Lecture Notes in Electrical Engineering 322

Jiasong Mu
Qilian Liang
Wei Wang
Baoju Zhang
Yiming Pi
Editors

The Proceedings of the Third International Conference on Communications, Signal Processing, and Systems

Springer

Lecture Notes in Electrical Engineering 322

More information about this series at http://www.springer.com/series/7818

Jiasong Mu • Qilian Liang • Wei Wang
Baoju Zhang • Yiming Pi
Editors

The Proceedings of the Third International Conference on Communications, Signal Processing, and Systems

Springer

Editors
Jiasong Mu
College of Physical and Electronic Information
Tianjin Normal University
Tianjin, China

Wei Wang
College of Physical and Electronic Information
Tianjin Normal University
Tianjin, China

Yiming Pi
School of Electronic Engineering
University of Electronic Science and Technology
Chengdu, China

Qilian Liang
University of Texas at Arlington
TX, USA

Baoju Zhang
College of Physical and Electronic Information
Tianjin Normal University
Tianjin, China

ISSN 1876-1100 ISSN 1876-1119 (electronic)
Lecture Notes in Electrical Engineering
ISBN 978-3-319-08990-4 ISBN 978-3-319-08991-1 (eBook)
DOI 10.1007/978-3-319-08991-1

Library of Congress Control Number: 2015936616

Springer Cham Heidelberg New York Dordrecht London

Printed on acid-free paper

Springer International Publishing AG Switzerland is part of Springer Science+Business Media (www.springer.com)

Preface

The Third International Conference on Communications, Signal Processing, and Systems (CSPS) was held in Hohhot on July 14 and 15, 2014. Hohhot is a famous historical city in north-central China and the capital of the Inner Mongolian Autonomous Region, serving as the region's administrative, economic, and cultural centre. CSPS 2014 brings together Chinese and international researchers and practitioners in communications, signal processing, and systems.

The accepted papers of CSPS 2014 are by researchers from around the world, including nine different technical sessions: 'Cognitive Radio System, Short Range Wireless Network', 'Radar and Sonar Networks, Radar Signal Processing', 'Mobile Networks, Wireless Communication', 'Millimeter Wave, UWB technology', 'Localization, Pattern Recognition', 'Ethernet, Fiber Communication', 'Image and Video Processing, Digital Signal Processing', 'Biological and Medical Signal Processing,' and 'Circuit Processing System, Intelligent System and Technology'.

The technical program team did an excellent job in soliciting submissions, coordinating the review process, and promoting the technical program. We would like to thank everyone of them for taking leadership roles in organizing the various aspects of the technical program.

We would also like to express our thanks to all of the members of the organizing committee as well as all of the volunteer reviewers who worked very hard over the days and nights of the conference. We are grateful to the host institution, Tianjin Normal University, Inner Mongolia University, and sponsorships from IEEE Fort Worth Section, University of Texas at Arlington, Beijing University of Posts and Telecommunications, University of Electronic Science & Technology of China (UESTC). Finally, the publication support from Springer is deeply appreciated.

Tianjin, China — Jiasong Mu
TX, USA — Qilian Liang
Tianjin, China — Wei Wang
Tianjin, China — Baoju Zhang
Chengdu, China — Yiming Pi

Welcome Message from the General Chairs

It is our great honor and pleasure to welcome you to Hohhot for the 3rd International Conference on Communications, Signal Processing, and Systems (CSPS) held during July 14–15 2014. During this conference, scholars and practitioners from all over the world in communications, signal processing, and electronic systems will get together in Hohhot.

Hohhot, a city was founded by Mongol ruler Altan Khan in the late 16th century. It was chosen as the region's administrative centre in 1952. As a city with a rich cultural background, Hohhot is known for its historical sites and temples and is one of the major tourist destinations of Inner Mongolia. It has many ancient relics, including Zhaojun Tomb, Five Pagoda Temple, and White Tower. Besides, it is nationally known as the center of Chinese diary industry and was declared "Dairy Capital of China" in 2005. It is also famous for barbecue and the production of mushrooms and hops. CSPS 2014 is organized by an international team. The conference features 9 technical sessions and 2 keynote sessions. We invite you to join us by attending the technical and social events held in CSPS 2014.

On behalf of the Organizing Committee, the Technical Program Committee, and all the volunteers that have been working hard for this conference, we warmly welcome you to CSPS 2014 and hope that you will enjoy the conference, and the beautiful city in which it takes place.

Tianjin, China	Yubao Gao
Glasgow, UK	Tariq S. Durrani
Washington, DC, USA	Rabinder N. Madan
TX, USA	Qilian Liang
Hohhot, China	Yongxin Liu

Contents

Part I
Cognitive Radio System, Short Range Wireless Network

Chapter 1
Cognitive Radio Interference Modeling and Application on Fading Channels

Jian Li, Shenghong Li, Xiang Lin, and Qiangwei Hang

Abstract Different from the statistical or bound method to build the interference model of cognitive wireless networks, in this paper, we propose an exact mathematical interference model based on the primary channel and the secondary interference channel under Rayleigh and Nakagami fading respectively. Under the rigorous mathematical derivation, the proposed model can cover many parameters such as spatial distribution, the spectrum sensing schemes, the transmission and channel propagation characteristics of nodes, etc. In addition, the analysis result can be extent to a number of applications including spatial density settlement of ST nodes, ST power control, spectrum sensing schemes analysis, irregular geographical shape evaluation of cognitive radio etc. The simulation results have verified our analytical model.

Keywords Cognitive network • Interference • Modeling

1.1 Introduction

As a promising technology to improve the spectrum resource utilization, cognitive radio is getting more and more attentions. Its principle is that the cognitive radio secondary users occupy the licensed spectrum to communicate when it

Foundation items: the National Natural Science Foundation of China (Nos. 61071152 and 61271316), the National Basic Research Program (973) of China (Nos. 2010CB731406 and 2013CB329605) and the National "Twelfth Five-Year" Plan for Science & Technology Support (No. 2012BAH38B04)

J. Li (✉)
Electronic Engineering Department, Shanghai Jiao Tong University, Shanghai, China

The Third Research Institute of Ministry of Public Security of P.R.C, Shanghai, China
e-mail: lijian2001@163.com

S. Li • X. Lin
Electronic Engineering Department, Shanghai Jiao Tong University, Shanghai, China

Q. Hang
The Third Research Institute of Ministry of Public Security of P.R.C, Shanghai, China

J. Mu et al. (eds.), *The Proceedings of the Third International Conference on Communications, Signal Processing, and Systems*, Lecture Notes in Electrical Engineering 322, DOI 10.1007/978-3-319-08991-1_1

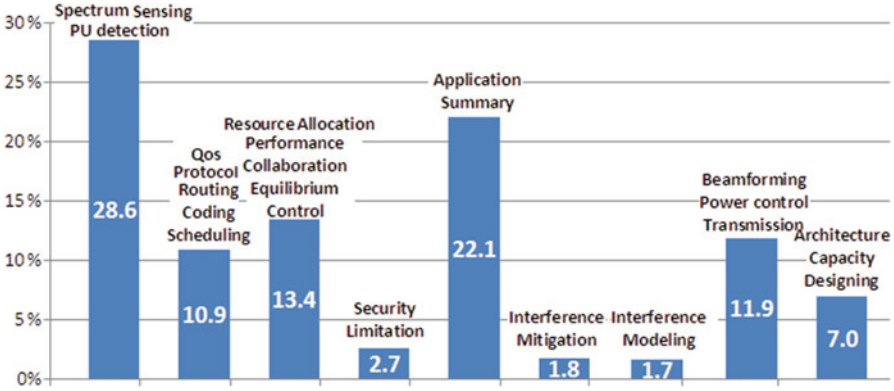

Fig. 1.1 Research status of cognitive radio

detects there is no activities conducted by the licensed primary users. Although the secondary users promise no interfering the normal communication of the licensed primary users by using the spectrum sensing technology, but due to the uncertain propagation channel and cognitive radio users etc., there is a certain probability for unlicensed users to generate the false-detection for the licensed users and to cause interference on the licensed users. Therefore, it is important to understand the potential influence of the secondary users' behaviors and build the models of the interference on the licensed users in achieving the goal of cognitive radio.

Most current researches for cognitive radio mainly focus on spectrum sensing, power control, networking, and other aspects of cognitive radio construction as shown in Fig. 1.1. The interference research on the primary network just received little attention. Moreover, the existing interference models mainly focus on identifying the statistical models or bounds of the interference. Statistical model can be derived by characteristic function (CF) [1–3] or Moment generating function (MGF) [4, 5]. Based on the cumulants from the CF and MGF, the aggregate interference is approximated to a number of distributions such as a shifted lognormal distributions [1], the symmetric stable distributions [3], the Gaussian distribution [5]. However, the statistical model to approximate the interference only shows some characteristic points of the interference, which is not sufficient to depict the exact interference and will introduce error in evaluating the interference. Moreover, the method finding interference bounds is a more rough way descripting the interference compared to the statistical model. Thus, in this paper, to overcome the insufficiency in the statistical and bounds model we propose an accurate mathematical model of the interference.

Spectrum sensing is the key component of cognitive radio and is the most popular technology being studied in cognitive radio. Then, the interference model should include the spectrum sensing scheme. However, there is just a small fraction of the proposed schemes [1, 2] to consider the spectrum sensing in the current

existing interference models. Therefore, in order to comprehensively evaluate the impact of the cognitive network interference on the performance of the primary network, this paper incorporates the spectrum sensing schemes in the proposed model and mathematically analyzes its effect on the interference.

1.2 Interference Modeling

In cognitive radio network, there are four types of nodes [6, 7]: primary transmitters (PTs), primary receivers (PRs), secondary transmitters (STs), secondary receivers (SRs). We assume that PR is the passive node and does not send out signal to PT. Therefore, SU should reliably monitor PTs' activities using spectrum-sensing and other technologies to detect the existence of the primary users. In the structure of cognitive radio networks, there are two kinds of channel [7]: (1) the primary channel between PT and PR, (2) the secondary interference channel between ST and PR. Most of the literatures [1–5] consider that the channels just experience the same channel environment, for instance Rayleigh fading in [8], Rice fading in [1]. However, in practice, the channels are often under different channel environment. In this paper, the primary channel is under Rayleigh fading and the secondary interference channel is under Nakagami fading. Their relationship is shown in Fig. 1.2, where R_{ao} and Φ_{ao} are the distance and angle between PT and PR respectively, r_i and φ_i are the distance and angle between i-th (ST_i) and PR, R_i is the distance from PT to ST_i.

From [7], when the primary channel is under Rayleigh fading channel, we obtain the outage probability (F_{out}):

$$F_{out} = 1 - \int_0^{+\infty} P_B(y)\mathrm{e}^{-sy}dy = 1 - \mathbf{L}_B(s) \tag{1.1}$$

where $s = \beta_{th}/\Omega_a$, Ω_a is the average envelope power of signal transmitted by PT, β_{th} denotes a threshold that PR can tolerate the interference when the signal-to-interference ratio (SIR) of the received PT's signal is above the threshold, $\mathbf{L}_B(s)$ is the Laplace transform of $P_B(y)$, $P_B(y)$ is the probability density function of aggregate

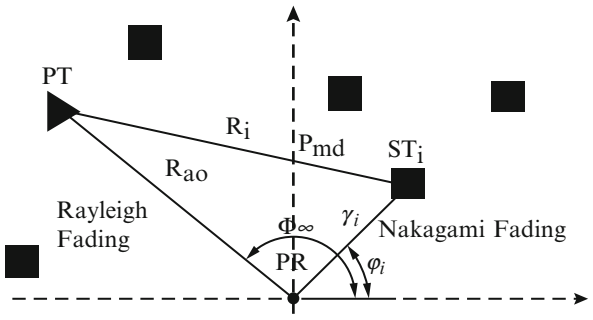

Fig. 1.2 Spatial structure. *PT* denotes the primary transmitter, *PR* denotes the primary receiver, and *ST* denotes the secondary transmitter

interfering signals transmitted by the cognitive radio secondary transmitters. Moreover, $P_B(y)$ is given as [7]:

$$P_B(y) = \sum_{I=0}^{\infty} \frac{(\lambda\Delta)^I}{I!} e^{-\lambda\Delta} (\mathrm{P}_{B_1}(y) \otimes \cdots \otimes \mathrm{P}_{B_i}(y) \otimes \cdots \otimes \mathrm{P}_{B_I}(y)) \tag{1.2}$$

where λ is the spatial density of STs distributed following Poisson point process, $\mathrm{P}_{B_i}(y)$ is the probability density function of interfering signal transmitted by i-th ST ($\mathrm{ST_i}$) and defined as [6]:

$$\mathrm{P}_{B_i}(y) = P_{S_i}(y) P_{g_i} + \delta(y)\left(1 - P_{g_i}\right) \tag{1.3}$$

where $\delta(y)$ is the delta function, P_{g_i} represents the effect of spectrum sensing on the interference and is a function of the missed detection probability (P_{md}) that $\mathrm{ST_i}$ falsely detected PT absent when PT is actually present [9], the probability distribution of signal (denoted by $s_i(t)$) transmitted by $\mathrm{ST_i}$ and received by PR under Nakagami fading is [10]:

$$P_{S_i}(y) = \left(\frac{m}{\Omega_i}\right)^m \frac{y^{m-1}}{\Gamma(m)} \exp\left\{-\frac{my}{\Omega_i}\right\} \tag{1.4}$$

where m is the fading figure. When $m = 1$, the Nakagami distribution becomes the Rayleigh distribution, and when $m \to \infty$ the distribution becomes an impulse, i.e., no fading [10].

By plugging (1.2) into $\mathbf{L}_B(s)$, so that $\mathbf{L}_B(s)$ can be expressed as [7]

$$\mathbf{L}_B(s) = \sum_{I=0}^{\infty} \frac{(\lambda\Delta)^I}{I!} e^{-\lambda\Delta} \prod_{i=1}^{I} \int_0^{\infty} e^{-sy} P_{B_i}(y) dy \tag{1.5}$$

Inserting (1.3) (1.4) into $P_{B_i}(y)$ and using variable substitution, then

$$\begin{aligned} \mathbf{L}_{B_i}(s) &= \int_0^{\infty} \mathrm{e}^{-sy} P_{B_i}(y) dy = \int_0^{\infty} \mathrm{e}^{-sy} \left[P_{S_i}(y) P_{g_i} + \delta(y)\left(1 - P_{g_i}\right)\right] dy \\ &= 1 - P_{g_i}\left(1 - \left(\tfrac{m}{s\Omega_i + m}\right)^m\right) \end{aligned} \tag{1.6}$$

We assume that the interference is iid uniformly distributed on the disk with radial density [5]. Then the mean of the $\mathbf{L}_{B_i}(s)$ is

$$E(\mathbf{L}_{B_i}(s)) = \int_r \int_{\varphi} \frac{r}{\Delta} \left(1 - P_{g_{(r,\varphi)}} \left(1 - \left(\frac{m}{s\Omega_{(r,\varphi)} + m}\right)^m\right)\right) dr d\varphi$$

where $P_{g_{(r,\varphi)}} = P_{md}\left(\sqrt{R_{ao}^2 + r^2 - 2R_{ao} r \cos\left(\Phi_{ao} - \varphi\right)}\right)$, $\Omega_{(r,\varphi)}$ is the average envelope power of signal transmitted by ST. Therefore $\mathbf{L}_B(s)$ can be written as

$$\mathbf{L}_B(s) = \sum_{I=0}^{\infty} \frac{(\lambda\Delta)^I}{I!} e^{-\lambda\Delta} \left(\int_r \int_\varphi \frac{r}{\Delta} \left(1 - P_{g_{(r,\varphi)}} \left(1 - \left(\frac{m}{s\Omega_{(r,\varphi)} + m} \right)^m \right) \right) dr d\varphi \right)^I \tag{1.7}$$

Interpreting the sum as the Taylor expansion of the exponential function, we obtain

$$\mathbf{L}_B(s) = \exp\left\{ -\lambda \int_r \int_\varphi r P_{g_{(r,\varphi)}} \left(1 - \left(\frac{m}{s\Omega_{(r,\varphi)} + m} \right)^m \right) dr d\varphi \right\} \tag{1.8}$$

Plugging (1.8) into (1.1), therefore the exact form of outage probability F_{out} can be obtained as

$$F_{out} = 1 - \exp\left\{ -\lambda \int_r \int_\varphi r P_{g_{(r,\varphi)}} \left(1 - \left(\frac{m}{s\Omega_{(r,\varphi)} + m} \right)^m \right) dr d\varphi \right\} \tag{1.9}$$

1.3 Numerical Results and Application

1.3.1 Default Parameters

In this section, we present numerical results based on the proposed model to illustrate the influence of interference on the primary users in cognitive radio networks. Unless otherwise specified, we use the following parameters in the simulation. Spatial density of ST is $\lambda = 0.00001$ node per square meter. The spatial shape is a circle with minimum radius equal to 1 meter and maximum radius equal to 100 m. $R_{ao} = 102$ m. Interference toleration threshold is $\beta_{th} = 10$. P_{md} is determined by the spectrum sensing schemes, therefore different spectrum sensing schemes will bring about great influence on the interference. In this paper, we adopt the spectrum sensing schemes in which P_{md} decreases linearly with signal noise ratio (SNR).

1.3.2 Numerical Results

To analyze the effect of the spatial density of ST nodes and the ST power on the outage probability F_{out} of the cognitive network interference, in Fig. 1.3, F_{out} versus spatial density of ST is depicted for the different power of ST. It is observed from Fig. 1.3 that F_{out} increases as the ST spatial density (λ) increases due to the fact that more ST nodes more likely result in interference on PR. Moreover, when the value

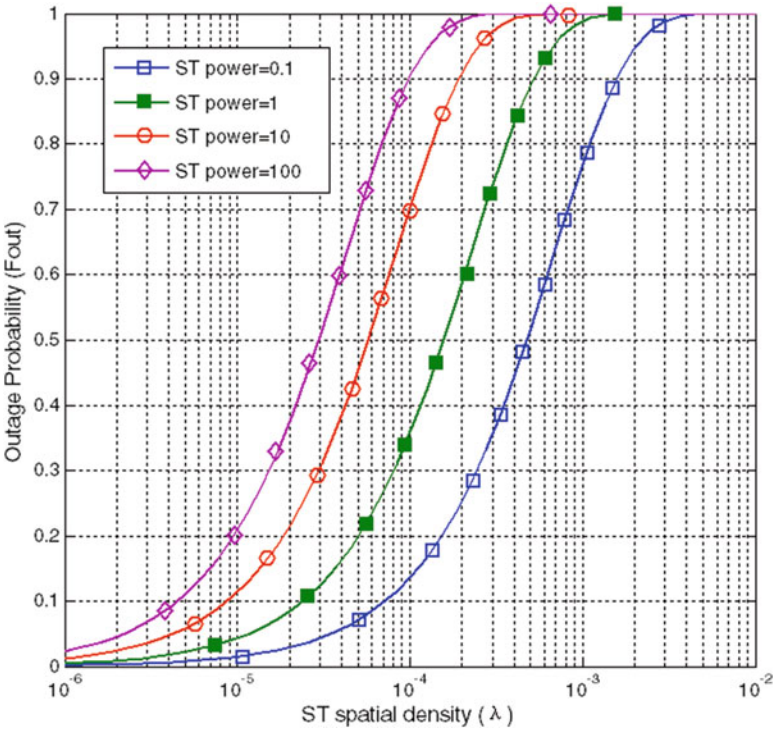

Fig. 1.3 CDF of the cognitive network interference as the function of the ST spatial density when ST power = 0.1, 1, 10, 100 (watts)

of λ is fixed, the outage probability rises as the ST power increases. This phenomenon well fits the expectation. From the example, we can get the conclusion that the power and spatial density of ST plays as an important role forming interference on primary network.

Figure 1.4 plots the outage probability as the function of ST power when PT transmits at different level power. The figure demonstrates that the outage probability rises as the ST power increases or the PT power decreases. In this example, the changing trend of the ST and PT power with outage probability also agrees well with the expectation. Therefore, it is reasonable to apply power control at secondary users in order to lower the potential interference.

Figure 1.5 plots the outage probability as the function of PT power when different interference toleration thresholds are adopted. We can learn from the figure that for a fixed threshold β_{th}, the larger PT power will cause the reduction of the interference. Moreover, for a fixed PT power, larger threshold will generate larger outage probability because larger threshold means that PU can tolerate less interference.

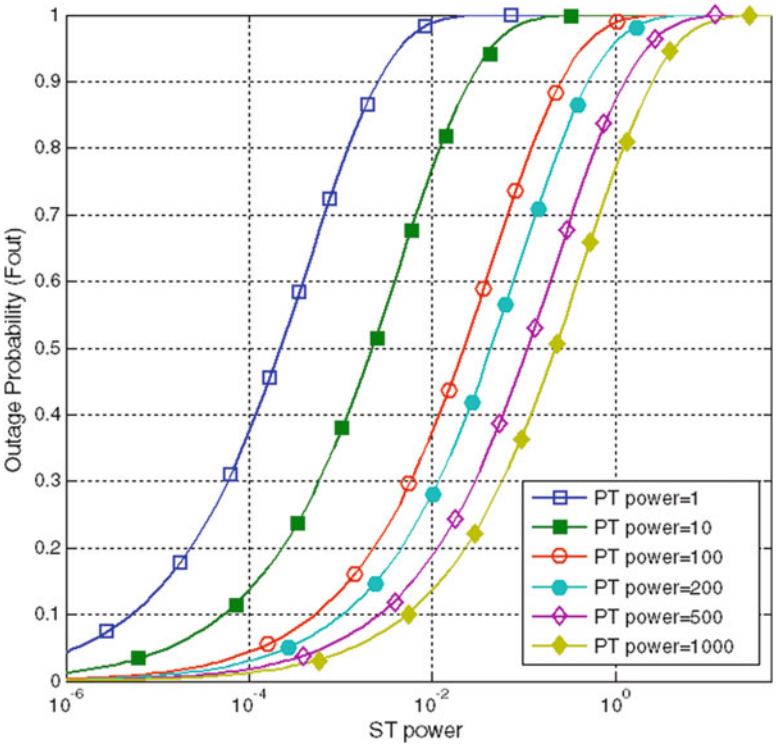

Fig. 1.4 CDF of the cognitive network interference as the function of ST power when PT power = 1, 10, 100, 200, 500, 1,000 (watts)

1.3.3 Application of the Model

The probability model is not only used in the theoretic analysis, but also can be put into more applications such as power control and the evaluation for spectrum sensing. From the above simulation results, we have verified that the ST power is a very important parameter to influence the interference on the primary networks. The proposed model in (1.9) is the function of ST power and provides an effective way accurately to analyze the influence of ST power on the interference in attempt to apply power controlling on the STs. Another application of the proposed model is that unlike some literatures such as [4], which are just suitable for a given spatial shape regions like circular or rectangle, the formula (1.9) can be used to evaluate the region with any geographic shape because the integral zone in (1.9) covers all region STs distributed. As discussed in section of introduction, there is small fraction of researches considering the influence of spectrum sensing on the interference. Since the missed detection probability (P_{md}) is the part of (1.9), then the proposed model can be changed to the function of the spectrum sensing and can analyze mathematically the effect of the cognitive network interference on the performance of the primary network.

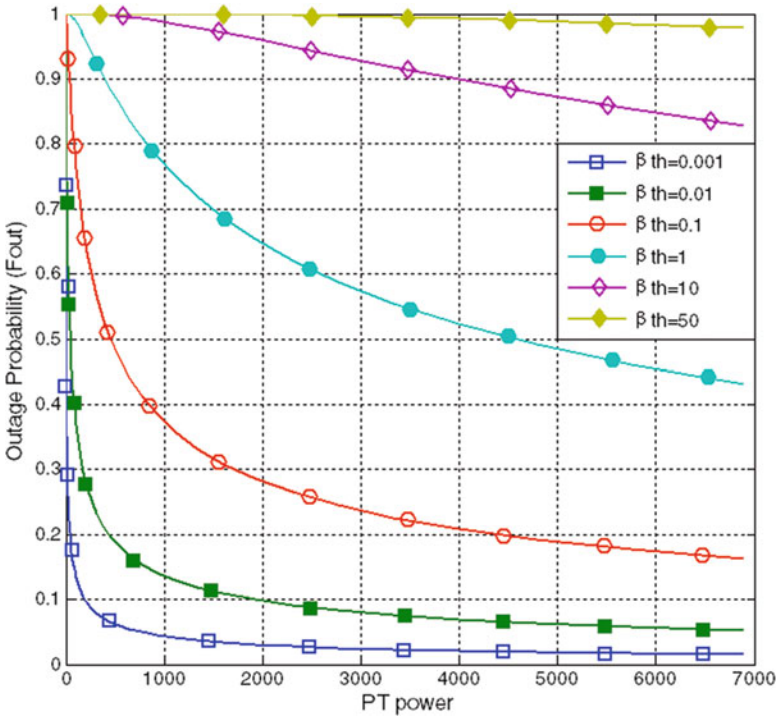

Fig. 1.5 CDF of the cognitive network interference as the function of PT power for the interference toleration threshold $\beta_{th} = 0.001, 0.01, 0.1, 1, 10, 50$

Conclusion

Current researches on the interference modeling mainly focus on building the statistical model and finding the bounds of interference. Moreover, the existing models may not cover sufficient factors such as spatial distribution, the spectrum sensing schemes, the transmission and channel propagation characteristics of nodes etc. Based on the primary channel channels and the secondary channel suffering Rayleigh and Nakagami fading respectively, we have mathematically derived an exact interference model of cognitive radio interference at the primary receiver caused by secondary users taking into account spectrum sensing schemes, ST and PT power, spatial density of ST nodes, spatial shape of the regions etc,. Beside the mathematical derivation, the proposed model can be put into some applications such as settling the spatial density of ST nodes, controlling for the transmitting power of ST, providing another method to analyze spectrum sensing schemes, evaluating any spatial shape that secondary users distributed. The numerical results verify the proposed theoretical model and the mathematical derivation.

References

1. Ghasemi A, Sousa ES (2008) Interference aggregation in spectrum-sensing cognitive wireless networks. IEEE J Select Topics Sign Process 2(1):41–56
2. Rabbachin A, Quek TQS, Shin H, Win MZ (2011) Cognitive network interference. IEEE J Select Areas Commun 29(2):480–493
3. Win MZ, Pinto PC, Shepp LA (2009) A mathematical theory of network interference and its applications. Proc IEEE 97(2):205–230
4. Salbaroli E, Zanella A (2009) Interference analysis in a Poisson interference analysis in a Poisson interference analysis in a Poisson field of nodes of finite area. IEEE Trans Veh Technol 58(4):1176–1783
5. Kusaladharma S, Tellambura C (2012) Aggregate interference analysis for underlay cognitive radio networks. IEEE Wireless Commun Lett 1(6):641–644
6. Li J, Li SH, Zhao F, Du R (2014) Co-channel interference modeling in cognitive wireless networks. IEEE Trans Commun 62(9):3114–3128
7. Li J, Li SH (2014) Interference of cognitive wireless networks on rayleigh and rice fading channels. Int J Distribut Sensor Netw 2014, Article ID 236891. doi: 10.1155/2014/236891
8. Pinto PC, Win MZ (2010) Communication in a Poisson field of interferers–part i: interference distribution and error probability. IEEE Trans Wireless Commun 9(7):2176–2186
9. Moghimi F, Nasri A, Schober R (2011) Adaptive *Lp*–norm spectrum sensing for cognitive radio networks. IEEE Trans Commun 59(7):1934–1945
10. Stüber GL (2002) Principles of mobile communication, 2nd edn. Kluwer, New York, pp 39–152

Chapter 2
Robust Localization with the Mobility of SUs for Cognitive Radio Networks

Fei Zhou and Yanhua Wang

Abstract For solving the problem of positioning primary user (PU) in cognitive radio networks (CRNs), we propose a new algorithm which is based on the mobility of secondary users (SUs). The algorithms has the following advantages. First, it needs minimal prior information of PU, so it is more suitable for CRNs; Second, the algorithm utilizes the relative span weighted factor as weight of each SU to overcome the drawback that Centroid Localization (CL) algorithm is too dependent on the connectivity of network; What is more, the algorithm is based on the mobility of SUs, therefore, it can improve the SUs density which fits the localization scenery with little SUs. Simulation results show that the proposed scheme has lower complexity and better robustness compared with traditional algorithms, meanwhile, the accuracy of the algorithm is relatively higher.

Keywords Cognitive radio networks • PU • SUs • CL • Robustness

2.1 Introduction

Spectrum has become a scare resource due to the tremendous development of wireless communication technologies. The inefficient usage of licensed spectrum has made the situation even worse. As a result, cognitive radio, which is a concept of opportunistically utilizing the spectrum holes in the time-frequency-space domain, was introduced [1]. In cognitive radio networks (CRNs), there are primary users (PUs) which are licensed users and have priorities in using the licensed bands, and secondary users (SUs) which are capable of sensing the spectrum holes in the licensed bands and reuse the unoccupied spectrum in an opportunistic fashion. Localization algorithms can be classified into two categories according to the level of estimated information available, i.e., range-free algorithms [2, 3] and range-based algorithms [4]. Range-based algorithms are more accurate than range-free algorithms. The reason is that the former require an accurate estimation of the

F. Zhou (✉) • Y. Wang
Chongqing Key Lab of Mobile Communications Technology, Chongqing University of Posts and Telecommunications, Chongqing 400065, People's Republic of China
e-mail: zhoufei@cqupt.edu.cn; wangyanhua920@sina.com

J. Mu et al. (eds.), *The Proceedings of the Third International Conference on Communications, Signal Processing, and Systems*, Lecture Notes in Electrical Engineering 322, DOI 10.1007/978-3-319-08991-1_2

distance between PU and SUs, however, range-free algorithms, instead of estimating the distance, depend on the connection of network. Furthermore, the range-free algorithms are more simple to implement and have lower hardware cost. More importantly, range-free algorithm is robust to channel variation [5]. In some actual positioning scenes, owing to limited hardware and less precision, range-free algorithm is a better choice. Among the range-free localization algorithms, CL is more attractive due to its simplicity and easy implementation [6].

The remainder of the paper is organized as follows. Section 2.2 provides two classical range-free algorithms. Section 2.3 presents a mobile relative span weighted method for CRNs; Sect. 2.4 analyzes simulation results; section "Conclusion" concludes the paper.

2.2 Classical Range-Free Algorithms

We assume that N SUs uniformly distribute in the communication range of the PU in CRNs. Therefore, according to the CL algorithm, the position of PU is the centroid of the polygon composed by SUs. Given the coordinates of the SUs and PU: $(x_1, y_1), (x_2, y_2) \cdots (x_N, y_N), (x_0, y_0)$, the coordinate of PU can be obtained as follows:

$$(x_0, y_0) = \left(\frac{x_1 + x_2 + \cdots x_N}{N}, \frac{y_1 + y_2 + \cdots y_N}{N}\right) \tag{2.1}$$

Because CL algorithm cannot obtain high positioning accuracy and is too dependent on network connectivity and node density, Weighted Centroid Localization (WCL) algorithm is further studied and become a hot issue. Here we introduce a WCL [7]. The expression is as follows:

$$P = \frac{\sum_{i=1}^{n} (w_i \times p_i)}{\sum_{i=1}^{n} w_i} \tag{2.2}$$

where

$$w_i = \frac{1}{(d_i)^g} \tag{2.3}$$

d_i is the distance between ith SU and PU, g is the weighted modification factor.

Because of no cooperation between PU and SUs in CRNs, we cannot obtain sufficient priori information of PU. And we also cannot estimate accurate path loss coefficient β, shadow fading factor σ and suitable weighting modification factor g. The exact closed-form solution for d cannot be derived. Therefore, we would like to have an algorithm which is able to take advantage of little prior information to locate PU.

2.3 Mobile Relative Span Weighted Method

According to [8], relative span weighted schemes can be classified as Relative Weighted Localization (RWL) and Relative Exponentially Weighted Localization (REWL). Now we propose a novel mobile relative span weighted method.

2.3.1 System Model

Existing positioning algorithms mostly assume SUs stationary. However, in most cases, SUs are dynamic. So we propose an algorithm to solve the problem based on the dynamical assumption. Figure 2.1 depicts the general system of mobile relative span weighted method which consists of a PU, a Cognitive Base Station (CBS) and many SUs. Given SUs, PU and CBS randomly distributed in CRNs, SUs with known coordinates collaborating with each other to locate PU. Assuming that the SUs are equipped with a radiometer for detection purposes, SUs send their received signal strength (RSS) values measured from PU and their own position information to CBS, and CBS preserve the information. When the SUs change their positions, CBS exploits the historical information and current position information of SUs to location PU using mobile relative span weighted method.

2.3.2 Algorithm Description

The algorithm we propose in this paper can be classified into two categories: Mobile Relative Weighted Localization (MRWL) and Mobile Exponentially Weighted Localization (MREWL).

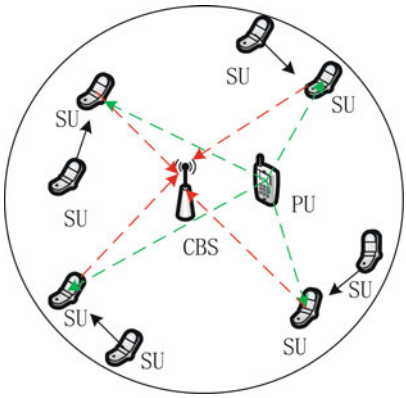

Fig. 2.1 A general system model of proposed algorithm

Definition 3.1 (Minimal/Maximal RSS). Given the number of SUs within the range of PU communication area is N. Let r_i denotes the RSS value measured by ith SU from PU. R represents the set of all RSS values, namely:

$$R = r_i : i \in N \tag{2.4}$$

Then we define the minimal and maximal RSS values, $r_{\min}$ and $r_{\max}$ as the smallest and largest RSS values in R:

$$r_{\min} = \min r_i \in R \tag{2.5}$$

$$r_{\max} = \max r_i \in R \tag{2.6}$$

Definition 3.2 (RSS Span). We define the RSS span r^{Δ} at a set of receivers which are all within the range of PU, namely:

$$r^{\Delta} = r_{\max} - r_{\min} \tag{2.7}$$

Assuming $P_i(i = 1 \cdots n)$ represents the two-dimensional vector coordinates of SUs, and $\widehat{P}$ represents the estimated position of PU. The MRWL can be expressed as:

$$\widehat{P} = \frac{\sum_{i=1}^{n} [(r_i - r_{\min}) \times P_i]}{\sum_{i=1}^{n} (r_i - r_{\min})} \tag{2.8}$$

where

$$w_i = \frac{r_i - r_{\min}}{r_{\max} - r_{\min}} \tag{2.9}$$

The MREWL can be obtained as:

$$\widehat{P} = \frac{\sum_{i=1}^{n} [(1-\lambda)^{(r_{\max} - r_i)} \times P_i]}{\sum_{i=1}^{n} (1-\lambda)^{(r_{\max} - r_i)}} \tag{2.10}$$

where

$$w_i = (1-\lambda)^{(r_{\max} - r_i)} \tag{2.11}$$

λ is the modification coefficient of exponential weighted factor.

2.4 Simulation Results

In this section, to find an algorithm for CRNs, we first discuss the performance of RWL and REWL by comparing them with two classical range-free algorithms in the case of SUs immobility. Then we analyze the performance of proposed algorithm by comparing them with RWL and REWL.

2.4.1 SUs Immobility

The performance of localization algorithms is affected by many factors. Now we consider two main factors: node density and shadow fading, which play vital roles in terms of algorithms robustness. The most robust and suitable algorithm for CRNs is summarized through simulation among different weighted strategies centroid localization algorithms.

We conduct an outdoor field experiment with $1,000\,\text{m} \times 1,000\,\text{m}$ square area. The simulation results were obtained from the ensemble average from over 1,000 independent trails. And for each trail, we define our node densities as the number of nodes per $100\,\text{m} \times 100\,\text{m}$. For every node density $d \in \{1, 2, 3, 4, 5, 6, 7, 8\}$, the communication radius of PU is approximate 100 m. We assess the performance of each mechanism according to its location accuracy which is computed as the Euclidian distance between the estimated position $\widehat{P}$ and the actual transmitter location. Figure 2.2 analyzes REWL with different λ. In our experiment, we can conclude $\lambda = 0.1$ is the best choice for the REWL.

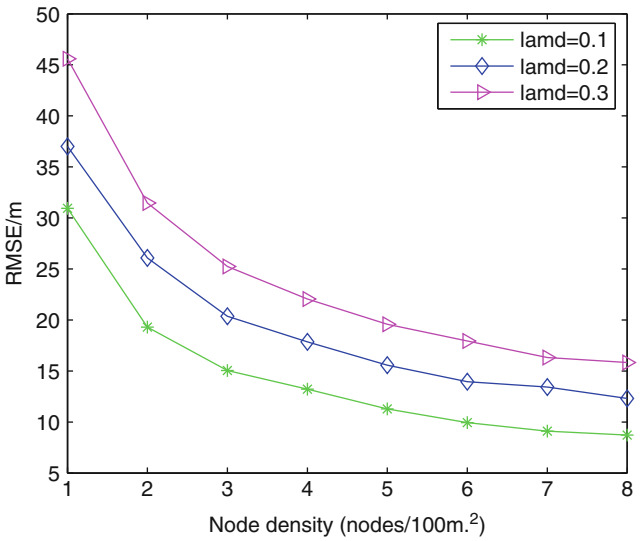

Fig. 2.2 REWL with different λ

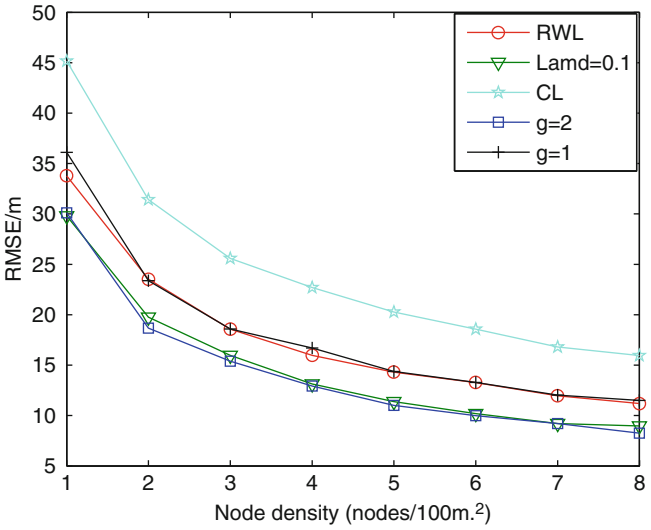

Fig. 2.3 Algorithms location error by node density

Figure 2.3 plots the average location error for each tested algorithm with all the priori defined node densities. It can be seen that higher densities results in greater location accuracy, and we can directly see the vulnerability of CL. In general, the average location error of RWL algorithm is the same with WCL ($g = 1$) algorithm, meanwhile, REWL ($\lambda = 0.1$) algorithm is also the same with WCL ($g = 2$) algorithm.

In order to gauge the performance of each tested algorithm for different levels of shadow fading. We execute each algorithm with $\sigma \in \{4, 6, 8\}$ dB. As can be seen from Fig. 2.4, higher levels of shadow fading results in lower location accuracy. When the value of σ is greater, the situation is more atrocious. But RWL algorithm and REWL algorithm are all still robust. More importantly, the average location error of RWL algorithm is almost the same with WCL ($g = 1$) algorithm, and REWL ($\lambda = 0.1$) algorithm is also almost the same with WCL ($g = 2$) algorithm with different shadow fading.

Although CL is easy to implement and has low communication overhead, the location error is very great under the circumstances of low anchors node density and uneven distribution of nodes. WCL improves the positioning accuracy compared with CL, but it needs prior information of PU and assumes path loss model, model parameters. The model parameters are almost empirical values which do not reflect the actual environment well. Meanwhile the performance of RWL and REWL ($\lambda = 0.1$) are pretty from our simulations. Moreover it is worth emphasizing that RWL and REWL need few prior information of PU to accomplish positioning. Above all, RWL and REWL are the best choices for CRNs.

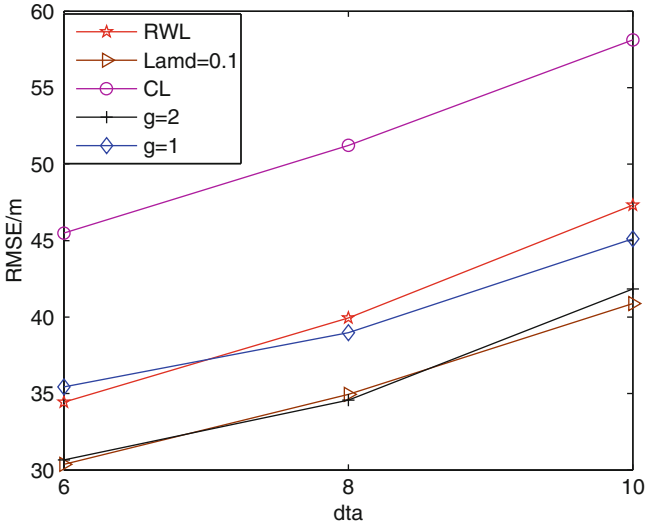

Fig. 2.4 Algorithms location error by shadow fading

2.4.2 SUs Mobility

In this section, we evaluate the performance of the proposed algorithms, MRWL and MREWL. We conduct an experiment with 100 m × 100 m square area. For each of 1,000 trails, we install eight SUs in the interesting area. The coordinates of SUs are (30,30), (30,50), (30,70), (50,20), (50,60), (80,20), (90,30), (80,60) and the actual position of PU is (60, 40). The communication range of PU is approximate 30 m. SUs move constantly with a speed of 10 m/s and measure RSS values every second. Each time the SUs move, CBS reorder all RSS values received from SUs and let the SU with the max RSS value as the reference node, then the other SUs move in the direction of the reference node. Next we discuss the robustness of MRWL and MREWL with different shadow fading.

Figure 2.5 depicts the performance of MRWL algorithm with different shadow fading. We can intuitively draw two conclusions from Fig. 2.5. One is that regardless of whether SUs move or not, the robustness of RWL algorithm is good. When SUs are immobile, the location error increases 2 m for every 2 dB of additional signal shadowing standard deviation. When SUs are mobile, the location error increases 0.5 m for every 2 dB of additional signal shadowing standard deviation. The other is that the positioning accuracy is improved by 50 % when SUs move one time compared with the immobile SUs, while the positioning accuracy is improved by 60 % when SUs move three times compared with the immobile SUs.

Figure 2.6 describes the performance of MREWL algorithm with different shadow fading. We can also intuitively draw two conclusions from Fig. 2.6. One is that regardless of whether SUs move or not, the robustness of REWL algorithm is

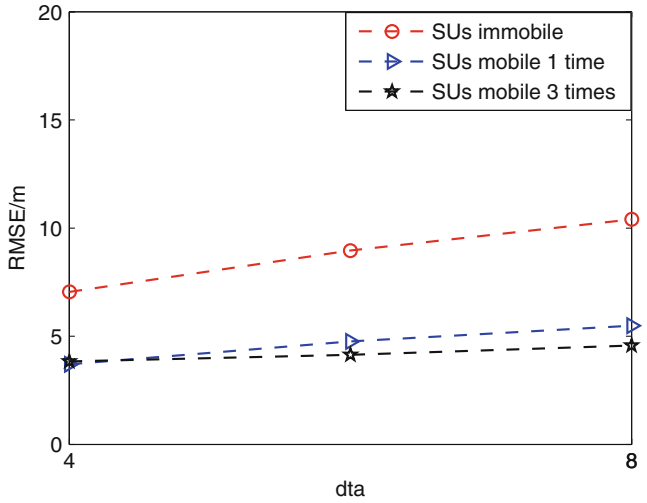

Fig. 2.5 MRWL location error by shadow fading

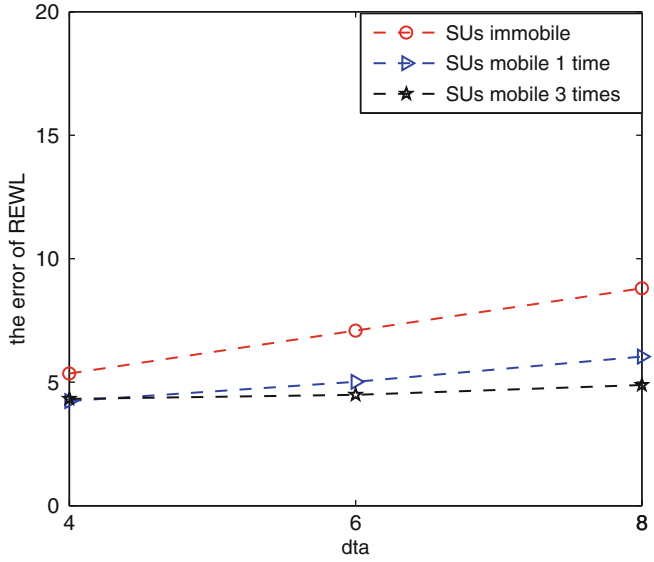

Fig. 2.6 MREWL location error by shadow fading

good. When SUs are immobile, the location error increases 1.5 m for every 2 dB of additional signal shadowing standard deviation. When SUs are mobile, the location error increases 0.5 m for every 2 dB of additional signal shadowing standard deviation. The other is that the positioning accuracy is improved by 35 % when

SUs move one time compared with the immobile SUs, while the positioning accuracy is improved by 45 % when SUs move three times compared with the immobile SUs.

Conclusion

We propose a Mobile Relative Span Weighted Method based on cognitive radio scene. It not only fits the feature of non-cooperation between PU and SUs in CRNs but also takes advantage of the nodes mobility which raises the node density to improve the positioning accuracy. Simulation results show that the location accuracy of MRWL improves by 50–60 % compared with RWL, meanwhile the location accuracy of MREWL improves by 35–45 % compared with REWL.

Acknowledgements This work was supported by the National Natural Science Foundation of China (61471077, 61301126), the Fundamental and Frontier Research Project of Chongqing (cstc2013jcyjA40034), the Science and Technology Project of Chongqing Municipal Education Commission (KJ1400413, KJ130528), the Program for Changjiang Scholars and Innovative Research Team in University (IRT1299), and the Special Fund of Chongqing Key Laboratory (CSTC).

References

1. Wang J, Urriza P et al (2010) Performance analysis of weighted centroid algorithm for primary user localization in cognitive radio networks. In: 2010 conference record of the forty fourth asilomar conference on signals, systems and computers (ASILOMAR), pp 966–970. doi:10.1109/ACSSC.2010.5757711
2. Lee J, Choi B et al (2013) Novel range-free localization based on multidimensional support vector regression trained in the primal space. IEEE Trans Neural Netw Learn Syst 24 (7):1099–1113. doi:10.1109/TNNLS.2013.2250996
3. Chen H, Chan Y et al (2010) Range-free localization with the radical line. In: 2010 I.E. international conference on communications (ICC), pp 1–5, 2010. doi:10.1109/ICC.2010.5502304
4. Wang H, Gao Z et al (2012) A survey of range-based localization algorithms for cognitive radio networks. In: 2012 2nd international conference on consumer electronics, communications and networks (CECNet), pp 844–847. doi:10.1109/CECNet.2012.6201449
5. Min AW, Kim K-H et al (2011) Robust cooperative sensing via stat estimation in cognitive radio networks. In: 2011 I.E. symposium on new frontiers in dynamic spectrum access networks (DySPAN), pp 185–196. doi:10.1109/DYSPAN.2011.5936205
6. Jun W, Paulo U et al (2011) Weighted centroid localization algorithm: theoretical analysis and distributed implementation. IEEE Trans Wirel Commun 10(10):3403–3413. doi:10.1109/TWC.2011.081611.102209
7. Chen Y, Pan Q et al (2010) AWCL: adaptive weighted centroid target localization algorithm based on RSSI in WSN. In: 2010 3rd IEEE international conference on computer science and information technology (ICCSIT), pp 331–336. doi10.1109/ICCSIT.2010.5565022
8. Laurendeau C, Barbeau M (2010) Centroid localization on uncooperative nodes in wireless networks using a relative span weighting method. EURASIP J Wirel Commun Netw 2010:1–10. doi:10.1155/2010/567040

Chapter 3
A Primary User Localization Method in Cognitive Radio Networks

Xinyue Fan, Chao Tong, and Fei Zhou

Abstract Localization of primary user (PU) is the key problem for location-aware spectrum allocation in cognitive radio networks (CRNs). In order to improve spectrum efficiency and reduce the interference from secondary users (SUs) to PU, localization of PU must be rapid and accurate enough. Aiming at the drawback of existing localization algorithm for PU localization, a PU localization algorithm based on node selection is proposed. The algorithm is suitable for PU localization with unknown transmit power and selects nodes based on geometric precision. The simulation results show that the proposed scheme has a good performance in terms of localization accuracy. Meanwhile, the complexity and communication traffic are reduced because of selecting part of the secondary users.

Keywords CRNs • PU localization • Node selection • Weighted least squares (WLS)

3.1 Introduction

The localization of PU and SUs are very important in cognitive radio networks [1]. The PU localization problem in CRNs is generally different from Global Positioning System (GPS). Localization of PU should use passive localization techniques, and the required number of SUs is relatively large and cooperation among SUs is necessary [2]. Some basic requirements for localization algorithm are proposed based on basic features of CRNs (i.e., localization of PU must be rapid enough and less computational complexity) [3]. Received signal strength (RSS) based localization algorithm is suitable for CRNs, because it is easy to obtain in many measurements [4]. An iterative search algorithm based on grid is proposed in [5]. In [6], a WLS algorithm is proposed to estimation the location of the target node. In [7], Adrian N. Bishop proposed a Cayley-Menger matrix based localization algorithm to estimate the transmission power. In [8], an algorithm based on

X. Fan (✉) • C. Tong • F. Zhou
Chongqing Key Lab of Mobile Communications Technology, Chongqing University of Posts and Telecommunications, Chongqing 400065, People's Republic of China
e-mail: fanxy@cqupt.edu.cn; jacktchao@163.com

J. Mu et al. (eds.), *The Proceedings of the Third International Conference on Communications, Signal Processing, and Systems*, Lecture Notes in Electrical Engineering 322, DOI 10.1007/978-3-319-08991-1_3

construction of a Gram matrix is proposed to estimate the path loss exponent and transmit power parameters. From [9], we can see that utilizing part of nodes to estimation the location of target node can also obtain good location accuracy. Meanwhile, the computation complexity and communication traffic are reduced because of selecting part of the secondary users. A utility based node selection scheme is proposed in [10]. From [11], it can be seen that nodes being distributed around the target node are the basic condition for a good geometry structure. A node selection algorithm based on partition is proposed in [12].

Since a PU does not cooperate or communicate with SUs, the information of PU signaling is very limited (e.g., transmit power or modulation scheme). Therefore, we propose a localization algorithm which is suitable for PU localization with unknown transmit power. Algorithm is divided into two steps. First, selecting nodes based on geometry structure. Second, estimating the localization of PU based on two steps WLS localization algorithm. We can obtain a good geometric structure by selecting part of the SUs, so the estimation accuracy is higher. Meanwhile, the complexity and communication traffic are reduced. The proposed algorithm meets the requirement of practical application, because its complexity is lower and it is easy to implement.

The rest of the paper is organized as follows. In Sect. 3.2, we propose a WLS localization algorithm based on node selection. In Sect. 3.3, we present simulation analyses for the proposed algorithm under different scenarios. Conclusions are given in section "Conclusion".

3.2 PU Localization Algorithm

3.2.1 WLS Localization Algorithm with Unknown Transmit Power

In the paper, we use RSS path-loss model:

$$P_i = P_s - 10\gamma \lg d_i + n_i, \quad i = 1, 2, \cdots, N \tag{3.1}$$

where P_i is the signal strength in dB received at the ith SU, P_s is the unknown transmit power, γ is the known path-loss factor, d_i is the distance between ith SU and PU, $\{n_i\}$ is uncorrelated zero-mean Gaussian variables with known variances $\left\{\sigma_i^2\right\}$. The number of SU is $N \geq 4$.

We consider two-dimensional positioning, as follows:

$$d_i = \sqrt{(x - x_i)^2 + (y - y_i)^2} \tag{3.2}$$

where $\mathrm{X} = [x\ y]^{\mathrm{T}}$ is the unknown PU position, (x_i, y_i) is the known coordinates of the ith SU.

From [13], we have:

$$A\theta = b + w \tag{3.3}$$

where

$$A = \begin{bmatrix} 2x_2 - 2r_{2,1}x_1 & 2y_2 - 2r_{2,1}y_1 & r_{2,1} - 1 \\ \vdots & \vdots & \vdots \\ 2x_N - 2r_{N,1}x_1 & 2y_N - 2r_{N,1}y_1 & r_{N,1} - 1 \end{bmatrix},\ b = \begin{bmatrix} x_2^2 + y_2^2 - r_{2,1}\left(x_1^2 + y_1^2\right) \\ \vdots \\ x_N^2 + y_N^2 - r_{N,1}\left(x_1^2 + y_1^2\right) \end{bmatrix}$$

$$\theta = [X\ R]^T, \quad E(w) = 0_{(N-1)\times 1}, \quad r_{i,1} = e^{-\frac{2}{\gamma}P'_{i,1} - \frac{2}{\gamma^2}\left(\lambda_i^2 + \lambda_1^2\right)} \quad i = 2, 3, \cdots, N$$

where $P'_{i,1} = 0.1In(10)(P_i - P_1)$, $\lambda_i^2 = 0.01(In(10))^2\sigma_i^2$ and $R = x^2 + y^2$.

Based on (3.3), we can obtain:

$$\widehat{\theta} = \left(A^{\mathrm{T}}C_W^{-1}A\right)^{-1}A^{\mathrm{T}}C_W^{-1}b \tag{3.4}$$

where $C_W = cov(w)$, so we have:

$$C_W = \sum \Lambda \sum \tag{3.5}$$

where

$$\Lambda = \begin{bmatrix} e^{\frac{4}{\gamma^2}\left(\lambda_2^2 + \lambda_1^2\right)} - 1 & e^{\frac{4}{\gamma^2}\lambda_1^2} - 1 & \cdots & e^{\frac{4}{\gamma^2}\lambda_1^2} - 1 \\ \vdots & \vdots & \ddots & \vdots \\ e^{\frac{4}{\gamma^2}\lambda_1^2} - 1 & e^{\frac{4}{\gamma^2}\lambda_1^2} - 1 & \cdots & e^{\frac{4}{\gamma^2}\left(\lambda_N^2 + \lambda_1^2\right)} - 1 \end{bmatrix},$$

$$\sum = diag(r_{2,1}, \cdots, r_{N,1})$$

So we can obtain: $\widehat{X} = \left[\left[\widehat{\theta}\right]_1 \left[\widehat{\theta}\right]_2\right]^{\mathrm{T}}$.

3.2.2 *Optimal WLS Localization Algorithm*

By utilizing the relationship between the unknown-position X and the introduced variable R, we can increase the estimation accuracy [13]. So an equation is constructed:

$$GZ = h + q \tag{3.6}$$

where

$$G = \begin{bmatrix} 1 & 0 & 1 \\ 0 & 1 & 1 \end{bmatrix}^T \quad Z = [x^2\ y^2]^T \quad h = \left[\left[\widehat{\theta}\right]_1^2 \left[\widehat{\theta}\right]_2^2 \left[\widehat{\theta}\right]_3 \right]^T$$

$$q = \begin{bmatrix} x^2 - \left[\widehat{\theta}\right]_1^2 \\ y^2 - \left[\widehat{\theta}\right]_2^2 \\ R - \left[\widehat{\theta}\right]_3 \end{bmatrix} = \begin{bmatrix} \left(x + \left[\widehat{\theta}\right]_1\right)\left(x - \left[\widehat{\theta}\right]_1\right) \\ \left(y + \left[\widehat{\theta}\right]_2\right)\left(y - \left[\widehat{\theta}\right]_2\right) \\ R - \left[\widehat{\theta}\right]_3 \end{bmatrix} \approx \begin{bmatrix} 2x\left(x - \left[\widehat{\theta}\right]_1\right) \\ 2y\left(y - \left[\widehat{\theta}\right]_2\right) \\ R - \left[\widehat{\theta}\right]_3 \end{bmatrix}$$

So the WLS estimation of Z is

$$\widehat{Z} = \left(G^{\mathrm{T}} C_q^{-1} G\right)^{-1} G^{\mathrm{T}} C_q^{-1} h \tag{3.7}$$

where $C_q = cov(q) = diag(2x, 2y, 1) C_{\widehat{\theta}} diag(2x, 2y, 1)$. Since x, y and $\overline{A}$ are not available, we replace $x, y, \overline{A}$ by $x \approx \left[\widehat{\theta}\right]_1, y \approx \left[\widehat{\theta}\right]_2, C_{\widehat{\theta}} \approx \left(A^{\mathrm{T}} C_W^{-1} A\right)^{-1}$.

So we can obtain an optimal WLS estimator as follow:

$$\widehat{X}^o = \left[sgn\left(\left[\widehat{\theta}\right]_1\right)\sqrt{\left[\widehat{Z}\right]_1} \quad sgn\left(\left[\widehat{\theta}\right]_2\right)\sqrt{\left[\widehat{Z}\right]_2} \right]^{\mathrm{T}} \tag{3.8}$$

3.2.3 *Node Selection Based Localization Algorithm with Unknown Transmit Power*

For a particular scenario, we usually cannot obtain the optimal geometric structure. But it is easy to see that nodes which are spaced around the target are the basic condition for a good geometry structure from some literatures which research the influence of the geometric structure of localization algorithm. In [12], a partition based node selection algorithm is proposed. The algorithm divides the sensing area into many partitions equally on angle at the PU. So it can ensure selection nodes are spaced around the PU, as shown in Fig. 3.1.

Since we need divide the sensing area into many partitions equally on angle at the PU, a coarse estimation for PU is required. A coarse localization algorithm should be performed as soon as possible and has a lower complexity. In this paper, we adopt the traditional centroid localization algorithm for coarse estimated

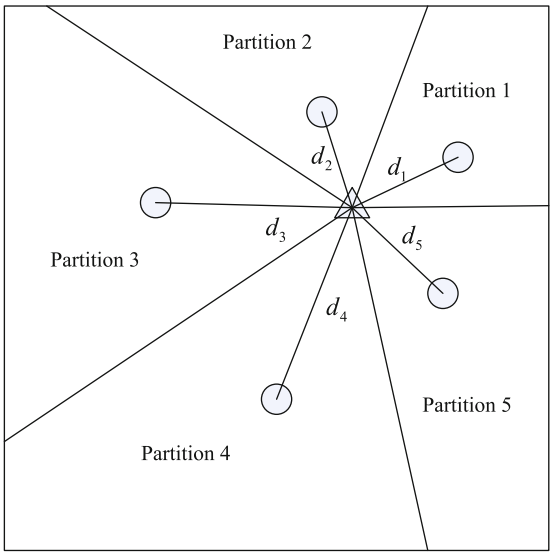

Fig. 3.1 Example of five partitions

position. By selecting five secondary users with the highest received signal strength, we can obtain the coarse estimated position of PU, as follows:

$$\widehat{u} = \sum_{j=1}^{5} \tilde{s}_j \frac{P_j}{\sum_{j=1}^{5} P_j} \tag{3.9}$$

where $\tilde{s}$ are the positions of five secondary users with the highest received signal strength and P are their measurements.

Five secondary users with the highest received signal strength are selected as preferred nodes. We can obtain the coarse estimated position of PU based on the preferred nodes. Then, we divide the whole area into many partitions equally on angle at the coarse estimated position of PU. If there is at least one preferred node in each partition, a good geometry structure is guaranteed, and these five preferred nodes are selected for PU localization; If there are some partitions which are not filled with preferred nodes, we try to fill each empty partition by selecting one SU with the highest received signal strength which is in this partition, and we let the selected SUs as backup nodes. Then we let all preferred nodes and backup nodes as selected nodes. Figure 3.2 is a flow chart of our PU localization algorithm.

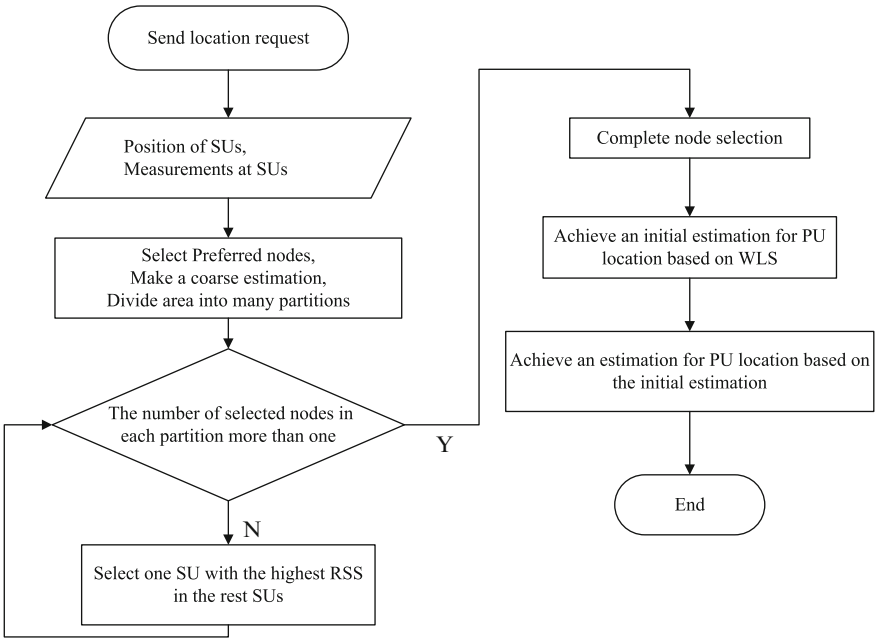

Fig. 3.2 A flow chart for our PU localization algorithm

3.3 Simulation Results

In most cases, one PU and 80 SUs are randomly placed in a 100 m $\times$ 100 m square area, and $\gamma = 4$. In the simulation diagrams, "S-" represents localization algorithm based on node selection.

The effects on localization accuracy for different numbers of selected SUs are presented in Fig. 3.3. Two scenarios, in which 30 and 50 nodes are uniformly distributed respectively, are considered. Many SUs with the highest RSS are selected and the number of selected SUs varies in the range of 4–20. Figure 3.3 shows that localization error is very high by only selecting four SUs. The reason is that four SUs cannot form a good geometry structure when SUs are deployed uniformly. The localization error by selecting five SUs is much smaller than that by selecting four SUs. When the number of selected SUs is more than five, the decrease of localization error is not obvious. So we adopt five partitions in the paper.

Figure 3.4 shows the effects of node selection in a uniformly distributed scenario. It can be seen that the RMSE of localization algorithm based on node selection is smaller than the RMSE of algorithm without node selection. And the RMSE of EWLS (optimal WLS localization algorithm without node selection) is higher than the RMSE of S-WLS. Figure 3.5 depicts the effects of PU position on

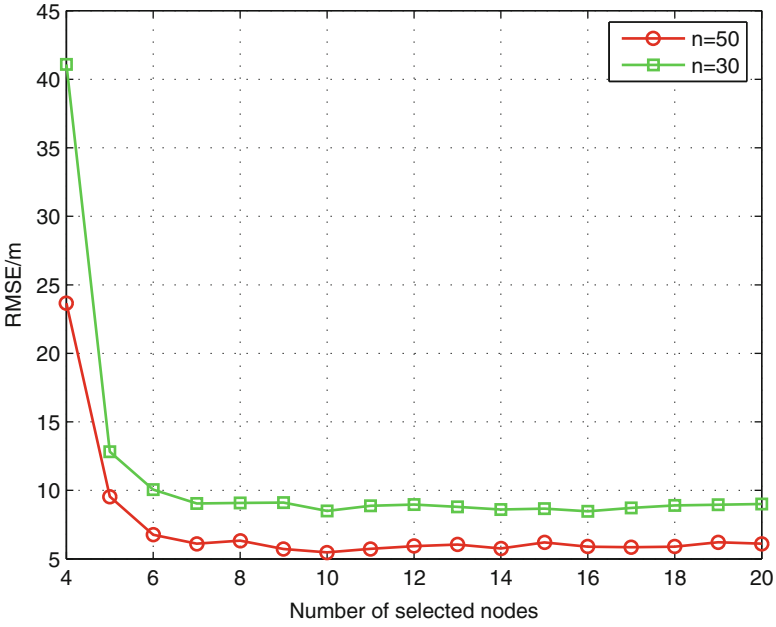

Fig. 3.3 Localization error versus the number of selected SUs

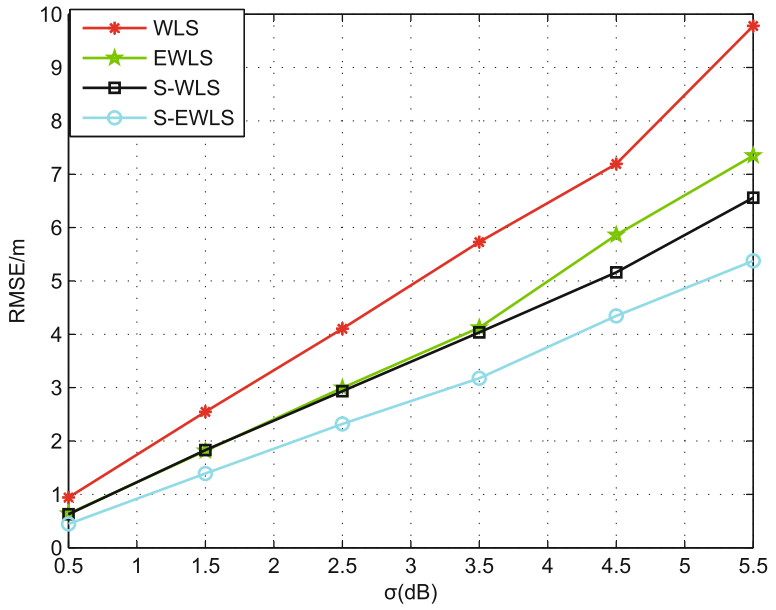

Fig. 3.4 A PU is uniformly placed in the whole area

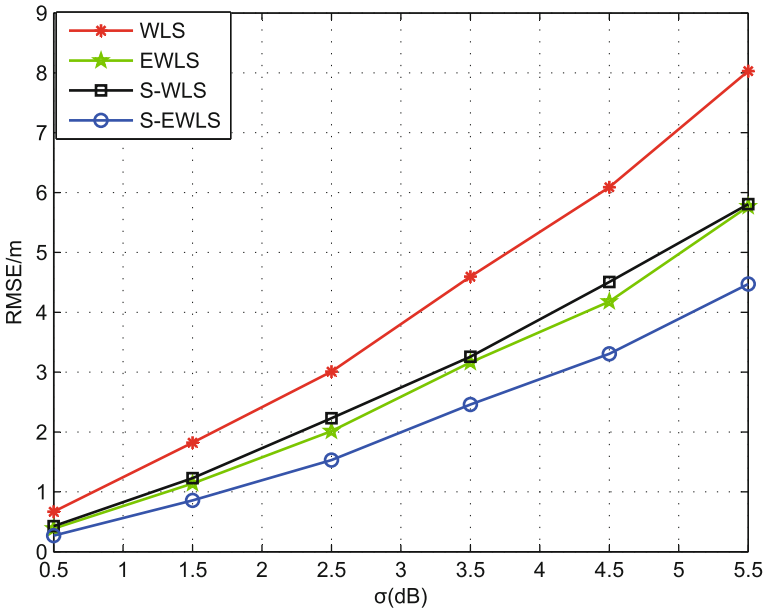

Fig. 3.5 A PU is uniformly placed in a specific area

localization error. In this simulation, a PU is uniformly distributed in a 20 m × 20 m square area which is in the center of the whole area (100 m × 100 m square area). By comparing Fig. 3.4 with Fig. 3.5, we can see that the localization error for a PU which is uniformly placed in the specific area is smaller than that in the whole area. The reason is that a PU may be on the edge of the whole area when the PU is uniformly placed in the whole area. In this case, selected nodes cannot obtain a good geometric structure.

Figure 3.6 shows the effects of node selection in a non-uniformly distributed scenario. In this simulation, the coordinates of PU is (40 40). With the PU as origin, the whole area is divided into four parts (i.e. two square areas and two rectangular areas).The left bottom and right top parts are the two square areas. There are 30, 10, 30 and 10 SUs uniformly distributed in the left bottom, right bottom, right top and left top parts, respectively. We can conclude that the RMSE of WLS method is higher than the RMSE of S-WLS method, the RMSE of EWLS method is higher than the RMSE of S-EWLS method.

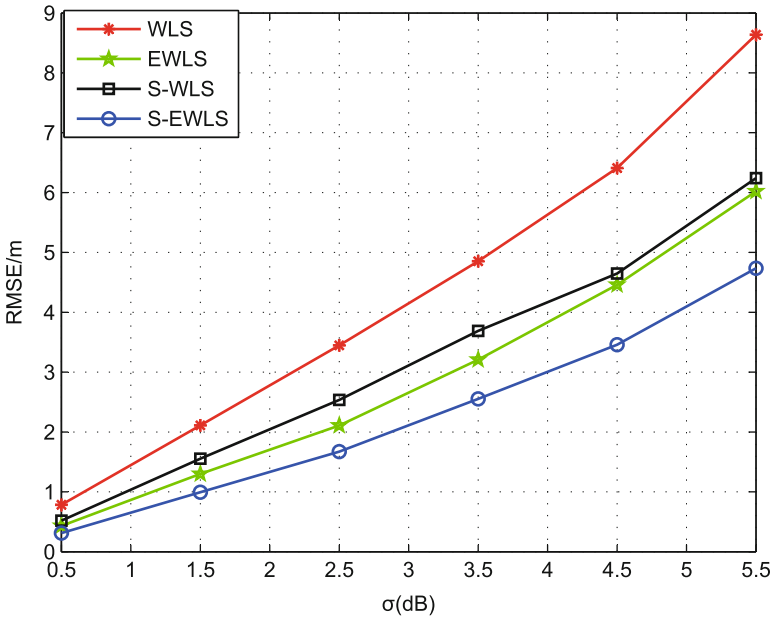

Fig. 3.6 Effects of node selection in a non-uniformly distributed scenario

Conclusion

In this paper, a PU localization algorithm with unknown transmit power is proposed. The algorithm ensures a good geometric structure for selected nodes and obtains a good tradeoff between localization accuracy and complexity. Simulation result shows localization algorithm based on node selection is superior to localization algorithm without node selection. When a PU is on the edge of the whole area, the localization error is higher because selected nodes cannot form a good geometric structure.

Acknowledgements This work was supported by the National Natural Science Foundation of China (61471077, 61301126), the Fundamental and Frontier Research Project of Chongqing (cstc2013jcyjA40034), the Science and Technology Project of Chongqing Municipal Education Commission (KJ1400413, KJ130528), the Program for Changjiang Scholars and Innovative Research Team in University (IRT1299), and the Special Fund of Chongqing Key Laboratory (CSTC).

References

1. Celebi H, Aslan H (2007) Utilization of location information in cognitive wireless networks. IEEE Wirel Commun 14(4):6–10. doi:10.1109/MWC.2007.4300977

2. Wang J et al (2013) Cramer-rao bounds for joint RSS/DOA Cbased primary-user localization in cognitive radio networks. IEEE Trans Wirel Commun 12(3):1363–1375. doi:10.1109/TWC.2013.012513.120966
3. Zhao B et al (2011) Sensor selection for an accurate closed form localization in cognitive radio networks: the trade-off between model accuracy and geometry structure. In: The 6th IEEE conference on industrial electronics and applications (ICIEA), pp 1987–1992. doi:10.1109/ICIEA.2011.5975918
4. Kim S et al (2007) Robust localization with unknown transmission power for cognitive radio. In: IEEE military communications conference (MILCOM), pp 1–6. doi:10.1109/MILCOM.2007.4455295
5. Mankar P et al (2012) A cooperative secondary user localization based primary user localization method for cognitive radio networks. In: 2012 National conference on communications (NCC), pp 1–5. doi:10.1109/NCC.2012.6176751
6. Tarrio P et al (2011) Weighted least squares techniques for improved received signal strength based localization. Sensors 11:8569–8592. doi:10.3390/s110908569
7. Bishop AN (2011) Transmitter power estimation for uncooperative emitters with the Cayley-Menger determinant. In: Mediterranean conference on control & automation (MED), pp 1166–1169. doi:10.1109/MED.2011.5983220
8. Gorji AA, Anderson BDO (2013) Emitter localization using received-strength-signal date. Signal Process 93:996–1012. doi:10.1016/j.sigpro.2012.11.020
9. Patwari N et al (2005) Locating the nodes: cooperative localization in wireless sensor networks. IEEE Signal Process Mag 22(4):54–69. doi:10.1109/MSP.2005.1458287
10. Hadzic S, Rodriguez J (2011) Utility based node selection scheme for cooperative localization. In: International conference on indoor positioning and indoor navigation (IPIN), pp 1–6. doi:10.1109/IPIN.2011.6071914
11. Bishop AN, Jensfelt P (2009) An optimality analysis of sensor-target geometries for signal strength based localization. In: The 5th international conference on intelligent sensors, sensor networks and information processing (ISSNIP), pp 127–132. doi:10.1109/ISSNIP.2009.5416784
12. Zhao B et al (2011) Sensor selection for received signal strength-based source localization in wireless sensor networks. J Control Theory Appl 9(1):51–57. doi:10.1007/s11768-011-0229-6
13. Lin L et al (2013) Accurate and simple source localization using differential received signal strength. Digit Signal Process 23:736–743. doi:10.1016/j.dsp.2012.12.020

Chapter 4
Management Mechanism of Key Leakage Avoidance in Hybrid ZigBee Network

An Wu and Zhuo Sun

Abstract The existing ZigBee security system shows less attention to forward security especially when a node leaves the network. In this paper, we present a key management mechanism in ZigBee hybrid network. This mechanism includes a rekeying method for hierarchical network key and a prompt revoking process of application link key, which can efficiently prevent the damage caused by the key leakage of leaving node. We build a network model to verify the key management mechanism. A modified routing protocol based on LEACH is adopted in the model to gain a cluster topology. Then we use MATLAB to evaluate the performance of this mechanism. Results show that the reduction of consumption is considerable especially in large scale network.

Keywords ZigBee security • Cluster • Key management

4.1 Introduction

ZigBee is a wireless specification for short distance and low rate communication. With the features of low complexity, low power consuming and low cost, it is widely used in wireless sensor network. Wireless sensor networks are mainly used in consumer electronics, industrial control, automatic control of medical equipment and agriculture automation etc. In such cases, a high degree of security is required.

ZigBee Alliance provides an independent module to realize the security mechanism of ZigBee protocol, which includes key establishing, key transmission, frame protection and equipment management. These security services constitute the structure of ZigBee security. The ZigBee Alliance and many other researchers make a significant effort to improve the security weakness of ZigBee protocol. Many improved encryption algorithms are proposed, such as chaotic algorithm [1, 2] and proxy re-encryption algorithm [3]. Furthermore, researchers dedicate themselves to analyze the weak points in ZigBee [4, 5] and put forward some efficient security

A. Wu (✉) • Z. Sun
Key Laboratory of Universal Wireless Communications, Ministry of Education, Beijing University of Posts & Telecommunications, Beijing 100876, China
e-mail: wuan@bupt.edu.cn

J. Mu et al. (eds.), *The Proceedings of the Third International Conference on Communications, Signal Processing, and Systems*, Lecture Notes in Electrical Engineering 322, DOI 10.1007/978-3-319-08991-1_4

schemes to fit different application scenarios [6]. However, the forward security is easier to be ignored compared with other aspects. Now the lastest ZigBee Specification still indicate nothing about how to manage the network key and link key after a node leaving the network. The lack of management for these keys will be utilized by the adversaries and then causes damage to the network. Actually a node which has left the network still reserves the network key and the application link key (APP LK) of peer units. If the keys are not revoked and redistributed in time, attackers will utilize these information easily to intercept or tamper messages transferring in the network.

In this paper we first introduce a network model in which we verify our key management mechanism. Second, we present a new management mechanism of security key in hybrid network. Nodes update the network key and delete application link key stored in peer ZigBee nodes instantly when a ZigBee node leaves the network. This method can improve the ignored forward security in wireless senor network. In the last section, the performance of this mechanism is evaluated.

4.2 The Network Model

In this section, we design a network model to verify the key management mechanism. In hybrid network, devices usually are divided into different levels to complete task. The topology structure of the system is showed in Fig. 4.1.

We choose a modified LEACH (Low Energy Adaptive Clustering Hierarchy) protocol [7] in this model. LEACH is one of the most famous routing protocols, with the features of saving energy consumption and easy to implement.

The basic idea of the algorithm is: select the cluster-head randomly in a cyclic manner. These senor nodes will choose a random number between zero and one. If the number is less than the threshold value, then this node will be selected as a cluster-head node.

However, the selecting of cluster-head is totally random. In a cluster, the node which has less energy left will be easier to exhaust if it is selected as cluster-head

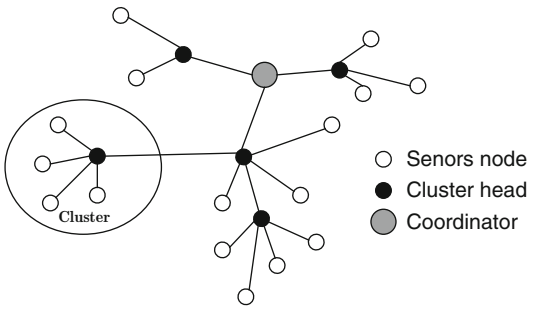

Fig. 4.1 Topology structure of hybrid network

node. The death of cluster-head node will lead to the paralysis of entire cluster. So we choose nodes which have more energy left to extend the life cycle of the entire cluster through the analysis of the energy of whole cluster nodes.

Each node in the cluster sends the remaining value of their current energy E_i in the cluster-reconstruction process. The average energy of entire cluster is $\overline{E_{lef}} = \frac{\sum_i E_i}{N}$. The node which is qualified for head node compares own E_i with $\overline{E_{lef}}$. If E_i is less than $\overline{E_{lef}}$, abandon the node and reselect a node until all head nodes are selected.

4.3 Management Mechanism of Security Key

In this section, we present a new mechanism of security key in hybrid network to manage the network key and link key after a node leaves. It can effectively prevent the damage caused by the key leakage.

4.3.1 Rekeying Mechanism of Hierarchical Network Key

In general, an access to any further data transmitting in the network should not be given to the leaving node in case that the node may be compromised or suspected by attackers [3]. If an adversary gets the network key from the left node, he can utilize it to eavesdrop or jam the network.

Updating the current network key entirely whenever a node leaves the network can effectively strengthen forward security. However, the flooding of network key updating frame will take a large amount of network resources consumption. Therefore, we present a new updating method of network key based on the characteristic of hybrid network. This updating mechanism can achieve higher security requirement with a less burden to entire network.

As shown in Sect. 4.2, the hierarchical network is a cluster-shaped network. Data of each non-cluster-head node will be sent to the cluster-head node at first. The cluster-head nodes act as a convergence node. So we adopt a multi-level network keys, which maximizes the advantage of this feature.

Each cluster maintains an internal network key. Meanwhile all cluster-heads preserve a public network key besides the internal network key of own cluster. The sensor nodes use the internal network key to encrypt data directly. The cluster-head nodes are responsible for the re-encryption and re-decryption of data in own cluster. The detail process of encryption and decryption is as follows:

Fig. 4.2 The pseudo code of encryption and decryption procedure

```
Cluster-head N_{head_i} receives Data_i{Dst,Scr,Key_i}
If (Dst ∈ Cluster_{head_i}{•}), where Cluster_{head_i}{•} means the set
of nodes in the cluster of N_{head}
  If( Scr ∈ Cluster_{head_i}{i} )
       Transmit Data_i directly to Dst
  else
       decrypt Data_i with NK_{public}, then set Key_i=NK_{internal}
        encrypt Data_i with Key_i
        transmit Data_i to another N_{head_j}, i ≠ j
else
  If( Scr ∈ Cluster_{head_i}{i} )
       decrypt Data_i with NK_{internal}, then set Key_i=NK_{public}
        encrypt Data_i with Key_i
        transmit Data_i to another N_{head_j}, i ≠ j
  else
       transmit Data_i directly to Dst
```

When a non-cluster-head node leaves the network, the public network key is unchanged. All we need is to update the internal network key in its cluster. When a cluster-head node leaves the network, updating the public network key within cluster-heads of each cluster is enough. We use INK to represent the internal network key. PNK is the short for public network key. n_1 is the number of cluster-head nodes. n_2 is the number of all nodes in a cluster. The network key update process is shown as below:

```
Trust center TC receives a leaving notification of node N_i
If( N_i ∈ N_{heads}{i} ),where N_{heads}{•} means a set of cluster-head nodes
in network
  Generate a new PNK_i
  Broadcast PNK update frame {Public,PNK_i} in whole network
  For i = 1 to n_1
        N_{heads}{i} set PNK = PNK_i
else
  Broadcast INK update frame {Internal,clusterID} in whole network
  For i = 1 to n_1
     If( i = clusterID)
        Generate a new INK_i
        Broadcast NK update frame in cluster
        For i = 1 to n_2
           N_{non_head}{i} set NK= INK_i
     else
        Abandon frame
```

Fig. 4.3 The pseudo code of key updating procedure

We can cut down the amount of frame needed in process of updating network key by restricting the update scope into a cluster. The consumption of network resource reduces through the new update mechanism of network key.

4.4 Revoking Mechanism of Application Link Key

According to ZigBee Specification, a device (e.g. parent node)will send a frame to inform trust center about the leaving of another node (e.g., child node). Then the trust center will delete the corresponding route table entries (RT) and application support sublayer mapping table entry (APS MT).

But ZigBee Specification provides no solution about how to handle the application link keys which stored in peer-nodes. More precisely, the other peer nodes are not aware of the device's leaving. They still remain the APPLK assigned to the leaving node. If aggressor gets the link key stored in the leaving node, he can eavesdrop on data which is encrypted by these keys and even communicate with the peer nodes by camouflage the leaving node.

A revoke mechanism of application link key is present in this paper to avoid this security threat. When trust center notices that a node is leaving the network, it will delete the trust center link key (TCLK) corresponding to the node. Then the trust center broadcast a message to inform the partner devices of the leaving node. The partner device which receives the broadcast frame will check its own application link key table. If any corresponding entry exists, it will delete the link key. The flow chart of revoke mechanism is shown in Fig 4.4.

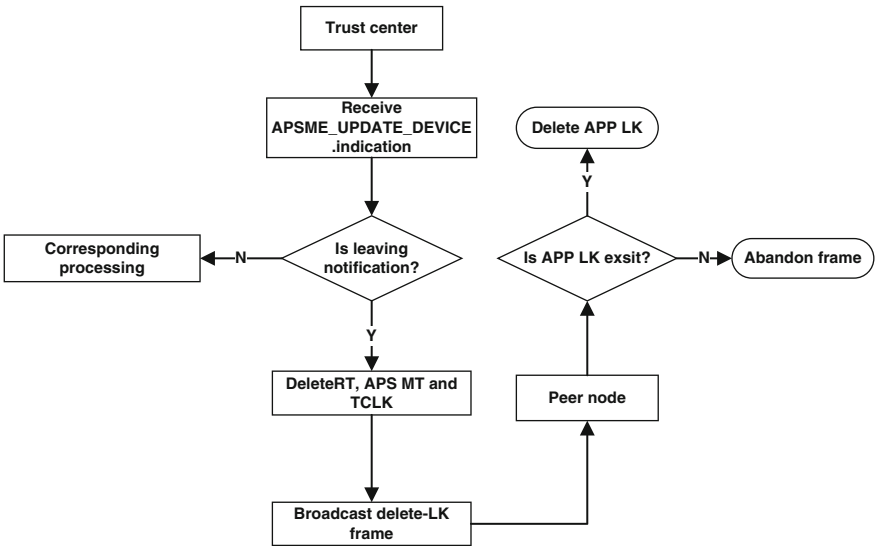

Fig. 4.4 Link key revoke process

In the model, the deleting mechanism of link key makes up the deficiency of ZigBee Specification. By deleting link key after peer device leaving, it strengthens the security of key.

4.5 Performance Evaluation

In this section, we analyze the performance of rekey mechanism of hybrid network key. In traditional update process of network key, the trust center will periodically broadcast a transport-key frame carrying a new network key and then broadcast a switch-key frame to inform FFD (Full Functional Device) to change network key. Nevertheless, the number of frames in our update mechanism of network key just relates to the scale of each cluster and number of cluster-heads nodes.

We use MATLAB to evaluate the performance of new mechanism. To simplify evaluation, we maintain the ratio of leaving nodes in a network at 0.1. Assuming the overhead of each frame is same. The number of frames produced in update key process can reflect the consumption of network resource in some degree.

In Fig. 4.5, we compare the resource consumption of updating network key in two networks. One updates network key as the way stated in ZigBee Specification and the other one updates as the proposed mechanism in this paper. It is assumed that the ratio of cluster is 0.05 which means each cluster has 20 nodes in total. We

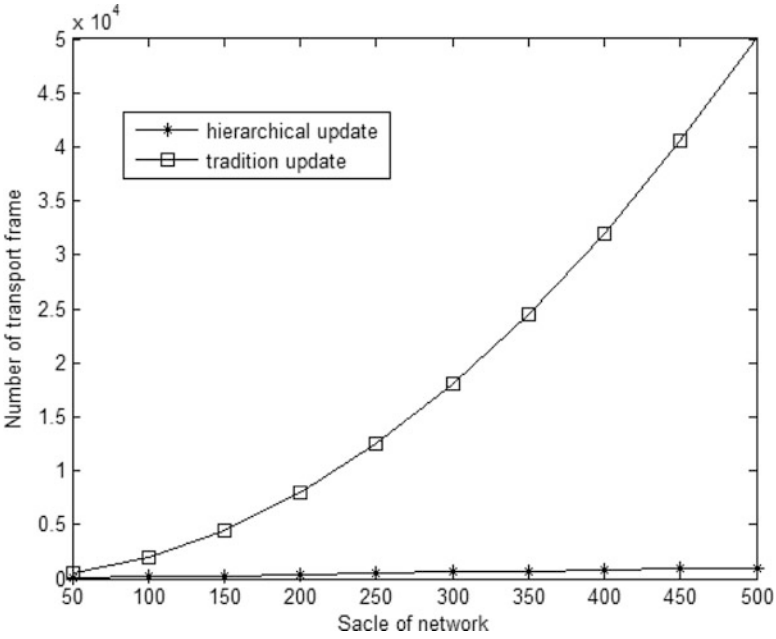

Fig. 4.5 Comparison of consumption in network key update process

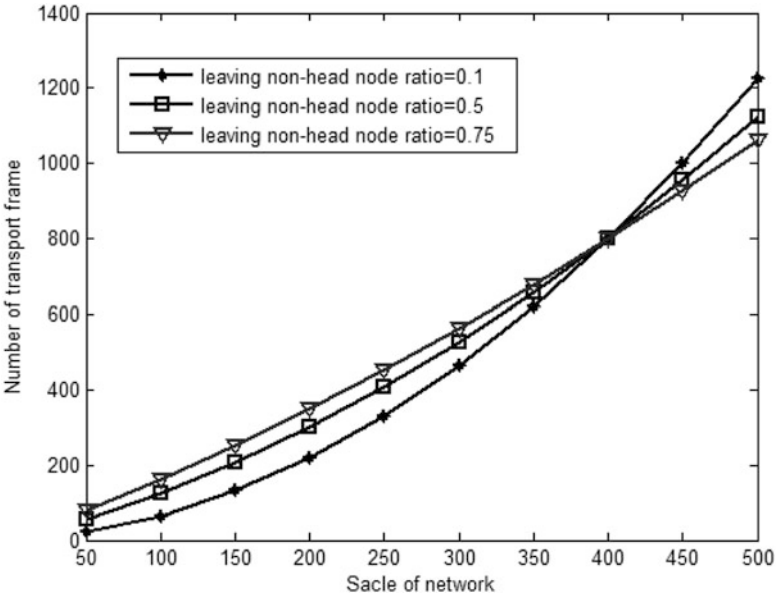

Fig. 4.6 Comparison of different ratio of non-cluster-head nodes

observe that the frame needed to update network key in rekeying mechanism of hierarchical network key is less than traditional way. The gap increases with the scale of the network.

Figure 4.6 provides the comparison of different ratio of non-cluster-head nodes in total leaving nodes. Though initially the number of produced frame is in proportion to the ratio of non-cluster-head nodes, as the scale of network increases it tends to be inverse proportion. The reason is that the scale of each cluster is fixed. Each non-cluster-head node leaving will trigger an internal network key updating. In a small network, a change of internal network key has greater effect than the change of public network key. As the scale of network becomes larger, the ratio of the number of nodes in a cluster to nodes in entire network is smaller, on the contrary, the significant effect of public network key rekey appears.

In Fig. 4.7, we change the scale of each cluster. As shown, the resource saving effect is inverse proportional to the cluster scale.

According to the results above, we can choose a proper scale of cluster and the number of cluster-head nodes to retrench the network resource consumption considering the scale of network and the ratio of leaving non-cluster-head nodes.

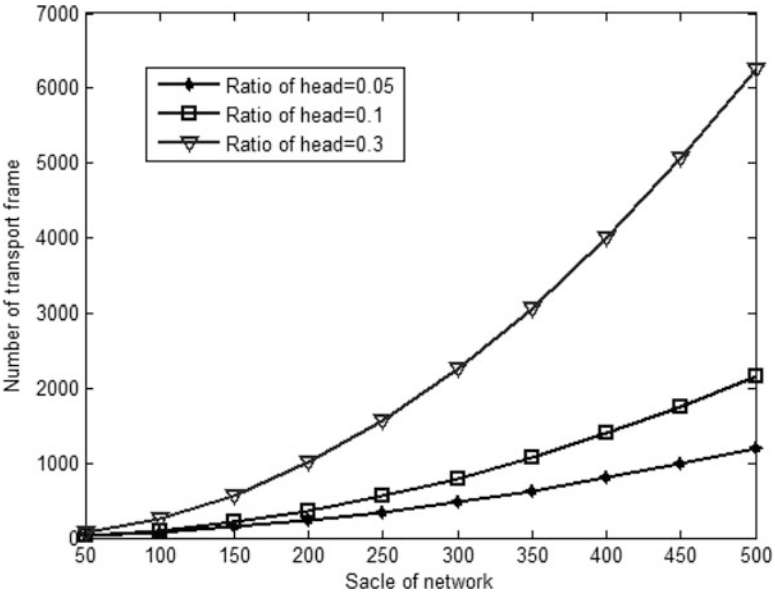

Fig. 4.7 Comparison of consumption in different cluster scale

Conclusion and Future Work

Now ZigBee security is one of research focus areas. Although the ZigBee Alliance has done a lot of effort, the forward security is one aspect easy to be overlooked. In this paper, we conduct a deep research of the ZigBee security system. A network model of hybrid network with a new mechanism is built. The mechanism of security key management reduces the security risk by updating network key in time and deleting peer application link key.

The updating mechanism of network key utilizes the feature of cluster structure in hybrid network and has a local trait to lower the consumption of network resource by creatively putting forward a concept of hierarchical network key. Furthermore, the deleting mechanism of link key makes up the deficiency of lack of control for link key after device leaving.

Future work will extend to different topology structures of network, since the rekey mechanism of network key in this paper is most suitable to cluster network. It will bring some unnecessary routing overhead in non-cluster topology.

Acknowledgments This work was supported by the National Science and Technology Major Project of China under grant 2013ZX03001003-003, and the BUPT Research Innovation Project under grant 2013RC0104.

References

1. Bakhache B, Ghazal JM, Assad SE (2013) Improvement of the security of zigbee by a new chaotic algorithm[J]
2. Bakhache B, Ghazal J, El Assad S (2011) Enhancement of zigbee and wi-fi security by a robust and fast chaotic algorithm[C]//Network and System Security (NSS). In: 2011 5th international conference on IEEE, pp 300–304
3. Seo H, Kim H (2011) Zigbee security for visitors in home automation using attribute based proxy re-encryption[C]//Consumer Electronics (ISCE). In: 2011 I.E. 15th international symposium on IEEE, pp 304–307
4. Vidgren N, Haataja K, Patino-Andres JL et al (2013) Security threats in zigbee-enabled systems: vulnerability evaluation, practical experiments, countermeasures, and lessons learned[C]//System Sciences (HICSS). In: 2013 46th Hawaii International Conference on IEEE, pp 5132–5138
5. Dini G, Tiloca M (2010) Considerations on security in zigbee networks[C]//Sensor Networks, Ubiquitous, and Trustworthy Computing (SUTC). In: 2010 I.E. international conference on IEEE pp 58–65
6. Nyamasvisva TE, Hasbullah H (2010) Multi-level security algorithm for random ZigBee wireless sensor networks[C]//Information Technology (ITSim). In: 2010 international symposium in IEEE, vol. 2. pp 612–617
7. Panahi N, Rohi HO, Payandeh A et al (2012) Adaptation of LEACH routing protocol to cognitive radio sensor networks[C]//Telecommunications (IST). In: 2012 sixth international symposium on IEEE, pp 541–547

Chapter 5
A Spectral Efficient Cognitive Radio Resource Management Method for Low-energy Cognitive Networks

Liaoyuan Zeng

Abstract For Cognitive Radio (CR) systems operating within the range of low power incumbent wireless systems, effective and efficient radio resource management (RRM) technique is vital for the spectrum efficiency improvement. By using robust and efficient channel estimation and synchronization techniques, CR based RRM algorithms can be integrated into CR enabling techniques such as Ultra Wideband (UWB) to dynamically allocate the radio resource across the operating frequency band for the optimal spectrum usage. For OFDM based CR-UWB system, we proposed a hybrid RRM (HRRM) algorithm aiming to optimize spectrum efficiency. The HRRM algorithm involves the joint optimization of power and time resource allocation, in which the spectrum sensing window size is dynamically assigned in order to optimize the use of the optimal power distribution algorithm. Our numerical simulation indicates that HRRM algorithm outperforms traditional RRM in terms of spectrum efficiency enhancement and the gain contributed by the HRRM algorithm outperforms the complexity generated.

Keywords Radio resource management • Cognitive radio • Ultra wideband

5.1 Introduction

A critical objective of the future cognitive radio (CR) [7] is to optimize the use of the spectrum resource, and one of the key determinants is the CR-based radio resource allocation (RRM) methods involving the processes of spectrum sensing, sharing and management. Ultra Wideband (UWB) operates [4] with an extremely low power spectrum density (PSD) [12], which facilitates the underlay spectrum sharing technique to co-exist with the primary users (PUs) that operate within the UWB's wide spectrum band [1]. Generally, to protect the PUs from being harmfully interfered, the CR-UWB's transmit power can be decreased to a level that is

L. Zeng (✉)
University of Electronic Science and Technology of China, Chengdu, China
e-mail: liaoyuan.zeng@ul.ie

J. Mu et al. (eds.), *The Proceedings of the Third International Conference on Communications, Signal Processing, and Systems*, Lecture Notes in Electrical Engineering 322, DOI 10.1007/978-3-319-08991-1_5

significantly lower than the UWB's regular PSD, which can result in considerably low spectral efficiency. By using orthogonal frequency division multiplexing (OFDM) [5], the UWB system can adaptively adjust the transmit power of the OFDM subcarriers according to the spectrum sensing results within the interested spectrum segments. The spectral efficiency of the overlapped spectrum is critical to the overall spectral efficiency of the CR-UWB system and is dependent on the performance of the spectrum sensing algorithm [9]. Thus, the performance of the RRM scheme is coupled with the performance of the spectrum sensing scheme, which jointly dictates the final spectrum efficiency of the CR-UWB system.

Generally, the CR-RRM design problem for spectrum efficiency optimization features multi-objective and NP-hard characteristics, which is nontrivial to solve. The design requires swift feedback of the meters such as BER, SNR and FER, and delicate tweak of various knobs including power, bandwidth, frame size, etc. for different purposes. The methodology of joint RRM design provides a great opportunity for CR professionals to find the optimal tradeoff among contradictive objectives. For capacity-based optimization, the optimal power can be derived as a function of a given sensing time by using convex optimization methods such as subgradient method [10], ellipsoid method [2] and Newton's method [8]. Then, one-dimensional exhaustive search or bisection search method is commonly used to obtain the optimal sensing time since it is NP-hard to derive an analytical form. Using convex optimization method to solve the power allocation problem requires relaxation of constraints, which will cause the optimization algorithm cannot be implemented in practical CR-UWB systems. Furthermore, the convex optimization algorithm often converges slowly near to the optimum and needs a large number of iterations to reach the desired accuracy [15].

In MB-OFDM CR-UWB receiver, incoming UWB signals are demodulated by a Fast Fourier Transform (FFT) engine, which facilitates the use of Discrete Fourier Transform (DFT) based energy detection (ED) for spectrum sensing. However, when PUs operate in low-SNR regime, waveform-based detection (WD) methods encompass superior performance than ED in terms of reliability and convergence time, because of the use of the coherent processing based techniques [13]. Thus, we assume the CR-UWB system uses WD method. In this paper, we derive a hybrid RRM (HRRM) method that includes a quasi-analytical solution for the optimal sensing window size based on WD method, which can provide an optimized transmit window for the greedy based power allocation algorithm to distribute the transmit power with.

5.2 System Model

We assume that the interleaved spectrum sharing mechanism is used in the CR-UWB system [3, 6]. The CR-UWB's spectrum efficiency is defined as

$$\zeta = \frac{B_{cog}}{T_s W}, \tag{5.1}$$

where $\mathbf{B}_{\text{cog}}$ represents the total number of bits allocated on the CR-UWB subcarriers, W is the bandwidth used by the transmitted OFDM symbol, and T_s denotes the OFDM symbol period.

The probability that an overlapped spectrum will contain less than energy threshold power at any instant of time, is determined by the probability that a PU is operating within the overlapped spectrum, and is written as

$$P(\mathcal{H}_1) = p(x;\lambda t) = \frac{e^{-\lambda t}(\lambda t)^x}{x!}, \tag{5.2}$$

where $\mathcal{H}_1$ represents the hypothesis that a PU is activated, x denotes the expected number of PU's occurrences during the period of t, and λ is the average number of PU's occurrence per μ s.

By using robust and efficient channel estimation and synchronization techniques, WD can be integrated into CR systems to dynamically allocate the radio resource across the operating frequency band for the optimized spectrum usage. For WD based sensing, assuming the received signal at CR-UWB has the form of [11]

$$y(n) = s(n) + w(n), \tag{5.3}$$

where $s(n)$ is the signal to be detected, $w(n)$ is the additive white Gaussian noise (AWGN) sample, and n is the sample index. The metric for the WD can be written as

$$M = R\rceil[\sum_{n=1}^{N} y(n)s^*(n)], \tag{5.4}$$

where M denotes the decision metric, and $*$ represents the conjugation operation. Furthermore, in the presence of a PU's signal, the sensing metric is

$$M = \sum_{n=1}^{N} |s(n)|^2 + R\rceil[\sum_{n=1}^{N} w(n)s^*(n)], \tag{5.5}$$

and the decision can be made by comparing M against a threshold.

5.3 Joint Optimization Method

In a CR-UWB system, the sensing window size determines the time ratio, α, for the system to apply the spectrum management function for useful data transmission, i.e., $\alpha = T_{txop} - \tau_s T_{txop}$, where T_{txop} is a pre-defined time segment for a certain type of application in the CR-UWB MAC layer, called Transmission Opportunity

(TXOP). We assume that the CR-UWB system starts sensing the channel prior to the start of a TXOP. Then, the CR-UWB system's spectrum efficiency (5.1) is re-written as

$$\zeta = \frac{1}{T_s W}\mathbf{B}\alpha(1 - P_f)(1 - P(\mathcal{H}_1)), \tag{5.6}$$

where **B** denotes the total number of bits loaded in the UWB subcarriers when all the subcarriers are available. To maximize a CR-UWB system's spectrum efficiency, an optimal SST value is needed to maximize α while meet the target value of P_d and P_f.

Figure 5.1 illustrates the value of α as a function of the received PU's SNR at the CR-UWB's side, we can see that the value of α obtained by WD based sensing significantly outperforms the ED based sensing, which provides grater opportunities for the use of the power allocation algorithm during the transmission period, especially at low-SNR situation.

In line-of-sight (LOS) channel condition, i.e., channel mode (CM) 1, of UWB system, Fig. 5.2 shows that by using a typical power allocation algorithm, i.e., equal power allocation, there exists peak spectrum efficiency value under a certain value of sensing window size in terms of milliseconds (ms). Furthermore, under different PU's SNR conditions, WD based sensing provides significantly higher peak value of spectrum efficiency compared with the ED based sensing. Under both sensing

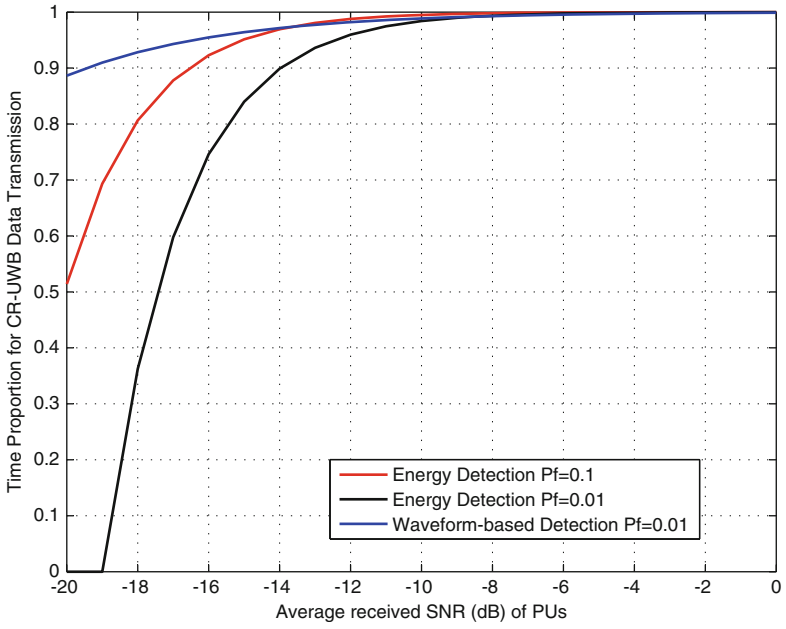

Fig. 5.1 Time proportion of data transmission as a function of PU's SNR

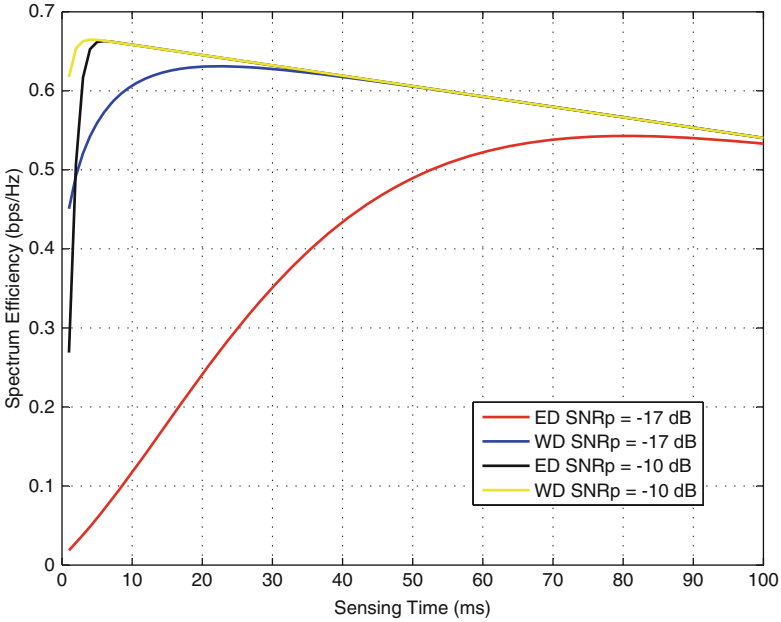

Fig. 5.2 The maximum spectrum efficiency as a function of received PU's SNR in CM1

mechanisms, the optimal point of sensing window size corresponding to the maximum spectrum efficiency can be identified through efficiency search algorithms.

By integrating the dynamic power allocation algorithm proposed by [14], spectrum efficiency achieved without using the SST optimization algorithm and the spectrum efficiency obtained when the HRRM optimization algorithm is applied. Observations in Fig. 5.3 show that by using the HRRM optimization algorithm equipped with WD based sensing, the spectrum efficiency is significantly increased compared with ED based sensing and normal sensing. For example, at $\gamma_p = -18$ dB, the spectrum efficiency of the CR-UWB system is 0.61 bps/Hz which is significantly higher than the spectrum efficiency that is achieved by the ED based sensing and normal sensing mechanisms. With the increase of the PU's SNR, the difference between the three lines decreases exponentially. At high SNR regime (i.e., > -12 dB), the spectrum efficiencies of the different CR-UWB systems are very close because the large SNR value becomes dominant, the target P_d is reached at a very small sensing window size. Figure 5.3 indicates that the HRRM optimization algorithm is more suitable for the situation where the received SNR is low.

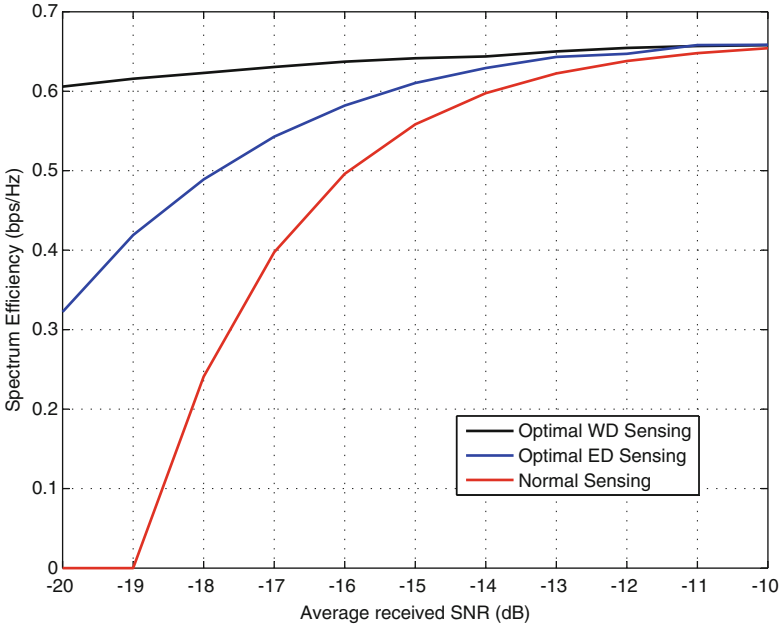

Fig. 5.3 The maximum spectrum efficiency as a function of received SNR γ_p in CM1

Conclusion

In this paper, we proposed a hybrid RRM algorithm for OFDM based CR-UWB systems, aiming to maximize the spectrum efficiency by jointly optimize the allocation of spectrum sensing window size and subcarrier transmit power. First, the WD-based spectrum sensing algorithm adaptively allocate the sensing window length for the CR-UWB system within a limited TXOP under the constraint of the target PF. Then, during the optimized window of transmission, the dynamic power allocation algorithm can adaptively assign the transmit power to the CR-UWB subcarrier groups according to the channel conditions. By using the HRRM algorithm, the CR-UWB system's spectrum efficiency can be enhanced obviously, and the complexity is relatively low especially when the CR-UWB operates within low-SNR regime of the PUs.

References

1. Akyildiz IF, Lee WY, Vuran MC (2006) Next generation dynamic spectrum access cognitive radio wireless networks: a survey. Comput Networks 50:2127–2159
2. Fan R, Jiang H, Guo Q, Zhang Z (2011) Joint optimal cooperative sensing and resource allocation in multichannel cognitive radio networks. IEEE Trans Veh Technol 60(2):722–729

3. FCC (2003) Facilitating opportunities for flexible, efficient, and reliable sprctrum user employing cognitive radio technologies. Technical report, Federal Communications Commission, Washington, DC
4. Gharpurey R, Kinget P (2008) Ultra wideband circuits, transceivers and systems. Springer Science+Business Media, LLC
5. Liu G, Zhu W (2004) Compensation of phase noise in ofdm systems using an ici reduction scheme. IEEE Trans Broadcast 50(4):399–407
6. Malik WQ, Stevens CJ, Edwards DJ (2008) Ultrawideband antenna distortion compensation. IEEE Trans Commun Syst 56(7):1900–1907
7. Mitola III J (1999) Cognitive radio for flexible mobile multimedia communications. In: Proceedings of the IEEE international workshop on mobile multimedia communications, 15–17 November 1996, San Diego
8. Pei Y, Liang YC, Teh KC, Li KH (2011) Energy-efficient design of sequential channel sensing in cognitive radio networks: optimal sensing strategy, power allocation, and sensing order. IEEE J Select Areas Commun 29(8):1648–1659
9. SPTF (2002) Report of the spectrum efficiency working group. Technical report, Federal Communications Commission Spectrum Policy Task Force, Washington, DC
10. Stotas S, Nallanathan A (2011) Optimal sensing time and power allocation in multiband cognitive radio networks. IEEE Trans Commun 59(1):226–235
11. Tang H (2005) Some physical layer issues of wide-band cognitive radio systems. In: Proceedings of international symposium on new frontiers in dynamic spectrum access networks, pp 151–159
12. Yang L, Giannakis GB (2004) Ultra-wideband communications: an idea whose time has come. IEEE Signal Process Mag 21:26–54
13. Yucek T, Arslan H (2009) A survey of spectrum sensing algorithms for cognitive radio applications. IEEE Commun Surv Tutor 11:116–130
14. Zeng L, McGrath S, Cano E (2010) Spectrum efficiency optimization in multiuser ultra wideband cognitive radio networks. In: Proceedings of the 7th international symposium on wireless communication systems, pp 1006–1010
15. Zhang YJ, Letaief K (2004) Multiuser adaptive subcarrier-and-bit allocation with adaptive cell selection for ofdm systems. IEEE Trans Wireless Commun 3(5):1566–1575

Chapter 6
An Efficient Authenticated Key Exchange Protocol for Wireless Body Area Network

Rui Yan, Jingwei Liu, and Rong Sun

Abstract Security protocol issues is an essential factor in network communication. The research of authenticated key exchange protocol is a hotspot in information security field at present, and the related research theories are quite mature. However with respect to the emerging wireless body area network (WBAN), there is few appropriate security protocol to guarantee the security of this network. This paper proposes an authenticated key exchange protocol for wireless body area network, which support the selective authentication between nodes pertain to the net, simultaneously two pairs of session key being generated efficiently and succinctly in the process of each certification, afterwards the security proof by BAN logic of such protocol is given out. The analysis indicates that the proposed protocol meets the expectative objectives.

6.1 Introduction

It is generally known that the information security is of vital importance in communication process while the issue is particular prominent in physically vulnerable wireless network [6]. Message exchange protocol based on cryptography called cryptographic protocol.

Key exchange protocol which furnished network authentication between users, is divided into password-based, symmetric key-based and public key infrastructure-based, named authenticated key exchange protocol [7]. And symmetric key-based authenticated key exchange protocol is common employed and provided with plenty of projects, such as the well-know NSSK protocol and improved NSSK protocols [1], the noted Yahalom protocol and its modified protocols [3] and the like.

With the development of wireless communication technique and sensor technology, research on WSN (wireless sensor network) security protocol [5] have gained gigantic progress. WBAN (wireless body area network) is the embranchment of WSN, it takes human bodies as the carrier of sensors, along with smart mobile device and long-distance information center constitute the network system. The international organization for standardization adopted the

R. Yan • J. Liu (✉) • R. Sun
Xidian University, Xi'an 710071, China
e-mail: yanrui19901028@gmail.com; jwliu@mail.xidian.edu.cn; rsun@mail.xidian.edu.cn

J. Mu et al. (eds.), *The Proceedings of the Third International Conference on Communications, Signal Processing, and Systems*, Lecture Notes in Electrical Engineering 322, DOI 10.1007/978-3-319-08991-1_6

WBAN standard IEEE802.15.6 in December 2011, which makes us have regulations to abide by in designing security protocol. On account of specificity of human bodies and WBAN [2], simple and accurate model is required, low redundancy rate messages and less message interactions is needed and flexible access of authentication nodes and higher protocol operation efficiency is the guarantee during the designing procedure of the security protocol.

By analyzing the existing protocols, meanwhile in accordance with the characteristics of the wireless body area network and the designing requirements of security protocol, a new security protocol right for the net is proposed in this paper, which accomplishes generating the session key and realizing the authentication of relevant nodes. In view of the calculation and storage capacity of sensor nodes and network complexity, new protocol is designed based on symmetric key cryptography.

Security analysis is the necessary step of security protocol design. Formalization analytical method for its capacity to detected the wispy bug of the security protocol comprehensively and thoroughly becomes the mainstream verification technology in security analysis, BAN logic is the emblematic representation which is a faith-based logic. The protocol in this paper is analysed by BAN logic and obtain the final faith through a series of logical deduction for case of achieving the security targets.

6.2 Network Model of the WBAN

The wireless body area network standard gives out the topology model of such net, the two-hop star topology network structure, which is composed of a hub node and dozens descendants. Here we differentiate the node as primary node and secondary node logically while the nodes have the same attribute, the affiliation of the nodes is shown in Fig. 6.1. We may considered the net as two-tier architecture, the control sensor node is linked together with the primary sensor node S_1, $S_2 \cdots S_n$ logically, simultaneously a portion of primary nodes in the first layer represented by S_i are connected with the corresponding secondary nodes S_{i1} in the second layer, the primary node here is amount to the relay node. In the initial condition authentication process of each node should be conducted at first place, then the session key is generated, to which the authenticated key exchange protocol is contributed.

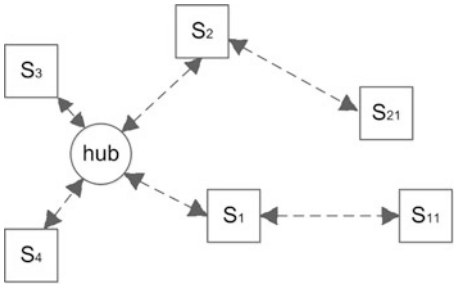

Fig. 6.1 The structure of two-hop star topology WBAN. hub denotes the control node, S_1 and S_2 denote relayed primary nodes, S_3 and S_4 denote primary nodes, while S_{11} and S_{21} denote relaying secondary nodes

6.3 New Authenticated Key Exchange Protocol for Wireless Body Area Network

This paper comes up with an emerging authenticated key exchange protocol for the newly spring up wireless body area network (for the sake of simplicity we make S denote the control node and B, C, D represent the primary nodes, A for secondary node). In the initial state, the control node S keeps the pre-shared key K_{bs} with primary node B, and K_{cs} with C, also K_{ds} with D, S shares the pre-shared key K_{as} with secondary nodes A identically. The protocol begins with a message broadcasted by secondary node A, after receiving the message from A the adjacent nodes B, C, D generate encrypted messages respectively according to the received message afterwards send it to the control node S, S determines the most appropriate primary node which to be connected with node A. Assumes that B is most applicable one, the protocol accomplishes the authentication between S and A, S and B, as well as A and B, also generate a session key named KEY between S and B, session key K_{ab} between A and B. At the same time S replies to C, D to inform the connection failure, authentication flow diagram is shown in Fig. 6.2.

The formalizing description of the new protocol:

Message1: A broadcast:A,Na
Message2: B→ S:B,$\{A,B,Na,Nb\}_{K_{bs}}$
Message3: S→ B:$\{B,Na,K_{ab}\}_{K_{as}}$,$\{A,Nb,K_{ab},KEY\}_{K_{bs}}$
Message3′: S→ C:$\{Nc,text\}_{K_{cs}}$
Message4: B→ A:$\{B,Na,K_{ab}\}_{K_{as}}$,$\{Na,Nb\}_{K_{ab}}$
Message5: A→ B:$\{Nb\}_{K_{ab}}$

Protocol analysis by step:

1. The secondary node A which is supposed to access to the network for authentication, broadcasts Message1 including its own identifier A and produces a random number Na. After receiving the broadcasted message, B, C, D send Message2 to S.

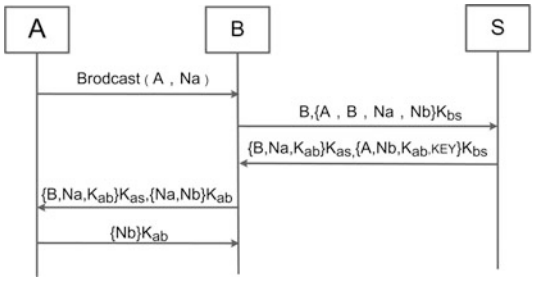

Fig. 6.2 The flow chart of the certification process

2. B sends a message encrypted under the pre-Shared key K_{bs} and its identifier B to S, which contains identifier A, random Na, identifier B and random number Nb generated by node B. Node C, D also send the same type of messages.
3. After receiving the request messages sent by primary nodes, S decrypts the messages by pre-shared key, noticed that it is secondary node A who want to join the net and being authenticated, S determines the suitable primary node to be connected with A and sends Message3 to the right node B as a reply, meanwhile sends Message3′ to C, D. Message3 contains $\{B,Na,K_{ab}\}$ encrypted with K_{as}, and$\{A,Nb,K_{ab},KEY\}$ encrypted with K_{bs}, K_{ab} is the session key for A and B generated by S, KEY is the session key between B and S generated by S.
4. After receiving Message3, B decrypts the message with K_{bs} and get the session KEY and K_{ab}, then encrypts the random number Na, Nb with K_{ab}, together with $\{B,Na,K_{ab}\}_{K_{as}}$ forwarded to A. At the same time node C, D have received the replied messages from S, knows it is unable to connect with A and replies noting.
5. After receiving the previous message, A decrypts message $\{B,Na,K_{ab}\}_{K_{as}}$ with K_{as} firstly, obtains the session key K_{ab}, then decrypts message $\{Na,Nb\}_{K_{ab}}$ with K_{ab} in order to get two random number assumed Na and assumed Nb, verified to observe whether they are the same, if so send Nb encrypted with K_{ab} to B, otherwise authentication failed.

After receiving the message from node A, node B test whether the assumed Nb is identical with the original one, if so manifests that node A have received the correct session key, end the protocol.

6.4 Formalizing Analyze of the New Protocol

We testify the security of the emerging protocol by the celebrated BAN logic, BAN logic formalizing analysis the authenticated key exchange protocol to deducted the final specified objectives from the prime faith. In BAN logic messages being idealized as the formulas in the first place, after that give out the initial state assumptions as the case may be, then make use of the known conditions and the logic regulations to judge whether the protocol meet the goals or not, the procedure is as follows.

6.4.1 Logical Symbol

Below are logical symbols of BAN logic used in this paper, P and Q are the subjects those are the principles participant in the protocol, while X stands for message and K signify the secret key, X is encrypted with K denoted by $\{X\}_K$.

1. P| ≡ Q: P believes Q
2. P◁ X: P has received message X
3. P | □ X: P has sent message X
4. Q⇒ X: Q has the jurisdiction to X
5. ♯(X): X is fresh
6. $P \overset{K}{\leftrightarrow} Q$: K is the common pre-share key of P and Q

6.4.2 Inference Rule

BAN logic contains message-meaning rules, nonce-verification rule, jurisdiction rules and so forth. seven rules as follow, the messages above the horizontal line are known conditions while below line are the results deduced from the known conditions. Assuming that P and Q are different principals participant, we judge the identities of actors from the encryption key and the content contained in the message. The following are main logical rules.

1. M1: $\frac{P|\equiv P \overset{K}{\leftrightarrow} Q, P \triangleleft \{X\}_{K_X}}{P|\equiv Q|\Box X}$
2. N1: $\frac{P|\equiv \sharp(X), P|\equiv Q|\Box X}{P|\equiv Q|\equiv X}$
3. J1: $\frac{P|\equiv Q \Rightarrow X, P|\equiv Q|\equiv X}{P|\equiv X}$
4. F1: $\frac{P|\equiv \sharp(X)}{P|\equiv \sharp(X,Y)}$
5. B1: $\frac{P|\equiv X, P|\equiv Y}{P|\equiv (X,Y)}$, B2: $\frac{P|\equiv Q|\equiv (X,Y)}{P|\equiv Q|\equiv Y}$

6.4.3 Logical Deduction

6.4.3.1 Protocol Idealization

- MS2:B→ S:$\{A,B,Na,Nb\}_{K_{bs}}$
- MS3:S → B:$\{Na, A \overset{K_{ab}}{\leftrightarrow} B, \sharp(A \overset{K_{ab}}{\leftrightarrow} B)\}_{K_{as}}$, $\{Nb, A \overset{K_{ab}}{\leftrightarrow} B, \sharp(A \overset{K_{ab}}{\leftrightarrow} B), S \overset{KEY}{\leftrightarrow} B, \sharp(S \overset{KEY}{\leftrightarrow} B)\}_{K_{bs}}$
- MS3′:S→ C:$\{Nc,text\}K_{cs}$
- MS4:B→ A: $\{Na,A \overset{K_{ab}}{\leftrightarrow} B,\sharp(A \overset{K_{ab}}{\leftrightarrow} B)\}_{K_{as}}$, $\{Na,Nb,A \overset{K_{ab}}{\leftrightarrow} B\}_{K_{ab}}$
- MS5:A→ B:$\{Nb,A \overset{K_{ab}}{\leftrightarrow} B\}_{K_{ab}}$

The idealization of messages1 is omitted since it does not contribute to the logical properties of the protocol.

6.4.3.2 Initial State Assumptions

P1: $A| \equiv A \overset{K_{as}}{\leftrightarrow} S$

P2: $B| \equiv B \overset{K_{bs}}{\leftrightarrow} S$

P3: $A| \equiv S \Rightarrow A \overset{K_{ab}}{\leftrightarrow} B$

P4: $B| \equiv S \Rightarrow A \overset{K_{ab}}{\leftrightarrow} B$

P5: $B| \equiv S \Rightarrow B \overset{KEY}{\leftrightarrow} S$

P6: $A| \equiv \sharp(Na)$

P7: $B| \equiv \sharp(Nb)$

P8: $S| \equiv \sharp(Ns)$

P11: $S| \equiv A \overset{K_{as}}{\leftrightarrow} S$

P12: $S| \equiv B \overset{K_{bs}}{\leftrightarrow} S$

6.4.3.3 Protocol Annotation

P13: $S \lhd \{A,B,Na,Nb\}_{K_{bs}}$

P14: $B \lhd \{Na, A \overset{K_{ab}}{\leftrightarrow} B, \sharp(A \overset{K_{ab}}{\leftrightarrow} B)\}_{K_{as}}, \{Nb, A \overset{K_{ab}}{\leftrightarrow} B, \sharp(A \overset{K_{ab}}{\leftrightarrow} B), S \overset{KEY}{\leftrightarrow} B, \sharp(S \overset{KEY}{\leftrightarrow} B)\}_{K_{bs}}$

P15: $A \lhd \{Na, A \overset{K_{ab}}{\leftrightarrow} B, \sharp(A \overset{K_{ab}}{\leftrightarrow} B)\}_{K_{as}}, \{Na, Nb, A \overset{K_{ab}}{\leftrightarrow} B\}_{K_{ab}}$

P16: $B \lhd \{Nb, A \overset{K_{ab}}{\leftrightarrow} B\}_{K_{ab}}$

6.4.3.4 Final Faith (Primary Faith and Secondary Faith)

① $A| \equiv A \overset{K_{ab}}{\leftrightarrow} B$

② $B| \equiv A \overset{K_{ab}}{\leftrightarrow} B$

③ $B| \equiv S \overset{KEY}{\leftrightarrow} B$

④ $A| \equiv B| \equiv A \overset{K_{ab}}{\leftrightarrow} B$

⑤ $B| \equiv A| \equiv A \overset{K_{ab}}{\leftrightarrow} B$

6.4.3.5 Derivation Process

1. According to P12, P13 and M1, yields: $S| \equiv B \mid \square \{A,B,Na,Nb\}_{K_{bs}}$
2. According to P2, P14 and M1 yields:
   $B| \equiv S \mid \square \{Nb, A \overset{K_{ab}}{\leftrightarrow} B, \sharp(A \overset{K_{ab}}{\leftrightarrow} B), S \overset{KEY}{\leftrightarrow} B, \sharp(S \overset{KEY}{\leftrightarrow} B)\}_{K_{bs}}$

3. According to P7, F1 yields:
   $B|\equiv \sharp\{Nb, A \overset{K_{ab}}{\leftrightarrow} B, \sharp(A \overset{K_{ab}}{\leftrightarrow} B), S \overset{KEY}{\leftrightarrow} B, \sharp(S \overset{KEY}{\leftrightarrow} B)\}_{K_{bs}}$
4. According to 2, 3 and N1 yields:
   $B|\equiv S|\equiv \sharp\{Nb, A \overset{K_{ab}}{\leftrightarrow} B, \sharp(A \overset{K_{ab}}{\leftrightarrow} B), S \overset{KEY}{\leftrightarrow} B, \sharp(S \overset{KEY}{\leftrightarrow} B)\}_{K_{bs}}$
5. According to 4 and B2 yields: $B|\equiv S|\equiv A \overset{K_{ab}}{\leftrightarrow} B\ B|\equiv S|\equiv B \overset{KEY}{\leftrightarrow} S$
6. According to 4 and B2 yields: $B|\equiv S|\equiv \sharp(A \overset{K_{ab}}{\leftrightarrow} B)\ B|\equiv S|\equiv \sharp(B \overset{KEY}{\leftrightarrow} S)$
7. According to 5, P4, P8 and J1 yields:
   $B|\equiv A \overset{K_{ab}}{\leftrightarrow} B$ ——-② $B|\equiv S \overset{KEY}{\leftrightarrow} B$ ——-③
8. According to P15, P1 and M1 yields: $A|\equiv S|\Box\{Na, A \overset{K_{ab}}{\leftrightarrow} B, \sharp(A \overset{K_{ab}}{\leftrightarrow} B)\}_{K_{as}}$
9. According to P6, P15 and F1 yields: $A|\equiv \sharp(A \overset{K_{ab}}{\leftrightarrow} B)$
10. According to 8, 9 and N1 yields: $A|\equiv S|\equiv \sharp(A \overset{K_{ab}}{\leftrightarrow} B)$
11. According to 10, P3 and J1 yields: $A|\equiv A \overset{K_{ab}}{\leftrightarrow} B$ ——-①
12. According to ②,P16 and M1 yields: $B|\equiv A|\Box A \overset{K_{ab}}{\leftrightarrow} B$
13. According to P7, P16 and F1 yields: $B|\equiv \sharp(A \overset{K_{ab}}{\leftrightarrow} B)$
14. According to 12, 13 and N1 yields: $A|\equiv B|\equiv A \overset{K_{ab}}{\leftrightarrow} B$ ——-④
15. According to ①,P15 and M1 yields: $A|\equiv B|\Box A \overset{K_{ab}}{\leftrightarrow} B$
16. According to P6, P15 and F1 yields: $A|\equiv \sharp(A \overset{K_{ab}}{\leftrightarrow} B)$
17. According to 15, 16 and N1 yields: $B|\equiv A|\equiv A \overset{K_{ab}}{\leftrightarrow} B$ ——-⑤

The analysis above indicates that the design of the protocol is successful and effective.

In conclusion the said protocol judges the freshness of the messages by random number, replay attacks and fake base attack is hold back through demonstration, the parallel session attack and the type-flaw attack is prevented by the different sequence of messages content and the distinct encryption types. The emerging protocol can prevent flooding attack in particular. Assuming that Message2:B → S:A,B,Na,Nb is plain text without encryption, the special attack exist (I -B represents for malicious attackers).

1. A Brodcast:A,Na
2. I -B→ S:A,B,Na,Nb
3. S→ I -B:$\{B, Na, _{K_{ab}}\}_{K_{as}}$,$\{A, Nb, K_{ab}, KEY\}_{K_{bs}}$
4. I -B discard the message

If I -B sends malicious information (A,B,Nb,Na) to S, S cannot aware whether the sender is legitimate nodes or not due to the message is plaintext. Thus S generates $\{B, Nb, K_{ab}\}_{K_{as}}$ and $\{A, Na, K_{ab}, KEY\}_{K_{bs}}$, after received the messages form S, I -B discarded the messages, the control node S cannot be informed that the messages emitted have been discarded throughout, for the computational cost of encrypt in Message3 is much larger in the protocol, therefore if

several malicious nodes sending messages to S in the network, the resources of the hub node S may be exhausted, indeed give rise to paralysis the network, yet the emerging protocol avoids this drawbacks effectively by encrypting Message2.

Conclusion

The article presents an emerging authenticated key exchange protocol for wireless body area network and gives out the security proof by BAN logic, the result reveals that the proposed protocol achieves the stated goals. The new protocol posses several advantages. Good security, it is provided with favourable security performance and capable of resisting sundry common attacks guarantee communication security; concise and efficient, the principals accomplish authentication and generate session key by merely five steps without tanglesome cryptographic operation; resources saving, on account of majority security protocols, timestamps is utilized to guarantee the freshness of message while the intrant principals must keep clock synchronization which is rather untoward, the new protocol adopts random number instead of timestamps, reduced the complex rate of the network as well as lowering the cost. How to design more and fantastic protocols for wireless body area network is the next target for further research.

Acknowledgements This work is supported by National Natural Science Foundation of China (No. 61100232), National Science and Technology Major Project of the Ministry of Science and Technology of China (No. 2013ZX03005007) the Fundamental Research Funds for the Central Universities (No. K5051301012), the 111 Project (B08038).

References

1. Chen H, Shi G (2013) Formal analysis validate an improved NSSK protocol. J Lanzhou Jiaotong Univ. doi:10.3969/j.issn.1001-4373.2013.01.018
2. Chen H, Zhang W (2013) The composition and application of WBAN. Netw Technol. doi:1003-9767-2013-01-0080-02
3. Gao G, Tang J (2013) YAHALOM protocol and its formal analysis based on BAN logic. China Comput Commun. doi:1003-9767-2012-12-0183-02
4. Jin B (2012) The application of BAN logic in the formal protocol analysis. Inf Sci 550025
5. Liu L, Xue X, Luo X, et al (2012) Wireless body area network architecture and the challenge it faced. Comput Knowl Technol 8(29). doi:1009-3044(2012)29-6918-03
6. Ren W (2012) Elementary exploration of the wireless network security problem. Netinfo Secur. doi:10.3969/j.issn.1671-1122.2012.01.003

Chapter 7
Expected Frame Cancellation: A Simulation Study on Performance Influencing Factors

Yao Ming Wu, Zhu Feng, and Zhang Cheng

Abstract Expected frame cancellation is a cross-layer interference cancellation technique proposed to increase the degree of concurrence in WLANs. Using the strong semantic correlation of the control frames exchanged in a typical 802.11 WLAN, a receiving node sometimes is able to know every digits of an incoming interfering frame. Thus it is possible for the receiver to reconstruct the signal of the interfering frame and then linearly cancel it from the receiving streams. In this paper we present our simulation study on the performance influencing factors to this technology, including SINR, frequency and timing differences. It is shown that the signal reconstruction and cancellation method based on the information provided by the preamble can greatly improve the BER performance, especially when the expected interfering frame and the frame to be received are synchronized.

Keywords Expected frame cancellation • WLAN • Simulation study • BER

7.1 Introduction

The hidden and exposed terminal problems are intrinsic to 802.11 based multi-hop WLANs [1]. The distributed coordination function (DCF) is introduced in the IEEE 802.11 standard [2] to resolve the hidden terminal problem. But this method may prevent the exposed node to transmit while in some cases such concurrent transmissions would not cause severe interference on the primer sender–receiver pair [3, 4]. Many enhanced protocols are proposed to solve the issue by introducing some mechanism to allow the exposed node to simultaneously transmit when it detects the transmission will bring spatial reuse benefits [3–7]. Most of these proposals are built on an adapted version of DCF signaling, e.g., carrying more information of neighboring nodes status in the RTS frame and the CTS frame so that the exposed node will know if it is harmful to initiate a concurrent transmission [5].

Y.M. Wu (✉) • Z. Cheng
State Key Laboratory of Integrated Services Networks, Xidian University, Xi'an, China

Z. Feng
Detection and Control Technology Research Institute, The Fourth Academy of CASIC, Beijing, China

J. Mu et al. (eds.), *The Proceedings of the Third International Conference on Communications, Signal Processing, and Systems*, Lecture Notes in Electrical Engineering 322, DOI 10.1007/978-3-319-08991-1_7

When the spatial reuse is high [8], collision will be frequent. In many cases collision is caused by two-way link interference: the DATA frame in one direction and the ACK frame in the reverse direction, and the ACK replied by one receiver would cause collision of the DATA intending to another receiver. MACA-P synchronizes the two concurrent transactions to let two neighboring receivers send ACK simultaneously, avoiding interfering each other [6]. CTMAC leaves enough waiting gaps between handshaking frames to achieve similar results [9]. In recent years some method of solving instead of preventing the collision is brought on to the desk of researchers. The overlapped signal from one receiver front end is said to be separated by vector decomposition [10]. In this way both of the overlapped signals can be received. Such ideas are previously proposed when the two signals are about 10 dB in power difference and capture effects occur, but the power difference is not necessary [10]. A method named ZigZag decoding is proposed [11], in which two frames will be successively decoded if they are collided twice. The only requirement of the two collisions is they have different overlapping parts, which leaves room for signal cancellation recursively.

These previous works show that if one of the interfering frames is known, it is possible for the receiver to cancel out the known one and decode another [12]. No matter what kind of handshaking method it uses, a DCF-like MAC protocol will give neighboring wireless nodes chances to guess what will happen next when it utilizes the 'semantic dependency' of the signaling frames exchanging process. For example, when a node named C hearing another node, namely node A, sending an RTS frame to node B, then it is natural for this node to guess, according to 802.11, a CTS frame will be returned to node A fixed period after the preceding RTS being completed. More precisely, if node C can overhear both the RTS frame sending from A to B and the CTS frame sending from B to A, then it will certainly know every digit of the upcoming ACK frame from B to A after the sending of the data frame from A to B is completed, including its arrival time. In such cases, any node like C could get a chance to 'expect' an interfering frame in an unavoidable upcoming collision, as we will explain more clearly in Part 2. Based on incoming frame predictions, we have proposed a cross-layer MAC protocol to promote spatial reuse. The main benefits of this technique is of collision resolution in a multi-hop WLAN which using the DCF. The system throughput will increase because of the collision resolution method may reduce the rates of retransmissions. In this paper we present simulations and results on the performance of the 'expected frame cancellation'.

The paper is organized as follows. Section 7.1 introduces related works and the backgrounds. Section 7.2 describes the expected frame cancellation technique, puts forward the simulation platform we established, and focuses the on the preamble of the interfering frame. Section 7.3 presents the simulation results about the main concerned factors affecting system performance, namely SNR, frequency and timing differences. A short conclusion is given in the last section.

7.2 Expected Frame Cancellation and the Simulation Platform

According to the semantic correlation, the content of the expected interfering frame is known. Given the known coding scheme and the frame incoming time, the known SYNC words can be slide over the received signal to compute the correlation. The position the peak appears is the accurate position of the expected frame. If the synchronization between the contending nodes is perfect, the reconstruction of the expected frames in samples would be easy. However, there is frequency and timing errors need to be corrected. After ascertaining the position, the frequency error and the timing error, the modulated and coded frame can be reconstructed with ease according to the known content, modulation and coding scheme. Cancelling the reconstructed interference of the expected frame, the remaining signal will be processed normally. This method has an advantage of lowering packet loss during a high spatial reuse MAC transaction. This paper will investigate the influential factors of this method in its BER performance (Fig. 7.1).

As the system diagram shows, the simulation platform using Simulink/Matlab was established. Two random frames are constructed in accordance with 802.11b's data frame format which includes PLCP Preamble, PLCP Header and PSDU. Then they are encoded and modulated using DBPSK, and each bit is spread by an 11-chip Barker code. The sampling rate is eight times of the chip rate. At the receiver, the overlapped signal passes through the channel filter first, which could eliminate some noise brought by the AWGN channel. Next, either the frequency error rectification method or the timing error rectification method in synchronization block is used to detect and correct the error. Then, the receiver begins to find the accurate position of the expected frame as interference detection. Before the sample position obtained, in this simulation system the chip position is acquired first with the help of the known preamble. Next, around the rough sample position (within 800 samples) the searching for the accurate sample position starts. This searching

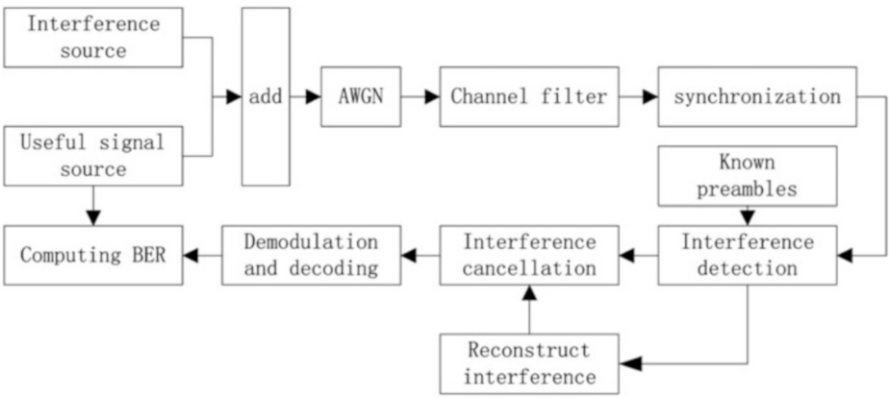

Fig. 7.1 System diagram

scheme decreases the amount of calculation a lot. According to the obtained knowledge including the content of the interference, the starting point, and the modulation and encoding scheme, the interference is to be reconstructed for the following cancellation. After removing the 'expected' interference frame, the rest will be decoded and demodulated. And the final stage of comparing with the sender's signal bits will show the BER performance.

7.3 The Influence of SIR, Frequency and Timing Errors

We analyzed the influence of SIR, relative frequency error and timing error on the BER of the method using extensive simulations. The two sources both transmit 20 8,384 bits long physical frames with 802.11b format in every test. And the BER in our analysis is the mean bit error rate in ten tests. Two models are in our simulation. One is the PID&C (preamble interference detection & cancellation) model, the other is the conventional model which doesn't include interference detection and cancellation blocks.

7.3.1 SINR

Under the 10 dB Gaussian white noise, the BERs of the two models with perfect synchronization are obtained. The simulation result is as follows (Fig. 7.2).

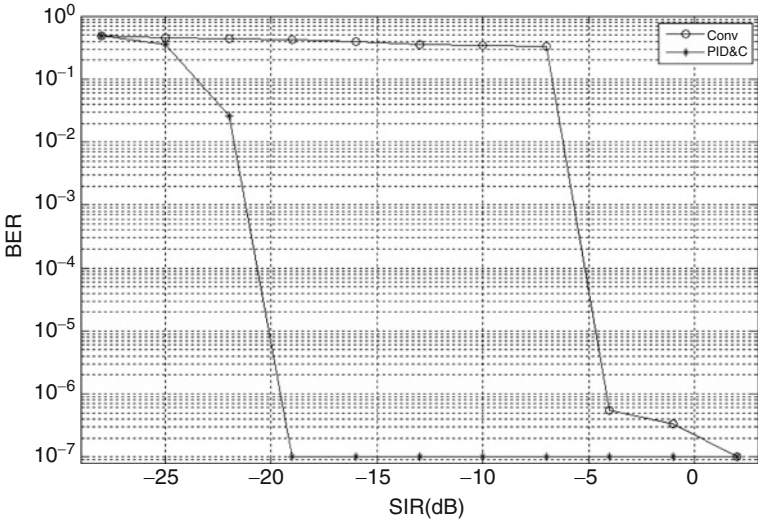

Fig. 7.2 BERs of PID&C and conventional model under different SIRs

When SIR < -19 dB, the PID&C model cannot demodulate the useful interfered signal steadily, because the power of the useful signal is too low. When -19 dB $<$ SIR < -7 dB, the PID&C model can do it well, but the conventional model cannot, since the former could detect and cancel the interference effectively, and the latter is affected seriously by the strong interference. When SIR > -7 dB, both of the two perform well. And if the power of the useful signal keeps on increasing, the performance of the PID&C model will be no better than that of the conventional one, because the locating mistake of the interference will appear.

7.3.2 *Frequency Difference*

To research the influence of frequency difference, 30 and 10 kHz frequency deviations are added to the useful signal and interference signal, respectively. In the PID&C model, the carrier synchronization block (i.e. Costas loop in software) is introduced. Through the simulation, the BERs are obtained.

As Fig. 7.3 shows, the PID&C model cannot demodulate the interfered useful signal steadily when SIR is lower than -22 dB, because the power of the useful signal is too low. But when -22 dB $<$ SIR < -4 dB, the PID&C model can do it, because the receiver is able to detect and eliminate the interference signal effectively. To make a further analysis, the output samples of the Costas loop at this time is shown in Fig. 7.4.

In the part of the useful signal samples which is not interfered, the Costas loop can work out the 10 kHz frequency error accurately, but in the overlapped part, the

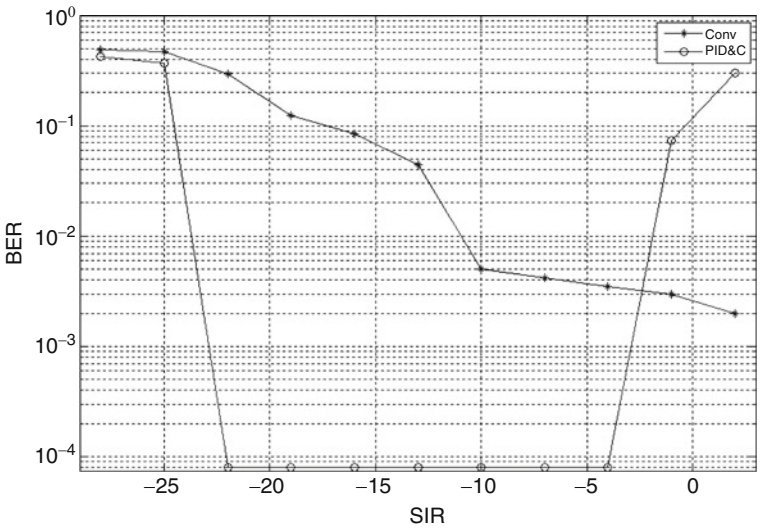

Fig. 7.3 BERs of PID&C and conventional models under constant frequency differences

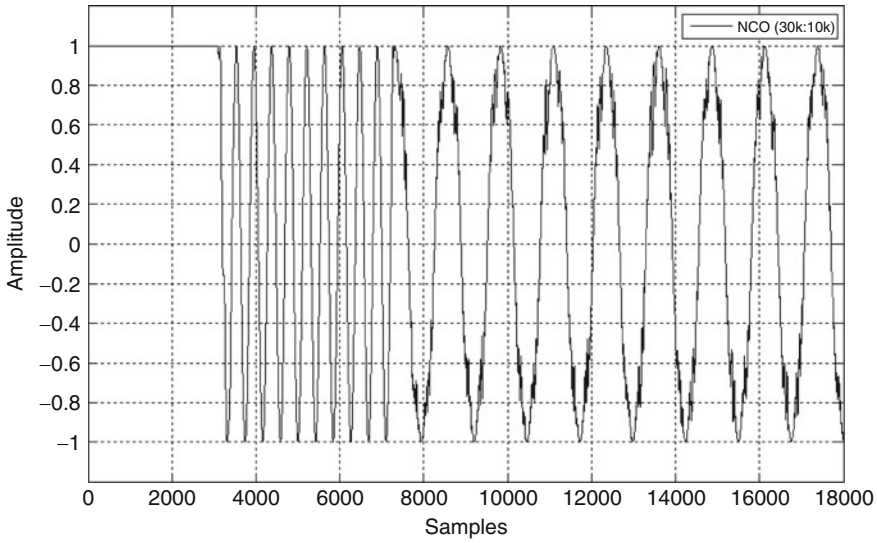

Fig. 7.4 Output samples of the Costas loop

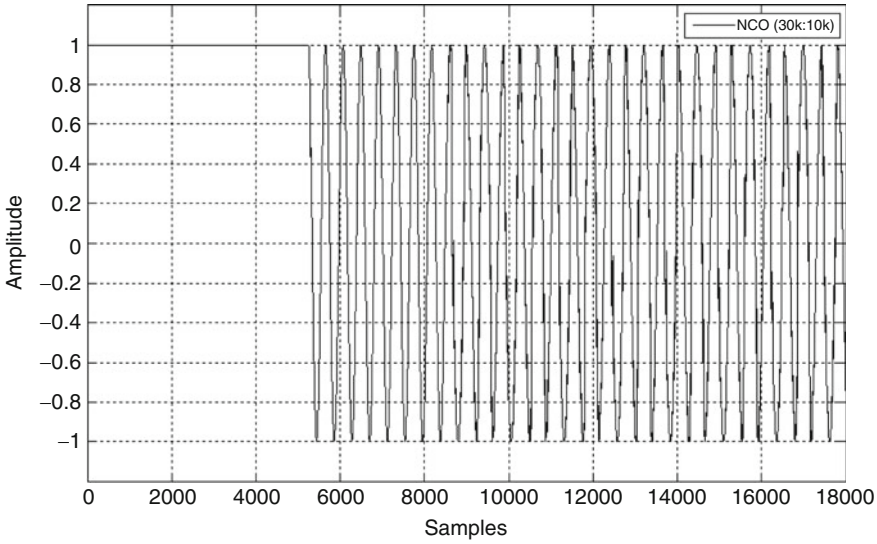

Fig. 7.5 Output samples of the Costas loop when SIR = 2 dB

frequency error estimation output is that of the useful signal (30 kHz). When SIR > -4 dB, the BER of the PID&C model decreases conspicuously. The output samples of the Costas loop at this time shown in Fig. 7.5 can be used to explain it.

The loop is keeping rectifying the 30 kHz frequency deviation, and this is the frequency deviation of the signal with stronger power, known as "the capture effect

of Costas loop". Hence, when the PID&C model detects the interference, the carrier synchronization block uses the frequency error of the useful signal to rectify that of the interference. It leads to the wrong estimation on the position of the interference. On the contrary, for the conventional model, when SIR > -10 dB, the receiver can demodulate the interfered signal with some stability.

7.3.3 *Timing Difference*

The constant timing error and corresponding timing synchronization block (i.e. the improved M&M algorithm) are added to show the results of the error rates as SIR changes in two models.

As Fig. 7.6 shows, when there is constant timing error, the PID&C model doesn't perform well. But through observing the output of the interference detection block, it can be seen that the interference has been detected and cancelled. The reason of wrong demodulation maybe is the improvement of the SIR threshold of correct demodulation by adding the M&M block. When SIR > 25 dB, the receiver performs well, because the SIR is high enough for demodulation after interference being eliminated. But the BER increases quickly when SIR > 27 dB. After the M&M synchronization, the interference is affected by the strong useful signal. It makes the receiver cannot detect the position of interference accurately, and the performance

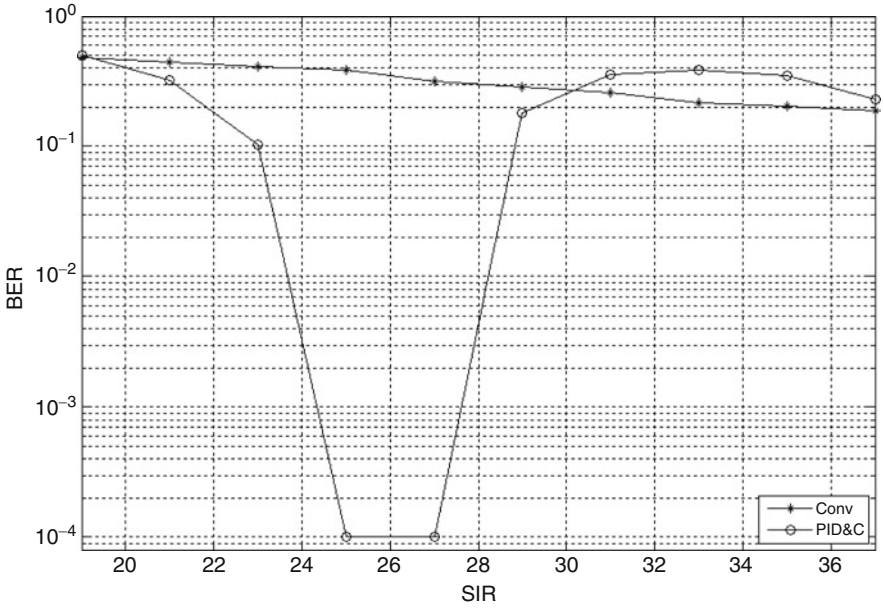

Fig. 7.6 Error rates of PID&C and basic models when timing error exists

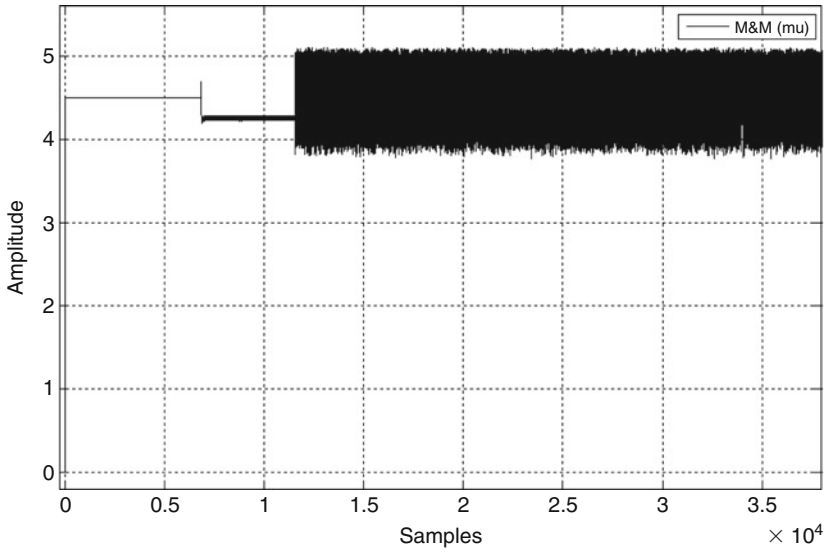

Fig. 7.7 Output samples of the M&M block

of the receiver gets worse. In the conventional model, as the SIR increases, the performance of the receiver doesn't get remarkable improved. By the output samples shown in Fig. 7.7, this phenomenon can be explained. The M&M algorithm could predict the position of timing error in signal which is not interfered. But when the overlapped part enters the M&M block, instead of the position of timing error, the output will be chaotic vibration which makes the interference detection harder.

The M&M timing synchronization algorithm generally used in USRP cannot adjust the timing error effectively, but increase the difficulty of interference cancellation. When this algorithm is in use, the receiver may eliminate the interference in wrong position, which will increase the error rates.

Conclusions

From the results and the analyses, we know that when the synchronization problems are solved, the PID&C model could improve the performance of demodulation. When constant frequency differences added, the PID&C model can significantly improve the performance if the interference signal is stronger. When constant timing differences exist between the two overlapping signals, the receiver in the PID&C model cannot detect and eliminate the interference well because of the unstable timing error adjustment on the interference of the M&M block. Hence, the timing synchronization block is important to PID&C, although this is not a new problem in interference cancellation.

(continued)

(continued)

In a summary, it is shown that the proposed method is capable of cancelling a short previously known interfering frame when it collides with another longer frame in a WLAN. Some timing and frequency differences will not affect the decoding performance severely. With some modification to the DCF mechanism, it is potential to use this method to increase the spatial reuse and thus improve the overall performance.

Acknowledgements The study of the cross layer interference cancellation and the single carrier full duplex technologies is jointly supported by the Natural Science Foundation of China (NSFC 61001129) and the Fundamental Research Funds for the Central Universities.

References

1. Panagiotakis A, Melidis P, Nicopolitidis P, Obaidat MS (2012) Power-controlled reduction of exposed terminals in ad-hoc wireless LANs. In: 2012 international conference on computer, information and telecommunication systems (CITS). IEEE, pp 1–5
2. IEEE Computer Society LAN MAN Standards Committee (1997) Wireless LAN medium access control (mac) and physical layer (phy) specifications.
3. Haiying Z, Jilong L, Mingwu Y (2012) An interference tolerance aware multiple access protocol for wireless networks. In: 2012 international conference on wireless communications and signal processing (WCSP). IEEE, pp 1–6
4. Karn P (1990) Maca-a new channel access method for packet radio. In: ARRL/CRRL Amateur radio 9th computer networking conference, vol 140, pp 134–140
5. Abichar ZG, Chang JM (2005) Conti: constant-time contention resolution for WLAN access. In: Networking 2005. Networking technologies, services, and protocols; performance of computer and communication networks; mobile and wireless communications systems. Springer, pp 358–369
6. Acharya A, Misra A, Bansal (2003) Maca-p: a mac for concurrent transmissions in multi-hop wireless networks. In: Proceedings of the first IEEE international conference on pervasive computing and communications, 2003 (PerCom 2003). IEEE, pp 505–508
7. Shukla D, Chandran-Wadia L, Iyer S (2003) Mitigating the exposed node problem in IEEE 802.11 ad hoc networks. In: Proceedings of the 12th international conference on computer communications and networks, 2003 (ICCCN 2003). IEEE, pp 157–162
8. Ye F, Yi S, Sikdar B (2003) Improving spatial reuse of IEEE 802.11 based ad hoc networks. In: IEEE Global telecommunications conference, 2003 (GLOBECOM'03), vol 2. IEEE, pp 1013–1017
9. Yu W, Cao J, Zhou X, Wang X, Chan KCC, Chan ATS, Va Leong H (2008) A high-throughput mac protocol for wireless ad hoc networks. IEEE Trans Wirel Commun 7(1):135–145
10. Halperin D, Anderson T, Wetherall D (2008) Taking the sting out of carrier sense: interference cancellation for wireless LANs. In: Proceedings of the 14th ACM international conference on Mobile computing and networking. ACM, pp 339–350
11. Gollakota S, Katabi D (2008) Zigzag decoding: combating hidden terminals in wireless networks, vol 38. ACM, New York
12. Bottomley GE (1996) Improved successive cancellation of DS-CDMA signals using signal orthogonalization. In: 1996 5th IEEE international conference on universal personal communications, 1996, Record, vol 1. IEEE, pp 141–144

Chapter 8
On the Security of Wireless Sensor Networks via Compressive Sensing

Ji Wu, Qilian Liang, Baoju Zhang, and Xiaorong Wu

Abstract Due to energy limitation of sensor nodes, the conventional security algorithms with high computation complexity are not suitable for wireless sensor networks (WSNs). We propose a compressive sensing-based encryption for WSNs, which provides both signal compression and encryption guarantees, without introducing additional computational cost of a separate encryption protocol. In this paper, we also discuss the information-theoretical and computational secrecy of compressive sensing algorithm. For proposed WSN, if only a fraction of randomizer bits is stored by an eavesdropper, then the probability that he/she cannot obtain any information about the plaintext approaches zero. Simulation results show a trade-off can be made between the sparsity of a random measurement matrix and the number of sensor nodes used to reconstruct the original signal at the fusion center.

Keywords Wireless sensor networks • Compressive sensing • Perfect secrecy and data reconstruction

8.1 Introduction

Sensor nodes in wireless sensor networks (WSNs) are inherently resource-constrained. These battery-operated nodes have limited processing capability and low storage capacity. In most practical situations, sensor nodes are unattended and even deployed in the hostile environments, which demands careful security consideration in the design of WSNs. Because of those constraints, the conventional security mechanisms with high computation complexity are not suitable for WSNs.

J. Wu (✉) • Q. Liang
Electrical Engineering, University of Texas at Arlington, 416 Yates Street, Arlington, TX 76019, USA
e-mail: ji.wu@mavs.uta.edu; liang@uta.edu

B. Zhang • X. Wu
College of Physics and Electronic Information, Tianjin Normal University, Tianjin 300387, China
e-mail: wdxyzbj@mail.tjnu.edu.cn; wu.xiaorong@sohu.com

J. Mu et al. (eds.), *The Proceedings of the Third International Conference on Communications, Signal Processing, and Systems*, Lecture Notes in Electrical Engineering 322, DOI 10.1007/978-3-319-08991-1_8

In order to design encryption that is suitable for WSNs, it is necessary to be aware about the constraints of the sensor nodes [1].

Our proposed compressive sensing-based encryption for WSNs is quite simple since it provides both signal compression and encryption guarantees, without introducing additional computational cost of a separate encryption protocol. Every sensor node and the fusion center share a short randomly-select secret key, which is independently chosen by each sensor node. We also exploit the difference in computational power and energy between sensor nodes and the fusion center in WSNs. It is assumed that an individual sensor node possesses far less computational power and energy than the fusion center. Then we propose placing the major computations and public key broadcast on the fusion center. The randomizer, which is a burst of random data, is broadcasted by the fusion center and the key used by each sensor node is determined by the secret key and a few randomizer bits. Each sensor node stores the product of key bit with received data if key bit is nonzero. The process is repeated until receiving all the data. Then, every sensor node simply sends the aggregated data to the fusion center.

The remainder of paper is organized as follows. In Sect. 8.2, we introduce the background of compressive sensing. Information-theoretical and computational secrecy of compressive sensing are discussed in Sects. 8.3 and 8.4, respectively. Section 8.5 discusses the signal reconstruction process at the fusion center. Section 8.6 gives numerical results and we draw the conclusion in the last section.

8.2 Compressive Sensing Overview

Compressive sensing (CS) provides a framework for integrated sensing and compression of discrete-time signals that are sparse in a known basis. A rich literature has been published to investigate the theoretic bounds [2–4] as well as its applications in radar sensor network and wireless communication systems [5–14]. Consider a discrete signal $f \in \mathbb{R}^N$ which can be expanded in an orthonormal basis $\Psi = [\psi_1 \ \psi_2 \ \ \cdots \psi_n]$ as follows:

$$f(t) = \sum_{i=1}^{N} x_i \psi_i(t), \tag{8.1}$$

where x is the coefficient sequence of f. Then, the discrete signal f is K-sparse in the domain Ψ, $K << N$, if only K out of N coefficients in the sequence x are nonzero. Sparsity of signal is a fundamental principle used in the compressive sensing.

The new M-length observation vector y can be represented by:

$$y = \Phi f, \tag{8.2}$$

where Φ is an $M \times N$ measurement matrix. It can be re-written as

$$y = \Phi\Psi x. \tag{8.3}$$

With the new observation vector y, the signal f could be recovered using ℓ_1-norm minimization; the proposed reconstruction f^* is given by $f^* = \Psi x^*$, where x^* is the solution to the convex optimization program ($\|x\|_{\ell_1} \equiv \sum_i |x|$)

$$\min_{\tilde{x} \in \mathbb{R}^N} \|\tilde{x}\|_{\ell_1} \text{ subject to } y = \Phi\Psi\tilde{x}. \tag{8.4}$$

That is, among all the objects $\tilde{f} = \Psi\tilde{x}$ consistent with the data, we choose the one with minimal ℓ_1-norm as the original coefficient sequence.

8.3 Information-Theoretic Secrecy of Compressive Sensing

An encryption method provides perfect secrecy only if the ciphertexts appear sufficiently random to the eavesdropper whose computation capability is unbounded. Shannon addressed the security problem by introducing the idea of perfect secrecy [15]. The encryption E is perfectly secret if ciphertext, c, and message, m, are independent, i.e., $\text{prob}(m, c) = \text{prob}(m) \cdot \text{prob}(c)$.

Theorem 1 states compressive sensing-based encryption is perfectly secret if the length of message X goes to infinity.

Theorem 1 *If message* $X = [X_1, X_2, \ldots, X_n]$ *is independent and the length of* X *goes to infinity, then perfect secrecy can be achieved by compressive sensing.*

Proof By the Central Limit Theorem, we know that message X follows Gaussian distribution. Suppose the measurements vector $\mathbf{Y} = \Phi\mathbf{X}$, then we have

$$\begin{aligned}
I(\mathbf{X};\mathbf{Y}) &= H(\mathbf{Y}) - H(\mathbf{Y}|\mathbf{X}) \\
&= H(\mathbf{Y}) - H(\mathbf{Y}|\mathbf{X} = \mathbf{0})P_{\mathbf{x}}(\mathbf{X} = \mathbf{0}) - \\
&\quad \sum_{\mathbf{x} \in \chi, \mathbf{x} \neq \mathbf{0}} H(\mathbf{Y}|\mathbf{X} = \mathbf{x})P_{\mathbf{x}}(\mathbf{X} = \mathbf{x}) \\
&=^{(a)} H(\mathbf{Y}) - \sum_{\mathbf{x} \in \chi, \mathbf{x} \neq \mathbf{0}} H(\mathbf{Y}|\mathbf{X} = \mathbf{x})P_{\mathbf{x}}(\mathbf{X} = \mathbf{x}) \\
&\leq^{(b)} \log|T| - \sum_{\mathbf{x} \in \chi, \mathbf{x} \neq \mathbf{0}} H(\mathbf{Y}|\mathbf{X} = \mathbf{x})P_{\mathbf{x}}(\mathbf{X} = \mathbf{x}) \\
&\leq^{(c)} \log|T| - \log|T - 1| \\
&=^{(d)} 0,
\end{aligned}$$

where

(a) follows from the fact that if message $\mathbf{X}=\mathbf{0}$, then $\mathbf{Y}=\mathbf{0}$ with probability one. Thus, $H(\mathbf{Y}\,|\,\mathbf{X}=\mathbf{0})=0$.
(b) follows from the maximum value of $H(Y)$ equals to $\log|T|$ only if Y is uniformly distributed, i.e., $H(\mathbf{Y})\leq\log|T|$.
(c) follows from the fact that let Φ be a random $m\times n$ matrix and $y=\Phi x$. If $m>2k$ (in our case $m\approx 4k$), then any k-sparse signal has a unique projection with probability one (see Appendix in [16]).
(d) follows that the value of $I(\mathbf{X};\mathbf{Y})$ is always non-negative.

Therefore, we can conclude that as the length of message X goes to infinity ($T\rightarrow+\infty$), $I(\mathbf{X};\mathbf{Y})=0$, and perfect secrecy can be achieved by compressive sensing. □

However, Theorem 2 shows that compressive sensing-based encryption cannot achieve perfect secrecy.

Theorem 2 *For any message $x\in\mathbb{R}^n$, $p_{\mathbf{X}}(\mathbf{x})>0$, and Φ is a $m\times n$ measurement matrix, $\mathbf{Y}=\Phi\mathbf{X}$. Then, perfect secrecy can never be achieved.*

Proof Since $\mathbf{x}=\mathbf{0}$ and $\mathbf{Y}=\Phi\mathbf{X}$, we have $\mathbf{y}=\mathbf{0}$ and $p_{\mathbf{Y}\,|\,\mathbf{X}}(\mathbf{Y}=\mathbf{0}\,|\,\mathbf{X}=\mathbf{0})=1$. It is noted that $\mathbf{y}=\mathbf{0}$ if and only if $\mathbf{x}=\mathbf{0}$. Since $p_{\mathbf{X}}(\mathbf{x})>\mathbf{0}$ for any message $\mathbf{x}\in\mathbb{R}^n$, then we can conclude that $p_{\mathbf{Y}}(\mathbf{Y}=\mathbf{0})<1$. Therefore, $p_{\mathbf{Y}\,|\,\mathbf{X}}(\mathbf{Y}=\mathbf{0}\,|\,\mathbf{X}=\mathbf{0})\neq p_{\mathbf{Y}}(\mathbf{Y}=\mathbf{0})$ and the secrecy of compressive sensing-based encryption is not perfect. □

Although compressive sensing-based encryption cannot achieve perfect secrecy, the security of our proposed compressive sensing-based encryption could approach perfect information-theoretic security, which is proved in [21].

8.4 Computational Secrecy of Compressive Sensing

The secrecy of many currently used encryption is based on the hardness of an underlying computational problem. In our approach, the computational secrecy of compressive sensing-based encryption relies on the computation hardness of finding the correct measurement matrix among a large number of candidates.

Assume an eavesdropper, Eve, has the information of ciphertext y and the sparsity of x. One possible way for Eve is to try all possible measurement matrix Φ and attempt to recover the original data x. If the recovered data is k-sparse, Eve could claim that the plaintext is successfully decrypted.

Lemma 1 shows $\mathrm{rank}(\Phi\,\Psi)=\mathrm{rank}(\Phi)$ if Ψ is a Bernoulli basis matrix.

Lemma 1 *If Φ is a $m\times n$ measurement matrix of rank m and Ψ is a $n\times n$ Bernoulli basis matrix of rank n, then $\mathrm{rank}(\Phi\Psi)=\mathrm{rank}(\Phi)$.*

Proof Since $\mathrm{rank}(\Psi)=\mathrm{n}$, there exist Ψ^{-1} such that $\Psi\,\Psi^{-1}=I$. $\mathrm{rank}(\Phi)=\mathrm{rank}(\Phi\,\Psi\,\Psi^{-1})=\mathrm{rank}\,((\Phi\,\Psi)\Psi^{-1})\leq\mathrm{rank}(\Phi\,\Psi)$. The reverse inequality rank

$(\Phi\ \Psi) \leq \text{rank}(\Phi)$ follows directly from the theorem $\text{rank(AB)} \leq \text{rank(A)}$. Hence, $\text{rank}(\Phi\ \Psi) = \text{rank}(\Phi)$. □

Theorem 3 states if an eavesdropper has the wrong measurement matrix, then the original data x can never be recovered. Here we only consider the case using the Bernoulli sensing matrix, the Gaussian sensing matrix case is discussed in [17].

Theorem 3 *Let Φ and Φ' be the original and generated $m \times n$ matrices with Bernoulli ensembles. For the original k-sparse data x, we have $\mathbf{x} = \Psi\theta$ and $\mathbf{y} = \Phi\mathbf{x}$. Then, for all recovered data $\mathbf{x}'$ and generated matrix Φ' such that $\mathbf{x}' = \Psi\theta'$ and $\mathbf{y} = \Phi'\mathbf{x}'$ satisfy $||\theta'||_0 = m$ if $m > k$, which indicates the original data x can never be recovered.*

Proof Since Ψ is a orthonormal Bernoulli sensing matrix, $\text{rank}(\Psi) = \text{n}$,

$\text{rank}(\Phi\ \Psi) = \text{rank}(\Phi'\Psi) = \text{m}$ if $m \leq n$, which directly follows from Lemma 1. Without loss of generality, we assume Ψ is the identity matrix and $\mathbf{y} = \Phi\ \theta$.

Let Φ'_m be a matrix obtained by taking m columns of Φ', which are linearly independent since $\text{rank}(\Phi'_m) = \text{m}$. We can use matrix inversion to uniquely determine m entries of θ' that satisfy $\mathbf{y} = \Phi'\theta'$.

Then, we prove a p-sparse ($p < m$) solution ϑ that satisfies $\mathbf{y} = \Phi'\vartheta$ does not exist by way of contradiction. If $\mathbf{y} = \Phi'\vartheta$, then we have $\mathbf{y} = \Phi'\theta' = \Phi'\vartheta$. Since, by assumption, θ' and ϑ are m-sparse and p-sparse solutions ($p < m$), it is easy to show that m columns of the sensing matrix Φ' can be represented by only p columns of Φ', where $p < m$. It contradicts the conclusion in Lemma 1 that $\text{rank}(\Phi')$=m and this happens with probability zero. Hence, a p-sparse ($p < m$) solution x' that satisfies $\mathbf{y} = \Phi'\mathbf{x}'$ does not exist.

Assume $\mathbf{y} = \Phi'\mathbf{x}' = \Phi\mathbf{x}$ with $||\theta'||_0 = m$ and $||\theta||_0 = k$ ($m > k$). It implies that $(m - k)$ columns of Φ' are linearly dependent, which contradicts the assumption we made above. Therefore, $\mathbf{x}' \neq \mathbf{x}$ and the eavesdropper cannot recover the original data x. □

The amount of computation required to find the correct measurement matrix is proportional to the number of candidates. Once an eavesdropper recovers a k-sparse vector using a measurement matrix, he/she could claim it is correct. Thus, compressive sensing-based encryption only provides computational secrecy.

8.5 Data Reconstruction at the Fusion Center

Due to the energy constraint and limited computation capability of sensor nodes, our proposed compressive sensing-based encryption for WSNs is quite simple. Please refer to [21] for more details. In many situations, eavesdroppers will not only eavesdrop sensor nodes but also inject some bogus data to the network as well as compromise certain sensor nodes, which can degrade the performance of data reconstruction at the fusion center. In this section, we will derive the relation

between the reconstruction error and uncompromised sensor nodes with different sparsity of measurement matrices. In our study, we prove Theorem 4. However, due to the limited space, we will not present the proof in this paper.

Theorem 4 states that if nearly sparse data satisfies certain conditions, one can produce an estimate of data within a small error in the existence of bogus data, and the performance is comparable to that of the best k-term approximation.

Theorem 4 *Suppose data* $\mathbf{u} \in \mathbb{R}^n$, $\frac{||\mathbf{u}||_\infty}{||\mathbf{u}||_2 \leq M}$, *where* $||\mathbf{u}||_\infty = \max(|x_1|, |x_2|, \ldots, |x_n|)$ *and measurement matrix* $\Phi \in \mathbb{R}^{m \times n}$ *with entries as shown in* [21]. *h be the bogus data that disseminated by the attacker and the corresponding transformation coefficientse* $= [e_1, e_2, \ldots, e_n]$. *Let* $\frac{||\theta||_2}{|e_i|} = \frac{1}{\gamma}$, $\mathbf{x} = \frac{1}{\sqrt{m}} \Phi \mathbf{u}$ *and* $\theta = \Psi \mathbf{u}$. *If the k largest transform coefficients in magnitude gives an approximation error* $||\theta - \theta_{app}||_2^2 \leq \eta ||\theta||_2^2$, *then one can produce an estimate with m uncompromised sensor nodes such that*

$$||\mathbf{u} - \widehat{\mathbf{u}}||_2^2 \leq (1 + \varepsilon)\eta ||\mathbf{u}||_2^2$$

with probability $\geq 1 - \delta$, *where* $\delta = ne^{-\frac{(\sqrt{3+\frac{\varepsilon\eta}{k}} - \gamma - \sqrt{3})^2 \tau m}{8+4(s-3)M^2}} (0 < \tau < \frac{1}{4})$.

8.6 Numerical Results

We use simulations to investigate the effects of various parameters on the data reconstruction process. Figure 8.1 compares the approximation error of data versus the number of selected sensor nodes with various sparsity s of a random measurement matrix. Note that $1/s = 1$ implies the conventional compressive sensing with Bernoulli ensemble is employed. It is noted that the performance is almost the same for sparsity $s = 1, 3$ and 5. This is because in our case $M = 0.458$, which is very small and the length of data is 2,000, which is comparably large. From Theorem 4, we can see the extra approximation error introduced by the sparsity of the measurement matrix could be ignored.

Figure 8.2 compares the approximation error of data versus the number of selected sensor nodes when $s = 3$ and a different number of compromised sensor nodes. As we can expect from the theoretical analysis, the fusion center could achieve better performance with larger SIR, smaller value of sparsity, s, and less sensor nodes that is compromised by the eavesdropper.

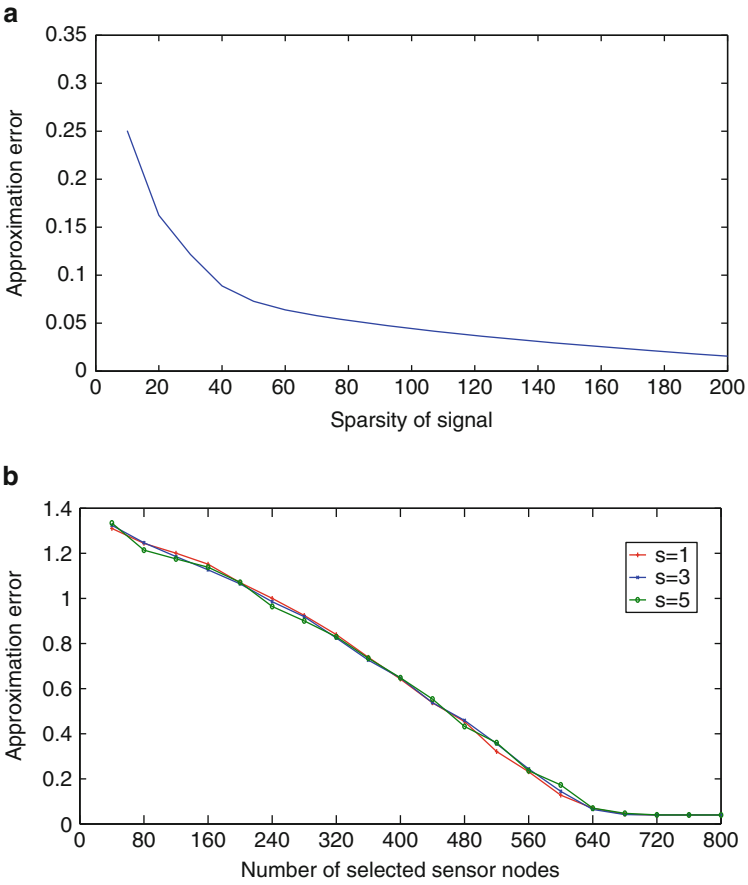

Fig. 8.1 The approximation error of data $\frac{||u-\widehat{u}||_2^2}{||u||_2^2}$ versus (**a**) the number of sensor nodes queried (**b**) the number of sensor nodes queried and various sparsity of random measurement matrix in normal condition

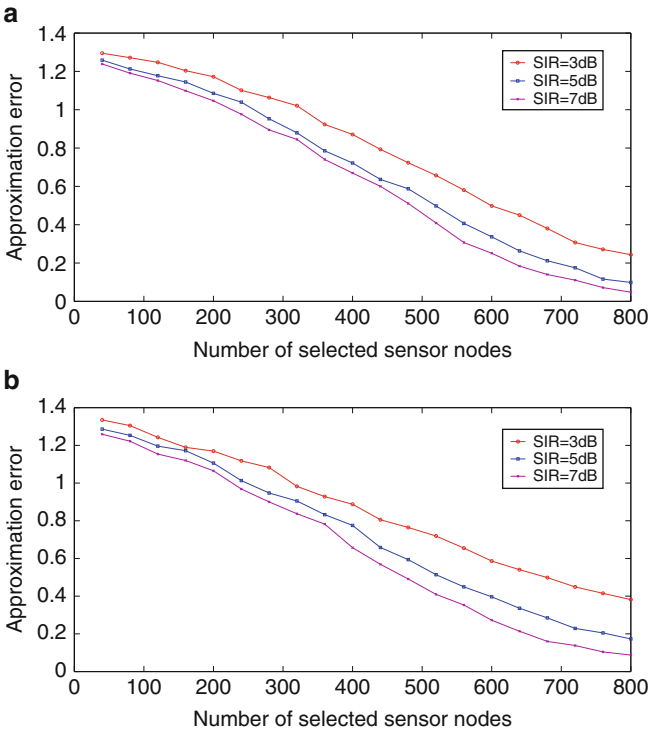

Fig. 8.2 The approximation error of data $\frac{||u-\widehat{u}||_2^2}{||u||_2^2}$ versus the number of sensor nodes queried with (**a**) 10 % and (**b**) 30 % of sensor nodes are compromised by the eavesdropper

Conclusions

Due to limited energy and physical size of the sensor nodes, the conventional security mechanisms with high computation complexity are not feasible for WSNs. This motivates us to design a compressive sensing-based encryption scheme for WSN with simple structure. We also studied the information-theoretic and computational secrecy of compressive sensing-based encryption scheme.

Simulation results show a trade-off can be made between the sparsity of a random measurement matrix and the number of uncompromised sensor nodes used to reconstruct the original signal.

Acknowledgements This work was supported in part by U.S. Office of Naval Research under Grants N00014-13-1-0043, N00014-11-1-0071, N00014-11-1-0865, and U.S. National Science Foundation under Grants CNS-1247848, CNS-1116749, CNS-0964713.

References

1. Carman DW, Krus PS Matt BJ (2000) Constraints and approaches for distributed sensor network security. Technical Report 00-010, NAI Labs, Network Associates Inc., Glenwood
2. Chen J, Liang Q (2011) Rate distortion performance analysis of compressive sensing In: IEEE Globecom. IEEE, Houston
3. Chen J, Liang Q, Paden J (2012) Compressive sensing analysis of synthetic aperture radar raw data. In: IEEE international conference on communications. IEEE, Ottawa
4. Kirachaiwanich D, Liang Q (2011) Compressive sensing: to compress or not to compress. In: Asilomar conference on signals, systems, and computers. Pacific Grove
5. Xu L, Liang Q (2012) Compressive sensing in radar sensor networks using pulse compression waveforms. In: IEEE International conference on communications. IEEE, Ottawa
6. Xu L, Liang Q, Cheng X, Chen D (2013) Compressive sensing in distributed radar sensor networks using pulse compression waveforms. EURASIP J Wirel Commun Netw. doi:10.1186/1687-1499-2013-36
7. Xu L, Liang Q, Zhang B, Wu X (2012) Compressive sensing in radar sensor networks for target RCS value estimation. In: IEEE Globecom, workshop on radar and sonar networks. IEEE, Anaheim
8. Wu, J, Wang W, Liang Q, Wu X, Zhang B (2012) Compressive sensing-based signal compression and recovery in UWB wireless communication system. Wiley Wirel Commun Mob Comput. doi:10.1002/wcm.2228
9. Wu, J, Wang W, Liang Q, Zhang B, WU X (2013) Compressive sensing based data encryption system with application to sense-through-wall UWB noise radar. Wiley Secur Commun Netw. doi:10.1002/sec.670
10. Wu J, Liang Q, Cheng X, Chen D, Narayanan R (2012) Amplitude based compressive sensing for UWB noise radar signal. In: IEEE Globecom, workshop on radar and sonar networks. IEEE, Anaheim
11. Wu J, Liang Q, Kwan C (2012) A novel and comprehensive compressive sensing-based system for data compression. In: IEEE Globecom, workshop on radar and sonar networks. IEEE, Anaheim
12. Liang Q, Ji Wu, Cheng X, Chen D, Liang J (2012) Sparsity and compressive sensing of sense-through-foliage radar signals. In: IEEE International conference on communications. IEEE, Ottawa
13. Liang Q (2011), Compressive sensing for synthetic aperture radar in fast-time and slow-time domains. In: Asilomar conference on signals, systems, and computers. Pacific Grove
14. Liang Q (2010) Compressive sensing for radar sensor networks. In: IEEE Globecom IEEE, Miami
15. Shannon CE (1949) Communication theory of secrecy systems Bell Syst Tech J 28(4):656–715
16. Weiss Y (2007) Learning compressed sensing
17. Rachlin Y, Baron D (2008) The secrecy of compressed sensing measurements. In: 46th annual Allerton conference on communication, control, and computing, pp 813–817
18. Achilioptas D (2003) Database-friendly random projections: Johnson-Lindenstrauss with binary coins. J Comput Syst Sci 66(4):671–687
19. Griffin A, Panagiotis T (2007) Compressed sensing of audio signals using multiple sensors. Reconstruction 3(4):5
20. Maurer UM (1992) Conditionally-perfect secrecy and a provably-secure randomized cipher J Cryptol 5(1):53–66
21. Wu J, Liang Q, Zhang B, Wu X (2013) Security analysis of distributed compressive sensing-based wireless sensor networks. In: Second international conference on communications, signal processing and systems

Chapter 9
Home Area Network Security in Smart Grid: A Hybrid Model of Wireless and Power Line Communications

Zhuo Li, Qilian Liang, Baoju Zhang, and Xiaorong Wu

Abstract Traditionally, jamming to the wireless in-home system is a fatal threat for Smart Grid communications, which impedes the two-way data transmission between electric devices and the smart meter, and thus deteriorates the reliability of the in-home communication of Smart Grid. To enhance Home Area Network (HAN) security for Smart Grid application, in this paper, orthogonal frequency division multiplexing (OFDM)-based power line (PL) system is incorporated into HAN, and a hybrid model of PL and wireless communications are proposed with transmit diversity. For the combinational model with transmit diversity, Alamouti code is employed at the transmitter part. Simulation results validate the feasibility of the presented combinational solution, and furthermore show that the hybrid model could tolerate jamming to the wireless system effectively.

Keywords Smart Grid security • Power line communications • OFDM • Diversity

9.1 Introduction

Smart Grid, which is achieved by overlaying the communication infrastructure with an electrical system infrastructure, is considered as a network of many systems and subsystems which are interconnected intelligently to provide cost-effective and reliable energy supply for increasing demand response [1].

Security is a critical as well as challenging issue in Smart Grid communications, especially within the scope of in-home system, where the HAN is subject to security threat either from an eavesdropper or from a PHY jamming. With a low-level security, the eavesdropper may easily obtain customers' private information [2]. On

Z. Li (✉) • Q. Liang
Department of Electrical Engineering, University of Texas at Arlington, Arlington, TX, USA
e-mail: zhuo.li@mavs.uta.edu; liang@uta.edu

B. Zhang • X. Wu
College of Physics and Electronic Information, Tianjin Normal University, Tianjin, China
e-mail: wdxyzbj@mail.tjnu.edu.cn; wu.xiaorong@sohu.com

J. Mu et al. (eds.), *The Proceedings of the Third International Conference on Communications, Signal Processing, and Systems*, Lecture Notes in Electrical Engineering 322, DOI 10.1007/978-3-319-08991-1_9

the other hand, the PHY jamming attack will deteriorate the availability of the communication channel. With jamming, the wireless channel would be sensed "busy" before data transmission between in-home devices and the smart meter is initiated, or the transmitted data could be distorted by the jamming signals. Therefore, PHY jamming critically reduces the stability and reliability of Smart Grid.

In order to enhance the reliability, stability, and security of the HAN in Smart Grid, a combination of advanced communication techniques, ranging from fiber optics to wireless and to wireline, as well as a hybrid architecture for Smart Grid, are highly required. Wireless communications have some advantages over PLC, such as low-cost infrastructure, connection simplicity, and high mobility, while wireless communications are vulnerable to environmental effects and also PHY attacks. However, PL communication has always been a promising technique for the communication with the smart meter, which is treated as the bridge between user behavior and power consumption metering for Smart Grid [3].

In the existing literatures, Li et al. investigated the performance improvement by introducing WiFi Direct as well as multiuser selection scheme in HANs [4–7]. The PL communication was validated as a good candidate for Smart Grid application in [8]. Home Plug Green PHY^{TM} has emerged as the leading Specification for implementing Smart Grid functionality across HAN PL-based networks [9]. Korki pointed out that the performance of the PL system are affected by noise and multipath propagation in the PL channel [10]. In addition, the Middleton's Class A model was employed as the noise in the simulation to evaluate the performance of the PL communication network. A classic multipath model for the PL channel was presented by Zimmermann, which was based on fundamental physical effects, and was analyzed by numerical measurements [11]. Furthermore, it was concluded that the average channel gain for PL communication is lognormally distributed [12]. Lai and Messier evaluated the performance of the wireless and PL diversity channel by applying maximum ratio combining (MRC) at the receiver part [13], but multipath propagation and attenuation were not considered in the evaluation, and the PL channel was only supposed to be static.

Based on the above considerations, we take an in-depth look at the characteristics of wireless and PL communications of in-home system for Smart Grid application, and propose a hybrid model with transmit diversity, under the environment of a potential jamming attack to the wireless channel. Since the reliability of Smart Grid directly relies on the performance on the communication infrastructure [14], which could be evaluated by bit error rate (BER), BER of the proposed hybrid model are evaluated and compared.

The rest of this paper is organized as follows: Sect. 9.2 presents the combinational model of OFDM-based wireless and PL communications with Alamouti-code transmit diversity. Characteristics of both the wireless channel and PL channel, the noises in these two channels, and the jamming signals emitted to the wireless system are presented in Sect. 9.3, followed by Monte-Carlo simulation results in Sect. 9.4; this paper finishes with a concluding discussion in section "Conclusion".

9.2 Hybrid Model with Alamouti-Code Transmit Diversity

Since OFDM technique is used in both wireless system and PL system, the same OFDM symbols are generated at the transmitter part, which are thus up-converted to the wireless channel (2.4 GHz) and the PL channel (2–30 MHz), separately. For the hybrid model with transmit diversity, Alamouti scheme is adopted as the space time block code (STBC), and the desired transmission data are decoded using maximum likelihood (ML) detector.

Figure 9.1 shows the hybrid model of OFDM-based wireless and PL communications with transmit diversity. At the transmitter part, the same OFDM symbols are generated, and thus transmitted through wireless channel and PL channel by Alamouti code. At the receiver part, only one receiver with ML detector is used to recover the transmitted OFDM symbols. At a given OFDM symbol period t_{2k}, two generated OFDM symbols $s[2k]$ and $s[2k+1]$ are simultaneously transmitted to the wireless channel and the PL channel. During the next OFDM symbol period t_{2k+1}, $-s^*[2k+1]$ is up-converted to the wireless channel while $s^*[2k]$ is up-converted to the PL channel. At the receiver, the received OFDM symbols from the wireless channel and the PL channel are combined to get:

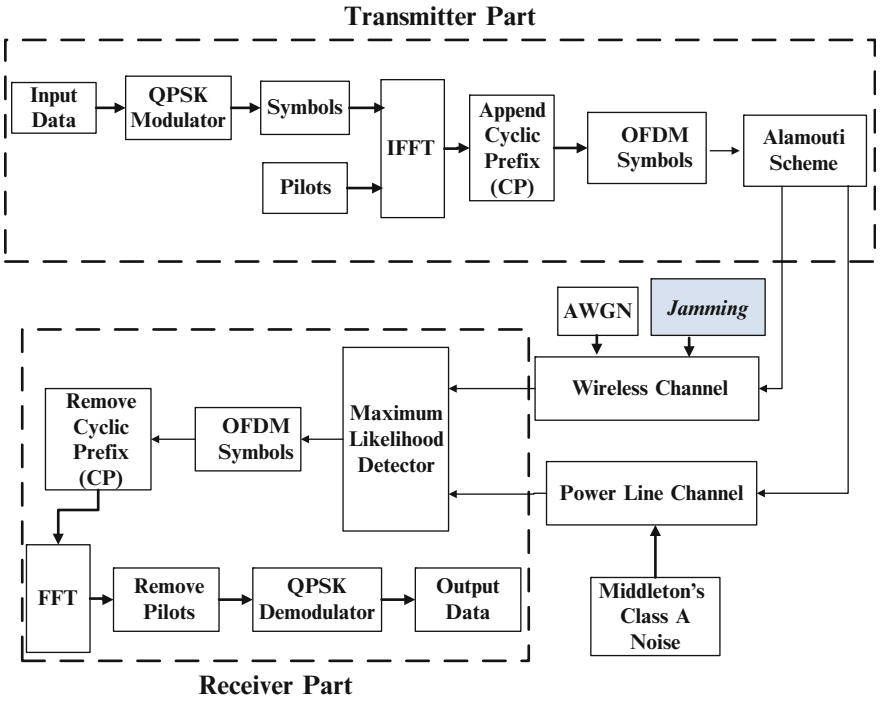

Fig. 9.1 The hybrid model with transmit diversity

$$r[2k] = s[2k]h_{RF}[2k] + s[2k+1]h_{PL}[2k] + j[2k] + n_{RF}[2k] + n_{PL}[2k] \tag{9.1}$$

$$r[2k+1] = -s^*[2k+1]h_{RF}[2k] + s^*[2k]h_{PL}[2k] + j[2k+1] + n_{RF}[2k+1] + n_{PL}[2k+1] \tag{9.2}$$

where h_{RF} and h_{PL} are the wireless channel and the PL channel respectively, and the fading across two adjacent OFDM symbols are assumed to be constant. j is the jamming signal added to the wireless channel. n_{RF} and n_{PL} are the noise in the wireless channel and the PL channel. The received OFDM symbols in (9.1) and (9.2) are thus sent to ML detector, and the desired transmitted OFDM symbols are estimated as[15]:

$$\tilde{s}[2k] = h_{RF}^*[2k]r[2k] + h_{PL}[2k]r^*[2k+1] \tag{9.3}$$

$$\tilde{s}[2k+1] = h_{PL}^*[2k]r[2k] - h_{PF}[2k]r^*[2k+1] \tag{9.4}$$

9.3 Hybrid Model Characteristics

This section renders an in-depth investigation of the properties of the hybrid models of OFDM-based wireless and PL communications, including the characteristics of wireless and PL channels, noises in these two channels, as well as jamming to the wireless channel.

9.3.1 Channel Characteristics

Generally, Rayleigh fading is a statistical model to describe signal attenuation over a non-LOS wireless channel environment. In this paper, Rayleigh flat fading channel is adopted as the wireless channel in the hybrid architectures, and the magnitude of the wireless channel follows Rayleigh distribution.

The PL channel differs from the wireless channel considerably in topology, structure, and physical properties. Zimmermann proposed a multipath model for the PL channel based on physical signal propagation effects including branches and impedance mismatching [11]. The complex frequency response that describes the typical transfer characteristics of PL channel ranging from 500 kHz to 20 MHz is:

$$H_{PL}(f) = \sum_{i=1}^{N_p} g_i \cdot e^{-(\alpha_0+\alpha_1 f^k)d_i} \cdot e^{-j2\pi f(d_i v_p)} \tag{9.5}$$

where i is the number of the path, and the path with the shortest delay has index $i = 1$; N_p is the total number of paths of the PL channel; α_0 and α_1 are attenuation parameters; k is the exponent of the attenuation factor, and the typical values are between 0.5 and 1; f is the operating frequency of the PL channel; d_i is the distance for path i; v_p is the propagation velocity along the PL cable, and v_p is calculated by $v_p = ce$, where c is the speed of light, and e is the dielectric constant of the PL cable, so that the term $d_i v_p$ can be denoted as the time delay for path i, namely τ_i; g_i the is the weighting factor for path i, and Galli [12] points out that the path amplitude of the PL channel is log-normally distributed;

9.3.2 Noise Characteristics

The wireless channel mainly experiences a thermal noise that is generally modeled as addictive white Gaussian noise (AWGN). But as to the PL channel, not only background noise, but also impulsive noise exist in power lines, so that AWGN is not suitable to represent the PL noise any more. The PDF of impulsive noise can be expressed as a sum of Gaussian functions with different variances [16]. The Middleton's Class A model is employed in this paper to characterize the PL noise, and the probability density function (PDF) of Middleton's Class A model is given as:

$$p_{n_{PL}}(z) = \sum_{m=0}^{\infty} \frac{e^{-A}A^m}{m!} \frac{1}{\sqrt{2\pi\sigma_m^2}} \exp(-\frac{z^2}{2\overset{2}{\underset{m}{\sigma}}}) \tag{9.6}$$

where

$$\sigma_m^2 = (\sigma_g^2 + \sigma_i^2)\frac{mA + \Gamma}{1 + \Gamma} \tag{9.7}$$

is the variance represented by a weighted sum of Gaussian distribution.

9.3.3 Jamming Characteristics

Jamming is defined as the act of deliberately directing electromagnetic energy towards an RF communication system in an attempt to disrupt or prevent signal transmission, and is viewed as a special case of denial of service (DoS) attacks.

In this paper, a random complex Gaussian signal $P(Jam)$ is selected as jamming which is inserted to the wireless channel with a certain probability in time domain.

9.4 Simulation and Results

Considering the vulnerability of the wireless system to the security threat from jamming, the in-home PLC system is incorporated into the HAN for Smart Grid. In this section, BER performance of the hybrid architectures presented in Sect. 9.2 is investigated by Monte-Carlo simulation. At the transmitter part, QPSK is employed to constellate the input data bits into complex symbols, which are thus assembled into 52 OFDM subcarriers, and the symbol duration is 4×10^{-6} s. Twelve pilots are inserted to mitigate intercarrier interference (ICI) and the FFT size is 64. The size of cyclic prefix (CP), which effectively eliminates intersymbol interference (ISI), is 16. In the simulation, Rayleigh flat fading channel is generated by Jake's model method, with the maximum Doppler shift as 100 Hz. For the signal propagation along PL cables, the OFDM symbols generated at the transmitter are up-converted to the 3 MHz four-path PL channel, in which the attenuation parameters α_0 and α_1 are -2.03×10^{-3} and 3.75×10^{-7}; the exponent of the attenuation factor is 0.7; the lengths of the four paths are set as 10, 10.3, 10.6, and 11 m; the dielectric constant of the PL cable is 1.4. GIR of the Middleton's Class A noise is set as 0.01. In addition, the channel side information (CSI) is assumed to be known at the receiver. Thus in the simulation, the channel equalization is simply achieved by removing the channel information from the data after receive diversity processing.

For the combinational model with Alamouti-code transmit diversity, Fig. 9.2 shows its BER performance with three different values of E_bN_{0PL}. The three solid lines are with no jamming to the wireless channel, and the three dashed plots are with a potential jamming of $P(Jam) = 2\,\%$ and $SJR = 5$ dB. For the PL channel, the impulsive index A is still 0.3. Figure 9.3 illustrates the impact of Middleton's Class A noise in the PL channel on the BER performance of the hybrid model. The solid lines are the BER performance with no jamming added to the wireless channel, but for the PL channel, E_bN_{0PL} is set to be 15 dB, and A is selected as 1, 0.3, and 0.1, which indicate various probabilities of pulses overlapping in time. When the wireless channel experiences a jamming of $P(Jam) = 2\,\%$ and $SJR = 5$ dB, the three BER plots totally overlap no matter what the value of A is.

Remark 1. An interesting observation from Fig. 9.3 is that as A increases BER decreases. This could be explained by the property of the impulsive index A, which is mentioned in Sect. 9.3.2. Large A indicates that the statistics of Middleton's Class A noise approaches Gaussian distribution, while small A means that the noise in the PL is more like impulsive noise. For $A = 1$, approximately 1 dB gain is obtained at $BER = 2 \times 10^{-4}$ compared to $A = 0.3$, and 3 dB gain compared with $A = 0.1$.

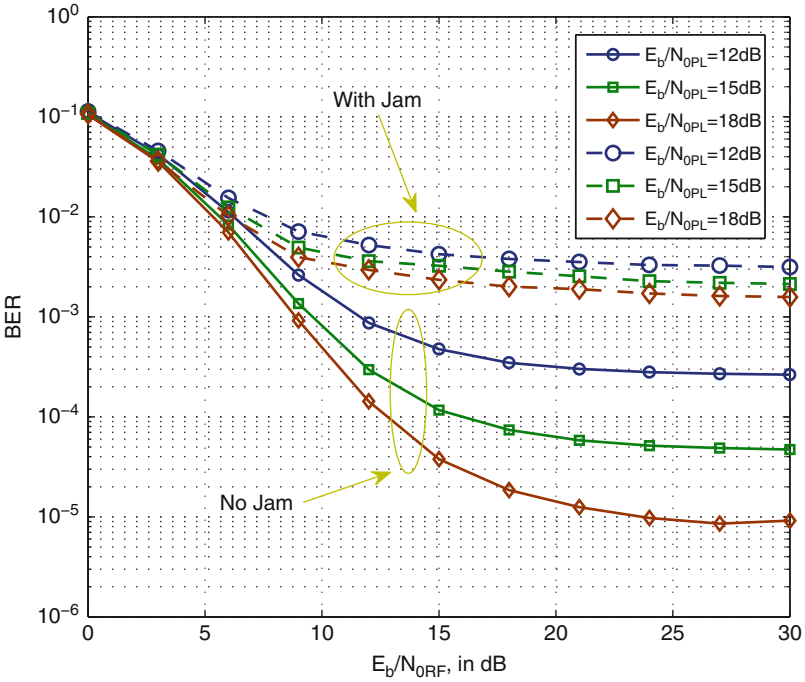

Fig. 9.2 BER of the hybrid model with transmit diversity, $P(Jam) = 2\,\%$, $A = 0.3$, and $SJR = 5$ dB

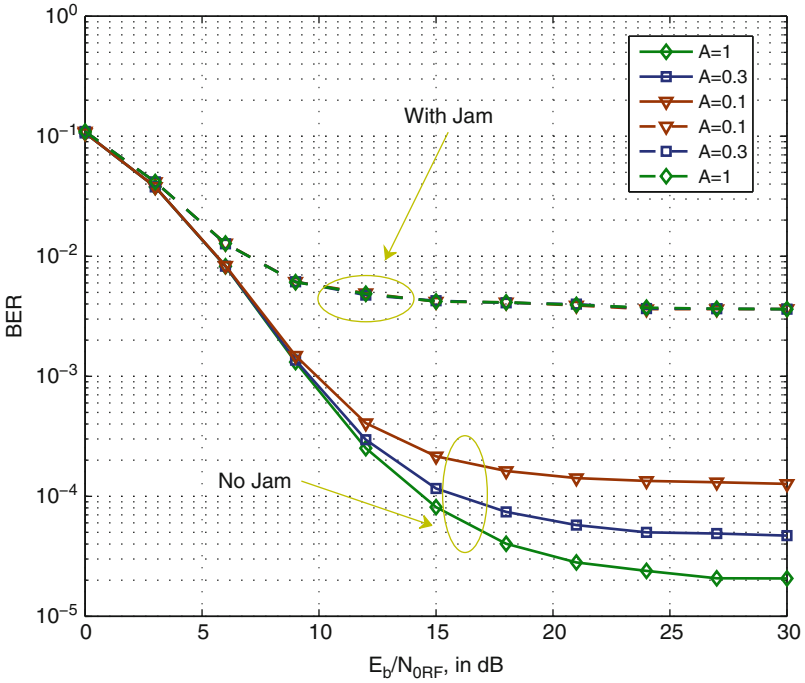

Fig. 9.3 BER comparison of hybrid models, $P(Jam) = 2\,\%$, and $SJR = 5$ dB

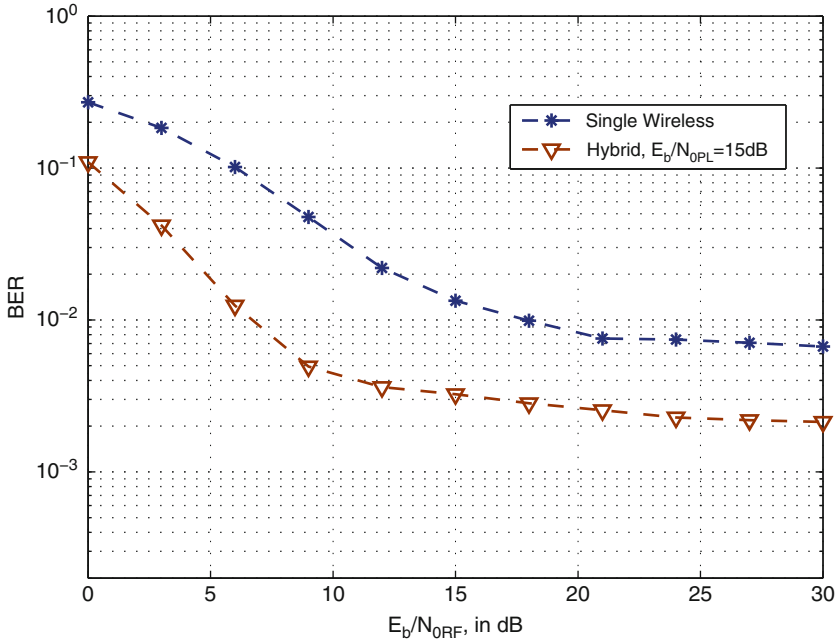

Fig. 9.4 BER comparison of hybrid models, $P(Jam) = 2\,\%$, and $SJR = 5$ dB

Figure 9.4 is the BER comparison of a single wireless communication system, and the hybrid model of wireless and PL communication systems with transmit diversity. The wireless channels are all threatened by a potential jamming of $P(Jam) = 2\,\%$ and $SJR = 5$ dB. It is shown that the hybrid model with Alamouti-code transmit diversity maintains BER improvement over the single wireless system.

Conclusion

In this paper, a combination of the OFDM-based wireless communication and the existing in-home PL system is proposed as a hybrid HAN for Smart Grid. Particularly, Alamouti-code is adopted for transmit diversity. Monte-Carlo simulation results show that the proposed hybrid structure effectively enhances the BER performance of the HAN, even when the wireless channel experiences a potential jamming. The combination of wireless communication and PL communication provides a new concept of the reliable and secure HANs for Smart Grid, with the advantages as:

(1) *Low cost*: due to the ubiquity of power lines and wall outlets, the combinational structures of wireless communication and the existing PL networks in HANs for Smart Grid are cost-effective;
(2) *Easy to implement*: in the hybrid model with Alamouti-code transmit diversity, only one receiver is required to recover the transmitted signals;

(continued)

(continued)

(3) *High security and reliability*: the hybrid model tolerate jamming to the wireless channel well, provide a reliable communication system, and thus the security is guaranteed in HANs for Smart Grid.

Acknowledgements This work was supported in part by U.S. Office of Naval Research under Grants N00014-13-1-0043, N00014-11-1-0071, N00014-11-1-0865, and U.S. National Science Foundation under Grants CNS-1247848, CNS-1116749, CNS-0964713.

References

1. Hossain E, Han Z, Poor HV (2012) Smart grid communications and networking. Cambridge University Press, New York, p 6
2. Li H, Lai L, Zhang W (2011) Communication requirement for reliable and secure state estimation and control in smart grid. IEEE Trans Smart Grid 2(3):476–486
3. Zaballos A, Vallejo A, Selga JM (2011) Heterogeneous communication architecture for the smart grid. IEEE Netw 25(5):30–37
4. Li Z, Liang Q (2013) Performance analysis of multiuser selection scheme in dynamic home area networks for smart grid communications. IEEE Trans Smart Grid 4(1):13–20
5. Li Z, Liang Q, Cheng X (2014) Emerging WiFi-direct technique in home area networks for smart grid power consumption and outage performance. Ad Hoc Networks J 22:61–68
6. Li Z, Liang Q, Mu J et al (2013) The hybrid architecture of wireless and power line communications in HANs for smart grid security. Secur Commun Netw. doi:10.1002/sec. 763
7. Li Z, Liang Q, Cheng X, Znati T (2012) Outage performance evaluation over rayleigh fading channels of WiFi direct networks in smart grid application. In: The proceeding of 2012 I.E. PES innovative smart grid technologies Asia, 2012
8. Galli S, Scaglione A, Wang Z (2011) For the grid and through the grid: the role of power line communications in the smart grid. Proc IEEE 99(6):998–1027
9. HomePlug Powerline Alliance, Inc. (2012) HomePlug Green PHY^{TM}1. 1 The standard for in-home smart grid powerline communications: an application and technology overview
10. Korki M, Hosseinzadeh N, Moazzeni T (2011) Performance evaluation of a narrowband power line communications for smart grid with noise reduction technique. IEEE Trans Consum Electron 57(4):1598–1606
11. Zimmermann M, Dosert K (2002) A multipath model for the powerline channel. IEEE Trans Commun 50(4):553–559
12. Galli S (2011) A novel approach to the statistical modeling of wireline channels. IEEE Trans Commun 59(5):1332–1345
13. Lai SW, Messier GG (2010) The wireless/power-line diversity channel. In: Proceedings of 2010 I.E. international conference on communications (ICC), pp 1–5
14. Azarm MA, Bari R, Yue M et al (2004) Electrical substation reliability evaluation with emphasis on evolving interdependence on communication infrastructure. In: Proceedings of international conference on probabilistic methods applied to power systems, pp 487–491
15. Alamouti SM (1998) A simple transmit diversity technique for wireless communications. IEEE J Select Areas Commun 16(8):1451–1458
16. Katayama M, Yamazato T, Okada H (2006) A mathematical model of noise in narrowband power line communication systems. IEEE J Select Areas Commun 24(7):1267–1276

Chapter 10
An Improved Grouping Spectrum Allocation Algorithm in Cognitive Radio

Bingxin Yan, Shubin Wang, and Yuanyuan Bao

Abstract In cognitive radio network, a Grouping spectrum allocation algorithm allocates lots of spectrum to cognitive users, but not to care for the users' requirement, which leads to unreasonable spectral allocation. For this problem, this paper proposes an improved Grouping algorithm based on users' requirement. According to the graph theory, the topology of network is divided into many groups by two different grouping ways (frequency Grouping and user Grouping) respectively. In the distributing process, each group reports the distributed information after completing one distribution. Whenever a user's demand is satisfied, every group is informed to not allocate the spectrum for the user any more, and delete it from the topology in every group at the same time. The improved method can get high spectrum utilization with little sacrifice of time that cost on the spectrum allocation. In addition, the fairness is improved by deleting the node whose demand had already been met. Because of doing this, the other nodes being interference with the node on the same channel can participate into spectrum allocation. The simulation result proves that the utilization of the improved algorithm is much higher than the traditional parallel algorithm, and users' satisfaction increases a lot.

Keywords Bandwidth requirement • Spectrum allocation • Topology • Users' satisfaction

10.1 Introduction

With the development of wireless communication, spectrum resource is becoming more and more scarce [1]. However, the way of fixed spectrum management leads to spectrum utilization rate much lower. As a result, being a new kind of intelligent spectrum sharing method, cognitive radio technology arises at the historic moment. In the cognitive radio, spectrum allocation is established on the basis of the detected idle spectrum. Just as our algorithm is proposed on the basis of detected idle spectrum.

B. Yan • S. Wang (✉) • Y. Bao
College of Electronic Information Engineering, Inner Mongolia University, Hohhot, China
e-mail: wangsb09@gmail.com

J. Mu et al. (eds.), *The Proceedings of the Third International Conference on Communications, Signal Processing, and Systems*, Lecture Notes in Electrical Engineering 322, DOI 10.1007/978-3-319-08991-1_10

At present, there are three spectrum allocation models of cognitive radio. Among them, the graph model is commonly used. Variety of algorithms based on graph coloring model introduced the factor of users' demand [2, 3]. It is a kind of method that takes the users' demand for spectrum into consideration. Whenever a user's requirement is met, the allocation of spectrum will stop to it.

A lot of spectrum allocation algorithms are proposed based on graph coloring model. Among them, list coloring algorithm [1] does not consider the difference between channels. However, coloring sensitive graph algorithm (CSGC) [4] overcomes this shortcoming, and puts forward several different rules based on the target label distribution. But the CSGC also has shortcomings—only one spectrum can be allocated in one distribution cycle. To enhance the time usage, a parallel spectrum allocation algorithm [5, 6] is proposed. It is known as a short time-consuming allocation method, for it allocates lots of spectrum to users at the same time. But it [5, 6] does not take the users' demand into consideration, which leads to the waste of spectrum [2] improves the CSGC on the aspect of waiting time and users' requirement by using new wait parameter but very sophisticated. To sum up, the parallel algorithm has advantage of shorter cost of time, and the algorithm based on users' demand can greatly improves the utilization of spectrum. In order to combine the advantages of both, our paper improved the parallel algorithm by taking the users' demand into consideration.

10.2 Grouping Algorithm Based on Users' Demand

10.2.1 Algorithm Principle

Assume a cognitive radio network is composed of N1 primary users (PU) and N2 secondary users (SU) in the area of $d \times d$. The whole available spectrum can be divided into m different channels which is orthogonal to each other. Assume in a cycle, the location of users and the available spectrum is fixed. According to graph theory, the spectrum allocation problem can be viewed as an equivalent graph coloring problem by mapping each SU into a vertex and each channel into a color. When we allocate channel m to user n, it is just similar to assign color m to vertex n. Take Fig. 10.1 as an example, where N_1 is 4, N_2 is 4, and the available channel number CH is 3. It also can be expressed as Fig. 10.2. Then we can use the known matrices to describe the distribution of process.

The process of improved Grouping algorithm is as follows:

Step1 delete nodes whose demand is larger than its total number of available spectrum from topology. For even if all of the available spectrum are allocated to it, the user's demand is still not satisfied.

Step2 topology can be divided by user grouping and frequency grouping respectively. In frequency grouping, the topology can be divided according to the number of available spectrum. Label and Color can be calculated in each group according to

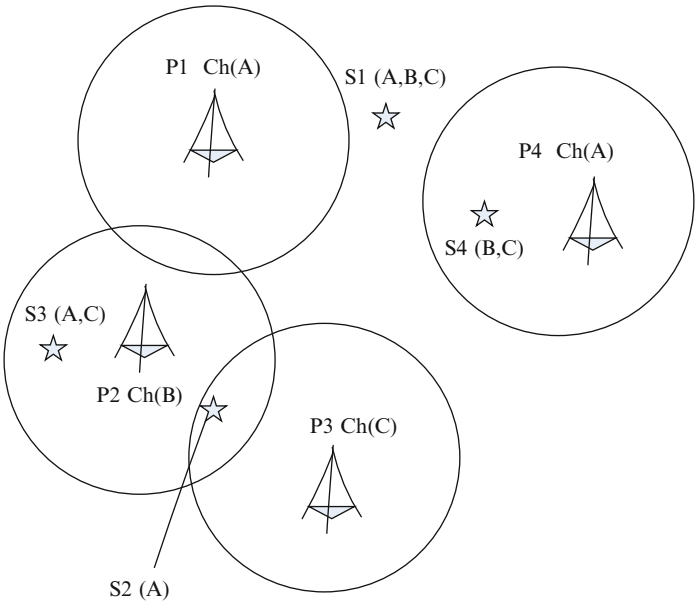

Fig. 10.1 A network of cognitive radio

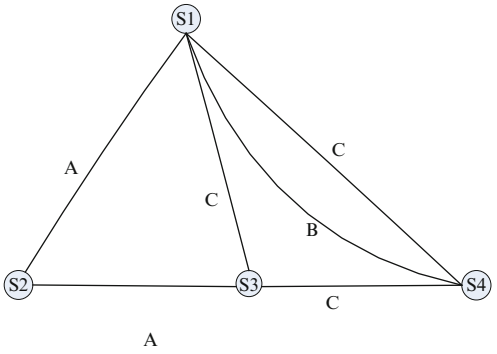

Fig. 10.2 Topology of cognitive radio

Eqs. (10.2) and (10.3). Then select the maximum value of Label, and allocate the corresponding Color to it (If there are two or more largest Labels, choose one of them randomly.). After this, delete the nodes that can't simultaneously use the spectrum with it in the topology of the group.

However, user grouping is another matter. More specifically, the topology can be divided according to the number of users. Because the different groups may choose the same frequency on which users can gain maximum Label, but these interfering users cannot use the frequency at the same time. In this case, the spectrum is assigned to the largest value of Label. While the other Labels correspond to the

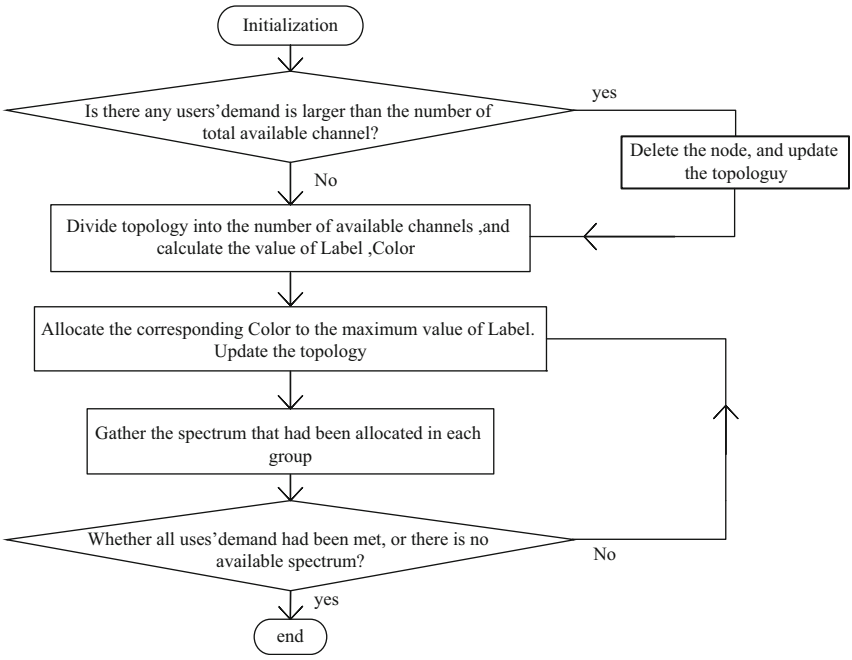

Fig. 10.3 Flow of procedure

other users are not allowed to take part in current allocating spectrum cycle. Otherwise, allocate spectrum to different users simultaneously.

Step3 in the loop of allocation, each group reports the distributed information after completing a distribution. Whenever a user's demand is met, it will receive no spectrum any more. By deleting the node from every topology, those who have interference constraints with the node on that channel can use that channel. The loop of allocation will be terminated, when there is no available spectrum or all of the users' requirements are met.

The flow of the algorithm is as follows (Fig. 10.3).

10.2.2 Objective Function and Labeling Standards

Our objective function is maximum the system spectrum utilization, on the premise of not allocating spectrum to users whose demand is larger the number of available channel. Therefore, the objective function can be expressed as:

$$f = \max \sum_{n=1}^{N} \sum_{m=1}^{M} an, m \cdot \gamma \cdot bn, m \tag{10.1}$$

where $\gamma = \frac{Demandn}{\sum_{n=1}^{N} Tn} <= 1$, and Tn indicates the number of available spectrum for the user n. When allocating spectrum with the function, we will introduce the labeling method. In order to achieve the purpose of maximizing the spectrum utilization, the labeling standards changed as follows:

$$Label\ln = \max \frac{\gamma \cdot \frac{bn,m}{Rn,m+1}}{\sum_{n=1}^{N} \ln, m \cdot bn, m} \tag{10.2}$$

$$Colorn = \operatorname{argmax} \frac{\gamma \cdot \frac{bn,m}{Rn,m+1}}{\sum_{n=1}^{N} \ln, m \cdot bn, m} \tag{10.3}$$

10.3 Simulation and Analysis

10.3.1 Simulation Conditions

Assume that PU and the SU are distributed in 10×10 region randomly. Each user can use any of M orthogonal channels. The bandwidth of available channel is generated from 1 to 3 MHz in TV spectrum. The demand of user n–Demand_n is a integer. The parameters are as follows (Table 10.1):

10.3.2 Results and Analysis

First we vary the number of available channels to compare the utilization of spectrum among the algorithms, as shown in Fig. 10.4. Because the traditional Parallel algorithm does not consider the requirement of SU's, when a SU's requirement has been satisfied, it still allocates channel to the SU. In fact, the SU will not use that channel. So the total utilization rate is not very high. At the same time, those who have interference constraints with the SU on that channel cannot use that channel. This also decreases the total spectrum utilization. Even when the number of available channels increases, the traditional parallel's total spectrum utilization has little change. However, the improved Groping algorithm would not allocate extra channel to the SU whose requirement is satisfied. So the total utilization rate of the improved algorithm is higher than the traditional parallel algorithm.

Table 10.1 Parameters table

The parameter name	Value
The number of primary user	4
The number of channel	3–20
The number of secondary user	20
The primary user's coverage radius	5
The secondary user's coverage radius	3.5
The user's demand of spectrum	Randomly generated from 0 to largest (T_n)

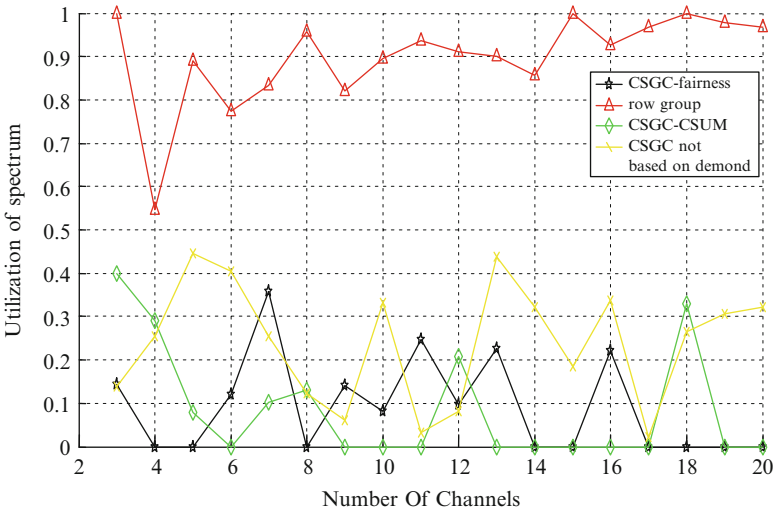

Fig. 10.4 Utilization rate versus number of channel

Then we compare the satisfaction rate of algorithms. Assume that the Demand matrix is [4, 2, 1, 3] as shown in Fig. 10.5. It shows that satisfaction rate of the improved Grouping algorithm is higher than the other algorithms.

Next, we pay attention to the time that algorithm cost on spectrum allocation as Fig. 10.6. It shows that the improved Groping algorithm is much shorter than the CSGC algorithm. Because the improved algorithm allocates lots of spectrum to many users simultaneously. Compared with parallel algorithm that based on demand, the improved Grouping algorithm spent a little longer of time on allocating spectrum. For it is time consuming thing to report allocation information in each cycle.

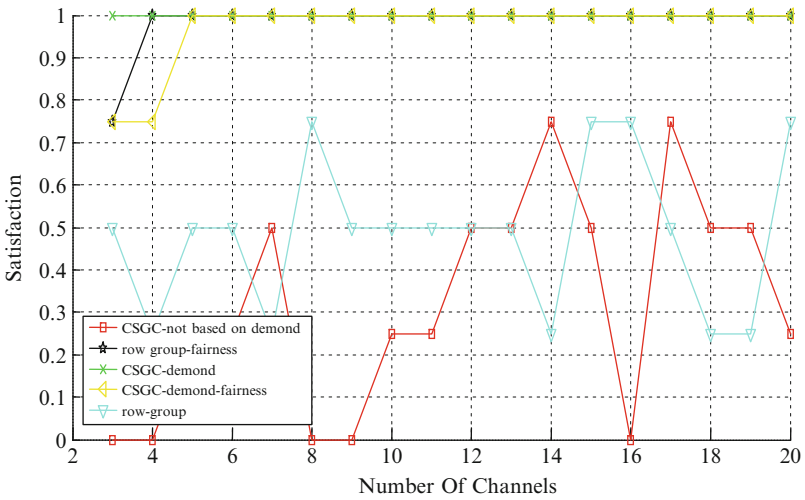

Fig. 10.5 Satisfaction versus number of channel

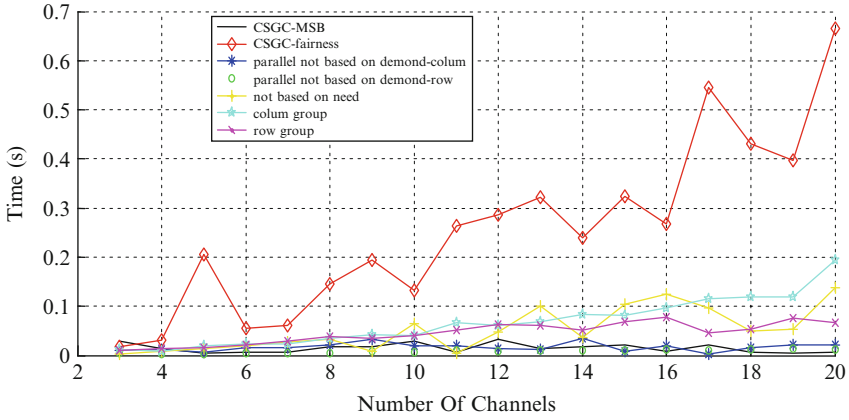

Fig. 10.6 The cost of time versus number of channel

Conclusion

This paper presents an improved parallel algorithm based on users' demand of spectrum. Two methods are used to illustrate the algorithm, finally we draw a conclusion that the improved Grouping algorithm not only has much higher spectrum utilization rate, but it improves the fairness and customers' satisfaction with the little sacrifice of time as well. However, it also has shortcomings—it is undeniable that the complexity is increased.

Acknowledgments Shubin Wang (wangsb09@gmail.com) is the correspondent author and this work was supported by the National Natural Science Foundation of China (61261020), and the Natural Science Foundation of Inner Mongolia, China (2012MS0903), and the Scientific Research Initial Fund for Higher Talents Program of Inner Mongolia University, China.

References

1. Wang W, Liu X (2005) List coloring based channel allocation for open spectrum wireless networks. In: Proceedings of IEEE 62nd vehicular technology conference, vol 1. pp 690–694
2. Liu P, Xu JY (2010) Improvement of CSGC algorithm based on users waiting time and bandwidth demand. In: Proceedings of international conference on multimedia technology, pp 1–4
3. Yang LL, Xie XZ, Zheng Y (2009) A historical-information-based algorithm in dynamic spectrum allocation. In: Proceedings of IEEE international conference on communication software and networks, pp 731–736
4. Zheng HT, Peng CY (2005) Collaboration and fairness in opportunities spectrum access. In: Proceedings of the 40th annual IEEE international conference on communications, vol 5, pp 3132–3136
5. Liao CL, Chen J, You X, Li S (2007) Parallel algorithm of spectrum allocation in cognitive radio. J Electron Inf Technol 7:1608–1611
6. Mo WC (2008) Reach on spectrum allocation in cognitive radio. Dissertation, Xi'an Electronics Science and Technology University

Chapter 11
Monitoring and Controlling Packets Transmission Improvement Based on the Physical Depth in the ZigBee Networks

Jiasong Mu, Liang Han, and Sijie Cheng

Abstract ZigBee provides a simple and reliable solution for the low cost networks. However, the current routing algorithms cannot fully satisfy the energy consumption issue. In this paper, we propose a minimum physical distance (MPD) broadcasting algorithm the transmission of the monitoring and command packets which are from or to the ZC. The physical depth is introduced to indicate the least hops to the ZC, and the transmission paths are decided based on the neighbour table information. The simulation results show that the MPD could improve the performance of the monitoring and controlling packets transmission by providing shorter paths lower delay.

Keywords ZigBee • Physical depth • Broadcasting transmission • Neighbour table

11.1 Introduction

ZigBee uses a mixed routing mechanism combined with HRP (hierarchical tree routing) and Z-AODV (ZigBee ad-hoc on demand distance vector) [1]. HRP is based on the address distribution and provides a simple and reliable measure for data transmission, though it is not always efficient and robust. For Z-AODV, each node may initiate routing discovery when necessary, a global shortest path between the source and destination is obtained during the process and the data frame was sent along the route. However, since the HRP and Z-AODV are designed for different topologies, their benefits are alternative. Moreover, ZigBee devices have limited processing capabilities, storage, power supplies and communication bandwidth. They may also move about randomly, which results in topology changes of the network. These constraints make it very difficult to find proper routing mechanisms that ensure high network throughput in different environments [2]. For that

J. Mu (✉) • L. Han • S. Cheng
College of Electronic and Communication Engineering,
Tianjin Normal University, Tianjin 300387, China
e-mail: mujiasong@aliyun.com

J. Mu et al. (eds.), *The Proceedings of the Third International Conference on Communications, Signal Processing, and Systems*, Lecture Notes in Electrical Engineering 322, DOI 10.1007/978-3-319-08991-1_11

reason, current network formation and routing protocols described in the ZigBee specification cannot fully address power consumption issues [3]. The deployment in smart gird is newly presented and the characteristics of application need to be more considered [4].

One can see at least two separate modes in the AODV: route discovery/maintenance and the actual forwarding of application packets, with the first mode involving special traffic that does not directly originate at the network's application [5]. The prevailing wisdom regarding the organization of wireless networks assumes point-to-point communication, whereby each node forwarding the packet on its way to the destination sends it to a specific neighbour [6]. Note that the benefits of unicast mechanism tend to be questionable and much more so in sensor networks, where packets tend to be very short [7]. Firstly, the action of announcing the transmission with the handshake may take more bandwidth than the actual transmission; so the probability of damage to an unannounced transmission is in fact lower than the one to the announcement [8]. Secondly, the neighbour identifier requires room in the packet header and thus incurs extra framing, which significantly inflates the otherwise short packet. Owing to the open nature in the wireless channel, the unicast is essentially a broadcasting that only a specified device would respond by identifying address information. If other parameters which are able to control the data flow and restraint the flooding can be found, we can design a proper delivery protocol to overcome the mentioned defects and achieve better performance in data transmission.

The MPD proposed in this paper is based on the hierarchical structure, in which the HRP is commonly used. In [9], the authors propose an improved routing algorithm for hierarchical topology. The information in neighbour tables was used to get the shorter paths. Based on the DAAM, if the addresses of source and destination nodes are given, the hierarchical route can be decided without any other information. The local device may calculate the hierarchical hop counts for every device in the neighbourhood and choose the one with the least hops as the next hop node. This mechanism can only grant the best hierarchical path, while our work may find the route with the shortest physical distance.

For the monitoring and controlling communication, as the ZC is the root of tree structure, these packets are transmitted along the hierarchical paths, where the depths of nodes are strictly monotonic (increasing for command and decreasing for monitoring frames). The depth is defined as the hop counts in the HRP, and it indicates the topological distance to the ZC. Nevertheless, the parameter that implies the spatial distance is needed to find the best route. In our work, we introduce the physical depth (PD), which is the minimal hops to the sink, to indicate the physical distance from a local device to the ZC. Since all the one hop neighbour nodes information is required to be stored by each device according to the ZigBee specification, the physical distance can be easily updated by diffusion. On that basis, the transmission of the command and monitoring packets could be optimized by the principle of seeking the receiver with the least physical depth in broadcasting transmission. In this way, the monitoring and command frames can be transmitted in the global shortest path without the handshake nor the routing discovery.

The rest of this paper is organized as follows. Section 11.2 briefly introduces the ZigBee specification, and the minimum physical distance broadcasting algorithm is proposed in Sect. 11.3. In Sect. 11.4, simulation results are presented. Finally, the conclusion is shown in Sect. 11.5.

11.2 ZigBee Specification and Routing Methods

ZigBee devices support the function of testing the link quality indication (LQI) measurement every time they receive a frame. The LQI measurement is a characterization of the strength and/or quality of a received packet. The measurement may be implemented using receiver energy detection (ED), a signal-to-noise ratio estimation, or a combination of these methods. The use of the LQI result by the network or application layers is not specified in IEEE 802.15.4 standard [10].

In ZigBee specification, it is recommended to use Distributed Address Allocation Mechanism (DAAM) for address assignment to form tree structure. The parameter *Cm* represents the largest number of children nodes, *Rm* means the number of children nodes which can be a router and *Lm* decides the maximum depth in the network. And for the same network, different nodes usually have constant *Cm* and *Rm*. Every potential parent is provided with a finite sub-block of the address space, which is used to assign network addresses to its children. Given *Cm*, *Lm*, and *Rm*, we can compute the function *Cskip(d)* as the size of the address sub-block distributed by each parent at depth d as (11.1) [10].

$$Cskip(d) = \begin{cases} 0, & Rm = 0, \\ 1 + Cm \times (Lm - d - 1), & Rm = 1, \\ \left(1 + Cm - Rm - Cm \times R^{Lm-d-1}\right)/(1 - Rm), & Rm > 1. \end{cases} \tag{11.1}$$

The network addresses $A_{d+1,rn}$ and $A_{d+1,el}$ shall be assigned to the nth router child and lth end device child at depth $d + 1$ in a sequential manner, respectively, as shown in (11.2):

$$\begin{aligned} A_{d+1,rn} &= A_{parent} + Cskip(d) \cdot (n - 1) + 1 \\ A_{d+1,el} &= A_{parent} + Cskip(d) \cdot R_m + l \end{aligned} \tag{11.2}$$

where A_{parent} represents the address of the parent and $1 \leq n \leq Rm$.

The hierarchical topology in ZigBee network is based on DAAM. In this tree shape structure, if the destination address is in the address space that a node is managing, the node forwards the packet to one of its child nodes. Otherwise, it forwards the packet to its parent.

Each ZigBee device maintains a neighbour table which has all its neighbours' information in the one-hop transmission range. The contents for a neighbour entry are the network's PAN (Personal Area Network) identifier; node's extended address, network address, device type, relationship, LQI and etc. Optionally,

additional information such as the depth can be included. Entries in the table are created when the node joins to an existing network. Conversely, the neighbour entry is removed when the neighbour node leaves the network. Since the information on the neighbour table is updated every time a device receives any frame from the some neighbour node, the information of the neighbour table can be said to be up-to-date all the time.

11.3 Minimum Physical Distance Broadcasting Algorithm

In ZigBee networks, the depth is defined as the transmission hops in the HRP. It indicates the topology distance between the local device and the ZC. This information is not helpful to find the global shortest path since the hierarchical topology limits the transmission to parent–child links. We introduce the concept of the physical depth (PD), which is defined as the minimum hop counts to the ZC. So the PD is able to indicate the spatial distance to some extents.

Thus, the ZC is the only device with the PD 0 in the network. For a device in the neighbourhood of the ZC, its PD may be set 1 since it may find the entry of the ZC in its neighbour table. If the PD information is required in the neighbour table, all the nodes within the transmission range of the PD 1 devices may have PD 2, the PD of any device can be recursively decided. The principle can be simply stated as: the PD value of a certain node is one plus the minimum PD value in its neighbour table.

However, there is no such content in the neighbour table in the ZigBee specification. Fortunately, the node depth is an optional term. Moreover, if the network address is assigned as the DAAM and the network address is given, the depth of the node can be calculated as the following pseudo codes [9]:

```
Pseudo codes: Algorithm of deciding the topology depth for node X
Q_0 = ADDR(X)
for d = 0 to Lm do
if Q_d == 0 then
D(X) = d break;
else if d > 0 and Q_{d-1} ≥ Rm · Cskip(d-1) then
D(X) = d break;
else
Q_{d+1} = (Q_d-1) mod (Cskip(d))
end if
```

Where Q_d is introduced to determine whether node X is a router node or an end device at depth d. One can see that the depth information is redundant in this case. Therefore, it can be replaced by the PD. On that basis, the delivery protocol is investigated.

In the MPD, we focus on the following parameters in the transmission. The address of the other terminal except the ZC, *S/D add* (this device is also called S/D

node in the following for convenience); the frame type, *M*/*C* (1 for monitoring frame and 0 for command); the sequence number, *SN*; the retired times, *RT*; the PD of the *S*/*D* node, *PDs*; the remaining hops to the destination, *PD*r; a flag, *f*Opt, indicates whether this frame is allowed to be rebroadcasted by other nodes which cannot find the routing table entries corresponding to the *S*/*D add* (1 for True and 0 for false). All the variables above are included in the frame header. With the array of [*S*/*D*, *M*/*C*, *SN*, *RT*], which we called broadcasting frame identity array (BFIA), the frame can be uniquely recognized. And the other parameters, *PDs*, *PD*r, and *f*Opt are used to control the transmission.

Our algorithm is based on an assumption that all the transmission links are half-duplex and symmetric. On the first attempt to communicate with the ZC for a certain node, suppose it is a monitoring frame (the principle is the same for the controlling one), the *S*/*D add* is set the address of this device, *M*/*C* is 1, *SN* is one plus the *SN* value in the last monitoring packets transmission, *RT* and *PD*s depends on the real situation, *PD*r is equal to the *PDs* minus 1, and *f*Opt has to be 1. And the packet is broadcasted to its neighbourhood by the S/D device.

Each node that receives this packet may compare the *PD*r value with its own PD, if the *PD*r is smaller, the frame is abandoned. Otherwise, the device may rebroadcast the packet. Meanwhile, the *PD*r value is decremented by 1 and an entry containing the *S*/*D add* and the *PD*r is built in the routing table. The sending node is asked to monitor the channel, if some packet with the same BFIA and the *PD*r is received, it may regard the packets as the transmission acknowledgement and reserve the corresponding routing entry, otherwise, the entry is deleted after a preset expiration time. Based on this mechanism, the frame is forwarded to the ZC and the path must be the global shortest.

When a packet is successfully delivered to the ZC, all the nodes in the transmission path may update their routing tables. The entry should at least includes the *S*/*D add*, *PD*s and *PD*r. For the later communication between this device and the ZC, the *f*Opt could be set 0, and the nodes only have to check the existence of the corresponding routing table entry to decide whether it should rebroadcast this packet or abandon it. For the monitoring packets, the *PD*r is the PD value of the local device, while it is equal to (*PD*s-PD) for the controlling ones.

However, if more than one receiving nodes have the same minimum PD in one delivery, it leads to the multipath problem, as shown in Fig. 11.1. Node 2 sends a packet with the *PD*r set 3, both the node D and F may rebroadcast this packet. Since all the candidates of next hop, including the LQI information, are in the neighbour table, a device may be aware of the branches before the transmission by checking whether there is more than 1 neighbour having the same minimum PD. If so, the sending device is asked to specify the network address of the receiving node. Such packets seem like the ones in the traditional unicast mechanism, but they have simpler frame header, e.g. the address of sending device is not necessary. Moreover, the address specifying only happens when the parameter *f*Opt is 1 (always in the first communication attempt), and the separate acknowledgement is removed to save the bandwidth.

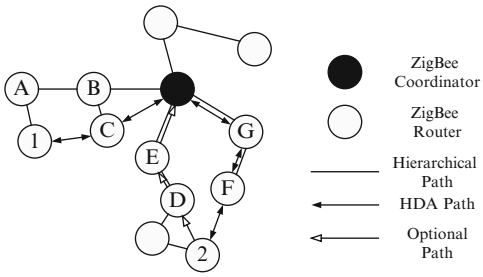

Fig. 11.1 An example of the minimum physical distance broadcasting algorithm

An example of the MPD routing is shown in Fig. 11.1. We can see that the node 1 could send frames via node C to the ZC, the hop counts is 2, reduced by 1 compared with the value in the HRP. For the node 2, the transmission path is also shortened. The link can be uniquely determined since node 2 can specify the address of the next hop device when it finds both the node D and F have the same minimum PD in its neighbour table. And the links not chosen can be used as a backup for link failures. Similarly, the path length from node is also reduced by 1.

11.4 Simulations

The performance of the proposed minimum physical depth delivery protocol is discussed in this section. The simulation was implemented by the MATLAB. Some parameters in the simulation were set as following: the time duration was 300 s; the simulation area was 300 m$\times$300 m; the network is consist of 50 nodes except the ZC, and all of them were the ZigBee routers; the nodes were randomly deployed following the uniform distribution; *Cm, Rm* and *Lm* were set 4, 4 and 5 separately; the data packet size was 100 bits; the packet interval time was 1 s; the first packet arrival time followed a uniform distribution from 10 to 11 for each node; the maximum retries was 4 times; the transmitter power of the ZC is five times the power of other devices; for each scenario, the simulation was carried out 500 times to calculate the average. To make a comprehensive comparison, the two modes of the MPD in which the *f*Opt was 0 and 1 were both tested. Our algorithm was compared with the two specified routing algorithms, the HRP and the Z-AODV. As a classic method in the hierarchical topology, the EHRP in [9] was also included.

The node mobility should be considered in the wireless networks. In our simulations, each node was stationary for a random time that followed a uniform distribution form $ts - 50$ to $ts + 50$ s. Then the node moved to a new position which is randomly chosen, and the moving speed was uniformly distributed from 1 to 10 m/s. The devices in the smart grid application did not move a lot, so the *ts* value was ranged from 100 to 350 s. As the duration was 300 s, the $ts = 350$ meant all the nodes may not move during the scenario.

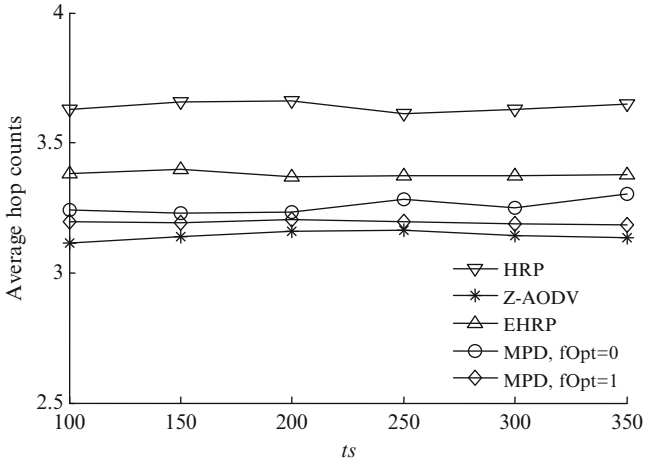

Fig. 11.2 The hop counts of different routing algorithms

We also made a mapping from the LQI in received data to the signal power. In our simulation, the channel followed Rayleigh fading with the δ^2 is 5. We mapped the best LQI (−3 dB loss) to 0xff (255) and the lowest quality compliant signals detectable by the receiver (−20 dB loss) to 0x00 (0), the values in between were uniformly distributed.

The path length obtained by each method is also shown in Fig. 11.2. The HPR had the most hop counts due to the limit of parent–child link, while the Z-AODV could always use the global shortest paths. The EHRP could reduce the path length effectively by using the neighbour table information. We might find that the MPD could further shorten the path, the concept of the PD was similar as the global shortest. However, when one node had more than one neighbour nodes with the same minimum PD, the path was decided only based on the link quality in the current hop, that might lead to the worse performance compared with the Z-AODV. But our algorithm could significantly improve the routing without any routing discovery operations and communication. Moreover, the asymmetric link in the neighbourhood of the ZC was considered for better performance. From the figure we could conclude that the hop counts were less related to the node mobility since each curve did not change much as the *ts* increased.

Although the routing method is mainly a NWK layer protocol, its performance is not only based on the NWK behaviours but also the MAC schemes. The MPD is quite different from the existing algorithms, even if it is designed for the ZigBee specification; some functions in the IEEE 802.15.4 (e.g. the beacon enable mode, GTS allocation, the superframe structure and etc.) may be incompatible with our algorithm. It has two meanings, the MPD cannot support such modes, and on the other hand, the MAC and NWK headers are redundant if we just consider the transmission. To make a meaningful comparison, we did not include the entire

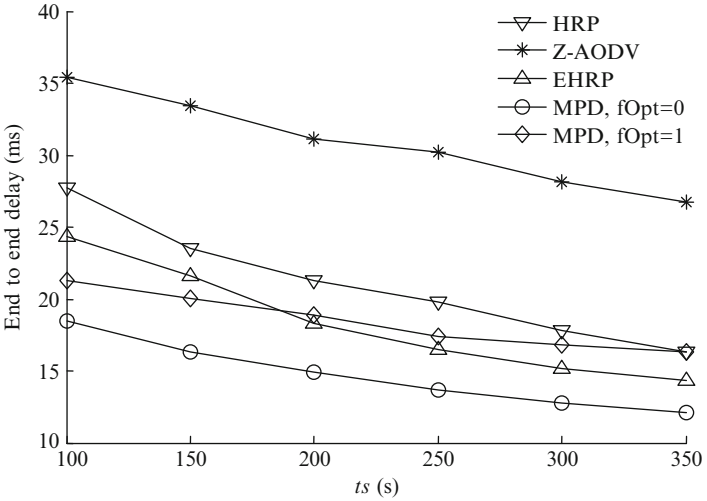

Fig. 11.3 The end to end delay in different routing algorithms

frame header in our simulations, only the information related to the routing and the used transmission mechanism was focused on.

Since the carrier transmission time is so short that can be ignored, the delay is mainly caused by the device processing time and the CSMA/CA mechanism. The former factor was tested in the OPNET as reference; we made a simple network with two nodes (not including the ZC) and watched the processing time of the intermediate node with the fixed packet size (100 bit). When trying to send the message, a node may listen to the channel and decide to transmit or wait for a random time based on the CSMA/CA scheme. The simulation in our work is a rough comparison, as a comprehensive work, the accurate test data may be obtained by designing compatible models in our further work.

Shown in Fig. 11.3 is the transmission delay in different routing algorithms. The Z-AODV had the highest latency owing to its routing discovery process. The delay of the HRP was shorter since the transmission was limited in the hierarchical links. And the EHRP could further reduce the delay by shortening the path length. We could see that the latency of the MPD was greatly decreased. Even the *f*Opt was 1; the delay was similar as the hierarchical routing methods. When the *f*Opt was 0, the delay could be obviously reduced. It had two mainly reasons, one was the shortest path and hop counts, the other was that the bandwidth was saved by removing the receiving acknowledgement and the channel was more likely to be free. Compared with the EHRP, the MPD could improve the performance on the delay for about 19.2 %.

Conclusions

In this paper, we proposed a minimum physical depth delivery protocol to improve the monitoring and controlling data transmission in the ZigBee networks. By introducing the concept of the physical depth, the packet was forwarded along the trajectory of the devices with the least PD in the neighbourhood. Considering the low payload of the frames, the broadcasting mechanism was used to save the bandwidth and the receiving acknowledgement was removed. Our algorithm was compared with the ones specified in the ZigBee and some classic improved methods. The simulation results showed that the MPD could improve the routing performance for the monitoring and controlling packets, It could reduce the hop counts effectively, and the end to end delay was also slightly decreased.

Our further work will focus on two issues. One is to design a fully compatible MAC scheme for the minimum physical depth delivery protocol to test the performance more accurately and apply the algorithm in the real application. The other one is to improve the algorithm for high reliability.

Acknowledgements This work is funded by the Project of Tianjin University Technology Development Fund (20130714), the Doctoral Scientific Foundation of Tianjin Normal University (52XB1106) and the University Students' Innovative Training Program.

References

1. Cuomo F, Luna SD, Monaco U, Melodia T (2007) Routing in ZigBee benefits from exploiting the IEEE 802.15.4 association tree. In: Paper presented at the IEEE international conference on communications, Glasgow, pp 3271–3276. doi: 10.1109/ICC.2007.542
2. Tareq AA, Yang SH (2008) A ZigBee-based mobile tracking system through wireless sensor networks. Int J Adv Mechatron Syst 1(1):63–70. doi:10.1504/IJAMechS.2008.020839
3. Metin T, Ibrahim K (2012) PSAR: power-source-aware routing in ZigBee networks. Wirel Netw 18(6):635–651. doi:10.1007/s11276-012-0424-5
4. Chien HY, Lee CF, Liu SB, Wu TC (2010) Enhancing convenience and situation-aware intelligence of smart home services using passive RFID and intelligent controls. Int J Internet Protoc Technol 5(3):166–173. doi:10.1504/IJIPT.2010.035387
5. Ran P, Zou SM (2006) ZigBee routing selection strategy based on data services and energy-balanced ZigBee routing. In: Paper presented at the IEEE Asia-Pacific conference services computing, Guangzhou, Guangdong, pp 400–404. doi: 10.1109/APSCC.2006.116
6. Sahinoglu Z, Orlik P, Zhang J, Bhargava B (2011) Tree-based data broadcast in IEEE 802.15.4 and ZigBee networks. IEEE Trans Mobile Comput 5(11):1561–1574
7. Ajgaonkar P (2010) Simulation studies on ZigBee communications for home automation and networking. In: IEEE AUTOTESTCON, Orlando, pp 1–6, 13–16 September 2010. doi:10.1109/AUTEST.2010.5613588
8. Liang Q, Wang L, Ren Q (2007) Fault-tolerant and energy efficient cross-layer design for wireless sensor networks. Int J Sens Netw 2(3):248–257

9. Ha JY, Park HS, Choi S, Kwon WH (2007) EHRP: Enhanced hierarchical routing protocol for ZigBee mesh networks. IEEE Commun Lett 11(12):1028–1103. doi:10.1109/LCOMM.2007.071325
10. ZigBee Standard Organization (2007) ZigBee Specification Document 053474r17. ZigBee Alliance, San Ramon

Chapter 12
An Improved Routing Discovery Algorithm Based on the Relative Position Information in the Zigbee Networks

Jie Fang and Jiasong Mu

Abstract In the ZigBee networks, the Z-AODV routing algorithm could use the global shortest path for data transmission by flooding the routing quest when necessary. However, this mechanism may lead to a heavy routing overhead. In this paper, we propose a directional broadcasting algorithm in routing discovery (DBRD) to reduce the routing overhead. The network is divided into several continuous "clusters" based on their relative position information. The devices which are not in the clusters covering the shortest path may not take part in the routing request rebroadcasting. The simulation results show that the DBRD could improve the performances of routing discovery; the routing overhead was effectively reduced.

Keywords ZigBee • Routing discovery • Directional broadcasting • Relative position

12.1 Introduction

ZigBee uses a mixed routing mechanism combined with HRP (hierarchical tree routing) and Z-AODV (ZigBee ad-hoc on demand distance vector) [1]. For the Z-AODV, each node may initiate routing discovery when necessary. However, ZigBee devices have limited processing capabilities, storage, power supplies and communication bandwidth. They may also move about randomly, which results in topology changes of the network. These constraints make it very difficult to find proper routing mechanisms that ensure high network throughput [2]. The routing protocols described in the specification still need more improvement [3].

In this paper, we focus on the improvement of the performance in routing discovery. In the original Z-AODV, an intermediate node may rebroadcast a certain

J. Fang • J. Mu (✉)
College of Electronic and Communication Engineering, Tianjin Normal University, Tianjin 300387, China
e-mail: mujiasong@aliyun.com

J. Mu et al. (eds.), *The Proceedings of the Third International Conference on Communications, Signal Processing, and Systems*, Lecture Notes in Electrical Engineering 322, DOI 10.1007/978-3-319-08991-1_12

routing request only once and abandon the other duplications. The coverage of the routing request broadcasting should be the whole network theoretically to ensure the global shortest path can be found. However, this range can be reduced if some prior knowledge is available. The path length and direction are two common parameters to optimize the routing discovery if they are predictable in some level. Some improved broadcasting strategies based on the length control have been proposed in the ZigBee networks. By contrast, the path direction is more difficult to forecast because of the lack of the nodes' spatial information and the high cost of operation and maintenance [4].

In our method, these two difficulties are solved as follows. In the ZigBee networks, the recommended Distributed Address Allocation Mechanism (DAAM) guarantees a hierarchical topology, in which each subtree and its root can be regarded as the cluster and the cluster head. The transmission link between the nodes in different clusters can be described by a sequence of clusters. If the clusters are organized based on the location information, this sequence may also contain the directional information. The relative position information would be enough to indicate the direction, and it can be easily obtained from the neighbour table, which is specified in the ZigBee specification. To address the energy cost issue, all the needed information are sent to the ZC, which has sufficient computing and storage capabilities. The ZC is responsible to calculate the cluster sequence to represent the direction and announce it to all the other devices. On that basis, a simple directional rebroadcasting algorithm in routing discovery (DBRD) which follows the ZigBee specification is proposed.

In [5], an effective broadcast algorithm called ZBARD (ZigBee broadcasting algorithm on route discovery) is proposed. As a known path, the HRP hop counts, which can be obtained when the network addresses of the source and destination devices are given, must be no less than the shortest path. And it can be used as the maximum retransmission times of the routing request. The ZBARD sets the broadcast radius to this value to reduce the control packets issued by the route discovery. This work effectively limits the retransmission range of routing requests, yet the direction of the coverage is not considered.

The rest of this paper is organized as follows. Section 12.2 briefly introduces the ZigBee specification, and the directional broadcasting algorithm in routing discovery is proposed in Sect. 12.3. In Sect. 12.4, simulation results are presented. Finally, the conclusion is drawn in Sect. 12.5.

12.2 ZigBee Specification and Routing Methods

ZigBee devices support the function of testing the link quality indication (LQI) measurement every time they receive a frame. The LQI measurement is a characterization of the strength and/or quality of a received packet. The measurement may be implemented using receiver energy detection (ED), a signal-to-noise ratio

estimation, or a combination of these methods. The use of the LQI result by the network or application layers is not specified in IEEE 802.15.4 standard [6].

In ZigBee specification, it is recommended to use Distributed Address Allocation Mechanism (DAAM) for address assignment to form tree structure. The parameter *Cm* represents the largest number of children nodes, *Rm* means the number of children nodes which can be a router and *Lm* decides the maximum depth in the network. And for the same network, different nodes usually have constant *Cm* and *Rm*. Every potential parent is provided with a finite sub-block of the address space, which is used to assign network addresses to its children. Given *Cm*, *Lm*, and *Rm*, we can compute the function *Cskip(d)* as the size of the address sub-block distributed by each parent at depth d as (12.1) [6].

$$Cskip(d) = \begin{cases} 0, & Rm = 0, \\ 1 + Cm \times (Lm - d - 1), & Rm = 1, \\ \left(1 + Cm - Rm - Cm \times R^{Lm-d-1}\right)/(1 - Rm), & Rm > 1. \end{cases} \tag{12.1}$$

The network addresses $A_{d+1,rn}$ and $A_{d+1,el}$ shall be assigned to the nth router child and lth end device child at depth $d+1$ in a sequential manner, respectively, as shown in (12.2):

$$\begin{aligned} A_{d+1,rn} &= A_{parent} + Cskip(d) \cdot (n-1) + 1 \\ A_{d+1,el} &= A_{parent} + Cskip(d) \cdot R_m + l \end{aligned} \tag{12.2}$$

where A_{parent} represents the address of the parent and $1 \leq n \leq Rm$.

The hierarchical topology in ZigBee network is based on DAAM. In this tree shape structure, if the destination address is in the address space that a node is managing, the node forwards the packet to one of its child nodes. Otherwise, it forwards the packet to its parent.

Each ZigBee device maintains a neighbour table which has all its neighbours' information in the one-hop transmission range. The contents for a neighbour entry are the network's PAN (Personal Area Network) identifier; node's extended address, network address, device type, relationship, LQI and etc. Optionally, additional information such as the depth can be included. Entries in the table are created when the node joins to an existing network. Conversely, the neighbour entry is removed when the neighbour node leaves the network. Since the information on the neighbour table is updated every time a device receives any frame from the some neighbour node, the information of the neighbour table can be said to be up-to-date all the time.

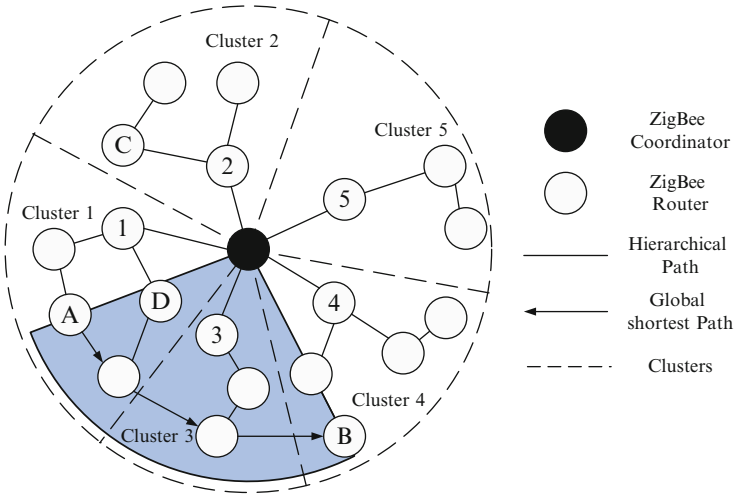

Fig. 12.1 An example of the directional broadcasting algorithm in routing discovery

12.3 Directional Broadcasting Algorithm in Routing Discovery

Considering the case in the Fig. 12.1, we assume the parameter *Cm* is 5, the network can be seen as being consist of five clusters that take the nodes in depth 1 as the cluster heads. If node A tries to send a packet to node B by Z-AODV, the global shortest path must start in the cluster 1 and finish in the cluster 4. Moreover, when we treat the network as a round, the two radiuses through the node A and B divide it into two sectors, the intermediate nodes of the global shortest path are almost certainly in the smaller one (including the ZC), as the shaded area shown in the Fig. 12.1. By limiting the routing request within this region, the overhead in the routing discovery can be reduced.

Firstly, we have to find a proper method to represent the area and the direction. Based on the DAAM, one device can easily decide its cluster by searching its ancestor in the a cluster head list. So the cluster headers should contain all the network addresses without overlapping. The number of clusters is preset, the cluster heads are chosen based on the principle mentioned above by the ZC, for a simple case, if the cluster count is equal to the *Cm*, all the routers in the depth 1 are selected. According to the Eq. (12.2), the A_{parent} is the address of its parent, which is also a router. For the depth 1 routers, their parent is the ZC whose address is 0. So we can use the sequential number k to differentiate the clusters. Since the clusters are fan shaped and not overlapping with a common vertex, each one may have at most two neighbours on the both sides. Their relative poisoning information can be represented by a sequence of adjacency (SoA). Since the neighbour devices

information is maintained by the neighbour table for each node, and we can tell which cluster a node belongs to if its network address is given, the SoA can be easily obtained. In Fig. 12.1, the node 1 and C can find each other in their neighbour tables, so it is the case with the node D and 3, therefore it can be concluded that the cluster 1 is adjacent to the cluster 2 and 3. However, if two clusters are too far apart to communicate, it may lead to the isolation. If all the nodes in one cluster can only find neighbours for the only other cluster, the cluster is isolated on one side, and if the communication is limited in the cluster, it is completely isolated. We use an isolation indicator (II) to announce such situations. Cluster 5 is a completely isolated cluster, the whole SoA of the network is [2,1,3,4,II,5,II]. The SoA is recursive, the last and the first clusters are adjacent by default, so another II is needed at the last.

The ZigBee network is organized as a hierarchical structure based on the DAAM, so the only task in the clustering is to choose the proper heads. Since the nodes in the same depth have different address spaces, it results in the fact that the number of the clusters can be only some specific integers, such as Cm, $2 \times Cm$-1 and etc. This may decline the performance of the algorithm. In the hierarchical network, the address subblocks overlapping of two routers (not including the ZC) only occurs when one node is the ancestor of the other, and the smaller space must be part of the greater one. So we may allow the overlapping by making the nodes in the common parts only belong to the cluster with the smaller address space. For the cluster members, if it finds more than one ancestor in the cluster head list, the principle can be simply implemented by joining the cluster with the greatest depth. The above mechanism guarantees that the clusters are not overlapping by any cluster numbers.

In our algorithm, the clustering begins a short time after the network initialized. The ZC is in the charge of deciding the cluster heads (will be explained later). Then all the devices that may find neighbours from other clusters are asked to report the adjacency to the head. Considering the overhead, if a certain device has announce its neighbour nodes from another cluster, all its descendants may be allowed to not monitor their neighbour tables any more. Each cluster head may also report its adjacent cluster to the ZC, and the ZC may work out the SoA and announce it to the whole network.

During the routing discovery, besides the range and duplications control, all the receiving nodes have to decide whether to rebroadcast or not based on the following principle: the node may find which clusters the source and the destination belong to separately, if possible, it may obtain the intervals between the two clusters in the SoA for both the forward and the reverse sequence; if the node is in the cluster which is part of the shorter path, it may rebroadcast the request, otherwise, the frame is abandoned. As shown in the Fig. 12.1, the nodes in the cluster 2 and 5 may not participate the routing discovery from node 1 to 2. By this method, the routing request rebroadcasting can be roughly limited in the smaller sector. If there is one II in the SoA, the mechanism of calculating the length of the bi-directional sequence is similar, whereas, if the II is in the shorter part, it can be deduced that the best link is a polyline whose inflection point is or near the ZC, so only the nodes in the source

and target clusters may rebroadcast the routing request. In the case of at least two IIs in the SoA, the network is absolutely segmented into more than two parts. If the start and the end devices are in the same section, the rebroadcasting is limited in the area from the source cluster to the destination one, otherwise, the request can be transmitted within only these two clusters.

Based on the principle above, the direction of the routing request flooding can be well controlled. However, its effectiveness and efficiency is closely related to the geometric parameters of the clusters. The expected clustering should have the similar scales, be uniformly distributed and not overlapping. The original networking method in the ZigBee specification cannot meet this requirements. So a cluster head decision method is also proposed. Suppose the cluster number is n, the ZC has to decide n cluster heads, denoted as CHi. Based on the ZigBee specification, the LQI is a mandatory term in the neighbour table, and this value could reflect the distance between two devices (is approximately proportional to the square of the space). So the distance between a node to the ZC, d_i, and that between two nodes $d_{i,j}$, can be denoted by the LQI of the corresponding links $1/\mathrm{LQI}_i$ and $1/\mathrm{LQI}_{i,j}$ respectively. The cosine of the angle between the two lines of the ZC to the devices CHi and CHj, $\alpha_{i,j}$, can be calculated by the Cosine Theorem, as (12.3):

$$\begin{aligned} \cos a_{i,j} &= \left(d_i^2 + d_j^2 - d_{i,j}^2\right)/2 \cdot d_i \cdot d_j \\ &= \frac{1}{2}\left(1/\mathrm{LQI}_i + 1/\mathrm{LQI}_j - 1/\mathrm{LQI}_{i,j}\right) \cdot \sqrt{\mathrm{LQI}_i \cdot \mathrm{LQI}_j} \end{aligned} \tag{12.3}$$

For n clusters, there should be n lines from the ZC to the cluster heads. We only focus on the angles between two adjacent lines, $\alpha_{<i,j>}$. To a uniformly distributed clustering, each $\alpha_{<i,j>}$ is $2\pi/n$. Based on the neighbour table information, the mechanism of finding the adjacent lines is similar as the one of deciding the relative position relationship in the SoA. Among all its neighbours, the ZC will choose n nodes that have the root mean square error (MSE) of the $\cos\alpha_{ij}$ to be the cluster heads, as shown in (12.4):

$$RMSE = \sum_{i,j} \left(\cos a_{<i,j>} - \cos \frac{2\pi}{n} \right)^2 \tag{12.4}$$

In our algorithm, the transmission range is also limited by a similar method as the ZBARD. As a known path, the length of the hierarchical path that passes through the first common ancestor is used as the maximum hops in the routing discovery, and that length can be worked out if the network addresses of the source and destination are given.

12.4 Simulations

The performance of the proposed directional broadcasting algorithm in routing discovery is discussed in this section. The simulation was implemented in the MATLAB. Some parameters in the simulation were set as following: the time duration was 300 s; the simulation area was 300 m × 300 m; the node numbers in the network varied from 25 to 200 (with the interval was 25), and all of them were the ZigBee routers; the nodes were randomly deployed following the uniform distribution; *Cm, Rm* and *Lm* were set 4, 4 and 5 separately; the packet interval time was 1 s; the first packet arrival time followed a uniform distribution from 10 to 11 for each node; the source and destination were randomly chosen; the cluster number was 5. For one scenario, the simulation was carried out 500 times to calculate the average.

The node mobility should be considered in the wireless networks. Since the ZigBee network is not for mobile communication, the node mobility is not high. In our simulations, each node was stationary for a random time that followed a uniform distribution from 50 to 150 s. Then the node moved to a new position which is randomly chosen, and the moving speed was uniformly distributed from 1 to 10 m/s.

We also made a mapping from the LQI in received data to the signal power. In our simulation, the channel followed Rayleigh fading with the δ^2 is 5. The slow fading was also considered. The amplitude loss followed a log-normal distribution, where the γ was 2.6 and the $\delta 2$ was 15 dB based on the empirical coefficient values tested in indoor with soft partition. We mapped the best LQI (−3 dB loss) to 0xff (255) and the lowest quality compliant signals detectable by the receiver (−20 dB loss) to 0×00 (0), the values in between were uniformly distributed.

To the best of our knowledge, we cannot find similar direction controlling algorithms based on the ZigBee specification, thus the DBRD was compared with the original Z-AODV and the ZBARD. An example of the network clustering by the DBRD is shown in Fig. 12.2. The cluster head candidates were decided according to the Eqs. (12.3) and (12.4). However, these 5 nodes did not cover the whole network. Based on the mechanism described in Sect. 12.3, their ancestors that containing the missing addresses might be chosen as the real cluster heads if they had already distributed some address blocks to other children. For the two candidates on the left side of the ZC, their father devices were selected as the grey nodes shown in the figure. On the other hand, although the candidate at the right bottom also had limited address subblock, its parent would not be selected because of the nonexistence of other descendants. And the other two candidates were decided as the cluster heads since they were able to cover all the devices in their direction. We can see that the network was successfully divided into five parts with similar sizes. On that basis, the directional broadcasting algorithm in routing discovery could be effectively applied.

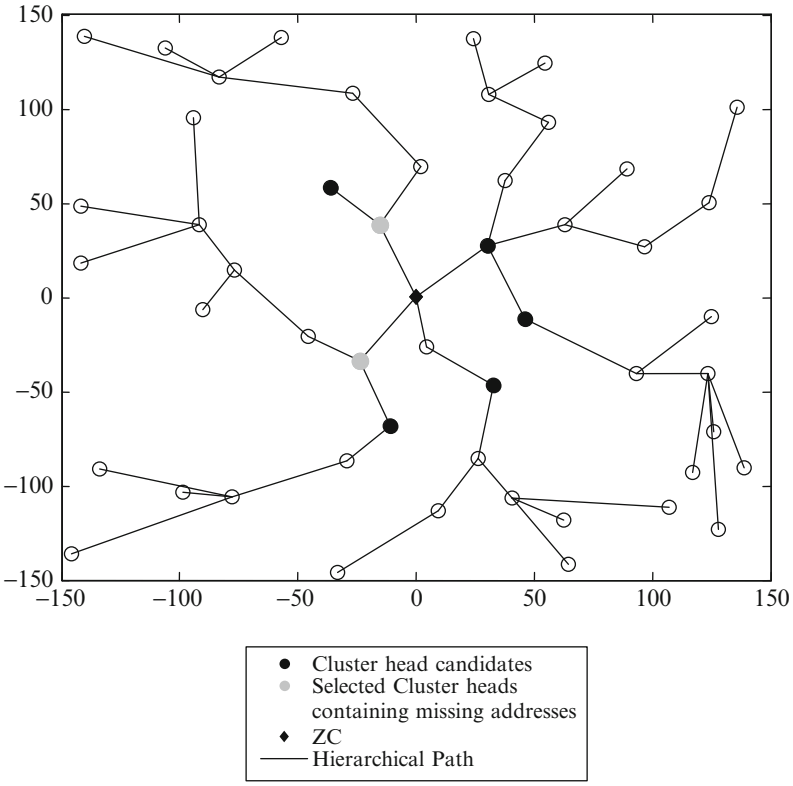

Fig. 12.2 An example of the network clustering in the DBRD

The normalized routing overhead, which was defined as the ratio of the number of routing packets transmitted per data packets sent to the destination, was used to evaluate the performance in our simulations. The performances of different algorithms are shown in Fig. 12.3. The Z-AODV had the greatest routing overhead for a fixed node number, because the routing request was flooding without any extra control. The ZBARD performed better due to its range limitation. We could see the DBRD could significantly reduce the cost in the routing discovery. That was mainly because it could suppress the rebroadcasting that probably not benefits the shortest path. Ideally, the overhead should be 50 % less than the ZBARD, however, due to the nodes' uneven distribution, the improvement in our simulation was about 40.7 % on average. Also, all the three methods had increasing normalized routing overhead according to the nodes number added. The DBRD curve had the least slope which implied the slowest increasing.

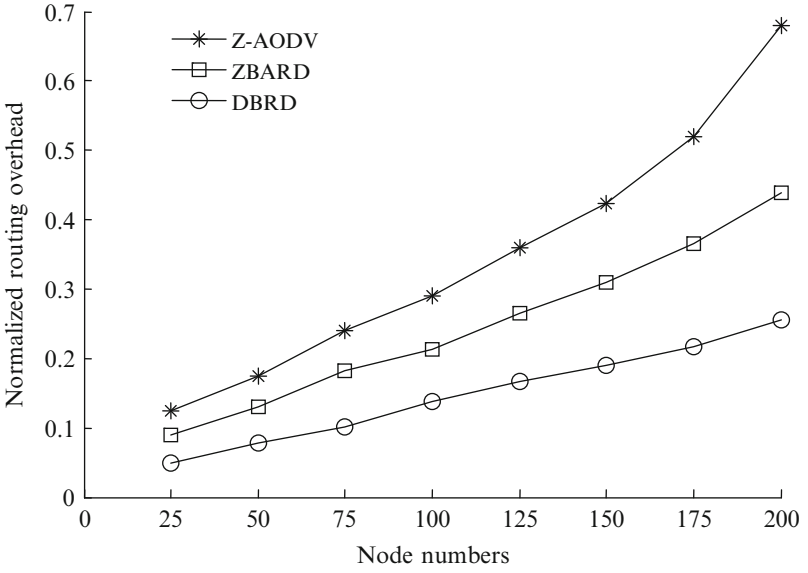

Fig. 12.3 The normalized routing overhead of different methods

Conclusions

In this paper, we proposed a directional broadcasting algorithm in routing discovery (DBRD) to reduce the routing overhead. The ZC was required to gather the node distribution information and clustering the network into parts with similar coverage. The adjacency of the clusters, also the direction, was represented by the SoA that was announced to every device in the network. The routing request was limited in the area of the shorter path in the SoA to reduce the routing overhead. Our algorithm was compared with the ones specified in the ZigBee and some classic improved methods. The simulation results showed that the DBRD could significantly lower the routing overhead. The normalized routing overhead might be 40 % cut and the latency was slightly reduced.

Our further work will further evaluate the algorithm in the aspects of the path length, delay and etc. Also, we may keep optimizing the clustering method in the directional broadcasting algorithm since the routing overhead is closely related to the size and node numbers in each cluster.

Acknowledgement This work is funded by the University Students' Innovative Training Program (201443).

References

1. Cuomo F, Luna SD, Monaco U, Melodia T (2007) Routing in ZigBee benefits from exploiting the IEEE 802.15.4 association tree. In: Paper presented at the IEEE international conference on communications, Glasgow, pp 3271–3276. doi:10.1109/ICC.2007.542
2. Tareq AA, Yang SH (2008) A ZigBee-based mobile tracking system through wireless sensor networks. Int J Adv Mechatron Syst 1(1):63–70. doi:10.1504/IJAMechS.2008.020839
3. Metin T, Ibrahim K (2012) PSAR: power-source-aware routing in ZigBee networks. Wirel Netw 18(6):635–651. doi:10.1007/s11276-012-0424-5
4. Liang Q (2003) Designing power aware self-reconfiguring topology for mobile wireless personal area networks using fuzzy logic. IEEE Trans Syst Man Cybern C Appl Rev 33(3):390–394
5. Lee KK, Kim SH, Park HS (2008) An effective broadcast strategy for route discovery in the ZigBee network. In: Paper presented at the 10th international conference on advanced communication technology, Gangwon-Do, vol 2. pp 1187–1191. doi:10.1109/ICACT.2008.4493977
6. ZigBee Standard Organization (2007) ZigBee Specification Document 053474r17. ZigBee Alliance, San Ramon

Part II
Radar and Sonar Networks, Radar Signal Processing

Chapter 13
Optimal Multiple Kernel Local Discriminant Embedding for SAR ATR

Hao Han, Yulin Huang, Xiaojia Liu, Jianyu Yang, and Jifang Pei

Abstract Feature extraction is a crucial step in synthetic aperture radar (SAR) automatic target recognition (ATR). This paper proposes a new feature extraction algorithm named optimal multiple kernel local discriminant embedding (OMKLDE). Based on kernel local discriminant embedding (KLDE), OMKLDE introduces multiple kernel functions and constructs an optimal model. Under this model, we use optimal method to obtain the expected mapping, which enhances interclass separability and maintains intraclass compactness, and more important, solves the parameter selecting problem in kernel trick. Experimental results based on MSTAR database show that the proposed method improves the stability and accuracy of recognition effectively.

Keywords Feature extraction • SAR • ATR • Manifold • Kernel

13.1 Introduction

With the capabilities of all-weather, all-time and high-resolution, SAR is widely applied in civilian and military fields. In order to detect and classify the targets efficiently, we need to use the technology named automatic target recognition (ATR). As an important part of ATR, feature extraction draws lots of attractions. The main task of feature extraction is to reduce dimension and reveal discriminatory information, which improves the speed of classification and accuracy of recognition greatly.

In the past decades, many effective feature extraction algorithms have been proposed. Principle component analysis (PCA) [1] and linear discriminant analysis (LDA) [2] are linear feature extraction algorithms. They are popular algorithms because of their simplicity and effectiveness. However, PCA and LDA are only optimal when the dataset satisfies a linear separable structure.

H. Han (✉) • Y. Huang • X. Liu • J. Yang • J. Pei
School of Electronic Engineering, University of Electronic Science and Technology of China, Chengdu Sichuan 611731, PR China
e-mail: haohanpapers@163.com

J. Mu et al. (eds.), *The Proceedings of the Third International Conference on Communications, Signal Processing, and Systems*, Lecture Notes in Electrical Engineering 322, DOI 10.1007/978-3-319-08991-1_13

Afterwards, kernel trick somehow expands the application of linear algorithms. The representative algorithms of kernel trick are kernel principle component analysis (KPCA) [3] and kernel linear discriminant analysis (KLDA) [4]. Both of the two methods firstly project the original space into a relatively high-dimensional space by nonlinear mapping, then extract features using linear method in that high-dimensional space. In other words, kernel trick transforms the linear inseparable dataset lying on lower-dimensional space to linear separable dataset of higher-dimensional space. However, since different parameters of kernel function effect recognition results dramatically, the selection of the parameters is an inevitable problem in kernel trick.

All the algorithms mentioned before have not considered the local structure of dataset, which fail to reveal essential features meeting special distribution. In recent years, literatures indicate that high-dimensional images may reside on a nonlinear manifold [5]. Manifold learning aims to find low-dimensional manifold which is embedded in high-dimensional space. Based on manifold learning, locally linear embedding (LLE) [6] and laplacian eigenmap (LE) [7] are two representative algorithms. However, these algorithms only get maps of the training dataset and how to extract features of novel testing dataset remains unclear. Afterwards, locality preserving projections (LPP) [8] is proposed to solve this problem, which gives a specific mapping from high-dimensional space to low-dimensional space. Although LPP extracts features which maintain local spatial structure successfully, it may not be suitable for SAR ATR due to its ignorance of interclass information. Local discriminant embedding (LDE) [9] is proposed with the consideration of interclass information, which performs better than LPP. By maximizing the distance of interclass and preserving local spatial structure, LDE reveals effective features to discrimination. The variant of LDE, kernel local discriminant embedding (KLDE) [9], combines manifold learning and kernel trick, even performs better than LDE. However, KLDE is sensitive to the parameter of kernel function, which is known as an inevitable problem of kernel trick. This problem can be solved by multiple kernel learning (MKL) [10], which finds optimal weight of kernel functions adaptively through solving an optimal model. However, MKL may not be effective to handle SAR images because it minimize the distance of interclass samples. As a result, the features are gathered but not separated well, which is adverse to discriminant.

In this paper, we propose a new feature extraction algorithm named optimal multiple kernel local discriminant embedding (OMKLDE), which combines the advantages of manifold learning and kernel trick. By introducing multiple kernel functions (the parameters of kernel function are different), OMKLDE constructs optimal model, by which obtains essential mapping, and more important, solves the selecting problem of kernel function parameter.

The rest of this paper is organized as follows. OMKLDE is proposed in Sect. 13.2. Experimental results are discussed in Sect. 13.3. Final section concludes this paper.

13.2 Optimal Multiple Kernel Local Discriminant Embedding

In order to solve the selecting problem of parameter of kernel function, we propose OMKLDE. Based on the mathematic model of KLDE, OMKLDE introduces a set of kernel functions $\mathbf{K} = [\mathbf{K}_1, \mathbf{K}_2, \ldots, \mathbf{K}_M]$ ($\mathbf{K}_\mathrm{i}$ is the kernel function, and they are with different parameters). Aiming at maximizing the distance of interclass samples and maintaining local spatial structure, OMKLDE constructs optimal model, by which obtains essential mapping.

The original SAR samples are $\{\mathbf{x}_i\}_{i=1}^N$ ($\mathbf{x}_i$ is the i-th sample and N is the number of samples), and their labels are $\{y_i\}_{i=1}^N$ (y_i is the label of $\mathbf{x}_i$). We project the original dataset to high-dimensional space by nonlinear mapping, and the dataset transforms to $\{\phi(\mathbf{x}_i)|\phi(\mathbf{x}_i) \in \mathbb{R}^m\}_{i=1}^N$ (m is the dimension of new space and $m \gg n$). In this $\mathbb{R}^m$ space, we can find an embedding $\mathbf{V}$, which maps the database $\{\phi(\mathbf{x}_i)|\phi(\mathbf{x}_i) \in \mathbb{R}^m\}_{i=1}^N$ to the feature space, and the transformed images can be denoted as (13.1).

$$\begin{aligned} \phi(\mathbf{z}_i) &= \mathbf{V}^T\phi(\mathbf{x}_i) \\ &= \sum_{p=1}^{N}\sum_{m=1}^{M}\alpha_p^T\beta_m K_m(p,i) \\ &= \alpha^T\mathbf{K}^{(i)}\beta \end{aligned} \tag{13.1}$$

Where $\mathbf{V}$ is the projection, $\alpha = [\alpha_1, \alpha_2, \ldots, \alpha_N]^T$, $\beta = [\beta_1, \beta_2, \ldots, \beta_M]^T$, $\mathbf{K}^{(i)} = \begin{bmatrix} K_1(1,i) & \cdots & K_M(1,i) \\ K_1(2,i) & \cdots & K_M(2,i) \\ \vdots & \ddots & \vdots \\ K_1(N,i) & \cdots & K_M(N,i) \end{bmatrix}_{N\times M}$ and $K_\mathrm{m}(i,j)$ is kernel function. α is the weight matrix to linear combine images $\{\phi(\mathbf{x}_i)\}_{i=1}^N$, while β is the weight to adjust the effect of different kernel functions, which can measure the importance of different kernel function to the optimal model. We use Gaussian kernel function in this paper: $K_m(i,j) = \exp\left(-\mathbf{x}_i - \mathbf{x}_j{}^2 t_m\right)$, where t_m is the parameter of kernel function.

Finally, we can obtain the optimal model.

$$\begin{aligned} \text{maxmize}: &\sum_{i=1}^{N}\sum_{j=1}^{N} \| \phi(\mathbf{z}_i) - \phi\left(\mathbf{z}_j\right) \|^2 w_{ij} \\ \text{subject to}: &\sum_{i=1}^{N}\sum_{j=1}^{N} \| \phi(\mathbf{z}_i) - \phi\left(\mathbf{z}_j\right) \|^2 w_{ij}{}' = constant \end{aligned} \tag{13.2}$$

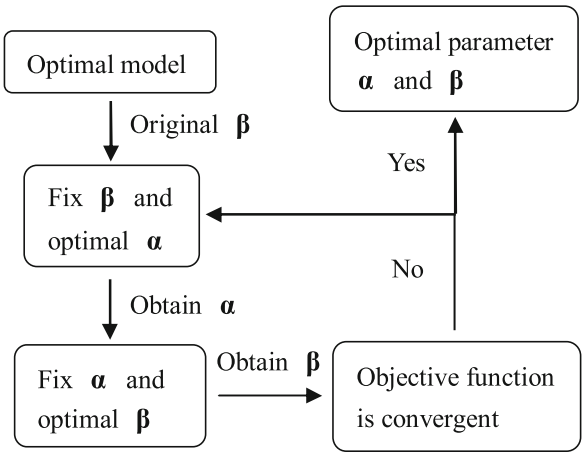

Fig. 13.1 Procedure of OMKLDE

where

$$w_{ij} = \begin{cases} \exp\left[-\| \mathbf{x}_i - \mathbf{x}_j \|^2 / \varepsilon\right] & y_i \neq y_j \\ 0, & y_i = y_j \end{cases}, \text{and } w'_{ij} = \begin{cases} \exp\left[-\| \mathbf{x}_i - \mathbf{x}_j \|^2 / \varepsilon\right] & y_i = y_j \\ 0, & y_i \neq y_j \end{cases},$$

ε is a constant.

The meaning of the optimal model is to maximize the distance of interclass samples and reserve the distance of intraclass samples. This model has two parameters, which are used for mapping to feature space and adjusting the effect of different kernel functions respectively. Since there are two parameters α and β still unknown, it is infeasible to use the same method like KLDE.

We solve the problem by iterating [9]. Through fixing one parameter and obtaining optimal result of the other parameter, we can get the optimal parameters after several times of iterations. Specific procedure is as follows (Fig. 13.1).

According to this procedure, specific derivation is as follows:

Step 1 *fix β and optimal α*:

Randomly select a set of parameters for β and transform objective function of (13.2) to (13.3):

$$\begin{aligned} J(\alpha) &= \max \sum_{i=1}^{N} \sum_{j=1}^{N} \mathbf{V}^T \phi(\mathbf{x}_i) - \mathbf{V}^T \phi(\mathbf{x}_j)^2 w_{ij} \\ &= \max \left(\text{trace} \left(\sum_{i=1}^{N} \sum_{j=1}^{N} \left(\alpha^T \mathbf{K}^{(i)} \beta - \alpha^T \mathbf{K}^{(j)} \beta \right) \left(\alpha^T \mathbf{K}^{(i)} \beta - \alpha^T \mathbf{K}^{(j)} \beta \right)^T w_{ij} \right) \right) \\ &= \max \left(\text{trace} \left(2\alpha^T \left(\mathbf{K} D \mathbf{K}^T - \mathbf{K} W \mathbf{K}^T \right) \alpha \right) \right) \\ &= \max \left(\text{trace} \left(\alpha^T \mathbf{K} (\mathbf{D} - \mathbf{W}) \mathbf{K}^T \alpha \right) \right) = \max \left(\text{trace} \left(\alpha^T \mathbf{S}_w^B \alpha \right) \right) \end{aligned} \tag{13.3}$$

where $\mathbf{K} = \sum_{m=1}^{M} \beta_m \mathbf{K}_m$ and $\mathbf{S}_w^B = \mathbf{K}(\mathbf{D} - \mathbf{W})\mathbf{K}^T$. $\mathbf{D}$ is a diagonal matrix which diagonal elements are $d_{ii} = \sum_{j=1}^{N} w_{ij}$ and $\mathbf{W} = \{w_{ij}\} \in \mathbb{R}^{N \times N}$. Obtain limiting condition according to:

$$\begin{aligned} J'(\alpha) &= \sum_{i=1}^{N}\sum_{j=1}^{N} \| \mathbf{V}^T\phi(\mathbf{x}_i) - \mathbf{V}^T\phi(\mathbf{x}_j) \|^2 w'_{ij} \\ &= 2\text{trace}\left(\alpha^T \mathbf{K}\left(\mathbf{D}' - \mathbf{W}'\right)\mathbf{K}^T\alpha\right) = 2\text{trace}\left(\alpha^T \mathbf{S}_{w'}^B \alpha\right) \end{aligned} \tag{13.4}$$

where $\mathbf{S}_{w'}^B = \mathbf{K}\left(\mathbf{D}' - \mathbf{W}'\right)\mathbf{K}^T$. Set $J_\alpha{}'$ to a constant, we can obtain the model, which fix β and obtain optimal α:

$$\begin{aligned} &\text{Maxmize} : \left(\text{trace}\left(\alpha^T \mathbf{S}_w^B \alpha\right)\right) \\ &\text{Subject to} : \text{trace}\left(\alpha^T \mathbf{S}_{w'}^B \alpha\right) = \text{constant} \end{aligned} \tag{13.5}$$

By computing the first l maximal eigenvalues and its corresponding eigenvectors of $\mathbf{S}_w^B \mathbf{S}_{w'}^B$, we can get the suitable α.

Step 2 *fix α and optimal β*:

We can obtain β by fixing α, which is obtained by (13.5). The objective function of (13.2)–(13.6):

$$\begin{aligned} J(\beta) &= \max \sum_{i=1}^{N}\sum_{j=1}^{N} \mathbf{V}^T\phi(\mathbf{x}_i) - \mathbf{V}^T\phi(\mathbf{x}_j)^2 w_{ij} \\ &= \max\left(\sum_{i=1}^{N}\sum_{j=1}^{N}\left(\alpha^T\mathbf{K}^{(i)}\beta - \alpha^T\mathbf{K}^{(j)}\beta\right)^T\left(\alpha^T\mathbf{K}^{(i)}\beta - \alpha^T\mathbf{K}^{(j)}\beta\right)w_{ij}\right) \\ &= \max\left(\sum_{i=1}^{N}\sum_{j=1}^{N}\beta^T\left(\left(\mathbf{K}^{(i)} - \mathbf{K}^{(j)}\right)^T\alpha\alpha^T\left(\mathbf{K}^{(i)} - \mathbf{K}^{(j)}\right)\right)\beta w_{ij}\right) \\ &= \max\left(\beta^T\mathbf{S}_w^A\beta\right) \end{aligned} \tag{13.6}$$

where $\mathbf{S}_w^A = \sum_{i=1}^{N}\sum_{j=1}^{N}\left(\left(\mathbf{K}^{(i)} - \mathbf{K}^{(j)}\right)^T\alpha\alpha^T\left(\mathbf{K}^{(i)} - \mathbf{K}^{(j)}\right)\right)w_{ij}$.

The constraint transformed into:

$$J^{'}(\beta) = \sum_{i=1}^{N}\sum_{j=1}^{N} \| \mathbf{V}^T\phi(\mathbf{x}_i) - \mathbf{V}^T\phi(\mathbf{x}_j) \|^2 w_{ij}^{'} = \beta^T \mathbf{S}_{w'}^{A} \beta \tag{13.7}$$

where $\mathbf{S}_{w'}^{A} = \sum_{i=1}^{N}\sum_{j=1}^{N}\left(\mathbf{K}^{(i)} - \mathbf{K}^{(j)}\right)^T \alpha\alpha^T \left(\mathbf{K}^{(i)} - \mathbf{K}^{(j)}\right) w_{ij}^{'}$. Set $J_{\beta}^{'}$ to a constant, we can obtain the optimal model:

$$\begin{aligned} &\text{Maxmize} : \beta^T \mathbf{S}_{w}^{A} \beta \\ &\text{Subject to} : \beta^T \mathbf{S}_{w'}^{A} \beta = \text{constant} \end{aligned} \tag{13.8}$$

This is a quadratically constrained quadratic programs (QCQP) problem, which can be solved by semidefinite programming (SDP) method [11].

Step 3 *Iteration:* According to the procedure, we can get the parameter of α and β by iteration. Repeat step 1 and 2 until the objective function is convergent.

Finally, we can use α and β to obtain feature of dataset $\{\mathbf{x}_i\}_{i=1}^{N}$ by (13.1).

13.3 Experiment

In the experiments, we will comprehensive analyze OMKLDE in three aspects. First, analyze the convergence of applying OMKLDE to SAR images. Second, compare the performance of OMKLDE with other representative algorithms. Third, investigate the stability of OMKLDE.

All the experiments use the Moving and Stationary Target Acquisition and Recognition (MSTAR) dataset. Three classes targets of MSTAR dataset are used, and they are BMP2, BTR70, T72. In this paper, training dataset contains SAR images at depression angle 17, and testing dataset at the depression 15. The detailed information of training and testing dataset is shown in Table 13.1.

Table 13.1 Detailed information of training and testing dataset

Training sets	Size	Testing sets	Size
		BMP2sn-c9563	195
BMP2sn-c9563	233	BMP2sn-c9566	196
		BMP2sn-c21	196
BTR70	233	BTR70	196
		T72sn-132	196
T72sn-132	232	T72sn-812	195
		T72sn-S7	191
Total	698	Total	1,365

All the experiments are carried out according to the steps as follows:

(a) **Image preprocessing**

In order to deduce the amount of calculation, we utilize centroid registration and incise the training and testing dataset to 64×64 matrixes, which contain the whole information of targets. Then, use two-parameter CFAR and geometric clustering to remove the false alarming areas. Finally, gray enhancement based on power function is utilized to enhance information of SAR images.

(b) **Feature extraction**

By utilizing feature extraction algorithms, we can obtain the features of training and testing dataset. All the kernel functions we used in this paper are Gaussian function ($K_m(i,j) = \exp\left(-\mathbf{x}_i - \mathbf{x}_j{}^2 t_m\right)$, t_m is the parameter of kernel function). The proposed algorithm OMKLDE, has five kernel functions (the kernel functions are different with the parameters of kernel function t_m) in the experiment.

(c) **Classification**

The nearest neighbor classifier (NNC) is used as the classifier in the experiments. The experiment results and analysis are shown as follows:

13.3.1 Analysis of the Convergence of OMKLDE

We will analyze the values of objective function through iterative optimization. Experimental results are shown in Fig. 13.2.

OMKLDE is iterated 20 times in the experiment. In Fig. 13.2, the values of objective function have slight changes in first three times of iteration, and then stay constant. Therefore, OMKLDE is convergent when apply to SAR images.

13.3.2 Compare the Recognition of Different Algorithms

In this part, we will compare OMKLDE with other representative algorithms. First, we compare OMKLDE with PCA, LDA and LDE, which do not consider the selection of kernel function. The parameters of kernel function of OMKLDE are selected as 1, 2, 3, 4 and 5. The feature dimension extracted by LDA is restricted by the number of class in training dataset. The result of stimulation is shown in Fig. 13.3.

As is shown in Fig. 13.3, OMKLDE reaches the highest recognition rate with 40 feature dimension, so it is superior to PCA, LDA and LDE. Generally, PCA and LDA are linear algorithms and only optimal when the dataset satisfies a linear separate structure. Based on manifold learning theory, LDE remains the local

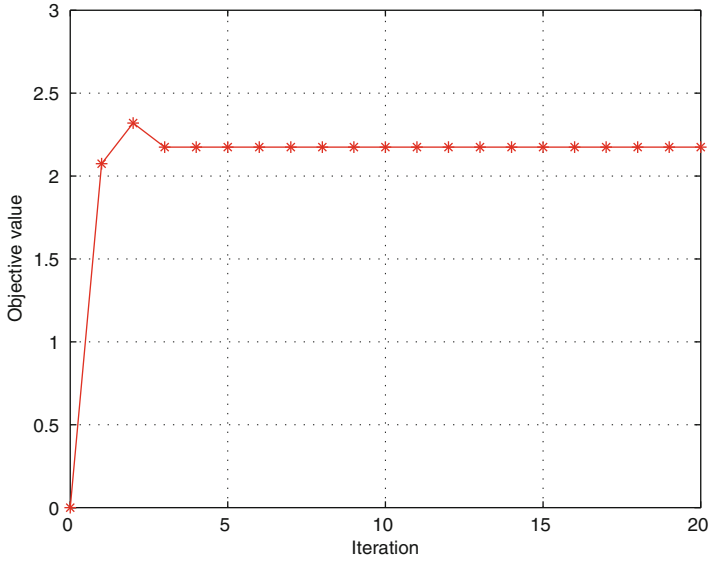

Fig. 13.2 Objective value vs iteration

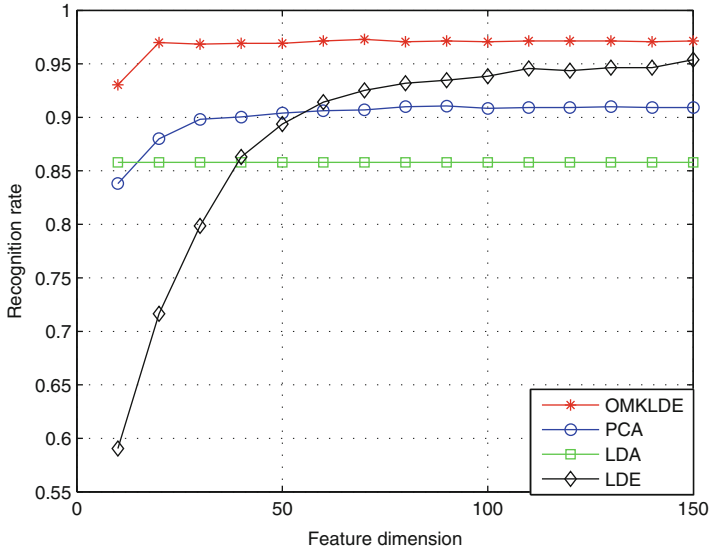

Fig. 13.3 The recognition rate of OMKLDE, PCA, LDA and LDE

structure and maximizes the distance of interclass samples, so LDE is suitable for SAR ATR. However, combined manifold learning theory and kernel trick, OMKLDE obtains better performance than LDE.

Table 13.2 The parameters of KPCA, KLDA, KLDE and OMKLDE

Algorithms	Parameters of kernel function (five sets)
KPCA	$t_1 = 1, t_2 = 2, t_3 = 3, t_4 = 4, t_5 = 5$
OMKLDE	$t_1 = 1, t_2 = 2, t_3 = 3, t_4 = 4, t_5 = 5$
KLDA	$t_1 = 5, t_2 = 10, t_3 = 15, t_4 = 20, t_5 = 25$
OMKLDE	$t_1 = 5, t_2 = 10, t_3 = 15, t_4 = 20, t_5 = 25$
KLDE	$t_1 = 1, t_2 = 5, t_3 = 10, t_4 = 15, t_5 = 20$
OMKLDE	$t_1 = 1, t_2 = 5, t_3 = 10, t_4 = 15, t_5 = 20$

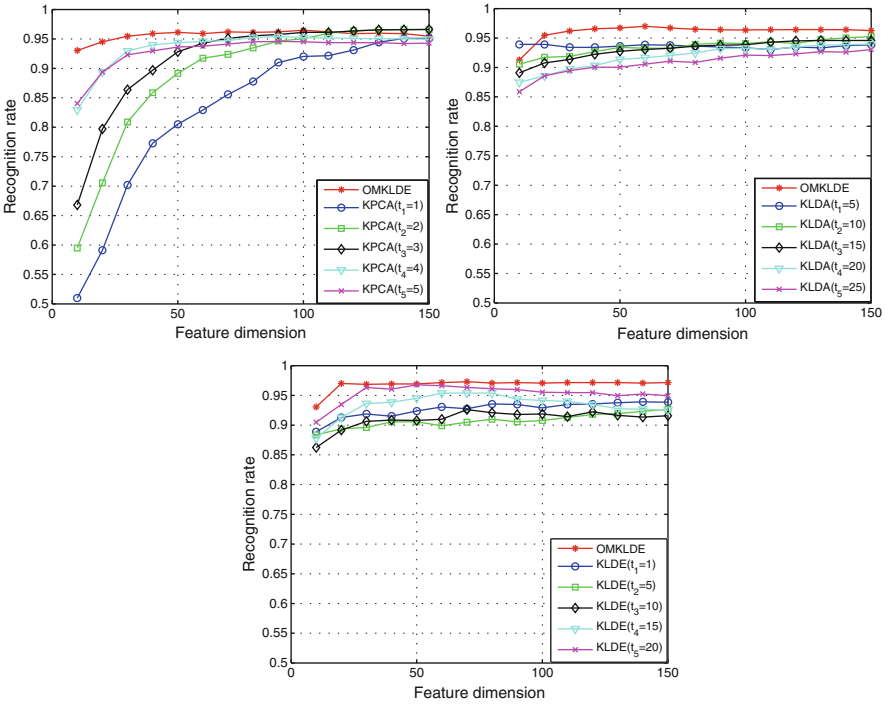

Fig. 13.4 Recognition rate of OMKLDE, KPCA, KLDA and KLDE

Then, compare OMKLDE with KPCA, KLDA and KLDE, which is considered as representative application of kernel trick. The parameters of these algorithms are shown in Table 13.2.

The experiment results are shown in Fig. 13.4.

As is shown in Fig. 13.4, OMKLDE obtains the highest recognition rate in all the comparisons. More important, the recognition rate is changed obviously with the change of parameters of kernel function for KPCA, KLDA and KLDE, while OMKLDE is insensitive to the parameter.

It is considered that SAR images may reside on a manifold structure. As linear algorithm, PCA and LDA can not reveal the essential feature of SAR dataset.

Table 13.3 Detailed information of training and testing dataset

No.	OMKLDE	KPCA	KLDA	KLDE
1	$t_1 = 1, t_2 = 2, t_3 = 3, t_4 = 4, t_5 = 5$	5	5	5
2	$t_1 = 6, t_2 = 7, t_3 = 8, t_4 = 9, t_5 = 10$	10	10	10
3	$t_1 = 11, t_2 = 12, t_3 = 13, t_4 = 14, t_5 = 15$	15	15	15
4	$t_1 = 16, t_2 = 17, t_3 = 18, t_4 = 19, t_5 = 20$	20	20	20
5	$t_1 = 21, t_2 = 22, t_3 = 23, t_4 = 24, t_5 = 25$	25	25	25
6	$t_1 = 26, t_2 = 27, t_3 = 28, t_4 = 29, t_5 = 30$	30	30	30

Although KPCA and KLDA somehow solve the restriction of linear algorithm by utilizing kernel trick, they only analyze the whole structure while ignore the importance of local structure. Based on manifold learning theory, LDE retains local structure and obtains better performance than others. As a variant of LDE, KLDE utilizes kernel trick and gets better performance than LDE. However, KLDE has to face with the selecting problem of kernel function parameter, which is known as the general problem of kernel trick. By solving an optimal model of multiple kernel functions, OMKLDE gets even better performance than KLDE, and more important, solves the problem of selecting the parameter of kernel function.

13.3.3 Analyze the Stability of Different Algorithms

In order to analyze the stability of OMKLDE, especially for the sensitivity of parameter selecting, we analyze the recognition rate with different parameters of kernel function.

We compare the sensitivity of OMKLDE with KPCA, KLDA and KLDE. The parameters are selected as Table 13.3.

We can see the error bars in Fig. 13.5.

As is shown in Fig. 13.5, we can get two conclusions. First, OMKLDE has the highest recognition. Second, the standard deviation of OMKLDE is the lowest for randomly feature dimension. In other words, OMKLDE is a stable algorithm while KPCA, KLDA and KLDE are sensitive to the parameter of kernel function.

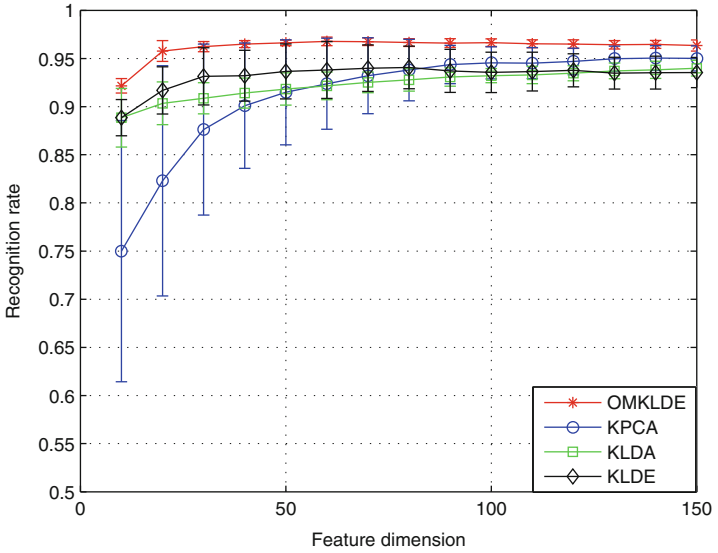

Fig. 13.5 Error bar of OMKLDE, KPCA, KLDA, KLDE

Conclusions

In this paper, we proposed a new feature extraction algorithm named as OMKLDE. This algorithm considers the SAR images are resided on a manifold which embedding in high-dimensional space. By introducing multiple kernel functions, OMKLDE constructs optimal model, which is solved by optimal method. Therefore, OMKLDE has better recognition rate and solves the selecting problem of kernel function parameters. Based on MSTAR dataset, a series of experiments are shown in this paper, which verify the effectiveness of OMKLDE.

References

1. Turk M, Pentland A (1991) Eigenfaces for recognition. J Cogn Neurosci 3(1):71–86
2. Belhumeur PN, Hespanha JP, Kriegman D (1997) Eigenfaces vs. fisherfaces: recognition using class specific linear projection. IEEE Trans Pattern Anal Mach Intell 19(7):711–720
3. Scholkopf B, Smola A, Müller KR (1999) Kernel principal component analysis. In: Advances in kernel methods-support vector learning, Citeseer. MIT, Cambridge
4. Scholkopft B, Mullert KR (1999) Fisher discriminant analysis with kernels
5. Seung HS, Lee DD (2000) The manifold ways of perception. Science 290(5500):2268–2269
6. Roweis ST, Saul LK (2000) Nonlinear dimensionality reduction by locally linear embedding. Science 290(5500):2323–2326
7. Belkin M, Niyogi P (2001) Laplacian eigenmaps and spectral techniques for embedding and clustering. Neural Inf. Process. Syst. 14:585–591

8. He X, Niyogi P (2003) Locality preserving projections. Neural Inf. Process. Syst. 16:234–241
9. Chen HT, Chang HW, Liu TL (2005) Local discriminant embedding and its variants. In: IEEE computer society conference on computer vision and pattern recognition (CVPR) 2005, vol 2, pp 846–853
10. Lin YY, Liu TL, Fuh CS (2011) Multiple kernel learning for dimensionality reduction. IEEE Trans Pattern Anal Mach Intell 33(6):1147–1160
11. Lanckriet GR, Cristianini N, Bartlett P, Ghaoui LE, Jordan MI (2004) Learning the kernel matrix with semidefinite programming. J Mach Learn Res 5:27–72

Chapter 14
Cubature Kalman Filter Based on Strong Tracking

Zhang Cun, Zhao Meng, Yu Xue-Lian, Cui Ming-Lei, Zhou Yun, and Wang Xue-Gang

Abstract To improve the ability of dealing with inaccurate of model and statistic characteristics of noise, as well as the abrupt change of state of cubature Kalman filter (CKF), a new nonlinear filter, called Cubature Kalman Filter based on strong tracking (CKF-ST), is proposed in this paper. Inspired by the idea of strong tracking, a time-variant factor is introduced into the recursive process of cubature Kalman filter such that the filter gain can be updated along with the measured values, thus endowing CKF-ST powerful ability to deal with abrupt changes of state. Meanwhile, such merits of CKF as high accuracy and being easy to implement can be entirely preserved in CKF-ST. Simulation results on one classical examples demonstrate that CKF-ST is overall superior to CKF and other filters involved, especially when target motion changes suddenly.

14.1 Introduction

Nonlinear filtering obtains a very wide use in both military and industrial applications. However, since the posterior probability density function (PDF) of system state is very difficult to acquire in most cases, it is too far to get an optimal solution to the state estimation of nonlinear dynamic system. Therefore, a lot of sub-optimal filtering techniques have been proposed.

The most representative one is the extended Kalman filter (EKF) [1], which have a simple structure and is easy to be implemented. Nevertheless, some linear features are ignored in EKF, which may lead to large errors and even divergence when the system is severely nonlinear. Moreover, the calculation of the Jacoby matrix is difficult in many practices. Some improved algorithms based on EKF can improve the calculation accuracy and stability, but at the same time they all increase the

Z. Cun (✉) • Z. Meng • Y. Xue-Lian • C. Ming-Lei • Z. Yun • W. Xue-Gang
University of Electronic Science and Technology of China (UESTC), No. 2006, Xiyuan Avenue, West High-Tech Zone, 611731 Chengdu, China
e-mail: 870697437@qq.com; zhaom0524@163.com

J. Mu et al. (eds.), *The Proceedings of the Third International Conference on Communications, Signal Processing, and Systems*, Lecture Notes in Electrical Engineering 322, DOI 10.1007/978-3-319-08991-1_14

computational burden [2, 3]. Zhou et al. (1999) and Ye (2000) proposed the strong tracking filter (STF) [3, 4]. The essence of STF is introducing a fading factor into the prediction error covariance matrix so that the filter gain will change along with the measured value. It has been verified that STF has better tracking performance than EKF, but it still need linearization operation.

To overcome the shortcomings of EKF mentioned above, many algorithms free from differential have been developed. Simon. J. Julier established the unscented Kalman filter (UKF) [5, 6]. Instead of linearization, UKF uses a set of weighted samples to approximate the probability density distribution of nonlinear function. It has been proved that UKF has a good estimation performance. But it is elusive to get satisfactory estimation results when the dimension of state vector is greater than three. It had been proved that Particle Filter (PF) [7], which approximates the posterior PDF by generating a large number of particles randomly, could achieve very high precision long as the number of particles meets the requirement. But large number of particles may cause an enormous amount of calculation, thus limiting the widely use of PF in practical application.

The cubatures Kalman filter (CKF), which is proposed in recent years by... [8], can obtain some good estimation accuracy with an acceptable computation complexity. In CKF, the mean and variance of the system state are propagated through a set of cubature points whose number is twice the dimension of state vector. Different from UKF [9, 10], the cubature points and weights of CKF are determined uniquely by the dimension of state vector so that the complicated work of parameter selection is removed. Experimental results show that the performance of CKF is better than that of UKF in most case. However, CKF will no longer have the superiority when sudden change occurs.

Aiming at the above problem of CKF, an improved nonlinear filter, named Cubature Kalman Filter based on strong tracking (CKF-ST), is presented in this paper. By introducing a time-variant factor into CKF, CKF-ST can continuously update the gain matrix along with residual error, which enables it huge power to deal with sudden change of states and uncertainty of system model. At the same time, the inherent merits of CKF are well preserved in CKF-ST.

The rest of the paper is organized as follows. In Sect. 14.2, CKF and the strong tracking filter are reviewed in short. In Sect. 14.3, CKF-ST is presented and the derivation process is detailed. Then in Sect. 14.4, one simulation is carried out to demonstrate the effectiveness of the proposed CKF-ST. Finally, conclusions are drawn in Sect. 14.5.

14.2 Reviews

14.2.1 Mathematical Model

The discrete nonlinear system can be expressed as:

$$\begin{cases} \mathbf{x}_k = f(\mathbf{x}_{k-1}) + \mathbf{w}_{k-1} \\ \mathbf{z}_k = h(\mathbf{x}_k) + \mathbf{v}_k \end{cases} \tag{14.1}$$

where $\mathbf{x}_k \in \Re^{n_x}$ is the state vector of the dynamic system at discrete time k, $\mathbf{z}_k \in \Re^{n_z}$ is the measurement, f and h are some known functions, $\mathbf{w}_{k-1}$ and $\mathbf{v}_k$ denote the process and measurement noise with corresponding covariance matrices $\mathbf{Q}_{k-1}$ and $\mathbf{R}_k$, respectively.

14.2.2 Cubature Kalman Filter

By reference [8], we can know that CKF use spherical-radial rule to get the basic cubature points and the opposite weights:

$$\xi_j = \sqrt{\frac{m}{2}}[1]_j, \quad \omega_j = \frac{1}{m}, \quad j = 1, \cdots m, \quad j = 1, \cdots m, \quad m = 2\mathrm{n}_x \tag{14.2}$$

m is the number of basic cubature points. $[1]_j$ is denoted as jth member from the point group. Let's take $n = 2$ for example, the point-group is $\left\{ \begin{bmatrix} 1 \\ 0 \end{bmatrix}, \begin{bmatrix} 0 \\ 1 \end{bmatrix}, \begin{bmatrix} -1 \\ 0 \end{bmatrix}, \begin{bmatrix} 0 \\ -1 \end{bmatrix} \right\}$.

The derivation process of CKF based on Eq. (14.1) can be summarized as follow:

(1) Evaluate the cubature points ($j = 1, 2, \cdots 2n_x$):

$$\mathbf{X}_{j,k-1|k-1} = \mathbf{S}_{k-1|k-1}\xi_j + \hat{\mathbf{x}}_{k-1|k-1} \tag{14.3}$$

(2) Propagated cubature points and the predicted state can be calculated as:

$$\begin{cases} \mathbf{X}^*_{j,k|k-1} = f\left(\mathbf{X}_{j,k-1|k-1}\right) \\ \hat{\mathbf{x}}_{k|k-1} = \dfrac{1}{m}\displaystyle\sum_{j=1}^{m} \mathbf{X}^*_{j,k|k-1} \end{cases} \tag{14.4}$$

(3) The calculation of predicted error covariance which has introduced time varying factor can be described as:

$$\mathbf{P}_{k|k-1} = \left\{ \frac{1}{m}\sum_{j=1}^{m} \mathbf{X}^*_{j,k|k-1}\mathbf{X}^{*\,T}_{j,k|k-1} - \hat{\mathbf{x}}_{k|k-1}\hat{\mathbf{x}}_{k|k-1} + \mathbf{Q}_{k-1} \right\} \tag{14.5}$$

(4) Evaluate the cubature points and the propagated cubature points

$$\begin{cases} \mathbf{X}_{j,k|k-1} = \mathbf{S}_{k|k-1}\xi_j + \hat{\mathbf{x}}_{k|k-1} \\ \mathbf{Z}_{j,k|k-1} = h\left(\mathbf{X}_{j,k|k-1}, \mathbf{u}_k\right) \end{cases} \tag{14.6}$$

Where $\mathbf{S}_{k|k-1} = \text{chol}(\mathbf{P}_{k|k-1})$.

(5) Calculate predicted measurement and the innovation covariance matrix as:

$$\begin{cases} \hat{\mathbf{z}}_{k|k-1} = \dfrac{1}{m}\sum_{j=1}^{1}\mathbf{Z}_{j,k|k-1} \\ \mathbf{P}_{zz,k|k-1} = \dfrac{1}{m}\sum_{j=1}^{m}\mathbf{Z}_{j,k|k-1}\mathbf{Z}_{j,k|k-1}^{T} - \hat{\mathbf{z}}_{k|k-1}\hat{\mathbf{z}}_{k|k-1}^{T} + \mathbf{R}_k \end{cases} \tag{14.7}$$

(6) Estimate the cross-covariance matrix:

$$\mathbf{P}_{xz,k|k-1} = \frac{1}{m}\sum_{j=1}^{m}\mathbf{X}_{j,k|k-1}\mathbf{Z}_{j,k|k-1}^{T} - \hat{\mathbf{x}}_{k|k-1}\hat{\mathbf{z}}_{k|k-1}^{T} \tag{14.8}$$

(7) Update the state and the corresponding error covariance as:

$$\begin{cases} \hat{\mathbf{x}}_{k|k} = \hat{\mathbf{x}}_{k|k-1} + \mathbf{W}_k\left(\mathbf{z}_k - \hat{\mathbf{z}}_{k|k-1}\right) \\ \mathbf{P}_{k|k} = \mathbf{P}_{k|k-1} - \mathbf{W}_k\mathbf{P}_{zz,k|k-1}\mathbf{W}_k^T \end{cases} \tag{14.9}$$

Where $\mathbf{W}_k = \mathbf{P}_{xz,k|k-1}\mathbf{P}_{zz,k|k-1}^{-1}$ is the gain of filter.

14.2.3 Strong Tracking Filter

Based on the EKF and principle of orthogonality, STF is deduced by introducing a time varying factor λ_k into the predicted error covariance of EKF [4]. It makes the residual error series orthogonal to each other. Therefore all the useful information in the residual error series could be extracted. The time varying factor can be calculated as [4, 11]:

$$\lambda_{k+1} = \begin{cases} \lambda_0, \lambda_0 > 1 \\ 1 \quad , \lambda_0 \leq 1 \end{cases} \tag{14.10}$$

$$\lambda_0 = \frac{\mathbf{tr}[\mathbf{N}_{k+1}]}{\mathbf{tr}[\mathbf{M}_{k+1}]} \tag{14.11}$$

in which $\mathbf{N}_{k+1} = \mathbf{V}_{k+1} - \mathbf{H}_k\mathbf{Q}_k\mathbf{H}_k^T - \beta\mathbf{R}_{k+1}$ and $\mathbf{M}_{k+1} = \mathbf{H}_k\mathbf{F}_k\mathbf{P}_{k|k}\mathbf{F}^T(k)\mathbf{H}^T{}_k$.

$$\mathbf{V}_{k+1} = E\{\boldsymbol{\gamma}_k\boldsymbol{\gamma}_k^T\} = \begin{cases} \boldsymbol{\gamma}_1\boldsymbol{\gamma}_1^T & k = 0 \\ \dfrac{[\rho\mathbf{V}_k + \boldsymbol{\gamma}_{k+1}\boldsymbol{\gamma}_{k+1}^T]}{1+\rho} & k \geq 1 \end{cases} \tag{14.12}$$

where, $0 < \rho \leq 1$ is the forgetting factor and $\beta \geq 1$ is the weakening factor. Both are set empirically.

14.3 Cubature Kalman Filter Based on Strong Tracking

In this section, the idea of strong tracking filter is merged into CKF, which gives rise to an improved nonlinear filter called CKF based on strong tracking (CKF-ST). By introducing the time varying factor into CKF, CKF-ST not only inherits the merits of CKF but also enhance the quick-response ability to deal with state sudden change.

The essence of the introduction of time varying factor is that the predicted error covariance can be changed along with the residual vector. Only difference between CKF and CKF-ST is the calculate of $\mathbf{P}_{k|k-1}$. In CKF-ST,

$$\mathbf{P}_{k|k-1} = \lambda_k\left\{\frac{1}{m}\sum_{j=1}^{m}\mathbf{X}^*_{j,k|k-1}\mathbf{X}^{*\,T}_{j,k|k-1} - \hat{\mathbf{x}}_{k|k-1}\hat{\mathbf{x}}_{k|k-1} + \mathbf{Q}_{k-1}\right\} \tag{14.13}$$

In the above derivation, λ_k is the time varying factor, but if we calculate λ_k according to the method given in previous section, a problem will be caused. Form Eqs. (14.4)–(14.8) we can know that, in order to calculate the time varying factor λ_k at time k, the residual error series should be known:

$$\boldsymbol{\gamma}(k) = \mathbf{z}_k - \hat{\mathbf{z}}_{k|k-1} \tag{14.14}$$

Meanwhile, the calculation of $\hat{\mathbf{z}}_{k|k-1}$ at time k must be on the basis of $\mathbf{P}_{k|k-1}$. Therefore, a logical error will be caused if we introduced the time varying factor in the derivation of CKF-ST directly. In order to solve this problem, we made a revise in the calculation of λ_k, and changed $\boldsymbol{\gamma}(k)$ as follow:

$$\boldsymbol{\gamma}(k) = \mathbf{z}_k - \hat{\mathbf{z}}_{k-1|k-2} \tag{14.15}$$

Respectively, the residual covariance matrix should be changed as:

$$\mathbf{S}_0(k+1) = \begin{cases} 0 & k = 0 \\ \dfrac{\left[\rho \mathbf{S}_0(k) + \boldsymbol{\gamma}(k+1)\boldsymbol{\gamma}(k+1)^T\right]}{1+\rho} & k \geq 1 \end{cases} \tag{14.16}$$

14.4 Simulation Analyses

To verify the effectiveness of the proposed CKF-ST, a bearings-only tracking system is used to validate the effective of CKF-ST, the detail description of this system can be seen in [11]. In the following simulations, the performance of CKF-ST is compared with others, and then the tracking results are analyzed.

State vector $\mathbf{x}_k = \begin{bmatrix} x_k & v_k^x & y_k & v_k^y \end{bmatrix}^T$, where x_k and y_k are the displacement components of east and north, v_k^x and v_k^y are the velocity components of east and north. We assumed that the velocity of target is a constant. The state equation and the measurement equation can be established as:

$$\mathbf{x}_k = \begin{bmatrix} 1 & T & 0 & 0 \\ 0 & 1 & 0 & 0 \\ 0 & 0 & 1 & T \\ 0 & 0 & 0 & 1 \end{bmatrix} \mathbf{x}_{k-1} + \mathbf{w}_{k-1} \tag{14.17}$$

$$\mathbf{z_k} = \begin{bmatrix} \alpha_k \\ \beta_k \end{bmatrix} = \begin{bmatrix} \arccos\left[x_k \Big/ \sqrt{x_k^2 + y_k^2}\right] \\ \arccos\left[(x_k - D) \Big/ \sqrt{(x_k - d)^2 + y_k^2}\right] \end{bmatrix} + \mathbf{v_k} \tag{14.18}$$

In this experiment, $\mathbf{w}_k$ of Eq. (14.1) and $\mathbf{v}_k$ are Gaussian sequence with zero mean and covariance matrix of them are $\mathbf{Q}_{k-1}$ and $\mathbf{R}(k)$. The system parameters are:

$$\mathbf{Q}_k = \begin{bmatrix} \mathbf{Q}_1 & \mathbf{0} \\ \mathbf{0} & \mathbf{Q}_1 \end{bmatrix}, \quad \mathbf{Q}_1 = \begin{bmatrix} T^3/2 & T^2/2 \\ T^2/2 & T \end{bmatrix},$$

$$\mathbf{R}_k = diag\{0.001, 0.001\} \times \pi/180$$

$$\mathbf{x}_0 = \begin{bmatrix} 200 & 15 & 200 & 9 \end{bmatrix}^T, \quad \mathbf{P}_0 = diag\{7, 0.01, 7, 0.01\}$$

In order to prove the good performance of CKF-ST when state have a sudden change, we introduce a state change in 30–40 s, the trajectory of target is shown in Fig. 14.1.

From Fig. 14.2 and Table 14.1 we can see that the error curve of CKF-ST is stable and the RMSE of both X- and Y-displacement is much smaller than those of another two methods. Moreover, the tracking performance of CKF-ST is free from the effect of sudden change in target motion. By contrast, the error curves of UKF and CKF show large fluctuations when the target motion began to change. Results show that CKF-ST exceeds CKF and UKF in capability of dealing with sudden change.

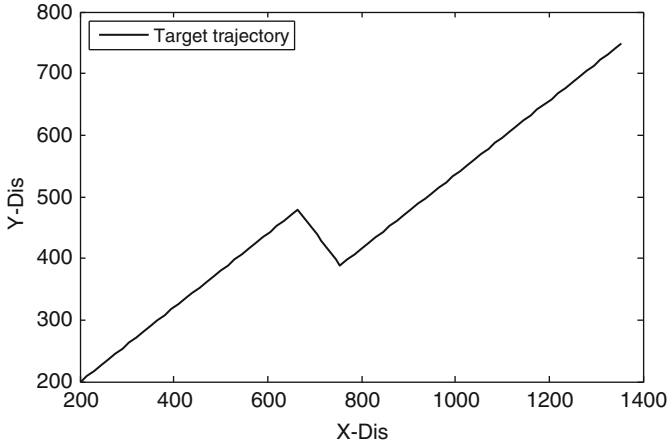

Fig. 14.1 Trajectory of target in the bearings-only tracking system

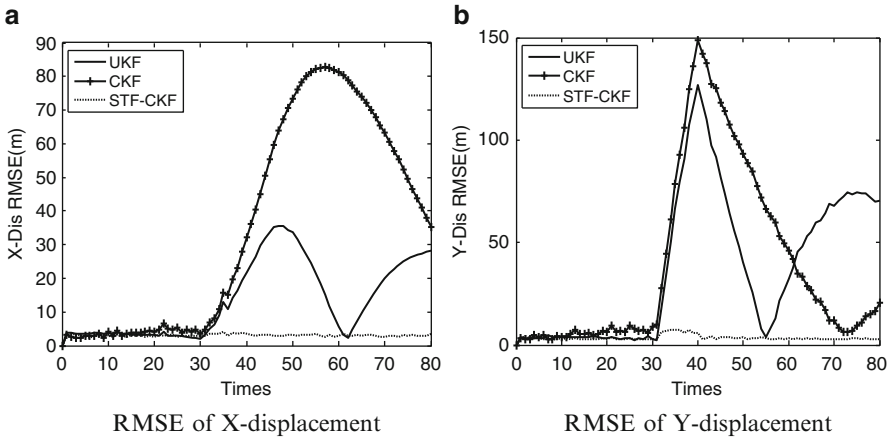

Fig. 14.2 RMSE of X-displacement and Y-displacement (**a**) RMSE of X-displacement (**b**) RMSE of Y-displacement

Table 14.1 Comparison of the three filters in RMSE

	RMSE (m)		
Displacement	UKF	CKF	CKF-ST
X	6.0260	9.6014	3.0726
Y	11.8160	13.0044	3.5139

Conclusion

A more accurate and stable nonlinear filter algorithm named cubature Kalman filter based on strong tracking (CKF-ST) is developed in this paper. There are at least two obvious merits for CKF-ST. At first, CKF-ST is easy to implement and has better estimate accuracy. Second, CKF-ST has a good ability to track the target which has abrupt changes in the motion. Simulation results on two different examples indicate that the tracking performance of CKF-ST has better capability when there has abrupt state change.

Acknowledgments This research was supported by Key Program of National Natural Science Foundation of China (61139003), the Fundamental Research Funds for the Central Universities (ZYGX2010J022), National Natural Science Foundation of China (No. 61139003), and the China Postdoctoral Science Foundation (No. 2013M531948).

References

1. Jazwinski AH (1970) Stochastic processes and filtering theory [M]. Academic, New York
2. Sadeghi B, Moshiri B (2007) Second-order EKF and unscented kalman filter fusion for tracking maneuvering targets, [C]. In: IEEE international conference on information reuse and integration, pp 514–519
3. Wu C, Han C (2007) Strong tracking finite-difference extended kalman filtering for ballistic target tracking. In: ROBOI 2007 IEEE. doi:10.1109/ROBOI.2007.4522393
4. Bin Y, Yu X (2002) Comparison between a strong tracking filter and kalman filter for target tracking. J Air Force Radar Acad 16:17–22 (in Chinese)
5. Changyun L, Penglang S, Song L (2011) Unscented extended kalman filter for target tracking. Syst Eng Electron 22(2):188–192. doi:10.3969/j.issn.1004-4132.2011.02.002
6. Guobin C, Jiangning X, An L (2011) A target tracking method of iterative unscented kalman filter. J Xi'an JiaoTong Univ 45:70–74 (in Chinese)
7. Wang Z, Liu Z, et al (2011) Particle filter algorithm based on adaptive resampling strategy. In: 2011 international conference on EMEIT. doi:10.1109/EMEIT.2011.6023752
8. Arasaratnam I, Haykin S (2009) Cubature kalman filters. IEEE Trans Automat Contr 54 (6):1254–1269
9. Arasaratnam I, Haykin S et al (2010) Cubature kalman filtering for continuous–discrete systems: theory and simulations. IEEE Trans Signal Process 58(10):4977–4993
10. Mu J, Cai Y-L (2011) Iterated cubature kalman filter and its application. [C] In: 2011 conference on cyber technology in automation, control, and intelligent systems
11. Li W, Ge Q (2010) UKF-STF tracking with correlated noises for the nonlinear system. In: 8th World congress on intelligent control and automation, pp 3466–3471

Chapter 15
Nonlinear Radar Tracking Data Filtering with Unscented Kalman Filter

Jihong Shen, Yanan Liu, Siyuan Liu, and Zhuo Sun

Abstract This paper focuses on the issue of nonlinear data filtering in radar tracking. By through the analysis on nonlinear filters, we find that the accuracy of the extended Kalman filtered (EKF) data image was not ideal for radar tracking data filtering. In our study the unscented Kalman filter (UKF) was introduced to achieve better performance. The evidences show that, while comparing with using EKF, using UKF for radar tracking can get more accurate results because the mean and variance of the nonlinear function can be estimated more accurately with unscented transformation, and the computation complexity is reduced significantly by avoiding to calculate the Jacobian matrix.

Keywords: Radar tracking • Kalman filter (KF) • Nonlinear filter • Unscented Kalman filter

15.1 Introduction

Gaussian applied generalized least squares method to radar data processing in the early nineteenth century. He created a mathematical approach to deal with observations, which then became the basis of the modern filter theory. Tracking filter is an important part of radar data processing technology. Its main goal is to estimate target location, speed and other parameters in real time base on the metrical information. And at the same time, tracking filter should extrapolate the location

J. Shen • Y. Liu
Faculty of Science, College of Automation, Harbin Engineering University, Harbin 150100, China

S. Liu (✉) • Z. Sun
Key Laboratory of Universal Wireless Communications, Ministry of Education, Beijing University of Posts & Telecommunications, Beijing 100876, China
e-mail: lsy0627@bupt.edu.cn

J. Mu et al. (eds.), *The Proceedings of the Third International Conference on Communications, Signal Processing, and Systems*, Lecture Notes in Electrical Engineering 322, DOI 10.1007/978-3-319-08991-1_15

information of the target in the next antenna scan period. The location information will then be used to examine the rationality of the measurement in the next time and can be used for track-related processing in searching radars [1].

Target tracking with combined multi-sensor is widely used in practical applications. The problem of nonlinear filtering is to estimate the optimal state of the common nonlinear stochastic dynamic systems. It is essential to find out an effective filtering method to estimate and predict the dynamic system status and the statistics of error from the sequential measurements in real-time. The result of Kalman filter is the optimal closed solution for linear systems, while for non-linear systems, it is very difficult or even impossible to get an accurate optimal solution. So a lot of methods on suboptimal approximate filtering are proposed.

Following 1960s, when Rudolph. E. Kalman invented and named Kalman filter, there emerged many modern filtering technologies, and most of them are created based on Kalman filter. Kalman filter plays an irreplaceable role in the development of filter which has been applied to many fields such as radar and computer vision. At the beginning, most of Kalman filters are linear filter, which are the minimum variance state estimation of linear dynamic system. However, as technology develops, linear filtering technique was hard to meet the demands and nonlinear filter got more use. Gaussian filter and particle filter are mainly applied to nonlinear filtering estimation, and general Gaussian approximation methods include linearization and sampling approximation with applicants of extended Kalman filter (EKF) and unscented Kalman filter (UKF) separately [2].

In the following paper, we first present the process of radar tracking. Then the unscented Kalman data filtering (UKDF) algorithm is state and analysed compared with EKF method. In the simulation, we do filtering by UKF and compared the data image with that of EKF algorithm. The experimental results show that it is more accurate when using Unscented Kalman Filter on radar tracking data filtering problem.

15.2 Radar Tracking

Modern radar usually process data with digital computer. Using parameter estimation techniques, we can estimate a lot of motion parameters such as the specific location of the target, velocity and acceleration basing on the radar measurements, and generate a variety of information about the target such as the expected position and the current and the next state of the target. There are five steps when processing TT&C radar data and the procedure is as shown in Fig. 15.1.

- Data formatting: Store the measurements by unified format.
- Data correction: Do unbiased estimation and defection compensation according to data theory.

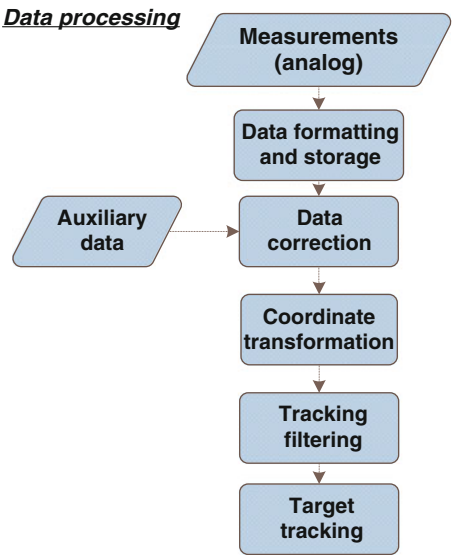

Fig. 15.1 Procedure of radar data processing

- Coordinate transformation: Most of the data measured by radar is based on the spherical coordinate system, which needs to be converted to the Cartesian coordinate system in order to simplify the calculation.
- Tracking filter processing: Tracking filter is the core device of a radar data processing system. It can estimate the state of the dynamic system using a series of measurements containing noise and other inaccuracies, and predict the coordinate position and velocity of the object according to the observation sequence of the noise.
- Target track processing: The tracking filter should estimate the target's motion parameters like speed and position in real time using radar measurements, and calculates the position and orientation of the target in the next time using the iteration formula.

15.3 Unscented Kalman Data Filtering (UKDF)

State equation and observation equation of nonlinear systems [3] are as follows:

$$\begin{aligned} X_{k+1} &= f_k(x_k) + u_k \\ z_k &= h_k + v_k \end{aligned} \tag{15.1}$$

where x_k is the state vector of the target, z_k is the observation vector, f_k and h_k are the state transition and the observation of the system, u_k and v_k are the unrelated status noise and measurement noise of system.

15.3.1 UKDF Algorithm

The Basic idea of UFDK is unscented transformation (UT) [4]. When doing unscented Kalman data filtering, we would firstly construct the Sigma points.

In the first place, work out the sampling points ξ_i and its corresponding weights W_i according to the following [5],

$$\begin{cases} \xi_0 = \overline{X} & , \quad i = 0 \\ \xi_i = \overline{X} + \left(\sqrt{(n_x + \kappa)P_x}\right)_i & , \quad i = 1, \ldots, n_x \\ \xi_{i+n_x} = \overline{X} - \left(\sqrt{(n_x + \kappa)P_x}\right)_i & , \quad i = 1, \ldots, n_x \end{cases} \tag{15.2}$$

$$\begin{cases} W_0 = \dfrac{\kappa}{(n_x + \kappa)} & , \quad i = 0 \\ W_i = \dfrac{\kappa}{[2(n_x + \kappa)]} & , \quad i = 1, \ldots, n_x \\ W_{i+n_x} = \dfrac{\kappa}{[2(n_x + \kappa)]} & , \quad i = 1, \ldots, n_x \end{cases} \tag{15.3}$$

where κ is a scale parameter that can be any value satisfying $(n_x + \kappa) \neq 0$, $\left(\sqrt{(n_x + \kappa)P_x}\right)_i$ is the ith line and the ith column of the Root mean square (RMS) matrix $(n_x + \kappa)P_x$ and n_x denotes the dimension of the state vector.

Give nonlinear transformation to the Sigma points. Each of δ samples are transmitted by non-linear function and we obtain,

$$y_i = g(\xi_i), \quad i = 0, \ldots, 2n_x \tag{15.4}$$

Then, we would calculate the mean and variance of y as follows,

$$\begin{aligned} \overline{y} &= \sum_{i=0}^{2n_x} W_i y_i \\ P_x &= \sum_{i=0}^{2n_x} W_i (y_i - \overline{y})(y_i - \overline{y})' \end{aligned} \tag{15.5}$$

UKDF conducts recurrence and updates of the nonlinear model status and error covariance by nonlinear UT method. It is not about the approximation of the nonlinear model, but the approximation of the state's probability density function. The similarity between UKDF and EKDF is that the used parametric analytical form are both based on the Gaussian assumption [6].

15.3.2 Discussion for UKDF

According to the statements in [7], by using EKF, it's obvious that besides some improvements, we can see that the magnitude of the error correction is small from the image after the radar data filtering and simulation. In our work, we try to use UKF who is more accurate than EKF, what's more, in the method of UKDF, the approximation of the maximum term of Tylor expression and the calculation of the Jacobian matrix can be avoided.

When do interpolation filtering, we need more samples in order to achieve ideal precision. In the method, Taylor expansion should be used and approximation must be done. We are not interested in IF, considering that the performance of applications on digital data is worse than applications on image data.

In practical, the estimation of nonlinear and non-Gaussian stochastic systems is more significant. An effective way to solve this problem is non-parametric particle filtering. There would be particle degradation when do particle filtering practically, which means that as the increase of the number of samples the weight of many particles may get smaller, and the variance of the sample would increase over time. Based on the judgments in, the system is under the assumption of Gaussian noise, so, we wouldn't use particle filtering algorithm here.

Although with a short history, Neural network filtering algorithm can be combined with the other filters like EKF and generates new adaptive extended Kalman filters. However, we don't choose it for it is better used under similar systems.

From the procedure of UKDF, we can see that the method is faster than EKDF for there is no need to calculate the Jacobian matrix. And the mean and variance of the nonlinear function can be estimated more accurately with UT, so get a higher accuracy. For any non-linear functions, the posterior mean and covariance by UKDF can be accurate to the second-order so that UKDF can be used in any dynamic model, while by EKDF we can only obtain a precision of the first-order.

Basing on the above analyses, we choose the method UKDF which can provide more accurate data for further calculation. And it has a great significance for practical applications by applying UKDF, which is bound to lay better foundation for the future data fusion problem.

15.4 Numerical Results

Using the data in [7], by overall analyses, we get the radar data map as follows (Fig. 15.2):

When simulating the extended Kalman filtering algorithm and the unscented Kalman filtering algorithm by Matlab, we set the initial values as follows:

- Radar period: $T = 2$.
- Random error of radar distance and the position: 200 and 0.3.

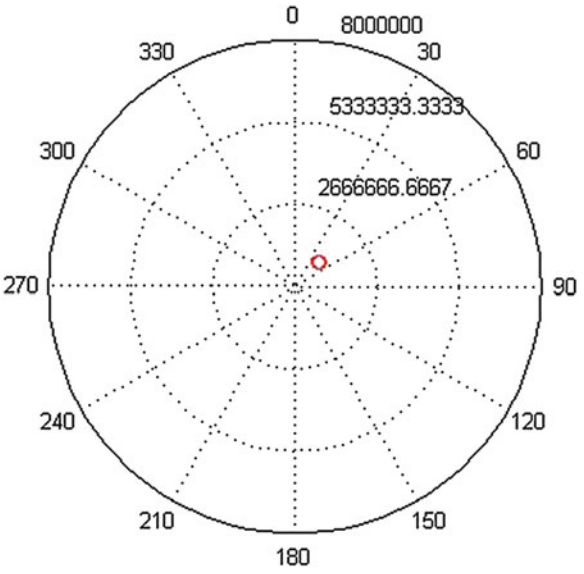

Fig. 15.2 Figure of overall radar data

- Initial value of the state are:

$$X_0 = \left\{ Z(1,2), \frac{Z(1,2) - Z(1,1)}{T_s}, Z(2,2), \frac{Z(2,2) - Z(2,1)}{T_s} \right\}$$
$$H = \begin{pmatrix} 1 & 0 & 0 & 0 \\ 0 & 0 & 1 & 0 \end{pmatrix}, \qquad F = \begin{pmatrix} 1 & T_s & 0 & 0 \\ 0 & 1 & 0 & 0 \\ 0 & 0 & 1 & T_s \\ 0 & 0 & 0 & 1 \end{pmatrix} \tag{15.6}$$

- Initial covariance is as follows

$$P = \begin{pmatrix} R(1,1) & \frac{R(1,1)}{T_s} & R(1,2) & \frac{R(1,2)}{T_s} \\ \frac{R(1,1)}{T_s} & \frac{2R(1,1)}{{T_s}^2} & \frac{R(1,2)}{T_s} & \frac{2R(1,2)}{{T_s}^2} \\ R(1,2) & \frac{R(1,2)}{T_s} & R(2,2) & \frac{R(2,2)}{T_s} \\ \frac{R(1,2)}{T_s} & \frac{2R(1,2)}{{T_s}^2} & \frac{R(2,2)}{T_s} & \frac{2R(2,2)}{{T_s}^2} \end{pmatrix}, \quad Q$$
$$= \begin{pmatrix} 50 & 50 & 10 & 10 \\ 50 & 50 & 10 & 10 \\ 10 & 10 & 50 & 50 \\ 10 & 10 & 50 & 50 \end{pmatrix} \tag{15.7}$$

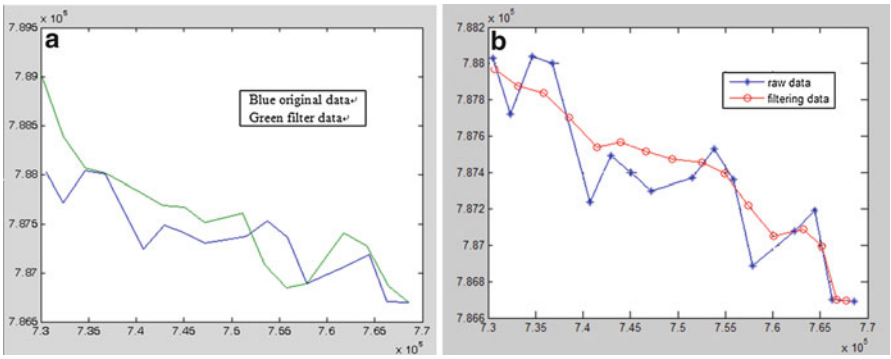

Fig. 15.3 Filter image of applying (**a**) EKDF algorithm and (**b**) UKDF algorithm

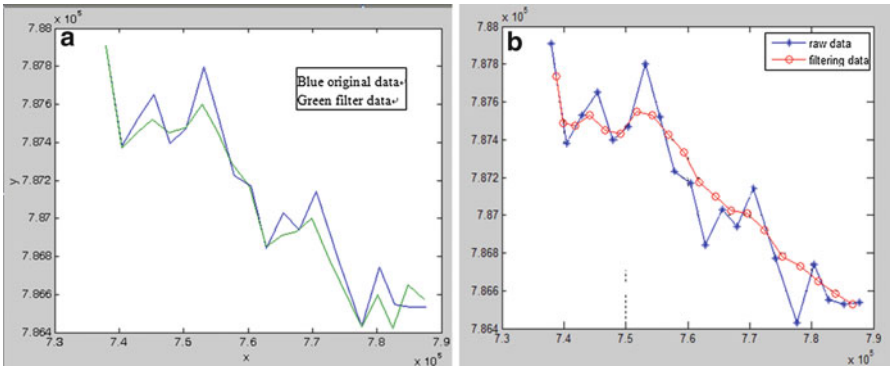

Fig. 15.4 Filter image of applying (**a**) EKDF algorithm and (**b**) UKDF algorithm

When using the extended Kalman filtering algorithm, we select 16 sets of data, where x_0 is the horizontal spatial position of the plane and y_0 is the vertical spatial position. After filtering data (x_0, y_0) by EKDF and UKDF, we get value (x_1, y_1) and (x_1', y_1'). The tracks of (x_1, y_1) after UKDF and (x_1', y_1') after EKDF are shown in Fig. 15.3a, b.

From the above images we can clearly see that the track in the second figure by UKDF is smoother especially around the point 8 and 9. Since actually the flight path of an aircraft cannot be poignant as broken line form, the smooth curve in Fig. 15.3b is much closer to the actual trajectory of the aircraft. That is to say, in the test cases UKDF algorithm is a more suitable method.

In the following, we choose 20 sets of data, and then smooth and track the path of aircraft using the Kalman filtering algorithm. We obtain the tracks of data as are shown in Fig. 15.4a by EKDF and Fig. 15.4b by UKDF.

Compared with the curve in Fig. 15.3b, the track by UKDF is much smoother. And the curve behind point 9 is almost in a smooth form. Although the curve by EKDF algorithm is close to the original measurement data, according to the actual principles

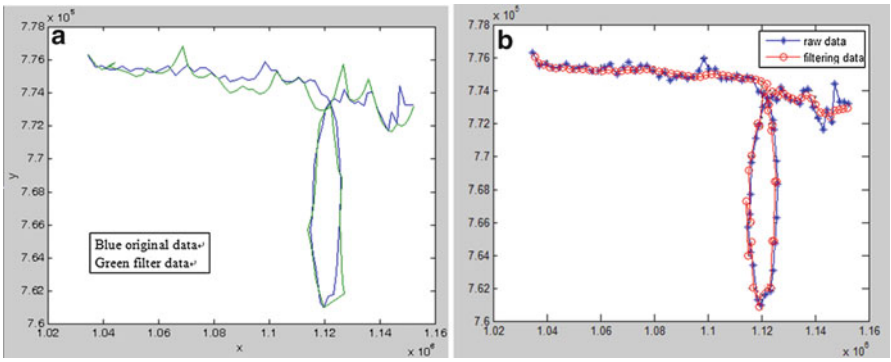

Fig. 15.5 Filter image of applying (**a**) EKDF algorithm and (**b**) UKDF algorithm

of flight, the aircraft should have a smooth movement, which fully illustrates that there is measurement error, and we should filter the data before using it.

In the next test case, we select 80 sets of data, then smooth and track the path of aircraft using the Kalman filtering algorithm, and we obtain the track after EKDF shown in Fig. 15.5a and the track after UKDF shown in Fig. 15.5b.

From Fig. 15.5a, we can find that after unscented Kalman filtering, the curve is almost a smooth one. It states that filtering the set of measurements by UKDF, the curve we obtain is much closer to the actual track.

Conclusion

The simulation results show that the precision of data and images we get by UKDF are superior to the other filters, especially better than the result by EKDF and shows smoother and better tracking performance. From the simulations above we can also find that for nonlinear function, UKDF algorithm is superior to EKDF and UKDF algorithm, thus can greatly improve the accuracy of the calculation in practical applications, if we apply the UKDF algorithm to the method in [2], the issue would be a preferable basis for data fusion in the future and may have great significance for practical applications.

Acknowledgements This work was supported by the National Science and Technology Major Project of China under grant 2013ZX03001003-003, and the BUPT Research Innovation Project under grant 2013RC0104.

References

1. Yong G (2012) Monitoring radar target tracking and localization studies. 91,913 troops of the PLA Navy, Dalian
2. Liu B, Chen Z, Liu X, Yang F, Geng J (2013) A new method based on the polytopic linear differential inclusion for the nonlinear filter. Beijing Institute of Technology, Beijing

3. Liu B, Chen Z, Liu X, Yang F (2013) A new method based on polytypic linear inclusion for nonlinear filter with non-Gaussian noise. Beijing, Beijing Institute of Technology
4. Xu J, Dimirovski GM, Jing Y, Shen C (2007) UKF design and stability for nonlinear stochastic systems with correlated noises. In: Proceedings of the 46th IEEE CSS conference on decision and control CDC07 (David Castanon, General Chair, and James Spall, Program Chair), New Orleans, 12–14 December 2007. The IEEE, Piscataway, pp 6226–6231
5. Ma Y, Wang Z (2010) An UKF algorithm based on the singular value decomposition of state covariance. Graduate School of the Chinese Academy of Sciences, Beijing
6. Simon D (2009) Kalman filtering with state constraints: a survey of: linear and nonlinear algorithms. Cleveland State University, Cleveland
7. Lin Z (2005) Research information fusion systems engineering design criteria [D]. Harbin Engineering University, Harbin

Chapter 16
Human Detection Through Wall using Information theory

Ishrat Maherin and Qilian Liang

Abstract Ultra wide band (UWB), can be used to detect human target hidden by walls. Information theoretic algorithms like entropy, relative entropy and mutual information are proven methods that can be applied to data collected by various sensors for detecting target. In this paper, we propose to use entropy and relative entropy to detect target. Breathing motion in human will cause periodic changes in the received signal at a distance where target is located. Relative entropy can detect the change in histogram quickly. After applying weight using relative entropy, we can apply entropy based detection. We conducted study in three different kinds of walls. When target is behind gypsum wall, accurate detection can be achieved by applying this method. We can identify the human behind the brick wall as well. However, human was undetected using this algorithm while hidden by wooden doors.

Keywords Human detection through wall • Information theory • Entropy • Relative entropy • UWB

16.1 Introduction

The detection of human hidden by walls are of interest for rescue, surveillance and security operations. The problem of rescuing people from beneath the collapsed buildings does not have an ultimate technical solution that would guarantee efficient detection and localization of victims. Due to the ability to penetrate through typical building materials, UWB radar is considered as preferred tool for detection. Detection of human beings with radars is based on movement detection such as respiratory motions and movement of body parts. These motions cause changes in frequency, phase, amplitude and time-of-arrival as scattered pulses come from the target. In this study, we implemented an information theory based human detection

I. Maherin (✉) • Q. Liang
Department of Electrical Engineering, University of Texas at Arlington, 416 Yates St, Arlington, TX 76019, USA
e-mail: ishrat.maherin@mavs.uta.edu; liang@uta.edu

J. Mu et al. (eds.), *The Proceedings of the Third International Conference on Communications, Signal Processing, and Systems*, Lecture Notes in Electrical Engineering 322, DOI 10.1007/978-3-319-08991-1_16

using UWB radar. We applied relative entropy based weighting for preprocessing and in second step we calculated the entropy for several fixed window.

There have been several successful attempt to detect human using breathing motion [1–3]. Staderini [2] has developed an UWB radar for non-intrusive breathing and heartbeat detection for medical purposes in LOS conditions. Ossberger et al. [3] investigated feasibility of using UWB radar for through-wall detection of breathing persons. The experimental data used in this study was collected by [4–6]. They applied several techniques such as short time fourier transform, singular value decomposition and doppler based detection to detect human target. As an alternative to these approaches we propose information theory based human detection. In a recent study, we proposed entropy based method to detect target in forest with good signal quality [7]. The current scenarios are different as human target behaves differently than the metallic target. Human body has complex shape and spatial extent is larger than the transmitted UWB pulse. Returned UWB signals are consists of multipath components as signals, returned from different body parts, are scattered independently. Even the dielectric of the wall will have significant effect on detection. Antenna coupling with the wall and multiple reflections from the wall will further deteriorate the performance. In order to reduce the performance degradation we, propose to use relative entropy based weighting after the clutter reduction on several scans collected from the same radar.

The rest of the paper is organized as follows: Data collection is described in Sect. 16.2. Two step information theory based detection is discussed in Sect. 16.3. In Sect. 16.4, we present the simulation results. We conclude this paper and propose some future research in section “Conclusions”.

16.2 Data Collection

This study considers PulseON P220 UWB radar, developed by time domain, in monostatic mode. Here waveform pulses are transmitted from a single Omni-directional antenna and the scattered waveforms are received by a collocated Omni-directional antenna as shown in Fig. 16.1. It has a center frequency of 4.3 GHz. An Ethernet cable is used to connect the radio to the PC and radar can be controlled using application software provided with the radios. Extremely low power, spectral efficiency, immunity to interference and excellent wall penetration characteristics make this radar suitable for indoor human detection. In general, UWB signal is noise-like due to the low energy density. Random noise waveform is inherently low probability of intercept (LPI) and low probability of detection (LPD). The large bandwidth along with discontinuous transmission makes UWB signal resistant to severe multi-path interference and jamming. Thus, it is an ideal candidate to work as a sensor for obscured regions in hostile environments [8].

Few important related parameters related to radio configuration are important in analyzing captured scans. These are hardware and software integration, window size, number of pulses per scan, number of sample per scan, pulse rate and scan rate.

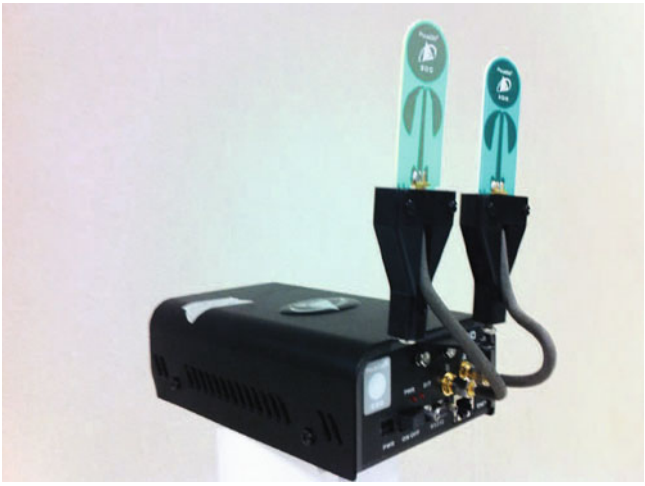

Fig. 16.1 P220 in monostatic mode

The total integration is the total number of UWB pulses per waveform sample, and is found by multiplying hardware and software integration. Window Size (ft) is the difference between stop position and the start position. Pulses per waveform is the number of UWB radio pulses required for the entire waveform (single scan). If we denote number of sample point per scan as nsample, then

$$nsample = \frac{2 * window\ size * .3048}{c * \text{step}\ size} \tag{16.1}$$

Now number of pulses per scan can be denoted as npulse and can be calculated as,

$$npulse = hi * si * nsample \tag{16.2}$$

here hi is hardware integration and si is software integration. Thus the scan rate can be calculated as follows,

$$\frac{ScanRate = npulse}{pulserate} \tag{16.3}$$

$$Totalscan = Scanrate * data - collecton - time \tag{16.4}$$

16.3 Two Step Information Theory Based Method

In this paper, we use two information theoretic criterion entropy and relative entropy to detect human in indoor environment. In our previous study, we have successfully applied our algorithm in sensing through foliage for metallic target, in UWB Radar Sensor Network. The current scenario is totally different from our

previous study. Here the target is human, the environment is indoor and the human is behind three different kind of wall; gypsum wall, brick wall and wooden door. Also here we have single radar collecting multiple scans in contrast with Radar Sensor Network. Before we explain the algorithm, we can define entropy and relative entropy. Entropy is a measure of uncertainty of a random variable n [9]. Let X be a discrete random variable with alphabet size of n, so $X = x_1, x_2 \ldots x_n$. Maximum entropy method (MEM) finds the distribution which maximizes the entropy. Then entropy H(X) of the discrete random variable with probability mass function p_i, can be expressed as [9],

$$H(X) = -\sum_{i=1}^{n} p_i log_2 p_i \tag{16.5}$$

The K-L divergence is defined for probability mass functions of p and q as [9],

$$D_{KL}(p||q) = \sum_{i=1}^{n} p_i \log(\frac{p_i}{q_i}) \tag{16.6}$$

For detecting the target with maximum entropy method, we assume the targeted region is more random and has more uniform distribution than the clutter. However, we need to do the preprocessing to make the detection more effective. For preprocessing, we generally use the methods of estimation. Two mostly used method of non recursive estimation are weighted average and least square estimation (LSE) [10]. In this study we use relative entropy or K-L divergence based weighted average as fusion technique and the foundation of this is in information theory. As in [11], it is shown that the KL divergence can detect the change in histogram quickly and can be used for the weighting. Breathing motion in human will cause periodic changes in the received signal at a distance where target is located. So in order to reduce the clutter in the environment we need to take the difference in multiple scans. For that purpose we create two N × M matrix "A1" and "A2" with and without target, which is constructed using $M = 100$ scans, each of length $N = 6400$,

$$A = \begin{vmatrix} scan1 & scan2 & scan3 & \ldots & scanM \\ sample1 & sample1 & sample1 & \ldots & sample1 \\ sample2 & sample2 & sample2 & \ldots & sample2 \\ \vdots & \vdots & \vdots & \vdots & \vdots \\ sampleN & sampleN & sampleN & \ldots & sampleN \end{vmatrix}$$

Two other matrix C1 and C2 can be constructed, where difference is taken between successive columns of the matrix A1 and A2, which captures changes from one scan to another and helps to suppress the static clutter signal. The matrix construction for the difference matrix C is shown below:

$$C = \begin{vmatrix} scan1 - scan2 & scan2 - scan3 & scan3 - scan4 & \dots & scan(M-1) - scan(M) \\ sample1 & sample1 & sample1 & \dots & sample1 \\ sample2 & sample2 & sample2 & \dots & sample2 \\ \vdots & \vdots & \vdots & \vdots & \vdots \\ sampleN & sampleN & sampleN & \dots & sampleN \end{vmatrix}$$

We invert that difference matrix C and construct two C_{inv} matrices for with target and without target and applied relative entropy based weighting on each of this row. Now the matrix C_{inv} is a$(M-1) \times N$ matrix. Now each row corresponds to the number of scans and weight is applied on each row based on their KL divergence. Q_i be the pmf of the quantized echoes of the ith row of the C_{inv} matrix and B be pmf related with the quantized echoes of the C_{inv} without target then the K-L divergence based weighting, w_i for each row of can be applied by the following,

$$w_i = \frac{D_i}{\sum_{i=1}^{100} D_i} \tag{16.7}$$

and

$$D_i = D_{KL}(Q_i||B) \tag{16.8}$$

where D_{KL} is the divergence calculated from the (16.6). The returned echoes are quantized and pmf are calculated before applying (16.7). After this weight we take the summation of the matrix C_{inv}. Then we applied our second step and applied entropy based detection with 16 level of quantization.

16.4 Simulation Results

In this study we considered the measurement taken at three different positions: behind gypsum wall, behind brick wall and behind wooden door. The hardware integration was 512 and software integration was 2. Pulse repetition frequency was 9.6 MHz, step size was 1 bin and window size was 10 ft.

Figure 16.2 shows the location of the radar and human target on different sides of a 1 ft thick Gypsum partition wall. Person is at a distance of 6.5 ft from the radar on the other side of the wall and the height of the antennas from ground is 3 ft 4 in. In this case matrix A is constructed using 100 scans captured at scan rate of 0.6827 scans/s for total time duration of 68 s. Total number of sample was 6400. We applied our algorithm and calculated entropy for 128 different window with 50 size of samples on each. Human was detected around sample 4200 as shown in Fig. 16.3.

Fig. 16.2 Location of the human target and UWB radar on different sides of a 1 ft thick Gypsum partition wall (**a**) human target and (**b**) UWB radar

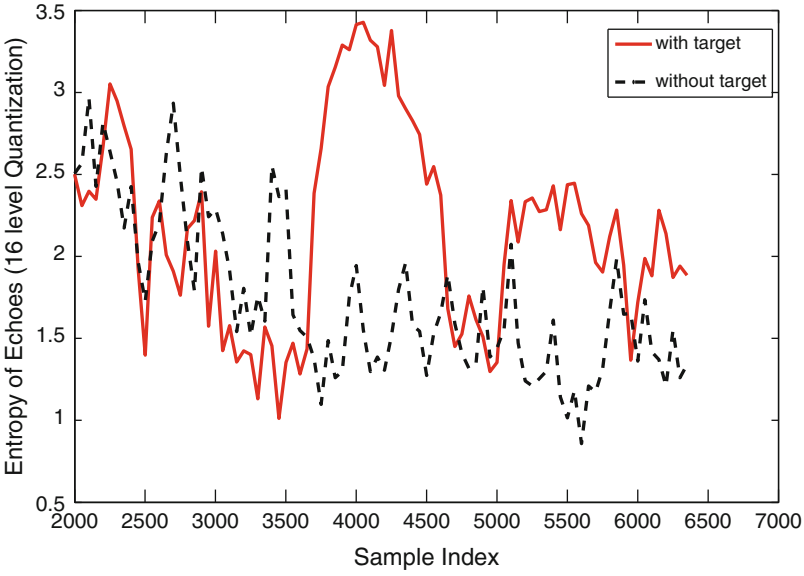

Fig. 16.3 Human target detection using two step information fusion. Target is detected around sample 4200

Figure 16.4 shows the location of the radar in one sides of a 12 cm Brick wall. Person is standing at a distance of 8′ from the radar on the other side of the door. After applying our algorithm we can see in Fig. 16.5 that there is a pick around the

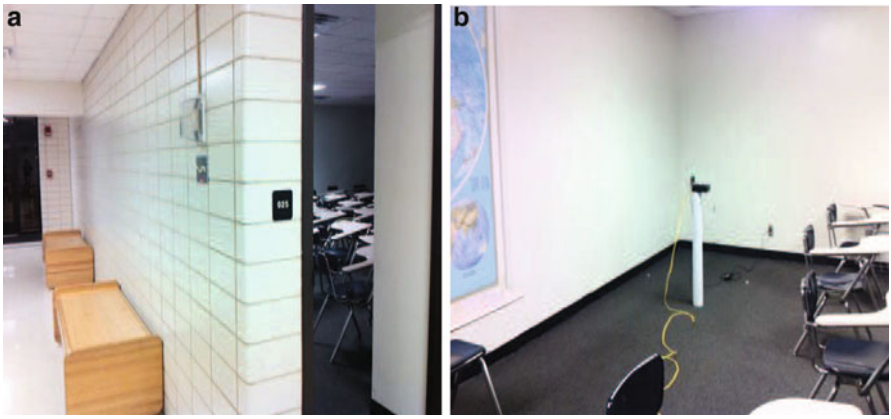

Fig. 16.4 Location of UWB radar on different sides brick wall (**a**) brick wall and (**b**) UWB radar

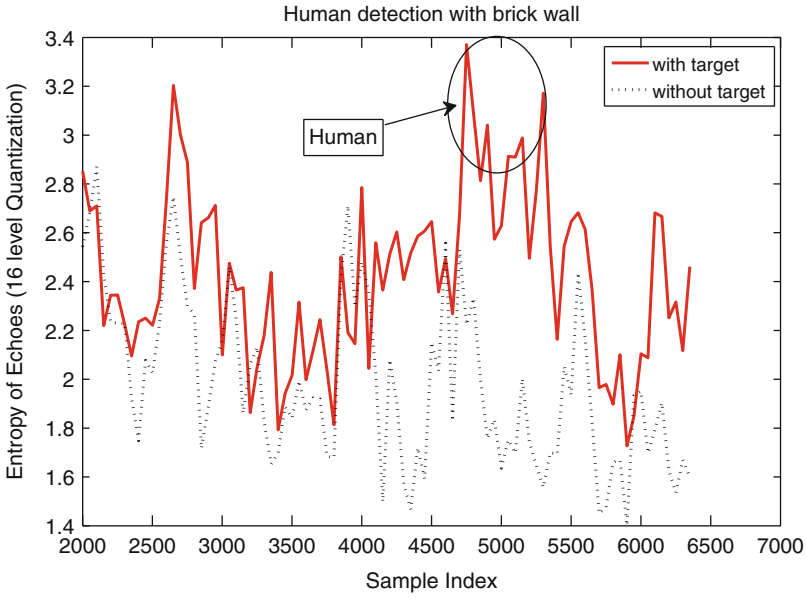

Fig. 16.5 Human target detection using two step information fusion. Target is detected around sample 5120

5120 sample. Since human was located about 8 ft away from the wall, it was expected in that range.

Figure 16.6 shows the location of the radar and Human target on different sides of a 4 cm wooden door. Person is standing at a distance of 7.5 ft from the radar on the other side of the door. For this particular case human was

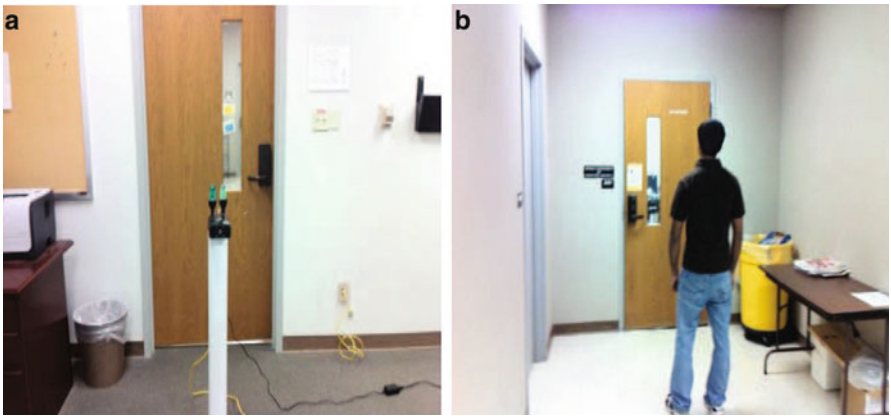

Fig. 16.6 Location of the Human target and UWB radar on different sides wooden door (**a**) human target and (**b**) UWB radar

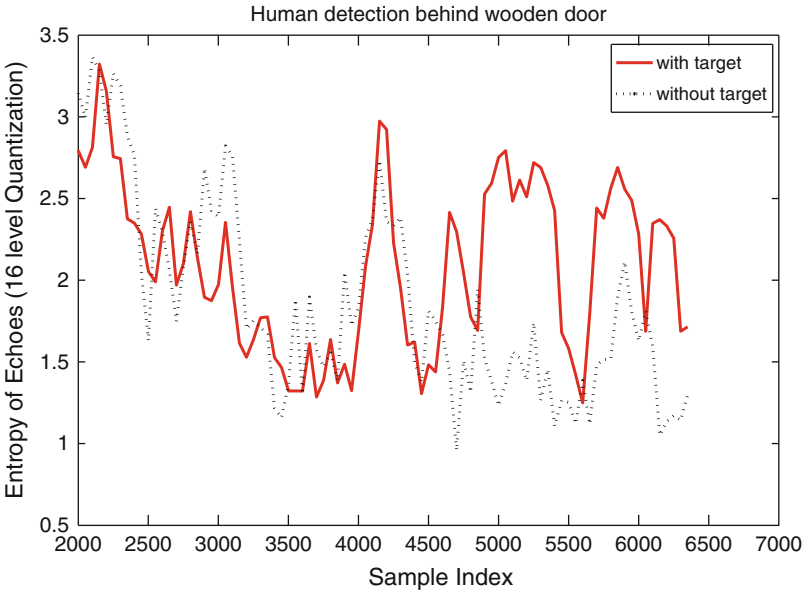

Fig. 16.7 Human target detection using two step information fusion. Target is behind door and expected around sample 4800

around sample 4800. In Fig. 16.7, we can see a pick around sample 4800, however that is not the highest point. In that case this algorithm is not suitable for wooden door.

Conclusions
Detection of human hidden behind the walls is a challenging task. In this paper, we propose to use information theory to UWB radar to detect human target. We applied relative entropy based preprocessing and entropy based detection. Results show that with this novel approach, accurate detection can be achieved when human is hidden behind the gypsum wall. This method could also detect human hidden behind the brick wall. However this method did not work for detecting human behind the wooden door. In future, we can acquire data on multi position of the radar and apply our method in Radar Sensor Network.

Acknowledgements This work was supported in part by U.S. Office of Naval Research under Grants N00014-13-1-0043, N00014-11-1-0071, N00014-11-1-0865, and U.S. National Science Foundation under Grants CNS-1247848, CNS-1116749, CNS-0964713.

References

1. Nezirovic A, Yarovoy AG, Ligthart LP (2006) Experimental study on human being detection using UWB radar. In: International radar symposium, 2006. IRS 2006, Krakow, pp 1–4, 24–26 May 2006
2. Staderini EM (2002) UWB radars in medicine. IEEE Aerosp Electron Syst Mag 17(1):13–18
3. Ossberger G, Buchegger I, Schimback E, Stelzer A, Weigel R (2004) Non-invasive respiratory movement detection and monitoring of hidden humans using ultra wideband pulse radar. In: International workshop on ultra wideband systems, pp 395–399, May 2004
4. Singh S, Liang Q, Chen D, Sheng L (2011) Sense through wall human detection using UWB radar. EURASIP J Wirel Commun Netw 2011:20
5. Kumar A, Liang Q, Li Z, Zhang B, Wu X (2012) Experimental study of through-wall human being detection using ultra-wideband (UWB) radar. In: IEEE globecom workshops (GC Wkshps), Anaheim, pp 1455–1459, 3–7 Dec 2012
6. Kumar A, Li Z, Liang Q, Zhang B, Wu X (2014) Experimental study of through-wall human detection using ultra wideband radar sensors. Measurement 47:869–879
7. Maherin I, Liang Q (2011) An entropy based approach for sense- through foliage target detection using UWB radar. In: 6th international conference on wireless algorithms, systems and applications (WASA), Chengdu, pp 180–189
8. Yarovoy AG, Matuzas J, Levitas B, Ligthart LP (2009) UWB radar for human being detection
9. Cover TM, Thomas JA (1991) Elements of information theory. Wiley-Interscience Press, New York
10. Luo RC, Chang CC, Lai CC (2011) Multisensor fusion and integration: theories, applications, and its perspectives. IEEE Sensors J 11(12):3122–3138
11. Maherin I, Liang Q (2014) Radar sensor network based target detection using Chernoff information and relative entropy. Phys Commun J

Chapter 17
A Feature Fusion-Based Visual Attention Method for Target Detection in SAR Images

Qiang Zhang and Zongjie Cao

Abstract Target detection is the front-end stage in any automatic recognition system for synthetic aperture radar (SAR) imagery (SAR-ATR). The efficiency of the detection directly impacts the succeeding stages in the SAR-ATR processing chain. This paper proposes a target detection method for SAR images based on visual attention mechanism. In the paper, a new texture feature extracting method using Local Walsh Transform (LWT) is employed and a target-saliency map is computed based on fusing the primary visual feature maps. Experiments are tested on two kinds of images with simple or complex background. The experimental results show that the detection time cost by the proposed algorithm is less than traditional visual attention methods and the detection results are visually more accurate.

Keywords: Visual attention • SAR image • Target detection • Local Walsh Transform (LWT) • Target-saliency map

17.1 Introduction

With the increasing volume of images collected from air- and space-borne synthetic aperture radar (SAR) systems, it is becoming more and more desirable to develop the targets detection technique for the expanding requirements of intelligence, surveillance and reconnaissance. Detecting objects in complex-background area can be time consuming, as the capabilities for image acquisition are growing rapidly. How to detect objects in large image data both quickly and reliably has become an emergency.

In order to solve this problem, a variety of approaches have been proposed in the literature. Target region extraction is one of the most popular applications applied to SAR images. Several SAR targets detection methods, based on geometric structure, fractal feature, probability models, level set and clustering, are generalized in current

Q. Zhang • Z. Cao (✉)
School of Electronic Engineering, University of Electronic Science and Technology of China, Chengdu, China
e-mail: zjcao@uestc.edu.cn

J. Mu et al. (eds.), *The Proceedings of the Third International Conference on Communications, Signal Processing, and Systems*, Lecture Notes in Electrical Engineering 322, DOI 10.1007/978-3-319-08991-1_17

researches. We broadly classify the detection algorithms reported in the open literature into three major taxa: single-feature-based, multi-feature based, and expert-system-oriented [1]. Primarily, under the single-feature-based taxon, constant false alarm rate (CFAR) based approaches are commonly preferred in the literature since they have reasonable computational requirements, constant false alarm rate, adaptive threshold selection capability, and fast detection performance [2]. The strong dependence of CFAR schemes on prior knowledge about targets and background observation limits their application in target detection. Methods under the multi-feature based taxon include the discrete wavelet transform (DWT) [3], the continuous wavelet transform (CWT) [4]. Finally, a more robust taxon is the expert-system-oriented approach, which incorporates intelligence into the process to guide the decision making. These methods only consider the image itself, they ignore the important role which human visual system (HVS) acts in SAR targets detection.

Nowadays, the selection of interest (ROI) based on visual attention is more and more popular in the targets detection area. Visual attention mechanism is what primates used to detect, in real time, conspicuous objects in cluttered visual environments. By using the sensitivity of the features including intensity, chromatic, orientation and color, visual attention mechanism could extract the interest information and orientation of salient objects rapidly in complicated visual scene and can accelerate the object detection process. In 1985, Koch and Ullman proposed the first visual attention mechanism model [8] based on the research of human cognitive psychology. This model first extracts several different characteristics, and then fuses them into a visual significant figure to simulate the process of finding interested region of human eye. On this basis, Itti put forward a new visual attention model suitable for processing natural image [9]. By analyzing the log-spectrum of an input image, Hou and Zhang [10] extracted the spectral residual for an image in the spectral domain and proposed a fast method for constructing a corresponding saliency map in the spatial domain. Elazary and Itti [11] proposed a new attention guide model for primary search and recognition, which was proved faster and more reliable. Visual attention mechanism has been more and more popular due to its broad applications, such as active information selection [12] and intelligent perception system [13–15]. In our letter, we use it to accelerate the target detection process in SAR images.

The innovation is inspired by the fact that targets, such as tanks, aircrafts, and vehicles can often attract attention of human eyes in images. Given a SAR image, first, we extract the intensity, orientation and LWT [16] information called feature maps from input SAR image. Second, a target-saliency map is calculated by combining these feature maps linearly. Third, we detect targets by a designed target detection method based on the target-saliency map. The experimental results show that the new algorithm can not only effectively reduce the computational complexity of the detection of SAR targets, but also to accurately describe the targets regions.

The rest of the letter is organized as the follows. In the next section, the method building feature maps and the target detection algorithm are described in detail. Section 17.3 presents experimental results for our detection approach. Conclusions are drawn in last section.

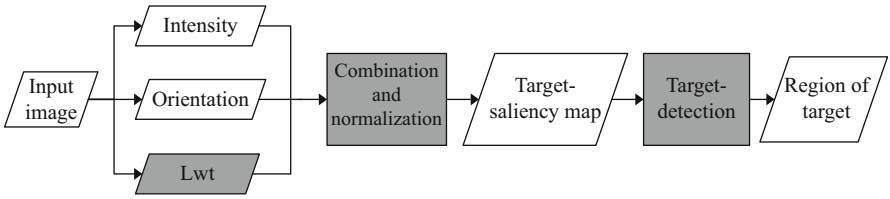

Fig. 17.1 The proposed method

17.2 Theory and Methodology

Our model is proposed to improve the computational efficiency and the accuracy of targets detection for SAR images. The methodology involves the following steps: (1) building feature maps; (2) target-saliency map computation; (3) targets detection. Figure 17.1 shows the framework of the proposed model, the parts with gray background are the innovations of our method.

17.2.1 Feature Maps Calculation

17.2.1.1 Calculating the Intensity Map

Since the pixel values of a SAR image I reflect the intensity information, image I is regarded as the intensity map directly.

17.2.1.2 Calculating the Orientation Map

Gabor filter is employed to extract the orientation feature. Gabor filter can be considered as orientation and scale tunable edge and linear feature detectors. It is described as (17.1):

$$H(\mathrm{x},\mathrm{y},\sigma,\theta) = \frac{1}{\sigma^2}\exp\left(-\pi\frac{x^2+y^2}{\sigma^2}\right) \times \left[\exp(\mathrm{i}2\pi f(\mathrm{x}\cos\theta + \mathrm{y}\sin\theta)) - \exp\left(-\frac{\pi^2}{2}\right)\right] \tag{17.1}$$

where σ is the scale parameter, f is the frequency of the sine wave and θ is the orientation. Generally, the value of θ is

$$\theta = \left[0, \frac{\pi}{4}, \frac{\pi}{2}, \frac{3\pi}{4}\right] \tag{17.2}$$

Fig. 17.2 Encoded mode

f_0	f_1	f_2
f_7	f_8	f_3
f_6	f_5	f_4

It means that four maps are computed in four directions finally. Then we combine these four maps linearly as the orientation map:

$$\overline{O} = \sum_{i=1}^{4} N(ori(i)) \tag{17.3}$$

where)N$ a normalized operation. It can normalize the values in the map to a fixed range [0, M] and eliminate modality-dependent amplitude differences. The major steps of normalization are: (a) find the global maximum Max and minimum Min of the image; (b) compute the ratio $\frac{image - Min}{Max - Min}$; and (c) globally multiply the ration by |*M*|. This operation is computationally simple.

17.2.1.3 Calculating the Texture Map

Since human eyes are always attracted by the abnormal objects in images, in this part, we employed Local Walsh Transform to extract the texture feature. According to [16], the texture feature based on LWT can express the difference between the central pixel and the surround pixels accurately. This method encodes the image as Fig. 17.2 shows.

In order to express the difference between the central pixel and the surround pixels accurately, we use (17.4) to get a 1-D discrete series.

$$f(\mathrm{n}|\mathrm{x},\mathrm{y}) = f_n - f_8 \ , \quad n = 0, 1, \ldots, 7 \tag{17.4}$$

Then the Discrete Walsh Transform (DWT) of $f(\mathrm{n}|\mathrm{x},\mathrm{y})$ is computed as follows, where $W(\mathrm{u}|\mathrm{x},\mathrm{y})$ indicates the transformation coefficient, $Wal(\mathrm{u},\mathrm{n})$ is the Walsh function, n is the code of pixels:

$$W(\mathrm{u}|\mathrm{x},\mathrm{y}) = \sum_{n=0}^{7} f(\mathrm{n}|\mathrm{x},\mathrm{y}) \cdot Wal(\mathrm{u},\mathrm{n}), \qquad \mathrm{u} = 0, 1, \ldots, 7 \tag{17.5}$$

For actual calculation, those coefficients can be individually computed by convolutions between image and masks. In this paper, we only use eight transformation coefficients. However, the coefficients we got from (17.5) cannot

distinguish different textures effectively. So, variances of them are used as texture features. Now, we have eight texture submaps.

$$texturesubmap(\mathrm{u}) = \frac{1}{W^2} \sum_{(\mathrm{i},\mathrm{j}) \in \mathrm{W}(\mathrm{x},\mathrm{y})} \left[\mathrm{W}\left(\mathrm{u}\middle|\mathrm{x},\mathrm{y}\right) - \mathrm{M}\left(\mathrm{u}\middle|\mathrm{x},\mathrm{y}\right)\right]^2 \tag{17.6}$$

where $W(\mathrm{x}, \mathrm{y})$ is neighborhood window, in which the pixel is at the center, W is the size of the window, let $W = 3$, $M(\mathrm{ulx}, \mathrm{y})$ is the mean of eight coefficients.

In our model, the final texture map $\overline{T}$ is computed by a linear combination of eight texture sub-maps.

$$\overline{T} = \sum_{i=0}^{7} texturesubmap(\mathrm{i}) \tag{17.7}$$

17.2.2 Target-Saliency Map Computation

Before computing the target-saliency map, a normalization operation $N(\cdot)$ is applied to each of the maps, which is described in the second part of Sect. 17.2.1. The final target-saliency map S is computed as follows:

$$S = \frac{1}{3}\left(\mathrm{N}\left(\overline{\mathrm{I}}\right) + N\left(\overline{\mathrm{O}}\right) + \mathrm{N}\left(\overline{\mathrm{T}}\right)\right) \tag{17.8}$$

17.2.3 Targets Detection Using a Designed Detection Method

The traditional models define the regions of targets (ROT) as a disk with a fixed radius, but they have problems with identifying random regions with much redundancy. To establish an accurate target detection model, a fast segment method with adaptive threshold is used to obtain ROTs. The algorithm consists of: (1) finding the location of the current target-saliency map's global maximum as the conspicuous point; (2) the traditional Otsu's method is applied to the target-saliency map to obtain the threshold T0; (3) computing binary mask as follows:

$$binary(\mathrm{x}, \mathrm{y}) = \begin{cases} 1, \dfrac{img(\mathrm{x}, \mathrm{y})}{seedVal} \geq T0 \\ 0, \dfrac{img(\mathrm{x}, \mathrm{y})}{seedVal} < T0 \end{cases} \tag{17.9}$$

where seedVal is the value of conspicuous point. To eliminate the influence of noise and generate well-defined regions, some morphology operations, including dilation, hole filling, and erosion, will be carried out. Finally, the current target region R is

achieved; (4) set R to zero, then updating the target-saliency map and repeat step (2), (3) until all target regions are searched.

17.3 Experiments and Results

To evaluate the performance of the proposed model (the PM), several experiments are conducted using selected SAR images, including simple and complex background. According to the prior information, true targets are framed by blue rectangles in all original images.

Experiment results are shown in Figs. 17.3 and 17.4. In result maps, yellow circles describe the regions of targets, and the red lines shows location shift route. As Fig. 17.3 shows, in the image with simple background, both the two methods can detect targets accurately. But compare to Itti et al. method, the PM achieves targets regions with less redundant information. Figure 17.4 shows the model of Itti et al. fails to detect targets entirely, and there exists false regions without targets. On the contrary, the PM detects all the targets accurately. Experimental results also reflect that the PM can achieve target saliency map more accurately.

Table 17.1 shows the time trends for detecting targets of the two different models. We can see that the detection time cost of the proposed method is less than the model of Itti et al. In summary, the proposed method shows its great performance and robustness for SAR images targets detection under various kinds of SAR images.

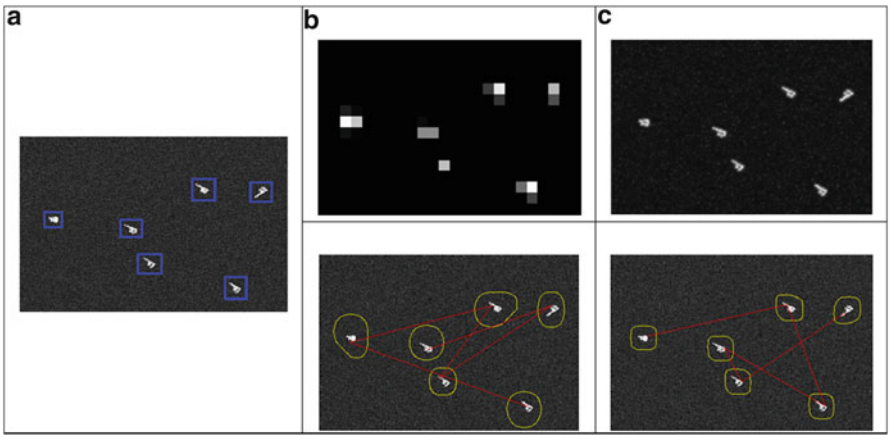

Fig. 17.3 (**a**) Original image; (**b**, **c**) target-saliency map (*top*) and detection result (*bottom*) of Itti et al. method and the PM method

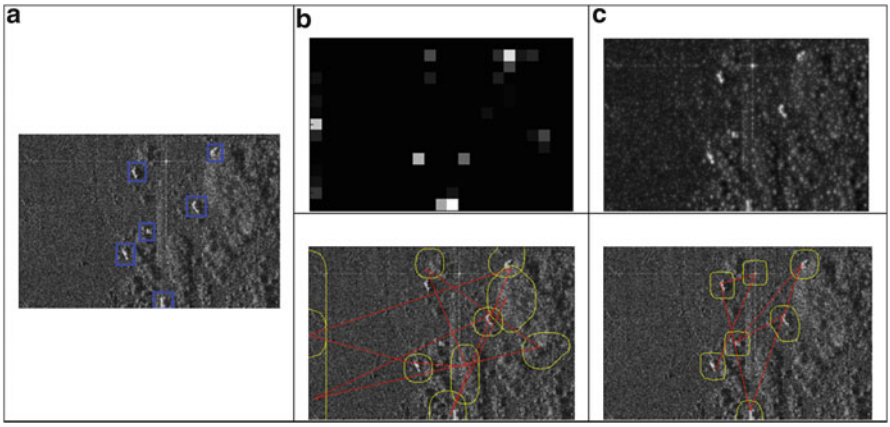

Fig. 17.4 (**a**) Original image; (**b**, **c**) target-saliency map (*top*) and detection result (*bottom*) of Itti et al. method and the PM method

Table 17.1 Average run time of two different methods

Method	Image1	Image2
Itti	7.504	7.816
PM	3.526	3.650

Conclusion

In this paper, we have presented a robust method for SAR targets detection inspired by visual effect of human eyes between SAR targets and backgrounds. Target-saliency detection is used to enhance the difference between targets and background before we detect the targets. For fair and comprehensive evaluation, SAR images with different typical backgrounds are used in the experiments, and the average run time is employed as an evaluation criteria. The results indicate that the proposed algorithm is more robust and has better performance than traditional visual attention methods.

Acknowledgement This work is supported in part by the National Natural Science Foundation of China under Grants 61271287, 61371048, 61301265.

References

1. El-Darymli K, McGuire P, Power D, Moloney C (2013) Target detection in synthetic aperture radar imagery: a state-of-the-art survey. J Appl Remote Sens 7(1). doi:10.1117/1.JRS.7.071598

2. Gao G, Liu L, Zhao L, Shi G, Kuang G (2009) An adaptive and fast CFAR algorithm based on automatic censoring for target detection in high resolution SAR images. IEEE Trans Geosci Remote Sens 47(6):1685–1697
3. Tello M, Lopez-Martinez C, Mallorqui JJ (2005) A novel algorithm for ship detection in SAR imagery based on the wavelet transform. IEEE Geosci Remote Sens Lett 2(2):201–205
4. Antoine JP et al (2004) Two-dimensional wavelets and their relatives. Cambridge University Press, Cambridge
5. Treisman AM, Gelade G (1980) A feature-integration theory of attention. Cogn Psychol 12 (1):97–136
6. Itti L (2000) Models of bottom-up and top-down visual attention. Dissertation, California Institute of Technology
7. Itti L, Koch C (2001) Computational modeling of visual attention. Nat Rev Neurosci 2 (3):194–230
8. Koch C, Ullman S (1985) Shifts in selective visual attention: towards the underlying neural circuitry. Hum Neurobiol 4(4):219–227
9. Itti L, Koch C, Niebur E (1998) A model of saliency-based visual-attention for rapid scene analysis. IEEE Trans Pattern Anal Mach Intell 20(11):1254–1259
10. Hou X, Zhang L (2007) Saliency detection: a spectral residual approach. In: IEEE conference on CVPR, Minneapolis
11. Elazary L, Itti L (2010) A Bayesian model for efficient visual search and recognition. Vis Res 50(14):1338–1352
12. Yu C, Smith L, Shen H, Pereira A, Smith T (2009) Active information selection: visual attention through the hands. IEEE Trans Auton Ment Dev 1(2):141–151
13. Yu Y, Mann G, Gosine R (2012) A goal-directed visual perception system using object-based top-down attention. IEEE Trans Auton Ment Dev 4(1):87–103
14. Miao J, Qing L, Zou B, Duan L, Gao W (2010) Top-down gaze movement control in target search using population cell coding of visual context. IEEE Trans Auton Ment Dev 2 (3):196–215
15. Navalpakkam V, Itti L (2006) An integrated model of top-down and bottom-up attention for optimizing detection speed. In: IEEE computer society conference on computer vision and pattern recognition, vol 2. IEEE, pp 2049–2056
16. Zhilong Z, Jichen L, Zhenkang S (2005) On texture feature extraction based on Local Walsh Transform. Signal Process 6(21)

Chapter 18
Sub-dictionary Based Joint Sparse Representation for Multi-aspect SAR Automatic Target Recognition

Liyuan Xu and Zongjie Cao

Abstract Joint sparse representation (JSR) is mostly used in face recognition area. While in this paper, JSR is adopted in the area of SAR automatic target recognition (ATR). In our method, the whole training dictionary is divided into several sub-dictionaries, according to the label of training samples. And classification is based on the minimum representation error criterion. Independent and identically distributed (IID) Gaussian random projection is used to extract feature of SAR images. Experiments are carried out on moving and stationary target acquisition and recognition (MSTAR) public database. Experiments results show that recognition rates can be improved by our method, by combining more useful information and reducing interference information of target.

Keywords SAR ATR • Multi-aspect • Sparse representation • Joint sparse representation • IID Gaussian random projection

18.1 Introduction

Synthetic aperture radar based automatic target recognition (SAR ATR) has been an important research subject, considering its key role in surveillance, homeland security and military. However, SAR ATR is not a simple problem, because SAR image is produced by specular reflection of coherent light. Images change obviously, even though azimuth or depression angle has a little variation.

According to the problem mentioned above, some researchers suggest that a combination of classifiers is applicable to different interval of pose [1]. There exist two traditional ways. The first way, estimate the pose of target. Then choose a corresponding classifier from combination of classifiers, which are trained by certain pose of target images. However, estimating target's pose is a challenging

L. Xu • Z. Cao (✉)
School of Electronic Engineering, University of Electronic Science and Technology of China, Chengdu, China
e-mail: zjcao@uestc.edu.cn

J. Mu et al. (eds.), *The Proceedings of the Third International Conference on Communications, Signal Processing, and Systems*, Lecture Notes in Electrical Engineering 322, DOI 10.1007/978-3-319-08991-1_18

problem, because of the unstable scattering of artificial objects [2]. The second way, considering most technology is developed based on single image classification, deal with single image separately with certain classifier, then fuse its' decisions [3–5]. Obviously, this method is not the optimal, for ignoring association of images. What is more, result relies too much on the performance of classifier.

Recently, some novel methods have been proposed for making full use of SAR images of target. Some researchers take full advantage of images by building a hierarchical structure with different kinds of features and classifiers [6]. But in practice, this kind of structure is complicate and time consuming sometimes. Some researchers put a few images with similar azimuth as a group, and choose samples from the whole training group to represent target [7]. But the method is based on an assumption that atoms selected from the whole dictionary to represent the test sample are from the same class. But the assumption is not verified. However, our method can get a better rate of recognition and solve all the problems at the same time.

The rest of the paper is organized as follows. Section 18.2, give basic knowledge about joint sparse representation. Our method will be described in detail in Sect. 18.3. And experimental results are shown in Sect. 18.4. In "Conclusion" section, conclusion is drown.

18.2 Joint Sparse Representation ATR

18.2.1 Sparse Representation Based Classification

We suppose that the size of training image is $w \times w$ and arrange the n^{th} training sample from the i^{th} class as one column of matrix $D_i = [v_{1i}, \ldots, v_{ni}]$, where $v \in \mathbb{R}^m$, $m = w \times w$. If there are k classes in the training set, a matrix $D = [D_1, \ldots D_k]$ is built to store all training samples. According to J. Wright et al. [8], a test sample x can be represented by a linear combination of training samples in the same class of test sample. So a test sample can be written in terms of all training examples as

$$y = Dx \tag{18.1}$$

where $x \in \mathbb{R}^n$ is a coefficient vector with most entries having a zero element. L_0 minimization is used to get the sparse solution of (18.1) [9], written as:

$$\hat{x} = \text{argmin}\|x\|_0, \text{s.}t. \;\; Dx = y \tag{18.2}$$

It's a NP-hard problem for solving underdetermined system of linear equations. However, theory in compressing sensing shows that if the solution of $\hat{x}$ is sufficiently sparse, solving (18.2) is equal to solve the equation below:

$$\hat{x} = \text{argmin}\|x\|_1, s.t.\ Dx = y \tag{18.3}$$

A new test sample y^i from class i can be represented by a linear combination of the training samples of the same class.

$$y^i = D_i x^i \tag{18.4}$$

In ideal case, the recovered sparse representation vector has the property that only the coefficients associated with the atoms belonging to the ground-truth class are non-zeroes. After recovering the sparse representation vector, the class label of the test sample is decided, based on the minimum reconstruction error criteria as

$$\hat{i} = \text{argmin}\left|\left|y - D\delta^i(\hat{x})\right|\right|_2 \tag{18.5}$$

where $\delta^i(\cdot)$ selects the elements of the vector corresponding to class i and set other elements to be zero.

18.2.2 Joint Sparse Representation Based Classification

A test group is made by M aspects of the same target. The test group $Y = [y_1, y_2, \ldots, y_M]$ can be rewritten as:

$$Y = DX \tag{18.6}$$

where $X = [\mathrm{x}_1, \ldots, \mathrm{x}_\mathrm{M}]$ is a coefficient matrix, whose entries are mostly zeroes.

As the same as the theory mentioned in part *2.1*, the reconstruct coefficient matrix is as follows:

$$\hat{X} = \text{argmin}\|Y - DX\|_F^2, s.t.\ \left|\left|\mathrm{X}\right|\right|_{\mathrm{l}_0\backslash\mathrm{l}_2} \le K \tag{18.7}$$

where K is an integer defining the sparse level. $\left|\left|\mathrm{X}\right|\right|_{\mathrm{l}_0\backslash\mathrm{l}_2}$ is obtained by first applying l_2 norm on each row of X and then apply l_0 norm on the resulting vector. This norm can promotes the degree of sparse at row level [10].

After recovering the sparse representation coefficient matrix $\hat{X}$, we can estimate the class label of target with the similar theory mentioned in part *2.1*.

$$\hat{i} = \arg\min_i \left\|Y - \hat{Y}^i\right\|_F = \arg\min_i \left\|Y - A\delta^i\left(\hat{X}\right)\right\|_F \tag{18.8}$$

18.3 Sub-dictionary Based Joint Sparse Representation for Multi-aspect ATR

According to basic knowledge in Sect. 18.2, joint sparse representation treats multi-aspect of target as a whole group. So the inter-correlations among the multi-aspect observations of the same physical target are fully used for recognition. But SAR image has some attributes, like obviously noise jamming and dramatically changing with pose variations. When targets are similar to each other, it is hard to distinguish them. As shown in Fig. 18.1, images of different targets with the same aspect are more similar than images of the same target with different aspects. In human face recognition area, the application of joint sparse representation is based on a hypothesis. The hypothesis is that a test sample can be well represented by a linear combination of training samples in the same class of test sample [11]. But Fig. 18.2 shows that traditional joint sparse representation cannot satisfy the hypothesis, while our method does. Combining multi-aspect images can improve the amount of information for ATR, but it can also improve the interference. Our method can control the interference while reserve the advantage of traditional sparse representation based classification.

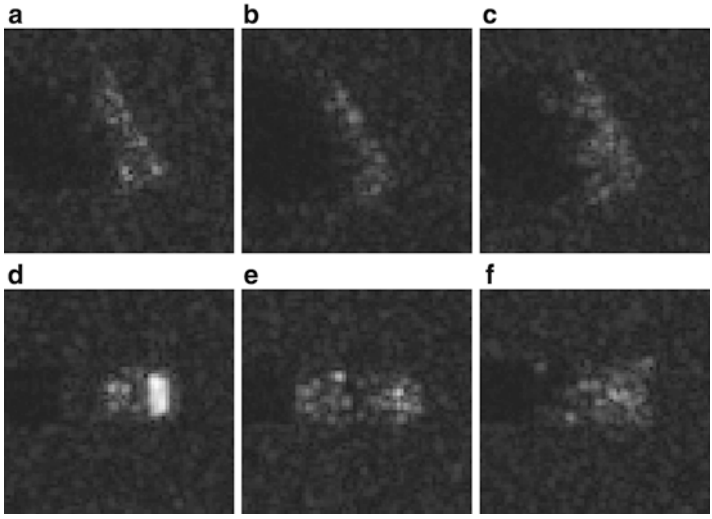

Fig. 18.1 Part of samples in MSTAR database. (**a**) BMP2, azimuth 120°; (**b**) BTR70, azimuth 120°; (**c**) T72, azimuth 120°; (**d**) BMP2, azimuth 0°; (**e**) BTR70, azimuth 0; and (**f**) T72, azimuth 0°

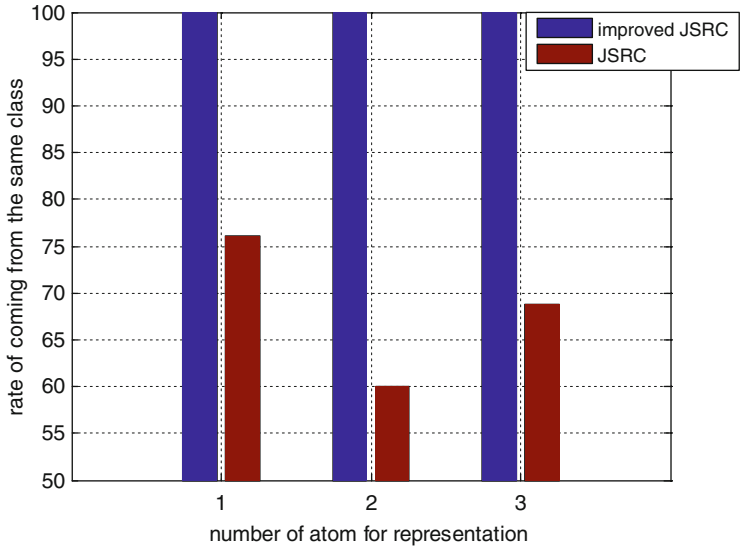

Fig. 18.2 Correct rate of selecting atoms for JSRC

18.3.1 Feature Extraction Use IID Gaussian Random Projection

For traditional SAR ATR, the extracted feature is one of decisive factors, but in our method, feature extraction is not so important. As a powerful tool for reducing dimension and compressing high-dimension data, independent and identical distribution Gaussian random projection is used [12]. Unlike traditional method (PCA, LDA, NMF and so on) [13–17], IID Gaussian random transformation matrix is generated randomly. When train dictionary changes, the transformation matrix stays the same, while a new projection matrix is needed in other methods.

Suppose N training samples are in dictionary $D = \{d_1, \ldots, d_i, \ldots, d_N\}, D \in \mathbb{R}^{T \times N}$, every image is reformed as a column of dictionary d_i, $i = 1, 2, \ldots, N$.

$$\widetilde{d}_i = R \times d_i \tag{18.9}$$

R is a standard orthogonal matrix, with distribution that elements in every raw satisfies $Norm(0, 1)$. $R \in \mathbb{R}^{t \times T}$, $t \ll T$, $\widetilde{d}_i$ is the compressed low dimensional vector obtained by random projection of d_i.

18.3.2 ATR via Improved Joint Sparse Representation

The greatest advantage of joint sparse representation is using relation among different pose of target, meanwhile using information of single image. In the field

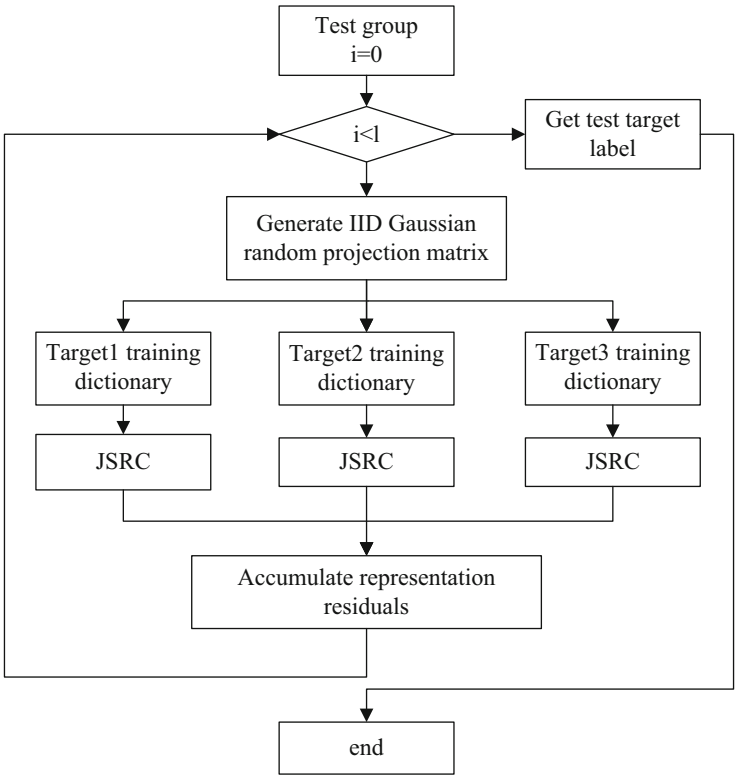

Fig. 18.3 The flow chart of improved joint sparse representation

of compressive sensing, simultaneous orthogonal matching pursuit (S-OMP) is used for signal representation [18]. We use the theory, S-OMP, to solve the equation:

$$\hat{x} = \text{argmin}\|y - Dx\|, s.t.\ \|x\|_1 \leq K \tag{18.10}$$

In our method, multi-aspect images of target are treated as a test group, so that more information of target can be used. And considering the assumption for sparse representation is too ideal to reach, the whole training group is divided into several parts, in accordance with its' class, to satisfy the assumption. $D = \{D_1, \ldots, D_k\} = \{d_{11}, d_{12}, \ldots, d_{ij}, \ldots, d_{k1}, \ldots, d_{kp}\}$, and D_i is a sub-dictionary with training samples of class i. The improved algorithm is shown in Fig. 18.3. And the algorithm used to deal with JSRC is M-CosAmp [18].

18.4 Experiment

In this section, we use MSTAR public database to evaluate the performance of our method. In MSTAR database, three types of targets, (BMP2, BTR70, T72), are used to test some certain performances of our method. All the images are cropped by extracting patches from the center of the image. Independent and identically distributed (IID) Gaussian random projection is used for feature extraction. For comparison, single-aspect ATR via sparse representation and multi-aspect ATR via unimproved joint sparse representation are used.

In this experiment, three classes (BMP2, BTR70 and T72) are used to prove that our method can improve the rate of recognition. Images captured at depression 17° are used for training and images captured at depression 15° are used for testing. As shown in Table 18.1, we only use some certain models (BMP2-sn9563, BTR70-snc71, and T72-sn132) as training data. But use all images at depression 15° as testing data.

Images, including training images and testing images, are all reshaped to one column, then dimension is reduced from 4096(64×64) to 144 by IID Gaussian random projection. Then run SAR ATR 10 times with IID Gaussian random projection matrix and combine distance matrixes to reach a final result. The repeating work is to reduce the unstable of IID Gaussian random projection.

After feature extraction, three methods are used separately. The test group is combined by three images, the sparse level is 3, and azimuth interval is 120°. The rate of recognition is shown in Table 18.2. Our method can improve the recognition rate obviously.

Table 18.1 Summary of the used MSTAR database

Target Number	1			2	3		
Target Type	BMP2			BTR70	T72		
	sn-c9563	sn-c9566	sn-c21	sn-c71	sn-132	sn-812	sn-s7
Train (φ =17°)	233			233	232		
Test (φ =15°)	195	196	196	196	196	195	191

Table 18.2 Recognition rate (%) of three methods

	Target type						
	BMP2			BTR70	T72		
Method	sn-9563	sn-9566	sn-c21	sn-c71	sn-132	sn-812	sn-s7
SRC	94.8187	68.5567	77.3196	98.4536	93.8144	64.2487	68.254
JSRC	99.4624	82.7957	96.2366	98.3871	98.3871	93.5135	89.9441
Improved JSRC	100	88.1356	100	100	98.3051	99.4318	93.5249

Conclusion

Sub-dictionary based joint sparse representation is proposed in this paper to combine more information of target. The whole training dictionary is divided into several sub-dictionaries based on class of training samples. And JSR is used in sub-dictionaries separately to force it in accordance with the premise. From experiments' results, we can prove that our method can raise recognition rate than traditional sparse representation.

Acknowledgement This work is supported in part by the National Natural Science Foundation of China under Grants 61271287, 61371048, 61301265.

References

1. Sun Y et al (2007) Adaptive boosting for SAR automatic target recognition. IEEE Trans Aerospace Electronic Syst 43:112–125
2. Principe JC, Xu D, Fisher III JW (1998) Pose estimation in SAR using an information theoretic criterion. In: Proceeding of SPIE, vol 3370. pp 218–229
3. Vespe M, Baker CJ, Griffiths HD (2005) Multi-perspective target classification. In: IEEE International radar conference, pp 877–882
4. Huan R, Pan Y (2011) Decision fusion strategies for SAR image target recognition. Radar, Sonar Navigation, IET 5:747–755
5. Huan R et al (2010) SAR target recognition with data fusion. In: WASE International Conference on Information Engineering (ICE), date 14–15, vol 2. pp 19–23
6. Cui Z, Cao Z, Fan Y, Zhang Qi (2012) SAR automatic target recognition using a hierarchical multi-feature fusion strategy. In: Globecom workshops (GC Wkshps), pp 1450–1454
7. Zhang H, Nasrabad NM, Zhang Y, Huang TS (2012) Multi-view automatic target recognition using joint sparse representation. IEEE Trans Aerospace Electronic Syst 48:2481–2497
8. Wright J et al (2010) Sparse representation for computer vision and pattern recognition. In: Proceedings of the IEEE–special issue on applications of sparse representation & compressive sensing, vol 98. pp 1031–1044
9. Donoho DL (2004) For most large underdetermined systems of linear equations the minimal l1-norm solution is also the sparsest solution. Commun Pure Appl Math 59:797–829
10. Tropp JA, Gilbert AC, Strauss MJ. (2006) Algorithms for simultaneous sparse approximation. EURASIP J Appl Sign Proc 83(3):589–602
11. Wright J, Yang AY, Ganesh A, Sastry SS, Ma Y (2009) Pattern analysis and machine intelligence. IEEE Trans 31:210–227
12. Yang AY et al (2007) Feature selection in face recognition: a sparse representation perspective. University of California Berkeley, Technical Report UCB/EECS-2007-99
13. Martinez AM, Kak AC (2001) PCA versus LDA. IEEE Trans Pattern Anal Mach Intell 23(2):228–233
14. Changzhen Q, Hao R, Huanxin Z, Shilin Z (2009) Performance comparison of target classification in SAR images based on PCA and 2D-PCA features. In: Proceeding of 2009 2nd Asian-Pacific Conference on Synthetic Aper ture Radar (APSAR), pp 868–871
15. Belhumeur PN, Hespanha JP, Kriegman DJ (2009) Eigenfaces vs. fisherfaces: recognition using class specific linear projection. IEEE Trans Pattern Anal Mach Intell 19(7):711–720

16. Lee DD, Seung HS (1999) Learning the parts of objects by non-negative matrix factorization. Nature 401:788–791
17. Nikolaus R (2007) Learning the par ts of objects using non-negative matrix factorization (Term Paper, MMER Team)
18. Rakotomamonjy A (2010) Surveying and comparing simultaneous sparse approximation (or group lasso) algorithms. University of Rouen, France, Technical Report

Chapter 19
Target Detection Performance Analysis of SAR Image with Different Resolutions Based on Template Matching

Haiyi Yang and Zongjie Cao

Abstract As the importance of analyzing system resource constrains on SAR automatically target recognition (ATR) has been noticed, more researchers start contributing to this field. In this paper, we focus on discussing the relationship between the performance of target detection and the resolution of SAR image which is regarded as one of the most important parameters of SAR imaging system. It is assumed that the resolution does not need to be good enough in target detection, but the modest reduction of resolution will provide a better trade-off between accuracy and speed. Firstly, an empirical operation is used to modify the resolution of raw images. Actually, the images with different resolutions should be derived by SAR imaging independently, but that's not the point in this paper. Then the comparison using two methods is described, the optimal detector based on Bayesian expression and the sub-optimal detector, which is known as CFAR detection. The simulated data is used to evaluate the performance of detection, and the correctness of our suspicion is demonstrated in the experiment.

Keywords Target detection performance • Resolution of SAR image • CFAR

19.1 Introduction

With the developing of SAR imaging technology, high resolution SAR image is much easier to get while the computation complexity grows rapidly. Due to the demands of wide scene imaging and speedy target detection, using high resolution SAR image to detect target is difficult, because the targets spread multiple image cells and the RCS of targets are usually non-uniform [1]. The detection could be influenced by many system resource constraints such as aspect sensitivity. Here, we concentrate on how the target detection performance is affected with the different

H. Yang • Z. Cao (✉)
School of Electronic Engineering, University of Electronic Science and Technology of China, Chengdu, China
e-mail: zjcao@uestc.edu.cn

J. Mu et al. (eds.), *The Proceedings of the Third International Conference on Communications, Signal Processing, and Systems*, Lecture Notes in Electrical Engineering 322, DOI 10.1007/978-3-319-08991-1_19

resolutions of SAR images. Though nowadays extensive applied methods which based on strong scattering point model is not well fit with spread target detection in high resolution SAR images yet, without loss of generality, some conventional methods are exploited to compare the performance at different resolutions.

Researching the influence of system resource constraints is started with Lincoln lab's contribution, about the ATR performance comparison related to different resolutions and polarizations of SAR images [2, 3]. An intuitive conclusion has been indicated that images with better resolution have better performance.

Michael D. DeVore et al. [4–6] expand the work theoretically and experimental. So far, many scientific institutes begin this research, since its importance is noticed.

The article is organized as follows. Section 19.2 presents the data format and the processing, and introduces the experiment for comparing the performance. Section 19.3 describes the methods of SAR target detection which is used in the paper. In Sect. 19.4, the result is given and the disadvantage of our methods is discussed. Conclusions are drawn in "Conclusion" section.

19.2 Data and Experiment Analysis

SAR images at same scene are used for the comparability, and some spatial filters and digital processors are exploited to reduce the resolution of SAR images. After filtering, the spatial resolution of the images has been changed by down sampling. However, when spatial resolution is reduced, the radiation resolution against raw images may be changed by this procedure. The filter constructed by sinc function often smears the images [7], on the contrary, directly reducing pixel number may cause the improvement of radiation resolution [8], though the quality of image has been decreased notably. Here in our experiment, adjacent cells are added directly, and the mean value of cells is set as new cell's value in lower resolution image. Then the images with different resolutions are derived, meanwhile aspect and other parameters of target keep fixed.

Another step is named as template matching, which will be mentioned in next section. The template for matching contains almost the same size of region or numbers of scatters against actual targets, and the size of template changes adaptively at each resolution. Here the matching step is a similar multiply-accumulate weighted by template. After this step, the variance of clutter is unified at different resolutions, as well as the SCR is unified.

The optimal detector is employed to estimate the target detection performance of simulated SAR images, because the essential information of a real SAR image might hardly get known. In the simulation each condition is taken into account and the mathematical formula based on Bayesian conditional probability equation is deduced later. As in the CFAR detection, the results are indeed evaluated by both simulations and experiments. However, the data which consists of a series of comparable data cannot complete the whole situations and the CFAR detector is a sub-optimal method. So in this premise, results of CFAR detection may miss out

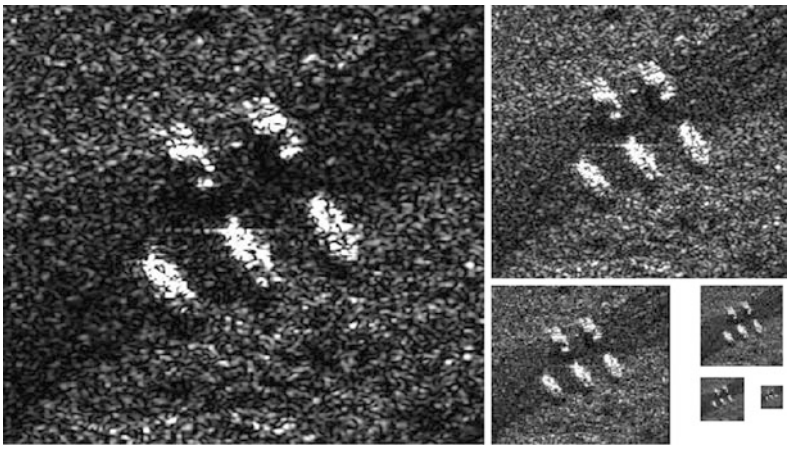

Fig. 19.1 Different resolution images used in experiments

some particular case while the variances of result at different conditions are indicated in optimal detection. We will weigh and analysis contrastively the result of two methods.

In the experiments, the mentioned methods are employed to derive images with different resolutions, and a graphic is shown in Fig. 19.1. We assume that the raw image owns the resolution of 1×1 and the resolutions of the rest images are 2×2, 4×4 until the size of cells getting close to size of targets. Then the detectors with a Pfa of 0.001 are applied, and the potential target regions are found out. Finally number of detected pixels indicates the performance in CFAR detection, and the statistical results show the performance in optimal detection, respectively.

19.3 Methodology

Two kinds of detectors are applied. One is optimal detector which utilizes prior knowledge about target, and the other is sub-optimal detector without prior knowledge. The first method here is noted as conditional Bayesian detector [9], and CFAR detector [10] is selected as the second one.

Here the template matching is used to accumulate power of spatial spread targets in high resolution SAR images. The template is decided by the minimum target which we focus on and its strong scatters if it might be known. Here the value of template is unitary and fixed in order to avoid unnecessary deviation. The size of template changes when resolution changes, since it's correlated to the actual size of targets.

For convenience, our process is described by the one-dimension chart. Assuming the target consists of four strong scatters and they distribute in range cells as shown in Fig. 19.2a. The presence of strong scatters is shown at four waveform peaks. The

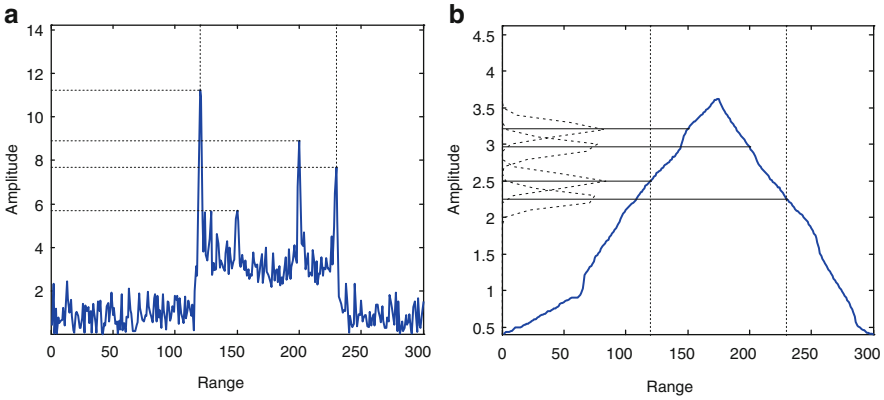

Fig. 19.2 Strong scatters signal and template matching output. (**a**) The waveform of target with four strong scatters. (**b**) The waveform after template matching

target size is regarded as the number of range cells between the first and last strong scatters accordingly.

After template matching, the pdf of four strong scatters are indicated by the left side dashed lines in Fig. 19.2b, and the values of region between two vertical lines are above the right boundary. The continuous curve is an ideal result, and the actual discrete values can be derived by sampling the result according to resolution and position of targets.

The conditional Bayesian method will be analyzed in the following. Assuming that target in SAR images is presented as the summation of target scatters and clutter:

$$I_{tar} = \left\{ \alpha(x_k, y_k) + w(x_k, y_k) \middle| x_k, y_k \in \Omega; k = 1, 2, \ldots, n \right\} \tag{19.1}$$

where Ω denotes target region, and n denotes the number of pixel in Ω. From the expression (19.1), target zone is a collection of many cells, consisting of low intensity scatters and strong scatters. As accumulating the cells in the template, if the target position and the resolution are certain, the collection after template matching and the values are determined. The expression is shown as:

$$F_{match}(x, y) = \sum_{k=0}^{M} a(x_k + x, y_k + y) + w(x_k + x, y_k + y) \tag{19.2}$$

$$C_{match\left|(x,y,D)\right.} = \left\{ F_{match}(x + iD, y + iD) \middle| (x, y) \in \Omega; i = 1, 2, \ldots, \lfloor n/D \rfloor \right\} \tag{19.3}$$

where D indicates the resolution parameters, and the (x, y) is the position related to the reference cells. In expression (19.2), M is the size of template, correspond to number of pixels at raw resolution divided by D.

Substituting the values into pdf under Gaussian assumption, since here the template matching result has satisfied the central limit theorem [11] for simplicity. Indeed if the speckle is multiplication model [12], the Gamma distribution might be more accurate. The expression of conditional distribution [13] is:

$$p\left(z\middle|\{(x_0,y_0),D\}\right)=\frac{1}{\sqrt{2\pi\widetilde{\sigma}}}\exp\left(-\frac{[z-F_{match}(x_0,y_0)]^2}{2\widetilde{\sigma}^2}\right) \tag{19.4}$$

where $\widetilde{\sigma}$ stands for clutter variance after template matching. As we mentioned, the values in target region are over one boundary, so the collection C_{match} could be detected sequentially, and each element has similar pdf and different mean values. The cpdf of C_{match} is:

$$p\left(C\middle|\{(x_0,y_0),D\}\right)=\left\lfloor\frac{D}{n}\right\rfloor\sum_{\Omega}p\left(z\middle|\{(x_0,y_0),D\}\right) \tag{19.5}$$

then the Bayesian equation is used:

$$p(C_{match})=\iint\limits_{(x_0,y_0)\in\Phi,D}p\left(C\middle|\{(x_0,y_0),D\}\right)p(x_0,y_0)p(D)d\Phi dD \tag{19.6}$$

This probability is integration of cpdf multiply by probability of conditions. In expression (19.5) the summation means if one cell in Ω is detected so that we consider the target is detected. Hence you can instead that by product of cpdf, and it means if all cells in Ω are detected so that the target is detected. At first, we should decide and separate the target cells against boundary. If prior information is enough, the boundary is set by manmade, such as the minimal value in target region. Then, the pdf of clutter can be determined. For comparison, a constant probability of false alarm is chosen and the threshold will be counted. Finally, the probability of detection will be derived. The optimal detection needs enough information, including the knowledge about targets and conditions. The statistical result will support our suspicion about the influence of SAR target detection performance at different spatial resolutions.

One contestation is about the boundary above. Since in traditional detection the threshold is determined by the distribution of clutter, while in this paper, the template matching result plays a prime role. However, it has been noticed that the template matching drops most of false alarm and numbers of weak scatters. The CFAR detection output will present that.

The CFAR detector has simplified the process because it only utilizes the information of clutter, and many conditions are fixed. The boundary is unknown since it is correlated to the targets. In our experiments using real SAR images, the boundary is chosen empirically, and the changes of target against aspects and/or postures are ignored. A trade-off boundary is computed by the mean value of whole

image multiply by a constant coefficient. It actually has little effect on target region which owns high values of amplitude. In the optimal experiments, the boundary is determined adaptively by template matching output.

19.4 Result

At first, an output is given by the experiments using simulated images. A statistical output of the optimal detector is analyzed, since all the conditions is counted, and the detection result are given independently. The evaluation of detection performance includes the variance of performance and probability of detection described by Pd. Results are shown in Fig. 19.3.

From the comparison, the worse resolution has better probability of detection in the optimal detection, while that costs a price of larger variance especially at the

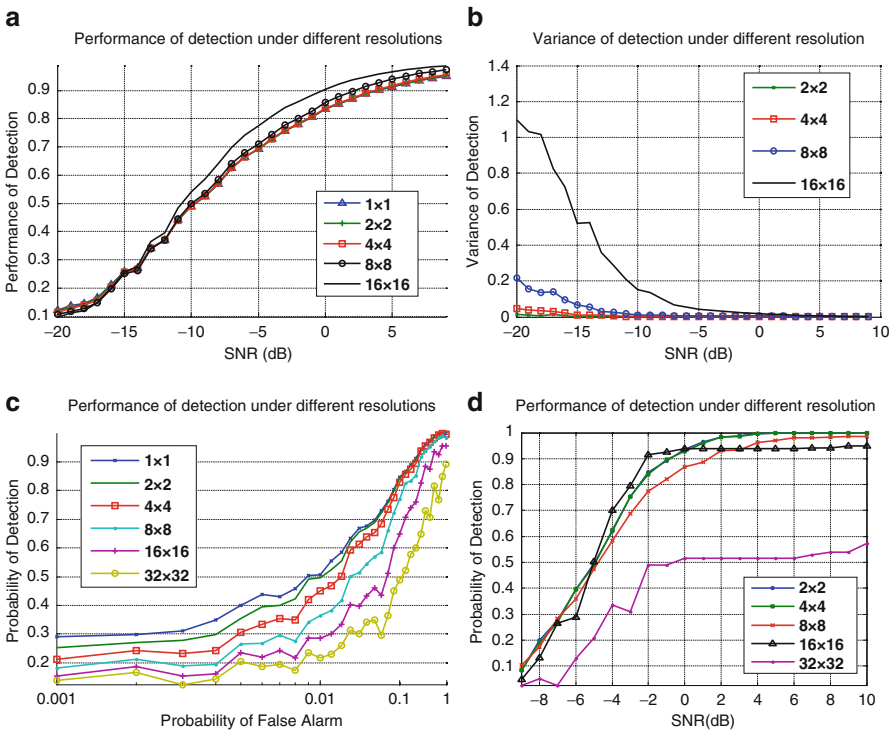

Fig. 19.3 Performance of simulated experiments under different resolutions. (**a**) The Pd–SNR curves using optimal detector; (**b**) the variance of Pd; (**c**) the Pd–Pfa curves using optimal detector; (**d**) the Pd–SNR curves using CFAR detector

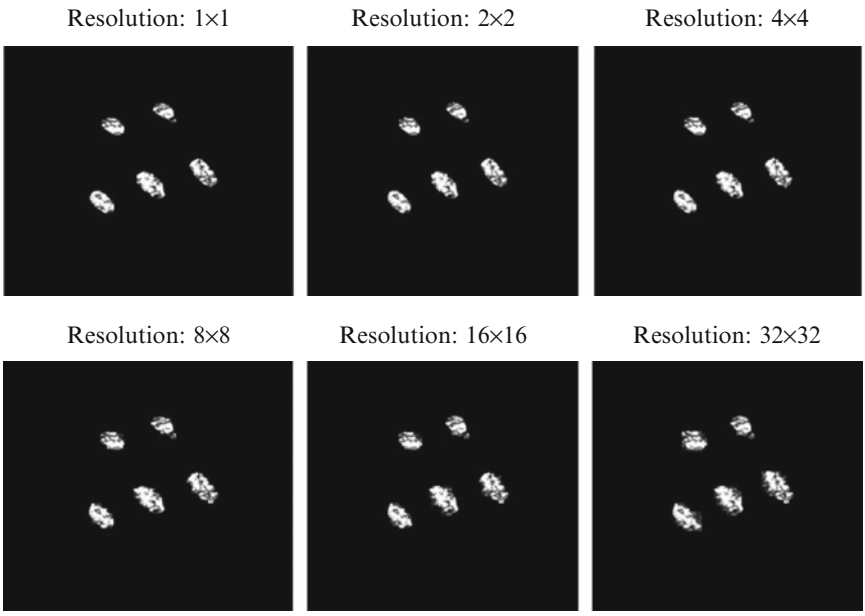

Fig. 19.4 CFAR detector output multiply by raw image at different resolutions

16×16 resolution. That means the Pd has a high value in most conditions, but has very low values of Pd in others. According to Fig. 19.3a, c, detection performance at worse resolution is more sensitive to SNR, since the larger cells consist of more scatters of both targets and clutters. In Fig. 19.3d, the similar result will be obtained. In CFAR detection, another distinction is shown that Pd at 32×32 resolution are significantly decreased, and it may occurs when the resolution cells become as large as the size of target and the aspect of template is improper matched.

Real SAR images are used then. Here the template is a rectangle but aspect angle of target is 45°, and the boundary is two times mean value of whole image. However, the detector archives a good performance. The detection results are presented in Fig. 19.4.

We can see the results of detection using CFAR detectors are similar when the size of resolution cell is less than 16×16. And when it raises to 32×32, the edges of regions detected as target get sharp and jagged. It is possible to deduce the decay of performance while resolution becomes worse. Here the size of target in raw images is 64×25 and the azimuth of targets is an approximate 45° rotation. Hence the template size is chosen as 32×32 at raw resolution. The CFAR detector has a satisfying output in our experiments under each resolution.

Conclusion

The target detection performance under different resolutions is compared by using simulated data and real SAR images. In most situations, the diminution of resolution would lead to negligible detection loss, even the performance can be better. When the resolution becomes worse, the variance of detection performance gets larger. And if the resolution cells is closing to the proper size of target, the probability of detection might significantly decrease.

The high resolution SAR imaging is the trend, and many articles contribute to the detection at high resolution [14, 15]. In view of constraints of nowadays system resource, the target detection at lower resolution has an advantage over speed and accuracy. Our future research is focus on improving the existing conclusion and expanding more aspects about system resource constraints.

Acknowledgments This work is supported in part by the National Natural Science Foundation of China under Grants 61271287, 61371048, 61301265.

References

1. Conte E, De Maio A, Galdi C (2004) Statistical analysis of real clutter at different range resolutions. IEEE Trans Aerosp Electron Syst 40(3):903–918. doi:10.1109/TAES.2004.1337463
2. Novak LM, Halversen SD, Owirka GJ, Hiett M (1995) Effects of polarization and resolution on the performance of a SAR automatic target recognition system. Lincoln Lab J 8(1):49–68
3. Novak LM, Owirka GJ, Netishen CM (1993) Performance of a high-resolution polarimetric SAR automatic target recognition system. Lincoln Lab J 6(1)
4. DeVore M, Chamberlain R et al (2002) Tradeoffs between quality of results and resource consumption in a recognition system. In: Proceedings of IEEE international conference on IEEE application-specific systems, architectures and processors, pp 391–402. doi:10.1109/ASAP.2002.1030738
5. Devore MD (2001) Recognition performance from synthetic aperture radar imagery subject to system resource constraints. Dissertation, Washington University
6. Huddleston SH, Zhou X et al (2007) Statistical models for target detection in infrared imagery. Proc SPIE Autom Target Recognit 17:65661A. doi:10.1117/12.747148
7. Terzuoli A, McGowan J, et al. (2010) The effect of synthetic aperture radar image resolution on target discrimination. In: 38th COSPAR scientific assembly, vol 38. p 391
8. Dumitru CO, Datcu M (2013) Information content of very high resolution SAR images: study of feature extraction and imaging parameters. IEEE Trans Geosci Remote Sens 51(8):4591–4610
9. Schonhoff TA, Giordano AA (2006) Detection and estimation theory and its applications. Pearson College Division, America
10. El-Darymli K, McGuire P, Power D, Moloney C (2013) Target detection in synthetic aperture radar imagery: a state-of-the-art survey. J Appl Remote Sens 7(1):071598–071598. doi:10.1117/1.JRS.7.071598

11. Gao G (2010) Statistical modeling of SAR images: a survey. Sensors 10:775–795. doi:10.3390/s100100775
12. López-Martínez C, Fabregas X (2003) Polarimetric SAR speckle noise model. IEEE Trans Geosci Remote Sens 41(10):2232–2242. doi:10.1109/TGRS.2003.815240
13. O'Sullivan JA, DeVore MD et al (2001) SAR ATR performance using a conditionally Gaussian model. IEEE Trans Aerosp Electron Syst 37(1):91–108. doi:10.1109/7.913670
14. Shui PL, Xu SW, Liu HW (2011) Range-spread target detection using consecutive HRRPs. IEEE Trans Aerosp Electron Syst 47(1):647–665. doi:10.1109/TAES.2011.5705697
15. Bandiera F, Besson O, Ricci G (2011) Adaptive detection of distributed targets in compound-Gaussian noise without secondary data: a Bayesian approach. IEEE Trans Signal Process 59(12):5698–5708. doi:10.1109/TSP.2011.2167613

Chapter 20
Sequential LOUD Test for Genuine and Dummy Warhead Identification Using MIMO Radar

Xue Wang, Qian He, and Dongyang Cai

Abstract This paper studies genuine and dummy ballistic warheads identification using multiple-input and multiple-output (MIMO) radar. State space model (SSM) is used to describe the kinetic characteristics of the warheads. Identification of the genuine and dummy warheads is accomplished by solving a binary hypothesis testing problem. Sequential detection method is employed. Since sophisticated dummy warhead are made very similar to the genuine one, it is very difficult for conventional sequential detectors to tell them from the genuine ones. We consider to employ locally optimal unknown direction (LOUD) test, which has been proved to have the advantage of distinguishing small differences. Sequential LOUD (SLOUD) test is proposed. It is shown that the performance of the SLOUD test based identification method is superior than the sequential detection method based on the conventional mismatched likelihood ratio (LR) test or the generalized LR (GLR) test.

Keywords MIMO radar • Sequential detection • State space model

20.1 Introduction

By launching dummy warheads in the middle-course phase which look similar to the genuine ones, the enemy intends to mislead the anti-missile system to fail to protect the genuine warheads. Identification of genuine and dummy ballistic warheads is the premise of an anti-missile system that determines the system prosperity. Warhead identification is usually performed during the middle course phase [1–7] based on feature extraction. The feature can be micro-Doppler signature [3–6], or polarization signature [7], etc. In this paper, a state space model (SSM) is developed for warheads travelling in the middle course phase. The difference between a genuine and a carefully designed dummy warhead usually lies in their micro-motion behaviors,

X. Wang • Q. He (✉) • D. Cai
EE Department, University of Electronic Science and Technology of China, Sichuan, China
e-mail: qianhe@uestc.edu.cn

J. Mu et al. (eds.), *The Proceedings of the Third International Conference on Communications, Signal Processing, and Systems*, Lecture Notes in Electrical Engineering 322, DOI 10.1007/978-3-319-08991-1_20

featuring different SSM system parameters, based on which, the observed data are directly used for the identification of genuine and dummy warheads.

Considering that the identification performance depends on the accuracy of the observed data, we propose to adopt multiple-input multiple-output (MIMO) radar with dispersed antennas which is capable of obtaining accurate multi-dimensional measurements [8], to observe the movements of the warheads. With the MIMO radar measurements, we formulate the identification problem as a binary hypothesis testing problem. As time is vital in the application of warhead identification, we use sequential detection to make a decision as quickly as possible. Since the SSM system parameters for the dummy warheads are usually unknown to the anti-missile system,[1] the binary hypothesis test is composite. The standard approach to solve this problem is to employ the generalized likelihood ratio (GLR) test based sequential detection (SGLRT). However, the SGLRT requires estimation of the unknown parameters and may lead to heavy time delay, which may be unaffordable to the genuine and dummy warhead identification system. Further, when the dummy warhead is made very similar to the genuine one, the identification performance of SGLRT-based method may not be acceptable.

In this work, we propose to employ a locally optimal unknown direction (LOUD) test based sequential detection approach to identify the genuine and dummy warheads. The LOUD test has been proved to be capable of distinguishing small differences, without causing processing delays. The expression of the sequential LOUD (SLOUD) detector is developed. We show by numerical examples that the performance of the SLOUD detector is superior than the SGLRT detector and the sequential mismatched likelihood ratio test (SMLRT) based detector.

20.2 State Space Model For Warhead

Consider the scenario where a ballistic warhead is flying in the middle course phase in a three dimensional radar coordinate system *UVW* as shown in Fig. 20.1. The warhead is composed of a few strong scatterers including a main scatterer.

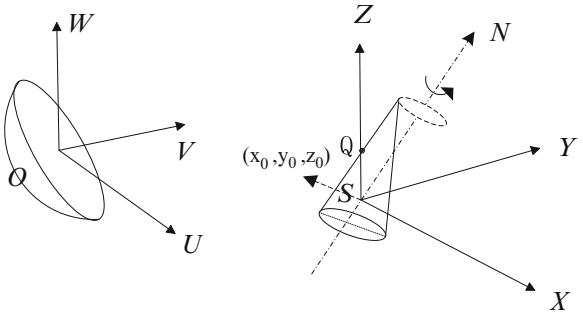

Fig. 20.1 Warhead movement in radar *UVW* and reference *XYZ* coordinate systems

[1] Assume the SSM system parameters are known for the genuine warheads based on some preprocessing or the available data base.

For simplicity and without loss of generality, here we focus on the movement of the main scatterer Q, which undergoes translation and micro-motion, such as vibration, precession, and nutation [5], etc. Without loss of generality, only precession is considered. To explicitly analyze the micro-motion of the main scatterer, a reference coordinate system XYZ centered at the intersection of the geometric symmetry axis and the precession axis of the target, initially located at (x_0, y_0, z_0) in UVW, is employed. Assume that the reference coordinate system has the same translation as the warhead and is parallel to the radar system along all axes. The warhead flies with initial translational velocity $(v_{x,0}, v_{y,0}, v_{z,0})$ and acceleration of gravity (g_x, g_y, g_z). Let $[q_x(t), q_y(t), q_z(t)]$ and $\left[q_x^{'}(t), q_y^{'}(t), q_z^{'}(t)\right]$ denote the instant micro-motion position and the micro-motion velocity of the main scatterer at time t. The instant position $[x(t), y(t), z(t)]$ in UVW and the instant velocity $\left[v_x(t), v_y(t), v_z(t)\right]$ of the main scatterer at time t can be described by the kinetic equation as follows [9, 10]

$$\begin{cases} x(t) &= x_0 + v_{x,0}t + 0.5g_x t^2 + q_x(t) \\ y(t) &= y_0 + v_{y,0}t + 0.5g_y t^2 + q_y(t) \\ z(t) &= z_0 + v_{z,0}t + 0.5g_z t^2 + q_z(t) \\ v_x(t) &= v_{x,0} + g_x t + q_x^{'}(t) \\ v_y(t) &= v_{y,0} + g_y t + q_y^{'}(t) \\ v_z(t) &= v_{z,0} + g_z t + q_z^{'}(t) \end{cases} \tag{20.1}$$

Define the state vector $\mathbf{x}(t)$ to include the instant position, the instant velocity and the instant micro-motion position of the warhead, i.e.,

$$\mathbf{x}(t) = \left[x(t), y(t), z(t), v_x(t), v_y(t), v_z(t), q_x(t).q_y(t).q_z(t)\right]^{\dagger}, \tag{20.2}$$

where † denotes transpose. According to (20.1) and (20.2), the noise-free state equation that describes the dynamic behavior of the warhead can be written as

$$\mathbf{x}^{'}(t) = \mathbf{R}_t \mathbf{x}(t) + \mathbf{u}(t), \tag{20.3}$$

where $\frac{x^{'}(t) = \partial \mathbf{x}(t)}{\partial t}$, $\mathbf{u}(t) = [0,0,0,g_x,g_y,g_z,0,0,0]^{\dagger}$ is time invariant, and

$$\mathbf{R}_t = \begin{bmatrix} \mathbf{0}_3 & \mathbf{I}_3 & \mathbf{0}_3 \\ \mathbf{0}_3 & \mathbf{0}_3 & \mathbf{E}_2 \\ \mathbf{0}_3 & \mathbf{0}_3 & \mathbf{E}_1 \end{bmatrix} \tag{20.4}$$

is the state transition matrix, where $\mathbf{I}_3$ is a 3×3 identity matrix, $\mathbf{E}_1$ and $\mathbf{E}_2$ depend on the micro-motion parameters which satisfy [11] $\mathbf{q}^{'}(t) = \mathbf{E}_1 \mathbf{q}(t)$ and $\mathbf{q}^{''}(t) = \mathbf{E}_2 \mathbf{q}(t)$, where $\mathbf{q}(t) = \left[q_x(t), q_y(t), q_z(t)\right]^{\dagger}$, $\mathbf{q}^{'}(t) = \partial \mathbf{q}(t) \partial t$ and $q^{''}(t) = \partial^2 \mathbf{q}(t) \partial^2 t$.

Assume that the sampling interval is T ($T>0$). Denote $\mathbf{u}_k=\mathbf{u}(kT)$, and $\mathbf{x}_k=\mathbf{x}(kT)$, where k is a positive integer. Discretizing (20.3) and taking into account the state noise $\mathbf{w}_k$, the discreet time state equation can be written as [11]

$$\mathbf{x}_{k+1}=\mathbf{F}_{k+1}\mathbf{x}_k+\mathbf{G}_{k+1}\mathbf{u}_k+\mathbf{w}_k, \tag{20.5}$$

where $\mathbf{F}_{k+1}=e^{\mathbf{R}_t T}$, $\mathbf{G}_{k+1}=\int_0^T e^{\mathbf{R}_t \tau}\mathrm{d}\tau$, $\mathbf{w}_k$ is assumed to be white Gaussian with zero mean and covariance matrice Σ_w, i.e., $\mathbf{w}_k\sim\mathcal{N}(\mathbf{0},\Sigma_w)$.

Suppose the measurements, possibly obtained from a radar estimator etc., is linear with respect to the state vector $\mathbf{x}_k$ [11], which can be expressed as

$$\mathbf{y}_k=\mathbf{H}\mathbf{x}_k+\mathbf{e}_k, \tag{20.6}$$

where $\mathbf{e}_k$ is the white Gaussian observation noise with zero mean and covariant matrix $\boldsymbol{\Sigma}_e$, i.e., $\mathbf{e}_k\sim\mathcal{N}(\mathbf{0},\Sigma_e)$, assumed mutually independent of the state noise $\mathbf{w}_k$ and $\mathbf{H}$ is the observation matrix.

Equations (20.5) and (20.6) together compose the SSM that describes the kinetic movement of the warhead flying in the middle course phase. In this way, the identification of the genuine and dummy warheads are transferred into hypothesis testing of the SSM parameters. Without loss of generality, we consider the case where the state transition matrix $\mathbf{F}_k$ differs.

20.3 Sequential Hypothesis Testing for Warheads Identification

The genuine and dummy warheads move together initially with the system transition matrix $\mathbf{F}_0$ which is assumed known possibly from preprocessing[1]. They separate from each other in the middle course phase at time k_0, where k_0 is unknown. After the separation, the genuine warhead moves with transition matrix $\mathbf{F}_0$, which is assumed known possibly from some data base or preprocessing, while the dummy warhead moves with transition matrix $\mathbf{F}_c$, where $\mathbf{F}_c\neq\mathbf{F}_0$ is usually unknown. Therefore, given the observation at time n, denoted by $\mathbf{y}_{1:n}=(\mathbf{y}_1,\cdots,\mathbf{y}_n)^\dagger$, the identification of the warhead can be formulated as

$$\begin{aligned}
&H_0:\text{observe }\mathbf{y}_{1:n}=(\mathbf{y}_1,\cdots,\mathbf{y}_n)^\dagger\text{with }\mathbf{y}_k\text{ defined in (20.6)}\\
&\mathbf{F}_k=\begin{cases}\mathbf{F}_0 & 1\le k\le k_0\\ \mathbf{F}_0 & k_0+1\le k\le n\end{cases},\\
&H_1:\text{observe }\mathbf{y}_{1:n}=(\mathbf{y}_1,\cdots,\mathbf{y}_n)^\dagger\text{with }\mathbf{y}_k\text{ defined in (20.6)}\\
&\mathbf{F}_k=\begin{cases}\mathbf{F}_0 & 1\le k\le k_0\\ \mathbf{F}_c\neq\mathbf{F}_0 & k_0+1\le k\le n\end{cases}.
\end{aligned} \tag{20.7}$$

Since $\mathbf{F}_c$ and k_0 in (20.7) are unknown, the sequential hypothesis testing problem is composite. Based on the SSM (20.5) and (20.6), the observation at $k+1$ $\mathbf{y}_k$ is independent of the observations prior to time k. Thus $\mathbf{y}_k$ is a Markov process. Then the conditional probability density function (pdf) of $\mathbf{y}_{k+1}$ given the previous observation $(\mathbf{y}_1, \ldots, \mathbf{y}_k)$ is

$$p_{\mathbf{y}_{k+1}|\mathbf{y}_1,\cdots,\mathbf{y}_k}(\mathbf{y}_{k+1}|\mathbf{y}_1, \cdots, \mathbf{y}_k; \mathbf{F}_k) = \frac{e^{-0.5(\mathbf{y}_{k+1}-\mu_{k+1})^\dagger \Sigma_{k+1}^{-1}(\mathbf{y}_{k+1}-\mu_{k+1})}}{(2\pi)^{N2}|\Sigma_{k+1}^{-1}|^{12}}. \tag{20.8}$$

Assuming the initial value of the observation is deterministic known or Gaussian distributed, $\mathbf{y}_{k+1}$ given $\mathbf{y}_k$ is a Gaussian sequence where the conditional mean of the observation at time $k+1$ given $\mathbf{y}_k$ as $\boldsymbol{\mu}_{k+1}$,

$$\boldsymbol{\mu}_{k+1} = \mathrm{E}\{\mathbf{y}_{k+1}|\mathbf{y}_k\} = \mathbf{H}\mathbf{F}_k\mathbf{H}^+\mathbf{y}_k + \mathbf{H}\mathbf{G}_k\mathrm{E}\{\mathbf{u}_k\}, \tag{20.9}$$

with E· denoting expectation, denotes $\mathbf{H}^+$ the pseudo-inverse of $\mathbf{H}$, the conditional covariance matrix is

$$\begin{aligned}\boldsymbol{\Sigma}_{k+1} &= \mathrm{E}\Big\{(\mathbf{y}_{k+1} - \mu_{k+1})^\dagger(\mathbf{y}_{k+1} - \mu_{k+1})|\mathbf{y}_k\Big\} \\ &= \mathbf{H}\mathbf{F}_k\mathbf{H}^+\Sigma_e(\mathbf{H}\mathbf{F}_k\mathbf{H}^+)^\dagger + \mathbf{H}\Sigma_w\mathbf{H}^\dagger + \Sigma_e^2,\end{aligned} \tag{20.10}$$

Suppose the warhead is deemed to be genuine by default and our goal is to identify the possible dummy warhead as soon as possible. Towards this goal, we employ sequential detection, which computes test statistic $T^n(\mathbf{y}_{1:n})$ at time n using all available observations $(\mathbf{y}_{1:n})$ and compares it with a predetermined threshold η. A dummy warhead is declared immediately, once

$$t_d = \inf\{n : T^n(\mathbf{y}_{1:n}) > \eta\}, \tag{20.11}$$

is satisfied, where inf· denotes the essential infimum. Define the conditional mean detection delay

$$\overline{\tau} = \mathrm{E}_{H_1}\{t_d - k_0 | t_d > k_0\}. \tag{20.12}$$

where the expectation is taken under H_1. Define the mean time between false alarms

$$\overline{t} = \mathrm{E}_{H_0}\{t_d\}, \tag{20.13}$$

where the expectation is taken under H_0. For a fixed t, smaller τ means better performance. For a fixed $\overline{\tau}$, smaller $\overline{t}$ is preferable [12]. The exact expression of $T^n(\mathbf{y}_{1:n})$ is dependent on specific sequential detection method, such as the sequential likelihood ratio (SILRT) and sequential general likelihood ratio test (SGLRT), as we present in the next section.

20.3.1 SILRT

Consider the hypothesis testing problem in (20.7), SILRT assumes $\mathbf{F}_c$ in (20.7) is perfectly known and compares the LR of the observation $\mathbf{y}_{1:n}$ to a threshold. The SILRT declares for H_1 at time n, if

$$T_{LR}^{n} = \frac{p_{\mathbf{y}_{1:n}}(\mathbf{y}_{1:n}; \mathbf{F}_k | H_1)}{p_{\mathbf{y}_{1:n}}(\mathbf{y}_{1:n}; \mathbf{F}_k | H_0)} = \frac{\prod_{k=k_0+1}^{n} p_{\mathbf{y}_k|\mathbf{y}_{k-1}}(\mathbf{y}_k|\mathbf{y}_{k-1}; \mathbf{F}_c)}{\prod_{k=k_0+1}^{n} p_{\mathbf{y}_k|\mathbf{y}_{k-1}}(\mathbf{y}_k|\mathbf{y}_{k-1}; \mathbf{F}_0)} > \eta_{LR}, \tag{20.14}$$

where η_{LR} is a constant. For SILRT, where $\mathbf{F}_c$ is perfectly known, the canonical cumulative sum (CUSUM) procedure performs well for its small mean detection delay and small calculation quantity. However, SILRT is an unachievable benchmark, because $\mathbf{F}_c$ are impossible to be obtained perfectly by the antimissile system.

20.3.2 SGLRT

SGLRT estimates the value of $\mathbf{F}_c$ using maximum likelihood estimation (MLE) and compares the LR of the observation using the estimated value of $\mathbf{F}_c$, the SGLRT declares for H_1 at time n, if

$$T_{SG}^{n} = \frac{p_{\mathbf{y}_{1:n}}(\mathbf{y}_{1:n}; \hat{\mathbf{F}}_k^n | H_1)}{p_{\mathbf{y}_{1:n}}(\mathbf{y}_{1:n}; \mathbf{F}_k | H_0)} = \frac{\prod_{k=k_0+1}^{n} p_{\mathbf{y}_k|\mathbf{y}_{k-1}}(\mathbf{y}_k|\mathbf{y}_{k-1}; \hat{\mathbf{F}}_c^n)}{\prod_{k=k_0+1}^{n} p_{\mathbf{y}_k|\mathbf{y}_{k-1}}(\mathbf{y}_k|\mathbf{y}_{k-1}; \mathbf{F}_0)} > \eta_{SG}, \tag{20.15}$$

where $\widehat{F}_c^n$ is the estimation of $\mathbf{F}_c$, and η_{SG} is a constant. Performance of SGLRT depends largely on the estimation accuracy which toboggans when the differences are small. SGLRT has large time delay due to estimation.

20.4 New Sequential Locally Optimal Unknown Direction Detector

Here we propose SLOUD test, based on LOUD test which can make quick decision and is proved to perform well in distinguishing small differences [13].

20.4.1 Locally Optimum Unknown Direction Test

Consider the case where the value of θ is from two disjoint sets Θ_0 and Θ_c, $p_{\mathbf{y}}(\mathbf{y};\theta)$, the pdf of the N-dimensional random observation vector $\mathbf{y}$ is dependent only on the value of θ, the hypothesis is

$$\begin{aligned} H_0 &: \mathbf{y} \text{ has pdf } p_{\mathbf{y}}(\mathbf{y};\boldsymbol{\theta}) \text{ with } \theta \in \Theta_0 \\ H_1 &: \mathbf{y} \text{ has pdf } p_{\mathbf{y}}(\mathbf{y};\theta) \textit{ with } \theta \in \Theta_c \end{aligned} \tag{20.16}$$

Assume $\Theta_0 = \theta_0$ and Θ_c includes all θ in a very small ball around θ_0. By employing N-dimensional spherical coordinate system, assume the false alarm probability $p_f(\delta, \theta_0) = \alpha$, the test function of LOUD test is [13]

$$\delta_{LOUD} = \sum_{i=1}^{N} \frac{\partial^2 p_{\mathbf{y}}(\mathbf{y};\mathbf{F}_0)}{\partial \mathbf{F}_{0i}} > \eta p_{\mathbf{y}}(\mathbf{y};\mathbf{F}_0), \tag{20.17}$$

where η is a constant and $0 \le \gamma(\mathbf{y}) \le 1$, $\delta = \delta_{LOUD}$ is optimal, $\delta \ne \delta_{LOUD}$ would not be optimal.

20.4.2 SLOUD Test

In binary hypothesis testing problem for LOUD test described in (20.16), the observation $\mathbf{y} = \mathbf{y}_{1:n}$, while Θ_0 is $\mathbf{F}_k$ under H_0, while Θ_c is $\mathbf{F}_k$ under H_1.

Assuming the pdf of the observation $p_{\mathbf{y}} 1 : n(\mathbf{y}_{1:n};\mathbf{F}_k)$ satisfies certain regularity conditions that allow interchanging the order of differentiation and integration operations. Based on LOUD test, the SLOUD test decares H_1 and stops detecting at time n if

$$T_{LS}^n = \frac{0 \le \overset{\max}{k_0} < n \left\{ \frac{\partial^2 p_{\mathbf{y}_{1:n}}(\mathbf{y}_{1:n};\mathbf{F}_k|H_1)}{\partial \mathbf{F}_k^2}|_{\mathbf{F}_k \in \Theta_c} \right\}}{p_{\mathbf{y}_{1:n}}(\mathbf{y}_{1:n};\mathbf{F}_k|H_0)|_{\mathbf{F}_k \in \Theta_0}} > \eta_{LS}, \tag{20.18}$$

where η_{LS} is a constant. To identify the genuine and dummy warhead as soon as possible is vital to the antimissile system, thus to reduce the calculation quantity is necessary. Analyzing (20.9) with (20.18), the stopping condition at time n that declares H_1 for SLOUD test can be further simplified as

$$T_{LS1}^n = c_n - e_n > \eta_{LS}, \tag{20.19}$$

where $c_n = \sum_{k=1}^{n}[b_k - a_k^2], e_n = 1 \leq \min k_0 \leq n \sum_{k=1}^{k_0}(a_k^2 - b_k) - (d_n - \sum_{k=1}^{k_0} a_k)^2, d_n = \sum_{k=1}^{n} a_k$, $a_k = \frac{1}{p_{y_k|\mathbf{y}_{k-1}}(\mathbf{y}_k|\mathbf{y}_{k-1};\mathbf{F}_k)} \frac{\partial p_{\mathbf{y}_k|\mathbf{y}_{k-1}}(\mathbf{y}_k|\mathbf{y}_{k-1};\mathbf{F}_k)}{\partial \mathbf{F}_k}$, $b_k = \frac{1}{p_{y_k|\mathbf{y}_{k-1}}(\mathbf{y}_k|\mathbf{y}_{k-1};F_k)} \frac{\partial^2 p_{\mathbf{y}_k|\mathbf{y}_{k-1}}(\mathbf{y}_k|\mathbf{y}_{k-1};\mathbf{F}_k)}{\partial \mathbf{F}_k}$, η_{LS} is a constant.

20.5 Numerical Results

In this section, performances of various sequential detectors for the identification of the warheads are measured in terms of the τ versus t curves. The performance of SLOUD test is compared with that of the SGLRT and SMLRT. The observations $\mathbf{y}_k$ about the warhead information are obtained using a MIMO radar with distributed antennas. Assuming the observation is the MMSE estimation of the warhead micro-motion parameters, the covariance matrix Σ_e of the observation noise $\mathbf{e}_k$ is approximated by the Cramer-Rao lower bound, such that the statistical behavior of $\mathbf{e}_k \sim \mathcal{N}(\mathbf{0}, \Sigma_e)$ is known.

Ignoring gravity and air resistance, the state transition matrix is assumed to be $\mathbf{F}_0 = \mathbf{I}$, where $\mathbf{I}$ is an identity matrix, $\mathbf{F_c} = \mathbf{F}_0 + \Delta\mathbf{F}$, where $\Delta\mathbf{F}$ indicates the difference between the genuine and the dummy warhead. Assume the covariance matrices of $\mathbf{e}_k$ and $\mathbf{w}_k$ are $\Sigma_e = 0.05\mathbf{I}$, and $\Sigma_w = 0.01\mathbf{I}$, $\mathbf{u}_k = \mathbf{0}$, $\mathbf{H} = \mathbf{I}$, and $k_0 = 20$. The results are obtained with 1000 Monte-Carlo runs.

In Fig. 20.2, we consider the scalar case where $\Delta\mathbf{F} = r$ with r uniformly distributed in $(-0.1, 0.1)$. The SILRT assumes perfectly known $\mathbf{F}_c$, while SMLRT assumes $\mathbf{F}_{mis} = 0.8$. The initial observation of the warhead is $\mathbf{y}_1 = 2$. It is observed that in all the curves that τ increases as t grows. The SILRT curve is below all curves which provides a benchmark for sequential detection problem. The SMLRTs performs the worst. The SLOUD test outperforms the SGLRT.

The example in Fig. 20.3. assumes that $\Delta\mathbf{F} = [0,\ r;\ 0,\ -r]$, $\mathbf{F}_{mis} = [1,\ 0.1;\ 1,\ -0.2]$ for SMLRT, and $\mathbf{y}_1 = [2,2]^{\dagger}$. It is observed that the SLOUD test still outperforms the SMLRT and SGLRT. We have tested many other examples and obtained similar findings.

It is worth noting that the computation time for SGLRT is much longer than that for the SLOUD test, which shows the effectiveness of SLOUD test.

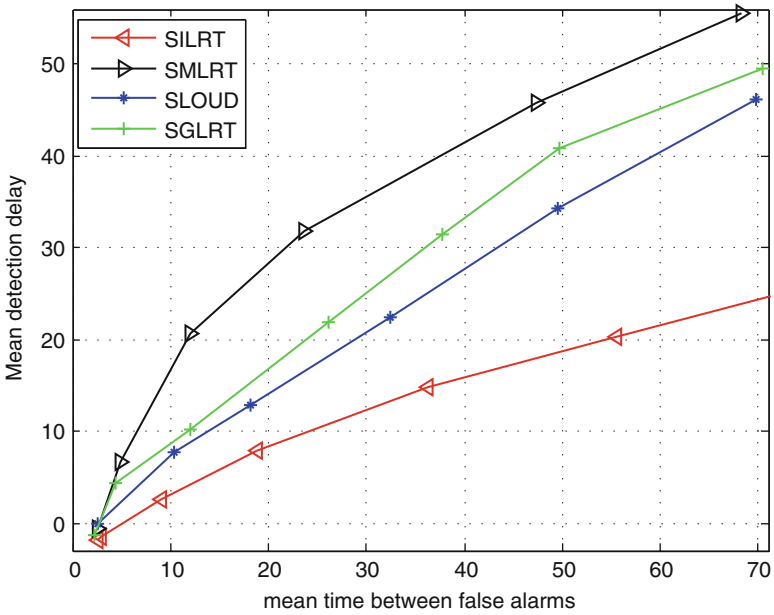

Fig. 20.2 Mean detection delay versus average time between false-alarms in one dimension

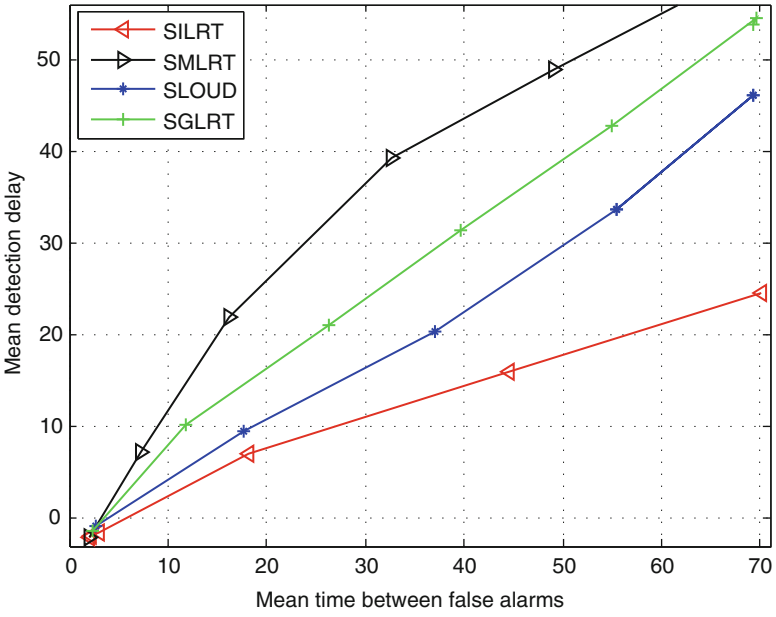

Fig. 20.3 Mean detection delay versus average time between false-alarms in two dimension

Conclusions
Based on observations coming from the estimation output of MIMO radar with distributed antennas, SSM is developed to describe the kinetic motion of the warhead. The differences between genuine and dummy warheads can be characterized by the differences of the SSM parameters. The problem of identifying the genuine and dummy warhead are translated into a binary hypothesis testing problem. To identify the genuine and dummy warheads as quickly as possible, sequential hypothesis test is employed. We consider the carefully made dummy warheads that look very similar to the genuine warheads. LOUD test is employed, which has the advantage in detecting small differences, to develop the SLOUD test. The performance of the SLOUD test is compared with conventional sequential methods (SILRT, SGLRT and SMLRT). The results show that the SLOUD test is superior than the SGLRTs in both detection performance and computational complexity in the studied examples.

Acknowledgements This work was supported by the National Nature Science Foundation of China under Grants 61102142, 61032010, and 61371184, the International Science and Technology Cooperation and Exchange Research Program of Sichuan Province under Grant 2013HH0006, and the Fundamental Research Funds for the Central Universities under Grant ZYGX2013J015.

References

1. Lemnios WZ, Grometstein AA (2002) Overview of the lincoln laboratory ballistic missile defense program. Lincoln Lab J 13(1):9–32
2. Li XR, Jilkov VP (2010) Survey of maneuvering target tracking. part ii: Motion models of ballistic and space targets. IEEE Trans Aerosp Electron Syst 46(1):96–119
3. Chen VC (2003) Micro-Doppler effect of micromotion dynamics: A review. In: AeroSense 2003. international society for optics and photonics, pp 240–249
4. Chen VC, et al. (2006) Micro-Doppler effect in radar: phenomenon, model, and simulation study. IEEE Trans Aerosp Electron Syst 42(1):2–21
5. Chen VC, Li F, Ho SS, et al. (2003) Analysis of micro-Doppler signatures. IEE Proc Radar Sonar Navig 150(4):271–276
6. Sun H, Liu Z (2008) Micro-Doppler feature extraction for ballistic missile warhead. In: IEEE international conference on information and automation ICIA, 2008
7. Steedly WM, Moses RL (1991) High resolution exponential modeling of fully polarized radar returns. IEEE Trans Aerosp Electron Syst 273:459–469
8. Haimovich AM, Blum RS, Cimini LJ (2008) MIMO radar with widely separated antennas. IEEE Signal Process Mag 251:116–129
9. Mehra RK (1971) A comparison of several nonlinear filters for reentry vehicle tracking. IEEE Trans Autom Control 16:307–319
10. Farina A, Ristic B, Benvenuti D (2002) Tracking a ballistic target: Comparison of several nonlinear filters. IEEE Trans Aerosp Electron Syst 38(3):854–867

11. Xue Wang, Dongyang Cai, Qian He. A new method of true-false warhead identification in MIMO radar using LOUD test. prepare to be published in Globalsip 2014
12. Basseville M, Nikiforov IV (1993) Detection of abrupt changes: Theory and application, vol 104. Englewood Cliffs, Prentice Hall
13. He Q, Blum RS (2011) Smart grid monitoring for intrusion and fault detection with new locally optimum testing procedures. In: IEEE international conference on acoustics, speech and signal processing (ICASSP), pp 3852–3855
14. Xu L, Li J, Stoica P (2008) Target detection and parameter estimation for MIMO radar systems. IEEE Trans Aerosp Electron Syst 443:927–939

Chapter 21
Improving Angular Resolution Algorithm Based on Landweber's Iteration for Scanning Radar Systems

Jinchen Guan, Jianyu Yang, Yulin Huang, Wenchao Li, and Junjie Wu

Abstract Scanning radar systems have extensive and significant applications, but theirs angular resolution usually is low because of many constraints. In this paper, a Landweber iteration algorithm of improving the angular resolution is proposed. Firstly, a signal model in the azimuth of the scanning radar system is illustrated. Then the Landweber algorithm is derived in theory. At last, Simulations and real radar data experiments show that the algorithm can effectively improve the angular resolution of the scanning radar system.

Keywords Angular resolution • Landweber iteration • Scanning radar system

21.1 Introduction

Scanning radar systems have extensive and significant applications, such as surveillance, navigation, autonomous landing of aircrafts, guidance. However, for a scanning radar system, the angular resolution (resolution in azimuth) is low, and is determined by the antenna beamwidth and the slant range [1, 2]. The angular resolution is approximately proportional to the slant range and the antenna beamwidth. The antenna beam B is limited by the ratio of signal wavelength to the antenna aperture size D

$$B \propto \lambda / D \tag{21.1}$$

where λ is the wavelength.

Although the antenna beamwidth of the scanning radar could be improved by increasing the physical radar antenna aperture, in most military and civil systems the size of the antenna aperture is limited by physical and/or cost constrains.

J. Guan • J. Yang (✉) • Y. Huang • W. Li • J. Wu
School of Electronic Engineering, University of Electronic Science and Technology of China, Chengdu, Sichuan 611731, PR China
e-mail: jchguan@163.com; jyyang@uestc.edu.cn

J. Mu et al. (eds.), *The Proceedings of the Third International Conference on Communications, Signal Processing, and Systems*, Lecture Notes in Electrical Engineering 322, DOI 10.1007/978-3-319-08991-1_21

Therefore, many signal processing methods have been proposed to obtain a finer angular resolution than the limit of the slant range and the antenna beamwidth.

In [3], digital inverse filtering is presented to improve signal resolution, but the method is difficult to achieve composite signal decomposition in the presence of noise. A fast constrained iterative deconvolution (CID) algorithm is provided avoiding division in frequency domain, but angular resolution improvement is approximately two times in [4]. An improved Wiener filter technique is presented to enhance the resolution in high signal noise ratio (SNR) in [5]. Attempts of improving the angular resolution were often unsuccessful because the deconvolution is an inherent ill-posed problem caused by noise and low-pass character of the antenna [6].

This research presents a statistical optimization method to enhance angular resolution. The algorithm uses the maximum likelihood criterion to regularize the inverse problem. The rest of the paper is organized as follows. In Sect. 21.2, signal model in azimuth of the scanning radar system is illustrated, and is rewritten with matrix–vector form for mathematical simplicity. In Sect. 21.3, principle of the improving angular resolution algorithm is proposed. In Sect. 21.4, simulation and experiments prove that the method can efficiently improve the angular resolution. Finally, the paper concludes in the last section.

21.2 Signal Model in Azimuth

The signal model of the scanning radar system in azimuth is shown simply in Fig. 21.1. The range is a fixed parameter, and only the angle value in azimuth is a variation. As the radar antenna scans the targets field including three ideal points in

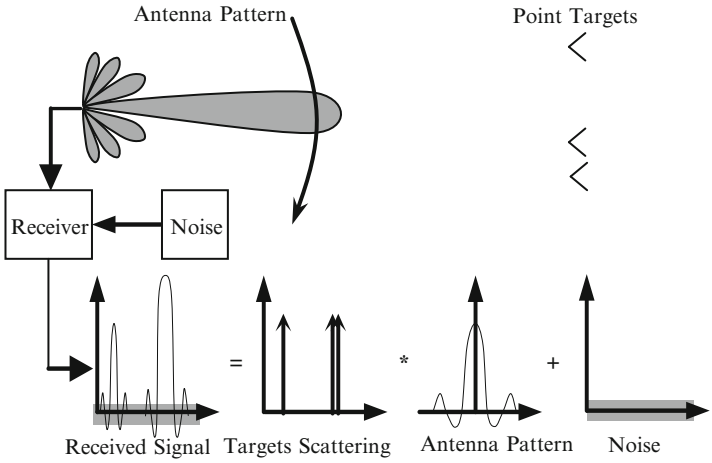

Fig. 21.1 Illustration of scanning radar system in azimuth

azimuth, for an isolated target scattering, the radar baseband signal received is proportional to the antenna pattern. So a graph of the radar signal received mimics the antenna pattern in azimuth. Assuming the scanning radar system as a linear receiver, then convolution superposition applies for the system [7]. In Fig. 21.1, radar signal received of two closely spaced point targets is proportionate to superposition of the two antenna pattern. While two targets are close enough, composite response signal will have a single peak as illustrated in Fig. 21.1, and each response signal is not resolved.

In the scanning radar system, the impulse response is the antenna pattern, and is of duration because the beam pattern is finite. Therefore, the radar signal is the convolution of many targets' angle information and the radar antenna beam pattern. At one range bin, the radar signal is

$$r(\theta) = h(\theta) * f(\theta) + n(\theta) \tag{21.2}$$

where $f(\theta)$ is the scattering coefficient of targets, $h(\theta)$ is the radar antenna pattern, $n(\theta)$ is the additive noise, $r(\theta)$ is the received signal, '*' is convolution operation.

Furthermore, the radar signal model in azimuth could be written clearly with matrix-vector form for mathematical description

$$R = HF + N \tag{21.3}$$

H is the convolution operation matrix which is circular matrix model. If size of H is $M \times M$, R, H, F are vectors of size $M \times 1$, and are the radar received signal, the targets' scattering, and noise respectively. In the angular spatial frequency domain, (21.2) is recast

$$R(\omega) = H(\omega)F(\omega) + N(\omega) \tag{21.4}$$

where $R(\omega)$, $F(\omega)$, $H(\omega)$ and $N(\omega)$ are the Fourier transforms of $r(\theta)$, $f(\theta)$, $h(\theta)$ and $n(\theta)$ respectively, and ω is the angular spatial frequency.

21.3 Improving Angular Resolution Landweber Algorithm

Based on the Bayes formula the maximum likelihood criterion finds the estimated value $\widetilde{F}$ which satisfies

$$P\left(R|\widetilde{F}\right) = \max_{F}\left(P(R|F)\right) \tag{21.5}$$

where $P(\bullet)$ represents the probability density function. The signal received R is the convolution of the antenna pattern and the targets' scattering. Then the original value at the ith element in the signal received is:

$$E(R_i) = \sum_j H_{ij} F_j \;\; \mathrm{j} = 1 \cdots M \tag{21.6}$$

where H_{ij} is the (i, j)th element of matrix H, F_j is the jth element of vector F.

Ignoring other noise, the actual ith pixel value R_i in R is the result of Gaussian distribution of the mean $\sum_j H_{ij} F_j$. Thus, the relation of R_i and F is written as follows

$$P\left(R_i \middle| F\right) = \frac{1}{\sqrt{2\pi}\sigma} \exp\left(- \frac{\left[R_i - (HF)_i\right]^2}{2\sigma^2} \right) \tag{21.7}$$

Each element in the received signal R is regarded as an independent Gaussian distribution and has the same variance σ, and

$$P\left(R \middle| F\right) = \prod_{i=1}^{M} \frac{1}{\sqrt{2\pi}\sigma} \exp\left(- \frac{\left[R_i - (HF)_i\right]^2}{2\sigma^2} \right) \tag{21.8}$$

Then the value estimated $\widetilde{F}$ which satisfies the maximum likelihood criterion is

$$\widetilde{F} = \arg \max_F \left[\prod_{i=1}^{M} \frac{1}{\sqrt{2\pi}\sigma} \exp\left(- \frac{\left[R_i - (HF)_i\right]^2}{2\sigma^2} \right) \right] \tag{21.9}$$

Function $ln(x)$ is a monotonic function in terms of x, and $\ln P(R|F)$ is much easier to deal with. The logarithm of $P(R|F)$ will be considered. Maximizing the logarithm of $P(R|F)$ is equal to minimizing the objective function

$$L(F) = \frac{\left(\left| \left| R - HF \right| \right|_2 \right)^2}{2} \tag{21.10}$$

where $\| \bullet \|_2$ is L_2 norm. To acquire the maximum value of $P(R|F)$, differentiating $L(F)$ with respect to F and the gradient vector is:

$$\frac{\partial L(F)}{\partial F} = HHF - HR = 0 \tag{21.11}$$

where H^{T} is transposition of H. The corresponding Euler equation is

$$HHF - HR = 0 \tag{21.12}$$

The Landweber algorithm is equal to the simplest iterative method for approximating the least-square solutions of Eq. (21.12). The iterative process is

$$F^{k+1} = F^k + \tau H^T \left(R - HF^k\right) \tag{21.13}$$

where k denotes the kth iteration, τ is a relaxation parameter controlling the convergence of the iterative process. In order to guarantee the convergence, the value of τ are given by

$$0 < \tau < \frac{2}{\sigma_1^2} \tag{21.14}$$

where σ_1 is the largest singular value of matrix H [8, 9]. The value of τ is usually set to 0.01.

Because the Landweber algorithm is a linear iteration method, it has limited capability of super-resolution from the frequency domain explanation. That is, the algorithm does not realize spectral extrapolation. Furthermore, for the received radar signal which contains intensities near zero, it is likely that negative intensities will be introduced the following iteration step, due to the lack of high spatial frequencies. Thus, the iteration process must guarantee the positivity of the estimated signal. Spectral extrapolation is reliable estimation of high frequencies. Utilization of a priori known information during the iteration processing is an effective method. Projection On Convex Sets (POCS) can modifies the Landweber algorithm to take into account priori information of the solution [10, 11]. Combing with the POCS method, the improved Landweber algorithm is

$${F_P}^{k+1} = P_C\left[F^{k+1}\right] \tag{21.15}$$

where P_C is the projection operator onto the constraint set C. It produces frequencies beyond the passband because P_C is non-linear operator. The improved Landweber algorithm can enhances the convergence rate and stabilize the solution.

The simple and natural convex set is nonnegative constraint of the solution. We can impose the constraint that the radar signal is nonnegative on the iteration.

$$P_C F = \begin{cases} F & if \ \ F > 0 \\ 0 & if \ \ F \le 0 \end{cases} \tag{21.16}$$

21.4 Simulations and Experiments

21.4.1 Simulations

Improving angular resolution Landweber algorithm for the scanning radar system is proved by the simulations. In Fig. 21.2, the top chart demonstrates the normalized radar antenna beam pattern, and the 3 dB antenna beam width of the radar real beam

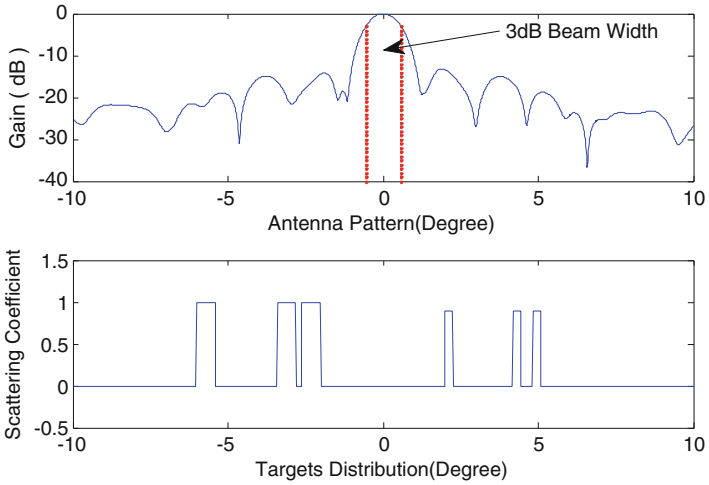

Fig. 21.2 Radar antenna beam pattern and targets' information

is about 3°. In Fig. 21.2, the bottom chart gives information about the targets' scattering. Two groups of extended targets have different amplitude (0.7 and 1) that denotes scattering coefficient of the targets. Each group includes an isolated target and a pairs of adjacent targets. Width of narrow targets is almost 1°, and its space between two adjacent targets is almost 1.5°. Width of wide targets is almost 3°, and its space between two adjacent targets is approximately 0.75°.

In Fig. 21.3, the top part illustrate the radar signal received that is generated by Fig. 21.2 (the radar antenna beam pattern and the targets' information), and SNR is 15 dB. Because the targets' distribution is smoothed by the radar antenna beam, isolated targets become bigger and obscure, furthermore adjacent targets cannot be distinguished and become one target. The middle part of Fig. 21.3 demonstrates the signal processed by Wiener filter. The group of the narrower targets is difficult to distinguish completely. The group of the wider targets is distinguished nearly. So performance of improving angular resolution of Wiener filter is affected seriously by SNR of the radar signal. The bottom part of Fig. 21.3 show the Landweber algorithm result of the signal and iteration is 50 times. Compared with the received signal, targets are distinguished completely and become clearer. However, the improving angular resolution result is distorted apparently because of the existence of noise.

Compared with the Wiener filter method, the Landweber algorithm is affected more trivially by SNR of the radar signal, and can keep performance at low SNR conditions. Furthermore, the algorithm is not related to the parameter of received signal processed, e.g. the value of SNR that is often difficult to obtain directly and precisely.

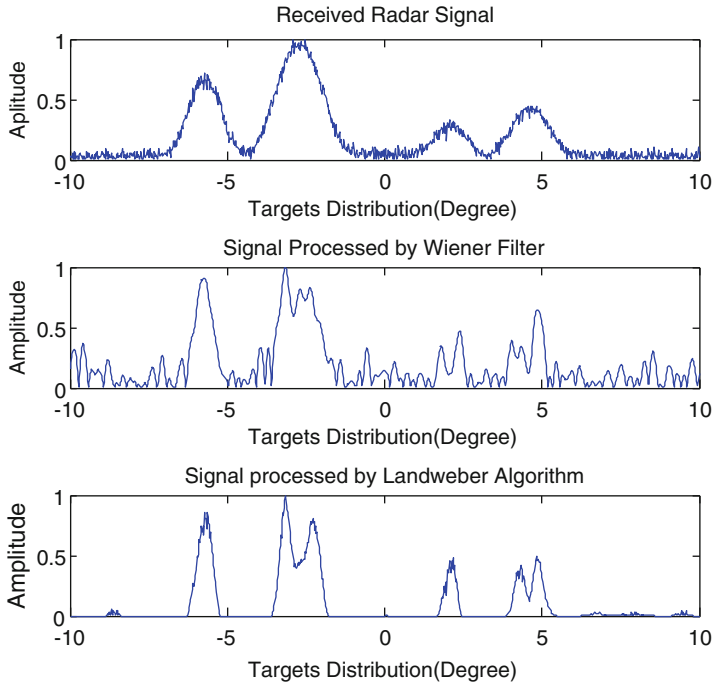

Fig. 21.3 Received signal and superresolution result with 15 dB Guassian white noise

21.4.2 Experiments

A real millimeter wave radar data is given in Fig. 21.4, mainly including two adjacent two metal targets and two isolated small metal targets. The original real beam radar imagery is shown in the top part of Fig. 21.4, and metal targets are difficult to be distinguished. The improving angular resolution result processed by the Wiener filter technique is illustrated in the middle part. Then main metal targets become clearer, and are separated approximately. The bottom part shows the result processed by the Landweber algorithm. It proves that the proposed method sharpens targets and clearly distinguishes the adjacent targets, especially the main targets.

A comparative result of the signal in a range bin in the scene is shown in Fig. 21.5. It demonstrates the proposed Landweber algorithm more clearly. The top part is the radar signal received, the middle part is the signal processed by the Wiener filter, and the bottom part is the signal processed by the Landweber algorithm.

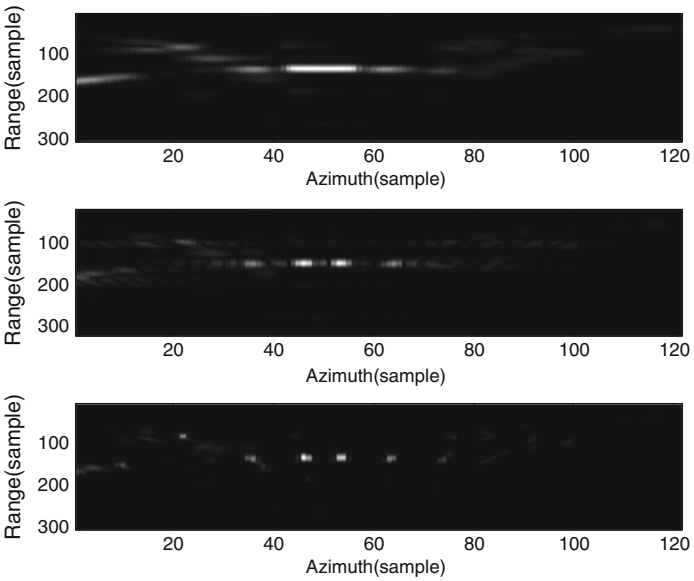

Fig. 21.4 A part of real radar imagery data

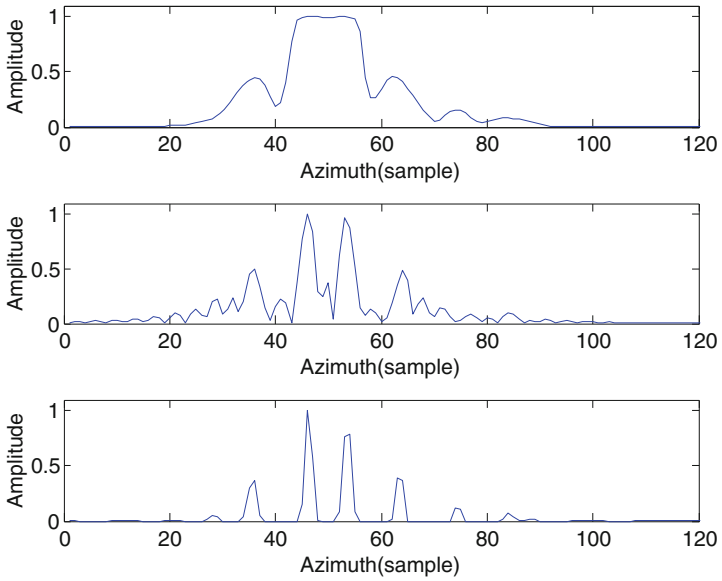

Fig. 21.5 Real radar signal in one range bin

Conclusion

This paper studies the improving angular resolution method based on maximum likelihood criterion. The optimal probability based on the statistical theory method can endure noise disturbance than conventional approaches. Maximum likelihood criterion is applied to regularize the deconvolution. Simulations and real radar data have proved effectiveness of the proposed method by comparing with the conventional technique–Wiener filter. The next step will consist in restraining the distortion of targets in our research work.

Acknowledgments This work is supported by the National Basic Research Program of China under Grant B1420110182 and National Natural Science Funds of China under Grant 61301273.

References

1. Skolnik MI (2008) Radar handbook, 3rd edn. McGraw-Hill, NewYork
2. Li W, Yang J, Huang Y (2012) Keystone transform-based space-variant range migration correction for airborne forward-looking scanning radar. Electron Lett 48(2):121–122
3. Senmoto S, Childers DG (1972) Signal resolution via digital inverse filter. IEEE Trans Aerosp Electron Syst AES-8(5):633–640
4. Richards MA (1988) Iterative noncoherent angular superresolution. In: IEEE National Radar conference, 3rd, Ann Arbor, 20–21 April 1988, pp 100–105
5. Suzuki T (1998) Radar beamwidth reduction techniques. IEEE Aerosp Electron Syst Mag 13 (5):43–48
6. Gambardella A, Migliaccio M (2008) On the superresolution of microwave scanning radiometer measurements. IEEE Geosci Remote Sens Lett 5(4):796–800
7. Richards MA (2008) Fundamentals of radar signal processing. McGraw-Hill, NewYork
8. Landweber L (1951) An iteration formula for Fredholm integral equations of the first kind. Am J Math 73:615–624
9. Wang L, Yuntao L, Xiaohui X, Xiaopeng W (2009) WSN multilateration algorithm based on Landweber iteration. In: Ninth international conference on electronic measurement & instruments, 2009 (ICEMI'09), pp 1250–1254
10. Piana M, Bertero M (1997) Projected Landweber method and preconditioning. Inverse Prob 13 (2):441–463
11. Li R, Gan Z, Cui Z, Wu M, Zhu X (2013) Distributed adaptive compressed video sensing using smoothed projected Landweber reconstruction. China Commun 10:58–69

Chapter 22
The Application of Digital Baseband Transmit in Hydrophone Linear Array

Jin Chen, Rong-rong Zhang, Ying Tong, Mao-lin Ji, Wen-shuo Zhang, Bao-ju Zhang, and Ying Liu

Abstract For the data transmission in hydrophone linear array, This paper focused on digital baseband transmission system and proposed the cascade channel transmission model, introduced the application of Turbo codes and Turbo channel coding and decoding system briefly, studied and verified the feasibility of improving the channel performance that add Turbo codes through computer-aided simulation.

Keywords Hydrophone linear array • Baseband transmission • Cascade channel • Turbo codes

22.1 Introduction

With the rapid development of science and technology, oil and gas exploration, power plant construction, as well as the construction of bridge and laying of submarine pipelines projects also will have a rapid development, especially marine engineering seismic exploration technology [1–4]. The increase of exploration requirements and difficulty is complementary to the development of exploration technologies. The artificial seismic waves are used in marine seismic exploration works, the hydrophone streamer receive seismic signals. By the processing and explaining of recording seismic data to invert seabed geological structures [5–7], study the development of faults situation, activity and regional seismic hazard [8, 9], we will determine the feasibility of ocean engineering.

The hydrophone which receives seismic has been made a big progress in marine seismic exploration and development, the more people attention, the more resources are afforded. With the line hydrophone array development, the amount of data transmitted cascade channel will increase. However, the actual marine seismic hydrophone streamer line array required to support a variety of real-time

J. Chen • R.-r. Zhang • Y. Tong (✉) • M.-l. Ji • W.-s. Zhang • B.-j. Zhang • Y. Liu
College of Electronics and Communications Engineering, Tianjin Normal University, Tianjin 300380, China
e-mail: tongying2334@163.com

J. Mu et al. (eds.), *The Proceedings of the Third International Conference on Communications, Signal Processing, and Systems*, Lecture Notes in Electrical Engineering 322, DOI 10.1007/978-3-319-08991-1_22

data collection under different hydrophone spacing, which requires to expand on the basis of the existing 100 m in the underwater distance between circuit nodes, up to 200 or 300 m long. In the actual transmission, more transmission error rate will increase as the transmission distance increase. The traditional design is unable to meet the rapid development of communication systems. This paper analysised and modeled the channel of hydrophone line array, proposed and applied Turbo channel coding technology, to improve the transmitter and receiver performance of digital baseband transmission system, which meets the need of future expansion in the physical distance of cascade channel on the basis of maintaining the digital baseband transmission the channel.

22.2 Digital Baseband Transmission System

In digital transmission system, although digital baseband transmission is not as widespread as digital frequency band transmission in the application, it still occupies an important position in industrial production. The baseband means the band which is occupied by transformed unmodulated signal, and the baseband transmission is a mode of transmission without spectrum move. Digital baseband transmission is the basis of transport technology, which has more simple equipments, line attenuation, and it is beneficial to increase the transmission distance, etc. The entire system consists of encoder, transmission filter, channel, receive filter, equalizer and decoder sampling decider, etc. Figure 22.1 shows the Baseband transmission system. As the hydrophone linear array cascade channel is limited by streamer physical size, power consumption and electromagnetic environment in vivo cable, it is not suitable for the mode of frequency band transmission, also the power shouldn't be a substantial increase, so we make use of the mode of baseband transmission.

In order to obtain excellent transmission characteristics in transmission channel, we use the encoder converts the signal into a transmission channel which is suitable for the pattern of the baseband signal at first. After the input stream encoding

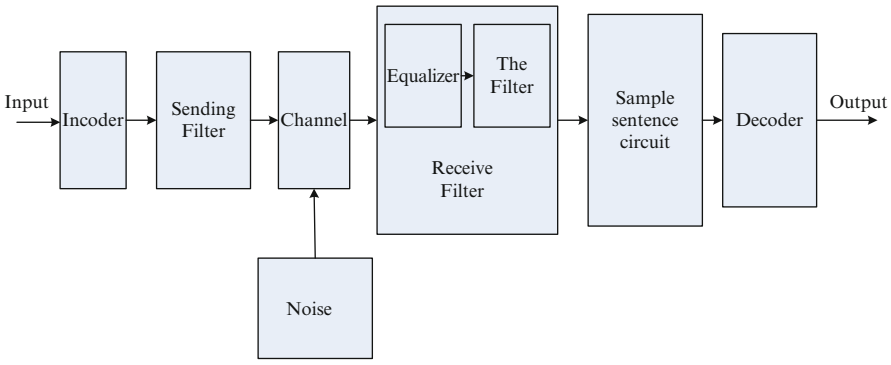

Fig. 22.1 Baseband transmission system

shaping filter [10], the stream is converted to a differential form of waveform unshielded twisted pair transmission channel cascade, then outputs to cascade channel. In the channel transmission, the limited bandwidth and superimposed channel noise will have an impact on waveforms and cause the judgment errors of receiving end. It can use the balance approach to correct the ISI and other multiplicative noise. This article discussed hydrophone line array in digital baseband channel receiver achieve a multiplicative noise filter equalizer through independent channels. For the additive channel noise, we use FEC (Former Error Correction) to filter it out [11], and reduce the error rate, improve the reliability of the transmission channel. Then we decode the signal to make output pattern meet the requirement of receiving terminal by the decoder, and sent it to the sink.

In Baseband transmission system, the channel is usually limited by DC blocking channel content and low-end of the transmission band, so that the transmission baseband signal and the DC component of the low frequency component hampered by them. Therefore, not all the original baseband digital signals can be transmitted in the channel. For the baseband signal forms, it is often represented by a rectangular square wave in the form of electrical pulses, because the expressions rectangular square wave spectrum is more simple, while the other wave spectrum is complex that is not conducive to transmit for signals. We must choose the appropriate pattern that can make rectangular square wave signal transmitted in baseband channel. Meanwhile, signal will be affected with various devices characteristics in baseband transmission system, as the result of interference and distortion, if it affects the judgment of received signals, it will generate errors. So the problem which we need to solve is to reduce the interference of signals from transmission characteristics in the baseband transmission system.

22.3 Hydrophone Linear Array Cascade Channel

Since the linear array is the main array of hydrophone array in this paper, the physical layer of linear array channel is wired, and the seawater has a constant temperature, and shield the electromagnetic [12], it can weaken the external or internal impulse noise, fluctuation noise and so on. Therefore, the various parameters of the channel in the frequency domain and time domain hardly change with time, so the hydrophone linear array channel can be regarded as a typical cascaded linear bandpass filter channel which mixed in BAWGN (Band-passed Additive White Gaussian Noise). That means the cascade channel in Hydrophone line array streamer can be modeled as a filter and BAWGN.

Every hydrophone converted sound waves in seawater to electrical signal and send it to each appropriate underwater circuit node. Apart from the farthest node, each node all complete the local data acquisition, collecting, framing and upload. They still need to complete the task of forwarding post-stage cascade channel data. The level of the input serial data stream synchronization code stream are extracted by the synchronous clock waveform analysis filter module receiving circuit and a

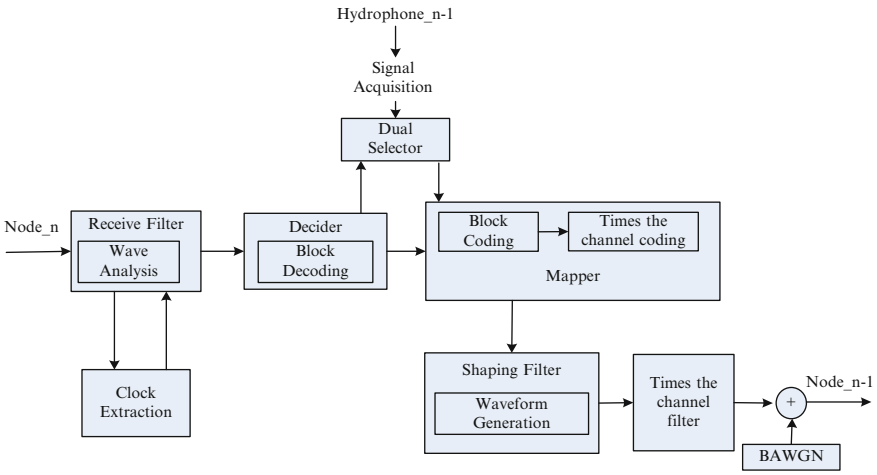

Fig. 22.2 Hydrophone linear array model

waveform equalizer receiving end. The digital baseband transmission is commonly used in the binary quantizer, inputting the code "0" or "1" to the block decoder module. We use 8–10 bit encoding in this article. The collected signal is converted into digital with AD converter. It will be signal combiner and selection with the frame-level data, and chose one way to access output channels. Output channel includes mapping and shaping filter. Bitstream mapper block coding and channel coding. In terms of stream channel transmission in later level, the decoding and re-coding operation can eliminate the accumulated error in channel to improve the reliability of transmission. The code after coding stream input shaping filter. The stream channel transform waveform into a non-shield twisted-pair transmission of differential forms, then it is outputted to cascade channel. Involving local-level data and the channel model shown in Fig. 22.2.

22.4 Digital Baseband Channel Design

22.4.1 Baseband Signal Transmission Channel Encoding

22.4.1.1 Transmission Channel Selection Pattern

According to the transmission characteristics of transmission channel, we first use the encoder converts the quantized signal into a digital code suitable for baseband signal transmission in the channel. The analog signal from the source changes into the pulse signal by digital processing, they are electrical pulse sequence binary. And the digital baseband signal which generally contains a DC component and low

frequency component. The transmission channel will be hindered for capacitance coupling circuit device or transmission band low-end constrained, there may be "0" or "1" data continuously. Because there is not internal association between level transitions or digital pulses at a long time. The receiver cannot obtain timing information from the received digital signal, and it cannot determine whether contains the error code [11].

In the baseband transmission, in order to fit the channel transmission, the baseband signal waveform is converted into a code which is suitable for transmission type. Transmission code design principles to be followed:

- For the low end of the band-limited transmission channel, the transmission pattern of the line spectrum shall not contain a DC component;
- Easy to extract the bit timing information from the symbol;
- There is a capability of certain error detection and correction;
- High transmission efficiency;
- Code should be independent of the statistical properties of information sources;
- Encoding and decoding devices should be simple and easy to implement.

22.4.1.2 Error Control Technology

Data communication request is transmitted with high reliability, which requires a sufficiently low error rate. Due to the presence of undesirable noise and channel characteristics in the channel, errors occur in the transmission channel inevitably, which causes noise and inter-symbol interference, resulting in error. In order to improve the reliability of the transmission channel, we use error control techniques to reduce the error rate [13]. Error control technique is sending termination add the number of check symbol in the digital information by the channel encoder, and we advance to establish the relationship between both sides, with these additional information to detect errors in transmission (Error detection coding), or correct errors (Error correction coding) [11]. Channel coding reduces the error by adding redundancy to reduce the transmission rate information and get the reliability of communication, which is specific and regular redundancy code. So it can be used to performs error detection and correction at the receiving end. There are basically four types of error control methods: forward error correction, retransmission error detection, error correction and feedback mixed parity. In digital communication systems, the receiver according to the received code words judged to detect and correct transmission errors in the channel, which is called as FEC mode. The transmission code which is sent can correct erroneous information in this way. The receiver corrects errors in the information stream independently without any information feedback to the sender. The main advantage of this approach is that one-way communication can be performed without increasing the separate feedback channel, the transmission channel and the receiver control logic is simple and good real-time decoding.

22.4.1.3 Turbo Code Encoder Design

In channel coding and decoding methods research has appeared in a variety of various types of coding systems and methods, such as block codes, cyclic codes, convolution codes, etc. However, because of the increased complexity of the coding of these with the block length or constraint of exponentially growing, and there is always a gap of more than 2 dB of gain between them with the theoretical Shannon limit. In order to improve the error correction capability, we use a special link code–Turbo Code [11]. Turbo is large codes in code length, approaching the theoretical limit can greatly achieve the best performance. The basic structure of Turbo Codes consists of a pair of recursive systematic convolutional codes RSCC (Recursive Systematic Convolution Code) encoder and an interleaver. Because the use of baseband transmission error control techniques, while improving the reliability of the transmission system, but the only drawback is that it increases redundancy and decreases coding efficiency with adding supervision Code. Therefore, the puncturing device is introduced before the final output stream in the actual Turbo Code encoder [14, 15]. And cut parts of the puncturing matrix of parity bits to reduce the redundancy (Fig. 22.3).

Hydrophone line array uses Turbo codes as component encoder channel coding to select recursive systematic convolutional code structure. Compared to the NSCC (Non-recursive Systematic Convolutional Codes), RSCC encoders can be used for components of the input data sequence to generate the minimum weight code word which is maximized for optimal performance [16]. By introducing parallel cascade component codes, in sequence so that the information generated to maximize the minimum weight codewords, but also to make the number of minimum distance codeword minimized [17]. Compared with the serial encoding, parallel coding can be more greatly reduce coding time, but we need more hardware resource consumption. In view of the line array herein have higher requirements for real-time data transmission channel, so the system uses the parallel encoding.

Another factor affecting the performance of Turbo codes is whether they can be able simultaneously to zero after the end of the encoding component encoder.

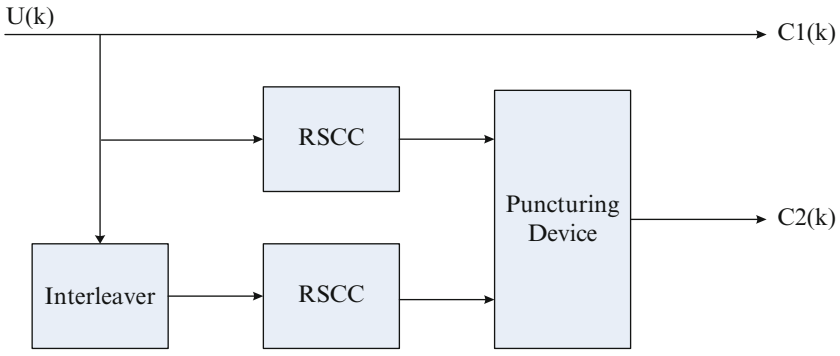

Fig. 22.3 The typical structure of turbo code encoder

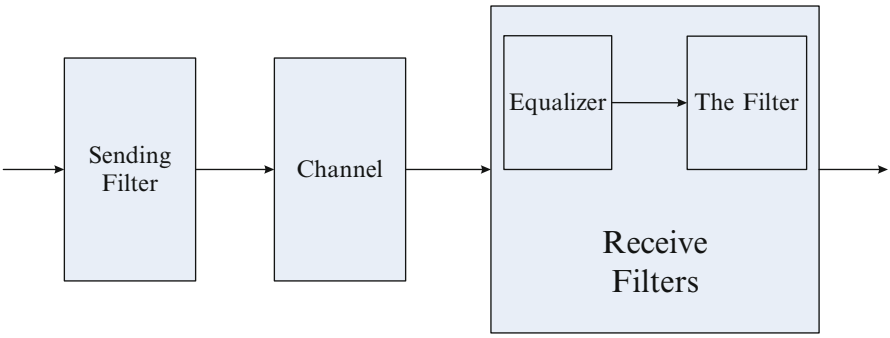

Fig. 22.4 The structure of shaping filter

This is one of the important measures to ensure the performance of Turbo codes to achieve tail-biting encoding function that is the end of each component encoder zero simultaneously in the encoding process. We adopt a kind of tail biting packet interleaver in this article [18]. Introducing interleaver can increase the distance of each component coding encoder to improve the output random data sequence and reduce the correlation between the data sequence at the receiving end of Turbo decoding. The interleaver uses a ROM for storing a mapping table to be stored with multi-port RAM interleaved sequence. Compared with the other way, ROM storage interleaving uses a mapping table to achieve intertwined mapping more flexible and targeted. The Multi-port RAM stores data which will be encoded in order to improve the encoding speed and complete interleaving the plurality of bits in each clock cycle based on the method of area exchange rate.

22.4.2 Shaping Filter Network

In modern communication, we need to compress the signal spectrum for effective utilization of the channel before the signal is transmitted out. Which greatly improve the spectrum efficiency in the premise to eliminate interference between the detector and the optimum code. In the digital baseband transmission system, the main method of compressing the baseband signal spectrum is to use the shaping filter. Shaping filter usually consists of transmit filter, channel, receive filter. The structure shown in Fig. 22.4.

The code after being encoded is inputted in transmitting filter for waveform transformation to convert into the differential form in the cascade of unshielded twisted pair transmission channel, making the channel signal waveform match channel to reduce inter-code interference, which has advantages with sync extraction and sampling judgment at the same time. Data transmission link can be equivalent to a more stable additive Gaussian noise channel model with parameters constant, and the twisted pair is a typical uniform transmission line. So the unshielded twisted pair

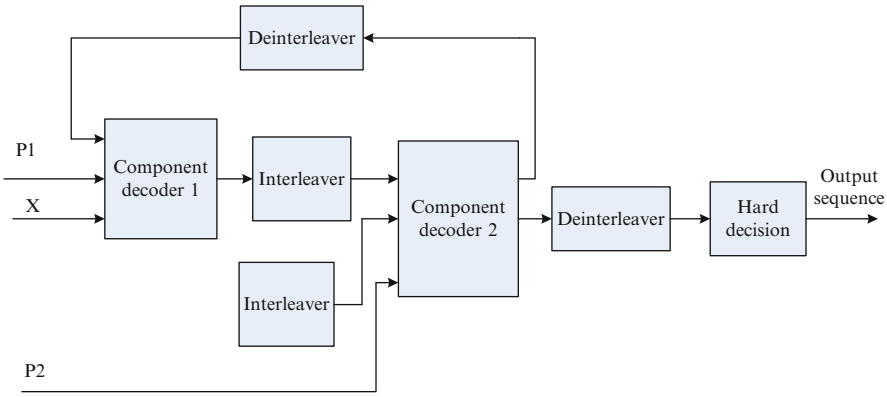

Fig. 22.5 The structure of turbo code decoder

CAT-6 type is used in the transmission medium of hydrophone array line transmission channel when a cable is immersed in the sea close to the speed of sound with special oil or gel inside. Limited bandwidth and channel noise superimposed will have an impact on waveform in channel transmission, resulting in error due to the receiving end of judgment errors. We can use the balanced approach to correct the ISI and other multiplicative noise. This article discussed that hydrophone line array achieved multiplicative noise which is filtered in the receiving end of the digital baseband channel by receiving filter equalizer channel. But we use the filter in the reception filter to filter out for the purposes of additive noise channel. That is mentioned earlier in the error control coding.

22.4.3 Baseband Transmission Channel Decoding of the Signal

Turbo decoder consists of the decoder, interleaver and deinterleaver. Decoder structure shown in Fig. 22.5. P1 is a non-interleaved parity sequence, P2 is interleaved parity sequence, X is an information sequence.

The probability P1 and X are multiplied by the confidence level Lc information symbols and coded symbols obtained logarithmic likelihood ratio, which is inputted into a component decoder for a complete decoding of the data frame. After interleaving, the Lc and P2 obtained by multiplying the confidence of the probability of the number of coded symbols likelihood ratio Λ_k, then they are inputted into the component decoder 2 together and decoded by the decoder 2. After deinterleaving, and then complete decoded again by the component decoder 1, which decode iteratively like this over and over again until the correct decoding or it can no longer correct mistakes so far. Component 1 and the decoder 2 decodes

the interactive component data characterizing the probability of passing the external information Λa. The information sequence is calculated iteration, while the information is passed to the other external decoder by decoder with each information symbol, the code symbol probability log-likelihood ratio and external information as input. We will make decoding converge to the correct decoding results after a finite number of iterations. First, we should make the processing of decoding the received information, the decoder is passed between two components of external information to form a loop iteration structure. As the role of external information, the bit error rate will reduce as the number of cycles increase under certain SNR. But the correlation between external information and receiving sequence number also increases gradually with increase the number of decoding. Error correction capability provided by external information also weakens. It will not improve decoding performance after a certain number of cycles.

Channel receiving access the source of the original sequence data by the inverse operation of Turbo stream sequence. Since the Turbo encoding side use two or more component encoder and interleaver. The receiving end need to adopt an iterative method to achieve MLD decoding [13]. Shannon information theory tells us that the optimal decoding algorithm is the probability decoding algorithm. That is the maximum a posteriori probability algorithm (MAP) [19–21]. Including classical MAP algorithm, the number of Log-MAP algorithm, the maximum number of Max-Log-MAP algorithm, the modified M-MAP, a sliding window MAP (SW-MAP) algorithm and etc. Before Turbo code appears, the channel coding using probability decoding algorithm is the Maximum Likelihood (ML). ML algorithm is a simplified MAP algorithm. On the assumption that the source symbols such as the probability of appearance, it is sub optimal decoding algorithm. Using the MAP algorithm decoding algorithm of Turbo codes improve in decoding structure and introduce the concept of feedback again, and achieved the tradeoff between performance and complexity. At the same time, the decoding using the iterative decoding of Turbo code that is completely different with the classical algebraic decoding. The System is used more commonly in this paper is the Log-MAP algorithm, namely the logarithmic form of the MAP. The main difference between logarithmic domain of multiplication with classic MAX algorithm is that can be converted to add operation in order to convenient the FPGA implementation and execution.

The calculation process of decoding is as follows:

$$M_k(e) = \begin{cases} \Lambda_a(u_k) - \ln\left(1 + e^{\Lambda_a(u_k)}\right) + \frac{1}{2}L_c y_k^s + \frac{1}{2}L_c y_k^p x_k^p & \mathrm{u_k} = 1 \quad \text{(a)} \\ -\ln\left(1 + e^{\Lambda_a(u_k)}\right) + \frac{1}{2}L_c y_k^s + \frac{1}{2}L_c y_k^p x_k^p & \mathrm{u_k} = 0 \quad \text{(b)} \end{cases} \tag{22.1}$$

x_k^p is receives the element of standard values, this value is ± 1 for the positive and negative level signal. y_k^p is receives the element of standard values, is receiving coding sequence, Lc is channel confidence level. And $\Lambda_a(u_k)$ is the a priori information of information sequence.

22.5 Results and Analysis

22.5.1 The Performance Comparison of Whether There Are Turbo Channel Coding or Not

Signal transmission via a transmission channel directly, the signal will be affected by the additive noise. As the transmission distance increases, the noise power spectral density will be increased, it will lead to increased bit error rate. In order to test the performance of Turbo code, the accuracy of the simulation under different SNR conditions in its data transmission in this paper. We use the BER (Bit Error Rate) as the reference index. In each SNR (Signal-to-noise Ratio) conditions, we reduce the influence of random factors by tests averaged 1,000 times. The results shown in Fig. 22.6.

From Fig. 22.6, the data transmission channel coding which has not been through channel coding, it's error rate is approximate linearly with the SNR, which is caused by additive noise. When the SNR over 10 dB level, direct transmission has a lower error rate. So in short distance transmission, channel coding system is not required, you can use the base-band direct transmission to reduce system complexity and overhead. When the SNR is reduced to about 6 dB, BER direct transmission will rise faster with the decline in SNR. This is due to the excessive noise in the received signal power will increasingly high noise component, which affect the result of the hard decision directly. With respect to the direct transmission, Turbo coding can be maintained over time 4 dB SNR low error rate,

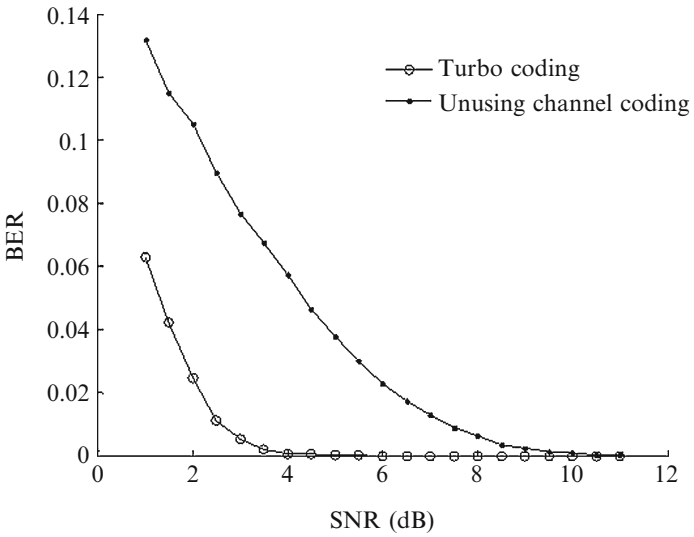

Fig. 22.6 Turbo coding performance under different SNR conditions

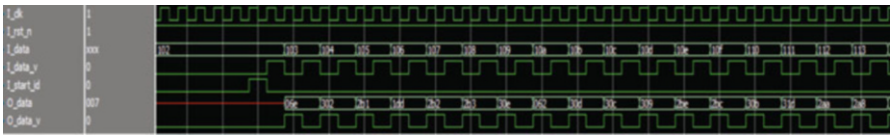

Fig. 22.7 Turbo coding module simulation map

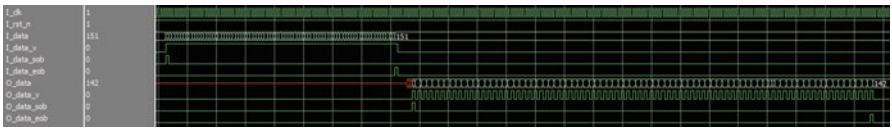

Fig. 22.8 Interleaving block diagram simulation

the soft-decision coding and randomization make the system significantly improved noise immunity. When the signal to noise ratio is reduced to 1 dB, that is equal to the average noise power signal power, Turbo coded BER is still only about 6.2 %.

22.5.2 Turbo Code Simulation Program Functions

22.5.2.1 Turbo Coding Simulation

Turbo encoded uses a convolutional code in parallel, encoding each clock cycle 10 bit to improve efficiency. The results shown in Fig. 22.7. I_data is Data to be encoded and O_data is the encoded data.

We uses the parallel weaves at the input of the second convolutional code encoder, each data using two clock cycles to complete the parallel weaves and weigh the resources and efficiency. I_data is Data to be encoded in Fig. 22.8. I_data_v is valid indication signal which is entered, O_data is the interleaved data and valid indication signal which is outputted.

22.5.2.2 Turbo Decoding Simulation

I_data is a data sequence which is input into Turbo decoding system in Fig. 22.9. Data width is 10 bit. The analog signal is got by the ADC converted from the data line. One bit signal that is generated to correspond to the Turbo coded signal 10 bit. 10 bit quantization purpose is to provide a soft decision information required for Turbo decoding, I_data_v is an effective indicator of data. Calculation requires sequential execution, so the single iterative operation time is long, which requires

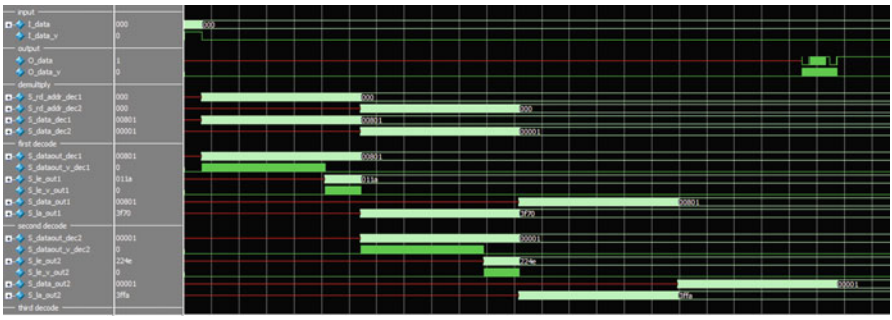

Fig. 22.9 Turbo decoding the top simulation diagram (using 2 iterations)

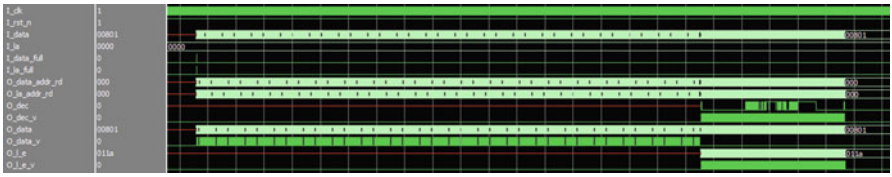

Fig. 22.10 Log-MAP decoding simulation figure

eight times the frame length of time. When the plurality of decoders in parallel, pipelined execution can be used for high-bandwidth applications between the decoders. Demultiplexing module separating two Turbo coded data, and the corresponding data sequence S_data_dec1 S_data_dec2. In order to improve data bandwidth, we use multiple decoding module performs pipelined manner Turbo decoding. The first decoding module reads the first set of coding sequences S_data_dec1, and produce a priori S_le_out1 signal, then becomes into S_la_out1 signal by interleaver. And it is inputted into the second decoding module with the second group of coding sequence S_data_dec2 together. The decoding produce a priori S_le_out2 signal, the signal is fed into the deinterleaver to become S_la_out2, then put into the next group to completing the first iteration. It output decoding sequence O_data after two times of iterative decoding. The width is 1 bit, consistent with Turbo coding sequence before.

From Fig. 22.10, I_data is coding sequence inputted, width is 10 bit. I_la is a priori information obtained by decoding the last bit and width is 14 bit. O_dec is decoding result, width is 1 bit. O_data is coding sequence for the cache to the next level decoding, width is 10 bit. O_l_e is a priori information which outputs to the next level. Log-MAP decoding execution index calculation involved, the number of operations using a lookup table to achieve, look-up data and the calculation is the value of the process variable 14 by tests.

Conclusion

This paper mainly for ocean exploration project to extend the line hydrophone arrays each circuit node spacing facing underwater noise ratio decreased transmission error rate increases and other practical issues. We Research digital baseband transmission type cascade channel design and application of Turbo codes. This article Introduces the cascade channel transmission model in detail and the related design of Turbo codes, briefly describes the coding and decoding process of Turbo codes with computer simulation method of adding the Turbo code on the channel performance. The content of this paper has an important basic role to further enhance the future hydrophone line array transmission performance.

Acknowledgments Thanks for the supporting by the National Natural Science Foundation of China (61271411), Tianjin Research Program of Application Foundation and Advanced Technology (14JCYBJC15800), Development Foundation of Tianjin Normal University (52XK1206), Tianjin Outstanding Young Teacher Support Program.

References

1. Wang ZQ, Tan J (2012) Solid streamer technology research and application in offshore exploration. Equipment Geophys Prospect 22(1):1–5. doi:10.3969/j.issn.1671-0657.2012.01.001
2. Song HB, Dong CZ, Chen L, Song Y (2008) Reflection seismic methods for studying physical oceanography: introduction of seismic oceanography. Progr Geophys 23(4):1156–1164
3. Lu JA, Wu ZL, Zeng XJ (2006) The synthesized effect of seismic wave and ghost reflection and its application in marine seismic survey. Ocean Technol 25(4):76–78. doi:10.3969/j.issn.1003-2029.2006.04.020
4. Jiang HY, Zhao WZ, Yan CZ, Qi RL, Ju BS, Wang Y (2008) Review on marine petroleum resources and exploration models in the Globe. Mar Orig Pet Geol 13(3):5–10. doi:10.3969/j.issn.1672-9854.2008.03.002
5. Luo SR (2003) Comprehensive utilization of side scan sonar and multibeam sounding system in oceanographic research. Hydrographic Surv Charting 23(1):22–24. doi:10.3969/j.issn.1671-3044.2003.01.006
6. Liu JN, Zhao JH (2002) The present status and developing trend of the multibeam system. Hydrographic Surv Charting 22(5):3–6. doi:10.3969/j.issn.1671-3044.2002.05.001
7. Zhang YL (2010) the research and DSP algorithms achievement of multibeam interferometric sounding technology. Ms. Thesis, Harbin Engineering University. doi:10.7666/d. y1808176
8. Ruan FM, Song KZ, Cao P (2006) Research and design of marine time-lapse seismic survey's research system. J Electron Meas Instrum 20(4):37–41
9. Cheng JY, Song KZ, Wang YF, Yang JF, Lu ZY (2006) Data gathering and transferring sub-system designing of time-lapse marine seismic data acquisition and recording system. J Basic Sci Eng 14(2):181–193
10. Ling YZ, Chen XM (2008) Research and design on digital baseband transfer systems. Foreign Electron Meas Technol 27(9):21–24. doi:10.3969/j.issn.1002-8978.2008.09.007
11. Fan CX, Cao LN (2006) Communication theory. Defense Industry Press, Beijing
12. Lv QH (2012) Physical oceanography foundation. Ocean Press, Beijing, pp 27–46

13. Liu DH (2003) The key technology and application research of turbo codes. PhD Thesis, University of Defense Technology
14. Benedetto S, Garello R, Montorsi G (1998) A search for good convolutional codes to be used in the construction of turbo codes. IEEE Trans Commun 46(9):1101–1105
15. Divsalar D, Pollara E (1995) Low-rate turbo codes for deep-space communications. In: Proceedings of 1995 I.E. international symposium on information theory, Pasadena, p 35
16. Benedetto S, Montorsi G (1996) Design of parallel concatenated convolutional codes. IEEE Trans Commun 44(5):591–600
17. Ho MSC (2000) Serial and parallel concatenated turbo codes. PhD Thesis, School of Physics and Electronic Systems Engineering, The University of South Australia
18. Breiling M, Peeters S, Huber J (1999) Class of double terminating turbo code interleavers. Electron Lett 35(5):389–391
19. Pietrobon SS, Barbulescu AS (1994) A simplification of the modifed bahl decoding algorithm for systematic convolutional codes. In: National conference publication–institution of engineers Australia NCP, pp 1073–1077
20. Robertson P, Villebrum E, Huber P (1995) A comparison of optimal and suboptimal MAP decoding algorithms operating in the log domain. In: Proceedings of 1995 I.E. international conference on communications, Seattle, pp 1009–1013
21. Franz V, Anderson JB (1998) Concatenated decoding with a reduced-search BCJR algorithm. IEEE J Sel Areas Commun 16(2):186–195

Chapter 23
A New Approach for Terrain Following Radar Based on Radar Angular Superresolution

Wen Jiang, Yulin Huang, Junjie Wu, Wenchao Li, and Jianyu Yang

Abstract Terrain following radar (TFR) is a particular airborne equipment that can assist the pilot in his task of staying close to the ground and yet avoiding obstacles. Angular resolution is crucial for TFR, but it is limited by the beam width of antenna. To overcome this problem, angular superresolution technique is adopted in TFR. First, received signal in vertical plane is modeled as a mathematical convolution of the antenna pattern and the targets' scattering. Then principles of the angular superresolution algorithm and range migration correction method are presented. Simulation result validates that the method can effectively improve the angular accuracy of TFR in vertical plane.

Keywords Terrain following radar • Radar angular superresolution • Deconvolution • Bayesian approach

23.1 Introduction

In the modern battlefield environment, helicopters and cruise missiles have to fly at low altitude to avoid easy detection by ground radars. In many civilian applications, such as agricultural insecticide spaying operations or aerial photography, the vehicle has to fly at low altitudes close to the ground. For both commercial and military aircraft flying at low altitude, the vehicle is likely to encounter both natural and man-made obstacles. These obstructions give rise to challenging problems to low-altitude flight missions [1].

Terrain following (TF) guidance system is a very important flight control technology for low altitude flight. The main objective of terrain following flight for an aircraft is to maintain a minimum preselected clearance above a give terrain and to fly fast enough so as to minimize the perils of being detected of or tacked.

W. Jiang (✉) • Y. Huang • J. Wu • W. Li • J. Yang
School of Electronic Engineering, University of Electronic Science and Technology of China, Chengdu, Sichuan 611731, PR, China
e-mail: wjianguestc@163.com

J. Mu et al. (eds.), *The Proceedings of the Third International Conference on Communications, Signal Processing, and Systems*, Lecture Notes in Electrical Engineering 322, DOI 10.1007/978-3-319-08991-1_23

Therefore, maintaining low altitude and high speed at the same time are the typical tactics in terrain following flights [2].

In fact, development of a complete TF guidance system consists of four steps [2, 3]:

1. Trajectory generation of the target terrain with survivability and mission effectiveness.
2. Control law development to follow the modeled or actual trajectory within the aircraft maneuvering capabilities.
3. Sensor blending for terrain data update.
4. Evaluation of the integrated system for different scenarios as well as emergencies.

This paper mainly studies the sensor technology in TF flight, with the focus on terrain following radar (TFR). TFR is a particular airborne equipment that can assist the pilot in his task of staying close to the ground and yet avoiding obstacles.

TFR have been operational for several decades. Signal processing has always been a significant part of TFR system [4]. Bert Bechtel at Texas Instruments invented the terrain-following radar system. The technology was patented in 1971 [5]. To obtain angular accuracy, a monopulse radar system is usually used [6], but monopulse radar is very sensitive to angular glint and system noise.

In this paper, we introduce a new signal processing method for TFR, which is based on scanning antenna and radar angular superresolution. The method can dramatically improved the angular accuracy of TFR. Simulation result also validates that the method can effectively improve the altitude measurement precision of TFR in the vertical plane.

23.2 Terrain Following Radar

In the modern battle environment and many civilian applications, aircrafts has to fly at low altitudes close to the ground. For both commercial and military aircraft flying at low altitude, the vehicle is likely to encounter both natural and man-made obstacles. So to assist the pilot in his task of staying close to the ground and yet avoiding obstacles, a particular type of airborne equipment has been developed called, generally, terrain following radar [6, 7].

23.2.1 Scan Pattern

In order to obtain height information of obstacle in flight path, TFR scans the terrain ahead by sweeping a pencil beam vertically, as shown in Fig. 23.1a.

A TFR system also forms a wedge of data in both the altitude and azimuth direction. An antenna scan pattern to produce this wedge is shown in Fig. 23.1b. In

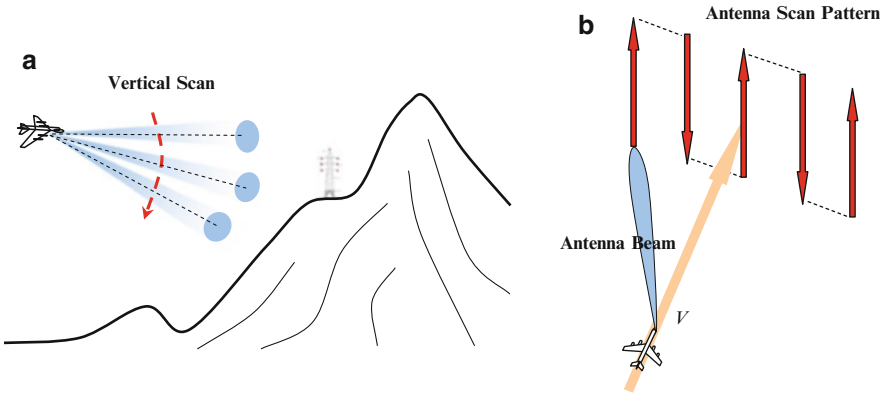

Fig. 23.1 Terrain following scan (**a**) side view (**b**) overhead view

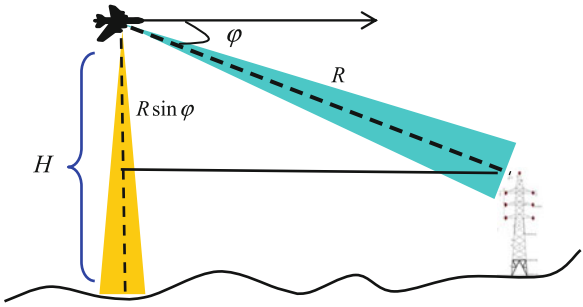

Fig. 23.2 Altitude measurement method

this type of scan, the horizon will be near the middle of the vertical scans, which will produce the wedge to the left, right, above and below the aircraft. All ground return gathered by this scan are collected and measured.

23.2.2 Altitude Measurement

The method of altitude measurement is shown in Fig. 23.2. As the aerial scans, the radar sends out a stream of pulses, and for each pulse the range R from radar to the obstacle along the aerial boresight and pitch angle φ of TFR is measured. Meanwhile, as the terrain-following radar scans the ground ahead of the aircraft, the actual clearance height H is measured by the radio altimeter.

After put all these information together, can obtain the height information of obstacle:

$$h = H - R\sin\varphi \tag{23.1}$$

A terrain following radar forms a closed loop control system between the radar, the aircraft, and in most cases the pilot. For this purpose, a TFR computer is usually used. The TFR computer uses radar return from the terrain and inputs from other sensor to generate these commands. Then the TFR algorithm compares the current aircraft condition to the desire aircraft condition required to safely maintain a set clearance above the terrain, and generates the appropriate pull-up or push-over command.

23.3 Radar Angular Superresolution

From Fig. 23.2 and expression (23.1), we can see that the computation of altitude relies on the range and angle to the ground with the required accuracy. In traditional TFR system, the aerial produces a single beam whose width is a function of the size of the aerial size and the frequency used. The beam width is big, which is quite inadequate for terrain following. In order to obtain better angular accuracy of TFR, we proposed a novel method based on scanning aerial and radar angular superresolution.

This section first research the range history of point target, then introduces range migration correction method, and ends with derivation of radar angular superresolution algorithm.

23.3.1 Range History of Point Target

Geometry model of TFR is illustrated in Fig. 23.1, and the range history between the radar and a point target in the flight path is

$$R(t) = \sqrt{V^2t^2 + r_0^2 \sec^2 \varphi - 2r_0Vt\cos\theta} \tag{23.2}$$

where r_0 is the range between radar and target when azimuth time is zero, θ is the angle between the direction of the antenna to the target and the flight direction when azimuth time is zero, we call it azimuth angular, φ is pitch angle of scanning aerial, t is slow time, and V is platform velocity.

Formula (23.2) can be expanded into a Taylor series. Due to the range migration is dominated by the range walk for TFR, the range history of scatterer can be expressed as:

$$R(t) \approx r_0 \sec\varphi - Vt \sec^{-1} \varphi \cos\theta \tag{23.3}$$

Based on range history of point target (23.3), let the TFR transmits chirp signal, the echo of point target after range compression can be expressed as

$$s(t,\tau) = \sigma(x_0, y_0)w(t)sinc(B(\tau - \frac{2R(t)}{c}))\exp(-j\frac{4\pi}{\lambda}R(t)) \tag{23.4}$$

where $\sigma(x_0, y_0)$ is backscattering coefficients of point target, $w(t)$ is the antenna pattern in vertical plane, which is a Gaussian envelope in generally, $sinc(\cdot)$ is response function in range direction, B is bandwidth of signal, τ is fast time, and λ is wavelength.

23.3.2 Range Migration Correction

It can be seen from (23.3) that the slope of range migration trajectory varies with θ and φ, which means that the range migration is variant with different azimuth and pitch angle. One might call it apace variant range migration.

Migration through resolution cell will arises if the system parameters meet the condition of

$$VT_a \overset{-1}{\sec}\ \varphi\cos\theta > \frac{c}{2F_s} \tag{23.5}$$

where T_a is time vector when the antenna beam is across the target, c is speed of light, F_s is sampling rate of rang direction. The space variant range migration makes the correction is difficult, and an apace variant range migration correction algorithm based on Keystone transform is proposed in [8]. Discussions in this paper are based on the case that migration is not through resolution cell or range walk is corrected.

After range migration correction, the signal model of point target a can be expressed as:

$$s(t,\tau) = \sigma(x_0, y_0)w(t)sinc(B(\tau - r_0))\exp(-j\frac{4\pi}{\lambda}R(t)) \tag{23.6}$$

After performs a modulus on (23.6), we get the following expression:

$$|s(t,\tau)| = \sigma(x_0, y_0)w(t)sinc(B(\tau - r_0)) \tag{23.7}$$

It can be seen from (23.7) that amplitude of point target echo in vertical plane is modulated by antenna pattern, which means we can restore the target by angular super-resolution.

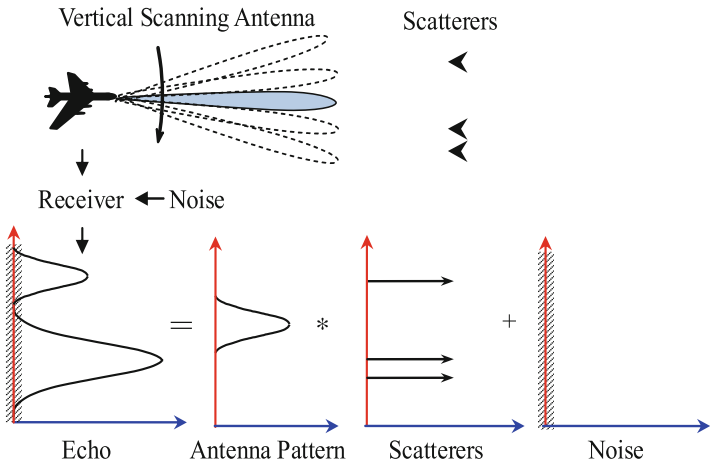

Fig. 23.3 Signal model of TFR

23.3.3 Radar Angle Superresolution Algorithm

The signal model of TFR is shown in Fig. 23.3. The baseband video output signal will trace out the antenna voltage pattern as it scans past a scatterer in the vertically direction, if two scatterers are close together, the output voltage will be proportional to the superposition of two replicas of the antenna pattern.

The echoes in vertical direction are the convolution of the antenna pattern and the surface scatterers when radar scanning a region vertically, antenna pattern is equivalent to the angular impulse response. Consider return signal at one range bin: $x(\varphi)$ denotes the surface scatterers, $h(\varphi)$ and $n(\varphi)$ denote antenna pattern and noise respectively. Then signal model of the return is expressed as

$$s(\varphi) = x(\varphi) * h(\varphi) + n(\varphi) \tag{23.8}$$

where $s(\varphi)$ is return signal, $*$ indicates convolution operator. We can recast (23.8) in the frequency domain as

$$S(\omega) = X(\omega)H(\omega) + N(\omega) \tag{23.9}$$

where ω is spatial frequency.

In time domain, the output voltage will be proportional to the superposition of many replicas of the antenna pattern, modulation of antenna pattern leads to the poor azimuth resolution. In frequency domain, typical antenna pattern results in strong low-pass filtering, and low resolution in the output data results from filtering out high spatial frequencies from the true scene.

Based on signal model, we can restore the scatterers by deconvolution. In theory, using knowledge of the operator inverse H^{-1} can restores surface scatterers:

$$\tilde{s}(\varphi) = H^{-1}s(\varphi) = x(\varphi) + H^{-1}n(\varphi) \tag{23.10}$$

In frequency domain, (23.10) can be expressed as

$$\tilde{S}(\omega) = \frac{S(\omega)}{H(\omega)} = X(\omega) + \frac{N(\omega)}{H(\omega)} \tag{23.11}$$

In practice, conventional inverse filter does not work. Since $H(\omega)$ has zeros for spatial frequencies above some cutoff value, it results in tremendous amplification of noise. Thus, the deconvolution becomes an ill-posed inverse problem. To overcome this problem and obtain radar angular super-resolution, various regularization methods are proposed in [9–11].

23.4 Simulation

Radar angular superresolution algorithm for TFR is verified in the simulation. The radar system parameters are listed in Table 23.1.

The simulations are shown in Fig. 23.4. Figure 23.4a, b show normalized antenna pattern and distribution of scatterers, where the 3 dB bandwidth of antenna pattern is 2.5 °. Figure 23.4c, d show return signal and the range compressed result.

Range migration correction result is illustrated in Fig. 23.4e. It can be seen that the range migration is presented as straight lines in the range compressed domain, and the space variant range migration can be corrected using the keystone transform.

As shown in the Fig. 23.4e, the amplitude of return signal in vertical plane is proportional to the superposition of antenna pattern. Then deconvolution can be conducted along the vertical plane.

Here, the radar angular superresolution algorithm based on [11] is adopted, and the result is shown in Fig. 23.4f. Obviously, a better resolution is obtained compare with the real beam echo shown in Fig. 23.4e. Compared with the distribution of scatterers in Fig. 23.4b, the angular super-resolution result is also satisfactory.

Table 23.1 Simulation parameters

Scan Coverage	±10°	Frequency	30 GHz
Frequency	30 GHz	Bandwidth	10 MHz
Scanning Rate	60 °/s	PRF	2,000 Hz
Original location of scatterers		Distance (1,900 m, 2,000 m, 2,100 m)	
		Azimuth angle (0 °, 0 °, 0 °)	
		Pitch angle (−5 °, 0 °, 5 °)	

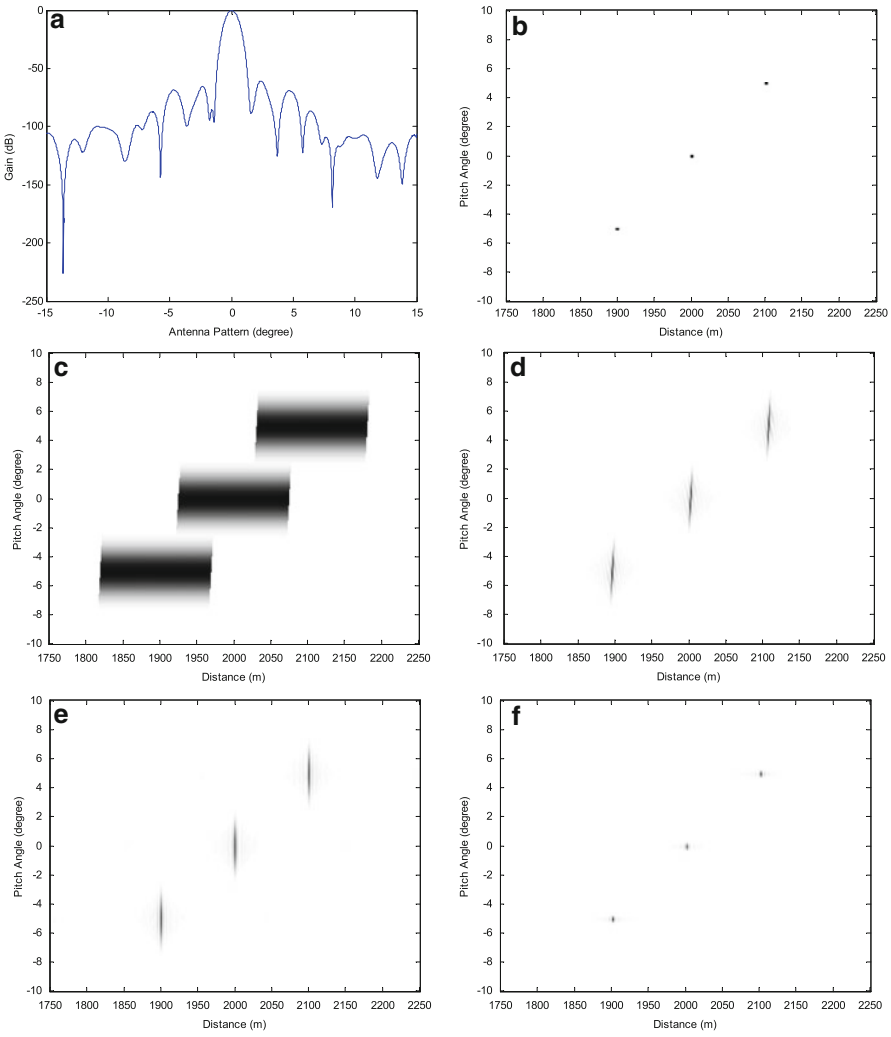

Fig. 23.4 Simulation results. (**a**) antenna pattern (**b**) distribution of scatterers (**c**) return signal (**d**) range-compressed result (**e**) migration correction result (**f**) superresolution result

Conclusion

This paper has discussed the application of angular super-resolution technique on TFR. The range migration is apace-variant for TFR, and it can be corrected using the keystone transform. Moreover, the angular resolution of TFR can be greatly improved using the angular superresolution algorithm. Simulation result validates that the method can effectively improve the angular accuracy of TFR in vertical plane. In the future, this method will be evaluated on the extended target and measured data.

References

1. Ajith Kumar B, Ghose D (2001) Radar-assisted collision avoidance/guidance strategy for planar flight. IEEE Trans Aerosp Electron Syst 37(1):77–90
2. Malaek SM, Kosari AR (2007) Novel minimum time trajectory planning in terrain following flights. IEEE Trans Aerosp Electron Syst 43(1):2–12
3. Malaek SM, Kosari AR (2012) Dynamic based cost functions for TF/TA flights. IEEE Trans Aerosp Electron Syst 48(1):44–63
4. Chapoton CW Jr (1989) Future terrain following radars. In: Proceedings of the IEEE National Radar conference, Texas, pp 20–23
5. Bechtel B, Satterwhite GD, Sharp JH (1971) Terrain avoidance radar system. US Patent 3,568,187
6. Starling RJ, Stewart MS (1971) The development of terrain following radar: an account of the progress made with an airborne guidance system for low flying military aircraft. Aircr Eng Aerosp Technol 43(4):13–15
7. Stimson GW (1998) Introduction to airborne radar. SciTech Publishing, Mendham, pp 37–38
8. Li WC, Yang JY et al (2012) Keystone transform-based space-variant range migration correction for airborne forward-looking scanning radar. Electron Lett 48(2):121–122
9. Jiang W, Li WC et al (2013) Radar angular superresolution algorithm based on Fourier-wavelet regularized deconvolution. In: IEEE international geoscience and remote sensing symposium, Melbourne, Australia, pp 1669–1772
10. Guan JC, Huang YL et al (2012) Improving angular resolution based on maximum a posteriori criterion for scanning radar. In: IEEE Radar conference, Atlanta, pp 451–454
11. Zhou DL, Huang YL et al (2010) Radar angular superresolution algorithm based on Bayesian approach. In: Proceedings of ICSP, Beijing, pp 1894–1897

Chapter 24
Similarity Factor Based on Coherence in PolSAR Change Detection

Yulin Huang, Yangchi Liu, Junjie Wu, and Jianyu Yang

Abstract This paper presents a new change detection method based on coherence characteristics between channels in Polarimetric Synthetic Aperture Radar (PolSAR) images to change detection. It aims at solving the problem that information sources of change detection measure are limited to image intensity information usually in PolSAR change detection. In this method, by using channel coherence information extracted from polarimetric covariance matrix, and relying on the entropy character, we obtain the similarity factor of improved information sources to change detection. Finally, set a threshold to distinguish the changed targets. Simulations and experiments are carried out to assess and evaluate the performance of the proposed method. A comparison between the proposed and the other well-known change detection methods is shown, which indicates that the proposed method performs well in change detection.

Keywords Synthetic Aperture Radar (SAR) • Change detection • Coherence parameter • Similarity factor

24.1 Introduction

Multi-temporal analysis of SAR images has been recognized to play a fundamental role in the field of remote sensing applications. As an important part of multi-temporal analysis, change detection in images of a given scene acquired at two different times has received increasing interest in earth science, especially in environmental monitoring, land-use/land-cover dynamics, damage assessment, and forest or vegetation monitoring [1].

For several years, researchers have made a great deal of studies on change detection. Many methods have been proposed for change detection in single channel SAR images. The scene difference measures as a change detection metric is limited by the utilization of radar image data. Compared with single channel SAR

Y. Huang • Y. Liu (✉) • J. Wu • J. Yang
School of Electronic Engineering, University of Electronic Science and Technology of China, Chengdu, Sichuan 611731, PR China
e-mail: liuyangchi@163.com

J. Mu et al. (eds.), *The Proceedings of the Third International Conference on Communications, Signal Processing, and Systems*, Lecture Notes in Electrical Engineering 322, DOI 10.1007/978-3-319-08991-1_24

data, Polarimetric Synthetic Aperture Radar (PolSAR) data contains both phase and amplitude information from radar returns transmitted in different polarizations. PolSAR has become an important research and application area in microwave imaging technology, which effectively improves the radar information acquisition ability for objects, and the polarization information in radar echo signal of targets owns great application space in filtering and recognition fields.

Conradsen et al. [2] introduced a test statistic for equality of two covariance matrices and derived an associated asymptotic probability measure for obtaining a smaller value of the test statistic which was applied to change detection in airborne fully polarimetric SAR images. In [3], a contextual unsupervised change-detection technique (based on a data-fusion approach) is proposed for two-date multichannel SAR images. Each SAR channel is modeled as a distinct information source, and a Markovian approach to data fusion is adopted. In [4], a new coherent similarity measure has analytically been derived for temporal polarimetric SAR images based on complex Wishart process in time, since the mathematical formulation is general, it can equally well be implemented into any kind of multivariate remote sensing data, such as multispectral optical and interferometric images after small continuation.

In PolSAR, the ability to detect changes depends on utilization of image data including its amplitude and phase [5, 6]. The information sources are defined by the power value of images which is limited to gary information. It results in the loss of multi-polarization information. Then in article [7], the source of change detection metric comes from the covariance matrices of a polarimetric image pair. It utilizes polarimetric information to determine the pixels that have changed. However, for different coherence, the statistic of change detection matrice have different expression. The algorithm has lack of adaptability for the complex situations. Some information is not being fully utilized. Detection sensitivity needs to be improved because some changes are very weak.

As discussed in the previous paragraph, taking into account the accuracy and adaptability of change detection algorithm, this paper proposes a change detection method increasing polarimetric information utilization rate to improve the detection performance of change detection. By calculating coherence parameter between polarization channels, then get a corresponding amplitude image pair of multiple correlation coefficient. And analyse the similarity factor between the image pair to find the changed targets. The performance of the change detection algorithm is quantified by means of comparison with the other well-known algorithm.

The paper is organized as follows. Section 24.2 presents the coherence of multi-polarization SAR. Section 24.3 describes the process of the new change detection method. Simulations and experiments are given in Sect. 24.4. Final section concludes this paper.

24.2 Coherence of Multi-Polarization SAR

PolSAR is widely used in microwave imaging. It is usually a multi-channel system. There is a certain mutual contact relationship between the channels, which is often overlooked.

24.2.1 Coherence Parameters Between Channels in Multi-Polarization SAR

In order to dig out and make full use of the polarimetric information from multi-polarization SAR images, we consider the relationship between the channels. The multi-channel properties of multi-polarization SAR provide a possibility to explore much more information.

For reciprocal medium (suitable for most nature objects), the polarization scattering matrix has three independent parameters, and correspondingly there are three separate channels in multi-polarization SAR: HH, HV and VV.

For the full polarization SAR images, each pixel corresponds to a polarized vector and the polarization vector contains three basic polarization informations, HH, VV, HV. We assume that S is a complex vector in Pol-SAR image corresponding to the pixel x.

$$S = \begin{bmatrix} HH_x \\ HV_x \\ VV_x \end{bmatrix} = \begin{bmatrix} s_1 \\ s_2 \\ s_3 \end{bmatrix} \tag{24.1}$$

While S is subject to complex Gaussian distribution. HH, HV and VV indicate the polarization combinations of antenna transmit-receive.

The corresponding complex covariance matrix C of polarization SAR image composed of the polarization vector can be denoted:

$$\begin{aligned} C &= < \overline{S}\overline{S}^H > \\ &= \begin{bmatrix} \sigma_1 & \rho_{12}\sqrt{\sigma_1\sigma_2} & \rho_{13}\sqrt{\sigma_1\sigma_3} \\ \rho_{12}{}^*\sqrt{\sigma_1\sigma_2} & \sigma_2 & \rho_{23}\sqrt{\sigma_2\sigma_3} \\ \rho_{13}{}^*\sqrt{\sigma_1\sigma_3} & \rho_{23}{}^*\sqrt{\sigma_2\sigma_3} & \sigma_3 \end{bmatrix} \end{aligned} \tag{24.2}$$

In which

$$\sigma_h = < |s_h|^2 > \quad (h = 1, 2, 3) \tag{24.3}$$

σ_h is the S_{th} backscattering coefficient and h is the channel number.

$$\rho_{kl} = \frac{< s_k s_l^* >}{(\sigma_k \sigma_l)^{1/2}} (k, l = 1, 2, 3) \tag{24.4}$$

where ρ_{kl} is the multiple correlation coefficient between channels k and l in Pol-SAR system.

Polarization covariance matrix C contains all the information of the radar polarization measurements, which is the basis of our data analysis and processing. Once the polarization covariance matrix is obtained and the nine parameters are estimated accurately, the image describing the data information can be shown out, which can show the nature in the same texture region composed by independent pixels in the image.

Now, ρ_{kl} is the parameter of polarization covariance matrix waiting to be estimated, which indicates the coherence between channels k and l.

As we known, within a certain range around the interested pixel, RCS (Radar Cross Section) is stable. In this case, L values of individual pixels around the interested pixel behave statistical consistency. Generally, we can place a window around the interested pixel. Every independent look in the same position is formed by pixels from different positions in the window. For gaussian polarized data, covariance matrix C of the MLE [5] can be expressed as:

$$C_{mle} = \frac{1}{N} \sum_{K=1}^{N} S^{(k)} S^{(k)H} \tag{24.5}$$

MLE estimation is the average of multi-look relying on pixels around the central pixel. S^k is the k^{th} complex vector. Multi-look provides the best estimation for parameters carrying information. For any two-channel:

$$\sigma_{kmle} = \frac{1}{N} \sum_{k=1}^{N} \left| s_k^{(k)} \right|^2 \tag{24.6}$$

$$\sigma_{lmle} = \frac{1}{N} \sum_{k=1}^{N} \left| s_l^{(k)} \right|^2 (k, l = 1, 2, 3) \tag{24.7}$$

$$R_{mle} = \frac{1}{N} \sum_{k=1}^{N} s_k^{(k)} s_l^{(k)*} \tag{24.8}$$

$|\rho_{klmle}|$ is the amplitude value of multiple correlation coefficience, always being called coherence.

$$\gamma_{kl} = \left| \rho_{klmle} \right| = \frac{|R_{mle}|}{\sqrt{\sigma_{kmle} \sigma_{lmle}}} \tag{24.9}$$

The correlation coefficient between the same polarized channel and cross-polarized channel show low correlation either in amplitude or phase in average. But the coherence of same polarized channels carries much more information in amplitude and phase. It is possible to make full use of the polarimetric information from multi-polarization SAR images by obtaining the γ_{kl} between the channel HH and VV.

Thus, we try to make use of covariance matrix of multi-polarization SAR as the information source for change detection.

24.2.2 Similarity Factor Based on Coherence Characteristics

In this section, we will discuss how to use the coherence information γ_{kl} between same polarized channels of multi-polarization SAR as the information source for change detection.

Assume A, B are two images to be detected, and γ_A, γ_B are the coherence information of pixels in two images. The entropy corresponding to the two coherence parameters images can be expressed as:

$$H(A) = -\frac{1}{N}\sum h_A(\gamma_A)\log\frac{h_A(\gamma_A)}{N} \tag{24.10}$$

$$H(B) = -\frac{1}{N}\sum h_B(\gamma_B)\log\frac{h_B(\gamma_B)}{N} \tag{24.11}$$

where $h_A(\gamma_A)$ and $h_B(\gamma_B)$ is the corresponding histograms, N is the number of all pixels in the histogram. The joint entropy is defined as:

$$H(A,B) = -\frac{1}{N}\sum h_{AB}(\gamma_A,\gamma_B)\log\frac{h_{AB}(\gamma_A,\gamma_B)}{N} \tag{24.12}$$

where $h_{AB}(\gamma_A,\gamma_B)$ is joint histogram, N is the number of all pixels in the joint histogram.

The coherence information γ is used to get the $H(A)$, $H(B)$ and $H(A,B)$. Similarity factor is defined as:

$$\begin{aligned} SF(A,B) &= H(A) + H(B) - H(A,B) \\ &= \frac{1}{N}\sum h_{AB}(\gamma_A,\gamma_B)\log\frac{h_{AB}(\gamma_A,\gamma_B)N}{h_A(\gamma_A)h_B(\gamma_B)} \end{aligned} \tag{24.13}$$

The similarity factor makes full use of the polarimetric information from multi-polarization SAR images, which represents the similarity of two images. Similarity factor takes a value within the interval [0, 1]. If the value of similarity factor close to 1, it is reasonable to assume that there is no change between the two images;

otherwise there is change. Accordingly, we use the similarity factor for PolSAR change detection.

24.3 The Change Detection Algorithm

Consider that a multi-polarization SAR image pair of size $H \times W$ pixels acquired on the same geographical area but at different time instances. The experimental procedure for studying the change detection is implemented as follows:

1) Compute the respective coherence parameter between channels HH and VV of the image pair according to γ_{kl}. We get a corresponding amplitude image pair of multiple correlation coefficient A and B;
2) Set the initial interested pixel of the image pair. Place a sliding window of size $n \times n$ around the interested pixel;
3) Compute the similarity factor in the sliding window between A and B according to 1) and 2);
4) Repeat the above steps for all interested pixels to obtain the similarity factor of all interested pixels;
5) Set a threshold to distinguish the changed targets.

24.4 Experiments and Results

In this section, experiments are carried out on SAR images to assess and evaluate the performance of the proposed method for change detection.

24.4.1 Simulation

Simulations are performed to assess the feasibility of the method. Two difference images are shown in Fig. 24.1a is the reference image and Fig. 24.1b is the mission image to be detected.

Choose 200 interested pixels as is shown in Fig. 24.2a. Then place a sliding window of size 5×5 around the interested pixels and compute the similarity factor in the sliding window between the reference image and mission image. The results obtained are shown in Fig. 24.2b.

Set the threshold of 0.3. The corresponding interested pixels of the part which below the threshold are changed. As we can see in Fig. 24.2, the results consist with the actual situation. The experiment shows that this method is feasible.

To evaluate the robustness and adaptability of the proposed method, we take a SAR image as the reference image. Then add change with different size, different intensity and position randomly distributed to the image as the mission image. 1000

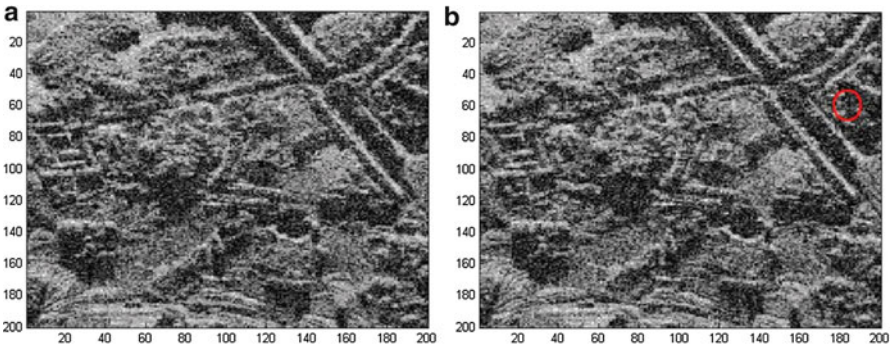

Fig. 24.1 (**a**) The reference image. (**b**) The mission image, the circled part is changed

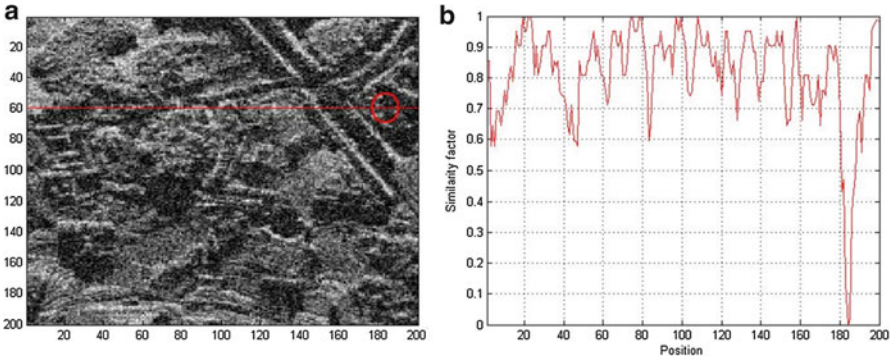

Fig. 24.2 (**a**) The parts which are marked by the *red line* are our interested pixels. (**b**) The similarity factor obtained from the interested pixels

Monte Carlo detection experiments are carried out under a certain SNR to get the detection probability (Pd). Statistic results under different SNR environments are shown in Fig. 24.3.

Simulation results indicate the method has a good performance when the SNR is low, which show that the method is robust.

24.4.2 Experiment

In order to assess the effectiveness of the change detection method for the analysis of the measured data, we considered the real multi-polarization SAR image. The images we used are shown in Fig. 24.4, which were acquired over the same area at different times. The change area is circled in Fig. 24.4b.

Place a sliding window of size 5×5 from the upper left to the lower right corner. The contour of the similarity factor obtained is shown in Fig. 24.5.

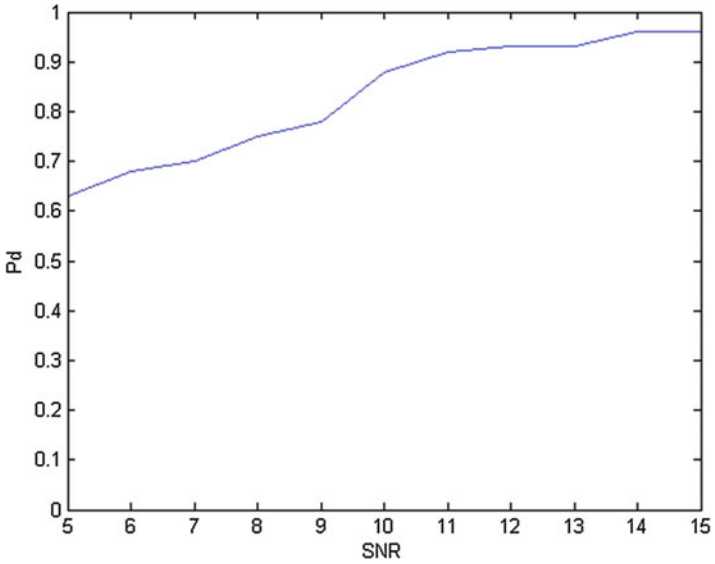

Fig. 24.3 The detection probability under different SNR environments

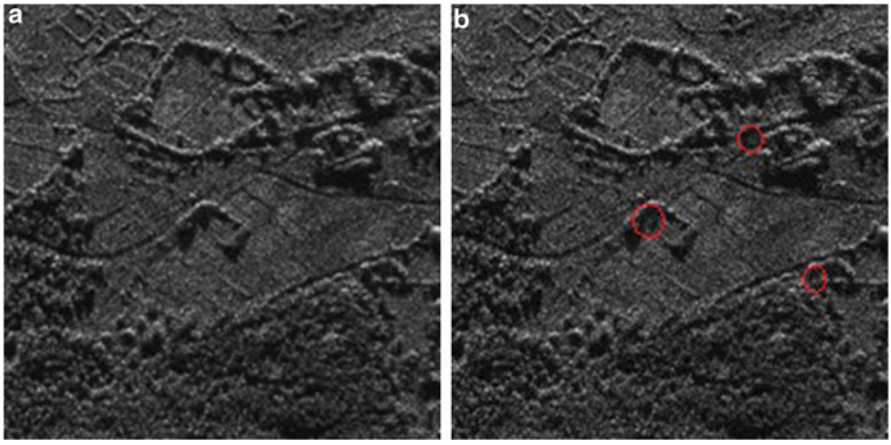

Fig. 24.4 (**a**) The reference image. (**b**) The mission image, the circled part is changed

Set the threshold of 0.3. The white area as is shown in Fig. 24.6 is the part below the threshold, which represent the change area. The results show that the proposed method performs well in practical applications.

Compare our proposed change detection method with mutual information (MI) [1, 9] and maximum-likelihood ratio test (MLRT) [6, 10] change detection method. In order to evaluate the quality of a change image independently of the choice of the thresholding algorithm, the evolution of the detection probability

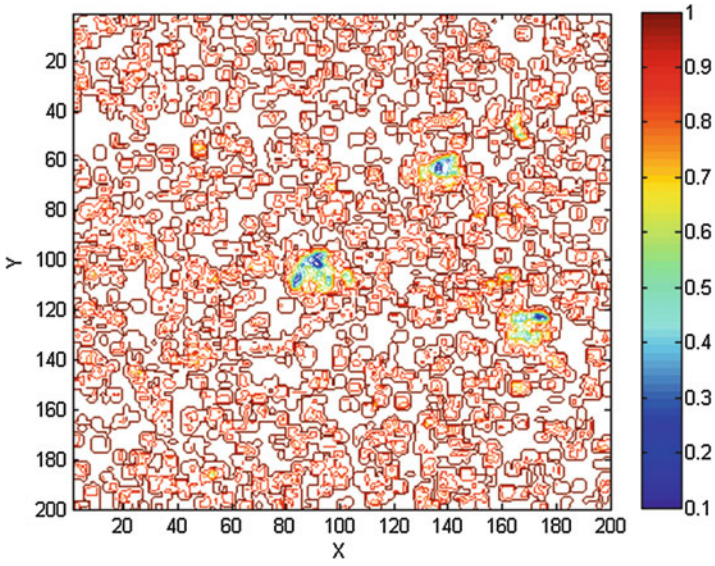

Fig. 24.5 The contour of the similarity factor obtained

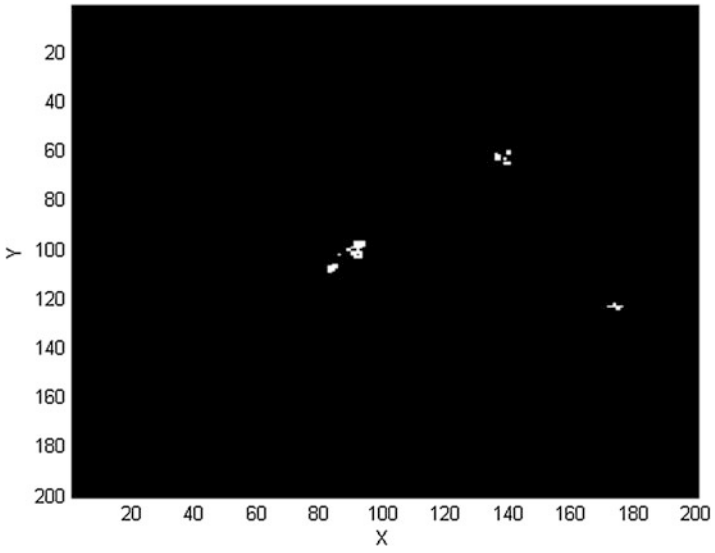

Fig. 24.6 The change detection results

(Pd) as a function of the false-alarm probability (Pfa) may be evaluated in the case where a set of constant thresholds is applied to the whole image. The result obtained is shown in Fig. 24.7.

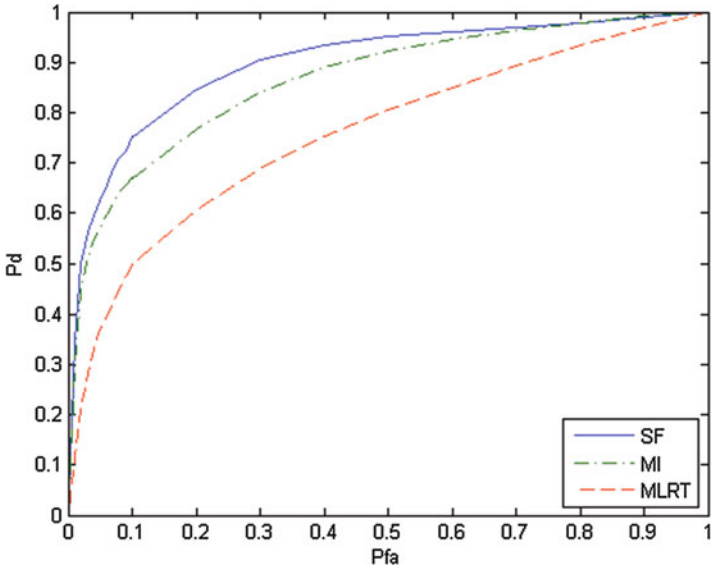

Fig. 24.7 The performance of different change detection method

As is shown in Fig. 24.7, the detection probability of the method based SF is higher than MI and MLRT method when the false-alarm probability is the same. The result show that the performance of the proposed method is better than MI and MLRT change detection method.

Conclusion

This paper proposed a strategy to the PolSAR change detection by changing the original information sources into coherence parameters between channels. In this way, we maked full use of the polarimetric information from multi-polarization SAR images. Simulations and experiments assessed and evaluated the feasibility and performance of the proposed method.

Acknowledgment This work is supported by the National Natural Science Foundation of China (No. 61201272).

References

1. Cui S, Datcu M, Gueguen L (2011) Information theoretical similarity measure for change detection. In: Joint Urban Remote Sensing Event (JURSE), Munich, 2011. IEEE, pp 69–72
2. Conradsen K, Nielsen AA, Schou J, Skriver H (2003) A test statistics in the complex Wishart distribution and its application to change detection in polarimetric SAR data. IEEE Trans Geosci Remote Sensing 41:4–19

3. Moser G, Serpico SB (2009) Unsupervised change detection from multichannel SAR data by Markovian data fusion. IEEE Trans Geosci Remote Sensing 47:2114–2128
4. Erten E, Reigber A, Ferro-Famil L, Hellwich O (2012) A new coherent similarity measure for temporal multichannel scene characterization. IEEE Trans Geosci Remote Sensing 50:2839–2851
5. Chaney RD, Burl MC, Novak LM (1990) On the performance of polarimetric target detection algorithms. In: Record of the IEEE Radar conference, Arlington, 1990. IEEE, pp 10–15
6. Novak LM (2005) Coherent change detection for multi-polarization SAR. In: Conference record of the thirty-ninth Asilomar conference on signals, systems and computers, Pacific Grove, 2005. IEEE, pp 568–573
7. Irving WW, Owirka GJ, Novak LM (2011) A new model for high-resolution polarimetric SAR clutter data. In: SPIE conference on synthetic aperture Radar, pp 567–576
8. Goodman NR (2012) Statistical analysis based on a certain multivariate Gaussian distribution. IEEE Trans Geosci Remote Sensing 34:152–177
9. Gueguen L, Pesaresi M, Ehrlich D, Lu L (2011) Urbanization analysis by mutual information based change detection between SPOT 5 panchromatic images. In: Sixth international workshop on the analysis of multi-temporal remote sensing images (multi-temp), 2011, pp 157–160
10. Kersten PR, Lee JS, Ainsworth TL (2005) A comparison of change detection statistics in POLSAR images. In: Proceedings of the IEEE international conference on geoscience and remote sensing symposium (IGARSS'05), pp 4836–4839

Chapter 25
Analysis of Angular Accuracy of Amplitude Comparison Mono-Pulse Angle Measurement for MIMO Radar

J. Li, Z. Wang, H. Liu, Z. He, and J. Zhang

Abstract The paper focuses on the angle measuring technology and analyses the angular accuracy. The total differential method is used to derive the angle measurement precision in the MIMO radar and the phased array radar. A strict formula of the angle measurement error is proposed, while the angular accuracy of the two types of radars are compared under the same SNR condition. The simulation results show that the formula of the angular accuracy is accordant with the simulation and the angular accuracy of MIMO radar is better than the phased array radar.

Keywords MIMO radar • Amplitude comparison mono-pulse angle measurement • Analyses of the angular accuracy • Total differential method

25.1 Introduction

MIMO radar [1, 2] transmits orthogonal signals, so a low-gain wide-beam can be formed in the spatial domain. And the receiver can handle multi-beam forming. MIMO radar has many new features compared to conventional phased array radars, such as better performance in the target velocity resolution, low-speed target detection, anti-interception and so on, so it is widely studied all over the world.

In the frequently-used measurement methods, mono-pulse angle measurement technology has the merits of simple structure and high accuracy, so it is widely used in the angle measurement of precise tracking radar [3]. Paper [4] implemented mono-pulse amplitude comparison angle measurement algorithm in the angle measurement of MIMO radar successfully. The applications of the mono-pulse phase comparison angle measurement in MIMO radar are studied in paper [5]. Paper [6] analyzed how the signal correlation effects the error of angle measurement. These research of mono-pulse angle measurement technology often

J. Li • Z. Wang (✉) • H. Liu • Z. He • J. Zhang
School of Electronic Engineering, University of Electronic Science and Technology of China, Chengdu, Sichuan 611731, PR China
e-mail: 946233793@qq.com

J. Mu et al. (eds.), *The Proceedings of the Third International Conference on Communications, Signal Processing, and Systems*, Lecture Notes in Electrical Engineering 322, DOI 10.1007/978-3-319-08991-1_25

proposed the relationship between the angular accuracy and SNR [7],but all of them are lacking in the theoretical derivation of the angular accuracy and the quantitative analysis of the angle measurement accuracy for MIMO radar and PA radar (phased array radar).

In this paper, the theoretical expression of the angle measurement accuracy is derived in detail and the relationship between the angular accuracy, number of array elements, SNR, and the beam spacing is obtained by the total differential method.

25.2 The Principle of the Sum and Difference Amplitude Comparison Mono-Pulse Angle Measurement [4]

The principle of the amplitude comparison angle measurement is shown in Fig. 25.1. The angle can be measured by comparing the signal strength of the target echo from the left and the right beams. The corresponding left, right and sum beam patterns are $F(\theta_l)$, $F(\theta_r)$ and $F(\theta_s)$ respectively. Then, the error voltage can be obtained

$$u = (|F(\theta_l)| - |F(\theta_r)|)/|F(\theta_s)| \tag{25.1}$$

The pattern function of MIMO radar [4] is:

$$F(\theta_s) = \frac{\sin\left[\frac{N\pi}{\lambda}d_r(\sin\theta - \sin\theta_s)\right]}{\sin\left[\frac{\pi}{\lambda}d_r(\sin\theta - \sin\theta_s)\right]} \frac{\sin\left[\frac{M\pi}{\lambda}d_t(\sin\theta - \sin\theta_s)\right]}{\sin\left[\frac{\pi}{\lambda}d_t(\sin\theta - \sin\theta_s)\right]} \tag{25.2}$$

$F(\theta_l)$ and $F(\theta_r)$ have the same expressions with $F(\theta_s)$, and N, M are the number of arrays for sending and receiving, d_r, d_t are the element spacing of the sending and receiving.

The difference between the phased array radar and MIMO radar about the sum and difference amplitude comparison mono-pulse angle measurement method is that the received signal of MIMO radar not only needs to get through the matched filter and form the receive beams, but also needs to get through the equivalent transmitting beam-forming to get the joint beam pattern to measure the angle.

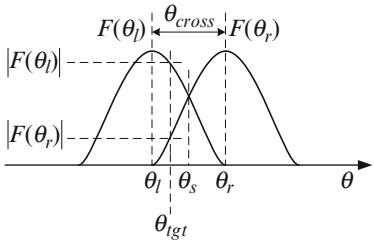

Fig. 25.1 Two adjacent beams overlap each other

Under the same arrangement of the antenna array, the main lobe width of MIMO radar joint beam pattern is narrower than the beam pattern of the phased array radar [4], which indicates that the angular accuracy of MIMO radar should be higher than that of the phased array radar.

25.3 The Angular Accuracy of MIMO Radar

Assume the deviation angle from the direction of the target to the direction of the sum beam is $\Delta\theta$. In a continuous tracking state, there are usually $\Delta\theta \ll \theta_{3dB}$, which means the target is located near the zero value (maximum of the sum beam) of the difference beams. So the pattern of the difference beam $F_{\Delta}(\Delta\theta)$ (the difference between the left and the right beam) can be expanded at the very location as

$$F_{\Delta}(\Delta\theta) = F_{\Delta}(0) + F_{\Delta}^{'}(0)\Delta\theta + \frac{1}{2!}F_{\Delta}^{''}(0)\Delta\theta^2 + \cdots\cdots, \tag{25.3}$$

Ignoring the second derivative above, and $F_{\Delta}(0) \approx 0$ as the low depth of difference beams zero value, then

$$F_{\Delta}(\Delta\theta) \approx F_{\Delta}^{'}(0)\Delta\theta. \tag{25.4}$$

Similarly near the maximum of the sum beam [3]

$$F_{\Sigma}(\Delta\theta) \approx F_{\Sigma}(0). \tag{25.5}$$

The $\Delta\theta$ is normalized by the half-power beam-width of the sum beam θ_{3dB}. The error voltage can be expressed as

$$u = \frac{F_{\Delta}(\Delta\theta)}{F_{\Sigma}(\Delta\theta)} = \frac{F_{\Delta}^{'}(0)}{F_{\Sigma}(0)}\Delta\theta = \left[\frac{F_{\Delta}^{'}(0)}{F_{\Sigma}(0)}\theta_{3dB}\right]\frac{\Delta\theta}{\theta_{3dB}}. \tag{25.6}$$

The error voltage is proportional to the value of $\Delta\theta$ which is the deviation angle from the direction of the target to the direction of the sum beam (the equal signals axis), so the value of $\Delta\theta$ is determined by obtaining the value of u and then the target orientation can be obtained.

Therefore, according to the formula (25.6), the RMS value of angle measurement error of the target, corresponding to the RMS of the error voltage caused by the receiver noise $\sigma_{\Delta u}$ is

$$\sigma_{\Delta\theta_{tgt}} = \sigma_{\Delta u}\theta_{3dB} / \left[\left(F_{\Delta}^{'}(0)/F_{\Sigma}(0)\right)\theta_{3dB}\right] = \sigma_{\Delta u}\theta_{3dB}/k_m, \tag{25.7}$$

where $k_m = (F_{\Delta}^{'}(0)/F_{\Sigma}(0))\theta_{3dB}$ is the normalized slope.

Fitting the pattern to obtain k_m by the Gaussian function [5], the $F(\theta_s)$, $F(\theta_l)$, $F(\theta_r)$ can be expressed

$$\begin{cases} |F(\theta_s)| = e^{-\frac{\alpha}{2}\left(\theta_{tgt}-\theta_s\right)^2} = e^{-\frac{\alpha}{2}(\Delta\theta)^2} \\ |F(\theta_l)| = e^{-\frac{\alpha}{2}\left(\theta_{tgt}-\theta_l\right)^2} = e^{-\frac{\alpha}{2}\left(\theta_{tgt}-\theta_s+\frac{\theta_{cross}}{2}\right)^2} = e^{-\frac{\alpha}{2}\left(\Delta\theta+\frac{\theta_{cross}}{2}\right)^2} \\ |F(\theta_r)| = e^{-\frac{\alpha}{2}\left(\theta_{tgt}-\theta_r\right)^2} = e^{-\frac{\alpha}{2}\left(\theta_{tgt}-\theta_s-\frac{\theta_{cross}}{2}\right)^2} = e^{-\frac{\alpha}{2}\left(\Delta\theta-\frac{\theta_{cross}}{2}\right)^2} \end{cases} \tag{25.8}$$

θ_{cross} is the beam spaced of the left and right beams, and $\alpha = 8\ln\sqrt{2}/\theta_{3dB}^2$. Because the value of $\alpha\cdot\Delta\theta\cdot\theta_{cross}/2$ is small, so $e^x \approx 1+x$ can be used for reduction

$$u = \frac{F_\Delta(\Delta\theta)}{F_\Sigma(\Delta\theta)} = \frac{e^{-\frac{\alpha}{2}\left(\Delta\theta+\frac{\theta_{cross}}{2}\right)^2} - e^{-\frac{\alpha}{2}\left(\Delta\theta-\frac{\theta_{cross}}{2}\right)^2}}{e^{-\frac{\alpha}{2}(\Delta\theta)^2}} = e^{-\frac{\alpha}{2}\left(\frac{\theta_{cross}}{2}\right)^2}\left(-\alpha\Delta\theta\cdot\theta_{cross}\right) \tag{25.9}$$

Into the value of α and derivation

$$\begin{aligned} \frac{F_\Delta{}'(\Delta\theta)}{F_\Sigma(\Delta\theta)} &= e^{-\ln\sqrt{2}\cdot\left(\frac{\theta_{cross}}{\theta_{3dB}}\right)^2}\cdot\frac{8\ln\sqrt{2}}{\theta_{3dB}^2}\cdot\theta_{cross}, \\ k_m &= 8\ln\sqrt{2}\cdot e^{-\ln\sqrt{2}\cdot\left(\frac{\theta_{cross}}{\theta_{3dB}}\right)^2}\cdot\frac{\theta_{cross}}{\theta_{3dB}} \end{aligned} \tag{25.10}$$

The left, right, and sum beam pattern functions of MIMO radar of the reception about the transmit-receive ULA of M array elements are

$$F_l = X_l + j\cdot Y_l,\ \ F_r = X_r + j\cdot Y_r,\ \ F_s = X_s + j\cdot Y_s. \tag{25.11}$$

The error voltage of the sum and difference amplitude comparison mono-pulse angle measurement

$$u = \frac{|F_l| - |F_r|}{|F_s|} = \frac{\sqrt{X_l^2+Y_l^2} - \sqrt{X_r^2+Y_r^2}}{\sqrt{X_s^2+Y_s^2}}, \tag{25.12}$$

Its total differential is

$$\begin{aligned} du = {} & \frac{(2X_l\cdot dX_l + 2Y_l\cdot dY_l)}{2\sqrt{X_l^2+Y_l^2}\sqrt{X_s^2+Y_s^2}} - \frac{(2X_r\cdot dX_r + 2Y_r\cdot dY_r)}{2\sqrt{X_r^2+Y_r^2}\sqrt{X_s^2+Y_s^2}} \\ & + \left(\sqrt{X_l^2+Y_l^2} - \sqrt{X_r^2+Y_r^2}\right)\left[-\frac{(2X_s\cdot dX_s + 2Y_s\cdot dY_s)}{2\left(\sqrt{X_s^2+Y_s^2}\right)^3}\right] \end{aligned} \tag{25.13}$$

Set $|\theta_l - \theta_r| = \theta_{cross}$, then the amplitudes of the left, right, and sum beams at the direction of the sum beam can be represented respectively as $|F_l| = |F_r| = A_1$, $|F_s| = A_0 = M^2$, so the total differential can be obtained

$$du = [(X_l \cdot dX_l + Y_l \cdot dY_l) - (X_r \cdot dX_r + Y_r \cdot dY_r)]/\left(A_1 \cdot M^2\right). \tag{25.14}$$

Considering the receiver noise, and in order to simplify the analysis, it is assumed that $\theta_s = \theta_{tgt} = 0$, which means the target is located in the normal direction of the array and the received beam points to the target, then $b(\theta_s) = a(\theta_{tgt}) = [1, 1, \cdots, 1]^T \in N^{M \times 1}$, noting

$$b(\theta_l) = b^*(\theta_r) = b_I + j \cdot b_Q, \quad V = v_I + j \cdot v_Q \in C^{M \times M}, \tag{25.15}$$

where $v_{I_{ij}}, v_{Q_{ij}} \sim N(0, \sigma^2/2)$, that is $V_{ij} \sim N(0, \sigma^2)$ (i, $j = 1, 2, \cdots M$), and

$$b_I = \mathrm{Re}\left\{\exp\left(-j \cdot m\frac{2\pi}{\lambda}d\left(-\frac{\theta_{cross}}{2}\right)\right)\right\},$$
$$b_Q = \mathrm{Im}\left\{\exp\left(-j \cdot m\frac{2\pi}{\lambda}d\left(-\frac{\theta_{cross}}{2}\right)\right)\right\} \quad (m = 0, 1, 2, \cdots, M-1).$$

The received left and right beams of MIMO radar are

$$\begin{aligned} Z_l &= b^H(\theta_l)\left[a(\theta_{tgt})a^T(\theta_{tgt}) + \frac{\sigma}{\sqrt{2}}V\right]b^*(\theta_l) \\ &= \left\{\left(\sum_{m=1}^{M} b_{I_m}\right)^2 - \left(\sum_{m=1}^{M} b_{Q_m}\right)^2 + \frac{\sigma}{\sqrt{2}}\left(b_I^T v_I b_I + b_Q^T v_Q b_I + b_I^T v_Q b_Q - b_Q^T v_I b_Q\right)\right\} \\ &\quad + j \cdot \left\{-2 \cdot \left(\sum_{m=1}^{M} b_{I_m}\right)\left(\sum_{m=1}^{M} b_{Q_m}\right) + \frac{\sigma}{\sqrt{2}}\left(-b_I^T v_I b_Q - b_Q^T v_Q b_Q + b_I^T v_Q b_I - b_Q^T v_I b_I\right)\right\} \\ &= \left[C_I^2 - C_Q^2 + \frac{\sigma}{\sqrt{2}} \cdot A\right] + j \cdot \left[-2 \cdot C_I C_Q + \frac{\sigma}{\sqrt{2}} \cdot B\right] \\ &= (X_l + dX_l) + j \cdot (Y_l + dY_l) \end{aligned}$$

$$
\begin{aligned}
Z_r &= b^H(\theta_r)\left[a(\theta_{tgt})a^T(\theta_{tgt}) + \frac{\sigma}{\sqrt{2}}V\right]b^*(\theta_r) \\
&= \left\{\left(\sum_{m=1}^{M} b_{I_m}\right)^2 - \left(\sum_{m=1}^{M} b_{Q_m}\right)^2 + \frac{\sigma}{\sqrt{2}}\left(b_I^T v_I b_I - b_Q^T v_Q b_I - b_I^T v_Q b_Q - b_Q^T v_I b_Q\right)\right\} \\
&\quad + j\cdot\left\{2\cdot\left(\sum_{m=1}^{M} b_{I_m}\right)\left(\sum_{m=1}^{M} b_{Q_m}\right) + \frac{\sigma}{\sqrt{2}}\left(b_I^T v_I b_Q - b_Q^T v_Q b_Q + b_I^T v_Q b_I + b_Q^T v_I b_I\right)\right\} \\
&= \left[C_I^2 - C_Q^2 + \frac{\sigma}{\sqrt{2}}\cdot C\right] + j\cdot\left[2\cdot C_I C_Q + \frac{\sigma}{\sqrt{2}}\cdot D\right] \\
&= (X_r + dX_r) + j\cdot(Y_r + dY_r)
\end{aligned}
\tag{25.16}
$$

substituting (25.16) into (25.14), it can be obtained

$$
du = \frac{1}{A_1\cdot M^2}\cdot\frac{\sigma}{\sqrt{2}}\cdot\left\{\left(C_I^2 - C_Q^2\right)\cdot A - 2\cdot C_I C_Q\cdot B - \left(C_I^2 - C_Q^2\right)\cdot C - 2\cdot C_I C_Q\cdot D\right\}. \tag{25.17}
$$

Because the output SNR of the direction of the sum beam is $SNR = M^2/\sigma^2$, the variance of the error voltage is

$$
\begin{aligned}
\sigma_{\Delta u}^2 = \frac{4}{A_1^2\cdot M^2\cdot SNR}\cdot\Bigg\{ & 2{C_I}^2{C_Q}^2\left[\left(\sum_{i=1}^{M} b_{I_i}^2\right)^2 + \left(\sum_{i=1}^{M} b_{Q_i}^2\right)^2\right] \\
& + \left(C_I^2 - C_Q^2\right)^2\left(\sum_{i=1}^{M} b_{Q_i}^2\right)\left(\sum_{i=1}^{M} b_{I_i}^2\right) + \left(C_I^4 - 6{C_I}^2{C_Q}^2 + C_Q^4\right)\left(\sum_{i=1}^{M} b_{I_i}b_{Q_i}\right)^2\cdot \\
& - 4\left(C_I^2 - C_Q^2\right)C_I C_Q\left[\left(\sum_{i=1}^{M} b_{I_i}^2\right) - \left(\sum_{i=1}^{M} b_{Q_i}^2\right)\right]\left(\sum_{i=1}^{M} b_{I_i}b_{Q_i}\right)\Bigg\}
\end{aligned}
\tag{25.18}
$$

where $C_I = \sum_{m=1}^{M} b_{I_m}, C_Q = \sum_{m=1}^{M} b_{Q_m}$. According to (25.18), the mean square error $\sigma_{\Delta u}^2$ of the error voltage of MIMO radar is connected with the beam spacing of the left and right beams $|\theta_l - \theta_r| = \theta_{cross}$, By substituting (25.18) and (25.10) into (25.7), the angular accuracy of MIMO radar can be obtained.

$\sigma_{\Delta\theta_{tgt}}$, $\sigma_{\Delta u}$, k_m and θ_{3dB} of the phased array radar have the same relationship with MIMO radar. So the variance of the error voltage $\sigma_{\Delta u}^2$ of the PA radar is

$$
{\sigma_{\Delta u}}^2 = \frac{1}{SNR}\cdot\frac{M}{A_1^2}\cdot\Big\{M\left(C_I^2 + C_Q^2\right) - \left({C_I}^2 - {C_Q}^2\right), \cdot\left(b_I^T b_I - b_Q^T b_Q\right), -2C_I C_Q, \cdot \left(b_I^T b_Q + b_Q^T b_I\right)\Big\} \tag{25.19}
$$

Then the angular accuracy of the phased array radar can be obtained.

25.4 Simulation Results

In order to prove the validity of the formula of the angular accuracy, the simulation is taken on the condition that the numbers of the phased array radar with uniform linear arrays is ten at the transmitter and receiver, spaced by $d = \lambda/2$, so $\sigma_{\Delta\theta_{tgt}} = 0.4771 \cdot \theta_{3dB}/\sqrt{SNR}$; and the numbers of the MIMO radar is $M = 10$ spaced by $d = \lambda/2$, so $\sigma_{\Delta\theta_{tgt}} = 0.4546 \cdot \theta_{3dB}/\sqrt{SNR}$.

Figure 25.2 is the simulation measurements value and the theoretical value of the angular accuracy. Figure 25.2a shows the error between the simulation measurements value and the theoretical value by the formula (25.18) is very small for the PA radar, but they are not equal by 2,000 Monte Carlo independent experiments while the beam spacing of the left and right beams is θ_{3dB}. The reason is that the fitting width is 0.002 under the simulation, which means the fitted slope is the approximation of the angle measurement error slope near the zero value. So the simulated value of the angle measurement error slope is 11.9069, while the normalized theoretical value of the slope is 11.0126. Although the theoretical values of the slope are very close to the simulated values, there is still a little error. Moreover, there also is the randomness of the simulation. So all these elements bring the error between the measured value with the theoretical value of $\sigma^2_{\Delta\theta_{tgt}}$. Figure 25.2b shows the results of MIMO radar which are the same with the phased array radar about the contrast and verification of the angular accuracy.

It should be pointed out that, in this paper, the angular accuracy is the approximation (not the lower bound) which is derived by the gauss function fitting, so it may appear that the simulation value is superior to the theoretical value in Fig. 25.2.

Comparing the theoretical angular accuracy of the MIMO radar with that of the phased array radar, we can get the angular accuracy of MIMO radar is higher than the phased array radar (θ_{3dB} of MIMO radar is smaller firstly, then the constant 0.4546 is smaller than 0.4771) under the same SNR condition. From Fig. 25.3, we can also obtain the same result.

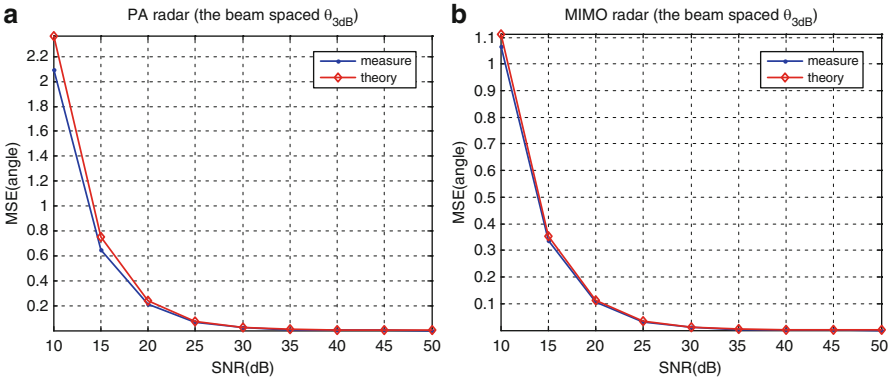

Fig. 25.2 The angular accuracy of PA radar and MIMO radar (**a**) the angular accuracy of PA radar and (**b**) the angular accuracy of MIMO radar

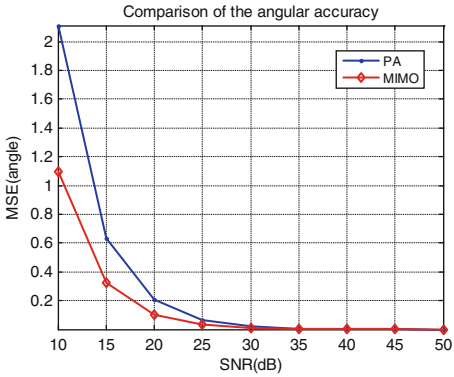

Fig. 25.3 Comparison of the angular accuracy (simulation measurements)

Conclusion

In this paper, the total differential method is employed to derivate the error voltage in the MIMO radar and phased array radar, and a theoretical formula of the angular accuracy has been educed on the basis of the relationship between the angular accuracy with k_m, the mean square error of error voltage, the beam spacing θ_{3dB}, and the angular accuracy are connected with the beam spaced of the left and right beams. The error between the simulation measurements and the theoretical value is very small by simulations. And the angular accuracy of two kinds of radar system is compared under the same simulation conditions, turning out that the angular accuracy of MIMO radar is really better than the phased array radar.

Acknowledgments This work is supported partly by the National Natural Science Foundation of China (no. 61201280 and no. 61101173).

References

1. Li J, Stoica P (2007) MIMO radar with collocated antennas. IEEE Signal Process Mag 24 (5):106–114
2. Zishu HE, Chun-lin H, Bo L (2005) MIMO radar and its technical characteristic analyses. Acta Electronica Sinica 33(12A):2441–2445
3. Guangyi Z (2001) Phased array radar principle. National Defense Industry Press, Beijing
4. He Q, He ZS, Li HY (2007) Multibeam amplitude comparison problems for MIMO radar's angle measurement. In: Asilomar conference on signal, systems and computers, pp 2163–2167
5. Juanjuan Z, Hongming L, Jun L (2011) Research on the mono-pulse phase comparison angle measurement algorithm of MIMO radar. In: International workshop on microwave and millimeter wave circuits and system technology (MMWCST), pp 1–4
6. Zhou L, Jun L, Hongming L (2013) The mono-pulse angle measurement of non-strictly orthogonal signals for MIMO radar. Radar Sci Technol 3(11):262–266
7. Lufei D (2009) Radar theory. Electronic Industry Press, Beijing

Chapter 26
Big Data Stream Anomaly Detection with Spectral Method for UWB Radar Data

Ying Yun and Wei Wang

Abstract Different from the traditional static data anomaly detection, the subjects of big data stream anomaly detection has been attracting extensive attention. Through wall human being detection with UWB radar has become popular recently due to its many merits. And it is a typical big data stream mining problem when detected human being in real time. In this paper, we proposed a statistical algorithm based on spectral method for big data stream anomaly detection. The through brick wall human detection experiment was designed and the results showed that the proposed method could detect the human being with high confidence level.

Keywords: Big data stream • Anomaly detection • Spectral method • UWB radar

26.1 Introduction

"Big Data" refers to large, diverse, complex, longitudinal and distributed data sets generated from instruments, sensors, internet transactions, email, video, click streams, and other digital sources available today and in the future. The developments of information and communication technologies dramatically change the data storing and processing. Especially, unbounded sequences of data objects that are continuously generated at rapid rates, the so-called data stream which have three features: huge amounts, real time and dynamic variation [1]. These big data stream can be considered as streaming data or as a snapshot of streaming data, and widely exists in fields such as sensor networks, network monitoring system, traffic management, telecom business records and web searching. Big data stream has become a challenge to today's analytic processes in data mining due to its large size and dynamic characteristics when being generated. In this paper, we will study the anomaly detection algorithm in big data stream.

Anomaly detection refers to find inconsistent with the desired pattern in data, also known as novelty detection, anomaly mining, noising mining. Anomaly

Y. Yun • W. Wang (✉)
College of Electronic and Communication Engineering, Tianjin Normal University, Tianjin, China
e-mail: weiwangvip@163.com

J. Mu et al. (eds.), *The Proceedings of the Third International Conference on Communications, Signal Processing, and Systems*, Lecture Notes in Electrical Engineering 322, DOI 10.1007/978-3-319-08991-1_26

detection has many applications, such as credit card fraud detection, medical diagnostics information anomaly detection, industrial equipment fault detection and structural defect detection, network intrusion detection and novel theme of text mining. Currently, anomaly detection methods include anomaly detection based on classification, anomaly detection based on the nearest neighbor method, anomaly detection based on clustering, statistical anomaly detection, anomaly detection based on information theory, spectral theory anomaly detection and so on [2].

Due to its penetration ability from non-metallic media to detect life signal in far-off areas and not require any contacting with the living body, the through wall human detection has become popular in recent years. The Ultra-wideband (UWB) radar, which has many merits such as strong anti-interference ability, high resolution performance and good target recognition capabilities, can launch very short duration pulses to penetrate non-metallic wall and obstacles. It has emerged as one of the most optimal choices for through wall human detection. In [3], Qilian Liang proposed Doppler approach, singular value decomposition and STFT and SVD method for through wall human detection. The results showed that these methods can work for some kind material of wall. In [2, 4–6], Wei Wang proposed statistical method based on SPC and Wavelet Packet Transform, SVD algorithm to detect human through gypsum, brick and concrete wall with uncompressed and compressed data. These methods needed to store the whole radar data for human detection. But in reality, we should detect human being through wall in real time. In other words, we should detect the anomaly through big data stream.

In this paper we will propose an algorithm for through wall human detection with spectral method in big data stream. The remainder of the paper is organized as follows. In the Sect. 26.2 the anomaly detection algorithm with spectral method will be introduced. Then the experimental procedure of UWB radar will be presented and the results will be showed based on the proposed anomaly detection algorithm in Sect. 26.3. Conclusion is in final section.

26.2 Spectral Method and Anomaly Detection

Let a part of big data stream be represented by a matrix $X = [x_1, x_2, \ldots x_L]$ where each data instance $x_i \in R^N$. It can be a network reading at one time or a snapshot of data stream. For notational simplicity, we assume the data stream matrix has been centralized. Then we can get the covariance matrix of data stream matrix Σ_X:

$$\Sigma_X = U \Lambda U^T \tag{26.1}$$

where the principal eigenvectors of Σ_X corresponding to the largest K eigenvalues $\lambda_1 \ldots \lambda_K$ builds the matrix $U = [u_1, u_2, \ldots u_K]$. The residual subspace is $P = (I - UU^T)$. Thus, for any snapshot of big data stream x, its projection into the

residual subspace is $z = Px$. According to the spectral method, the squared prediction error (SPE) statistic is given as

$$t_{SPE} = \|z\|_2^2 \tag{26.2}$$

Where the t_{SPE} follows a non-central chi-square distribution under the null hypothesis that the matrix is normal. Hence, the anomaly detection can be achieved based on whether t_{SPE} exceeds a certain threshold corresponding to a desired false alarm rate. The threshold is called $Q-$ statistic, and it is a function of non-principal eigenvalues in residual subspace. For a significance level β, the $Q-$ statistic can be computed by the followed equation:

$$Q = \alpha_1 \left[\frac{(1-\beta)\sqrt{2\alpha_2 h^2}}{\alpha_1} + 1 + \frac{\alpha_2 h(h-1)}{\alpha_1^2} \right]^{\frac{1}{h}} \tag{26.3}$$

where $h = 1 - \frac{2\alpha_1\alpha_3}{3\alpha_2^2}$, $\alpha_i = \Sigma_{j=K+1}^{N} \lambda_j^i$. An anomaly can be detected when $t_{SPE} > Q$ [7, 8].

26.3 Experiment and Results Analysis

The experimental procedure is the same as the depiction in [4–6]. The P220 UWB radar of Time Domain Company is chose as the detection tool and it worked in monostatic mode which the waveform pulses were transmitted from a single Omni-directional antenna and scattered waveforms were acquired by a collocated Omni-directional antenna. In the project, the P220 UWB radar was positioned one side of Brick wall (see Fig. 26.1) and the radar parameters were: Hardware Integration = 512, Software Integration = 2, Pulse Repetition Frequency 9.6 MHz, Step Size 7 bin. We collected echo signals at two statuses: no person behind wall and still human standing behind wall. Thirty echo signals were collected for each status and the data of under no person status were used for training and the other data were used for testing.

We constructed the big data stream matrix with 30 echo signals under no person status and acquired the principle eigenvectors to build matrix U. Then each test echo signal was used for anomaly detection based on the proposed spectral method.

In Figs. 26.2 and 26.3, two echo signals are showed under the two statuses. It can be seen that there are only some tiny differences in amplitude. In other word, we can not directly detect the human through the echo signal in time domain.

In Fig. 26.4 we computed the squared prediction errors of testing data based on the training data. The threshold limit Q was also computed according the $(1-\beta)$ confidence level and β was varied between 0 and 1 with the increment 0.1.

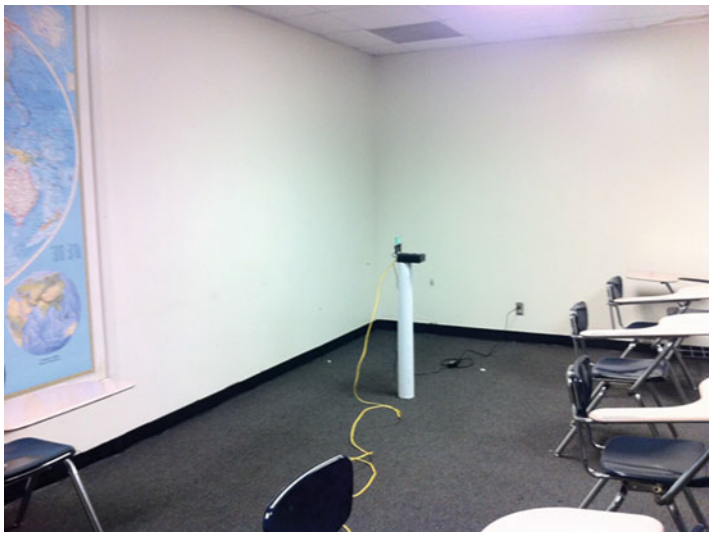

Fig. 26.1 The location of P220 UWB radar

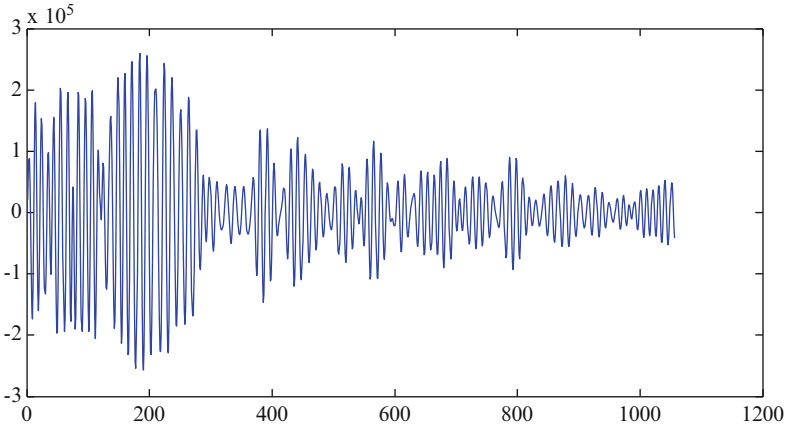

Fig. 26.2 An echo signal under no person status

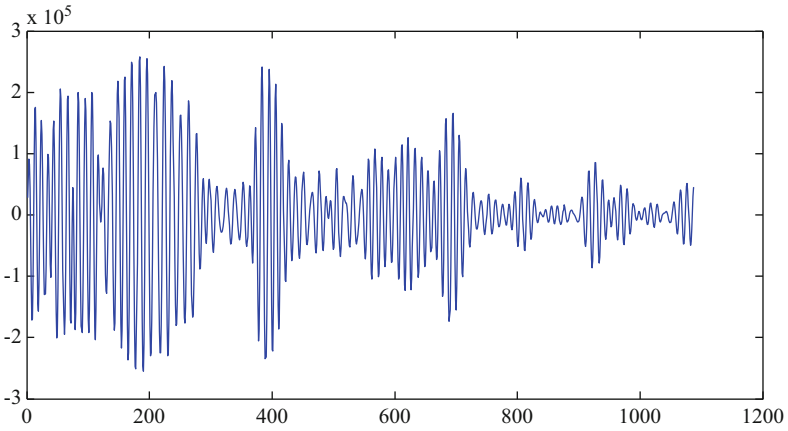

Fig. 26.3 An echo signal under still person standing behind the brick wall

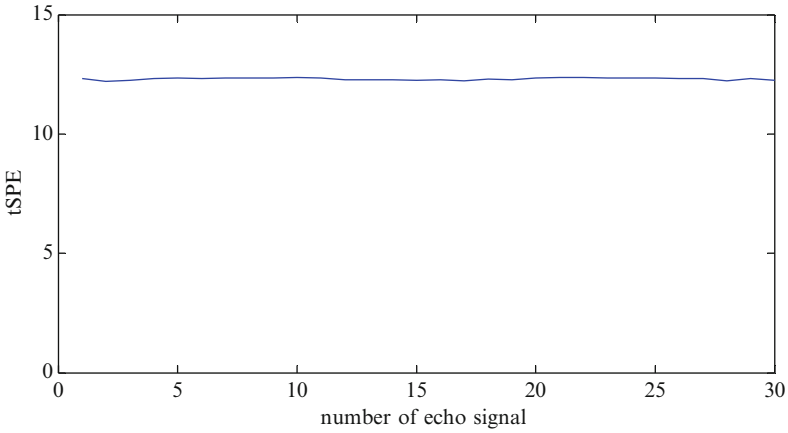

Fig. 26.4 The squared prediction error of test echo signals

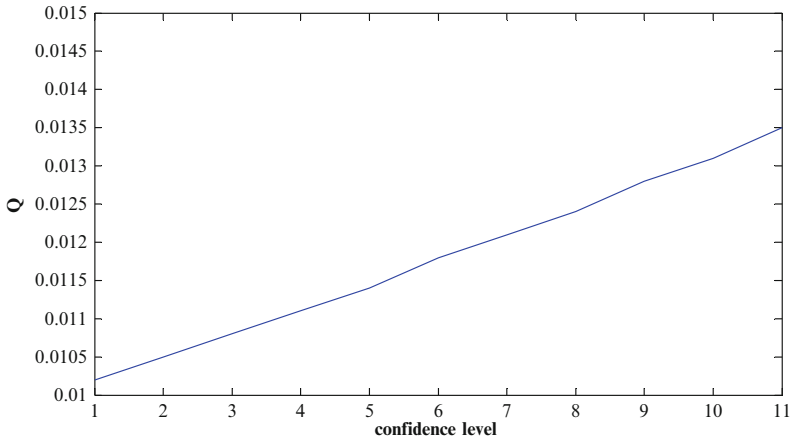

Fig. 26.5 Q value under different confidence level

Obviously, the proposed anomaly detection method with spectral method can detect human being through brick wall in real time (Fig. 26.5).

Conclusion
Through wall human detection is of great interest for military reconnaissance, anti-terrorism, medical and natural disasters ambulance. According to the requirement of real time detection, we proposed a big data stream anomaly detection algorithm based on spectral method. The experimental results showed that the method can detect human being through brick wall with high probability.

Acknowledgement The authors would love to thank Professor Qilian Liang in University of Texas at Arlington for providing the UWB radar data. This research was supported by the Tianjin Younger Natural Science Foundation (12JCQNJC00400) and National Natural Science Foundation of China (61271411).

References

1. Silva JA, Faria ER, Barros RC et al (2013) Data stream clustering: a survey. ACM Comput Surv 46(1):1–31 (Article 13)
2. Wang W, Lu D, Zhou X, Zhang B, Mu J (2013) Statistical wavelet-based anomaly detection in big data with compressive sensing. EURASIP J Wireless Commun Netw 2013:269. doi:10.1186/10.1186/1687-1499-2013-269
3. Singh S, Liang Q, Chen D, Sheng L (2011) Sense through wall human detection using UWB radar. EURASIP J Wireless Commun Netw 2011:20

4. Wang W, Zhang B, Mu J (2013) Through wall detection of human being based on SPC and wavelet packet transform by UWB radar. In: IEEE international conference on communications workshop, 6, pp 955–958
5. Wang W, Zhou X, Zhang B, Mu J (2013) Anomaly detection in big data from UWB radars. Secur Commun Netw 3. doi:10.1002/sec.745
6. Zhang B, Wang W (2013) Through-wall detection of human being with compressed UWB radar data. EURASIP J Wireless Commun Netw 2013:162
7. Pham D-S, Venkatesh S, Lazarescu M, Budhaditya S (2014) Anomaly detection in large-scale data stream networks. Data Min Knowl Disc 28(1):145–189
8. Lakhina A, Crovella M, Diot C (2004) Diagnosing network-wide traffic anomalies. In: Proceedings of the 2004 conference on applications, technologies, architectures, and protocols for computer communications, pp 219–230

Chapter 27
An Autofocus Technique for Sub-aperture Processing of Video-SAR

Ruizhi Hu and Rui Min

Abstract Video-SAR can produce sequential images at high frame rate, providing a continuous surveillance over a region of interest (ROI). To accelerate the speed of image processing, the whole circular path of Video-SAR is divided into several sub-apertures. However, due to the severe coupling of range and cross-range direction of the circular path, standard autofocus techniques as Phase Gradient Autofocus (PGA) fail since the direction of image blur changes for each sub-aperture image (sub-image). We have developed an algorithm for sub-aperture processing of Video-SAR that estimates the phase errors from strong scatters in the unfocused sub-image based on echo regeneration, regardless of the sub-aperture position. After phase compensation, more focused sub-images can be obtained before they are compiled into a SAR video. Thus the efficiency and utility of Video-SAR sub-aperture processing is retained, while image quality is not compromised due to platform motion errors.

Keywords Video-SAR • Sub-aperture processing • Autofocus • Echo regeneration

27.1 Introduction

Video-SAR can provide a sequential images of the entire ROI at a given resolution and high frame rate, which allows for easier observation of moving targets and more natural interpretation by human analysts. During the imaging process of Video-SAR, each frame image is formed to the same pixel and must be oriented to a fixed direction on the ground coordinate system (GCS) so that the ROI does not appear to rotate as the platform flies along its circular path. In Video-SAR mode, the time required to achieve the desired cross-range resolution typically exceeds the frame interval. As a result, successive frames of Video-SAR have overlapped sub-apertures. In order to utilize this overlap property, back-projection

R. Hu • R. Min (✉)
School of Electronic Engineering, University of Electronic Science and Technology of China, Chengdu, China
e-mail: minrui@uestc.edu.cn

J. Mu et al. (eds.), *The Proceedings of the Third International Conference on Communications, Signal Processing, and Systems*, Lecture Notes in Electrical Engineering 322, DOI 10.1007/978-3-319-08991-1_27

(BP) algorithm [1] was selected as the imaging algorithm for its pulse-wise processing, which allows intermediate results to be reutilized. To overcome the $O(N^3)$ computational requirements of BP and achieve high frame rate, fast BP algorithms based on sub-aperture processing have been developed [2, 3] and applied to circular SAR processing [4]. After processing of sub-apertures, the sub-images are coherently summed up to form the frame image in full cross-range resolution. Different frame image formation techniques [5, 6] have been proposed to mitigate the high side-lobes effects of cross-range windowing.

However, the image quality is very sensible to sub-wavelength motion errors of platform position uncertainty. Due to the limit of accuracy of GPS systems and the inertial measurement units (IMU), a robust autofocus technique has to be put forward to fulfill the demands of Video-SAR image formation. However, because of the serious coupling between range and cross-range for circular path, the robust PGA [7] technique that is widely used in linear SAR scenario cannot readily be applied to Video-SAR. To overcome this problem, a method by image rotation has been proposed [8], which applies the PGA technique in the sub-aperture coordinate system (SCS) and then rotate the focused sub-images back to GCS. However, this method requires image rotations that is time-consuming and will introduce extra interpolation error. Ash et al. [9] proposed an autofocus method that can be combined with their ARBP [5] sequential imaging algorithm. However, for this method, the focusing criterion of the current sub-image is based on image sharpness, which imposes restrictions on the size of sub-aperture, thus further limits the efficiency of fast BP processing and storage overhead of intermediate images. In this paper, we proposed an autofocus method for Video-SAR based on echo regeneration of sub-apertures, which is independent of rotation of coordinate system and can accomplish sub-image focusing in GCS directly. The method is proved to be both accurate and efficient, which facilitates real-time sequential imaging of Video-SAR.

The rest of this paper is organized as follows. Firstly, the geometry of Video-SAR sub-aperture processing is introduced, followed by an analysis of the difference for Video-SAR imaging in GCS and SCS. Then a GCS autofocus method based on echo regeneration of sub-apertures is proposed. Afterwards results for simulated data are shown. Finally, the conclusions are presented.

27.2 Theory and Methodology

27.2.1 Geometry of Video-SAR by Sub-aperture Processing

Typical geometry of Video-SAR is illustrated in Fig. 27.1, the platform of Video-SAR flies along a circular flight path around a fixed scene centered at a constant elevation $_H$, with the sensor directed inward and perpendicular to the platform heading, which enables a persistent surveillance of the entire ROI. Here, R_g denotes

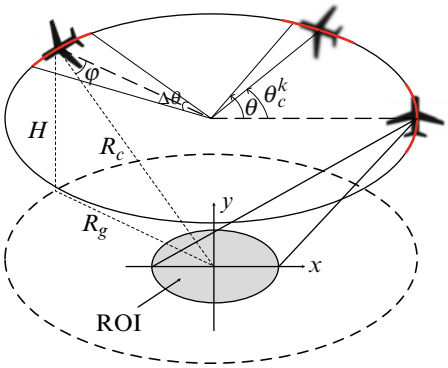

Fig. 27.1 Video-SAR geometry

the radius of the circular path while θ denotes the aspect angle. In order to utilize the fast BP algorithm, the entire circular aperture is divided into several sub-apertures. Each sub-aperture has an angular extent of $\Delta\theta$ and is centered at $\theta_c^k, \theta_c^k = k\Delta\theta$, where k denotes the index of sub-aperture.

However, to take the sequential imaging process as a whole, the sub-image and phase errors will behave differently in SCS and GCS. The geometry of SCS and GCS are illustrated in Fig. 27.2a, b respectively, and SCS equals GCS when $\theta_c^k = 0$.

For SCS, the image region and the coordinate axis $x^k - y^k$ rotates as the center aspect angle of the sub-aperture θ_c^k grows from 0 to 2π. For a fixed scatter (x_p, y_p) in GCS, it is located at (x_p^k, y_p^k) in the kth sub-image, resulting a series of rotated sub-images. In SCS, let (x_a^k, y_a^k) denote the position of platform in the kth sub-aperture and $R_p(x_a^k, y_a^k)$ denote the measured slant range from target (x_p^k, y_p^k) to the platform. If $\Delta\theta$ is small enough, each sub-aperture can be approximated as linear and parallel to the cross-range direction of each sub-image, thus the geometry of each sub-aperture can be approximate as linear Spotlight-SAR. By combing the motion error and the linear approximation error together and denoting it with $\varepsilon(y_a^k)$, $R_p(x_a^k, y_a^k)$ can be calculated as (27.1),

$$\begin{aligned} R_p\left(x_a^k, y_a^k\right) &\approx \sqrt{\left(R_g - x_p^k\right)^2 + \left(y_a^k - y_p^k\right)^2 + H^2} - \varepsilon\left(y_a^k\right) \\ &= R_p\left(y_a^k\right) - \varepsilon\left(y_a^k\right) \end{aligned} \tag{27.1}$$

where $R_p(y_a^k)$ is the measured slant range from the target to the ideal approximate linear sub-aperture in SCS. According to the theory of PGA, for linear Spotlight-SAR, the phase errors caused by motion error mainly manifest in the cross-range direction, and the corrupted range-compressed profile for sub-aperture $\widetilde{I}_p\left(x_a^k, y_a^k\right)$ is equivalent to the Fourier transform of sub-image $J(x^k, y^k)$ along the cross-range direction y^k, i.e.,

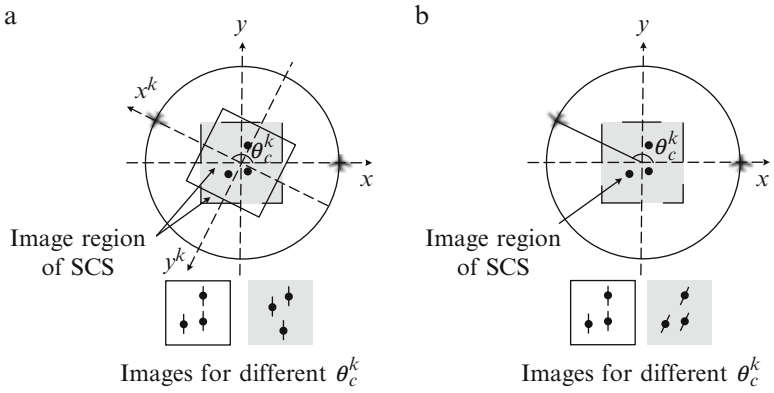

Fig. 27.2 (**a**) Geometry of SCS. (**b**) Geometry of GCS

$$\begin{aligned}\mathcal{F}_{y^k}\left\{J\left(x^k,y^k\right)\right\} &= \widetilde{I}_p\left(x_a^k,y_a^k\right)=\sigma_p\left(x_p^k,y_p^k\right)\exp\left\{-j2kR_p\left(x_a^k,y_a^k\right)\right\}\\ &\approx \sigma_p\left(x_p^k,y_p^k\right)\exp\left\{-j2kR_p\left(y_a^k\right)\right\}\exp\left\{j\phi_\varepsilon\left(y_a^k\right)\right\}\end{aligned} \tag{27.2}$$

where $\phi_\varepsilon(y_a^k)$ denotes the total phase error.

27.2.2 Autofocus in GCS

For GCS, the geometry of GCS is illustrated in Fig. 27.2b. The target is output in the fixed location (x_p, y_p) for kth sub-image $J^k(x, y)$, which is the rotated version of the corresponding sub-image $J(x^k, y^k)$ in SCS. Let $\square_k(\cdot)$ denotes the rotation transform from $x^k - y^k$ to $x - y$. According to the rotation property of Fourier transform,

$$\begin{aligned}&\mathcal{F}_y\left\{J^k(x,y)\right\}\\ &=\sigma_p\left(x_p,y_p\right)\exp\left\{-j2kR_p^k(x_a,y_a)+j\phi_\varepsilon\left(-x_a\sin\theta_c^k+y_a\cos\theta_c^k\right)\right\}\end{aligned} \tag{27.3}$$

where $R_p^k(x_a, y_a)$ is the measured slant range from the target to the kth ideal linear sub-aperture in GCS. From (27.3), in GCS, the target is output in the same location (x_p, y_p), which is accord with the demand of Video-SAR imaging and can avoid image rotations. However, the phase information and phase errors are functions of (x_a, y_a) and θ_c^k, which means the direction of image blur caused by phase errors changes for each sub-image and PGA is not applicable.

To solve the autofocusing problem in GCS, we proposed a new method for autofocus in Video-SAR based on echo regeneration [10] of sub-apertures. This

method can estimate the phase error in GCS directly, which is both computational efficient and accurate.

For the kth sub-aperture, with aspect angle $\theta \in \left[\theta_c^k - \frac{\Delta\theta}{2}, \theta_c^k + \frac{\Delta\theta}{2}\right]$. Assume the measurement error in the slant range $\varepsilon(\theta)$ is a function of aspect angle θ, $R_p(\theta)$ and $R(\theta)$ are the measured distance and the actual distance respectively, where $R_p(\theta)$ is described as (27.4)

$$R_p(\theta) = \sqrt{\left[x_a(\theta) - x_p\right]^2 + \left[y_a(\theta) - y_p\right]^2 + H^2} \tag{27.4}$$

According to SAR theory, the range-compressed profile received by the radar at aspect angle θ is the aggregate of echo from all the targets in the scene. Assuming the target P is a strong target and its location in the kth unfocused GCS sub-image $J^k(x, y)$ is (x_p, y_p), the regenerated range compressed profile from P is

$$\begin{aligned} I_{ps}(\theta) &= \iint W\left(x - x_p, y - y_p\right) J(x, y) \exp\left(-j2kR_{xy}(\theta)\right) dxdy \\ &\approx \sigma_p\left(x_p, y_p\right) \exp\left\{-j2kR_p(\theta) + j2k\varepsilon(\theta)\right\} \end{aligned} \tag{27.5}$$

where W is a window function, which preserves the information of the target P and rejects information from other targets and clutter. $R_{xy}(\theta)$ denotes the range from radar to ground pixel (x, y) , i.e.,

$$R_{xy}(\theta) = \sqrt{\left[x_a(\theta) - x\right]^2 + \left[y_a(\theta) - y\right]^2 + H^2} \tag{27.6}$$

When there is no measurement error, the ideal echo signal from P is

$$I_{p0}(\theta) = \exp\{-j2kR(\theta)\} = \exp\left\{-j2kR_p(\theta)\right\} \tag{27.7}$$

The phase error function can be obtained from the phase difference between $I_{ps}(\theta)$ and $I_{p0}(\theta)$,

$$\phi_\varepsilon(\theta) = \arg\left\{I_p(\theta) \cdot I_{p0}^*(\theta)\right\} = 2k\varepsilon(\theta) + \arg\left(\sigma_p\right) \tag{27.8}$$

After sub-aperture imaging in GCS, several strong targets can be selected from the unfocused sub-image. For each strong target, the phase error function can be estimated from (27.8), only with a constant bias of $\arg(\sigma_p)$, which has no influence on the amplitude of the output sub-image and can be reduced by averaging across several strong targets. For a given $_\theta$, assume the phase errors are the same for different targets, the received range-compressed profile of sub-aperture can be compensated and thus a more focused sub-image can be obtained.

27.3 Simulation and Results

In this section, simulation results are presented to prove the effectiveness of the proposed approach. The simulation parameters are shown in Table 27.1. The whole circular aperture is divided into 40 sub-apertures, that is $\Delta\theta = 9°$. The scene consists of 4 point targets, two strong and two weak, the distribution of targets are shown in Table 27.2.

Figure 27.3a, b are the 3rd and 17th sub-image in GCS respectively. In the two sub-images, the targets are output in the right position, but the image blur is in different slant direction. Figure 27.3c, d are the 3rd and 17th sub-image after using our autofocus method in GCS. After autofocus process, all the targets are located accurately and the image quality is enhanced significantly.

The actual phase error and estimated phase error of the whole aperture are shown in Fig. 27.4, it is obviously that our autofocus algorithm of Video-SAR can estimate the phase errors quite accurately.

To further prove the validity of our method, we applied it to Gotcha Public Release dataset [11], the results are shown in Fig. 27.5.

The data of aspect angle form 0–5° and 55–60° are extracted from one path of Gotcha as measured echo of two sub-apertures, after that different phase error are added. Figure 27.5a, b are the unfocused sub-image before autofocusing processing, Fig. 27.5c, d are the corresponding focused sub-images by our method. It is shown that our method improved the image quality remarkably and is applicable to real data.

Table 27.1 Simulation parameters

Parameters	Value
Center frequency	0.5 GHz
Band width	300 MHz
Platform height	4 km
Trajectory radius	4 km
Scene radius	25 m

Table 27.2 Distribution of targets

Targets	Range (m)	Cross-range (m)	Reflectivity
Target 1 (Strong)	0	0	1
Target 2 (Strong)	3	−15	0.85
Target 3 (weak)	−15	−10	0.47
Target 4 (weak)	15	15	0.31

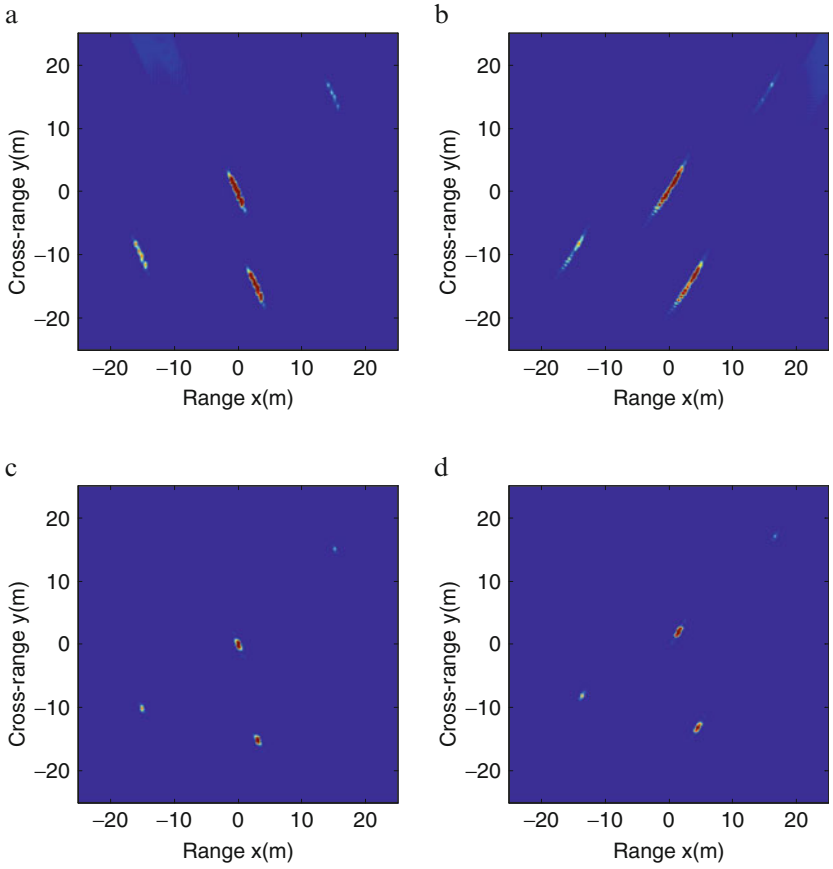

Fig. 27.3 Simulation results. (**a**) Original third sub-image. (**b**) Original 17th sub-image. (**c**) Third sub-image after autofocus. (**d**) Seventeenth sub-image after autofocus

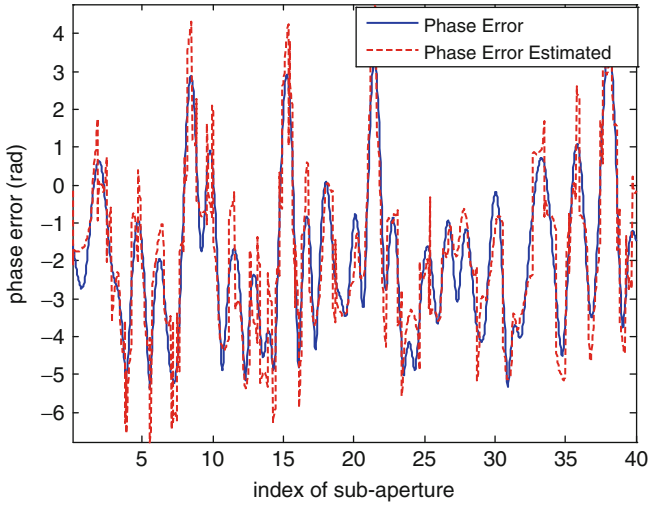

Fig. 27.4 Actual and estimated phase error

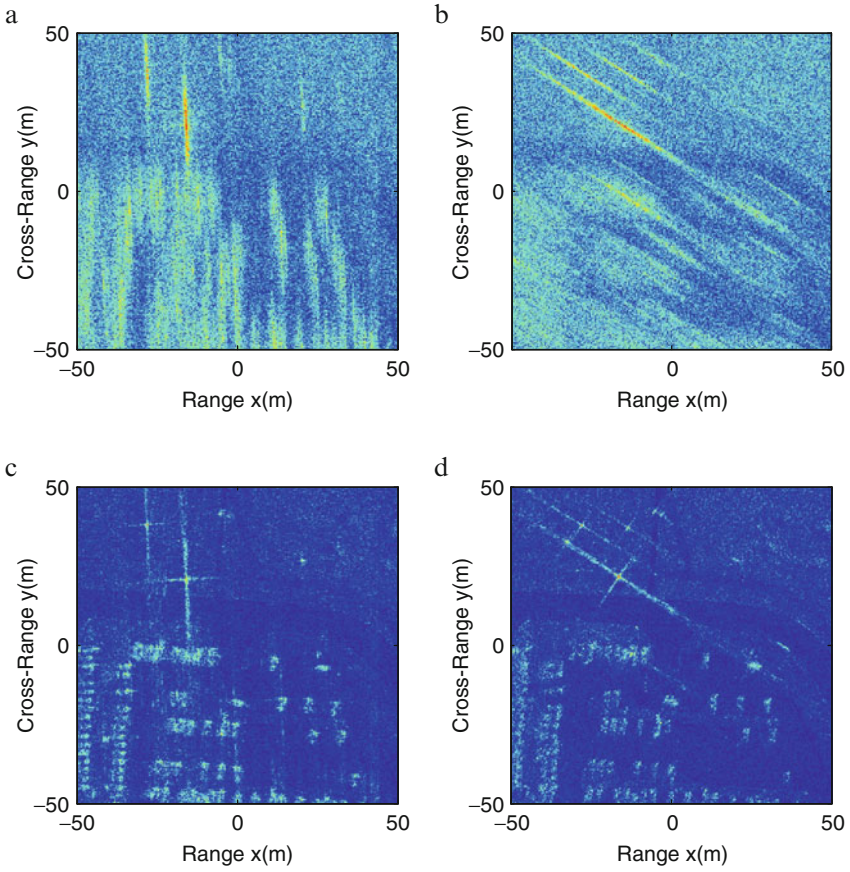

Fig. 27.5 Results of Gotcha data set

Conclusion

In this paper, we have presented a new autofocus method for sub-aperture processing of Video-SAR. This method takes the space-variant property of circular Video-SAR into account and can accomplish autofocusing of unfocused sub-image in GCS directly, which avoids rotation of sub-image and is proven to be both accurate and efficient.

Acknowledgments This work is supported in part by the National Natural Science Foundation of China under Grants 61271287, 61371048, 61301265.

References

1. Gorham LRA, Moore LJ (2010) SAR image formation toolbox for MATLAB. In: SPIE algorithms synthetic aperture radar imagery. International Society for Optics and Photonics, pp 769906–769906
2. Yegulalp AF (1999) Fast backprojection algorithm for synthetic aperture radar. In: Radar conference, 1999. The record of the 1999 IEEE, pp 60–65
3. Gorham LA, Majumder UK, Buxa P et al (2006) Implementation and analysis of a fast backprojection algorithm. In: SPIE algorithms synthetic aperture radar imagery, defense and security symposium. International Society for Optics and Photonics, pp 62370G–62370G
4. Ponce O, Prats P, Rodriguez-Cassola M et al (2011) Processing of circular SAR trajectories with fast factorized back-projection. In: Geoscience and Remote Sensing Symposium, pp 3692–3695
5. Moses RL, Ash JN (2008) Recursive SAR imaging. In: Proceedings of the SPIE Algorithms Synthetic Aperture Radar Imagery, pp 69700P–69700P
6. Hawley RW, Garber WL (2011) Aperture weighting technique for video synthetic aperture radar. In: SPIE Defense, Security, and Sensing, pp 805107–805107
7. Wahl DE, Eichel PH, Ghiglia DC et al (1994) Phase gradient autofocus-a robust tool for high resolution SAR phase correction. In: IEEE Trans Aerosp Electron Syst, pp 827–835
8. Linnehan R, Miller J, Bishop E, Horndt V (2013) An autofocus technique for video-SAR. In: SPIE algorithms synthetic aperture radar imagery, SPIE defense, security, and sensing. International Society for Optics and Photonics, pp 874608–874608
9. Ash JN (2012) An autofocus method for backprojection imagery in synthetic aperture radar. Geosci Remote Sens Lett 9:104–108
10. Lin Y, Hong W, Tan WX, Wang YP, Wu YR (2011) A novel PGA technique for circular SAR based on echo regeneration. In: IEEE CIE international conference on vol 1. IEEE
11. Gotcha Volumetric SAR data set, Version 1.0 (2007) https://www.sdms.afrl.af.mil/DataSets/gotcha.index.php

Part III
Mobile Networks, Wireless Communication

Chapter 28
Bandwidth Allocation Based on Personality Traits on Smartphone Usage and Channel Condition

Junjie Chen, Qilian Liang, and Jie Wang

Abstract A bandwidth allocation method based on smartphone users' personality traits and channel condition is studied in a unified mathematical framework in this paper. Based on the relationship between automatically extracted behavioral characteristics derived from rich smartphone data and Big-Five personality traits, the service provider could estimate each user's probability of each personality trait using diagnostic inference, and then based on predictive inference to calculate each user's usage of bandwidth using Bayesian Network. This could help the service provider to better allocate the smartphone bandwidth. For our proposed smart bandwidth allocation scheme, both the outage capacity and the outage probability are studied in fading channel. The service provider could adjust the bandwidth allocated further on account of the real channel condition, which makes our proposed algorithm more robust.

Keywords Bandwidth allocation • Big data • Bayesian network inference • Personality traits • Channel condition

28.1 Introduction

Smartphones are everywhere these days, and they have become an indispensable part of our daily lives. As the smartphone supports interpersonal interaction, smartphone data might be a function of personality. The study of the relationship between mobile phone usage and user personality has attracted a lot of researchers. Personality traits

J. Chen (✉) • Q. Liang
Electrical Engineering, University of Texas at Arlington, 416 Yates St, Arlington, TX 76019, USA
e-mail: junjie.chen@mavs.uta.edu; liang@uta.edu

J. Wang
Department of Computer Science, University of Massachusetts Lowell, Lowell, MA 01854, USA
e-mail: wang@cs.uml.edu

J. Mu et al. (eds.), *The Proceedings of the Third International Conference on Communications, Signal Processing, and Systems*, Lecture Notes in Electrical Engineering 322, DOI 10.1007/978-3-319-08991-1_28

can predict the patterns of mobile phone use was concluded in [1] by self reported data. In 2011, a paper was published concerning changes in consumer privacy in relation to smartphones [2], which discussed research that found correlations between styles of phone usage and personality traits of users. Papers [3] and [4] studied the impact of the "Big Five" personality traits on smartphone ownership and use, which was the first study that specifically examines smartphone use.

These studies facilitate further research on the usage of personality traits for personalizing services on smartphone users. Although a lot of approaches of efficiently using spectrum was studied [5–9], with the increasing consumption of data and limited bandwidth [18, 19], the best way to solve this problem should be efficiently and effectively allocation the bandwidth dynamically. Bayesian Network (BN) is an important approach of prediction in data analysis [10, 11]. BN could be drawn based on the relationship concluded in [2–4]. Personalizing bandwidth allocation could be done based on smartphone users' personality traits, resulting in business intelligence, a smart and efficient usage of the limited bandwidth.

Main Contributions: A bandwidth allocation method based on smartphone users' personality traits and channel condition is studied in a unified mathematical framework in this paper. Based on the relationship between automatically extracted behavioral characteristics derived from rich smartphone data and Big-Five personality traits, the corresponding Bayesian Network could be drawn. Further, the service provider could estimate each user's probability of each personality trait using diagnostic inference, and then based on predictive inference to calculate each user's usage of bandwidth. Personalizing bandwidth allocation could be done based on smartphone users' personality traits, resulting in a smart and efficient usage of the limited bandwidth. For our proposed smart bandwidth allocation scheme, both the outage capacity and the outage probability are studied in fading channel. The service provider could adjust the bandwidth allocated further on account of the real channel condition, which makes our proposed algorithm more robust.

The remainder of this paper is organized as follows. In Sect. 28.2, we describe the principle of our proposed smart bandwidth allocation scheme. The outage throughput capacity in fading channel is analyzed as well, which helps the service provider to adjust the allocated bandwidth based on real channel condition. Numerical results are shown in Sect. 28.3, and conclusions are given in section "Conclusions".

28.2 Bandwidth Allocation Scheme

28.2.1 Bayesian Network Modeling

Extraverts are sociable, gregarious and ambitious, who are optimistic and seek out new opportunities and excitement[12]. Agreeable people are sympathetic, good natured, cooperative and forgiving [13, 14]. Conscientious people are strong-willed, deliberate, and reliable [12]. People score high in neuroticism tend to be fearful, sad, embarrassed, distrustful, and have difficulty managing stress [14, 15].

People high in openness have flexibility of thought and tolerance of new ideas, and they actively seek out new and varied experiences and value change [15, 17].

The corresponding BN could be drawn based on the relationship concluded in [2–4] as shown in Fig. 28.1. Extroverts had heavy usage of calendars and office apps and their smartphone habits were with less games and Internet functions. Less agreeable people were heavier users of office, Internet, Video/Audio/Music, mail, calendar and SMS apps. Less conscientious people were less likely to use multimedia and YouTube applications. Emotional stable people were found to use less of office and calendar apps. Curious people had less usage of office, calendar and SMS apps.

The conditional probability tables (CPT) of "Calls", "Youtube", "Video/Audio/Music", "SMS", "Mail" and "Internet" could be calculated based on the results in [2–4]. For short, we only use the first three letters to represent each node, for example, "LBW" stands for "Less BW".

28.2.2 Bandwidth Allocation: Bayesian Network Inference

Both diagnostic inference and predictive inference could be calculated based on personality traits and their usage of smartphone apps in Fig. 28.1. Diagnostic inference provides the probability of each personality trait with the data of each user's bandwidth usage, for example, what is the probability of one user's personality traits if this smartphone user occupies above 10 GB data per bill cycle? Differently, Predictive inference calculate the probability of the usage of bandwidth based on each node's parent nodes, for example, if a user score high on extraversion, what is the probability of this user occupies more bandwidth?

Since the structure of a BN implies that the value of a particular node is conditional only on the values of its parent nodes, we can simplify its joint probability expressions.

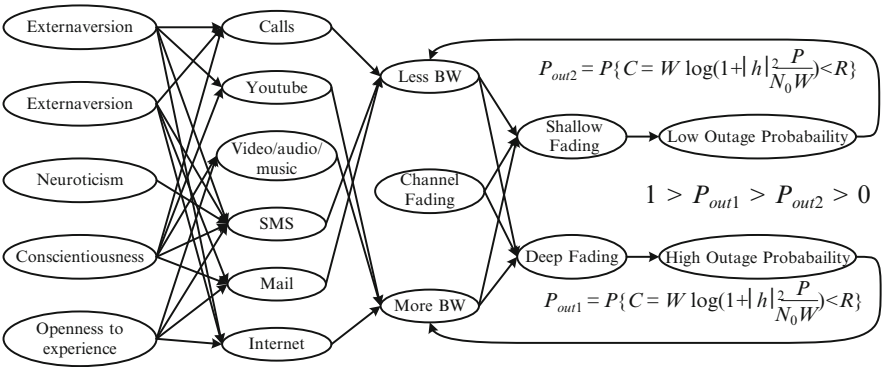

Fig. 28.1 Bandwidth allocation scheme on personality traits and channel condition

$$
\begin{aligned}
&P(Ext, Agr, Neu, Con, Ope, Cal, You, Vid, SMS, Mai, Int, LBW) \\
&\quad = P(Ext)P(Agr)P(Neu)P(Con)P(Ope) \cdot P(Cal|Ext, Agr, Neu, Con, Ope) \\
&\qquad \cdot P(You|Ext, Agr, Neu, Con, Ope) \cdot P(Vid|Ext, Agr, Neu, Con, Ope) \\
&\qquad \cdot P(SMS|Ext, Agr, Neu, Con, Ope) \cdot P(Mai|Ext, Agr, Neu, Con, Ope) \\
&\qquad \cdot P(Int|Ext, Agr, Neu, Con, Ope) \cdot P(LBW|C, Y, V, S, M, I)
\end{aligned} \tag{28.1}
$$

28.2.2.1 Diagnostic Inference

First, let's look at diagnostic inference. Here, we only show one example of given "LBW", the probability of Extraversion. For other probability with other personality traits, the principal is the same.

$$
P(Ext = y|LBW = y) = \frac{P(Ext = y, LBW = y)}{P(LBW = y)} \tag{28.2}
$$

where

$$
\begin{aligned}
&P(Ext = y, LBW = y) = \sum P(Ext = y)P(Agr)P(Neu)P(Con)P(Ope) \\
&\quad \cdot P(Cal|Ext = y, Agr, Neu, Con, Ope) \cdot P(You|Ext = y, Agr, Neu, Con, Ope) \\
&\quad \cdot P(Vid|Ext = y, Agr, Neu, Con, Ope) \cdot P(SMS|Ext = y, Agr, Neu, Con, Ope) \\
&\quad \cdot P(Mai|Ext = y, Agr, Neu, Con, Ope) \cdot P(Int|Ext = y, Agr, Neu, Con, Ope) \\
&\quad \cdot P(LBW = y|Cal, You, Vid, SMS, Mai, Int)
\end{aligned} \tag{28.3}
$$

and

$$
\begin{aligned}
&P(LBW = y) = \sum P(Ext)P(Agr)P(Neu)P(Con)P(Ope) \cdot P(Cal|Ext, Agr, Neu, Con, Ope) \\
&\quad \cdot P(You|Ext, Agr, Neu, Con, Ope) \cdot P(Vid|Ext, Agr, Neu, Con, Ope) \\
&\quad \cdot P(SMS|Ext, Agr, Neu, Con, Ope) \cdot P(Mai|Ext, Agr, Neu, Con, Ope) \\
&\quad \cdot P(Int|Ext, Agr, Neu, Con, Ope) \cdot P(LBW = y|Cal, You, Vid, SMS, Mai, Int)
\end{aligned} \tag{28.4}
$$

28.2.2.2 Predictive Inference

Similarly, the predictive inference could be calculated for each personality trait. We also only show one example of knowing a user's personality of extraversion, the probability of less BW assignment as

$$
P(LBW = y|Ext = y) = \frac{P(Ext = y, LBW = y)}{P(Ext = y)} \tag{28.5}
$$

We assume the original probability for all personality traits is unknown, that is $P(Ext = y) = 0.5$, $P(Agr = y) = 0.5$, $P(Neu = y) = 0.5$, $P(Con = y) = 0.5$, and $P(Ope = y) = 0.5$.

28.2.3 Bandwidth Allocation in Fading Channel

As we know that the capacity of wireless channels is also based on channel conditions[16]. We can build a smart bandwidth allocation scheme that adaptively allocates channel bandwidth to each smartphone user depending on what the current channel condition is.

For a bandwidth-limited system, the capacity is $C = Wlog(1 + |h|^2 \frac{P}{N_0 W})$ [16], where h is the fading channel gain, and $|h|$ is the amplitude of h. W is the channel bandwidth. P is a given received power, and additive white Gaussian noise power spectral density is $N_0/2$.

Suppose the transmitter encodes data at a rate R bits/s. If h is small that $C < R$, then the system is in outage, with outage probability [16]

$$P_{out}(R) = Pr\left\{ Wlog\left(1 + |h|^2 \frac{P}{N_0 W}\right) < R \right\} \tag{28.6}$$

For fading channels, we consider ε-outage capacity C_ε, which is the largest transmission rate R such that $P_{out}(R)$ is less than ε.

$$C_\varepsilon = Wlog\left(1 + F^{-1}(1-\varepsilon)\frac{P}{N_0 W}\right) \quad bit/s \tag{28.7}$$

where $F(x) = Pr\left\{|h|^2 > x\right\}$.

When h is complex Gaussian $\mathscr{CN}(0,1)$, the outage probability $P_{out}(R)$ for Rayleigh fading

$$\begin{aligned} P_{out}(R) &= Pr\left\{ Wlog\left(1 + |h|^2 \frac{P}{N_0 W}\right) < R \right\} \\ &= Pr\left\{ |h| < \sqrt{\frac{\left(2^{\frac{R}{W}} - 1\right) N_0 W}{P}} \right\} \overset{(a)}{\approx} \frac{\left(2^{\frac{R}{W}} - 1\right) N_0 W}{P} \end{aligned} \tag{28.8}$$

where (a) follows from the fact that $|h|$ follows Rayleigh distribution. Therefore,

$$Pr\left\{|h| < \sqrt{\frac{\left(2^{\frac{R}{W}}-1\right)N_0W}{P}}\right\} = \int_0^{\sqrt{\frac{\left(2^{\frac{R}{W}}-1\right)N_0W}{P}}} f(|h|)d|h| = 1 - exp\left(-\frac{\left(2^{\frac{R}{W}}-1\right)N_0W}{P}\right) \approx \frac{\left(2^{\frac{R}{W}}-1\right)N_0W}{P} \tag{28.9}$$

where the last step follows from the fact of the Taylor series for the exponential function e^{-x} that $e^{-x} \approx 1 - x$.

Above is the relationship of the outage probability with bandwidth W in our smart bandwidth allocation scheme. Next, let's think about the effect of channel fading.

(1). For deep fading, $|h| \to 0$, with high probability that $C < R$, and the system will be in outage, more bandwidth W should be allocated to reduce the outage probability, as shown in Fig. 28.1.

$$P_{out1}(R) = Pr\left\{Wlog\left(1 + |h|^2\frac{P}{N_0W}\right) < R\right\} \tag{28.10}$$

(2). For shallow fading, the channel quality is good, so with high probability that $C > R$, reliable communication with small error probability could be achieved. Therefore, taking advantage of the better channel conditions, less bandwidth W could be assigned.

$$P_{out2}(R) = Pr\left\{Wlog\left(1 + |h|^2\frac{P}{N_0W}\right) < R\right\} \tag{28.11}$$

with

$$0 < P_{out2}(R) < P_{out1}(R) < 1 \tag{28.12}$$

28.3 Numerical Results

Based on one smartphone user's data usage in one billing cycle, the service provider could calculate this user's probability of each personality trait using diagnostic inference, and then based on predictive inference to calculate this user's usage of bandwidth in the next billing cycle. We can see that both diagnostic inference and

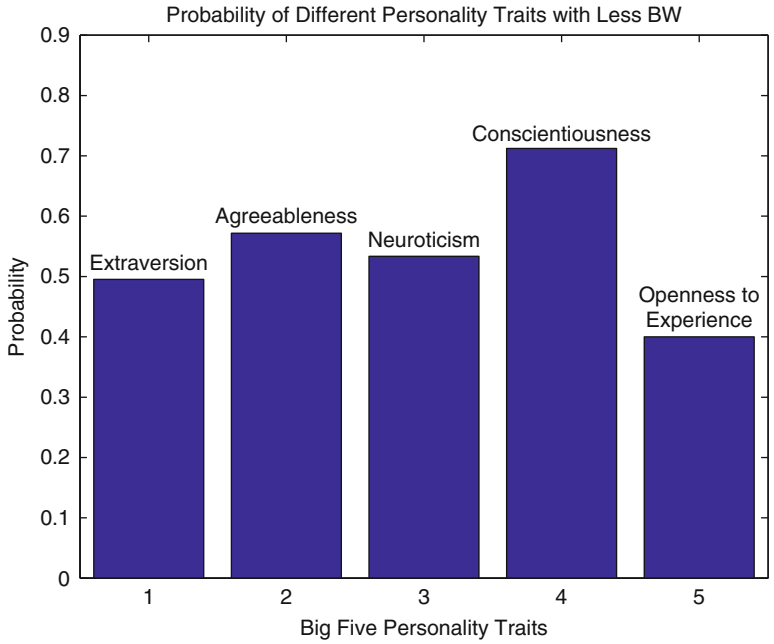

Fig. 28.2 Diag. prob.-lessBW

predictive inference could help the service provider to better allocate the smartphone bandwidth based on each user's personality.

Figure 28.2 show the diagnostic inference for the probability of personality traits with less bandwidth allocated. We can observe that $P(Con = y|LBW = y) = 0.7123$ with the highest probability, which means that when less bandwidth is occupied, with the probability of 0.7123 that the user scoring high on conscientiousness.

In the simulation, we assume the original probability for all personality traits is unknown, that is $P(Ext = y) = 0.5$, $P(Agr = y) = 0.5$, $P(Neu = y) = 0.5$, $P(Con = y) = 0.5$, and $P(Ope = y) = 0.5$.

Figure 28.3 give the diagnostic inference for the probability of personality traits with more bandwidth. It can be observed that $P(Ope = y|MBW = y) = 0.5426$, which means that when more bandwidth is allocated, with the probability of 0.5426 that the user scoring high on openness. We can notice that with more bandwidth allocated, users are more likely to score high on openness.

Figures 28.4 and 28.5 provide the predictive inference probability. Given a user's personality trait, the probability of this user occupying less bandwidth is shown. For an extravert person, the probability of less bandwidth occupation is 0.2962, while the probability of more bandwidth occupation is 0.7038. For an open-minded user, the case of less bandwidth is 0.2392, and more bandwidth is 0.7608. Open-minded user has the highest probability to occupy more bandwidth.

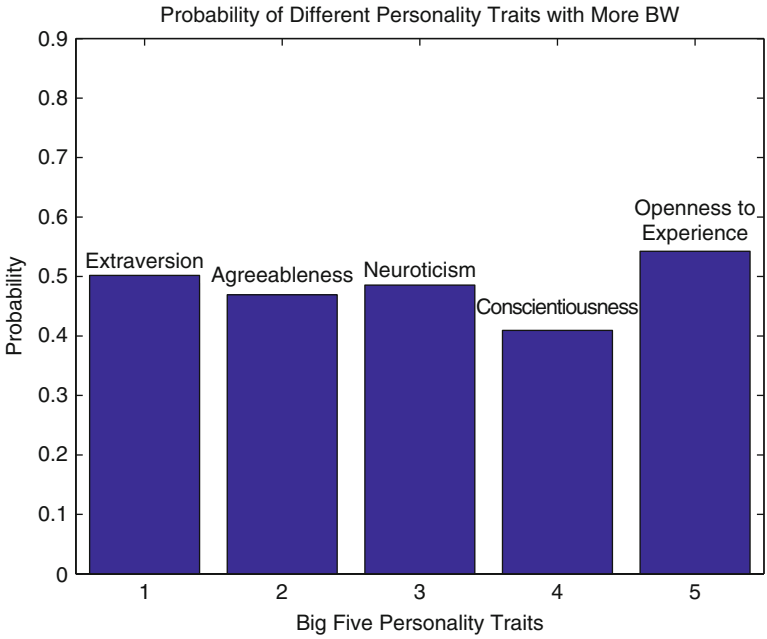

Fig. 28.3 Diag. prob.-moreBW

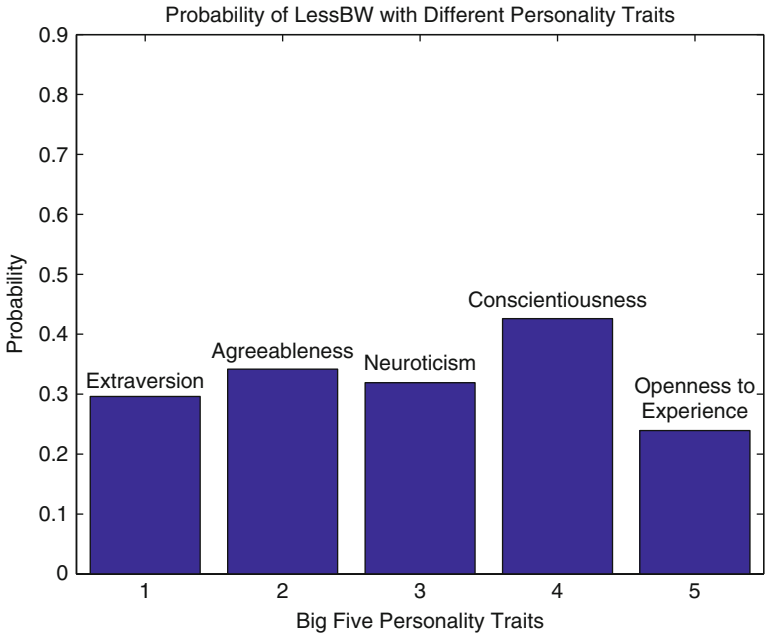

Fig. 28.4 Pred. prob.-lessBW

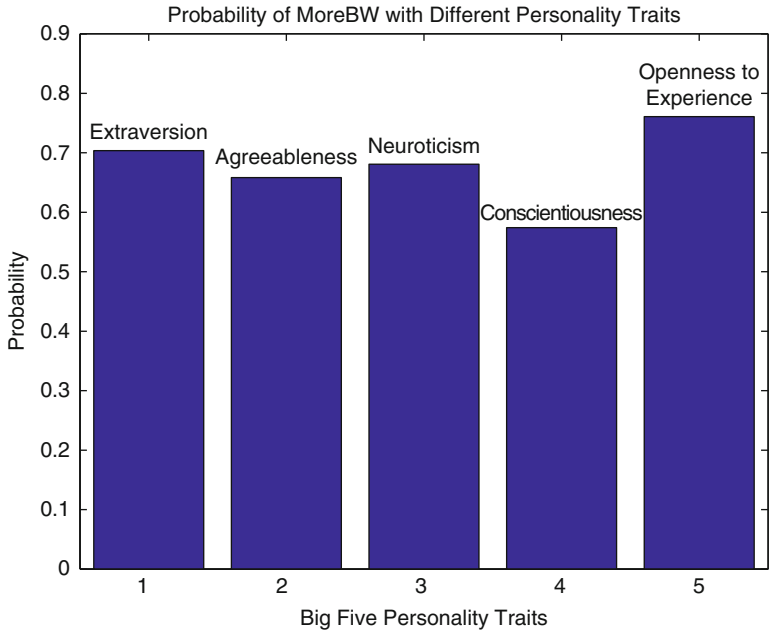

Fig. 28.5 Pred. prob.-moreBW

Manufacturers and service providers in the cell phone industry could provide more personal service to each user based on the results calculated. For example, for two smartphone users A and B, in the last billing cycle, user A used 3 GB data, and the other one used 20 MB data, with high probability that user A is open-minded, and user B is conscientious. Smartphone service provider could store each user's personality trait and provide the corresponding service to each user.

Conclusions

A bandwidth allocation method based on smartphone users' personality traits and channel condition is studied in a unified mathematical framework. Based on one user's data usage, the service provider could estimate this user's probability of each personality trait using diagnostic inference, and then based on predictive inference to calculate this user's usage of bandwidth in the future. Personalizing bandwidth allocation could be done based on smartphone users' personality traits, resulting in a smart and efficient usage of the limited bandwidth.

For our proposed smart bandwidth allocation scheme, both the outage capacity and the outage probability are studied in fading channel. In deep fading scenario, the outage probability will become too high to support the service. One possible solution is to assign more bandwidth to guarantee the service performance.

Acknowledgements This work was supported in part by U.S. Office of Naval Research under Grants N00014-13-1-0043, N00014-11-1-0071, N00014-11-1-0865, and U.S. National Science Foundation under Grants CNS-1247848, CNS-1116749, CNS-0964713.

References

1. Butt S, Phillips JG (2008) Personality and self reported mobile phone use. Comput Human Behav 24(2):346–360
2. Chittaranjan G, Blom J, Gatica-Perez D (2013) Mining large-scale smartphone data for personality studies. Pers Ubiquitous Comput 17(3):433–450
3. Lane W, Manner C (2011) The impact of personality traits on smartphone ownership and use. Int J Bus Soc Sci 2(17):22–28
4. Lane W, Manner C (2012) The influence of personality traits on mobile phone application preferences. J Econ Behav Stud 4(5):252–260
5. Liu T, Chen J (2009) Joint downlink transmit and receive beamforming under per-antenna power constraints. In: IEEE 7th international conference on information, communications and signal processing, 2009, pp 1–5
6. Chen J, Liang Q, Zhang B, Wu X (2013) Spectrum efficiency of nested sparse sampling and co-prime sampling. EURASIP J Wirel Commun Netw 2013(1):47
7. Chen J, Liang Q, Choi H-A (2012) Spectrum efficiency of nested sparse sampling. In: Wireless algorithms, systems, and applications. Springer, Berlin/Heidelberg, pp 574–583
8. Chen J, Liang Q, Wang J (2013) Secure transmission for big data based on nested sampling and coprime sampling with spectrum efficiency. Secur Commun Netw. doi:10.1002/sec.785
9. Chen J, Liang Q, Zhang B, Wu X (2013) A new secure transmission for big data based on nested sampling and coprime sampling. In: The 2nd international conference on communications, signal processing, and systems (CSPS'13)
10. Bouchaffra D (2012) Mapping dynamic bayesian networks to-shapes: application to human faces identification across ages. IEEE Trans Neural Netw Learn Syst 23(8):1229–1241
11. Neapolitan RE (2004) Learning bayesian networks. Pearson Prentice Hall, Upper Saddle River
12. McElroy JC, Hendrickson AR, Townsend AM, DeMarie SM (2007) Dispositional factors in internet use: personality versus cognitive style. MIS Q 31:809–820
13. Phillips JG, Butt S, Blaszczynski A (2006) Personality and self-reported use of mobile phones for games. CyberPsychol Behav 9(6):753–758
14. Ehrenberg A, Juckes S, White KM, Walsh SP (2008) Personality and self-esteem as predictors of young people's technology use. CyberPsychol Behav 11(6):739–741
15. Devaraj S, Easley RF, Crant JM (2008) Research note - how does personality matter? Relating the five-factor model to technology acceptance and use. Inf Syst Res 19(1):93–105
16. Tse D, Viswanath P (2005) Fundamentals of wireless communication. Cambridge University Press, Cambridge, ISBN 0521845270
17. Russell SJ, Norvig P (2010) Artificial intelligence: a modern approach, 3rd edn. Pearson Education, Prentice Hall, Upper Saddle River
18. Chen J, Liang Q (2014) Rate distortion performance analysis of nested sampling and coprime sampling. EURASIP J Adv Signal Process 1–8
19. Chen J, Liang Q, (2013) Theoretical performance limits for compressive sensing with random noise. In: Global telecommunications conference (GLOBECOM, (2013) Atlanta. December 2013:3400–3405

Chapter 29
Frequency-Domain Equalization of Channel Inconsistency for Wideband Navigation Anti-jamming Receiver Based on Uniform Circular Array

Shangce Yuan, Zishu He, and Donghui Huang

Abstract The channel inconsistency will generally degrade the performance of a multichannel system. So it's necessary to equalize the mismatch of each channel. In the navigation anti-jamming receiver based on array antennas, the channel inconsistency will lead to a distortion of the beam and degrade the anti-jamming capability. This paper proposes a frequency-domain equalization method to compensate the channel inconsistency and improve the anti-jamming capability of the receiver. The simulations show that the method is highly effective and can improve the system performance.

Keywords Channel Inconsistency • Channel Equalizer • Navigation anti-jamming Receiver

29.1 Introduction

Global navigation satellite system (GNSS) plays an important role in civilian and military fields. As the GNSS-signal is susceptible to interference, the anti-jamming technologies based on digital beam forming (DBF) of array antennas have been widely studied [1].

But the mismatch between channels will generally lead to a distortion of the array beam and degrade the anti-jamming performance of DBF [2, 3].

Time-domain equalization methods have been studied in [3, 4]. By utilizing adaptive algorithm, time-domain equalization can help calibrate the channel inconsistency effectively. But time-domain equalization is generally not accurate enough.

S. Yuan (✉) • Z. He • D. Huang
School of Electronic Engineering, University of Electronic Science and Technology of China, Chengdu, Sichuan 611731, P. R. China
e-mail: ysctrnt@126.com

J. Mu et al. (eds.), *The Proceedings of the Third International Conference on Communications, Signal Processing, and Systems*, Lecture Notes in Electrical Engineering 322, DOI 10.1007/978-3-319-08991-1_29

Frequency-domain equalization method is presented in [5]. By taking advantage of Fast Fourier transform (FFT), the complexity of implementation can be greatly reduced.

Considering wideband navigation anti-jamming receiver based on uniform circular array, this paper proposes a frequency-domain equalization method. By adding an equalization filter after each channel and assuming one channel is the reference one, it makes the frequency response of the channel to be calibrated approximate that of the reference one, utilizing the least squares criterion. An improved method is also proposed to increase the approximation accuracy within the system band. The comparison of the simulation results shows that this method can equalize the channels effectively and increase the anti-jamming performance.

29.2 Equalization Model

The channel equalization model is showed in Fig. 29.1. T is the sampling interval, and L is the order of the equalization filter (assuming L is an odd number). The delay time of reference channel can be denoted by $D = (L-1)T/2$. Since the finite impulse response (FIR) filter is stable and causal and has linear phase response, FIR filter is chosen as the equalizer. The power divider feeds each channel a wideband correcting signal, and which is often chosen as the linear frequency modulation (LFM) signal. The process of equalization is to calculate the weights of equalizers, so that the frequency response of the channel to be calibrated can approximate that of the reference one within the receiver band.

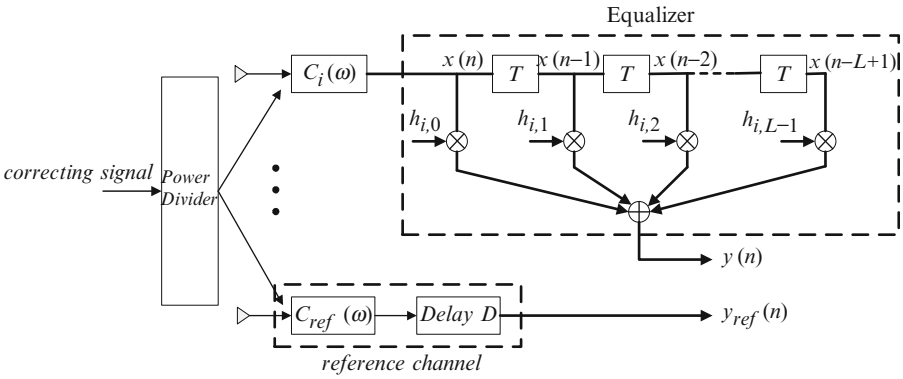

Fig. 29.1 Equalization mode of multi-channel system

29.3 Frequency-Domain Equalization Method

We generally choose the channel which has the least fluctuation in frequency response as the reference channel. And then make a least squares approximation of the frequency response between the reference channel and the channel to be calibrated.

29.3.1 Conventional Frequency-Domain Equalization Method

The discrete frequency response of the reference channel and the i channel to be calibrated can be denoted respectively by

$$\begin{array}{l} C_{ref}(k), k = 0, 1, \ldots, N-1 \\ C_i(k), k = 0, 1, \ldots, N-1 \end{array} \tag{29.1}$$

Where N is the point to do Discrete Fourier Transform (DFT).

Since the order of calibration filter is $L(L < N)$, the group delay of calibration filter can be denoted by $D = (L-1)T/2$. A filter is added into the reference channel to compensate the group delay. And the discrete frequency response of which can be denoted by

$$H_{ref}(k) = e^{-j\frac{2\pi kD}{N}}, k = 0, 1, \ldots, N-1 \tag{29.2}$$

So the desired discrete frequency response of the calibration filter is expressed as

$$H_i(k) = \frac{C_{ref}(k)H_{ref}(k)}{C_i(k)}, k = 0, 1, \ldots, N-1 \tag{29.3}$$

It can be seen that the desired discrete frequency response of the equalization filter can be calculated by $C_{ref}(k)$ and $C_i(k)$, which can be estimated by doing N-point DFT of the received signal in the case of feeding correcting signal.

The actual discrete frequency response of the equalization filter is

$$\hat{H}_i(k) = \sum_{l=0}^{L-1} h_{i,l} e^{-j\frac{2\pi}{N}kl} = \boldsymbol{a}^T(k)\boldsymbol{h}_i, k = 0, 1, \ldots, N-1 \tag{29.4}$$

Where

$$\boldsymbol{a}(k) = \left[1, e^{-j\frac{2\pi}{N}k}, e^{-j\frac{2\pi}{N}2k}, \ldots, e^{-j\frac{2\pi}{N}(L-1)k}\right]^T, k = 0, 1, \ldots, N-1 \tag{29.5}$$

$$\boldsymbol{h}_i = [h_{i,0}, h_{i,1}, \ldots, h_{i,L-1}] \tag{29.6}$$

Then we make an approximation between $\hat{H}_i(k)$ and $H_i(k)$, and the approximation error vector of i channel is denoted by

$$\boldsymbol{e}_i = \boldsymbol{A}\boldsymbol{h}_i - \boldsymbol{H}_i \tag{29.7}$$

Where

$$\boldsymbol{e}_i = [e_i(0), e_i(1), \ldots, e_i(N-1)]^T \tag{29.8}$$

$$\boldsymbol{H}_i = [H_i(0), H_i(1), \ldots, H_i(N-1)]^T \tag{29.9}$$

$$\boldsymbol{A} = \begin{bmatrix} \boldsymbol{a}^T(0) \\ \boldsymbol{a}^T(1) \\ \vdots \\ \boldsymbol{a}^T(N-1) \end{bmatrix} = \begin{bmatrix} 1 & 1 & \cdots & 1 \\ 1 & e^{-j\frac{2\pi}{N}} & \cdots & e^{-j\frac{2\pi(L-1)}{N}} \\ \vdots & \vdots & \cdots & \vdots \\ 1 & e^{-j\frac{2\pi(N-1)}{N}} & \cdots & e^{-j\frac{2\pi(N-1)(L-1)}{N}} \end{bmatrix} \in \mathbb{C}^{N\times L} \tag{29.10}$$

According to the least squares criterion, the cost function is constructed as

$$J = \min_{\boldsymbol{h}_i} \sum_{k=0}^{N-1} \left|\boldsymbol{e}_i(k)\right|^2 = \min_{\boldsymbol{h}_i} \|\boldsymbol{e}_i\|^2 = \min_{\boldsymbol{h}_i} \|(\boldsymbol{A}\boldsymbol{h}_i - \boldsymbol{H}_i)\|^2 = \boldsymbol{e}_i^H \boldsymbol{e}_i \tag{29.11}$$

Here, $\|\bullet\|$ denotes the Frobenius norm. The expanded form of the cost function is

$$\begin{aligned} \boldsymbol{J} &= \left(\boldsymbol{h}_i^H \boldsymbol{A}^H - \boldsymbol{H}_i^H\right)(\boldsymbol{A}\boldsymbol{h}_i - \boldsymbol{H}_i) \\ &= \boldsymbol{h}_i^H \boldsymbol{A}^H \boldsymbol{A}\boldsymbol{h}_i - \boldsymbol{h}_i^H \boldsymbol{A}^H \boldsymbol{H}_i - \boldsymbol{H}_i^H \boldsymbol{A}\boldsymbol{h}_i + \boldsymbol{H}_i^H \boldsymbol{H}_i \end{aligned} \tag{29.12}$$

To get the minimum of J, we assume that

$$\nabla J = 2\boldsymbol{A}^H \boldsymbol{A}\boldsymbol{h}_i - 2\boldsymbol{A}^H \boldsymbol{H}_i = 0 \tag{29.13}$$

As $L < N$, $\boldsymbol{A}^H\boldsymbol{A}$ is nonsingular, the coefficients of the calibration filter is

$$\hat{\boldsymbol{h}}_i = \left(\boldsymbol{A}^H \boldsymbol{A}\right)^{-1} \boldsymbol{A}^H \boldsymbol{H}_i \tag{29.14}$$

29.3.2 Improved Method of Frequency-Domain Equalization

In the actual process of equalization, since the order of the equalizer is limited, we often hope to have higher approximation accuracy within the system band and lower accuracy outside the system band. The cost function can be modified as

$$J = \min_{\boldsymbol{h}_i} \|\boldsymbol{\Gamma e}_i\|^2 = \min_{\boldsymbol{h}_i} \|\boldsymbol{\Gamma}(\boldsymbol{A h}_i - \boldsymbol{H}_i)\|^2 \tag{29.15}$$

Where

$$\boldsymbol{\Gamma} = diag\{w_0, w_1, \ldots, w_{N-1}\} \tag{29.16}$$

Here, $diag\{\bullet\}$ denotes a diagonal matrix, w_k means how much impact the corresponding frequency point has on the cost function. The w_k is bigger, the approximation accuracy is higher in the corresponding frequency point.

The coefficients of the improved calibration filter is

$$\hat{\boldsymbol{h}}_i = \left(\boldsymbol{A}^H \boldsymbol{\Gamma}^H \boldsymbol{\Gamma A}\right)^{-1} \boldsymbol{A}^H \boldsymbol{\Gamma}^H \boldsymbol{\Gamma H}_i \tag{29.17}$$

When the order of calibration filter is big enough, the $\boldsymbol{A}^H \boldsymbol{\Gamma}^{\mathbf{H}} \boldsymbol{\Gamma A}$ might be ill conditioned. Diagonal loading is brought in to mend this case. The final form of the coefficients is denoted by

$$\hat{\boldsymbol{h}}_i = \left(\boldsymbol{A}^H \boldsymbol{\Gamma}^{\boldsymbol{H}} \boldsymbol{\Gamma A} + \delta \boldsymbol{I}\right)^{-1} \boldsymbol{A}^H \boldsymbol{\Gamma}^{\boldsymbol{H}} \boldsymbol{\Gamma H}_i \tag{29.18}$$

In this expression, $\boldsymbol{I}$ is an identity matrix with L orders.

29.4 Simulation Results

In this section, considering the actual circumstance of navigation receiver, simulation results of equalization methods as depicted before are presented. The distribution of array elements is showed in Fig. 29.2, and it's a uniform circular array with 4 elements. The array radius is 0.095 m. The sampling clock is 65.28 MHz. The bandwidth of the system is 20.46 MHz.

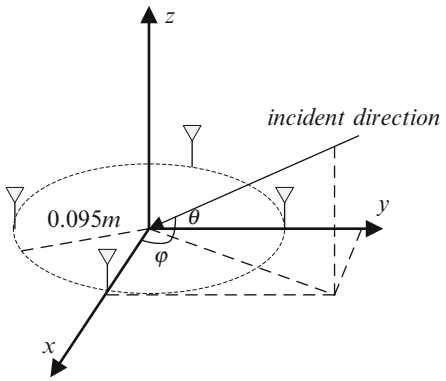

Fig. 29.2 Distribution of array elements

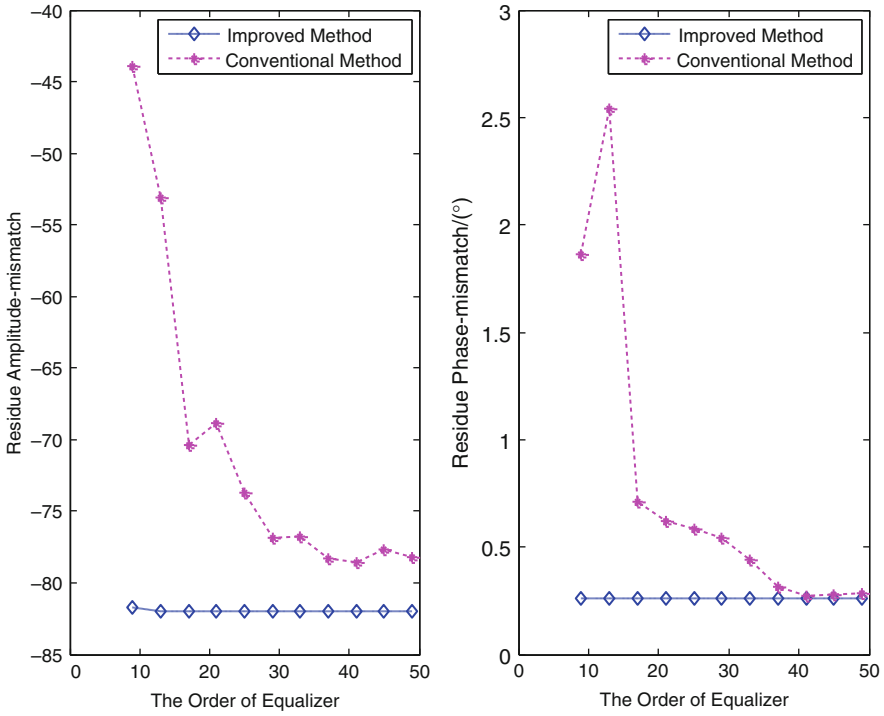

Fig. 29.3 The residue amplitude-phase mismatch of equalization methods

The carrier frequency of correcting signal is 1,268.52 MHz, and it's a LFM signal from the normal direction ($\theta = 90^{\circ}$), with bandwidth $B = 25MHz$. Noise is assumed to be white gaussian noise with zero-mean, and signal-noise ratio $SNR = 40dB$. To simulate the inconsistency of each channel, the channel frequency response $C_i(\omega)$ is descripted as [6]

$$C_i(\omega) = \left[a_{i,0} + a_{i,1}\cos\left(K_{i,1}\omega/B_s + \varphi_{i,1}\right)\right] \times \exp\left\{j\left[-b_{i,0}\omega + b_{i,1}\cos\left(K_{i,2}\omega/B_s + \varphi_{i,2}\right)\right]\right\} \tag{29.19}$$

Here, $a_{i,0} \sim U(0.5, 1.5)$, $a_{i,1} \sim U(0, 0.5)$, $b_{i,0} \sim U(-3 \times 10^{-11}, 3 \times 10^{-11})$, $b_{i,1} \sim U(0, 0.5)$, $K_{i,1} \sim U(0, 10)$, $K_{i,2} \sim U(0, 10)$, $\varphi_{i,1} \sim U(-\pi, \pi)$, $\varphi_{i,2} \sim U(-\pi, \pi)$. B_s is the digital bandwidth of the system, which is expressed as $\frac{2\pi \times 20.46}{65.28} rad$.

The residue amplitude-phase mismatch of the two methods depicted before is showed in Fig. 29.3. It can be seen that the improved method is more accurate, especially when L is small.

Figure 29.4 shows the ratio of frequency response between the reference channel and the channel to be calibrated. Within the receiver band, the improved equalization method is highly effective.

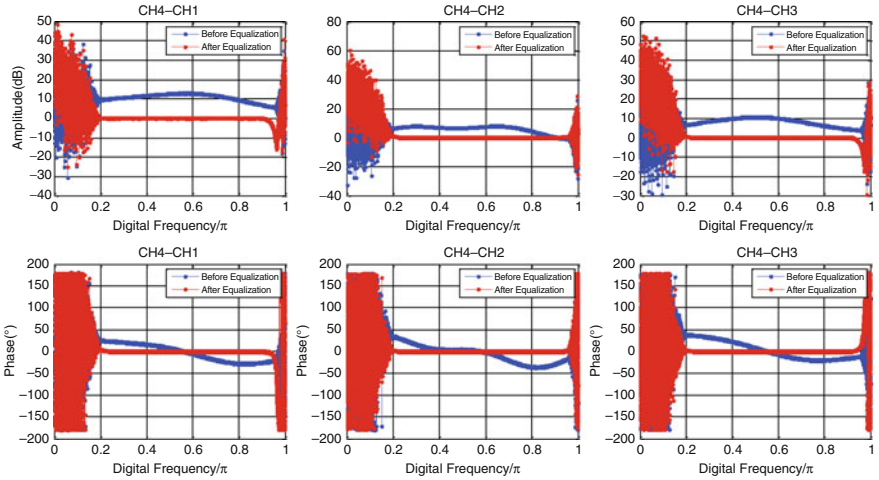

Fig. 29.4 The ratio of frequency response within the receiver band with $L = 21$

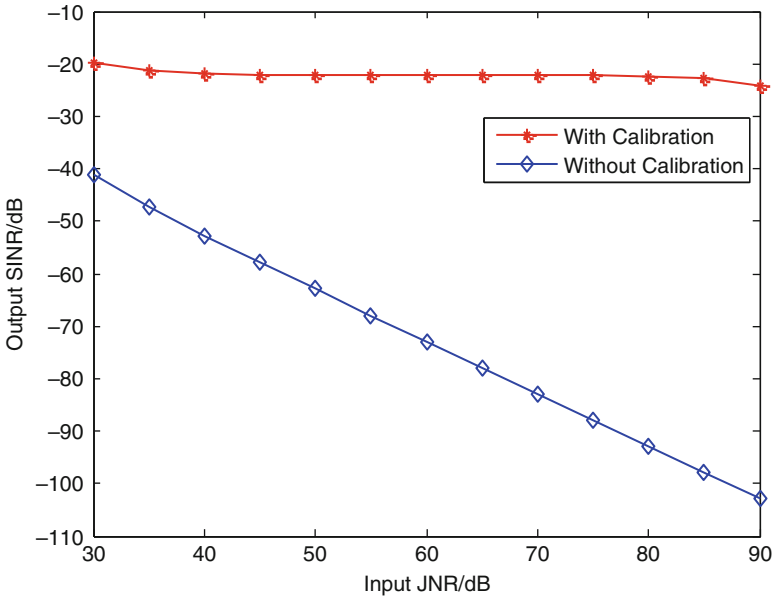

Fig. 29.5 The output SINR of DBF with and without calibration

Then remove the correcting signal, and add the interference signal and the GNSS-signal which are from $(70^\circ, 150^\circ)$ and $(45^\circ, 30^\circ)$ respectively. Both signals are modulated by QPSK with different Gold sequences. $SNR = -20dB$, JNR ranges from $30dB$ to $90dB$. MVDR method is used to do DBF, and the output $SINR$ is showed in Fig. 29.5 to indicate the effect of mismatch between channels.

Without calibration, the output SINR falls rapidly along with the increase of input JNR. When output SINR falls below $50dB$, the system will lose the capability to capture the GNSS-signal.

29.5 Summary

This paper proposes a frequency-domain equalization method in wideband navigation anti-jamming receiver. The anti-jamming performance is greatly susceptible to the beam distortion caused by channel inconsistency in the GNSS case. The equalization method and its improved form proposed in this paper can help compensate the inconsistency between channels. In the process of actual implementation, the improved method is more accurate with low filter order, and can also reduce the amount of calculation.

References

1. Misra P, Burke B, Pratt M (1999) GPS performance in navigation. Proc IEEE 87(1):65–85
2. Aalfs DD, Holder EJ (2000) Impact of wideband channel-to channel mismatch on adaptive arrays. In: IEEE Proc SAMSP, Cambridge, pp 459–463
3. Gerlach K (1990) The effects of IF bandpass mismatch errors on adaptive cancellation. IEEE Trans AES 26(3):455–468
4. Russell Johnson J, Fenn AJ, Aumann M (1991) An experimental adaptive nulling receiver utilizing the sample matrix inversion algorithm with channel equalization. IEEE Trans Microware Theory Tech 39(5):798–808
5. Wu S, Li Y (1995) Adaptive channel equalization for space-time adaptive processing. IEEE. In: International conference, Alexandria, 624–628
6. Monzigo RA, Miller TW (1980) Introduction to adaptive arrays. Wiley, New York, 461–475

Chapter 30
A Newly Adaptive Beamforming Method for Vector Sensor Array

Fang Liu, Huiyong Li, and Julan Xie

Abstract In order to improve the stability of the beam pattern, a newly adaptive beamforming method (SPAPES, Space-Polarization Amplitude and Phase EStimation) for vector sensor array is presented in this paper. The signal model is introduced first, and the principle of the proposed method has been discussed, and then the optimal weight vector is derived. The desired signal will be cancelled out when calculating the covariance matrix, thus the optimal weight vector is irrelevant to the desired signal. Simulation results indicate that SPAPES can achieve a good filtering performance under the circumstances of high desired signal power, low sampling snapshots and coherent interference signal.

Keywords Beamforming • APES • Vector sensor array • Space-polarization filtering

30.1 Introduction

In the past few decades, many array processing techniques including both parameter estimation and beamforming for vector sensor array have been developed rapidly. For parameter estimation, the ESPRIT algorithm has been extensively investigated for vector sensor array in [1, 2]. MUSIC-based direction finding algorithms using vector sensor array have been proposed in [3]. For beamforming, minimum-noise-variance beamformer with a vector sensor has been introduced in [4] and the output SINR is given in [5]. The SPMVDR (Space-Polarization Minimum Variance Distortionless Response) method is introduced in [6]. However, the performance of the SPMVDR will be severely degraded under the circumstances of high desired signal power, low sampling snapshots and correlated interferences.

Conventional APES algorithm has been widely used in many fields [7, 8]. It has been applied to scalar sensor array beamforming and a performance comparison with different filtering methods is given in [9]. The forward-backward spatial APES

F. Liu (✉) • H. Li • J. Xie
School of Electronic Engineering, University of Electronic Science and Technology of China, Chengdu, Sichuan 611731, PR China
e-mail: dafangr@163.com

J. Mu et al. (eds.), *The Proceedings of the Third International Conference on Communications, Signal Processing, and Systems*, Lecture Notes in Electrical Engineering 322, DOI 10.1007/978-3-319-08991-1_30

is introduced in [10]. In order to overcome the shortcomings of SPMVDR and obtain a more stable beam pattern, the conventional spatial APES is expanded into the joint space-polarization adaptive beamforming and the SPAPES is presented in this paper. Simulation results are shown to verify the effectiveness of the proposed method.

30.2 Signal Model

In Fig. 30.1, the uniform linear array consists of M vector sensors and each sensor is composed of the crossed electric pair. The sensor spacing is equal to d. The form of the array manifold is also called the two-component vector sensor array.

There is one desired signal and J interferences impinging on the array. The direction of arrival (DOA) and polarization parameter of the desired signal are known. The received signal model $\boldsymbol{X}(t)$ can be described as:

$$\begin{aligned}\boldsymbol{X}(t) &= \boldsymbol{a}_d \cdot s_d(t) + \sum_{i=1}^{J} \boldsymbol{a}_i \cdot s_i(t) + \boldsymbol{N}(t) \\ &= \boldsymbol{A} \cdot \boldsymbol{S}(t) + \boldsymbol{N}(t)\end{aligned} \tag{30.1}$$

where $s_d(t)$ represents the desired signal and $s_i(t)$ is the interference. $\boldsymbol{N}(t)$ denotes the additive complex white Gaussian noise, $\boldsymbol{S}(t) = \mathrm{diag}(s_d(t),\ s_1(t),\ \cdots,\ s_J(t))$, $\boldsymbol{A} = [\boldsymbol{a}_d, \boldsymbol{a}_1, \cdots, \boldsymbol{a}_J]$. $\boldsymbol{a}_d$ and are the joint space-polarization steering vectors of the desired signal and the interference. By using the polarization steering vector $\boldsymbol{a}_{ip}$ and space steering vector $\boldsymbol{a}_{is}$, the joint space-polarization steering vector is

$$\boldsymbol{a}_i = \boldsymbol{a}_{is} \otimes \boldsymbol{a}_{ip} i = d,\ \ 1, \cdots, J \tag{30.2}$$

where symbol $\otimes$ represents the Kronecker product. The space steering vector $\boldsymbol{a}_{is}$ is

$$\boldsymbol{a}_{is} = \left[1, e^{-\mathrm{j}\phi_i}, \cdots, e^{-\mathrm{j}(M-1)\phi_i}\right]^{\mathrm{T}} \tag{30.3}$$

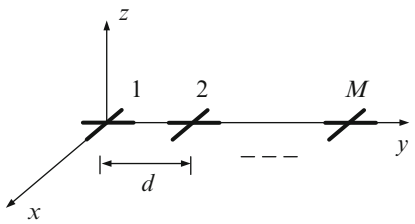

Fig. 30.1 The structure of the vector sensor array

The polarization steering vector of each sensor in Fig. 30.1 can be described as

$$\boldsymbol{a}_{ip} = \begin{bmatrix} p_{ix} \\ p_{iy} \end{bmatrix} = \begin{bmatrix} -\sin\varphi_i & \cos\theta_i\cos\varphi_i \\ \cos\varphi_i & \cos\theta_i\sin\varphi_i \end{bmatrix} \begin{bmatrix} \cos\gamma_i \\ \sin\gamma_i e^{\mathrm{j}\eta_i} \end{bmatrix} \tag{30.4}$$

where $0 \le \gamma < \pi/2$ signifies the auxiliary polarization angle, and $-\pi \le \eta < \pi$ represents the polarization phase difference. $-\pi/2 \le \theta \le \pi/2$ and $0 \le \phi < 2\pi$ denote the elevation angle and azimuth angle, respectively. Assume the azimuth angle of each incident signal to be $\varphi = \pi/2$, then Eq. (30.4) can be simplified as

$$\boldsymbol{a}_{ip} = \begin{bmatrix} p_{ix} \\ p_{iy} \end{bmatrix} = \begin{bmatrix} -\cos\gamma_i \\ \cos\theta_i\sin\gamma_i e^{\mathrm{j}\eta_i} \end{bmatrix} \tag{30.5}$$

The joint space-polarization steering vector of the desired signal can be written as

$$\boldsymbol{a}_d = \left[p_{dx},\ p_{dy},\ p_{dx}e^{-\mathrm{j}\phi_d}, p_{dy}e^{-\mathrm{j}\phi_d},\ \cdots,p_{dx}e^{-\mathrm{j}(M-1)\phi_d},\ p_{dy}e^{-\mathrm{j}(M-1)\phi_d}\right]^{\mathrm{T}} \tag{30.6}$$

The steering vector of interference signal has the similar form with (30.6). The covariance matrix of received signal can be represented as

$$\boldsymbol{R}_{\boldsymbol{X}} = \mathrm{E}\left\{\boldsymbol{X}(t)\boldsymbol{X}(t)^{\mathrm{H}}\right\} = \boldsymbol{A}\boldsymbol{R}_{\boldsymbol{S}}\boldsymbol{A}^{\mathrm{H}} + \sigma_{\mathrm{n}}^2\boldsymbol{I} \tag{30.7}$$

where $\boldsymbol{R}_{\boldsymbol{S}}$ is the autocorrelation matrix of the incident signals and σ_{n}^2, $\boldsymbol{I}$ represent the noise power and $2M \times 2M$ identity matrix, respectively.

30.3 Method Description

The two-component vector sensor array is divided into K subarrays and each subarray is of size $L = M - K + 1$. The received signal of the kth subarray is

$$\begin{aligned} \boldsymbol{X}_k(t) &= \left[x_{kx},\ x_{ky},\ \cdots,x_{(k+L-1)x},\ x_{(k+L-1)y}\right]^{\mathrm{T}} \\ &= \boldsymbol{A}_k \cdot \boldsymbol{S}(t) + \boldsymbol{N}_k(t) \end{aligned} \tag{30.8}$$

where $\boldsymbol{X}_k(t)$ is a $2L$-dimensional column vector. The $2k-1$ to the $2k+2L-2$ lines of the matrix $\boldsymbol{A}$ constitutes the matrix $\boldsymbol{A}_k$. Similar, $\boldsymbol{A}_1$ can be expressed as

$$\begin{aligned}\boldsymbol{A}_1 &= [\widetilde{\boldsymbol{a}}_d \quad \widetilde{\boldsymbol{a}}_1 \quad \cdots \quad \widetilde{\boldsymbol{a}}_J] \\ &= \begin{bmatrix} p_{dx} & p_{1x} & \cdots & p_{Jx} \\ p_{dy} & p_{1y} & \cdots & p_{Jy} \\ \vdots & \vdots & & \vdots \\ p_{dx}e^{-\mathrm{j}(\mathrm{L}-1)\phi_d} & p_{1x}e^{-\mathrm{j}(\mathrm{L}-1)\phi_1} & & p_{Jx}e^{-\mathrm{j}(\mathrm{L}-1)\phi_J} \\ p_{dy}e^{-\mathrm{j}(\mathrm{L}-1)\phi_d} & p_{1y}e^{-\mathrm{j}(\mathrm{L}-1)\phi_1} & \cdots & p_{Jy}e^{-\mathrm{j}(\mathrm{L}-1)\phi_J} \end{bmatrix}\end{aligned} \tag{30.9}$$

Diagonal matrix $\boldsymbol{\psi}$ is defined as

$$\boldsymbol{\psi} = \mathrm{diag}\left(e^{-\mathrm{j}\phi_d}, e^{-\mathrm{j}\phi_1}, \cdots, e^{-\mathrm{j}\phi_J}\right) \tag{30.10}$$

It is obvious that $\boldsymbol{A}_k = \boldsymbol{A}_1 \cdot \boldsymbol{\psi}^{k-1}$, $k = 1,\ 2,\ \cdots K$. Rewrite the received signal of the kth subarray as below

$$\boldsymbol{X}_k(t) = \widetilde{\boldsymbol{a}}_d e^{-\mathrm{j}(k-1)\phi_d} s_d(t) + \boldsymbol{z}_k(t) \tag{30.11}$$

where $\boldsymbol{z}_k(t) = \sum_{i=1}^{J} \widetilde{\boldsymbol{a}}_i \cdot e^{-\mathrm{j}(k-1)\phi_i} \cdot s_i(t) + \boldsymbol{N}_k(t)$ represents the interference plus noise signal vector.

The output $y_k(t)$ of each subarray after adaptive beamforming is

$$y_k(t) = \boldsymbol{w}_0^{\mathrm{H}} \boldsymbol{X}_k(t) = \boldsymbol{w}_0^{\mathrm{H}} \widetilde{\boldsymbol{a}}_d e^{-\mathrm{j}(k-1)\phi_d} s_d(t) + \boldsymbol{w}_0^{\mathrm{H}} \boldsymbol{z}_k(t) \tag{30.12}$$

where $\boldsymbol{w}_0$ is the optimal weight vector. Notice that $e^{-\mathrm{j}(k-1)\phi_d} s_d(t)$ is the desired signal's component received by the kth subarray and let $\boldsymbol{w}_0^{\mathrm{H}} \widetilde{\boldsymbol{a}}_d = 1$, then the Eq. (30.12) can be rewritten as

$$y_k(t) = e^{-\mathrm{j}(k-1)\phi_d} s_d(t) + \boldsymbol{w}_0^{\mathrm{H}} \boldsymbol{z}_k(t) \tag{30.13}$$

Choose the weight vector $\boldsymbol{w}_0$ to ensure the output power of $\boldsymbol{w}_0^{\mathrm{H}} \boldsymbol{z}_k(t)$ minimal and consider all the K subarrays, then the beamformer can be derived by solving the following constrained optimization problem

$$\min \left\{ J(\boldsymbol{w}_0,\ s_d(t)) = \frac{1}{K} \sum_{k=1}^{K} \left| y_k(t) - e^{-\mathrm{j}(k-1)\phi_d} s_d(t) \right|^2 \right\} \quad \text{st.} \ \ \boldsymbol{w}_0^{\mathrm{H}} \widetilde{\boldsymbol{a}}_d = 1 \tag{30.14}$$

Define vector $\boldsymbol{f} = \frac{1}{K} \sum_{k=1}^{K} \boldsymbol{X}_k(t) e^{\mathrm{j}(\mathrm{k}-1)\phi_d}$, the optimization problem in (30.14) after simplification can be described as

$$\min \quad \boldsymbol{w}_0^{\mathrm{H}} \hat{\boldsymbol{R}}_{in} \boldsymbol{w}_0 \qquad \text{st.} \qquad \boldsymbol{w}_0^{\mathrm{H}} \widetilde{\boldsymbol{a}}_d = 1 \tag{30.15}$$

where $\hat{\boldsymbol{R}}_{in}$ is the estimation of covariance matrix of interferences plus noise signal.

$$\hat{\boldsymbol{R}}_{in} = \frac{1}{K}\sum_{k=1}^{K} \boldsymbol{X}_k(t)(\boldsymbol{X}_k(t))^{\mathrm{H}} - \boldsymbol{f}\boldsymbol{f}^{\mathrm{H}} \tag{30.16}$$

Usually, $\hat{\boldsymbol{R}}_{in}$ is obtained by sampling $\boldsymbol{X}_k(t)$. Consider N sampling snapshots

$$\begin{aligned}\hat{\boldsymbol{R}}_{in} &= \frac{1}{N}\sum_{n=1}^{N}\left(\frac{1}{K}\sum_{k=1}^{K}\boldsymbol{X}_k(t)(\boldsymbol{X}_k(t))^{\mathrm{H}} - \boldsymbol{f}\boldsymbol{f}^{\mathrm{H}}\right) \\ &= \frac{1}{K}\sum_{k=1}^{K}\hat{\boldsymbol{R}}_k - \frac{1}{N}\sum_{n=1}^{N}\boldsymbol{f}\boldsymbol{f}^{\mathrm{H}}\end{aligned} \tag{30.17}$$

where $\hat{\boldsymbol{R}}_k = \frac{1}{N}\sum_{n=1}^{N}\boldsymbol{X}_k(t)(\boldsymbol{X}_k(t))^{\mathrm{H}}$ is the estimation of covariance matrix of the kth subarray. By averaging the covariance matrix of all the subarrays, the spatial smoothing technique is applied to the two-component vector sensor array. When the incident interference is correlated with the desired signal, the proposed algorithm can complete the decorrelation well.

Matrix $\boldsymbol{f}$ is expressed as the following

$$\begin{aligned}\boldsymbol{f} &= \frac{1}{K}\begin{bmatrix} 1 & 0 & e^{\mathrm{j}\phi_d} & \cdots & 0 & e^{\mathrm{j}(K-1)\phi_d} & 0 & 0 & 0 & 0 \\ 0 & 1 & 0 & e^{\mathrm{j}\phi_d} & \cdots & 0 & e^{\mathrm{j}(K-1)\phi_d} & 0 & \cdots & 0 \\ \vdots & & & & & \ddots & & & \ddots & 0 \\ 0 & \cdots & & & 1 & 0 & & e^{\mathrm{j}\phi_d} & \cdots & 0 & e^{\mathrm{j}(K-1)\phi_d} \end{bmatrix}\begin{bmatrix} x_{1x} \\ x_{1y} \\ \vdots \\ x_{Mx} \\ x_{My} \end{bmatrix} \\ &= \frac{1}{K}\boldsymbol{T}\boldsymbol{X}(t)\end{aligned} \tag{30.18}$$

where $\boldsymbol{T}$ is a Toeplitz matrix of size $2L \times 2M$, then

$$\begin{aligned}\frac{1}{N}\sum_{n=1}^{N}\boldsymbol{f}\boldsymbol{f}^{\mathrm{H}} &= \frac{1}{K^2}\cdot\frac{1}{N}\sum_{n=1}^{N}\boldsymbol{T}\boldsymbol{X}(t)(\boldsymbol{T}\boldsymbol{X}(t))^{\mathrm{H}} \\ &= \frac{1}{K^2}\boldsymbol{T}\hat{\boldsymbol{R}}_X\boldsymbol{T}^{\mathrm{H}}\end{aligned} \tag{30.19}$$

where $\hat{\boldsymbol{R}}_{\mathbf{X}} = \frac{1}{N}\sum_{n=1}^{N}\boldsymbol{X}(t)\boldsymbol{X}^{\mathrm{H}}(t)$ is the estimation of covariance matrix of received signal, then Eq. (30.17) can be abbreviated as

$$\hat{\boldsymbol{R}}_{in} = \frac{1}{K}\sum_{k=1}^{K}\hat{\boldsymbol{R}}_k - \frac{1}{K^2}\boldsymbol{T}\hat{\boldsymbol{R}}_{\mathbf{X}}\boldsymbol{T}^{\mathrm{H}} \tag{30.20}$$

Equation (30.20) completes the estimation of covariance matrix of interference plus noise signal, then the optimal weight vector $\boldsymbol{w}_0$ in (30.15) can be obtained by applying the Lagrange multiplier method. We can draw the solution as below

$$\boldsymbol{w}_0 = \frac{\hat{\boldsymbol{R}}_{in}^{-1}\widetilde{\boldsymbol{a}}_d}{\widetilde{\boldsymbol{a}}_d^{\mathrm{H}}\hat{\boldsymbol{R}}_{in}^{-1}\widetilde{\boldsymbol{a}}_d} \tag{30.21}$$

From (30.21), the optimal weight vector of SPAPES beamforming algorithm for vector sensor array is obtained. It is obvious that the calculation of $\boldsymbol{w}_0$ is only related to the interference plus noise signal but irrelevant to the desired signal. Therefore, even if under the condition of high desired signal, SPAPES beamforming algorithm can also obtain the stable beam pattern and it performs well when the incident interferences are correlated with the desired signal because of the spatial smoothing technique.

30.4 Simulation Results

In this section, we evaluate the performance of the SPAPES and SPMVDR. In the simulations, a ten-element linear array of two-component vector sensor with half-wave-length element spacing is chosen and the number of subarray is set 3.

In the first scenario, one desired signal and the uncorrelated interference signal are considered. The DOA angles of desired signal and interference are $(\theta_d, \varphi_d) = (0^\circ, 90^\circ)$ and $(\theta_1, \varphi_1) = (50^\circ, 90^\circ)$. The polarization parameters are $(\gamma_d, \eta_d) = (30^\circ, 60^\circ)$ and $(\gamma_1, \eta_1) = (60^\circ, 90^\circ)$, respectively. The sampling snapshot is $N = 300$ and the interference to noise ratio (INR) is 20dB. Figure 30.2 shows the beam pattern versus the elevation angle at a fixed SNR 15dB.

In Fig. 30.2, the proposed algorithm has a deep nulling point at the direction of the interference and the main-lobe of the beam pattern points at the elevation angle of the desired signal. While the SPMVDR has an obvious main-lobe offset and a higher side-lobe level. So the SPAPES performs well, but the SPMVDR fails to filter the interference under the condition of high desired signal power.

In the second scenario, the same desired signal and interference signal parameters with the first scenario are considered. The SNR is 5dB and the INR is 20dB. Figure 30.3 shows the beam pattern versus the elevation angle at a fixed sampling snapshot $N = 50$. In Fig. 30.3, the proposed method has a lower side-lobe level and deeper nulling point at the direction of the interference signal. The main-lobe of the SPAPES points at the direction of the desired signal while the main-lobe of the SPMVDR deviates from the direction of the desired signal. So the proposed method can obtain a good filtering performance even in the case of low snapshots, but the SPMVDR has a serious performance degradation when the sampling number is small due to the inaccurate estimation of covariance matrix.

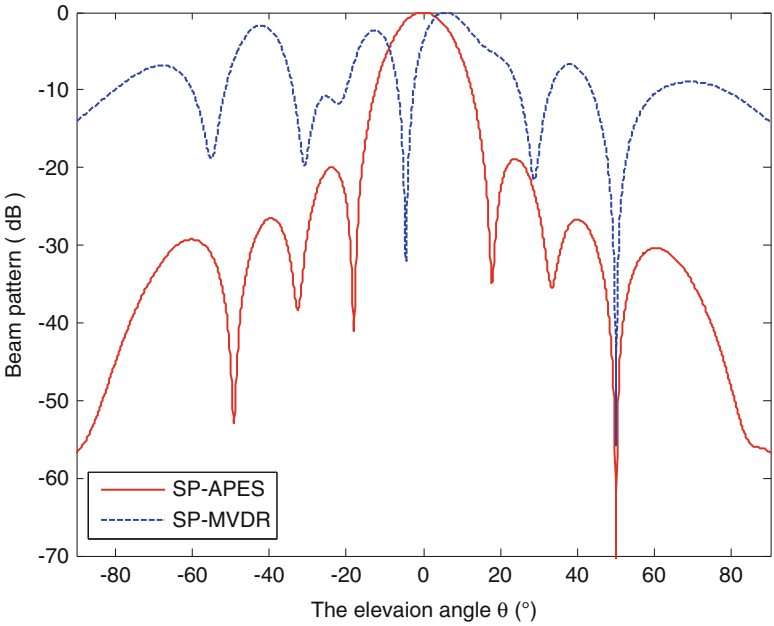

Fig. 30.2 Beam pattern versus θ at a fixed SNR 15dB

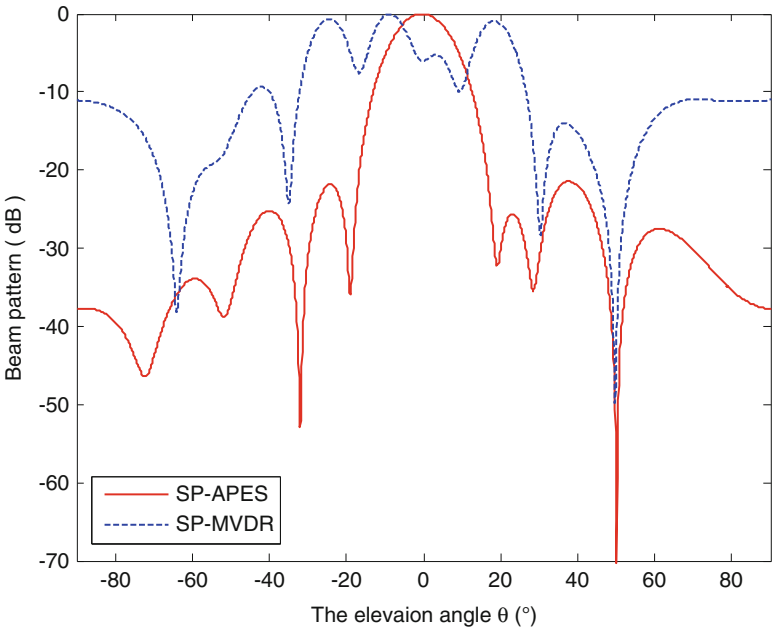

Fig. 30.3 Beam pattern versus θ at a fixed snapshots $N = 50$

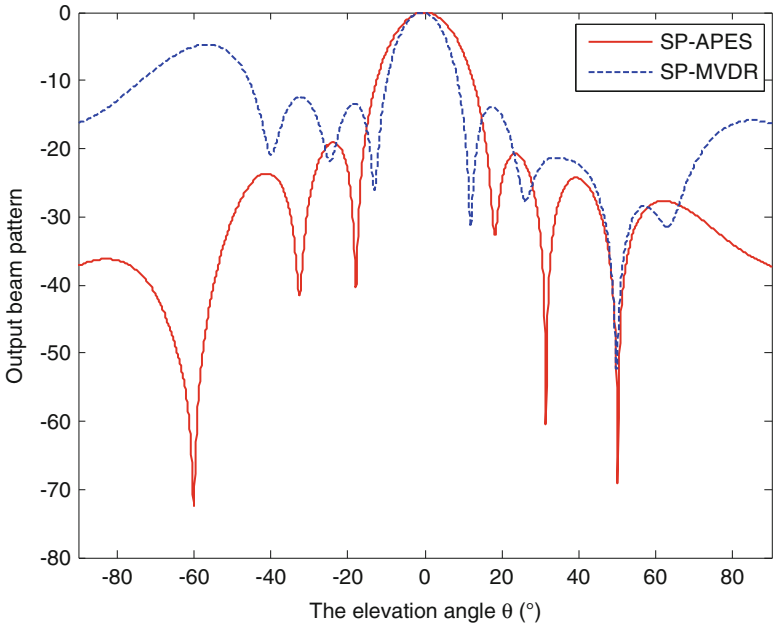

Fig. 30.4 Output beam pattern versus θ in the situation of correlated interference

In the third scenario, the desired signal parameters and sampling snapshot are set to be the same as the first scenario. Two interference signals are considered with the same INR = 20dB, and one is fully correlated with desired signal while the other is uncorrelated with them. The parameters of the first interference are $(\theta_1, \varphi_1) = (-60^\circ, 90^\circ)$, $(\gamma_1, \eta_1) = (53^\circ, 90^\circ)$ and the second are $(\theta_2, \varphi_2) = (50^\circ, 90^\circ)$, $(\gamma_2, \eta_2) = (57^\circ, 90^\circ)$. Figure 30.4 shows the beam pattern versus the elevation angle at a fixed SNR 5dB.

From Fig. 30.4, one can observe that the beam pattern of SPAPES appears deep nulling points at the elevation angle of incident interference but SPMVDR cannot deal with correlated interference as the beam pattern of the SPMVDR forms a spectrum peak at the elevation angle of correlated interference. So the proposed algorithm is not sensitive to the coherent interference, but SPMVDR algorithm fails to filter when existing coherent signal.

30.5 Summary

A newly space-polarization adaptive beamforming method is proposed in this paper. The theoretical derivation of the method is given and the optimal filtering weight vector is obtained. Simulation results show that the proposed method can overcome the deficiencies of SPMVDR and has a better filtering performance in situations of high desired power, low sampling snapshots and coherent interferences.

Acknowledgments This work is supported partly by the China Postdoctoral Science Foundation (No. 2012M520077) and the National Nature Science Foundation of China (No. 61371184).

References

1. Wong K, Zoltowski M (1997) Uni-vector-sensor ESPRIT for multisource azimuth, elevation, and polarization estimation. IEEE Trans Antennas Propag 45(10):1467–1474
2. Wong K, Zoltowski M (2000) Closed-form direction finding and polarization estimation with arbitrarily spaced electromagnetic vector-sensors at unknown locations. IEEE Trans Antennas Propag 48(5):671–681
3. Wong K, Zoltowski M (2000) Self-initiating MUSIC-based direction finding and polarization estimation in spatio-polarizational beamspace. IEEE Trans Antennas Propag 48(8):1235–1241
4. Nehaorai A, Ho K (1999) Minimum-noise-variance beamformer with an electromagnetic vector sensor. IEEE Trans Signal Process 47(3):601–618
5. Xu YG, Liu T, Liu ZW (2004) Output SINR of MV beamformer with one EM vector sensor of and magnetic noise power. In: Proceedings of the 7th international conference on signal processing, pp 419–422
6. Guo YH, Chang QM, Yu DJ (2012) An improved polarization-space adaptive beamforming algorithm. Acta Electronica Sinica 46(6): 1279–1283 (in Chinese)
7. Li H, Li J, Stoica P (1998) Performance analysis of forward-backward matched-filterbank spectral estimators. IEEE Trans Signal Process 46(7):1954–1966
8. Glentis G (2008) A fast algorithm for APES and Capon spectral estimation. IEEE Trans Signal Process 56(9):4207–4220
9. Russell D, Palmer R (2004) Application of APES to adaptive arrays on the CDMA reverse channel. IEEE Trans Veh Technol 53(1):3–17
10. Jakobsson A, Stoica P (2006) On the forward–backward spatial APES. Signal Process 86 (4):710–715

Chapter 31
Design and Implementation of MARG Sensors Based Positioning Method Using a Mobile Phone

Zengshan Tian, Guang Qian, and Mu Zhou

Abstract Due to the problems of high cost and complication in indoor positioning, a new kind of positioning method by using a mobile phone based on magnetic, angular, rate, and gravity (MARG) sensors is more favored in recent years. This method estimates the orientation of pedestrian by quaternion. The quaternion-based extended Kalman filter (EKF) used for data fusion and orientation correction reduces the error of linear acceleration and avoids magnetic-field interference. We conduct pedestrian gait detection and step length estimation by using an accelerometer and verify the positioning performance of this method in an mobile phone. Testing results indicate that the positioning accuracy can reach 30‰ and 20‰ in the complex magnetic-field and non-magnetic interference environments respectively.

Keywords Indoor positioning • Pedestrian dead reckoning • Extended Kalman filter • Gait detection • Quaternion

31.1 Introduction

Global Navigation Satellite System (GNSS) is currently one of the most sophisticated positioning systems which is normally categorised into the conventional satellite positioning systems. The positioning precision of civilian GNSS is around 10 m [1], while in the indoor environment, since the signal strength is weak, the receiver cannot receive the data reliably. On this basis, the development of indoor positioning technology is necessary to supply the gap of GNSS systems in indoor positioning.

The conventional indoor positioning technologies are mainly based on WLAN, RFID, UWB, and cellular network and use the methods of AOA (Angle of Arrival),

Z. Tian (✉) • G. Qian • M. Zhou
Chongqing Key Lab of Mobile Communications Technology, Chongqing University of Posts and Telecommunications, Chongqing 400065, People's Republic of China
e-mail: tianzs@cqupt.edu.cn; qg0624@163.com

J. Mu et al. (eds.), *The Proceedings of the Third International Conference on Communications, Signal Processing, and Systems*, Lecture Notes in Electrical Engineering 322, DOI 10.1007/978-3-319-08991-1_31

TOA (Time of Arrival), TDOA (Time Difference of Arrival), and RSSI (Received Signal Strength Indication) [2–4].

With the development of sensor technology, Micro-Electro-Mechanical-System (MEMS) is increasingly applied to the wide use of indoor positioning systems. Currently, the most representative method for MEMS based indoor positioning is known as PDR (Pedestrian Dead Reckoning). Based on MEMS-IMU toes, the authors in [5] addressed a pedestrian navigation system by using ZUPT (zero speed update) for gyro dynamic error estimation and correction. The shortage of this system is mainly about the complicated process which is not beneficial to sensor data acquisition. In [6], the authors provided an attitude measurement algorithm which is based on quaternion extended Kalman filter. The large number of system state variables and high computation complexity indicate that this algorithm cannot be applied to handheld platforms. By taking the power consumption of handheld platform and system implementation into account, this paper proposed MARG sensors based positioning method using a mobile phone. We test and verify the stability and efficiency of our proposed method in an Android mobile phone. This paper describes the system structure in Sect. 31.2. Section 31.3 introduces the design of the system modules. Finally, the testing results are present in Sect. 31.4.

31.2 System Overview

The indoor positioning technology develops rapidly due to the remarkable development of highly-precise and low-cost sensor manufacturing technology. The benefits of inventing an indoor positioning system on Android platform are about the cost saving, ease for use, and needless for hardware platform selection.

Figure 31.1 shows a block diagram of the indoor positioning system based on Android platform. The modules of data fusion and attitude calculation, gait detection, and step length estimation are integrated into algorithm library. The algorithm layer uses attitude information which is obtained by computing gait information and step length information to calculate pedestrian location coordinates, total distance, and total displacement in a real-time manner. The purpose of application layer of the

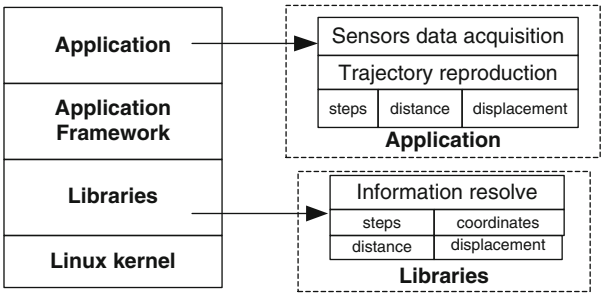

Fig. 31.1 Structure diagram of indoor positioning system

system is to acquire the raw sensor data from the accelerometer, magnetometer, and gyro, conduct trajectory reproduction, and display track information.

31.3 System Design

31.3.1 Objectives

Considering the disadvantages of the conventional indoor positioning systems, a new positioning method is designed for Android mobile phones based on MARG sensors in this paper. The four main objectives of our method are as follows. (1) Data acquisition from MARG sensors. (2) Attitude measurement for handheld device. (3) Pedestrian gait recognition and step length estimation. (4) Walking trajectory reconstruction.

The positioning accuracy to be achieved is also listed below. (1) The compliance rate is more than 20‰-1σ in non-magnetic interference environment, where 20‰ means that on a testing path with the lengths of 1,000 m, the distance between the start and end points is less than 20 m, and 1σ indicates that the compliance rate is no less than 66.7 %. (2) The compliance rate is more than 30‰-1σ in complex magnetic environment.

31.3.2 System Description

31.3.2.1 Dead Reckoning

We assume that the walking speed is constant in every short time interval. If we have the information of the current position, the coordinates of the next position (x_{k+1},y_{k+1}) can be inferred based on the current pedestrian heading direction and step length, as shown in (31.1), where d_{k+1} and θ_{k+1} are the step length and the heading direction at the kth position.

$$\begin{cases} x_{k+1} = x_k + d_{k+1}\cos\theta_{k+1} \\ y_{k+1} = y_k + d_{k+1}\sin\theta_{k+1} \end{cases} \tag{31.1}$$

The flow chart of our proposed positioning method by PDR is show in Fig. 31.2. First of all, we use the Hamming window to filter the acceleration data for the sake

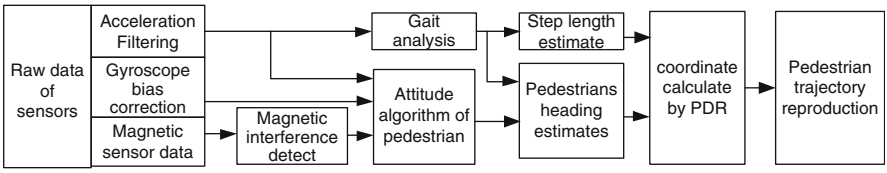

Fig. 31.2 Flow chart of dead reckoning

of eliminating the outlier data and correct the bias of gyro. Second, we conduct gait detection and step length estimation based on the triaxial accelerometer modulus values and estimate the real-time attitude.

Furthermore, we fuse the data from accelerometer, magnetometer, and gyroscope by EKF to correct attitude angles and calculate pedestrian coordinates by PDR. Finally, we show the results of pedestrian trajectory reconstruction.

31.3.2.2 Gait Detection and Step Length Estimation

According to the pedestrian walking model and motion law of handheld sensor, the triaxial accelerometer modulus value can be used to detect the pedestrian gait law. The variations of acceleration modulus values when the pedestrian is walking are shown in Fig. 31.3a. In Fig. 31.3, the notation Acc stands for the difference between the triaxial accelerometer modulus value and the local acceleration of gravity.

The phenomenon of multiple peaks and sudden jumps in acceleration modulus values could occur when the pedestrian is walking. Thus, the error step and missing step have significant impact on positioning results. After the acceleration modulus values are filtered, a single peak curve is obtained in Fig. 31.3b. Compared to the results in Fig. 31.3a, the errors caused by jitter and sudden jump have been effectively eliminated.

Considering the resource constraints of Android platform, we rely on the following two steps to improve the accuracy of gait detection in a real-time manner. (1) Find the peaks of acceleration values based on the threshold A_{th}^{+}. (2) Find the trough of acceleration values based on the threshold A_{th}^{-}. The thresholds A_{th}^{+} and A_{th}^{-} are adjusted dynamically with respect to different pedestrians.

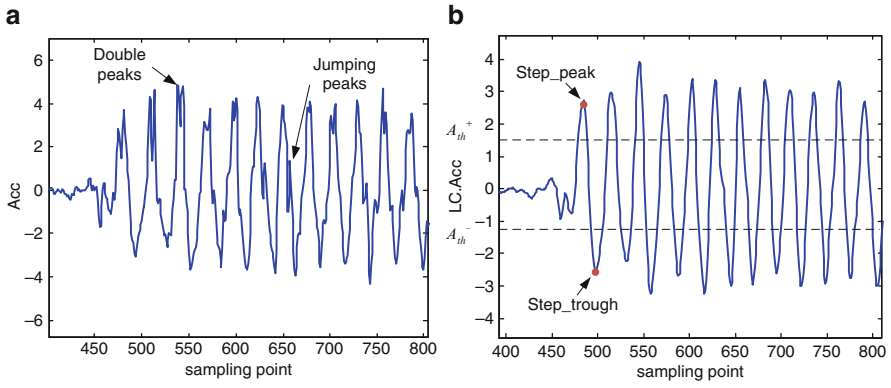

Fig. 31.3 Acceleration modulus values. (**a**) Variations of acceleration modulus values. (**b**) Results of acceleration modulus values after filtering

As defined in (31.2), an empirical model is used to estimate step length, where $Acc_{\max}$ and $Acc_{\min}$ stand for the maximum and minimum of acceleration modulus values, which are obtained from gait detection. C is the scale factor. We use a backpropagation (BP) neural network to estimate the value C by constructing the nonlinear relations of pedestrian height, cadence, and stride.

$$StepLen = C^4\sqrt{Acc_{\max} - Acc_{\min}} \tag{31.2}$$

31.3.2.3 Attitude Estimation and Data Fusion

By assuming that b and n stand for carrier coordinates and navigation coordinates, the coordinate transformation matrix, notated as C_b^n, from b to n is defined in (31.3).

$$C_b^n = \begin{bmatrix} \cos\gamma\cos\psi & \cos\theta\sin\psi + \sin\theta\sin\gamma\cos\psi & -\cos\theta\sin\gamma\cos\psi + \sin\theta\sin\psi \\ -\cos\gamma\sin\psi & -\sin\theta\sin\gamma\sin\psi + \cos\theta\cos\psi & \cos\theta\sin\gamma\sin\psi + \sin\theta\cos\psi \\ \sin\gamma & -\sin\theta\cos\lambda & \cos\theta\cos\gamma \end{bmatrix} \tag{31.3}$$

where, ψ, θ and γ are yaw, pitch, and roll. Based on the relationship between quaternion and gesture rotation matrix, $C_b{}^n$ can be converted into

$$C_b^n = \begin{bmatrix} q_0^2 + q_1^2 - q_2^2 - q_3^2 & 2(q_1q_2 - q_0q_3) & 2(q_1q_3 + q_0q_2) \\ 2(q_1q_2 + q_0q_3) & q_0^2 - q_1^2 + q_2^2 - q_3^2 & 2(q_2q_3 - q_0q_1) \\ 2(q_1q_3 - q_0q_2) & 2(q_2q_3 + q_0q_1) & q_0^2 - q_1^2 - q_2^2 + q_3^2 \end{bmatrix} \tag{31.4}$$

Therefore, θ, γ and ψ can be calculated in (31.5) by using (31.3) and (31.4).

$$\begin{cases} \theta = \arctan\left(-\dfrac{2(q_2q_3 + q_0q_1)}{q_0^2 - q_1^2 - q_2^2 + q_3^2}\right) \\ \gamma = \arcsin(2(q_1q_3 - q_0q_2)) \\ \psi = \arctan\left(-\dfrac{2(q_1q_2 + q_0q_3)}{q_0^2 + q_1^2 - q_2^2 - q_3^2}\right) \end{cases} \tag{31.5}$$

Since the extended Kalman filter (EKF) which is recognized as a non-linear estimation algorithm inhibits the cumulative drift effectively in long time duration [7], it can reduce the influence on orientation estimation by the external magnetic interference. In our system, the state vector is a quaternion, while the observations are the acceleration and magnetometer data. The EKF model to be used in this paper is as follows.

$$\begin{cases} X_{k+1} = AX_k + w_k \\ Z_{k+1} = HX_{k+1} + v_k \end{cases} \tag{31.6}$$

where, X is calculated by rotation quaternion. A is the state transition matrix. w_k is the process noise vector. v_k is the measurement noise vector.

Based on the EKF model in (31.6), the state equation of EKF is defined in (31.7).

$$\mathbf{Q}_{k+1} = A\mathbf{Q}_k + w_k \tag{31.7}$$

where, $A = \exp(\frac{1}{2}\Omega(wT_s))$. The observation equation is shown in (31.8).

$$\begin{bmatrix} \mathbf{a}_{k+1} \\ \mathbf{m}_{k+1} \end{bmatrix} = \begin{bmatrix} C_n^b\mathbf{Q}_{k+1} & 0 \\ 0 & C_n^b\mathbf{Q}_{k+1} \end{bmatrix} \begin{bmatrix} \mathbf{g}_{k+1} \\ \mathbf{m}_{k+1} \end{bmatrix} + \begin{bmatrix} v_{ak} \\ v_{mk} \end{bmatrix} \tag{31.8}$$

where $\mathbf{g}_{k+1}$ is the gravitational acceleration vector at the moment k+1. $\mathbf{m}_{k+1}$ is the magnetic field vector. The covariance matrix of v_k is R, such that

$$R = \begin{bmatrix} \delta_a^2 & 0 \\ 0 & \delta_m^2 \end{bmatrix} \tag{31.9}$$

which is affected by the external magnetic field during the movement. To reduce the external magnetic field interference, we adjust the weight of measurements in a real-time manner by using the covariance matrix R. Then, we obtain

$$\delta_a^2 = k_a var\left(\left\|\mathbf{a}_{i-N/2}\right\| : \left\|\mathbf{a}_{i+N/2}\right\|\right) \tag{31.10}$$

$$\delta_m^2 = k_m var\left(\left\|\mathbf{m}_{i-N/2}\right\| : \left\|\mathbf{m}_{i+N/2}\right\|\right) \tag{31.11}$$

where k_a and k_m are the scale factors. N is the size of sliding window.

Since the covariance matrix structure becomes complicated when a large linear acceleration or a large magnetic field occurs, the proportion of gyro should be raised to calculate orientation and reduce the effect of linear acceleration and magnetic disturbance. We can obtain stable attitude information with the help of quaternion estimation and updating in (31.6), the result is shown in Fig. 31.4

We compute the coordinates in (31.1) based on the step length d_k in Sect. 31.3.2.2 and the steady information of direction θ_k in Sect. 31.3.2.3.

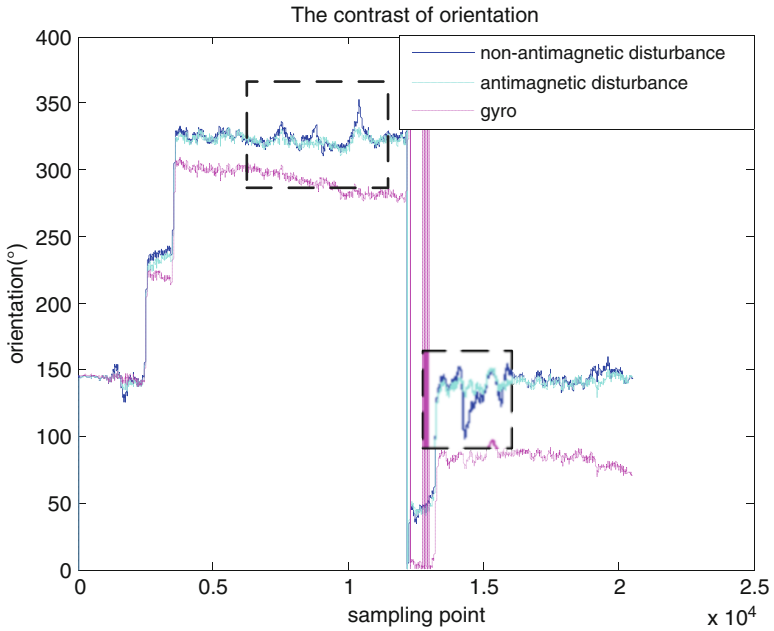

Fig. 31.4 Results of orientation

31.4 Testing Results

To verify the reliability and stability of our system, we conduct the experiments in four testing scenarios, as shown in Fig. 31.5. In our testing, the data acquisition frequency is set to be 50 Hz and the testing Android device is hold by a person.

31.4.1 Test of Gait Detection Precision

We invite 30 persons including men and women as the volunteers to walk 1,000 steps for the sake of testing the stability of gait detection in our system. The number of actual steps and the number of detected steps are compared in Table 31.1.

The results of gait detection show that there is no significant difference in gait detection between men and women, while the recognition accuracy is about 99 %.

31.4.2 Test of Trajectory Precision

As shown in Fig. 31.5, we choose four typical environments as our testing scenarios, a stadium where the magnetic interference does not exist, an indoor commercial

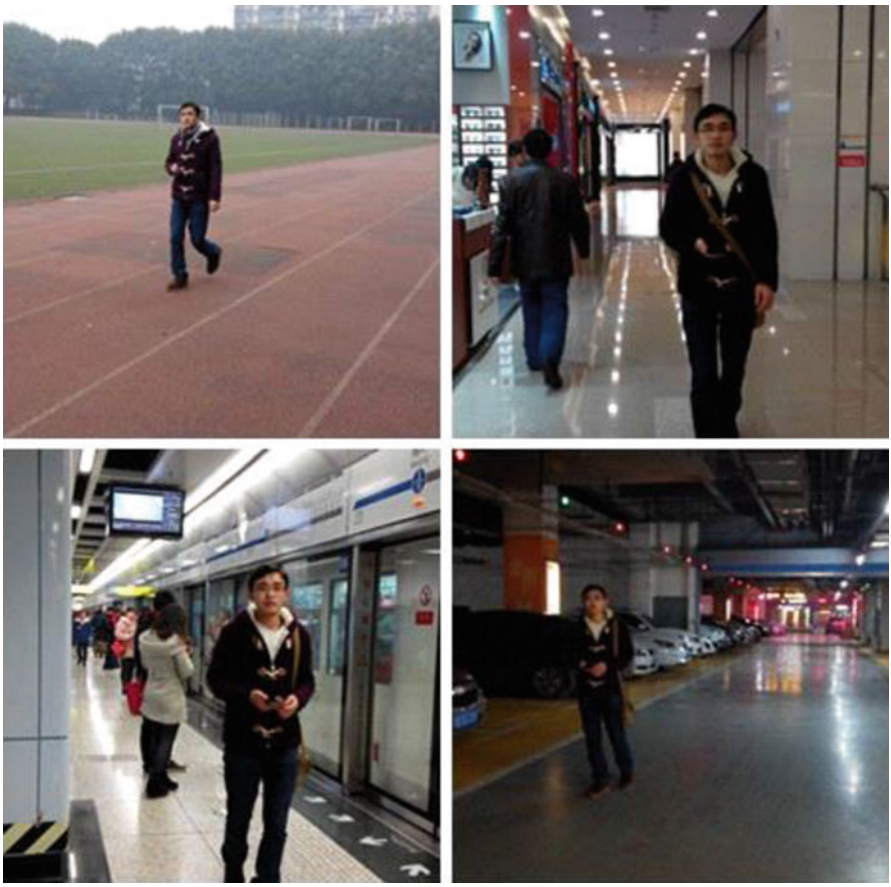

Fig. 31.5 Testing scenarios

Table 31.1 Results of gait detection

Number of detected steps	Number of persons
≤ 990	0
≥ 991 and ≤ 995	2
≥ 996 and $\leq 1,000$	14
$\geq 1,001$ and $\leq 1,005$	11
$\geq 1,006$ and $\leq 1,010$	3
$\geq 1,011$	0

pedestrian street, an underground garage, and a subway station where the magnetic interference exists, to examine the trajectory precision. The standard-reaching rates for the environments with non-magnetic interference and with magnetic interference are about 88 % and 91 % respectively, as shown in Table 31.2. The results in Table 31.2 show that the magnetic interference can be reduced efficiently by our proposed system, while the standard-reaching rates of our system are above 85 %.

Table 31.2 Results of trajectory precision

Place	Total number	Number of standard-reaching	Standard-reaching rate (%)
Stadium	50	44	88
Indoor commercial pedestrian street	50	45	90
Underground garage	45	44	97.78
Subway station	50	44	88

Conclusion

This paper proposes a handheld positioning system which is designed based on MARG sensors to solve the problems of high-cost, high complexity, and cumbersome wearing requirement by the existing positioning systems. Based on Android platform, in our system, we use the accelerometers to detect the gait of pedestrian, a quaternion to estimate attitude information, and EKF to conduct data fusion and heading correction. Compared to the conventional systems which are suffered by the high hardware cost and the significant power consumption, our system has achieves higher trajectory precision, as well as better anti-interference ability.

References

1. Li C, Liu W, Wu J (2010) High-precision positioning algorithm based on GPS. In: International conference on advanced computer control, vol 5, pp 364, 368, 27–29, 2010
2. Prasithsangaree P, Krishnamurthy P, Chrysanthis, PK (2002) On indoor position location with wireless LANs. In: IEEE International symposium on personal, indoor and mobile radio communications, vol 2, pp 720, 724, 15–18, 2002
3. Nakamori E, Tsukuda D, Fujimoto M, Oda Y, Wada T, Okada H, Mutsuura K (2012) A new indoor position estimation method of RFID tags for continuous moving navigation systems. In: International conference on indoor positioning and indoor navigation. pp 1, 8, 13–15, 2012
4. Xu J, Lu X (2010) Design and simulation of indoor positioning system based on UWB. In: International conference on e-business and e-government, pp 3872, 3875, 7–9, 2010
5. Abdulrahim K, Hide C, Moore T, Hill C (2010) Aiding MEMS IMU with building heading for indoor pedestrian navigation. In: Ubiquitous positioning indoor navigation and location based service (UPINLBS), pp 1, 6, 14–15, 2010
6. Sabatini AM (2006) Quaternion-based extended Kalman filter for determining orientation by inertial and magnetic sensing. IEEE Trans Biomed Eng 53(7):1346, 1356
7. Yudan Yi, Dorota A, Grejner-Brzezinska (2001) Nonlinear bayesian filter: alternative to the extended kalman filter in the GPS/INS fusion systems. In: Proceedings of the 18th international technical meeting of the satellite division of the institute of navigation, 2001

Chapter 32
An Ultra-Low Sidelobe Suppression Method About NLFM

Ping Liu, Xue-gang Wang, Lin Zou, Yun Zhou, and Xue-lian Yu

Abstract Pulse compression technology is very useful in modern radar system, with the reason that it can solve the contradiction between the radar range and range resolution. Now, nonlinear frequency modulation (NLFM) is researched widely, because the pulse compression of the NLFM signal can lower the range sidelobe better than −40 dB without window weighting. But in some applications, the reducing level also cannot meet the requirements. This paper put forward a continuous nonlinear FM waveform designed bring down the level of the range sidelobe, which can suppress the range sidelobe to −86 dB. Therefore, it can be used in many radar systems, especially in some kind of weather radar.

Keywords Pulse compression • NLFM • Continuous nonlinear FM waveform design

32.1 Introduction

In radar system, in order to increase the operating distance as far as possible, we should transmit wide pulse, but the biggest disadvantage of this is that wide pulse will result in the decline of the range resolution. So in order to compromise this contradiction, pulse compression is brought in.

Nowadays, linear frequency modulation (LFM) signal and nonlinear frequency modulation (NLFM) signal are widely used in pulse compression. Although LFM is easy to generate, the output of the pulse compression is unsatisfactory. So in order to decrease the sidelobe of the signal, windowing weighting is essential, but which will result in the loss of signal-to-noise ratio and the main lobe of the signal will also be widen. So researchers want to find other signal to improve this problem. NLFM has the ability that it needn't weighting, and the result of the pulse compression is very good. Because of no window weighting, so it will not result in the

P. Liu (✉) • X.-g. Wang • L. Zou • Y. Zhou • X.-l. Yu
University of Electronic Science and Technology of China (UESTC), No. 2006, Xiyuan Avenue, West High-Tech Zone, Chengdu 611731, China
e-mail: liuping_2012@126.com; 1053432306@qq.com

J. Mu et al. (eds.), *The Proceedings of the Third International Conference on Communications, Signal Processing, and Systems*, Lecture Notes in Electrical Engineering 322, DOI 10.1007/978-3-319-08991-1_32

loss of SNR and the width of the main lobe also will not be widened. So it is researched more and more widely.

The traditional method of nonlinear frequency modulation waveform design is based on the stationary of phase principle and then uses the window function to design it. But this method can't get a good range sidelobe; it can only achieve range sidelobe levels about −40 dB, which is far not meeting the need of the engineer application, therefore this paper proposes another method to design nonlinear frequency modulation waveform, which is based on a continuous nonlinear FM function. Using this method, we can get a level of range sidelobe better than −86 dB, which is very useful in the satellite-borne precipitation radar. Because in this kind of radar, the echo of the ground clutter can almost reach a level to 30–55 dB, and the strong echo may submerge the weak objective signal, this will cause the target residual, so in order to measure the strength of the rain, the normalized sidelobe level must reach better than −60 dB.

32.2 Traditional Method of Designing NLFM

Assuming the expression of NLFM signal can be expressed as following:

$$\mathrm{s(t)} = \mathrm{a(t)exp(j}\theta\mathrm{(t))} \tag{32.1}$$

Normally, we will let $a(\mathrm{t}) = 1$, so if we want to design the waveform of the NLFM, all we should do is determining the phase function θ(t). When the phase function is determined, the remaining work will be simple. According to the stationary phase principle, we can know that the spectrum's modular square of output signal is equal to spectrum of the window function, it can be expressed as:

$$\left|S(\mathrm{f})\right|^2 = W(\mathrm{f}) \tag{32.2}$$

So the group delay can be expressed as:

$$T(\mathrm{f}) = \mathrm{K} \cdot \int_{-\infty}^{f} W(\mathrm{x})\mathrm{dx} \quad -B/2 \le \mathrm{f} \le \mathrm{B}/2 \tag{32.3}$$

For K is a constant, whose expression is:

$$K = T/\int_{-B/2}^{B/2} W(\mathrm{x})\mathrm{dx} \tag{32.4}$$

Where W(x) is a window function; B is the signal bandwidth; T is the pulse width; and the group delay's inverse function is a frequency function. It can be expressed as:

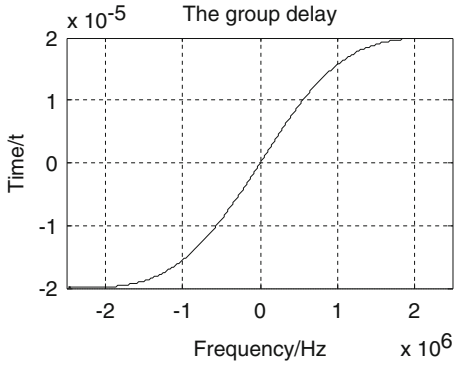

Fig. 32.1 The group delay of nonlinear frequency modulation signal

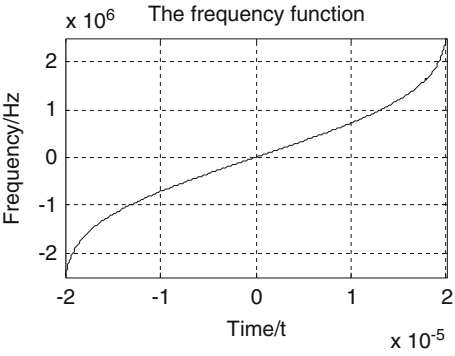

Fig. 32.2 The frequency function of NLFM

$$f(\mathrm{t}) = \mathrm{T}^{-1}(\mathrm{f}) \quad -T/2 \le \mathrm{t} \le T/2 \tag{32.5}$$

Hence, on the basis of the frequency function, we can get the phase function, whose expression is in this form:

$$\theta(\mathrm{t}) = 2\pi \cdot \int_0^t f(\mathrm{t})\mathrm{dt} \quad -T/2 \le \mathrm{t} \le \mathrm{T}/2 \tag{32.6}$$

If the phase function is already known, the waveform of the NLFM can be worked out easily.

Although all we need are known, in fact the simulation process is very difficult. Because the group delay of signal is not a simple expression, so if we want to solve its inverse function, it is hard to achieve. Therefore, in actual circumstances, we must use interpolation and fitting method to get an approximate value. And when we solve phase function, we also should use approximate integration to get.

In the following, we will use matlab to simulate the following derivation, assuming the simulation conditions are: pulse width $\mathrm{T} = 40$ μs; bandwidth $\mathrm{B} = 5$ MHz, sampling frequency $\mathrm{fs} = 4\mathrm{B}$. The simulation results are illustrated Figs. 32.1, 32.2, 32.3, and 32.4.

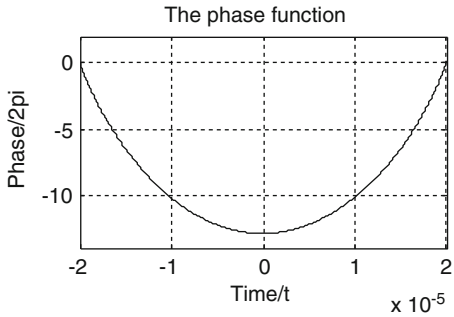

Fig. 32.3 The phase function of NLFM

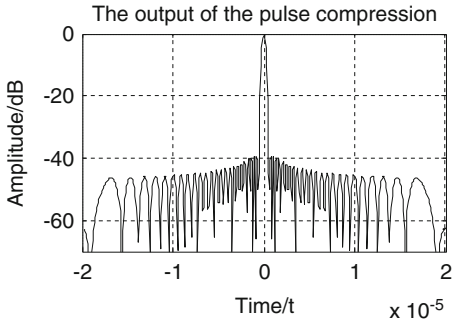

Fig. 32.4 The result of pulse compression using traditional method

From Fig. 32.4 we can know that the ratio of main to minor lobes is only reached −39.2, which cannot meet requirements in some new radar systems, so in order to lower the minor lobes of the output further, other improved method to design nonlinear frequency modulation function must be put forward.

32.3 Modified Method of Designing NLFM

In order to improve the performance of pulse compression of NLFM signal, an improved method is put forward.

The modified method to design NLFM is based on a continuous nonlinear FM function, which is derived from the piecewise nonlinear FM function, shown in Fig. 32.5. As we can see that the waveform is composed of three linear parts. But the performance of this function is also not very ideal, so on the basis of this, a continuous nonlinear FM function is put forward, which is shown in Fig. 32.6.

In contrast to the piecewise nonlinear FM function, the continuous nonlinear FM waveform can be divided into three parts. The center of the waveform is a linear part, which is the major part of the waveform, and both of the ends of the linear part are small portions of higher FM rate curve signal. By introducing the curve part, the result of pulse compression will be better.

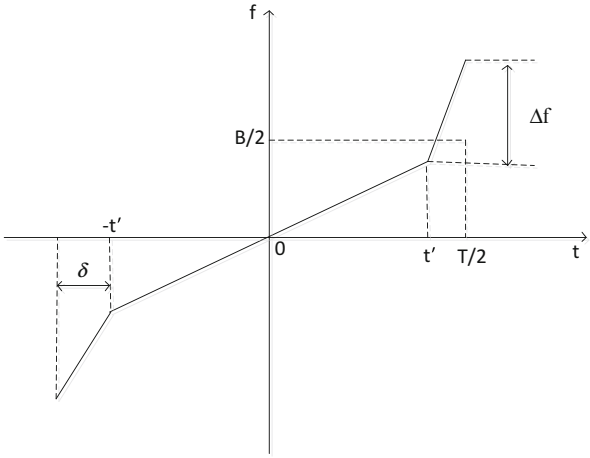

Fig. 32.5 Piecewise nonlinear FM waveform

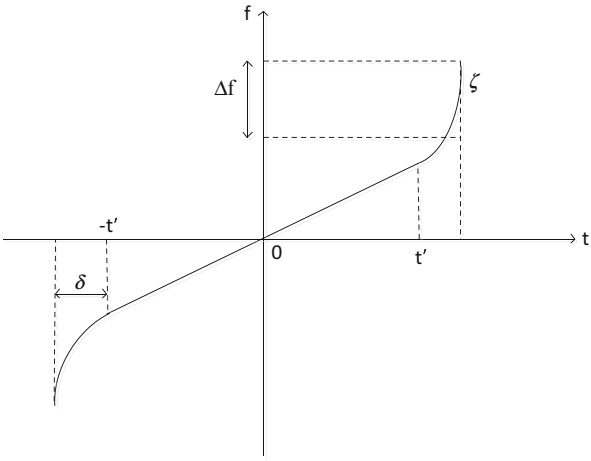

Fig. 32.6 Continuous nonlinear FM waveform

Using this method, there is no need to design the group delay of the signal, because we directly use continuous nonlinear frequency function to design the phase function.

From Fig. 32.6 we can see that there are some parameters that determine the structure of the waveform, such as t', determining the duration of the linear part, and δ, representing the nonlinear part. In the process of the design, what makes the matter most is how to choose the parameters' value. From Fig. 32.6 we can get the formal definition of the continuous nonlinear FM function,

$$f(\mathrm{t}) = \begin{cases} \chi/t + T/2 + \chi/\zeta & -T/2 \le t \le -t' \\ Kt & -t' < t < t' \\ -\chi/t - T/2 - \chi/\zeta & t' \le t \le T/2 \end{cases} \tag{32.7}$$

Where T is the length of the whole pulse; the duration of the center linear part is $-t'$ to t'; $K = B/T$ is the rate of frequency; ζ is the instantaneous frequency of pulse at time T/2; τ is the instantaneous frequency of pulse at time (T/2−t′); the expression of τ can be expressed as:

$$\tau = K \cdot (\mathrm{T}/2 - \mathrm{t}') \tag{32.8}$$

The parameter χ has the form in the following:

$$\chi = \tau\zeta \cdot (\mathrm{T}/2 - \mathrm{t}')/(\zeta - \tau) \tag{32.9}$$

Therefore, if we can determine the value of these parameters, the frequency function f(t) can be determined.

But the value of ζ is already unknown, so we should use successive approximation method to determine it.

Because of the uncertainty of some parameters, and they are very difficult to determine, so doing plenty of simulation will be of great significance. According to the plenty of simulation results, we can get the conclusion that when the value of t' is between 0.452 and 0.496 T and ζ is between $2B - 1$ and $2B + 1$, the simulation result will be better. Because the expression of τ and ζ are not highly accurate, in the process of the design, we should do enough simulation near the value range; only in this way can we get the optimum result. Through simulation we found that sidelobe can be brought down well below −86 dB with appropriate window function.

32.4 Simulation Results

Assuming the simulation conditions are expressed as following:

(1) $T = 40\,\mu\mathrm{s}$
(2) $B = 5\,\mathrm{MHz}$
(3) $f_s = 4B$
(4) $t' = 18.4\,\mu\mathrm{s}$
(5) $\tau = \mathrm{K} \cdot (\mathrm{T}/2 - \mathrm{t}') = (\mathrm{B}/\mathrm{T}) \cdot (\mathrm{T}/2 - \mathrm{t}') = 0.2\,\mathrm{MHz}$
(6) $\zeta = 2B + 1 = 11\,\mathrm{MHz}$
(7) Window function = Blackman

Where f_s is the sampling frequency of signal. But in the process of simulation, we found when $\tau = 0.21\,\mathrm{MHz}$, the result will be better, so we can get the results as follows (Figs. 32.7 and 32.8)

From Fig. 32.9, it is seen that the range sidelobe is suppressed to a certain extent, which is brought down well below −86 dB. This kind of performance meets the requirement of the satellite-borne precipitation radar measuring the amount of the precipitation pretty well. Although using this method we can achieve range sidelobe levels better than −86 dB, the width of the main lobe is not small enough, and other

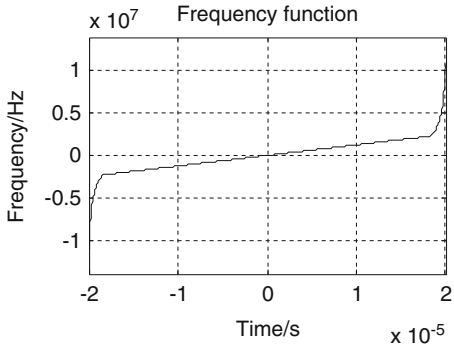

Fig. 32.7 The frequency function using modified method

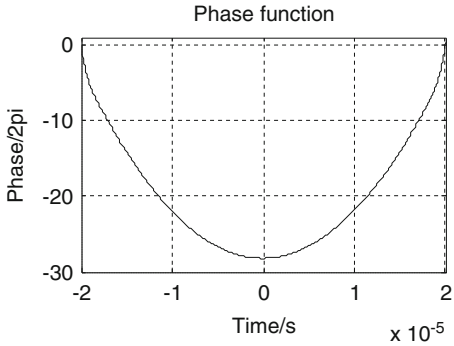

Fig. 32.8 The phase function using modified method

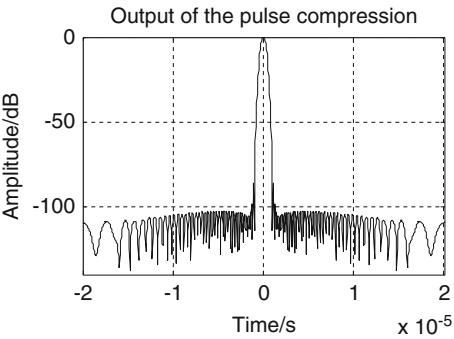

Fig. 32.9 The result of pulse compression using modified method

aspects also will affect the pulse compression result, such as the parameter t', when it is chosen too small, the performance of the pulse compression will decline greatly. At the same time, the weighting window function is another impact factor, so we should operate so many simulations to determine which function has the best performance. At last, the sampling frequency will also affect the performance. So in order to achieve the best result, doing plenty of simulations is essential.

Conclusion

Pulse compression is of great importance in modern radar systems, which can solve the problem between detection distance of radar and range resolution. So it is used more and more widely.

This paper proposes a design method of continuous nonlinear frequency modulation waveform, which can achieve range sidelobe levels of better than −86 dB. This method is suitable for the application of satellite-borne precipitation radar. But there are also some problems, like unideal main lobe, so other methods should be put forward to improve the performance of pulse compression.

Acknowledgments This research was supported by the Key Program the China Postdoctoral Science Foundation (No. 2013M531948), National Natural Science Foundation of China (No. 61139003) and the National Key Technology Support Program of China (No. 2011BAH24B05).

References

1. Hong-gang Y, Xiao-long D (2008) Pulse compression with ultra-low range sidelobe for space-borne meteorology radars. IEEE Conference Publications
2. De White E, Griffiths HD (2004) Improved ultra-low range sidelobe pulse compression waveform design. Electron Lett 40(22):1448–1450
3. Ge Z, Huang P (2008) Matched NLFM pulse compression method with ultra-low sidelobes. In: Proceedings of the 5th radar conference, European
4. Collins T, Atkins P (1999) Nonlinear frequency modulation chirps for active sonar. IEE Proc Radar Sonar Navig 146(6):312–316
5. Nuttall AH (1981) Some windows with very good sidelobe behavior. IEEE Trans Acoust Speech Signal Process 29:84–91
6. Griffiths HD, Vinagre L (1994) Design of low-sidelobe pulse compression waveforms. Electron Lett 30:1004–1005
7. Feng L, Liting R, Shunjun W (2009) Design of modified spectrum filter based on mismatched window for NLFM signal. IEEE
8. Liang Z (1994) An improved method of designing NLFM signal. Modern Radar 27–34

Chapter 33
Optimization of Power Allocation and Relay Location for Decode-and-Forward Relaying in the Presence of Co-channel Interference

Liang Han, Jiasong Mu, Shuang Liu, and Zhong Zhang

Abstract This paper focuses on the power allocation and relay location for decode-and-forward (DF) relaying in the presence of co-channel interference. Firstly, we derive the approximation outage probability in the high signal-to-interference ratio (SIR) regime. Then, three optimization problems are formulated to minimize the obtained approximation outage probability, namely optimal relay location with fixed power allocation, optimal power allocation with fixed relay location, and joint optimization of relay location and power allocation. The simulation results validate our analysis and show that joint optimization obtains the best outage performance.

Keywords Co-channel interference • Decode-and-forward • Power allocation • Relay location

33.1 Introduction

Relay technologies have been adopted in IMT-Advanced (4G) standards, such as LTE-Advanced and WiMAX to extend network coverage and improve the throughput of the cell edge users [1, 2]. So far, there has been much research in this field.

Since the performance of relaying can be improved by power allocation among the source and relay nodes, the strategy used to allocate power has attracted much attention. Various power allocation schemes have been proposed in the literatures. In [3], the authors studied capacity bounds and obtained optimal power allocation for three-node wireless relay channels in a Rayleigh fading environment. In [4], the authors presented optimal power allocation schemes that maximize the instantaneous received signal-to-noise ratio (SNR) in an AF multi-hop transmission system under short-term and long-term power constraints. For the cases with and without

L. Han (✉) • J. Mu • S. Liu • Z. Zhang
College of Electronics and Communication Engineering,
Tianjin Normal University, Tianjin 300387, China
e-mail: hanliang@mail.tjnu.edu.cn

J. Mu et al. (eds.), *The Proceedings of the Third International Conference on Communications, Signal Processing, and Systems*, Lecture Notes in Electrical Engineering 322, DOI 10.1007/978-3-319-08991-1_33

perfect feedback of CSI at the source and relay, the optimal power control methods were investigated in [5]. Also, the optimal power allocations were obtained in [6, 7] by minimizing the bit error rate (BER) over Rayleigh fading channels for AF and DF relaying, respectively.

On the other hand, the benefits of relaying can be further exploited by optimization of the relay locations. As such, how to place the relay node to achieve the best system performance has attracted much attention in recent years. In [8], Kramer et al. investigated the impact of the relay location on the achievable rates by using various relaying schemes, such as decode-and-forward (DF) and compress-and-forward (CF). As an extension of [8], Aggarwal et al. [9] addressed the problem on how to deploy relays to maximize the system coverage with a given transmission rate, where the relay locations become design parameters. In [10], the average transmission rate was adopted as the performance metric, and a vector quantization algorithm was proposed to compute the optimal relay placement, with given cell size and the number of relays. In [11], the authors jointly optimized the power allocation at the source and the relay and the relay position for amplify-and-forward (AF) relaying over Weibull fading channels.

Although there has been growing interests on the optimization of power allocation and relay location, the current literatures are mainly limited to the noise-limited environment. There have been no results on the joint optimization of the power allocation and relay location in the presence co-channel interference. This is the objective of the present work.

33.2 System Model

The system model is shown in Fig. 33.1. We consider a cooperative relaying system consisting of three nodes, namely a source, a relay and a destination. Assume that the source, relay, destination and one interferer are located in a straight line, where l_{SD}, l_{SR}, l_{RD}, l_{ID} and l_{IR} denote the distances of source-to-destination, source-to-relay, relay-to-destination, interferer-to-destination and interferer-to-relay, respectively. The DF relaying scheme adopted is carried out in two time slots. In the first time slot, the source transmits a signal to the relay and the destination, and the received signals at the relay and the destination are given as

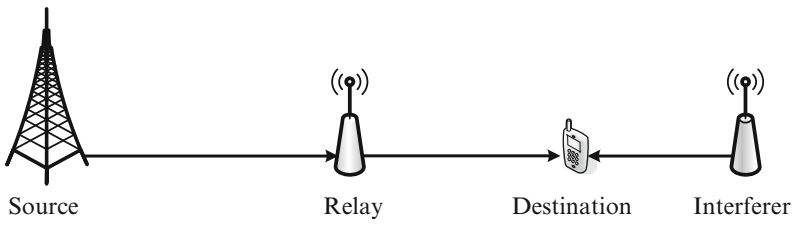

Fig. 33.1 System model

$$y_R = \sqrt{P_S l_{SR}^{-\alpha}} h_{SR} x + \sqrt{P_I l_{IR}^{-\alpha}} h_{IR} c_1 + n_R \tag{33.1}$$

$$y_{D,1} = \sqrt{P_S l_{SD}^{-\alpha}} h_{SD} x + \sqrt{P_I l_{ID}^{-\alpha}} h_{ID,1} c_1 + n_{D,1} \tag{33.2}$$

respectively, where P_S and P_I are the transmit power of the source and the interferer, respectively, α is the path loss exponent, x and c_1 denotes the transmitted symbol of the source and the interferer with unit power, respectively. If the relay decodes the received symbol successfully, it forwards the decoded symbol to the destination in the second time slot, and the received signal at the destination is

$$y_{D,2} = \sqrt{P_R l_{RD}^{-\alpha}} h_{RD} x + \sqrt{P_I l_{ID}^{-\alpha}} h_{ID,2} c_2 + n_{D,2} \tag{33.3}$$

where P_R is the transmit power of the relay node. In (33.1)–(33.3), h_{SD}, h_{SR}, h_{RD}, h_{ID} and h_{IR} denote the small-scale fading coefficients of source-to-destination, source-to-relay, relay-to-destination, interferer-to-destination and interferer-to-relay, respectively, which are assumed to be independent and identically distributed (i.i.d.) zero-mean complex Gaussian random variables with unit-variance; n_R, $n_{D,1}$, $n_{D,2}$ denote i.i.d. complex additive white Gaussian noise (AWGN) with zero mean and variance σ_n^2.

33.3 Outage Probability Analysis

In this section, we derive the outage probability for the DF relaying systems. The outage probability is defined as the probability that the instantaneous received SNR falls below a specified threshold β. Instead of using maximal ratio combining (MRC), which requires the channel state information (CSI), we use selection combining (SC) at the destination. Therefore, the outage probability is given by

$$P_{\text{out}} = P_{\text{out}}^{D,1} P_{\text{out}}^{R} + P_{\text{out}}^{D,1} \left(1 - P_{\text{out}}^{R}\right) P_{\text{out}}^{D,2} \tag{33.4}$$

where $P_{\text{out}}^{D,1}$, P_{out}^{R}, $P_{\text{out}}^{D,2}$ denote the outage probabilities of the source-to-destination, source-to-relay, and relay-to-destination, respectively. We can obtain

$$P_{\text{out}}^{R} = \Pr\left(\frac{P_S l_{SR}^{-\alpha} |h_{SR}|^2}{P_I l_{IR}^{-\alpha} |h_{IR}|^2 + \sigma_n^2} < \beta\right) = 1 - \exp\left(-\frac{\beta \sigma_n^2}{P_S l_{SR}^{-\alpha}}\right) \frac{P_S l_{SR}^{-\alpha}}{P_S l_{SR}^{-\alpha} + \beta P_I l_{IR}^{-\alpha}} \tag{33.5}$$

$$P_{\text{out}}^{D,1} = \Pr\left(\frac{P_S l_{SD}^{-\alpha}|h_{SD}|^2}{P_I l_{ID}^{-\alpha}|h_{ID,1}|^2 + \sigma_n^2} < \beta\right)$$
$$= 1 - \exp\left(-\frac{\beta\sigma_n^2}{P_S l_{SD}^{-\alpha}}\right)\frac{P_S l_{SD}^{-\alpha}}{P_S l_{SD}^{-\alpha} + \beta P_I l_{ID}^{-\alpha}} \tag{33.6}$$

$$P_{\text{out}}^{D,2} = \Pr\left(\frac{P_R l_{RD}^{-\alpha}|h_{RD}|^2}{P_I l_{ID}^{-\alpha}|h_{ID,2}|^2 + \sigma_n^2} < \beta\right)$$
$$= 1 - \exp\left(-\frac{\beta\sigma_n^2}{P_R l_{RD}^{-\alpha}}\right)\frac{P_R l_{RD}^{-\alpha}}{P_R l_{RD}^{-\alpha} + \beta P_I l_{ID}^{-\alpha}} \tag{33.7}$$

By substituting (33.5)–(33.7) into (33.4), we can obtain the outage probability. Since the closed-form expression is complex, we consider the interference-limited environment, which means that the noise can be ignored. Therefore, the outage probability can be given as

$$P_{\text{out}} \approx \frac{\beta P_I l_{ID}^{-\alpha}}{P_S l_{SD}^{-\alpha} + \beta P_I l_{ID}^{-\alpha}}\frac{\beta P_I l_{IR}^{-\alpha}}{P_S l_{SR}^{-\alpha} + \beta P_I l_{IR}^{-\alpha}} + \frac{\beta P_I l_{ID}^{-\alpha}}{P_S l_{SD}^{-\alpha} + \beta P_I l_{ID}^{-\alpha}}\frac{\beta P_I l_{ID}^{-\alpha}}{P_R l_{RD}^{-\alpha} + \beta P_I l_{ID}^{-\alpha}} \tag{33.8}$$

In the high signal-to-interference ratio (SIR) regime, the outage probability can be further approximate as

$$P_{\text{out}} \approx \frac{\beta P_I l_{SD}^{\alpha}}{P_S l_{ID}^{\alpha}}\frac{\beta P_I l_{SR}^{\alpha}}{P_S l_{IR}^{\alpha}} + \frac{\beta P_I l_{SD}^{\alpha}}{P_S l_{ID}^{\alpha}}\frac{\beta P_I l_{RD}^{\alpha}}{P_R l_{ID}^{\alpha}} \tag{33.9}$$

33.4 Optimization of Power Allocation and Relay Location

33.4.1 Power Allocation Optimization Under Fixed Relay Location

In this case, we derive the optimal power allocation by assuming fixed relay location. We fix the total transmitted power of the source and the relay as P_T, then the optimization problem can be formulated as

$$\begin{cases} \left(P_S^*, P_R^*\right) = \arg\min\limits_{P_S, P_R} \quad P_{\text{out}}(P_S, P_R) \\ \text{subject to}: \; P_S + P_R = P_T \quad \text{and} \quad P_S, P_R \geq 0 \end{cases} \tag{33.10}$$

Substituting $P_R = P_T - P_S$ into (33.9), taking the first derivative with respect to P_S, and letting the derivative be equal to zero, we obtain

$$P_S^* = \frac{1+\sqrt{1+8l_{SR}^{\alpha}l_{ID}^{\alpha}l_{IR}^{-\alpha}l_{RD}^{-\alpha}}}{3+\sqrt{1+8l_{SR}^{\alpha}l_{ID}^{\alpha}l_{IR}^{-\alpha}l_{RD}^{-\alpha}}}P_T, P_R^* = \frac{2}{3+\sqrt{1+8l_{SR}^{\alpha}l_{ID}^{\alpha}l_{IR}^{-\alpha}l_{RD}^{-\alpha}}}P_T \quad (33.11)$$

It is easy to check that $\frac{\partial^2 P_{\text{out}}}{\partial P_s^2} > 0$ for $0 \le P_s, P_r \le P_t$,which means the objective function is convex. Therefore, we conclude that the solution is optimal. From (33.11), we observe that the optimal power allocation depends on the relay location and the interferer location. Moreover, we can see that $P_s \in (P_t/2, P_t)$,$P_r \in (0, P_t/2)$, which means the equal power strategy is not optimal.

33.4.2 Relay Location Optimization Under Fixed Power Allocation

In this case, we derive the optimal relay location under fixed power allocation. The optimization problem can be formulated as

$$\begin{cases} x^* = \arg\min\limits_{x} \ P_{\text{out}}(x) \\ \text{subject to}: \ 0 < x < l_{SD} \end{cases} \quad (33.12)$$

where $x = l_{SR}$. Taking the first derivative with respect to x, and letting the derivative be equal to zero, we obtain

$$P_S(l_{SD}+l_{ID}-x)^{\alpha+1}(l_{SD}-x)^{\alpha-1} = P_R l_{ID}^{\alpha}(l_{SD}+l_{ID})x^{\alpha-1} \quad (33.13)$$

It is easy to check that $\frac{\partial^2 P_{\text{out}}}{\partial x^2} > 0$ for $\alpha > 1$ and $0 < x < l_{SD}$,which means the objective function is convex. Therefore, we conclude that the solution in (33.13) is optimal to problem (33.12).

33.4.3 Joint Optimization of Power Allocation and Relay Location

In this case, we jointly optimize the power allocation and relay location to further improve the outage performance. By substituting $l_{RD} = l_{SD} - x$ and $P_R = P_T - P_S$ into (33.9), we obtain

$$P_{\text{out}}(P_S, x) \approx \frac{\beta^2 P_I^2 l_{SD}^{\alpha}}{l_{ID}^{\alpha}} f(P_S, x) + \frac{\beta^2 P_I^2 l_{SD}^{\alpha}}{l_{ID}^{2\alpha}} g(P_S, x) \tag{33.14}$$

where $f(P_S, x) = \frac{x^{\alpha}}{P_S^2 (l_{SD} - x + l_{ID})^{\alpha}}$ and $g(P_S, x) = \frac{(l_{SD} - x)^{\alpha}}{P_S (P_T - P_S)}$. The optimization problem can be formulated as

$$\begin{cases} \left(P_S^*, x^*\right) = \arg\min\limits_{P_S, x} \; P_{\text{out}}(P_S, x) \\ \text{subject to}: \; 0 < x < l_{SD}, \;\; 0 < P_S \le P_T \end{cases} \tag{33.15}$$

Though the matrix of the second partial derivative (Hessian matrix) of the objective function is complex, we can check the Hessian matrix of $f(P_S, x)$ and $g(P_S, x)$ are positive definite for $\alpha > 3$. Therefore, the Hessian matrix of the objective function is positive definite for $\alpha > 3$. For analytical tractability, we assume $\alpha > 3$ in this paper. Then, the optimal power allocation and relay location can be obtained by setting the first derivatives of the objective function with respect to P_S and x to zero.

33.5 Numerical and Simulation Results

In this section, we present some numerical and simulation results to validate our analysis. Basic simulation parameters are given as follows: $l_{SD} = 1,000$ m, $\alpha = 3$, $\beta = 10$ dB, $\sigma^2 = -114$ dBm.

In Fig. 33.2, we show the relationship between the power allocation and the outage probability for different relay locations, where $l_{ID} = 500$ m, $P_T = 30$ dBm, and $P_I = -3$ dBm. As shown in Fig. 33.2, the simulation results approximately agree with the analytical results. Moreover, we can see that as the relay gets closer to the destination, we should put more power at the source.

In Fig. 33.3, we show the relationship between the relay location and the outage probability for two different interference scenarios, where $P_T = 30$ dBm, $P_S = P_R = 0.5 P_T$. From Fig. 33.3, we can observe that the different interference environment will impact the optimal relay location. It is further proved from Fig. 33.3 that the simulation results approximately agree with the analytical results.

In Fig. 33.4, we compare the outage performance for different optimization schemes. Using the proposed optimization schemes, we can obtain the optimal $P_S = 0.55 P_T$ for the relay locating in the middle of the source and the destination, the optimal $l_{SR} = 0.63 l_{SD}$ for equal power allocation, and the optimal $(P_S, l_{SR}) = (0.79 P_T, 0.73 l_{SD})$ for the joint optimization. It is observed from Fig. 33.4 that the joint optimization outperforms the other two optimization schemes and achieves the minimum outage probability.

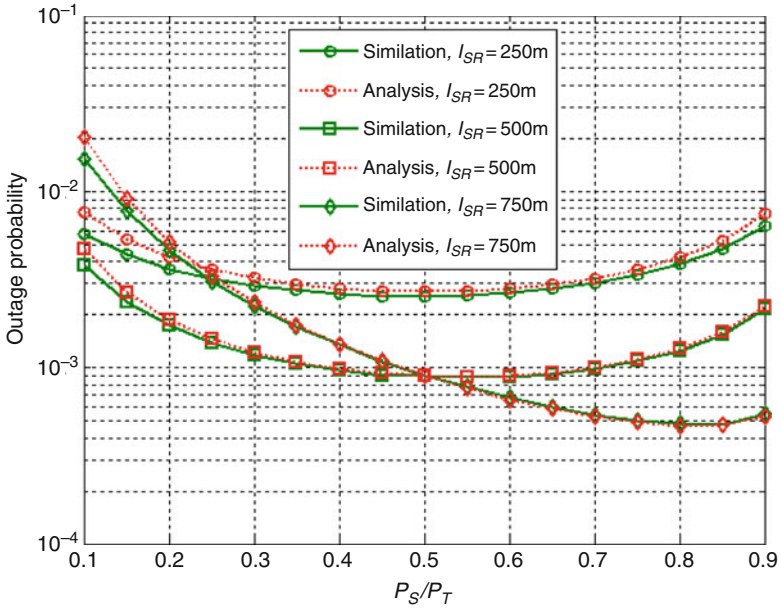

Fig. 33.2 Outage performance versus power allocation with different relay location

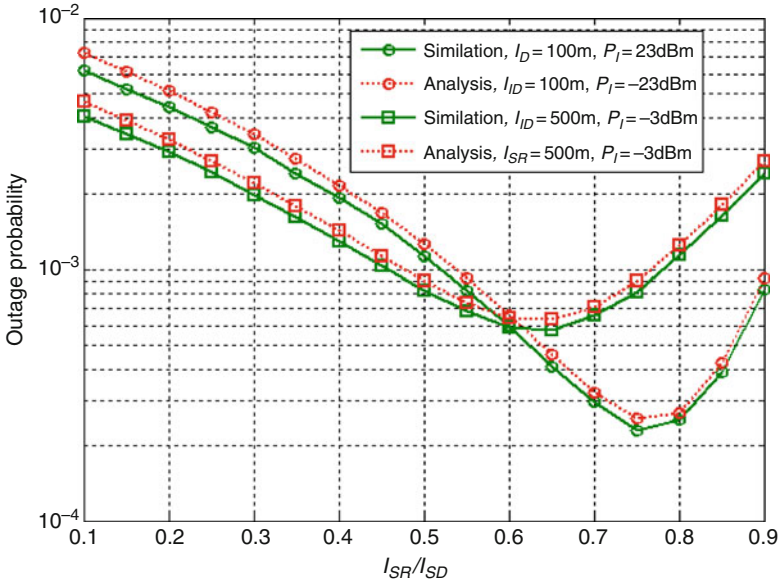

Fig. 33.3 Outage performance versus relay location for two different interference scenarios

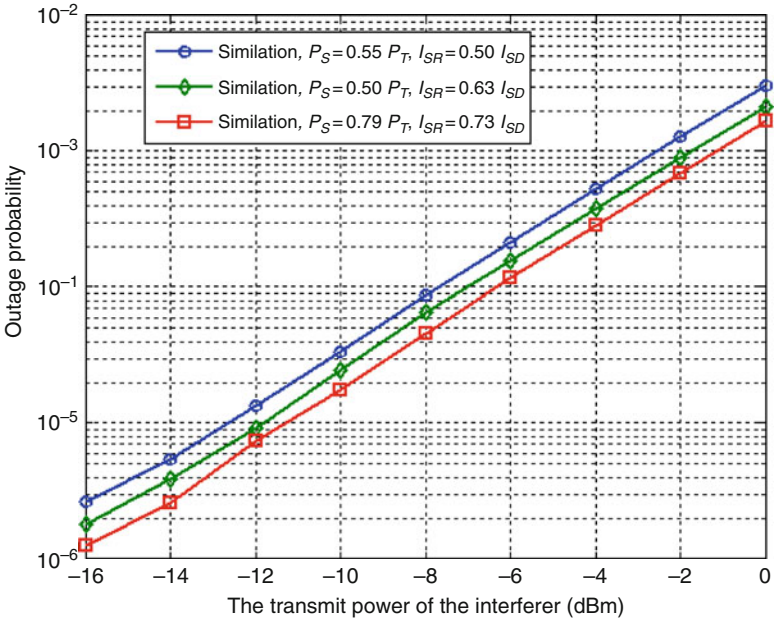

Fig. 33.4 Outage performance under different optimization schemes

Conclusion

In this paper, we investigated the optimization of power allocation and relay location in the presence of co-channel interference. It was shown that the co-channel interference has significant impacts on the outage performance and hence on the optimal power allocation and relay location. We compared three optimization schemes and showed that joint optimization obtains the best outage performance.

References

1. Yang Y, Hu H, Xu J, Mao G (2009) Relay technologies for WiMAX and LTE-advanced mobile systems. IEEE Commun Mag 47(10):100–105
2. Hoymann C, Chen W, Montojo J, Golitschek A, Koutsimanis C, Shen X (2012) Relaying operation in 3GPP LTE: challenges and solutions. IEEE Commun Mag 50(2):156–162
3. Host-Madsen A, Zhang J (2005) Capacity bounds and power allocation for wireless relay channels. IEEE Trans Inf Theory 51(6):2020–2040
4. Farhadi G, Beaulieu NC (2009) Power-optimized amplify-and-forward multi-hop relaying systems. IEEE Trans Wirel Commun 8(9):4634–4643
5. Ahmed N, Khojastepour MA, Sabharwal A, Aazhang B (2006) Outage minimization with limited feedback for the fading relay channel. IEEE Trans Commun 54(4):659–669
6. Fareed MM, Uysal M (2008) BER-optimized power allocation for fading relay channels. IEEE Trans Wirel Commun 7(6):2350–2359

7. Khabbazibasmenj A, Vorobyov SA (2011) Power allocation based on SEP minimization in two-hop decode-and-forward relay networks. IEEE Trans Signal Process 59(8):3954–3963
8. Kramer G, Gastpar M, Gupta P (2005) Cooperative strategies and capacity theorems for relay networks. IEEE Trans Inf Theory 51(9):3037–3063
9. Aggarwal V, Bennatan A, Calderbank AR (2009) On maximizing coverage in Gaussian relay networks. IEEE Trans Inf Theory 55(6):2518–2536
10. Pourahmadi V, Fashandi S, Saleh A, Khandani AK (2011) Relay placement in wireless networks: a study of the underlying tradeoffs. IEEE Trans Wirel Commun 10(5):1383–1388
11. Ikki SS, Aissa S (2011) A study of optimization problem for amplify-and-forward relaying over Weibull fading channels with multiple antennas. IEEE Commun Lett 15(11):1148–1152

Chapter 34
A Robustness Enhanced Beamformer

Ying Zhang, Chuanyi Pan, and Huapeng Zhao

Abstract In this paper, we propose a robustness enhanced beamformer which does not involve any additional constraint on weight vector beside the distortionless response constraint. The proposed algorithm enhances its robustness against steering vector error by incorporating a term which aims to minimize the cross-correlation between the real and the imaginary parts of the desired signal in the objective function. Extensions of the proposed algorithm to l_1-norm minimization and incorporation of robust constraint are also addressed. Computer simulations verify validity and advantage of the proposed algorithm.

Keywords Beamforming • Impulsive noise • Robustness • Steering vector error

34.1 Introduction

One of the most well-known techniques is the minimum variance distortionless response (MVDR) beamformer [1] which produces output with desired magnitudes and phases using the preset steering vector. However, in real applications, the performance of the MVDR beamformer is shown to deteriorate significantly due to distinction between the nominal and actual steering vector [2]. In this letter, we propose a robustness enhanced beamformer which does not involve additional constraint on the weight vector beside the distortionless response constraint. The proposed beamformer achieves robustness by incorporating a term which aims to minimizing the cross-correlation of the real and the imaginary parts of the desired signal in the objective function. Simulation results show that the proposed algorithm outperforms the MVDR beamformer and the norm constrained MVDR beamformer [3] in the presence of steering vector error.

Y. Zhang (✉) • C. Pan • H. Zhao
College of Electronic Engineering, University of Electronic Science and Technology of China, Chengdu, China
e-mail: zh0045ng@e.ntu.edu.sg; zdpcy2008@163.com

J. Mu et al. (eds.), *The Proceedings of the Third International Conference on Communications, Signal Processing, and Systems*, Lecture Notes in Electrical Engineering 322, DOI 10.1007/978-3-319-08991-1_34

34.2 The Proposed Algorithm

In real applications, signals are received and transmitted in real-valued form. Denoting the snapshots of array as u, its Hilbert transform as v, the real-valued optimization problem of the MVDR beamformer is given by

$$\min_{\mathrm{a,b}} \begin{pmatrix} \mathbf{a} \\ \mathbf{b} \end{pmatrix}^{\mathrm{T}} \begin{pmatrix} \mathbf{A} \\ \mathbf{B} \end{pmatrix} \begin{pmatrix} \mathbf{a} \\ \mathbf{b} \end{pmatrix} \tag{34.1a}$$

$$\text{Subject to } \left(\mathbf{a}^{\mathrm{T}}, \mathbf{b}^{\mathrm{T}}\right)\mathbf{c}_0(\theta)=1 \tag{34.1b}$$

Where $\mathbf{c}_0(\theta) = [\mathrm{Real}(\mathbf{a}_0(\theta))^T \ \mathrm{Imag}(\mathbf{a}_0(\theta))^T]^T$, and

$$\mathbf{A} = \begin{pmatrix} \mathbf{R}_{uu} + \mathbf{R}_{vv} & \mathbf{R}_{uv} - \mathbf{R}_{vu} \end{pmatrix} \tag{34.2}$$

$$\mathbf{B} = \begin{pmatrix} \mathbf{R}_{vu} - \mathbf{R}_{uv} & \mathbf{R}_{uu} + \mathbf{R}_{vv} \end{pmatrix} \tag{34.3}$$

In (34.2) and (34.3), $\mathbf{R}$ denotes the correlation matrix.

In this letter, we propose the following optimization problem to design a beamformer:

$$\min_{z} E\left(\left|\mathbf{z}^T\mathbf{y}\right|^2\right), \tag{34.4a}$$

$$\text{Subject to} \mathbf{z}^T\mathbf{c}_0(\theta) = 1 \tag{34.4b}$$

Where

$$\mathbf{z} = \left[\mathbf{c}^T, \mathbf{d}^T\right]^T, \ \mathbf{y} = \begin{bmatrix} \mathbf{u} + \mathbf{v} \\ \mathbf{v} - \mathbf{u} \end{bmatrix},$$

Using the Lagrange multiplier technique, the solution of (34.4) is given by

$$\mathbf{z}_{opt} = \frac{\mathbf{R}_{yy}^{-1}\mathbf{c}_0(\theta)}{\left(\mathbf{c}_0^{\mathrm{T}}\mathbf{R}_{yy}^{-1}\mathbf{c}_0(\theta)\right)} \tag{34.5}$$

After deriving $\mathbf{z}_{opt} = [\mathbf{c}_{opt}^T, \mathbf{d}_{opt}^T]^T$, the desired signal is recovered using

$$\hat{s}\,(t) = \left(\mathbf{c}_{opt} + j\mathbf{d}_{opt}\right)^H(\mathbf{u}(\mathrm{t}) + j\mathbf{v}(\mathrm{t})) \tag{34.6}$$

From the definition of $\mathbf{y}$, it can be shown that (34.5) is equivalent to

$$\begin{pmatrix}\mathbf{c}\\ \mathbf{d}\end{pmatrix}_{opt} = \frac{\begin{pmatrix}\mathbf{A}+\mathbf{C}\\ \mathbf{B}+\mathbf{D}\end{pmatrix}^{-1}\mathbf{c}_0(\theta)}{\mathbf{c}_0^T(\theta)\begin{pmatrix}\mathbf{A}+\mathbf{C}\\ \mathbf{B}+\mathbf{D}\end{pmatrix}^{-1}\mathbf{c}_0(\theta)}, \tag{34.7}$$

Where

$$\mathbf{C} = (\mathbf{R}_{uv} + \mathbf{R}_{vu} \quad \mathbf{R}_{vv} - \mathbf{R}_{uu}),$$
$$\mathbf{D} = (\mathbf{R}_{vv} - \mathbf{R}_{uu} \quad -\mathbf{R}_{uv} - \mathbf{R}_{vu}),$$

From (34.7), it is equivalent to express the proposed optimization problem (34.4) as

$$\min_{\mathrm{a,b}} \begin{pmatrix}\mathbf{c}\\ \mathbf{d}\end{pmatrix}^{\mathrm{T}} \begin{pmatrix}\mathbf{A}+\mathbf{C}\\ \mathbf{B}+\mathbf{D}\end{pmatrix} \begin{pmatrix}\mathbf{c}\\ \mathbf{d}\end{pmatrix} \tag{34.8a}$$

$$\text{Subject to } (\mathbf{c}^{\mathrm{T}}, \mathbf{d}^{\mathrm{T}})\mathbf{c}_0(\theta)=1 \tag{34.8b}$$

Comparing (34.1) and (34.8), we see that for the proposed algorithm, the term $\begin{pmatrix}\mathbf{c}\\ \mathbf{d}\end{pmatrix}^{\mathrm{T}} \begin{pmatrix}\mathbf{C}\\ \mathbf{D}\end{pmatrix} \begin{pmatrix}\mathbf{c}\\ \mathbf{d}\end{pmatrix}$ is added to the objective function of the MVDR beamformer. It can be deduced that

$$\begin{pmatrix}\mathbf{C}\\ \mathbf{D}\end{pmatrix} = E\left[\begin{pmatrix}\mathbf{u}\\ \mathbf{v}\end{pmatrix}(\mathbf{v}^{\mathrm{T}} \quad -\mathbf{u}^{\mathrm{T}}) + \begin{pmatrix}\mathbf{v}\\ -\mathbf{u}\end{pmatrix}(\mathbf{u}^{\mathrm{T}} \quad \mathbf{v}^{\mathrm{T}})\right]$$

From (34.6), we see that

$$(\mathbf{c}^{\mathrm{T}}, \mathbf{d}^{\mathrm{T}})_{opt} \begin{pmatrix}\mathbf{u}\\ \mathbf{v}\end{pmatrix} = Real(\hat{s}(t)), \tag{34.9a}$$

$$(\mathbf{c}^{\mathrm{T}}, \mathbf{d}^{\mathrm{T}})_{opt} \begin{pmatrix}\mathbf{v}\\ -\mathbf{u}\end{pmatrix} = Imag(\hat{s}(t)), \tag{34.9b}$$

Which means that the added term is a measurement of cross-correlation of the real part and imaginary part of the source. Since the real part and imaginary part are orthogonal, minimizing their cross-correlation helps enhance the beamformer's robustness.

34.3 Extension of the Proposed Algorithm

34.3.1 Extension of the Proposed Algorithm with Weight Constraint

Supposing that the steering vector uncertainty is contained in a sphere [2] the proposed robust beamformer can be derived by

$$\min_{\mathbf{z}} E\left(\left|\mathbf{z}^{\mathrm{T}}\mathbf{y}\right|^2\right), \tag{34.10a}$$

$$\text{Subjecting to}\, \mathbf{z}^{\mathrm{T}}\mathbf{c}(\theta) \geq 1, \mathbf{c}(\theta) = \mathbf{c}_0(\theta) + \mathbf{e}, \|\mathbf{e}\|_2 \leq \varepsilon. \tag{34.10b}$$

Using Lagrange multiplier technique, its solution is derived as

$$\mathbf{z} = -\lambda\left(\mathbf{R}_{\mathrm{yy}} + \lambda\mathbf{Q}\right)^{-1}\mathbf{c}_0(\theta) \tag{34.11}$$

Where λ is the root of the equation:

$$f(\lambda)=\lambda^2\sum_{\mathrm{i}=1}^{2\mathrm{L}}\frac{c_{\mathrm{i}}^2\gamma_{\mathrm{i}}}{\left(1+\lambda\gamma_{\mathrm{i}}\right)^2} - 2\lambda\sum_{\mathrm{i}=1}^{2\mathrm{L}}\frac{c_{\mathrm{i}}^2}{\left(1+\lambda\gamma_{\mathrm{i}}\right)} - 1 \tag{34.12}$$

In (34.11), $\mathbf{Q} = \varepsilon^2\mathbf{I} - \mathbf{c}_0(\theta)\mathbf{c}_0^{\mathrm{T}}(\theta)$. In (34.12), c_{i} is the *ith* element of $\mathbf{c} = \mathbf{V}^T\mathbf{R}_{yy}^{-1/2}\mathbf{c}_0(\theta)$, γ_i is the *ith* element of the diagonal elements of Γ. $\mathbf{V}$ and Γ denote the matrices consisting of eigenvectors and eigenvalues of $\mathbf{R}_{yy}^{-1/2}\mathbf{Q}(\mathbf{R}_{yy}^{-1/2})^T$, respectively.

The proposed optimization problem is given by

34.3.2 Extension of the Proposed Algorithm Using l_1-Norm Minimization

There have been literatures demonstrating that impulsive noise appears on the signal at wireless receiver in a form of impulsive noise bursts [4]. To enhance the performance of beamformers in the presence of impulsive noise, some beamforming algorithms have been introduced [5, 6]. In this letter, we choose the l_1-norm criterion because of its computational simplicity.

The proposed optimization problem is given by

$$\min_{z} E\left(\left|\mathbf{z}^T\mathbf{y}\right|\right), \text{ subject to } \mathbf{z}^T\mathbf{c}_0(\theta) \geq 1 \tag{34.13}$$

Because closed form of the solution is not available, the solution to (34.13) can be iteratively obtained via

$$\mathbf{z}(\mathrm{k}+1) = \mathbf{P}\left[\mathbf{z}(\mathrm{k}) - \mu\left|\mathbf{z}^T(\mathrm{k})\mathbf{y}(\mathrm{k})\right|^{-1}\mathbf{z}^T(\mathrm{k})\mathbf{y}(\mathrm{k})\mathbf{y}(\mathrm{k})\right] + \mathbf{f}, \tag{34.14}$$

Where

$$\mathbf{P} = \mathbf{I} - \mathbf{c}_0(\theta)\mathbf{c}_0^T(\theta)/\mathbf{c}_0^T(\theta)\mathbf{c}_0(\theta),$$
$$\mathbf{f} = \mathbf{c}_0(\theta)/\mathbf{c}_0^T(\theta)\mathbf{c}_0(\theta),$$

And μ is the stepsize.

34.4 Computer Simulations

A uniform linear array (ULA) with 10 half-wavelength spaced sensors is considered. The source from 20°is the Signal of Interest (SOI), while the interferences are from $-50°$, 0°, 35°, 70°. The Signal-to-Interference Ratio (SINR) is -10 dB. Additive Gaussian noise is added which gives the Signal-to-Noise Ratio (SNR) as 3 dB. Two thousand independent trials are conducted to compute the output SINR.

34.4.1 In the Presence of Steering Vector Error

First of all, look direction mismatch is assumed. Figure 34.1 shows the derived beampatter of various algorithms with look direction mismatch equal to 3°. We plot the output SINR versus look direction mismatch in Fig. 34.2. It is observed from Fig. 34.1 that at the direction of SOI, the proposed algorithms do not suffer from the problem of SOI cancelation compared with the MVDR beamformer and the MVDR beamformer with norm constraint which suppress the SOI about -15 dB. From Fig. 34.2, we see that the output SINR of the proposed algorithms are much higher than that of the other two algorithms. The performance of all algorithms deteriorates as the look direction error increases.

Then, we add sensor position error to array steering vector error. Sensor position error is assumed to be a Gaussian variable with zero mean and standard deviation 10 % of inter-element spacing. Figure 34.3 plots the output SINR versus standard deviation of sensor position error. From Fig. 34.3, we can see that the proposed algorithms have higher output SINR than that of the other algorithms.

In Fig. 34.4, the output SINR versus SNR is plotted. We assume that the look direction of the beamformer is $20° + \Delta$, where Δ is a Gaussian variable with zero mean and standard deviation $\sqrt{2}°$. It is observed from Fig. 34.4 that the proposed

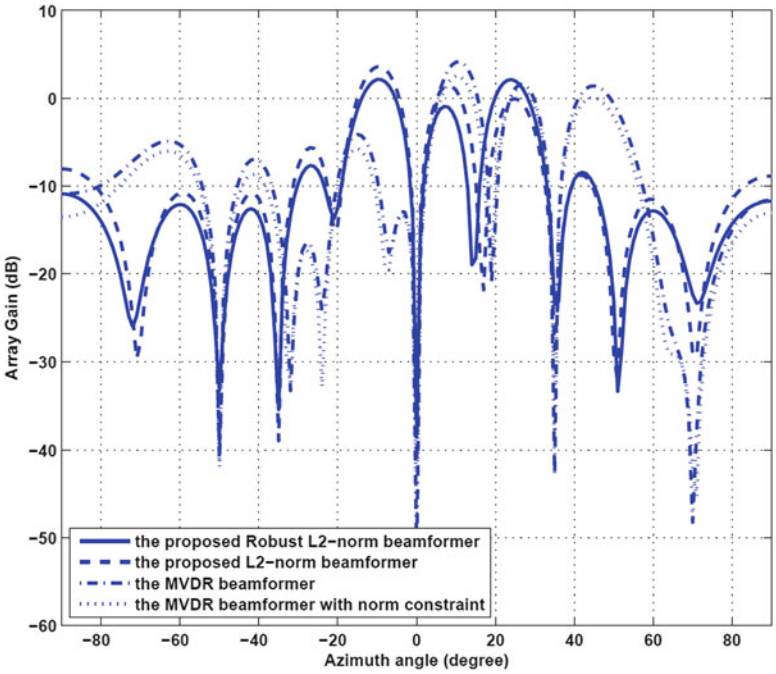

Fig. 34.1 Array gain of algorithm in the presence of look direction mismatch

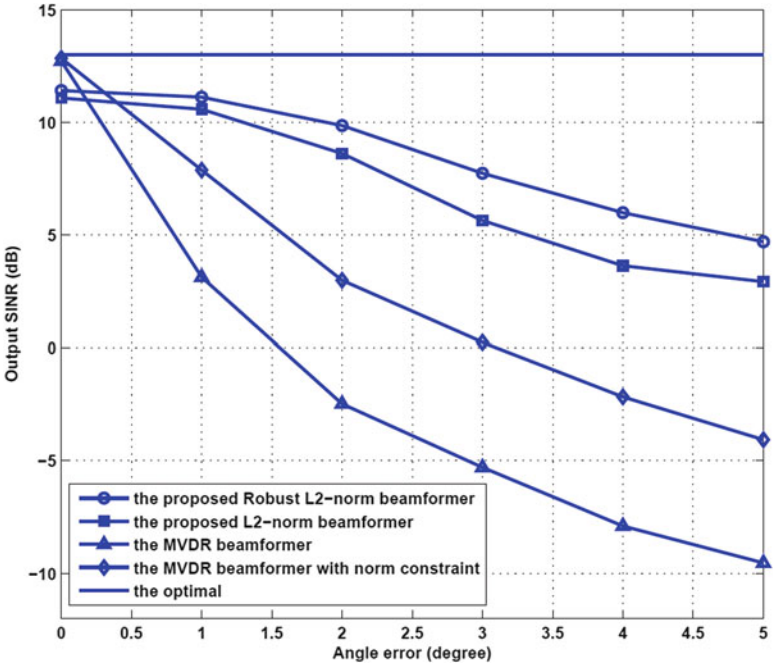

Fig. 34.2 Output SINR versus look direction mismatch

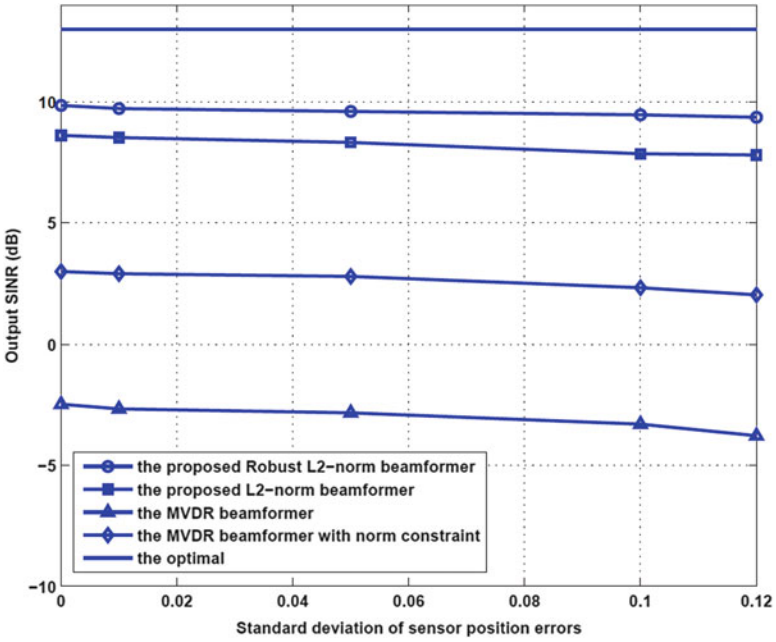

Fig. 34.3 Output SINR versus standard deviation of the sensor position error

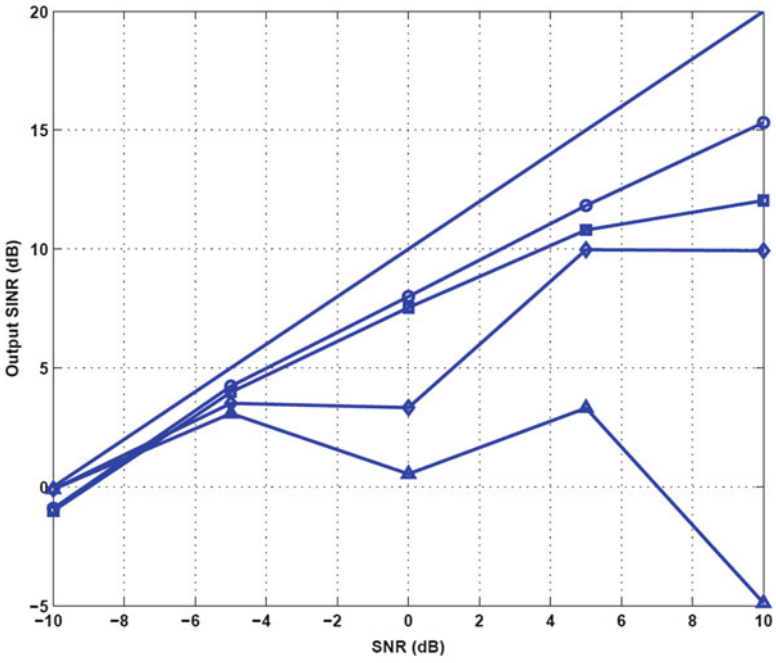

Fig. 34.4 Output SINR versus SNR in the presence of steering vector error

algorithms given higher output SINR than that of the other algorithms. The robust constraint given by (34.10b) helps enhance robustness of the proposed algorithm.

34.4.2 In the Presence of the Intermittent Impulsive Noise and Steering Vector Error

In this simulation, we take both impulsive noise and steering vector error into account. We generate impulsive noise using ϵ mixture of two Gaussian random variables. We assume that the first, fifth and sixth sensors are failed. We evaluate the performance of the proposed algorithm with l_1-norm minimization. Figure 34.5 shows the array gain using different methods. Figure 34.6 gives the output SINR of the algorithms. It is observed that the proposed beamformer gives array gain closed to 0 dB at the direction of SOI, while other algorithms suppress the SOI about 10 dB. The proposed algorithm has the highest output SINR among all the algorithms.

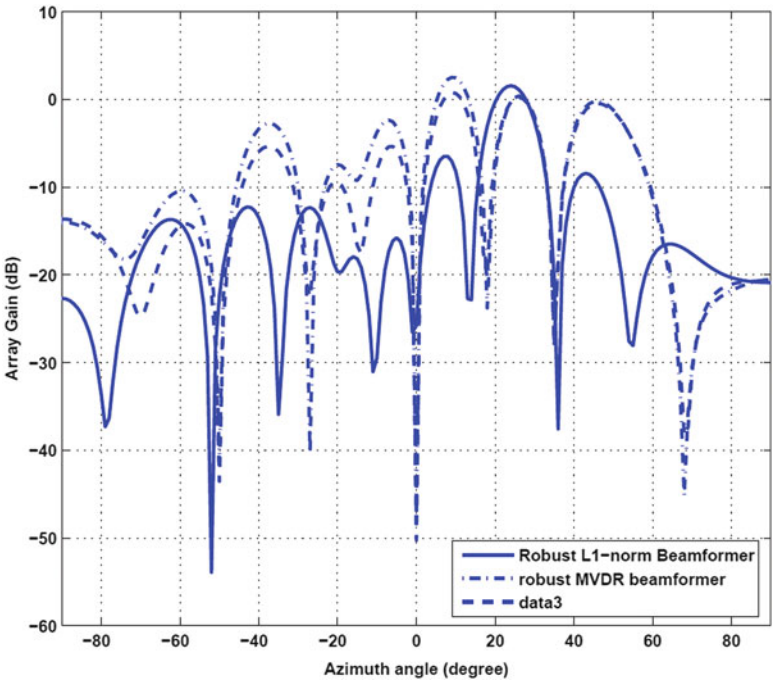

Fig. 34.5 Array gain of the algorithms in the presence of steering vector error and impulsive noise

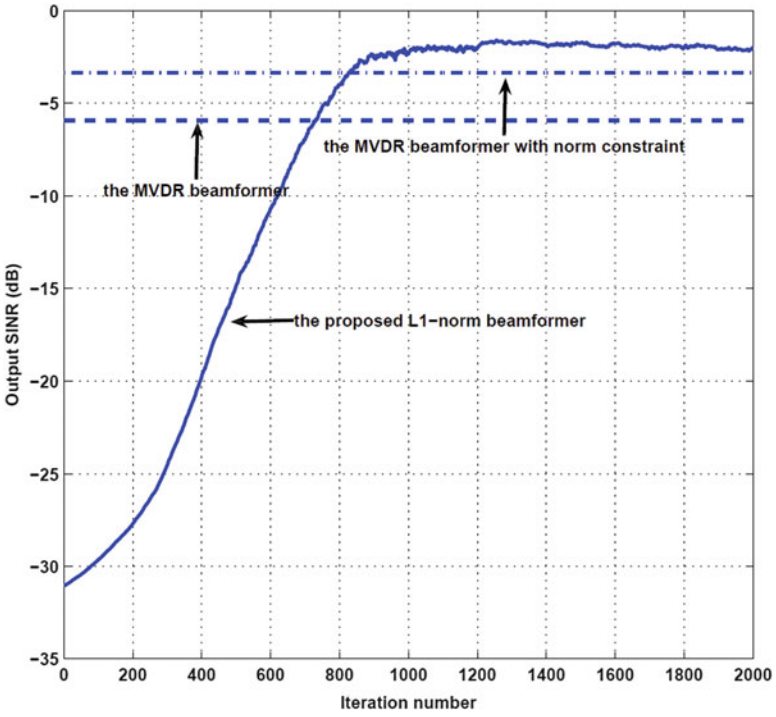

Fig. 34.6 Output SINR of various algorithms in the presence of sensor position error and impulsive noise

Conclusions

This letter proposes a new adaptive beamforming algorithm which is robust against array steering vector error. The proposed algorithm enhance its robustness by incorporating a term which aims to minimize the cross-correlation of the real and imaginary parts of the desired signal in objective function. Extension of the proposed algorithm to other applications is applicable. Computer simulations demonstrate the validity and superiority of the new algorithm.

Acknowledgment The author wishes to acknowledge the financial support of the National Science Foundation of China through Grant Nos. 61101094 and 61201275.

References

1. Capon J (1969) High-resolution frequency-wavenumber spectrum analysis. Proc IEEE 57:1408–1418
2. Li J, Stoica P (2005) Robust adaptive beamforming. Wiley, USA
3. Li J, Stoica P, Wang Z (2004) Doubly constrained robust capon beamformer. IEEE Trans Signal Process 52:2407–2423
4. Hu B, Beaulieu NC (2008) On characterizing multiple access interference in TH-UWB systems with impulsive noise models. In: IEEE radio and wireless symposium, Orlando, pp 879–882
5. Kivinen J, Warmuth MK, Hassibi B (2006) The p-norm generalization of the LMS algorithm for adaptive filtering. IEEE Trans Signal Process 54:1782–1793
6. He J, Liu Z, Wong KT (2007) Linearly constrained minimum-geometric power adaptive beamforming using logarithmic moments of data containing heavy tailed noise of unknown statistics. IEEE Antennas Wirel Propag Lett 6:600–603

Chapter 35
An Improved Clustering Cooperative Spectrum Sensing Algorithm

Huiqin Liu, Shubin Wang, Fei Li, Sarina Liu, and Hongyue Wang

Abstract For the fading channel effect on the performance of cooperative spectrum sensing in cognitive wireless network, an improved clustering cooperative spectrum sensing algorithm based on double-threshold energy detection is presented in this paper. Within each cluster, the cognitive user that the channel quality is best to the data fusion center (DFC) is chosen as the cluster head (CH), other cognitive users in the cluster use the double-threshold energy detection on the local position. The detective information is sent to the CH, the CH makes the decision of the cluster, and then the decision information of each cluster is sent to the DFC by each CH. The DFC use the "or" rule to fuse each clusters' results, and make a final decision whether the authorized user (AU) exists. Simulation results show that the proposed algorithm can further improve the detection probability of cognitive wireless network than traditional cooperative spectrum sensing based on double threshold detection.

Keywords Cognitive radio networks • Cooperative sensing • Clustering • Double-threshold energy detection

35.1 Introduction

Cognitive radio is an effective solution scheme for spectrum sharing [1], spectrum sensing is one of key technologies of cognitive radio network [2, 3], which main function is to detect idle frequency band named the spectrum hole. Meanwhile, the detection technology also requires the ability to quickly identify authorized users (AU), so that the cognitive users can stop to use the band immediately when authorized users emerge, and ensure the cognitive users to authorized users communicate without causing interference.

Traditional double-threshold energy detection [3] is one of key technologies of spectrum sensing, as shown in Fig. 35.1, there are two thresholds λ_L and λ_H, E_k denotes

H. Liu • S. Wang (✉) • F. Li • S. Liu • H. Wang
College of Electronic Information Engineering,
Inner Mongolia University, Hohhot, China
e-mail: wangsb09@gmail.com

J. Mu et al. (eds.), *The Proceedings of the Third International Conference on Communications, Signal Processing, and Systems*, Lecture Notes in Electrical Engineering 322, DOI 10.1007/978-3-319-08991-1_35

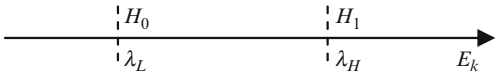

Fig. 35.1 Double-threshold energy detection

the signal energy which is the kth cognitive user received. The kth cognitive user will think that the authorized user is not exist when E_k is less than λ_L, and make H_0 detection, then reports the result to the data fusion center (DFC). If E_k greater than λ_H, the kth cognitive user determines the authorized user (AU) is present, correspondingly, make H_1 detection and reports the result to the DFC. If E_k is between λ_L and λ_H, the kth cognitive user not make detection, and not send any information to the DFC.

The cooperative spectrum sensing based on traditional double-threshold detection method now is a relatively new kind of judgment program in cognitive radio network, but when the number of cognitive users tends to be very large, the detection performance of cooperative spectrum sensing will seriously be affected by channel fading. For the question, this paper proposes an improved clustering cooperative spectrum sensing algorithm, and gives concrete expression to determine the cluster head. This paper also improves double-threshold detection, each cognitive user within a cluster adopt improved double-threshold energy detection locally. The detective performance of improved cooperative spectrum detection algorithm has been greatly improved compare with the algorithm that cooperative spectrum sensing based on traditional double threshold detection [3, 4].

35.2 Cluster Algorithm

All cognitive users of the whole cognitive radio network are divided into several clusters [5, 6], as shown in Fig. 35.2. For selecting cluster heads [7, 8], the distances is calculated from all the cognitive users in each cluster to the fusion center, the user with the shortest distance to fusion center is cluster head (CH), then the CH sends the cooperative sensing result of its cluster to the fusion center. In this way, not only ensure the accuracy of the information transmission, but also be able to save transmission channel bandwidth.

35.3 An Improved Clustering Cooperative Spectrum Sensing Algorithm

35.3.1 Improved Double-Threshold Energy Detection

The improved double-threshold energy detection is as following. When E_k is between λ_L and λ_H, the kth cognitive user cannot make a local decision, but E_k is send to the DFC. In this way DFC collects two possible information-local decision results and the reception signal energy value-from cognitive users.

For the improved double-threshold energy detection, $P_{d,k}$ and $P_{f,k}$ and $P_{m,k}$ respectively mean the detection probability, false alarm probability and leakage

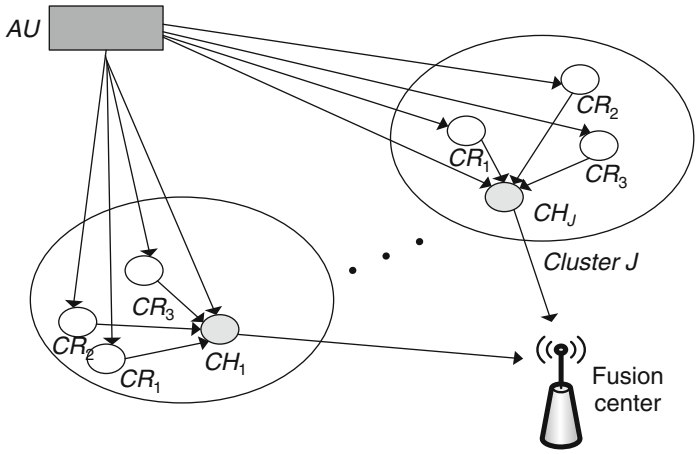

Fig. 35.2 Multi-cluster model of cooperative spectrum sensing

alarm probability of the kth cognitive user. In order to facilitate the following discussion, two parameters $\theta_{0,k}$ and $\theta_{1,k}$ are introduced, which respectively denote the probability of the kth cognitive user that cannot make local decision in case of two hypothesis H_0 and H_1,

$$\theta_{0,k} = P\{\lambda_L < E_k \le \lambda_H | H_0\} \tag{35.1}$$

$$\theta_{1,k} = P\{\lambda_L < E_k \le \lambda_H | H_1\} \tag{35.2}$$

so it can get

$$P_{d,k} = P(E_k > \lambda_H | H_1) = Q_u\left(\sqrt{2\gamma_k}, \sqrt{\lambda_{H,k}}\right). \tag{35.3}$$

$$P_{f,k} = P(E_k > \lambda_H | H_0) = \frac{\Gamma(u, \lambda_{H,k}/2)}{\Gamma(u)} \tag{35.4}$$

$$P_{m,k} = P(E_k < \lambda_L | H_1) = 1 - \theta_{1,k} - P_{d,k} \tag{35.5}$$

where $\Gamma(a)$ and $\Gamma(a, b)$ respectively represent the complete and incomplete gamma function, $Q_{\mathcal{U}}(x, y)$ is the generalized Marcum function, γ_k represents the SNR of the kth cognitive user in a cluster, u represents the time-bandwidth product.

35.3.2 Selecting Cluster Head

In front narrative, the selection of cluster heads is to assume that the channel without decline in the ideal. In reality, the channel is fading channel. The following assumes that the channel between all cognitive users in each cluster and the fusion center of network is Rayleigh fading channel, the probability density function of Rayleigh distribution as follows.

$$f\left(d_{k,j,r}\right) = \frac{d_{k,j,r}}{\alpha^2} \exp\left(\frac{d_{k,j,r}}{2\alpha^2}\right) \qquad d_{k,j,r} \geq 0$$

where "$d_{k,j,r}$" is the distance from the kth cognitive users of cluster "j" to the fusion center of network, "α^2" is the average power of the detected signal on the perception bandwidth when cognitive users detecting whether AU exists.

Using this formula to calculate the channel fading that between all cognitive users in each cluster and the fusion center of network, and finding out the cognitive user of each cluster whose channel fading is minimum, this cognitive user is chosen as cluster head whose channel quality is best, indicated as "h_{headj}". The collection of each cluster and the cluster head ID is stored as"b_j" and "h_{headj}".

35.3.3 An Improved Clustering Cooperative Spectrum Sensing Algorithm

Assuming that there are N number of cognitive users in cognitive wireless network, and dividing them into J numbers clusters, so there are D numbers cognitive users in each cluster, where "D = N/J". Next, the improved double-threshold energy detection and improved clustering cooperative spectrum sensing algorithm are combined to increase the detective performance of network.

$P_{d,j}$ and $P_{f,j}$ respectively represent the collaborative detection probability, collaborative false alarm probability and collaborative leakage alarm probability of a cluster, as follows,

$$P_{d,j} = 1 - P_{m,j} \tag{35.6}$$

$$\begin{aligned} P_{f,j} = 1 - \prod_{k=1}^{D} \left(1 - \theta_{0,k} - P_{f,k}\right) - \sum_{M=0}^{D-1} \binom{D}{M} \\ \prod_{k=1}^{M} \left(1 - \theta_{0,k} - P_{f,k}\right) \prod_{k=M+1}^{D} \theta_{0,k} \left[1 - \Gamma\left[\frac{(D-M)u, ½]}{\Gamma[(D-M)u]}\right]\right. \end{aligned} \tag{35.7}$$

Assuming the channel between authorized users and cognitive users or between CH and cognitive users is Rayleigh fading channel, the cooperative detection

probability and cooperative false alarm probability of a cluster in CH location can be expressed as follows:

$$P_{d,j} = 1 - \prod_{k=1}^{D} \left((1 - P_{d,k})(1 - P_{e,k}) + P_{d,k} P_{e,k} \right) \tag{35.8}$$

$$P_{f,j} = 1 - \prod_{k=1}^{D} \left((1 - P_{f,k})(1 - P_{e,k}) + P_{f,k} P_{e,k} \right) \tag{35.9}$$

where $P_{e,k}$ is the bit error rate (BER) of the kth cognitive user when it sending perceptual information to its CH in a cluster.

Each CH sends the perceptive result of its cluster to the fusion center, then it consolidates these perceptive results to get the final perceptive result of the whole cognitive wireless network. So the detection probability and false alarm probability of the whole cognitive wireless network can be calculated by the following two formulas.

$$P_d = 1 - \prod_{j=1}^{J} \left[(1 - P_{e,j}) \prod_{k=1}^{D} \left(1 - P_{d,j,k}\right) + P_{e,j} \left(1 - \prod_{k=1}^{D} \left(1 - P_{d,j,k}\right) \right) \right] \tag{35.10}$$

$$P_f = 1 - \prod_{j=1}^{J} \left[(1 - P_{e,j}) \prod_{k=1}^{D} \left(1 - P_{f,j,k}\right) + P_{e,j} \left(1 - \prod_{k=1}^{D} \left(1 - P_{f,j,k}\right) \right) \right] \tag{35.11}$$

where $P_{f,j,k}$ and $P_{d,j,k}$ respectively denote the false alarm probability and detection probability of the kth cognitive user in cluster "j"; $P_{e,j}$ represents the BER when the CH_j sends the perceptual information to the fusion center.

In the condition of the Rayleigh fading channel, there are several parameters need to calculate, which are used to calculate the detection probability of the multi-cluster cooperative spectrum sensing. The channel between AU and cognitive users or between CH and cognitive users is Rayleigh fading channel. According to Eq. (35.3), $P_{d,j,k}$ can be expressed as follows:

$$P_{d,j,k} = Q_u \left(\sqrt{2\gamma_{j,k}}, \sqrt{\lambda_H} \right) \tag{35.12}$$

where $\gamma_{j,k}$ is the SNR of the kth cognitive user in a cluster.

For Rayleigh fading channels, the probability density function of $\gamma_{j,k}$ as follows,

$$f\left(\gamma_{j,k}\right) = \frac{1}{\gamma_j} \exp\left(-\frac{\gamma_{j,k}}{\overline{\gamma_j}} \right) \tag{35.13}$$

where $\overline{\gamma}_j$ is the average received SNR of the cognitive users in the cluster.

According to Eqs. (35.12) and (35.13), for Rayleigh fading channel, the detection probability of the kth cognitive user in the cluster "j" is expressed as follows,

$$\begin{aligned} P_{d,j,k} &= \int_0^\infty P_{d,j,k} f\left(\gamma_{j,k}\right) d_{\gamma_{j,k}} \\ &= \int_0^\infty Q_u\left(\sqrt{2\gamma_{j,k}}, \sqrt{\lambda_H}\right) \frac{1}{\gamma_j} \exp\left(-\frac{\gamma_{j,k}}{\overline{\gamma}_j}\right) d_{\gamma_{j,k}} \end{aligned} \tag{35.14}$$

Assuming that the CH adopts the BPSK modulation way to send 1 bit perceptual information to fusion center of the network, the information is the decision result of its cluster. The error rate of the CH sends information is expressed as follows,

$$P_{e,j} = Q\left(\sqrt{2\rho_{j,max}}\right)$$

where $\rho_{j,max}$ is the SNR when the CH of the cluster "j" sends perceptual information to the fusion center, it is the largest SNR in the cluster among all cognitive users.

For Rayleigh fading channel, the probability density function of $\rho_{j,max}$ is expressed as follows,

$$\mathrm{f}\left(\rho_{j,max}\right) = \frac{D}{\overline{\rho}_j} e^{-\frac{\rho_{j,\max}}{\rho_j}} \left(1 - e^{-\frac{\rho_{j,\max}}{\rho_j}}\right)^{D-1}$$

where $\overline{\rho}_j$ is the average SNR when CH of cluster "j" sends perceptual information". The error rate is expressed as follows,

$$\begin{aligned} P_{e,j} &= \int_0^\infty P_{e,j} \mathrm{f}\left(\rho_{j,max}\right) d_{\rho_{j,max}} = \sum\nolimits_{m=0}^{D-1} C_{D-1}^m \\ &(-1)^{D-m-1} \frac{D}{2(D-m)} \left(1 - \sqrt{\frac{\overline{\rho}_j}{D-m+\overline{\rho}_j}}\right) \end{aligned} \tag{35.15}$$

35.4 Simulation

In this part, the simulation is given to demonstrate the performance of the improved clustering algorithm based on improved double-threshold energy detection. Assuming that the sensing area has only one authorized user and one DFC. N numbers cognitive users are divided into J numbers clusters, and D numbers cognitive users in each cluster. The noise and signal power of each cognitive user is same. Set $P_{f,j} = 0.1$, the time-bandwidth product $\mathrm{u} = 5$, $\lambda_\mathrm{L} = 0.8\lambda$, $\lambda_H = 2\lambda$, $\theta_{1,\mathrm{k}} = 0.01$. The simulation results are shown in Figs. 35.3 and 35.4.

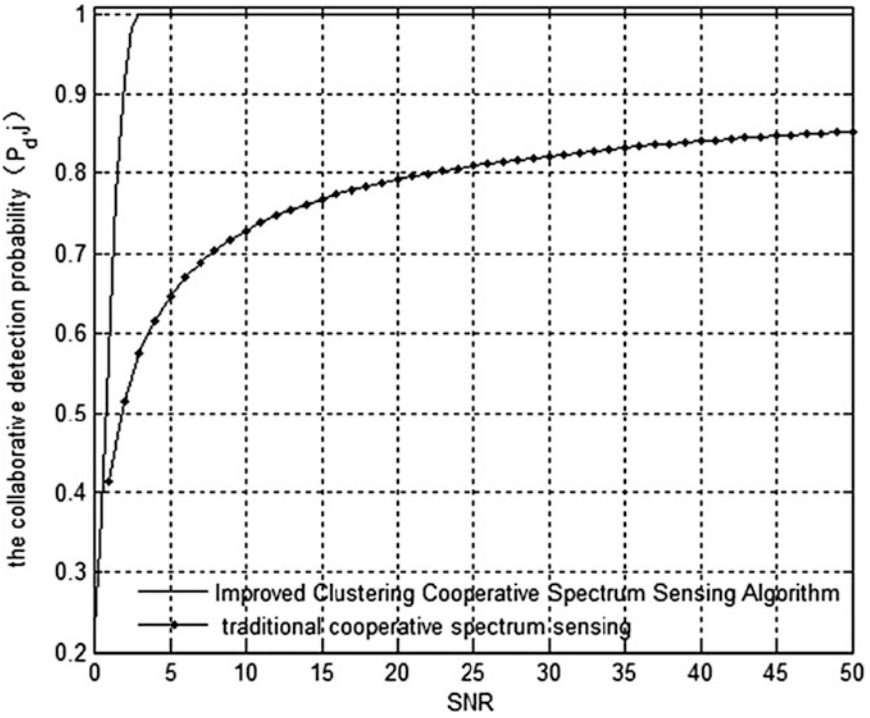

Fig. 35.3 Compared the collaborative detection probability of two algorithms

It is apparently seen from Fig. 35.3, the collaborative detection probability of total cognitive radio network is gradually increases as SNR increases, and corresponding to the same SNR, the collaborative detection probability of improved clustering cooperative spectrum sensing algorithm is higher than traditional cooperative spectrum sensing. So it verified the performance of the proposed algorithm has been greatly improved.

In Fig. 35.4, the collaborative false alarm probability of total cognitive radio network is gradually decreases as SNR increases, and corresponding to the same SNR, the collaborative detection probability of improved clustering cooperative spectrum sensing algorithm is lower than traditional cooperative spectrum sensing. So the detection accuracy of the proposed algorithm has been greatly improved.

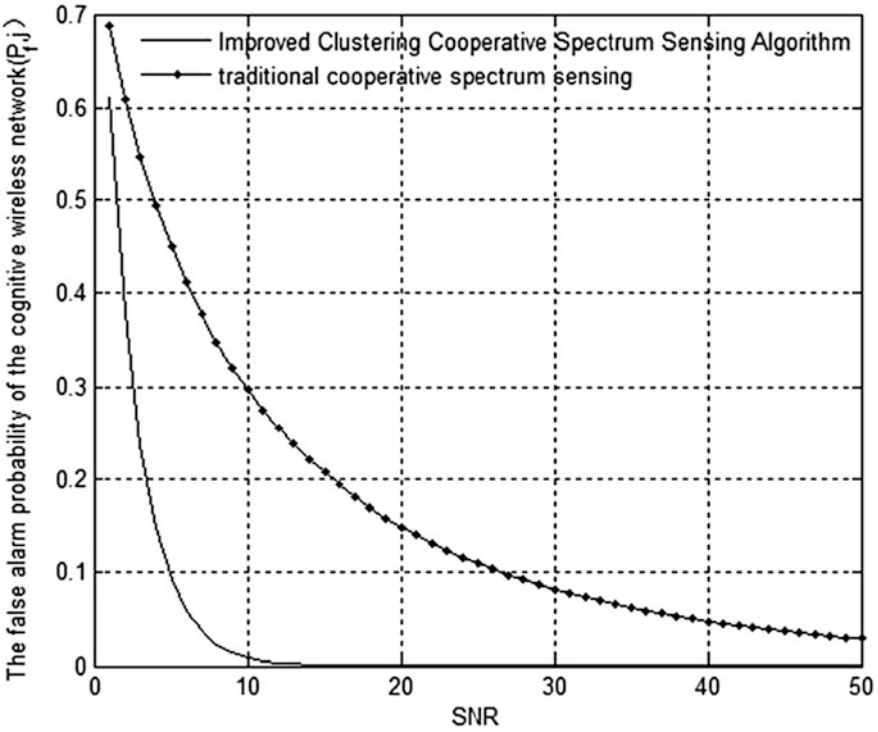

Fig. 35.4 Compared the collaborative false alarm probability of two algorithm

Conclusion

This paper proposes an improved clustering cooperative spectrum sensing algorithm based on improved double-threshold energy detection, and analyzes the algorithm's detective performance. The simulation results show that the proposed method performance is obviously much better than traditional cooperative spectrum sensing based on double threshold energy detection.

Acknowledgments Shubin Wang (wangsb09@gmail.com) is the correspondent author and this work was supported by the National Natural Science Foundation of China (61261020), and the Natural Science Foundation of Inner Mongolia, China (2012MS0903), and the Scientific Research Initial Fund for Higher Talents Program of Inner Mongolia University, China.

References

1. Huang XL, Wang G, Hu F (2011) Multitask spectrum sensing in cognitive radio networks via spatiotemporal data mining. IEEE Trans Veh Technol 62:809–823
2. Wang SB, Zhou Z, Kwak KY (2012) Two pulse designs for ultra wideband-cognitive radio by using multiple modified transform domain communication system. Appl Math Inf Sci 6:619–628
3. Valenta V, Fedra Z, Marsaalek R (2009) Towards cognitive radio networks: spectrum utilization measurements in suburb environment. In: Proceedings of IEEE radio and wireless symposium, pp 352–355
4. Chen HG, Liu J (2010) Cooperative spectrum sensing based on double threshold detection and Dempster–Shafer theory. In: Proceedings of IEEE international communication technology conference, pp 1212–1215
5. Jun M, Zhao GD, Li Y (2008) Soft combination and detection for cooperative spectrum sensing in cognitive radio networks. IEEE Trans Wirel Commun 7:4502–4507
6. Yu GC, Long CZ (2011) Research on energy detection algorithm in cognitive radio systems. In: Proceedings of 2011 international conference on computer science and service system, pp 3460–3463
7. Herath SP, Rajatheva N, Tellambura C (2009) Unified approach for energy detection of unknown deterministic signal in cognitive radio over fading channels. In: Proceedings of IEEE international conference on communications workshop, pp 1–5
8. Hu Y, Feng ZY, Wang ZL, Song JQ (2010) A novel triggered asynchronous spectrum sensing scheme in cognitive radio networks. In: Proceedings of 2010 I.E. 72nd vehicular technology conference fall, pp 1–5

Chapter 36
An Improved Time-Domain Autocorrelation Spectrum Detection Algorithm

Sarina Liu, Shubin Wang, Hongyue Wang, and Huiqin Liu

Abstract When a primary user uses frequency hopping communication, cognitive radio users using typically spectrum detection method is the time-domain autocorrelation. But the primary users signal is interfered by a fixed-frequency interference (FFI), the method is invalid. For the problem, this paper improves the traditional time-domain autocorrelation method by using the power spectrum cancellation, and the improved method can effectively avoid the fixed-frequency spectrum interference to increase the spectrum detection performance. Simulation results show that signal-to-noise ratio (SNR) is below −10 dB, and the false alarm probability is 0.05, the detection probability of improved method is greater than that of the traditional time-domain autocorrelation method. In low SNR, the improved method has a good detection performance, and also can prevent the collision between frequency of FFI and frequency of the primary user as well.

Keywords Cognitive radio • Hopping signal • Time-domain autocorrelation detection • Power spectrum • Spectrum detection

36.1 Introduction

Spectrum detection is the key technology of cognitive radio (CR) [1], its purpose is to find spectrum hole [2]. With the development of cognitive radio technology, the spectrum detection method continues to increase. When a primary user adopts frequency hopping (FH) communication, the spectrum detection commonly uses a time-domain autocorrelation method. But the primary users signal is interfered by fixed-frequency interference (FFI), the algorithm is almost undetectable to the primary users. For the question, this paper firstly analyzes the traditional time-domain autocorrelation method containing fixed-frequency interference (FFI) and power spectrum cancellation algorithm [3]. Next, according to that power spectrum of frequency hopping signal changing with time is different, this paper uses the power spectrum cancellation algorithm to improve the traditional time-domain

S. Liu • S. Wang (✉) • H. Wang • H. Liu
College of Electronic Information Engineering, Inner Mongolia University, Hohhot, China
e-mail: wangsb09@gmail.com

J. Mu et al. (eds.), *The Proceedings of the Third International Conference on Communications, Signal Processing, and Systems*, Lecture Notes in Electrical Engineering 322, DOI 10.1007/978-3-319-08991-1_36

autocorrelation method, thereby overcomes the FFI to raise the detection performance. At the same time, the collision between frequency of FFI and frequency of the primary user is also prevented.

36.2 Traditional Time-Domain Autocorrelation Detection

The time-domain autocorrelation algorithm is also known as a multiple hops autocorrelation detection [4]. The received signal containing FH signal and noise can be expressed as

$$x(t) = S_H(t) + n(t) \tag{36.1}$$

where $x(t)$ represents received signal of the cognitive radio user. $S_H(t)$ represents the FH signal with a cycle T_H. The sampling time T is greater than the FH cycle and less than the frequency hopping sequence cycle, which ensure that a sampled signal contains multiple hopping frequency information. $n(t)$ with the mean 0 represents the bandpass Gaussian white noise, and a single sideband power spectral density for $n(t)$ is $\frac{N_0}{2}$.

The received signal autocorrelation $R_x(\tau)$ can be expressed as

$$R_x(\tau) = R_{SS_{HH}}(\tau) + R_{NN}(\tau) + R_{S_HN}(\tau) \tag{36.2}$$

where $R_{SS_{HH}}(\tau)$ represents the FH signal autocorrelation, $R_{NN}(\tau)$ represents the noise autocorrelation, $R_{S_HN}(\tau)$ represents the cross-correlation of FH signal and noise. When signal-to-noise ratio (SNR) is really small, $R_{S_HN}(\tau)$ has a little effect on the detection performance [5]. The equation (36.2) also can be expressed as

$$R_x(\tau) = R_{SS_{HH}}(\tau) + R_{NN}(\tau) \tag{36.3}$$

Gaussian white noise is non-correlation in time-domain, so $R_x(\tau)$ depends on $R_{SS_{HH}}(\tau)$ in (36.3). When $\tau < T_H$, $S_H(t)$ has the very strong correlation within one hop period, and its value is non-zero. When $\tau > T_H$, $S_H(t)$ is random, and is not relevant in a few adjacent hop, so $R_{SS_{HH}}(\tau) \cong 0$.

For the received signal containing FH or non-FH signal, the characteristic parameter can be calculated respectively as following.

$$\rho_1 = \frac{E_1}{E_2} = \frac{(T - T_H)\int_0^{T_H} \left| R_{SS_{FF}}(\tau) + PR(\tau)\big|_{\sigma^2=1} \right| d\tau}{T_H \int_{T_H}^{T} \left| PR(\tau)\big|_{\sigma^2=1} \right| d\tau} \tag{36.4}$$

$$\rho_2 = \frac{E_1}{E_2} = \frac{(T - T_H)\int_0^{T_H} \left|PR(\tau)\right|_{\sigma^2=1}\left|d\tau\right.}{T_H \int_{T_H}^{T} \left|PR(\tau)\right|_{\sigma^2=1}\left|d\tau\right.} \tag{36.5}$$

where P and $R(\tau)\big|_{\sigma^2=1}$ represent respectively the noise power and autocorrelation of Gaussian white noise with power being unit value. ρ_1 and ρ_2 are associated with the probability distribution of noise.

The $S_H(t)$ has a strong correlation in one hop interval so that the mean of $S_H(t)$ has a very significant increment, so ρ_1 can be used as a parameter to detect whether the FH signal exist.

Estimating the expectation and variance of ρ_2, and combining with the probability density distribution of Gauss distributed random variables, and according to the false alarm probability, the suitable threshold value can be obtained.

36.3 Improved Time-Domain Autocorrelation Detection

Assuming the received signal contains the FH signal and noise and FFI, it can be expressed as

$$x(t) = S_H(t) + S_F(t) + n(t) \tag{36.6}$$

where $S_F(t)$ means FFI of the whole detecting frequency band, $x(t), S_H(t), n(t)$ is the same with the Sect. 36.2.

The autocorrelation of received signal can be expressed as follows

$$\begin{aligned} R_x(\tau) = E[x(t)x(t+\tau)] = R_{SS_{HH}}(\tau) + R_{SS_{FF}}(\tau) + R_{NN}(\tau) + R_{S_HS_F}(\tau) \\ + R_{S_FS_H}(\tau) + R_{S_HN}(\tau) + R_{NS_H}(\tau) + R_{S_FN}(\tau) + R_{NS_F}(\tau) \end{aligned} \tag{36.7}$$

where $R_{SS_{FF}}(\tau)$ represents FFI autocorrelation, $R_{S_HS_F}(\tau)$ and $R_{S_FS_H}(\tau)$ mean the cross-correlation between FH signal and FFI. $R_{S_HN}(\tau)$ and $R_{NS_H}(\tau)$ and $R_{S_FN}(\tau)$ and $R_{NS_F}(\tau)$ represent the cross-correlation of noise and FH signal and FFI. $R_{SS_{HH}}(\tau)$ and $R_{NN}(\tau)$ are the same with the previous section.

Based on the literature [5], the cross-correlation of noise and FH signal and FFI can be ignored, so the formula (36.7) can be expressed as

$$R_x(\tau) = R_{SS_{HH}}(\tau) + R_{SS_{FF}}(\tau) + R_{NN}(\tau) + R_{S_HS_F}(\tau) + R_{S_FS_H}(\tau) \tag{36.8}$$

The FFI has a very strong autocorrelation in the whole detection band, so the FFI autocorrelation value is not 0.

If $x(t)$ only contains noise and FFI, the formula (36.8) can be expressed as

$$R_x(\tau) = R_{SS_{FF}}(\tau) + PR(\tau)\big|_{\sigma^2=1}, \quad 0 < \tau < T \tag{36.9}$$

If $x(t)$ contain the FH signal and noise and FFI, the formula (36.8) can be expressed as

$$R_X(\tau) = \begin{cases} R_{SS_{HH}}(\tau) + R_{SS_{FF}}(\tau) + R_{S_HS_F}(\tau) + R_{S_FS_H}(\tau) + PR(\tau)\big|_{\sigma^2=1}, \\ 0 < \tau < T_H \\ R_{SS_{FF}}(\tau) + R_{S_HS_F}(\tau) + R_{S_FS_H}(\tau) + PR(\tau)\big|_{\sigma^2=1}, \\ T_H < \tau < T \end{cases} \tag{36.10}$$

where $P$and $R(\tau)\big|_{\sigma^2=1}$ are the same with the Sect. 36.2.

Because the FFI of each frequency point has a good autocorrelation, depended on the formula (36.9) and (36.10), even if the detecting frequency band contain the FH signal, the autocorrelation of received signal does not tend to 0 whatever τ taking any values.

For the received signal not containing FH signal, the characteristic parameter can be expressed as following

$$\rho_3 = \frac{E_1}{E_2} = \frac{(T - T_H)\displaystyle\int_0^{T_H} \left|R_{SS_{FF}}(\tau) + PR(\tau)\big|_{\sigma^2=1}\right| d\tau}{T_H \displaystyle\int_{T_H}^{T} \left|R_{SS_{FF}}(\tau) + PR(\tau)\big|_{\sigma^2=1}\right| d\tau} \tag{36.11}$$

For the received signal containing FH, the characteristic parameter can be expressed as following

$$\begin{aligned} \rho_4 &= \frac{E_1}{E_2} \\ &= \frac{(T - T_H)\displaystyle\int_0^{T_H} \left|R_{SS_{HH}}(\tau) + R_{SS_{FF}}(\tau) + 2R_{S_HS_F}(\tau) + PR(\tau)\big|_{\sigma^2=1}\right| d\tau}{T_H \displaystyle\int_{T_H}^{T} \left|R_{SS_{FF}}(\tau) + 2R_{S_HS_F}(\tau) + PR(\tau)\big|_{\sigma^2=1}\right| d\tau} \end{aligned} \tag{36.12}$$

where $R_{S_HS_F}(\tau)$ equals $R_{S_FS_H}(\tau)$.

Based on the formula (36.4) and (36.5) and (36.12) and (36.13), ρ_3 compared to ρ_2, FFI can make the false alarm probability increase. The cognitive radio user lose more opportunities to use the spectrum holes, and the spectral efficiency is reduced. ρ_1 compared to ρ_4, ρ_4 relative to ρ_3, the mean has no an obvious increment.

For the improved time-domain autocorrelation detection method, firstly, the original power spectrum of cognitive signal subtracts its average power spectrum to offset FFI and save the FH signal. Next, using time-domain autocorrelation to detect these retained information in order to determine whether the spectrum holes.

A non-stationary signal can be divided into several stationary signals [6], the FH signal is a non-stationary signal [7], and the segmented FH signals must ensure to contain the multiple FH information. A signal with length N can be expressed as

$$x_N(n) = \sum_{i=1}^{a} S_{Fi}(n) + \sum_{j=1}^{b} S_{Hj}(n) + n(n) \tag{36.13}$$

where $S_{Fi}(n)$ represents a FFIs, $i = 1, 2, \cdots, a$. $S_{Hj}(n)$ represents b FH signals, $j = 1, 2, \cdots, b$. $n(n)$ means Gaussian white noise.

The signal is divided into L segments, and the length of one segment being expressed as $x_{MK}(n)(K = 1, 2, 3, \cdots, L)$ is M. Each segment carries out Fast Fourier Transform (FFT) to obtain the power spectrum $P_{xMK(n)}(\omega)$ as follow.

$$P_{xMK(n)}(\omega) = \frac{1}{M}\left|\sum_{n=0}^{M-1} x_{MK}(n)e^{-j\omega n}\right|^2 \tag{36.14}$$

The averaging power spectrum of each segment can be obtained as follow.

$$\overline{P}_{x_{N(n)}}(\omega) = \frac{1}{L}\sum_{K=1}^{L} P_{MK}(n)e^{-j\omega n} = \frac{1}{ML}\sum_{K=1}^{L}\left|\sum_{n=0}^{M-1} x_{MK}(n)e^{-j\omega n}\right|^2 \tag{36.15}$$

Making FFT on the whole signal, the power spectrum of the signal is calculated as follow.

$$P_{xN(n)}(\omega) = \frac{1}{N}\left|\sum_{n=0}^{N-1} x_N(n)e^{-j\omega n}\right|^2 \tag{36.16}$$

The power spectrum cancellation $P_{SUB}(\omega)$ can be calculated as following

$$P_{SUB}(\omega) = P_{xN(n)}(\omega) - \overline{P}x_{N(n)}(\omega) \tag{36.17}$$

After power spectrum cancellation, the most information of FFI is offset, and the most information of FH signal is retained.

According to Wiener–Khinchin theorem [8], and taking inverse Fourier transform on $P_{SUB}(\omega)$, the autocorrelation after the FFI suppression can be obtained as following

$$R_{X1}(\tau) = F^{-1}{}_{\tau}[P_{SUB}(\omega)] = \int_{-\infty}^{+\infty} P_{SUB}(\omega)e^{j\omega\tau}d\omega \tag{36.18}$$

36.4 Simulation

36.4.1 Relationship Between Correlation Coefficient and Time Delay for Different Signals

Assuming the cognitive band contains the FH signal and noise, and total data point number is 3,000. The sampling point number of each hop is 120, and FH frequency is respectively 1,000, 2,000, 3,000, 4,000, 5,000, 6,000, 7,000, 8,000 Hz. The noise is Gaussian white noise, and the relationship between normalized autocorrelation coefficients of received signal and time delay is shown in Fig. 36.1a.

Assuming the cognitive band contains the FH signal and noise and FFI, and the frequency of FFI is respectively 1,000 and 8,000 Hz. The other simulation conditions keep the above, and the relationship between normalized autocorrelation coefficients of received signal and time delay is shown in Fig. 36.1b.

From Fig. 36.1a, we can kwon that the autocorrelation only appears a large peak in one hop cycle, and is relatively smooth in other time delay range. From Fig. 36.1b, we can kwon that the entire detection band appears larger correlation values. Once the FFI emerges, the detection accuracy is reduced for the traditional time-domain autocorrelation detection.

36.4.2 Fixed-Frequency Interference Suppression

The simulation conditions is set as the Sect. 36.4.1, and the original power spectrum of the signal is shown in Fig. 36.2a depended on the formula (36.16), and the cancelling power spectrum is shown in Fig. 36.2b based on the Eq. (36.17).

In Fig. 36.2b, the Point 1 (1,000 Hz) and Point 2 (7,000 Hz) are respectively the frequency collision point between the FH signal and FFI. Compared with the

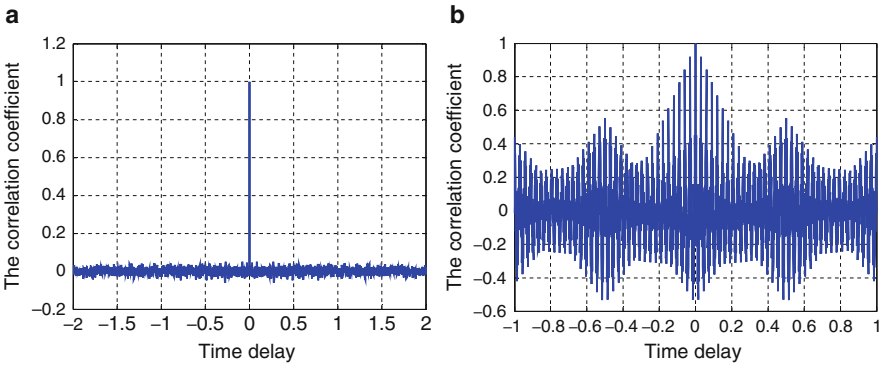

Fig. 36.1 (**a**) Autocorrelation coefficient and time delay for the FH signal and noise; (**b**) autocorrelation coefficients and time delay for the FH signal and FFI and noise

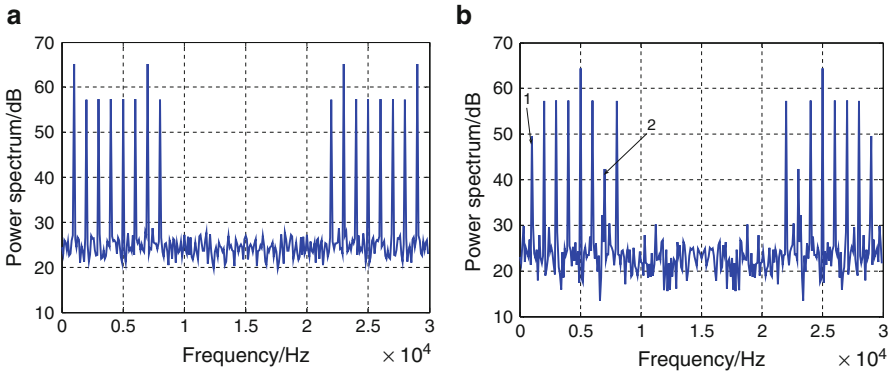

Fig. 36.2 (**a**) Signal power spectrum; (**b**) power spectrum after the fixed frequency suppression

corresponding frequency point in Fig. 36.2a, the FH power spectrum of two frequency point is decreased after the power spectrum cancellation. But the detection performance isn't affected, and the FH information of other frequency point is also not damaged.

36.4.3 Relationship Between Correlation Coefficient and Time Delay After FFI Suppression

After the power spectrum cancellation, the autocorrelation of received signal can be obtain depended on (36.18), and is shown in Fig. 36.3.

Comparing Fig. 36.3 with Fig. 36.1b, the autocorrelation after the power spectrum cancellation only appears a larger peak in one hop cycle, and closes to zero in other time delay range. So the improved time-domain autocorrelation detection can increases the detection performance.

36.4.4 Performance Comparison

Taking the false alarm probability $P_f = 0.05$, we compare the performance of traditional time-domain autocorrelation method and that of improved method, and the results is shown in Fig. 36.4.

From Fig. 36.4, we know the detection probability of improved method obviously increase than that of traditional time-domain autocorrelation method in low SNR.

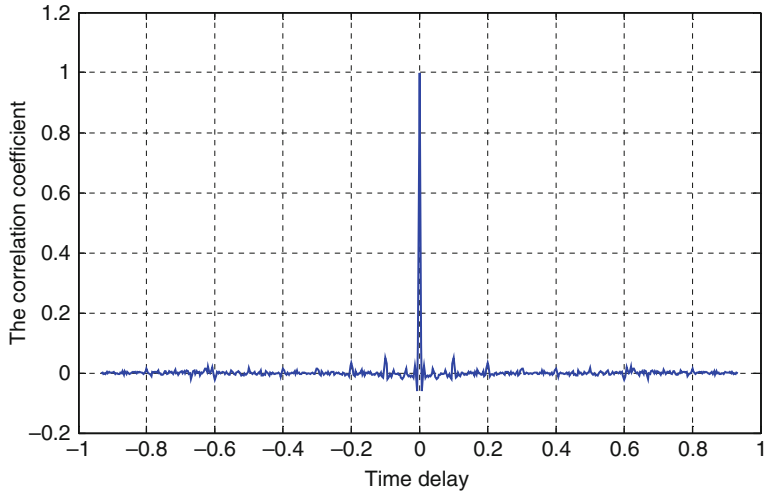

Fig. 36.3 Inverse Fourier transform to get the autocorrelation function

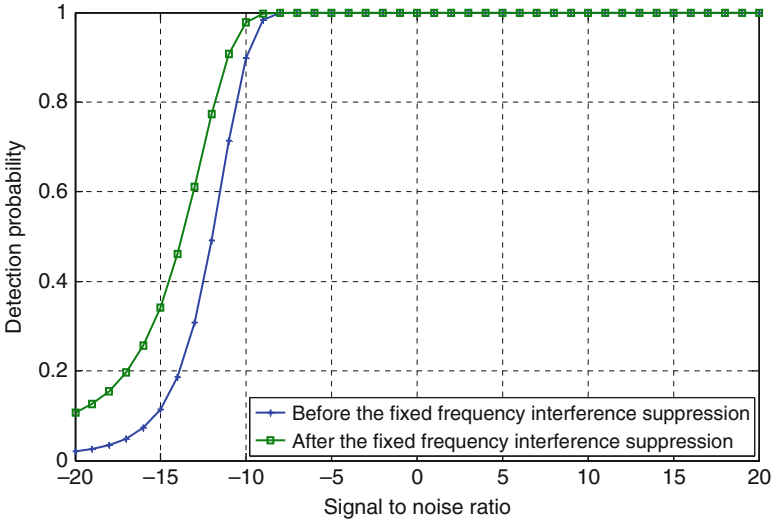

Fig. 36.4 Comparing the detection probability for two methods

Conclusion

The traditional time-domain autocorrelation method only can detect signals containing FH and noise. Depended on Wiener–Khinchin theorem, using power spectrum cancellation, this paper improves time-domain

(continued)

(continued)

autocorrelation method. Not only the improved method can detect the spectrum of containing FFI to get a good detection performance, but also prevent the collisions between the primary user and the FFI frequency.

Acknowledgments Shubin Wang (wangsb09@gmail.com) is the correspondent author and this work was supported by the National Natural Science Foundation of China (61261020), and the Natural Science Foundation of Inner Mongolia, China (2012MS0903), and the Scientific Research Initial Fund for Higher Talents Program of Inner Mongolia University, China.

References

1. Wang SB, Zhou Z, Kwak KY (2012) Two pulse designs for ultra wideband-cognitive radio by using multiple modified transform domain communication system. Appl Math Inform Sci 6:619–628
2. Haykin S (2005) Cognitive radio: brain-empowered wireless communications. IEEE J Select Areas Commun 23:201–220
3. Gao XJ, Li DX et al (2008) Algorithm for frequency-hopping signal detection based on suppressing power spectrum. J Jilin University 26:239–243
4. Chung CD (1994) Generalised likelihood-ratio detection of multiple-hop frequency-hopping signals. IEE Proc Commun 141:70–78
5. Chung CD, Polydors A (1995) Parameter estimation of random FH signals using autocorrelation techniques. IEEE Trans Commun 43:1097–1106
6. Barbarossa S, Scaglione A (1997) Parameter estimation of spread spectrum frequency hopping signals time–frequency distribution. In: Proc of first IEEE signal processing workshop on signal processing advance in wireless communications, pp 213–216
7. Lavielle M (1998) Optimal segmentation of random processes. IEEE Sign Proc 46:1365–1373
8. Norbert W (1930) Generalized harmonic analysis. Acta Math 55:117–258

Chapter 37
An Improved Spectrum Sensing Data-Fusion Algorithm Based on Reputation

Hongyue Wang, Shubin Wang, Sarina Liu, and Huiqin Liu

Abstract A false sensing information attack can cause the detection performance down for cognitive radio, for this problem, this paper presents an improved weighted sequential probability ratio test (WSPRT) algorithm by based on an accuracy combining effectively using the user data of small weight. The method enhances weight by recording the accordant times between the previous spectrum sensing report and the final spectrum sensing decision, at the same time, the malicious users are distributed smaller weights in order to use the sending data of malicious users. Simulation results show that the improved algorithm can be effectively resist spectrum sensing data falsification (SSDF) attacks by comparing with traditional WSPRT when there are more malicious users.

Keywords Cognitive radio • Cooperative spectrum sensing • Reputation • Malicious users • Weighted sequential probability ratio test

37.1 Introduction

Cognitive Radio [1] is a kind of spectrum sharing technology, and this technology's key problem is reliable spectrum detection. In cooperative spectrum sensing technology [2–4], multiple cognitive radio users complete spectrum sensing process cooperatively, each unlicensed user complete local spectrum sensing independently, and sends the local detection result to the fusion center, and fusion center make a final decision by appropriate fusion rule.

In the actual wireless communication, due to the uncertainty of the wireless environment, the error decision of unlicensed users usually appears and it is inevitable that a malicious user send an error report to fusion center, lead to affect the detection performance of the whole system. An attacker may send false local spectrum sensing results to a data collector, causing the data collector to make a wrong spectrum-sensing decision [5]. Therefore, sensing data falsification attack is

H. Wang • S. Wang (✉) • S. Liu • H. Liu
College of Electronic Information Engineering, Inner Mongolia University, Hohhot, China
e-mail: wangsb09@gmail.com

J. Mu et al. (eds.), *The Proceedings of the Third International Conference on Communications, Signal Processing, and Systems*, Lecture Notes in Electrical Engineering 322, DOI 10.1007/978-3-319-08991-1_37

a security threat. In cooperative detection, usually appears Byzantine failure problem, this problem can lead to Spectrum Sensing Data Falsification (SSDF)[6, 7] attacks. In SSDF attack, malicious user send tampered local spectrum report to the fusion center intentionally, in order to cause the fusion center make wrong spectrum sensing decision. Therefore, the paper [8] proposed a Weighted Sequential Probability Radio Test (WSPRT) algorithm, is assigned each node to the corresponding weights based on reputation.

The literature [9] proposed a WSPRT algorithm, and set the memory byte by fusion center, and record the recent sensing report of cognitive user in accord with final decision, then decide the SSDF existence by the correct rate of decision result. In the actual detection process, due to the uncertainty of the wireless environment, the normal node may not sent correctly normal report, so it is possible that a malicious user is misinterpreted, then the data of this node will be wasted. Because some users send the error report intermittently, some malicious user don't have to send an error report, if its reputation is greater than the decision threshold, then at this time the user would have been considered a normal user by the fusion center, so using data sent by the user. However, this method in literature [9] only can identify routinely malicious users, and give up user data of small weight, but don't use the malicious user data, therefore, the method wastes mass data of malicious user. Therefore, using the data sent by the smaller weight user, malicious user is assigned to reverse weight when dealing with the weight, 0 come from detection terminal is treated 1 in the fusion center by weight, 1 is treated 0. Two methods are only applicable for the case of less malicious users, opposing SSDF attack is not obvious when malicious users increase. Therefore, in the case of a malicious user is more, combining two methods adopt its advantages and overcome the system disadvantages, it resists effectively the SSDF attack and reduce the probability of error detection.

37.2 Weighted Sequential Probability Radio Test

Weighted Sequential Probability Radio Test (WSPRT) is a cooperative algorithm based on traditional sequential detection, r_i is each user's reputation, its weight is w_i, and the decision variable is:

$$W_n = \prod_{i=0}^{n} \left(\frac{P[u_i/H_1]}{P[u_i/H_0]} \right)^{w_i} \tag{37.1}$$

Decision rule is as follows:

$$\begin{aligned} &W_n \geq \lambda_1 \Rightarrow accept\, H_1 \\ &W_n \leq \lambda_0 \Rightarrow accept\, H_0 \\ &\lambda_0 < W_n < \lambda_1 \Rightarrow take\ another\ observation \end{aligned} \tag{37.2}$$

Decision threshold λ_0 and λ_1 is identified by false alarm probability Q_f and miss detection probability Q_m:

$$\lambda_0 = \frac{Q_m}{1-Q_f}, \lambda_1 = \frac{1-Q_m}{Q_f} \tag{37.3}$$

Assuming reputation of a single cognitive user is expressed as r_i, each user's local decision is u_i,it compared with the fusion center the final decision u, then update the reputation according to the rules: $r_i : r_i = r_i + (-1)^{u_i+u}$, and adjust weights w_i for each user:

$$w_i = f(r_i) = \begin{cases} 0 & , r_i \leq g \\ \dfrac{r_i + g}{max(r_i) + g}, & r_i > g \end{cases} \tag{37.4}$$

where $w_i = 0$ judges the user to the malicious user.

37.3 M-WSPRT Cooperation Detection Algorithm

The literature [9] proposed memory byte records recent decision report of cognitive user, considering the time's one-dimensional factor, overcoming short period of dramatic changes in users, the introduction of the correct rate:

$$a_i = 1 - \frac{\sum_{m=1}^{N} b_{im}}{N} \tag{37.5}$$

where N represents the number of detecting in the past.

When considering the time's one-dimensional factor, in order to use the data of less reputation users, reversing weights and giving it a negative weights. Greater reputation users stand on the original algorithm, and redefining the weighting coefficient as follows:

$$w_i = f(r_i) = \begin{cases} \dfrac{r_i}{max(r_i) + g}, & r_i \leq g \\ \dfrac{r_i + g}{max(r_i) + g}, & r_i > g \end{cases} \tag{37.6}$$

Formula (37.4) can be expressed as:

$$W_n = \prod_{i=0}^{n} \left(\frac{P[u_i/H_1]}{P[u_i/H_0]} \right)^{w_i \times a_i} \tag{37.7}$$

The simulation proved that combination of the two methods effectively resists the SSDF attacks, and reduces the error probability of the system.

37.4 Performance Simulation and Analysis

We carried out the compartment the sequential test with weighted sequential test and M-WSPRT's performance. In the simulations, *N* unlicensed users are randomly located in a 2,200 × 2,200 m square area, there are *Na* malicious users launched SSDF attack among N cognitive users. Using HATA path loss model, the licensed users of the operating band is the UHF frequency of 617 MHz, the height of the transmitting and receiving antennas is 100 and 1 m. The receiver sensitivity is −94 dBm, and $Q_m = 10^{-5}$, $Q_f = 10^{-6}$, $g = 5$. WSPRT detection probability is greater than 0.98, Fig. 37.1 shows the improved method does not significantly improve the detection probability of the system.

Figure 37.1 shows that with the number of malicious user increase, correct detection probability of traditional sequential detection is significantly reduced, in this case of a malicious user is more. So the traditional sequential detection is not appropriate for spectrum detection in the system when system exist more malicious users. Improved Weighted Sequential Detection don't substantially increase correct detection probability of the system, but is still above the weighted sequential detection, to a certain extent to improve the probability of correct detection. As can be seen from Fig. 37.2, improved method greatly reduces the probability of incorrect detection compared with weighted sequential detection, and effectively against SSDF attacks when the malicious user is more.

Conclusion

This paper proposes an improved weighted sequential probability ratio test algorithm, which is based on combining accuracy and effectively using user data of small weight, and recorded reports of unlicensed users in a period of time, meanwhile the less reputation user reverse weights. Simulation shows that it is compared with the weighted sequential test, and this algorithm significantly reduces the probability of error detection system and effectively resists the SSDF attacks, and improves system detection performance.

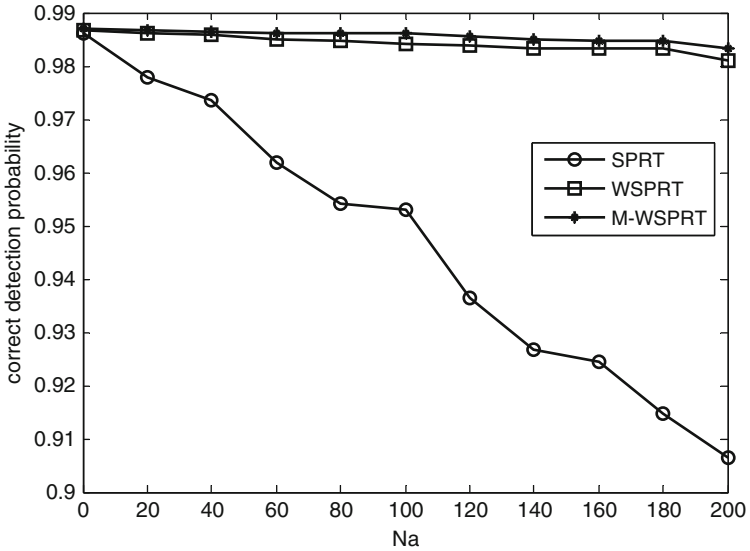

Fig. 37.1 Relationship with the probability of correct detection and malicious users

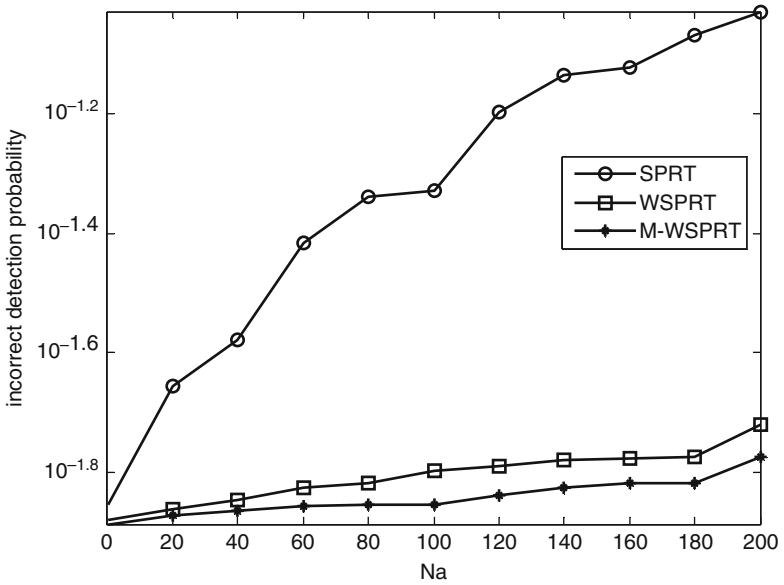

Fig. 37.2 Relationship with the probability of incorrect detection and malicious users

Acknowledgments Shubin Wang (wangsb09@gmail.com) is the correspondent author and this work was supported by the National Natural Science Foundation of China (61261020), and the Natural Science Foundation of Inner Mongolia, China (2012MS0903), and the Scientific Research Initial Fund for Higher Talents Program of Inner Mongolia University, China.

References

1. Zhang Y, Ge LJ, He W, Chen S (2010) Research on key technologies in cognitive radio system. Network Commun 26:99–101
2. Tan XZ, Jiang J, Sun HJ (2007) Cognitive radio spectrum perception technology research. Commun Technol 3:61–63
3. Mao XM, Yu GD, Qiu PL (2009) Cooperation communications in cognitive radio. J Zhejiang Univ 43:111–116
4. Unnikrishnan J, Veeravalli VV (2008) Cooperative sensing for primary detection in cognitive radio. IEEE Select Top Sign Proc 2:18–27
5. Chen R, Park JM, Hoh YJ (2008) Toward secure distributed spectrum sensing in cognitive radio network. IEEE Commun Mag 46:50–55
6. Gao F, Yuan W, Liu W (2010) A robust and efficient cooperative spectrum sensing scheme in cognitive radio network. In: Proc of IEEE Communications Workshops (ICC), pp 1–5
7. Liu Q, Gao J, Guo YW, Liu SX (2011) Consistency cooperative spectrum sensing scheme to resist SSDF attack. Electronic J 39:2643–2647
8. Chen R, Park JM, Bian K (2008) Robust distributed spectrum sensing in cognitive radio network. In: Proc of the 27th Conference on Computer Communication (IEEE INFOCOM 2008), pp 1876–1884
9. Yu F, Song CL, Tan CP (2012) Spectrum sensing data fusion algorithm based on credibility. Commun Technol 5:12–14

Chapter 38
Doubly Selective Channel Estimation in OFDM System Using Optimized Discrete Prolate Spheroidal Sequences

Xi Quan, Fei Qi, Xiaojun Jing, Songlin Sun, Hai Huang, and Na Chen

Abstract In orthogonal frequency division multiplexing (OFDM) system, basis expansion model (BEM) has been commonly used because of the significant variation of doubly-selective channels. In such a model, the channel taps are estimated by linear combinations of prescribed basis function. We propose a method of making better use of discrete prolate spheroidal sequence, also called Slepian sequence with an optimized parameter in a mathematical relationship with Doppler shift, and then using inverse reconstruction method to recover the BEM coefficients of the channel taps. Simulation results have confirmed the validity of this improvement and also proved an enhanced use of Slepian sequence than other basis functions in high mobility environments.

Keywords Basis expansion model (BEM) • Slepian sequence • Channel estimation • Doubly-selective • OFDM

38.1 Introduction

Orthogonal frequency division multiplexing (OFDM) is a high-speed transmission technology in wireless environment, which takes advantage of the multicarrier modulation technique.

Usually, OFDM systems are designed that channel is time-invariant within a single OFDM symbol duration. Recently, future wireless applications are expected to operate in mobile communications where high speed of terminals and scatters causes Doppler effects, resulting in both frequency-selective and time-selective fading [1].

X. Quan (✉) • F. Qi • X. Jing • S. Sun • H. Huang • N. Chen
School of Information and Communication Engineering, Beijing University of Posts and Telecommunications, Beijing, China

Key Laboratory of Trustworthy Distributed Computing and Service (BUPT), Ministry of Education, Beijing, China
e-mail: quanxi613@126.com

J. Mu et al. (eds.), *The Proceedings of the Third International Conference on Communications, Signal Processing, and Systems*, Lecture Notes in Electrical Engineering 322, DOI 10.1007/978-3-319-08991-1_38

Basis expansion model (BEM) has been commonly used to model doubly selective channel, whose taps vary with time, and implement channel estimation [2–4]. The BEM approximates the channel taps by combinations of prescribed basis functions in the time domain. The BEM with complex exponentials (CE-BEM) uses a truncated Fourier series as the basis function [5, 6]. There are also many other BEMs, including the generalized CE-BEM (GCE-BEM) [7], the polynomial BEM (P-BEM) [8, 9], the prolate spheroidal sequences BEM (DPSS-BEM) [2].

In Zemen and Mecklenbrauker [3], the prolate spheroidal sequences (DPSSs) are used as a basis instead of complex exponentials which allows more accurate representation of wireless channels in a high mobility environment. The performance of the BEM with DPSSs depends on a proper choice of the Slepian sequence.

In this paper, we propose a Slepian sequence with an optimized parameter called time-bandwidth product, and it has a mathematical relationship with Doppler shift f_d, and channel taps from pilots and the received signals is recovered by inverse method. The performance of DPSS-BEM with the enhanced use of Slepian sequence is better than other basis functions in high mobility environment.

The remainder of this paper is organized as follows. Section 38.2 introduces the OFDM system model and some theoretical foundations of the estimation algorithm. Section 38.3 shows theory basis on acquiring optimized Slepian Sequence. We present our simulation results in Sect. 38.4, and our conclusions in final section.

38.2 System Model

38.2.1 Transmitter–Receiver Model

The OFDM system with K subcarriers and a cyclic prefix of length N_{cp} is considered. The transmission bandwidth is denoted by B and the sampling period is denoted by $T_s = 1/B$. We assume that $N_{cp}T_s$ exceeds the channel's maximum path delay to avoid inter symbol interference (ISI). The time-domain transmit signal $s[n]$ is obtained by modulating the frequency-domain transmit symbols $S[k]$ using inverse discrete Fourier transform (IDFT) as follows

$$s[n] = \frac{1}{\sqrt{K}} \sum_{k=0}^{K-1} S[k] \mathrm{e}^{j2\pi \frac{nk}{K}}, \qquad n = -N_{cp}, \ldots, K-1. \tag{38.1}$$

The channel tap is denoted as h_l with discrete-time delay changes from 0 to L − 1, where L is the maximum discrete-time delay. We express the taps on sampling points as $h_l[n]$, where $n = NT_s$. At the receiver, after cutting off the cyclic prefix, signal $r[n]$ in time domain is shown in the following formula

$$r[n] = \sum_{l=0}^{L-1} h_l[n]\mathrm{s}[n-1] + w[n], \qquad n = 0, \ldots, K-1, \tag{38.2}$$

where $w[n]$ is the samples of additive white Gaussian noise (AWGN).

38.2.2 Fourier and BEM Coefficients of Channel Taps

In BEM framework, each channel tap h_l can be represented as a linear combination of the basis functions. Q is denoted as the model order, then Q basis functions is used for each delay path in rapid varying channels within one single OFDM symbol duration. Consequently, the lth channel tap is represented as

$$h_l(\mathrm{n}) = \sum_{q=0}^{Q-1} b_{lq} B_q(\mathrm{n}), \quad 0 \le \mathrm{n} \le \mathrm{K}, \tag{38.3}$$

where l changes from 0 to $L-1$, b_{lq} is the qth basis coefficient of the lth channel tap, and $B_q(\mathrm{n})$ is the basis function matrix.

We can approximate the channel taps with D-term Fourier series

$$h_l[n] \approx \sum_{d=D^-}^{D^+} H_l[m] e^{-j2\pi\frac{dn}{K}} \tag{38.4}$$

D denotes a positive integer, $D^- = -\lfloor (D-1)/2 \rfloor$, $D^+ = \lfloor D/2 \rfloor$ ($\lfloor . \rfloor$ is the floor operation). Then the dth Fourier coefficient of the lth channel tap $H_l[\mathrm{m}]$ can be reconstructed from formula below

$$\mathrm{H}_l[m] = \frac{1}{\sqrt{K}} \sum_{n=0}^{K-1} \mathrm{h}_l[n] \mathrm{e}^{-j2\pi\frac{nm}{K}} \tag{38.5}$$

Reconstruction of the channel taps from the estimated Fourier coefficients corresponds to the CE-BEM. However, because of the Gibbs phenomenon, the CE-BEM is not accurate for estimation of doubly selective channels.

38.2.3 Pilot Arrangement

We use a frequency-domain Kronecker delta (FDKD) pilot arrangement [9]. In each OFDM symbol, we distribute L pilot groups of size $2D-1$ each, uniformly spaced every K/L subcarriers. The location of the first pilot subcarrier is k_0,

$0 \le k_0 \le I - (2\mathrm{D} - 1)$, and then the pilot location is formed as $k_0 + q + iI$, where $q = 0, \ldots, 2D - 2$, $i = 0, \ldots, L - 1$. In each group, all the pilot values are zero except for the central pilot, which is set to a value a_0.

38.2.4 Estimation of Fourier Coefficients

According to the method in [9], we can estimate the Fourier coefficients from the received signal and the known pilots at the receiver end

$$\hat{H}_l[d] = \frac{1}{a_0\sqrt{K}} e^{-2\pi \frac{l(k_0+D-1)}{K}} \tilde{r}(d - D^-)[l], \tag{38.6}$$

where $d = D^-, \ldots, D^+$, and $l = 0, \ldots, L - 1$, r is the received signal. Estimated Fourier coefficients can be used to estimate the BEM coefficients with respect to a fixed arbitrary basis.

However, the DFT has an effect similar to the Gibbs phenomenon. The Slepian basis expansion represents bandlimited sequences with a minimum number of basis functions avoiding the deficiencies of the Fourier basis expansion.

38.2.5 Basis Coefficient Estimation

The inverse reconstruction method is used to reconstruct a function as a linear combination of given basis functions from a finite number of Fourier coefficients of the function [11].

The BEM coefficients can be calculated by minimizing the norm of the difference between the Fourier coefficients in (38.6) and the dth Fourier coefficients of h_l(n) in (38.3)

$$\sqrt{\sum_{D^- \le d \le D^+} \left|\hat{H}_l[d] - H_l[d]\right|^2}. \tag{38.7}$$

The coefficients b_l minimizing the problem of the expression (38.8) is solved to deal with the over-determined least squares problem

$$\min_{b_l \in \mathbb{C}^M} P b_l - \hat{H}_l, \tag{38.8}$$

where P is the $D \times Q$ matrix whose entries are the respective Fourier coefficients of the basis functions B_q(n).

When P has full rank, the BEM coefficients are solved by LS problem

$$\hat{b}_l = P^{\dagger}\hat{H}_l, \tag{38.9}$$

where $P^{\dagger}$ is the Moore–Penrose pseudoinverse of the matrix P.

38.3 Slepian Basis Expansion Model

38.3.1 Slepian Sequence

Since Slepian sequence shows energy conservation property in time and frequency domain either in finite or infinite limit, it outperforms CE-BEM when tap delay is unknown to the receiver [10].

Slepian sequences $\{v(n)\}$ is assumed of length N defined on $[0, N-1]$ with unit energy, and the sequences are bandlimited to the frequency range $[-W, W]$.

$$\sum_{n-0}^{N-1} v(n)^2 = 1 \tag{38.10}$$

The sequences $\{v(n)\}$ are the eigenvectors of the following eigenvalue equation

$$\sum_{m=0}^{N-1} v_k(m) \frac{sin\, 2\pi W(n-m)}{\pi(n-m)} = \lambda_k(N, W)\nu_k(n), \tag{38.11}$$

where λ_k denotes the corresponding eigenvalues, and indicates the fraction of energy contained in the band $[-W, W]$. The eigenvalues are ordered $\lambda_1 > \ldots > \lambda_{N-1} > 0$. Then v_k(n) is the kth most time concentrated Slepian sequence. Kim et al. [12] derived that the first $2NW$ eigenvalues λ_k are very close to 1. Thus we only need $2NW$ Slepian sequences to approximate time and frequency concentrated functions.

38.3.2 Optimized Slepian Sequences

To create desirable Slepian sequences for our proposed estimator, a parameter time-bandwidth product is employed. The expression of the parameter is NW, where N denotes the length of Slepian sequences, W denotes the effective bandwidth of the sequence. The time-bandwidth product can greatly affect the concentration of energy of Slepian sequences and consequently influence performance of such sequences.

Let B_w denote the total system bandwidth. The subchannel bandwidth is $B_s = B_w/N_s$. We assume that the subchannel bandwidth B_s is much less than the channel coherence

bandwidth $B_c \approx 1/\tau_{\max}$, where $\tau_{\max}$ is the maximum delay spread. Therefore, each subchannel can be assumed to be frequency flat fading [11]. In the perspective of time-selectivity, owing to time domain limit, h is bandlimited over $f_d * T_s$, which corresponds to the range W.

$$NW = Nf_d T_s = N\frac{v}{c} f_c T_s \tag{38.12}$$

From (38.12), if receiver is in low velocity, then W is small, and λ_k is close to zero, which is a worst case due to the property of Slepian sequence.

From the view of frequency-selectivity, since frequency domain H is limited to $[0,\ \tau_{\max}]$ and $H[k]$ is the channel frequency response sampled at the kth subcarrier frequency with sampling period of B_s, the inverse DFT of H is limited to $[0,\ \tau_{\max} B_s]$, which also corresponds to the range W.

$$NW = N\tau_{\max} B_s = N\frac{B_s}{B_c} \tag{38.13}$$

38.4 Numerical Simulations

38.4.1 Simulation Parameters

The merits of the proposed channel estimator are illustrated in terms of MSE by comparing with the CE-BEM, P-BEM and DCT-BEM through computer simulation. In the simulations, the number of subcarriers is 256, the intercarrier spacing is 10.9 kHz, sampling time is 0.357 μs, carrier frequency is 5.8 GHz.

38.4.2 Results of Simulation

We compare the MSE of the estimators as function of the signal-to-noise ratio (SNR). Figure 38.1a shows MSE of these methods with a fixed receiver velocity of 5 m/s. The Doppler shift is low, the performance of these methods are similar especially in low SNR. The inverse method with DCT-BEM performs little better than other ones with low SNR, while the inverse method with Legendre-BEM and DPSS-BEM perform the best with high SNR. In this scenario *NW* in DPSS-BEM is 0.00883 which is figured out by Eq. (38.12).

In Fig. 38.1b, the velocity is changed to 30 m/s, we can find the robustness of inverse methods with Legendre-BEM and DPSS-BEM. Here *NW* for DPSSs is 0.053. Inverse methods with Legendre-BEM and DPSS-BEM perform similarly.

As the receiver velocity increases to 90 m/s in Fig. 38.2a, the performance of DPSS-BEM is better than others. In Fig. 38.2b, several *NW* values are exhibited for simplicity, one is the optimized value 0.16704, while other values are 0.01, 0.07,

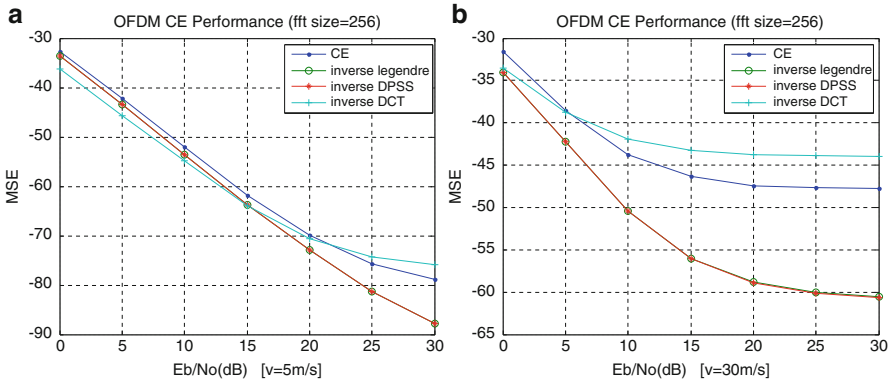

Fig. 38.1 (**a**) MSE versus SNR with velocity of 5 m/s, and *NW* equals 0.00883, (**b**) velocity equals 30 m/s and *NW* equals 0.053

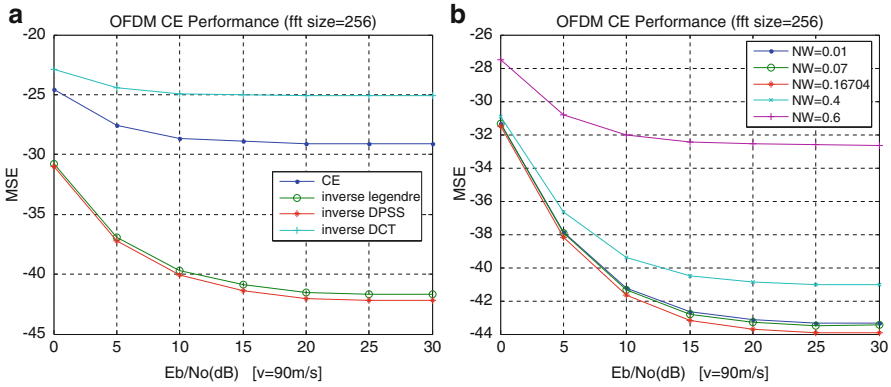

Fig. 38.2 MSE versus SNR velocity of 90 m/s. (**a**) *NW* equals 0.16875. (**b**) *NW* equals 0.01, 0.07, 0.16704, 0.4, 0.6

0.4, 0.6 which are bigger or smaller than the optimized one. As expected, the simulation result proves 0.16704 which is worked out by Eq. (38.12) are the optimized value of *NW*.

Through comparisons among Figs. 38.1 and 38.2, we find that the higher the velocity, the better performance of DPSS-BEM is. Meanwhile, a high Doppler spread estimation with the DPSSs created with a proper time-bandwidth product is significantly more accurate than that with the Legendre Polynomials.

Conclusion

In this paper, we combine the DPSSs with inverse reconstruction method to estimate channel taps in OFDM systems. The performance of the BEM with DPSSs depends on a proper choice of the time-bandwidth product *NW* for the DPSSs. By using the theory of mathematics, we calculate the value of *NW* by the formula to produce the optimal DPSSs, and then we employ the inverse method to reconstruct the channel. The computer simulations have confirmed that with the enhanced use of Slepian sequence, the DPSS is better than other basis functions, and it is more suited for the high mobility environments.

Acknowledgments This work is supported in part by NSFC 61143008, National High Technology Research and Development Program of China (No. 2011AA01A204), the Fundamental Research Funds for the Central Universities.

References

1. Haas E (2002) Aeronautical channel modeling. IEEE Trans Veh Technol 51(2):254–264
2. Tang Z, Cannizzaro RC, Leus G, Banelli P (2007) Pilot-assisted timevarying channel estimation for OFDM systems. IEEE Trans Signal Process 55(5):2226–2238
3. Zemen T, Mecklenbrauker CF (2005) Time-variant channel estimation using discrete prolate spheroidal sequences. IEEE Trans Signal Process 53(9):3597–3607
4. Tang Z, Leus G (2007) Pilot schemes for time-varying channel estimation in OFDM systems. In: IEEE workshop signal processing advances in wireless communication, Helsinki, pp 1–5
5. Cirpan HA, Tsatsanis MK (1999) Maximum likelihood blind channel estimation in the presence of Doppler shifts. IEEE Trans Signal Process 47(6):1559–1569
6. Guillaud M, Slock DTM (2003) Channel modeling and associated intercarrier interference equalization for OFDM systems with high Doppler spread. Int Conf Acoust Speech Signal Process (ICASSP) IV:237–240
7. Leus G (2004) On the estimation of rapidly time-varying channels. Eur Signal Process Conf (EUSIPCO) 4:2227–2230
8. Borah DK, Hart BD (1999) Frequency-selective fading channel estimation with a polynomial time-varying channel model. IEEE Trans Commun 47(6):862–873
9. Hrycak T, Das S, Matz G, Feichtinger H (2011) Practical estimation of rapidly varying channels for OFDM systems. IEEE Trans Commun 59(11):3040–3048
10. Slepian D (1978) Prolate spheroidal wave functions, Fourier analysis, and uncertainty ŀV: the discrete case. Bell Syst Tech J 57(5):1371–1430
11. Hrycak T, Das S, Matz G (2012) Inverse methods for reconstruction of channel taps in OFDM systems. IEEE Trans Signal Process 60(5):2666–2671
12. Kim J, Wang C-W, Stark WE (2007) Frequency domain channel estimation for OFDM based on Slepian basis expansion. In: IEEE International Conference on Communications 2007 (ICC'07), Glasgow

Chapter 39
SEMOPIAS: A Novel Secure and Efficient Mutual Open PKI Identity Authentication Scheme for Mobile Commerce

Wang Yue

Abstract Although the mobile commerce has wide prospect, it has to face with huge challenges because of potential security risks, privacy problems and efficiency due to its limitations of processing capability, and storage space and power supply in mobile terminal. The secure and efficient open PKI (Public Key Infrastructure) identity authentication scheme is one of the possible solutions in secure identity authentication of the mobile commerce. In this paper, we propose a novel secure and efficient mutual open PKI identity authentication scheme, named SEMOPIAS, to solve the problems of validity, one-time use of identification and unauthorized application system in open PKI identity authentication scheme. Analysis and evaluation are performed to demonstrate that the SEMOPIAS achieves stronger security and higher efficiency by simplifying the message format and optimizing the authentication processes. Especially, the advantages of the SEMOPIAS will be achieved more significantly when there are multiple clients or merchants participated in the scheme.

Keywords Efficiency • Identity authentication • Mobile commerce • PKI • Security

39.1 Introduction

The mobile commerce [1] has been the new development direction of the electronic commerce, because of the characteristics of convenience and ubiquitous. However, because of the susceptibility in wireless environment [2] and the limitations of processing capability, and storage space and power supply in mobile terminal, the mobile commerce has to face with huge secure challenges [3, 4], such as identity authentication, information confidentiality, integrity, and non-repudiation. The secure issues restrict the development of mobile terminal greatly. So it is very important to solve the security problems in mobile commerce, especially the security and efficiency of the identity authentication.

W. Yue (✉)
School of Physics and Mechatronics Engineering, Xi'an University, Xi'an, China

J. Mu et al. (eds.), *The Proceedings of the Third International Conference on Communications, Signal Processing, and Systems*, Lecture Notes in Electrical Engineering 322, DOI 10.1007/978-3-319-08991-1_39

In recent years, there are some identity authentication schemes. Some schemes [1, 3, 5–9] had different electronic payment architectures and identity authentication methods by setting up different electronic payment agencies. In these schemes, mobile terminals had to authenticate themselves with servers many times. They had to authenticate with not only bank or payment server, but also merchants, payment gateway [3] and agency. Payment gateway was worked as a CA (Certificate Authority) in the scheme proposed by Karnouskos [4]. Because all the information exchange among entities must pass by the payment gateway and the identity authentication had to be done during each exchange, the processes were very complex in the scheme. Clients and merchants only authenticated with their own banks in the mobile payment architecture of the typical European Union mobile payment system SEMOPS [7]. The authentication was not only one time, and not only the payment instructions but also all the commerce information were transmitted by the bank, so banks had to bear the additional burden of information processing and it is not agree with the requests of information confidentiality. So the schemes above are not secure and efficient enough. With the popularization of mobile commerce, the solutions of security and efficiency become more urgent and essential.

Most of the mobile commerce schemes are based on the PKI or WPKI (Wireless Public Key Infrastructure). They are both the core of information security technology and the basic technology of the mobile commerce. So it is very important and significant to improve and optimize PKI identity authentication scheme in mobile commerce. The SEMOPIAS proposed in this paper is just improved and optimized the open PKI identity authentication scheme.

In this paper, we propose a novel secure and efficient mutual open PKI identity authentication scheme (SEMOPIAS), to solve the problems of validity, one-time use of identification and unauthorized application system in open PKI identity authentication scheme. Analysis and evaluation are performed to demonstrate that the SEMOPIAS achieves stronger security and higher efficiency by simplifying the message format and optimizing the authentication processes. Especially, the advantages of the SEMOPIAS will be achieved more significantly when there are multiple clients or merchants participated in the scheme.

The remainder of this paper is organized as follows. In Sect. 39.2, the open PKI identity authentication scheme is introduced; in Sect. 39.3, the SEMOPIAS is proposed; in Sect. 39.4, the security and efficiency of the SEMOPIAS is provided; finally, concluding remarks are given in “Conclusions”.

39.2 Open PKI Identity Authentication Scheme

39.2.1 Open PKI Identity Authentication Scheme

In this part, we will introduce the open PKI identity authentication scheme. It improves and combines the PKI identity authentication scheme and OCSP (Online Certificate Status Protocol) reply mechanism into the scheme of providing identity

authentication file. Thereby the problems of trust, OCSP clients diversity (incompatibility) and certificate validity can be solved in the scheme. In order to solve the problems of the mutual trust between key verification logic and OCSP response service and the OCSP service differentiation, it is necessary to consolidate the key verification logic and OCSP response service into a standard identity authentication scheme, whose identity authentication service is provided by CA.

The processes of the open PKI identity authentication scheme are as follows:

1. When clients access the application system, the application system requests for CA to verify clients' identity.
2. Clients access the authentication interface of CA to complete their identity authentication.
3. Clients and CA complete clients' identity authentication by executing the digital certificate authentication processes. After completing the identity authentication, CA issues clients' identification attached the CA's digital signature.
4. Clients access the application system using their identification.

In step (3), the process of clients' identity authentication includes clients' private key verification and clients' certificate validity verification. After CA verifies clients' private key and certificate validity, it generates the identification validity, which is an important part of the identification (Fig. 39.1).

39.2.2 Some Problems

There are some problems in the open PKI identity authentication scheme.

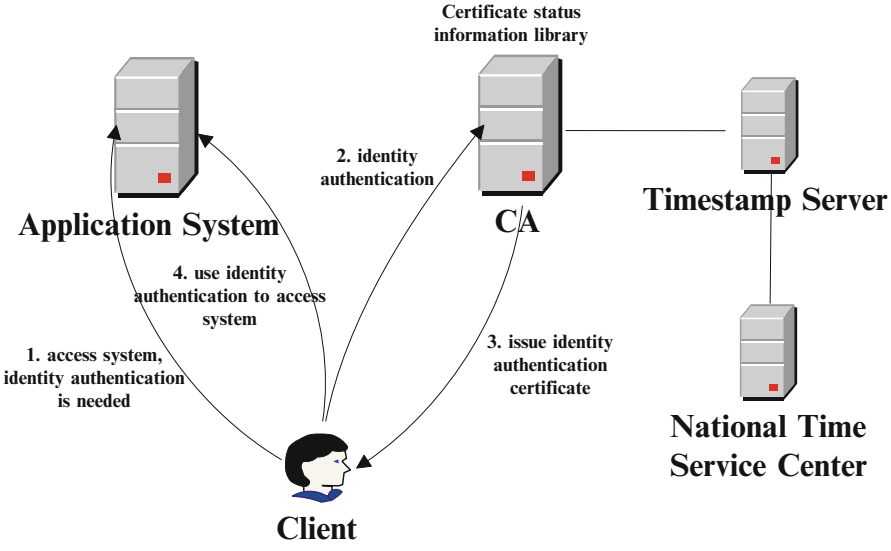

Fig. 39.1 The open PKI identity authentication scheme

1. Validity

The validity is purpose to prevent the identification from being used when the permission period is over. Thus, illegal using of identification in invalid time can be avoided. However, because the validity is a time period, the identification information could be copied and used infinitely after it is stolen within its validity.

2. One-time use of identification

The identification issued by CA in the open PKI identity authentication scheme includes the requester's ID, client's ID, validity, and so on. This identification can only be used for the mutual authentication only between the client and the requester. Identification still needs to be get from CA for the mutual authentication between the client and the other requester. Because clients' identification only can be used one time, clients who already have a legal identification have to access CA to be authenticated and get a new identification to access a different application system every time. So that is an unnecessary waist in source and time. It is a big problem in mobile terminal which is a limitation system in source.

3. The application system is not be verified.

Any entity involved in mobile commerce should be authenticated. If the application system is not been verified illegal users could pretend to be the application system to get clients' identification, so that they can pretend to be the legal clients to produce the mobile commerce. The legal clients will have to face a huge loss.

39.3 Secure and Efficient Mutual Open PKI Identity Authentication Scheme

39.3.1 Improvement Strategy

To solve the problems of the open PKI identity authentication scheme, we propose the improvement strategy.

1. Validity

Clients, who request identification, apply for an authorization from CA, so that they can apply for different validity independently. In addition, clients apply for a number of identification use times within its validity, which can prevent the identification from being used infinitely by illegal users.

2. Identification

Instead of using the previous full identification information, we use the certificate validity proof (CVP) in SEMOPIAS. The main difference is that the CVP no longer contains the authentication requester's (application system) ID. After the requester's ID is authorized in the improvement strategy (1), clients can add its ID independently. The authorized clients can add different application system ID on their CVP. So they only need to verify their identity from CA one time. CA only

verifies clients' certificate. The clients' identity can be verified using their signature signed by clients' private key.

3. The application system is not be verified.

The application system can be looked as a network node, which is the same status with clients. So the authentication processes are the same as clients' identity authentication processes.

39.3.2 SEMOPIAS

According to the improvement strategies above, we propose the SEMOPIAS (Table 39.1).

1. Interaction between the client and CA
   (1) C → CA:$ID_C, N, SIG_C(ID_C||N)$
   C applies for the certificate validity authentication to CA. The message from C contains the digital certificate ID of C and his signature signed on the message. SIG_C is used to ensure that this message is sent by C. N is a random number to prevent the reply attack (Fig. 39.2).
   (2) CA → C:$CVP_C, N, SIG_{CA}(CVP_C||N)$

Table 39.1 Symbol instruction

Symbol	Meaning
ID_i	Digital certificate ID of i
CVP_i	The CVP of i
N	A random number
SIG_i	The message is signed by using the private key of i
T_i	The validity of CVP of i
N_i	The number of using CVP within its validity
NUM_i	The number of used CVP of i
AS	Application system
C	Client

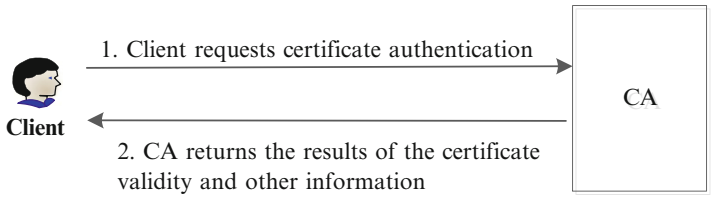

Fig. 39.2 The processes of the interaction between the client and CA

$$CVP_C = SIG_{CA}(ID_C||T_C||N_C) \tag{39.1}$$

CA checks the validity of the certificate after it receives IDC. If ID_C is valid, CVPC will be returned to C, which is the signature of CA to the CVP information. The CVP information contains ID_C (the digital certificate ID of C), T_C (the validity of CVP), and N_C (the number of using CVP within its validity).

After C receives the message from CA, he uses the public key of CA stored before to verify the message, and save CVP_C.

2. The interaction between application system and CA is the same as the interaction between the client and CA.
3. Interaction between the client and application system
   (1) C → AS:$CVP_C, ID_{AS}, N, NUM_C, SIG_C(CVP_C||ID_{AS}||N||NUM_C)$
   The client sends the identification information and its signature signed by C to AS. The identification information contains CVP, the ID of application system ID_{AS}, the number of used CVP NUM_C and the random number N.

   After AS receives the message from the client, it first uses the public key of CA to verify the CVP_C is the right CVP of C, which is issued by CA. Then, according to the validity of CVPC, AS verifies whether it is within the valid period. Finally, AS verifies whether NUM_C is less than N_C (the number of using CVP within its validity). If NUM_C is less than N_C, AS authenticates C successfully.
   (2) AS → C:$CVP_{AS}, ID_C, N, NUM_{AS}, SIG_{AS}(CVP_{AS}||ID_C||N||NUM_{AS})$
   AS sends its identification information and its signature to C like the process C → AS above.
   (3) After the two-way authentication is completed, the trust relationship is established successfully. Then, the mobile commerce can be conducted securely.

Before C and AS send CVP to each other, they should both check whether their CVP is within its validity. If not, they should access CA to apply for a new one. Otherwise, they check whether the available number is zero. If it is not zero, they sent CVP to each other (Fig. 39.3).

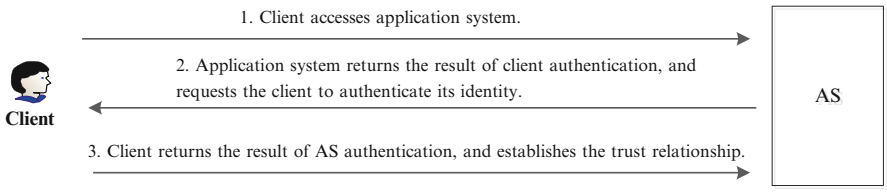

Fig. 39.3 The model of the improved protocol (2)

39.4 Security and Efficiency Analysis

39.4.1 Security Analysis

In this part, we will mainly discuss the security of identity authentication.

When the client applies for the CVP from CA, the applying message is signed by using client's own private key. After CA receives the massage, it verifies the validity of client's certificate again to guarantee the request is sent by the claimed client indeed. Then, CA signs the information of CVP, validity and the number of using CVP within its validity using its private key, to ensure that the CVP received by client is signed by CA.

After the client obtains CVP, he sends the message and its signature to AS. The message includes CVP and the ID of application system ID_{AS}. Even if the attacker gets CVP_C, he cannot forge the message because the message is signed by the client by using his own private key.

After AS receives the message, he use CA's public key to decrypt of CVP_C. If the decryption result is correct, it can believe CVP_C is issued by CA. At the same time the client's public key is also decrypted, and AS can use the client's public key to verify whether the received message is actually sent by the client. The client can verify the identity of AS though the same processes.

Because the random number is used in the message, the timeliness of the message can be verified. The random number can use to prevent the reply attack.

Because the identities of participated entities are authenticated in SEMOPIAS, the problem that the application system identity is not verified in the open PKI identity authentication scheme is also been optimized. So the security can be guaranteed in SEMOPIAS.

39.4.2 Efficiency Analysis

One of the most important advantages of SEMOPIAS is the identity authentication in the open PKI identity authentication scheme is replaced by a simple CVP. That will not restrict the objects who will receive the CVP. That is because after CA authenticates the client's identity, it will give an authorization to the client and the authorization allows the client to add the receiver's ID. The number of using CVP within its validity is used in SEMOPIAS. It can solve the problem that the identification information could be copied and used infinitely after it is stolen within its validity in the open PKI identity authentication scheme. It can restrict the client's permission, not fully authorized. CA can control the number of using CVP, and it is responsible for the security of the client's identity information. Within the number of using CVP, the client can authenticated with multiple AS after he authenticates with CA once. The advantages are as follows:

(1) Because the amount of CVP information sent by CA in SEMOPIAS is less than the amount of identity authentication in the open PKI identity authentication scheme, the transmission resource and budget are saved.
(2) The receiver's ID, which is removed from CVP, can be added by the client when it will be used. This method improves the usage efficiency of CVP, and reduces the authentication number of the client with CA.
(3) When there are multiple clients or Ass in SEMOPIAS, the transmission number of messages can be reduced greatly. So resources can be saved and the possibility of the message being stolen can be reduced too.

Conclusions
A novel secure and efficient mutual open PKI identity authentication scheme is proposed in this paper. The scheme can solve the problems of validity, one-time use of identification and unauthorized application system in open PKI identity authentication scheme. The scheme also achieves stronger security and higher efficiency by simplifying the message format and optimizing the authentication processes. For our future work, we will further explore other challenging security issues, such as the privacy protection in mobile payment.

Acknowledgements This work has been financially supported by the Xi'an Science and Technology Plan funded project (CXY1352WL30).

References

1. Hoepner P, Karnouskos S, Vilmos A, et a1. (2003) Secure mobile payment–architecture and business model of semops. European Institute for Research and Strategic summit, pp 1–8
2. Trchina E, Hassinen M, Hypponen K (2008) Utilizing national public-key infrastructure in mobile payment systems. Electron Commer Res Appl 7(20):214–231
3. Javier L, Mildrey C, JoséMaría S (2009) Secure multiparty payment with an intermediary entity. Comput Secur 28(50):289–300
4. Kungpisdan S (2009) Accountability in centralized payment environments. In: 9th international symposium on communications and information technology, pp 1022–1027
5. Lee CS, Chong C, Chua HN (2006) Towards flexible mobile payment via mediator-based service model. In: 8th international conference on electronic commerce, pp 295–301
6. Apostolopoulos T, Kousaridas A, Parissis G (2008) An open financial services architecture based on the use of intelligent mobile devices. Electron Commer Res Appl 7(2):232–246
7. Pierre S, Lei YH, Quintero A (2009) Mobile services access and payment through reusable tickets. Computer Commun 32(4):602–610
8. Li H, Fan K, Wang Y (2009) A new abuse-free fair electronic payment protocol. In: 5th international conference on information assurance and security, pp 633–636
9. Li H, Fan K, Wang Y (2012) Fairness electronic payment protocol. Int J Grid Util Comput 3 (1):53–58

Chapter 40
Uplink Capacity Analysis of Noncooperative Cellular Systems with Multiple Antennae

Wen-Liang Nie and Xiang-Yong Mou

Abstract Multi-Input Multi-Output (MIMO) are known as increasing the link throughput by providing a multiplexing gain which scales with the number of antenna cellular systems. Based on noncooperative cellular systems with multiple antennas, uplink capacity is analyzed in this paper. The concise expression of the approximated capacity is derived in the reverse link by utilizing Bernoulli's law of large number. Furthermore, the impact of several factors on the noncooperative cellular systems in practical application is discussed. Finally, computer Simulation is presented to verify the theoretical analysis.

Keywords Noncooperative cellular wireless • MIMO • Multiplexing gain • Uplink capacity

40.1 Introduction

MIMO technique is a key feature in all of advanced cellular wireless systems [1], but it has yet to be adopted on a scale commensurate with its true potential. There are several reasons for this. Cheaper alternatives to increase throughput, such as purchasing more spectrums, are invariably adopted rather than more expensive and technologically sophisticated solutions. An easy alternative to a point to point MIMO system is a multiuser MIMO system [2] in which an antenna array simultaneously serve a multiplicity of autonomous terminals. It provides high capacity gains when the terminal has channel state information (CSI). In [3] author considers a single cell time division duplex (TDD) scenario, through reciprocity, an estimate CSI is obtained by the base station. A larger excess of more base station antennas is always beneficial and one can always recover from low SNR conditions by adding a sufficient number of antennas in [3]. In [4], author considers multiuser MIMO

W.-L. Nie (✉)
CK Telecom Corporation, Chengdu 610000, China
e-mail: wenleon.nie@gmail.com; joyodsp@163.com

X.-Y. Mou
Chengdu University of Information Technology, Chengdu 610225, China

J. Mu et al. (eds.), *The Proceedings of the Third International Conference on Communications, Signal Processing, and Systems*, Lecture Notes in Electrical Engineering 322, DOI 10.1007/978-3-319-08991-1_40

operation with an infinite number of base station antennas in a multi-cellular environment.

We consider a cellular system consisting of noncooperative hexagonal cells with frequency reuse of one, three, or seven, TDD operation, Orthogonal Frequency Division Multiplexing (OFDM), and base station arrays comprising antennas where $M \to \infty$, where each base station serves single antenna terminals. We obtain closed form expressions for capacities on the reverse link and cumulative distribution functions for the SIRs in a particular scenario.

The rest of this paper is organized as follows. In the next section, we describe the proposed cellular system model. In the third section, we derive a deterministic equivalent of the capacity and the signal-to-noise rate in the reverse link. In fourth section, the simulation results are presented in special scenario. And the paper is concluded in the fifth section.

40.2 Scenario

40.2.1 Hexagonal Cells

The cells are hexagonal with a radius (from center to vertex) of r_c, every cell has K terminals having single antenna, which are placed randomly, uniformly distributed over the cell, and at the center of the cell is a base station, which comprise M omnidirectional antennas, where in the subsequent analysis, the number of M tends to infinite.

40.2.2 OFDM

We assume that OFDM is utilized, T_s denotes a symbol interval, T_u denotes a useful symbol duration, which is equal to the reciprocal of the subcarrier spacing, namely $T_u = \frac{1}{\Delta_f}$, T_g denotes a guard interval, which denotes $T_u = T_u - T_u$, "frequency smoothness interval" can be expressed as

$$N_{smooth} = 1/(T_g \Delta_f) \tag{40.1}$$

The maximum number of terminals is given as:

$$K = \tau N_{smooth} = \frac{\tau}{T_d \Delta_f} = \frac{(\tau T_s) T_u}{T_d T_s} = \left(\frac{T_{pilot}}{T_d}\right)\left(\frac{T_u}{T_s}\right) \tag{40.2}$$

where $T_{pilot} = \tau T_s$ is the time spent on sending reverse pilots, we assume that a guard interval T_g equals to the delay spread time T_d.

40.2.3 Propagation

We denote the complex propagation coefficient between the mth base station antenna in the jth cell, and the kth terminal in the lth cell in the nth subcarrier by g_{nmjkl} which, in turn, is equal to a complex fast fading factor times an amplitude factor that accounts for geometric attenuation and shadow fading,

$$g_{nmjkl} = h_{nmjkl} \bullet \beta_{jkl}^{1/2} \beta_{jkl} = \frac{Z_{jkl}}{r_{jkl}^{\gamma}} \tag{40.3}$$

$$\beta_{jkl} = \frac{Z_{jkl}}{r_{jkl}^{\gamma}} \tag{40.4}$$

where r_{jkl} is the distance between the kth terminal in the lth cell and the base station in the jth cell, γ is the decay exponent, and Z_{jkl} is a log-normal random variable.

Let $\hat{G}_{jj}$ denotes the estimate for the MK propagation matrix between the M base station antennas of the jth cell, and the K terminals in the jth cell;

$$\hat{G} = \sqrt{\rho_p} \sum_{l=1}^{L} \hat{G}_{jl} + V_j \tag{40.5}$$

where $\hat{G}_{jl}$ denotes the estimate for the MK propagation matrix between the M base station antennas of the lth cell, and the K terminals in the jth$|G_{jl}| = g_{nmjkl}$,$m = 1,\ldots,$ $k = 1,\ldots,K$,V_j denotes a MK matrix of receiver noise, ρ_p denotes a measure of pilot signal to noise ratio.

40.3 Reverse Link Data Transmission

The K terminals in each cell independently transmit data streams to their respective base station. The base station uses its channel estimate to perform maximum ratio combining.

40.3.1 Signal Model

$$\overline{x}_j = \sqrt{\rho_r} \sum_{l=1}^{L} G_{jl} \overline{a}_j + \overline{w}_j \tag{40.6}$$

where $\overline{a}_j$ is the $1 \times K$ vector of message bearing symbols from the terminals of the lth cell, which are transmitted by the terminals are independent and distributed as

zero mean, unit variance, complex Gaussian. $\overline{w}_j$ is a vector of receiver noise whose components are zero-mean and uncorrelated with the propagation matrices, and ρ_r is a measure of signal-to-noise ratio.

40.3.2 Maximum Ratio Combining

According to Eqs. (40.4) and (40.6), by exploiting maximum ratio combining method, let received signal multiply the conjugate transpose of the channel estimate, we can obtain the received signal expression at the base station:

$$\overline{y}_j \equiv \widehat{G}_{jj}^{\dagger}\overline{x}_j = \sqrt{\rho_p}\sum_{l=1}^{L} G_{jl} + V_j = \left(\sqrt{\rho_p}\sum_{l=1}^{L} G_{jl} + V_j\right)^{\dagger}\left(\sqrt{\rho_r}\sum_{l=1}^{L} G_{jl_2}\overline{a}_j + \overline{w}_j\right) \tag{40.7}$$

where the superscript † denotes conjugate transpose. The components of $\overline{y}_j$ comprise sums of inner products between M component random vectors. The propagation matrices can be written as:

$$\frac{1}{M}G_{jl_1}^{\dagger}G_{jl_2} = D_{\overline{\beta}_j l_1}^{1/2}\left(\frac{H_{jl_1}^{\dagger}H_{jl_2}}{M}\right)D_{\overline{\beta}_j l_2}^{1/2} \tag{40.8}$$

where H_{jl} is the MK matrix of fast fading coefficients between the K terminals of the lth cell, and the M antennas of the jth base station, $|H_{il}| = h_{nmjkl}$, and $D_{\overline{\beta}_j l_1}^{1/2}$ is a MK diagonal matrix whose diagonal elements comprise the vector $|\beta_{il}|_k = \beta_{ikl}, k = 1, \cdots, K$. According to law of large numbers, as the scale of M grows larger, we have the following expression.

$$\frac{1}{M}H_{jl_1}^{\dagger}H_{jl_2} = I_K\delta_{l_1 l_2} \tag{40.9}$$

where I_K is the $K \times K$ identity matrix.

$$\frac{1}{M\sqrt{\rho_r\rho_p}}\overline{y}_j \to \sum_{l=1}^{L} G_{jl}\overline{a}_j (j = 1, \cdots, L) \tag{40.10}$$

The kth component of the processed signal becomes:

$$\frac{1}{M\sqrt{\rho_r}\rho_p}\overline{y}_{kj} \to \beta_{jkj}a_{kj} + \sum_{l\neq j}\beta_{jkl}a_{kl} \tag{40.11}$$

The effective signal to interference ratio is a random quantity which depends on the random positions of the terminals and the shadow fading coefficients.

$$SIR_{rk} = \frac{\beta_{jkl}^2}{\sum_{j \neq k} \beta_{jkl}^2} \tag{40.12}$$

40.3.3 Reverse Link Capacity

The instantaneous capacity of the terminal within each subcarrier is equal to the logarithm of one plus the signal-to-interference ratio. The throughput per terminal, in units of bits/sec/terminal, accounts for the total bandwidth and frequency re-use, the pilot overhead and the overhead of the cyclic prefix.

$$C_{rk} = \left(\frac{B}{\alpha}\right)\left(\frac{T_{slot} - T_{pilot}}{T_{slot}}\right)\left(\frac{T_u}{T_s}\right)\log_2(1 + SIR_{rk}) \tag{40.13}$$

where B is the total bandwidth in Hz, α is the frequency reuse factor (equal to either one, three, or seven in our subsequent analysis), T_{pilot} is the slot length, T_u is the time spent transmitting reverse link pilots, T_u is the useful symbol duration, and T_s is the OFDM symbol interval, where the times are measured in seconds.

The sum of the net throughputs per terminal is given as:

$$C_{rk} = \sum_{k=1}^{K} C_{rk} \tag{40.14}$$

40.4 Numerical Simulation

40.4.1 Scenario for Numerical Study

We assume OFDM parameters identical to Long Term Evolution (LTE) reverse link parameters (Table 40.1).

Table 40.1 Set parameters for link

Link parameters	Parameters set
Symbol interval	71.4 ms
Useful symbol duration	66.7 ms
Training efficiency time	3/7
System bandwidth	20 MHz
Frequency reuse factor	1,3,7
Decay exponent	3.8
Shadow fading	8 dB
Simulation times	5,000

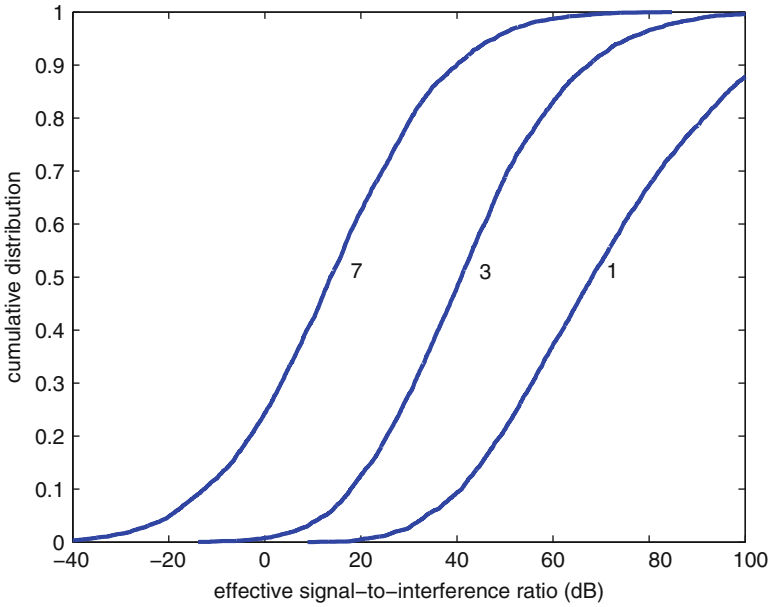

Fig. 40.1 Cumulative distribution of the reverse effective signal to interference ratio (dB) for frequency-reuse factors of one, three, and seven

The cell radius is 1,600 m, and the cell hole radius is 100 m. The set of cells that interfere with a particular cell by finding all cells which reuse the same frequency band and are within eight cell diameters of the cell.

40.4.2 Simulation Results

Figure 40.1 shows that cumulative distribution of the reverse effective signal to interference ratio (dB) for frequency-reuse factors of one, three, and seven. Frequency reuse of three instead of one increases the SIR by about 21 dB, and reuse of seven adds an additional 15 dB. It clearly shows that frequency reuse can help improve the system SIR. Figure 40.2 shows that cumulative distribution of the net reverse capacity per terminal (megabits/second) for frequency-reuse factors of one, three, and seven. When the SIR is low, reuse factors are beneficial; When the SIR is already high, a greater frequency reuse factor causes a net decrease in throughput. Capacity gains due to the large increase in SIR more than offset the loss due to less aggressive frequency reuse.

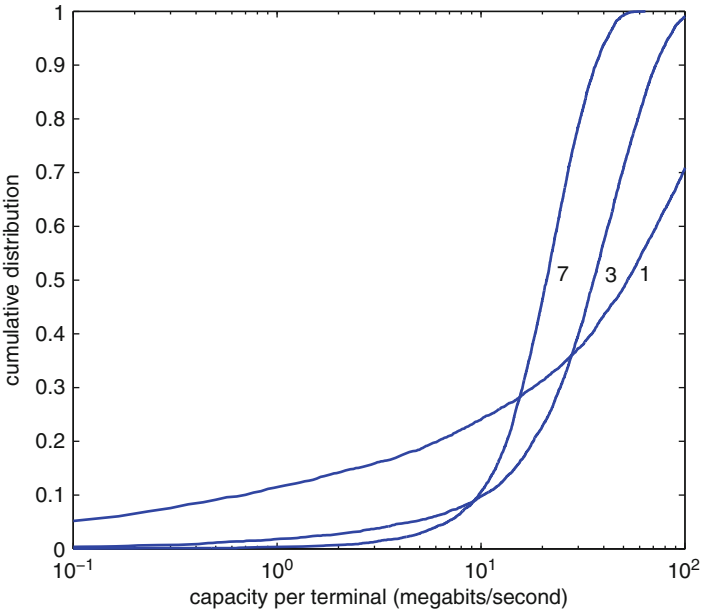

Fig. 40.2 Cumulative distribution of the net reverse capacity per terminal (megabits/second) for frequency-reuse factors of one, three, and seven

Conclusions

This paper outlined a compelling case for a time division duplex cellular system which employs base stations equipped with large numbers of antennas that communicate simultaneously with smaller numbers of cheap, single-antenna terminals through multi-user MIMO techniques. Numerical results verify this system has the potential to deliver high throughputs reliably on both the forward and the reverse link in fast changing propagation environments. As the number of base station antennas grows without limit all of the effects of uncorrelated noise and fast fading disappear. However, it remains inter cellular interference that results from pilot contamination.

References

1. Telatar IE (1999) Capacity of multi-antenna gaussian channels. Trans Telecommun 10:586–595
2. David G, Marios K, Thomas S From single user to multiuser communications: shifting the MIMO paradigm. IEEE Signal Process Mag 36–46
3. Marzetta TL (2006) How much training is required for multiuser MIMO? In: Fortieth Asilomar conference on signals, systems, computers, pacific grove, 2006
4. Marzetta TL (2010) Noncooperative cellular wireless with unlimited numbers of BS antennas. IEEE Trans Wirel Commun 9:3590–3600

Chapter 41
An Improved Slow-Start Algorithm Based on Bandwidth Estimation

Hong Jie, Rui-Qing Wu, and Nan Ding

Abstract Aimed at these problems that the transmission rate changes greatly, the slow start threshold (ssthresh) sets statically and the abrupt transition causes the multiple packets losses from a window of data and retransmission timeouts on the stage of slow-start of TCP congestion, this paper proposes an improved slow-start algorithm called TCPBP, which utilizes a passive end-to-end bandwidth estimation technique to estimate in real time the available bandwidth, then realizes the dynamical updating of ssthresh according to the network status. Furthermore, we adopt a phased approach to adjust the size of the congestion window (cwnd) during slow-start phase. Simulation results show that TCPBP can effectively avoid the phenomenon of multiple packets losses with respect to the traditional TCP and achieve the smooth access and the transition to congestion avoidance stage, which improve the performance of network, increase the bandwidth utilization and throughput, and lower the packet loss rate.

Keywords Congestion control • Slow-start • Bandwidth estimation • Multiple packets losses

41.1 Introduction

The transmission control protocol (TCP) is widely used in the network as the transport layer protocol based on sliding window. It can automatically adjust the size of cwnd to make the data transmission rate adapt to network congestion. Many studies have done about congestion control and made some improvements. The original TCP Tahoe has used slow-start and congestion avoidance mechanisms, TCP Reno has realized fast retransmission and fast recovery mechanisms, TCP NewReno and TCP SACK have acquired more information on the sender side based on the confirming message from the receiver side to find out the lost packet. When a TCP connection is established or the retransmission timeout occurs,

H. Jie (✉) • R.-Q. Wu • N. Ding
School of Electronic Engineering, University of Electronic Science and Technology of China, Chengdu, China
e-mail: jieqionghong@126.com

J. Mu et al. (eds.), *The Proceedings of the Third International Conference on Communications, Signal Processing, and Systems*, Lecture Notes in Electrical Engineering 322, DOI 10.1007/978-3-319-08991-1_41

slow-start begins with gradually increasing the size of cwnd due to unknown network status instead of immediately transmitting a larger window of data into the network. During this phase, cwnd is exponentially increased at every round trip time (RTT), i.e. an acknowledgment received at the sender side increases the size of cwnd by 1. Due to the way slow-start probes the network bandwidth, it suffers from the following two problems. On one hand, since the slow-start algorithm begins with sending one segment, it takes many RTTs to reach the optimal operating point, thus resulting in poor utilization of the available bandwidth for short transfers. On the other hand, since a TCP sender has no knowledge about the capacity of the available resources on the networks and uses default parameters at the beginning of transmission, the exponential growth of cwnd in the last part often misleads the sender to send too many packets, causing a severe buffer overflow at the bottleneck link and resulting in multiple packets losses and network instability. Researchers have proposed a series of improved methods. Allman et al. [1] designed a bigger initial window and reduced the slow-start time to improve the efficiency of the short lifetime connection slow-start stage. Hoe [2] replaced the default setting of ssthresh with estimated threshold at the receiver side to ensure cwnd to the appropriate values. But it is insensitive to the changes of network load, leading to multiple packets losses when more than one data stream start or a new flow injects into the network at the same time. Padmanabhan and Katz [3] proposed TCP Fast-start, which shortened the next slow-start time by caching the parameters of recent network, thereby significantly reducing the burst transmission latency. It requires the network run smoothly, but with the Internet scale extending and the network bandwidth larger, the amplitude of network oscillation is bigger. TCP Vegas [4] increased the value of cwnd every two RTT to limit the exponential growth rate, but still not avoiding multiple packets losses, and reducing the network transmission performance in some extent.

Many scholars have devoted a lot of meaningful works [5–8]. In this paper, we presents a phased and successive approximation of slow-start algorithm called TCPBP, which dynamically adjusts the value of ssthresh with respect to the default setting based on the available bandwidth by the end-to-end passive estimation method. TCPBP makes ssthresh close to the value of network bandwidth to improve the network resource utilization, and changes the growth way of cwnd in the second half of slow-start i.e. entering the stage of congestion avoidance in a more gentle way. Combined with exponential and negative exponential growth window of gradually approximation method, the smoothness of slow-start is improved.

The rest of the paper is organized as follows. The available bandwidth estimation is presented in Sect. 41.2. Section 41.3 discusses the improved slow-start mechanism. In Sect. 41.4, the simulation results and analysis are shown. Some conclusions are given in the last section.

41.2 Improved Slow-Start Algorithm Based on the Available Bandwidth Estimation

41.2.1 Available Bandwidth Estimation

The technique of the bandwidth measurement, divided into passive and active method, are applied to end-to-end flow control by acquiring in real time network status to adjust the network behavior so as to make full use of network resources. Passive estimation has no effect on the actual behavior of the network, only to record and count network behavior, not increasing and modifying the data load into the network. However, active estimation, where injecting specific probe packet into the network is needed, affects the network operation flow. Therefore, TCPBP adopts passive estimation method to estimate in real time the available bandwidth by monitoring the ACK stream and the RTT values corresponding to a TCP flow. The mechanisms for calculating the bandwidth sample and estimating the available bandwidth are described below.

Assume that an ACK arriving at the sender at time t_i means that d_i bytes corresponding to the flow have been received at the receiver. So the initial bandwidth sample for the flow is defined as follows:

$$bw_i = \frac{d_{i+1} - d_i}{t_{i+1} - t_i} = \frac{\Delta d}{\Delta t} \tag{41.1}$$

However, due to the burstiness in the ACK arrival process, Δt is very small in most cases. Therefore, bw_i may not reflect the fair share of bandwidth for the corresponding TCP flow. Assume that the lifetime of a TCP flow is a collection of burst periods (during when it receives ACKs and transmits TCP segments) and off periods (during when there is no ACK reception and transmission). Therefore, consider that an RTT period includes burst period, gap period, and diffRTT. Figure 41.1 shows the different parts in an RTT period, where minRTT represents the minimum RTT seen by the flow in its lifetime, and currRTT stands for the measured value of the RTT from previous RTT period and the current RTT period is in progress.

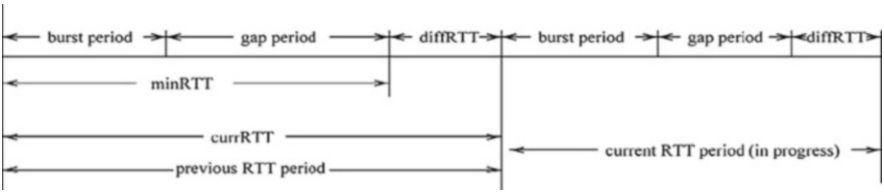

Fig. 41.1 Different parts of a RTT period

During a burst period from t_i to t_{i+nack}, the sender receives (nack + 1) ACKs for data ranging from d_i to d_{i+nack}. So the bandwidth for the flow can be calculated as follows:

$$bw_s = \frac{d_{i+nack} - d_i}{t_{i+nack} - t_i} = \frac{(d_{i+1} - d_i) * nack}{(t_{i+1} - t_i) * nack} = \frac{\Delta d_i}{\Delta t_i} \tag{41.2}$$

Under the bottleneck bandwidth, RTT is equal to the burst period and diffRTT, therefore, the estimated bandwidth is as follows:

$$bw_e = \frac{d_{i+1} - d_i}{(t_{i+1} - t_i) + diffRTT/nack} \tag{41.3}$$

Define the parameter $\alpha(0 \leq \alpha \leq 1)$ which determines the degree of congestion. Let α be equal to β*(diffRTT/minRTT), where β is a scaling factor for the normalized diffRTT with respect to minRTT. For all of our simulations, we set the value of β to be equal to 1.5. Note that, the value of α approaches one as the congestion in the network increases. Let T_{gap} stands for the gap period, then the approximate fair share of bandwidth for the flow can be defined as follows:

$$bw_a = \frac{d_{i+1} - d_i}{t_{i+1} - t_i + diffRTT/nack + \alpha * T_{gap}/nack} \tag{41.4}$$

To estimate the available bandwidth from the bandwidth sample, we use an EWMA filter whose gain varies with the change in the bottleneck link capacity.

$$\mathrm{bw_i} = \xi * \mathrm{bw_{i-1}} + (1 - \xi) * \mathrm{bw_s} \tag{41.5}$$

Where $\mathrm{bw_i}$, $\mathrm{bw_s}$ and ξ represents current bandwidth, the bandwidth sample, and exponential smoothing factor respectively. We take $\beta = 19/21$ empirically.

41.2.2 Improved Slow-Start Algorithm

The network bandwidth of the TCP flow can be computed by bw = cwnd/RTT. Therefore, TCPBP adjusts dynamically the value of ssthresh based on the estimated bandwidth instead of the default value. The expression of ssthresh is defined as follows:

$$\mathrm{ssthresh} = \mathrm{bw} * \mathrm{RTT} \tag{41.6}$$

The key idea of TCPBP includes two aspects. On one hand, the value of ssthresh is adjusted based on the estimated bandwidth. At the beginning of slow-start, the sender estimates the available bandwidth according to the expression (41.4) and

(41.5), then updating the value of ssthresh according to the expression (41.6). In the process of slow-start, TCPBP adjusts in real time the value of ssthresh to adapt to the current link state. On the other hand, TCBP improves the increasement rule of the size of cwnd. The slow-start phase of the traditional TCP increases exponentially the size of cwnd from one to the value of ssthresh. This fixed increasement is easy to cause the low bandwidth utilization rate during the initial stage of slow-start. In addition, when the size of cwnd soars to the half of the value of ssthresh, the way of exponential increasement is easy to cause congestion due to big amplitude change, leading to the oscillation of cwnd, triggering the resumption of slow-start, and seriously impacting on throughput. TCPBP proposes the improved process described below. In the initial stage of the TCP flow, when the size of cwnd is less than the half of the value of ssthresh i.e. the available bandwidth lager than cwnd, the size of cwnd increases exponentially. After the size of cwnd soars to the half of the value of ssthresh, cwnd increases the half value of difference between ssthresh and cwnd every RTT until the difference exceeds regulatory factor θ. The improved slow-start is described as follows.

Step1: Initialize the size of cwnd and the value of ssthresh;
cwnd=2, ssthresh=$ssthresh_{init}$,θ=θ_0;
Step2: Send packets with the number according to the size of cwnd;
Step3: After receiving the ACK packet, the sender estimates the available bandwidth by expression (2.4) and (2.5), and sets the value of ssthresh by expression (2.6);
Step4: Adjust the size of cwnd described below;

```
if (cwnd<ssthresh){
   if (cwnd<ssthresh/2) cwnd=2*cwnd;
      else if (cwnd>=ssthresh/2&&(ssthresh-cwnd)>θ)
           cwnd=cwnd+(ssthresh-cwnd)/2; }
else{ cwnd=ssthresh; go to Step6;}
```

Step5: When retransmission timer occurs, slow-start restart and return to Step1.
Step6: Enter the congestion avoidance phase.

41.3 Performance Simulation

In this section, we use NS2 to simulate and evaluate the performance of the improved slow-start algorithm compared to TCP Reno and TCP Vegas. The performance of improved algorithm focuses on the following three: (1) the accuracy of available bandwidth estimation; (2) the number of packet loss under different size of the window; (3) the change of throughput and packet loss rate under different bottleneck capacity. The network topology used in the simulation is depicted in Fig. 41.2.

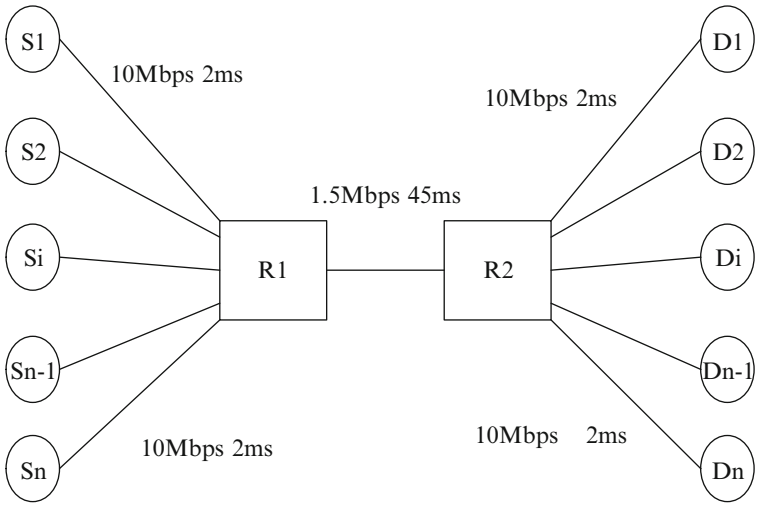

Fig. 41.2 Network topology

The TCP senders S_1 to S_n are connected to the router R1 via a 10 Mbps link with 2 ms one-way delay; The TCP receivers D_1 to D_n are connected to the router R2 via a 10 Mbps link with 2 ms one-way delay; The link between R1 and R2 is the bottleneck link with 1.5 Mbps bandwidth and 45 ms one-way delay; The maximum segment size of TCP is set to 1,000 bytes and the buffer capacity is set to 25 packets.

41.3.1 Accuracy of the Bandwidth Estimation

The method of bandwidth measurement and the accuracy of bandwidth estimation are directly related to the performance of the improved algorithm. The scenario including non-adaptive UDP flow is set up to test the accuracy of bandwidth estimation of TCPBP. Figure 41.3 illustrates the results for a bottleneck link with 5 Mbps capacity and 30 ms one-way propagation delay shared by one TCPBP connection based on FTP traffic and two UDP connection based on CBR traffic with a fixed rate of 1 Mbps. The first UDP connection is from 0 to 300 s. The duration of the send UDP connection is from 50 to 100 s, 150 to 200 s, 250 to 300 s. Simulation results show that the estimated bandwidth is basically consistent with actual bandwidth. TCPBP is estimated around 4 Mbps when one UDP connection exists. Besides, the estimated bandwidth of TCPBP is about 3 Mbps when the other UDP connection occurs.

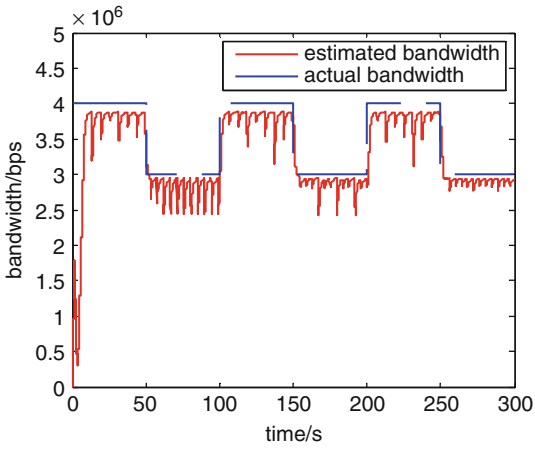

Fig. 41.3 The result of bandwidth estimation

41.3.2 Packets Losses Under Different Size of the Window

We set up the simulation environment including background traffic with a fixed rate of 0.5 Mbps and a TCPBP flow (Vegas or Reno) sharing 1 Mbps bandwidth and a cache area of eight groups. Meanwhile routers use FIFO scheduling and the bottleneck link uses Droptail strategy. The network bandwidth delay product is calculated about 12 groups according to the characteristics of the network. Figure 41.4 shows the tendency of grouping discarding along with the increasement of the size of window in different slow-start mechanism. Reno increases the sending rate in a constant manner without the real-time knowledge of the network status, resulting in packet loss seriously. Although Vegas increases the sending rate every two RTT, but still not avoiding the packets losses. While TCPBP by accurately estimating the available bandwidth to dynamically set the sending rate, reduce the number of packet loss with respect to Reno and Vegas. Especially when allowed that the sending rate is greater than the network bandwidth, TCPBP can acquire better performance. Figure 41.5 shows that when the size of advertised window from the receiver is set to be large enough, the number of packet loss varies along with the size of FTP file. We can see from Fig. 41.5, when the size of FTP is small, there is no packet discarded. The reason is that before the data flow is filled with the connecting pipe, the file has been transferred. But, with the continuous increase the size of the file, Reno and Vegas send too much packets in excess of the network capacity due to the inaccurate judgement of the network state, leading to buffer overflow and more packet discard. However TCPBP greatly reduces the number of packet loss based on the adaptive bandwidth estimation which dynamically adjusts the value of ssthresh and the smooth method of increasement of the cwnd.

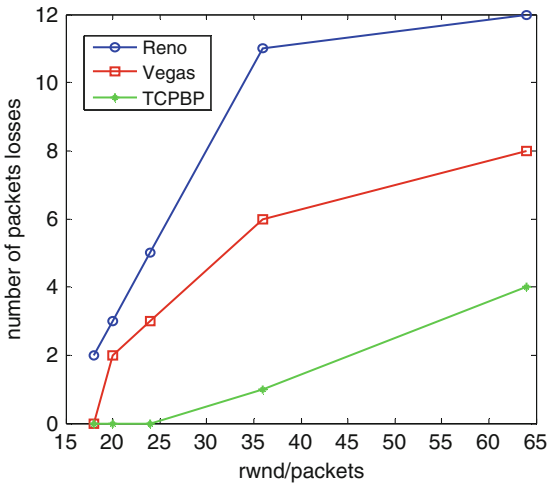

Fig. 41.4 Number of Packets losses with window

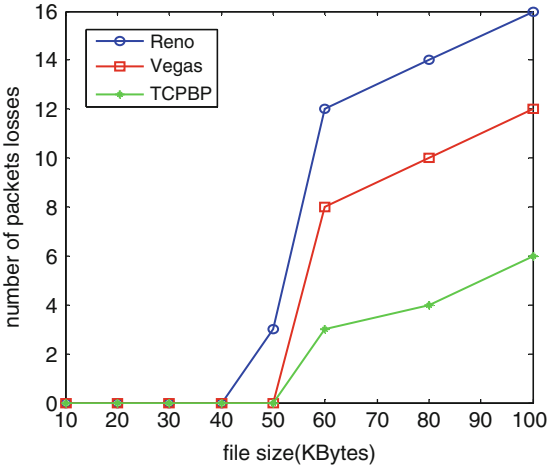

Fig. 41.5 Number of Packets losses with file size

41.3.3 Throughput and Packet Loss Rate Under Different Bottleneck Capacity

To evaluate the performance of TCPBP in different network environment, we range the bottleneck capacity from 5 to 40 Mbps, compared with Reno and Vegas. We calculate the throughput of the three kinds of slow-start algorithm within the first 20 s. Simulation results shown in Fig. 41.6 illustrate that the throughput of Reno can not increase as the increasement of the network capacity due to the fixed ssthresh. And the increasement of throughput of Vegas is not obvious after the value soaring to 8 Mbps. The reason is that Vegas estimates the network bandwidth by monitoring round-trip delay. However, the throughput of TCPBP can be increased in

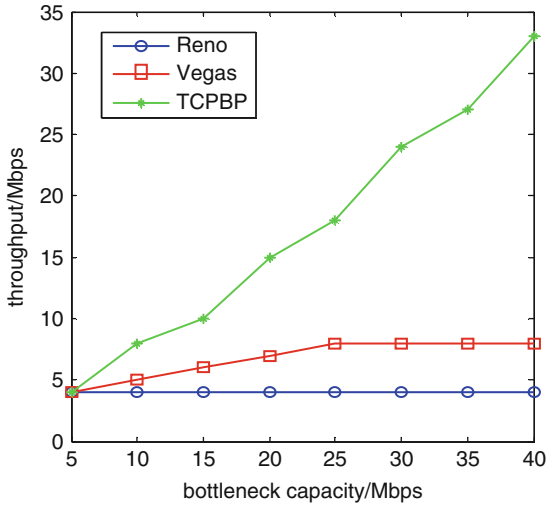

Fig. 41.6 Throughput with bottleneck capacity

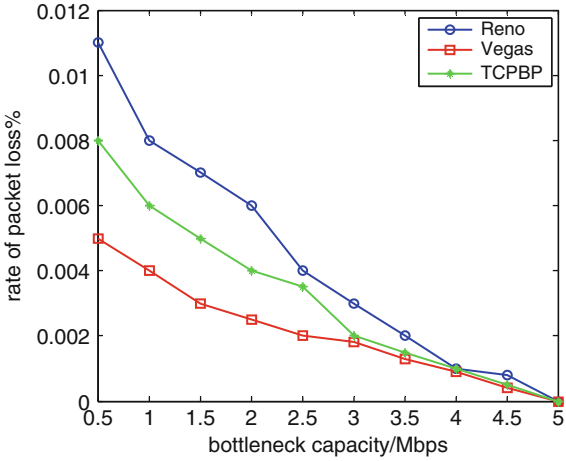

Fig. 41.7 Packet loss rate with bottleneck capacity

approximately linear with network capacity depending on real-time estimation network bandwidth. Therefore, the transmission efficiency of TCPBP is improved in a great extent compared with Reno and Vegas.

As seen in Fig. 41.7, packet loss rate of TCPBP and Reno are reduced with the growth of the bottleneck bandwidth. When the bottleneck link bandwidth is small, the packet loss rate of TCPBP is less than Reno. The reason is that TCPBP can effectively control the increase speed of cwnd according to the degree of congestion, thus reducing the packet loss probability and improving the TCP performance effectively.

Conclusion

This paper analyzes the influence and the defect of the slow-start mechanism of TCP for network transmission. An improved slow-start algorithm TCPBP based on the bandwidth estimation is proposed, which adjusts dynamically the value of ssthresh by in real time estimating network available bandwidth. Besides we improve the exponential growth rule of cwnd by adopting a kind of more smooth access to the congestion avoidance. Simulation results show that the improved algorithm can greatly improve the performance of TCP and avoid the occurrence of the phenomenon of multiple packets losses, and the bandwidth utilization and throughput are improved, and the error rate of packet loss is reduced compared with Reno and Vegas.

Acknowledgment This work is supported by the Fundamental Research Funds for the Central Universities Project No. ZYGX2012J020.

References

1. Allman M, Hayes C, Ostermann S (1998) An evaluation of TCP with larger initial windows. ACM SIGCOMM Comput Commun Rev 28:41–52
2. Hoe JC (1996) Improving the start-up behavior of a congestion control scheme for TCP. ACM SIGCOMM Comput Commun Rev 26:270–280
3. Padmanabhan VN, Katz RH (1998) TCP fast start: a technique for speeding up web transfers
4. Samios CB, Vernon MK (2003) Modeling the throughput of TCP Vegas. ACM SIGMETRICS Perform Evaluat Rev 31:71–81
5. Niu L, Wang F, Liu DD et al (2014) A dynamic adjustment algorithm of slow-start threshold based on RTT. Appl Mech Mater 536:782–785
6. Petrov I, Janevski T (2013) Improved TCP slow start algorithm. In: 21st Telecommun Forum (TELFOR), 2013. IEEE, pp 121–124
7. Sallantin R, Baudoin C, Chaput E et al (2013) Initial spreading: a fast start-Up TCP mechanism. In: IEEE 38th conference on local computer network (LCN). IEEE, pp 492–499
8. Feroz A, Lai WL, Stabile JJ (2011) Slow-start adaptive mechanisms to improve efficiency of bandwidth allocation: U.S. Patent 8,031,601

Chapter 42
Efficient Joint Spectrum Sensing Algorithm Under Time-Variant Flat Fading Channel

Mengwei Sun, Xingjun Lai, Xiao Peng, Chenglin Zhao, and Bin Li

Abstract In this paper, we propose a new spectrum sensing method which could detect the time-variant fading channel gain and primary user state jointly. This joint estimation algorithm is based on the maximum a posteriori probability criteria and the particle filtering technology. Experimental simulations verify the superior performance of our presented joint detection scheme over traditional detection methods such as matched filtering detection and energy detection under time-variant flat fading channel.

Keywords Spectrum sensing • Time-variant flat fading channel • Joint estimation • Maximum a posteriori probability criteria • Particle filtering

42.1 Introduction

Cognitive radio (CR) is considered as an effective solution for scarcity of spectrum resources [1]. Unlicensed users (second users, SUs) detect the assigned spectrum by spectrum sensing technology and exploit the unused part of the spectrum [2]. In some emerging wireless services such as IEEE 802.11n and LTE-A, time-variant fading channel has become common and brings grim challenge to spectrum sensing. This is because the most common spectrum sensing techniques such as matched filter detection (MFD) [3] and energy detection (ED) [4, 5] are designed for time-invariant channel.

We propose a novel method to address this problem. The creativity of this method could be manifest in the following aspects. Firstly, the time-variant flat fading channel gain and the PU state are estimated jointly at the receiver. This joint estimation framework is accomplished by maximum a posteriori probability (MAP) criteria and particle filtering (PF) technology and could be applied to both coherent and incoherent reception systems. Secondly, we redefine detection probability which could balance the quality of data transmission and utilization rate of

M. Sun (✉) • X. Lai • X. Peng • C. Zhao • B. Li
Key Lab of Universal Wireless Communications, Beijing University of Posts and Telecommunications, Beijing, China
e-mail: 18810536430@163.com

J. Mu et al. (eds.), *The Proceedings of the Third International Conference on Communications, Signal Processing, and Systems*, Lecture Notes in Electrical Engineering 322, DOI 10.1007/978-3-319-08991-1_42

spectrum [6]. The purpose of the proposed algorithm for spectrum sensing is to maximize the detection probability.

The remaining part of this paper is organized as follows. Section 42.2 provides the DSM for spectrum sensing over time-variant flat fading (TVFF) channel. In Sect. 42.3, the joint blind estimation algorithm is provided in detail. Numerical simulations and performance analysis are provided in Sect. 42.4. Finally, conclusions of this study are presented in section "Conclusion".

42.2 System Model

In this paper, we develop a dynamic state-space model (DSM) which takes full consideration of the evolution of primary user state and the time-varying fading channel gain, and it could be represented as

$$\begin{cases} S_n = f(S_{n-1}) \\ a_n = h(a_{n-1}) \\ y_n = g(a_n, x_n, \mathbf{v}_n) \end{cases} \qquad n = 0, ..., N-1 \tag{42.1}$$

Here, S_n denotes the state of PU, x_n is the transmitted signal. The fading channel gain is denoted by a_n. The observation equation $g(.)$ have a reference to x_n, a_n and additive Gaussian white noise $\mathbf{v}_n$. These three parts will be described in detail below.

42.2.1 PU States

The working status of PU is active or idle. We abstract this evolution process by a hidden Markov model (HMM). The transition probability matrix (TPM) it could be expressed as

$$\mathbf{\Pi} = \begin{bmatrix} p_{idle \to idle} & p_{idle \to active} \\ p_{active \to idle} & p_{active \to active} \end{bmatrix} = \begin{bmatrix} p_{00} & p_{01} \\ p_{10} & p_{11} \end{bmatrix} \tag{42.2}$$

Here, $p_{01} = 1 - p_{00}$ and $p_{10} = 1 - p_{11}$. The configurations of the transition probability should be established based on the practical application.

42.2.2 TVFF Channel

The particularity of the TVFF channel is that the channel gain changes over time in a correlated manner and it could be viewed as the output of a Markov chain. Thus, we use finite-state Markov channel (FSMC) model to describe it. The main idea of FSMC model is partitioning the fading channel gain into finite discrete states, i.e. the number of discrete states is designated by K, and each discrete state transfers to others with specified probability [7].

42.2.3 Observation

When pilot, synchronization code or spread spectrum code is utilized and known to receiver, we get the observation by using MFD scheme for reference which could obtain the optimum for detection of PUs. The observation could be written as

$$y_n = \begin{cases} \mathbf{v}_n \otimes \mathbf{s}_c & H_0 \\ (a_n \times \mathbf{x}_n + \mathbf{v}_n) \otimes \mathbf{s}_c & H_1 \end{cases} \tag{42.3}$$

Here, $\mathbf{s}_c$ to denote the pilot. There are two hypotheses: (1) H_0 denotes that the pilot signal does not exist, i.e., $\mathbf{x}_n = \mathbf{0}$; (2) H_1 represents that the pilot signal exists, i.e. $\mathbf{x}_n = \mathbf{s}_c$, [6].

It is obvious from (3) that the observation y_n follows a Gaussian distribution and could be depicted as

$$f_y(y_n) = \begin{cases} \dfrac{1}{\sqrt{2\pi\|s_c\|\sigma^2}} \exp\left[-\dfrac{(y_n - \mathbf{v}_n \otimes \mathbf{s}_c)}{2\|s_c\|\sigma^2}\right] & H_0 \\ \dfrac{1}{\sqrt{2\pi\|s_c\|\sigma^2}} \exp\left\{-\dfrac{[y_n - (a_n \times \mathbf{x}_n + \mathbf{v}_n) \otimes \mathbf{s}_c]}{2\|s_c\|\sigma^2}\right\} & H_1 \end{cases} \tag{42.4}$$

Otherwise, we use ED sensing scheme for reference, the observation is the summed energy of sampling data in a specified sample size

$$y_n = \begin{cases} \sum_{m=1}^{M} v_{n,m}^2 & H_0 \\ \sum_{m=1}^{M} (a_{n,m} x_{n,m} + v_{n,m})^2 & H_1 \end{cases} \tag{42.5}$$

where M represents the sample size; $a_{n,m}$ and $x_{n,m,}$ denote the mth fading channel gain and sampling signal in the nth sensing slot respectively; $v_{n,m}$ represents the additive white Gaussian noise value, and $v_{n,m} \sim N(0, \sigma^2)$. In this paper, we normalize the energy of sampling signal, i.e. $x_{n,m} = 1$, H_1; $x_{n,m} = 0$, H_0.

It could be deduced from (42.5) that the observation y_n follows chi-square distribution with M degrees of freedom and could be written as [8]

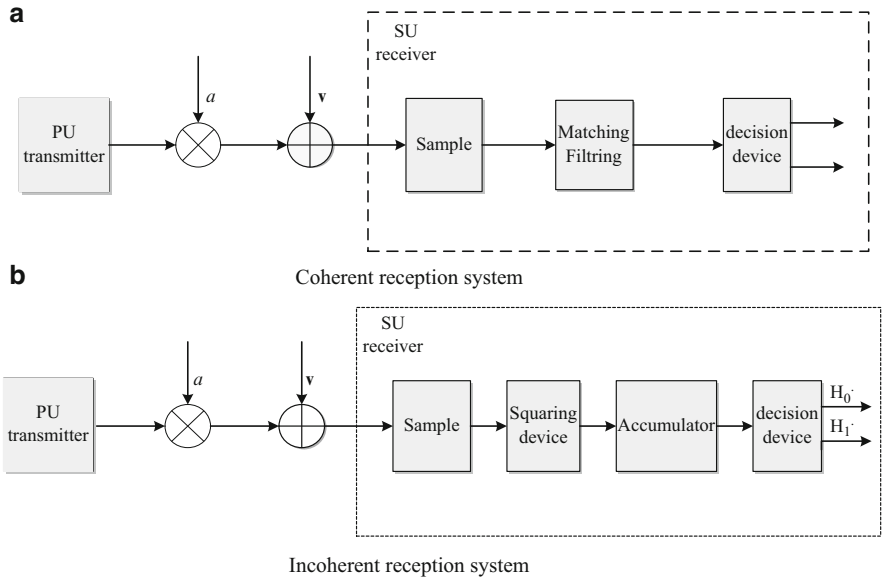

Fig. 42.1 System model block diagram. (**a**) Coherent reception system, (**b**) Incoherent reception system

$$f_y(y_n) = \begin{cases} \dfrac{1}{(2\sigma^2)^{M/2}\Gamma(M/2)} y_n^{\frac{M}{2}-1} \exp\left(-\dfrac{y_n}{2\sigma^2}\right) & H_0 \\ \dfrac{1}{2\sigma^2}\left(\dfrac{y_n}{\kappa}\right)^{\frac{M-2}{4}} \exp\left(-\dfrac{y_n+\kappa}{2\sigma^2}\right) \mathrm{I}_{M/2-1}\left(\dfrac{\sqrt{\kappa y_n}}{\sigma^2}\right) & H_1 \end{cases} \tag{42.6}$$

Here, κ denotes a non-centrality parameter and the value is related to $a_{n,m}$, $\mathrm{I}_{M/2-1}$ denotes the '$M/2-1$'-order modified Bessel function of the first kind and σ^2 represents the variance of Gaussian noise.

In general, the system models of sensing spectrum adopted in this paper is shown in Fig. 42.1.

42.3 Joint Estimation

The PU state and channel gain are estimated jointly to maximize the probability of detection. Given the quality of data transmission and spectral utilization rate, we adopt a novel definition of detection probability [6].

$$P_d \triangleq 1 - p_f p(x_n = 0) - p_m p(x_n = 1) \tag{42.7}$$

The proposed sensing algorithm at receiver consists of three steps. I.e., (1) coarse detection; (2) estimation of fading channel gain; (3) PU state detection.

42.3.1 Coarse Detection

The PU state is detected roughly by comparing the observation with specified threshold:

$$S_n = \begin{cases} idle & y_n < \tau_{CD} \\ active & y_n \geq \tau_{CD} \end{cases} \tag{42.8}$$

The thresholds for MFD scheme and ED scheme are achieved by (42.9a) and (42.9b)

$$\text{MFD}: \quad \tau_{CD} = \frac{1}{2} \times \left[a_{\min} \cdot \left(\mathbf{s}_c \cdot \mathbf{s}_c^H \right) \right] \tag{42.9a}$$

$$\text{ED}: \quad \tau_{CD} = \frac{M}{2} \times a_{\min}^2 \tag{42.9b}$$

It should be noted that the purpose of the coarse detection is to provide the basis channel estimation. The accuracy will be modified by the subsequent process.

42.3.2 Estimation of Fading Channel Gain

We design three different channel gain estimation mechanisms for two specific reasons. Firstly, the results of coarse detection are different. Secondly, in the majority of practical wireless communication systems, the channel is slow fading. For the convenience of analysis, we set the period of channel fading state is integral multiples of the sensing period, i.e. $T_c = JT_s$. Thus, the sensing slots are classified into two categories due to the different location in a channel variation period: first slot and non-first slot. At the first sensing slot, the state of fading channel gain may transfer [9].

Due to this law, we could refine the estimation of channel state in the same channel state period by making full use of the historical observations and estimations of PU states. For these reasons, the specified mechanisms are designed as follows:

(1) If the result of coarse detection is idle, and the sensing slot is the first slot, we may obtain the estimation of a_n relying on the prior transition probability:

$$\hat{a}_n = \arg\max_{a_n \in A} p\left(a_n \middle| \hat{a}_{n-1}\right) \tag{42.10}$$

(2) If the result of coarse detection is idle, and the sensing slot is non-first, the estimation of fading channel gain will remain unchanged, i.e. $\hat{a}_n = \hat{a}_{n-1}$.
(3) If the result of coarse detection is active, we could obtain the estimation of channel gain based on MAP criterion.

$$\hat{a}_n = \arg\max_{a_n \in A} p\left(a_n \middle| \hat{a}_{pre}, x_n^{\dagger}, y_n, M\right) \propto \arg\max_{a_n \in A} p\left(y_n \middle| a_n, x_n^{\dagger}, M\right) p\left(a_n \middle| \hat{a}_{pre}\right) \tag{42.11}$$

Here, $\hat{a}_{pre}$ represents the final estimation of previous channel coherent period. The likelihood function in (42.11) follows different distribution over MFD and ED systems as shown in (42.12a) and (42.12b).

$$p\left(y_n \middle| a_n, \mathbf{x}_n^{\dagger} = \mathbf{s}_c, M\right) = \frac{1}{\sqrt{2\pi \|\mathbf{s}_c\| \sigma^2}} \exp\left[-\frac{\left(y_n - a_n \cdot \mathbf{s}_c \cdot \mathbf{s}_c^H\right)}{2\|\mathbf{s}_c\|\sigma^2}\right] \tag{42.12a}$$

$$p\left(y_n \middle| a_n, x_n^{\dagger} = 1, M\right) = \frac{1}{2\sigma^2}\left(\frac{y_n}{\lambda}\right)^{\frac{M-2}{4}} \exp\left(-\frac{y_n + \lambda}{2\sigma^2}\right) \mathrm{I}_{M/2-1}\left(\frac{\sqrt{\lambda y_n}}{\sigma^2}\right) \tag{42.12b}$$

where $\lambda = Ma_n^2$ and σ^2 denotes the variance of white Gaussian noise.

42.3.3 PF-Based PU State Detection

Due to the transfer of channel state does not synchronize with the shift of PU state, the DSM shows non-stationary property. Meanwhile, the observation is non-linear under ED system. These bring grim challenges for sequential detection of PU state. As a promising signal detection technique, the PF could solve these problems effectively by approximating complex continuous distribution with discrete particles $x^{i)}$ and associated weights $w^{i)}$ ($i = 1,2,\ldots,I$). On this basis, the MAP estimation could be drawn [10]:

$$\hat{x} = \arg\max_{x \in X} \left\{ \sum_{i=1}^{I} \delta\left(x - x^{(i)}\right) w^{(i)} \right\} \tag{42.13}$$

The specific process of PF-based PU state detection includes two steps. (1) Draw particles based on the sequential importance sampling (SIS) and compute the associated importance weight of each particle. (2) Normalize the importance weights and conduct a re-sampling procedure [10].

Firstly, according to the SIS algorithm, we build the state trajectories and compute the importance weights sequentially. More specifically, we begin SIS

algorithm by drawing particles from the important distribution $x_n^{(i)} \sim \pi(x_n | x_{0:n-1}, y_{0:n})$. The design of the important distribution is a critical step in particle filtering and it varies according to the actual situation. In this paper, we adopt the importance distribution as follow:

$$\pi\left(x_n \middle| x_{0:n-1}^{(i)}, \hat{a}_n, y_{0:n}\right) \propto p\left(y_n \middle| x_n, x_{0:n-1}^{(i)}, \hat{a}_n, y_{0:n-1}\right) p\left(x_n \middle| x_{0:n-1}^{(i)}\right) \tag{42.14}$$

After the particles are sampled from the importance function sequentially, the associated importance weights could be computed recursively in time as follow [11]:

$$\overline{w}_n^{(i)} = \overline{w}_{n-1}^{(i)} \times \frac{p\left(y_n \middle| x_{0:n}^{(i)}, \hat{a}_n, y_{0:n-1}\right)}{\pi\left(x_n^{(i)} \middle| x_{0:n-1}^{(i)}, y_{0:n}\right)} = \overline{w}_{n-1}^{(i)} \times p\left(y_n \middle| x_{n-1}^{(i)}, \hat{a}_n\right) \tag{42.15}$$

Secondly, normalize the importance weights. To overcome the weight degeneracy after several times of iteration, re-sampling procedure is conducted after the normalization process. The basic idea of re-sampling method is to eliminate particles with small normalized importance weight while concentrate upon those particles having larger normalized importance weight [10].

42.4 Computer Simulation

Figure 42.2 shows the contrast of detection performance between proposed algorithm and tradition methods, i.e. MFD and ED methods. In this simulation, the sample size M is set to be 15, and the size of partitioned states number K for the TVFF channel is 5. The configuration of maximum Doppler frequency shift f_d is 0.05.

It is obvious that the sensing performance could be improved significantly utilizing the proposed algorithm when operating the TVFF channel. For example, in MFD systems, when the detection probability surpasses 0.95, the desired SNR of new algorithm and traditional MFD method is -2 and 4 dB respectively. Furthermore, the performance achieved by MFD is higher than ED. That's because the way to obtain observations in MFD systems is coherent reception, the information of transmitted signal is known.

Figure 42.3 shows the effects that the variations of sample size M for the TVFF channel have on the sensing performance. For coherent reception systems, M refers to the size of pilot, synchronization code or spread spectrum code. In this simulation, $f_d = 0.05$ and $K = 5$. The values of sample size M are 15 and 31 respectively. It is observed from Fig. 42.3 that with the advance of M. the performance of proposed algorithm in this paper will increase. In practice, a larger M means the observation

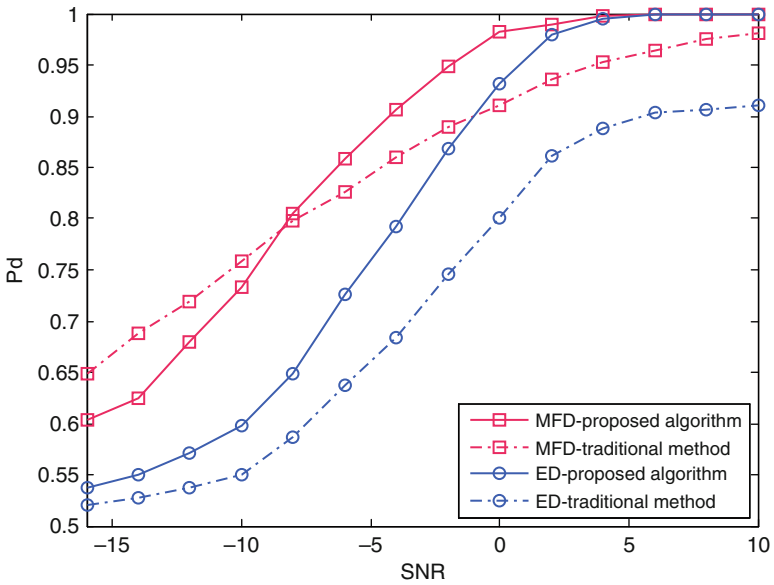

Fig. 42.2 Sensing performance of the proposed joint estimation algorithm and traditional methods under different receiver systems

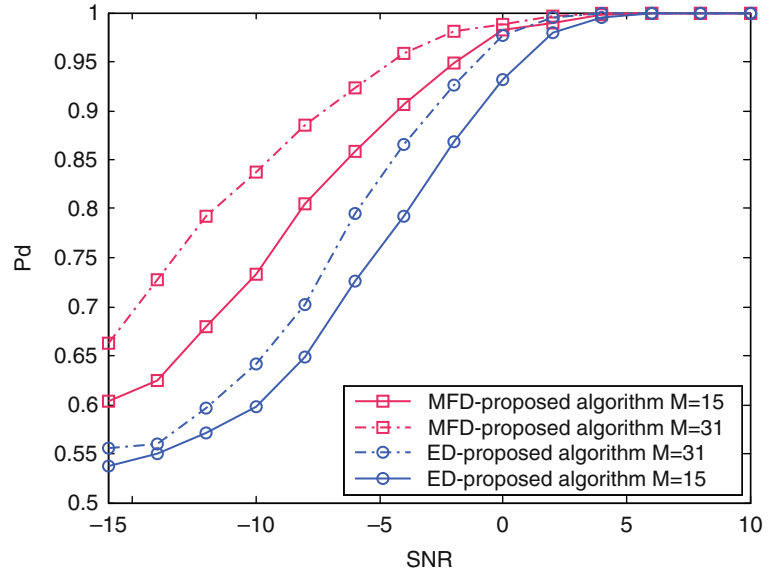

Fig. 42.3 Sensing performance under different sample size *M*

contains more information of the PU state and the fading channel state. As a result, the more information to be utilized, the more accurate the estimation is.

Conclusion
Effective spectrum sensing is essential for CR systems, particularly those exhibiting time-variant fading channel. Simulation results have demonstrated our proposed algorithm could be applied to either coherent reception system or incoherent reception system and achieve better detection performance.

Acknowledgments This work was supported by the National Natural Science Foundation of China (61271180, 61379016), Research Fund for the Doctoral Program of Higher Education of China (20130005110016), Major National Science and Technology Projects (2013ZX03001015-003).

References

1. Federal Communication Commission (2002) Spectrum Policy Task Force Report, ET Docket, no. 02-155, Nov 02, 2002
2. Ma J, Li GY, Juang BH (2009) Signal processing in cognitive radio. Proc IEEE 97(5):805–823
3. Chen HS, Gao W, Daut DG. Signature based spectrum sensing algorithms for IEEE 802.22 WRAN. In: Proceedings of IEEE International Conference on Communications (ICC), Glasgow, Scotland, Jun 2007, pp 6487–6492. MF
4. Digham, FF, Alouini, MS, Simon, MK (2003) On the energy detection of unknown signals over fading channels. In: Proceedings of IEEE International Conference on Communications (ICC), Anchorage, AK, May 2003, pp 3575–357
5. López-Benítez M, Casadevall F (2012) Improved energy detection spectrum sensing for cognitive radio. Commun IET 6(8):785–796
6. Zhao C, Sun M, Li B, Zhao L, Peng X (2014) Blind spectrum sensing for cognitive radio over time-variant multipath flat-fading channels. EURASIP J Wirel Commun Netw 2014:84
7. Sadeghi P, Kennedy R, Rapajic P, Shams R (2008) Finite-state Markov modeling of fading channels: a survey of principles and applications. IEEE Signal Process Mag 25(5):57–80
8. Li B, Zhou Z, Nallanathan A (2013) Joint estimation based spectrum sensing for cognitive radios in time variant flat fading channel. In: Proceedings of IEEE global communications conference (Globecom 2013), Atlanta, Georgia, USA, Dec. 2013, pp 1–6
9. Sun M, Li B, Song Q, Zhao L, Zhao C (2014) Joint detection scheme for spectrum sensing over time-variant flat fading channel. IET Commun. (2014, in press)
10. Djuric PM, Kotecha JH, Zhang JQ, Huang YF, Chirmai T, Bugallo MF, Miguez J (2003) Particle filtering. IEEE Signal Process Mag 20(5):19–38
11. Li B, Zhao C, Sun M, Zhou Z et al. (2014) Spectrum sensing for cognitive radios in time-variant flat fading channels: a joint estimation approach. IEEE Trans Commun. (in press, 2014)

Chapter 43
Optimal Threshold of Welch's Periodogram for Spectrum Sensing Under Noise Uncertainty

Tingyu Lu, Chenglin Zhao, Yongjun Zhang, and Xiao Peng

Abstract In this paper, spectrum sensing is investigated when the decision statistic is computed using energy detection (ED) with Welch's method in the frequency domain. First, we assume an estimated noise variance is used to calculate the threshold, instead of the priori exact noise. We present an analytical model to evaluate the performance of the conventional Welch's ED. The characteristics of this model are also analyzed to show the effect for the performance of spectrum sensing. Then an optimal threshold is proposed to achieve high detection probability and low false alarm probability at low SNR levels. The analytical results and simulations demonstrate the effectiveness of the proposed optimal threshold.

Keywords Spectrum sensing • Energy detection • Welch method • Estimated noise • Optimal threshold

43.1 Introduction

Cognitive Radio (CR) has been viewed as a intelligent wireless communication technology in recent years [1]. Primary users (PU) are the owners of the licensed spectrum while the secondary (unlicensed) users (SU) transmit and receive signals over the licensed spectra or portions when the primary users are inactive [2].

Spectrum sensing is one of the most challenging tasks in CR systems. Quite a few methods have been proposed for this, including likelihood ratio test (LRT), matched filter (MF)-based methods, cyclostationary detection (CSD) methods and energy detection (ED), each of which has different requirements [4, 5]. LRT needs the distribution of the source signal and noise. MF-based methods requires perfect knowledge of the channel responses and accurate synchronization. CSD performs well at the expense of extensive computational requirements and the acquisition of

T. Lu (✉) • C. Zhao • Y. Zhang • X. Peng
Key Lab of Universal Wireless Communications, MOE Wireless Network Lab, Beijing University of Posts and Telecommunications, Beijing, China
e-mail: lty615@126.com

J. Mu et al. (eds.), *The Proceedings of the Third International Conference on Communications, Signal Processing, and Systems*, Lecture Notes in Electrical Engineering 322, DOI 10.1007/978-3-319-08991-1_43

the cyclic frequencies of the primary signals. Though ED is simpler than the aforementioned methods, its performance is susceptible to noise uncertainty. Moreover, it is quite inflexible when the SU needs to sense multiple channels with different characteristic bandwidths [6]. A different approach is to implement energy detection in frequency domain, which can provide the flexibility to process wider bandwidths and sense multiple channels simultaneously. There are various methods proposed for PSD estimation in [7]. In these works, periodogram method is considered to estimate the PSD of the PU's signal.

In our paper, we focus on Welch's periodogram method to compute the spectrum.

The idea of the Welch's periodogram method is to compare the estimated energy with a threshold, which can be calculated if the exact noise variance is known, to decide whether a signal is transmitted or not [8]. The difficulty is that we can only estimate the noise power in practice. The simple but reasonable method is to regard the estimated power of noise as the true power to obtain the threshold. The estimated noise power is used to set the threshold in energy detection in [9]. In [10], the impact of noise uncertainty on the performance of spectrum sensing is addressed. All the aforementioned works is about the analysis of threshold in time-domain. However, they did not mention the performance of the threshold based on the estimated noise in the frequency domain. Our work is to approach the target requirements for spectrum sensing with the optimal threshold based on a real time estimation of the noise power using Welch's periodograms method. We believe our analysis is more applicable to the practical spectrum sensing.

43.2 System Model

43.2.1 Welch Energy Detection

In spectrum sensing field, the decision problem can be formulated into a binary hypothesis form

$$\begin{array}{llll} H_0: & y[n] = g[n] & n = 1, 2, ...N & (signal\ \ absent) \\ H_1: & y[n] = x[n] + g[n] & n = 1, 2, ...N & (signal\ \ present) \end{array} \tag{43.1}$$

Where H_0 and H_1 denote the PU absent or present respectively. $y[n]$ are the received signal. g[n] represent the additive white Gaussian noise with zero mean and variance of σ_w^2. $x[n]$ is the PU's signal which also assumed to be random process with zero mean and variance of σ_s^2. N is the sample points.

The Welch's method is a modified periodogram. The principle of the Welch's algorithm is to divide the data sequence into several segments to obtain the PSD. The block diagram of energy detection with Welch's method is depicted in Fig. 43.1.

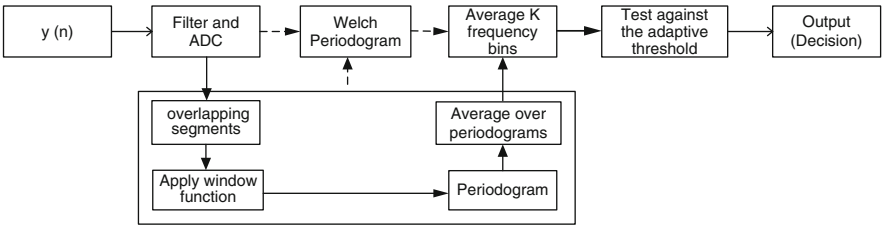

Fig. 43.1 Block diagram of energy detection with Welch's method

After filtered and A/D converted, the data sequence is partitioned into L segments of length M, allowing overlapping between successive segments as follows,

$$y_i(n) = y(n + iD), \qquad n = 0, ..., M-1, \qquad i = 0, ..., L-1 \tag{43.2}$$

Where iD is the starting point and D is the overlapping sequence for each segment. D = M means no overlapping. The second step is to apply a window function to each of the L segments to perform FFT. The samples of each segment are squared and averaged over the M samples to obtain the periodogram for each sequence.

$$S_y^i(k) = \frac{1}{MU}\sum_{n=0}^{M-1} \left| y_i(n) w(n) e^{-j2\pi kn/K} \right|^2 \tag{43.3}$$

Where w(n) is the window function. U is the power in the window function calculated as

$$U = \frac{1}{M}\sum_{n=0}^{M-1} w^2(n) \tag{43.4}$$

Due to discontinuities at the end points, the spectrum of a finite-length signal always exhibits side-lobes. The window function alleviates the discontinuities. K is the number of DFT points for the periodograms. Then, the Welch power spectrum estimate corresponds to the average of L periodograms as

$$S_y = \frac{1}{L}\sum_{i=0}^{L-1} S_y^i \tag{43.5}$$

We can get the number of spectral averages L from N, M and D as

$$L = \frac{N-M}{D} + 1 \tag{43.6}$$

We define $f_R = W/K$ as the frequency resolution. Then, making use of Eq. (43.5), we get the power content over the frequency bins of interest as the test statistic:

$$T = P = \sum_{k=0}^{K-1} f_R S_y(k) \tag{43.7}$$

This T is then compared with the pre-defined fixed threshold λ to determine whether the primary signal is present or not. The detail description of λ will be shown in section B.

43.2.2 Fixed Threshold Based Welch's Algorithm

We assume that the elements of y(n) are drawn from a Gaussian process, then the elements of its Fourier transform are also Gaussian random variables. Then, T follows a central and non-central chi square distribution with LK degrees of freedom. According to Central Limit Theorem, when LK is sufficiently large, T approaches a Gaussian distribution with mean and variance as follows,

$$\begin{aligned} T|\ H_0 &\sim N\left(\sigma_w^2, 2\sigma_w^4/LK\right) \\ T|\ H_1 &\sim N\left((1+\gamma)\sigma_w^2, 2(1+\gamma)^2\sigma_w^4/LK\right) \end{aligned} \tag{43.8}$$

$\gamma = \sigma_s^2/\sigma_w^2$ is the signal to noise ratio. Then, we derive P_d and P_f as follows,

$$\begin{aligned} P_d &= P(T > \lambda|H_1) = Q\left(\frac{\lambda - (1+\gamma)\sigma_w^2}{\sqrt{2/LK}(1+\gamma)_S\sigma_w^2}\right) \\ P_f &= P(T > \lambda|H_0) = Q\left(\frac{\lambda - \sigma_w^2}{\sqrt{2/LK}\sigma_w^2}\right) \end{aligned} \tag{43.9}$$

Q(·) is Gaussian Q function. It can be seen that both P_d and P_f are related to λ. Therefore, the threshold can be derived using a target detection or false alarm value. If the required probability of constant detection rate (CDR) is predetermined, the threshold can be set accordingly as

$$\lambda_d = (1+\gamma)\sigma_w^2\left(1 + Q^{-1}(P_D)/\sqrt{LK/2}\right) \tag{43.10}$$

Similarly, under hypothesis H_0, we can derive the threshold λ_f for a constant false alarm rate (CFAR) as

$$\lambda_f = \sigma_w^2\left(1 + Q^{-1}(P_F)/\sqrt{LK/2}\right) \tag{43.11}$$

The Nyman–Pearson criterion states that we can construct a decision rule that maximizes P_d, constrained to a fixed value of P_f [9]. From Eq. (43.9), we notice that σ_s^2 is a must to maximize P_d. However, it is neither available nor easy to obtain for the signal. On the contrary, it is possible to set λ_f based on the distribution of the test statistic under H_0. Then, we opt for λ_f to be the detection-threshold and the rest of the paper will be discussed based on this point. The detection based on λ_d can be derived in the same way.

We note that the values of λ_f in Eq. (43.11) are derived from the exact noise variance, σ_w^2. According to the difficulty of acquisition of the real noise variance, the SU always estimate noise variance $\hat{\sigma}_w^2$ from the samples collected and regard it as the true noise variance. Then, here comes the question: If we use σ_w^2 simply replace the exact noise variance σ_w^2 in Eq. (43.11), will the pre-set P_F be achieved and what kind of detection performance can be expected using threshold as follows?

$$\hat{\lambda}_f = \hat{\sigma}_w^2\left(1 + Q^{-1}(P_F)/\sqrt{LK/2}\right) \tag{43.12}$$

43.3 Proposed Optimal Threshold Based on Welch's Algorithm

43.3.1 Asymptotic Analysis Model Based on Uncertain Noise

We assume that the number of samples used to estimate the noise and the number of samples used to perform spectrum sensing are the same. Then, we denote W and Y are the energy power from the sampling points respectively.

$$w = \frac{1}{LK}\sum_{i=1}^{LK}|w(i)|^2 \tag{43.13}$$

$$y = \frac{1}{LK}\sum_{i=1}^{LK}|y(i)|^2 \tag{43.14}$$

Since we use CFAR based detection, H_0 should be the true condition when deriving the probability of false alarm. The PDF of w and y must be the same. Then, the probability of false alarm based on $\hat{\lambda}_f$ can be written as follows.

$$\hat{P}_f = P\left(Y > \hat{\lambda}_f | H_0\right) = Q\left(\left(w\left(1 + Q^{-1}(P_F)/\sqrt{LK/2}\right) - \mu_y\right)/\sigma_y\right) \tag{43.15}$$

Where μ_y and σ_y^2 are the estimate of the mean and variance of Y. Then, the mean expected probability of false alarm by integrating Eq. (43.15) over the PDF of W is given by

$$\overline{\hat{P}}_f = \int_0^{\infty} Q\left(\left(w\left(1+Q^{-1}(P_F)/\sqrt{LK/2}\right)-\mu_y\right)/\sigma_y\right)\frac{1}{\sqrt{2\pi}\sigma_w}e^{\frac{-(w-\mu_w)^2}{2\sigma_w^2}}dw \quad (43.16)$$

Where μ_w and σ_w^2 are the estimate of the mean and variance of W. We define $\tau = (w-\mu_w)/\sigma_w$ and $\eta = Q^{-1}(P_F)$ in order to simplify Eq. (43.16) as (43.17),

$$\overline{\hat{P}}_f = \int_{-\sqrt{LK/2}}^{\infty} Q\left(\eta+\tau\left(1+\eta/\sqrt{LK/2}\right)\right)\frac{1}{\sqrt{2\pi}}e^{\frac{-\tau^2}{2}}d\tau \quad (43.17)$$

The estimate $\overline{P}_f$ model has been complicated analyzed in [10]. In this paper, we give a simple analysis method. We use the property of Gaussian Q function that $E[Q(\alpha+\beta X)] = Q\left(\alpha/\sqrt{1+\beta^2}\right)$ when X is assumed to be random process with zero mean and unit variance. Assuming η, τ as α, X respectively, the approximate closed-form expression of $\overline{\hat{P}}_f$ can be written by

$$\overline{\hat{P}}_f(LK) \approx Q\left(\eta/\sqrt{1+\left(1+\eta/\sqrt{LK/2}\right)^2}\right) = Q(\eta, LK) \quad (43.18)$$

We use $Q(\eta, LK)$ to denote the approximate estimate probability of false alarm. When LK is sufficiently large, the limiting $\overline{\hat{P}}_f$ should be

$$\lim_{LK\to\infty}\overline{\hat{P}}_f(LK) = Q\left(\eta/\sqrt{2}\right) \quad (43.19)$$

According to the above derivation, the characteristics of the function $Q(\eta, LK)$ can be given that $Q(\eta, LK) > Q(\eta, \infty) > P_F$ when $P_F < 0.5$. In the cognitive radio application scenarios, P_F is always expected to be less than 0.5. Therefore, we can conclude that simply using Eq. (43.12) to calculate the estimated threshold will never achieve the expected target P_F, no matter how sufficiently the sampling points are. The only way to achieve $\overline{\hat{P}}_f = P_F$ is to raise the detection threshold. If CDR based detection is used, the results shown above also apply except $\overline{\hat{P}}_f$ and P_F, which should be replaced by $\overline{\hat{P}}_d$ and P_D respectively.

43.3.2 Proposed Optimal Threshold Model

In this section, we will give an optimal detection threshold model based on the above analysis. Since $\overline{\hat{P}}_f = Q(\eta, LK)$ is related to the variable of η and the variable of LK, we define a new variable u to replace η, which satisfies $Q(\eta, LK) = P_F$. Then, the optimal threshold can be obtained as

$$\lambda_f^{optimal} = \hat{\sigma}_w^2\left(1 + u/\sqrt{LK/2}\right) \tag{43.20}$$

Substitute u into Eq. (43.1) to get the mean probability of false alarm under the optimal threshold,

$$\overline{\hat{P}}_f^{optimal}(LK) \approx Q\left(u/\sqrt{1 + \left(1 + u/\sqrt{LK/2}\right)^2}\right) \tag{43.21}$$

In order to achieve the expected probability of false alarm, the equation $\overline{\hat{P}}_f^{optimal}(LK) = P_F$ should be true. The solution is

$$u = \frac{\sqrt{2LK}\eta^2 + \sqrt{2LK\eta^2(LK - \eta^2)}}{LK - 2\eta^2} \tag{43.22}$$

This optimal threshold is then implemented with Welch's algorithm to perform spectrum sensing. In addition, we can observe that $\lambda_f^{optimal}$ is only related to the variables of L and K. The effect of varying L and K on the performance of spectrum sensing will also be analyzed in this paper.

43.4 Simulation and Performance Analysis

The results correspond to the performance of the Welch obtained by varying the parameters K and the types of window for each segment. For our simulations, we considered a fixed number of sample points [N = 3,000] and the overlapping rates [D/M = 0.5]. The number of points in the DFT equals to the number of samples contained in each segment. According to the values for N, M and D considered, and from Eq. 43.6, the number of LK can be simplified as LK = 2(N − K/2), which is only related to K. Performance curves were obtained by Monte Carlo realizations and results are averaged over 500 realizations.

Figure 43.2 shows the curve of $\overline{\hat{P}}_f$ based on the fixed threshold with the change of LK points. The expected P_F is set as 0.05 and $\eta = Q^{-1}(0.05)$. Then, $\overline{\hat{P}}_f = Q(\eta, LK)$ can be the function of LK. We can observe that when LK goes to infinity, $\overline{\hat{P}}_f$ converges to $Q\left(\eta/\sqrt{2}\right)$. In addition, no matter how many samples are averaged ($LK \to \infty$), $\overline{\hat{P}}_f$ is always higher than P_F and will never converge to P_F. This observation matches our analysis in Sect. 43.3.

Figure 43.3 shows a comparison of the detection performance between traditional fixed and proposed optimal threshold based on the SNR of −14 dB. The expected P_F is set as 0.1. K varies from 128 to 2,048. When K is higher than 1,024, Eq. (43.18) will no longer conform to Eq. (43.19) since LK is not so large according

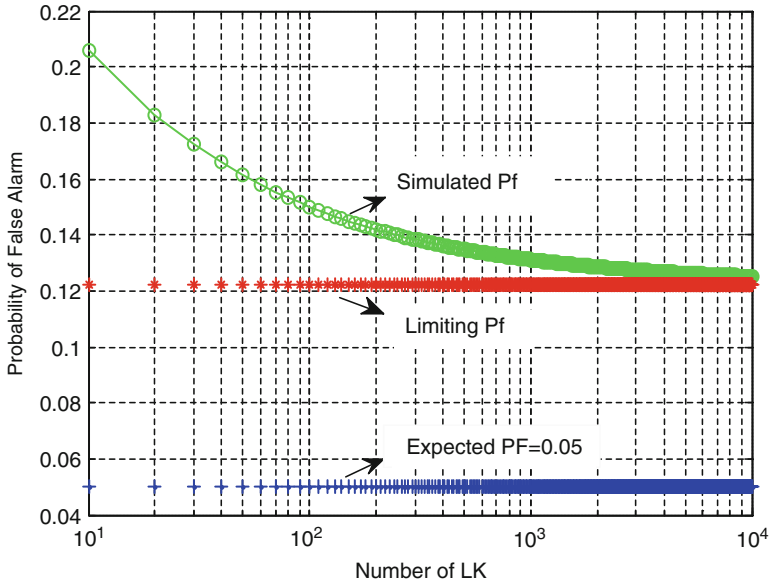

Fig. 43.2 Characteristics of $\overline{\widehat{P}}_f$ as the function of LK

to LK = 2(N − K/2), leading to the fast attenuation of P_d and the trend of a constant P_f under the fixed and optimal threshold respectively. When K is lower than 1,024, the number of LK increases along with the decrease of K. It can be seen that P_f of the fixed threshold drops and converges to 0.22, which is still two times of P_F while P_f of the optimal threshold converges to 0.1 and P_d approaches to 0.98. Then, we can conclude that the proposed optimal threshold performs better than the fixed threshold on the premise of an expected detection probability. The results in Fig. 43.3 are also accord with the theoretical analysis in Fig. 43.2.

Figure 43.4 shows the detection performance for different windows using in Welch's method at SNR = −15 dB and K = 256. From this figure, we observe that Kaiser is the best window shape for each segment. This is because with the same settings, the side lobe attenuation of Kaiser is much more severe than the window shape of Hamming, Rectangular, Bartlett and Blackman, leading to a fast attenuation of the end points of the signal and less noise involved.

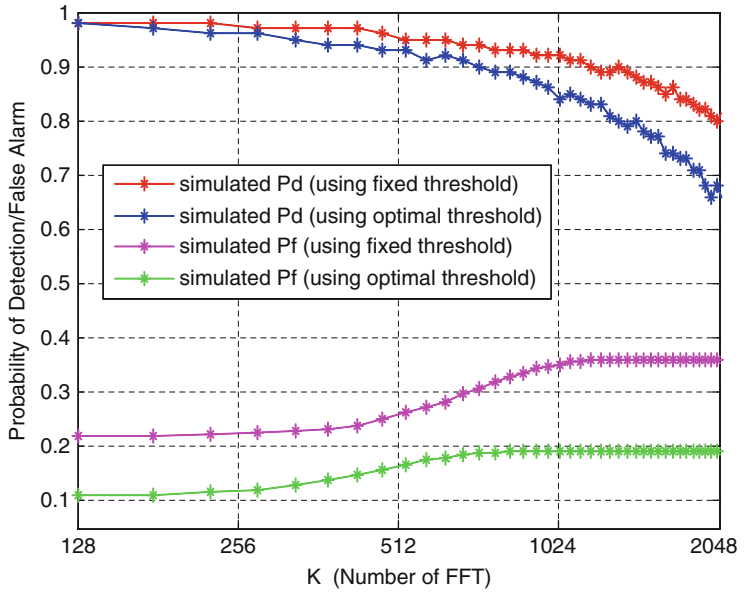

Fig. 43.3 Comparison of the fixed and optimal threshold at SNR = −14 dB

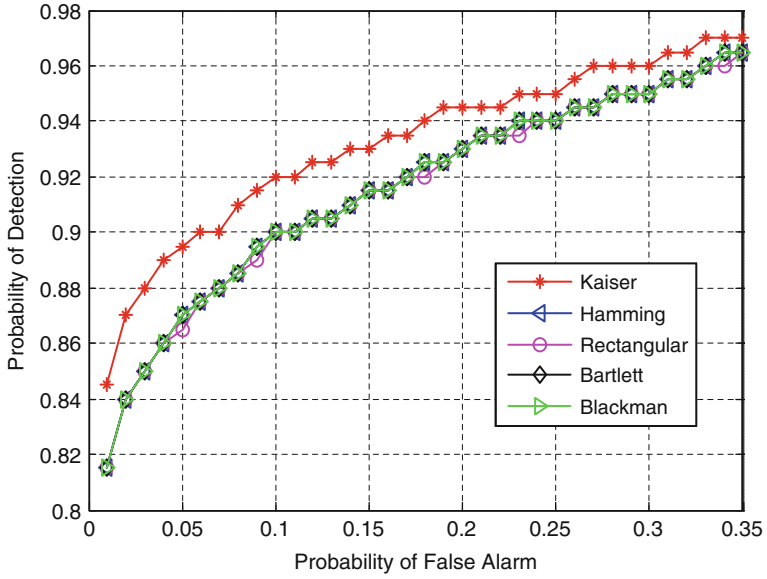

Fig. 43.4 Comparison of different window shapes for ED with Welch's method

Conclusion

In this paper, we analyze the performance of energy detection with Welch's method in the frequency domain for spectrum sensing. An asymptotic analytical model is shown to evaluate the probability of false alarm and detection under the fixed threshold, assuming only set by an estimated noise variance, instead of the exact noise variance. The theoretical analysis shows that we will never achieve the expected false alarm probability if we use the fixed threshold. Based on the analytical model, we propose an optimal threshold model using estimated noise variance. By studying the characteristics of this optimal threshold, we show how the number of points in the DFT and the shape of window for each segment affect the performance of spectrum sensing. The simulation results based on a CFAR detection show that our proposed optimal threshold can achieve the expected false alarm probability and guarantee a high detection probability, which performs much better than the fixed threshold.

Acknowledgements This work was supported by the National Natural Science Foundation of China (61379016、61271180), Major National Science and Technology Projects (2013zx03001015).

References

1. Clanton C, Kenkel M (2010) Cognitive radio: an integrated architecture for software defined radio. Ph. D. Thesis, Royal Institute of Technology, Sweden, May 2010
2. Elramly S, Newagy F, Yousry H (2011) Novel modified energy detection spectrum sensing technique for FM wireless microphone signals. IEEE Int Conf Commun Softw Netw 6 (4):59–63
3. Van Wesemael P, Pollin S, Lopez E (2013) Performance evaluation of sensing solutions for LTE and DVB-T. IEEE symposium on new frontiers in dynamic spectrum access networks, vol 3. pp 531–537
4. Yucek T, Arslan H (2009) A survey of spectrum sensing algorithms for cognitive radio applications. IEEE Commun Surv Tutor 9:116–130
5. Martinez DM, Andrade AG (2013) Performance evaluation of Welch's periodogram-based energy detection for spectrum sensing. IET Commun 5:1117–1125
6. Welch PD (1967) The use of fast Fourier transform for the estimation of power spectra: a method based on time averaging over short, modified periodograms. IEEE Trans Audio Electroacoust 8(11):70–73
7. Cabric D, Tkachenko A, Brodersen RW (2006) Experimental study of spectrum sensing based on energy detection and network cooperation. In: Proceedings of the first international workshop on technology and policy for accessing spectrum, Boston, MA, USA, June 2006. Article no. 12
8. Gismalla EH (2011) Performance analysis of the periodogram-based energy detector in fading channels. IEEE Trans Signal Process 8(59):3712–3721
9. Chen H-S, Gao W, Daut, DG (2008) Spectrum sensing for wireless microphone signals. IEEE annual communications society conference on sensor, mesh and ad hoc communications and networks, pp 1–5
10. Tandra R, Sahai A (2011) Fundamental limits on detections in low SNR under noise uncertainty. IEEE Trans Parallel Distrib Syst 22:1564–1577

Chapter 44
Compressed Sensing Method for Secret Key Generation Based on MIMO Channel Estimation

Yuqi Li, Ting Jiang, and Jingjing Huang

Abstract In searching for alternative solutions of secret key generation in wireless networks, many physical-layer-based methods have been proposed. These methods exploit the inherent randomness and reciprocity of the multipath fading channel to generate secret keys. Multiple-antenna system provide higher key bit generation rate than single-antenna one because of more channel randomness. However, traditional MIMO key generation schemes produce prohibitively high bit mismatch. To address the tradeoff between key bit generation rate and key agreement probability, we propose a compressed sensing (CS) method for key generation in single carrier MIMO sparse multipath channel. Theory analysis shows that the CS-based key generation scheme provides high entropy key bits from fewer probes. Performance simulation reveals the proposed scheme achieves a high key agreement probability at a high key generation rate.

44.1 Introduction

Due to the open and shared nature of the wireless channels, a third-party eavesdropper can easily hear the message transmitted between two legitimate parties [1]. To protect the confidentiality and security of the communication, secret key must be established to encrypt the message transmitted. Recently, many key generation methods exploiting physical layer (PHY) information are caught in hot discussion [2]. These PHY-based methods are less expensive and more flexible because they extract secret bits from the inherently random spatial and temporal variation of the

Y. Li (✉) • T. Jiang • J. Huang
School of Information and Communication Engineering, Beijing University of Posts and Telecommunications, Beijing, China

Key Laboratory of Universal Wireless Communications (BUPT), Ministry of Education, Beijing, China
e-mail: 173897054@qq.com

J. Mu et al. (eds.), *The Proceedings of the Third International Conference on Communications, Signal Processing, and Systems*, Lecture Notes in Electrical Engineering 322, DOI 10.1007/978-3-319-08991-1_44

reciprocal wireless channels. So far, many prior works on PHY-based security techniques have focused on single antenna systems. However, exploiting the increased randomness afforded by MIMO channels remains an elusive task [3]. Traditional MIMO key generation schemes, like random pre-encryption method and channel quantization algorithm [4, 5], produce prohibitively high bit mismatch.

To address the tradeoff between key bit generation rate and key agreement probability, the CS-based secret key generation protocol (CS-SKGP) is proposed. Simulations show based on CS techniques [5], this method gains larger agreement probabilities and longer key lengths.

The rest of the paper is organized as follows. In Sect. 44.2 we outline the system model. Introduction and block diagram of CS-SKGP is provided in Sect. 44.3. Section 44.4 analyzes the performance of the proposed method, and section "Conclusions" concludes the paper.

44.2 System Model

44.2.1 Attack Model

Figure 44.1 illustrates the attack model for a wireless communication system. Alice and Bob are legitimate users who need to communicate securely by establishing a pairwise key from channel measurement, while Eve is a potential adversary that aims to derive the message by eavesdropping.

In our system model, channels h_{AB} and h_{BA} are estimated by Alice and Bob during the coherence time respectively. Because the signals experience the same fading in the coherence time, $h_{AB} = h_{BA}$.

On the other hand, channels h_{AE} and h_{BE}, which is estimated by Eve, convey information of all the communication between Alice and Bob to Eve. According to communication theory, an entity that is at least $\lambda/2$ away from the network nodes experiences fadings statistically independent of the fadings between the communicating nodes [2]. Therefore, $h_{AE} \neq h_{AB}$ and $h_{BE} \neq h_{BA}$.

44.2.2 Secret Key Generation Model

As shown in Fig. 44.2, a PHY-based key generation scheme generally includes three steps.

- **Channel measurement**: The typical channel profiles are received signal strength (RSS) and phase estimates [6]. In this article, we use RSS as a channel statistic.
- **Quantization**: The constructed channel profile is then quantized into vector bits to obtain preliminary key. The typical quantization methods include

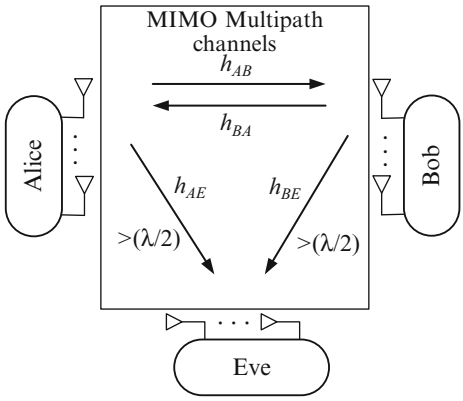

Fig. 44.1 Attack model for MIMO system scenario

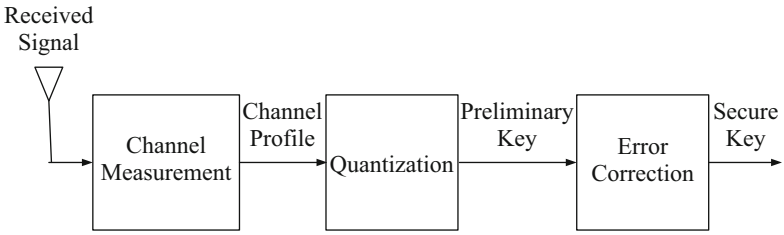

Fig. 44.2 Standard method of key generation

level-crossing algorithm [7], Adaptive Secret Bit Generation (ASBG) [6], and deep fade thresholding [8].

- **Error correction**: Due to the errors in channel measurement, bit mismatch exists. Researchers suggest using two well-known techniques to tackle the challenge—information reconciliation [9] and privacy amplification [10].

44.2.3 MIMO Channel Estimation Model

We assume the number of transmit antennas is $M_{\mathbf{t}}$ and the number of reception antennas is $M_{\mathbf{r}}$. The channel tap between the mth transmit antenna and the nth reception antenna is defined as:

$$\boldsymbol{h}_{mn} = [h_{mn}(0), h_{mn}(1), \ldots, h_{mn}(L-1),] \in \boldsymbol{C}^{L\times 1} \tag{44.1}$$

where L is the maximum discrete time delay. We define K as the number of non-zero elements in h_{mn}, which is much smaller than L. Assuming the number of pilot symbols is N. Thus, the pilot symbols sent by the mth transmit antenna and received by the nth reception antenna can be expressed as.

$$\boldsymbol{y}_n(i) = \sum_{m=1}^{M_t} \sum_{l=0}^{L-1} \boldsymbol{x}_m(l)\boldsymbol{h}_{mn}(i-l) + \boldsymbol{n}_n(i) = \sum_{m=1}^{M_t} \boldsymbol{H}_{mn}\boldsymbol{x}_m(i) + \boldsymbol{n}_n(i) \tag{44.2}$$

where $\boldsymbol{H}_{mn}$ is a $N \times N$ cyclic matrix. It is the channel time-domain response between the mth transmitting antenna and the nth receiving antenna. $\boldsymbol{n}_n(i) \tilde{} \mathcal{N}\left(\boldsymbol{0}_{N\times 1}, \sigma_r^2 \boldsymbol{I}_N\right)$ represents the n-dimensional noise vector. We express (44.2) in matrix form:

$$\boldsymbol{y}(i) = \boldsymbol{H}\boldsymbol{x}(i) + \boldsymbol{n}(i) \tag{44.3}$$

Specific definition of $\boldsymbol{H}$ as follow:

$$\boldsymbol{H} = \begin{bmatrix} \boldsymbol{H}_{11} & \cdots & \boldsymbol{H}_{M_t 1} \\ \vdots & & \vdots \\ \boldsymbol{H}_{1M_r} & \cdots & \boldsymbol{H}_{M_t M_r} \end{bmatrix} \in \boldsymbol{C}^{M_r N \times M_t N} \tag{44.4}$$

Based on the matrix theory and discrete Fourier transform, $\boldsymbol{H}_{mn}$ can be expressed as:

$$\boldsymbol{H}_{mn} = \boldsymbol{F}^H diag\{H_{mn}(0), \cdots, H_{mn}(N-1)\}\boldsymbol{F} \tag{44.5}$$

The expression $\boldsymbol{F}$ in (44.5) is an N-point discrete Fourier transform matrix:

$$\boldsymbol{F} = \frac{1}{\sqrt{N}} \begin{bmatrix} W_N^{00} & W_N^{01} & \cdots & W_N^{0(N-1)} \\ W_N^{10} & W_N^{11} & \cdots & W_N^{1(N-1)} \\ \vdots & \vdots & \ddots & \vdots \\ W_N^{10} & W_N^{(N-1)10} & \cdots & W_N^{(\mathrm{N}-1)(\mathrm{N}-1)} \end{bmatrix} \tag{44.6}$$

As for the received vector, $\mathbf{y}(k)$ it can be transformed as $\mathbf{Y}(k) = \mathbf{F}\mathbf{y}(k)$. As a consequence of the DFT, the expression in (44.3) can be rewrote as:

$$\boldsymbol{Y}(k) = \boldsymbol{X}(k)\overline{\boldsymbol{H}}(k) + \boldsymbol{N}(k), k = 0, 1, \ldots N-1 \tag{44.7}$$

where $\overline{\boldsymbol{H}}(k) = \boldsymbol{F}_1(k)\boldsymbol{h}$, $\boldsymbol{h} \triangleq \left[\boldsymbol{h}^T(0), \boldsymbol{h}^T(1), \cdots \boldsymbol{h}^T(L-1)\right]^T \in \boldsymbol{C}^{M_r M_t L \times 1}$, $\boldsymbol{X}(k) = \boldsymbol{F}\boldsymbol{x}(k)$. Therefore, the expression in (44.3) can be wrote as:

$$\boldsymbol{Y} = \boldsymbol{X}\boldsymbol{F}_1\boldsymbol{h} + \boldsymbol{N} = \boldsymbol{Z}\boldsymbol{h} + \boldsymbol{N} \tag{44.8}$$

44.3 Compressed Sensing Based Secret Key Generation Protocol

44.3.1 CS Background

In CS theory, if $\overline{\boldsymbol{h}}$ is a vector in R^N we plan to acquire and then reconstruct, there is a basis $(\psi_i : i = 1, \cdots, N)$ for R^N can transform $\overline{\boldsymbol{h}}$ into coefficients $h_i = \langle , \overline{h}, \psi_i \rangle$:

$$\overline{\boldsymbol{h}} = \boldsymbol{\Psi h} \tag{44.9}$$

where the transformed coefficients $\boldsymbol{h}$ only have K non-zero values. Therefore $\boldsymbol{h}$ is the sparse representation of $\overline{\boldsymbol{h}}$. The N-length sparse signal can be compressed into and measured by vector $\boldsymbol{y}$ in R^M, and M satisfies $M \geq cK \log(N/K)$ where c is a constant. The measure vector $\boldsymbol{y}$ can be defined as:

$$\boldsymbol{y} = \boldsymbol{\Phi}\overline{\boldsymbol{h}} = \boldsymbol{\Phi\Psi h} = \boldsymbol{Zh} \tag{44.10}$$

where $\boldsymbol{\Phi}_{M \times \mathrm{N}}$ is defined as the observation matrix which is independent from $\boldsymbol{\Psi}$. $\boldsymbol{Z}$ is the measure matrix which is defined as $\boldsymbol{Z} = \boldsymbol{\Phi\Psi}$.

The reconstruction of $\boldsymbol{h}$ can be transformed into solving minimum $l1$ norm of the convex optimization problem:

$$\hat{\boldsymbol{h}} = \min \|\boldsymbol{h}\|_1, \quad \text{s.t. } \boldsymbol{y} = \boldsymbol{\Phi\Psi h} = \boldsymbol{Zh} \tag{44.11}$$

A sufficient condition for perfect reconstruction of $\boldsymbol{h}$ from $\boldsymbol{y}$ is that $\boldsymbol{\Phi}$ should satisfy the restricted isometric property (RIP):

$$\exists \delta : (1 - \delta)\|\boldsymbol{h}\|_2^2 \leq \|\boldsymbol{y}\|_2^2 \leq (1 + \delta)\|\boldsymbol{h}\|_2^2, \forall \text{k}-\text{sparse } \boldsymbol{h} \tag{44.12}$$

44.3.2 CS-SKGP

Figure 44.3 shows the block diagram of proposed key generation scheme. In our algorithm, the two users use the synchronized key Q_{AB} and a same reference signal $\boldsymbol{r_{AB}}$ to calculate the RSS value respectively. Moreover, $\boldsymbol{r_{AB}}$ is uncorrelated to the probing signal $\boldsymbol{x}_{AB}$ so as to obtain independent channel measurements.

In the beginning of our algorithm, Alice sends the pilot symbols $x(t)$ to Bob. The signal received by Bob is expressed as:

$$y_B(t) = h_{AB}(t) \cdot x(t) + n_{AB}(t), \tag{44.13}$$

where $n(t) \sim \mathcal{N}(0, N_0/2)$ is the Gaussian noise. After that, Bob sends the same pilot symbols back to Alice. The signal received by Alice is expressed as:

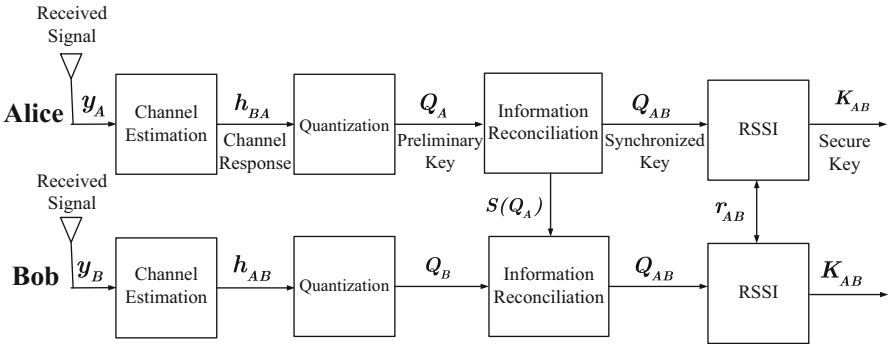

Fig. 44.3 Enhanced key generation method with channel estimation

$$y_A(t) = h_{BA}(t) \cdot x(t) + n_{BA}(t), \tag{44.14}$$

Note that due to the channel reciprocity $h_{AB}(t) = h_{BA}(t)$ holds, $y_A(t) = y_B(t)$.

Alice and Bob use the received signal to compute imperfect estimates (due to noise) of the channels, $\hat{h}_{AB}(t)$ and $\hat{h}_{BA}(t)$:

$$\hat{h}_{AB}(t) = h_{AB}(t) + \varepsilon_{AB}(t) \tag{44.15}$$

$$\hat{h}_{BA}(t) = h_{BA}(t) + \varepsilon_{BA}(t) \tag{44.16}$$

where ε_{AB} and ε_{BA} are the zero-mean complex Gaussian estimation errors.

Channel estimation can be viewed as a l_1 norm optimization problem, which is generally solved by basic pursuit (BP) algorithms or matching pursuit (MP) algorithms. As a combination of these two kinds of algorithm, CoSaMP algorithm [11] has good stability and robustness, and is easy to implement. Therefore, this paper adopts the CoSaMP algorithm for channel estimation in MIMO system.

After channel estimation, a binary quantization is needed to convert the analog $\hat{h}_{AB}(t)$ and $\hat{h}_{BA}(t)$ yields the binary preliminary key. Then, in the stage of key agreement, the preliminary keys are synchronized by using turbo encoder to remove bit mismatch.

44.4 Performance Evaluation

44.4.1 Simulation Parameters

In this article, we analyze the performance of the proposed CS-SKGP by comparing with these two existing key generation schemes. In [9], Mathur et al. proposed the level crossing key generation algorithm, which uses random sub-sampling of the

Table 44.1 Simulation setup

Number of transmitting antennas (Tx)	2
Number of receiving antennas (Rx)	2
Sampling time (Ts)	0.357 us
Carrier frequency (fc)	2.4 GHz
Average path gain	−2 dB
Fading	Rayleigh
Doppler spectrum	Jakes
Coherence time (Tc)	3.75 ms

extracted key bits to increase the entropy. In [3] Azimi-Sadjadi et al. present a key generation methodology which is based on detecting deep fades to extract correlated bit streams.

Table 44.1 presents parameters used in the simulation.

44.4.2 Performance Metrics

The performance of the proposed method measured in terms of three metrics:

- **Bit mismatch rate**: Bit mismatch rate characterizes the robustness of the key generation schemes. It is defined as the ratio of the number of bits that do not match to the number of all the bits extracted from quantization.
- **Secret bit rate**: Secret bit rate measures the efficiency of the schemes. We define the secret bit rate as the average number of secret bits extracted per receives channel probing signal.
- **Entropy**, which measures the randomness of the generated keys. The entropy of a random variable X is defined as

$$H(X) = E[I(x_i)] = -\xi p(x_i)\log_2 p(x_i) \tag{44.17}$$

44.4.3 Results

(1) **Performance of Key Bit Mismatch Rate:** Figure 44.4 shows the bit mismatch rate. The number of probes is set to 64. We can observe that CS-SKGP has the lowest mismatch rate for higher SNRs, while Mathur's scheme has the lowest mismatch rate for lower SNRs. On the other hand, Azimi-Sadjadi's scheme performs the highest mismatch rate for any SNR. In fact, CS-SKGP always finds a secret key in our simulations for the SNRs of larger than 45 dB.

(2) **Performance of Bit Generation Rate:** Figure 44.5 shows the secret bit rate. We set the number of probes ranges from 50 to 110. It can be clearly seen that the bit rates of CS-SKGP are always above 1 while other two schemes' bit rates

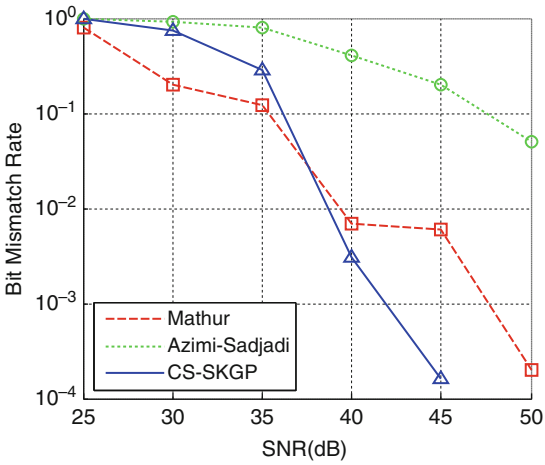

Fig. 44.4 Bit mismatch rate of Mathur's scheme, Azimi-Sadjadi's scheme and CS-SKGP

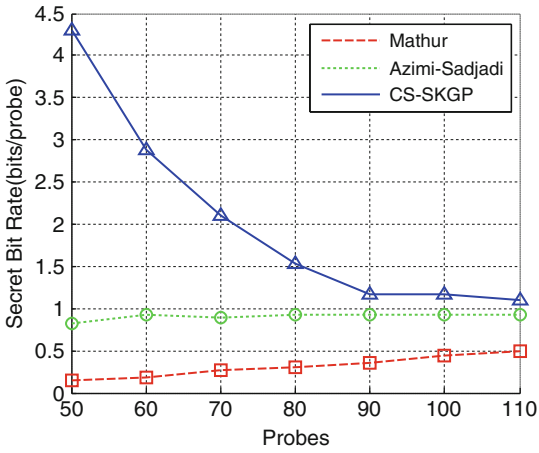

Fig. 44.5 Secret bit rate of Mathur's scheme, Azimi-Sadjadi's scheme and CS-SKGP

are under 1. The reason is that, in CS-SKGP, the probing signals for CS-based channel estimation are much less than the probes for the RSS measurements in Mathur's and Azimi-Sadjadi's quantization schemes.

(3) **Randomness Test:** We assume the number of probes ranges from 45 to 75 and the SNR is fixed in 15 dB. As shown in Fig. 44.6, Azimi-Sadjadi's scheme produces bit streams with the lowest entropy, while CS-SKGP generates secret bits with highest entropy at basically steady situation. The result shows that the smaller correlation between the pilots and the key bits results greater entropy.

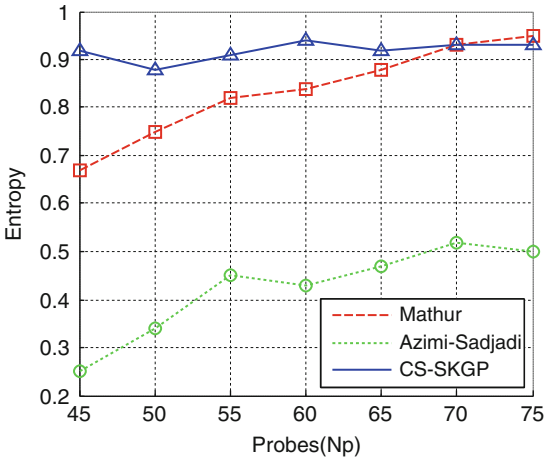

Fig. 44.6 Key bit entropy of Mathur's scheme, Azimi-Sadjadi's scheme and CS-SKGP

Conclusions

This paper presents a secret key generation scheme based on compressed sensing, CS-SKGP. This technique generates secret keys by exploiting the common randomness and the sparsity of MIMO channel coefficients. Simulations show that CS-SKGP minimizes number of probing signals by performing CS-based channel estimation, and generates secret keys with higher entropy, higher generation rate and lower mismatch rate.

Directions for future work include improving the efficiency and secrecy of the channel quantization technique, investigating the CS-based key generation protocols for low SNR region, and finding sensing matrices that can achieve the upper bound of the secret key length.

References

1. Limmanee A, Henkel W (2010) Secure physical-layer key generation protocol and key encoding in wireless communications. In: GLOBECOM workshops IEEE, pp 94–98
2. Ren K, Su H, Wang Q (2011) Secret key generation exploiting channel characteristics in wireless communications. Wirel Commun IEEE 18(4):6–12
3. Kai Z, Wu D, An C, Mohapatra P (2010) Exploiting multiple-antenna diversity for shared secret key generation in wireless networks. In: Proceedings of INFOCOM'10, pp 1837–1845
4. Wallace JW, Sharma RK (2010) Experimental investigation of MIMO reciprocal channel key generation. Communications (ICC) IEEE international conference IEEE, pp 1–5
5. Bajwa WU, Haupt J, Sayeed AM, Nowak R (2010) Compressed channel sensing: a new approach to estimating sparse multipath channels. Proc IEEE 98(6):1058–1076
6. Jana S, Premnath SN, Clark M et al (2009) On the effectiveness of secret key extraction from wireless signal strength in real environments. In: Proceedings of the 15th annual international conference on mobile computing and networking ACM, pp 321–332

7. Suhas M, Narayan M, Chunxuan Y, Alex R (2008) Radio-telepathy: extracting a secret key from an unauthenticated wireless channel. In: Proceedings of the 14th ACM international conference on mobile computing and networking. ACM, pp 128–139
8. Babak A, Alejandra M, Bulent Y et al (2007) Robust key generation from signal envelopes in wireless networks. In: Proceedings of the 14th ACM conference on computer and communications security. ACM, pp 401–410
9. Gilles B, Louis S (1994) Secret key reconciliation by public discussion. Lect Notes Comput Sci 765:410–423
10. Impagliazzo R, Leonid AL, Michael L (1989) Pseudo-random generation from one-way functions. In: Proceedings of the twenty-first annual ACM symposium on theory of computing. ACM, pp 12–24
11. Needell D, Joel AT (2009) CoSaMP: iterative signal recovery from incomplete and inaccurate samples. Appl Comput Harmon Anal 26(3):301–321

Chapter 45
Interference Management Research in DCF Infrastructure Networks Based on Boolean Model

Xiaokun Zheng and Ting Jiang

Abstract In traditional CDMA networks, transmit power control (TPC) is main technology to mitigate interference of cell-edge users (CEU), and in 4G-LTE networks with OFDM, fractional frequency reuse (FFR) for CEU is main technology for its flexibility of subcarrier pre-coding. In this paper, we propose a FFR scheme based on cell-edge interference alignment (IA) in DCF infrastructure networks first, then present a performance analysis and compare it with TPC by using probability theory with same node density based on BM model, simulation are given at last. Results show that TPC and soft FFR are almost same in terms of average throughput, former has a little more outage or error probability; TPC with upload and download in different channel has the best throughput performance.

45.1 Introduction

For the ever increasing demand of higher rates and dense nodes, interference between users is a main challenge. In traditional CDMA infrastructure networks, TPC is main technology to mitigate interference of CEU. However, in 4G-LTE networks with OFDM, FFR is main method because of its flexibility of subcarrier pre-coding; of course TPC can also be used in OFDM. The advantage of TPC is all nodes can use entire band, by using FFR method both aggressor and victim can only use part of band to mitigate interference. But if the aggressor is very near, transmit power and rate must reduce much or even TPC is not efficient anymore.

Recent years many references have discussed lots of approaches based on TPC and FFR. In [1], a download FFR in cellular network based on interference

X. Zheng (✉) • T. Jiang
Beijing University of Posts and Telecommunications, Beijing, China

Key Laboratory of Universal Wireless Communications, Ministry of Education, Beijing, China
e-mail: 1053072637@qq.com

J. Mu et al. (eds.), *The Proceedings of the Third International Conference on Communications, Signal Processing, and Systems*, Lecture Notes in Electrical Engineering 322, DOI 10.1007/978-3-319-08991-1_45

alignment (IA) is proposed. Kim and Kwon [2], Venturino and Prasad [3] discussed FFR combined with subcarrier power allocation to mitigate download interference. Xu [4] proposed a FFR approach combined with general MIMO. In [5], performance analysis of IA in ad-hoc based on BM model is proposed. Galindo [6] discussed FFR combined with load balancing in relay work. A Generic Mathematical Model Based on Fuzzy Set is given in [7] to derive various FFR in cellular networks. Novlan and Andrews [8] analysis different FFR and fixed FR in same scene based on Poisson point process; In [9], different interference management approaches including TPC and FFR are compared by literature review method, also indicates that FFR combined with power control is promoting but is complicated somewhat and power setting would need standardized.

In this paper, we research soft FFR based on cell-edge IA in DCF infrastructure network first, then propose a performance compare between TPC and FFR by using BM. Boolean model (BM) [10] is a famous new stochastic geometry model proposed recently, often used to assess wireless coverage or interference performance.

The remainder of the paper is organized as follows. Section 45.2 presents system model based on BM model and introduce outage probability, multiplexing gain [11] and normalized throughput used in this paper. Section 45.3 illustrates FFR based on cell-edge IA, then analysis FFR and TPC by using probability method based on BM. Section 45.4 discusses the analysis result and simulation result, both analysis and simulation result are in accord with qualitative comparison result in [9]. Finally, conclusion is given in section "Conclusions".

45.2 Mass Deployment System Model

45.2.1 TPC and FFR in Cell-Edge Interference Mitigation

The advantage of TPC is all nodes can use entire band while both aggressor and victim can only use part of band to mitigate mutual interference by using FFR method. However, if the interference node is very near to cell node, transmit power and rate must reduce too much or even TPC is not efficient anymore (Fig. 45.1).

45.2.2 BM Model of Dense Infrastructure Network

Boolean model (BM) [10] consists of one basis father process (germs) and some sub process (grains), sub processes usually consider using Poisson point process or uniform distribution. Adding some amendment to the basic model, BM can be used to a variety of different structure network, such as DCF infrastructure network discussed in this paper.

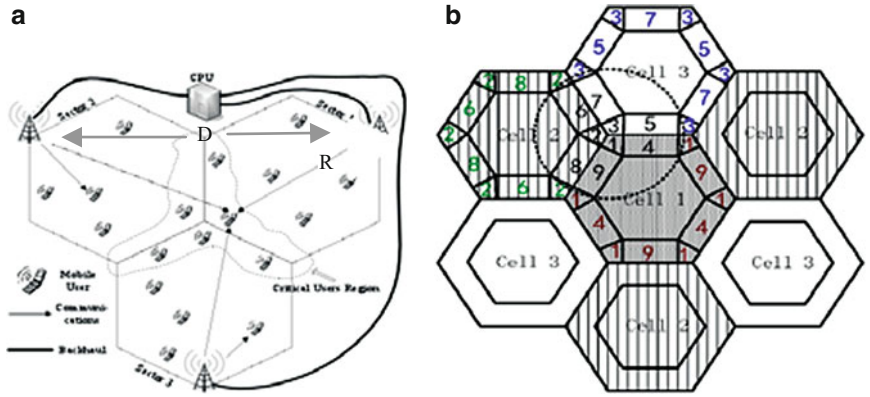

Fig. 45.1 Dense infrastructure network $R < D < 3R$ (**a**) FFR based on cell-edge IA&TPC (**b**) cell edge FFR model in [10]

45.2.3 Normalized Average Throughput and Outage Probability

Firstly we introduce normalized throughput and multiplexing gain [11]. If there are seven pairs of user interfere with each other, by using CDM method with spreading factor $p = 15$, each pair would get 1/15 bandwidth; by using FDM or TDM, each pair get 1/7. As to OFDM, each pair can get 2/7. While by using fixed frequency reuse, each pair obtain 1/3 capacity or each pair's average throughput is 0.33 when total bandwidth and rated power are fixed. That's to say fixed FR obtain 4/3 multiplexing gain comparing with FDM/TDM (1/7–1/3). Outage probability discussed here is caused when interference can't be mitigated by TPC if aggressor is fairly close.

45.3 FFR Based on Cell-Edge IA and TPC

To research FFR and TPC in non-clustered scene, we mainly consider each cell has eight nodes (density = 8), mainly analysis the case of eight nodes distributed as Fig. 45.2c, then analysis four cases of other distribution, give the average at last (Fig 45.5).

Last we give brief analysis for Poisson distribution ($\lambda = 4$) in non-clustered (Fig. 45.2a)

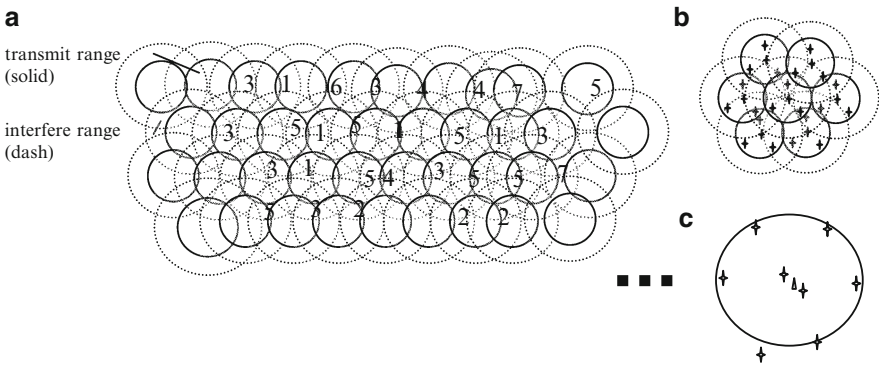

Fig. 45.2 Node uniform and Poisson distribution. (**a**) A realization of BM model AP(R < D < 3R) nodes Poisson distribution λ = 4 [matlab generation]; (**b**) nodes uniform distribution density = 4; (**c**) nodes uniform distribution density = 8

45.3.1 Clustered Scene (n = 7)

45.3.1.1 Layering Frequency Cell-Edge IA

Layering frequency IA is illustrated as Fig. 45.3a, divide total F into four parts of subcarrier, use two parts if there is mutual interference with up/down cell or left/right cell, or say using 1/2 band; use one parts if there is mutual interference with up/down cells and left/right cells simultaneously, or say 1/4 band to avoid interfering. Of course if there is no mutual interference with all cells around, one can use total band (see Fig. 45.3a), this approach also can refer to other literature [7–9].

Such as for A2 cell (see Fig. 45.3a), if there is mutual interference with B1 or B2, select f3, f4 to transmit and set f1, f2 to zero (meanwhile B1 or B2 select f1, f2). To obtain average transmit band or average throughput, we need to calculate the probability of each case. If the probability of mutual interference with A1 is $P_{shrinkLR}$, then the probability of shrink with above and below B cell is

$$P_{shrinkUD} = 2P_{shrinkLR} - {P_{shrinkLR}}^2 \tag{45.1}$$

Because four B cells above and below can be thought as two couple of cell pairs on the left and right (see Fig. 45.4a). The average throughput of A2 can be written as:

$$\overline{V}_{A2} = 1 \times (1 - P_{shrinkLR})(1 - P_{shrinkUD}) + \frac{1}{2}[P_{shrinkLR}(1 - P_{shrinkUD}) + (1 - P_{shrinkLR})P_{shrinkUD}] + \frac{1}{4}P_{shrinkLR}P_{shrinkUD}$$

So if we get $P_{shrinkLR}$, The average throughput of A2 can be worked out.

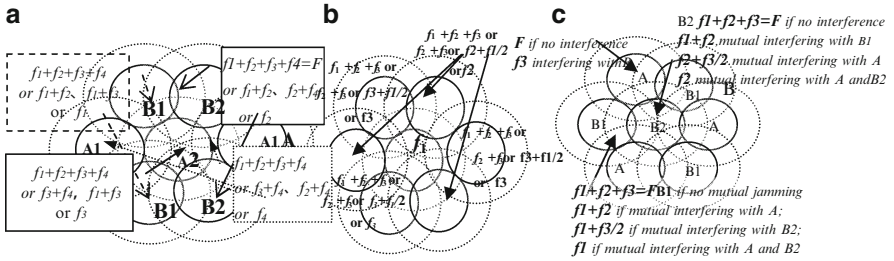

Fig. 45.3 Clustered FFR based on cell-edge IA, (**a**) layering FFR cell-edge IA, (**b**) triangle FFR cell-edge IA, (**c**) triangle FFR cell-edge IA

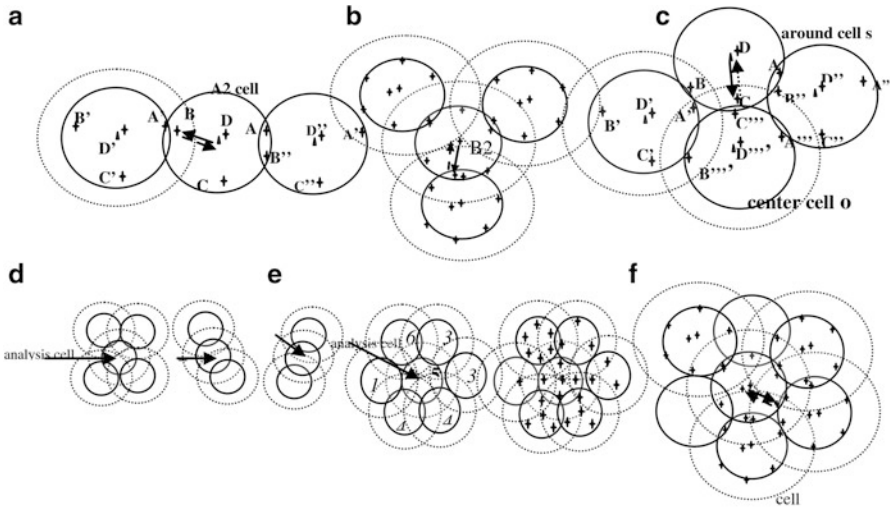

Fig. 45.4 Analysis of shrink probability to eliminate clutter edge, (**a**) P_{shrik} LR analysis of laying FFR, (**b**) P_{shrink} analysis of triangle FFR, (**c**) TPC P_{shrink} analysis of around cell, (**d**) P_{shrink} UD analysis of laying FFR, (**e**) node Poisson distribution, (**f**) TPC Pshrink analysis of center

Following we discuss $P_{shrinkLR}$ in detail. According to Fig. 45.4a, first we assume node A, B, C, D's access probability are all 1/8, whether uplink or downlink, each node or AP has ideal CSI (Channel state information) around. AP has 100 % saturation of access. Node D is in the center of cell, not CEU, so its uplink (UL) or downlink (DL) would not interfere neighbor cell's node, but could be interfered by neighbor A' node's UL.

Let us inspect node B in A2 cell firstly (Fig. 45.4a), when B downlinks, left A', B', C' nodes' DL and A's UL would interfere B's transmission. so $P_{left} = 3/8 + 1/8 = 1/2$; Besides that, B's DL would interfere right B"s DL, $P_{right} = 1/8$, then we can get node B's DL shrink probability,

$$P\{shrink|Bdown\} = P_{left} + (1 - P_{left})P_{right} = \frac{1}{2} + \left(1 - \frac{1}{2}\right) \times \frac{1}{8} = \frac{9}{16} \quad (45.2)$$

when B uplinks, it could interfere left cell's all UL and A', D' node's DL, $P_{left} = 1/2 + 1/8 + 1/8$; right B" node's UL could interfere B uplink, $P_{right} = 1/8$, then we can get node B's UL shrink probability,

$$\begin{aligned} P\{shrink|Bup\} &= P_{left} + (1 - P_{left})P_{right} \\ &= \frac{1}{2} + \frac{1}{8} + \frac{1}{8} + \left[1 - \left(\frac{1}{2} + \frac{1}{8} + \frac{1}{8}\right)\right] \times \frac{1}{8} = \frac{25}{32} \end{aligned} \quad (45.3)$$

As to node A, there is equivalence between B, so $P\{shrink|A_{up}\} = P\{shrink|B_{up}\}$ and $P\{shrink|A_{down}\} = P\{shrink|B_{don}\}$. **As to node C**, when C downlinks, could interfere left A' node's DL($P_{left} = 1/8$) and right B" node's DL(1/8)

$$P\{shrink|Cdown\} = P_{left} + (1 - P_{left})P_{right} = \frac{1}{8} + \left(1 - \frac{1}{8}\right) \times \frac{1}{8} = \frac{15}{64} \quad (45.4)$$

C UL could be interfered by A' and B" node's UL

$$P\{shrink|Cup\} = P_{left} + (1 - P_{left})P_{right} = \frac{15}{64} \quad (45.5)$$

As to node D, could not interfere neighbor, but could be interfered by left A' and right B" node's UL

$$\begin{aligned} P\{shrink|Dup\} = P\{shrink|Ddown\} &= P_{left} + (1 - P_{left})P_{right} = \frac{1}{8} + \left(1 - \frac{1}{8}\right) \times \frac{1}{8} \\ &= \frac{15}{64} \end{aligned}$$

According to Total probability theorem, to avoid mutual interference with left and right, cell A2 's all transmissions shrink probability $\boldsymbol{P_{shrinkLR}}$ is

$$\begin{aligned} P_{shrinkLR} &= P\{A_{up}\}\, P\{shrink|A_{up}\} + P\{A_{down}\}\, P\{shrink|A_{down}\} + P\{B_{up}\}\, P\{shrink|B_{up}\} \\ &+ P\{B_{down}\} P\{shrink|B_{down}\} + P\{C_{up}\}\, P\{shrink|C_{up}\} + P\{C_{down}\}\, P\{shrink|C_{down}\} \\ &+ P\{D_{up}\}\, P\{shrink|D_{up}\} + P\{D_{down}\}\, P\{shrink|D_{down}\} \end{aligned} \quad (45.6-1)$$

Bring Eqs. (45.2)–(45.5)'s result into (45.6-1),we get

$$\begin{aligned} P_{shrinkLR} &= 1/8x(25/32 + 9/16 + 25/32 + 9/16 + 15/64 + 15/64 + 15/64 + 15/64) \\ &= 232/512 = 0.453 \end{aligned} \quad (45.6-2)$$

then according to (1), $P_{shrinkUD} = 2P_{shrink} - P_{shrink}{}^2 = 2 \times 0.453 - 0.453^2 = 0.7$.

So the average transmit bandwidth or normalized average throughput of A2 cell

$$\begin{aligned}\overline{V}_{A2} &= 1 \times (1 - P_{shrinkLR})(1 - P_{ud}) \\ &\quad + \frac{1}{2}[P_{shrinkLR}(1 - P_{ud}) + (1 - P_{shrinkLR})P_{ud}] + \frac{1}{4}P_{shrinkLR}P_{ud} \\ &= (1 - 0.453)(1 - 0.7) + \ldots = 0.503\end{aligned} \tag{45.7}$$

Next we discuss A1 cell in Fig. 45.3d, its interference from above and below might comes from two cells,so $P_{shrinkUD}$ can use (45.6)'s result PshrinkUD = 0.453 its interference from left or right only comes from one cell, just keep (45.2), (45.3), (45.4), and (45.5)'s Pleft left (get rid of $(1 - P_{left}) \cdot P_{right}$) could get $P\{shrink|B_{down}\}$, $P\{shrink|B_{up}\}$, $P\{shrink|C_{down}\}$ and so on. Bring these conditional probability into Total probability theorem,

$$\begin{aligned}&P_{shrinkone} = P\{shrink|A_{up}\}P_{A_{up}} + P\{shrink|B_{up}\}P_{B_{up}} + P\{shrink|C_{up}\}P_{C_{up}} \\ &+P\{shrink|D_{up}\}P_{D_{up}} + P\{shrink|A_{down}\}P_{A_{down}} + P\{shrink|B_{down}\}P_{B_{down}} \\ &+P\{shrink|C_{down}\}P_{C_{down}} + P\{shrink|D_{down}\}P_{Ddown} \\ &= \frac{1}{8}\left(\frac{3}{4} + \frac{1}{2} + \frac{3}{4} + \frac{1}{2} + \frac{1}{8} + \frac{1}{8} + \frac{1}{8} + \frac{1}{8}\right) = \frac{3}{8}\end{aligned} \tag{45.8}$$

$P_{shrinkone} = 3/8 = 0.375$, then the average transmit bandwidth or normalized average throughput of A1 cell

$$\begin{aligned}\overline{V}_{A1} &= 1 \times (1 - P_{shrinkUD})(1 - P_{shrinone}) + \frac{1}{2}[P_{shrinkUD}(1 - P_{shrinone}) + (1 - P_{shrinkUD})P_{shrinone}] \\ &\quad + \frac{1}{4}P_{shrinkUD}P_{shrinone} = (1 - 0.45)(1 - 0.37) + 1/2(0.450.63 + 0.550.37) \\ &\quad + 1/40.450.37 = 0.628\end{aligned}$$

There is equivalence between cell B1, B2 and A1, so $\overline{V}_B = \overline{V}_{A1} = 0.628$, then average throughput of all cell in Fig. 45.3d

$$\overline{V} = \left(4\overline{V}_B + 2\overline{V}_{A1} + \overline{V}_{A2}\right)/7 = (6 \times 0.628 + 0.503)/7 = 0.61$$

45.3.1.2 Triangle Frequency IA

According to Fig. 45.3b, divides F into three parts $f_1 = f_2 = f_3 = F$. Center cell use f_1 regular, cells around use F if no interference with center and two sides, use two parts (such as $f_2 + f_3$) if there is mutual interference with center only, use 1.5 parts of F (such as $f_2 + f_1/2$,cell near by $f_3 + f_1/2$) if there is interference with two sides only, use one pars if there is mutual interference both with center and tow sides. So the six cells around have four choice of bandwidth to transmit.

As to the shrink probability with tow sides, here use the result of Eq. (45.6-2) $P_{shrinkLR} = 0.453$, the shrink probability with center, we use the result of (8), $P_{cent} = P_{shrinkone} = 3/8$, so each around cell in Fig. 45.3b's average throughput could be calculated

$$\begin{aligned}\overline{V_{round}} &= \left[\frac{1}{3}P_{cen}P_{shrinkLR} + 1 \times (1 - P_{shrinkLR})(1 - P_{cen})\right. \\ &\quad \left. + \frac{2}{3}P_{cen}(1 - P_{shrinkLR}) + \frac{1}{2}(1 - P_{cen})P_{shrinkLR}\right] \\ &= 45.3\% \times \frac{3}{8} \times \frac{1}{3} + \ldots = 67.7\%\end{aligned}$$

the center cell throughput is $V_{cen} = 1/3$, the average throughput of all cell in Fig. 45.3b is

$$\overline{V} = \overline{V_{round}} \times \frac{6}{7} + V_{cen} \times \frac{1}{7} = 67.7\% \times \frac{6}{7} + 33.33\% \times \frac{1}{7} = 0.628$$

45.3.1.3 TPC with Half-Deplux

In this section we analysis TPC with half-deplux, that means UL and DL transmission are in same channel F, interference may come from neighbor UL or DL and interference strength may differ with distance change, so power reduce level differ in accordance with distance, here we simply assume average transmit power and rate reduce level is 2/5 (see 802.11a or other) (when UL and DL channel is not the same, interference level is few smaller, we set average reduce level 3/5 in next Sect. 45.3.1.4),according to $\overline{V} = \frac{2}{5}P_{shrink} + (1 - P_{shrink}) \times 1$, we discuss P_{shrink} in TPC below.

Let us inspect cell *s* not at center in Fig. 45.4c first. **As to C node's DL**, would interfere neighbor A', C'", B" nodes' DL, need to, so conditional shrink probability of C DL is

$$\begin{aligned}P\{shrink | Cdown\} &= P_{A'down} + \overline{P_{A'down}}P_{B''down} + \overline{P_{A'down}} \cdot \overline{P_{B''down}} \cdot P_{C'''down} \\ &= P_{A'down} + (1 - P_{A'down})P_{B''down} + (1 - P_{A'down})(1 - P_{B''down})P_{C'''down} \\ &= \frac{1}{8} + \frac{7}{8} \times \frac{1}{8} + \frac{7}{8} \times \frac{7}{8} \times \frac{1}{8} = \frac{169}{512}\end{aligned} \tag{45.9}$$

Similarly B, A, node's DL interfere neighbor A', C'", B" nodes' DL too, so $P\{shrink|A_{down}\} = P\{shrink|B_{down}\} = P\{shrink|C_{down}\} = 169/512$

D node is in the center region, its DL would not interfere neighbor, $P\{shrink|Ddown\} = 0$, then s cell downlink's total shrink probability is

$$P_{Sdown} = P\{Adown|down\}P\{shrink|Adown\} + P\{Bdown|down\}P\{shrink|Bdown\} + P\{Cdown|down\}P\{shrink|Cdown\} = 3 \times \frac{1}{4} \times \frac{169}{512} = 0.248 \quad (45.10)$$

(*note*: when DL, each node access probability is 1/4, such as $P\{Adown/down\} = 1/4$)

Similarly, cell s UL

$$P_{Sup} = P_{Aup}P\{shrink|Aup\} + P_{Bup}P\{shrink|Bup\} + P_{Cup}P\{shrink|Cup\} = 2 \times \frac{1}{4} \times 0.78 + \frac{1}{4} \times 0.81 = 0.593 \quad (45.11)$$

(in Eq. (45.11) $\{shrink/Aup\} = P\{shrink/Bup\} = 0.78$, $P\{shrink/Cup\} = 0.81$)

Assuming $P_{up} = P_{down} = 1/2$, we get all transmission's average shrink probability is

$$P_{shrink} = 1/2xP_{Sdown} + 1/2xP_{Sup} = 1/2x0.248 + 1/2x0.593 = 0.42$$

Thus average throughput of cells (Fig. 45.4c) around

$$V_{around} = \frac{2}{5}P_{shrink} + (1 - P_{shrink}) \times 1 = 0.42 \times 0.4 + 0.58 = 0.748$$

Similarly we can obtain center cell's (Fig. 45.4f) average throughput $\overline{V}_{中心} = 0.66$

At last we work out the average throughput of TPC with half-deplux

$$\overline{V} = \left(6\overline{V}_{around} + \overline{V}_{center}\right)/7 = (6 \times 0.748 + 0.66)/7 = 0.735$$

However, when node C in Fig. 45.4c UL, interference to neighbor C"' is too severe to mitigate; Similarly B node's UL to A' DL, A node's UL to B" DL and A, B, C node's DL to A', B", C"' DL, interference these case all couldn't be mitigated, then $P_{outage} = 1/8 \cdot 1/8 + 1/8 \cdot 1/8 + 1/8 \cdot 1/8 + 3/8 \cdot (1/8 + 7/8 \cdot 1/8 + 7/8 \cdot 7/8 \cdot 1/8) =$ 14.7 %

Outage or error probability is 0.147, reduce throughout

$$\overline{V} = 0.735 - 0.147 \approx 0.59 \quad (45.12)$$

45.3.1.4 TPC with Full Duplex

If DL and UL transmit in two separate channel, each channel is equal to half of total bandwidth F, there is no inference between DL and UL, interference level is few smaller, we set average reduce level 3/5. Similar to 45.3.1.3 section, we analysis the

cell not in center first (*s* cell in Fig. 45.4c), then analysis the central (Fig. 45.4f). The transmit is full deplux, DL/UL can transmit simultaneously, each node's DL or UL access probability is 1/4. When C node DL (Fig. 45.4c), neighbor A', B", C'" node's DL would be interfered, B, A node's DL would also interfere A', B", C'" nodes'DL,

$$P\{shrnk|A_{down}\} = P\{shnk|B_{dwn}\} = P\{shrnk|C_{dwn}\} = 37/64 \tag{45.13}$$

Node d is in cell's center region, $P\{shrink|Ddown\} = 0$. So the cell's DL shrink Probability

$$\begin{aligned} P_{down} &= P_{Adown}P\{_{shrink}|_{Adown}\} + P_{Bdown}P\{_{shrink}|_{Bdown}\} \\ &\quad + P_{Cdown}P\{_{shrink}|_{Cdown}\} \\ &= 3 \times \frac{1}{4} \times \frac{37}{64} = \frac{111}{256} \end{aligned} \tag{45.14}$$

In considering of DL channel is equal to half of total bandwidth F, average rate of DL is

$$\overline{V_{up}} = \frac{1}{2} \times \left(\frac{3}{5} \times P_{down}, +1, \times (1 - P_{down}) \right) = \frac{3}{10} \times \frac{111}{256} + \frac{1}{2} \times \frac{145}{256} = 0.413$$

Similarly, average rate of UL

$$\overline{V_{up}} = \frac{3}{5} \times \frac{1}{2} \times P_{Sup} + \frac{1}{2}(1 - P_{Sup}) = \frac{3}{10} \times \frac{3}{4} + \frac{1}{2} \times \frac{1}{4} = 0.35$$

When full deplux, average transmit rate of cell is $\overline{V}_{\text{around}} = \overline{V_{up}} + \overline{V_{down}} = 0.35 + 0.4133 = 0.76$

As to the cell in center, according to Fig. 45.4f, we work out $\overline{V}\text{cen} = 0.72$, so the whole cluster's average throughput is $\overline{V} = (6\overline{V}_{\text{center}} + \overline{V}_{\text{non-cent}})/7 = (6\text{x}0.7633 + 0.72)/7 = 0.76$

45.3.2 Non-clustered

When there are much more mutual interference cells and can't be clustered, each cell need more CSI and greater shrink probability, such as in Fig. 45.2a, each cell need six cells' CSI around we just give some brief analysis results below.

45.3.2.1 Layering and Triangle Frequency IA

Layering frequency IA approach non-clustered is the same as clustered (see Fig. 45.3a) except that each cell's shrink probability calculation need six CSI around itself. The analysis is nearly same with 45.3.1.1 subsection and according to Eq. (45.7) we get

$$\begin{aligned}\overline{V} &= 1 \times (1 - P_{shrinkLR})(1 - P_{shrinkUD}) \\ &\quad + \frac{1}{2}[P_{shrinkUD}(1 - P_{shrinkLR}) + P_{shrinkLR}(1 - P_{shrinkUD})] + \frac{1}{4}P_{shrinkLR}P_{shrinkUD} \\ &= 0.547 \times 0.3 + \ldots = 0.503\end{aligned}$$

As to triangle frequency IA here we use scheme according to Fig. 45.3c. Each cell has four subcarrier options which is little more than clustered Fig. 45.3b.

$$\begin{aligned}\overline{V_{B1}} &= 1 \times (1 - P_{shrink})^2 + \frac{1}{3}{P_{shrink}}^2 + \frac{2}{3}P_{shrink}(1 - P_{shrink}) + \frac{1}{2}P_{shrink}(1 - P_{shrink}) \\ &= (1 - 0.617)^2 + \ldots = 0.55 = \overline{V_{B2}} \\ \overline{V_A} &= 1 \times (1 - P_{shrink})^2 + \frac{1}{3}{P_{shrink}}^2 + \frac{1}{3}2P_{shrink}(1 - P_{shrink}) = 0.432 \\ \overline{V} &= \frac{1}{3}\overline{V_{B1}} + \frac{1}{3}\overline{V_{B2}} + \frac{1}{3}\overline{V_A} = \frac{2}{3}0.55 + \frac{1}{3}0.432 = 0.511\end{aligned}$$

45.3.2.2 TPC with Upload and Download in Same or Different Channel

In case of non-clustered and half-deplux, the analysis of TPC is almost same with 45.3.1.3 subsection, except that each cell has six cells around (see Fig. 45.4 f),

$$\overline{V} = \frac{2}{5}\ P_{shrink} + \overline{P_{shrink}} \times 1 = \frac{2}{5} \times 0.57 + 1 - 0.57 = 0.658 \tag{45.15}$$

In consideration of some interference can't be mitigated, according to Eq. (45.12) the throughput reduced to $\overline{V} = 0.658 - 0.147 = 0.511$

In case of non-clustered and full duplex communication, interference is decreased somewhat, we assume that power drops to 3/5 averagely and nearly all interference can be mitigated here. The analysis of shrink probability is similar to 45.3.1.4 subsection (see Fig. 45.4f), shrink probability of DL and UL are $P\{_{\text{shrink}}|\text{down}\} = 0.62$, $P\{_{\text{shrink}}|\text{up}\} = 0.75$, finally we get

$$\overline{V} = \overline{V}_{up} + \overline{V}_{down} = 0.375 + 0.35 = 0.72 \tag{45.16}$$

45.3.2.3 Layering Frequency IA with Poisson Process

When nodes in each cell are Poisson distribution, first we analysis the cell with five nodes in it (Fig. 45.4e)

$$\overline{V} = 1(1 - P_{shrinkLR})(1 - P_{shrinkUD}) + \frac{1}{2}\left[P_{shrinkUD}(1 - P_{shrinkLR}) + P_{shrinkLR}(1 - P_{shrinkUD})\right] + \frac{1}{4} P_{shrinkLR} P_{shrinkUD} = 0.467$$

Then analysis four other cells in Fig. 45.2a, the average is $\overline{V}_{poiss} = 0.485$

45.4 Analysis and Simulation Results

We present a simulation based on BM model introduced in this paper, assumed each AP has 100 % saturation of access, DCF access mode, nodes density of each cell is four or eight (Poisson distribution with $\lambda = 4$), ideal CSI, run 40 simulations totally.

Both analysis and simulation result are in accord with qualitative comparison result by literature review method in [9]. TPC and FFR are almost same in terms of average throughput, clustered is better than non-clustered. TPC has 14.7 % outage probability for some rest interference. TPC has nearly no outage and best throughput performance in case of duplex when UL and DL have separate channel (Figs. 45.5 and 45.6).

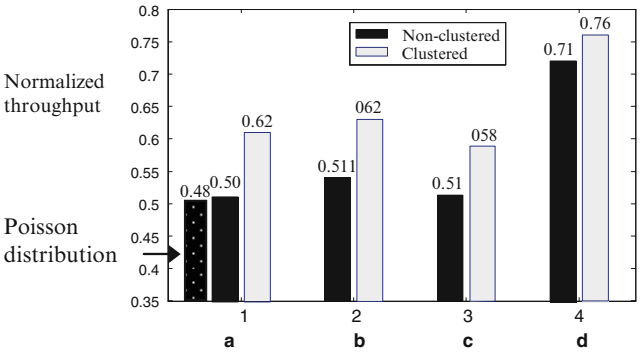

Fig. 45.5 Normalized throughput result. (**a**) Layering frequency, (**b**) triangle frequency, (**c**) TPC in half-duplex, (**d**) TPC in full duplex

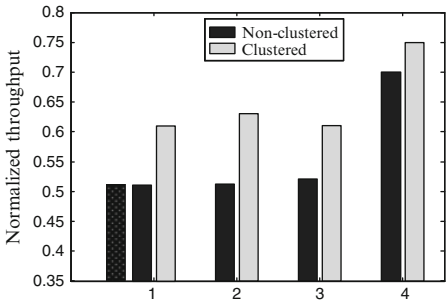

Fig. 45.6 Throughput simulation result. (If there is enough distance between cellular, normalized throughput of each cellular is 1.0—note)

Conclusions

In this paper, we proposed two FFR schemes based on cell-edge IA to mitigate interference in infrastructure network, then make a compare between FFR and TPC. Analysis and simulation results are in accord with qualitative comparison [9]. Results show they are almost same in terms of average throughput, former has some outage probability, TPC with full-deplux has best throughput performance.

References

1. Da Bin, Zhang R (2011) Exploiting interference alignment in multi-cell cooperative OFDMA resource allocation. GLOBALCOM
2. Kim S-Y, Kwon J-A (2013) Resource allocation for the multi-cell OFDM system and its capacity bounds. In: 11th WiOpt, IEEE Press
3. Venturino L, Prasad N (2009) Coordinated scheduling and power allocation in downlink multicell OFDMA networks. IEEE Trans Veh Technol 58(6):2835–2848
4. Xu F-M (2008) A fractional frequency reuse scheme supporting generalized MIMO technique. J Beijing Univ Posts Telecommun 31:46–49
5. Dong H, Song R-F (2011) Transmit capacity of wireless networks with interference alignment. J Nanjing Univ Posts Telecommun 31(6):11–15
6. Galindo A (2012) Managing femto to macro interference without *X*2 interface support through POMDP. Mob Netw Appl 17:633–647, Springer
7. Tao X (2013) A generic mathematical model based on fuzzy set theory for frequency reuse in cellular networks. IEEE JSAC 31:861–869
8. Novlan TD, Andrews JG (2013) Analytical evaluation of uplink fractional frequency reuse. IEEE Trans Commun 61:2098–2108
9. Saquib N, Hossain E (2012) Interference management in OFDMA femtocell networks: issues and approaches. IEEE Wirel Commun 19:86–95
10. Haenggi M (2009) Stochastic geometry and random graphs for the analysis and design wireless networks. IEEE JSAC 27:1029–1046
11. Cadambe VR, Jafar SA (2008) Interference alignment and degrees of freedom of the K-user interference channel. IEEE Inf Theory 54:3425–3441

Chapter 46
The Resolution for Wireless Coverage of Important Activity Regions

Fei Fei Dong and Xin Chen Wang

Abstract Teletraffic demand in important activity regions is high, thus congestion shappen frequently. So how to meet the wireless communication demands of these places become a major concern of operator. In this paper, we have explored this problem by careful analysis of business statistics, business model building and total demand prediction. Relevant radio network construction scale and need were then introduced. Finally, we designed the corresponding three-dimension network scheme.

Keywords Important activity regions • Wireless coverage • Macro base

46.1 The Analysis of Business Demand in Important Regions

46.1.1 Definition of the Major Activity Region

Major activity region, refers to the dense flow and intensive communication requirements of important activities, the places are often high traffic demanded. Due to the frequency of the mobile communication, the channel resources is very limited, such as how to meet the demand of the sites of wireless communication, become a topic of carrier's attention.

Refer to the voice traffic demand of typical important activities region, make the voice call density of 200,000 people per square meter and 4,000 Erl/km^2 as an evaluation in the important activities region, for qualitative calculation.

F. Fei Dong (✉) • X. Chen Wang
Chengdu Monitoring Station of the State Radio Regulation of China, 610000 Chengdu, China

Fujian Monitoring Station of the State Radio Regulation of China, 361000 Xiamen, China
e-mail: dong.f.f@srrc.org.cn; Wangxinchen@srrc.org.cn

J. Mu et al. (eds.), *The Proceedings of the Third International Conference on Communications, Signal Processing, and Systems*, Lecture Notes in Electrical Engineering 322, DOI 10.1007/978-3-319-08991-1_46

46.1.2 Types of Business

The types of public mobile network includes three different kinds of that, voice service, value-added service and wireless data service (video call, MMS, wireless network, mobile email, mobile games, WAP, JAVA, etc.)

46.1.3 Business Model and the Total Predication

The user's business model is associated to the setting of network scale, though the difference of standard, we can conclude the business just voice service and data service for simple. Refer to the business level of every carrier, we set the 0.02 Erl per person in voice service, and 500 bps in data service in common. The table is calculated by 1 km^2 and 200,000 people per square kilometers as sample, which is demanded in the important activities region.

46.1.4 Classification of Important Activity Regions

There are three kinds of important activity regions as follow: (1) Airport, station, port, dock, etc; (2) Permanent exhibition venues and Stadiums (3) Temporary exhibition venues and Stadiums.

46.2 The Demand of Wireless Network Construction Scale for Important Activities Regions

46.2.1 Coverage of Voice and Data Service

According to the related standard, combined the experience of local carrier, considering that the height of base station is 20–35 m, the formula of each typical coverage will be given as follow, the loss caused by the building will be considered.

$$L_b = 69.55 + 26.16\log f - 13.82\log h_b - a(\mathrm{h}_m) + (44.9 - 6.55\log \mathrm{h}_b)\log d$$

h_b–the efficient antenna height.

- The coverage of voice service

Considered the system limited by the up-link, we estimated the coverage of voice service of each main standard single base station as follow (Table 46.1):

Table 46.1 Coverage estimation of voice service of single station

	GSM 900	DCS 1800	CDMA 800	WCDMA	TD-SCDMA
Up-link load	–	–	75 %	50 %	50 %
Coverage radius (km)	0.6	0.58	0.63	0.57	0.5
Coverage area (km^2)	0.7	0.66	0.77	0.63	0.49
Amount of base station per square kilometers	1.43	1.52	1.3	1.59	2.05

- The coverage of data service

We estimated the data service coverage of single base station of each main standard, for limited by many factor, the coverage will be calculated by the data as follow (Table 46.2):

Compared to the voice service, to fulfill the data service will need more macro base station.

46.2.2 The Analysis of System Capacity

Based on the characteristic of mobile communication, there are many factors will influence the system capacity, it's difficult to calculate the capacity of mobile network system with a simple formula. Assumed that all voice service will be loaded by Macro station, and the total demand of voice service in 2G net occupied 90 %, the construction demand will be given as follow (Table 46.3).

In conclusion, the main influence of net construction and plan is voice service, in the important activity region, the capacity is the most important thing, much more methods should be considered by net.

46.3 Three-Dimensional Networking Solutions on Major Events Region

46.3.1 Ideas of Three-Dimensional Network Building

According to the analysis in the previous section, the major activity regions, a single macro base station network can hardly meet the teletraffic demand. Therefore, in order to meet the high traffic need in the major activity region, a wireless three-dimension network has to be built.

The core connotation of wireless three-dimension network is hierarchy and partition, which means covering the target are a stratified and subregionally. "Layered" architecture of wireless network is constructed by the upper layer

Table 46.2 Coverage estimation of data service of single station

	CDMA 800	Ev-Do (2000 band)	WCDMA	TD-SCDMA
Up-link load	75 %	50 %	50 %	50 %
Coverage radius (km)	76.8	153.6	128	144
Coverage area (km^2)	0.5	0.45	0.43	0.4
Amount of base station per square kilometers	0.49	0.39	0.36	0.31
Up-link load	2.05	2.57	2.78	3.23

Table 46.3 2G construction demand of each standard data service

2G net with full capacity	User per single base station	Market shares	Users per square kilometers (10,000) (%)	The construction demand of macro base
Mobile GSM 900/1800	13,250	70	12.6	10
Unicom GSM 900/1800	3,500	35	6.3	18
Telecom CDMA 800	11,000	15	2.7	3

network and the lower layer network. The upper layer network is formed by the macro stations, which cover a wide area to offer continuous coverage of the target area, and the underlying network is constructed by the micro-cellular stations and street stations, which offer regional coverage combined with emergency communications vehicles. "Partition" wireless network structure is efficient methods that provide differentiated customer-facing network configure and services in the process of three-dimensional mesh network. The structure gives full consideration to the imbalance of the business development region, and thus covers the target area into multiple units.

46.3.2 Deployment of Outdoor Macro stations (Upper Layer Network)

The first step to build 3-dimension wireless network is deploying the Outdoor macro base stations. In the important activity area, macro stations provide continuous coverage of roads and outdoor areas. Due to the small number, the traffic carrying capacity of macro stations is weak, so they work only as reserves. The teletraffic within the important region are mainly covered by indoor coverage system and street station.

Macro station planning should cover overall demand for the operators of each network. The deploying principles are as follows:

(1) Macro station should planed based on the planning of regional plan, facilitate early consideration of resource requirements, including transmission, machine room, antenna and aesthetics requirements.
(2) Multi-system station, room, antenna and other resources would prefer to be built and installed in the same site.
(3) Try to meet the communication needs of business peak by comprehensive way.

46.3.3 Indoor Coverage System Deployments (Lower Layer Network)

In the important activity area, were commend an "indoor distribution system plus source generator" methods to cover important buildings or buildings that need traffic sharing. Distribution system should be configured based on the actual building characteristics. Small-scale establishments can be distributed passively, and large-scale exhibition can use an active way after carefully considered the equipment selection and location requirements.

Indoor coverage system should be planned based on structural characteristics, traffic and teletraffic demand. Therefore, Indoor coverage system can be divided into two parts, sources and distribution systems.

46.3.3.1 Signal Source Settings

Signal source selection scheme should be determine according to the characteristic of target place, the construction area, the teletraffic level.

The technical factors should be considered first, including building coverage requirements, capacity requirements, network environment, and the signal source installation position. Second, the economic factor, especially the investment should be considered. Other important factors are project implementation factors including regional planning requirements and engineering aspects and long-term development factor such as building's long-term business development.

46.3.3.2 Distributed Antenna Scheme

Distributed antenna system is designed for allocating the electric power generate by signal source to required antenna, thus realize uniform distribution of the signal, and solve the problem of indoor signal coverage.

Among three distributed antenna systems (the ordinary cable systems, leakage cable systems and optical fiber systems), the ordinary cable system is most common used, and usually use with passive device like coupler, splitter and antenna. Active devices like trunk amplifier can also used with it when necessary.

The construction of indoor distribution system is an important activity, so the type of distribution system should be chosen carefully according to building size or coverage characteristics. General building and stadium usually use ordinary cable system and when signal extension is needed, a mixed indoor coverage system consisted of ordinary cable system and optical system can be constructed to expand the service scope. Leakage cable systems, on the other hand, can cover elevator and subway tunnels.

46.3.3.3 Multi-System Building

After considered problems such as saving investment, client environment, many indoor coverage system adopt the POI (POI, POINT OF INTERFACE). POI combine signals on the descending signal path, at the same times hunt signals on the uplink path of different systems. It also suppressed unwanted disturbance components between bands. So POI scheme is selected according to the different requirements of system isolation. In recent years, POI are widely and successfully used in new indoor coverage systems developed by operators, including 3G, 2.4 GHz WLAN and 800 MHz clusters (Iden, TETRA) systems.

With the issuance of 3G licenses, the number of combined systems in important region increased greatly, and main problem is still the interference between multi-systems. These interference signals are not only related to the quality of equipment, buy also related to its output power and bandwidth that is related to the degree of deviation. The bearability of the system to interference is determined by two factors, namely its own signal strength and interference signal strength. So we can reduce interference by spatial isolation, reducing the transmitter power, or using filter in the transmitter or receiver.

46.3.4 Lower Net Street Station Deployment

Street station name originated in the 2G network, and nature is replacing the function of a base station with several entities modules. The modules should be separately installed and easy to implement. This way is an important technical innovation in addressing station and covering the complex wireless environment.

3G often called it “remote radio (RRU)”, while 2G systems called it “street station”.

Street station are generally distributed in both sides of the street, the height of the antenna must be installed beneath the roof height. The coverage control is achieved by reducing the transmission power or by using the building block. Frequency arrangement adopts frequency hopping with high load and even some macro cellular layer of the frequency. The macro cellular equipment can adjust the equipment configuration according to the capacity needs, and then choose the

right transmit power and antenna to improve indoor coverage of tall buildings on both sides of the streets. Coverage of each street station is generally 300 m.

Street station is used for absorbing the teletraffic of outdoor people and sharing outdoor macro station traffic load. Therefore, Street Station scheme should be determined according to the regional planning and macro station deployment.

46.3.5 Emergency Vehicle Deployment (Lower Layer Networks)

Emergency communication vehicle is equivalent to the movable outdoor macro station, and also, it can be used as a temporary traffic hotspot coverage solution. Without the need for civil construction, Emergency communication vehicle can quickly setup, but still need to power, transmission and park location. Emergency vehicle deployment can be adjusted according to the traffic distribution and site operator's temporary deployment. Generally, it should be setup in temporary traffic hotspot and the areas that are difficult to construct outdoor macro station and street station.

46.3.6 Different Solutions in the Important Activities Region

46.3.6.1 Airport, Station, Port, Wharf

Because the airport, station, port, dock are often long-term fixed with relatively stable traffic and high traffic demand characteristics in most of the time in a year, mobile communication network deployment should adopt the following methods:

(1) Establish massive and permanent macro stations on suitable building to offer continuous coverage and thus, solve traffic problems in outdoor area.
(2) Construct street station or radio remote base station on the position of billboards, banners, lamp pole, and solve teletraffic demand at the entrance, check point, and the pick-up drop-off areas.
(3) Indoor areas should be covered by the indoor distribution system that can meet the rush hour traffic demand.
(4) Macro equipments with large capacity or microcellular indoor are preferred to cover indoor areas.

46.3.6.2 Permanent Exhibition Venues and Stadiums

Permanent exhibition venues and stadiums always have an extremely uneven teletraffic distribution, the flow of people and traffic can reach the peak features

in a short time. So the network deployment is similar to the airport terminal, station, port.

(1) Macro station are built to offer continuous coverage of the outdoor area and meet the daily traffic problems, high configuration will cause the inactive waste.
(2) Construct street station or radio remote base station on the position of bill-boards, banners, lamp pole, and solve teletraffic demand at the entrance, checkpoint, and the pick-up drop-off areas.
(3) Indoor areas should be covered by the indoor distribution system that can meet the rush hour traffic demand.
(4) All source configurations should take idle waste into account therefore, arriver channel resource sharing, scheduling problems should be considered carefully.

46.3.6.3 Temporary Exhibition Venues and Major Sports Venues

Temporary exhibition venues and sports venues also has the characteristics of high traffic and high impact, but because of the temporary premises, the demolition will be a waste of equipment, materials and other aspects. So the large-scale network construction isn't necessarily desirable. In these temporary venues, selection of meshing scheme shall be measured according to the activity duration, degree of importance, and there use of old level. Anyway, a lot of investment in construction of fixed macro base station and indoor distribution system is not needed, and may be the use of emergency communication vehicle is appropriate.

References

1. Shihe L (2003) TD-SCDMA, the third generation mobile communication standard. People's Posts and Telecommunications Press, Beijing
2. Laiho J (2004) UMTS wireless network planning and optimization (in Chinese translated by Xianpu S, et al.). Publishing House of Electronics Industry, Beijing
3. Holma H (2005) WCDMA technology and system design (third edition translated by Zeqiang C, et al.). Mechanical Industry Press, Beijing
4. YD/T1026-2001 technical requirement for the interface between mobile service switching center and base station subsystem in 800 MHz CDMA digital cellular mobile communication network

Part IV
Millimeter Wave, UWB Technology

Chapter 47
Design and Implementation of UWB Microstrip Equalizer

Hao Wang, Yu Liu, Wenbao Liu, Ziqiang Yang, and Tao Yang

Abstract In this paper, the basic theory of amplitude equalizer was mentioned, with the main specification and type. Model of resistor-aided ultra wide band (UWB) microstrip equalizer was presented and the equivalent circuit was analyzed. According to the analysis result, the length of a short circuit resonance stub was calculated roughly. Microwave simulating software High Frequency Structure Simulator (HFSS) was used to develop the model and perform simulation optimizing design. At last the equalizing module was produced, and the 2–18 GHz microstrip equalizer was finished. The measure results showed good performance, what's more, the power equalizer was small in size and was already in use.

Keyword UWB equalizer microstrip

47.1 Introduction

With the development of modern radar electronic technology in the modern radar system, high precision microwave measuring system and Traveling-wave tube amplifier (TWTA), the equalizer plays an important role. In the process of transmission of the circuit, the signals of different frequency will appear in the inconsistency of change, which is called the amplitude distortion. To correct the amplitude distortion, generally a balanced network, to be called amplitude equalizer, is inserted before or after the signal distortion, the amplitude frequency characteristics of which is contrary to the amplitude frequency characteristics of signal distortion, so that signal amplitude distortion can be corrected, equilibrium characteristics is a frequency selective attenuation characteristics. In short, a balanced characteristic is the attenuation characteristic which has the feature of frequency selective [1, 2].

There are two important technical requirements for the power equalizer: 1. the power attenuation characteristics should conform to the requirements within the

H. Wang (✉) • Y. Liu • W. Liu • Z. Yang • T. Yang
School of Electronic Engineering, University of Electronic Science and Technology of China, Chengdu, China
e-mail: wanghaoyu55@126.com

J. Mu et al. (eds.), *The Proceedings of the Third International Conference on Communications, Signal Processing, and Systems*, Lecture Notes in Electrical Engineering 322, DOI 10.1007/978-3-319-08991-1_47

working frequency band; 2. VSWR should be as small as possible and match the external circuit. In general, the power equalizer is passive. To implement the power equalizer, there are two main methods: one is to use an isolator and a lossless equalizing network, which can make the energy that the equalizer reflected be absorbed in the isolator; the second is to use a lossy equalizing network, the appropriate design makes the equalizer can satisfy the two requirements mentioned at the same time [3, 4]. There are four main types of the power equalizer, which are Lumped parameter type, Coaxial line type, Waveguide type and integrated transmission line type. However, the power equalizer of integration transmission line type has been widely used because of its various advantagements such as its small size, light weight, high bandwidth, high reliability, simple structure, easy fabrication and low cost. The majority of integrated transmission line power equalizers are mainly made of resistance loaded microstrip branch type, which is suitable for broadband microstrip equalization network [5, 6].

Based on the design principle and the equivalent model of broadband equalizer, a microstrip equalizer is proposed in this paper. Because of the RC parallel circuit installed in series, its high-pass characteristic makes the equilibrium effect better, the bandwidth wider, about 2–18 GHz, and structure simpler. The insertion loss and the Voltage Standing Wave Ratio (VSWR) of the equalizer are simulated, and the results show the feasibility and effectiveness of the design.

47.2 Basic Structural Analyses

As resonant network is the basic unit of the power equalizer, through reasonable topology of resonant network, we can get accurate equilibrium response curves. In this design, to reduce the size, the resonant network unit was structured by the terminals of the resistance load short circuit. A schematic view of the resonant cell structure of microstrip equalizer is shown in Fig. 47.1.

By the transmission line theory [7], the length of the microstrip short circuit branch is d, the input impedance of which is

$$Z_{\text{in}} = Z_0 \tanh(\alpha + \text{j}\beta)\text{d} \tag{47.1}$$

For the loss of the transmission line is very low, it can be approximately considered as the lossless transmission line, the attenuation constant $\alpha = 0$,

$$Z_{\text{in}} = Z_0 \text{j}\tan\beta\text{d} \tag{47.2}$$

As microstrip line has periodicity, when we lengthening the transmission line with quarter-wavelength's even times, we will get the same impedance at the input port. So, we can choose $n\lambda/4$as the value of the branches length, where n = 1, 3, 5. . .. . .etc. According to the relevant knowledge of microwave resonator, when $d = n\lambda/4$, n = 1.3.5. . .. . .etc, the short-circuited transmission line can be equivalent

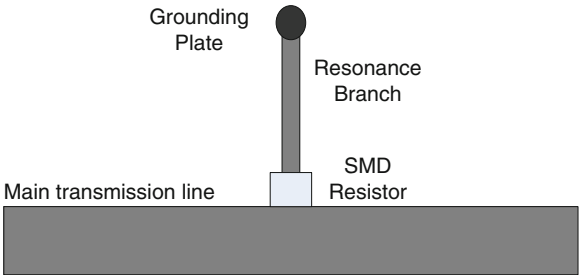

Fig. 47.1 Schematic of the resonant cell structure of microstrip equalizer

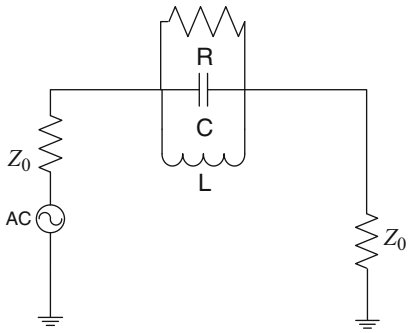

Fig. 47.2 Equivalent circuit of the microstrip resonance branch

to parallel resonance. We can get the equivalent circuit of the model in Fig. 47.1. Figure 47.2 shows the equivalent circuit.

The capacitance of the equivalent circuit is

$$C = \frac{\pi}{4\omega_0 z_0} \tag{47.3}$$

The inductance of the equivalent circuit is

$$L = \frac{1}{\omega_0^2 C} = \frac{4z_0}{\omega_0 \pi} \tag{47.4}$$

Among which, Z_0 is the characteristic impedance of transmission line, $\omega_0^2 = 1/LC$, ω_0 is the resonant frequency.

The input impedance of parallel RLC resonance circuit is

$$z_{in} = \left(\frac{1}{R} + \frac{1}{j\omega L} + j\omega C\right)^{-1} \tag{47.5}$$

According to the function, we can get

$$|z_{in}(\omega)|_{\max} = |z_{in}(\omega_0)| = R \tag{47.6}$$

As mentioned above, $d = \frac{n\lambda}{4}$, where n = 1, 3,5,7..... etc. When n = 1, $d = \frac{\lambda_g}{4} = \frac{v_p}{4f_0} = \frac{c}{4f_0\sqrt{\varepsilon_e}}$, is the Effective dielectric constant of the micro strip line. At this point, we can design the length of the resonance branch in the light of the required resonance frequency.

When designing the equalizer, we often make multiple resonance branches cascade together to obtain the results of the design requirements. For the microstrip resonant branch, changing the loading resistance R can turn the attenuation and Q value; Adjusting the length of the resonance branch, the resonance frequency and bandwidth can be adjusted accordingly; And the modification of the branch width is often used to fine tune the resonant frequency and attenuation [8, 9].

47.3 Design of Simulation and Implementation

We can use the microwave simulation software, HFSS, for modeling and simulation according to the principle mentioned above. In this paper, the plate type of microstrip transmission line used is RO4350, relative dielectric constant of which is 3.66, substrate thickness is 0.254 mm, and the microstrip line width is 0.5 mm. From the above formula, we can reckon d = 2.48 mm, when f_0 =18 GHz. When using single branch to simulate, we found that the value of equalization is too small, and the bandwidth is not enough wide, However, the equalizer is required to realize bandwidth of 2–18 GHz UWB, so we use the form of resistance loaded resonant branches with the similar length which are cascaded to establish the model in order to get good equalizing effect. Figure 47.3 is the equalizer's simulation model in HFSS.

In this figure, a number of rectangular blocks are set on both sides of resonance branches, which can be used to fine tune the transmission line width, and then the resonant frequency and attenuation. After model established, we optimize the length and width of each branch and the value of SMD resistor to get the transmission curve as shown in Fig. 47.4.

Simulation result shows that the curve of insertion loss within 6–18 GHz frequency band has good linearity and can well meet the requirements, but within 2–6 GHz, the curve rises, which indicates that it can't achieve the value of equalization within the required frequency band. Therefore, we make a RC parallel circuit connect in series with the main transmission line, which is used to suppress low frequency transmission, and makes the insertion loss satisfy the linearity in the whole frequency band. After optimization, we ultimately determine to add the RC parallel circuit between the first resonance stub and the second one to satisfy the requirements and get nice result. Figure 47.5 shows the improved simulation model.

In the Fig. 47.5, yellow rectangle block and black one represent the capacitance C and resistance R of parallel circuit in the red round frame, respectively.

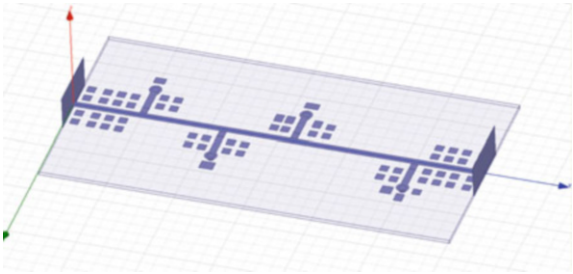

Fig. 47.3 Simulation model of equalizer in HFSS

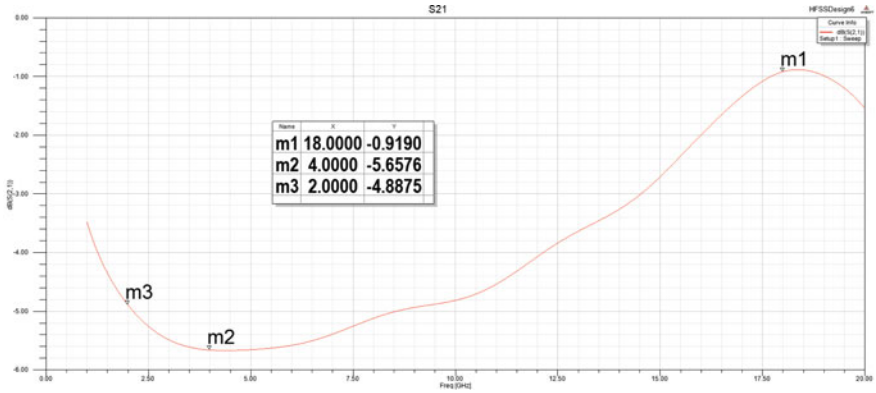

Fig. 47.4 The simulation result in HFSS

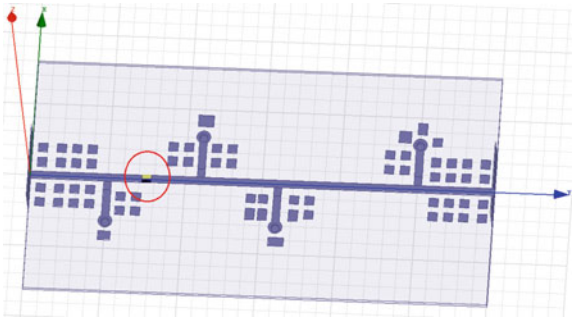

Fig. 47.5 The improved model

Through the optimization of HFSS, we get the result, the solid line, shown in Figs. 47.7 and 47.8. We can see, in the frequency band, the max attenuation is about 8 dB at 2 GHz. Insertion loss is less than 1.2 dB at 18 GHz, the value of equalization is about 7 dB, The input and output VSWR are both less than 2.

The amplitude equalizer is manufactured according to the modified model. The photograph of the equalizer is shown in Fig. 47.6. Finally, using vector network analyzer (VNA) to measure, we can get the measurement results, the dotted line, which are shown in Figs. 47.7 and 47.8. Compared to simulation results, we can see,

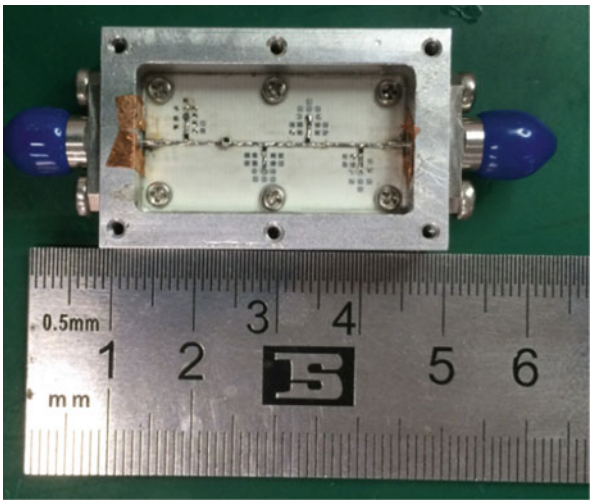

Fig. 47.6 Manufacture of the amplitude equalizer

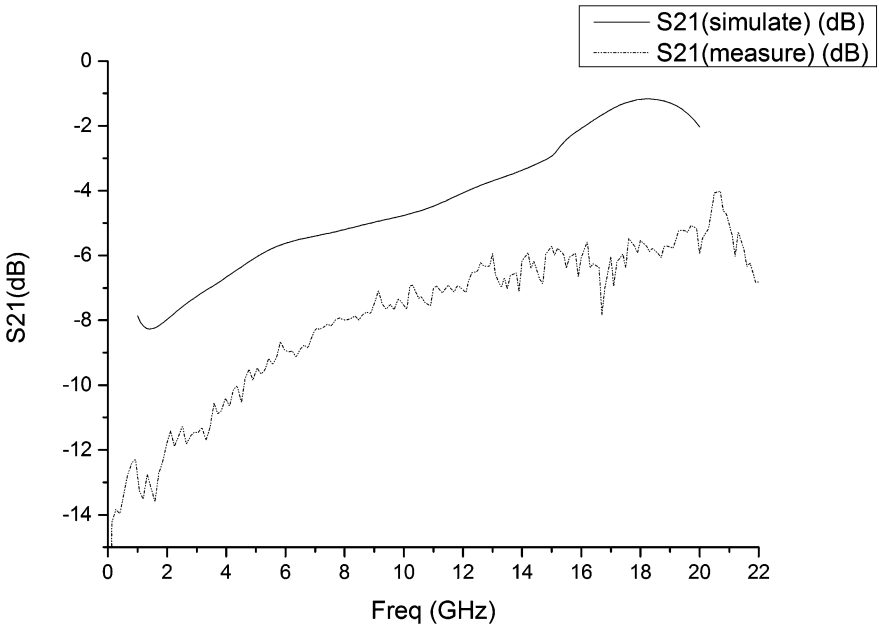

Fig. 47.7 The test results compared with the simulation results: S21

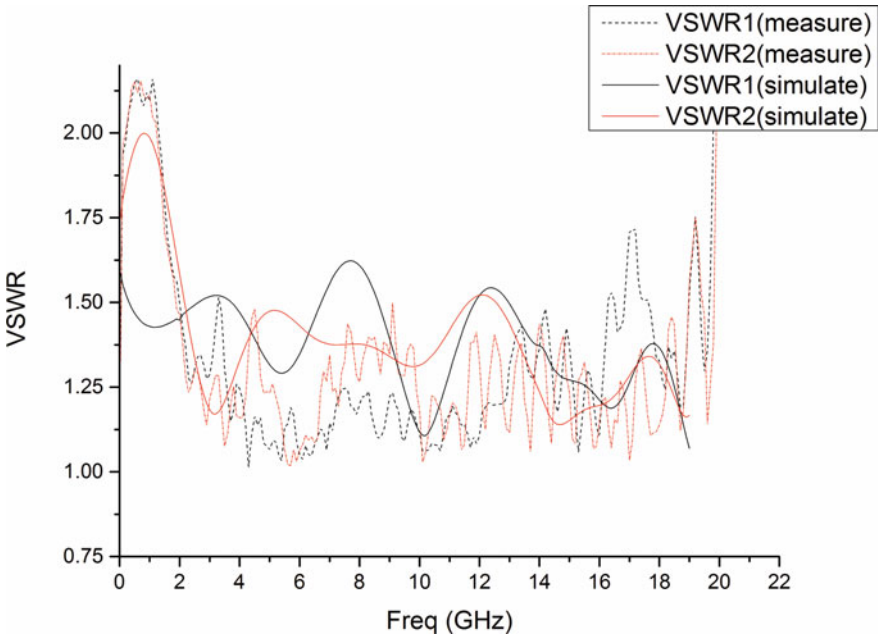

Fig. 47.8 The test results compared with the simulation results: VSWR

in consideration of the discontinuity of joint and the actual loss, the measurement results of insertion loss is inferior to the simulation results about 3 dB. But the input and output reflection coefficient is very well in the operating frequency band. By and large, the measurement result and the simulation curve meets well.

Conclusion

In this paper, we analyzed the basic structure of microstrip equalizer, and optimized the design by using the commercial software, Ansoft HFSS. In the design process, the frequency band whose attenuation characteristic was undesirable appeared near 2 GHz. In order to solve this problem, we added the RC parallel circuit, and finally worked out the microstrip equalizer. Its operation bandwidth is 2–18 GHz ultra-wideband, the value of equalization is about 7 dB, and input and output VSWR is less than 1.8. Compared the results we can see, the measured results meet with the simulation results well.

Acknowledgment This work was supported by the Fundamental Research Funds for the Central Universities Grant No.ZYGX2012J030.

References

1. Zhou T, Wang Z, Huan W, Xu R (2012) Design of microwave wave gain equalizer using microstrip shorted SIR. In: IEEE International Conference on Microwave and Millimeter Wave Technology (ICMMT), vol 5. pp 1–4
2. Kahng S, Moon W, Ju J (2007) Developing the 150%-FBW Ku-band linear equalizer. In: IEEE Asia-Pacific Microwave Conference (APMC) pp 1–3
3. Zhang S, Hua G, Wang P (2012) Design of UWB microstrip amplitude equalizer. Fire Control Radar Technol 41(2):51–54
4. Zhang Y, Xue K (2008) Microstrip power equalizer with great equal range. High Power Laser Part Beams 7:1147–1149
5. Liu Y, He Q, Hao J et al (2010) Design and implementation of 6 GHz ~18 GHz super-broadband micros-trip equalizer. Semicond Technol 35(1):23–26
6. Zhao Y, Zhou D, Niu Z et al (2007) A 12 GHz branch matched broad- band microstrip equalizer. Mod Radar 29(2):70–72
7. Pozar DM (2006) Microwave engineering, 3rd edn. Hoboken, Wiley
8. Lv D, Zhou D, Wang Z, Liu J (2012) Design of broadband equalizer. J Microw 28(5):93–96
9. Zhang Y, Yu M, Yan B, Xu R (2007) Research on the millimeter wave power equalizer. In: IEEE International Symposium on Microwave, Antenna, Propagation and EMC Technologies for Wireless Communications, pp 446–449

Chapter 48
Polar Code for Future 60 GHz Millimeter-Wave Communications

Zhuangkun Wei, Bin Li, and Chenglin Zhao

Abstract With high operating frequencies and high emission power, 60 GHz millimeter communications may suffer seriously from realistic hardware impairments. Among this, nonlinear power amplifier (PA) will significantly degrade its transmission performance. In order to decrease the bits error rate (BER) of 60 GHz millimeter communications, in this investigation a promising polar coding scheme is proposed. Based on the derivation of the general formulas of polar code, a new construction scheme for polar code is proposed. This designed polar code is further applied to 60 GHz systems with nonlinear PA. Experimental simulations verified the proposed coding scheme, which may significantly promote the transmission performance of 60 GHz communications. It is also demonstrated that the proposed polar coding scheme will surpass the popular LDPC code, which hence provides a great promise to practical use.

Keywords 60 GHz communication system • Nonlinearity • Polar code • LDPC

48.1 Introduction

With the potential of providing high data rate of Gbps, 60 GHz millimeter-wave (mm-Wave) communications have drawn the wide–wide attentions in recent years, which have also been considered as the promising candidate for the emerging 5th-generation (5G) communications. A major advantage of 60 GHz communications over other techniques is the enormous vacant bandwidth available at this mm-Wave band. For instance, the United States has assigned 57–64 [1] GHz for 60 GHz communications. Further adopting a large effective isotropic radiated power (EIRP), the achieved transmission rate may easily surpass IEEE 802.11n or UWB [2]. The carrier frequency modulation has also been recommended as a physical layer (PHY) solution due to its flexibility and implementation simplicity.

Z. Wei (✉) • B. Li • C. Zhao
Key Lab of Universal Wireless Communications, Beijing University of Posts and Telecommunications, Beijing, China
e-mail: zhuangkun1993@163.com; 1572833546@qq.com; Binli@bupt.edu.cn; clzhao@bupt.edu.cn

J. Mu et al. (eds.), *The Proceedings of the Third International Conference on Communications, Signal Processing, and Systems*, Lecture Notes in Electrical Engineering 322, DOI 10.1007/978-3-319-08991-1_48

However, 60 GHz communication also encounters some challenges from practical hardware impairments. Due to its high operating frequencies and high emission power, 60 GHz millimeter communications may suffer seriously from nonlinear power amplifier (PA) [3, 4], which will significantly degrade its transmission performance. It is well known the coding approach may reduce the bit error ratio (BER) even in the presence of nonlinear distortions, which can be suggested as a feasible approach to combat the performance degradation aroused by nonlinear PA.

Since the 60 GHz communications are mainly oriented toward high speed transmissions, the date rate is very huge and the frame length is therefore long. This may facilitate the designed coding scheme by concentrating on improving the transmission performance. For example, in the IEEE 802.11ad standard draft, low density parity code (LDPC) with a length of 672 bits can be specified in the encoding method [5]. Unfortunately, with the nonlinear PA, it is shown that even the long LDPC code is applied, the BER seems still to be less attractive to practical use (especially for the high-order modulations).

In this paper, we proposed a promising coding scheme to further promote the BER performance of 60 GHz communication with nonlinear PA. Firstly, based on the derivations of general formulas of polar code, a new construction scheme for polar code is proposed. This designed new polar code is further applied to 60 GHz systems. Experimental simulations verified the proposed coding scheme, which may significantly promote the transmission performance of 60 GHz communications. It is also demonstrated that, compared with the popular LDPC code, the proposed polar coding scheme may acquire more competitive BER performance, which hence provides a great promise to practical use.

In Sect. 48.2, we will introduce the channel model and hardware impairments in 60 GHz communication system. In Sect. 48.3, we discuss the property of polar code with arbitrary core matrix, and provide a new method for construction. In Sect. 48.4, we compare the BER performances of polar code with LDPC respectively utilizing QPSK, and 16QAM for modulation.

48.2 System Model

In order to compare the performances of polar code with LDPC in 60 GHz communication system, a simulation system has been designed in Fig. 48.1. The source port generates random binary bits of data into code part where the polar code and LDPC is used respectively. Then, the codes pass through modulation part that will map them into baseband complex signals. Next, signals are distorted by nonlinear PA, and go through the channel by adding complex Gaussian noise to the receiver. Finally, signals demodulate into binary bits and get decoded.

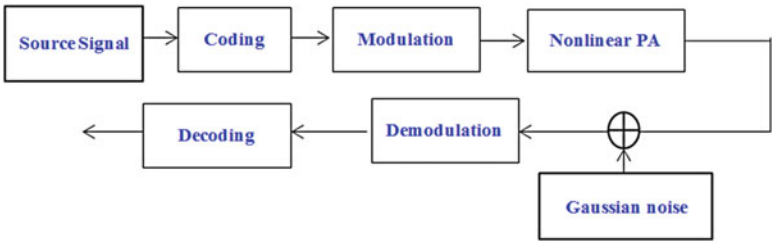

Fig. 48.1 System model

48.2.1 Nonlinearity of PA

After modulation signals passed through a PA with a high frequency, the nonlinear distortions will occur. The influences of nonlinearity contain the distortions of amplitudes and phases on out-put signals [5], which may be usually characterized by the (amplitude-modulation amplitude modulation) AM–AM model and (amplitude-modulation phase modulation) AM–PM respectively. The two mathematical models care specified as following,

$$G(A) = g\frac{A}{\left(1+\left(\frac{gA}{A_{sat}}\right)^{2s}\right)^{\frac{1}{2s}}} \tag{48.1}$$

$$\varphi(A) = \frac{\alpha A^{q1}}{\left(1+\left(\frac{A}{\beta}\right)^{q2}\right)} \tag{48.2}$$

According to IEEE 802.11ad, A and $G(A)$ represent the amplitude of input and output respectively, the latter of which has a saturation that $A_{sat} = 0.58$, while g, the linear gain, take the value at 4.65. Parameter $s = 0.81$ denotes smoothness of the inflection point of distortion. In the latter expression, $\varphi(A)$ denotes the distortion of PM, and parameters $\alpha, \beta, q1, q2$ take value at 2,560, 0.114, 2.4, 2.3, respectively.

Figure 48.2 shows the mapping curve of AM–AM and AM–PM, from which we may note that the distortions are massive with the increasing of input amplitudes.

48.3 Polar Code for 60 GHz Communications

Polar code is a kind of $\mathbf{G}_N$-Coset Code inspired by a phenomenon called channel polarization, which can be achieved by recursively combining with N channel $W : \mathbf{X} \rightarrow \mathbf{Y}$, and then splitting the combined channels into N channels through information theory. With this method, the capacity of some channels is nearly to 1, while the rest of them are close to 0.

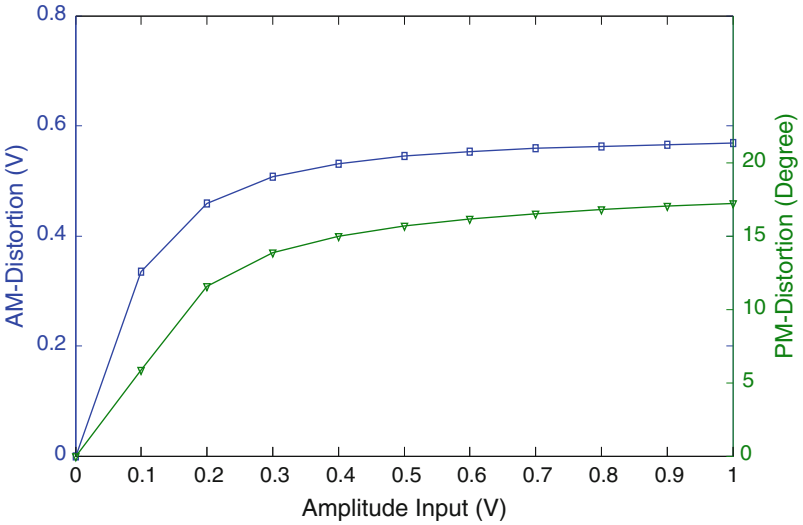

Fig. 48.2 Plot of distortions of nonlinear PA

We firstly utilize a_i^j to denote a vector $(a_i, a_{i+1}, \ldots, a_j)$, where i, j are natural numbers with normally $i \le j \cdot a_i^j$ is regarded as void while $i > j$.

We define $\mathbf{F}$ is a l - by - l matrix with entries in $\{0, 1\}$, and U_1^l is a l-vector, whose elements are all random variables (RV) with a uniformly distributed over $\{0, 1\}$.

48.3.1 Channel Combining

In Fig. 48.3, for any $N = l^n$, the recursive process that produces W_{N} through $W_{N/l}$, is called channel combining [7].

The parameter $\mathbf{R}_N^l$ is a permutation matrix, mapping the vector $\mathbf{V}_1^{\mathrm{N}}$ onto the vector $\mathbf{V}_{1,k}^N = (V_k, V_{l+k}, \ldots, V_{ml+k})$, $k = 1, 2, \ldots, l$, where $ml \le N < (m+1)l$. Base on the above recursive structure, the propagations of transition probabilities can be calculated below,

$$W_N\left(y_1^N \middle| u_1^N\right) = \prod_{k=1}^{l} W_{N/l}\left(y_{kN/l+1}^{(k+1)N/l} \middle| \mathbf{V}_{1,k}^N\right) \tag{48.3}$$

48.3.2 Channel Splitting

Based on the information theory, we can split the combining channel back to N-numbers of channels $\{W_N^i : \mathbf{X} \to \mathbf{Y}^N \times \mathbf{X}^{i-1} \;\; 1 \le i \le N\}$, each of which has the

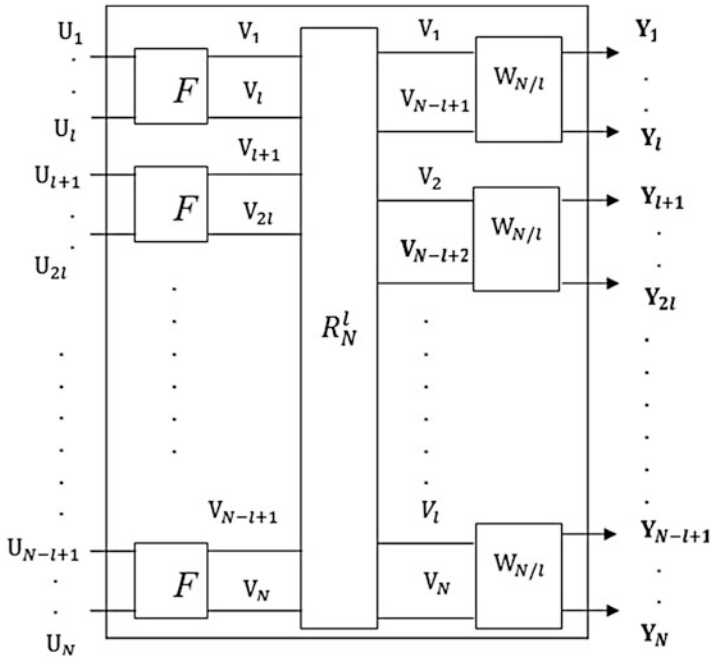

Fig. 48.3 *N*th recursive step of channel combining

recursive transition probabilities in expression (48.4), where we have $v_{(i-1)l+1}^{il} = u_{(i-1)l+1}^{il} \cdot \mathbf{F}$. For any $1 \le i \le \frac{N}{l}$ and $1 \le j \le l$,

$$\begin{aligned} & W_N^{l(i-1)+j}\left(y_1^N, u_1^{l(i-1)+j-1} \middle| u_{l(i-1)+j}\right) \\ & = \frac{1}{2^{l-1}} \sum_{u_{l(i-1)+j+1}}^{u_{li}} \prod_{k=1}^{l} W_{N/l}^{i}\left(y_{kN/l+1}^{(k+1)N/l}, \mathbf{v}_{1,k}^{l(i-1)} \middle| \left(u_{l(i-1)+1}^{li} \cdot \mathbf{F}\right)_k\right. \end{aligned} \tag{48.4}$$

48.3.3 Construction of Polar Code

In this section, we give an examples of construction based on a different form of matrix **F**. The basic idea of polar coding is to create a coding system where one can access each coordinate channel W_N^i individually, and send data only through those for which $Z(W_N^i)$ is approaching to 0.

G_N-Coset Code:
The main task is to create $\mathbf{G}_N$ for coding. Given any $N = l^n$, we have u_1^N as the source block waiting for coding, among which k, $(k < n)$ bits are for data transmission, and the rest of which are frozen bits that can be transmit any arbitrary bits. Thus, we have expression below,

$$x_1^N = u_1^N \mathbf{G}_N \tag{48.5}$$

Then we define $\mathbf{I}_m$ as a m-dimensional Identity matrix for any $m \geq 1$. By recursively operating the process in Fig. 48.3, we have the recursive formulas below,

$$\mathbf{G}_N = \mathbf{B}_N \mathbf{F}^{\otimes \mathrm{n}} \tag{48.6}$$

$$\mathbf{B}_N = \mathbf{R}_N^l \left(\mathbf{I}_l \otimes \mathbf{B}_{N/l}\right) \tag{48.7}$$

with $\mathbf{G}_1 = \mathbf{I}_1$.

If a subset $\mathcal{A} \subseteq \{1, 2, \ldots, N\}$ that satisfies $\forall i \in \mathcal{A}, \forall j \in \mathcal{A}^{\mathrm{C}}$, $Z\left(W_N^i\right) < Z\left(W_N^j\right)$, with $|\mathcal{A}| = k$, where $Z(W)$ is a Bhattacharyya parameter, the subset $\mathcal{A}$ is chosen for data transmission and $\mathbf{u}_{\mathcal{A}^{\mathrm{C}}}$ are frozen bits.

Example Here we give an example of polar code based on the matrix $\mathbf{F} = \begin{bmatrix} 1 & 0 & 0 \\ 1 & 0 & 1 \\ 1 & 1 & 1 \end{bmatrix}$ instead of $\mathbf{F} = \begin{bmatrix} 1 & 0 \\ 1 & 1 \end{bmatrix}$, the classical example offered by Erdal Arikan. The channel $W : \mathbf{X} \to \mathbf{Y}$ is a BEC whose input alphabet $\mathbf{X}$ is $\{0, 1\}$, and output alphabet $\mathbf{Y}$ is $\{0, E, 1\}$ with an erasure probability $\epsilon = 0.1$. Hence, we have $l = 3$.

For any $1 \leq i \leq N/3$, we have,

$$Z\left(W_N^{3i-2}\right) = -Z\left(W_{N/3}^i\right)^3 + Z\left(W_{N/3}^i\right)^2 + Z\left(W_{N/3}^i\right) \tag{48.8}$$

$$Z\left(W_N^{3i-1}\right) = -Z\left(W_{N/3}^i\right)^2 + 2Z\left(W_{N/3}^i\right) \tag{48.9}$$

$$Z\left(W_N^{3i}\right) = Z\left(W_{N/3}^i\right)^3 \tag{48.10}$$

$$\text{with } Z\left(W_1^1\right) = \epsilon$$

Successive Cancellation Decode: We firstly define the likelihood ratio below,

$$L_N^i\left(y_1^N, \hat{u}_1^{i-1}\right) = \frac{W_N^i\left(y_1^N, \hat{u}_1^{i-1} \middle| \hat{u}_i = 0\right)}{W_N^i\left(y_1^N, \hat{u}_1^{i-1} \middle| \hat{u}_i = 1\right)} \tag{48.11}$$

The parameter $\hat{u}_i$ is the decision for u_i. Obviously, if $L_N^i(y_1^N, \hat{u}_1^{i-1}) > 1$, we consider the sending $u_i = 0$, and $u_i = 1$ otherwise.

Now, we create a recursive butterfly process for the *SC* decoding, whose complexity can be measured by $O(N \log N)$. Especially in the example we mentioned above, the log base is 3. Before we give the full recursive expression, a group of variables are defined for clarity.

$$\begin{cases} \alpha = L_{N/3}^{i}\left(y_1^{N/3}, \hat{u}_{1,1}^{3i-3} \oplus \hat{u}_{1,2}^{3i-3} \oplus \hat{u}_{1,3}^{3i-3}\right) \\ \beta = L_{N/3}^{i}\left(y_{N/3+1}^{2N/3}, \hat{u}_{1,3}^{3i-3}\right) \\ \gamma = L_{N/3}^{i}\left(y_{2N/3+1}^{N}, \hat{u}_{1,2}^{3i-3} \oplus \hat{u}_{1,3}^{3i-3}\right) \end{cases}$$

Then, the recursive expressions are below,

$$L_N^{3i-2}\left(y_1^N, \hat{u}_1^{3i-3}\right) = \frac{\alpha\beta\gamma + \alpha\gamma + \beta + 1}{\beta\gamma + \alpha\beta + \alpha + \gamma} \tag{48.12}$$

$$L_N^{3i-1}\left(y_1^N, \hat{u}_1^{3i-2}\right) = \left(\frac{\alpha\beta\gamma + 1}{\beta + \alpha\gamma}\right)^{(1-\hat{u}_{3i-2})} \cdot \left(\frac{\beta\gamma + \alpha}{\alpha\beta + \gamma}\right)^{\hat{u}_{3i-2}} \tag{48.13}$$

$$L_N^{3i}\left(y_1^N, \hat{u}_1^{3i-1}\right) = \alpha^{(1-2\hat{u}_{3i-2})(1-2\hat{u}_{3i-1})}\beta\gamma^{(1-2\hat{u}_{3i-1})} \tag{48.14}$$

48.4 Experimental Evaluations

In the experimental simulations, we mainly focus on the line-of-sight (LOS) scenarios, in which the first LOS path may have an extremely strong energy [11]. This is justified by wide adoptions of beam-forming techniques [12]. In this case, the single-path complex Gaussian channel can be used for the simplicity of analysis. The code rate is fixed at 1/2, the erasure probability (ϵ) is 0.1. We choose $\mathbf{u}_{\mathcal{A}^c}$ as a $\mathbf{0}$ vector. In the experiments, the classical polar code posed by Erdal Arikan (i.e., $l = 2$), which is denoted by polarcode2, is also used for comparative analysis. Meanwhile, the popular LDPC scheme approved by the IEEE 802.11ad standard is adopted.

In our analysis, two high-order modulation schemes, i.e., QPSK and 16-QAM are employed. The BER performances of these two modulated signals are plotted by Figs. 48.4 and 48.5, respectively. First, we note that, the BER performance of both polar code and LDPC will be reduced, compared with the non-code situation. Thus, the coding scheme can be viewed as the effective approach to combat the realistic nonlinearity. Second, it is seen that, in both QPSK and 16-QAM signals, the polar code may surpass the popular LDPC in high SNR regions. Taking the QPSK signals of SNR = 2dB for example, the BER may even approach 8×10^{-3}. In comparison, the BER value of LDPC is only 4×10^{-2}. Roughly, a detection gain of 0.6 dB can be acquired by the polar code. Third, it is shown that the 16-QAM is more vulnerable to 60 GHz nonlinear PAs (NLPA), compared with the ideal linear PA (LPA). Finally, we may note that, in the case of NLPA with 16QAM signals, the designed polar code seems to be comparative with the class polar code of $l = 2$, which (with $l = 3$), however, may be of more flexibility and efficiency in frame designing and multicomplexity.

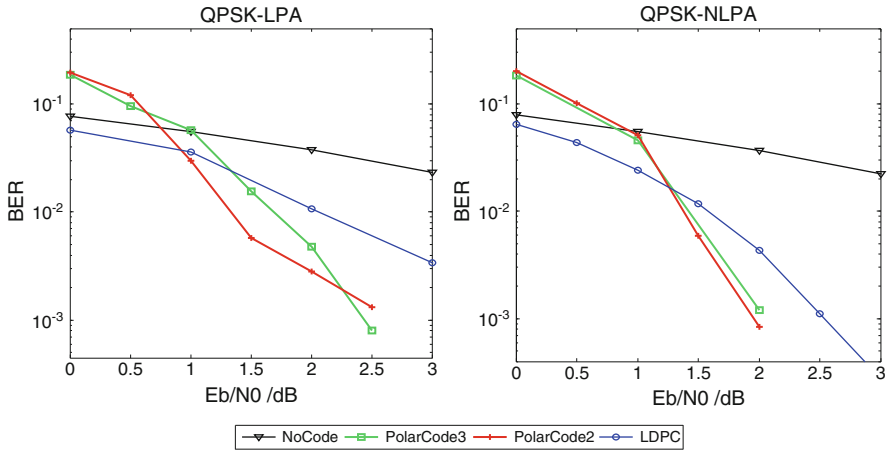

Fig. 48.4 BER performance of QPSK modulated signals

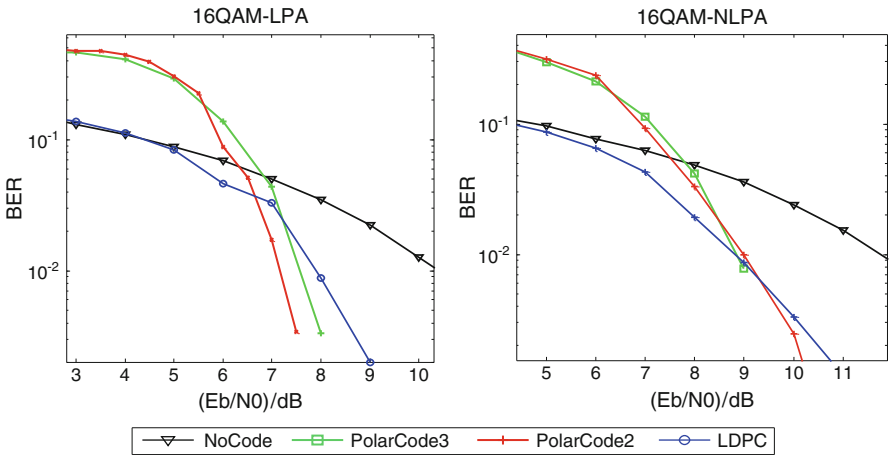

Fig. 48.5 BER performance of 16-QAM modulated signals

Conclusion

The transmission performance of 60 GHz mm-Wave communications is significantly subjected to hardware impairments, especially the evitable nonlinearity of PA. To deal with such drawbacks, polar code is proposed for 60 GHz systems in this investigation. The provided experimental simulations have verified the proposed polar coding scheme, which may obtain more promising BER performance in the presence of either linear PA or nonlinear PA. By significantly reducing the BER, this new polar code scheme may be considered as a potential candidate for the emerging 5G mm-Wave communications of extremely high data rates.

References

1. Federal Communications Commission (2001) Code of federal regulations, part 15-radio frequency devices section 15.255: operation within the band 57.0–64.0 GHz. http://law.justia.com/cfr/title47/47-1.0.1.1.12.html#47:1.0.1.1.12.3.236.35. Jan 2001
2. Yong SK, Xia P, Valdes-Garcia A (2011) 60 GHz technology for Gbps WLAN and WPAN. Wiley, Chichester, pp 2–5
3. Lei M, Lakkis I, Sum CS et al (2008) Hardware impairments on LDPC coded SC-FDE and OFDM in multi-Gbps WPAN (IEEE 802.15.3c). In: Wireless communications and networking conference, New Jersey, Mar. 31–Apr. 3, pp 442–446
4. Sum CS, Funada R, Wang J et al (2009) Error performance and throughput evaluation of a multi-Gbps millimeter-wave WPAN system in multipath environment in the presence of adjacent and co-channel interference. IEEE J Sel Area Commun 27(8):1433–1442
5. IEEE 802.11ad (2012) Part 11: wireless LAN medium access control (MAC) and physical layer (PHY) specifications amendment 3: enhancements for very high throughput in the 60 GHz band
6. Perahia E, Park M, Stacey R et al (2010) IEEE P802.11 wireless LANs TGad evaluation methodology. IEEE 802.11 TGad technology report 09/0296r16, 2010: 3–5, 9–15.
7. Arikan E (2009) Channel polarization: a method for constructing capacity achieving codes for symmetric binary-input memoryless channels. IEEE Trans Inf Theory IT-55:3051–3073
8. Gallager RG (1968) Information theory and reliable communication. Wiley, New York
9. Kato S, Harada H, Funada R et al (2009) Single carrier transmission for multi-gigabit 60-GHz WPAN system. IEEE J Sel Area Commun 27(8):1466–1478
10. Xu H, Liu K (2010) Research on wireless communication networks in the 60 GHz frequency band. In: International conference on internet technology and applications, Wuhan, 20–22 Aug 2010, pp 1–4
11. Li B, Zhao C et al (2014) Joint channel estimation and signal detection for 60 GHz millimeter-wave communication with nonlinear power amplifier. In: Proceedings of international communication conference (ICC 2014), Sydney, Aug 2014, pp 1–6
12. Li B, Zhou Z, Zou W et al (2013) On the efficient beam forming training for 60 GHz wireless personal area networks. IEEE Trans Wireless Commun 12(2):504–515

Chapter 49
The Recognition of Human Activities Under UWB Communication

Yi Zhong, Zheng Zhou, and Ting Jiang

Abstract This paper presents a novel human activity recognition method that uses UWB signals to enable a low clutter outdoor environment sensing and recognition of human activities, which can transmit the information and identify human activities simultaneously. Since UWB signals do not require line-of-sight and have very good ability of penetration, the proposed method can enable a low clutter outdoor environment human activities recognition using the UWB signals in wireless communication. Further, it achieves this goal for a through-targets scenario and without requiring seeing devices (e.g., camera, radar). We evaluate the proposed method using UWB signals in a playground, with eight human subjects performing eight different activities. The type of the human activities performed between the transmitter and receiver of UWB communication system can have significant effects on the shape of the received signal waveform. From these time-varying signals, we extract features that are representative of the activities types based on 1-D diagonal slice of fourth-order cumulant within a time window. Then, we use support vector machine (SVM) to realize the human activities identification. Our results show that proposed method can identify and classify a set of eight activities with an average accuracy of 99.2 %.

Keywords Human activities recognition • UWB signals • Fourth-order cumulant • Support vector machine

49.1 Introduction

Recognition of human activities is currently one of the most active research topics in computer vision and radar to both military and civilian research. This strong interest is driven by a wide spectrum of promising applications in many areas such as smart surveillance, virtual reality, advanced user interface, etc.

Y. Zhong (✉) • Z. Zhou • T. Jiang
Key Laboratory of Universal Wireless Communication, Ministry of Education, Beijing University of Posts and Telecommunications, Beijing 100876, China
e-mail: zhongyim2m@gmail.com

J. Mu et al. (eds.), *The Proceedings of the Third International Conference on Communications, Signal Processing, and Systems*, Lecture Notes in Electrical Engineering 322, DOI 10.1007/978-3-319-08991-1_49

There have been many studies in the past to identify human activities based on computer vision and visual analysis from image sequences involving humans. Two types techniques are used in feature tracking for recognition: template matching [1] and state-space approaches [2]. Although recognition of human actions has been accomplished in many computer vision studies, there exists a trade-off between computational cost and accuracy. The use of radar is another unique way to detect and monitor humans. In recent years, there have been many efforts undertaken to investigate human motion detection with Doppler radar [3], ultra-wide band (UWB) radar [4] and WiFi-Based Passive Bistatic Radar [5]. However, the use of radar is limited for the through-targets scenario because all the targets are identified by analyzing echo data. All above typical method for human activities recognition involves the burdens of instrumentations (e.g., camera, radar) or complex iterative computation. Especially, recognition with computer vision are limited to detect people for a dark environment, and may be infeasible in many scenarios (e.g., in a shower) that people are not willing to be recorded in the camera.

UWB are frequently employed for target identification in recent years owning to the following characteristics: (1) strong penetrability, (2) high resolution rate and (3) good anti-interference ability. Several studies have shown promising results on detecting and classifying humans in obscured by foliage environments using UWB signals without requiring specific novel sensing and vision devices [6, 7]. In their studies, all the targets such as humans are identified through the UWB wireless communication system. In [8], a shape of the received pulse is analyzed. The statistical characteristics of received signal that are representative of the target types were suggested to extract and a human could be successfully detected. The study focused on the detection of humans but not on the human's activity.

In this paper, we investigate the feasibility of classifying human activities using through-human UWB signals in wireless communication system. Depending on different human activities, the change of received signals has its own characteristics. By exploiting the features of the UWB signal, our approach can recognize eight different human activities including walking, running, rotating, boxing, jumping, transitioning between standing and sitting, crawling, and standing still with high recognition rate. The method is applied to classify human activities consists of extracting features of the received UWB signals using the fourth-order cumulant and analyzing the time-varying behaviors of those features. Then, we use a support vector machine (SVM) to realize the human activities identification based on the processed features. Low clutter outdoor environment experiments have been conducted to test the performance of the new approach.

The paper is organized as follows. In Sect. 49.2, a brief introduction of data measurement and collection in real scenarios is provided. In Sect. 49.3, fourth-order cumulant classification approach within a time window using SVM is explained. The obtained experimental results are illustrated in Sect. 49.4. Finally, conclusions are given in section "Conclusions".

49.2 Measurement of Different Human Activities Using UWB Signals

Measured data based on the received UWB signals of eight human subjects undergoing different activities are collected using a UWB communication system. The measurements were taken using PulsON 400 (P400) RCM by the Time Domain Co., Ltd. The P400 RCM operating band is from 3.1 to 5.3 GHz, with center frequency 4.2 GHz. Time Domain Broadspec toroidal dipole antennas are used for transmitting and receiving antennas, the gain of the antenna is about 3 dbi. The P400 RCM is controlled by a PC and data are recorded digitally. The measurements are performed in a low clutter outdoor environment (e.g., playground). Only a single human subject is tested at one time, with the subject moving directly forward and backward between the UWB-IR transmitter (TX) and UWB-IR receiver (RX) of the communication systems. The range of the measurement is 10 m.

In this study, data for human subjects undergoing eight different activities are collected by the received signals in the UWB communication system. They are (1) walking, (2) running, (3) rotating, (4) boxing, (5) jumping, (6) transitioning between standing and sitting, (7) crawling and (8) standing still as presented in Fig. 49.1a. A photo of the measurement set-up is shown in Fig. 49.1b. The descriptions of each activity are given in Table 49.1. This translates to each motion being recorded around 120 s. In the measurement, the human subject performs the eight activities between TX and RX of the UWB communication system.

49.3 Method of Human Activities Recognition

49.3.1 Features Extraction Based on Higher Order Cumulants

As the type of human activity varies, the complex scattering from the human subject changes the entire shape of the received signal. We can see that the waveforms of the received UWB signals show rather interesting differences depending on the activity. As we expect to capture the distinct differences of the received UWB signals when human perform different activities, it is necessary to extract features to compare the shape of the received signals of human subject.

In modern signal processing theory, there are many techniques available for feature extraction. They include higher order cumulant (HOC), time-frequency analysis, wavelet transform, etc. In this study, we use higher order cumulant because Gaussian noise can be completely inhibited by HOC and characteristics can be very rich after any HOC. A non-Gaussian signal can be decomposed into its higher order cumulant functions where each one of them may contain different information about the signals [9]. This can be very useful to extract distinct classification features of received UWB signals from human subject in higher

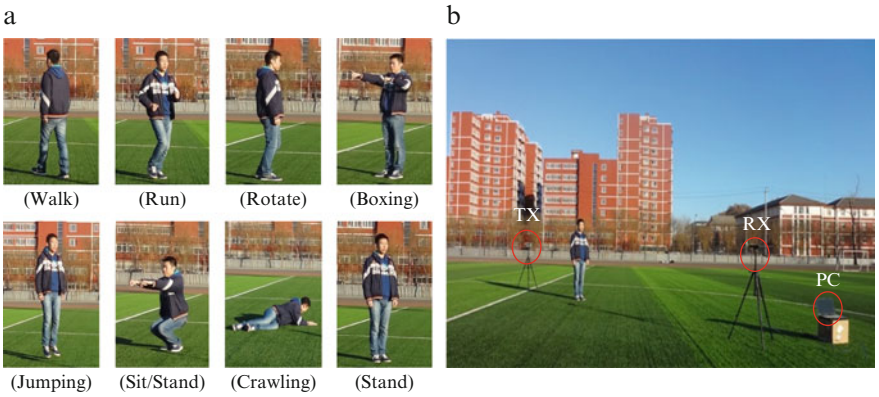

Fig. 49.1 Activities to be recognised under UWB communication. (**a**) Eight different human activities. (**b**) Measurement setup

Table 49.1 Eight human activities under study

Activity	Description
(i) Walking	The act of walking forward and backward at a moderate speed while moving arms and legs.
(ii) Running	The act of running forward and backward quickly by moving arms and legs.
(iii) Rotating	The act of rotating clockwise or counter clockwise at the same distance.
(iv) Boxing	The act of throwing punches using both arms continuously while standing still.
(v) Jumping	The act of jumping upward continuously while staying in one place.
(vi) Sitting/ standing	The act of transitioning between standing and sitting continuously while staying in one place.
(vii) Crawling	The act of crawling on both hand and knees while staying in one place.
(viii) Standing still	The act of standing still while staying in one place.

order domain. Furthermore, in order to extract distinct features from a waveform, it is necessary to distinguish the received UWB signal from noise. The noise is found to have a Gaussian-like distribution. Suppose UWB signals $x(t)$ exist in addition to Gaussian noise $e(t)$, and we have received UWB signals $y(t) = x(t) + e(t)$; then

$$\begin{aligned} &C_{ky}(\tau_1, \tau_2, \cdots, \tau_{k-1}) \\ &\quad = C_{kx}(\tau_1, \tau_2, \cdots, \tau_{k-1}) + C_{ke}(\tau_1, \tau_2, \cdots, \tau_{k-1}) \end{aligned} \tag{49.1}$$

where C_{ky}, C_{kx} and C_{ke} respectively denote the kth-order cumulant of $x(t)$.

Since $e(t)$ is Gaussian and $k \geq 3$ then, $C_{ky}(\tau_1, \tau_2, \cdots, \tau_{k-1}) = C_{kx}(\tau_1, \tau_2, \cdots, \tau_{k-1})$, whereas $C_{2y}(\tau) = C_{2x}(\tau) + C_{ke}(\tau)$. This makes the HOC of Gaussian process and even the colored Gaussian process constantly zero. In essence, cumulants can draw the UWB signals out of Gaussian noise, thereby boosting their signal-to-noise ratios.

However, if a random process is symmetrically distributed, then its third-order cumulant equals zero, whereas some nonsymmetrical process have extremely small third-order cumulant and much larger fourth-order cumulant; hence, we would use latter in many specific applications. In fact, to avoid the computation complexity of the fourth-order cumulant, 1-D slices of the fourth-order cumulant is usually applied in signal processing. In this paper, we derive the 1-D diagonal slice of fourth-order cumulant to extract features of received UWB signals. This means the received signal $x(t)$ can be represented using its 1-D diagonal slice of fourth-order cumulant, that is:

$$\begin{aligned} C_{4x}(\tau) &= E\{x(t)x(t+\tau)x(t+\tau)x(t+\tau)\} \\ &\quad - 3C_{2x}(\tau)C_{2x}(0) \\ &= E\left\{x(t)x^3(t+\tau)\right\} - 3E\{x(t)x(t+\tau)\}E\left\{x^2(t)\right\} \end{aligned} \tag{49.2}$$

where $C_{4x}(\tau)$ denotes the 1-D diagonal slice of fourth-order cumulant of $x(t)$, and $\tau_1 = \tau_2 = \tau_3 = \tau$.

49.3.2 Training Eature Set Generation

We require a training data set for a classifier implemented using a machine learning technique. The features can be represented as the 1-D diagonal slice of fourth-order cumulant of received signal. As some motions shows the similar or identical posture in time, there is a high chance that extracted features from different activity look nearly identical which cause high levels of error in the classification process. Therefore, the features must be further processed before the SVM could be trained for classification. To do this, the variance of features of each motion was computed across a 20 s overlapping sliding time window. In this paper, the data set is constructed by computing variance and mean of the features to classify each motion based on its instantaneous and time varying features, which consists of eight human subjects performing eight activities. Each human subject repeats a particular activity for 120 s for different times.

49.3.3 Classification Using Support Vector Machine

We use an SVM to classify the eight human activities based on the variance and mean of features of the received UWB signals from human target. SVM is a powerful data-driven model that has been used in a number of applications. As SVM is a binary classifier, we detect and classify the eight human activities by incorporate multi-classification techniques. In this paper, we choose one vs. one method (the majority vote) for the multi-class problem. This method process is rather fast and exhibit higher accuracy compared with other methods.

We use LibSVM, a freely available SVM library implemented by Chang and Lin [10]. The data recorded were separated into two sets for processing. The first set is referred to as the training set, which is used as the basis for training of SVM. The other set of data is the validation set, which is used to test the accuracy of the classification algorithm. To maintain a more realistic investigation of this classification technique, the training and testing sets do not include any overlap in data. We use 1/4 of the data as the training set for each SVM and 3/4 for testing the accuracy of the classification. In the SVM training process, the radial basis function (RBF) kernel function is selected because it is the most commonly used kernel for its powerful performance. The penalty parameter c of the SVM and the RBF kernel function width g is searched exhaustively by grid search parameter optimization approach to minimize average classification error for each SVM.

49.4 Experimental Results and Analysis

49.4.1 Experimental Results

In this paper, we investigate the feasibility and effect of detecting and classifying different human activities in a low clutter outdoor environment using UWB signals. The experiments were conducted in a playground, and the measurement data were collected in winter 2013. During the test period, the weather was little cold, with 10–12 °C temperature and 1–2 wind force level. The eight human activities and the test scene in the playground are shown in Fig. 49.1a and b, respectively.

In the experiments, the human activities were classified using SVM based on the 1-D diagonal slice of fourth-order cumulant of the received signals. For each type of human activity, we extracted 50 samples from the measurement data from each human target to form the data set for each human activity. So a dataset including 400 samples for each human activity is established. All samples in the dataset are divided into two sets, the training set includes 100 samples and the test set includes 300 samples. To increase the certainty of the results obtained, the training set were generated randomly and testing sets do not include any overlap in data. Then the target detection and recognition model is established based on the SVM method. The recognition rates using 1-D diagonal slice of fourth-order cumulant alone as the features are shown in Table 49.2. Given the same classifier SVM, we use the variance and mean of 1-D diagonal slice to recognize motion types. The recognition rates and identification results are shown in Table 49.3 and Fig. 49.2 respectively.

Table 49.2 Classification accuracy of human activity based on 1-D diagonal slice of fourth-order cumulant

Classification accuracy (%)			
Walking	Running	Rotating	Boxing
55	23	23	62
Jumping	Sitting/Standing	Crawling	Standing still
43.67	35.33	97	63.33

Table 49.3 Classification accuracy of human activity based on variance and mean of 1-D diagonal slice of fourth-order cumulant

Classification accuracy (%)			
Walking	Running	Rotating	Boxing
100	97	99.67	99.33
Jumping	Sitting/standing	Crawling	Standing still
99.33	99.67	100	98.67

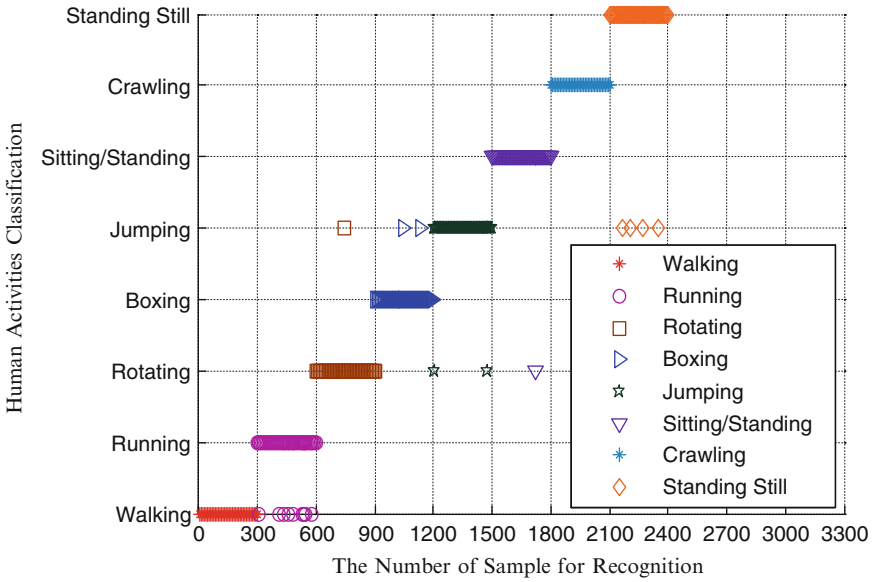

Fig. 49.2 Recognition results based on variance and mean of 1-D diagonal slice of fourth-order cumulant

49.4.2 Experimental Analysis

We can see from Table 49.2, the ability of the method only using 1-D diagonal slice as the features to classify human activity is, in general, not very accurate. Even though the crawling motion was quite easily classified, the average accuracy is 50.29 % which is not conclusive. This is because the position of a human in two different motions maybe looks nearly identical in a certain instant. Therefore the features directly extracted from signals may include identical information which causes high levels of error in the classification process. From Table 49.3, it can be seen that the recognition rates of the

variance and mean of 1-D diagonal slice are higher than those of 1-D diagonal slice alone, regardless of the types of motions. All human activities recognition rates are higher than 97 %, and the average accuracy of the classification is 99.2 %.

Conclusions

In this paper, we investigated the feasibility of classifying different human activities using the received UWB signals based. Data were collected using a UWB communication system and processed using 1-D diagonal slice of fourth-order cumulant. The statistical variance and mean as seen through a 20 s sliding time window were used for the features of SVM. Our experiments show that the average accuracy of recognition rate is more than 99.2 %. From the obtained experimental results, we can strongly recommend the use of the UWB communication approach for human activities detect and recognition. Compared with the traditional techniques, our experimental system cannot only detect the motion for a through-human scenario but also classify and recognize the types of motions with high recognition rate under environmental conditions such as haze, fog or at night.

Acknowledgment This work was supported by NSFC (61171176).

References

1. Bobick A, Davis J (2001) The recognition of human movement using temporal templates. IEEE Trans Pattern Recognit Mach Intell 23:257–267
2. Pavlovic V, Rehg JM, MacCormick J (2000) Learning switching linear models of human motion. In: Advances in neural information processing systems. MIT, Cambridge, pp 981–987
3. Kim Y, Ling H (2009) Human activity classification based on micro-Doppler signatures using a support vector machine. IEEE Trans Geosci Remote Sens 47(5):1328–1337
4. Bryan JD, Kwon J, Lee N, Kim Y (2012) Application of ultra-wide band radar for classification of human activities. IET Radar Sonar Navig 6(4):172–179
5. Guo H, Woodbridge K, Baker C (2009) Target detection in high clutter using passive bistatic WiFi radar. In: Proc. of IEEE Radar Conference 2009, 4–8 May 2009, pp 1–5
6. Zhai S, Jiang T (2013) A novel sense-through-foliage target recognition system based on sparse representation and improved particle swarm optimization-based support vector machine. Meas: J Int Meas Confed 46(10):3994–4004
7. Zhai S, Jiang T (2014) Target detection and classification by measuring and processing bistatic UWB radar signal. Meas: J Int Meas Confed 47:547–557
8. Zhai S, Jiang T (2014) Sparse representation-based feature extraction combined with support vector machine for sense-through-foliage target detection and recognition. IET Signal Process 8(5):458–466
9. El-Khamy SE, Elsayed HA, Rizk MRM (2012) Neural network for classification of multi-user chirp modulation signals using wavelet higher order statistics features. Int J Emerg Technol Adv Eng 2(8)
10. Chang C C, Lin C J. (2011) LIBSVM: a library for support vector machines[J]. ACM Transactions on Intelligent Systems and Technology (TIST) 2(3):27

Chapter 50
Application of Ultra-Wide Band Radar for Sense-Through-Foliage Target Detection and Recognition

Shijun Zhai and Ting Jiang

Abstract In this paper, we propose a new approach to detect and recognize the target obscured by foliage based on real data collected by an Ultra-wide band (UWB) radar sensor. The new proposed method is the combination of support vector machine (SVM) and memetic algorithm. SVM is a powerful tool for solving the recognition problem with small sampling, nonlinearity and high dimension. Memetic algorithm is applied to determine the optimal parameters for SVM with highest accuracy and generalization ability. Moreover, the feature vectors for target detection and recognition are obtained from target echo signal that processed by wavelet packet transform (WPT). The results of the experiments indicate that this proposed approach is an effective method for sense-through-foliage target detection and recognition, which has higher recognition accuracy than that of the artificial neural network and the SVM which has randomly extracted parameters.

Keywords Target recognition • Ultra-wide band radar • Support vector machine • Memetic algorithm

50.1 Introduction

Detection and recognition of target in foliage environment has been a long-standing subject of intensive study. But the propagation path in foliage environment is non-line of sight and scattering from tree trunk and ground reflectivity may overwhelm the returned target signals of interest. And when targets and trees appear to have similar dielectric and frequency properties, it is difficult to detect and recognize the target in such environments.

In recent years, there have been many efforts undertaken to investigate foliage penetration and sense through foliage target detection. Sheen et al. [1] measured

S. Zhai (✉) • T. Jiang
Key Laboratory of Universal Wireless Communication, Ministry of Education, Beijing University of Posts and Telecommunications, Beijing, China
e-mail: zhaishijun@bupt.edu.cn

J. Mu et al. (eds.), *The Proceedings of the Third International Conference on Communications, Signal Processing, and Systems*, Lecture Notes in Electrical Engineering 322, DOI 10.1007/978-3-319-08991-1_50

one-way transmission properties of foliage using a bistatic and coherent wide-band system. Based on Ultra-wide band (UWB) radar, Kapoor et al. [2] proposed an alpha-stable model while Liang et al. [3, 4] presented a log-logistic model for foliage clutter. These studies have showed that foliage contains many spikes and angular fluctuations, and it's difficult to achieve effective and accurate target detection and recognition in forest. Moreover, Liang et al. [5, 6] investigated sense through foliage target detection using UWB radar sensor network system. These studies mainly focus on target detection.

In this paper, we investigate the feasibility of detecting and recognizing target obscured by foliage using UWB radar. Although target echo signal contains useful information for the type of target, it is difficult for us to make accurate judgments due to the huge amount of data. With the development of the artificial intelligence, neural network as an intelligent technology has been widely applied to the automatic target recognition system [7, 8]. However, neural network is based on the traditional empirical risk minimization which may suffer from several drawbacks, such as over-fitting, slow convergence velocity and easily relapsing into local extremum and so on. Support vector machine, developed by Vapnik [9], is a novel machine learning method based on statistical learning theory. Based on the idea of structural risk minimization principle, SVM minimizes the empirical risk of the training samples, can overcomes the problems of over-fitting, failing local minimum and low-convergence rate existing in neural network and does well in the case of small sample size and high dimension. Nowadays, SVM has been successfully applied to numerous nonlinear classification and pattern recognition problems such as target detection and recognition [10, 11] and fault diagnosis [12]. However, the practicability of SVM is affected due to the difficulty of selecting appropriate SVM parameters. To overcome shortages of the SVM, a support vector machine method based on memetic algorithm is proposed in this paper.

50.2 Support Vector Machine Algorithm

Traditionally, SVM is a learning machine for two-class classification problems. The purpose of SVM classification is to find optimal separating hyperplane by maximizing the margin between the separating hyperplane and the data. Let $\{x_l, y_l\}_{l=1}^{L}$ be the training sample set, where x_l is the input vector, $y_l \in \{-1, +1\}$ is the class labels. SVM try to find an optimal hyperplane $f(x) = 0$ that separates the given data when two classes are linearly separable.

$$f(x) = \langle w \cdot x \rangle + b = 0 \tag{50.1}$$

where w is the normal to the optimal hyperplane, and b is a scalar threshold. w and b are used to define the position of separating hyperplane.

The optimal hyperplane can be found by solving the following constrained optimization problem:

$$\begin{aligned} &\text{Minimize} \quad \frac{1}{2}\|w\|^2 \\ &\text{Subject to} \quad y_l\langle w \cdot x_l + b\rangle \geq 1, l = 1, 2, \cdots, L \end{aligned} \tag{50.2}$$

In the case where the two classes can be separated the SVM determines the separating hyperplane which maximizes the margin between the two classes. Typically, most practical problems involve classes which are not separable. In this case, the SVM classifier is obtained by solving the following optimization problem:

$$\begin{aligned} &\text{Minimize} \quad \frac{1}{2}\|w\|^2 + C\sum_{l=1}^{L}\xi_l \\ &\text{Subject to} \quad \begin{cases} y_l\langle w \cdot x_l + b\rangle \geq 1\text{-}\xi_l, l = 1, 2, \cdots, L \\ \xi_l \geq 0, i = 1, 2, \cdots, L \end{cases} \end{aligned} \tag{50.3}$$

where the ξ_l are slack variables that allow the SVM to tolerate misclassifications and C is the penalization parameter, which used to control the trade-off between minimizing training errors and model complexity. By the Lagrangian multipliers algorithm, the above-mentioned optimization problem is transformed into the dual quadratic optimization problem, that is:

$$\begin{aligned} &\text{Maximize} \quad \sum_{l=1}^{L}\alpha_i\text{-}\frac{1}{2}\sum_{l,m=1}^{L}\alpha_l\alpha_m y_l y_m (x_l \cdot x_m) \\ &\text{Subject to} \quad \sum_{l=1}^{L}\alpha_l y_l = 0,\ C \geq \alpha_l \geq 0, l = 1, \cdots, L \end{aligned} \tag{50.4}$$

The linear decision function is created by solving the dual optimization problem, which can be written as

$$f(x) = sign\left(\sum_{l=1}^{L}\alpha_l y_l (x_l, x) + b\right) \tag{50.5}$$

SVM can also be used in non-linear classification by using kernel function $K(x_l, x_m)$. The value of $K(x_l, x_m)$ equals to $\varphi(x_l) \cdot \varphi(x_m)$, where $\varphi(x_l)$ is the transformation function, which makes the input data into high-dimensional feature space. Then, the non-linear decision function is described as below:

$$f(x) = sign\left(\sum_{l=1}^{L}\alpha_l y_l K(x_l, x) + b\right) \tag{50.6}$$

Since radial basis function kernel has excellent non-linear classification ability, in this paper, radial basis function (RBF) kernel function $K(x_l, x) = \exp(\text{-}\ \|x_l\text{-}x\|^2/2\sigma^2)$ is accepted for constructing SVM, where σ denotes the width of RBF kernel function.

50.3 Parameters Optimization of SVM with Memetic Algorithm

Memetic algorithms (MAs) [13, 14] are population-based heuristic search approaches which can be used to solve optimization problems based on cultural evolution. MA combines the advantages of genetic algorithms and local search for optimisation problems. Genetic algorithms are used in many disciplines because of their efficient optimisation capabilities. Based on a local search approach, the number of iterations of the dominance is limited in order to reduce its computational requirements. In addition, for the local search procedure, the current solution (initially obtained by a constructive heuristic) is replaced by the neighbouring solution that results in the greatest improvement in the object function to be optimised. The process continues until a solution with no improving neighbour in a fixed generation number has been reached, that is until an optimum has been found. Its advantage can set up reasonable stopping criteria flexibly and avoid the shortcoming for the stopping criteria of the trial and error of genetic algorithms. The framework of memetic algorithm can be depicted as following.

Memetic algorithm
Initialization: Generate an initial population
while stopping criteria are not satisfied **do**
  Evaluate all individuals in the population
  Evolve a new population using genetic algorithm operators: crossover, mutation and selection.
  for each individual **do**
    Perform local search around it with probability P.
  end for
end while

In the study, RBF kernel is used to construct SVM classifier in the paper, the selection of the width σ and penalization parameters C have a great influence on the performance of SVM. The MA method is applied to determine the parameters of SVM. Here, the chromosome is composed of the parameters C and σ. The basic steps of determining the parameters of SVM by MA (MA-SVM) are represented as follows:

Step 1: Initialization. Randomly generate an initial population of chromosomes. The two parameters C and σ are encoded in a binary format; and represented by a chromosome. The number of population size is N.

Step 2: Fitness valuation. In this study, the fitness function used in GA is based on classification accuracy of SVM, which is as follows:

$$fitness = \frac{N_t}{N_t + N_f} \tag{50.7}$$

where N_t and N_f denote the number of true and false classifications, respectively.

Step 3: Selection. Based on fitness functions, chromosomes with higher fitness values are more likely to yield offspriong in the nest generation. The roulette wheel selection principle is applied to choose chromosomes for reproduction.

Step 4: Crossover. Pairs of parents are selected from these survivors. Single point crossover is employed to produce the nest generation. Segments of paired chromosomes between two determined break-points are swapped. The rate of crossover is 0.5.

Step 5: Mutation. Mutation is performed to alter binary code. That is, if a bit is equal to 1, it is changed to 0; if it is equal to 0, it is changed to 1. The rate of mutation is set to 0.1.

Step 6: Local search. A hill-climber algorithm is used as local search.

Step 7: Termination criteria. The procedure proceeds until stopping criteria is satisfied, and then the global optimal values of C and σ are obtained, the MA ends the iteration. Otherwise, return to step 2.

50.4 Experimental Results and Analysis

In this study, an experimental setup is used for obtaining the real target echo signal data sets. The radar experiment set used in this study, is a bistatic UWB radar system (individual transmit and receive antennas). We investigate received UWB radar signals from the bistatic UWB radar system. The measurements were taken using PulsON 400 (P400) by the Time Domain Co., Ltd. The P400 operating band is from 3.1 to 5.3 GHz, with center frequency 4.2 GHz. Time Domain Broadspec toroidal dipole antennas are used for transmitting and receiving antennas, the gain of the antenna is about 3dbi. The P400 is controlled by a PC and data are recorded digitally.

Propagation measurements were performed in a park. The park contains a mix of hardwood trees along with low-lying underbrush/shrubs. Measurements were performed in two different forest environments: light forest and medium forest. And two data sets collected at light forest and medium forest are used in this paper. For both Light Forest and Medium Forest, transmitter (TX) and receiver (RX) were placed at fixed positions. The distances between TX and RX are more than 19 m in both light forest and medium forest. Three target types including human (target type I), wood board (target type II) and small iron cabinet (target type III) are employed as research object. Firstly, the penetration measurement was taken without target placed between TX and RX. Then, the penetration measurement data was collected with target placed at different locations in the forest. The targets were placed at different positions. Target echo signals are obtained and recorded digitally by a computer. More than 100 penetration measurement data were collected when a target placed at each position. The measurement scenes in the forests are shown in Fig. 50.1.

Fig. 50.1 The testing scene in forest

In these experimental studies, 200 radar target echo signals that placed at different locations in the forest are used for each target type. Therefore, a dataset including 800 samples for all target types is established. All samples in the dataset are divided into two sets, the training set includes 320 samples (select 80 samples for each target type) and the test set includes 480 samples. To maintain a more realistic investigation of this classification technique, the training and testing sets do not include any overlap in data. The testing samples are adopted to show the recognition performance of the proposed method compared with that of canonical support vector machine model, the back-propagation neural networks (BPNN) model and the k-nearest neighbor (KNN) model.

In this paper, wavelet packet transform (WPT) [15, 16] is used for feature extraction. By applying three layers WPT decomposition to the original signal with Db6 wavelet base, the WPT decomposition coefficients of eight frequency bands of the third layer are obtained. The dimension of the wavelet coefficients is reduced using Principal Component Analysis [17].

In the optimized SVM, the parameter C and σ are optimized by MA, the adjusted parameters with maximal classification accuracy are selected as the most appropriate parameters. Then, the optimal parameters are utilized to train SVM model. In the canonical SVM model, the parameter C and σ are randomly selected to construct the recognition model. The experimental results of MA-SVM are shown in Tables 50.1 and 50.2. The comparison of recognition results among MA-SVM, canonical SVM, BPNN and KNN are shown in Tables 50.3 and 50.4. It is indicated that the proposed MA-SVM has higher recognition accuracy than canonical SVM, BPNN and KNN in sense through foliage target recognition.

We can see from Tables 50.1 and 50.2 that the successful target detection rates of the proposed MA-SVM classifier are higher than 98 % and the recognition rates for each target type are higher than 91 %. From Tables 50.3 and 50.4, it can be seen that that the recognition rates of the MA-SVM classifier are higher than those of SVM,

Table 50.1 Test results of four target types each including 120 test samples in light forest

	No target	Target type I	Target type II	Target type III
Total number of samples	120	120	120	120
Correct classification	119	116	115	112
In correct classification	1	4	5	8
Recognition rate (%)	99.17	96.67	95.83	93.33

Table 50.2 Test results of four target types each including 120 test samples in medium forest

	No target	Target type I	Target type II	Target type III
Total number of samples	120	120	120	120
Correct classification	118	115	114	110
In correct classification	2	5	6	10
Recognition rate (%)	98.33	95.83	95.00	91.67

Table 50.3 The recognition results comparison of four kinds of target type in light forest

	Recognition accuracies (%)			
Target type	MA-SVM	SVM	BPNN	KNN
No target	99.17	97.50	97.50	96.67
Target type I	96.67	94.17	93.33	92.50
Target type II	95.83	92.50	89.17	87.50
Target type III	93.33	90.83	87.50	85.83
Average recognition	96.25	93.75	91.88	90.63

Table 50.4 The recognition results comparison of four kinds of target type in medium forest

	Recognition accuracies (%)			
Target type	MA-SVM	SVM	BPNN	KNN
No target	98.33	96.67	96.67	95.83
Target type I	95.83	92.50	91.67	91.67
Target type II	95.00	91.67	87.50	85.00
Target type III	91.67	90.00	85.83	84.17
Average recognition	95.21	92.71	90.42	89.17

BPNN and KNN classifiers, and the recognition rates of the SVM classifier are higher than KNN and BPNN classifier, this is because the SVM classifier is robust to small sample set, which is the case in our experiments. Nevertheless, the MA-SVM classifier outperforms all the classifiers as it obtains the highest recognition rates for all types of targets. This verifiers the effectiveness of the bistatic UWB radar and MA-SVM classifier in sense through foliage target detection and recognition.

Conclusion

In order to detect and recognize the target obscured by foliage, a novel recognition model based on support vector machine and memetic algorithm is proposed. WPT-based features are extracted from measured real radar echo signal waveforms using Ultra-wide band (UWB) radar sensor. Then, the support vector machine algorithm optimized by memetic algorithm is developed to perform target types detection and recognition. The obtained results clearly confirm the superiority of the proposed method for target recognition compared to the method of SVM, KNN and BPNN. This indicates that the proposed technique promises to be an effective tool for sense-through-foliage target recognition purposes. In the future, the proposed method needs to be tested on more sensing-through-foliage data to further optimize the proposed approaches and improve their robustness. And we also need to investigate the recognition performance of models on large size of training sets once enough samples are obtained.

Acknowledgement This work is supported by the National Natural Science Foundation of China (No. 61171176).

References

1. Sheen DR, Malinas NP, Kletzli DW, Lewis TB, Roman JF (1994) Foliage transmission measurements using a ground-based ultra-wideband (UWB) (300–1300 MHz) SAR system. IEEE Trans Geosci Remote Sens 32(1):118–130
2. Kapoor R, Tsihrintzis GA, Nandhakumar N (1996) Detection of obscured targets in heavy-tailed radar clutter using an ultra-wideband (UWB) radar and alpha-stable clutter models. In: Proceedings of the 30th Asilomar conference on signals, systems and computers, IEEE, 3–6 Nov 1996, pp 863–867
3. Liang J, Liang Q (2010) Outdoor propagation channel modeling in foliage environment. IEEE Trans Veh Technol 59(3):2243–2252
4. Liang Q (2011) Radar sensor wireless channel modeling in foliage environment: UWB versus narrowband. IEEE Sens J 11(6):1448–1457
5. Liang J, Liang Q (2009) UWB radar sensor networks detection of targets in foliage using short-time Fourier transform. In: IEEE international conference on communications, 14–18 June 2009, pp 1–5
6. Liang J, Liang Q (2010) Sense-through-foliage target detection using UWB radar sensor networks. Pattern Recogn Lett 31(11):1412–1421
7. Park S et al (2010) A neural network approach to target classification for active safety system using microwave radar. Expert Syst Appl 37(3):2340–2346
8. Sun G, Wang J, Qin S, Na J et al (2008) Radar target recognition based on the multi-resolution analysis theory and neural network. Pattern Recogn Lett 29(16):2109–2115
9. Vapnik VN (1995) The nature of statistical learning theory. Springer, New York
10. Lei P, Wang J, Guo P, Cai D (2011) Automatic classification of radar targets with micro-motions using entropy segmentation and time-frequency features. AEU-Int J Electron Commun 65(10):806–813

11. Eryildirim A, Onaran I (2011) Pulse doppler radar target recognition using a two-stage SVM procedure. IEEE Trans Aerosp Electron Syst 47(2):1450–1457
12. Qin Q et al (2012) A novel scheme for fault detection of reciprocating compressor valves based on basis pursuit, wave matching and support vector machine. Measurement 45(5):897–908
13. Urselmann M et al (2011) A Memetic algorithm for global optimization in chemical process synthesis problems. IEEE Trans Evol Comput 15(5):659–683
14. Wang H et al (2012) A memetic particle swarm optimization algorithm for multimodal optimization problems. Inform Sci 197:38–52
15. Vong CM, Wong PK (2011) Engine ignition signal diagnosis with wavelet packet transform and multi-class least squares support vector machines. Expert Syst Appl 38(7):8563–8570
16. Mallat SG (2009) A wavelet tour of signal processing: the sparse way. Academic, Washington
17. Jolliffe IT (2002) Principal component analysis, 2nd edn. Springer, New York

Part V
Localization, Pattern Recognition

Chapter 51
A Novel DOA Estimation Algorithm for Wideband LFM Source with Local Scattering

Liang Zhang, Jiexiao Yu, Kaihua Liu, and Deliang Liu

Abstract To realize the direction of arrival (DOA) estimation of wideband Linear Frequency-modulated (LFM) source with local scattering, an approximate model is derived by Taylor series expansion and a novel estimation algorithm using fractional Fourier transform (FrFT) is proposed. New array data models in both the time domain and the fractional Fourier domain are presented and the one-to-one relationship between the location vector in the Energy-concentrated domain and the spatial parameters is given. Then, the conventional Multiple Signal Classification (MUSIC) algorithm is exploited to estimate the spatial parameters of multiple wideband LFM sources with local scattering in the Energy-concentrated domain. Compared with the previous FrFT-MUSIC algorithm based on the assumption of point source model, the proposed algorithm has better performance on location position accuracy and anti-noise property.

Keywords Direction of arrival • Fractional Fourier transform • Linear frequency-modulated signal • Local scattering • Generalised array manifold

51.1 Introduction

Wideband linear frequency-modulated (LFM) signal is widely applied in radar, sonar, communication, geological exploration, and biomedical science fields [1] and its spatial parametric estimation has received increasing attention. Whereas, in the actual application environment, multipath propagation occurs in many scenarios. For example, in the case of a radar system performing low angle tracking, the diffuse components caused by the reflection from a rough sea surface should be considered a distributed source [2]. Similarly, because of local scattering and reflection from the mobile stations and the base stations, the point source presents significant angular scattering distributions in urban wireless communications

L. Zhang (✉) • J. Yu • K. Liu • D. Liu
School of Electronic Information Engineering, Tianjin University, Tianjin, China
e-mail: vfleon@163.com

J. Mu et al. (eds.), *The Proceedings of the Third International Conference on Communications, Signal Processing, and Systems*, Lecture Notes in Electrical Engineering 322, DOI 10.1007/978-3-319-08991-1_51

[3]. For acquiring the direction of arrival (DOA) parameter in the situations with multipath propagation from local scatters, a generalised array manifold model (GAM) has been proposed, and a corresponding algorithm is presented to implement DOA estimation by using a Vandermonde structure in [4]. However, this algorithm was aimed at the condition of narrowband signal in the far field.

In this paper, the calibrated location vector in fractional Fourier domain is proposed, which can be applied to estimating the spatial parameters of wideband LFM source with local scatting. And the separation of multiple uncorrelated LFM sources can be implemented by using the time–frequency properties of LFM signal in fractional Fourier domain. Finally, the spatial signatures of multiple LFM sources can be obtained.

51.2 Data Model

51.2.1 Array Model in Time Domain

Considering Q uncorrelated wideband LFM sources, each of which can be seen as a superposition of N_q scattered point sources. For an array of P sensors, the complex envelope of the output vector on the pth sensor can be modeled as

$$x_p(t) = \sum_{q=1}^{Q} \sum_{i=1}^{N_q} \beta_{qi} \mathrm{a}\left(\theta_i + \widetilde{\theta}_{qi}, t\right) s_q\left(t - \nu_{qi}\right) + n_p(t) \tag{51.1}$$

where

β_{qi}: the complex amplitude of the ith scattered source from the qth source;
$\mathrm{a}\left(\theta_i + \widetilde{\theta}_{qi}, t\right)$: the time-varying location vector of the array, θ_i is the incidence angle of the qth source and $\theta_i + \widetilde{\theta}_{qi}$ is the arrival of angle of the ith scattered source from the qth source;
$s_q(t)$: the qth source;
ν_{qi}: the time delay associated with the ith scattered source from the qth source;
$n_p(t)$: additive zero-mean noise at the pth sensor uncorrelated from the sources.

51.2.2 Location Vector in the Energy-Concentrated Domain

In the following derivation, a scenario with a source emitting LFM signal in the far field is considered. For simplicity, uniform linear array (ULA) has been taken as an example for derivation and the similar conclusions are easy to be generalized to the arrays with other types.

Assume that the interval of sensors is d and the first sensor is regarded as the reference sensor. The output of the reference sensor without noise can be written as

$$y_1(t) = a_0 e^{j\pi\left(2f_0 t+\mu_0 t^2\right)+j\varphi_0}, \qquad -T/2 \le t \le T/2 \tag{51.2}$$

where a_0 is the amplitude, f_0 is the initial frequency, φ_0 is the initial phase and $\mu_0 = B/T$ is the chirp rate with bandwidth B and duration time T.

The LFM signal presents best energy concentrated property in a proper fractional Fourier domain which is called the Energy-Concentrated domain of this signal. The energy concentrated property is suitable to implement the spatial parameter estimation of LFM source. The rotation angle of FrFT in the Energy-concentrated domain is

$$\alpha_e = -\text{arc}\cot\mu_0 \tag{51.3}$$

FrFT of rotation angle α_e is performed on $y_1(t)$ and $y_1(t)$ is transformed into the Energy-concentrated domain.

$$Y_1(u) = \sqrt{1-j\cot\alpha_e}\, e^{j\pi u_0^2\cot\alpha_e} T \frac{\sin\left(\pi(u\csc\alpha_e - f_0)T\right)}{\pi(u\csc\alpha_e - f_0)T} \tag{51.4}$$

According to [5], when $u_1 = f_0/\csc\alpha_e$, the spectrum peak of $Y_1(u)$ is

$$Y_1(u_1) = \sqrt{1-j\cot\alpha_e}\, e^{j\pi u_0^2\cot\alpha_e} T \tag{51.5}$$

The output of the pth sensor is

$$y_p(t) = y_1\left(t-\tau_p\right) = a_0 e^{j\varphi_0} e^{j\pi\left(-2f_0\tau_p+\mu_0\left(\tau_p\right)^2\right)} e^{j\pi\left(2\left(f_0-\mu_0\tau_p\right)t+\mu_0 t^2\right)} \tag{51.6}$$

where $\tau_p = (k-1)d\sin(\theta)/c$ represents time delay which performs on the pth sensor, θ is the incidence angle of the signal and c is the speed of light. Because the chirp rate of the delayed signal is invariable, the rotation angle of the time-delayed signal in the Energy-concentrated domain is invariable. According to the time shifting properties of FrFT [6],

$$F^{\alpha}[y(t-\tau)] = e^{\left(j2\pi\tau^2\sin\alpha\cos\alpha\right)} e^{(-j2\pi u\tau\sin\alpha)} Y_{\alpha}(u-\tau\cos\alpha) \tag{51.7}$$

FrFT of the rotation angle α_e of $y_p(t)$ is

$$Y_p(u) = B\sqrt{1-j\cot\alpha_e}\, e^{j\pi u_0^2\cot\alpha_e} T \frac{\sin\left(\pi\left(u\csc\alpha_e - f_0+\mu_0\tau_p\right)T\right)}{\pi\left(u\csc\alpha_e - f_0+\mu_0\tau_p\right)T} \tag{51.8}$$

where

$$B = a_0 e^{j\varphi_0} e^{j\pi\left(-2f_0\tau_p+\mu_0\left(\tau_p\right)^2\right)} \tag{51.9}$$

And the spectrum peak of $Y_p(u)$ with $u_p = u_1 + \tau_p \cos\alpha_e$ is

$$Y_p\left(u_p\right) = B\sqrt{1 - j\cot\alpha_e} e^{j\pi u_p^2 \cot\alpha_e} T \tag{51.10}$$

Compared (51.5) and (51.10), the relationship of the peaks of the output on the reference sensor and on the pth sensor in the Energy-concentrated domain can be given by

$$Y_p\left(u_p\right) = A_p(\theta) Y_1(u_1) \tag{51.11}$$

where

$$A_p(\theta) = e^{-j\pi\left[2\tau_p u_0 \sin\alpha_e + \left(\tau_p\right)^2 \sin\alpha_e \cos\alpha_e\right]} \tag{51.12}$$

In (51.12), the location vector is only related with the incidence angle, eliminating the influence of time parameter. As a result, the location matrix can be written as

$$\mathbf{A}(\theta) = [1, A_2(\theta), \cdots, A_P(\theta)]^{\mathrm{T}} \tag{51.13}$$

51.2.3 Approximating the Spatial Signature

According (51.11), we can obtain that the relationship between the peak $S_{qi}(u_{qi})$ of $F^{\alpha_e}\left[s_q\left(t - v_{qi}\right)\right]$ and that $S_q(u_q)$ of $F^{\alpha_e}\left[s_q(t)\right]$ satisfies

$$S_{qi}\left(u_{qi}\right) = e^{-j\pi\left[2v_{qi}u_q \sin\alpha_e + \left(v_{qi}\right)^2 \sin\alpha_e \cos\alpha_e\right]} S_q\left(u_q\right) \tag{51.14}$$

Because the time delay v_{qi} is very small in most of applications, the quadratic term of v_{qi} can be ignored and (51.14) can be approximate to

$$S_{qi}\left(u_{qi}\right) \simeq e^{-j2\pi v_{qi} u_q \sin\alpha_e} S_q\left(u_q\right) \tag{51.15}$$

Hence, FrFT of the output of the qth source, with a rotation angle α_d in the Energy-concentrated domain, can be given by

$$\sum_{i=1}^{N_q} \beta_{qi} e^{-j2\pi v_{qi} u_q \sin\alpha_e} \mathbf{A}_q\left(\theta_q + \widetilde{\theta}_{qi}\right) S_q\left(u_q\right) \tag{51.16}$$

where $\mathbf{A}_q(\theta)$ is the location vection of the qth source in the Energy-concentrated domain, and $S_q(u)$ is FrFT of $s_q(t)$.

Let $c_{qi} = \beta_{qi} e^{-j2\pi v_{qi} u_q \sin\alpha_e}$. We define that

$$v_q = \sum_{i=1}^{N_q} c_{qi} \mathbf{A}_q\left(\theta_q + \widetilde{\theta}_{qi}\right) \tag{51.17}$$

Assume that the deviation angle $\widetilde{\theta}_{qi}$ caused by local scattering is small relatively, a first-order Taylor series expansion of $\mathbf{A}_q\left(\theta_q + \widetilde{\theta}_{qi}\right)$ can be used to approximate (51.17).

$$\begin{aligned} \mathbf{v}_q &\simeq \sum_{i=1}^{N_q} c_i\left(\mathbf{A}_q(\theta_q) + \widetilde{\theta}_{qi}\mathbf{d}(\theta_q)\right) \\ &= \left(\sum_{i=1}^{N_q} c_i\right)\mathbf{A}_q(\theta_q) + \left(\sum_{i=1}^{N_q} c_i\widetilde{\theta}_{qi}\right)\mathbf{d}(\theta_q) = \mathbf{A}_q(\theta_q) + \phi_q\mathbf{d}(\theta_q) \end{aligned} \tag{51.18}$$

where $\phi_q = \sum_{i=1}^{N_q} c_i\widetilde{\theta}_{qi}, d(\theta) = \frac{\partial A_q(\theta)}{\partial\theta}$ and the spatial signature is assumed to be scaled so that $\sum_{i=1}^{N_q} c_{qi} = 1$. Then the compact matrix notation $\mathbf{V}$ can be given by

$$\mathbf{V} \simeq \mathbf{A}\left(\underline{\theta}, \underline{\phi}\right) = \mathbf{A}\left(\underline{\theta}\right) + \mathbf{D}\left(\underline{\theta}\right)\Phi(\phi) \tag{51.19}$$

where

$$\begin{aligned} \mathbf{A}\left(\underline{\theta}\right) &= \left[\mathbf{A}_1(\theta_1), \ldots, \mathbf{A}_Q\left(\theta_Q\right)\right] \\ \mathbf{D}\left(\underline{\theta}\right) &= \left[\mathbf{d}(\theta_1), \ldots, \mathbf{d}\left(\theta_Q\right)\right] \\ \Phi\left(\underline{\phi}\right) &= \mathrm{diag}\left\{\phi_1, \ldots, \phi_Q\right\} \end{aligned} \tag{51.20}$$

According to (51.19), $\underline{\theta} = \left[\theta_1, \ldots, \theta_Q\right]^{\mathrm{T}}$ and $\underline{\phi} = \left[\phi_1, \ldots, \phi_Q\right]^{\mathrm{T}}$ are the parameters which are needed to estimated in the approximated model. In the next section, we will give parameter estimation method for the proposed model.

51.3 Parameter Estimation Algorithm

As mentioned above, the location matrix in the Energy-concentrated domain has a one-to-one relationship with the time delay on the sensors, namely spatial parameters. Besides, the location vector under the condition of local scattering has been

calibrated by Taylor series expansion. Consequently, some of the narrowband point source DOA estimation algorithms can also be applied to the DOA estimation of wideband LFM sources with local scattering in the Energy-concentrated domain.

We choose MUSIC algorithm as an example to show how the proposed calibrated location vector can be applied to estimation. MUSIC is a classical DOA estimation algorithm based on the matrix feature subspace decomposition. The spatial estimation spectrum of standard MUSIC algorithm [7] is

$$V_{MUSIC}(\theta) = \frac{\mathbf{a}^*(\theta)\hat{\mathbf{E}}_n\hat{\mathbf{E}}_n^*\mathbf{a}(\theta)}{\mathbf{a}^*(\theta)\mathbf{a}(\theta)} \tag{51.21}$$

In the Energy-concentrated domain, the location vection of the proposed data model (51.6) should be replace by

$$\mathbf{A}(\theta) + \phi\mathbf{d}(\theta) = \overline{\mathbf{A}}(\theta)\overline{\phi} \tag{51.22}$$

where $\bar{\mathbf{A}}(\theta) = [\mathbf{A}(\theta) \quad \phi\mathbf{d}(\theta)]$ and $\overline{\phi}(\theta) = [1 \quad \phi]^{\mathrm{T}}$. For this case, the spatial estimation spectrum becomes

$$\overline{V}_{MUSIC}(\theta,\phi) = \frac{\phi^*\overline{\mathbf{A}}^*(\theta)\hat{\mathbf{E}}_n\hat{\mathbf{E}}_n^*\overline{\mathbf{A}}(\theta)\overline{\phi}}{\mathbf{A}^*(\theta)\mathbf{A}(\theta)} \tag{51.23}$$

The parameters θ and ϕ can be determined by the spectral peak position.

51.4 Simulation Study and Results

We verified the performance of the proposed algorithm by simulations. In the simulations, the ULA with eight sensors is used to estimate the spatial parameters of the proposed model which is consisted by 100 local scattering components. Two wideband LFM sources with local scattering are chosen to illustrate the location performance. The initial parameters of two LFM source are shown as follow: the first set are $f_1 = 12$ MHz and $\mu_1 = 1 \times 10^{12}$Hz/s and the second set are $f_2 = 10$ MHz and $\mu_2 = -10 \times 10^{12}$Hz/s. The central incident angles of two sources are taken as $\theta_1 = 30^\circ$ and $\theta_2 = -45^\circ$ with the extension widths from a uniform angular distribution of width $\Delta_1 = 4^\circ$ and a Gauss angular distribution of width $\Delta_2 = 4^\circ$ respectively. The signal-to-noise ratio (SNR) is 10 dB and 500 snapshots are collected.

Figure 51.1 shows the two-dimensional spectrum of continuous rotation angle FrFT of received signal on the reference sensor. Two distinct spectrum peaks correspond to the shock pluses of two LFM sources with local scattering in their Energy-concentrated domain. Consequently, the rotation angle in the Energy-concentrated domain and the incident source number can be determined from this figure.

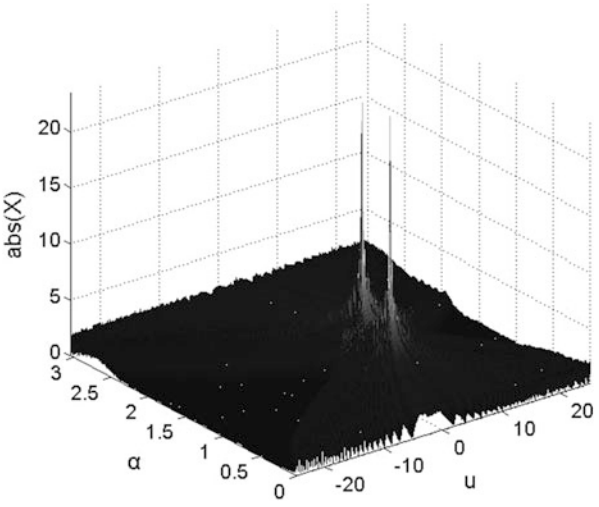

Fig. 51.1 Two-dimensional spectrum of two LFM sources in plane (α, u)

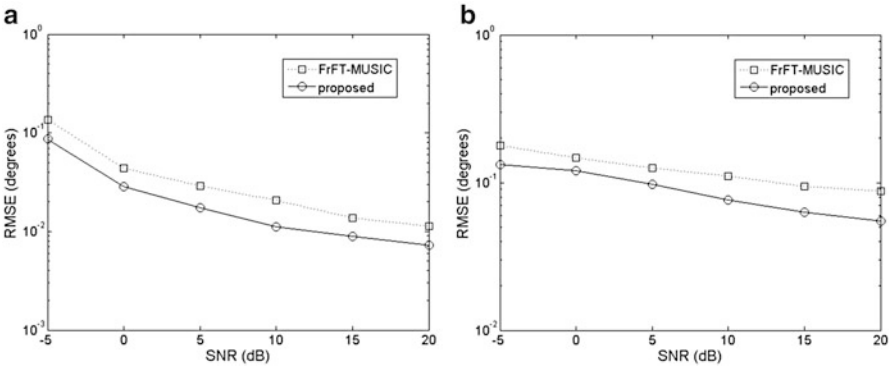

Fig. 51.2 The estimation RMSE for the central angle versus SNR. (**a**) Source 1; (**b**) Source 2

FrFT-MUSIC algorithm [8] which is applied to the DOA estimation of wideband LFM point source is chosen as the comparing algorithm to demonstrate the performance of the proposed algorithm for the LFM source with local scattering. A Monte Carlo simulation with 50 independent runs for each trial of two sources is performed for different SNRs. Figure 51.2 presents the root mean square error (RMSE) for the central angle estimator. Compared with the FrFT-MUSIC, the proposed algorithm provides a smaller bias in the DOA estimation. Figure 51.3 shows the RMSE for the DOA estimation versus extension width. With the increasing extension width, the proposed algorithm has location accuracy than the FrFT-MUSIC.

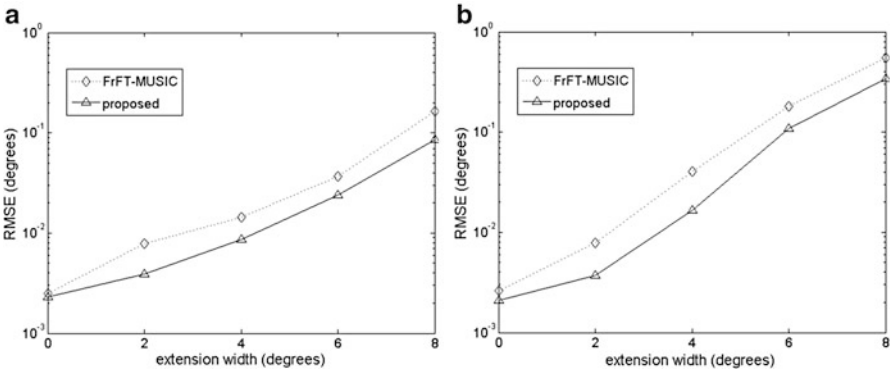

Fig. 51.3 RMSE for the central angle versus extension width. (**a**) Source 1; (**b**) Source 2

Conclusion

To estimate the DOA of wideband LFM source with local scattering, a novel estimation algorithm based on FrFT is proposed, which realized the determination of the number of sources and the spatial parameter estimation of each source based on the energy concentration property of array signals in the fractional Fourier domain. The proposed algorithm allow the source number exceed the sensor number. The simulation results showed that the proposed algorithm had higher location accuracy and obtained better spatial resolution performance than the FrFT-MUSIC algorithm for wideband LFM source with local scattering.

Acknowledgments This work is supported by Tianjin Research Program of Application Foundation and Advanced Technology under Grant 14JCQNJC01400.

References

1. Djuric P, Kay SM (1990) Parameter estimation of chirp signals. IEEE Trans Acoust Speech Signal Process 38(12):2118–2126
2. Meng Y, Stoica P, Wong KM (1996) Estimation of the directions of arrival of spatially dispersed signals in array processing. IEE Proc Radar Sonar Navig 143(1):1–9
3. Jin Y, Friedlander B (2004) Detection of distributed sources using sensor arrays. IEEE Trans Signal Process 52(6):1537–1548
4. Asztely D (1997) Spatial models for narrowband signal estimation with antenna arrays. Tech. Lic. thesis, Royal Institute of Technology
5. Qi L, Tao R, Zhou SY et al (2004) Detection and parameter estimation of multicomponent LFM signal based on the fractional Fourier transform. Sci China (Ser F, Info Sci) 47(2):184–198

6. Ozaktas HM, Kutay MA, Mendlovic D (1999) Introduction to the fractional Fourier transform and its applications. Adv Imaging Electron Phys 106:239–291
7. Schmidt RO (1986) Multiple emitter location and signal parameter estimation. IEEE Trans Antennas Propag 34(3):276–280
8. Ran T (2005) Novel method for the direction of arrival estimation of wideband linear frequency modulated sources based on fractional Fourier transform. Trans Beijing Inst Technol 25 (10):895–899

Chapter 52
A Novel Localization Algorithm for Coherently Distributed Wideband LFM Source

Jiexiao Yu, Liang Zhang, Kaihua Liu, and Deliang Liu

Abstract This article presents a novel algorithm to estimate the spatial parameters of the coherently distributed wideband linear frequency-modulated (LFM) source model, which is a generalization of the conventional distributed source parameter estimator (DSPE) algorithm. A new array data model is constructed through the energy concentrated property of LFM signal in proper fractional Fourier domain. The central angels and the extension widths of multiple LFM sources can be estimated separately using the proposed algorithm. Compared with previous FrFT-MUSIC algorithm, the proposed algorithm has a better performance on location accuracy and anti-noise property, and can determine the number of incident sources which in this algorithm is allowed to exceed the number of sensors in the array.

Keywords Distributed source • Fractional Fourier transform • Linear frequency-modulated signal • Localization

52.1 Introduction

Wideband linear frequency-modulated signal (LFM) signal is a kind of important non-stationary signal which is widely applied in radar, sonar, communications, geological exploration, and biomedical sciences fields [1]. In order to estimate spatial parameter of an LFM signal by sensor array, a method based on the time–frequency analysis of LFM signal has been presented in [2]. Based on fractional Fourier transform (FrFT) and fractional Fourier domain signal subspace decomposition, the FrFT-MUSIC algorithm is presented in [3]. Yuan [4] proposed a temporal-invariance ESPRIT algorithm to estimate the two-dimensional elevation-azimuth angle of an LFM signal by a triangle array. However, multipath transmission occurs in many scenarios. Frequently, the point source model will

J. Yu (✉) • L. Zhang • K. Liu • D. Liu
School of Electronic Information Engineering, Tianjin University, Tianjin, China
e-mail: yjx@tju.edu.cn

J. Mu et al. (eds.), *The Proceedings of the Third International Conference on Communications, Signal Processing, and Systems*, Lecture Notes in Electrical Engineering 322, DOI 10.1007/978-3-319-08991-1_52

be evolved into a distributed source model. Traditional distributed source spatial parameter estimation algorithms are mainly aimed at the condition of narrowband signal in the far field, such as classical distributed source parameter estimator (DSPE) algorithm [5] which is a generalization of multiple signal classification (MUSIC) algorithm, and its improved algorithm dispersed signal parametric estimation (DISPARE) [6].

Due to the location vector in time domain is temporal-varying, if the array received LFM signal, previous methods to estimate the parameters of distributed narrowband source are not suitable. Consequently, we propose a novel distributed wideband LFM source model firstly. For coherently source, the model in the Energy-concentrated domain is given through the time–frequency properties of LFM signal in the fractional Fourier domain. Then, combined with traditional DSPE algorithm, a novel algorithm to estimate the spatial parameters of the proposed model is presented. In this algorithm, the incident source number can be determined precisely and be allowed to exceed the number of sensors in the array. Meantime, the distribution of each source can differ from each other. Furthermore, the simulation shows a dramatic improvement in localization accuracy and anti-noise performance compared with FrFT-MUSIC algorithm.

52.2 Array Model

52.2.1 Fractional Fourier Transform

FrFT of the rotation angle α of signal $x(t)$ is defined as a linear integral transform.

$$X_\alpha(u) = F^\alpha[x(t)] = \int_{-\infty}^{\infty} x(t) K_\alpha(t,u)dt \tag{52.1}$$

where $K_\alpha(u,t)$ is kernel function.

$$K_\alpha(t,u) = \begin{cases} \sqrt{1-j\cot\alpha}\ e^{j\pi\left(t^2\cot\alpha - 2tu\csc\alpha + u^2\cot\alpha\right)}, & \alpha \neq n\pi \\ \delta(t-u), & \alpha = 2n\pi \\ \delta(t+u), & \alpha = (2n\pm 1)\pi \end{cases} \tag{52.2}$$

52.2.2 Array Model in Time Domain

A distributed wideband source can be considered to consist of a set of wideband point sources which is densely distributed in the space. Assume that the scattering point sources are continuous and an array of p sensors observing a wave field of q distributed wideband LFM sources. When the received signal components of a source at different angles are delayed and scaled replicas of the same signal, the

source can be considered as coherently distributed (CD) source. For CD source, the complex envelope of the output vector of the array is

$$\mathrm{x}(t) = \sum_{i=1}^{q} \int_{\vartheta \in \Theta} \mathrm{a}(\vartheta, t) s_i(t) \ell_i(\vartheta, \psi_i) d\vartheta + \mathrm{n}(t) \tag{52.3}$$

where $\mathrm{a}(\vartheta, t)$ is the location vector of the array, $s_i(t)$ is a random variable which reflects the time properties of distributed source and $\ell_i(\vartheta, \boldsymbol{\psi}_i)$ is the deterministic angular signal density of the ith source in the direction $\vartheta \in \Theta$, ψ_i is the ith source location parameter vector and $\mathrm{n}(t)$ is an additive zero-mean noise vector.

Considering the wideband non-stationary properties of LFM signal, there not exist one-to-one relationship between the spatial distribution parameters and $\mathrm{a}(\vartheta, t)$ which is also dependent on time parameter. Therefore, traditional estimation methods of distributed source are not suitable for LFM source. Because the time–frequency properties of LFM signal can be utilized to transform the received signal into a proper domain in which the influence of time parameter on the location vector is eliminated, we attempt to transform the model from the time domain into the fractional Fourier domain.

52.2.3 Array Model in Fractional Fourier Domain

As a kind of linear transformation, FrFT implemented on the scattering components of a single source or multiple sources won't bring in cross-term interference. Therefore, the location vector has the same form as that deduced by FrFT of a single point source in fractional Fourier domain. In the following derivation, a scenario with a source emitting LFM signal in the far field is considered. For simplicity, uniform linear array (ULA) has been taken as an example for derivation and the similar conclusions are easy to be generalized to the arrays with other types.

Assume the interval of sensors is d and the first sensor is regarded as the reference sensor. The output of the kth sensor is

$$y_k(t) = y_1(t - \tau_k) = a_0 e^{j\varphi_0} e^{j\pi\left(-2f_0\tau_k + \mu_0(\tau_k)^2\right)} e^{j\pi\left(2(f_0 - \mu_0\tau_k)t + \mu_0 t^2\right)} \tag{52.4}$$

where a_0 is the amplitude, f_0 is the initial frequency, φ_0 is the initial phase, $\mu_0 = B/T$ is the chirp rate with bandwidth B and duration time T, $\tau_k = (k-1)d\sin(\theta)/c$ is time delay which performs on the kth sensor, θ is the incidence angle of the signal and c is the speed of light.

The LFM signal presents best energy concentrated property in a proper fractional Fourier domain which is called the Energy-Concentrated domain of this signal and the rotation angle of FrFT in the Energy-concentrated domain is

$$\alpha_e = -\mathrm{arc}\cot\mu_0 \tag{52.5}$$

Transforming $y_1(t)$ into the Energy-concentrated domain:

$$Y_1(u) = \sqrt{1 - j\cot\alpha_e}\, e^{j\pi u_0^2 \cot\alpha_e} T \frac{\sin\left(\pi(u\csc\alpha_e - f_0)T\right)}{\pi(u\csc\alpha_e - f_0)T} \tag{52.6}$$

According to [7], when $u_1 = f_0/\csc\alpha_e$, the spectrum peak of $Y_1(u)$ is

$$Y_1(u_1) = \sqrt{1 - j\cot\alpha_e}\, e^{j\pi u_0^2 \cot\alpha_e} T \tag{52.7}$$

Because the chirp rate of the delayed signal is invariable, the rotation angle of the time-delayed signal in the Energy-concentrated domain is invariable. According to the time shifting properties of FrFT [8], FrFT of the rotation angle α_e of $y_k(t)$ is

$$Y_k(u) = B\sqrt{1 - j\cot\alpha_e}\, e^{j\pi u_0^2 \cot\alpha_e} T \frac{\sin\left(\pi(u\csc\alpha_e - f_0 + \mu_0\tau_k)T\right)}{\pi(u\csc\alpha_e - f_0 + \mu_0\tau_k)T} \tag{52.8}$$

where

$$B = a_0 e^{j\varphi_0} e^{j\pi\left(-2f_0\tau_k + \mu_0(\tau_k)^2\right)} \tag{52.9}$$

And the spectrum peak of $Y_k(u)$ with $u_k = u_1 + \tau_k\cos\alpha_e$ is

$$Y_k(u_k) = B\sqrt{1 - j\cot\alpha_e}\, e^{j\pi u_k^2 \cot\alpha_e} T \tag{52.10}$$

Compared (52.7) and (52.10), the relationship of the peaks of the output on the reference sensor and on the kth sensor in the Energy-concentrated domain can be given by

$$Y_k(u_k) = A_k(\theta) Y_1(u_1) \tag{52.11}$$

where

$$A_k(\theta) = e^{-j\pi\left[2\tau_k u_0 \sin\alpha_e + (\tau_k)^2 \sin\alpha_e \cos\alpha_e\right]} \tag{52.12}$$

In (52.12), the location vector is only related with the incidence angle, eliminating the influence of time parameter. As a result, the location matrix can be written as

$$\mathbf{A}(\theta) = \left[1, A_2(\theta), \cdots, A_p(\theta)\right]^{\mathrm{T}} \tag{52.13}$$

Therefore, in the Energy-concentrated domain, the ULA output model (52.3) with only one source can be transformed into

$$\begin{aligned}\mathbf{X} &= \int_{\vartheta\in\Theta} \mathbf{A}(\vartheta)S(u_1)\ell(\vartheta,\psi)\ d\vartheta + \mathbf{N} \\ \mathbf{X} &= \begin{bmatrix} X_1(u_1) & X_2(u_2) & \cdots & X_p(u_p) \end{bmatrix}^{\mathrm{T}} \\ \mathbf{N} &= \begin{bmatrix} N_1(u_1) & N_2(u_2) & \cdots & N_p(u_p) \end{bmatrix}^{\mathrm{T}}\end{aligned} \tag{52.14}$$

where, $S(u)$ is the FrFT of $s(t)$, and $N(u)$ is the FrFT of $n(t)$. In the next section, we will give parameter estimation method for the proposed model in the Energy-concentrated domain.

52.3 Parameter Estimation Algorithm

DSPE is a classical distributed narrowband signal parameter estimation algorithm which proposed a MUSIC-type distributed signal parameter estimator that is based on minimizing a norm of the transformed noise eigenvectors in the source subspace. Similarly, we propose that the parameter vector ψ of the distributed wideband LFM sources can be estimated by locating the peaks of

$$\hat{\psi} = \arg\max_{\psi} \frac{1}{\left\| b^H(\psi)E_n \right\|^2} \tag{52.15}$$

$$b(\psi) = \int_{\vartheta\in\Theta} A(\vartheta)\ell(\vartheta;\psi)d\vartheta \tag{52.16}$$

where E_n is noise subspace which is a $p \times (p-q)$ matrix with columns representing the eigenvectors of the covariance matrix $R_{\mathbf{XX}} = E(\mathbf{XX}^H)$ corresponding to the $(p-q)$ smallest eigenvalues.

As (52.5) shows LFM signals with different chirp rates have different rotation angels of the Energy-concentrated domain in which only one LFM signal can present an obvious peak and the energy distributions of other signals and noise are sparse. Therefore, the rotation angle of the Energy-concentrated domain can be determined by searching the coordination of spectrum peak in the two-dimensional plane (α, u). The spatial parameter of each source can be acquired by the proposed algorithm mentioned above individually in the corresponding Energy-concentrated domain. After that, received signal rotated with the rotation angle of the Energy-concentrated domain of others is processed successively with the same operation till the parameters of all sources are achieved. Thus, this method can be easily used in the condition with more sources than the number of sensors.

Main steps of the estimation algorithm are summarized as follows:

Step 1: FrFT of continuous orders are performed on received signals on the reference sensor, the source number and the rotation angles $\{\alpha_{ei}\}_{i=1}^{q}$ in the Energy-concentrated domain of all sources can be determined by the position information of the peak in the two-dimensional plane (α, u).

Step 2: Received signals on each sensor are calculated by FrFT of the rotation angle α_{ei}, and $\mathbf{X}$ is constructed by spectrum peak amplitudes of each sensor.
Step 3: The autocorrelation matrix $R_{\mathbf{XX}}$ in the Energy-concentrated domain is calculated and noise subspace E_n is solved using eigenvalue decomposition.
Step 4: The parameter ψ_i is estimated through (52.16).
Step 5: Steps 2–4 are repeated until acquiring the estimation parameters of all sources.

52.4 Simulation

In this section, the performance of our algorithm through some simulation experiments is investigated. The simulation assumes a ULA of $p = 8$ impinging from $q = 2$ far-field coherently distributed wideband LFM sources, whose initial parameters are $f_1 = 12\,\text{MHz}$ $f_2 = 10\,\text{MHz}$ and $\mu_1 = 1 \times 10^{12}\,\text{Hz/s}$ $\mu_2 = -10 \times 10^{12}\,\text{Hz/s}$. The central incident angles of two sources are taken as $\theta_1 = 60^\circ$ and $\theta_2 = -30^\circ$ with the extension widths from a Gauss angular distribution of width $\Delta_1 = 2^\circ$ and a uniform angular distribution of width $\Delta_2 = 4^\circ$ respectively. The signal-to-noise ratio (SNR) is 10 dB and 500 snapshots are observed.

As can be seen in Fig. 52.1, two obvious spectrum peaks are presented in the two-dimensional plane (α, u) which can determine the rotation angles of the Energy-concentrated domain of these two LFM sources. Figure 52.2 reveals the spatial parameters searching results of two LFM sources. As a result, the estimation central angles are $\hat{\theta}_1 = 60.02^\circ$ $\hat{\theta}_2 = -29.98^\circ$ and the extension widths are $\hat{\Delta}_1 = 2.01^\circ$ $\hat{\Delta}_2 = 4.01^\circ$.

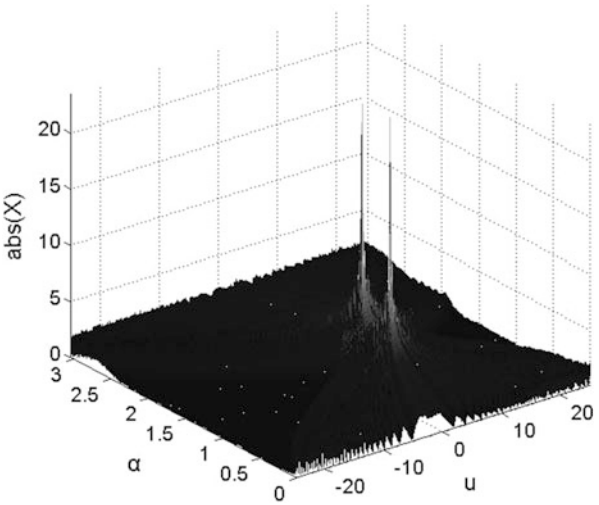

Fig. 52.1 Two-dimensional spectrum of two LFM sources in plane (α, u)

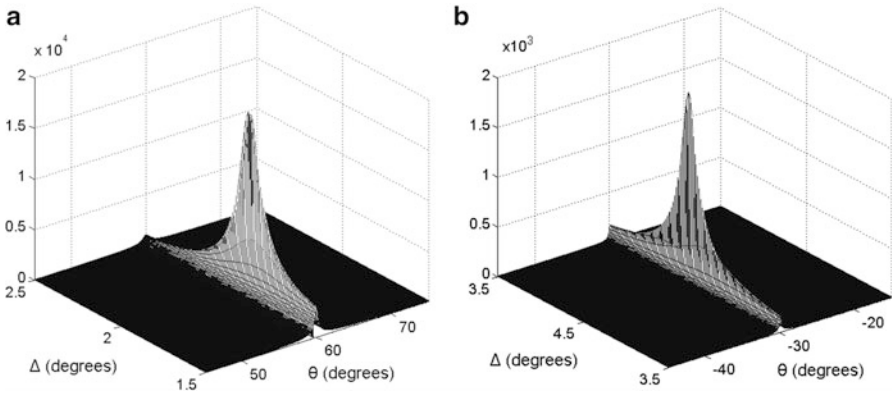

Fig. 52.2 The estimation spectrum of two LFM sources. (**a**) Source 1; (**b**) Source 2

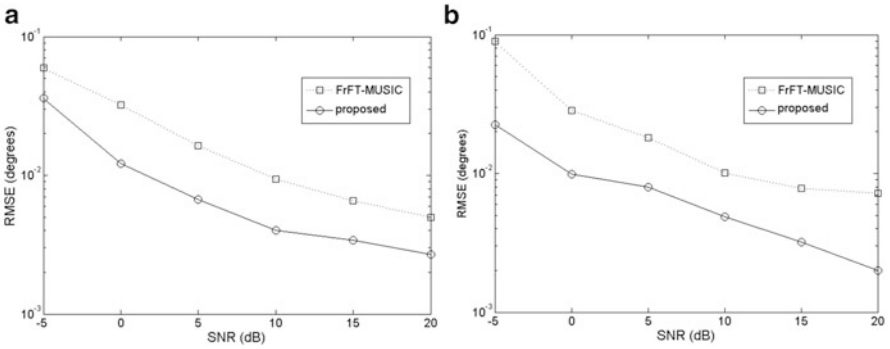

Fig. 52.3 The RMSE for the central angle versus SNR. (**a**) Source 1; (**b**) Source 2

For demonstrating the performance of the proposed algorithm in the condition of coherently distributed wideband LFM sources, the FrFT-MUSIC algorithm is chose as the comparing algorithm which is an estimation algorithm for wideband LFM point source. The Monte Carlo simulation is used 100 trials for each simulation using two algorithms. Figures 52.3 and 52.4 present the root mean square error (RMSE) for the central angle estimator versus different SNRs and different extension widths. Compared with the FrFT-MUSIC algorithm, the proposed algorithm provides a smaller RMSE in the estimation by increasing SNR and a more stable localization performance by increasing extension widths.

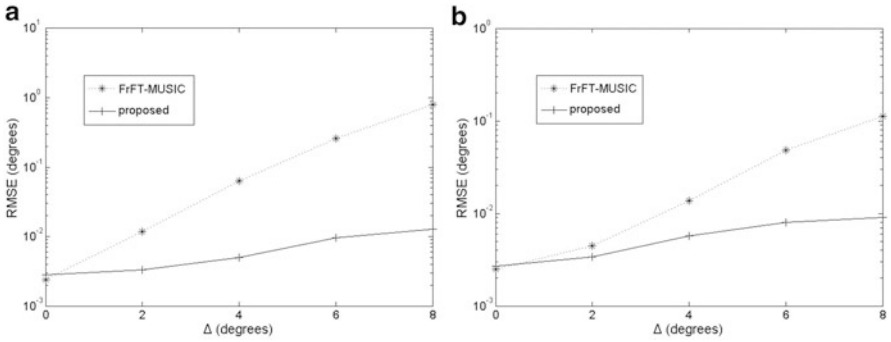

Fig. 52.4 The RMSE for the central angle versus extension width. (**a**) Source 1; (**b**) Source 2

Conclusion

To estimate the spatial parameters of coherently distributed wideband LFM source, a novel coherently distributed wideband LFM source model was proposed, and the estimation algorithm of the proposed model was presented using the time–frequency properties of LFM signal in fractional Fourier domain. In the proposed algorithm, the number of the estimation sources can be determined which was allowed to exceed the number of array, and the deterministic angular signal densities for all sources were not need to be identical. The simulation results show that the proposed algorithm had higher location accuracy and obtained better anti-noise performance than the FrFT-MUSIC algorithm.

Acknowledgments This work is supported by Tianjin Research Program of Application Foundation and Advanced Technology under Grant 14JCQNJC01400.

References

1. Djuric P, Kay SM (1990) Parameter estimation of chirp signals. IEEE Trans Acoust Speech Signal Process 38(12):2118–2126
2. Gershman AB, Amin MG (2000) Wideband direction-of-arrival estimation of multiple chirp signals using spatial time–frequency distributions. IEEE Signal Process Lett 7(6):152–155
3. Tao R, Zhou YA (2005) Novel method for the direction of arrival estimation of wideband linear frequency modulated sources based on fractional Fourier transform. J Beijing Inst Technol 25 (10):895–899
4. Yuan X (2012) Location-finding wideband linear FM sources with triangular arrays. IEEE Trans Aerosp Electron Syst 48(3):2416–2425
5. Valaee S, Champagne B, Kabal P (1995) Parametric localization of distributed sources. IEEE Trans Signal Process 43(9):2144–2153
6. Meng Y, Stoica P, Wong KM (1996) Estimation of the locations of arrival of spatially dispersed signals in array processing. Proc Inst Elect Eng Radar Sonar Navig 143:1–9

7. Qi L, Tao R, Zhou SY et al (2004) Detection and parameter estimation of multicomponent LFM signal based on the fractional Fourier transform. Sci China (Ser F Info Sci) 47(2):184–198
8. Ozaktas HM, Kutay MA, Mendlovic D (1999) Introduction to the fractional Fourier transform and its applications. Adv Imaging Electron Phys 106:239–291

Chapter 53
An Application of RFID Localization in Lane Recognition for Vehicles

Yingzhi Ren, Yongtao Ma, Xi Liu, Jiexiao Yu, and Kaihua Liu

Abstract Due to the surge in the number of vehicles throughout the world, traffic problems become increasingly severe. Thus, the implementation of lane recognition plays an important role in Intelligent Transportation Systems (ITS). In this paper, we present a RFID based positioning approach for lane recognition which is also practical for scenarios like tunnels or multilayer viaduct where GPS is not available now. As Phase Difference of Arrival is the essential information for localization, two UHF RFID phase extraction schemes have been discussed. Experimental results show that both of the two schemes can achieve an error recognition rate under 6.0 %. The sub-sampling scheme has a better performance than Zero-IF Receiver at the expense of system complexity.

Keywords Lane recognition • RFID based localization • Phase difference of arrival • Sub-sampling • Zero-IF

53.1 Introduction

With the advantages of low costs, powerless, easy deployment and relatively long communicating distance, localization techniques based on passive UHF RFID has been widely applied in warehouse [1–3], supply chains, office, parking lot, etc. It is foreseeable that this technique would be widely used in many fields in the near future.

In recent years, localization methods based on Phase Difference of Arrival (PDOA) has drawn researchers' attention, using sub-carrier AM modulation [4] or multi-frequency-based techniques [5] we could extract the phase difference information for localization, and overcome the phase ambiguity problem. Nikitin et al. used RF phase information of UHF RFID signal to get the spatial identification (determining position and velocity), and presented the experiments performed in a real RFID warehouse portal environment [6]. Yongtao Ma et al. utilized a joint iterative phase reconstruction algorithm to improve the localization precision in non-line-of sight environment [7].

Y. Ren (✉) • Y. Ma • X. Liu • J. Yu • K. Liu
School of Electronic Information Engineering, Tianjin University, Tianjin, China
e-mail: nancy@tju.edu.cn

J. Mu et al. (eds.), *The Proceedings of the Third International Conference on Communications, Signal Processing, and Systems*, Lecture Notes in Electrical Engineering 322, DOI 10.1007/978-3-319-08991-1_53

Due to the worldwide increase in the number of vehicles, research on Intelligent Transportation System (ITS) is becoming an urgent necessity [8]. With advantages described above, RFID techniques could be an appropriate option to be applied in lane recognition, which is important for lane keeping and lane changing assistance systems in ITS [9]. However, the vehicular localization in ITS nearly all depends on GPS, and the localization accuracy always could not meet the demands under some certain circumstances.

In this paper, we mainly introduce UHF RFID localization algorithms based on PDOA method into lane recognition for ITS. The main content is organized as follows. In Sect. 53.2, two phase extraction schemes based on different UHF RFID transceivers are discussed and compared. In Sect. 53.3, we propose a lane recognition method used for specific urban traffic environment. In Sect. 53.4, we establish a simulation environment, and evaluate the performance of the proposed method.

53.2 Discussion of Two UHF RFID Phase Extraction Schemes

UHF RFID localization algorithms based on PDOA have been studied for several years, however, phase extraction schemes based on UHF RFID transceivers and signals have yet to be discussed. In this section, using sub-carrier AM modulation method mentioned in [7], we demonstrate two phase extraction schemes: Sub-sampling (SS) scheme and Zero-IF Receiver (ZR) scheme. Under sub-carrier AM modulation method, the continuous wave is replaced by sub-carrier AM modulation signal during backscattering, the transmitting signal $S(t)$ could be defined as Eq. (53.1)

$$S(t) = A[1 + m_a \cos(2\pi f_{sub} t + \varphi_s)] \cos(2\pi f_c t + \theta_s) \tag{53.1}$$

Where A is the amplitude of the carrier, m_a is the modulation index, f_{sub} and f_c are sub-carrier and carrier frequency, φ_s and θ_s are the phase of sub-carrier and carrier signals.

During backscattering, the baseband signal (PC + EPC + CRC16) of the tag is modulated to the sub-carrier AM modulation signal using ASK and then backscattering to the space. At the antenna of the reader, the receiving signal $R(t)$ could be demonstrated as Eq. (53.2)

$$R(t) = A' m(t)[1 + m_a \cos(2\pi f_{sub} t + \varphi_R)] \cos(2\pi f_c t + \theta_R) + N(t) \tag{53.2}$$

Where A' is the amplitude of the carrier at the receiver, $m(t)$ is the baseband signal of the tag, φ_R and θ_R are the phase of sub-carrier and carrier signals of the receiving signal, $N(t)$ is the random noise. The phase φ_R is the phase information

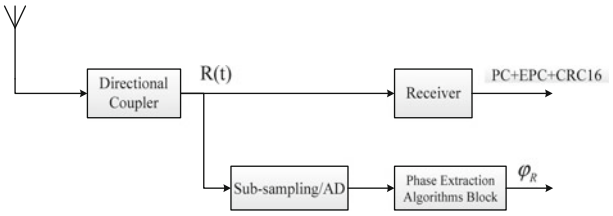

Fig. 53.1 Structure of sub-sampling scheme

needed to estimate the phase difference, and the phase extraction schemes will be discussed as follows.

53.2.1 Sub-sampling Scheme

Sub-sampling phase extraction scheme needs to modify the structure of the existing UHF RFID receiver, the structure of the scheme is shown in Fig. 53.1.

As is shown in Fig. 53.1, the receiving signal $R(t)$ would be separated into two paths, one path goes through the receiver to be demodulated and decoded, and then we could get the PC + EPC + CRC16 information; the other one is to be sub-sampled and Analog-Digital converted, then we could use phase extraction algorithm block to get receiving phase φ_R of the sub-carrier signal. The sub-sampling frequency f_s is far lower than the center frequency f_c of the signal $R(t)$. Though some information would be lost after sub-sampled, it has been proven in [4] that the phase information could be reconstructed without distortion. After sampling and A/D converting, digital domain signal $R(n)$ could be redefined as

$$R(n) = A' m(n/f_s)[1 + m_a \cos(2\pi n f_{sub}/f_s + \varphi_R)] \cos(2\pi n f_c/f_s + \theta_R) + N(n/f_s) \tag{53.3}$$

Introduce angular frequency $\omega_{sub} = 2\pi f_{sub}/f_s$ and $\omega_c = 2\pi f_c/f_s$ into Eq. (53.3), then

$$R(n) = A' m(n/f_s)\left\{ \cos(\omega_c n + \theta_R) + \frac{1}{2} m_a \cos[(\omega_c + \omega_{sub})n + \theta_R + \varphi_R] + \frac{1}{2} m_a \cos[(\omega_c - \omega_{sub})n + \theta_R - \varphi_R] \right\} + N(n/f_s) \tag{53.4}$$

Using phase extraction algorithms, we could get the receiving sub-carrier phase φ_R and then estimate the phase difference

$$\Delta\varphi = \frac{(\theta_R + \varphi_R) - (\theta_R - \varphi_R)}{2} - \varphi_S \tag{53.5}$$

And with Eq. (53.6), we could obtain the distance between the reader and the tag.

$$d = \frac{c\Delta\varphi}{4\pi f_{sub}} \tag{53.6}$$

In summary, SS scheme process the receiving signal on the UHF band and need not frequency conversion or filtering, interfere from circuit could be avoided to some extend. However, this scheme needs to modify the existing UHF RFID reader structure, additional sub-sampling component and phase extraction component is needed as well. Meanwhile, A/D converter works at UHF band is expensive, the system cost would rise a lot.

53.2.2 Zero-IF Receiver Scheme

Contrary to sub-sampling method, Zero-IF Receiver method is based on the existing UHF RFID receiver and needn't to modify the current structure of the reader. Zero-IF receiver is widely used in UHF RFID readers, and we should obtain the receiving sub-carrier phase φ_R and PC + EPC + CRC16 information at the same time. To accomplish this work, we need to integrate the receiving signal $R(t)$ and the Zero-IF receiver structure, as is shown in Fig. 53.2.

The extraction of PC + EPC + CRC16 information and phase information are undertaken under the same receiver structure. Before A/D converting, the receiving signal $R(t)$ needs to be down-converted to the baseband and the signal is separated into In-phase (I) and Quadrature (Q) path. Assuming the LO signal is $\cos(2\pi f_c t + \psi)$, then after down converting and filtering, the I and Q signal could be demonstrated as

$$\begin{aligned} R_I(t) &= \frac{1}{2}A' m(t) m_a \cos(2\pi f_{sub} t + \varphi_R)\cos(\theta_R - \psi) + N_I(t) \\ R_Q(t) &= \frac{1}{2}A' m(t) m_a \cos(2\pi f_{sub} t + \varphi_R)\sin(\theta_R - \psi) + N_Q(t) \end{aligned} \tag{53.7}$$

Where $N_I(t) = N(t)\cos(2\pi f_c t + \psi)$ and $N_Q(t) = N(t)\sin(2\pi f_c t + \psi)$. Then we use a sampling frequency f_s satisfied to the Nyquist theorem, thus the I/Q signal in digital domain could be redefined as

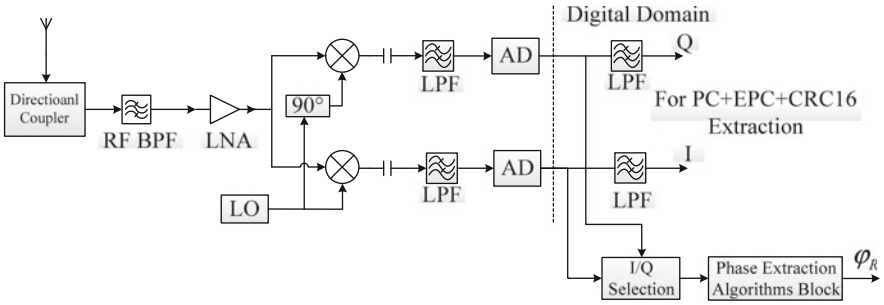

Fig. 53.2 Structure of zero-IF receiver scheme

$$\begin{aligned} R_I(n) &= \frac{1}{2}A^{'}m(n/f_s)m_a\cos(\omega_{sub}n+\varphi_R)\cos(\theta_R-\psi)+N_I(n/f_s) \\ R_Q(n) &= \frac{1}{2}A^{'}m(n/f_s)m_a\cos(\omega_{sub}n+\varphi_R)\sin(\theta_R-\psi)+N_Q(n/f_s) \end{aligned} \tag{53.8}$$

Signal in Eq. (53.8) are the signals we need to extract PC + EPC + CRC16 information and phase information. For PC + EPC + CRC16 information extraction, as the baseband signal is modulated to the sub-carrier signal, we need to design another low-pass filter (LPF) to filter out the sub-carrier signal before decoding. For phase extraction, we could use phase extraction algorithms to obtain the phase of the receiving sub-carrier signal φ_R, and then get $\Delta\varphi$ and d by Eq. (53.6). It's worth noting that in each path there is an attenuation index $\cos(\theta_R-\psi)$ or $\sin(\theta_R-\psi)$, with that the signal could be attenuated into zero. So before phase extraction, we need to choose one path of bigger amplitude from the I/Q signals.

As discussed above, ZR scheme needs not to modify the current structure of the RFID readers and need not extra hardware. To make the receiving signal compatible with the reader, what we need to do is just modify some parameters of the filters. Furthermore, all the signal processing procedures are done in digital domain, and it is convenient to design and control. However, this scheme seems vulnerable to interferes caused by the circuit, and some offset is needed in signal processing procedures.

53.3 Proposed Lane Recognition Method

In this paper, we consider that the three-dimension scenario is configured by one reader with four antennas and a passive tag adhered to the vehicle's front windshield, which is shown in Fig. 53.3. Considering the reality of road conditions, we assume there are four lanes in one-way road, each lane's width is 4 m. The four antennas of reader are placed in the middle of every lane, so the pitch of every neighboring antenna is 4 m as well. Antennas are set in a line and 6 m height from ground, the angle between antenna's main lobe direction and horizontal is 30°.

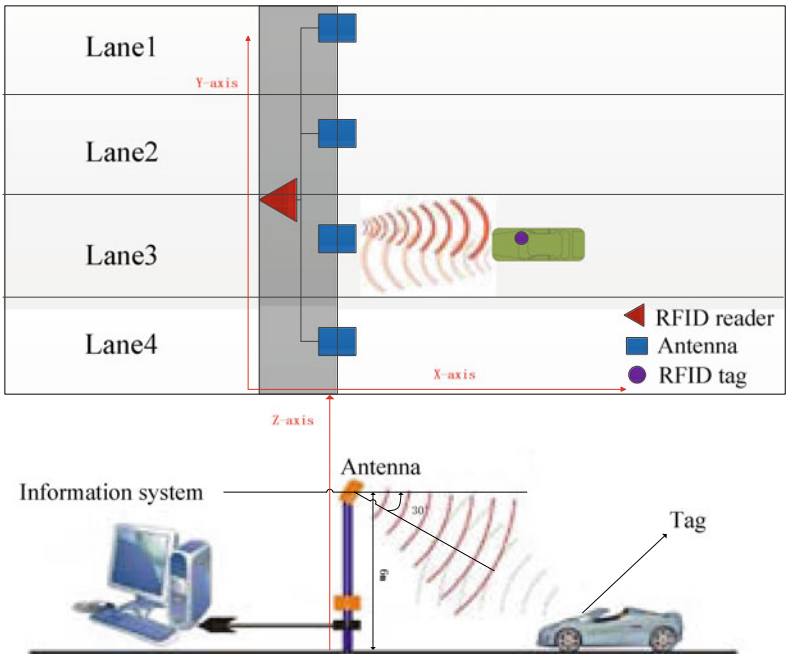

Fig. 53.3 Lane recognition scenario

The tag is adhered to the vehicle's front windshield so the antenna could contact with it as soon as vehicle enters antenna's radiation range.

When estimating the position of moving vehicles, antennas will work as a time division multiple access system for transmitting and receiving signals sequentially. The phase difference of sub-carrier can be calculated by the reader then converted into distance between antenna and tag according to Eq. (53.6).

The distance obtained by each antenna can be written as *d1*, *d2*, *d3*, *d4*. As demonstrated in Fig. 53.1, all the four antennas are put in the same height and also in a straight line. Hence, there will be innumerable solutions for the equations established by *d1*~*d4*. This is shown in Fig. 53.4, all the points in dashed arcs meet the requirements. Thereby, we can just achieve one-dimensional positioning through the present antenna layout scheme. Luckily, only the Y-axis dimensional positioning is needed for lane determination under the circumstance pictured in Fig. 53.3.

The position of each antenna is known as (x_i, y_i, z_i), $i = 1, 2, 3, 4$, and the position (x, y, z) of tag is unknown. There is no need for the tag to communicate with the reader, but it's important to backscatter radio wave of antennas. It is assumed that the sub-carrier phase difference from the *i*th antenna via tag and then back to *i*th antenna receiver is $\Delta\varphi_i$ (i = 1, 2, 3, 4), and we get these information through All-phase-FFT, the distance can be obtained by Eq. (53.6), then

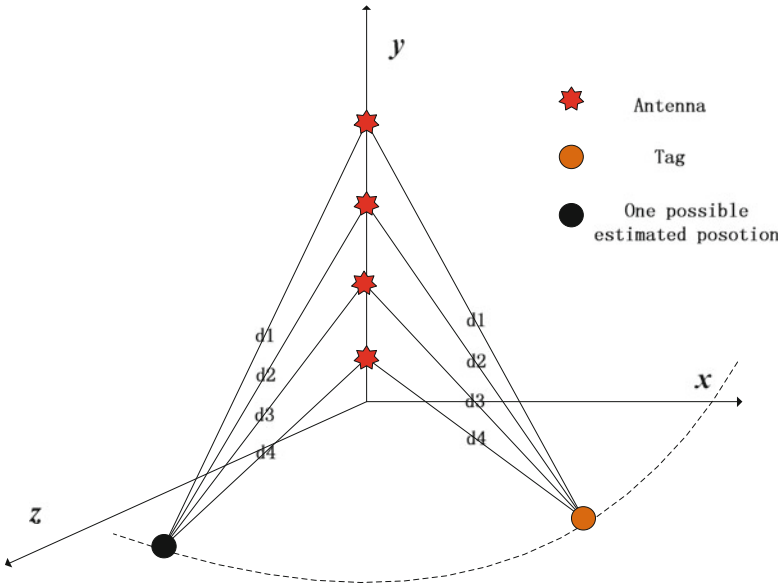

Fig. 53.4 Innumerable solutions

$$\begin{cases} \sqrt{(x_1 - x)^2 + (y_1 - y)^2 + (z_1 - z)^2} = d_1 \\ \sqrt{(x_2 - x)^2 + (y_2 - y)^2 + (z_2 - z)^2} = d_2 \\ \sqrt{(x_3 - x)^2 + (y_3 - y)^2 + (z_3 - z)^2} = d_3 \\ \sqrt{(x_4 - x)^2 + (y_4 - y)^2 + (z_4 - z)^2} = d_4 \end{cases} \tag{53.9}$$

Take square on both sides of Eq. (53.9), then execute subtraction operation on the both sides of the two adjacent equations. As the antennas are in a line, so that $x_i - x_{i-1} = 0, z_i - z_{i-1} = 0$. Then the equations can be obtained as

$$\begin{cases} (y_2 - y_1)y = \frac{1}{2}(y_2^2 - y_1^2 + d_1^2 - d_2^2) \\ (y_3 - y_2)y = \frac{1}{2}(y_3^2 - y_2^2 + d_2^2 - d_3^2) \\ (y_4 - y_3)y = \frac{1}{2}(y_4^2 - y_3^2 + d_3^2 - d_4^2) \end{cases} \tag{53.10}$$

Obviously Eq. (53.10) is a system of linear equations and can be solved by least squares algorithm, then we can get the tag's position of Y-axis, combined with the width of each lane, the lane number of vehicle is using can be determined as

$$\begin{cases} y < 4, & lane\,1 \\ 4 \le y < 8, & lane\,2 \\ 8 \le y < 12, & lane\,3 \\ 12 \le y, & lane\,4 \end{cases} \tag{53.11}$$

53.4 Experimental Results

For evaluating the location accuracy of our scheme, we conduct a series of simulation experiments. It is assumed that the experimental field is $16 \times 16 \times 6$ m which is three-dimension, the actual height of vehicle is generally 1–3 m, so the range of the location of tag is $0 \le x \le 16m, 0 \le y \le 16m, 1 \le z \le 3$. The four antennas are set in the middle of every 4-m-length lane, and 300 tags are randomly distributed in each lane. All antennas can receive the signal from tag without distortion, an average accuracy of position estimation of 1,000 independent simulation runs is considered.

In Fig. 53.5, we make a localization comparison between two schemes, location estimation error is shown as RMSE changing with signal to noise rate (SNR). As SNR is high, the estimation accuracy of positioning would become high. We can find that the SS scheme performs a better localization accuracy than the ZR scheme. The SS scheme can obtain RMSE < 0.5 m when SNR is higher than 11 dB, the ZR scheme may have a similar RMSE range when SNR is higher than 12 dB. The main reason may attribute to the mixing processing in receiver of ZR scheme, this may introduce additional noise. However, as SNR becomes high, the RMSE differences of the two schemes become smaller. It is 0.012 m when SNR is 20 dB.

As shown in Fig. 53.6, the error recognition rate (ERR) of two schemes will decrease rapidly with the increasing of SNR. The ERR of SS and ZR will reach their

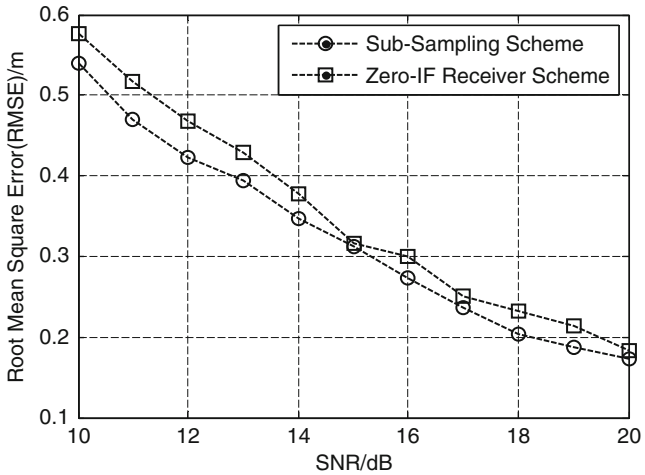

Fig. 53.5 Localization comparison

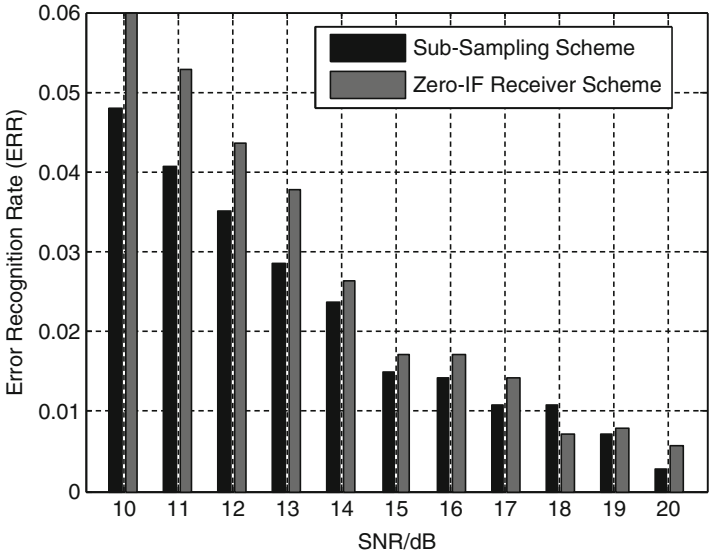

Fig. 53.6 Error recognition rate comparison

peak at 4.79 % and 6.00 %, respectively, when SNR = 10 dB. And both of the two schemes can almost obtain ERR ≦ 1.0 % when SNR ≧ 18 dB. The ERR of two schemes become closer when the SNR goes up which coincides with the performance in Fig. 53.5.

Conclusions

In this paper, the sub-sampling scheme and zero-IF receiver scheme are proposed as two novel signal processing procedures for localization. Firstly, the two phase extraction schemes have been presented and proved. Then we laid out a lane recognition method under a certain traffic scenario. Finally, simulation results are presented to verify that the proposed methods could successfully recognize the lane in most cases. The SS scheme had a better performance than ZR under diverse SNR, however, it will complicate the existing UHF RFID reader structure and cost more. On the contrary, the ZR scheme had a slightly worse ERR compared to SS but it's easy to deploy and with no extra cost. As a conclusion, the two schemes both had their strengths and weaknesses, we may choose one from the perspective of the actual needs. Both of them could fulfill high localization accuracy and reasonable ERR by numerical analysis.

References

1. Heidrich J, Brenk D, Essel J et al (2010) The roots, rules, and rise of RFID. IEEE Microw Mag 11(3):78–86. doi:10.1109/MMM.2010.936075
2. Costanzo A, Masotti D, Ussmueller T et al (2013) Tag, you're it: ranging and finding via RFID technology. IEEE Microw Mag 14(5):36–46. doi:10.1109/MMM.2013.2259392
3. Ni LM, Zhang D (2011) RFID-based localization and tracking technologies. IEEE Wirel Commun 18(2):45–51. doi:10.1109/MWC.2011.5751295
4. Shi WG, Liu KH, Fang JJ et al (2012) UHF RFID location algorithm based on dual frequency subcarriers amplitude modulation. Harbin Inst Tech 44(3):81–86
5. Li X, Zhang Y, Amin MG (2009) Multifrequency-based range estimation of RFID tags. RFID. doi:10.1109/RFID.2009.4911199
6. Nikitin PV, Martinez R, Ramamurthy S et al (2010) Phase based spatial identification of UHF RFID tags. RFID. doi:10.1109/RFID.2010.5467253
7. Ma Y, Zhou L, Liu K et al (2014) Iterative phase reconstruction and weighted localization algorithm for indoor RFID-based localization in NLOS environment. IEEE Sensor J 14 (2):597–611. doi:10.1109/JSEN.2013.2286220
8. Al-Naima FM, Al-Any H (2011) Vehicle location system based on RFID. DeSE. doi:10.1109/DeSE.2011.11
9. Togashi H, Borcea C, Yamada S (2012) Lane recognition for moving vehicles using multiple on-car RFID receiver antennas—algorithm and its experimental results. Intell Vehicles Symp (IV). doi:10.1109/IVS.2012.6232139

Chapter 54
Design and Implementation of Target Positioning System Based on Map API

Hongwei Liu, Yongxin Liu, Yonggang Ji, Hui Zhang, and Zhiqiang Zheng

Abstract This paper presents a method for target positioning on the map. It provides an intuitive and effective view of the target location. With this method the specific target positioning information can be gotten and the attribute of target can be viewed and analysed easily. The method is implemented using C# windows forms and JavaScript scripting based on Map API. The JavaScript scripting is used to create a page map and accomplish map coordinate covering and other necessary operations. The C# windows forms are used to build the operation and display interface in the VS2010 development environment. This approach is applied to the specific positioning of vessels. The results show that the vessel can be well positioned on the map, and can achieve a good purpose for the analysis of vessels.

Keywords Positioning • Map API • JavaScript • C# • Map coordinate • Covering

54.1 Introduction

The application field of the map positioning system are very extensive, such as ship positioning, vehicle navigation, aircraft cruising, typhoon warning, seismic surveys, and missile guidance and so on. Map positioning system can provide accurate location information of the target, the location of the target can be shown through the form of map unfolded, which can give an intuitive and profound impression to people. It effectively improves the way of people to monitor the target, and greatly enhances the monitoring efficiency at the same time. Therefore, map positioning system has gradually become an important part of the current target monitoring fields [1–4].

Looking at the present situation of the development of map positioning system in domestic and foreign, there are three main ways to achieve map positioning. One is through the establishment of the professional website, such as the query system of

H. Liu • Y. Liu (✉) • H. Zhang • Z. Zheng
College of Electronic Information Engineering, Inner Mongolia University, Hohhot 010021, China
e-mail: yxliu@imu.edu.cn

Y. Ji
First Institute of Oceanography, State Oceanic Administration, Qingdao 266061, China

J. Mu et al. (eds.), *The Proceedings of the Third International Conference on Communications, Signal Processing, and Systems*, Lecture Notes in Electrical Engineering 322, DOI 10.1007/978-3-319-08991-1_54

ship location of Ship Tracker, the second is to establish a dedicated map positioning software, such as Google Map and the third is by means of VC++ and other development software through calling Map API [5] interface for secondary development on the map. Professional map positioning website has a high efficiency development mode, but the amount of programming code is very large. The specialized map positioning software has high execution efficiency, but its expanding is poor and its update are more complex. With the software calling Map API interface for secondary development can both avoid large amount of programming code and has better application scalability, which is a popular way of research and development of map positioning system.

To achieve map positioning, we must resolve how to load the map, how to process the target data and using what methods to mark the target position on the map. Because of its geographical location information contained in the map is very large, extremely complex and diverse, the workload of map programming process is enormous. From the study of the current situation, the current map processing is mostly to put the map into the webpage through programming, and it will be presented in front of the user in the form of webpage. We can complete various operations on the map on this basis.

This paper presents a target map positioning method based on Map API and JavaScript technology, the technology platform is implemented in the VS2010 development environment. Using the C# windows forms application builds the control platform interface. To load and display in the WebBrowser control of windows forms program through the Map API interface. Then, we need programming to read the radar target data into the window and doing some pre processing. Finally, by calling windows forms and JavaScript, We can achieve the geographic location information of the target well display and match on the map.

54.2 Brief Introduction of JavaScript API

The way of secondary development on the map on API component provided by the current map website has been developed rapidly in recent years. Map JavaScript API is a set of application programming interface written by JavaScript language based on map service, using the interface can not only call the existing map, but also can realize secondary development on current map through independent coding. It provides convenience for the user to develop map, it can also help the developers to build rich and strong interactive map application, which can greatly improve the development efficiency of map application.

Map API provides the using of map basic functional interface and it also provides a series of map operation development options. Using the different development options can achieve different operations of the target, such as using map parameter setting function can conveniently set the map center point and zoom level. Using the map tool can conveniently get the distance of two points and get the latitude and longitude of the current position and so on.

Through adding covering function provided by map API can add the mark to the position of the target, it can both add the mark using the default label icon and also implement custom covering design through programming. In addition to the various operations on the map, it also provides a series of controls to view the map, with which can achieve a good purpose to analysis and view the target on the map.

54.3 Loading Map in the WebBrowser Control

Loading map is achieved primarily through the following two steps. First, it needs to create an HTML page map using the JavaScript scripting language. Then, it needs to load the created page map into C# WebBrowser control. Map loading process is shown in Fig. 54.1.

The establishing method of each part of the process is as follows:

54.3.1 Creating a Map in HTML Page

The page map creates primarily through the following steps:

- Designing a page to introduce Map API: JavaScript statement with Script tag is required to point to the API address, namely: <script type="text/javascript" src

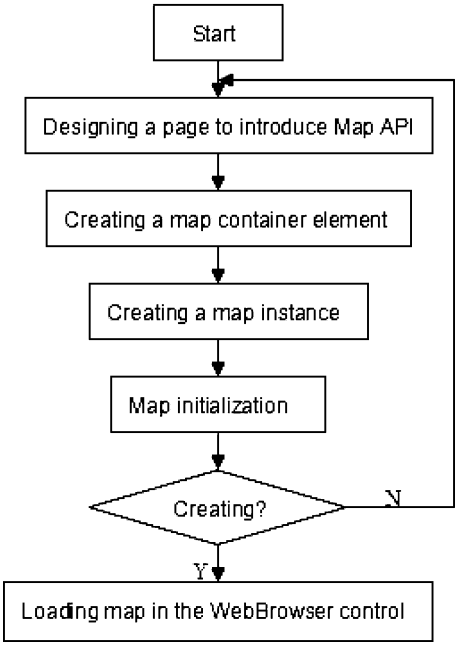

Fig. 54.1 Flow chart of map loading

=“http://api.map.baidu.com/api?v=1.3”></script>. Of which, URL points to the location of the JavaScript file that includes all symbols and definitions required when using Map API, v=1.3 means that the interface is the version 1.3.
- Creating a map container element: This creates a div element, namely: . Map requires an HTML element as a container, so as to show to the page.
- Creating a map instance: Using the Map class of the BMap namespace creates a new instance of the map, namely: var map = new BMap.Map(“allmap”). Among which, all map is the id attribute of div, and map is created in the allmap container.
- Map initialization: Using setCenter () and setZoom () methods complete the map initialization, including setting the display mode, setting latitude and longitude of the center point, and setting zooming factor.

54.3.2 Loading Map in the WebBrowser Control

Using the method of C# Forms program calls JavaScript to load the map. The main steps are as follows:

- Two pieces of code is needed to be added before the Form1 class [PermissionSet (SecurityAction.Demand,Name=“FullTrust”)]and[System.Runtime. InteropServices.ComVisible(true)].The purpose of these two pieces of code is to request permission for the assemblies, and make COM component visible for the application program [6].
- In the form loading function Form1_Load (), we need to write map loading program. To find the loaded map page, it needs to redefine the Uri address of the page file in the program, namely: string address = “File: \cr” + Application. StartupPath + “\cr baidumap.html”. It also needs to set the properties of the WebBrowser control, namely: webBrowser.ObjectForScripting = this, appointing the HTML page map as the access object of the control webpage.
- The display effect after loading the map is shown in Fig. 54.2.

54.4 Reading and Preprocessing Target Data

It needs to add a positioning button in C# Forms program, and add the reference of System.IO namespace of the system. So that the class can be used directly under the namespace to read and do other operations of the source file. According to the original data’s format and type, the appropriate processing program is needed to be added. Reading process of objective data is shown in Fig. 54.3.

Fig. 54.2 Display the map after loading

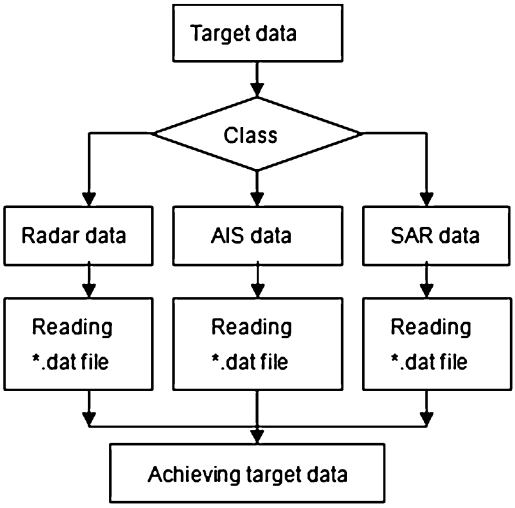

Fig. 54.3 Reading process of target data

The basic algorithm flow of reading the target data is as follows:

- A file input stream is needed to define, and using Read Line() method of Stream Reader class reads the input stream. It is used to read a line of the Characters from the input streams, and the result is returned as a string.
- Using the line.Split() method splits the string, then the divided string stores in an string array.
- In order to retain the accuracy of original data and be convenient to operate the data, it needs to converse the type of string data and double data, and the result is

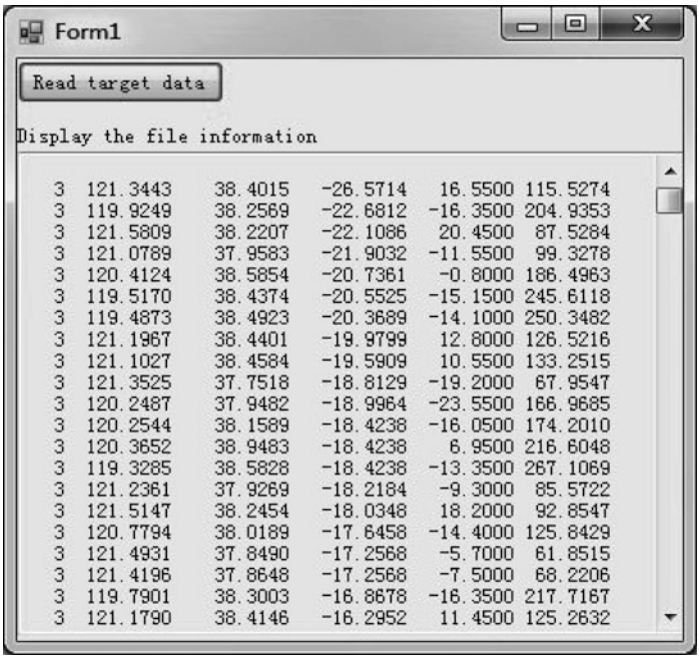

Fig. 54.4 The display result after reading of target data

stored in the converted double array. It can realize convenient processing and calling of the data.

- The display effect of target data after reading is shown in Fig. 54.4.

54.5 Achieving Target Map Positioning

By calling JavaScript script functions in HTML page of C# Forms class achieves target map positioning. The algorithm flow chart is shown in Fig. 54.5.

The basic process of the specific algorithm is as follows:

54.5.1 Positioning Method Written in HTML Pages

A positioning method of custom icon label is designed. Steps are as follows:

- Making an icon of the right size. If the background requires being transparent, images should be saved as .png format. Then it needs to take the picture into the Forms program debug folder.

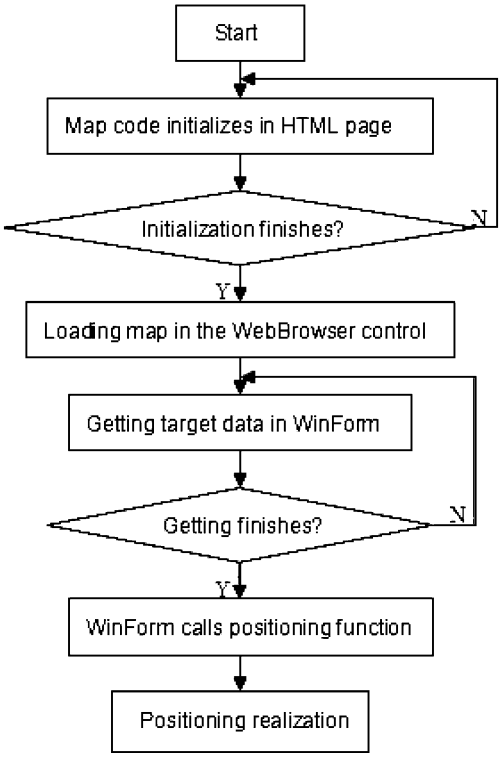

Fig. 54.5 Flow chart of target map positioning

- For icons of different labels, it needs to program corresponding positioning function in the HTML page. First, icons which have already been made needs to define and add the appropriate reference. Sizes and dimensions should be consistent between defined function icons and the actual icons. Then, according to the parameter of the function, we can create corresponding label points by using Marker class under the BMap namespace. Finally, using the method of map.addOverlay() [7] adds the appropriate label on created annotation points.

54.5.2 Calling Positioning Method of HTML Page in C# Form Class

Using webBrowser.Document.InvokeScript("method name", new object [] {parameter 1, parameter 2}) in C# Forms program calls positioning method of HTML page. The parameters in which are information in arrays when the target data is read and preprocessed, such as latitude and longitude, which are as actual parameters. It will be passed to parameters in the HTML page. Then the target location is determined, and we can add the icons calling this method.

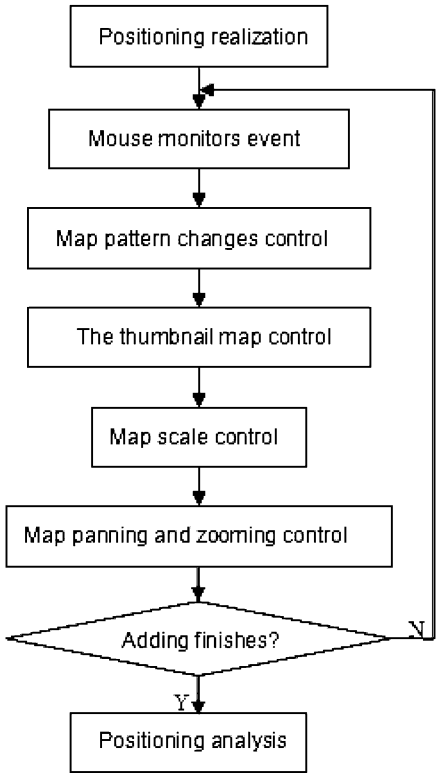

Fig. 54.6 Adding positioning analysis function module

After achieving positioning, in order to analyze and view the located target on the map, it needs to add some target analysis function on the map. It can achieve a well target analysis purpose by using a variety of map controls and events provided by Map API. The target map analysis module is defined and shown in Fig. 54.6.

54.6 Application Example

Figure 54.7 is the effect of co-locating of vessels' HFSWR and AIS data in a certain area of Chinese sea on October 31st, 2011. The small square represents the radar data. The small triangle represents the AIS data. They all use custom annotation icon. Left mouse clicking the labeled icon of the current target, it will appear a dialog to display the latitude and longitude of the current target position [8].

Through zooming function, it can easily get the view of the overall and local effect of the map. Partial image of interception in Fig. 54.7 is analyzed as follows:

It can be seen that some of the targets gathered in Fig. 54.8. The targets can not be effectively viewed and analyzed. Therefore, it needs to further amplify the map.

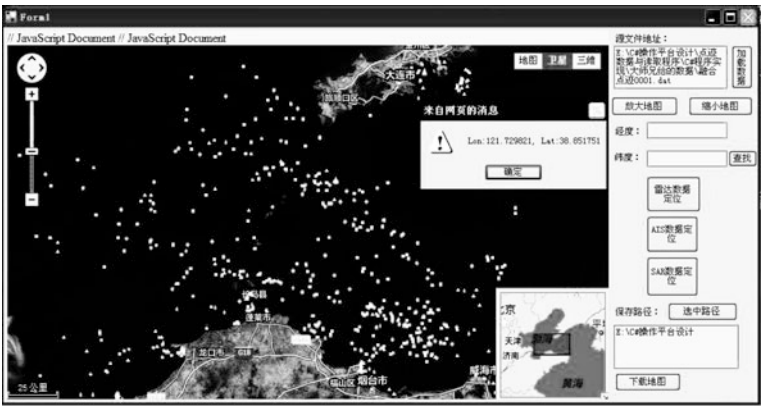

Fig. 54.7 The common display of HFSWR and AIS ship data

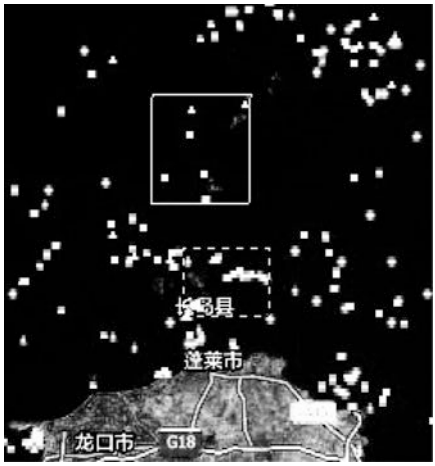

Fig. 54.8 Image of part of Fig. 54.7

We select partial area for analysis in Fig. 54.8. The dashed boxed section is enlarged and shown in Fig. 54.9.

By clicking the left mouse button to get the latitude and longitude information of the target, it can be further analyzed to obtain other relevant information. The solid line framed section in Fig. 54.8 is enlarged and analyzed, and the result is shown in Fig. 54.10.

After achieving positioning, through the radar and AIS data or SAR and AIS data available to demonstrate on one map, using the position and velocity matching algorithm [9] can analyze and recognize the target.

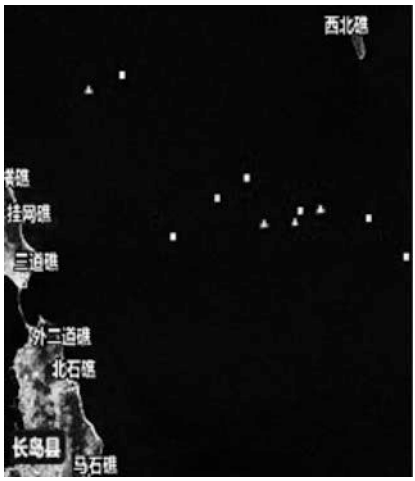

Fig. 54.9 Amplification and display of the dashed framed section of Fig. 54.8

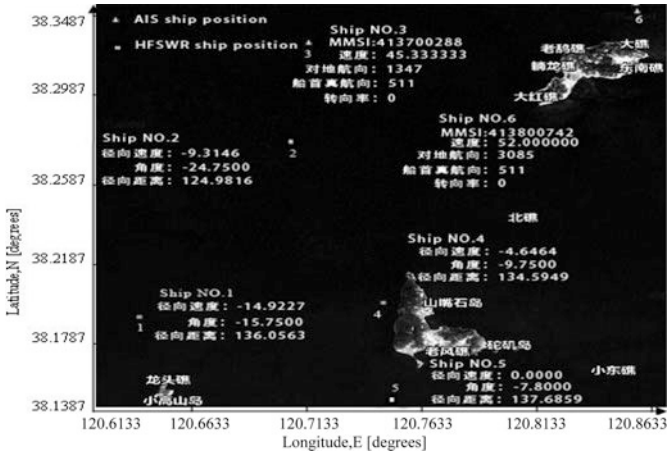

Fig. 54.10 Zooming display and analysis of the *solid line* framed section of Fig. 54.8

Conclusion

In the target location information display functions based on Map API, a target map positioning method using JavaScript programming language mixing with C# windows forms application is established. The results show that the location of the target can be clearly and precisely marked and displayed on the map. It can achieve the purpose of convenient observation

(continued)

and analysis of the target. The method has wide applicability, it can be applied to vehicles, vessels and other areas that are required target monitoring, and it also has important and positive significance in positioning technology applications.

Acknowledgments This research is sponsored by National Natural Science Foundation of China (61362002).

References

1. Almomani IM, Alkhalil NY, Ahmad EM et al (2011) Ubiquitous GPS vehicle tracking and management system. In: IEEE Jordan conference on applied electrical engineering and computing technologies (AEECT), Amman, pp 1–6
2. Chang SJ (2004) Development and analysis of AIS applications as an efficient tool for vessel traffic service. In: Oceans '04. MTTS/IEEE Techno-Ocean '04, Kobe, vol 4, pp 2249–2253
3. He L, Lai ZJ (2010) The study and implementation of mobile GPS navigation system based on Google Maps. In: International conference on computer and information application (ICCIA), Tianjin, pp 87–90
4. Lin J-Y, Yang B-K, Do T-A et al (2013) The accuracy enhancement of GPS track in Google Map. In: Eighth international conference on broadband and wireless computing, communication and applications (BWCCA), Compiegne, pp 524–527
5. Dong ZY (2013) The communication map shows based on Baidu Maps JavaScript API. Electron Des Eng 21:73–76
6. Xu CR, Zhou CB (2013) The research of methods to browse Google satellite map in AutoCAD. Bulletin of Surveying and Mapping, pp 77–79
7. Qiang JP, Yang XT, Liu XX et al (2011) Construction of fast graphics traceability system for agricultural products. Trans Chin Soc Agric Eng 27:167–171
8. Su YZ, Zhang KY (2009) Study and design on the engineering data management system based on Google Maps API technology. Bulletin of Surveying and Mapping, pp 48–69
9. Chaturvedi SK, Yang C-S, Ouchi K et al (2012) Ship recognition by integration of SAR and AIS. J Navig 65:323–337

Chapter 55
Interpolation Database Construction for Indoor WLAN Localization via Breakpoint Propagation Modeling

Mu Zhou, Feng Qiu, Zengshan Tian, Qiao Zhang, and Qing Jiang

Abstract Among different types of Wireless Local Area Network (WLAN) positioning systems, fingerprinting-based localization exhibits good accuracy performance, and thus becomes increasingly popular. Fingerprinting-based localization needs extensive calibration effort to construct a Received Signal Strength (RSS) fingerprint database, which hinders the large development of WLAN localization. In this paper, to reconstruct the raw sparse fingerprinting database and reduce manual effort, we propose a novel integrated Propagation Model-based Breakpoint Model Interpolation (PMBMI) and Multidimensional Linear Interpolation (MLI). We carry out extensive experiments in a ground-truth indoor environment to examine the localization accuracy of our proposed approach. Experimental results show that our proposed approach can be applied to reduce the labor cost in off-line phase, as well as guaranteeing high-enough accuracy performance.

Keywords WLAN • Interpolation • Propagation model • Multidimensional linear interpolation • Location fingerprint

55.1 Introduction

As the demand for real-time location information remarkably increases, the Location-based Services (LBSs) attract more and more attention in recent decade. On this basis, WLAN-based indoor localization technique is proposed to meet this goal. Among the different indoor Wireless Local Area Network (WLAN) localization systems, the fingerprinting-based localization [1] is more favored and has been widely used. There are normally two phases involved in fingerprinting-based localization, namely the off-line phase and on-line phase. In off-line phase, to

M. Zhou (✉) • F. Qiu • Z. Tian • Q. Zhang • Q. Jiang
Chongqing Key Lab of Mobile Communications Technology, School of Communication and Information Engineering, Chongqing University of Posts and Telecommunications, Chongqing 400065, China
e-mail: zhoumu@cqupt.edu.cn; 869024158@qq.com; tianzs@cqupt.edu.cn; 18716322725@139.com; jiangq@cqupt.edu.cn

J. Mu et al. (eds.), *The Proceedings of the Third International Conference on Communications, Signal Processing, and Systems*, Lecture Notes in Electrical Engineering 322, DOI 10.1007/978-3-319-08991-1_55

construct the fingerprint database (also named as radio-map), we calibrate Reference Points (RPs) in target area and collect Received Signal Strength (RSS) measurements from hearable Access Points (APs) at each RP. In on-line phase, we collect new RSS measurements and rely on radio-map to estimate target locations. Thus, radio-map construction is one of significantly important components of fingerprinting-based localization. Radio-map construction is normally based on propagation prediction modeling approach and point-by-point acquisition approach.

Since point-by-point acquisition approach is time-consuming, propagation prediction modeling approach is widely used to construct radio-map in a short period of time when the required localization accuracy is not very high. To achieve higher accuracy, the fingerprints predicted by propagation modeling should be similar to the real RSS loss. In general, the existed propagation models are divided into two categories: empirical model and deterministic model [2]. Empirical model is featured with two main advantages of low computation complexity and efficient calculation. Deterministic model consumes a large amount of computation cost to reveal the interaction of the electromagnetic and physical environments to improve prediction accuracy.

This paper focuses on empirical models, which mainly include Linear Attenuation Model (LAM) [3], Logarithmic Distance Loss Model (LDLM), Attenuation Factor Model (AFM) [4], COST231 Multi Wall Model (COST231-MWM) [5], and Breakpoint Model (BM) [6]. LAM needs a large number of test data to build a complete model for mini-test environment. LDLM is one of the simplest models without taking the environmental factors into consideration. LDLM is featured with low computation cost and can be applied to any simple environments. By considering the influence of different types of buildings and barriers, AFM is with the advantages of better flexibility and smaller standard deviations of predicted path loss compared to logarithmic distance loss model. In [5], to improve prediction accuracy, COST231-MWM considers not only the free space loss, but also the penetration parameters, like the wall attenuation factor (WAF) and floor attenuation factor (FAF). Based on the ground-truth data collected in indoor office environment, K. W. Cheung et al. proposed BM with higher accuracy by using electromagnetic unanimous theory of diffraction (UTD). In their experiments, they found that the propagation loss in indoor environment is similar to the free space loss with the distance between 5 and 20 m from the transmitter to receiver, while the propagation loss increases rapidly when the distance is over 20 m. Therefore, the loss exponent in breakpoint model varies unpredictably and irregularly, which is different from the constant loss exponent involved in the previous propagation models.

In this paper, we propose a novel integrated Propagation Model-based Breakpoint Model Interpolation (PMBMI) and Multidimensional Linear Interpolation (MLI) [7], to reduce the labor cost and improve the accuracy of the reconstructed fingerprinting database. The rest of this paper is organized as follows. In Sect. 55.2, we introduce the proposed RSS prediction model. Section 55.3 conducts performance evaluation with respect to different parameters and discusses prediction errors. Finally, we conclude the paper in Sect. 55.4.

55.2 RSS Prediction Model

55.2.1 Flow Chart

In this paper, we propose the integrated PMBMI and MLI to construct the RSS fingerprint database. To reconstruct the raw sparse fingerprinting database, we conduct MLI in the environment with Non Line of Sight (NLOS) and PMBMI in the Line of Sight (LOS) environment. The flow chart of our proposed RSS prediction model is shown in Fig. 55.1.

55.2.2 PMBMI

We carry out a testing in a straight corridor in real WLAN environment. The corridor is with the dimensions of 64.3 m × 1.6 m. In this corridor, 87 RPs are uniformly calibrated with the interval of 0.8 m. Figure 55.2 shows the relationship between RSS and the distance from the transmitter to receiver.

In Fig. 55.2, we find that the variations of RSS with respect to distance are not fully compliant with logarithmic distance loss model due to the existence of several growths at some locations. This observation is normally recognized as small-scale jitter which is attributed to normal random variable in many previous studies. To solve this problem, our proposed BM adds breakpoint gain by taking the situation

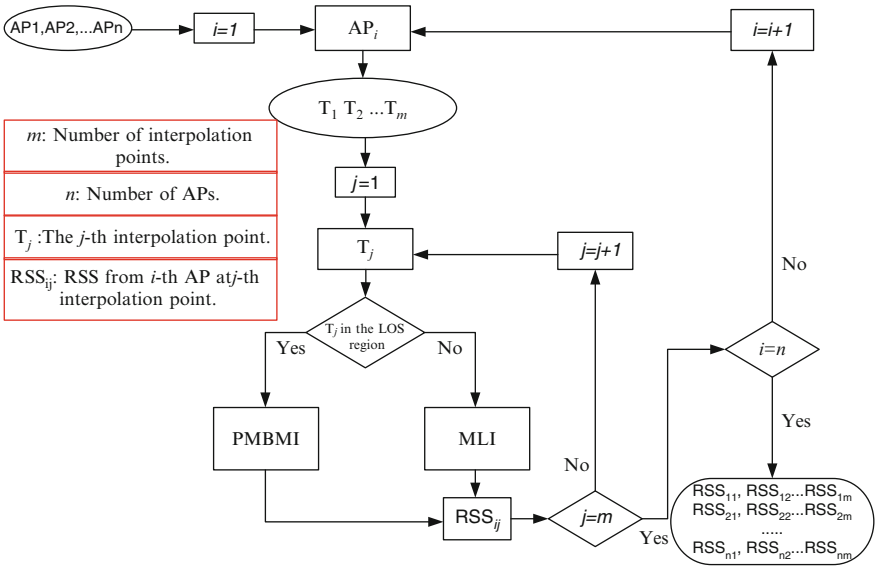

Fig. 55.1 Flow chart

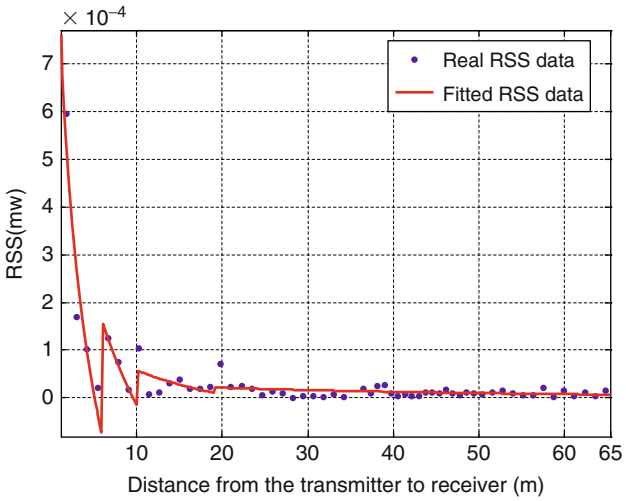

Fig. 55.2 Variations of RSS with respect to the distance from the transmitter to receiver

that RSS could vary suddenly and significantly into account. For indoor narrow areas, like the straight corridor, we propose indoor propagation model-based breakpoint model with multiple breakpoints in (55.1).

$$P = P(d_0) + \sum_{i=0}^{N-1} (10n_{i+1}\log(d) - \alpha_{i+1})\left[u(d - d_{bpi}) - u(d - d_{bpi+1})\right] + PL_{wf} \tag{55.1}$$

Where PL_{wf} is the attenuation by the walls and floors.

55.2.3 MLI

By assuming that an unknown variable distribution satisfies linear features on a single dimension, the linear interpolation can be used to deal with the unknown variables based on the characteristics of the same slop of a line function. Since the unknown variables are often affected by many factors, the spatial variables hardly satisfy linear feature property in practice. In response to this compelling problem, the multi-dimension linear interpolation is proposed to reflect the unknown multi-dimension variables. In this paper, the RSS at interpolation points is determined by three parameters d, x, and y, where d is the distance between the interpolation point and its adjacent RP. x and y stand for the horizontal and vertical coordinates

respectively. Based on the characteristics that the RSSs at adjacent locations are similar, we apply MLI to predict each interpolation point by using the RSSs at adjacent RPs. Specifically, the RSSs at every k adjacent RPs are used to calculate the RSS at an interpolation point in three dimensions, as shown below.

$$\begin{cases} P_d = \dfrac{\sum_{i=1}^{k} \frac{1}{d_i} \cdot RSSI_i}{S_d}, S_d = \sum_{j}^{k} \frac{1}{d_j} \\ P_x = \dfrac{\sum_{i=1}^{k} \frac{1}{|x_i - x|} \cdot RSSI_i}{S_x}, S_x = \sum_{j}^{k} \frac{1}{|x_j - x|} \\ P_y = \dfrac{\sum_{i=1}^{k} \frac{1}{|y_i - y|} \cdot RSSI_i}{S_y}, S_y = \sum_{j}^{k} \frac{1}{|y_j - y|} \end{cases} \tag{55.2}$$

The weighted sum is calculated by

$$P = \sum_{i=1}^{3} w_i \cdot P_i \tag{55.3}$$

$$w_i = \frac{\sum_{j=1}^{k} l_{ij}}{\sum_{i=1}^{3} \sum_{j=1}^{k} l_{ij}} \quad (i = x, y, d) \tag{55.4}$$

where w_i is the weight of the i - th parameter in multidimensional linear interpolation. The value of w_i is determined by the corresponding distance difference. l_{ij} is the absolute value of the distance between interpolation point and j-th RP with respect to the i - th parameter.

55.3 Performance Evaluation

55.3.1 Experimental Setup

We do the testing in real indoor WLAN environment with the size of 64.6 m by 18.5 m on the first floor in Administration Building at CQUPT. The environment is covered by five D-link DAP-2310 APs. A Samsung S7568 mobile phone is selected as the receiver which is installed with our developed Wi-Fi location Software.

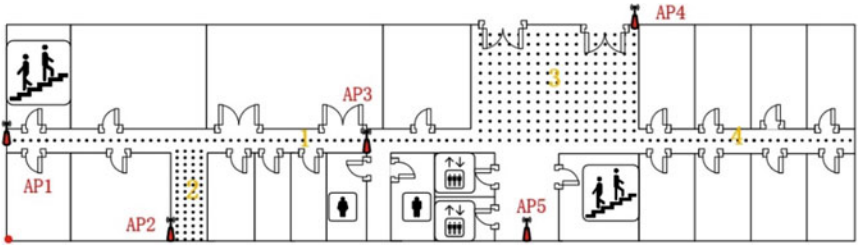

Fig. 55.3 Physical layout

Table 55.1 Location errors in different RP selection conditions

Types of RP selection	k	K	Location errors (m)
All the RPs	–	3	2.39
RPs with even no.	3	3	2.58
RPs with odd no.	3	3	2.58
Half RPs with Random no. (type 1)	3	3	2.51
Half RPs with Random no. (type 2)	3	3	2.72
Half RPs with Random no. (type 3)	3	3	2.55
Half RPs with Random no. (type 4)	3	3	2.52

The RSS measurements are stored into txt files. We uniformly calibrate 327 RPs in five regions in target environment, namely Regions 1, 2, 3, and 4. The physical layout of our experimental environment is shown in Fig. 55.3.

55.3.2 Experimental Results

55.3.2.1 Location Errors in Different RP Selection Conditions

To show the effectiveness of our proposed interpolation algorithm in fingerprinting database reconstruction, Table 55.1 compares the location errors in different RP selection conditions. In Table 55.1, k and K stand for the number of adjacent RPs used for MLI and the number of neighboring RPs by KNN.

55.3.2.2 Prediction Errors

In our testing, we use deviation which is defined in (55.5) to analyze the prediction errors by interpolation. The cumulative distribution functions of deviation with respect to different APs are shown in Fig. 55.4. Based on (55.5), we can find that larger deviation results in poorer performance of interpolation.

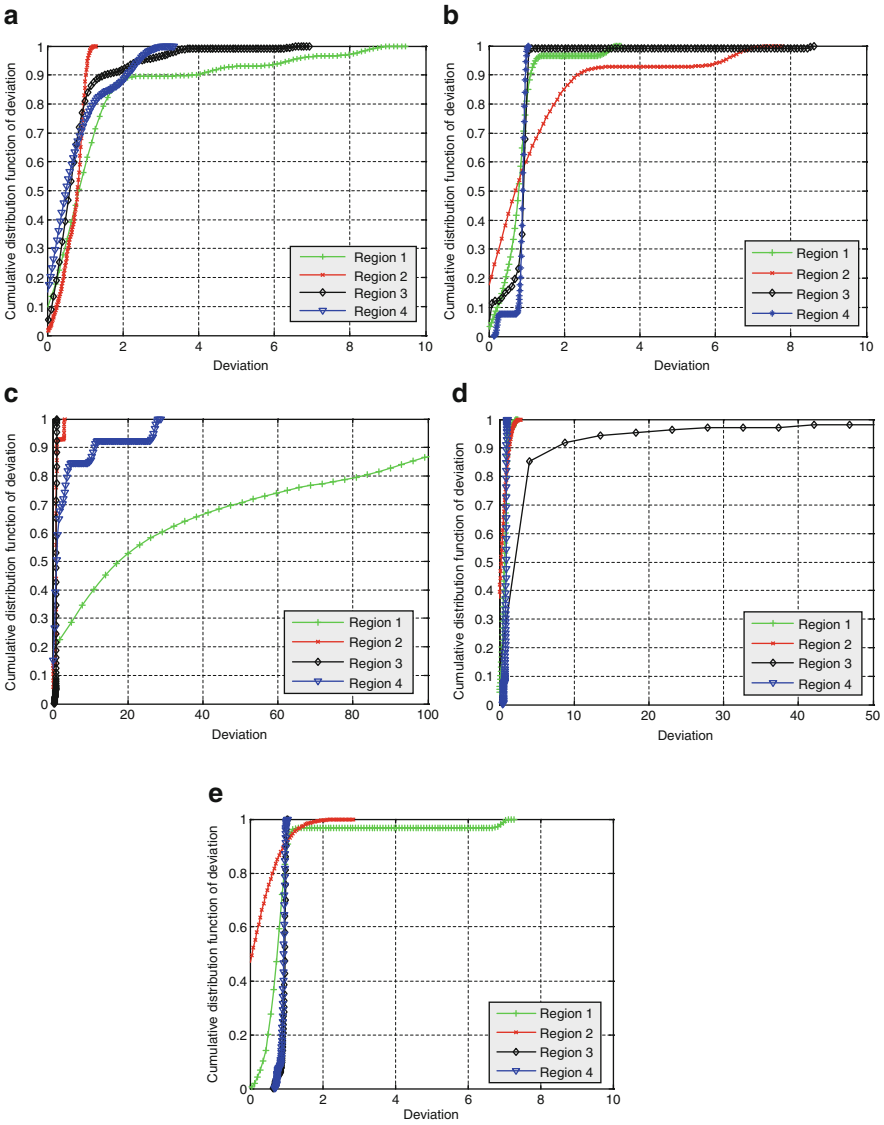

Fig. 55.4 Deviation with respect to different APs. (**a**) Deviation with respect to AP1. (**b**) Deviation with respect to AP2. (**c**) Deviation with respect to AP3. (**d**) Deviation with respect to AP4. (**e**) Deviation with respect to AP5

$$\text{Deviation} = \frac{\left|RSS_p\text{-}RSS_r\right|}{RSS_r} \tag{55.5}$$

where RSS_p and RSS_r stand for the predicted RSS by interpolation and the real recorded RSS respectively.

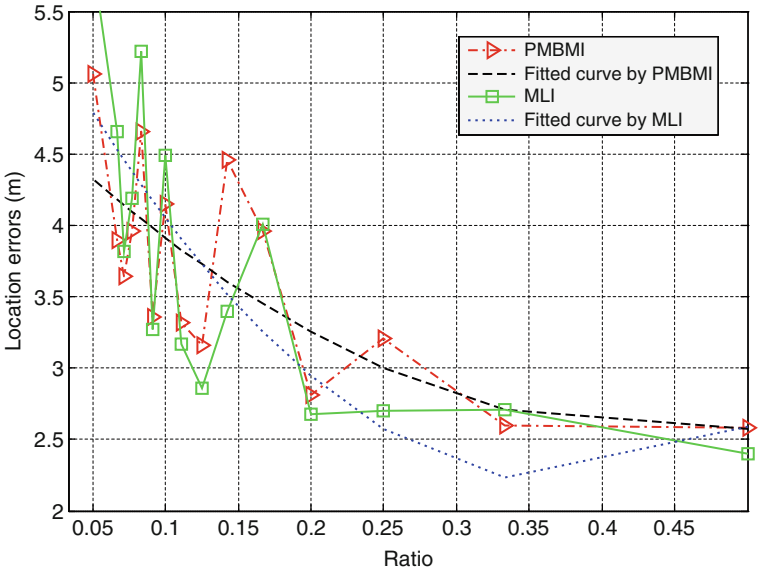

Fig. 55.5 Location errors by MLI and PMBMI in different ratio conditions

Table 55.2 Comparisons of MLI and PMBMI in different RP selection conditions

Types of RP selection	MLI (m)	PMBMI (m)
RPs with even no.	2.40	2.58
RPs with odd no.	2.26	2.58
Half RPs with Random no. (type 1)	2.55	2.72
Half RPs with Random no. (type 2)	2.48	2.55
Half RPs with Random no. (type 3)	2.37	2.52
Half RPs with Random no. (type 4)	2.37	2.51

55.3.2.3 Comparison of MLI and PMBMI

Experiments are carried out to compare the performance of MLI and PMBMI. Figure 55.5 shows the variations of location errors with respect to the ratio of the number of RPs used for MLI and PMBMI respectively in the conditions of $k = 3$ and $K = 3$. From Fig. 55.5 and Table 55.2, we can find that in the small ratio condition, the accuracy of PMBMI is higher than MLI, while in the large ratio condition, MLI exhibits higher accuracy compared to PMBMI.

55.3.2.4 Variations of the Number of RPs Used for Interpolation

Figure 55.6 shows the variations of location errors with respect to the ratio of the number of RPs used for interpolation and the total number of RPs in the conditions of $k = 3$ and $K = 3$. From Fig. 55.6, we find that in the small ratio condition, the

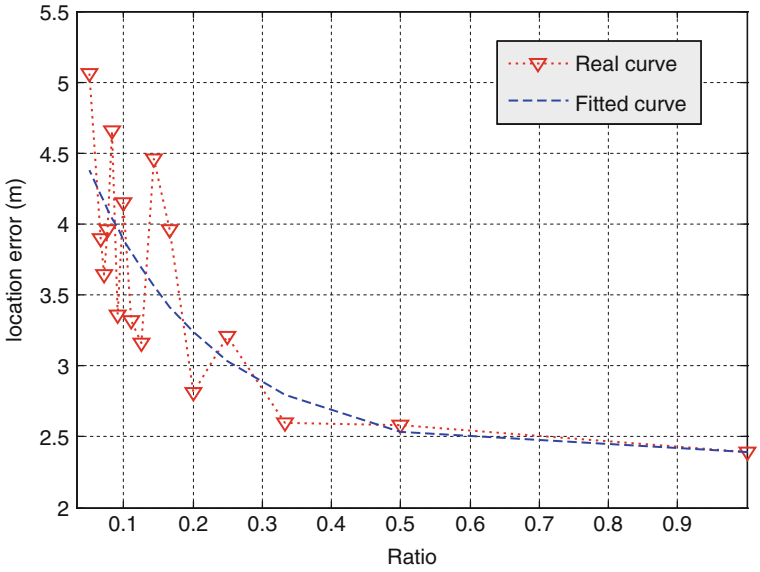

Fig. 55.6 Variations of location errors with respect to the ratio

increase of the number of RPs used for interpolation significantly reduces location errors, while when the ratio is over 0.5, the variations of the number of RPs used for interpolation have slight influence on location errors.

55.3.2.5 Variations of *k*

By setting $K = 3$, Fig. 55.7 shows the variations of location errors with respect to value k in different RP selection conditions. Table 55.3 compares the standard deviations of location errors in different RP selection conditions. The results in Fig. 55.7 indicate that location errors change slightly with the variations of value k, which can be interpreted that MLI is almost independent of value k. On this basis, we set the value k equal to two or three for the sake of reducing computation cost.

55.3.2.6 Variations of *K*

Figure 55.8 shows the variations of location errors with respect to value K. In Fig. 55.8, we observe that in different value k conditions, the optimal value K which achieves the lowest location error only equals to two, three or four.

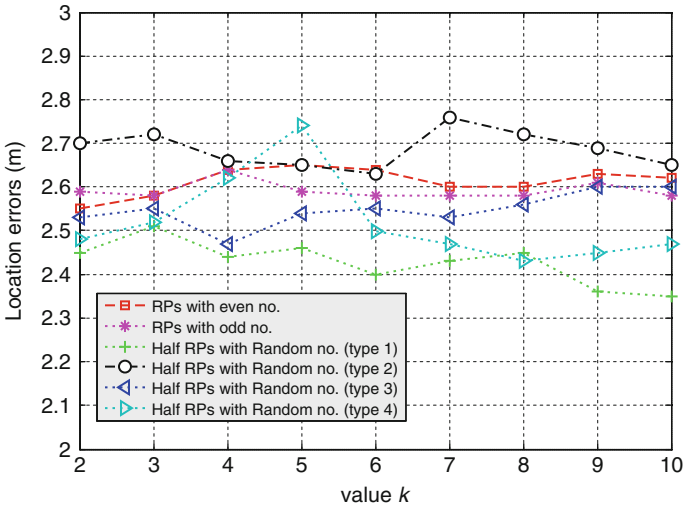

Fig. 55.7 Location errors in different value *k* conditions

Table 55.3 Standard deviation of location errors in different RP selection conditions

Types of RP selection	Standard deviations (mw)
RPs with even no.	0.0327
RPs with odd no.	0.0205
Half RPs with Random no. (type 1)	0.0504
Half RPs with Random no. (type 2)	0.0424
Half RPs with Random no. (type 3)	0.0393
Half RPs with Random no. (type 4)	0.099

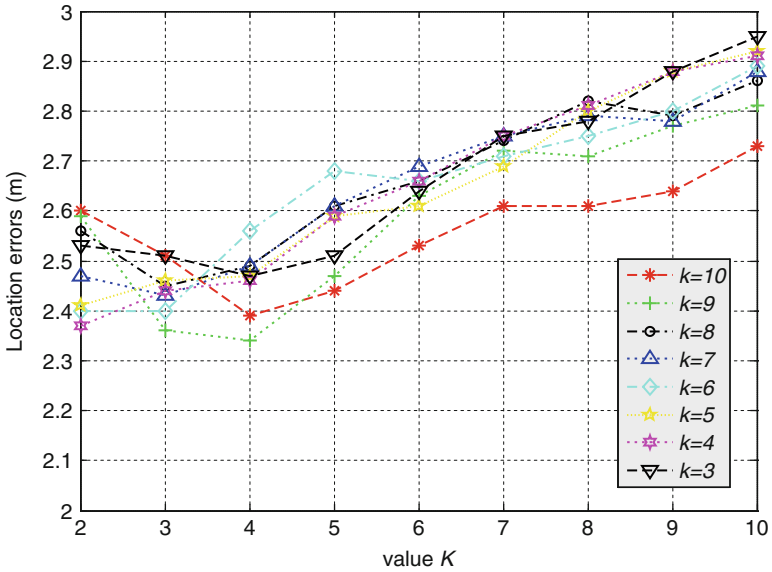

Fig. 55.8 Location errors in different value *K* conditions

Conclusions
In this paper, to reconstruct the raw collected sparse fingerprinting database and reduce the laboring effort for location fingerprinting in indoor WLAN localization, we propose the integrated PMBMI and MLI. The experimental results in real WLAN environment demonstrate that our proposed model can not only reduce RP density for RSS fingerprint database construction, but also improve computation efficiency for WLAN localization. The model optimization to improve the accuracy of RSS prediction further forms an interesting work in future.

Acknowledgement This work was supported in part by the Program for Changjiang Scholars and Innovative Research Team in University (IRT1299), National Natural Science Foundation of China (61301126), Special Fund of Chongqing Key Laboratory (CSTC), Fundamental and Frontier Research Project of Chongqing (cstc2013jcyjA40041, cstc2013jcyjA40032, cstc2013jcyjA40034), Scientific and Technological Research Program of Chongqing Municipal Education Commission (KJ130528), Startup Foundation for Doctors of CQUPT (A2012-33), Science Foundation for Young Scientists of CQUPT (A2012-77), and Student Research Training Program of CQUPT (A2013-64).

References

1. Zhou M, Tian Z, Xu K, Yu X, Hong X, Wu H (2014) SCaNME: location tracking system in large-scale campus Wi-Fi environment using unlabeled mobility map. Expert Syst Appl 41 (7):3429–3443
2. Chen Q, Huang G, Song S (2009) WLAN user location estimation based on receiving signal strength indicator. In: 5th international conference on wireless communications, networking and mobile computing
3. Herring KT, Holloway JW, Staelin DH (2010) Path-loss characteristics of urban wireless channels. IEEE Trans Antenn Propag 58(1):171–177
4. Ismail M, Ali BM, Khatun S, Thiagarajah S (2005) Empirical UWB path loss models for typical office environments. In: 2005 13th IEEE international conference on networks jointly held with the 2005 7th IEEE Malaysia international conference on communications, vol 2, pp 1023–1028
5. Ding G, Tan Z, Zhang J, Zhang L (2013) Regional propagation model based fingerprinting localization in indoor environments. In: 2013 I.E. 24th annual international symposium on personal, indoor, and mobile radio communications, PIMRC 2013, pp 291–295
6. Cheung KW, Sau JH, Fong MS, Murch RD (1994) Indoor propagation prediction utilizing a new empirical model. In: Proceedings of the IEEE international conference on communication systems. Part 1 (of 3), vol 1, pp 15–19
7. Liu S, Yan D, Wang G, Li C, Weng B (2013) Development and application of multidimensional linear interpolation. South-North Water Sci Tech 11(4):9–12

Chapter 56
WLAN Localization Without Location Fingerprinting Using Logic Graph Mapping

Mu Zhou, Qiao Zhang, Zengshan Tian, Feng Qiu, and Qing Jiang

Abstract In Wireless Local Area Network (WLAN) environment, most of the existed Received Signal Strength (RSS) based localization algorithms rely on RSS data collection at Reference Points (RPs) in off-line phase. The process of RSS data collection is usually time consuming and labor intensive. To solve this problem, we make use of the relationship between the raw RSS sequences and the architecture of ground-truth environment, as well as the correlation among different raw RSS sequences to construct logic graphs. After that, by conducting mapping from the ground-truth graph into logic graph and doing mapping selection, we locate the target in the subarea which the target really belongs to. Since our proposed approach does not require the exact locations of the collected RSS data, a large amount of time and laboring cost for site survey is saved. Experimental results show that our proposed approach can be used to locate target in WLAN environment without site survey on WLAN RSS data.

Keywords WLAN localization • Received signal strength • RSS sequence • Logic graph • Site survey

56.1 Introduction

With the significant deployment of Wireless Local Area Network (WLAN) technique, it is particularly valuable to rely on the public WLAN infrastructures to do localization in a cost-efficient manner. Up to now, Received Signal Strength (RSS) based indoor WLAN localization systems have been carefully studied, like the RADAR [1] and Horus [2].

As we know, there are two phases involved in most of the recent location fingerprinting-based localization systems, namely the off-line phase and on-line phase. In off-line phase, a large amount of RSS data are collected to construct a

M. Zhou (✉) • Q. Zhang • Z. Tian • F. Qiu • Q. Jiang
Chongqing Key Lab of Mobile Communications Technology, School of Communication and Information Engineering, Chongqing University of Posts and Telecommunications, Chongqing 400065, China
e-mail: zhoumu@cqupt.edu.cn; 18716322725@139.com; tianzs@cqupt.edu.cn; 869024158@qq.com; jiangq@cqupt.edu.cn

J. Mu et al. (eds.), *The Proceedings of the Third International Conference on Communications, Signal Processing, and Systems*, Lecture Notes in Electrical Engineering 322, DOI 10.1007/978-3-319-08991-1_56

radio map which is recognized as a mapping from RSS fingerprints into the corresponding ground-truth locations. In on-line phase, localization algorithms are conducted to track the target. To reduce the off-line site survey effort, we propose a novel localization approach which only relies on the raw RSS sequences to locate the target without location fingerprinting. Specifically, we first use off-the-shelf smart phones to sporadically collect WLAN RSS sequences in target environment. Second, we do the clustering on RSS data in each RSS sequence. Third, based on the relations of RSS clusters in difference RSS sequences, we construct logic graphs. Fourth, we do the mapping from the ground-truth graph into logic graphs. Finally, after the mapping selection, we locate the target with subarea-level accuracy.

The rest of this paper is summarized as follows. Section 56.2 gives some related work on WLAN localization, and also introduces the idea of indoor WLAN localization without site survey on location fingerprinting. In Sect. 56.3, we illustrate the process of our proposed approach in detail. The experimental results are shown in Sect. 56.4 based on the data collected in real indoor WLAN environment. Section 56.5 concludes this paper and provides some future directions.

56.2 Related Work

In the past decade, the angle of arrival (AOA), time of arrival (TOA), and time difference of arrival (TDOA) have been widely used in many indoor localization systems. Two significant problems to be considered by AOA, TOA, and TDOA are that: (1) both the exact locations of access points (APs) and the line-of-sight (LOS) property are required; and (2) some specialized hardware devices are needed to measure the arrival angle and arrival time of RSS.

To reduce infrastructure cost and improve system adaptability, the RSS-based WLAN localization systems are widely studied by a large number of universities and research institutes. One of the pioneer localization systems, RADAR, was proposed by Microsoft Research in 2000 [1]. Horus system [2] is recognized as another representative localization system which is also based on off-line and on-line phases. In [3], the authors rely on threshold classification and RSS weighting to enhance localization accuracy. Authors in [4] propose to use radio propagation model and multiple regressions to optimize AP placement in order to increase localization efficiency. Neural network based WLAN localization system can be found in [5] and [6]. In [7] and [8], a new probabilistic localization system by modeling RSS fingerprints as random variables are discussed.

For many existed indoor Location Based Services (LBS), there is no need to spend a lot of time and laboring cost in estimating the exact locations which we are located at. For example, in indoor office environment, we prefer to know the office we are really in, rather than the exact locations in this office. On this basis, the authors in [9] and [10] propose a simple algorithm to locate the target into the correct room by using raw RSS sequences without site survey on location fingerprinting, while in their algorithm, the accelerator is required to determine the

motion state of the target for the sake of eliminating the RSS data which are collected at each fixed location. Different from [9] and [10], the work in this paper only focuses on the RSS sequences which are sporadically collected to locate the target without any extra motion sensor. The prior information we require is a ground-truth graph, which can be easily obtained from the fire escape planes in modern buildings. In concrete terms, we first collect RSS sequences sporadically in target area. Second, the clustering algorithm is conducted on each RSS sequence to classify the RSS data into different clusters. Third, based on the correlation among different clusters in different RSS sequences, we obtain a number of logic graphs. Finally, by mapping the ground-truth graph into logic graphs, we locate the target in the correct subarea. Experiments show that our approach is efficient due to the independence of site survey on location fingerprinting and motion sensing.

56.3 Indoor Localization Without Site Survey

56.3.1 Characteristics of RSS

The reason of using RSS sequences to locate the target is based on the characteristics that the RSS data in different architectural environments vary significantly. Figure 56.1 shows an example of the RSS variations when crossing a wall.

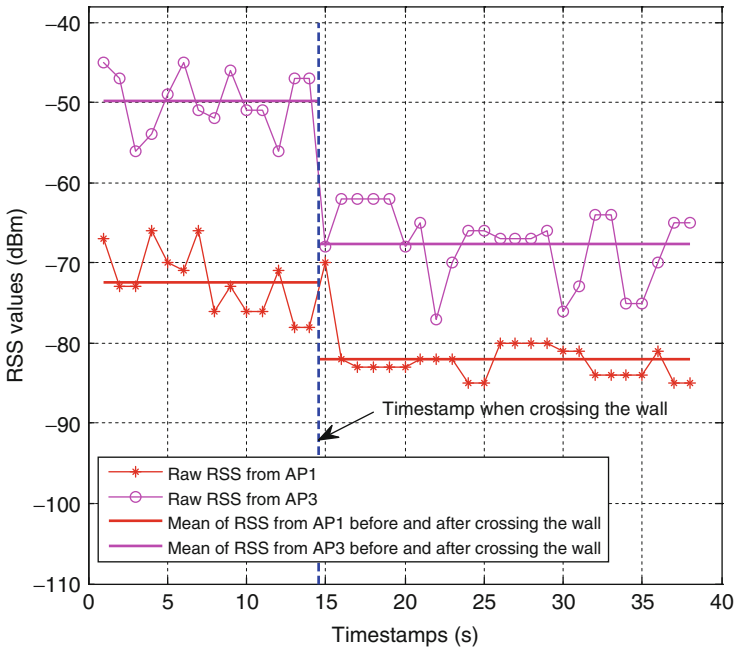

Fig. 56.1 Variations of RSS when crossing a wall

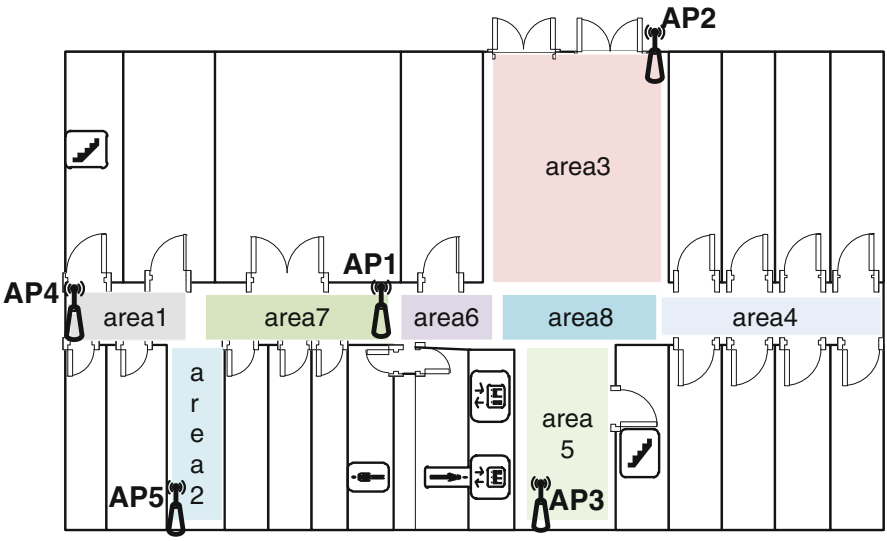

Fig. 56.2 Experimental layout

In Fig. 56.1, we can find that the RSS data on different sites of the wall vary a lot with respect to both the raw RSS and the mean of RSS. For example, the mean of RSS from AP1 before crossing the wall is about −50 dBm, while after crossing the wall, the mean of RSS decreases to about −67 dBm. On this basis, we can use RSS data to describe the architecture of the target environment.

56.3.2 RSS Collection

In our approach, RSS collection is conducted at any time and by different volunteers in target environment. The volunteers are not required to stay at each Reference Point (RP) to collect the RSS data, but use the off-the-shelf smart phones to sporadically collect the RSS data to form RSS sequences from each hearable Access Point (AP). The motion state of volunteers does not have significant influence on the construction of our proposed logic graphs. Figure 56.2 shows the layout of our experimental environment. We divide the area into eight subareas, namely as the areas 1, 2, 3, 4, 5, 6, 7, and 8. In our testing, there are in total 21 RSS sequences collected in this environment.

56.3.3 Construction of Logic Graphs

To construct logic graphs, we first need to construct a cluster graph for each RSS sequence. The steps of the construction of cluster graph are shown below.

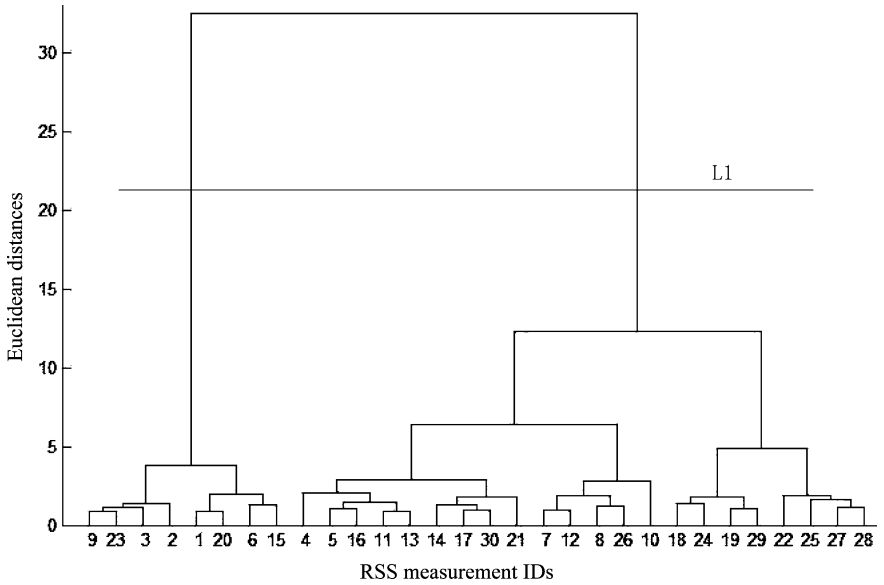

Fig. 56.3 An example of cluster tree

Step 1: In each RSS sequence, we calculate the Euclidean distance between every two RSS measurements. Thus, we can obtain a distance matrix, notated as M_d in (56.1).

$$M_d = \begin{bmatrix} d_{11} & d_{12} & \dots & d_{1n} \\ d_{21} & d_{22} & \dots & d_{2n} \\ \dots & \dots & \dots & \dots \\ d_{n1} & d_{n2} & \dots & d_{nn} \end{bmatrix} \tag{56.1}$$

where d_{ij} is the Euclidean distance between the i-th and j-th RSS measurements in the same RSS sequence. n is the length of RSS sequence.

Step 2: Choose the two RSS measurements with the smallest Euclidean distance to form a new cluster, and meanwhile calculate the mean of these two RSS measurements as the center of this new cluster.

Step 3: Put the center of the new cluster into the RSS sequence and repeat steps 1 and 2 until all the RSS measurements have been clustered.

For each RSS sequence, we can obtain a cluster tree, as shown in Fig. 56.3. The number of clusters, c_m, in cluster tree depends on the number of subareas in target environment. In our experiments, we set $c_m = 8$. For example, in Fig. 56.3, if $c_m = 2$, the cluster tree should be cut by L1 to form two clusters, $\{9, 23, 3, 2, 1, 20, 6, 15\}$ and $\{4, 5, 16, 11, 13, 14, 17, 30, 21, 7, 12, 8, 26, 10, 18, 24, 19, 29, 22, 25, 27, 28\}$.

After the cluster tree is constructed, each RSS measurement is assigned a cluster ID. Then, we can obtain a sequence of cluster IDs with the length equaling to the number of measurements. An average filter is applied to smooth the transitions of cluster IDs, and then the cluster IDs are reassigned in ascending order of

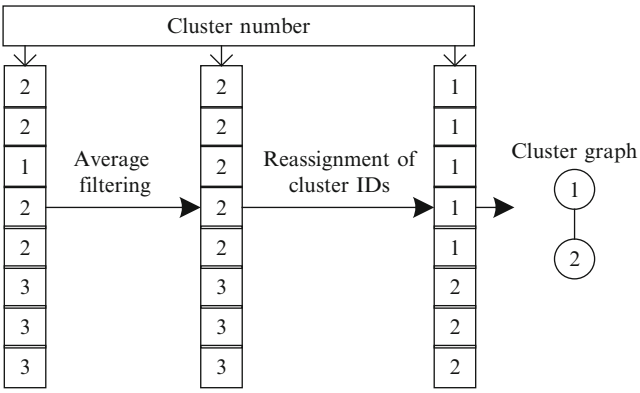

Fig. 56.4 Construction of cluster graph

timestamps starting from the first RSS measurement to the last measurement. We can obtain a cluster graph which indicates the transitions of clusters in each RSS sequence. Figure 56.4 shows the process of average filtering, reassignment of cluster IDs, and the construction of cluster graph. In our experiments, there are in total 21 cluster graphs to be assembled into logic graphs.

The process of the construction of logic graphs is as follows.

Step 1: Label the cluster graphs with IDs from 1 to 21 and choose the cluster graph with ID 1 as the reference graph.
Step 2: Calculate the Euclidean distances between the cluster centers in reference graph and the cluster centers in other cluster graphs.
Step 3: Merge every two clusters when the Euclidean distance of their corresponding cluster centers is smaller than the similarity threshold, s_{th}, and calculate the mean of these two cluster centers as the center of the new merged cluster.
Step 4: Repeat step 3 for all the clusters in cluster graphs.
Step 5: Modify the value of s_{th} , namely if the initial setting of s_{th} results in an unconnected graph, increase the step length by 1. On the contrary, increase the step length by ± 1. In our experiments, s_{th} is in the range of (3, 30). And repeat steps 2, 3, and step 4 to obtain the other fully connected graphs, namely the logic graphs.
Step 6: Select another reference graph and repeat steps 2, 3, 4, and 5. We end this process when all of the 21 cluster graphs have been selected as reference graphs.

56.3.4 Logic Graph Mapping

Considering the symmetry of the ground-truth graph (see Fig. 56.5) constructed from the experimental layout, we select three Calibration Points (CPs) to label the areas 2, 3, and 4 respectively. The labeled areas are the leaf nodes of the ground-truth graph, which can be used to avoid the symmetry problem.

We rely on the three selected CPs to conduct the first round selection of logic graphs. At each CP, we calculate the mean of 600 RSS measurements as

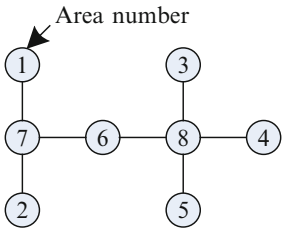

Fig. 56.5 Topological structure of the ground-truth graph

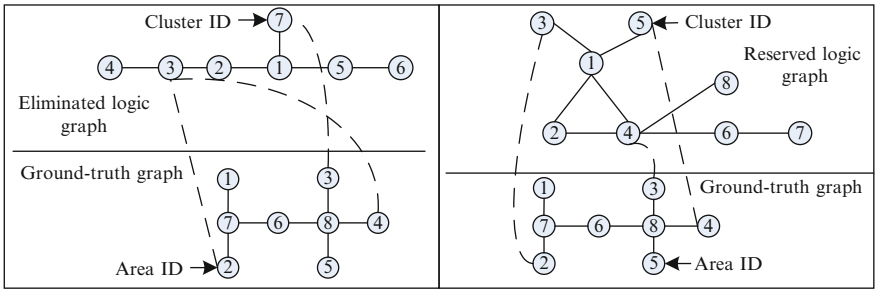

Fig. 56.6 An example of the eliminated logic graph and the reserved logic graph

Representative Vector (RV) of this CP. We match each CP to the cluster (in logic graphs) with the cluster center having the smallest distance to the RV of this CP. We eliminate the logic graph which contains one or more clusters matched by more than 1 CPs. Figure 56.6 gives an example of the eliminated logic graph and the reserved logic graph.

After the first round selection of logic graphs, we obtain in total 17 candidate logic graphs. Then, we continue to conduct the second round selection of logic graphs to find the optimal logic graph. First of all, we define the Adjacent Degree (AD) of each cluster (node) in logic graph as the sum of the degree of itself and the degrees of its adjacent nodes. For example, in Fig. 56.5, the AD of node 4 is 5 since the degree of node 4 is 1 and the degrees of its adjacent node, node 8, is 4. Then, the steps of mapping logic graphs into ground-truth graph are shown below.

Step 1: Find all the leaf nodes and nonleaf nodes in logic graphs and in ground-truth graph respectively.

Step 2: Order the nonleaf nodes in each logic graph and ground-truth graph with the ADs in descending order, and then map the nonleaf nodes in logic graph into the nonleaf nodes in ground-truth graph one by one starting from the nonleaf nodes with the largest ADs. If the number of nonleaf nodes in logic graph is larger, we map the excess nonleaf nodes in logic graph into the nonleaf nodes (in ground-truth graph) which are mapped by their adjacent nonleaf nodes in logic graph. On the contrary, we map excess nonleaf nodes in ground-truth graph into the nonleaf nodes (in logic graph) which are mapped by their adjacent nonleaf nodes in ground-truth graph.

Step 3: Map the leaf nodes containing CPs in ground-truth graph into the clusters (in logic graphs) which have been matched during the first round selection of

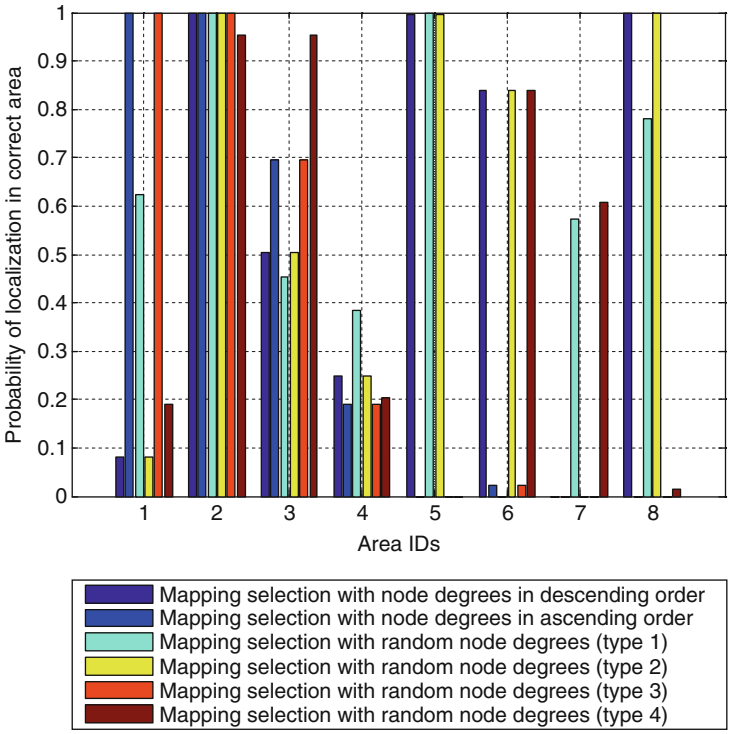

Fig. 56.7 Probability of localization in correct area

logic graphs. For the other leaf nodes in ground-truth graph, we first map all of leaf nodes in logic graph to them. If a leaf node in logic graph is matched into more than two leaf nodes in ground-truth graph, we only reserve the mapping from the leaf node in logic graph to the two leaf nodes (in ground-truth graph) which have the smallest number of hops between each other.

56.4 Experimental Results

In each area, we choose a random location at which 600 RSS measurements are collected to test localization accuracy. We discuss three types of mapping selection: (1) mapping selection with node degrees in descending order, (2) mapping selection with node degrees in ascending order, and (3) mapping selection with random node degrees. In types 1 and 2, we select nodes in the ground-truth graph with node degrees, namely AD, in descending order and ascending order to test the localization accuracy respectively. In type 3, nodes in the ground-truth graph are selected with random node degrees to test the localization accuracy. Figures 56.7, 56.8, and 56.9

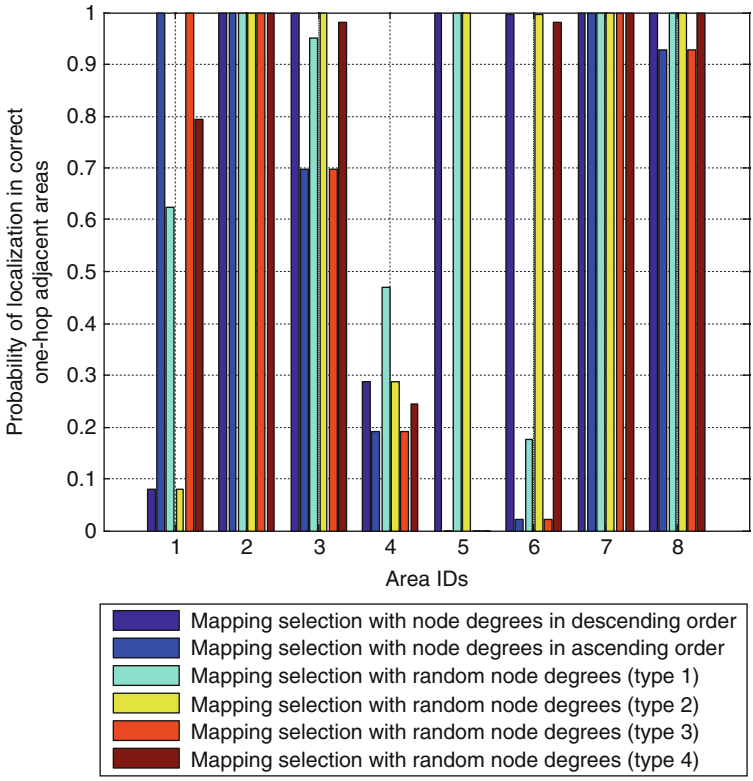

Fig. 56.8 Probability of localization in correct one-hop adjacent areas

show the Probability of Localization in Correct Area (PLCA), Probability of Localization in Correct One-hop Adjacent Areas (PLCOAA), and Probability of Localization in Correct Two-hop Adjacent Areas (PLCTAA) respectively by using different types of mapping selection. Table 56.1 compares the average probabilities of localization in correct area, correct one-hop adjacent areas, and correct two-hop adjacent areas.

Based on the previous results, we can find that type 1 performs better than type 2 since the PLCA, PLCOAA, and PLCTAA of type 1 are about 20, 18, and 17 % higher than the PLCA, PLCOAA, and PLCTAA of type 2. For the mapping selection with random node degrees, the localization performance varies significantly. Therefore, due to the consideration of localization accuracy and stability, we select type 1 as the mapping selection in our testing. Finally, Fig. 56.10 shows the mapping result between logic graph and ground-truth graph.

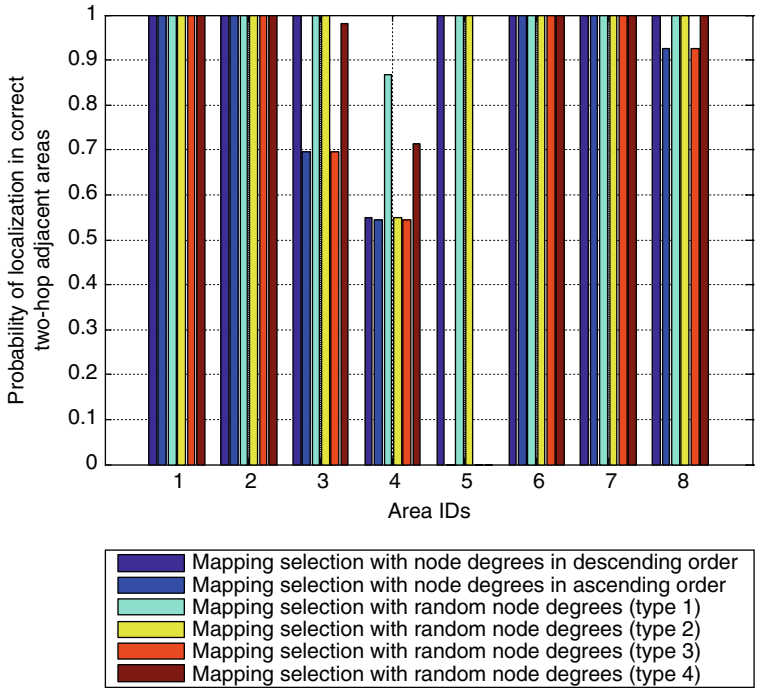

Fig. 56.9 Probability of localization in correct two-hop adjacent areas

Table 56.1 Average probabilities of localization

Types of mapping selection	Average probabilities of localization in correct area (%)	Average probabilities of localization in correct one-hop adjacent areas (%)	Average probabilities of localization in correct two-hop adjacent areas (%)
Area selection with node degrees in descending order	58.33	79.54	94.37
Area selection with node degrees in ascending order	36.35	60.44	77.08
Area selection with random node degrees (type 1)	60.17	77.75	98.33
Area selection with random node degrees (type 2)	58.33	79.54	94.37
Area selection with random node degrees (type 3)	36.35	60.44	77.08
Area selection with random node degrees (type 4)	46.98	74.98	83.67

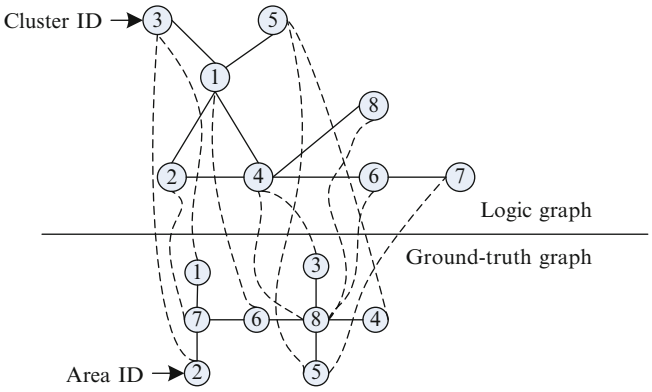

Fig. 56.10 Result of logic graph mapping

Conclusion

A novel approach of indoor WLAN localization without site survey on location fingerprinting is addressed in this paper. Based on the RSS sequences which are sporadically collected in indoor WLAN environment, we construct logic graphs, conduct mapping from logic graphs to ground-truth graph, and realize target localization. Experimental results show that our proposed mapping selection with node degrees in descending order can achieve high enough PLCA, PLCOAA, and PLCTAA. In our future work, we will apply our approach to a more general indoor environment containing not only office rooms, but also straight corridors, and also optimize area division in target environment.

Acknowledgment This work was supported in part by the Program for Changjiang Scholars and Innovative Research Team in University (IRT1299), National Natural Science Foundation of China (61301126), Special Fund of Chongqing Key Laboratory (CSTC), Fundamental and Frontier Research Project of Chongqing (cstc2013jcyjA40041, cstc2013jcyjA40032, cstc2013jcyjA40034), Scientific and Technological Research Program of Chongqing Municipal Education Commission (KJ130528), Startup Foundation for Doctors of CQUPT (A2012-33), Science Foundation for Young Scientists of CQUPT (A2012-77), and Student Research Training Program of CQUPT (A2013-64).

References

1. Bahl P, Padmanabhan VN (2000) RADAR: an in-building RF-based user location and tracking system. Proc IEEE INFOCOM 2:775–784
2. Youssef M, Agrawala A (2005) The Horus WLAN location determination system. In: Proceedings of mobile systems, applications, and services conference, pp 205–218

3. Yang X, Ye A, Ling Y (2013) Indoor localization algorithm based on threshold classification and signal strength weighting. J Comput Appl 33(10):2711–2714
4. Chen Y, Li X (2004) Signal strength based indoor geolocation. Acta Electronica Sinica 32 (9):1456–1458
5. Battiti R, Villani A, Nhat TL (2002) Neural network models for intelligent networks: deriving the location from signal patterns. In: Proceedings of annual autonomous intelligent networks and system symposium, pp 1–13
6. Battiti R, Nhat TL, Villani A (2002) Location-aware computing: a neural network model for determining location in wireless LANs. Technical Report DIT-02-0083, Dept. of Information and Comm. Technology, Univ. of Trento
7. Roos T, Myllymaki P, Tirri H, Misikangas P, Sievanen J (2002) A probabilistic approach to WLAN user location estimation. Wireless Inform Network 9(3):155–164
8. Fang SH, Lin TN (2007) Indoor localization by a novel probabilistic approach. In: Proceedings of signal processing advances in wireless communications workshop, pp 1–4
9. Wu C, Yang Z, Liu Y, Xi W (2012) Will: wireless indoor localization without site survey. In: Proceedings of IEEE INFOCOM, pp 64–72
10. Wu C, Yang Z, Liu Y, Xi W (2013) Will: wireless indoor localization without site survey. IEEE Trans Parallel Distr Syst 24(4):839–848

Chapter 57
Automatic Cell Cycle Localization Using Latent-Dynamic Conditional Random Fields

Jing Zhang, Peipei Li, Jing Yu, Anan Liu, Tong Hao, Yuting Su, and Zhaoxuan Yang

Abstract This paper proposes an automatic cell cycle localization method based on the Latent-Dynamic Conditional Random Fields (LDCRFs) model. Since the LDCRFs model can jointly capture both extrinsic dynamics and intrinsic sub-structure, it can simultaneously model the visual dynamics within one stage and visual transition between adjacent stages in one mitosis sequence. Based on our previous work on candidate mitosis sequence extraction and classification, this paper mainly focuses on the formulation of LDCRFs for cell cycle modeling. Besides, the model learning and inference methods are also presented. The evaluation on C2C12 dataset shows the superiority of the proposed method.

57.1 Introduction

Wide attention has been paid to stem cell proliferation especially in its biomedical applications, such as drugs discovery, biology research and quantitative cellular studies, recently. Previously, biologists usually recognized the proliferation of cells by observing the visual pattern transition. As shown in Fig. 57.1, it is obvious that a cell cycle can be divided into four stages, during which a cell retracts, rounds up, exhibits '8' shape and at last divides into two daughter cells. After identifying mitoses, biologists manually computed the biology parameters (density, mitosis rate, etc.) for the small scale and short-time dataset. However, facing the high-throughput time-lapse microscopy image sequences, it becomes extremely time-consuming to manually annotate each mitotic cell for quantitative analysis of stem cell proliferation. Therefore, automatic cell cycle localization method become necessary to discover the novel biology knowledge.

Most of the previous work only focuses on the recognition of mitosis, which is the beginning of stage 3 in Fig. 57.1. The stat-of-the-art mitosis identification methods can be generally classified into two categories, the appearance-based

J. Zhang (✉) • P. Li • J. Yu • A. Liu • Y. Su • Z. Yang
School of Electronics Information Engineering, Tianjin University, Tianjin, PR China

T. Hao
College of Life Sciences, Tianjin Normal University, Tianjin, China
e-mail: haotong2001@gmail.com

J. Mu et al. (eds.), *The Proceedings of the Third International Conference on Communications, Signal Processing, and Systems*, Lecture Notes in Electrical Engineering 322, DOI 10.1007/978-3-319-08991-1_57

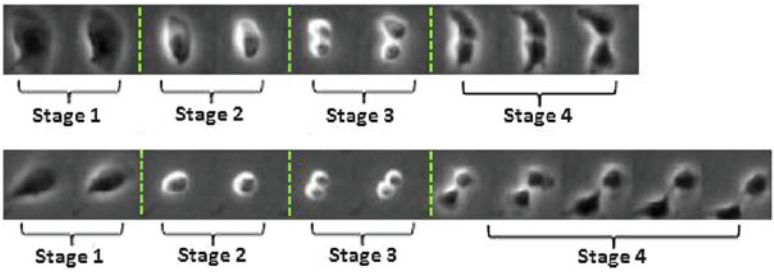

Fig. 57.1 Samples showing the cell cycle with four stages

method and the sequential structure-based method. Tripathi et al. [12] proposed a 2-Sieve model associated with Multiresolution wavelet features and Gray Level Entropy Matrix features to detect mitosis in breast cancer multispectral images. Using the Indirect Immunofluorescence (IIF) protocol, [13] described a novel system termed Cell Pyramid Matching (CPM) for automatic classification of images obtained from Anti-Nuclear Antibody (ANA) pathology tests on Human Epithelial type 2(HEp-2) cells. Coupled with the Multiple Kernel Learning framework, this method was composed of regional histograms of visual words. Agrawal et al. [1] adopted a combination of texture features and SVM classification to classify cell images achieving a relatively high accuracy. Becker and Madany [2] introduced a mitosis automatic detector according to morphological cell features by using a maximum likelihood (ML) estimator. Different from the appearance-based method only focusing on the visual representation of spatial regions, the sequential structure-based method can take advantage of temporal context for the inference. Siva et al. [10] demonstrates an algorithm by using the temporal intensity changes from time-lapse images to track the deformation of embryonic tissue, then to identify the localization of mitosis cells. Liu et al. [6] utilized the max-margin hidden conditional random fields enhance the results of mitosis classification and then implemented the max-margin Semi-Markov model to further segment each divided cell into four temporal stages. Thirusittampalam et al. [11] illustrated the process of development of a tracking algorithm, which can detect mitosis cells sequence, aiming to achieve the cell motility indicators and finally identify the cellular mitosis events.

Since the sequential structure-based method can model the dynamics during mitotic event, we follow this kind of method. Different from previous work only identifying mitosis or localizing the beginning of mitosis event, this paper will deal with the localization of the entire cell cycle, which will provide more quantitative analysis for biologists. The proposed method consists of three steps. First, candidate mitosis sequences are extracted by foreground detection and volumetric region growing. Then, we extract the appearance feature of each frame within a candidate sequence for visual representation. At last, we apply the Latent-Dynamic Conditional Random Field (LDCRF)[7] for cell cycle localization. Compared against classic CRF[4] and HCRF[9], LDCRFs can capture both extrinsic dynamics and

intrinsic sub-structure by combining the strengths of CRFs and HCRFs. Specifically, LDCRFs cannot only model the visual pattern dynamic of inner-class sub--sequence, but also learn the transition between inter-class sub-sequences. Therefore, LDCRFs can be directly applied to localize different cell cycles by taking advance of both the visual dynamics within individual cell cycle and the visual pattern transition between adjacent cell cycles. The experiment on C2C12 cell dataset will show the superiority of the proposed method.

The rest of this paper is organized as follows. In Sect. 57.2, the proposed framework will briefly stated. Then, the Latent-Dynamic Conditional Random Fields model will be detailed in Sect. 57.3. Experimental results with discussions will be presented in Sect. 57.4. The last section will conclude the paper.

57.2 Framework

The proposed method for cell cycle localization proceeds through three continuous steps.

- **Candidate Sequence Extraction**: The goal of this step is to extract spatiotemporal volumes within the image sequences, which probably contain mitosis events as well as eliminate most of the background regions. We first construct the background model by mixture Gaussian modeling with the entire image sequence. Then the background is subtracted from individual image in order to remove the stationary bright artifacts. At last, we implement the 3D region growing as we did previously [5] to extract all candidate sequences.
- **Candidate Refinement**: The step means to identify the candidates outputted in the previous step, which contain mitosis events. The refined candidates will be preserved for further cell cycle localization. Since this step corresponds to the task of sequence classification, we adopt the hidden-state conditional random fields-based method for mitosis sequence identification as we did previously [5].
- **Cell Cycle Localization**: This step aims to localize the beginning of stages 2–4 in each mitosis sequence, which is obtained in the second step. We leverage the Latent-Dynamic Conditional Random Fields model for cell cycle modeling. LDCRFs can be directly applied to localize different cell cycles by taking advance of both the visual dynamics within individual cell cycle and the visual pattern transition between adjacent cell cycles.

57.3 Latent-Dynamic Conditional Random Fields

As shown in Fig. 57.1, each mitosis sequence contains four sub-structures, which corresponding to four stages. Within each sub-structure, the visual dynamics varies gradually while the visual patterns changes obviously between adjacent

sub-structures. The intrinsic and extrinsic visual transitions can be well modeled by the Latent-Dynamic Conditional Random Fields (LDCRF) by taking advantage of the superiorities of CRF for frame-wise labeling within one segment and HCRF on segment classification. We will respectively introduce its graphical structure and model formulation, learning and inference in this section.

57.3.1 Formulation

Given a candidate sequence $X = x_{t_{t=1}}^{T}$, the task of LDCRF aims to predict a label sequence $Y = y_{t_{t=1}}^{T}$. Each y_t is a state label for the t^{th} frame of a candidate sequence and is a member of a set $\mathcal{Y}$ of possible state labels. Ideally, Y will contains four segments, each of which contains the same frame-wise label. The location of the first label within each segment denotes the beginning of each stage. $x_t \in {}^{d}$ corresponds to the visual feature of the t^{th} frame in the candidate sequence. The model contains a hidden layer $H = h_{t_{t=1}}^{T}$ ($h_t \in \mathcal{H}$), where $\mathcal{H}$ means the four segments as shown in Fig. 57.1. The graphical representation of LDCRF is shown in Fig. 57.2. With the above illustration, the conditional probabilistic model of LDCRF can be defined as:

$$p(Y|X,\theta) = \sum_{H} p(Y|H,X,\theta)p(H|X,\theta), \tag{57.1}$$

where θ is the parameter of the model.

The model is restricted to have disjoint sets of hidden states associated with each state label in order to keep learning and inference tractable. The state label y_t corresponds to a set $\mathcal{H}_{y_t}$ of possible hidden states, and $h_t \in \mathcal{H}_{y_t}$. If sequences have any $h_t \notin \mathcal{H}_{y_t}$, we can get $p(Y|H,X,\theta) = 0$ by definition, so the model can be expressed as:

$$p(Y|X,\theta) = \sum_{H:\forall h_t \in \mathcal{H}_{y_t}} p(Y|H,X,\theta)p(H|X,\theta). \tag{57.2}$$

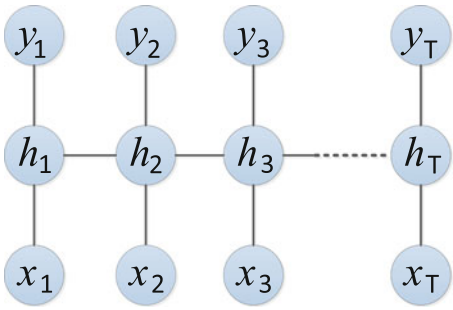

Fig. 57.2 Graphical structure of LDCRF

Using the usual conditional random field formulation, the $p(H|X,\theta)$ can be expressed by:

$$p(H|X,\theta) = \frac{1}{Z(X,\theta)}\exp(\sum_{k}\theta_k \cdot \mathbf{F}_k(H,X)), \tag{57.3}$$

where $Z(X,\theta)$ is a partition function computed as $Z(X,\theta) = \sum_{H}\exp(\sum_{k}\theta_k \cdot \mathbf{F}_k(H,X))$. Weights θ_k associated with the feature representation model both the intrinsic and extrinsic dynamics, and $\mathbf{F}_k$ is defined as $\mathbf{F}_k(H,X) = \sum (t=i)^T f_k(h_{t-1},h_t,X,t).f_k(h_{t-1},h_t,X,t)$ is feature function reflecting the transition feature extracted at frame t and $t-1$.

57.3.2 Learning

The training set is expressed as $T_r = (X_i,Y_i)_{i=1}^N$. Referring to [3], we use the following objective function to learn the parameter λ^*:

$$L(\lambda) = \sum_{i=1}^{N}\log p(Y_i|X_i,\lambda) - \frac{1}{2\sigma^2}\parallel \lambda\parallel^2 \tag{57.4}$$

This equation consists of two components, the first one is the conditional log-likelihood of the training data and the second one is the log of a Gaussian prior with variance σ^2.

L-BFGS can be leveraged for objective function optimization to search for the optimal model parameters $\lambda^* = \underset{\lambda}{\text{argmax}} L(\lambda)$. Due to the limited space, please refer to [7] for more details about objective function optimization.

57.3.3 Inference

The goal of testing is to estimate the most probable label sequence Y^* for a given test sequence X_{test}. The testing label sequence can be computed by:

$$Y^* = \arg\max_{Y} p(Y|X,\lambda^*), \tag{57.5}$$

where the parameter λ^* is learned from training examples. Assuming each label is associated with a disjoint set of hidden states, the previous equation can be rewritten as:

$$Y^* = \arg\max Y \sum_{H:\forall h_t \in \mathcal{H}_{y_t}} p(H|X, \lambda^*). \tag{57.6}$$

We use maximal marginal probabilities approach to estimate the sequence of labels since it minimizes the error per frame.

57.4 Experiment

57.4.1 Data

The proposed method was validated in a challenging phase contrast image sequence C2C12, prepared by our colleagues [6]. This dataset contains 1,010 images observed under a Zeiss Axiovert 135 TV inverted microscope, using a 5X, 0.15 N.A. objective lens with phase contrast optics. Images were acquired every 5 min for 120 h using a 12-bit Qimaging Retiga EXi Fast 1394 CCD camera at 500 ms exposure with a gain of 1.01. Each image consists of 1,392 $\times$ 1,040 pixels. The relatively low resolution was chosen in order to image a large cell population in the limited field of view. Totally 673 mitotic events were found in C2C12 image sequence.

57.4.2 Performance of Cell Cycle Localization

In our experiment, we utilized GIST feature [8] to represent low level feature of each frame because of its high discriminative capability since it can represent both structural and textural characteristics of each image. After getting the GIST feature of each frame, we can obtain the GIST feature sequence to represent each candidate sequence.

We manually annotated the mitosis events on each C2C12 image. Specifically, we labeled each frame within one mitosis sequence outputted by Step 2 from 1 to 4. In this way each mitosis sequence was segmented into four stages and the first frame of each segment denotes the beginning of the corresponding cell cycle. With the mitosis sequence and its sequence label groundtruth. LDCRFs can be trained to pinpoint each stages during one mitosis. In our experiment, the first half of the C2C12 mitosis events were used for model learning while the others were utilized for test. We trained LDCRF model with different window size and frame difference and utilized the area under ROC curve as the criteria to select the optimal parameters for modeling. Consequently, the comparison experiment shows that with the model trained with the hidden state 3 and the window size 1 can consistently outperformed the others on this dataset.

To evaluate the performance of localization, we utilized the mitosis stage localization error, which is defined as the difference in number of frames between the locations of the stage boundaries in segmentation result of LDCRF and the ground truth in [6].

Table 57.1 Performance of cell cycle localization

Frame difference	Stage 2	Stage 3	Stage 4
1	0.405	**0.263**	1.206
3	0.424	0.350	1.211
5	0.506	0.500	1.242

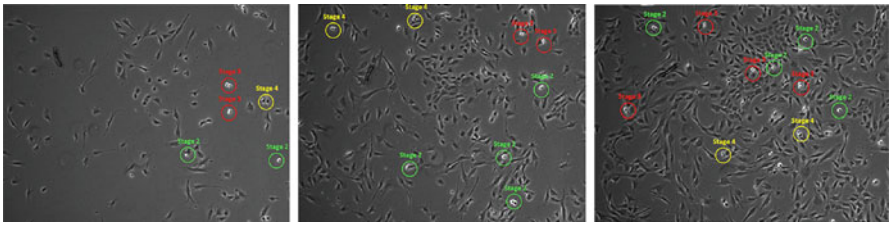

Fig. 57.3 Samples showing the localization performance

As summarized in Table 57.1, we utilized three different thresholds (1, 3, and 5) to further refine the performance of mitosis identification assuming that the mitosis sequence recognized in Step 2 will be discarded if the localization error of stage 3, the most important stage during one cell cycle, exceeds this threshold. With the refined mitosis sequence, we calculated the localization error of each stage. Performances of the LDCRF-based method (♯Hidden state = 3, window size = 1) are listed. It is obvious that the smaller a threshold is, the stricter the condition is. Therefore, when the value of frame difference comes to 1, the localization of mitosis cell achieves optimal by discarding more false positive mitosis sequences. When increasing the window sizes, the localization results of each stage become more inaccurate. Table 57.1 also shows that when the frame difference is fixed, the localization error of Stage 3 is the smallest and the localization error of Stage 4 is the largest since the drastic change from the zero shape pattern to the eight shape pattern at the beginning of Stage 3 can benefit temporal labelling. On C2C12 dataset the proposed method can achieve an average localization error of 0.263 frames for the start of Stage 3, and for the starting points of Stages 2 and 4, the localization errors are 0.405 and 1.206 frames, respectively. Some samples of the localization result are shown in Fig. 57.3.

Conclusion

In this paper, we propose a Latent-Dynamic Conditional Random Fields model-based method for automatic cell cycle localization. The LDCRF model can simultaneously model the visual dynamics within one stage and visual transition between adjacent stages in one mitosis sequence. Therefore, the proposed method can localize the beginning of each stage in one shot. The experiment on C2C12 dataset achieves the satisfactory performance of cell cycle localization. Especially, we achieve 0.26 frame for the localization error of Stage 3.

Acknowledgements This work was supported in part by the National Natural Science Foundation of China (61100124, 21106095, 61170239, and 61202168), the grant of Elite Scholar Program of Tianjin University, the grant of Introducing Talents to Tianjin Normal University (5RL123), the grant of Introduction of One Thousand High-level Talents in Three Years in Tianjin.

References

1. Agrawal P, Vatsa M, Singh R (2013) Hep-2 cell image classification: a comparative analysis. In: Machine learning in medical imaging. Springer, pp 195–202
2. Becker T, Madany A (2012) Morphology-based features for adaptive mitosis detection of in vitro stem cell tracking data. Methods Inf Med **51**(5):449
3. Kumar S, Hebert M (2003) Discriminative random fields: a discriminative framework for contextual interaction in classification. In: Proceedings of 9th IEEE international conference on computer vision, 2003. IEEE, pp 1150–1157
4. Liang L, Zhou X, Li F, Wong ST, Huckins J, King RW (2007) Mitosis cell identification with conditional random fields. In: Life science systems and applications workshop, 2007 (LISA 2007). IEEE/NIH, pp 9–12
5. Liu AA, Li K, Kanade T (2010) Mitosis sequence detection using hidden conditional random fields. In: 2010 I.E. international symposium on biomedical imaging: from nano to macro. IEEE, pp 580–583
6. Liu AA, Li K, Kanade T (2012) A semi-markov model for mitosis segmentation in time-lapse phase contrast microscopy image sequences of stem cell populations. IEEE Trans Med Imaging **31**(2):359–369
7. Morency L, Quattoni A, Darrell T (2007) Latent-dynamic discriminative models for continuous gesture recognition. In: IEEE conference on computer vision and pattern recognition, 2007 (CVPR'07). IEEE, pp 1–8
8. Oliva A, Torralba A (2001) Modeling the shape of the scene: a holistic representation of the spatial envelope. Int J Comput Vis **42**(3):145–175
9. Quattoni A, Wang S, Morency LP, Collins M, Darrell T, Csail M (2007) Hidden-state conditional random fields. IEEE Trans Pattern Anal Mach Intell **29**(10):1848–1852
10. Siva P, Brodland GW, Clausi D (2007) Automated detection of mitosis in embryonic tissues. In: Fourth Canadian conference on computer and robot vision, 2007 (CRV'07). IEEE, pp 97–104
11. Thirusittampalam K, Hossain J, Whelan PF (2013) A novel framework for cellular tracking and mitosis detection in dense phase contrast microscopy images. IEEE Trans Biomed Eng **17**(3):642–653
12. Tripathi AS, Mathur A, Daga M, Kuse M, Au OC (2013) 2-simdom: a 2-sieve model for detection of mitosis in multispectral breast cancer imagery. In: International conference on image processing. IEEE
13. Wiliem A, Sanderson C, Wong Y, Hobson P, Minchin RF, Lovell BC (2013) Automatic classification of human epithelial type 2 cell indirect immunofluorescence images using cell pyramid matching. Pattern Recognit

Chapter 58
Human Action Recognition using Salient Region Detection in Complex Scenes

Zhong Zhang, Shuang Liu, Shuaiqi Liu, Liang Han, Yunxue Shao, and Wen Zhou

Abstract Although the methods based on spatio-temporal interest points have shown promising results for human action recognition, they are not robust in complex scenes especially background clutter, camera motion, occlusions and illumination variations. In this paper, we propose a novel method to classify human actions in complex scenes. We suppress the false detection interest points by detecting salient regions. Furthermore, we encode the features according to their spatio-temporal relationship. Our method is verified on two challenging databases (UCF sports and YouTube), and the experimental results demonstrate that our method achieves better results than previous methods in human action recognition.

Keywords Human action recognition • Salient region detection • Complex scenes

58.1 Introduction

Automatically recognizing human actions is receiving increasing attention due to its wide range of applications such as video retrieval, human-computer interaction and activity monitoring. A large number of methods [1, 2] for humane action recognition have been proposed, ranging from trajectory-based methods [3] and local descriptor-based methods [4] to attribute-based method [5, 6].

Z. Zhang • S. Liu (✉) • S. Liu • L. Han
College of Electron and Communication Engineering, Tianjin Normal University, Tianjin, China
e-mail: zhong.zhang8848@gmail.com; shuangliu.tjnu@gmail.com; shdkj-1918@163.com; hanliang@mail.tjnu.edu.cn

Y. Shao
College of Computer Science, Inner Mongolia University, Inner Mongolia, China
e-mail: csshyx@imu.edu.cn

W. Zhou
The State Key Laboratory of Management and Control for Complex Systems, Institute of Automation, Chinese Academy of Sciences, Beijing, China
e-mail: wen.zhou@ia.ac.cn

J. Mu et al. (eds.), *The Proceedings of the Third International Conference on Communications, Signal Processing, and Systems*, Lecture Notes in Electrical Engineering 322, DOI 10.1007/978-3-319-08991-1_58

However, most of these previous approaches for human action recognition are constrained to well-controlled environments and fail to achieve desired results in complex scenes. Human action recognition in complex scenes is an extremely difficult task, due to several challenges, like background clutter, camera motion, occlusions and illumination variations. To address these challenges, several methods, such as tree-based template matching [7], tensor canonical correlation [8] and prototype based action matching [9] are proposed. Most of these methods are complex, time consuming and preprocessing requirement, such as segmentation, tree data structure building, target tracking or background subtraction. Other methods [10–12] for human action recognition in complex scenes apply spatio-temporal interest point detectors and local descriptors to characterize and encode the action video, which demand less or no preprocessing. Thus, this kind of methods achieve promising recognition accuracy. However, interest points are usually false detection in uncontrolled environments and Fig. 58.1 shows the result of interest point detection in complex scenes. We can see that the interest points outside the green rectangle are invalid owing to the actor inside the green rectangle.

In this paper, we propose a novel method to classify human actions in complex scenes. As is well-known, interest points inside or around the actor are beneficial to classification. Therefore, we utilize salient regions to select the interest points. Concretely, we reserve the interest points with high salient values, while we discard the interest points with low salient values. After selecting interest points, we apply CLC coding strategy [13] to consider the spatial and temporal relationship among interest points. Finally, we train the classification model using SVM.

The rest of this paper is organized as follows. Section 58.2 introduces the proposed method in detail. Section 58.3 demonstrates that our experimental results are more accurate than the state-of-the-art methods on UCF sports dataset and YouTube dataset. Finally, in section “Conclusion” we conclude this paper.

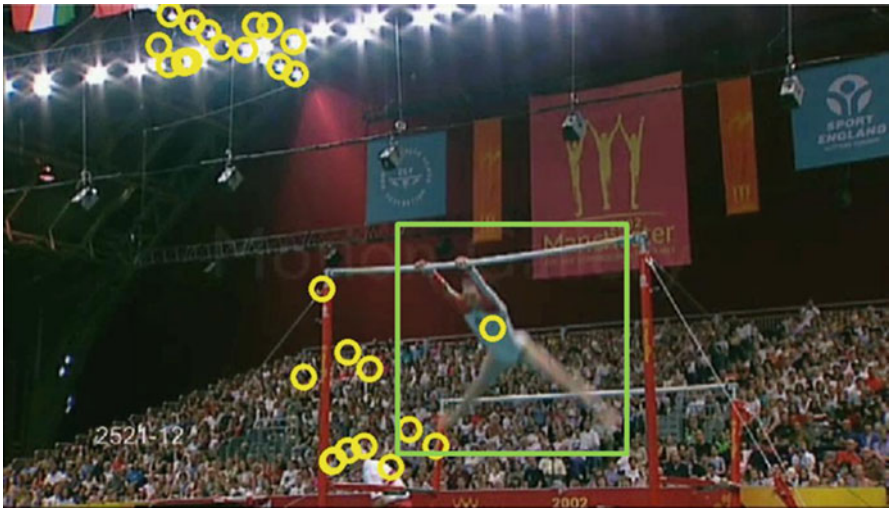

Fig. 58.1 Detecting interest points in complex scenes

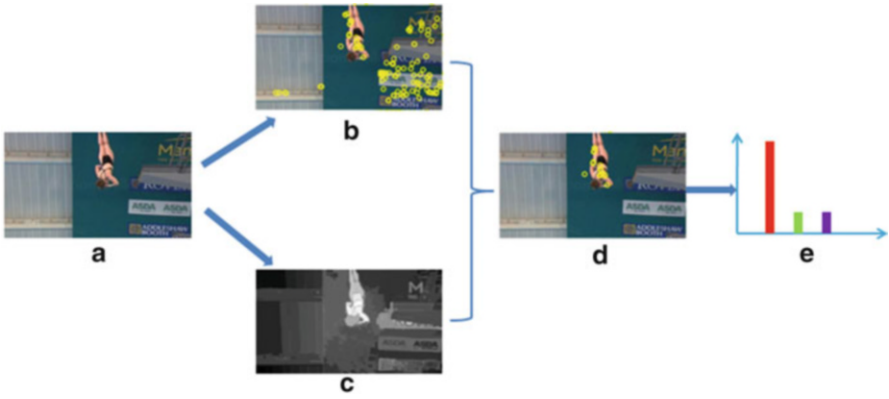

Fig. 58.2 Flowchart of the proposed method. (**a**) Original action video; (**b**) detecting spatio-temporal interest points; (**c**) detecting salient regions; (**d**) selecting significative spatio-temporal interest points; (**e**) generating feature histograms

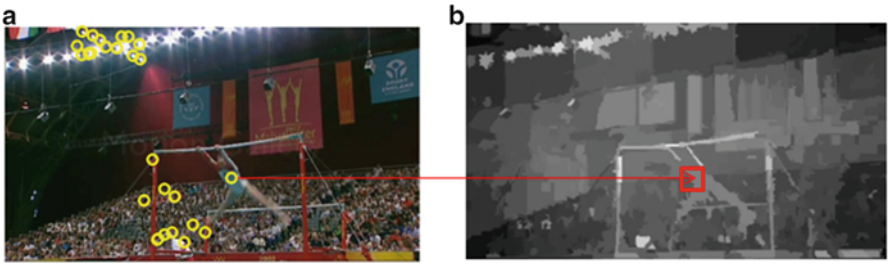

Fig. 58.3 Selective interest points

58.2 Approach

58.2.1 Method Overview

The proposed method consists of four stages: (a) detecting spatio-temporal interest points for each action video; (b) detecting salient regions for each frame of an action video; (c) selecting significative spatio-temporal interest points according salient regions; (d) generating feature histograms and training classifier. The flowchart of the proposed method is shown in Fig. 58.2 and the corresponding detailed description will be presented in the following sections.

58.2.2 Detection of Spatio-Temporal Interest Points

To detect interest points, we first use Harris3D corner detector [14] for each action video as shown in Fig. 58.2b. For each interest point, we characterize the local

appearance using histogram-of-gradients (HOG) and histogram-of-optical-flow (HOF) [15]. As a result, we obtain a set of interest points for an action video, $v = (\mathbf{x}_i, \mathbf{s}_i)_{i=1,\ldots,N}$, where N is the number of interest points for the action video v, $\mathbf{x}_i$ indicates the feature vector of the i-th interest point and $\mathbf{s}_i$ is the location of the i-th interest point. Here $\mathbf{s}_i = (x, y, t)$ where x, y and t are horizontal, vertical, and temporal coordinates respectively.

58.2.3 Salient Region Detection

We detect the salient regions for each frame by using region contrast (RC) [16]. First, we segment the frame into regions using a segmentation method based on graph cut [17]. Then, the color histogram is builded for each region. For each region a_k, we calculate the salient value by comparing its color contract with all other regions:

$$S(a_k) = \sum_{a_k \neq a_i} exp(D_s(a_k, a_i)/\sigma^2) w(a_i) D_r(a_k, a_i) \tag{58.1}$$

where $w(a_i)$ is the weight of region a_i, D_r represent the color distance between the two regions, D_s is the spatial distance between two regions, and σ controls the strength of spatial weight. From the above equation, we can see that all the pixels in one region share the same salient value. The number of pixels in a_i indicates the weight w_i. The spatial distance is defined as the Euclidean distance between the centroids of regions. The color distance between two regions a_1 and a_2 is defined as:

$$D_r(a_1, a_2) = \Sigma_{i=1}^{n_1} \Sigma_{j=1}^{n_2} f(c_{1,i}) f(c_{2,j}) D(c_{1,i}, c_{2,j}) \tag{58.2}$$

where $f(c_{k,i})$ is the probability of the i-th color $c_{k,i}$ among all n_k colors in the k-th region a_k, $k = 1, 2$. The result of salient region detection is shown in Fig. 58.2c.

58.2.4 Selective Interest Points

Since human actions are usually recorded in complex scenes, for example cluttered background, illumination variations, camera motion and occluded bodies, there are a lot of noise interest points. The location of these noise interest points are usually in the background, and therefore they are injurious to classification. To address this problem, we apply the salient regions to suppress these noise interest points. For each interest point $(\mathbf{x}, \mathbf{s})$, we compute the maximum salient value around its space location:

$$S_m = \max_{(x,y)\in R_l} S((x,y)) \tag{58.3}$$

where R_l is the local region around the interest point (see the red rectangle in Fig. 58.3b) and $S((x,y)$ is the salient value at (x,y). If $S_m > T_s$, we reserve this interest point due to its location in salient region; otherwise we discard this interest point. Here T_s is the salient threshold value. The result of selective interest points is illustrated in Fig. 58.2d.

58.2.5 Feature Coding

After selecting the interest points, we cluster all the interest points from all the action videos by using k-means clustering algorithm and generate the dictionary. Then, we utilize CLC [13] strategy to code the features, which not only considers the spatio-temporal relationships among interest points, but also alleviates the quantization error by using linear coding. Afterwards, each action video is represented by a histogram (see Fig. 58.2e). Finally, we use these feature histograms to train a multi-class SVM.

58.3 Experimental Results

To evaluate our proposed method for human action recognition, we conduct a series of experiments on two publicly available human action datasets: UCF Sports dataset [18] and YouTube action dataset [19]. These two datasets are challenging because these action videos are recorded in realistic scenes and suffer from cluttered background, illumination variations, camera motion and so on. The codebook is constructed by k-means algorithm and the number of codebook is empirically set to 4,000 [20]. The salient threshold value T_s is set to 180 and R_l is set to 15.

We present the results of selective interest points in Fig. 58.4. The first row is the original detected interest points, the second row is the salient regions, and the last row is the results of suppressing the noise interest points. From Fig. 58.3, we can see that most of interest points on background are discarded and the interest points on human are reserved which is beneficial to the subsequent classification. Next, we will objectively evaluate our proposed method on UCF Sports dataset and YouTube action dataset.

The UCF sports dataset [18] contains ten different types of sports action: swinging (on the pommel horse and on the floor), diving, kicking (a ball), weight-lifting, horse-riding, running, skateboarding, swinging (at the high bar), golf swinging and walking. The dataset consists of 150 real videos with a wide range of viewpoints and scene backgrounds. In order to increase the amount of

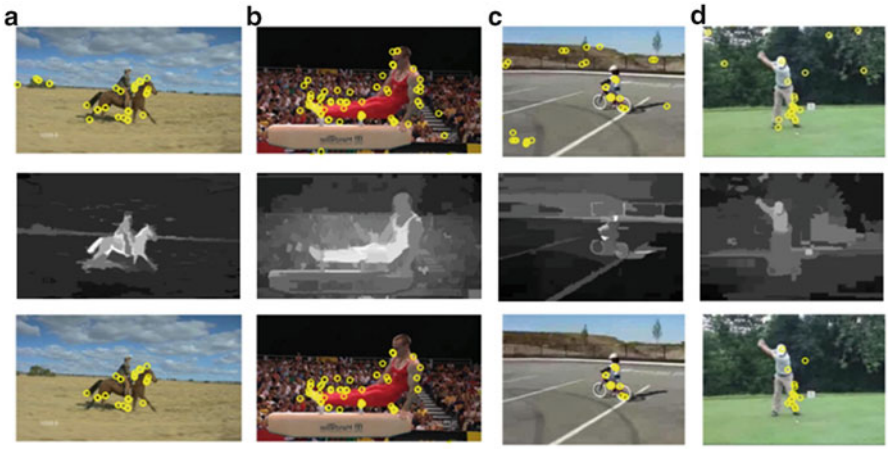

Fig. 58.4 Performance of the selective interest points in complex scenes. The action videos (**a**, **b**) are from UCF Sports dataset and the action videos (**c**, **d**) are from YouTube action dataset

Table 58.1 Recognition results of different methods on the UCF Sports dataset

Method	Accuracy (%)
Sullivan et al. [18]	69.2
Wang et al. [20]	85.6
Kovashka et al. [21]	87.27
Le et al. [22]	86.5
Zhang et al. [13]	87.33
Ours	**88.0**

training samples, we extend the dataset by adding a horizontally flipped version of each video sequence to the dataset as suggested in [20]. Table 58.1 compares our method with the other excellent methods, in which we can see that our method achieves the highest recognition accuracy of 88 %. Figure 58.5 shows the confusion table of recognition results on UCF sports dataset. From this figure, "horse-riding" are prone to be misclassified into "running" due to their similar appearance.

The YouTube dataset [19] is a collection of 1,168 complex and challenging YouTube videos of 11 human actions categories: basketball shooting, volleyball spiking, trampoline jumping, soccer juggling, horseback riding, cycling, diving, swinging, golf swinging, tennis swinging and walking (with a dog). The dataset has the following properties: a mix of steady cameras and shaky cameras, cluttered background, low resolution, and variation in object scale, viewpoint and illumination. Our method achieves 88.65 % recognition accuracy on this dataset and Table 58.2 compares our result with the other state-of-the-art methods.

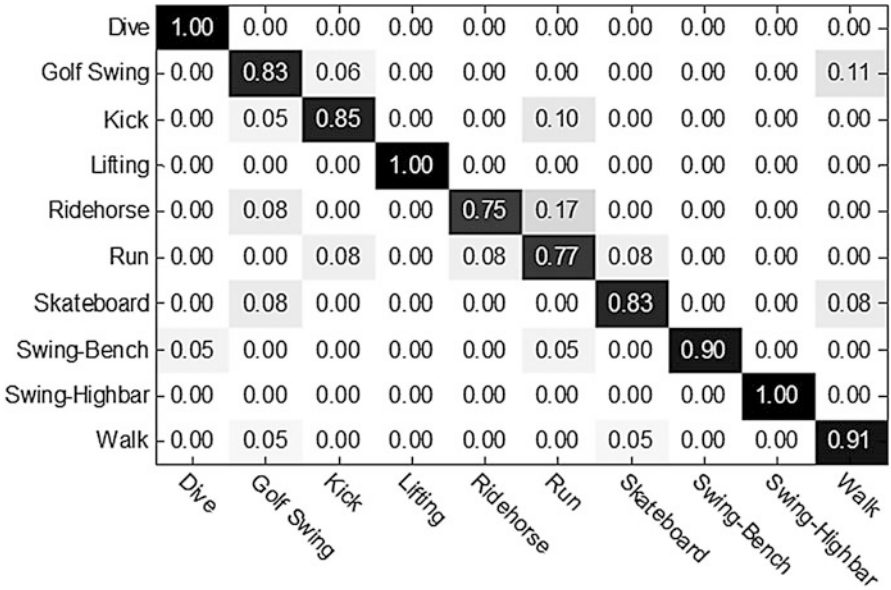

Fig. 58.5 Confusion table of our method on UCF Sports dataset

Table 58.2 Recognition results of different methods on the YouTube dataset

Method	Accuracy (%)
Bregonzio et al. [23]	64.0
Liu et al. [19]	71.20
Chakraborty et al. [4]	86.98
Ours	**88.65**

Conclusion

In this paper, a novel method has been proposed to classify human actions in complex scenes. We propose to select interest points by using salient regions. The selected interest points are beneficial to sequential classification because they are inside or around the actors. The proposed method has been validated on two challenging datasets, and the experimental results clearly demonstrate the superiority of our method over previous methods in human action recognition.

References

1. Poppe R (2010) A survey on vision-based human action recognition. Image Vis Comput 28(6):976–990
2. Zhang Z, Wang C, Xiao B, Zhou W, Liu S (2012) Contextual Fisher kernels for human action recognition. In: International conference on pattern recognition, pp 437–440
3. Raptis M, Soatto S (2010) Tracklet descriptors for action modeling and video analysis. In: European conference on computer vision, pp 577–590
4. Chakraborty B, Holte M, Moeslund T, Gonzàlez J (2012) Selective spatio-temporal interest points. Comput Vis Image Underst 116(3):396–410
5. Liu J, Kuipers B, Savarese S (2011) Recognizing human actions by attributes. In: IEEE conference on computer vision and pattern recognition, pp 3337–3344
6. Zhang Z, Wang C, Xiao B, Zhou W, Liu S (2013) Attribute regularization based human action recognition. IEEE Trans Inf Forensics Secur 8(10):1600–1609
7. Jiang Z, Lin Z, Davis L (2012) A tree-based approach to integrated action localization, recognition and segmentation. In: Trends and topics in computer vision, pp 114–127
8. Kim T, Wong K, Cipolla R (2007) Tensor canonical correlation analysis for action classification. In: IEEE conference on computer vision and pattern recognition, pp 1–8
9. Lin Z, Jiang Z, Davis L (2009) Recognizing actions by shape-motion prototype trees. In: IEEE international conference on computer vision, pp 444–451
10. Cao L, Liu Z, Huang T (2010) Cross-dataset action detection. In: IEEE conference on computer vision and pattern recognition, pp 1998–2005
11. Duchenne O, Laptev I, Sivic J, Bach F, Ponce J (2009) In: IEEE international conference on computer vision, pp 1491–1498
12. Yu T, Kim T, Cipolla R (2010) Real-time action recognition by spatiotemporal semantic and structural forests. In: British machine vision conference
13. Zhang Z, Wang C, Xiao B, Zhou W, Liu S (2012) Action recognition using context-constrained linear coding. IEEE Signal Process Lett 19(7):439–442
14. Laptev I (2005) On space-time interest points. Int J Comput Vis 64(2):107–123
15. Laptev I, Marszalek M, Schmid C, Rozenfeld B (2008) Learning realistic human actions from movies. In: IEEE conference on computer vision and pattern recognition, pp 1–8
16. Cheng M, Zhang G, Mitra N, Huang X, Hu S (2011) Global contrast based salient region detection. In: IEEE conference on computer vision and pattern recognition, pp 409–416
17. Felzenszwalb P, Huttenlocher D (2004) Efficient graph-based image segmentation. Int J Comput Vis 59(2):167–181
18. Sullivan M, Shah M (2008) Action MACH: maximum average correlation height filter for action recognition. In: IEEE conference on computer vision and pattern recognition
19. Liu J, Luo J, Shah M (2009) Recognizing realistic actions from videos in the wild. In: IEEE conference on computer vision and pattern recognition, pp 1996–2003
20. Wang H, Ullah M, Klaser A, Laptev I, Schmid C (2009) Evaluation of local spatio-temporal features for action recognition. In: British machine vision conference
21. Kovashka A, Grauman K (2010) Learning a hierarchy of discriminative space-time neighborhood features for human action recognition. In: IEEE conference on computer vision and pattern recognition, pp 2046–2053
22. Le Q, Zou W, Yeung S, Ng A (2011) Learning hierarchical invariant spatio-temporal features for action recognition with independent subspace analysis. In: IEEE conference on computer vision and pattern recognition, pp 3361–3368
23. Bregonzio M, Li J, Gong S, Xiang T (2010) Discriminative topics modelling for action feature selection and recognition. In: British machine vision conference, pp 1–11
24. Zhang Z, Wang C, Xiao B, Zhou W, Liu S, Shi C (2013) Cross-view action recognition via a continuous virtual path. In: IEEE conference on computer vision and pattern recognition, pp 2690–2697

Chapter 59
Semantic Analysis in Human Action Recognition: A Comprehensive Study

Zhong Zhang, Shuang Liu, Shuaiqi Liu, Liang Han, and Yunxue Shao

Abstract Human action recognition is a hot topic in computer vision and pattern recognition. Semantic analysis, as a kind of effective bridge to connect the human brains and computers, has been widely studied over the past several years and a number of methods have been proposed. However, there is no comprehensive study concerning semantic analysis in human action recognition. In this paper, we make a survey on various semantic analysis methods based on an approach-based taxonomy. We choose several representatives from semantic analysis methods and evaluate them on publicly available datasets.

Keywords Human action recognition • Semantic analysis • Computer vision

59.1 Introduction

59.1.1 Motivation

Human action recognition is a hot topic in computer vision and pattern recognition. It has a wide range of applications, like video surveillance, video retrieval, human-computer interaction and medical monitoring. The objective of human action recognition is to automatically assign class labels to an unknown action video. It is a challenging problem due to cognitive differences between human brains and computers. Specifically, for an action video, computers consider it as a set of binary digits, while human brains consider it as an action class. This results in semantic gap between human brains and computers, as shown in Fig. 59.1. To overcome this challenge, semantic analysis methods, which attempt to bridge the gap

Z. Zhang • S. Liu (✉) • S. Liu • L. Han
College of Electron and Communication Engineering, Tianjin Normal University, Tianjin, China
e-mail: zhong.zhang8848@gmail.com; shuangliu.tjnu@gmail.com; shdkj-1918@163.com; hanliang@mail.tjnu.edu.cn

Y. Shao
College of Computer Science, Inner Mongolia University, Inner Mongolia, China
e-mail: csshyx@imu.edu.cn

J. Mu et al. (eds.), *The Proceedings of the Third International Conference on Communications, Signal Processing, and Systems*, Lecture Notes in Electrical Engineering 322, DOI 10.1007/978-3-319-08991-1_59

Fig. 59.1 The cognitive differences between human brains and computers

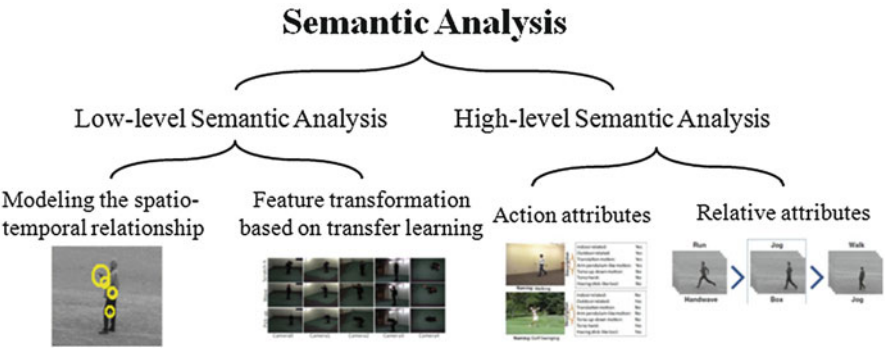

Fig. 59.2 A taxonomy of semantic analysis methods in human action recognition

between human brains and computers, have been proposed and have achieved the state-of-the-art performance in several datasets, for example, KTH dataset [1], UCF dataset [2] and YouTube dataset [3].

59.1.2 Taxonomy

The objective of this paper is to provide a complete overview and comparison of semantic analysis in human action recognition. Figure 59.2 illustrates an overview of the tree-structured taxonomy for semantic analysis. We have chosen an approach-based taxonomy. All the semantic analysis methods in human action recognition are first classified into two categories: low-level semantic analysis methods and high-level semantic analysis methods. Level-level semantic analysis methods are methods that automatically learn the semantic information from low-level features. On the other hand, high-level semantic analysis methods represent human actions using human-defined attributes, and then train the classification model. Low-level semantic analysis methods are again classified

into two types: modeling the spatio-temporal relationship among interest points and feature transformation based on transfer learning. High-level semantic methods are classified into two types: action attributes and relative attributes.

59.1.3 Contributions

The major contributions of this paper are summarized as follows:

- Provide a survey on recent process in semantic analysis for human action recognition. To the best of our knowledge, we are the first to review human action recognition in terms of semantic analysis. Thus, our work is different from the other surveys [4, 5].
- Evaluate several representative semantic analysis methods on standard action dataset and realistic action dataset.
- Summarize main problem and challenges of current studies, and point out some open directions in future.

59.2 Semantic Analysis Methods

59.2.1 Low-Level Semantic Methods

Level-level semantic analysis methods automatically learn the semantic information from low-level features. They are again classified into two types: modeling the spatio-temporal relationship among interest points and feature transformation based on transfer learning.

The methods, which model the spatio-temporal relationship among interest points, focus on overcoming the drawbacks of bag-of-words [6]. The relationship of interest points is a kind of low-level semantic information. The traditional bag-of-words model takes no consideration of the relationship among spatio-temporal points; furthermore, it also suffers serious quantization error. Savarese et al. [7] used a local histogram called ST-correlograms to measure feature co-occurrence patterns in a local 3-D region. Ryoo et al. [8] proposed a so-called "feature feature relationship histogram" to capture both appearance and relationship information between pair-wise interest points. Kovashka et al. [9] designed a hierarchy of codebooks using neighborhoods of spatio-temporal interest points. Wang et al. [10] presented a representation method that captures contextual interactions between interest points, based on the density of all features observed in each interest point's multi-scale spatio-temporal contextual domain. Zhang et al. [11] proposed a novel coding strategy called context-constrained linear coding (CLC), which not only considered spatio-temporal contextual information but also alleviated quantization

error. Zhang et al. [12] added a Gaussian function to represent contextual information into the generative model under the framework of Fisher kernel.

The methods using feature transformation based on transfer learning can address the problem of cross-view action recognition. Some approaches for cross-view action recognition rely on geometric constraints [13], body joints detection and tracking [14, 15], and 3D models [16]. However, these approaches require some sophisticated techniques, such as body joints detection and tracking, or alignment between views. Recently, transfer learning approaches are employed to address cross-view action recognition, which belong to low-level semantic methods due to transformation the original feature space to a discriminative one. Farhadi et al. [17] generated split-based features in the source view using Maximum Margin Clustering and then transferred the split values to the corresponding frames in the target view. Liu et al. [18] learned a cross-view bag of "bilingual words" using corresponding pairs. Then, the action videos are represented by "bilingual words" in both views. Zheng et al. [19] explored view-invariant features based on sparse representations using a transferable dictionary pair. The transferable dictionary not only learns the view knowledge from one source view but also from multiple source views. "Handkelet" [20] was proposed as a new type of feature which is robust to view variance by capturing the dynamics instead of simple spatial gradient information. Zhang et al. [21] utilized a continuous virtual path connected the source view and the target view to transform the original feature space to infinite-dimensional feature space.

59.2.2 High-Level Semantic Methods

High-level semantic analysis methods represent human actions using human-defined attributes, which explicitly represents the semantic information. High-level semantic methods are classified into two types: action attributes and relative attributes.

Attributes are defined additional concepts to describe action related properties that act as high-level semantic concept which bridge the gap between low-level features and class labels, shown in Fig. 59.3. In some recent work, it is shown that attributes are useful in many aspects. First, they are helpful for recognizing and describing familiar objects/actions [22, 23]. The described objects/actions can also help search people or merchandise in semantic terms [24]. Second, they are a powerful tool for the zero-shot learning problem [25], i.e., no training samples are available. Most methods utilize the prior knowledge provided by human-defined attributes to transfer knowledge. Third, some works [22, 23, 26, 27] treat attributes as middle-level features for object or video classification. Lampert et al. [23] proposed the direct attribute prediction (DAP) model, which learned to predict the presence of each attribute, and then used the predictions to train object models. Liu et al. [25] treated the action attributes as latent variables, where classifiers are pretrained by linear SVMs with outputs being the inputs of latent SVM. Zhang

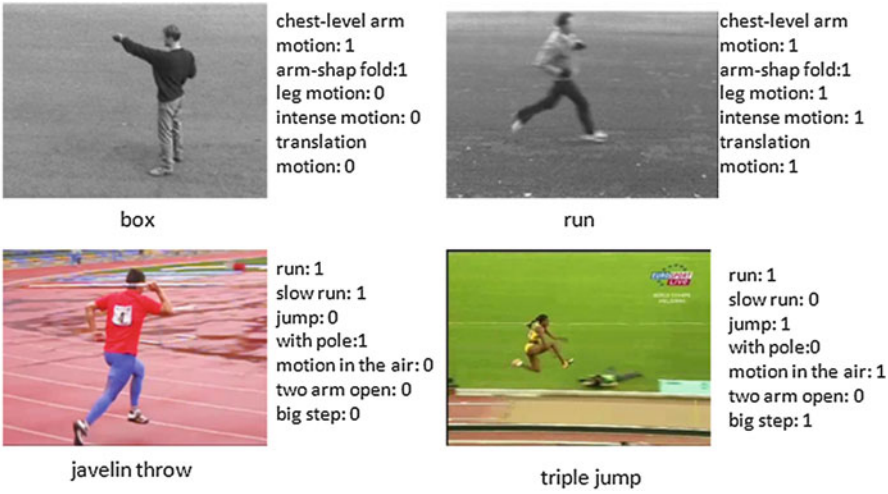

Fig. 59.3 Examples of action attributes. *1* Indicate the presence of this attribute; *0* indicate the absence of this attribute

et al. [28, 29] explicitly considers attribute-action relationship for human action recognition by adding attribute regularization under the multitask learning framework. In this way, the learned model not only shares the low-level features, but also gets regularized according to the semantic constrains.

The action attribute-based methods totally regard attributes as binary values which indicate the presence or absence of the corresponding attribute. In this way, the binary attribute fails to capture the degree of existence of attribute, so it could hardly represent objects veritably. So Parikh and Grauman [30] proposed the concept of *relative attributes* as a kind of high-level semantic analysis. It explores a semantically rich representation by describing relative relationships in the world. For example, 'running' has stronger presence of 'leg motion' than that of 'jogging', and 'walking' has weaker presence of 'jumping motion' than that of 'jumping from situp'. Zhong et al. [31] proposed a robust framework for relative attributes which is realized by simultaneously introducing Sigmoid and Gaussian envelopes into RankSVM loss objective and uses Gaussian Mixture models (GMM) to train generative model.

59.3 Experimental Study

To test the performance of different semantic analysis methods, an empirical study is conducted in this section. We first introduce the datasets and experimental setup. Then, we present the comparative results.

To detect interest points from videos of action, we adopt the Harris 3-D corner detector proposed in [32], which is an extension of the Harris 2-D corner. The

Harris 3-D detects the location where the video intensities have significant local variations in both space and time. For each interest point, the histogram of oriented gradients (HOG) [33] and histogram of optical flow (HOF) [34] are used as local appearance descriptors.

We validate our algorithm on three publicly available datasets: KTH dataset [1], UIUC action dataset [35] and UCF Sports dataset [2]. The KTH dataset is a standard benchmark for human action recognition. It contains six action classes (box, hand clap, hand wave, jog, run, and walk), each of which is performed in four different scenarios by 25 subjects, resulting in a total of 599 video clips. We quantize the descriptors by k-means clustering and the number of codebook is set to 4,000. We adopt the Leave One Out Cross Validation (LOOCV) strategy [8, 9], specifically 24 videos of actors as training and the rest one as test videos. The UIUC action dataset [35] contains about 532 videos of 14 actions including jump forward, push up, raise one hand, etc. These videos are performed by 8 actors. The action classes in this dataset are very diverse, which is useful for our study. We quantize the descriptors by k-means clustering and the number of codebook is set to 2,000. In addition, we adopt Leave One Actor Out (L1AO), namely excluding all sequences of the same actor from the training set. The UCF sports dataset [2] contains ten different types of sports action: swinging (on the pommel horse and on the floor), diving, kicking (a ball), weight-lifting, horse-riding, running, skateboarding, swinging (at the high bar), golf swinging and walking. The dataset consists of 150 real videos with a wide range of viewpoints and scene backgrounds. In order to increase the amount of training samples, we extend the dataset by adding a horizontally flipped version of each video sequence to the dataset as suggested in [5]. We adopt Leave One Video Out Cross Validation [5].

Table 59.1 shows the recognition accuracies of different state-of-the-art methods on the KTH, UIUC and UCF Sports datasets. Note that we obtain the results from their original literatures with the optimal parameters. From the table, we can see that the method [12] belonging to low-level semantic analysis methods achieves the best results on the KTH and UCF datasets, yet the method [29] belonging to high-level semantic analysis methods obtains the best results on the UIUC dataset. The method [12] projects the original feature to a high dimensional space. The human-

Table 59.1 State-of-the-art recognition accuracies (%) on the KTH, UIUC and UCF Sports datasets

Method	KTH	UIUC	UCF Sports
Kovashka et al. [9]	94.53	-	87.27
Le et al. [36]	93.8	-	86.5
Zhang et al. [11]	95.06	-	87.33
Perronnin et al. [37]	91.92	-	84.0
Zhang et al. [12]	**96.11**	-	**89.3**
Hwang et al. [38]	90.13	98.86	-
Zhang et al. [29]	96.07	**99.14**	-
Parikh et al. [30]	88.1	93.4	-
Zhang et al. [31]	95.98	98.87	-

defined attributes are adopted by Zhang et al. [29]. Each semantic analysis methods have their own merits. If human action is classified in complex scenes or different views, one should choose low-level semantic analysis methods. If zero-shot learning problem is expected to address, one should choose high-level semantic analysis methods.

Conclusion
In this paper, we have discussed various semantic analysis methods and evaluated their performance. Finally, we would like to discuss some open directions. The one is that recognize human action in complex scenes and the other one is that learn features from action videos under the framework of deep learning.

References

1. Schuldt C, Laptev I, Caputo, B (2004) Recognizing human actions: a local SVM approach. In: International conference on pattern recognition, pp 32–36
2. Sullivan M, Shah M (2008) Action MACH: Maximum average correlation height filter for action recognition. In: IEEE conference on computer vision and pattern recognition
3. Liu J, Luo J, Shah M (2009) Recognizing realistic actions from videos in the wild. In: IEEE conference on computer vision and pattern recognition, pp 1996–2003
4. Aggarwal JK, Ryoo MS (2011) Human activity analysis: a review. ACM Comput Surv (CSUR) 43(3):1–43
5. Wang H, Ullah M, Klaser A, Laptev I, Schmid C (2009) Evaluation of local spatio-temporal features for action recognition. In: British machine vision conference
6. Csurka G, Dance C, Fan L (2004) Visual categorization with bags of keypoints. In: ECCV workshop on statistical learning in computer vision, pp 1–22
7. Savarese S, DelPozo A, Niebles J, Fei-Fei L (2008) Spatial-temporal correlatons for unsupervised action classification. In: IEEE workshop on motion and video computing, pp 1–8
8. Ryoo M, Aggarwal J (2009) Spatio-temporal relationship match: video structure comparison for recognition of complex human activities. In: IEEE international conference on computer vision, pp 1593–1600
9. Kovashka A, Grauman K (2010) Learning a hierarchy of discriminative space-time neighborhood features for human action recognition. In: IEEE conference on computer vision and pattern recognition, pp 2046–2053
10. Wang J, Chen Z, Wu Y (2011) Action recognition with multiscale spatio-temporal contexts. In: IEEE conference on computer vision and pattern recognition, pp 3185–3192
11. Zhang Z, Wang C, Xiao B, Zhou W, Liu S (2012) Action recognition using context-constrained linear coding. IEEE Signal Process Lett 19(7):439–442
12. Zhang Z, Wang C, Xiao B, Zhou W, Liu S (2012) Contextual Fisher kernels for human action recognition. In: International conference on pattern recognition, pp 437–440
13. Yilmaz A, Shah M (2005) Actions sketch: A novel action representation. In: IEEE conference on computer vision and pattern recognition, pp 984–989
14. Parameswaran V, Chellappa R (2006) View invariance for human action recognition. Int J Comput Vis 66(1):83–101
15. Rao C, Yilmaz A, Shah M (2002) View-invariant representation and recognition of actions. Int J Comput Vis 50(2):203–226

16. Weinland D, Boyer E, Ronfard R (2007) Action recognition from arbitrary views using 3D exemplars. In: IEEE international conference on computer vision, pp 1–7
17. Farhadi A, Tabrizi M (2008) Learning to recognize activities from the wrong view point. In: European conference on computer vision, pp 154–166
18. Liu J, Shah M, Kuipers B, Savarese S (2011) Cross-view action recognition via view knowledge transfer. In: IEEE conference on computer vision and pattern recognition, pp 3209–3216
19. Zheng J, Jiang Z, Phillips P, Chellappa R (2012) Cross-view action recognition via a transferable dictionary pair. In: British machine vision conference, pp 7–16
20. Li B, Camps O, Sznaier M (2012) Cross-view activity recognition using hankelets. In: IEEE conference on computer vision and pattern recognition, pp 1362–1369
21. Zhang Z, Wang C, Xiao B, Zhou W, Liu S, Shi C (2013) Cross-view action recognition via a continuous virtual path. In: IEEE conference on computer vision and pattern recognition, pp 2690–2697
22. Farhadi A, Endres I, Hoiem D, Forsyth D (2009) Describing objects by their attributes. In: IEEE conference on computer vision and pattern recognition, pp 1778–1785
23. Lampert C, Nickisch H, Harmeling S (2009) Learning to detect unseen object classes by between-class attribute transfer. In: IEEE conference on computer vision and pattern recognition, pp 951–958
24. Vaquero D, Feris R, Tran D, Brown L, Hampapur A, Turk M (2009) Attribute-based people search in surveillance environments. In: IEEE workshop on applications of computer vision, pp 1–8
25. Liu J, Kuipers B, Savarese S (2011) Recognizing human actions by attributes. In: IEEE conference on computer vision and pattern recognition, pp 3337–3344
26. Kumar N, Berg A, Belhumeur P, Nayar S (2009) Attribute and simile classifiers for face verification. In: IEEE international conference on computer vision, pp 365–372
27. Wang Y, Mori G (2010) A discriminative latent model of object classes and attributes. In: European conference on computer vision, pp 155–168
28. Zhang Z, Wang C, Xiao B, Zhou W, Liu S (2012) Human action recognition with attribute regularization. In: IEEE international conference on advanced video and signal-based surveillance, pp 112–117
29. Zhang Z, Wang C, Xiao B, Zhou W, Liu S (2013) Attribute regularization based human action recognition. IEEE Trans Inf Forensics Secur 8(10):1600–1609
30. Parikh D, Grauman K (2011) Relative attributes. In: IEEE international conference on computer vision, pp 503–510
31. Zhang Z, Wang C, Xiao B, Zhou W, Liu S (2014) Robust relative attributes for human action recognition. Pattern Anal Appl. doi:10.1007/s10044-013-0349-3
32. Laptev I (2005) On space-time interest points. Int J Comput Vis 64(2):107–123
33. Dalal N, Triggs B (2005) Histograms of oriented gradients for human detection. In: IEEE conference on computer vision and pattern recognition, pp 886–893
34. Dalal N, Triggs B, Schmid C (2006) Human detection using oriented histograms of flow and appearance. In: European conference on computer vision, pp 428–441
35. Tran D, Sorokin A (2008) Human activity recognition with metric learning. In: European conference on computer vision, pp 548–561
36. Le Q, Zou W, Yeung S, Ng A (2011) Learning hierarchical invariant spatio-temporal features for action recognition with independent subspace analysis. In: IEEE conference on computer vision and pattern recognition, pp 3361–3368
37. Perronnin F, Sánchez J, Mensink T (2010) Improving the fisher kernel for large-scale image classification. In: European conference on computer vision, pp 143–156
38. Hwang S, Sha F, Grauman K (2011) Sharing features between objects and their attributes. In: IEEE conference on computer vision and pattern recognition, pp 1761–1768

Chapter 60
DOA Estimation of Coherent and Incoherent Wideband OFDM Signals Based on Fourth-Order Cumulants

Wei Min, Xiao Zhong Liu, Bao Gen Xu, Yi He Wan, Si Long Tang, Zhong Chu Rao, and Qun Wan

Abstract A novel algorithm based on fourth-order cumulants (FOC) was proposed when coherent and incoherent wideband OFDM signals coexist. The proposed algorithm comprises two steps. The first step is to estimate the DOA of incoherent OFDM signals, then a FOC matrix that only contains the information of coherent OFDM signals was constructed by eliminating the contribution of incoherent OFDM signals; the second step is to estimate the DOA of the coherent OFDM signals from the constructed matrix by using a sparse reconstruction method. The simulation results demonstrate the performance of our proposed algorithm.

Keywords Wideband OFDM signals • Coherent signals • Fourth-order cumulants • Direction-of-arrival • Sparse reconstruction theory

60.1 Introduction

With the increase of the bandwidth of the signal processing, the spatial spectrum of wideband OFDM signal has become one of the most important and difficult problems in the field of array signal processing due to their eliminating ISI effect of multipath channels and high frequency band utilization. Incoherent Signal Subspace Method (ISM) [1] was firstly introduced to estimate the DOA of incoherent wideband signals, but it failed to work in dealing with the DOA of coherent wideband signals. To solve this problem, Wang proposed the Coherent Signal

W. Min (✉) • Q. Wan
Department of Electronic Engineering, University of Electronic Science and Technology of China, Chengdu 611731, China
e-mail: 18081878741@163.com

X.Z. Liu
CETC38 Institute, Hefei 230031, China

B.G. Xu • Y.H. Wan • S.L. Tang • Z.C. Rao
Tong Fang Electronic Science and Technology Co. Ltd., Jiujiang 332007, China

J. Mu et al. (eds.), *The Proceedings of the Third International Conference on Communications, Signal Processing, and Systems*, Lecture Notes in Electrical Engineering 322, DOI 10.1007/978-3-319-08991-1_60

Subspace Method [2], based on which, Signal Subspace Transform [3] algorithm and Rotational Signal Subspace (RSS) [4] algorithm were proposed. However, they failed to work when the additive noise is colored Gaussian noise. FOC method in [5] can inhibit the influence of colored noise, but they could not estimate the DOA of coherent wideband signals when incoherent and coherent wideband signals coexisted because of the rank loss of the FOC matrix .To solve it, a novel algorithm based on FOC was proposed. The proposed algorithm comprises two steps. The first step is to estimate the DOA of incoherent OFDM signals, then a FOC matrix that only contains the information of coherent OFDM signals was constructed by eliminating the contribution of incoherent signals; the second step is to estimate the DOA of the coherent OFDM signals from the estimation of a sparse vector. The simulation results demonstrate the performance of our proposed algorithm.

60.2 Model Formulation

In Fig. 60.1, OFDM transmitter maps the message bits into a sequence of QPSK symbols which will be subsequently converted into N parallel streams. Each of N symbols from S/P conversion is carried out by different subcarrier. Let $X_l[h]$ denote the lth transmit symbol at the hth subcarrier. Then the base band OFDM signals in the continuous-time domain is $s(t) = \sum_{l=0}^{\infty} \sum_{h=0}^{N-1} X_l[h] e^{j2\pi f_h \left(t - lT_{sym}\right)}$, where T_{sym} is the period of an OFDM symbol, f_h is the frequency of hth subcarrier and $f_h = h/T_{sym}$.

Consider K wideband far-field OFDM signals with bandwidth B and center frequency f_0 impinge on a ULA with M identical array elements, where the inter-spacing of the sensors is $d = c/(2f_0)$. For simplicity, assume the first N_i signals $s_i(t)$ coming from the direction $\theta_i, i = 1, 2, \ldots, N_i$ are incoherent. The rests are D groups of coherent signals and the number of coherent signals in the kth group is d_k for $k = N_i + 1, N_i + 2, \ldots, N_i + D$ with $N_i + D = K$. In the kth group, the signal coming from the direction $\theta_{k,p}$ is corresponding to the pth multipath propagation of the source $s_k(t)$ with the complex fading coefficient $\alpha_{k,p}$ for $p = 1, 2, \ldots, d_k$. Assume that the incoherent signals and coherent signals in different groups are independent of each other. Let the first element of the array be the reference one, then the signal received at the mth $(m = 1, 2, \ldots, M)$ sensor can be expressed as

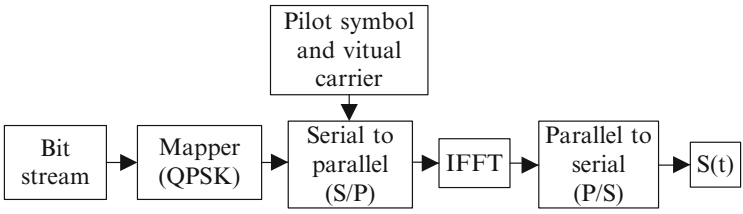

Fig. 60.1 OFDM base band signal model

$$x_m(t) = \sum_{i=1}^{N_i} s_i(t - \tau_m(\theta_i)) + \sum_{k=N_i+1}^{N_i+D} \sum_{p=1}^{d_k} \alpha_{k,p} s_k\left(t - \tau_m\left(\theta_{k,p}\right)\right) + n_m(t) \tag{60.1}$$

where $\tau_m(\theta_i)$ is the propagation delay between the mth sensor and the reference point for the ith incoherent OFDM signal, $\tau_m(\theta_{k,p})$ is the propagation delay between the mth sensor and the reference point for the pth coherent OFDM signal in the k^{th} group and $n_m(t)$ is the additive colored Gaussian noise at the mth sensor.

The observation time T_0 is divided into Z sub-intervals of period T_d each. We assume the narrowband component obtained from the η^{th} snapshot as $\mathbf{X}_\eta\left(f_j\right), j = 1, 2, \ldots, J, \eta = 1, 2, \ldots, Z$, then

$$\begin{aligned}\mathbf{X}_\eta\left(f_j\right) &= \left[X_{1,\eta}\left(f_j\right), \ldots, X_{M,\eta}\left(f_j\right)\right]^T = \sum_{i=1}^{N_i} \mathbf{a}\left(f_j, \theta_i\right) S_{i,\eta}\left(f_j\right) + \sum_{k=N_i+1}^{N_i+D} \sum_{p=1}^{d_k} \mathbf{a}\left(f_j, \theta_{k,p}\right) \alpha_{k,p} S_{k,\eta}\left(f_j\right) \\ &+ \mathbf{N}_\eta\left(f_j\right) = \mathbf{A_i}\left(f_j\right)\mathbf{S}_i\left(f_j\right) + \mathbf{A_c}\left(f_j\right)\mathbf{S}_c\left(f_j\right) + \mathbf{N}_\eta\left(f_j\right) = \mathbf{G}\left(f_j\right)\mathbf{S}_\eta\left(f_j\right) + \mathbf{N}_\eta\left(f_j\right)\end{aligned} \tag{60.2}$$

where $\mathbf{G}\left(f_j\right) = \left[\mathbf{A_i}\left(f_j\right), \mathbf{A_c}\left(f_j\right)\right], \mathbf{S}_\eta \quad \left(f_j\right) = \left[\mathbf{S}_i\left(f_j\right), \mathbf{S}_c\left(f_j\right)\right]^T, \quad \mathbf{S}_i\left(f_j\right) = \left[S_{1,\eta}\left(f_j\right), \ldots, S_{N_i,\eta} \quad \left(f_j\right)\right]^T, \quad \mathbf{S}_c\left(f_j\right) = \left[S_{N_i+1,\eta}\left(f_j\right), \ldots, S_{N_i+D,\eta}\left(f_j\right)\right]^T, \mathbf{A_i}\left(f_j\right) = \left[\mathbf{a}\left(f_j, \theta_1\right), \ldots, \mathbf{a}\left(f_j, \theta_{N_i}\right)\right], \mathbf{A_c}\left(f_j\right) = \left[\mathbf{A}_{N_i+1}\left(f_j\right)\boldsymbol{\beta}_{N_i+} \quad 1, \ldots, \mathbf{A}_{N_i+D}\left(f_j\right)\boldsymbol{\beta}_{N_i+D}\right], \mathbf{a}\left(f_j, \theta_i\right) = \left[1, e^{-j2\pi d \sin(\theta_i) f_j / c}, \ldots, e^{-j2\pi(M-1) d \sin(\theta_i) f_j / c}\right]^T, \boldsymbol{\beta}_k = \left[\alpha_{k,1}, \ldots, \alpha_{k,d_k}\right]^T, \mathbf{A}_k\left(f_j\right)$.

$X_{m,\eta}(f_j)$ denote the DFT of the output data at the mth sensor, $S_{i,\eta}(f_j)$ denote the DFT of the ith incoherent signal, $S_{k,\eta}(f_j)$ denote the DFT of the coherent signal source in the kth group and $N_{m,\eta}(f_j)$ denote the DFT of additive colored Gaussian noise at the ηth snapshot. For convenience in the following sections, we denote $\mathbf{X}_\eta(f_j)$ as $\mathbf{X}(f_j)$ and denote $\mathbf{S}_\eta(f_j)$ as $\mathbf{S}(f_j)$.

60.3 DOA Estimation of Incoherent Signals and Coherent Signals

Assuming the first row of $\mathbf{X}(f_j)$ as $\mathbf{x_1}(f_j)$, we define a $M \times M$ FOC matrix like [6]

$$\begin{aligned}\mathbf{C_4}\left(f_j\right) &= cum\left(\mathbf{x_1}\left(f_j\right), \mathbf{x_1}^*\left(f_j\right), \mathbf{X}\left(f_j\right), \mathbf{X}^H\left(f_j\right)\right) = E\left\{\mathbf{x_1}\left(f_j\right)\mathbf{x_1}^*\left(f_j\right)\mathbf{X}\left(f_j\right)\mathbf{X}^H\left(f_j\right)\right\} \\ &- E\left\{\mathbf{x_1}\left(f_j\right)\mathbf{x_1}^*\left(f_j\right)\right\}E\left\{\mathbf{X}\left(f_j\right)\mathbf{X}^H\left(f_j\right)\right\} - E\left\{\mathbf{x_1}\left(f_j\right)\mathbf{X}\left(f_j\right)\right\}E\left\{\mathbf{x_1}^*\left(f_j\right)\mathbf{X}^H\left(f_j\right)\right\} \\ &- E\left\{\mathbf{x_1}^*\left(f_j\right)\mathbf{X}\left(f_j\right)\right\}E\left\{\mathbf{x_1}\left(f_j\right)\mathbf{X}^H\left(f_j\right)\right\} = \sum_{v=1}^{N_i+D} c_{sv}\left|\mathbf{G}\left(f_j\right)_{1,v}\right|^2 \mathbf{g}_v\mathbf{g}_v{}^H \\ &= \mathbf{G}\left(f_j\right)\mathbf{C_s}\left(f_j\right)\mathbf{G}^H\left(f_j\right)\end{aligned} \tag{60.3}$$

where $c_{sv} = cum\left(S_v\left(f_j\right), S_v{}^*\left(f_j\right), S_v\left(f_j\right), S_v{}^*\left(f_j\right)\right)$ is the FOC of $S_v(f_j)$, which is the vth row of $\mathbf{S}(f_j)$, and $\mathbf{g}_v$ is the vth column of $\mathbf{G}(f_j)$, whose first row and vth column element is $\mathbf{G}(f_j)_{1,v}$, and $\mathbf{C_s}\left(f_j\right) = diag\left\{c_{s1}\left|\mathbf{G}\left(f_j\right)_{1,1}\right|^2, \ldots, c_{sN_i+D}\left|\mathbf{G}\left(f_j\right)_{1,N_i+D}\right|^2\right\}$.

The total array is firstly divided into three sub-arrays. Define $\mathbf{B_i}\left(f_j\right) = diag\{v_1, \ldots, v_{N_i}\}$ where $v_i = e^{-j2\pi d \sin(\theta_i) f_j/c}, i = 1, 2, 3, \ldots, N_i, \mathbf{B_c}\left(f_j\right) = blkdiag\left\{\mathbf{B}_{\mathbf{c},N_i+1}\left(f_j\right), \ldots, \mathbf{B}_{\mathbf{c},N_i+D}\left(f_j\right)\right\}$ with $\mathbf{B}_{\mathbf{c},k}\left(f_j\right) = diag\{v_{k,1}, \ldots, v_{k,d_k}\}$ where $v_{k,p} = e^{-j2\pi d \sin\left(\theta_{k,p}\right) f_j/c}, k = N_i + 1, \ldots, N_i + D, p = 1, 2, \ldots, d_k$.

Then the array output vectors of the three sub-arrays can be expressed as follows

$$\begin{aligned}\mathbf{X}_w\left(f_j\right) &= \left[X_{w,\eta}\left(f_j\right), X_{w+1,\eta}\left(f_j\right), \ldots, X_{M+w-3,\eta}\left(f_j\right)\right]^T \\ &= \left[\mathbf{A_{1i}}\left(f_j\right)\mathbf{B_i}^{w-1}\left(f_j\right)\mathbf{A_{1c}}\left(f_j\right)\mathbf{B_c}^{w-1}\left(f_j\right)\mathbf{\Gamma}\right]\mathbf{S}\left(f_j\right) + \mathbf{N}_w\left(f_j\right),\ \omega = 1, 2, 3\end{aligned} \tag{60.4}$$

where $\mathbf{A_{1i}}\left(f_j\right) = \mathbf{A_i}\left(f_j\right)(1 : M-2, 1 : N_i), \mathbf{A_{1c}}\left(f_j\right) = \mathbf{A_{c2}}\left(f_j\right)(1 : M-2, 1 : D \times d_k)$, $\mathbf{A_{c2}}\left(f_j\right) \in C^{M\times(d_k\times D)} = \left[\mathbf{A}_{N_i+1}\left(f_j\right), \ldots, \mathbf{A}_{N_i+D}\left(f_j\right)\right], \mathbf{A}_k\left(f_j\right) = \left[\mathbf{a}\left(f_j, \theta_{k,1}\right), \ldots, \mathbf{a}\left(f_j, \theta_{k,d_k}\right)\right], k = N_i + 1, \ldots, N_i + D, \mathbf{\Gamma} \in C^{(D\times d_k)\times D} = blkdiag\left\{\boldsymbol{\beta}_{N_i+1}, \ldots, \boldsymbol{\beta}_{N_i+D}\right\}, \boldsymbol{\beta}_k = [\alpha_{k,1}, \ldots, \alpha_{k,d_k}]^T$.

Combine $\mathbf{X}_1(f_j)$ and $\mathbf{X}_2(f_j)$ as a new vector $\mathbf{Z}\left(f_j\right) = \left[\mathbf{X}_1\left(f_j\right) \quad \mathbf{X}_2\left(f_j\right)\right]^T$. Define $\widetilde{\mathbf{C}}_\mathbf{4}\left(f_j\right)$ as the FOC matrix of $\mathbf{Z}(f_j)$ as the way used in Eq. (60.3), then we can prove that $\widetilde{\mathbf{C}}_\mathbf{4}\left(f_j\right) = \begin{bmatrix}\mathbf{C_4}\left(f_j\right)(1 : M-2, 1 : M-2) & \mathbf{C_4}\left(f_j\right)(1 : M-2, 2 : M-1) \\ \mathbf{C_4}\left(f_j\right)(2 : M-1, 1 : M-2) & \mathbf{C_4}\left(f_j\right)(2 : M-1, 1 : M-1)\end{bmatrix}$, and then perform Eigen-decomposition of $\widetilde{\mathbf{C}}_\mathbf{4}\left(f_j\right)$, we can obtain the signal subspace $\widetilde{\mathbf{U}}_\mathbf{4}\left(f_j\right) \in C^{2(M-2)\times(N_i+D)}$ whose columns are eigenvectors corresponding to the $N_i + D$ largest eigenvalues. Partition $\widetilde{\mathbf{U}}_\mathbf{4}(f_j)$ into two $(M-2) \times (N_i + D)$ matrices $\widetilde{\mathbf{U}}_\mathbf{41}(f_j)$ and $\widetilde{\mathbf{U}}_\mathbf{42}(f_j)$ as $\widetilde{\mathbf{U}}_\mathbf{4}\left(f_j\right) = \left[\widetilde{\mathbf{U}}_\mathbf{41}\left(f_j\right) \quad \widetilde{\mathbf{U}}_\mathbf{42}\left(f_j\right)\right]^T$. Then we can construct a new matrix $\widetilde{\mathbf{V}}_\mathbf{4}\left(f_j\right) = \left(\widetilde{\mathbf{U}}_\mathbf{41}\left(f_j\right)\right)^+ \widetilde{\mathbf{U}}_\mathbf{42}\left(f_j\right)$, where $(\cdot)^+$ denotes the operation of pseudo-inverse. Perform eigen-decomposition of $\widetilde{\mathbf{C}}_\mathbf{4}\left(f_j\right)$, we can obtain $N_i + D$

eigenvalues $\gamma_1\left(f_j\right), \gamma_2\left(f_j\right), \ldots, \gamma_{N_i+D}\left(f_j\right)$, thus the estimation of $\widetilde{\theta}_v\left(f_j\right)$ can be obtained as

$$\widetilde{\theta}_v\left(f_j\right) = -\arcsin\left\{\mathrm{Arg}\left(\gamma_v\left(f_j\right)\right)/\pi\right\}, v = 1, 2, \ldots, N_i + D \tag{60.5}$$

where $\mathrm{Arg}(\cdot)$ denotes the operation of phase angle. Add up all the $\widetilde{\theta}_v\left(f_j\right)$ at frequency bin f_j and calculate its average, we can obtain $\widetilde{\theta}_v = \frac{1}{J}\sum_{j=1}^{J}\widetilde{\theta}_v\left(f_j\right)$, then we can not only obtain N_i true DOA estimates of incoherent OFDM signals, but also obtain D DOA estimates of D virtual signals which correspond to the D groups of coherent OFDM signals.

To obtain the N_i true DOA estimates of incoherent OFDM signals, we define another matrix $\hat{\mathbf{C}}_4(f_j)$ as the FOC matrix of $\mathbf{H}\left(f_j\right) = \left[\mathbf{X}_2\left(f_j\right) \quad \mathbf{X}_3\left(f_j\right)\right]^T$ and we can prove that $\hat{\mathbf{C}}_4\left(f_j\right) = \begin{bmatrix} \mathbf{C_4}\left(f_j\right)(2:M-1, 2:M-1) & \mathbf{C_4}\left(f_j\right)(2:M-1, 3:M) \\ \mathbf{C_4}\left(f_j\right)(3:M, 2:M-1) & \mathbf{C_4}\left(f_j\right)(3:M, 3:M) \end{bmatrix}$, then repeat the same steps as $\widetilde{\mathbf{C}}_4\left(f_j\right)$,we can obtain another $N_i + D$ DOA estimated directions $\hat{\theta}_v, v = 1, 2, \ldots, N_i + D$, which also contain N_i true DOA direction of incoherent OFDM signals and direction of D virtual signals corresponding to the D groups of coherent OFDM signals.

For the DOA estimation of virtual signals obtained from the processing of $\hat{\mathbf{C}}_4(f_j)$ are different from those obtained from the processing of $\widetilde{\mathbf{C}}_4\left(f_j\right)$, while the difference between the DOA estimation of incoherent OFDM signals obtained from the two processing are very small, so we can select the true DOA estimation of incoherent OFDM signals $\widetilde{\theta}_i, i = 1, 2, \ldots, N_i$ from $\widetilde{\theta}_v, v = 1, 2, \ldots, N_i + D$ and select $\hat{\theta}_i, i = 1, 2, \ldots, N_i$ from $\hat{\theta}_v, v = 1, 2, \ldots, N_i + D$ respectively. Arrange $\widetilde{\theta}_1$, $\widetilde{\theta}_2, \ldots, \widetilde{\theta}_{N_i}$ and $\hat{\theta}_1, \hat{\theta}_2, \ldots, \hat{\theta}_{N_i}$ in the increasing order respectively to result in $\widetilde{\theta}'_1$, $\widetilde{\theta}'_2, \ldots, \widetilde{\theta}'_{N_i}$ and $\hat{\theta}'_1, \hat{\theta}'_2, \ldots, \hat{\theta}'_{N_i}$, then we can define $\widetilde{\widetilde{\theta}}_1 = \frac{\widetilde{\theta}'_i + \hat{\theta}'_i}{2}, i = 1, 2, \ldots, N_i$, thus $\widetilde{\widetilde{\theta}}_1, \widetilde{\widetilde{\theta}}_2, \ldots, \widetilde{\widetilde{\theta}}_{N_i}$ are the true DOA estimation of incoherent OFDM signal.

We can express Eq. (60.3) in another form as

$$\begin{aligned} \mathbf{C_4}\left(f_j\right) &= \mathbf{C_i}\left(f_j\right) + \mathbf{C_c}\left(f_j\right) \\ &= \mathbf{A_i}\left(f_j\right)\mathbf{C_{si}}\left(f_j\right)\mathbf{A_i}^H\left(f_j\right) + \mathbf{A_c}\left(f_j\right)\mathbf{C_{sc}}\left(f_j\right)\mathbf{A_c}^H\left(f_j\right) \end{aligned} \tag{60.6}$$

where $\mathbf{C_i}(f_j)$ is the FOC matrix of incoherent signals at f_j with $\mathbf{C_{si}}\left(f_j\right) = \mathbf{C_s}\left(f_j\right)(1:N_i, 1:N_i)$ and $\mathbf{C_c}(f_j)$ is the FOC matrix of coherent OFDM signals with $\mathbf{C_{sc}}\left(f_j\right) = \mathbf{C_s}\left(f_j\right)(N_i+1:N_i+D, N_i+1:N_i+D)$. From Eq. (60.6) we can see that the FOC matrix $\mathbf{C_i}(f_j)$ is a Toeplitz matrix and $\mathbf{C_i}\left(f_j\right) = \mathbf{TC_i}\left(f_j\right)^T\mathbf{T}$, where $\mathbf{T}$ is an exchange matrix with ones on its anti-diagonal and zeros elsewhere. Then we can define a new matrix $\mathbf{C_d}(f_j)$ as $\mathbf{C_d}\left(f_j\right) = \mathbf{C_4}\left(f_j\right) - \mathbf{TC_4}\left(f_j\right)^T\mathbf{T} = \mathbf{C_c}\left(f_j\right) - \mathbf{TC_c}\left(f_j\right)^T\mathbf{T}$, where $\mathbf{C_d}(f_j)$ only contains the information of coherent signals. Add up all the $\mathbf{C_d}(f_j)$ of each frequency bin and calculate its average, we can obtain $\mathbf{C_d} = \frac{1}{J}\sum_{j=1}^{J}\mathbf{C_d}\left(f_j\right)$. By performing the eigen-decomposition of $\mathbf{C_d}$, we can see that the eigenvalues of $\mathbf{C_d}$ appear in pairs with a positive and negative eigenvalue, and the two values of each pair have the same absolute value. Then we can obtain the subspace $\mathbf{U_{cn}} \in C^{M\times D}$, whose columns are eigenvectors corresponding to the D largest absolute values of eigenvalues. We can consider this problem as a spare recovery problem. Define $\widetilde{\theta}_1, \widetilde{\theta}_2, \ldots \widetilde{\theta}_{N_c}$ as all the possible coherent signal directions, then the DOA of coherent wideband OFDM signals can be described as [7]

$$\min_{\mathbf{q_{cn}}} \sum_{\wp=1}^{N_c} \left\|\mathbf{q_{cn}}^{\wp}\right\|_2 st. \left\|\mathbf{U_{cn}} - \widetilde{\mathbf{A}}\mathbf{q_{cn}}\right\|_2 \leq \varepsilon \tag{60.7}$$

where $\widetilde{\mathbf{A}} \in C^{M\times N_c} = \left[\mathbf{a}\left(\widetilde{\theta}_1\right), \mathbf{a}\left(\widetilde{\theta}_2\right), \ldots, \mathbf{a}\left(\widetilde{\theta}_{N_c}\right)\right]$ is an over-complete dictionary, $\mathbf{q_{cn}}^{\wp}(\wp = 1, 2, \ldots, N_c)$ is the $\wp$th row of matrix $\mathbf{q_{cn}} \in C^{N_c\times D}$ and ε is a parameter specifying how much estimation error we wish to allow. After solving the problem of Eq. (60.7) by the CVX software [8], we can obtain a spatial spectrum by plotting the l_2 norm of the $\mathbf{q_{cn}}^{\wp}(\wp = 1, 2, \ldots N_c)$, and then estimate the DOA of coherent signals by mapping indexes of sharp estimated peaks of the spatial spectrum.

60.4 Simulation Results

A linear array of ten sensors with equal element spacing of 0.5 wavelength at $f_0 = 240$ MHz is used. The bandwidth of all the OFDM signals with 64 subcarrier is 20 MHz and the additive colored Gaussian noise has the same bandwidth as OFDM signals. The sample frequency is 60 MHz and 64 snapshots are used, so the total observation time is $T_0 = 64/60 = 1.066\,\mu s$ and T_0 is sectioned into $Z = 20$ sub-intervals of duration $T_d = T_0/20 = 0.0533\,\mu s$, the DFT point is $J = 40$ at each

sub-interval. For each experiment we performed 500 Monte-Carlo trials, and the root mean square error (RMSE) of DOA estimation is as follows

$$RMSE = \sqrt{\sum_{n=1}^{200}\sum_{v=1}^{Ns}(\theta_v(n) - \theta_v)^2/(200N_s)} \tag{60.8}$$

where N_s is the number of all the incoherent signals or all the coherent signals and $\theta_v(n)$ is the estimation of θ_v for nth trial.

Consider three incoherent wideband OFDM signals from $\left[-9^0, 0^0, 27^0\right]$ and two groups of six coherent signals from $\left[-23^0, 40^0, 59^0\right]$ and $\left[-43^0, -4^0, 19^0\right]$, and the relative fading coefficients of coherent signals are $[1, -0.6332 - 0.2434j, 0.7421 - 0.1325j], [1, 0.5970 - 0.4317j, -0.6410 - 0.2812j]$ respectively. The DOA estimation of our algorithm is shown in Fig. 60.2 for $SNR = 10$ dB. Figure 60.3 shows the RMSE of the DOA estimation tested versus input SNR from 0 to 20 dB. Obviously our proposed algorithm can estimate wideband coherent OFDM signals. Besides, our proposed algorithm outperforms the reference method in [5] for the incoherent wideband OFDM signals.

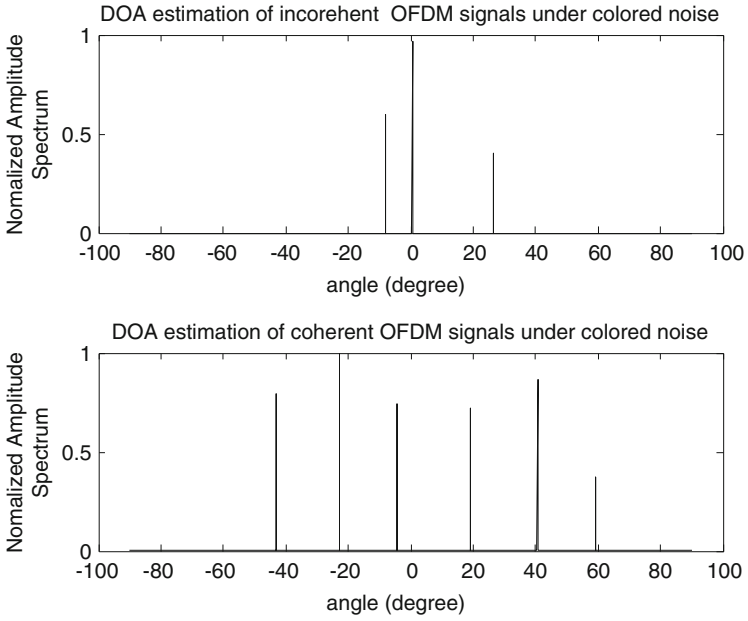

Fig. 60.2 DOA estimation of OFDM signals

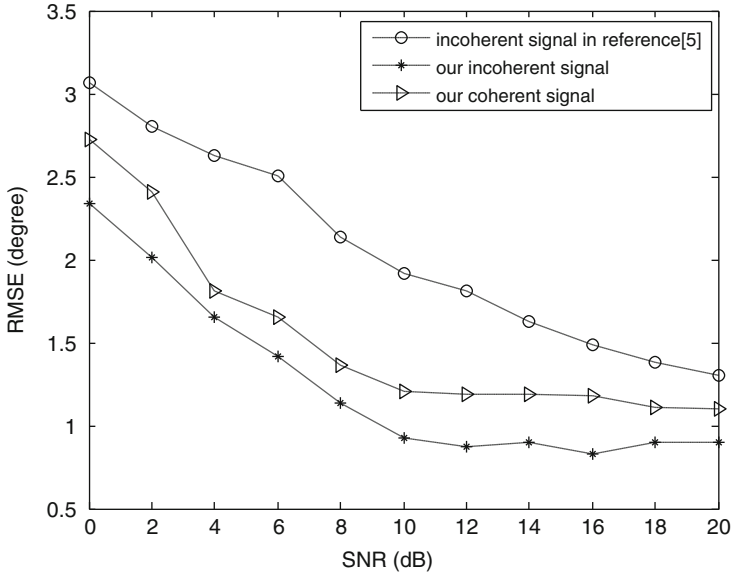

Fig. 60.3 RMSE of DOA estimation versus SNR

Conclusion

In this letter, we proposed an efficient algorithm for DOA estimation when incoherent and coherent wideband OFDM signals coexist. Our proposed algorithm can not only estimate the DOA of coherent OFDM signals without reducing array aperture or array geometry constraint, but also suppress colored Gaussian noise. The simulation results demonstrate the performance of our proposed algorithm.

Acknowledgments This work was supported in part by the National Natural Science Foundation of China under grant 61172140 and joint laboratory project of UESTC-713 short-wave &ultra-short-wave array signal processing.

References

1. Wax M, Shan TJ, Kailath T (1984) Spatio-temporal spectral analysis by eigenstructure methods. IEEE Trans SP 32:817–827
2. Wang H, Kaveh M (1985) Coherent signal-subspace processing for the direction and estimation of angles of arrival of multiple wide-band sources. IEEE Trans ASSP 33:823–831
3. Valaee S, Kabalp P (1995) Wideband array processing using a two-sided correlation transformation. IEEE Trans SP 43:160–172
4. Chun Jing Liu, Feng Liu, Shu Zhang (2010) Wideband DOA estimation based on focusing data matrix. Missiles Guidance 30:190–192

5. Zhi Chao Wang, Tian Qi Zhang (2013) DOA estimation for wideband OFDM signals based on focusing and cumulants. Comput Appl 33:1828–1832
6. Ye Z, Zhang Y (2009) DOA estimation for non-Gaussian signals using fourth-order cumulants. LET Microwaves Antennas Propag 3:1069–1078
7. Hui Chen, Qun Wan (2011) Robust DOA estimation for uncorrelated and coherent signals. IEICE Trans Fundam Electron Commun Comput Sci 94-A:2035–2038
8. Boyd S, Vandenberghe L (2003) Convex optimization. Cambridge University Press, Cambridge

Part VI
Ethernet, Fiber Communication

Chapter 61
QoS Multi-path Routing Scheme Based on ACR Algorithm in Industrial Ethernet

Jing Zhao and Xin Ge

Abstract Network congestion is the determinant of network transmission delay. The QoS differentiated multi-path routing mechanism is proposed in this paper to balance the network load of industrial Ethernet, under the limited network resource condition. ACR algorithm is used to obtain the path sets for data transmission with different QoS requirements. The mathematical model of differentiated multi-path routing algorithm in industrial Ethernet is established and described in detail. Furthermore, key metrics involved in design is analyzed deeply. Difficulties in implementation based on ACR algorithm is pointed out, and the solution is given in specific description.

61.1 Instruction

The requirements of data delivered decide the tasks of network undertaking. In industrial Ethernet, there is periodic, short control information coming from industrial fields, which is called hard real-time data due to its strict delay constrain. There also exists audio and video traffic for-warding around periodically or aperiodically. This kind of data usually has a wide changing range of frame size, and request the performance indexes of both delay and delay jitter. Meanwhile there are management data streams using large frame size with the need of bandwidth [1–4]. Therefore industrial Ethernet must ensure the hard real-time data is delivered at the designated time, and to meet the transmission requests of other types of data in the meantime.

J. Zhao (✉)
College of Computer and Information Engineering,
Tianjin Normal University, Tianjin 300387, P. R. China
e-mail: zhaojing8006@163.com

X. Ge
Tianjin Design and Research Institute of Civil Defence and Building,
Tianjin 300040, P. R. China

J. Mu et al. (eds.), *The Proceedings of the Third International Conference on Communications, Signal Processing, and Systems*, Lecture Notes in Electrical Engineering 322, DOI 10.1007/978-3-319-08991-1_61

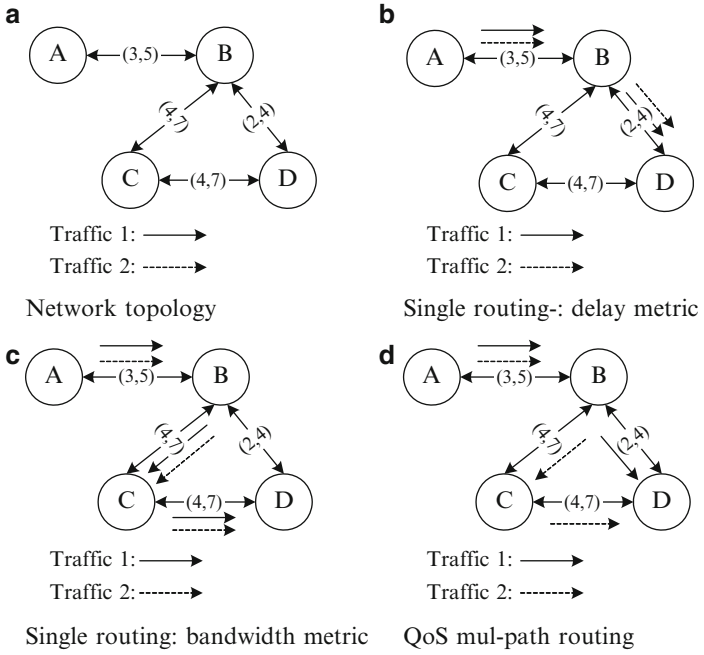

Fig. 61.1 Transmission mechanism of single routing and multi-path routing

QoS routing is presented to provide paths satisfying certain conditions for some kinds of data transmission [5, 6]. And routers in network differentiate them to forward according to their sources or destinations [7, 8]. Once the path in accordance with some QoS measure is established between two nodes, all traffics to the same destination converge, as shown in Fig. 61.1. It is a network topology with four nodes, and every link is labeled transmission delay and bandwidth. At node A, there are two types of data both going to node D, to be transmitted. Traffic 1 is 1 M production control information, while traffic 2 is 4 M FTP download. Subgraph b) and c) describe routing process following QoS metric delay and bandwidth respectively. In subgraph b), the path $A \rightarrow B \rightarrow D$ is a good choice to achieve low transmission delay, but the link BD must be blocked because of its insufficient bandwidth. Then congestion causes more delay. In order to meet the requirement of bandwidth, in subgraph c) path $A \rightarrow B \rightarrow C \rightarrow D$ is selected, but it brings the longest delay for traffic 1. Multi-path routing mechanism is applied in subgraph d). Routers build separate ways to node D, not only satisfy delay limits of traffic 1, but also bandwidth demand of traffic 2.

In this paper, a QoS differentiated multi-path routing scheme is presented based on ACR algorithm in industrial Ethernet. Choices of QoS measures, acquiring path sets, service assignment strategy, mathematical model and difficulties in the scheme design are analyzed in detail.

61.2 QoS Measures and Acquiring Path Sets

61.2.1 Choice of QoS Measures in Industrial Ethernet

QoS metrics usually include end-to-end delay, delay jitter, bandwidth, cost, the packet drop rate, and so on. In industrial Ethernet, control information with strict delay requirement is the main traffic, using short frames and to guarantee its punctual delivery is the primary task of industrial Ethernet. So end-to-end delay is its only QoS metric.

Real-time voice and video is sensitive to end-to-end delay and delay-jitter, besides it needs to be supported by a certain amount of bandwidth. The delay jitter metric may be mapped as the function of end-to-end delay. Management information can tolerate a relatively long transmission delay, but larger bandwidth is demanded.

So our requirements for QoS features consideration are end-to-end delay and bandwidth in industrial Ethernet. Because delay is additively metric but bandwidth is concavity, it is difficult to establish compound function following to the two different operation rules. In such circumstances the combination of main and auxiliary metric is adopted, and end-to-end delay is used as the main and bandwidth is the auxiliary.

61.2.2 Aquiring Path Sets by Using ACR Algorithm

In QoS multi-path routing mechanism, there are three methods of achieving path sets. One way is crankback, searching one path at a time. If the path found can't provide QoS satisfactions, the source restarts to seek the new route. Obviously, it can adapt the dynamical characteristics of network, but takes longer time to build up connection. The other way is multi-path parallel searching, by which routing information is set out along multiple links simultaneously, and resource is reserved on the route. The best path is selected to transmit data from full routine obtained and the resource on other paths is released. It reduces the time of path construction, but resource reserved forbid to be used before the final path is determined. A third method is that multiple paths work together to accomplish a transmission task. Its drawback is that information can't be synchronized and frames arrive with disorder.

Searching a way satisfying two or more QoS metrics at the same time on networks is a typical NP-complete problem. Due to the uncertainty and nonlinear, it is difficult to be solved by traditional analytic method and optimization technique. Heuristic algorithm is usually used to settle Multi-parameter QoS routing problem.

Parallel calculation, route-updated dynamically and inner information processing, all these intrinsic characteristics of ACR algorithm are well matched the network communication mode. It searches multiple paths in parallel, can feel the data processing ability of every node, link and resource usage dynamically, but

doesn't reserve resource along the path. The most important of all, path sets obtained by three ways mentioned above only service one type of data once, but ACR can provide after running each time not only the best way, but also large sub-optimal and local optima paths which other types of data can fully utilize to be transmitted. That means different kinds of data can choose paths from the same path sets.

61.3 Model of QoS Differentiated Multi-path Routing Scheme in Industrial Ethernet

In researching on routing algorithms, network usually is mapped as a directional weight graph $G = (V, E)$. V is the set of nodes in G, and E is the set of links between nodes. Link (i,j) connects node i and j $(i,j \in V)$, and end-to-end delay metric indicates $delay(i,j)$, bandwidth metric $band(i,j)$. Illustration of symbols is as follows.

C_{ij}: the channel capacity of link (i,j), $(i,j) \in E$
K: set of sending requests between source and destination
s_k: the source node of sending request k, $k \in K$
d_k: the destination of sending request k, $k \in K$
q^k: data quantity of sending request k, $k \in K$
P_k: set of sending request k available paths between source-destination, $k \in K$
x_p^k: quantity allocated to path p which belongs to sending request k, $k \in K$, $p \in P_k$
δ_{ij}^{pk}: if path p selected by sending request k includes link (i,j). True is 1, otherwise is 0. $k \in K$, $p \in P_k$
x_{ij}: total quantity on link (i,j), $(i,j) \in E$
$u_{\max}$: the maximum value of link utilization in E

Then the maximum utilization of network resource is obtained

$$x_{ij} = \sum_{k \in K} \sum_{p \in P_k} x_p^k \cdot \delta_{ij}^{pk} \tag{61.1}$$

The mathematical model of differentiated multi-path routing algorithm in industrial Ethernet is

$$\min\{u_{\max}\} = \min\left\{\max\left\{\frac{x_{ij}}{C_{ij}}\right\}\right\} \tag{61.2}$$

Three types of data in industrial Ethernet commonly abide constraint equations are

$$\sum_{p\in P_k}\sum_{j\in V,(i,j)\in E} x_p^k\cdot\delta_{ij}^{pk}-\sum_{p\in P_k}\sum_{j\in V,(i,j)\in E} x_p^k\cdot\delta_{ji}^{pk}=q^k,\quad i=s_k,\ \forall k\in K \tag{61.3}$$

$$\sum_{p\in P_k}\sum_{j\in V,(i,j)\in E} x_p^k\cdot\delta_{ij}^{pk}-\sum_{p\in P_k}\sum_{j\in V,(i,j)\in E} x_p^k\cdot\delta_{ji}^{pk}=-q^k,\quad i=d_k,\ \forall k\in K \tag{61.4}$$

$$\sum_{p\in P_k}\sum_{j\in V,(i,j)\in E} x_p^k\cdot\delta_{ij}^{pk}-\sum_{p\in P_k}\sum_{j\in V,(i,j)\in E} x_p^k\cdot\delta_{ji}^{pk}=0,\quad i\neq s_k,d_k,\ \forall k\in K \tag{61.5}$$

They need to abide constraint conditions respectively is as follows

$$delay(p)=\min\left\{\sum_{(i,j)\in p} delay(i,j),\ p\in P_k\right\} \tag{61.6}$$

$$\begin{cases}\min\left\{\sum_{(i,j)\in p} delay(i,j),\ p\in P_k\right\}\le delay(p)\le\max\left\{\sum_{(i,j)\in p} delay(i,j),\ p\in P_k\right\}\\ band(p)=\min\{band(i,j),(i,j)\in p\}\\ C\le band(p)\le C+\varepsilon,\ p\in P_k\end{cases} \tag{61.7}$$

and

$$\begin{cases} band(p)=\min\{band(i,j),(i,j)\in p\}\\ band(p)=\max\{band(p),p\in P_k\}\end{cases} \tag{61.8}$$

Equations (61.6), (61.7) and (61.8) direct separately hard real-time, soft real-time and non real-time data how to select their own from multiple paths. In (61.7) equal signs on both of $delay(i,j)$ represents that the equation holds when only the optimal path or the worst one satisfies bandwidth requirement of soft real-time information. C is the least bandwidth of soft real-time data and $C\le band(p)\le C+\varepsilon, p\in P_k$ refers to the nearest bandwidth path.

61.4 Description of QoS Differentiated Multi-path Routing Scheme

In this section, specific implementation of differentiated multi-path routing scheme is introduced based on ACR algorithm. Due to some disadvantages of the original ACR algorithm, improved ACR searching rule as in [8] is adopted here. The new searching mechanism presented in [8] solves the problem of ant stuck when routing,

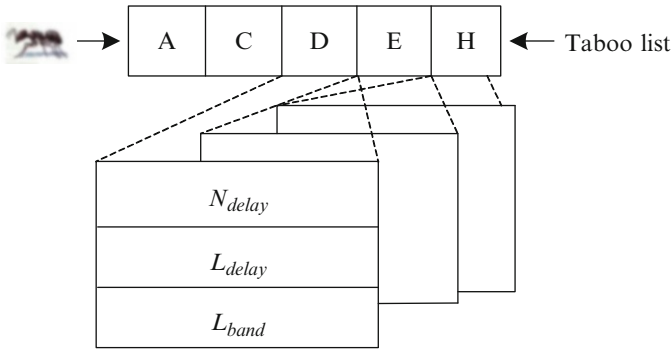

Fig. 61.2 Ant's taboo list

not only has a fast convergence speed, but achieve large effective sub-optimal and local optima paths comparable with the performance of the best way. So, all denotations used in the followings are synonyms with the meanings define in [8].

In our scheme, every ant dispatched to find path carries a taboo list to record each node it has visited. In the taboo list, each node has a data structure containing three parameters. One is Ldelay, indicating the delay caused by the link between two adjacent nodes, and another is Lband, pointing out available bandwidth of forward link. The third is Ndelay, the processing time in current node. The data structure is shown in Fig. 61.2.

Here are the definitions of new symbols.

Num: the number of ants released every iteration, remaining unchanged during the whole operation

Rset: update frequency of path set, referring to ACR running frequency in process of data sending continuously

Mhop: the maximum number of hops when finding the path with the biggest bandwidth

The steps of differentiated multi-path routing scheme are giving as follows.

Step 1: to initialize. According to the network topology, the distribution of nodes and links to initialize the parameters such as α, β, ρ, *Num*, *Rset*, *Mhop*.

Step 2: arrival of sending request. In accordance with the type of data to be transmitted, ACR algorithm works by the following equations:

$$\tau_{ij}(t+1) = \rho \cdot \tau_{ij}(t) + \sum_{k=1}^{m} \Delta\tau_{ij}^{k}(t,\ t+1) + \Delta\tau_{ij}^{*}(t,\ t+1) \tag{61.9}$$

$$\Delta\tau_{ij}^{k}(t,\ t+1) = \begin{cases} \dfrac{Q}{L_k(t)} & \text{if ant } k \text{ passed link } (i,\ j) \text{ in this iteration} \\ 0 & \text{otherwise} \end{cases} \tag{61.10}$$

$$P_{ij}^{k}(t) = \begin{cases} \dfrac{\tau_{ij}^{\alpha}(t)\eta_{ij}^{\beta}(t)}{\sum\limits_{s \in N_{\text{allowed}(k)}} \tau_{is}^{\alpha}(t)\eta_{is}^{\beta}(t)} & j \in N_{\text{allowed}(k)} \\ 0 & otherwise \end{cases} \tag{61.11}$$

and

$$\Delta\tau_{ij}^{*}(t,\ t+1) = \begin{cases} \mu \dfrac{Q}{L^{*}} & if\ link\ (i,\ j)\ is\ the\ part\ \ of\ optimization\ path \\ 0 & otherwise \end{cases} \tag{61.12}$$

1. If sending request is triggered by hard real-time or soft real-time data, $L_k(t)$ is the end-to-end delay obtained by ant k in (61.10).

$$L_k(t) = \sum_{\substack{i,\ j \in Tabu_k \\ (i,\ j) \in Tabu_k}} N_{delay}(i) + delay(i,\ j) \tag{61.13}$$

   In (61.11), η_{ij} is the delay resulting from link (i,j), the priori available heuristic value

$$\eta_{ij} = 1/delay(i,\ j) + N_{delay}(i) \tag{61.14}$$

   AND in (61.12), L^{*} is the shortest one of all optimal paths after all iterations

$$L^{*} = \min\{L_k(t),\ \ k = 1, 2, \ldots Num\} \tag{61.15}$$

2. If sending request is triggered by non real-time data, $L_k(t)$ is the bandwidth obtained by ant k in (61.10).

$$L_k(t) = \min\{band(i,\ j), (i,\ j) \in p\} \tag{61.16}$$

   and

$$\eta_{ij} = 1/band(i,\ j) \tag{61.17}$$

   If the number of nodes in the final taboo list is more than *Mhop*, ants backtrack along the final taboo list don't update the intensity of pheromone and the probability and restart to search routes from the source node.

   We take Fig. 61.3 as the reference for the above illustration.

Step 3: selecting paths. When the scheme converges, every type of data chooses their path as listed below.

1. At the same time, to the same destination, there is a single type of data waiting. Hard real-time data selects the lowest delay one of all optimal paths

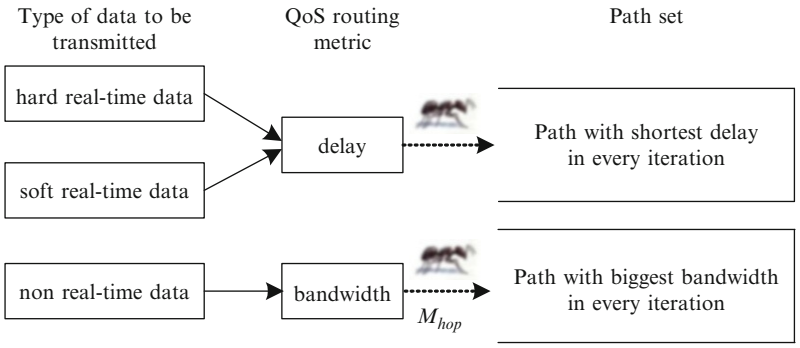

Fig. 61.3 Sketch map of ACR searching scheme

achieved from every iteration, and soft real-time data picks out the near-optimum delay path which satisfies the bandwidth request. Non real-time data makes a choice of the maximum bandwidth path and restriction on *Mhop* is must be kept.

2. At the same time, to the same destination, there are mixed types of data to be transmitted. The *Rset* timer is start and in the limited period, if the sending request is triggered by hard real-time or soft real-time data, the selection rule of paths is same as the first situation. If non real-time information triggers the request of data transmission, it chooses maximum bandwidth path with constraint on *Mhop*, and other data keeps waiting, until the step 2 restarts to establish new path set. If the *Rset* timer is over but non real-time data doesn't complete, step 2 repeats when the current transmitting ends.

Step 4: bandwidth requirement of path unsatisfied. When all paths receiving cannot meet bandwidth request of soft real-time data, it doesn't use this chance. If forwarding request is triggered by itself and there is no hard real-time data waiting for transmission, these searching results are discarded. Then ACR routing restarts. But if three types of data are mixed at current time, hard real-time data makes use of the path with the shortest delay, and non real-time data selects the one which is the most irrelevant with the lowest delay path.

Finally, two parameters are pointed out. One is *Rset*, set to avoid one path set keeping used when there is mass data waiting. The path sets is becoming obsolete and causes dynamic changes of network resource cannot be felt in time. So *Rset* provides a time limit, restarts ACR algorithm periodically and update path sets. *Rset* initialized not only can update path information, but also be proper for the running frequency of ACR.

The other is *Mhop* which is set separately for non real-time data transmission. When there is only non real-time data waiting, paths are searched by bandwidth indicator. Though this type is insensitive to delay, it is demanded to complete data delivery. So *Mhop* is used to prevent from a infinite searching trip.

Conclusion

Balancing network load to make the maximization of network resource is the basic solution to avoid congestion and control the transmission delay. In this paper, we present a QoS differentiated multi-path routing scheme based on improved ACR algorithm in industrial Ethernet. First, the mathematical model of the scheme is established. Then the choice of QoS measures, path sets establishing and path selections of every type data with different QoS requirements are discussed thoroughly. The implementation of the scheme proposed is given in detail. Furthermore, the difficulties in design are pointed out and given a rational parameter settings analysis.

Acknowledgments This work was jointly supported by the National Natural Science Foundation of China (51077015) and (60970060), and Scientific and Technology Support Key Project of Tianjin City (09ZCKFGX00500).

References

1. Piqqin RSH (2007) Developments in real-time control with Ethernet/IP. Assembly Autom 27 (2):109–117
2. Katzel J, Mark T, Hoske (2006) Industrial Ethernet protocols. Control Eng 53(12):58–63
3. Jasperneite J, Schumacher M, Welber K (2007) Limits of increasing the performance of industrial ethernet protocols. In: IEEE symposium on emerging technologies and factory automation, Greece, pp 17–24
4. Guo Y, Kuipers FA, Van Mieghem P (2003) A link-disjoint paths algorithm for reliable QoS routing. Int J Commun Syst 16(9):779–798
5. Van Mieghem P, Kuipers FA (2003) On the complexity of qos routing. Comput Commun 26 (4):376–387
6. Orda A, Sprintson A (2003) Precomputation schemes for QoS routing. IEEE/ACM Trans Network 11(4):578–591
7. Xiao W, Soony BH, Law CL (2004) Evaluation of heuristic path selection algorithm for multi-constrained QoS routing. In: Proceedings of the 2004 I.E. international conference on networking, sensing and control, Taipei, Taiwan, pp 112–116
8. Zhao J, Tong W (2009) Solution to the problem of ant being stuck by ant colony routing algorithm. J China Univ Posts Telecommun 16(1):100–105

Chapter 62
Link Prediction via a Neighborhood-Based Nonnegative Matrix Factorization Model

Yuxin Zhao, Shenghong Li, Chenglin Zhao, and Wen Jiang

Abstract Link prediction is an important issue to understand the dynamics and evolution mechanisms of complex networks. Traditional link prediction algorithms are based on the topological properties of the underlying network in terms of graph theory. In order to improve the accuracy of link prediction, recent researches increasingly focus on modeling the link behaviors from the latent structure information of the networks. In this paper, we propose a neighborhood-based nonnegative matrix factorization model to solve the problem of link prediction. Our model learns latent feature factors from the overall topological structure combing with local neighborhood structures of the underlying network. Extensive experiments on real-world networks demonstrate the effectiveness and efficiency of our proposed model.

Keywords Complex network • Link prediction • Nonnegative matrix factorization • Latent feature

62.1 Introduction

Many real-world systems can be represented by complex networks, where the nodes denote individuals and links indicate the interactions and relations between the nodes [1]. During recent years, extensive research efforts have been focused on the topology, organization and dynamics of complex networks. A fundamental problem in the field of complex network is link prediction, which aims at estimating the likelihood of the existence of a link between two nodes, based on the observed

Y. Zhao (✉) • S. Li
Department of Electronic Engineering, Shanghai Jiao Tong University, Shanghai, China
e-mail: zhaoyuxin1@sjtu.edu.cn; shli@sjtu.edu.cn

C. Zhao
School of Information and Communication Engineering, Beijing University of Posts and Telecommunications, Shanghai, China
e-mail: clzhao@bupt.edu.cn

W. Jiang
Department of Electronic Engineering, Shanghai Jiao Tong University, Shanghai, China
e-mail: wenjiang@sjtu.edu.cn

J. Mu et al. (eds.), *The Proceedings of the Third International Conference on Communications, Signal Processing, and Systems*, Lecture Notes in Electrical Engineering 322, DOI 10.1007/978-3-319-08991-1_62

links and the attributes of nodes [2]. Link prediction is an important issue to understand the dynamics and evolution mechanisms of complex networks and has great significance in many practical applications, such as social network analysis, recommendation system and so on [3].

However, the complexity of network structure makes link prediction a challenging task. Firstly, the correlations between nodes depend on the properties and characteristics of the underlying systems, which cannot be directly obtained from the network. Secondly, in most situations, network data is quit sparse that the observed links are only a small proportion of all possible links. Thirdly, real-world networks are often scalable and constituted by large numbers of nodes, which requires the link prediction algorithms to have low time complexity.

Motivated by the great practical significance, many algorithms for link prediction have been proposed recently. These algorithms can be categorized into two strategies: unsupervised models and supervised models. Unsupervised models use some specific measurements to evaluate the similarity between two nodes according to the topological properties of the network. On the other hand, supervised models propose some patterns of the link behaviors and learn a series of parameters according to the observed links in the networks.

In this paper, we proposed a nonnegative matrix factorization model for solving the problem of link prediction in complex networks. In our model, we associate the probability of a link with a nonnegative strength variable, which is related with the latent features of the nodes. We also consider the influence of the neighborhood structure and make the latent features of each node learnt from the overall topological structure combing with local neighborhood structures of the underlying network.

The rest of the paper is organized as follows. In Sect. 62.2, we introduce the related background of link prediction in complex networks. Our proposed neighborhood-based nonnegative matrix factorization model for link prediction is described in detail in Sect. 62.3. The experimental results and discussions are reported in Sect. 62.4. Finally, section "Conclusion" gives the conclusion of this paper.

62.2 Related Work

62.2.1 Problem Definition

Formally, a complex network can be represented by an undirected and unweighted graph $G = (V, E)$, where V is the set of nodes and $E = \{ (i, j) \mid i, j \in V \}$ is the set of links connecting the nodes. The states of the links in the network are indicated by the adjacency matrix $A = A_{ij} | i, j \in V$, where $A_{ij} = 1$ denotes an observed present link between node i and node j, and $A_{ij} = 0$ indicates nonexistent link between node i and node j. Assuming that some links are unobserved in the network, the task of link prediction is to find out these missing links.

62.2.2 Existing Link Prediction Models

Link prediction algorithms can be roughly classified into two classes: unsupervised models and supervised models. In unsupervised models, the probability of the existence of a link is measured by some specific similarity indices between the two nodes. Local similarity indices [4–8] only depend on the information of the neighborhoods, such as the common neighbors. Global similarity indices [9–11] require entire topological information of the network from the perspectives of paths, random walks and other properties. The similarity in unsupervised models is predefined and invariant to the specific structure of the input networks.

Supervised models, on the other hand, usually propose some patterns of the link behaviors and learn a series of parameters according to the observed links. We list some popular approaches as follows:

- Hierarchical Structure Model (HSM). This model proposed by Clauset et al. [12] infers the existence of a link between two nodes depending on the hierarchical structures of the network.
- Stochastic Block Model (SBM). In this model, nodes are partitioned into groups and the probability that two nodes are connected solely depends on the groups which they belong to [13].
- Latent Factor Model (LFM). This class of model [14, 15] maps the network topology into a latent feature space and assumes that two nodes are more likely to be connected if they have more similar latent features.

The former two models use the explicit topological properties of the network, while latent factor models depends on latent features of the network, which can be viewed as an implicit representation of the network topological information. The main drawback of the former two models is the high calculation complexity, which makes them inapplicable to large-scale networks [3]. By contrary, the latent factor models can be trained in linear time with the number of observed links.

62.3 Our Model

62.3.1 Basic Latent Factor Model

In basic latent factor model (LFM), each node i is associated with a latent feature vector $F_i \in \mathbb{R}^k$, where k is the number of latent features. The latent features of all the nodes in the network constitute the latent feature matrix $\mathbf{F} \in \mathbb{R}^{n \times k}$, where n is the number of nodes in the network. Under the assumption that two nodes are more likely to be connected if they have more similar latent features, the predicted score of the link between node i and j can be written as:

$$\hat{A_{ij}} = L\left(\sum_{f=1}^{k} F_{if} F_{jf}\right) = L(F_i F_j^T) \tag{62.1}$$

where, $L(\cdot)$ is a link function, which is monotonic increasing and usually taken as identity function or sigmoid function.

The latent features of each node can be learnt by solving the following optimization problem:

$$\min_{\mathbf{F}} \sum_{(i,j)\in O} \left(A_{ij} - L(F_i F_j^T)\right)^2 + \lambda\left(\|\mathbf{F}\|_F^2\right) \tag{62.2}$$

where, O is the set of the observed present and absent links, the first term is regularized square error loss function and the second term is L_2 norm regulation term that prevents overfitting. Stochastic gradient descent method is usually used to solve this optimization problem. The total training process exhibits linear time with the number of observed links.

62.3.2 Neighborhood-Based Nonnegative Matrix Factorization Model

In basic latent factor model, the latent features of some nodes may have negative values, which may mislead the whole approach. Moreover, the influences of the neighborhoods of the nodes in the network are not considered in basic latent factor model. It has been shown in [4] that several neighborhood-based similarity indices do correlate with the missing links in numerous real-world networks.

We first assume that the latent feature matrix $\mathbf{F}$ is a nonnegative matrix and each pair of nodes in the network have a latent interaction of nonnegative strength variable X_{ij}. The link between the two nodes is present only if the corresponding $X_{ij} > 0$. Consider that node i and j generate an interaction of strength $X_{ij}^{(f)}$ with each latent feature f using a Poisson distribution with mean $F_{if} \cdot F_{jf}$. The strength X_{ij} between node i and j is the sum of $X_{ij}^{(f)}$ for all the latent features:

$$X_{ij} = \sum_{f=1}^{k} X_{ij}^{(f)} \sim Pois\left(\sum_{f=1}^{k} F_{if} \cdot F_{jf}\right) = Pois\left(F_i F_j^T\right) \tag{62.3}$$

Then, the link probability between the pair of nodes (i, j) can be figured out:

$$P(X_{ij} > 0) = 1 - P(X_{ij} = 0) = 1 - exp\left(-F_i F_j^T\right) \tag{62.4}$$

It is expected that the nodes with larger values in the same latent features are more likely to have a link between each other.

Taking the node-specific biases into account and using $1 - exp(\cdot)$ as the link function, we can reformulate the optimization problem (62.2) as:

$$\min_{\mathbf{F}, b>0} \sum_{(i,j)\in O} \left(A_{ij} - 1 + exp(b_i + b_j - F_i F_j^T)\right)^2 + \lambda\left(\|b\|_2^2 + \|\mathbf{F}\|_F^2\right) \tag{62.5}$$

where, b is the node-specific bias vector, which is similar to the intercept terms in standard supervised learning.

Now, let us consider the influence of the neighborhoods on the link probability between the nodes. In unsupervised models, many similarity metrics are defined in the following form:

$$s_{ij} = \sum_{u\in\Gamma(i)\cap\Gamma(j)} w_u \tag{62.6}$$

where, $\Gamma(i)$ is the set of neighbors of node i and w_u is a measurement of the topological properties of node u. Common Neighbors Index (CN) [4] directly count the neighborhood overlap of the two nodes so that $w_u = 1$. For Adamic-Adar Index (AA) [7] and Resource Allocation Index (RA) [8], w_u is related with the node degree k_u that $w_u = 1/log(k_u)$ in AA index and $w_u = 1/k_u$ in RA index. Here, we extend this form by making each node have different influences upon the pairs of nodes:

$$\hat{A_{ij}} = \sum_{u\in\Gamma(i)\cap\Gamma(j)} (w_{ui} + w_{uj}) \tag{62.7}$$

The nonnegative parameters $\mathbf{w}$ are learnt by solving the optimization problem:

$$\min_{\mathbf{w}>0} \sum_{(i,j)\in O} (A_{ij} - \sum_{u\in\Gamma(i)\cap\Gamma(j)} \left(w_{ui} + w_{uj}\right))^2 + \lambda\left(\|\mathbf{w}\|_F^2\right) \tag{62.8}$$

In order to reduce the number of parameters, we factorize the matrix $\mathbf{w} = \mathbf{X}^T\mathbf{Y}$, $\mathbf{X}, \mathbf{Y} \in \mathbb{R}^{n\times k}$. Then, the optimization problem (62.8) can be reformulated as

$$\min_{\mathbf{X},\mathbf{Y}>0} \sum_{(i,j)\in O} \left(A_{ij} - (X_i + X_j) \sum_{u\in\Gamma(i)\cap\Gamma(j)} Y_u^T\right)^2 + \lambda\left(\|\mathbf{X}\|_F^2 + \|\mathbf{Y}\|_F^2\right) \tag{62.9}$$

Finally, we combine the previous two models and make predictions of link probabilities by:

$$\hat{A_{ij}} = 1 - exp\left(b_i + b_j - \alpha \cdot F_i F_j^T - \beta \cdot (F_i + F_j) \sum_{u \in \Gamma(i) \cap \Gamma(j)} Y_u^T\right) \tag{62.10}$$

where, α and β are two strength coefficients. Here, we arbitrarily let $\mathbf{F} = \mathbf{X}$ to reduce the number of parameters. Thus, model parameters are learnt by solving the optimization problem associated with

$$\min_{\mathbf{F}, b, \mathbf{Y} > 0} \sum_{(i,j) \in O} \left(A_{ij} - 1 + exp\left(b_i + b_j - \alpha \cdot F_i F_j^T - \beta \cdot (F_i + F_j) \sum_{u \in \Gamma(i) \cap \Gamma(j)} Y_u^T\right)\right)^2 + \lambda\left(\|b\|_2^2 + \|\mathbf{F}\|_F^2 + \|\mathbf{Y}\|_F^2\right) \tag{62.11}$$

An optimal solution of this optimization problem can be obtained using stochastic gradient descent method. Let the prediction error $A_{ij} - \widehat{A}_{ij}$ be denoted by e_{ij}. We loop through all observed links in the network. For a given observed link (i, j), we modify the parameters by moving in the opposite direction of the gradient, yielding:

- $b_i \leftarrow max(0, b_i + \gamma \cdot ((1 - \widehat{A}_{ij}) \cdot e_{ij} - \lambda \cdot b_i))$
- $b_j \leftarrow max(0, b_j + \gamma \cdot ((1 - \widehat{A}_{ij}) \cdot e_{ij} - \lambda \cdot b_j))$
- $F_i \leftarrow max\left(0, F_i + \gamma \cdot \left((1 - \widehat{A}_{ij}) \cdot e_{ij} \cdot \left(\alpha \cdot F_j + \beta \cdot \sum_{u \in \Gamma(i) \cap \Gamma(j)} Y_u\right) - \lambda \cdot F_i\right)\right)$
- $F_j \leftarrow max\left(0, F_j + \gamma \cdot \left((1 - \widehat{A}_{ij}) \cdot e_{ij} \cdot \left(\alpha \cdot F_i + \beta \cdot \sum_{u \in \Gamma(i) \cap \Gamma(j)} Y_u\right) - \lambda \cdot F_j\right)\right)$
- $\forall \quad u \in \Gamma(i) \cap \Gamma(j)$:
  $Y_u \leftarrow max\left(0, Y_u + \gamma \cdot \left(\beta \cdot (1 - \widehat{A}_{ij}\right) \cdot e_{ij} \cdot (F_i + F_j) - \lambda \cdot Y_u)\right)$

  where, γ is the learning rate.

62.4 Experimental Results

We apply our neighborhood-based nonnegative matrix factorization model on several real-world networks, which are widely used in link prediction literature. General information of these real-world networks is shown in Table 62.1. We also make comparisons with some unsupervised link prediction models, including Common Neighbors Index (CN) [4], Salton Index [6], Preferential Attachment Index (PA) [5], Adamic-Adar Index (AA) [7] and Karz Index [9].

Table 62.1 General information of the real-world networks

Network	Description	Node	Present link	Average degree
Karate	Zachary's karate club [17]	34	78	4.58
Dolphin	Social network of Lusseau's dolphins [18]	62	159	5.13
USair	US air transportation system [19]	332	2,126	12.81
Email	E-mail interchanges between members of the University Rovira i Virgili [20]	1,133	5,451	9.62
Blog	Hyperlinks between blogs on US politics [21]	1,222	16,174	27.36
Protein	The interaction between proteins [22]	2,473	6,269	5.09
Powergrid	The topology of the Power Grid of the United States [23]	4,941	6,594	2.67
PGP	The interactions between users of Pretty-Good-Privacy algorithm [24]	10,680	24,316	4.55

Table 62.2 The *AUC* values of different models on real-world networks

	CN	Salton	PA	AA	Karz	Basic LFM	Our model
Karate	0.7035	0.6387	0.7461	0.7313	0.7877	0.8058	**0.8294**
Dolphin	0.7786	0.7076	0.6907	0.7851	0.8103	0.8109	**0.8275**
Usair	0.9368	0.8624	0.9017	0.9461	0.4136	0.9433	**0.9598**
Email	0.8541	0.8129	0.7814	0.8550	0.6415	**0.9131**	0.9105
Blog	0.9175	0.8469	0.8977	0.9205	0.4804	0.9292	**0.9384**
Protein	0.7624	0.6543	0.7232	0.7626	0.6322	0.8849	**0.8867**
Powergrid	0.5879	0.4411	0.4395	0.5878	**0.6587**	0.6344	0.6291
PGP	0.8371	0.6805	0.7117	0.8373	0.5245	0.8775	**0.8983**

To evaluate the accuracy of the models, we adopt *AUC* proposed by Hanely and McNeil [16] as the basic measure for the experiments reported in this paper. The *AUC* value is defined as the probability that a randomly chosen missing link is assigned with a higher score than a randomly chosen nonexistent link. If among n independent comparisons, there are n_1 times the missing link having a higher score and n_2 times the scores are equal, the *AUC* value is

$$AUC = \frac{n_1 + 0.5n_2}{n} \tag{62.12}$$

If all the scores are randomly given, the *AUC* value should be approximate to 0.5. The degree to which the *AUC* value exceeds 0.5 indicates how much better the model performs than pure chance.

For each network, the present links are partitioned into training set (90 %) and test set (10 %). The evaluated *AUC* values of the models on each network are the average over ten repetitions. The performances of different models on real-world networks are shown in Table 62.2.

As is shown in Table 62.2, our model performs the best among all the other models on most real-world networks and is only inferior to basic LFM on Email network and Karz index on Powergrid network. Compared with unsupervised link prediction models, our model shows significant advantages on Karate network, Blog network and PGP network. In comparison with basic LFM, our model shows obvious improvement on Karate network, Dolphin network, USair network and PGP network.

Powergrid network is a very sparse network that about 60 % of the nodes only have one or two links connecting with other nodes. The sparsity makes a large part of model parameters get insufficient training, which results in that our model does not perform well on this network.

From the above experimental results on real-world networks, we see that our model is promising and effective for link prediction in complex networks.

Conclusion

In this paper, we propose a neighborhood-based nonnegative matrix factorization model for solving the problem of link prediction in complex networks. In our model, the probability of a link is associated with a nonnegative strength variable, which is related with the latent features of the nodes. The influence of the neighborhood structure is also taken into consideration. Thus, the latent features of each node are learnt from the overall topological structure combing with local neighborhood structures of the underlying network. We test our model on several real-world networks, which are widely used in link prediction literature. The experimental results demonstrate the effectiveness and efficiency of our model for link prediction in complex networks.

Acknowledgements This work is funded by National Science Foundation of China (61271316 and 61071152), 973 Program (2010CB731403, 2010CB731406 and 2013CB329605), Chinese National "Twelfth Five-Year" Plan for Science & Technology Support (2012BAH38 B04), Key Laboratory for Shanghai Integrated Information Security Management Technology Research and Chinese National Engineering Laboratory for Information Content Analysis Technology.

References

1. Strogatz SH (2001) Exploring complex networks. Nature 410:268–276
2. Getoor L, Diehl CP (2005) Link mining: a survey. ACM SIGKDD Explor Newslett 7:3–12
3. Lü L, Zhou T (2011) Link prediction in complex networks: a survey. Physica A 390:1150–1170
4. Newman MEJ (2001) Clustering and preferential attachment in growing networks. Phys Rev E 64:025102
5. Barabási AL, Albert R (1999) Emergence of scaling in random networks. Science 286:509–512

6. Salton G, McGill MJ (1983) Introduction to modern information retrieval. McGraw-Hill, Auckland
7. Adamic LA, Adar E (2003) Friends and neighbors on the Web. Soc Netw 25:211–230
8. Zhou T, Lü L, Zhang YC (2009) Predicting missing links via local information. Eur Phys J B 71:623–630
9. Katz L (1953) A new status index derived from sociometric analysis. Psychometrika 18:39–43
10. Chebotarev P, Shamis EV (1997) The matrix-forest theorem and measuring relations in small social groups. Autom Remote Control 58:1505–1514
11. Liu W, Lü L (2010) Link prediction based on local random walk. Europhys Lett 89:58007
12. Clauset A, Moore C, Newman MEJ (2008) Hierarchical structure and the prediction of missing links in networks. Nature 453:98
13. Guimera R, Sales-Pardo M (2009) Missing and spurious interactions and the reconstruction of complex networks. Proc Natl Acad Sci USA 106:22073
14. Menon A, Elkan C (2011) Link prediction via matrix factorization. In: ECML-PKDD 2011, Part II. Springer, Berlin, pp 437–452
15. Gao S, Denoyer L, Gallinari P (2012) Link prediction via latent factor Block Model. In: Proceedings of the 21st international conference companion on World Wide Web, Lyon, pp 507–508, 2012
16. Hanely JA, McNeil BJ (1982) The meaning and use of the area under a receiver operating characteristic (ROC) curve. Radiology 143:29–36
17. Zachary WW (1997) An information flow model for conflict and fission in small groups. J Anth Res 33:452–473
18. Lusseau D (2003) The emergent properties of a dolphin social network. Proc R Soc Lond B 270:S1860–S1888
19. Batageli V, Mrvar A, Pajek Datasets, available at http://vlado.fmf.uni-lj.si/pub/networks/pajek/data/gphs.htm
20. Guimera R, Danon L, Díaz-Guilera A, Giralt F, Arenas A (2003) Self-similar community structure in a network of human interactions. Phys. Rev. E 68:065103
21. Adamic LA, Glance N (2005) The political blogosphere and the 2004 US Election. In: Proceedings of the WWW-2005 workshop on the weblogging ecosystem. ACM, New York, pp 36–43
22. Palla G, Derényi I, Farkas I, Vicsek T (2005) Uncovering the overlapping community structure of complex networks in nature and society. Nature 435:814–818
23. Watts DJ, Strogatz SH (1998) Collective dynamics of small-world networks. Nature 393:440–442
24. Boguña M, Pastor-Satorras R, Díaz-Guilera A, Arenas A (2004) Models of social networks based on social distance attachment. Phys Rev E 70:056122

Chapter 63
Performance Research on Cascade Topology of Deterministic Ethernet Based on Network Calculus

Yu Xiang, Hui Jiang, Wei Wang, Yong Tang, and Siyu Zhan

Abstract The thesis adopts the theoretical tool of network calculus theory to conduct the performance research on the cascade topology of deterministic Ethernet. Based on the simple star topology, the thesis proposes the cascade topology which is the extension of the simple star topology. The thesis conducts the in-depth study of the network calculus theory and deterministic Ethernet. Firstly, we adopt the deconvolution theory to establish the network calculus model of the cascade topology. Secondly, we establish the simulation model. Lastly, we compare the simulation results with the theory results to analyze the determinacy and real-time of deterministic Ethernet. The conclusion shows that the cascade topology has a good performance.

Keywords Time-triggered • Deterministic • Cascade topology • Network calculus • Simulation

63.1 Introduction

Deterministic Ethernet [1] is compatible with the application of traditional Ethernet. Meanwhile, it also meets the requested real-time application to achieve the determinacy and real-time of Ethernet technology. Network calculus [2–4] is a good theory tool for the study of deterministic Ethernet. In [5], we study the simple star topology using network calculus theory [6]. The result shows that the real-time data is guaranteed service preferentially and has no conflict and no loss; the rate-constraint data has smaller priority than real-time data and usually has no loss due to the small amount; the best-effort data can't be guaranteed service and its end-to-end delay has very large value and the average value is under the theoretical

Y. Xiang (✉) • H. Jiang • W. Wang • Y. Tang • S. Zhan
School of Computer Science and Engineering, University of Electronic Science and Technology of China, Chengdu, China
e-mail: jcxiang@uestc.edu.cn; jh17326@sina.com; 874614101@qq.com; worldgulit@uestc.edu.cn; zhansy@uestc.edu.cn

J. Mu et al. (eds.), *The Proceedings of the Third International Conference on Communications, Signal Processing, and Systems*, Lecture Notes in Electrical Engineering 322, DOI 10.1007/978-3-319-08991-1_63

calculations, and the larger the amount of data the greater the loss rate. In general, in the simple star topology, deterministic Ethernet has good performance for determinacy and real-time [7]. Thus it can be further applied in industrial control and other fields.

The basic topologies of Ethernet are star, tree and mesh. We can mix with the basic topologies to establish complex topologies [8] to meet a variety of needs. The network topology is more complex in the practical applications. There will be the cascade of many switch nodes which is not only the simple star topology. Thus, the complex topology is much closer to our practical application, which needs us to conduct in-depth study in the complex topology of deterministic Ethernet. Based on the simple star topology, the thesis conducts in-depth study in deterministic Ethernet, proposes the cascade topology and researches on the performance of it.

The thesis is to conduct performance research on the cascade topology of the deterministic Ethernet. Firstly, we establish the network calculus model of the cascade topology. Secondly, we establish the simulation model. Lastly, we compare the simulation results with the theory results to obtain conclusion.

63.2 Establish the Network Calculus Model of Cascade Topologies

63.2.1 The Cascade Topology of Deterministic Ethernet

The definition of cascade topology is that more than one switch are cascaded, that is to say, data is transmitted by multiple switches nodes from the source node to the destination node. We use OPNET simulation tool to establish the simulation model of the cascade topology. Figure 63.1 shows the three switches cascade topology which is consist of four terminals nodes, three switches nodes and links. The workflow of the cascade topology is: the source node generates data, and the switch node receives data and forwards to the next node, and until the destination node receive the data. As the simple star topology, cascade topology transmits three kinds of data which are time-triggered (TT) data, rate-constraint (RC) data and best-effort (BE) data.

63.2.2 The Network Calculus Model of Cascade Topology

Network calculus model has a great relationship with the network topology. When multiple switches cascaded, we need to consider the data flow of two directions in the network. Thus, the network calculus model of the cascade topology is more complex than the simple star topology.

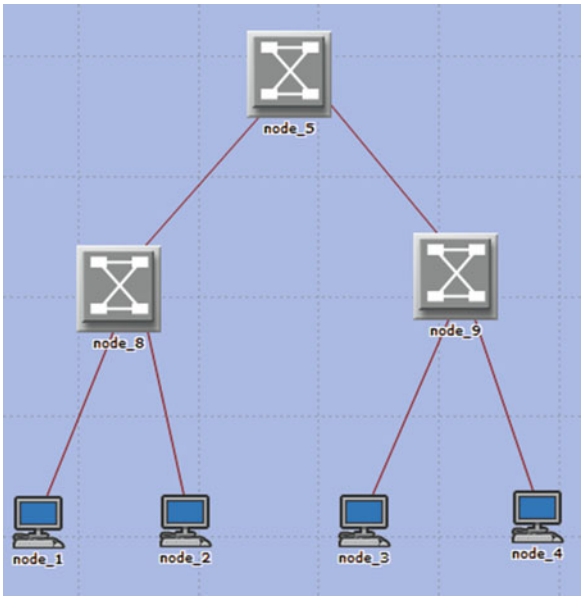

Fig. 63.1 The cascade topology

Table 63.1 Some new symbol definitions

Symbol	Definitions
$\alpha_{\max}$	The arrival curve of micro-data stream with maximum arrival rate
$A_{\max}$	The arrival curve of aggregated flow with maximum arrival rate
n_i	The number of terminal nodes connected to the level i of switch node
$r_{\max}$	The maximum arrival rate of the three kinds of data
$b_{\max}$	The maximum value of b of the three kinds of data
F_j^H	The micro-data stream with the highest priority

Based on the simple star topology, the section establishes the network calculus model of cascade topology. On the basis of the symbol definition in [5], there adds some symbol definitions showed in Table 63.1.

When establishing the theory model of cascade topology, we conduct analysis by levels. Considered the level I switch node, there are the formulas as follows.

$$\alpha_{\max}(t) = r_{\max}t + b_{\max} \quad A_{\max}(t) = n_i * \alpha_{\max}(t)$$

Now, we analyze the case of data aggregation. The micro stream F_j with the same low priority is aggregated into aggregation stream G_j. The micro stream F_j with the same high priority is aggregated into aggregation stream G_j^H. The stream G_j and G_j^H are aggregated into aggregation stream PG_j with mixed priority. Based on the network calculus theory, we establish the model reversely. Firstly, we establish the mathematical model of the aggregation stream with mixed priority. Secondly,

we establish the mathematical model of the aggregation stream with high priority and low priority respectively. Lastly, we obtain the mathematical model of the micro stream. In the modeling process, we consider the stream of two directions and add deconvolution and convolution theory, thus making the process more complex.

From [5, 9], we obtain the service curve of the aggregation stream PG_j is $\beta(PG_j, t) = [\beta_{R,T}(t) - l^j_{\max}]^+ = C[t - l^j_{\max}/C]^+$.

The service capability of switch node is fixed and is C. When there is data with the highest priority, the switch node deal with the data using its all service capability. Thus, the service curve of aggregation stream G^H_j is as follows:

$$\beta\left(G^H_j, t\right) = \beta\left(PG_j, t\right) = \left[\beta_{R,T}(t) - l^j_{\max}\right]^+ = C\left[t - l^j_{\max}/C\right]^+ \tag{63.1}$$

In the cascade topology, we consider the data of two directions. To analyze the aggregation stream with low priority, we consider not only the aggregation stream G^H_j, but also the aggregation stream $A_{\max}$ of reverse direction. From [5, 9], we obtain the service curve of the aggregation stream G_j with low priority as follows $\beta(G_j, t) = [\beta(PG_j, t) - A^H_j(t) - A_{\max}(t)]^+$.

Then, we can obtain as follows:

$$\begin{aligned}\beta(G_j, t) &= \left[C\left(t - \tfrac{l^j_{\max}}{C}\right) - \sum\nolimits_{\{i:\, p(i) > p(j)\}} r_i * t - \sum\nolimits_{i:\, p(i) > p(j)} b_i - A^H_{\max}\right]^+ \\ &= C - \sum\nolimits_{\{i:\, p(i) > p(j)\}} r_i - n_i * r_{\max}\Bigg) \left[t - \frac{l^j_{\max} + \sum_{\{i:\, p(i) > p(j)\}} b_i + n_i * b_{\max}}{C - \sum_{\{i:\, p(i) > p(j)\}} r_i - n_i * r_{\max}}\right]\end{aligned} \tag{63.2}$$

The minimum of the service rate is 0, so we define R^G_j non-negative. So, we obtain the service rate and delay of aggregation stream G_j with low priority as follows:

$$R^G_j = max\left(C - \sum\nolimits_{\{i:\, p(i) > p(j)\}} r_i - n_i * r_{\max}, 0\right) \tag{63.3}$$

$$T^G_j = \left(l^j_{\max} + \sum\nolimits_{\{i:\, p(i) > p(j)\}} b_i + n_i * b_{\max}\right) / R^G_j \tag{63.4}$$

Now, it is the turn to analyze the model of micro stream. For the data with the highest priority which is called the real-time data, it is no conflicts and needs timely response, and will be serviced by switch node preferentially. The service curve of micro stream F^H_j with high priority is similar to the aggregation stream G^H_j as follows:

$$\beta\left(F^H_j, t\right) = \beta\left(G^H_j, t\right) = \left[\beta_{R,T}(t) - l^j_{\max}\right]^+ = C\left[t - \frac{l^j_{\max}}{C}\right]^+ \tag{63.5}$$

Similarly, to analyze the micro stream F_j with low priority, we also consider the micro stream $\alpha_{\max}$ of two directions. From [5, 9], we obtain the service curve of micro stream with low priority as follows:

$$\beta[F_j,t] = [\beta(G_j,t) - (A_j(t-\theta) - \alpha_j(t-\theta)) - (r_{\max} * t + b_{\max})]^+$$
$$= \left(R_j^G - \sum_{\{i:p(i)=p(j)\}} r_i + r_j - r_{\max}\right) * \left[t - \frac{\left(R_j^G - \sum_{\{i:p(i)=p(j)\}} r_i + r_j\right)\left[T_j^G + \left(\sum_{\{i:p(i)=p(j)\}} b_i - b_j\right)/R_j^G\right] + b_{\max}}{R_j^G - \sum_{\{i:p(i)=p(j)\}} r_i + r_j - r_{\max}}\right]^+ \tag{63.6}$$

Similarly, the service rate and delay of micro stream with low priority are as follows

$$R_j = max\left(R_j^G - \sum\nolimits_{\{i:p(i)=p(j)\}} r_i + r_j - r_{\max}, 0\right) \tag{63.7}$$

$$T_j = \left\{\left[T_j^G + \left(\sum\nolimits_{\{i:p(i)=p(j)\}} b_i - b_j\right)/R_j^G\right]\left[R_j^G - \sum\nolimits_{\{i:p(i)=p(j)\}} r_i + r_j\right] + b_{\max}\right\}/R_j \tag{63.8}$$

Lastly, we analyze the case of cascaded switch nodes. Assuming that micro stream F_j passes through system S_1 and S_2 sequentially, the arrival curve and the service curve of system S_1 are $\alpha_{r,b}$ and $\beta_{R,T}$ respectively. From [9], we obtain the export curve of system S_1 which is also the arrival curve of system S_2 as follows:

$$\alpha_1^*(t) = \alpha_2(t) = (\alpha_{r,b} \oslash \beta_{R,T})(t) \tag{63.9}$$

From [9], we obtain the formula as follows:

$$\begin{aligned}
&(\alpha_{r,b} \oslash \beta_{R,T})(t) \\
&= \sup_{u \geq 0}\{\alpha_{r,b}(t+u) - R[u-T]^+\} \\
&= \sup_{0 \leq u \leq T}\{\alpha_{r,b}(t+u) - R[u-T]^+\} \vee \sup_{u>T}\{\alpha_{r,b}(t+u) - R[u-T]^+\} \\
&= \sup_{0 \leq u \leq T}\{\alpha_{r,b}(t+u)\} \vee \sup_{u \geq T}\{\alpha_{r,b}(t+u) - Ru + RT\} \\
&= \{\alpha_{r,b}(t+u)\} \vee \sup_{u>T}\{\alpha_{r,b}(t+u) - Ru + RT\}
\end{aligned}$$

When $t > -T$, there is as follows:

$$\begin{aligned}&\left(\alpha_{r,b} \varnothing \beta_{R,T}\right)(t)\\&= \{b + r(t+T)\} \vee \sup_{u>T} \{b + r(t+u) - Ru + RT\}\\&= \{b + r(t+T)\} \vee \{b + r(t+T)\}\\&= b + r(t+T)\end{aligned}$$

When $t \leq -T$, it has no practical significance. So $t > 0$, there is as follows:

$$\left(\alpha_{r,b} \varnothing \beta_{R,T}\right)(t) = b + r(t+T) \tag{63.10}$$

When obtaining the service of the cascaded network, we need to use convolution theory. From [9], the service curve of system S_1 and system S_2 is β_{R_1,T_1} and β_{R_2,T_2} respectively. Thus, the service curve of the cascaded network is as follows:

$$\beta = \beta_{R_1,T_1} \otimes \beta_{R_2,T_2} = \beta_{\min(R_1,R_2),T_1+T_2} \tag{63.11}$$

Compared with the simple star topology, the analysis process of cascade topology is added many complex factors, such as the data stream of two directions, deconvolution and convolution theory, making the theoretical analysis closer to the practical situation.

63.3 Network Calculus Analysis Process of Cascade Topology

In the topology, we set the three kinds of data as follows:

- Time-triggered (TT) data: During the TT data processing, there is only one packet in the network.
- Rate-constraint (RC) data: Each node transmits two packets every 25 ms.
- Best-effort (BE) data: Each node transmits 10,000 packets every second.

The size of packet varies from 100 to 500 bytes. To make it simple, we set that the size of packet is 100 bytes in the paper.

According to the setting, we obtain the arrival curve of three kinds of data of cascade topology. The arrival curve of TT data is $\alpha_{TT}^{S_1}(t)$, and the arrival curve of RC data is $\alpha_{RC}^{S_1}(t)$, and the arrival curve of BE data is $\alpha_{BE}^{S_1}(t)$.

$$\begin{aligned}\alpha_{TT}^{S_1}(t) &= (4000t + 100)\,(\text{bytes})\\\alpha_{RC}^{S_1}(t) &= (8000t + 100)\,(\text{bytes})\\\alpha_{BE}^{S_1}(t) &= (1000000t + 100)\,(\text{bytes})\end{aligned}$$

Based on the network calculus model of cascade topology in Sect. 63.2.2, we conduct the calculation process as follows:

The service curve of level 1 of switch node:

$$\beta_{TT}^{s_1}\left(R_{TT}^{s_1} = 1.048576{*}10^8\,\text{bps}, T_{TT}^{s_1} = 7.63{*}10^{-6}\,\text{s}\right)$$
$$\beta_{RC}^{s_1}\left(R_{RC}^{s_1} = 0.807616{*}10^8\,\text{bps}, T_{RC}^{s_1} = 5.94{*}10^{-5}\,\text{s}\right)$$
$$\beta_{BE}^{s_1}\left(R_{BE}^{s_1} = 0.726976{*}10^8\,\text{bps}, T_{BE}^{s_1} = 8.11{*}10^{-5}\,\text{s}\right)$$

The service curve of level 2 of switch node:

$$\beta_{TT}^{s_2}\left(R_{TT}^{s_2} = 1.048576{*}10^8\,\text{bps}, T_{TT}^{s_2} = 7.63{*}10^{-6}\,\text{s}\right)$$
$$\beta_{RC}^{s_2}\left(R_{RC}^{s_2} = 0.807616{*}10^8\,\text{bps}, T_{RC}^{s_2} = 8.354{*}10^{-5}\,\text{s}\right)$$
$$\beta_{BE}^{s_2}\left(R_{BE}^{s_2} = 0.726976{*}10^8\,\text{bps}, T_{BE}^{s_2} = 1.145{*}10^{-4}\,\text{s}\right)$$

The service curve of level 3 of switch node:

$$\beta_{TT}^{s_3}\left(R_{TT}^{s_3} = 1.048576{*}10^8\,\text{bps}, T_{TT}^{s_3} = 7.63{*}10^{-6}\,\text{s}\right)$$
$$\beta_{RC}^{s_3}\left(R_{RC}^{s_3} = 0.807616{*}10^8\,\text{bps}, T_{RC}^{s_3} = 1.118{*}10^{-4}\,\text{s}\right)$$
$$\beta_{BE}^{s_3}\left(R_{BE}^{s_3} = 0.726976{*}10^8\,\text{bps}, T_{BE}^{s_3} = 1.62{*}10^{-4}\,\text{s}\right)$$

Based on Xiang et al. [5], we obtain the end-to-end delay of the three kinds of data.

$$tt\_ete\_delay = T_{TT}^{s_1} + T_{TT}^{s_2} + T_{TT}^{s_3} + 4{*}send\_delay = 5.5{*}10^{-5}\,\text{s}$$
$$rc\_ete\_delay = T_{RC}^{s_1} + T_{RC}^{s_2} + T_{RC}^{s_3} + 4{*}send\_delay = 2.87{*}10^{-4}\,\text{s}$$
$$be\_ete\_delay = T_{BE}^{s_1} + T_{BE}^{s_2} + T_{BE}^{s_3} + 4{*}send\_delay = 3.90{*}10^{-4}\,\text{s}$$

63.4 Analysis of Simulation Result and Network Calculus Result

The section is to compare the simulation result with network calculus result to conduct analysis from three aspects including end-to-end delay, throughput and packet loss rate. We give that the definition of end-to-end delay jitter is the offset value between each end-to-end delay and the average value.

- End-to-end delay

1. The analysis of simulation value and theory value of end-to-end delay

   In the Sect. 63.3, we know that the size of packet is 100 bytes. From the simulation experiments and theoretical calculation process, we can obtain

the simulation value and theory value of the end-to-end delay of the three kinds of data as shown in Fig. 63.2.

The value of end-to-end delay of TT data is fixed. For RC data, it is queued for receiving and processing, and its end-to-end delay floats up and down within the scope of theoretical calculation. When there are TT data and RC data in the network, BE data needs to wait and may wait for long time. So, the end-to-end delay of BE data has very large value.

2. The analysis of the end-to-end delay jitter

In the cascade topology, we obtain the end-to-end delay jitter of three kinds of data as shown in Fig. 63.3.

For TT data, because its end-to-end delay is fixed, its end-to-end delay jitter is always 0. For RC data, there is end-to-end delay jitter, but not great. The end-to-end delay jitter of BE data is the largest.

At the same time, we analyze the end-to-end delay of simulation value and theory value of different size of packet. With the growing size of TT data, its end-to-end delay is also increasing. Meanwhile, the theory value is very close to the simulation value. The larger size of RC or BE data packet, the value of its end-to-end delay is greater. For RC data, its simulation value always within the scope of theoretical calculation. For BE data, when the size reaches a certain value, its average simulation value of end-to-end delay will be very large.

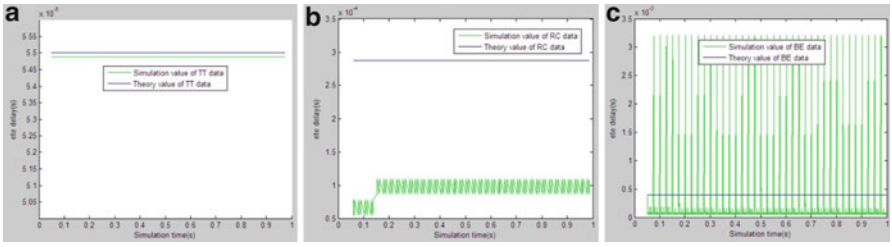

Fig. 63.2 The end-to-end delay of three kinds of data, (**a**) TT data (**b**) RC data (**c**) BE data

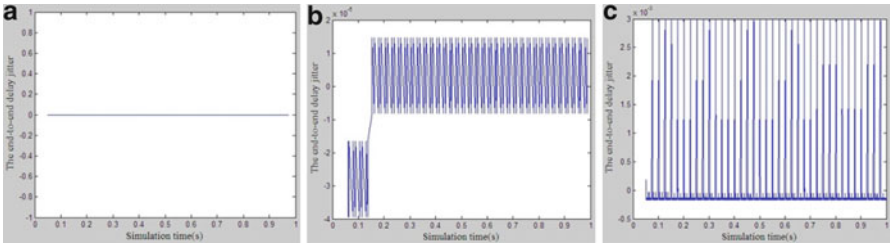

Fig. 63.3 The end-to-end delay jitter of three kinds of data, (**a**) TT (**b**) RC (**c**) BE

- Throughput

  In the cascade topology, we describe the throughput by the receiving and sending rate of switch node. Figure 63.4 shows the receiving and sending rate of switch node of three kinds of data.
- Packet loss

  In the cascade topology, we analyze the loss rate of different size of packet of three kinds of data. Deterministic Ethernet strictly ensure the conflict-free service of TT data. So, TT data has no packet loss. The priority of RC data is lower than TT data. Due to the small amount, RC data has low packet loss and is 0 generally. Unless the amount of RC data is large, there will be some packet loss. BE data is best effort data and can't get guaranteed service. When the size is small, the packet loss is low. When the size reaches to the 400 bytes, its packet loss is very large and is more than a third. Table 63.2 shows the packet loss of BE data with different size.

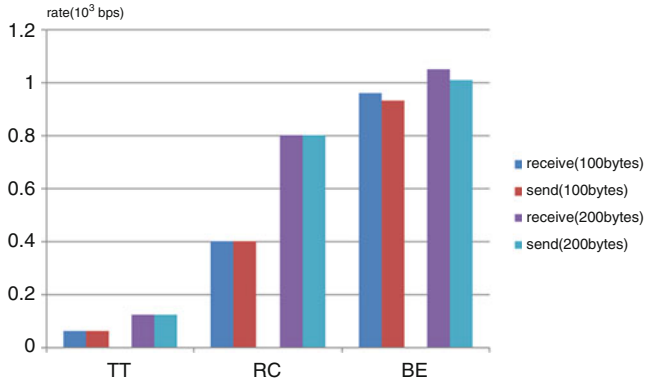

Fig. 63.4 The receiving and sending rate of switch node of three kinds of data

Table 63.2 The packet loss of BE data with different size

BE data (bytes)	Number of sending data	Number of receiving data	Number of losses	Loss rate (%)
100	1,880	1,824	56	2.98
150	1,880	1,824	56	2.98
200	1,880	1,823	57	3.03
250	1,880	1,822	58	3.09
300	1,880	1,819	61	3.24
400	1,880	1,244	636	33.8

Conclusion
The cascade topology is the extension of the simple star topology. In this topology, for TT data, it receives the real-time service and has no packet loss, and the simulation value is very close to the theory value. For RC data, its simulation value is within the scope of the theoretical calculations. BE data receive the best effort service and have some packet loss. To sum up, deterministic Ethernet of cascade topology which is compatible with the traditional Ethernet can provide real-time and rate-constraint service. So, it is competent for the requirements of high security, real-time and reliability.

References

1. TTEthernet Specification Document edition 0.9.1-22968 of 20-Nov-2008. Document number D-INT-S-10-002
2. Le Boudec JY, Thiran P (2000) A short tutorial on network calculus I: fundamental bounds in communication networks. In: Proceedings of ISCAS'2000, Geneva, May 2000
3. Le Boudec JY, Thiran P (2000) A short tutorial on network calculus II: min-plus system theory applied to communication networks. In: IEEE international symposium on circuits and systems (ISCAS 2000), May 2000
4. Lee KC, Lee S (2002) Performance evaluation of switched ethernet for real-time industrial communications. Comput Stand Interf 24:411
5. Xiang Y, Wang W, Zhang X, Li Z (2014) Performance research on time-triggered ethernet based on network calculus. EURASIP J Wirel Commun Netw. doi:10.1186/1687-1499-2014-12,2014:12
6. Le Boudec JY (1996) Network calculus made easy. Technical report EPFL-DI 96/218
7. Whitepaper (1999) Real time services (QoS) in ethernet based industrial automation networks. Technical report, Hirschmann Rheinmetall Elektronik
8. Albert R, Barabási A-L (2002) Statistical mechanics of complex networks. Rev Mod Phys 74:47–97
9. Le Boudec JY, Thiran P (2004) Network calculus: a theory of deterministic queuing system for the internet. Online version: Springer, Heidelberg

Chapter 64
TCP BRJ: Enhanced TCP Congestion Control Based on Bandwidth Estimation and RTT Jitter for Heterogeneous Networks

Nan Ding, Rui-Qing Wu, and Hong Jie

Abstract In this paper, we propose an improved TCP scheme, TCP BRJ, which is capable of adjusting the initial slow-start threshold and congestion window in real time according to the bandwidth estimation in slow-start phase, dividing the network congestion grades based on round-trip time (RTT) jitter in congestion avoidance phase, distinguishing the random packet losses from the congestion packet losses, and reacting accordingly. Simulation results by NS-2 show that TCP BRJ provides more significant performance improvement in throughput, bandwidth utilization and fairness than TCP Reno and TCP Westwood in heterogeneous networks with high random bit-error rate (BER), and shows friendliness towards the widely used algorithm TCP Reno.

Keywords Bandwidth estimation • Round-trip time jitter • Wired/wireless networks • TCP Westwood • Loss differentiation

64.1 Introduction

With the rapid development of emerging wireless communication, a number of wired/wireless heterogeneous networks have been widely deployed nowadays. However, the traditional TCP protocol originally designed primarily for the wired networks has been unable to meet the performance requirements of increasingly complex wired/wireless heterogeneous networks. In wired networks, the random bit-error rate (BER) is negligible and the congestion is the main cause of packet loss, while in wireless networks, frequent random packet losses are unavoidable due to some non-negligible factors, such as high BER, fading and blackout [1]. The traditional TCP's reactive congestion control and avoidance mechanism taken the assumption that all packet losses are due to congestions become incapable of

N. Ding (✉) • R.-Q. Wu • H. Jie
School of Electronic Engineering, University of Electronic Science and Technology of China, Chengdu 611731, China
e-mail: dingnan0807@qq.com

J. Mu et al. (eds.), *The Proceedings of the Third International Conference on Communications, Signal Processing, and Systems*, Lecture Notes in Electrical Engineering 322, DOI 10.1007/978-3-319-08991-1_64

differentiating the mixed packet losses. Therefore, TCP without modification suffers throughput degradations when used in heterogeneous networks.

In the past few years, many research efforts have been made to adapt TCP to heterogeneous networks. Such works can be classified into three main categories: split-connection schemes [2], localized link layer solution [3], and end-to-end schemes [4]. Among them, strictly end-to-end schemes at the transport layer have been paid much attention because they require no support from the network. As a representative end-to-end congestion control algorithm applied in wireless network nowadays, TCP Westwood [5], has evolved into many variants. When the packet loss occurs, it sets the slow-start threshold (ssthresh) and congestion window (cwnd) based on bandwidth estimation, which eliminates the influence of wireless random loss to some extent and provides significant throughput gains. However, the following shortages still exist in TCP Westwood when it is applied in heterogeneous networks with high BER. (1) It has no loss differentiation mechanism, which misinterprets random packet losses as congestion losses and results in an unnecessary congestion control. (2) It remains the slow-start phase intact as traditional TCP Reno [6] does, which initializes the ssthresh blindly with a fixed value leading to a decline of bandwidth utilization.

In order to overcome the above disadvantages, we propose a novel TCP BRJ scheme with loss differentiation mechanism and following improvements. (1) In slow-start phase, TCP BRJ adjusts the initial ssthresh according to bandwidth estimation in real time. (2) Every time after receiving an arrival acknowledgment (ACK) of new data segments, TCP BRJ calculates the RTT jitter and divide the network into five congestion grades based on the jitter in congestion avoidance phase. (3) When three duplicate ACKs occur, TCP BRJ differentiates the random packet losses from the congestion packet losses based on network congestion grades and reacts accordingly.

64.2 Overview of TCP Westwood

TCP Westwood (TCPW) is a sender-only modification of TCP NewReno [7]. The TCP sender determines bandwidth estimation (BWE) when each arrival ACK packet of new data is received. The estimation is based on information in the ACKs, and the rate at which the ACKs are received. After a packet loss indication, the sender uses BWE to set the cwnd and the ssthresh properly. Further details of BWE are presented in [5]. Here, we describe how the estimation is used to set the cwnd and ssthresh. Firstly, in TCPW, cwnd dynamics during slow start and congestion avoidance are unchanged, that is, they increase exponentially and linearly, respectively. A packet loss is indicated by (a) the reception of three duplicate ACKs, or (b) coarse timeout expiration. In case (a), TCPW sets cwnd and ssthresh as follows.

```
if (three DUPACKs are received) {      //packet loss
ssthresh = (BWE * RTTmin) /seg_size;
if (cwnd > ssthresh)   cwnd = ssthresh; } //congestion avoidance.
When coarse timeout expires, the cwnd and ssthresh are set as follows:
if (coarse timeout expires) {
cwnd = 1;
ssthresh = (BWE * RTTmin) / seg_size;
if (ssthresh < 2)   ssthresh = 2; }
```

64.3 RTT Jitter and Congestion Grade

A packet's round-trip time (RTT) consists of three parts: transmission delay, propagation delay and queuing delay. If all the packets pass through the same router and the packets are of the same size, the transmission delay and propagation delay are fixed. Then the changes of RTT are determined only by the queuing delay, which indicates the congestion degree of network. Therefore the network state can be characterized to a large extent by the RTT jitter, so TCP BRJ uses the adaptable RTT jitter to predict network states, and then divides the network congestion into different grades according to the previous forecast.

We use the following formula to calculate the RTT jitter based on RTT:

$$J_{sample}(k) = RTT_k - RTT_{k-1} \tag{64.1}$$

$$J_{estimate}(k) = \alpha * J_{estimate}(k-1) + (1-\alpha) * J_{sample}(k) \tag{64.2}$$

Where RTT_k and $J_{sample}(k)$ means respectively the RTT and RTT jitter measured when the kth ACK received at the sender. To improve the accuracy of RTT jitter, we use an exponentially-weighted moving average (EWMA) filter in formula (64.2) to calculate the estimation value of RTT jitter $J_{estimate}(k)$, where $\alpha \in [0, 1]$, and α is generally set to a fixed value equal to 0.125. From (64.2), we can see that if α is small, the value of $J_{estimate}(k)$ depends on $J_{sample}(k)$ and otherwise depends on $J_{estimate}(k-1)$. However, when the network state changes frequently, it is difficult to get accurate RTT jitter estimation adopting a fixed α. In TCP BRJ, we update the value of α dynamically according to the network states, which will be provided in following sections. If the network state changes quickly, α will be set to a smaller value, otherwise, if the network state is stable, we use a larger α. TCP BRJ obtains a more accurate RTT jitter estimation. The pseudo code is shown below.

```
if (network states change quickly) {
    α = | J_sample(k) - J_estimate(k-1) | / J_estimate(k-1);
    if (α > 1)  α = 1/ α;
} else  α = 0.875;       // network states are stable
```

Table 64.1 Division of congestion grade

NCF	Congestion grade	Congestion degree
$(-\infty, -4)$	1	Serious under-load
$(-4, -1)$	2	Slight under-load
$[-1, 0.5]$	3	Normal network
$(0.5, 1)$	4	Slight congestion
$(1, +\infty)$	5	Serious congestion

This paper takes advantage of the network congestion flag (NCF) to realize a fine-grained classification of network congestion degree. The NCF is given by $NCF = (J_{estimate}(k) - T)/T$, namely the difference rate between RTT jitter estimation and a constant variable T. Where T is set to 0.5 ms, which is an experience value gained from simulation experiments. According to the value of NCF, the network congestion degree will be specifically divided into five grades as shown in Table 64.1.

64.4 Congestion Control of TCP BRJ

We note that in TCPW, the initial value of ssthresh is set to 1 artificially, which is hard to be adaptable to the network states on the condition of unknown bottleneck link bandwidth. And an inappropriate value of ssthresh will lead to a decline of bandwidth utilization. In this paper, we propose an improved slow-start phase, which adjusts the initial ssthresh and cwnd in real time according to BWE. During the detection period, if the current ssthresh is lower than BWE, the sender will set the ssthresh equal to BWE and increase the cwnd at a slightly higher speed than exponentially growth in TCPW, which will then make the slow-start process astringed fast. The pseudo code of improved slow-start phase is shown below.

```
if (ssthresh < (BWE*RTT_min)/seg_size)
    ssthresh = (BWE*RTT_min)/seg_size;
if (cwnd < ssthresh)   cwnd = cwnd + 1.5;
else go to the congestion avoidance phase
```

The improved congestion avoidance phase of TCP BRJ realizes not only the division of congestion grade but also adopts a new cwnd adjustment strategy. The process of improved congestion avoidance phase is shown in Table 64.2.

Firstly, when the congestion grade is 1 and 2, the network utilization is very low, and the cwnd is increased by 1.1 and 1.2 respectively in order to make full use of the network resources as fast as possible. Secondly, the congestion grade equaled to 3 means a normal network state, and we increase the cwnd by 1. Thirdly, when the congestion grade grows to 4, which indicates a slight congestion, the sender will decrease the growth rate of cwnd appropriately. When the congestion grade is equal

Table 64.2 The adjustments in improved congestion avoidance phase

NCF range	Cwnd update	Grade	Remark
$(-\infty, -4]$	cwnd = cwnd + 1.2	1	Serious under-load network
$(-4, -1]$	cwnd = cwnd + 1.1	2	Slight under-load network
$(-1, 0.5]$	cwnd = cwnd + 1.0	3	Normal network
(0.5, 1]	cwnd = cwnd + 0.8	4	Slightly congestion network
$(1, -\infty)$	cwnd = cwnd + 0.6	5	Serious congestion network

to 5, the network is seriously congested, and then we increase the cwnd by a quite small value.

The proposed TCP BRJ also has a novel loss differentiation mechanism based on the bandwidth estimation and RTT jitter. When more than three duplicate ACKs occur, TCP BRJ differentiates the random packet losses from the congestion packet losses based on network congestion grades and reacts accordingly. If the congestion grade is larger than 3, TCP BRJ regards the packet loss as a congestion loss, otherwise, a random loss. More details are shown below.

```
More than three duplicate ACKs are received:
if (grade <= 3) {            //Wireless random loss
   ssthresh = int (cwnd * 4/5);
   cwnd = ssthresh + 3;
} else if (grade = 4) {          //Congestion loss
   sstemp = (BWE*RTT_min)/seg_size;
   ssthresh = int (sstemp);
   if (cwnd > sstemp)   cwnd = (cwnd + sstemp)/2;
} else {                 //Serious congestion loss
   ssthresh = int (sstemp);
   if (cwnd > sstemp)    cwnd = cwnd * 0.6;}
```

64.5 Performance Evaluations

In this section, we simulate and analyze the performance improvements of TCP BRJ in throughput, bandwidth utilization, fairness and friendliness compared with TCP WestwoodNR (NS-2 modules of TCP Westwood with the NewReno feature) and TCP Reno in heterogeneous networks by the NS-2 simulator.

Throughput is an important feature of network performance, which is calculated by the effective amount of data delivered through the network based on received ACKs at the sender. The simulation topology is depicted in Fig. 64.1.

A single TCP connection running a long-live FTP application delivers data from 0 to 100 s. We run the simulation for BRJ, Reno and WestwoodNR, respectively. The BER at the wireless bottleneck link varies from 0.01 to 10 %.

The comparison of throughput is shown in Fig. 64.2. For random loss rate smaller than 0.1 %, all TCP schemes perform closely to each other. Besides that,

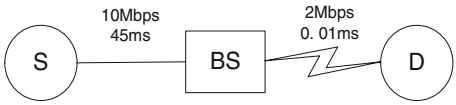

Fig. 64.1 Simulation topology for throughput

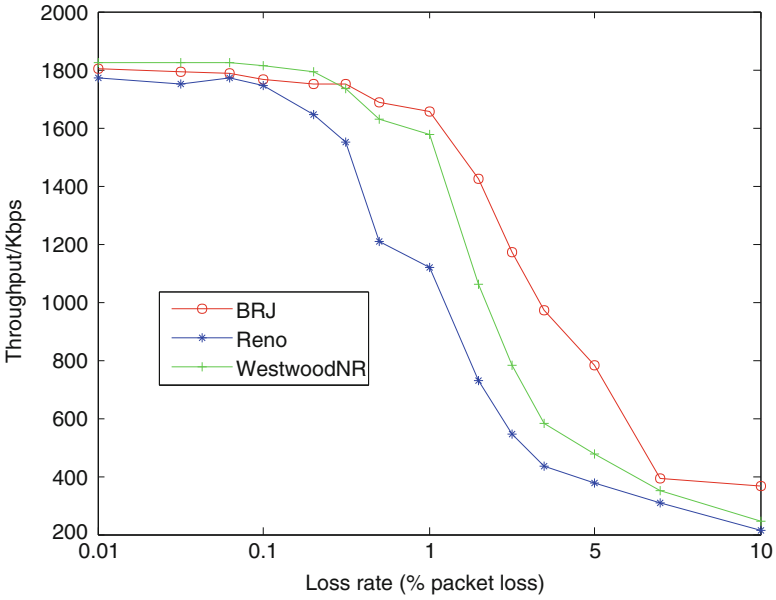

Fig. 64.2 Throughput comparison

BRJ starts to outperform the other TCP variants when loss rate is bigger than 0.1 %. What's more, the throughput of BRJ is especially superior to others when the loss rate varies from 1 to 5 %. At a very practical wireless loss rate, i.e., 2 %, BRJ outperforms WestwoodNR by 34.3 % and Reno by 95.3 %. Furthermore, the advantages of BRJ still exist in various bottleneck bandwidths as shown in Fig. 64.3.

We use the fairness index function proposed in [8] to evaluate the fairness of TCP schemes. Multiple connections of the same TCP scheme must interoperate and converge on their fair share. The simulation topology is shown in Fig. 64.4, where 10 same TCP flows share a 20 Mb/s bottleneck link with 1–5 % BER. We simulate different TCP schemes and the results are shown in Fig. 64.5. We can see that all TCP variants achieve satisfactory fairness index. What's more, from Fig. 64.6, which show the total throughput of 10 TCP flows, we can see that TCP BRJ greatly improves bandwidth utilization of bottleneck link compared to the others.

A friendly TCP scheme should be coexisted with other TCP variants and not cause them starvation. To verify the friendliness of TCP BRJ towards TCP Reno, we use the simulation topology in Fig. 64.4. There are 10 TCP flows running

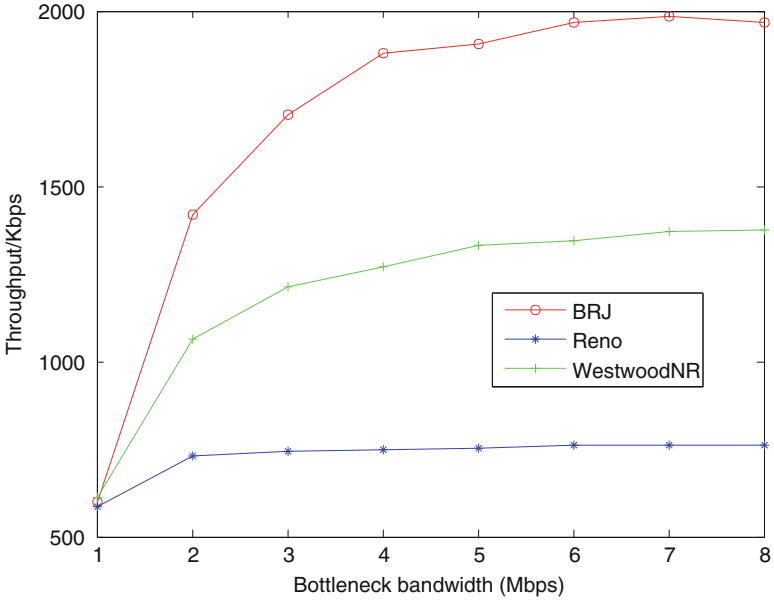

Fig. 64.3 Throughput in different bottleneck

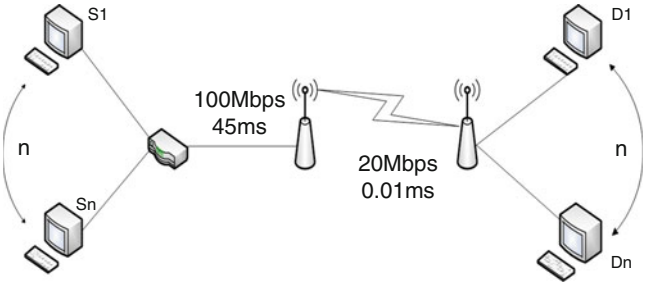

Fig. 64.4 Simulation topology for multiple flows

together through a bottleneck link with 0.1 % BER, where m TCP BRJ flows coexist with n TCP Reno flows. We vary the flows proportion of these two TCP schemes by adjusting the variables m and n. All ten connections are expected to share the bottleneck bandwidth equally, i.e., roughly 2 Mbps per connection.

The results are show in Fig. 64.7. It is observed that the bandwidth allocation of each TCP connection is close to its fair share at bottleneck link, except that TCP BRJ achieves a slightly higher throughput than Reno, but within a tolerable range.

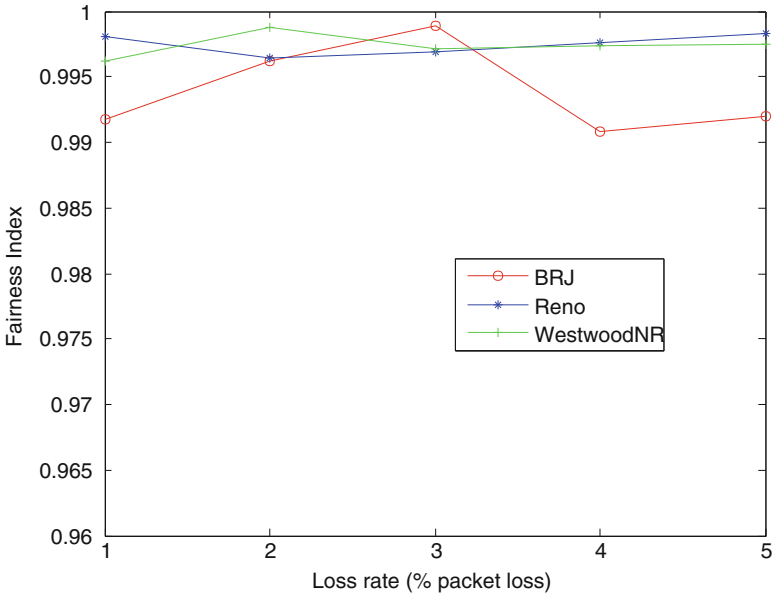

Fig. 64.5 Fairness index comparison

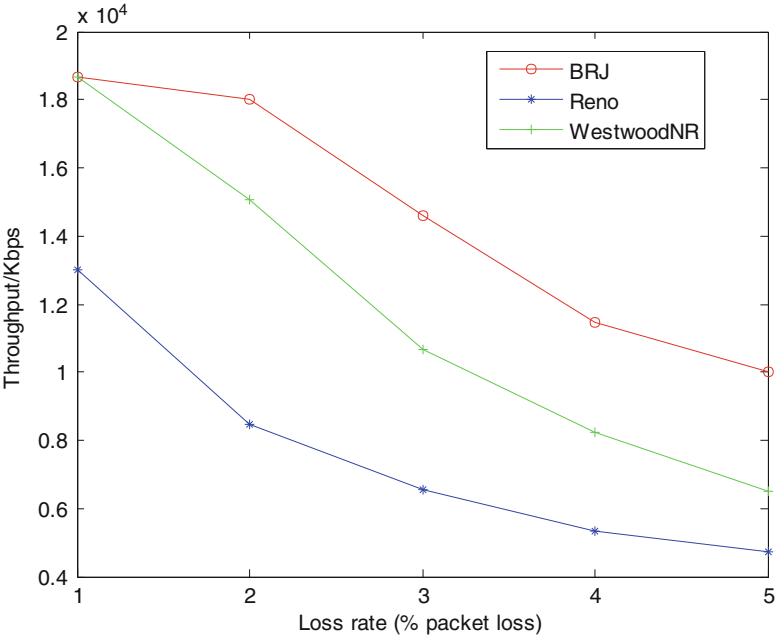

Fig. 64.6 Total throughput comparison

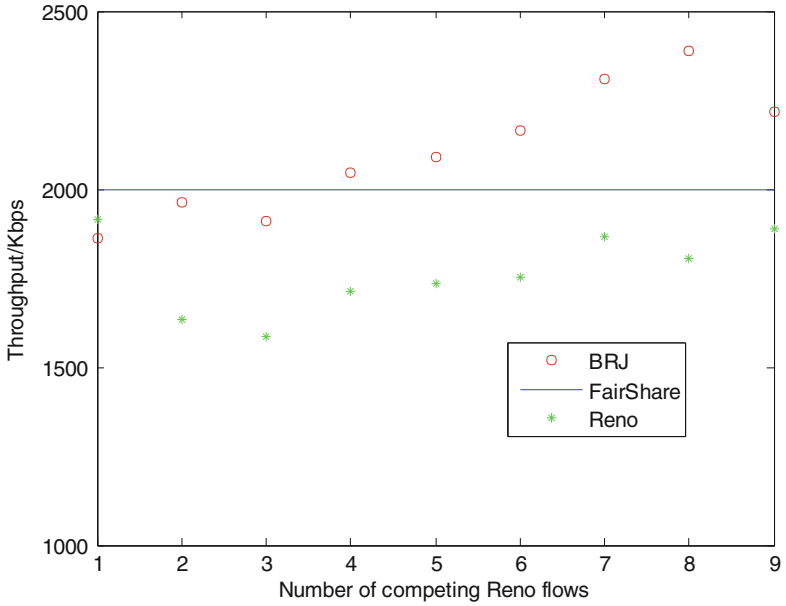

Fig. 64.7 Friendliness of BRJ towards Reno

Conclusion

In this paper, we propose a new TCP scheme, TCP BRJ, to improve the TCP performance in the wired/wireless heterogeneous networks. TCP BRJ has an improved slow-start phase and realizes a novel congestion avoidance phase. Moreover, it proposes a loss differentiation mechanism. The simulation results show that TCP BRJ provides a significant performance improvement in throughput, bandwidth utilization and fairness than others in heterogeneous networks with high BER, especially 1–2 %, a typical characteristic of wireless link. And for practical purpose, TCP BRJ is friendly towards TCP Reno.

Acknowledgment This work is supported by the Fundamental Research Funds for the Central Universities Project No. ZYGX2012J020.

References

1. Tsaoussidis V, Matta I (2002) Open issues on TCP for mobile computing. Wirel Commun Mob Comput 2:3–20
2. Byun HJ, Lim JT (2005) Explicit window adaptation algorithm over TCP wireless networks. IEE Proc Commun 152:691–696

3. Klemm F, Ye Z, Krishnamurthy SV et al (2005) Improving TCP performance in ad hoc networks using signal strength based link management. Ad Hoc Netw 3:175–191
4. Yanxiang Z, Fang S, Mingyan K (2010) A fuzzy packet loss differentiation algorithm based on Ack-timeout times ratio in heterogeneous network. In: IEEE international conference on Communications and Mobile Computing (CMC), vol 1, pp 453–457
5. Gerla M, Ng BKF, Sanadidi MY et al (2004) TCP Westwood with adaptive bandwidth estimation to improve efficiency/friendliness tradeoffs. Comput Commun 27:41–58
6. Stevens WR, Allman M, Paxson V (1999) TCP congestion control. Consultant
7. Henderson T, Floyd S, Gurtov A, Nishida Y (2012) The NewReno modification to TCP's fast recovery algorithm. RFC6582
8. Jain R, Chiu DM, Hawe WR (1984) A quantitative measure of fairness and discrimination for resource allocation in shared computer system. Digital Equipment Corporation, Eastern Research Laboratory, Hudson

Chapter 65
Unique Characteristics of Half-Filling Photonic Bandgap Fiber Sagnac Interferometer and Their Applications as Sensor and Switch

Tingting Han

Abstract Transmission characteristics of a half-filling photonic bandgap fiber Sagnac interferometer are investigated. The temperature responses of the interference dips are further studied. They are fully related to the temperature responses of the phase birefringence and group birefringence. Two of the interference dips have opposite shift direction and different temperature responses. An ultrahigh sensitivity temperature sensor with sensitivity of −20 nm/°C is achieved. In addition, the transmission loss at a certain wavelength changes with temperature changing, and an optical switch with extinction ratio of 45 dB is achieved.

Keywords Photonic crystal fiber • Photonic bandgap fiber • Sagnac interferometer • Fiber sensor

65.1 Introduction

High birefringent (HiBi) fiber Sagnac interferometers (SI) have been widely applied in the optical sensing and the optical communication [1]. Based on the high thermo-optic coefficient of the conventional HiBi fibers, temperature sensors based on SI with sensitivity of 0.94 nm/°C have been reported [2]. HiBi photonic crystal fibers (PCFs) with low thermo-optic coefficient have been widely used in the temperature insensitivity sensors based on SI [3, 4]. Besides, the air-holes structures of the PCFs provide more convenience for the infusion of the active functional materials. This opens up a new area for the realization of the HiBi PCFs. Based on the high thermo-optic coefficient of some materials, the sensors based on the SI have ultrahigh temperature sensitivity [5]. A compact temperature sensor based on a fiber loop mirror (FLM) combined with an alcohol-filled HiBi PCF is

T. Han (✉)
College of Electronic and Communication Engineering, Tianjin Normal University, Tianjin 300387, China
e-mail: hanting608@163.com

J. Mu et al. (eds.), *The Proceedings of the Third International Conference on Communications, Signal Processing, and Systems*, Lecture Notes in Electrical Engineering 322, DOI 10.1007/978-3-319-08991-1_65

demonstrated [5], and the sensitivity reaches to 6.6 nm/°C. In addition, the HiBi photonic bandgap fibers (PBGFs) possess unique birefringence characteristics, and the HiBi PBGFs based on the SI for sensing physical parameters have unique features, such as the temperature and the strain sensitivity are very much dependent upon the wavelength [6]. Nevertheless, few researches study the SI based on the HiBi PBGFs realized by filling the high index fluids. Only in 2008, Du et al. [7] first place a HiBi PBGF which is realized by infusing the anisotropic liquid crystal into a SI, and realize the electrically tunable Sagnac filter. The SI based on the HiBi filling PBGFs will have wide and bright prospects in sensing.

In this paper, we investigate the transmission characteristics of the SI based on a half-filling photonic bandgap fiber by only filling half of the air holes of the PCF with high index fluid. The temperature responses of these interference dips are further discussed. And they are fully related to the temperature responses of the phase birefringence and group birefringence. Not only some dips have opposite shift direction and different shift velocities, but also the transmission loss at a certain wavelength changes with the temperature. Utilizing the features, a high sensitivity temperature sensor with sensitivity of −20 nm/°C and an optical switch with extinction ratio of 45 dB are realized. We believe the SI based on the half-filling PBGFs have very large capacity for multi-sensing and optical devices.

65.2 Theoretical Simulation of Birefringence

The cross-section of the PCF used in our theoretical simulation fabricated by Yangtze Optical Fiber and Cable Corporation Ltd. of China, is shown in Fig. 65.1a. This pure silica PCF includes five rings of air holes arranged in a regular hexagonal pattern. The diameters of the holes, the inner holes distance, and the diameter of the core are 3.7, 5.8, and 7.9 μm, respectively. Figure 65.1b shows the theory model for simulation. The white holes are air holes, and the red holes are high index fluids produced by Cargille Laboratories Inc with the refractive index of 1.52 at wavelength of 583 nm and temperature of 25 °C and the thermal coefficient of −0.000407/°C.

The half-filled fiber guides light by both photonic bandgap effect and total internal reflection, and possesses birefringence characteristics. The phase birefringence B and group birefringence B_g are expressed as follows:

$$B = \left|n_x - n_y\right|, \tag{65.1}$$

$$B_g = B - \lambda \cdot \frac{dB}{d\lambda} \tag{65.2}$$

Where, n_x and n_y are the effective indices of the x-polarization and y-polarization core fundamental mode. Then we place the half-filling PBGF into

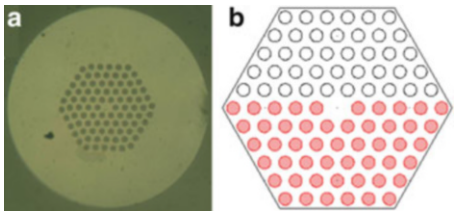

Fig. 65.1 (**a**) The cross-section of the PCF used in our paper. (**b**) The theory model for simulation, and the *white holes* are air holes and the *red holes* are high index fluids

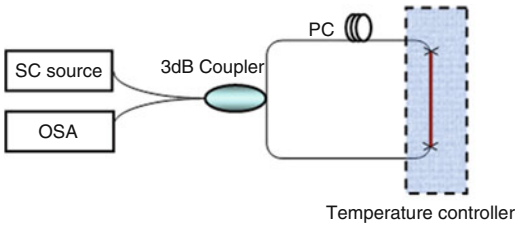

Fig. 65.2 The Sagnac interferometer device for simulation

the Sagnac interference device, as shown in Fig. 65.2, and the transmission *T*r can be expressed as the equation:

$$T\mathrm{r} = \sin^2(\delta/2) = \sin^2(\pi LB/\lambda), \tag{65.3}$$

Where, L is the filling length, and δ is the phase difference. The position of the interference dip λ(T) satisfies the equation:

$$\frac{2\pi B(\lambda, T)L}{\lambda(T)} = 2k\pi, \tag{65.4}$$

Where, k is the integer. We deduce the variation of the S (T) with the temperature changing as follows:

$$\frac{d\lambda}{dT} = \frac{\frac{dB(\lambda,T)}{dT} \times \lambda(T)}{B_g(\lambda, T)} \tag{65.5}$$

It can be seen that $\frac{d\lambda}{dT}$ is related to $\frac{dB(\lambda,T)}{dT}$ and $B_g(\lambda, T)$, hence we need to calculate the variation of the phase birefringence $\frac{dB(\lambda,T)}{dT}$ and the group birefringence $B_g(\lambda, T)$ with the temperature T changing.

We calculate the effective indices of the x-polarization (n_x) and y-polarization (n_y) core fundamental modes through the theory model as shown in Fig. 65.1b using the finite element method (FEM) [8]. According to Eq. (65.1) and the thermal coefficient of the high index fluid, we calculate the B, B_g with temperature increasing from 25 to 55 °C, as shown in Fig. 65.3. The B and the B_g have 10^{-5} and 10^{-4}

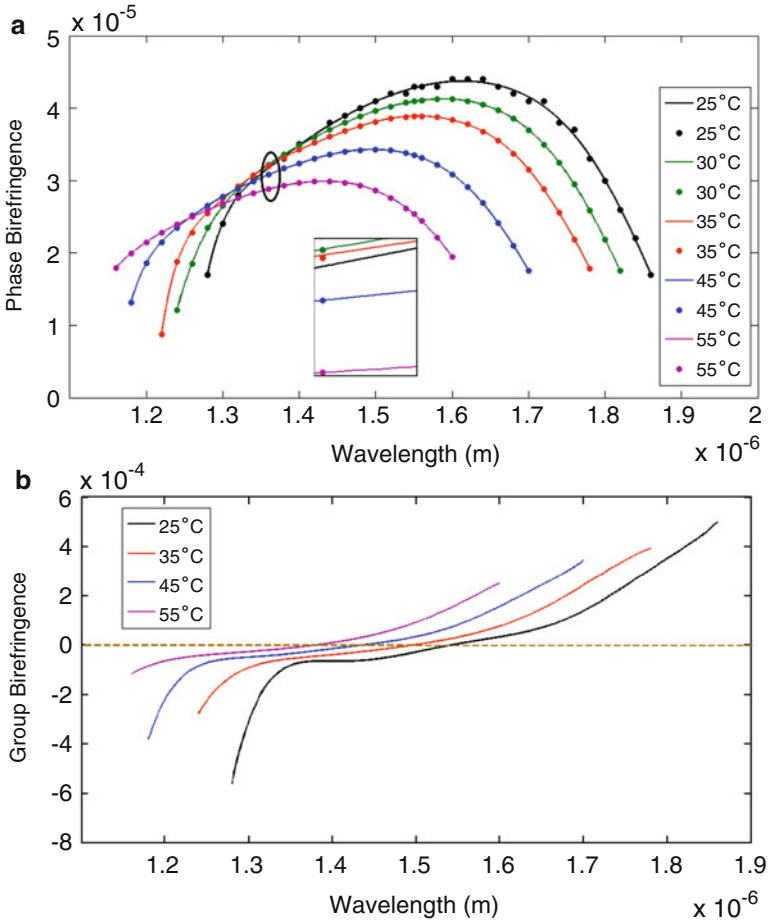

Fig. 65.3 The phase birefringence B (**a**) and the group birefringence Bg (**b**) dependence on the temperature

order of magnitude, respectively. And the B first increases and then decreases with wavelength increasing, and the B_g have a value $B_g = 0$ at a certain wavelength and increases monotonously with temperature. Besides, the B and the B_g both shift to the short wavelength with temperature increasing.

Furthermore, there is a wavelength area λ_a, if the wavelength $\lambda > \lambda_a$, the B decreases with temperature increasing, i.e. $dB(\lambda,T)/dT < 0$; on the contrary, if the wavelength $\lambda < \lambda_a$, the B increases with temperature increasing, i.e. $dB(\lambda,T)/dT > 0$. Combination with the $B_g(\lambda,T)$, we can deduce using Eq. (65.5) that the change of the interference dip with temperature changing will have inverse tendency in the λ_a area's two sides.

65.3 Theoretical Simulation of SI

According to Eq. (65.2), the filling length L and the phase birefringence B will affect the transmission Tr, so we will discuss the variation of the transmission spectra with the change of the L and the B, respectively.

Figure 65.4a, b show the transmission spectra with different filling length from 11 to 14 cm and from 15 to 18 cm, respectively. Contrast the two figures, we find with the L increasing, the two figures have similar variation trend. In each figure, with the L increasing, there are two groups of the interference dips which have opposite shift direction, resulting in the spacing between the two dips in the middle of the bandgap

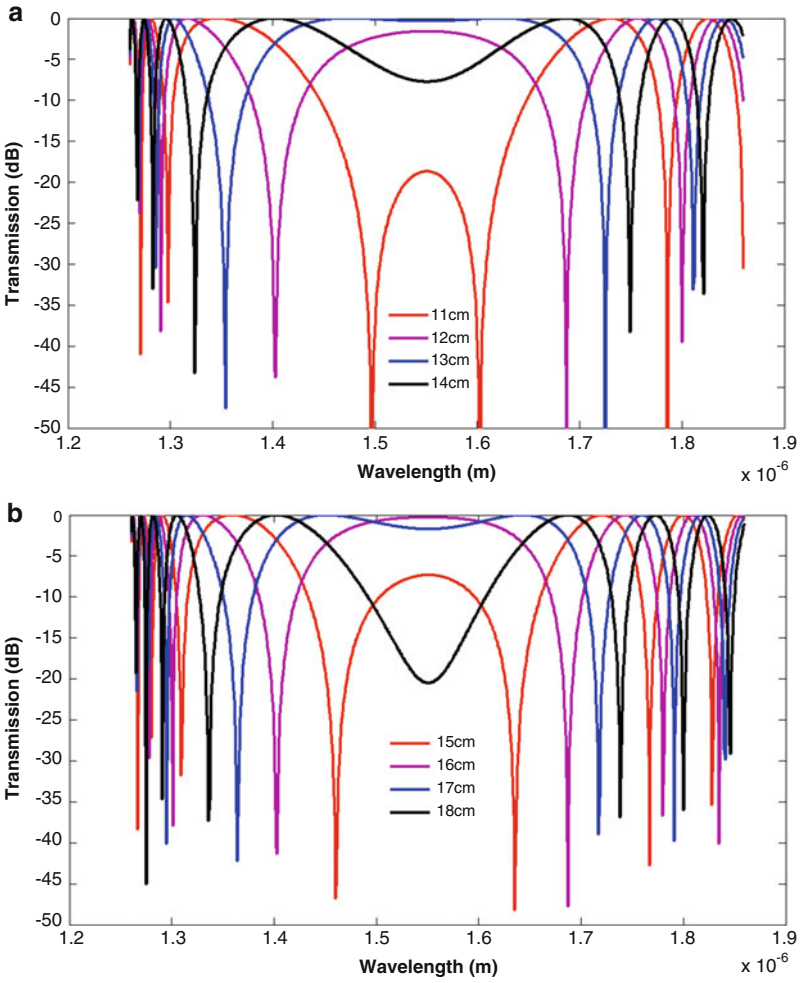

Fig. 65.4 The transmission spectra with different filling length (**a**) from 11 to 14 cm and (**b**) from 15 to 18 cm

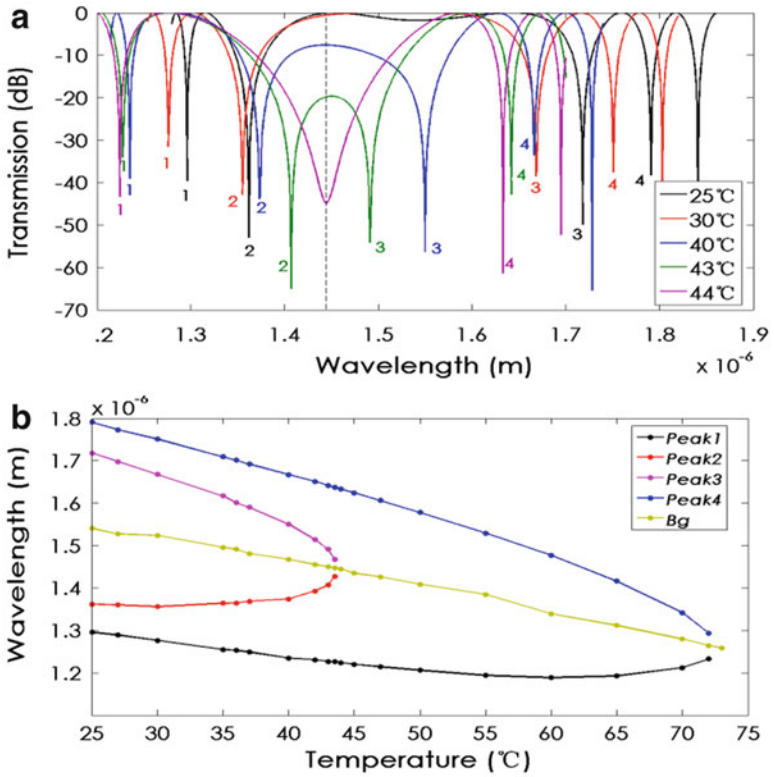

Fig. 65.5 (**a**) The transmission spectra at different temperature with the filling length of 17 cm. (**b**) The specific shift of the four dips as shown in (**a**) with temperature increasing

broadening. Furthermore, when the L increases to 14 cm (in Fig. 65.4a) or 18 cm (in Fig. 65.4b), a large loss appears in the middle of the bandgap.

Next, we depict the transmission spectra at different temperature with the filling length of 17 cm, as shown in Fig. 65.5. Five interference dips with unequal interval appear. We follow the four dips: dip 1 at 1,296 nm, dip 2 at 1,362 nm, dip 3 at 1,718 nm and dip 4 at 1,791 nm. With temperature increasing, dips 1, 3, 4 shift to the short wavelength. For dip 2, from 25 to 30 °C, it shifts to the short wavelength, and from 30 to 43 °C shifts to the long wavelength. The space between the two dips 2 and 3 reduces gradually, and at 44 °C they merge and a wide loss dip appears. If increasing the temperature continually, the depth of the wide dip decreases until it disappears at 55 °C. In addition, start with 55 °C, dip 1 starts change its shift direction and shifts to the long wavelength. The space between the dips 1 and 4 also decreases gradually. The specific variations of the interference dips versus wavelength are shown in Fig. 65.5b.

These unique variation tendencies of the interference dips can be explained using Eq. (65.5). The expression $\frac{d\lambda}{dT}$ is related to $\frac{dB(\lambda,T)}{dT}$ and $B_g(\lambda, T)$. We depict the

wavelength at which the B_g is zero dependence on the temperature in the Fig. 65.5b. It can be seen dips 1 and 2 locate the area in which the $B_g(\lambda, T)$ is negative, while dips 3 and 4 locate the area in which the $B_g(\lambda, T)$ is positive. From temperature 25 to 30 °C, for dip 2, the B increases with temperature increasing. Hence, according to Eq. (65.5), the value $\frac{d\lambda}{dT}$ is negative, resulting dip 2 shifts to the short wavelength. However, start with 30 °C, the B decreases with temperature increasing, and dip 2 shifts to the long wavelength. And for dip 3, the B always decreases with temperature increasing. Furthermore, at its wavelength the $B_g(\lambda, T)$ is positive. So it always shifts to the short wavelength. And with temperature increasing, dips 2 and 3 get closer to the wavelength at which the $B_g(\lambda, T)$ is zero, resulting in smaller value of $B_g(\lambda, T)$. Hence, with temperature increasing, the shift velocity of the two dips increases, as shown in Fig. 65.5b, and from 40 to 43 °C, a sensitivity of −20 nm/°C is achieved. Until the temperature reaches to 44 °C, two dips almost meet the wavelength at which the $B_g(\lambda, T)$ is zero, and they disappear. The variation tendencies of the dips 1 and 4 is similar to the dips 2 and 3, we won't repeat the details again.

In addition, from the inset of the Fig. 65.6, we find the transmission loss at wavelength of 1,445 nm changes with temperature increasing. And we show the variation of the transmission loss at the wavelength of 1,445 nm dependence on temperature in the Fig. 65.6. We can see obviously the loss increases with temperature increasing from 25 to 44 °C, and from 40 to 44 °C, it increases sharply. While, it decreases with temperature increasing from 44 to 55 °C, and from 44 to 47 °C, it decrease sharply. Utilizing this feature, we can realize high sensitivity optical switch with the extinction ratio of 45 dB.

65.4 Experimental Realization

In experimental, we utilize the high frequency CO_2 laser (CO_2–H10, Han's laser) to realize the half-filling PBGF. We fix the PCF on a stage and use the CO_2 laser to expose the side of the PCF. Figure 65.7a shows the cross-section of the PCF after

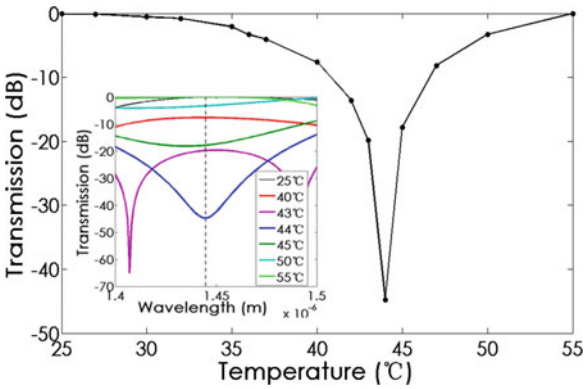

Fig. 65.6 The transmission of the wavelength of 1,445 nm with temperature changing

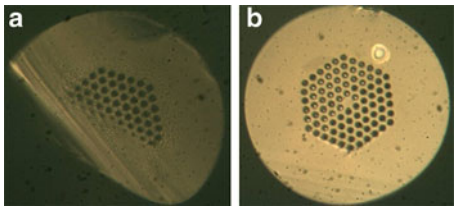

Fig. 65.7 (**a**) The cross-section of the PCF after CO2 laser's side exposure. (**b**) The cross section of the realized half-filling PBGF

CO_2 laser's side exposure, and we can find that half of the air holes are collapsed and the other holes keep open. On this basis, we fill the index-matching fluid into the treated PCF, and then cut off the exposed section of the PCF. The cross section of the half-filling PBGF is realized, as shown in Fig. 65.7b; obviously, only half of the air holes are filled by the fluids and the cross section is well matched with the simulation model shown in Fig. 65.1b.

And the further experiments will be carried out in the future.

Then we compare the unique characteristics of the SI based on the half-filling PBGF to the SIs based on the index guiding HiBi PCFs [5] and the HiBi PBGFs [6]. The phase birefringence of the index-guiding HiBi PCF is linear change with the wavelength and has 10^{-4} order of the magnitude, resulting in the same shift direction of the interference dips. The group birefringence of the HiBi PBGF in [6] has the tendency of low values in the middle of the bandgap and lager values in the edges of the bandgap. And the values are all positive at the bandgap. These results are different from our results. One of the reasons may be that the bandgaps studied by us are different bandgaps which are formed from the coupling of the different cladding modes. About the deep reason, we will take further study.

Conclusion

In conclusion, we theoretically analyze the temperature characteristics of the transmission spectra of the SI based on the HiBi half-filling PBGF. The shift features of the interference dips are related to the temperature response of the B and the B_g. And an optical switch with extinction ratio of 45 dB and a sensitivity of -20 nm/°C are achieved from temperature 40 to 43 °C.

Acknowledgement This work is funded by the Doctoral Scientific Foundation of Tianjin Normal University (52XB1307).

References

1. Vali V, Shorthill RW (1976) Fiber ring interferometer. Appl Opt 15:1099–1100
2. Liu Y, Liu B, Feng X, Zhang W, Zhou G, Yuan S, Kai G, Dong X (2005) High-birefringence fiber loop mirrors and their applications as sensors. Appl Opt 44:2382–2390

3. Zhao C, Yang X, Lu C, Jin W, Demokan MS (2004) Temperature-insensitive interferometer using a highly birefringent photonic crystal fiber loop mirror. IEEE Photon Technol Lett 16:2535–2537
4. Fu HY, Tam HY, Shao L-Y, Dong X, Wai PKA, Lu C, Khijwania SK (2008) Pressure sensor realized with polarization-maintaining photonic crystal fiber-based Sagnac interferometer. Appl Opt 47:2835–2839
5. Qian W, Zhao C, He S, Dong X, Zhang S, Zhang Z, Jin S, Guo J, Wei H (2011) High-sensitivity temperature sensor based on an alcohol-filled photonic crystal fiber loop mirror. Opt Lett 36:1548–1550
6. Kim G, Cho T, Hwang K, Lee K, Lee KS, Han YG, Lee SB (2009) Strain and temperature sensitivities of an elliptical hollow-core photonic bandgap fiber based on Sagnac interferometer. Opt Express 17:2481–2486
7. Du J, Liu Y, Wang Z, Zou B, Liu B, Dong X (2008) Electrically tunable Sagnac filter based on a photonic bandgap fiber with liquid crystal infused. Opt Lett 33:2215–2217
8. Cucinotta A, Selleri S, Vincetti L, Zoboli M (2002) Holey fiber analysis through the finite-element method holey fiber analysis through the finite-element method. IEEE Photons Technol Lett 14:1530–1532

Part VII
Image and Video Processing, Digital Signal Processing

Chapter 66
Image Fusion in Compressed Sensing Based on Non-subsampled Contourlet Transform

Xin Zhou, Wei Wang, and Rui-an Liu

Abstract A fusion method based on non-subsampled contourlet transform (NSCT) in compressed sensing was proposed. The method decomposes two or more original images using NSCT, and gets the sparse matrix by the NSCT coefficients sparse representation, and fuses the sparse matrices with the coefficients absolute value maximum scheme. The compressed sample can be received through randomly observed. The fused image is recovered from the reduced samples by solving the optimization. The simulations show that the proposed CS-based image fusion algorithm has the advantages of simple structure and easy implementation, and also can achieve a better fusion performance.

Keywords Image fusion • Compressive sensing • Non-subsampled contourlet transform

66.1 Introduction

Image fusion uses the different imaging modes of multi-sensor to provide complementary information and increase the amount of the image information for the further processing. It has been widely used in areas such as machine vision, geographic information system and biomedical engineering etc. [1].

Wavelet has become an important means in image fusion for its well-known time frequency localization analysis properties [2]. However, the advantages of the Wavelet transform primarily embody in the analysis and process towards the one dimension segmentation smooth and function of bounded variation. When it has been applied in two dimension or higher dimensional case, the separable wavelet formed by one-dimension wavelet has limited direction, and then can't optimally represent line singularity or face singularity high dimensional function. Therefore, the wavelet transform can only reflect the point singularity of the signal, and can't reflect the two-dimensional image's marginal, linear, characteristics.

X. Zhou (✉) • W. Wang • R.-a. Liu
College of Electronics and Communication Engineering,
Tianjin Normal University, Tianjin, China
e-mail: zhouxintjnu@126.com

J. Mu et al. (eds.), *The Proceedings of the Third International Conference on Communications, Signal Processing, and Systems*, Lecture Notes in Electrical Engineering 322, DOI 10.1007/978-3-319-08991-1_66

In multi-resolution decomposition fusion algorithm, the introducing of the wavelet transform algorithm would cause high frequency noise, and then the fused image's quality would be influenced by it [3]. To improve the above mentioned disadvantages of the wavelet transform, Minh. N. Do and Martin Vetterli proposed the two-dimensional image representation: contourlet transform theory in 2002. The anisotropic characteristics of the theory are beneficial to the high efficient representation of the image marginal information. The main features of the transform is the good directivity and anisotropy [4]. It not only has the multi-scale characteristic of the wavelet transform but also the good directivity and anisotropy which is not provided by the wavelet transform. Therefore, it can be better applied in the image process.

66.2 Non-subsampled Contourlet Transform

In the construction process of the contourlet, gibbs phenomenon would inevitably appear, because the under sampling operation in Laplacian pyramid and directional filter would make the contourlet transform not possessing the translation invariance [5–8]. To eliminate the phenomenon, A.L. Cunha, etc. have applied the non-under sampling pyramidal decomposition and the non-under sampling directional filter to realize the non-subsampled contourlet transform.

NSCT contains a series of filters. Figure 66.1 has given the structure diagram of NSCT. The filters have divided the two-dimensional frequency plane in the sub-band. The non-under sampling pyramidal decomposition, has made the NSCT acquiring multi-scale property. And the non-under sampling directional filter has made the NSCT acquiring multi-direction property. The integration of the two has made the NSCT not only inherit the multi-scale property and multi-direction property, but also has the translation invariance, and then the gibbs phenomenon can be effectively eliminated.

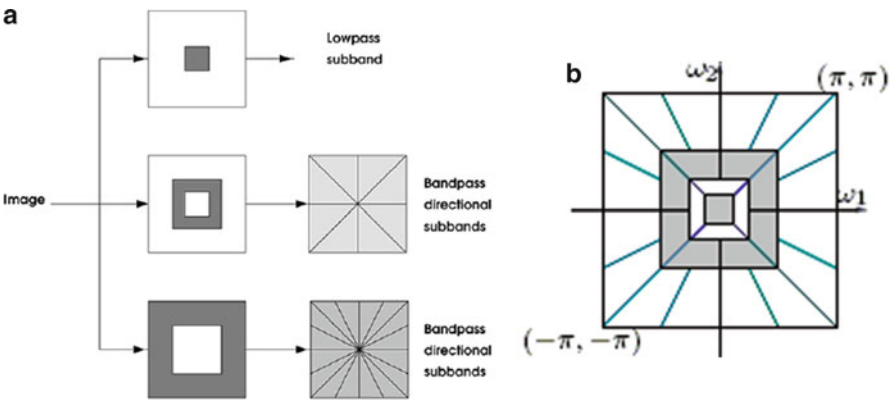

Fig. 66.1 Non-subsampled contourlet transform. (**a**) NSCT transform (**b**) frequency partitioning obtained with the NSCT

66.3 Compressive Sensing and Image Fusion

Compressive sensing enables a sparse or compressible signal to be reconstructed from a small number of non-adaptive linear projections, thus significantly reducing the sampling and computation costs [9]. CS has many promising applications in signal acquisition, compression and medical imaging. In this paper, we investigate its potential application in the image fusion.

As far as a real-valued finite-length one-dimensional discrete-time signal x is concerned, it can be viewed as a R^N space $N \times 1$ dimensional column vector, and the element is $x[n]$, $n = 1, 2, \ldots, n$. If the signal is sparse K, it can be shown as the following formula:

$$x = \psi s \tag{66.1}$$

ψ is the $N \times N$ matrix, s is the coefficient component column vector of dimension $N \times 1$ [10].

When the signal x in the base of ψ has only non-zero coefficients of $K \ll N$ (or greater than zero coefficients), ψ is called the sparse base of the signal x.

The CS theory indicates that if the signal x's (the length is N) transform coefficient which is at a orthogonal basis ψ is sparse (That is, only a small number of non-zero coefficients can be obtained.) if these coefficients are projected into the measurement basic ϕ which is irrelevant to the sparse base ψ, The $M \times 1$ dimensional measurement signal y can be get. By this approach, the signal x's compressed sampling can be realized. The expression can be expressed as:

$$y = \phi x = \phi \psi s = \Theta s \tag{66.2}$$

ϕ is the measurement matrix of $M \times N$, and $\Theta = \phi\psi$ is the $M \times N$ matrix, and it is called the projection matrix. y is the measurement value of the projection matrix Θ, which is relevant to the sparse signal s. Only when the orthogonal basis ψ is irrelevant to the measurement matrix ϕ, that is to say, the projection matrix can satisfy the requirement of Restricted Isometry Property (RIP), the signal x can be accurately recovered via these measured value by solving formula (66.2) in the best optimized way.

$$\min_s \|s\|_{l1} \quad \text{s.t.} \quad y = \phi\psi s \tag{66.3}$$

The advantage of CS theory is that the data obtained via the projection measurement is much smaller than the conventional sampling methods, breaking the bottleneck of the Shannon sampling theorem, so that the high-resolution signal acquisition becomes possible. The attraction of CS theory is that it is for applications in many fields of science and engineering and has important implications and practical significance, such as statistics, information theory, coding theory, computer science theory and other theories.

Compared with the traditional fusion algorithms, the CS-based image fusion algorithm theory has shown significant superiority: the image fusion can be conducted in the non-sampling condition of the image with the CS technique; the quality of image fusion can be improved by increasing the number of measurements; this algorithm can save storage space and reduce the computational complexity. The main ideas of the CS-based image fusion algorithm theory are: first of all, the two images which need to deal with should undergo the NSCT transform; the sparse matrix can be obtained after the NSCT coefficients processed with sparse treatment; and then determine the fusion rules for sparse matrix integration; obtaining compressive sampling through random sampling matrix; finally, the fused image can be obtained in the best optimized way.

The practical function of NSCT transform is the signal de-correlation [11, 12], and all the information of the signal is concentrated into the NSCT coefficients with large amplitude. These large NSCT coefficients contain far more energy than that contained in small coefficient, so that in the reconstruction of the signal, a large coefficient is more important than the smaller one.

This paper adopted the fusion rule which concentrated on the larger absolute value, comparing two NSCT coefficients of the same location in two images, the absolute value which is greater are selected as fusion NSCT coefficients. The expression is as follows:

$$D_f = D_M, \quad \text{and} \quad M = \underset{i=1,2,\cdots,I}{\operatorname{argmax}}(|D_i|) \tag{66.4}$$

The D_f is the fusion NSCT coefficient; D_M is the NSCT coefficient whose absolute value is the largest of the NSCT coefficients in the same location in different images; I is the number of the source image.

The NSCT transform is used to deal with the source image; NSCT coefficients obtained sparse treatment: small coefficient (or coefficient of close to zero) is set to zero, to obtain an approximate sparse coefficient matrix.

When the source image is conducted via sparse transformation, the NSCT is used as the sparse basis. To make the image can be reconstructed with less measurement value the reconstruction, we must ensure the sparse basis ψ and the measurement matrix ϕ is irrelevant, because any random sparse matrix has superiority that it is irrelevant to any sparse basis. That is the reason why it can be used as a measurement measure matrix.

The concrete realization of image fusion algorithm which is based on CS theory is as follows. For each $m \times n$ pixel image conducts NSCT transform to obtain the NSCT coefficients matrix. The NSCT coefficients are processed with sparse treatment, and then the NSCT coefficients are fused according to the larger absolute value rule. For the fused NSCT coefficients, the random matrix is selected as the measurement matrix ϕ, after the measuring, the measured value y can be obtained. By solving the linear programming of the l_1 norm, the approximate solution $\hat{x}$ can be acquired. Conducting the inverse transform to the obtained NSCT coefficients, and thus the fusion image can be acquired.

66.4 Experimental Results and Analysis

The experiments selected the infrared and visible images to conduct the fusion experiment with different approaches, firstly. Figure 66.2 shows image (a) and image (b) respectively represent the infrared and visible images, and the two images contain much detail and texture information; the image (c) represents the fusion result based on the Laplacian pyramid transform; the image (d) the fusion result based on CS and NSCT. As can be seen from the figure, the images (d) is clearer as far as the visual effect is concerned (Table 66.1).

The paper selected another fusion experiment for multi-focus image. Figure 66.3 is the multi-focus image fusion experiment. Figure 66.3 (a) is the in focus image, and image (b) is the far focus image. The image (c) represents the fusion result based on the Laplacian pyramid transform; the image (d) represents the fusion results based on CS and NSCT. As can be seen from the figure, the images (c) have different degrees of blur. Compared to (c), the image (d) is clearer as far as the visual effect is concerned. Figure 66.4 is the mutual information of different sampling rates for multi-focus image fusion. The mutual information values of the compressive sensing image fusion algorithm are the better between the two fusion methods.

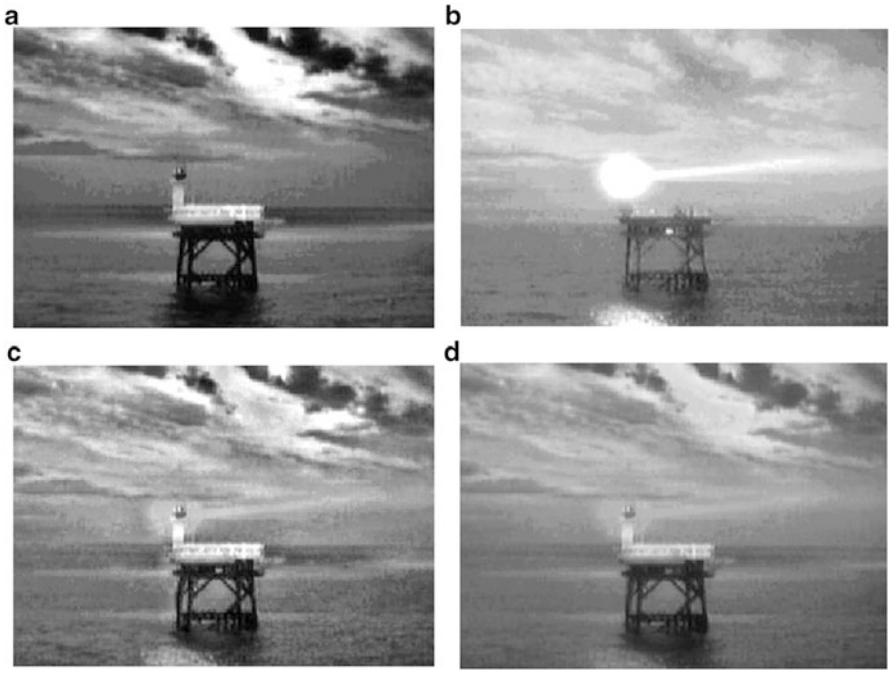

Fig. 66.2 Fusion experiment for infrared and visible image fusion. (**a**) Infrared image (**b**) visible image (**c**) fusion image based on Laplacian pyramid transform (**d**) fusion image based on CS and NSCT

Table 66.1 Comparison of statistical parameters about fusion results according to different fusion rules

	Entropy	Cross entropy	Standard deviation	Average gradient
LP	10.751	0.688	13.610	27.503
CS	11.904	0.977	15.427	29.011

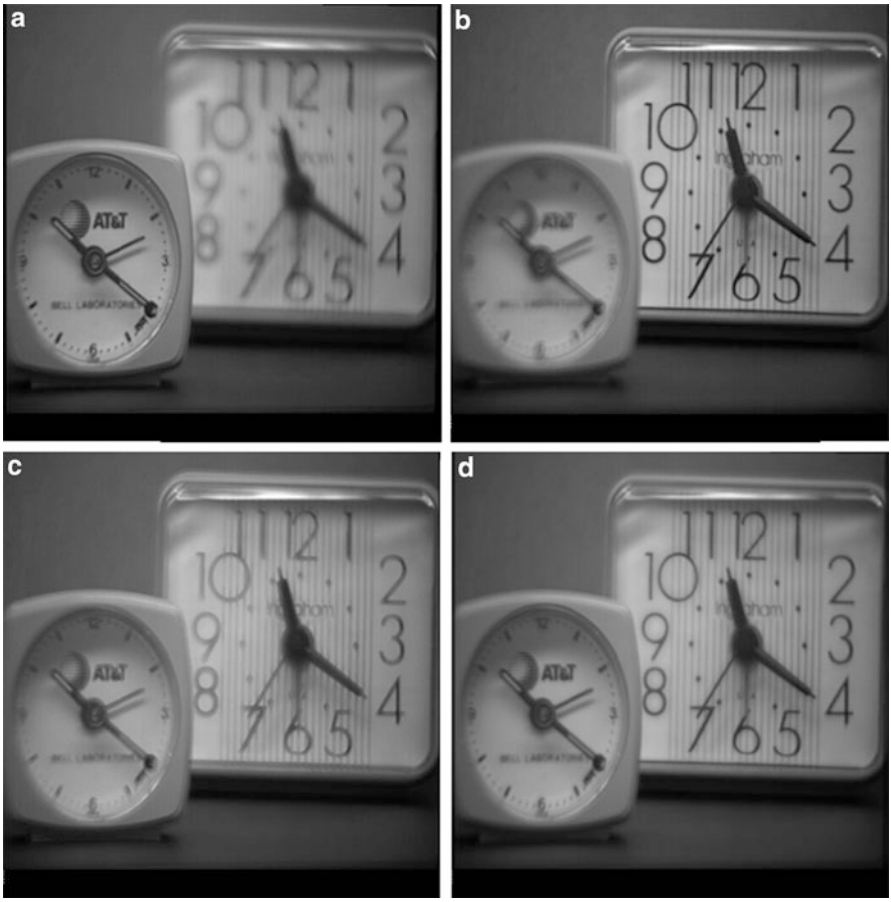

Fig. 66.3 Multi-focus image fusion experiment. (**a**) In focus image (**b**) far focus image (**c**) fusion image based on Laplacian pyramid transform (**d**) fusion image based on CS and NSCT

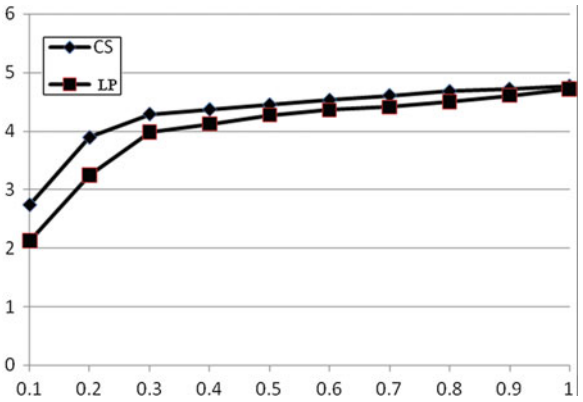

Fig. 66.4 Mutual information of different sampling rates for multi-focus image fusion

Conclusions

The paper put forward an fusion algorithm based on the compressed sensing and NSCT. Compared with the traditional transform, the proposed CS-based image fusion algorithm can preserve the image's feature information, enhance the fused image's space detail representation ability, and improve the fused image's information. The experiment proves that the approach in this paper is better than the wavelet transform and Laplace pyramid decomposition, etc.

Acknowledgment The authors are grateful to the anonymous referees for constructive comments.

References

1. Feng X, Wang X, Dang J, Shen Y (2013) Fusion method for visible light and infrared images based on compressive sensing of non-subsampled contourlet transformation sparsity. Inform Technol J 12(4):672–679
2. Zhou X, Liu R-A, Chen J (2010) Infrared and visible image fusion enhancement technology based on multi-scale directional analysis. IEEE Comput Soc
3. Aiazzi B, Alparone L, Baronti S (2002) Context-driven fusion of high spatial and spectral resolution images based on over-sampled multi-resolution analysis. IEEE Trans Geo-sci Remote Sens 40(10):2300–2312
4. Yi W-j, Yu M, Jiang G-y (2006) Contourlet: efficient directional and multiresolution analytic tool. Appl Res Comput 9(20):18–22
5. Guo X-j, Wang Z-l (2007) Nonsubsampled contourlet image denoising based on inter-scale correlations. J Opto-electron Laser 18(9):1116–1119
6. Zhang Y-f (2007) A fusion method based on nonsampled contourlet transform. Microcomput Inform 23(9–3):283–285
7. Do MN, Vetterli M (2005) The contourlet transform: an efficient directional multiresolution image representation. IEEE Trans Image Process 14(12):2091–2106

8. Zhou J, Cunha AL, Do MN (2005) Nonsubsampled contourlet transform: construction and application in enhancement. In: 2005 international conference on image processing, ICIP, pp 469–472
9. Candes E, Wakin MB (2008) An introduction to compressive sampling. IEEE Signal Process Mag 48(4):21–30
10. Provost F, Lesage F (2009) The application of compressed sensing for photo-acoustic tomography. IEEE Trans Med Imaging 28(4):585–594
11. Tao W, Nishan C, Alin A (2008) Compressive image fusion. IEEE Int Conf Image Process: 1308–1311
12. Jin W, Fu R-d, Ye M (2011) Multi-focus fusion using dual-tree contourlet and compressed sensing. Opto-Electron Eng 38(4):87–94

Chapter 67
Image Compressive Sensing Based on Blended Basis Functions

Ying Tong, Leilei Liu, Meirong Zhao, and Zilong Wei

Abstract Compressive sensing (CS) has given us a new idea at data acquisition and signal processing. It has proposed some novel solutions in many practical applications. Focusing on the image compressive sensing problem, the paper proposes an algorithm of compressive image sensing based on the multi-resolution analysis. We present the method to decompose the images by nonsubsampled contourlet transform (NSCT) and wavelet transform successively. It means that the images can be sparse represented by more than one basis functions. We named this process as blended basis functions representation. Since the NSCT and wavelet basis functions have complementary advantages in the image multi-resolution analysis, and the signals are more sparse after decomposed by two kinds of basis functions, the proposed algorithm has perceived advantages in comparison with compressive sensing in the wavelet domain which is widely reported by literatures. The simulations show that our method provides promising results.

Keywords Blended basis functions • Compressive sensing • NSCT • Wavelet transform

67.1 Introduction

In recent years, compressive sensing (CS) has inspired significant interests because of its compressive capability. It gives us great inspiration to balance the relationship between the quality of imaging and computation complexity.

Y. Tong (✉)
College of Electronic and Communication Engineering,
Tianjin Normal University, Tianjin, China

State Key Laboratory of Precision Measuring Technology and Instruments,
Tianjin University, Tianjin, China
e-mail: tongying2334@163.com

L. Liu • M. Zhao • Z. Wei
State Key Laboratory of Precision Measuring Technology and Instruments,
Tianjin University, Tianjin, China

J. Mu et al. (eds.), *The Proceedings of the Third International Conference on Communications, Signal Processing, and Systems*, Lecture Notes in Electrical Engineering 322, DOI 10.1007/978-3-319-08991-1_67

In this paper, in the first place, we provide a brief description of CS. Then we introduce two kinds of multi-resolution analysis tools as NSCT and wavelet transform, since they have good performances in the image multi-resolution analysis and their advantages are complementary. In Sect. 67.4, we explore the idea of applying blended basis functions to the CS domain. For this purpose, NSCT and wavelet blended basis functions and wavelet basis alone are employed to sparse represent the same image. The image is then reconstructed via OMP algorithm. The performances of the two methods show that blended basis functions provide a promising result in CS. Finally, conclusions and suggestions for future work are given in Sect. 67.5.

67.2 Brief Description of CS

In 2006, Donoho D. L. demonstrated that many natural signals which are sparse or compressible can be accurately represented by a set of low-dimensional projections that preserve the structure of the signal; the signal can be then reconstructed from these projections using an optimization process [1]. The theory is now known as compressive sensing.

Natural signals are usually not sparse in the time domain. But when we transform the signals into an appropriate basis (wavelet basis for example), most of the coefficients will turn to be zero or close to zero. That is the signals will present sparse features in some domain. Consider a real-valued, finite-length, one-dimensional signal [2] $f \in R^N$, if it can be represented as a linear combination of a set of standard orthogonal basis, such as:

$$f = \psi\theta \tag{67.1}$$

where ψ is some basis and θ is a vector containing only $K \ll N$ nonzero coefficients; we can say that f is K-sparse in domain ψ, and ψ is a sparse basis for signal f. If the signal is sparse in some domain, it means that it is compressible and it can be well approximated by K-sparse representations.

If a signal is compressible, the compressive measurements can be taken on it, it is represented as:

$$y = \phi f = \phi\psi\theta = \Theta\theta \tag{67.2}$$

where $y \in R^M$ and$\varphi$is an $M \times N$ matrix ($M < N$). In CS, φ is called the measurement matrix. It seems to be an ill-posed problem to recover signal f from the measurements y, but CS theory provides that it is possible to reconstruct the signal through some optimization algorithm. CS presents the method to capture and represent compressible signals at an incredible low rate.

67.3 Introduction to Multi-resolution Analysis Tools

In the image compressive sensing process, the commonly used sparse representation tool is wavelet transform, which is also a widely used multi-resolution analysis function. Some papers have reported that many multi-resolution analysis tools can be used as sparsifying transform [3–5]. In this section, two multi-resolution analysis tools, wavelet transform and nonsubsampled contourlet transform (NSCT), are selected for comparative analysis. It can be seen that the two basis functions have their own features and their advantages are complementary.

67.3.1 Wavelet Transform

Wavelet transform can decompose the signals into different scales with different levels of resolution by dilating a prototype function. That is to decompose the signal into shifted and scaled versions of the mother wavelet [6]. Any details of the signals can be focused adaptively by wavelet transform, so it is called "digital microscope". It also shows good performance in two-dimensional signals processing such as image denoising, enhancement and fusion. However, since the 2-D wavelet transform has only limited number of directions, it cannot express the high-dimensional signals that have line singularity optimally. But line singularity is a typical performance of the edges in natural images, wavelet transform show its deficiency in the processing of edge signals.

67.3.2 Nonsubsampled Contourlet Transform

Nonsubsampled contourlet transform is proposed based on the contourlet transform. NSCT not only has the frequency characteristic of multi-resolution, but also has the feature of anisotropic, so it can have a good grasp of the geometry of the image. The basic idea of NSCT is to use the nonsubsampled pyramid decomposition to decompose the image into multiple scales. And then through the nonsubsampled directional filter bank, the signals of each scale are decomposed into different directional sub-bands. The number of sub-bands in each scale can be any power of 2. NSCT has no down-sampling process in the two-step decomposition, so it has the feature of translation invariant [7]. Since NSCT has the directional characteristics, its advantage of image edge processing is obvious.

67.3.3 The Idea of Blended Basis Function

Through the above analysis on the characteristics of wavelet transform and NSCT, we can see that the two algorithms have complementary advantages. Literature [8] proposed a novel algorithm that combines two multi-resolution analysis functions to fuse the image. The method provides better result than the traditional multi-resolution based image fusion.

In this paper, we call the process of decomposing the signals by two basis functions successively as blended basis functions representation. Considering that the blended basis functions has given promising results in the multi-resolution based image fusion, and wavelet basis which is a commonly used basis function is also widely used in CS, we propose to explore the application of CS based on blended basis functions.

67.4 Applying Blended Basis Functions in CS

Blended basis functions are the combination of two multi-resolution analysis tools. The two functions, NSCT and wavelet, are cascaded. The image has already been decomposed into multi-scales by NSCT before the sparse representation of wavelet. After NSCT decomposition, the signals of each scale has already been sparse presented to some extend and the high-frequency parts are more sparse than low-frequency parts. And then these sparse signals are sparse represented by wavelet basis. That is the signals are sparse represented twice by two kinds of basis functions successively, which can effectively enhance the sparsity of the signals. From the theory of CS, we can see that if the signal is more sparse, the less measurements are needed to reconstruct the signal; or the reconstruction result will be more ideal when the same number of measurements are taken.

In order to test the feasibility of applying blended basis functions in CS, the experiments will compare the reconstruction results of blended basis functions as sparse basis with single wavelet basis as sparse basis. The comparison is performed on an image with the size of 256×256. The simulation results on Matlab platform are shown in Fig. 67.1. The measurement matrix is random matrix and OMP algorithm is chosen for the reconstruction algorithm.

In Fig. 67.1, the images in the left group are sparse represented by wavelet basis; while the images in the other group are sparse represented by blended basis functions. The images of the same row are recovered from the same number of measurements. From the comparison in the images of the same row, it can be seen obviously that the reconstruction results of the images on the right side are much better than the ones on the left, especially at the edges and details sections. When the images are compared vertically, we can find that with the reduction in the number of measurements, the reconstruction results of the images in the two columns are decline gradually, but there is a clear performance improvement by

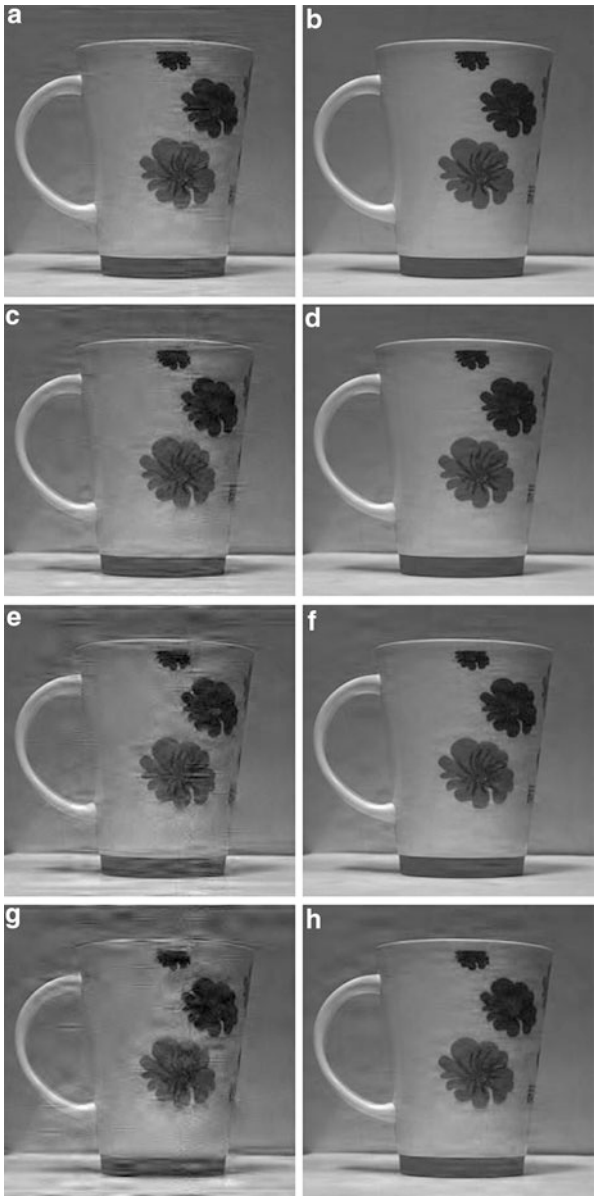

Fig. 67.1 The comparison of CS reconstruction results (**a**) wavelet basis M/N = 74.2 % (**b**) blended basis functions M/N = 74.2 % (**c**) wavelet basis M/N = 58.6 % (**d**) blended basis functions M/N = 58.6 % (**e**) wavelet basis M/N = 50.8 % (**f**) blended basis functions M/N = 50.8 % (**g**) wavelet basis M/N = 43.0 % (**h**) blended basis functions M/N = 43.0 %

using the blended basis functions when fewer measurements are used. The objective evaluation results in Table 67.1 confirm our conclusion. The values of PSNR show that the proposed algorithm improves the image reconstruction quality obviously.

Table 67.1 PSNR of the reconstructed image

	74.2 %	58.6 %	50.8 %	43.0 %
Wavelet basis	34.5160	32.3963	29.9405	27.9680
Blended basis functions	39.8186	38.0513	36.5466	34.6952

Conclusions

In the paper, we present a feasible image compressive sensing algorithm in the CS domain. Blended basis functions, two kinds of basis functions used successively, are used to sparse represent the images. Since the sparsity of the signals can be enhanced and the advantages of the two multi-resolutions tools are complementary, the proposed algorithm shows promising results in the CS domain.

However, there are still many issues that remain unsolved in this paper. For example, other multi-resolution tools such as directionlets transform, contourlet transform and so on, can be choose to form blended basis functions. And the performances of different combination of basis functions can be compared and analyzed. We will also explore the application of blended basis functions in the CS domain image processing.

References

1. Donoho DL (2006) Compressed sensing. IEEE Trans Inform Theor 52(4):1289–1306
2. Baraniuk RG (2007) Compressive sensing. IEEE Signal Process Mag: 118–124
3. Lian Q, Chen S (2010) Sparse image representation using the analytic contourlet transform and its application on compressed sensing. Acta Electron Sin 38(6):1–6
4. Kim D-O (2010) Evaluation of image quality using dual-tree complex wavelet transform and compressive sensing. Electron Lett 46(7):494–495
5. Zhou X, Wang W, Liu R-a (2014) Compressive sensing image fusion algorithm based on directionlets. EURASIP J Wireless Commun Netw 2014:19
6. Mallat SG (1989) A theory for multiresolution signal decomposition: the wavelet representation. Pattern Anal Mach Intell 11(7):674–693
7. Do MN, Vetterli M (2005) The contourlet transform: an efficient directional multiresolution image representation. IEEE Trans Image Process 14(12):2091–2106
8. Bin Y (2005) Researches on novel methods for pixel level multi-sensor image fusion. Zhengzhou University of Light Industry, Hunan, pp 31–33

Chapter 68
Cloud Storage Architecture with Meta-Data Service Layer in Cloud Computing

Kai Fan, Libin Zhao, Hui Li, and Yintang Yang

Abstract With the rise of cloud computing, cloud storage has become a challenging issue. It is a huge challenge to design a distributed file architecture to meet the requirements of cloud storage. In this paper, in order to improve the system reliability and performance, we propose a cloud storage architecture with a meta-data service layer. The proposed architecture is a distributed file storage system based on the master-slave architecture, which uses multiple proxy servers of the meta-data server to establish a peer-to-peer meta-data service layer. Each meta-data server and the proxy server, could be an access to service for clients rather than only one fixed access as usual, which can improve the parallel processing performance of a meta-data service layer greatly. Some P2P techniques are used between proxy servers to solve the disadvantages of the master-slave architecture efficiently. Analysis and evaluation are performed to demonstrate that the proposed architecture improves the system reliability and performance greatly.

Keywords Cloud storage • Architecture • Meta-data service layer • Reliability • Performance

68.1 Introduction

The master-slave and the peer-to-peer (P2P) are the two most basic architectures. The former has the advantages of simpleness, easy operation and maintenance. On the other hand, the latter has the advantages of reliability and stability. GFS [1], the representative of the master-slave storage architecture, has the bottlenecks of reliability and performance [2, 3], which leads to the inefficient concurrent access and the single point failure. In order to improve the parallel processing performance, the parallel optimization BlobSeer [3] storage layer is used to substitute the

K. Fan (✉) • L. Zhao • H. Li
State Key Laboratory of Integrated Service Networks, Xidian University, Xian, China
e-mail: kfan@mail.xidian.edu.cn

Y. Yang
Key Lab. of the Minist. of Educ. for Wide Band-Gap Semiconductor Materials and Devices, Xidian University, Xian, China

J. Mu et al. (eds.), *The Proceedings of the Third International Conference on Communications, Signal Processing, and Systems*, Lecture Notes in Electrical Engineering 322, DOI 10.1007/978-3-319-08991-1_68

distributed file storage system HDFS [4] in Hadoop cloud computing system. Although the BlobSeer improves the concurrency, it cannot address the single point reliability efficiently. The P2P based data sharing network [5, 6] is proposed to eliminate the single point failure and ensure the expansion and reliability. In addition, Amazon presents the decentralized P2P cloud storage architecture Dynamo, which is the top-down P2P structure. Although Dynamo ensures the balance of data distribution and node load, the update and search of large-scale P2P network will be delayed greatly. Furthermore, Dynamo improves the reliability, but it delays some data processing in consistency.

Although the consistency, reliability and availability cannot be achieved simultaneously, they can be balanced to some extent. We propose a cloud storage architecture with a meta-data service layer. The proposed architecture is a distributed file storage system based on the master-slave architecture, which uses multiple proxy servers of the meta-data server to establish a P2P meta-data service layer. The P2P server structure is only used in the meta-data service layer. All the meta-data is stored with one copy in each different meta-data servers, which can ensure the fault tolerance, and reduce the complexity of the file lock service in the case of one file being written by many clients. In the proposed architecture, each meta-data server or each proxy server could be an access to service for clients rather than only one fixed access as usual, which can improve the parallel processing performance of the meta-data service layer greatly. In addition, proxy servers share part of services of the meta-data server in GFS and HDFS to improve the performance. In addition, some P2P techniques, such as configuration, service scheduling, and searching, are used between the proxy servers to solve the disadvantages of the master-slave architecture efficiently. That can improve the reliability and the access concurrency, in which the meta-data can be used as the system cache in each proxy server. Analysis and evaluation are performed to demonstrate that the proposed architecture improves the system reliability and performance greatly.

The remainder of this paper is organized as follows: in Sect. 68.2, the cloud storage architecture with a meta-data service layer is proposed; in Sect. 68.3, the system service interaction protocol of the proposed architecture is proposed; and the analysis and evaluation of the proposed architecture is performed in Sect. 68.4; finally, concluding remarks are provided in the last section.

68.2 Cloud Storage Architecture with a Meta-Data Service Layer

The cloud storage architecture with a meta-data service layer is shown in Fig. 68.1. The block-data service layer, the meta-data service layer and the client application layer are defined from the inside out respectively.

The meta-data service layer is the key of the architecture. Compared with GFS system, the meta-data service layer is a P2P distributed service network using multiple proxy servers in the proposed architecture, which is like the meta-data server Master in GFS.

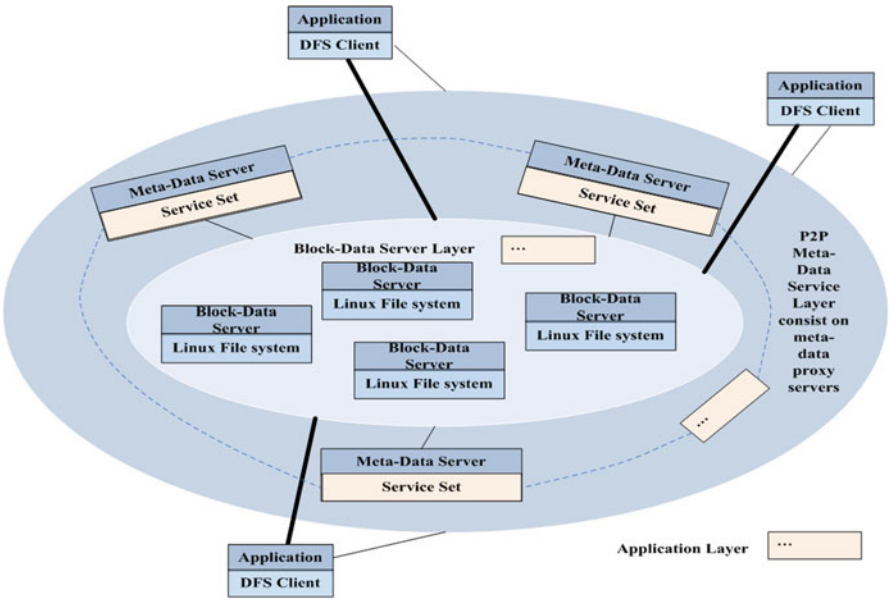

Fig. 68.1 The cloud storage architecture with a meta-data service layer

The definition of the function of the meta-data service layer is as follows.

1. Request listening: that is to listen on the request events of the client and the block-data server. The client events are the name space to be created and deleted, files to be created, wrote, read, deleted and renamed, list of files information to be accessed, resource lock to be obtained and released, and so on. The events of the block-data server are the heartbeat information, the file block information, the error information, and so on.
2. Request processing: that is to process the request listening events and return the result.
3. Meta-data management: the meta-data is mainly the name space, the mapping from file to the file block and the mapping from the file block to the block-data server.
4. Name space management: the name space is managed by using the directory tree structure.
5. File management: that is some basic operations to the file. For example, creating, writing, deleting and renaming.
6. File block management: that is to create or copy new files, delete the invalid file blocks and recover the orphaned file blocks.
7. Load balance of the block-data server: due to the uneven distribution of file blocks in different block-data servers, which caused by a large number of file blocks writing and deleting the file block load balance, should be performed.

8. Lease (session) management: that is to manage the lease of client. That includes the obtaining and releasing lease, and recovering lease, in which the lease is expired.
9. Heartbeat detection: the block-data server will report its load condition to the meta-data server though sending heartbeat information regularly.

The function of the block-data service layer is similar as the basic master-slave distributed file system. The definition of the function is as follows.

1. Data block information management: there may be tens of thousands of data blocks in the block-data servers, and the block-data server may operate any data block in anytime.
2. Data block writing and reading: client could write data blocks to or read data blocks from the block-data servers frequently. When the data block is being written, it also should be backed up.
3. Data block transmission: the data block transmission between block-data servers is frequent. When the writing operation and backup operation are performed, the data block transmission will be established between block-data servers.
4. Sending heartbeat information to the meta-data server: the meta-data server judges whether the block-data server is working normally based on the heartbeat information.
5. Processing the command information of the meta-data server: when the system is running, the meta-data server will tell the block-data server to back up, delete and move file blocks.
6. Reporting the file block information to the meta-data server: because file blocks will change in the block-data server, the block-data server should report the file block information to the meta-data server regularly. Then the newest block information will be in the meta-data server.
7. Processing client requests: the system interaction is the interaction between client and the block-data servers, such as the writing and reading of data blocks. Therefore, the interactive interface should be established between client and the block-data servers.

The client application layer is the service access layer, in which the compliable interface is provided as GFS. The storage interface is provided to client using the programming language in the proposed architecture, which can provide the function access using the command-line mode, and reduce the difficulty of the operation and maintenance. The definition of the function is as follows.

1. Directory management: that is to create, rename and delete directories.
2. File management: that is some basic operations to the file. For example, uploading, downloading, deleting and renaming.
3. Data flow operation: the output flow to file system will be created, when a client wants to upload a file to the system. Otherwise, the input flow reading from the system will be created when a client wants to download a file in the system.
4. The operation of resource lock: that is to obtain the resource lock and release it.

68.3 System Service Interaction Protocol

We can summarize the interaction in distributed file storage system as writing and reading operation. The data updating can be regarded as a special writing process, which is the same as the ordinary writing operation process. The processes of writing and reading are shown in Fig. 68.2.

The communication in the architecture consists of the control flow and the data flow, which are shown in the thin lines and thick lines. We define the main process in different layers.

68.3.1 The Writing Operation Step

W1: request writing, in addition, sending file information.
W2: returning the information of main storage block, including the mapping of file name, the size of the block, and so on.
W3: client writes files into the block-data server based on the result of W2.
W4: the block-data server backups files based on the result of W2.
W5: the backup node returns the backup result to main storage server.
W6: the result of block storage is sent to the meta-data server to generate the meta-data.
W7: confirming the meta-data.
W8: sending the result of client. If it fails, returning events, which will be completed by using control command and state recovering.

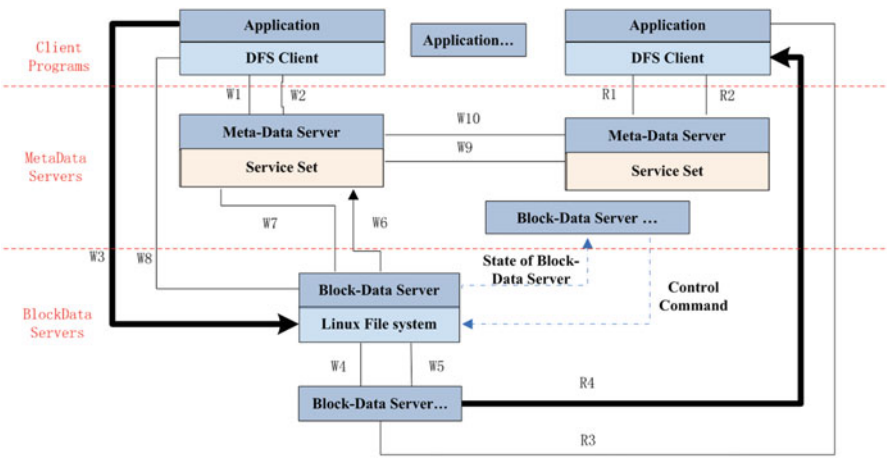

Fig. 68.2 The system service interaction process

W9: updating the local meta-data and the corresponding vector clock, and this operation information is transmitted to other main servers, meta-data proxy servers, by IP multicasting. Other servers choose to update their meta-data set or not based on the vector clock.
W10: checking the results returned from other main servers. The fault-tolerant processing is performed if there is a return warning with failure.

68.3.2 The Reading Operation Step

R1: request reading data.
R2: the main server returns the information of file blocks.
R3: client sends block information to the block-data server.
R4: the block-data server sends data blocks.

The copy process of the meta-data in servers is the key issue of the system performance improvement, such as W9 and W10 in Fig. 68.2.

68.4 Analysis and Evaluation

The architecture evaluation mechanism [3] we used is to determine the properties of the architecture by modeling or simulating one or many aspects in the system. We use theoretical modeling to qualitative analyze the proposed architecture. In addition, we code and implement the meta-data service layer model of meta-data proxy servers.

The analysis of reliability in Sect. 68.4 is valid based on following assumptions:

- life of each node follows an *exp* distribution.
- the life of all nodes is I.D.D.

68.4.1 The Analysis of System Scale

There are 40 servers in each cabinet in the condition of HDFS typical configuration. Every cluster can support about 1,000 nodes mostly in GFS. In the proposed architecture, the larger node scale can be supported. That is only the advantage of the proxy server model.

The proxy server in the meta-data service layer is a group of the P2P meta-data server. The scale should not be too large. One reason is to reduce the complexity of

consistency maintenance. The other reason is the P2P structure is used in this layer, in which when P2P network scale is too large, network changing and data updating would cause the problem of jitter and delay, and the higher searching complexity.

So the meta-data service layer based on small scale not only can reduce the design complexity of the large-scale P2P network, but also can support much larger block server node scale, except the simplified consistency. We can estimate as follow.

The number of the meta-data server node, the proxy server node, in the meta-data service layer is at least 2 and at most 256 in the proposed architecture. That is the number of preliminary estimating. The node scale of the block-data server can be expanded of at least 200 times in GFS and HDFS theoretically. In addition, because every proxy server is an access for client, the concurrent processing capability of the meta-data service can be enhanced at least 200 times. When the number of the proxy server is less than 256, this is already a considerable enhancement. In addition, there is no the single point failure. The performance enhancement will be quantitatively analyzed in the availability analysis.

68.4.2 The Analysis of Service Performance

There are higher concurrent responses in the proposed architecture, because the proxy server shares the work of the Master node in GFS. The enhancement of system performance will be analyzed in the two aspects of writing and reading, and the simulation is also performed.

The average writing time of concurrent file request with different number of proxy servers is shown in Fig. 68.3. We have performed eight concurrent processes

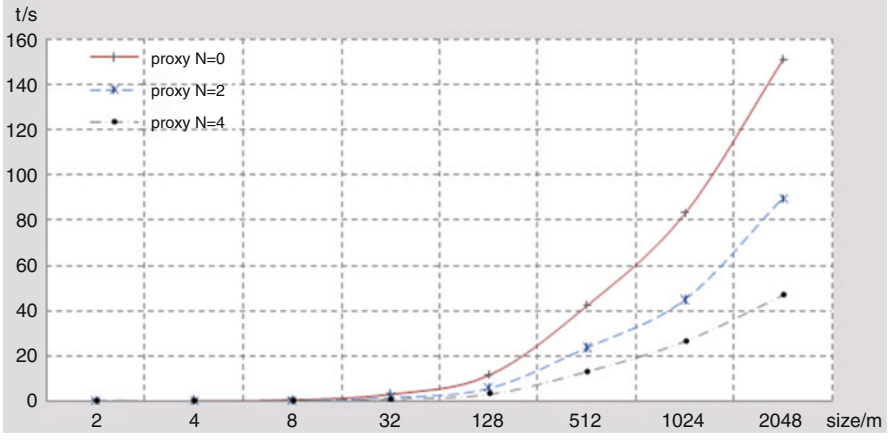

Fig. 68.3 The average writing time of concurrent file request with different number of the proxy servers

with 4,000 connections in each process. The size of files in each concurrent request is from 2 to 2,048 MByte.

From Fig. 68.3, the larger of the number of the proxy server and the larger of the file writing concurrent request, the less time cost in writing and the higher performance of the proposed architecture.

68.4.3 The Analysis of System Reliability

The reliability of the GFS and the proposed architecture with different server nodes is shown in Fig. 68.4.

From Fig. 68.4, the larger the system scale is, the higher reliability the proposed architecture achieves. The solution of the single point failure in GFS is the multiple nodes backed up. When the number of nodes is much larger, the reliability will not be improved obviously with the change of the number of nodes. Otherwise, the proposed architecture uses multiple proxy servers in service at the same time. Although the service performance will be decreased when many nodes cannot work, the availability will not be affected. Therefore, the proposed architecture has higher reliability with more nodes.

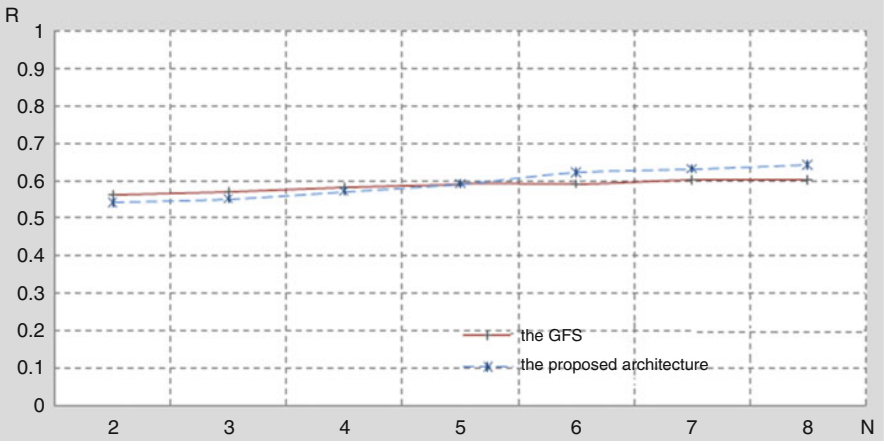

Fig. 68.4 The reliability of the GFS and the proposed architecture

Conclusions
In this paper, a cloud storage architecture with a meta-data service layer has been proposed. Compared with other existing cloud storage architectures, the proposed architecture achieves higher reliability and performance. For our future work, we will further explore other challenging issues, such as, file blocking storage method in cloud computing environment.

Acknowledgements This work has been financially supported by the National Natural Science Foundation of China (No. 61303216 and No. 61373172), the China Postdoctoral Science Foundation funded project (No.2013M542328), the Xidian-Ningbo Information Technology Institute Seed Foundation funded project, National 111 Program of China B08038, and the Xian Science and Technology Plan funded project (CXY1352WL30).

References

1. Zhan Y, Sun Y (2009) Cloud storage management technology. In: ICS, pp 301–311
2. Ye W (2009) SaaS architecture design. Publishing house of electronics industry, pp 56–78
3. Nicolae B, Moise D, Antoniu G (2010) BlobSeer: Bringing high throughput under heavy concurrency to Hadoop map-reduce applications. In: Parallel and Distributed Processing, pp 1–11
4. Shvachko K, Kuang H, Radia S, Chansler R (2010) The Hadoop distributed file system. In: Mass Storage Systems and Technologies, pp 1–10
5. Xu K, Song M, Zhang X, Song J (2009) A cloud computing platform based on P2P. In: IT in Medicine and Education, pp 427–432
6. Rivero M, Rubino G (2010) Priority-based scheme for file distribution in peer-to-peer networks. In: Communications, pp 1–6

Chapter 69
Bit Allocation for Spatial Scalable Video Coding with Rate–Distortion Analysis

Bo Wang, Songlin Sun, Xiaojun Jing, and Hai Huang

Abstract The spatial layer bit allocation problem of H.264/scalable video coding (SVC) is solved in this paper. The challenge of this problem lies in the fact that the low frequency information in spatial scalable video, which consists mainly of the mean absolute difference (MAD) of the residual texture in the base layer, is not always the suitable reference for inter-layer prediction. To overcome this issue, we first analyze the MAD prediction in the enhancement layer from both temporal and spatial aspects, then derive the Rate–Distortion (R–D) models of the spatial layer analytically, and finally develop a model-based bit allocation algorithm. Experimental results show that the proposed bit allocation algorithm can achieve a coding performance close to the optimal R–D performance based on the full search method, and outperforms two prior H.264/SVC bit allocation algorithms served as benchmarks.

Keywords Bit allocation • H.264/SVC • Rate–Distortion models • MAD prediction • Spatial layer

69.1 Introduction

H.264/scalable video coding (SVC) has been standardized to extend the capabilities of the H.264/advanced video coding (AVC) standard [1]. To improve coding efficiency, inter-layer prediction is employed to remove redundancies between layers [2]. Due to the inter-layer prediction, the problem of spatial bit allocation in H.264/SVC is very challenging. That is, the Rate–Distortion (R–D) behavior of an enhancement layer (EL) is dependent on its preceding layers, and although the reconstructed lower-resolution video represents the low frequency information in

B. Wang (✉) • S. Sun • X. Jing • H. Huang
School of Information and Communication Engineering,
Beijing University of Posts and Telecommunications, Beijing, China

Key Laboratory of Trustworthy Distributed Computing and Service (BUPT),
Ministry of Education, Beijing, China
e-mail: wang_bo@bupt.edu.cn

J. Mu et al. (eds.), *The Proceedings of the Third International Conference on Communications, Signal Processing, and Systems*, Lecture Notes in Electrical Engineering 322, DOI 10.1007/978-3-319-08991-1_69

spatial scalable video, it may not necessarily be the most suitable reference for inter-layer prediction.

Several works have been accomplished for the bit allocation problem of H.264/SVC. For example, the JVT-G012 rate control algorithm was implemented in the base layer (BL) of the Joint Scalable Video Model (JSVM) reference software. For the ELs, the target bit rate can be controlled by use of the FixedQptool in JSVM, with a logarithmic search algorithm applied to find the proper quantization parameter QP required to meet the target bit rate. Besides, a rate control algorithm was proposed for inter-layer prediction employment in SVC [3]. Particularly, a Rate–Quantization (R–Q) model for inter-layer prediction coding of the spatial ELs is developed first. Then an optimized mean absolute difference (MAD) prediction model for spatial ELs is constructed, where the predicted error of MAD in the BL is needed to be subtracted from predicted value of MAD in the EL, but the prediction errors of MAD in the BL and the EL are different. Liu et al. [4] proposed a rate control algorithm for the spatial and coarse-grain SNR scalability of H.264/SVC. The proposed algorithm operates on a fixed rate of each layer and implements an MB-layer bit allocation scheme. In [5], Liu et al. proposed a bit allocation algorithm for SVC when the inter-layer dependency is taken into consideration. Analytical R–D models can provide a simple solution to the complex bit allocation problems [6]. Based on the R–D models, the optimal bit allocation problem can be formulated using Lagrange multiplier approach and solved numerically.

Our paper's main contributions lie in three aspects: (1) In order to obtain accurate MAD prediction values of the residual texture in the EL, we develop a novel switched model using the K-means. (2) Based on the novel MAD prediction model, the R–D models for spatial scalability coding are derived. (3) To avoid collecting all the R–D data while retaining optimality, an efficient bit allocation algorithm for spatial scalability coding of H.264/SVC using the R–D models is developed. Experimental results show that the proposed algorithm can achieve the coding performance close to that based on the full search (FS) method, and outperforms two prior H.264/SVC bit allocation algorithms served as benchmarks.

The rest of this paper is organized as follows. In Sect. 69.2, a novel MAD prediction model of EL is established, and the R–D models for spatial scalability coding are derived. The bit allocation problem of spatial scalability coding is formulated and solved numerically in Sect. 69.3. The performance of the proposed bit allocation scheme in terms of coding efficiency is evaluated in Sect. 69.4. Finally, concluding remarks are given in final section.

69.2 Rate–Distortion Models for Spatial SVC

Based on the proposed MAD prediction model of EL and the BL's temporal prediction model [4], the R–D models for spatial scalability coding are derived.

69.2.1 Improved MAD Prediction Model for the Spatial EL

From observation and analysis, the temporal prediction model is very efficient when there is no abrupt change, while the spatial one works well in the presence of abrupt changes (high motion or scene change). Moreover, in the SVC encoding process, each frame of the BL is encoded first, prior to the EL's. Thus benefiting from the bottom-up coding structure of SVC, the detection of the abrupt changes is accomplished first in the BL based on the actual BL's MAD, then suitable MAD prediction model of the EL can be chosen.

69.2.1.1 Calculating the Threshold of the MAD's Abrupt Changes in the BL

Given a set of observations $(x_1, x_2, \ldots, x_i)$, the observation x_i is defined as: $x_i = MAD^*_{i+1,k} - MAD^*_{i,k}$, where i is the frame number, k is the layer number, and MAD^* is the actual MAD of the residual texture. The definition of the observation x_i is appropriate for different sequences, and the huge observations can be obtained easily. As to process the no tags clustering of large samples, K-means method is very efficient [7]. K-means is employed to partition the i observations into two sets $S_n (n = 1, 2)$ which contain MAD abrupt changes and no MAD abrupt changes, so as to minimize the within-cluster sum of squares: $\text{argmin}_s \sum_{n=1}^{2} \sum_{x_j \in S_n} \left\| x_j - \mu_n \right\|^2$, where μ_n is the mean of points in S_n, and j is the number between 0 and i. After the categorization is achieved, we choose the boundary $MAD_{B\_Threshold}$ of the two clusters as the threshold of the MAD's abrupt changes in the BL.

69.2.1.2 Calculating the MAD in the EL

The absolute value of difference between $MAD^*_{i+1,k}$ and $MAD^*_{i,k}$ is calculated first, then the absolute value is compared with the threshold $MAD_{B\_Threshold}$. If the absolute value is greater than the threshold, the spatial prediction is chosen. Otherwise, the temporal prediction is chosen. The switched MAD prediction scheme is presented as:

$$\begin{aligned} &If \quad \left| MAD^*_{i+1,k} - MAD^*_{i,k} \right| > MAD_{B\_Threshold} \\ &MAD_{i+1,k+1} = \sigma_1 \cdot MAD^*_{i+1,k} + \sigma_2 \quad else\ MAD_{i+1,k+1} = \tau_1 \cdot MAD^*_{i,k+1} + \tau_2, \end{aligned}$$

where $\sigma_1, \sigma_2, \tau_1, \tau_2$ are the model parameters, and MAD is the predicted value. With the above scheme, both the temporal and spatial correlations are used in the prediction. To estimate the accuracy of the MAD prediction method, the prediction errors are measured at the frame level for several sequences, as shown in Table 69.1,

Table 69.1 Mad prediction error

Sequence QCIF 15 Hz	Prediction error	Sequence CIF 30 Hz	Prediction error
Bus	0.11	City	0.08
Mobile	0.36	Harbour	0.16
Football	0.33	Soccer	0.82

in which the coding structure is IPPP, one CIF enhancement layer for QCIF sequence and one 4CIF enhancement layer for CIF sequence, and the initial quantization parameter QP is 30 for both the base layer and the enhancement layer.

69.2.2 Rate–Distortion Models Derivation

The simplified q-domain R–D models of residual signal are given in [8]: $R(q) = \alpha \cdot \frac{MAD}{q^p}$ and $D(q) = \beta \cdot MAD \cdot q^p$, where α and β are the model parameters. q is the quantization step size and p is the parameter that depends on the frame types. A frame is employed as a basic bit allocation unit in this paper, and the rate and distortion of the basic bit allocation unit are defined by $R(q_{i,k})$, $D(q_{i,k})$ respectively. The k^{th} layer's R–D models can be reformulated as:

$$\begin{aligned} R_k^{th}(q_{i,k}) &= \sum_{i=0}^{I} R(q_{i,k}) = \frac{\alpha_{i,k} \cdot MAD_{i,k}}{q_{i,k}^p} \\ D_k^{th}(q_{i,k}) &= \sum_{i=0}^{I} D(q_{i,k}) = \beta_{i,k} \cdot MAD_{i,k} \cdot q_{i,k.}^p \end{aligned} \tag{69.1}$$

The total number of frames and layers in a coded video stream are defined by I and K respectively. The total R–D models can be expressed as:

$$\begin{aligned} R_{tot}(q_{i,k}) &= \sum_{i=0}^{I}\sum_{k=0}^{K} R(q_{i,k}) = \frac{\alpha_{i,k} \cdot MAD_{i,k}}{q_{i,k}^p} \\ D_{tot}(q_{i,k}) &= \sum_{i=0}^{I}\sum_{k=0}^{K} D(q_{i,k}) = \beta_{i,k} \cdot MAD_{i,k} \cdot q_{i,k,}^p \end{aligned} \tag{69.2}$$

where the MAD predictions of ELs use the switched prediction scheme in Sect. 69.2.1, and the MAD prediction of BL uses the model in [4]. After each layer's MAD is calculated, R–D models in (69.1) and (69.2) can be used in the bit allocation algorithm in the next section.

69.3 Bit Allocation for Spatial SVC

In this section, the optimal bit allocation problem is formulated using Lagrange multiplier approach. Based on the R–D models above, the Lagrange solution of the bit allocation problem is worked out, and the bit allocation algorithm is also developed.

69.3.1 Bit Allocation Problem Formulation

The bit allocation problem for the spatial layer of H.264/SVC is formulated as an optimal quantization step size q decision problem, which targets to minimize the total distortion under a target bit rate R_k^T for each spatial layer. Mathematically:

$$\begin{aligned} Q^* &= \arg\ \min_{q_{i,k}\in\Omega} D_{tot}(q_{i,k}) \\ \textit{Subject to } R_0^{th}(q_{i,0}) &\le R_0^T, R_1^{th}(q_{i,1}) \le R_1^T \ldots, \textit{and}\ \ R_k^{th}(q_{i,k}) \le R_k^T, \end{aligned} \tag{69.3}$$

where Q^* is the optimal quantization step size vector, Ω is the set of all possible quantization step sizes. The Lagrange cost function is introduced to map the constrained optimization problem in (69.3) to an equivalent unconstrained optimization problem:

$$\begin{aligned} Q^* &= \arg\ \min_{q_{i,k}\in\Omega} J(q_{i,k},\lambda_k) \\ J(q_{i,k},\lambda_k) &= D_{tot}(q_{i,k}) + \lambda_0\left(R_0^{th}(q_{i,0}) - R_0^T\right) + \ldots + \lambda_k\left(R_0^{th}(q_{i,k}) - R_k^T\right), \end{aligned} \tag{69.4}$$

where λ_k represents the Lagrange multiplier. To solve the problem given in (69.4), the model-based bit allocation algorithm is developed to solve the complexity issue. The details will be discussed in the next section.

69.3.2 Solution to Lagrange

Since the variables are independent in (69.4), the optimization problem can be solved by deriving the partial derivatives with respect to $q_{i,k}$ and λ_k, which results in a system of nonlinear equations. Mathematically:

$$\begin{aligned} \frac{\partial J(q_{i,k},\lambda_k)}{\partial q_{i,k}} &= p\cdot\beta_{i,k}\cdot MAD_{i,k}\cdot q_{i,k}^{p-1} - p\cdot\lambda_k\cdot\frac{\alpha_{i,k}\cdot MAD_{i,k}}{q_{i,k}^{p+1}} = 0 \\ \frac{\partial J(q_{i,k},\lambda_k)}{\partial \lambda_k} &= \sum_{i=0}^{I}\frac{\alpha_{i,k}\cdot MAD_{i,k}}{q_{i,k}^{p}} - R_k^T = 0. \end{aligned} \tag{69.5}$$

Since the numbers of variables and equations are the same, the solution to the system of nonlinear equations in (69.5) is feasible, and it is solved by the gradient method. To apply a gradient method, a new equation is defined, where the sum of squares of the partial derivatives in (69.6) is set to be zero, namely:

$$g(q_{i,k},\lambda_k)=\sum_{i=0}^{I}\sum_{k=0}^{K}\left(\frac{\partial J(q_{i,k},\lambda_k)}{\partial q_{i,k}}\right)^2+\sum_{k=0}^{K}\left(\frac{\partial J(q_{i,k},\lambda_k)}{\partial \lambda_k}\right)^2=0. \tag{69.6}$$

Then the solution ($q_{i,k}$ and λ_k) is defined as the values that make $g(q_{i,k},\lambda_k)$ closest to zero. Quantization parameters QP can be determined using the one-to-one correspondence between quantization step size q and quantization parameter QP in [9]. Finally, each layer in the current basic coding unit is encoded to produce the final bit stream at the target bit rate.

69.4 Experiments and Results

To evaluate the coding efficiency of the proposed algorithm, the performance of the proposed algorithm is conducted on various test sequences. In the experiments, each video contains two spatial layers. The layer setting and the experimental configuration are described as follows. For Scenario 1, two layers are of QCIF–CIF format with three sequences (Bus, Football, and Mobile) at the frame rate of 15 frames/s. For Scenario 2, the two layers are of CIF–4CIF format with another three test sequences (City, Soccer, and Harbour) at the frame rate of 30 frames/s. The initial QP value is set to 30 and the search range is 32 in both layers.

The frame-by-frame peak signal-to-noise ratio (PSNR) performance comparison of FS method, JSVM algorithm and proposed algorithm are shown in Fig. 69.1. With the FS method, the input video sequence is encoded with all possible quantization step size values, which are set constant for the whole sequences in the FS method, and selects the one with the best R–D performance, showing the minimum value of the average distortion of the BL and the EL while meeting the requirement of the total target bit rate. Then, the optimal solution is determined as the optimized quantization step size group. From these figures, clearly the proposed bit allocation method outperforms the JSVM FixedQPEncoder tool significantly while the gap between the optimal performance (obtained by FS) and the proposed scheme is very small.

For further evaluation, performance of the proposed algorithm, JSVM algorithm and Xin's algorithm [3] in terms of Rate, PSNR are summarized in Table 69.2. Given the same target bit rates, the accuracy of the proposed algorithm is better than JSVM algorithm and Xin's algorithm in all cases. This is because the proposed optimized MAD prediction model results in a smaller prediction error. Consequently, it can be considered that bit rate is precisely controlled using the proposed algorithm. Moreover, the PSNR of each of the six sequences is increased at all ranges of target bit rate.

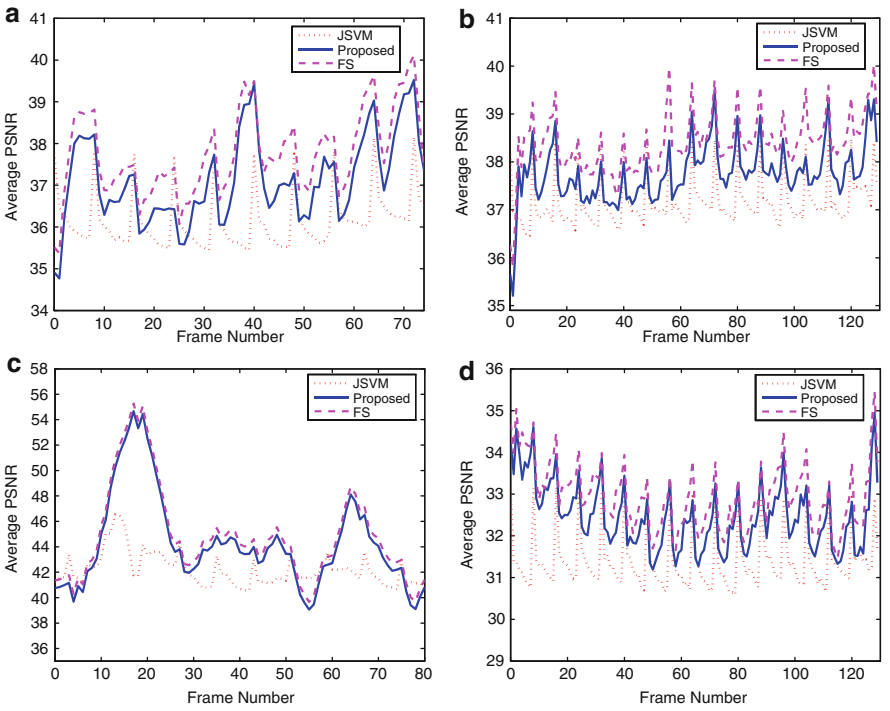

Fig. 69.1 Average PSNR value as a function of the frame number with the proposed, JSVM and FS. (**a**) Bus. (**b**) City. (**c**) Football and (**d**) Mobile

Table 69.2 Performance of the proposed, JSVM and Xin's in terms of PSNR, output rate

Seq.	Target rate (kbps)	JSVM 9.12		Xin's		Proposed	
		PSNR (dB)	Rate (kbps)	PSNR (dB)	Rate (kbps)	PSNR (dB)	Rate (kbps)
City	1,024	36.9032	1,002.6425	37.0663	1,027.6031	37.9774	1,025.7302
	1,536	37.4349	1,457.0345	38.4405	1,533.7631	39.2834	1,538.0192
Harbour	1,536	33.6957	1,463.8782	33.9546	1,529.8991	34.5241	1,537.3382
	2,048	33.2839	1,926.4098	34.0316	2,065.1471	35.4872	2,057.2165
Soccer	1,536	40.0197	1,564.3532	40.0498	1,543.5194	40.9134	1,533.3219
	2,048	39.7508	2,067.8418	40.1506	2,038.8123	41.0173	2,047.0235
Football	768	42.5091	753.2243	42.6807	769.6265	42.9671	768.0231
	1,024	41.1978	993.6471	41.3763	1,025.9788	41.9873	1,024.4638
Bus	384	35.4134	363.7040	36.9834	384.4768	37.3298	384.5716
	512	36.9396	503.0224	37.2923	517.7968	37.9563	515.3404
Mobile	256	31.2935	261.6148	31.3526	259.4649	31.9441	256.7302
	384	31.4774	365.1055	33.5818	391.7086	33.6012	383.3407

Conclusion

In this paper, a model-based spatial layer bit allocation algorithm for H.264/SVC is proposed by establishing the Rate–Distortion models for spatial layer of H.264/SVC. The accuracy of the residual MAD prediction in the enhancement layer is significantly improved by the switched prediction model, and the Rate–Distortion models of the spatial layer are also derived accordingly. It is shown by experimental results that the proposed bit allocation algorithm can achieve the coding performance close to the optimal R–D performance based on the full search algorithm. Moreover, the proposed algorithm outperforms two prior H.264/SVC rate control algorithms by a significant margin.

Acknowledgements This work is supported in part by NSFC 61143008, National High Technology Research and Development Program of China (No. 2011AA01A204), the Fundamental Research Funds for the Central Universities.

References

1. Schwarz H, Marpe D, Wiegand T (2007) Overview of the scalable video coding extension of the H.264/AVC standard. IEEE Trans Circuits Syst Video Technol 17(9):1103–1120
2. Li ZG, Rahardja S, Sun H (2006) Implicit bit allocation for combined coarse granular scalability and spatial scalability. IEEE Trans Circuits Syst Video Technol 16(12):1449–1459
3. Lu X, Martin GR (2013) Rate control for Scalable Video Coding with rate-distortion analysis of prediction modes. In: IEEE international workshop on Multimedia Signal Processing (MMSP), Pula, pp 289–294
4. Liu Y, Li Z, Soh YC (2008) Rate control of H.264/AVC scalable extension. IEEE Trans Circuits Syst Video Technol 18(1):116–121
5. Liu J, Cho Y, Guo Z, Kuo C (2010) Bit allocation for spatial scalability coding of H.264/SVC with dependent rate–distortion analysis. IEEE Trans Circuits Syst Video Technol 20 (7):967–981
6. Cho Y, Kwon D-K, Liu J, Kuo C-CJ (2013) Dependent R/D modeling techniques and joint T-Q layer bit allocation for H.264/SVC. IEEE Trans Circuits Syst Video Technol 23(6):1003–1015
7. Kanungo T, Mount DM, Netanyahu NS, Piatko CD, Silverman R, Wu AY (2002) An efficient k-means clustering algorithm: analysis and implementation. IEEE Trans Pattern Anal Mach Intell 24(7):881–892
8. Kwon D, Shen M, Kuo C-CJ (2007) Rate control for H.264 video with enhanced rate and distortion models. IEEE Trans Circuits Syst Video Technol 17(5):517–529
9. Richardson IEG (2003) H.264 and MPEG-4 video compression video coding: video coding for next-generation multimedia. Wiley, Chichester

Chapter 70
A Robust Lane Detection and Tracking Based on Vanishing Point and Particle Filter

Maopeng Xu, Mei Xie, and Daming Zhang

Abstract A lot of people die in every year all around the world in the traffic accidents caused by vehicle roadway departure crashes. A lane-detection system is an important part of intelligent transportation to avoid these accidents. In this paper, we novelly present an algorithm which can detect lanes though vanishing points, track lanes though particle filter on each control, and refresh these control points though an scoring algorithm. We can get some pairs of lines though an vanishing point in detecting parts, get some pairs of lines though particle filter on each control point, find the lane in all the pairs of lines though the scoring algorithm, and then refresh these control points by the end-points of each part of the lane. General process is that, we first use a Gabor filter to find the edge in an image. And then, we divide the image into five parts and use Hough transform to find the lines in each part. After that an algorithm based on particle filter and vanishing points is novelly proposed to generate a large number of hypotheses. Then we will use our scoring algorithm to mark every control point/pair of lines to select the control points/pair of lines whose score is highest. At last, a pair of lane is obtained by fitting function. Experimental results on real roads will be presented to prove the effectiveness of the proposed lane detection algorithm.

Keywords Image analysis • Image matching • Image recognition • Object detection • Particle tracking

70.1 Introduction

Lane-detection-and-tracking system from a road image is an important part of intelligent-transportation system or Lane Departure Warning System (LDWS). There has been active research on lane detection. Several approaches for lane detection and tracking were proposed and successfully demonstrated (including model-based, Hough transform, feature-based, region-based and modalities) [1, 2].

M. Xu (✉) • M. Xie • D. Zhang
University of Electronic Science and Technology of China (UESTC), Sichuan, China
e-mail: 452777728@qq.com; XIEMEI@uestc.edu.cn; 570523902@qq.com

J. Mu et al. (eds.), *The Proceedings of the Third International Conference on Communications, Signal Processing, and Systems*, Lecture Notes in Electrical Engineering 322, DOI 10.1007/978-3-319-08991-1_70

Because of a real-time constraint, although some of famous algorithms have a high detection rate, they need too much processing time which seriously affects the real-time performance of lane detection. Such as, Yue Wang in [3–5] which used B-Snake spline to detect lane.

Some algorithms for lane detection can get ideal detection result in weak light and lane missing cases, but for corner detection are error-prone. Such as Massimo Bertozzi in [3] which used stereo vision system for lane detection. Other algorithms, like Canny/Hough Estimation of Vanishing Points (CHEVP) which extracts the parameters for lace detection, can obtain results robustly and accurately. But the robustness of canny operator is sensitive to the initialization parameter. Dealing with different situation it can not get ideal results. Some recent studies deal with shadows, lane missing, curved lane have a good result. But they can't take real-time and ideal results in challenging scenes into account. The desired properties of lane detection techniques include [6]:

1. Lane detection result cannot be subject to shadow effects, such as trees, buildings, etc.
2. It should be should be able to detect crooked lane.
3. It should be able to get good result at night.
4. It should be able to detect uphill or downhill lane.
5. It should be able to detect lane in the effect of rule objects around, such as green belt.

A good lane detection and tracking algorithms need to meet all of the above requirements. In our paper, we provide an algorithm is different form the previous algorithm in the follows, as shown in Fig. 70.1.

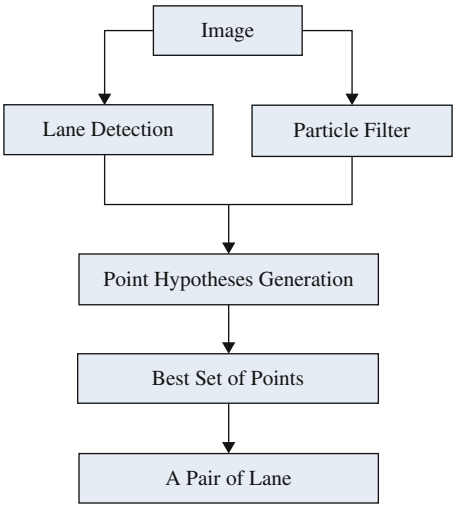

Fig. 70.1 Flow diagram of the algorithm. First, the image is divided into five parts. Possible parts of lane are detected in the five parts. Then, the endpoints of lines are grouped into lane-boundary hypotheses. A combined approach of a particle-filtering technique (for tracking) and a vanishing point technique (for detection) is introduced to robustly find lane-boundary hypotheses in real-time. Finally, a selecting algorithm is applied to choose the best set of points for fitting the lane

1. We divided one image into five parts. From each section we can get many ports form two end-points of a line. In these points, the lowest and vanishing points are most important.
2. Using the improved particle filter near the control points, we can get a series of candidate points.
3. Using the selection algorithm, we can get the optimal point form all candidate points. Then using the fitting function we can synthesize these points to a line.
4. It combines lane detection and tracking that can effectively deal with lane changes, emerging, ending, merging, or splitting lane.

70.2 Edge Detection

Many previous algorithms can only detect simple straight lines under the condition of good light. But for lane in shadow, a lack of part of the lane and curved lane, the algorithms do not get good results.

In order to solve these problems, we will first divide an image into five parts (each part accounts for one fifth of an image). Because each part is independent of others, so our algorithm is not sensitivity of the parameters and we can get more detailed results from each part.

Canny proposed a best edge detection operator (Canny operator). But when using canny operator for edge detection, gradient value of pixel should be the maximum inhibition and it must set high and low threshold values for edge point selection. At present, the two threshold selection is still no uniform standard. For the same image, due to the different shooting conditions, the result got by canny operator is not the same with the ideal result. Besides, due to the different gray level distribution in different images, the threshold adopted should also be different.

Due to the canny operator's defect, this paper will use Gabor filter for the image edge detection. Steps are as follows:

1. Use wavelet function to smooth the image noise.
2. Compute the amplitude and phase of the wavelet.
3. Inhibit the maximum in the wavelet image.
4. Judge the integration of wavelet coefficients.
5. Connect edge.

After the steps above, we can get a complete image and the edge detection image is shown in Fig. 70.2. Using this method for image edge detection, we find that we can get better edge detection without setting parameters. The details and the overall outline is better and it can remove unnecessary pseudo edge at the same time.

Then we will use Hough transform in the five parts. And then, we can get parts of the lines in five parts.

Fig. 70.2 Original image and image handled by Gabor filter. We can see that under the condition of not changing any parameter, Gabor filter can still get good effect of edge detection

70.3 Lane Detection and Tracking

We will use hough transformation in the five sections of the picture to find all the lines within each section. Calculated the coordinates of the intersection of every pair of line within each section. After above steps, we will choose the row whose num of coordinates nearby is the largest as the vanishing line. And then through ordinate of the vanishing line, we can choose the pair of line whose intersection is nearest the vanishing line as lane in each part.

Through the actual operation, we found that, there are a lot pairs of the line whose intersection near vanishing, so it is difficult to choose the best one form all pairs, as shown in Fig. 70.3.

So we novelly present an algorithm about how to choose control points [7, 8] and use particle filter on each points for tracking [9]. For the particle filter, it modeled moving objects as a Gaussian model, but the movement of the vehicle is not Gaussian model. So we will prevent it from modeling Gaussian model. Our particle filter algorithm is as follows: First, we can get control points from the process of lane detection for the first time. Second, the car movement is different from the Gaussian model. Car is go straight ahead, in other words, lane is always go down in our sight relatively. For the control points, they always move to the below until disappear in our sight. So when we use the particle filter to process control point, we only deal with the points which are below the control points (The top of the control points is vanishing point. It wont always like other points which will always

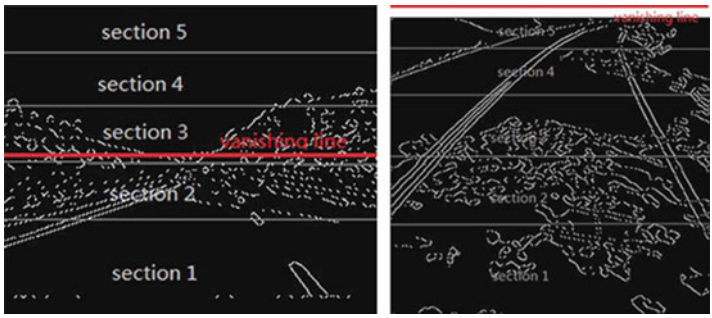

Fig. 70.3 Location of the vanishing line in an image. We selected the two representative images. In an image lane occupied the whole picture, and in the other lane only occupied half of the image. For this two images, our algorithm can find the precise vanishing line. So it is very robust

disappear in the field of vision, so we can handle this control point based on Gaussian distribution). Third, through particle filter resampling procedure, we can choose points each of which is below the control points and each of whose feature is most similar to the controls point as candidate points. Fourth, when the control points disappeared in the vision, we need to choose new control points below the vanishing point from candidate points.

Through lane detection and tracking, we can get many points. The answer of what points should we choose is in the part 4.

70.4 Select Lanes

Our next goal is to select the eligible points and pairs of lane. We use four types of evidence feature: support of the color of lanes, consistency of the two boundary hypotheses, consistency of a control point and the consistency of the vanishing point. We use capital letters, such as X, to represent variables and lowercase letters, such as x, to represent certain value. For the detection and tracking, when the pixel value of p is between red and yellow (the range of white or yellow is wide), $M(p) = 1$. On the contrary, $M(p) = 0$. Because there are many regular things in the roadside, such as buildings, green belts. These interferences beside the road are often treated as a lane. In addition, the shadow in the middle of a road will also affect the accuracy of the results. If the color range defined is small, we may rule out the lane directly when lanes are in different lighting conditions. So we have to balance the color range of interference and that of lane [10, 11]. Of course, we can't completely remove interference by the method above, as shown in Fig. 70.4.

Our goal is to choose the pair of lines which has the highest scores as the lane and refresh each control points by the end-point of each part of the lane.

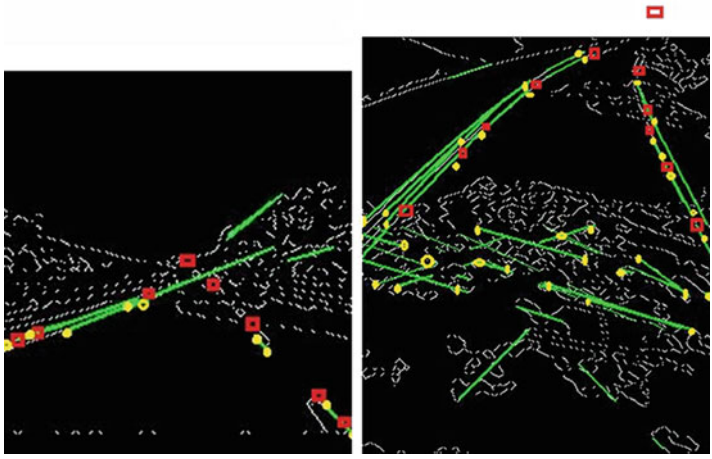

Fig. 70.4 Shows two images with control points and candidate points (control points in *red*, candidate points in *yellow*). We can see that there are still some parts which are not a part of a lane are treated as a lane, but they are relatively far away from the control points, so they will get a very loss weight and have less effect on the result. In addition, each candidate point is under a control point(the farther,the less weight). The control point on the top is special. There are no candidate points near it, and we will use it for scoring each pair of lines' intersection

$$maxF(X_i); \tag{70.1}$$

Where X is the random variable,$x_i = x_l, x_r$ denote a specific left and right of a pair lane, and m is a mark in four types of evidence. When we assume that the evidence variable m is a set of four types of independent evidence variables, $\mathrm{m} = (m_{c1}, m_v, m_p, m_{c2})$,where m_{c1} is a set of marks in the current frame, the value of m_{c1} is marked by the range of color, m_v is a set of marks which are marked by the relative between location of nodes and the disappear straight line, m_p is a set of marks which are marked by the consistency of a pair of a lane, m_{c2} is a set of marks which are mark by the particle filter. The mark of each pair of lane hypotheses is:

$$F(X_i) = M(x_i|m_{c1}) * M(x_i|m_v) * M(x_i|m_p) * M(x_i|m_{c2}) \tag{70.2}$$

where

$$M(x_i|m_{c1}) = \sum M_p \tag{70.3}$$

As previously said, it is depended on the color.

$$M(x_i|m_v) = \frac{1}{\sqrt{(x_i - x_v)^2 + (y_i - y_v)^2}} \tag{70.4}$$

Where (x_i, y_i) is the coordinates of the variable, (x_v, y_v) is the coordinates of the vanishing point.

$$M(x_i|m_{c2}) = \frac{1}{|k_l - k_r|} \tag{70.5}$$

Where k_l/k_r represents the curvature of the left/right lane. The last part $(M(x_i \mid m_{c2}))$ is calculated by the normalization of the particle filter.

70.5 Experimental Results

The algorithm has been thoroughly tested on several platforms. The testing sessions included different weather and lighting conditions. The amount of the recognition error rate is greatly reduced. To the lanes contains shadow or the curved lane, our algorithm also gets a good result. In addition, it can rule out regular construction and green belts which can influence the results deeply, as shown in Fig. 70.5.

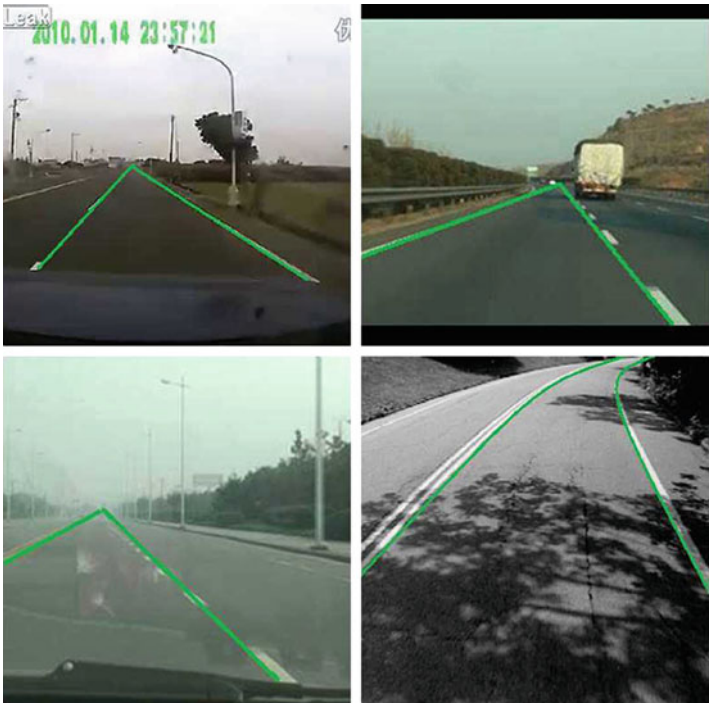

Fig. 70.5 Shows the final result after the algorithm processing

Conclusion

We novelly present an algorithm which is not the same with other as follows:

1. Our method uses vanishing point for obtaining initial control points in five sections and detecting lanes.
2. Track lanes through particle filter on each controls.
3. Refresh the control points through an scoring algorithm.

We can get some pairs of line though an vanishing point in detecting parts, get some pairs of lines though particle filter on each control points, find the lane in all the pairs of lines though the scoring algorithm, and then refresh these control points by the end-points of each part of the lane. The detection and tracking approach are able to deal with weak lighting situation, different weather conditions, lane markings, regular construction, green belts, in shadow, etc. In these challenging scenario, our algorithm accuracy is 0.94, rejection rate of 0.03, and is not sensitive to initialization of a parameter setting. Besides, we can deal with full and half horizons in an image. So this is a robust, high efficiency, simple operation, and shorter algorithm.

Acknowledgements This work is supported by National Nature Science Foundation of China (NSFC) grand No.61271288 and Specialized Research Fund for the Doctoral Program of Higher Education (SRFDP) grand No.74235986.

References

1. Serge B, Michel B (1944) Road segmentation and obstacle detection by a fast watershed transform. In: Proceedings of the intelligent vehicles'94 symposium, pp 296–301
2. Pomerleau D (1995) RALPH: Rapidly adapting lateral position handler. In: Proceedings of intelligent vehicle symposium, pp 506–511
3. Bertozzi M, Broggi A (1996) Real-time lane and obstacle detection on the gold system. In: Proceedings of IEEE intelligent vehicle, pp 216–218
4. Wang Y, Shen D, Teoh EK (1998) Lane detection using catmull-rom spline. In: Proceedings of the IEEE Intelligent Vehicles
5. Wang Y, Teoha EK, Shen D (2004) Lane detection and track using B-snake. Image Vis Comput 22(4):269–280
6. Hamburger C (1995) Quasimonotonicity, regularity and duality for nonlinear systems of partial differential equations. Ann Mat Pura Appl 169:321–354
7. Want JS, Knipling RR Single-vehicle roadway departure cranshes: problem size assessment and statistical description. National Highway Traffic Safety Administration Technical Report DTNH-22-91-C-03121
8. Zhang Z (2000) A flexible new technique for camer calibration. IEEE Trans Pattern Anal Mach Intell 22(11):1330–1334

9. Kim ZW (2008) Robust lane detection and tracking in challenging scenarios. IEEE Trans Intell Transp Syst 9(1):16–26
10. Tsai T, Chan V (2006) HSI color model based lane-marking detection. In: 2006 I.E. intelligent transportation systems conference, pp 1169–1172
11. Chin K, Lin S (2005) Lane detection using color-based segmentation. In: Proceedings of the IEEE intelligent vechicles symposium, pp 706–711

Chapter 71
A Dynamic Template Combination of Pixels for License Plate Recognition

Maopeng Xu, Jing Ni, and Mei Xie

Abstract This invention creatively puts forward a method that we can use a dynamic template combination of pixels for character segmentation in license plates. Firstly, we can obtain the dynamic vehicle monitoring area through the background modeling based on Gaussian mixture model and local license plate by using the edge information of license plate. Secondly, combining structure information, texture information, the rules of arrangement and maximum correlation among characters, we will find segmentation position after sliding this template. Then we can get the best position of license plate segmentation through calculating the number of nonzero pixels in the segmentation position in a binary image. At the end, after extracting the features of the characters, we should use the SVM for training and license plate character recognition [1, 2]. Compared with other solutions in the field, the invention has high accuracy, good robustness and stability in complex environment.

Keywords Image classification • Image recognition • Image segmentation • Image texture • Object detection

71.1 Introduction

With the development of machine learning and pattern recognition, labor management already cannot meet the actual needs. At the same time, microelectronics, communications and computer technology in the field of traffic greatly improve the efficiency of traffic management. License Plate Recognition (LPR) is an important part of modern intelligent transportation system, and the application is very extensive [3]. Based on digital image processing, pattern recognition and computer vision technology, it can analyze the vehicle images taken by a camera or video, and gets every car's license plate number [4]. Then it can complete the process of recognition. Through some subsequent processing, it can be used in the parking management, traffic flow control measurement, vehicle positioning, car alarm, automatic

M. Xu (✉) • J. Ni • M. Xie
University of Electronic Science and Technology of China (UESTC), Sichuan, China
e-mail: 452777728@qq.com; 814646634@qq.com; XIEMEI@uestc.edu.cn

J. Mu et al. (eds.), *The Proceedings of the Third International Conference on Communications, Signal Processing, and Systems*, Lecture Notes in Electrical Engineering 322, DOI 10.1007/978-3-319-08991-1_71

regulation of highway, and other places [5, 6]. It has realistic significance to maintain traffic safety and urban public security, prevent traffic jam, realize a traffic automation management and intelligent city. But the existing license plate recognition methods have many shortcomings, such as low recognizing precision, etc [7].

In general, vehicle license plate recognition system can be divided into three parts: the license plate location, vehicle license plate character segmentation and vehicle plate character recognition. Now with machine learning and pattern recognition techniques development, it is not a problem to get the license plate characters though neural network, template matching or support vector machines (SVM) method. How to accurately get the segmentation of plate characters has becoming the ultimate problem.

There are some challenges in segmentation of plate characters as follows:

1. According to People's Republic of China motor vehicle plate under (GA36-2007), motor vehicle plate contains seven characters, and width of characters is roughly same except "1". Among these characters whose width is roughly same, compared to other character, "j", "t" and "l" have their particularity; Characters in motor vehicle plates, except "Shaanxi", "Chuan", and minority characters which are not consortium, other are connected.
2. Vehicle license plate recognition system in adverse weather conditions, such as rain, fog, snow, will receive the fouled or blocked characters.

Current license plate character segmentation algorithms have the methods as follows:

1. The projection method. Projection method is the tradition of classical character segmentation algorithms, and has been widely applied in sophisticated character recognition systems. Although it is insensitive to slightly fuzzy license plate and is easy to be implemented, it's prone splitting. For "1", "j", "l", "t" and other special characters, it will be dealt as a noise and seriously affect the accuracy of license plate when the upper or lower boundaries are not cut precisely [8].
2. The connecting area analysis method. Connection area analysis method uses the characters from second to seventh which are English characters or numbers whose feature is consortium. But this method is poor adaptability to Chinese characters [9].

71.2 Licence Plate Detection

After obtaining the single vehicle license plate in the target area, we can achieve accurate segmentation of plate as follows:

1. Firstly, license plate recognition system receives the image data stream collected from monitoring device. Based on the Gaussian mixture background modeling method and the use of weights and variance, we can get sports scene in the foreground and background. By subtracting the foreground and background we

can get every movement vehicles within the scene. Due to model the moving object's background, we should update the parameters real-time. The corresponding formula is described in Eq. (71.1). As in (71.1), $M_{k,t}$ is the update parameter [10].

$$W_{k,t} = (1 - a)W_{k,t-1} + aW_k \tag{71.1}$$

2. Using Bayesian classifier as a core part of tracking algorithms, and the corresponding formula is described in Eq. (71.2). Details about this can be seen in [11].

$$H(v) = log\left(\frac{\prod_{i=1}^{n} p(v_i|y=1)p(y=1)}{\prod_{i=1}^{n} p(v_i|y=0)p(y=0)}\right) \tag{71.2}$$

3. Due to the inherent properties of the license plate, which has a jumping point edge, we use adaptive threshold method to binary the edge detection image obtained. In this way we can remove some of the obvious interference and interference noise generated point [12].
4. The target area was subjected to morphological closing operation after extracting connected domain. Then according to the aspect ratio to remove some pseudo plates. After this we should seek their smallest circumscribed rectangle as coarse position of license plates [13].
5. Use projection method to adjust the angle of the plates, we can get the fine position of license plates (Fig. 71.1) [14].

71.3 Licence Plate Character Segmentation

After obtaining the single vehicle license plate in the target area, we can achieve accurate segmentation of plate characters as follows:

1. Figure 71.2. Setting some plate parameters: The license plate obtained after above is normalized, and is scaled to the unity dimension h. Then the binary processing is made on the license plate (white standing for characters and black standing for background). According to the current standard for license plate, the whole license plate's length-width ratio is r_1. Second and third character have the maximum interval, whose length-width ratio is r_2. Others are r_3. Finally, the character width is $w_1 = r_1 * h$, second and third characters' interval width is $w_2 = r_2 * h$ and other characters interval is $w_3 = r_3 * h$. We can get $w = 7 * w_1 + w_2$. Set a template, as shown in Fig. 71.3. Because it may have a great margin of error in above steps, we should set the total width of the template is w/2 and height is h at first to improve the robustness and stability of the template.
2. Slide the templates on the precision positioning of plates from the left to the end of the right side (one pixel at a time). Keep the number of pixels in the position

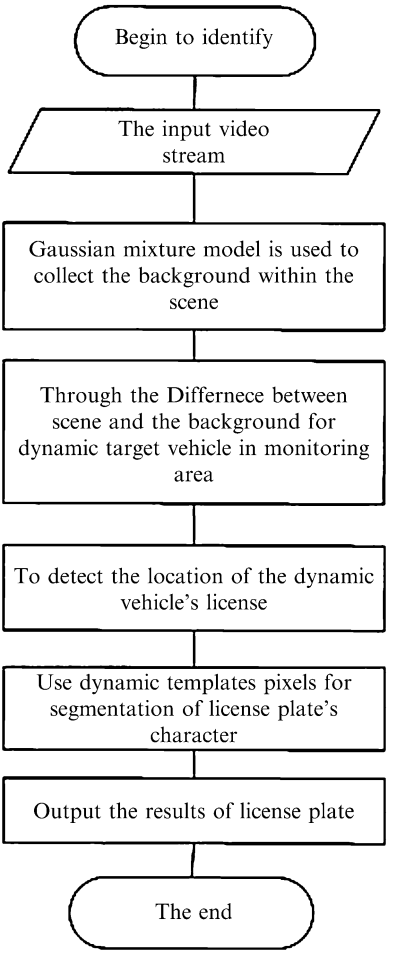

Fig. 71.1 Flow diagram of the algorithm

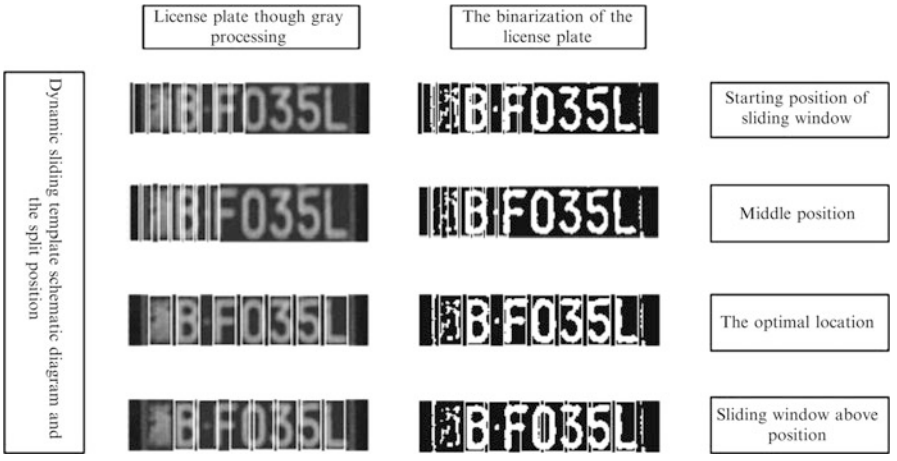

Fig. 71.2 Shows the effect on results by different sliding window

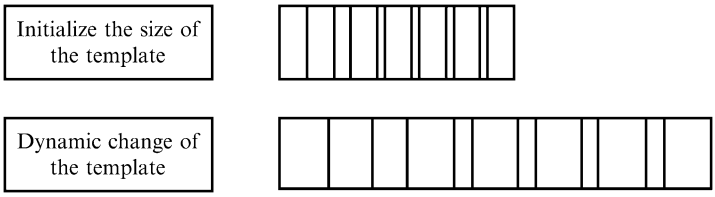

Fig. 71.3 Shows the sliding window

where the template local in the segmentation as well as binary plate. Because beginning of the plate is usually at the first one-third of the plate in the whole normalization plate, although the template does not reach the normalized plate right side, it still ended. Slide template again after increasing the total width of the template, template characters and interval between characters. Then slide template with this rule until the template equals the size of the normalized plate.

3. We can get multiple results based on dynamic template combined with pixels. Then select the location which contains a maximum of pixels as the final segmentation location.

71.4 Licence Plate Recognition

Identify the steps as follows:

1. We should normalize the known characters, and then extract the character features to a classifier for training. Finally, we can get the training results from all the characters. This invention using SVM in approach to training with license plate characters classified recognition.
2. Normalize the split characters and extract the characteristics of vehicle license plate character. Then vehicle use SVM classifier for license plate character recognition.
3. We can get multiple results based on dynamic template combined with pixels. Then select the location which contains a maximum of pixels as the final segmentation location.

71.5 Experimental Results

The present contribution is based on dynamic template pixels of license plate character segmentation. To get the character segmentation, verified by the experiment, the Chinese characters recognition rate reached 0.9755, letters of English character recognition rate of 0.9905, the digital character recognition rate of 99.56, the character of statistical average recognition rate of 0.98872. The results is shown in Fig. 71.4.

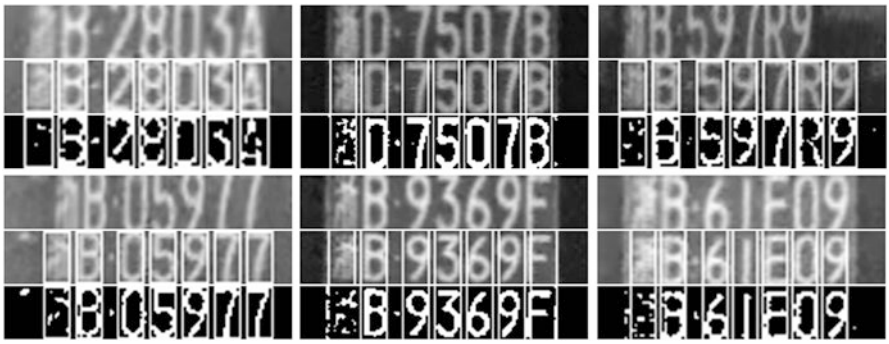

Fig. 71.4 Shows the results. Each image with three parts: the original *gray* image, the image after segmentation and binary image after segmentation

This contribution is carried out in the Matlab intuitive, and achieved very good results. Then port it to C + + platform (Visual Studio 2008). In the actual test, we use 5050 pictures which is taken in different weather field including sunny, cloudy, night, rain, fog, snow days. And in these pictures license plates are horizontal, inclined, shelter, etc. After a lot of valid test, compared with the traditional method, the method of the contribution has good robustness and versatility in a complex environment (Fig. 71.4).

Conclusion

The innovation of the present contribution as follows:

1. A new method of license plate character segmentation is presented. The method makes full use of the license plate structure and texture information, uses different characters between the rules of arrangement and maximum correlation of distribution among characters. It can get license plate character segmentation precisely. In addition, it can prevent inaccurately segmentation from characters in part of barrier and the dirty. Through character segmentation in the license plate in the same target vehicle for many times, we can get different segmentation results and number of nonzero pixels in the corresponding position of the binary image. Then take the position which contains the most nonzero pixels in the binary image as the final segmentation result of license plate character segmentation.
2. For the early stage of the plate coarse positioning and precision whose positioning is not very good, this method still has a good recognition result. Experiments prove that the new license plate character segmentation method can greatly improve the robustness of license plate recognition system and the stability of the results.

Acknowledgements This work is supported by National Nature Science Foundation of China (NSFC) grand No.61271288 and Specialized Research Fund for the Doctoral Program of Higher Education (SRFDP) grand No.74235986.

References

1. Comelli P, Ferragina P, Granieri MN, Stabile F (1995) Optical recognition of motor vehicle license plates. IEEE Trans Veh Technol 44(4):790–799
2. Draghici S (1997) A neural network based artificial vision system for license plate recognition. Int J Neural Syst 8(1)–126
3. Huang YP, Lai SY, Chuang WP (2004) A template-based model for license plate recognition. In: IEEE conference on networking, sensing and control, pp 737–740
4. Gao DS, Zhou J (2000) Car license plates detection from complex scene. In: Proceedings of the 5th international conference on signal processing, vol 2, pp 1409–1414
5. Hegt HA, De la Haye RJ, Khan NA (1998) A high performance license plate recognition system. In: Proceedings of IEEE international conference on system, man, and cybernetics, vol 5, pp 4357–4362
6. Hu Y, Zhu F, Zhang X (2005) A novel approach for licence plate recognition using subspace projection and probabilistic neural network. In: Wang J, Liao X, Yi Z (eds) Lecture notes on computer science, vol 3497, pp 216–221. Springer, New York
7. Hermida XF, Rodriguez FM, Lijo JLF, Sande FP, Iglesias MP (1997) A system for the automatic and real time recognition of VLP's (Vehicle License Plate). In: Proceedings of lecture notes in computer science, vol 1311, pp 552–558
8. Martín F, García M, Alba L (2002) New methods for automatic reading of VLP's (Vehicle Licence Plates). In: Proceedings of IASTED international conference on SPPRA
9. Kim KI, Jung K, Kim J (2002) Color texture-based object detection: An application to licence plate localization In: Lee S-W, Verri A (eds) Lecture notes on computer science, vol 2388, pp 293–309 Springer, New York
10. Hontani H, Koga T (2001) Character extraction method without prior knowledge on size and position information. In: Proceedings of the IEEE international conference on vehicle electronics, pp 67–72
11. Keller JM, Krishnapuram R, Yager RR, Zadeh LA (1994) Fuzzy decision models in computer vision. In: Fuzzy sets, neural networks, and soft computing, pp 213–232. Van Nostrand, New York
12. Anagnostopoulos C, Anagnostopoulos I, Vassili L, Eleftherios K (2006) A licence plate recognition algorithm for intelligent transportation system applications. IEEE Trans Intell Transp Syst 7(3):377–392
13. Duan TD, Hong Du TL, Phuoc TV, Hoang N (2005) Building an automatic vehicle licence plate recognition system. In: Proceedings of international conference on computer science RIVF, pp 59–63
14. Kim DS, Chien SI (2001) Automatic car license plate extraction using modified generalized symmetry transform and image warping In: Proceedings of IEEE International symposium in industrial electronics, vol 3, pp 2022–2027

Chapter 72
Spatial Context Constrained Characteristic View Extraction for 3D Model Retrieval

Anan Liu, Zhongyang Wang, Weizhi Nie, Xiaying Wu, Yuting Su, and Zhaoxuan Yang

Abstract With the development of 3D camera, efficient and effective 3D model retrieval algorithms are highly desired and attracted intensive research attentions. In this paper, we proposed a view-based 3D model retrieval method based on spatial context constrained characteristic view extraction method. First, according to the spatial constraints of views, we cluster all of 2D images, which capture 3D model from different angles. Second, the random-walk algorithm is utilized to update the weight of each view to help us to select the most representative view. Finally, we apply Bayesian model to compute the similarity between query model and candidate 3D model to find the best matching 3D model. Experimental comparisons have been conducted on the ETH and NTU 3D model datasets, and the results have demonstrated the superiority of the proposed method.

Keywords 3D model retrieval • Characteristic view • Spatial context • Energy maximization

72.1 Introduction

With the development of computer graphics, modeling tools, 3D graphic accelerated hardware, more and more equipments have been used to record 3D objects. Especially, the advent of Microsoft Kinect sensor strongly advocates this trend. These equipments generate large amounts of 3D models and 3D images. Therefore, the research on how to efficiently retrieve and manage these 3D models is becoming especially hot.

Many effective retrieval methods were proposed to handle this problem [3, 4, 14]. Ankerst et al. [1] proposed an optimal selection of 2D views from a 3D model, which focuses on numerical characteristics obtained from the 3D model representative features. Shih et al. [13] proposed Elevation Descriptor (ED) feature, which is

A. Liu • Z. Wang • W. Nie (✉) • X. Wu • Y. Su • Z. Yang
School of Electronic Information Engineering, Tianjin University, Tianjin, China
e-mail: truman.nie@gmail.com

J. Mu et al. (eds.), *The Proceedings of the Third International Conference on Communications, Signal Processing, and Systems*, Lecture Notes in Electrical Engineering 322, DOI 10.1007/978-3-319-08991-1_72

invariant to translation and scaling of 3D models. Tarik et al. [2] proposed a Bayesian 3D object search method. X-means is utilized [12] to select characteristics views and Bayesian model is used to compute the similarity between different 3D objects. Gao et al. [9] proposed a general framework for 3D object retrieval without the limitation of camera array restriction. Gaussian model is used to simulate the feature distribution of query model and candidate model. The high computation complexity makes it unsuitable in real world. Among all these retrieval methods, spatial information has not be considered, which might benefit the characteristic view extraction.

In this paper, we propose a new 3D model retrieval method based on the spatial constraint information of views. First, the spatial information of view is utilized to structure one graph model. We apply graph cluster method to cluster all of these views into a set of sub-clusters. Second, the random-walk algorithm is used to update and generate the weight for each view. We selected the maximum weight of view as the characteristic view for each sub-cluster. Finally, Bayesian Model is utilized to compute the posterior probability as similarity between query model and candidate 3D model.

The main contributions of our work are summarized as follows:

- Both spatial constraint and visual similarity are leveraged for objective function formulation to group all 2D images of one 3D model into different characteristic clusters,
- We utilized the random walk method to update the weights of individual 2D images of one characteristic cluster to select the characteristic view as the representative 2D image of this cluster,
- We propose a Bayesian model to compute the similarity between the query model and individual candidate 3D model.

This paper is organized as follows. In Sect. 72.2, we will detail the characteristic view extraction method. In this section, the spatial view clustering method and characteristic view selection method will be illustrated respectively. The similarity metric is defined to compute the similarity between query model and candidate 3D models will be illustrated in Sect. 72.3. Experimental results and discussions are provided in Sect. 72.4. Finally, we conclude the paper in section “Conclusions”.

72.2 Characteristic View Extraction

In this section, we will detail the characteristic view extraction method. In Sect. 72.2.1, we will introduce the view cluster method according to the spatial constraint information and visual feature of views. In Sect. 72.2.1, we will detail the characteristic view selection method for each cluster.

72.2.1 View Cluster Method

Each 3D model consists of a set of 2D images. To reduce the candidate 2D images for similarity measure during the process of model retrieval, it is necessary to extract the characteristic. To extract characteristic views, the original 2D images of one model need to be clustered by taking advance of both visual and spatial information. The rule for image clustering is to maximize the inner-class correlation while minimize the inter-class correlation. In terms of this rule, the view-constrained clustering method can be formulated as an energy minimization problem. The objective function consisting of two parts, data terms and smooth terms can be defined as:

$$\mathbb{C}' = arg\max_{\mathbb{C}} \sum_{i=1}^{m} E(v_i) + \sum_{i,j=1}^{m} E(v_i, v_j) \quad i \neq j, \quad v_i, v_j \in \mathbb{C}, \tag{72.1}$$

where $E(v_i)$ represents energy of view i. This term represents the contribution of this view for this cluster $\mathbb{C}$. $E(v_i, v_j)$ represents the correlation between different views. If two different views v_i and v_j belong to $\mathbb{C}$, $E(v_i, v_j)$ should have a higher value. The sum of $E(v_i, v_j)$ and $E(v_i)$ represents the entire energy of one specific clustering method for this 3D model.

Thus, $E(v_i)$ measures the agreement between cluster $\mathbb{C}$ and the observed data v_i. It can be computed by:

$$E(v_i) = D_1(f_i, f_{center}), \tag{72.2}$$

where f_{center} represents the feature of center point in $\mathbb{C}$. f_i represents feature of v_i. $D_1(f_i, f_{center})$ represents similarity between v_i and v_{center}, which is compute by:

$$D_1(f_i, f_{center}) = \frac{1}{\sqrt{(f_i - f_{center})^2}} \tag{72.3}$$

$E(f_i, f_j)$ affects the correlation among v_i, v_j and v_{center}. To this end, the computing function can be written:

$$E(v_i, v_j) = E(v_i) \cdot E(v_j) \cdot D_2(v_i, v_j) \quad i \neq j \tag{72.4}$$

where $E(v_i)$ and $E(v_j)$ are computed according to Eq. (72.3). $D_2(f_i, f_j)$ represents similarity between v_i and v_j, which is computed by:

$$D_2(v_i, v_j) = D_1(f_i, f_j) \cdot D_s(v_i, v_j), \tag{72.5}$$

where $D_1(v_i, v_j)$ is the computed by Eq. (72.3). $D_s(v_i, v_j)$ represents the spatial similarity between different two views, which is computed by:

$$D_s(v_i, v_j) = \frac{1}{Distance(v_i, v_j)}, \tag{72.6}$$

where $Distance(v_i, v_j)$ is the spherical distance between v_i and v_j. The centre of this sphere is the center of mass of this 3D model.

Finally, Eq. (72.1) can be converted to:

$$\begin{aligned} \mathbb{C}' = \underset{\mathbb{C}}{arg\max} \quad & \sum_{i=1}^{m} D_1(f_i, f_{center}) + \sum_{i,j=1}^{m} E(v_i) \cdot E(v_j) \cdot D_2(v_i, v_j) \\ s.t \quad & v_i, v_j \in \mathbb{C}, \end{aligned} \tag{72.7}$$

After the above process, we have successful convert our problem into one Energy Maximization problem. Many early proposed methods can be used to handle this problem [5, 11]. Graph cut [5] is applied in this paper. We applied many iterative to get a set of sub-clusters.

72.2.2 Characteristic View Selection

After clustering, we have a set of view clusters for each 3D model. Each cluster includes a set of 2D images. The fact is that all views do not have equal importance. The higher relevance photo has the higher weight exists among these photos. Thus, the random-walk method is utilized to update the weight for each image. This procedure can be formulated by

$$p^i_{rv_k} = \alpha w^0_i + (1 - \alpha) \sum_{i \neq k} s(v_i, v_k) w^n_i, \tag{72.8}$$

where α is a parameter determining how important the initial weight value is, w^0_i is the weight for each image, $S(v_i, v_k)$ is the similarity between two different image, which is computed by:

$$s(v_i, v_k) = \frac{1}{\sqrt{(f(v_i) - f(v_k))^2}} \tag{72.9}$$

This procedure is theoretically proved to converge after iterations. The initial weight is defined $w_{initial} = \frac{1}{N}$ for each image, where N is the size of cluster. Finally, we select the biggest weight of image as characteristic view.

72.3 Model Retrieval

Each model M_i of the collection $\mathbb{D} = \{M_1, \ldots, M_n\}$ can be represented by a set of characteristic views $M_i = \{v_1, v_2, \ldots, v_m\}$. m is the number of characteristic views. Considering a 3D request model Q, we wish to find the model $M_i \in \mathbb{D}$ which is the closest to Q. Therefore, M_i should corresponds to the highest probability $p(M_i \mid Q)$, which can be written:

$$P(M_i|Q) = \sum_{k=1}^{K} P(M_i|V_Q^k), \tag{72.10}$$

where K is the number of characteristic views of the model Q. By constraining that a represented view from Q can only match one view form M_i. The characteristic view with the maximum probability:

$$P(M_i|V_Q^k) = \max_{j=1}^{P} P(V_M^j|V_Q^k), \tag{72.11}$$

where P is the number of characteristic views of the model M. Till now, the Eq. (72.10) can be written as:

$$P(M_i|Q) = \sum_{k=1}^{K} \max_{j=1}^{P} P(V_M^j|V_Q^k), \tag{72.12}$$

where $P(V_M^j|V_Q^k)$ can be computed by Eq. (72.9). Finally, the matched model M of query model Q is:

$$M^{'} = arg\max_{i \in M} P(M_i|Q). \tag{72.13}$$

72.4 Experimental Setup

72.4.1 Dataset

In order to demonstrate the performance of the proposed method, two 3D model datasets are used. The first dataset is the The Eidgenössische Technische Hochschule Zürich (ETH) dataset [7], which is a-real-world 3D object multi-view dataset. It contains 80 objects from eight categories. Each category includes 10 objects and each object contains a group of 41 views which uniformly distribute in the upper viewing hemisphere, subdividing an octahedron to the third recursion level. Some simple example objects from the ETH are shown in Fig. 72.1.

The second dataset is the National Taiwan University (NTU) 3D Model Benchmark [6]. There are totally 1,833 objects from 48 categories. And 47 categories are

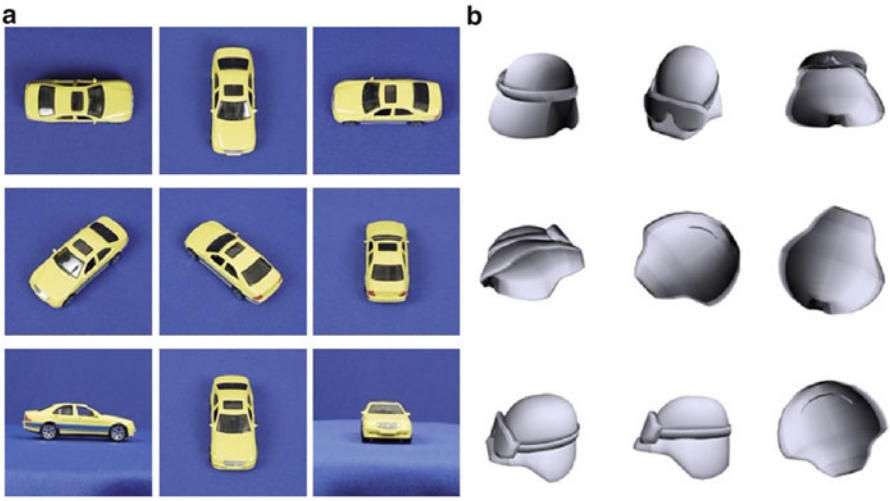

Fig. 72.1 Example 3D objects from the ETH dataset. (**a**) Example 3D objects from the ETH dataset; (**b**) Example 3D objects from the NTU-60 dataset

chosen as the testing database. Some example objects in the NTU dataset are shown in Fig. 72.1. In our experiments, we employed to the virtual cameras to capture initial views for 3D objects. The first camera array contains 60 cameras that are set on the vertices of a polyhedron with the same structure with Buckminsterfullerene (C60). This dataset is named as NTU-60. The second camera array contains 216 cameras, which are set on the six different views of the bounding box: front, top, right, rear, bottom and left. In each view, 36 cameras are uniformly placed. This dataset is named as NTU-216.

72.4.2 Experimental Results

We compare the proposed method with the Adaptive Views Clustering (AVC) [2] and the Camera Constraint-Free View-Based (CCFV) [10]. The two methods are view-based 3D object retrieval methods. AVC is an adaptive views clustering method based on Bayesian Model. This method applied X-means to select characteristic views for each 3D model, and a probabilistic Bayesian method for 3D model indexing based on these views. CCFV first builds a positive matching model and a negative matching model via positive and negative matching samples. Then, CCFV generates a query Gaussian model by combining the positive and negative models. Finally, query Gaussian model is used to judge the similarity between query and candidate 3D model.

In this paper, Nearest Neighbor Precision (NN), First Tier (FT), Second Tier (ST), E-Measure, Discounted Cumulative Gain (DCG) is used to evaluate the

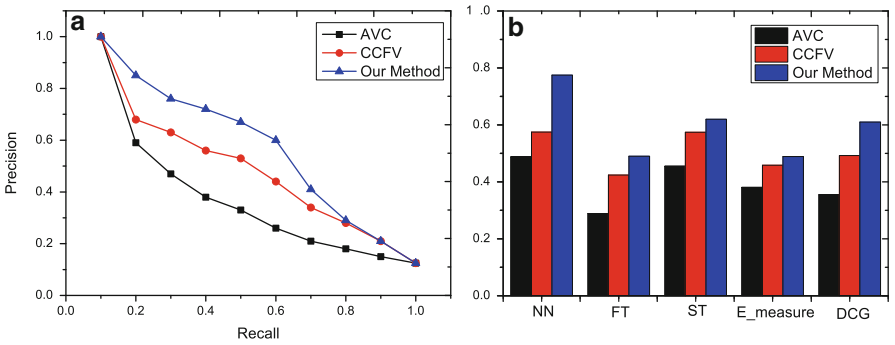

Fig. 72.2 The retrieval result in the ETH data set. (**a**) Precision-recall curves; (**b**) comparison of average NN, FT, ST, E-Measure and DCG

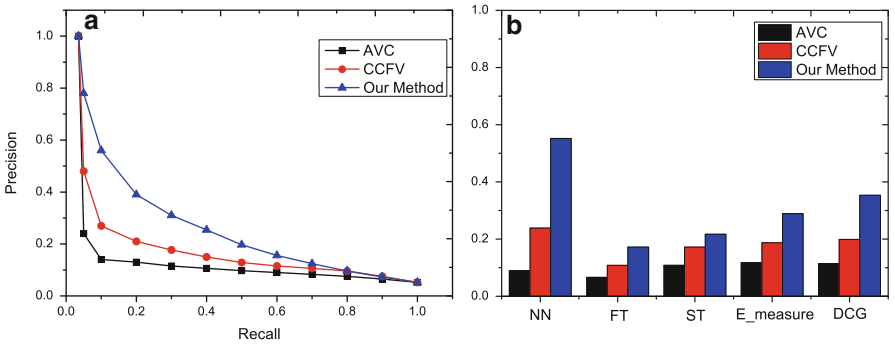

Fig. 72.3 The retrieval result in the NTU-60 data set. (**a**) Precision-recall curves; (**b**) comparison of average NN, FT, ST, E-Measure and DCG

performance of the proposed method [8]. The Precision-recall curves of the experimental and comparison results of the performance measure are shown in Figs. 72.2, 72.3 and 72.4 respectively.

From the experimental results, we can find that the proposed method is better than other comparative methods. Compared with AVC method, the biggest difference is characteristic views extraction. We consider spatial constraint information to construct graph model, and apply graph cut to cluster all of images instead of X-means in AVC. The experimental results prove the effective of the proposed method. Compared with CCFV method, the characteristic views of the proposed method can well represent the feature of 3D model. While Gaussian model in CCFV can not well model the distribution of features for each 3D object. The experimental results in NTU-60 and NTU-216 demonstrate this conclusion.

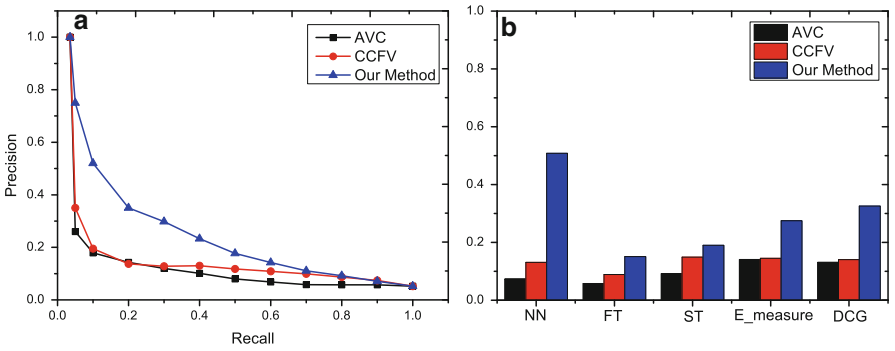

Fig. 72.4 The retrieval result in the NTU-216 data set. (**a**) Precision-recall curves; (**b**) comparison of average NN, FT, ST, E-Measure and DCG

Conclusions

In this paper, we consider spatial constraint information of view to propose a new characteristic view extraction method. First, we utilize spatial information of view to structure graph model. Graph cut is applied to handle graph clustering problem. Then, Random-walk algorithm generates the weight of view for characteristic view extraction. Finally, Bayesian approach is used to compute the matching score between query model and candidate 3D object as the basis of retrieval. Experimental results demonstrate the superiority of this method.

Acknowledgements This work was supported in part by the National Natural Science Foundation of China (61472275, 61170239), the Tianjin Research Program of Application Foundation and Advanced Technology (15JCYBJC16200), the grant of Elite Scholar Program of Tianjin University (2014XRG-0046).

References

1. Ankerst M, Kastenmüller G, Kriegel HP, Seidl T (1999) 3D shape histograms for similarity search and classification in spatial databases. In: SSD, pp 207–226
2. Ansary TF, Daoudi M, Vandeborre JP (2007) A bayesian 3-D search engine using adaptive views clustering. IEEE Trans Multimedia 9(1):78–88
3. Antini G, Berretti S, Bimbo AD, Pala P (2005) Retrieval of 3d objects using curvature correlograms. In: ICME, pp 735–738
4. Assfalg J, Bertini M, Bimbo AD, Pala P (2007) Content-based retrieval of 3-D objects using spin image signatures. IEEE Trans Multimedia 9(3):589–599
5. Boykov Y, Veksler O, Zabih R (2001) Fast approximate energy minimization via graph cuts. IEEE Trans Pattern Anal Mach Intell 23(11):1222–1239

6. Chen DY, Tian XP, Shen YT, Ouhyoung M (2003) On visual similarity based 3D model retrieval. Comput Graph Forum 22(3):223–232
7. Funkhouser TA, Min P, Kazhdan MM, Chen J, Halderman JA, Dobkin, DP, Jacobs DP (2003) A search engine for 3D models. ACM Trans Graph 22(1):83–105
8. Gao Y, Dai Q, Zhang N (2010) 3D model comparison using spatial structure circular descriptor. Pattern Recogn 43(3):1142–1151
9. Gao Y, Wang M, Shen J, Dai Q, Zhang N (2010) Intelligent query:open another door to 3D object retrieval. In: Proceedings of ACM conference on multimedia
10. Gao Y, Tang J, Hong R, Yan S, Dai Q, Zhang N, Chua TS (2012) Camera constraint-free view-based 3-D object retrieval. IEEE Trans Image Process 21(4):2269–2281
11. Goldberg AV, Tarjan RE (1988) A new approach to the maximum-flow problem. J ACM 35 (4):921–940
12. Pelleg D (2005) X-means: extending k-means with efficient estimation of the number of clusters. In: Computational intelligence, pp 91–96
13. Shih JL, Lee CH, Wang JT (2007) A new 3D model retrieval approach based on the elevation descriptor. Pattern Recogn 40(1):283–295
14. Tangelder JWH, Veltkamp RC (2003) Polyhedral model retrieval using weighted point sets. Int J Image Graph 3(1):209

Chapter 73
Unequal-Compressed Sensing Based on the Characteristics of Wavelet Coefficients

Weiwei Li, Ting Jiang, and Ning Wang

Abstract Compressed sensing (CS) has drawn quite an amount of attentions as a joint sampling and compression approach. Its theory shows that if a signal is sparse or compressible in a certain transform domain, it can be decoded from much fewer measurements than suggested by the Nyquist sampling theory. In this paper, we propose an unequal-compressed sensing algorithm which combines the compressed sensing theory with the characteristics of the wavelet coefficients. First, the original signal is decomposed by the multi-scale discrete wavelet transform (DWT) to make it sparse. Secondly, we retain the low frequency coefficients; meanwhile, one of the high frequency sub-band coefficients is measured by random Gaussian matrix. Thirdly, the sparse Bayesian learning (SBL) algorithm is used to reconstruct the high frequency sub-band coefficients. What's more, other high frequency sub-band coefficients can be recovered according to the high frequency sub-band coefficients and the characteristics of wavelet coefficients. Finally, we use the inverse discrete wavelet transform (IDWT) to reconstruct the original signal. Compared with the original CS algorithms, the proposed algorithm has better reconstructed image quality in the same compression ratio. More importantly, the proposed method has better stability for low compression ratio.

Keywords Discrete wavelet transform • Random Gaussian matrix • Unequal-compressed sensing • Image compression • SBL algorithm

73.1 Introdution

With the recent advances in computer technologies and Internet applications, the number of multimedia files increase dramatically. Thus, despite extraordinary advances in computational power, the acquisition and processing of signals in application areas such as imaging, video and medical imaging continues to pose a tremendous challenge. The recently proposed sampling method, Compressed

W. Li (✉) • T. Jiang • N. Wang
Key Laboratory of Universal Wireless Communication, Ministry of Education, Beijing University of Posts and Telecommunications, Beijing, China
e-mail: puma8566@bupt.edu.cn

J. Mu et al. (eds.), *The Proceedings of the Third International Conference on Communications, Signal Processing, and Systems*, Lecture Notes in Electrical Engineering 322, DOI 10.1007/978-3-319-08991-1_73

Sensing (CS) introduced in [1–3], can collect compressed data at the sampling rate much lower than that needed in Shannon's sampling theorem by exploring the compressibility of the signal. Suppose that $\boldsymbol{x} \in \mathbb{R}^{N \times 1}$ is a length-N signal. It is said to be K-sparse (or compressible) if $\boldsymbol{x}$ can be well approximated using only $K \ll N$ coefficients under some linear transform

$$\boldsymbol{x} = \boldsymbol{\Psi}\boldsymbol{\omega} \tag{73.1}$$

where $\boldsymbol{\Psi}$ is the sparse transform basis, and $\boldsymbol{\omega}$ is the sparse coefficient vector that has at most K (significant) nonzero entries.

According to the CS theory, such a signal can be acquired through the random linear projection:

$$\boldsymbol{y} = \boldsymbol{\Phi}\boldsymbol{x} + \boldsymbol{n} = \boldsymbol{\Phi}\boldsymbol{\Psi}\boldsymbol{\omega} + \boldsymbol{n} \tag{73.2}$$

where, $\boldsymbol{y} \in \mathbb{R}^{M \times 1}$ is the sampled vector with $M \ll N$ data points. $\boldsymbol{\Phi}$ represents a $M \times N$ random matrix, which must satisfy the Restricted Isometry Property (RIP) [4], and $\boldsymbol{n} \in \mathbb{R}^{M \times 1}$ is the measurement noise vector. Solving the sparsest vector $\boldsymbol{\omega}$ consistent with the Eq. (73.2) is generally an NP-hard problem [4]. For the problem of sparse signal recovery with $\boldsymbol{\omega}$, lots of efficient algorithms have been proposed. Typical algorithms include basis pursuit (BP) or l_1-minimization approach [5], orthogonal matching pursuit (OMP) [6], and Bayesian algorithm [7].

CS theory provides us a new promising way to achieve higher efficient data compression than the existing ones [8–10]. The reference [9] proposed a new kind of sampling methods, it sampled the edge of the high frequency part of the image densely and the non-edge part randomly in the encoder, instead of using the measurement matrix to obtain the lower-dimensional observation directly in the traditional compressed sensing theory. The reference [10] proposed an improved compressed sensing algorithm based on the single layer wavelet transform according to the properties of wavelet transform sub-bands. But this article doesn't consider the characteristic of high sub-band frequency coefficients. In this paper, the proposed unequal-compressed sensing algorithm combines the compressed sensing theory with the characteristics of the wavelet coefficients. The proposed algorithm has better reconstructed image quality in the same compression ratio. Usually, the coefficients are not zero but compressible (most of them are negligible) after sparse transform (e.g., DWT). Therefore, the sparse Bayesian learning (SBL) algorithm is used to resolve the reconstructed problem, which can recover the image correctly and effectively.

The remainder of this paper is organized as follows. Section 73.2 introduces the characteristics of wavelet coefficients. In Sect. 73.3, the proposed algorithm for image compression is presented. In Sect. 73.4, experiment results are given. Conclusions of this paper and some future work are given in Sect. 73.5.

73.2 Characteristics of Wavelet Coefficients

73.2.1 Characteristic One

Wavelet transform as the sparse decomposition has been widely used in compressed sensing. In this paper, we choose the discrete wavelet transform (DWT) as the sparsifying basis. As we know, the low frequency coefficients are much more important than the high frequency coefficients. Table 73.1 gives an idea about the PSNR (in dB) achieved that the image restoration only used low frequency coefficients or high frequency coefficients when the images are decomposed by four-scale DWT. In the Table 73.1, we can see that the low frequency coefficients make far greater contribution to the PSNR than the high frequency coefficients. Therefore, we retain the low frequency to ensure the quality of image restoration, and the high frequency coefficients are measured by the random Gaussian matrix to achieve compression.

Table 73.2 shows that the PSNR is achieved by the Lena images using multi-scale DWT. We can see that the scale of the decomposition S is smaller, the contribution to the PSNR which is made by low frequency coefficients is greater, and the length of the low frequency coefficients ($N/2^S$) is longer. Therefore, we can choose the proper the scale of the decomposition S according to the compression ratio.

Table 73.1 The PSNR of four-scale DWT

	PSNR	
Image	Low frequency	High frequency
Lena	22.51	7.38
Cameraman	20.72	5.72
Baboon	19.21	5.64
Boat	20.31	5.48
Peppers	21.36	5.85
Fruits	21.81	3.48

Table 73.2 The PSNR of multi-scale DWT

	PSNR		
Scale S	Low frequency coefficients	High frequency coefficients	The length of low coefficients
1	31.97	7.25	$N/2$
2	27.32	7.27	$N/4$
3	23.91	7.31	$N/8$
4	21.16	7.38	$N/16$

73.2.2 Characteristic Two

In order to reduce the computational complexity and storage space, we make each column of image $\boldsymbol{x}$ as a $N \times 1$ signal to be coded alone. It is compressible in the discrete wavelet basis $\boldsymbol{\Psi}$. The coefficients of the two-scale decomposition structure are shown in Fig. 73.1.

We can see that wavelet coefficient $\boldsymbol{c}$ consists of three parts, which are $\boldsymbol{cA_2}$ (low frequency coefficients), $\boldsymbol{cD_2}$ (one of the high frequency sub-band coefficients) and $\boldsymbol{cD_1}$ (the other high frequency sub-band coefficients). We choose one column of image 256×256 Lena as a 256×1 signal to be decomposed alone. The decomposed high frequency sub-band coefficients are shown in Fig. 73.2.

We can see that, the locations of the larger coefficients in $\boldsymbol{cD_1}$ are almost two times than the locations of the larger coefficients in $\boldsymbol{cD}_2$. Then, we extend $\boldsymbol{cD}_2$ using the zero insertion method, the comparison of the extended $\boldsymbol{cD}_2$ and $\boldsymbol{cD}_1$ are shown

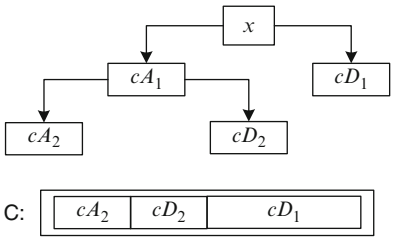

Fig. 73.1 The coefficients of the two-scale decomposition structure

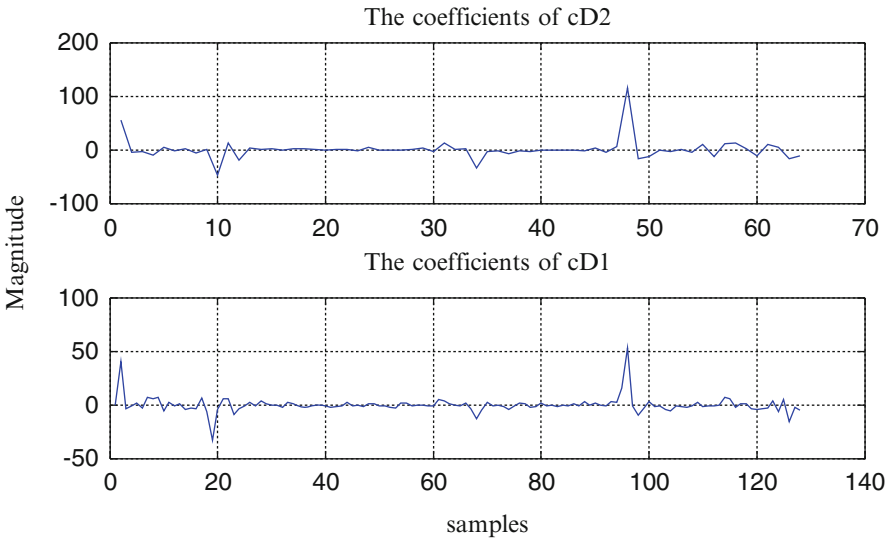

Fig. 73.2 The decomposed high frequency sub-band coefficients

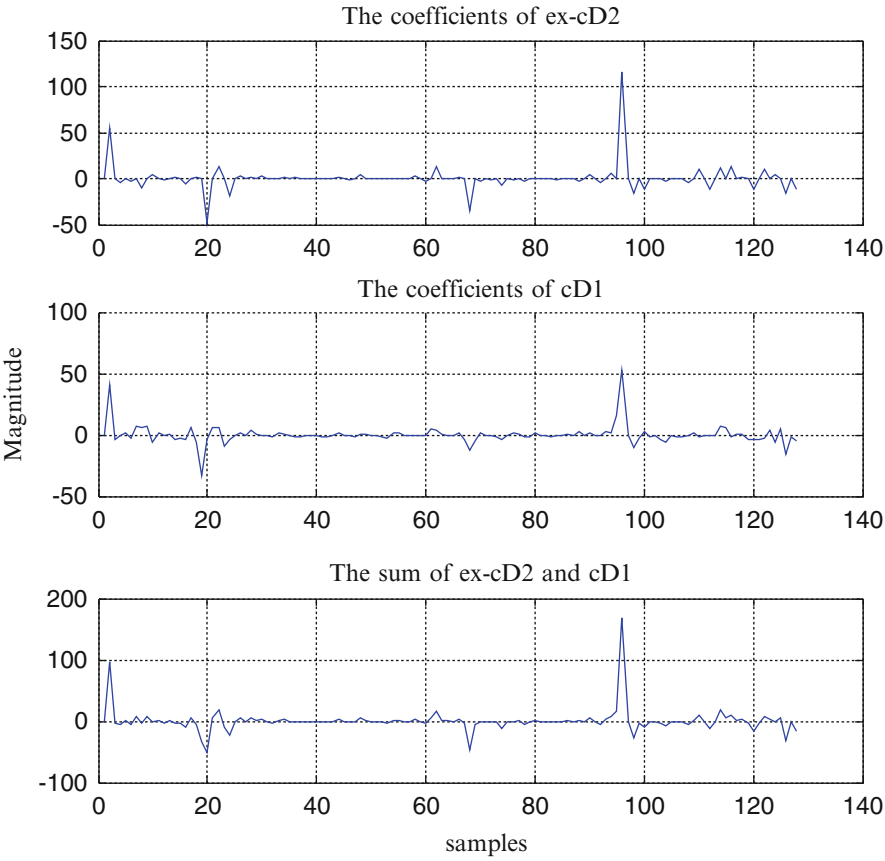

Fig. 73.3 The comparison of the extended cD_2 and cD_1

in Fig. 73.3. As can be seen from the Fig. 73.3, if the high frequency coefficient is lager (or smaller) at a certain location in $\boldsymbol{cD}_1$, the high frequency coefficient is also larger (or smaller) with a great probability at the same location in the extended $\boldsymbol{cD}_2(\boldsymbol{ex}\_\boldsymbol{cD}_2)$. Let $\boldsymbol{s}\_\boldsymbol{cD}_1\_\boldsymbol{cD}_2$ represents the sum of $\boldsymbol{ex}\_\boldsymbol{cD}_2$ and $\boldsymbol{cD}_1$, it has only a few of larger coefficients $\boldsymbol{c}_d$, other coefficients are almost close to zero. More importantly, the locations of the larger coefficients in $\boldsymbol{s}\_\boldsymbol{cD}_1\_\boldsymbol{cD}_2$ are almost the same as the locations of the larger coefficients in $\boldsymbol{cD}_1$ and $\boldsymbol{ex}\_\boldsymbol{cD}_2$. Let

$$\boldsymbol{s}\_\boldsymbol{cD}_1\_\boldsymbol{cD}_2 = \boldsymbol{ex}\_\boldsymbol{cD}_2 + \boldsymbol{cD}_1$$

Then

$$\boldsymbol{cD}_1 = \boldsymbol{s}\_\boldsymbol{cD}_1\_\boldsymbol{cD}_2 - \boldsymbol{ex}\_\boldsymbol{cD}_2$$

Let $\boldsymbol{c}_d$ represents the only a few of the largest coefficients in $\boldsymbol{s}\_\boldsymbol{cD}_1\_\boldsymbol{cD}_2$. According to $\boldsymbol{ex}\_\boldsymbol{cD}_2$ and $\boldsymbol{c}_d$, we can recover $\boldsymbol{cD}_1$ approximately.

73.3 The Proposed Algorithm for Image Compression

In the original CS algorithm for image compression, the $N \times N$ image is firstly decomposed by a certain sparse transform (e.g. wavelet transform). And then, random Gaussian matrix Φ is employed to measure the wavelet coefficients. At the decoder, the original image is recovered by SBL algorithm and inverse wavelet transform. However, we study that the high frequency sub-band coefficients have a strong relevance. The algorithm which combines compressed sensing theory with the characteristics of the wavelet coefficients is proposed. The specific steps are as follows:

- Step 1: in order to reduce the computational complexity and storage space, we make each column of image X as a $N \times 1$ signal x to be decomposed alone. It is compressible in the DWT Ψ. We decompose the signal x by S-scale DWT. Retain the low frequency coefficients $\boldsymbol{cA}_s$. The scale of the decomposition S is decided by the compression ratio.
- Step 2: let $\boldsymbol{s\_cD}_S\boldsymbol{\_cD}_i$ represent the sum of $\boldsymbol{ex\_cD}_S$ and $\boldsymbol{cD}_i$, $i = 1, \ldots S$–1. Restore the only a few of the larger coefficients $\boldsymbol{c}_i$, $i = 1, \ldots S$–1. Let m represents the number of the largest coefficients $\boldsymbol{c}_i$.
- Step 3: the random Gaussian matrix $M \times \frac{N}{2^s}(M < N/2^s)$ $\boldsymbol{\Phi}$ is employed to measurement sampling the $\boldsymbol{cD}_S$ to yield a sampled vector $\boldsymbol{y} = \boldsymbol{\Phi} \cdot \boldsymbol{cD}_S$.
- Step 4: we can use the SBL algorithm to recover the vector $\boldsymbol{c}\hat{\boldsymbol{D}}_S$ and then, according to $\boldsymbol{c}\hat{\boldsymbol{D}}_S$ and $\boldsymbol{c}_i$ to recover $\boldsymbol{c}\hat{\boldsymbol{D}}_i$, $i = 1, \ldots S$–1. Finally, we use the inverse discrete wavelet transform to reconstruct the original signal.

  The compression ratio of the proposed CS method is

$$\alpha = \frac{N/2^S + m \times i + M}{N} \tag{73.3}$$

Where, $N/2^S$ is the number of the low frequency coefficients, $m \times i$ represents the total number of the largest coefficients $\boldsymbol{c}_i$, $i = 1, \ldots S$–1. M is the dimension of measurement matrix $\boldsymbol{\Phi}$, and, $M < N/2^S$.

73.4 Experimental Results

The performance of the proposed algorithm has been evaluated by simulation. We choose the 256×256 Lena, Fruits, Baboon and Boat image as the original signals. We set the compression ratio α from 0.1 to 0.9. First, we determine the scale of the wavelet transform S according to the compression ratio α, and then get the length of the low frequency coefficients $N/2^S$. Secondly, we choose the proper the dimension M of measurement matrix to guarantee the high frequency coefficients $\boldsymbol{cD}_S$ transmits reliably. When the result is decimal, we choose the integer $\lfloor M \rfloor$. Thirdly, we get the number of the largest coefficients m according to the formula (73.3). When

the result is decimal, we choose the integer $\lfloor m \rfloor$. In conclusion, the principle of distribution of these parameters is to ensure the reliable transmission of more important information in the fixed compression ratio α.

Similarly, we conduct the simulation using two types of original CS algorithm. One method is that the signal is decomposed by four-scale DWT (In general, the decomposition level of 256×256 image should be more than four to satisfy the sparsity), and then, all of the wavelet coefficients are measured by random Gaussian matrix. (In this paper, we named the general CS method). The compression ratio is calculated by the formula $\alpha_1 = M/N$. The other method is that the signal is decomposed by single layer DWT, and then, the low frequency coefficients are retained, the high frequency coefficients are measured [10]. (In this paper, we named the single layer CS method). The compression ratio is calculated by the formula $\alpha_2 = \frac{N/2+M}{N}$, $\alpha_2 \geq 0.5$. Both of the two methods have not considered the characteristics of high frequency coefficients.

The PSNR of Lena, Fruits, Baboon and Boat images at different compression ratio using unequal-CS, general CS and single layer CS algorithms are shown in Fig. 73.4.

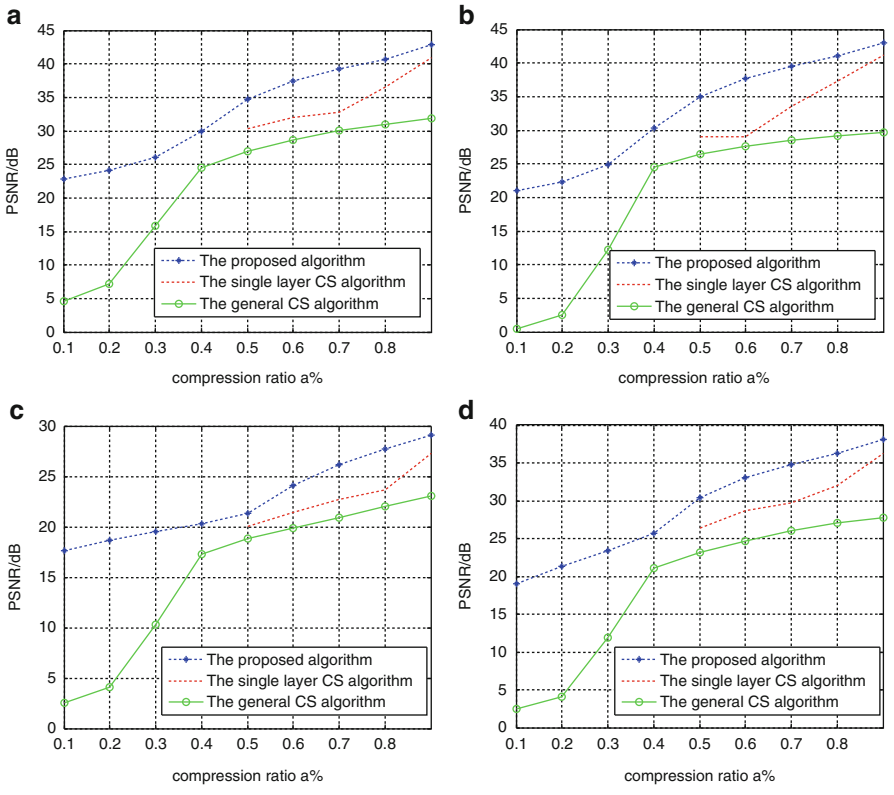

Fig. 73.4 The compared PSNR of (**a**) Lena, (**b**) Fruits, (**c**) Baboon and (**d**) Boat

These figure shows that the proposed unequal-CS method achieves much higher PSNR than the other two CS methods. Especially, the gap is much larger in low compression ratio. What's more, with the decrease of compression ratio, the PSNR of the rate of decline is much lower than the other two CS methods. And, the PSNRs which are achieved by the proposed unequal-CS method are not less than 18 dB. It indicates that the proposed method has a better stability for various compression ratios.

However, from the Fig. 73.4, we can see that the PSNR of Baboon image are lower than that of Lena, Fruits and Boat image at the same situations, because there are more high frequency coefficients in Baboon. After measurement, the loss is much. As this type of sources, the high frequency coefficients are larger relatively; the proposed method is not suitable for them.

Conclusion

An unequal-compressed sensing algorithm is proposed in this paper. According to the characteristics of the wavelet coefficients, we propose an unequal-compressed sensing algorithm which combines the compressed sensing theory with the characteristics of the wavelet coefficients and the PSNR of the proposed algorithm is greatly improved than the original CS algorithms. What's more, it indicates that the proposed method has a better stability for various compression ratios.

Acknowledgement This work was supported by National Science Foundation of China (61171176).

References

1. Donoho DL (2006) Compressed sensing. IEEE Trans Inform Theory 52(4):1289–1306
2. Tsaig Y, Donoho DL (2006) Extensions of compressed sensing. IEEE Trans Signal Process 86 (3):549–571
3. Candès EJ, Romberg J, Tao T (2006) Robust uncertainty principles: exact signal reconstruction from highly incomplete frequency information. IEEE Trans Inform Theory 5:489–509
4. Candès EJ (2008) The restricted isometry property and its implications for compressed sensing. CR Math 346(9):589–592
5. Chen SS, Donoho DL, Saunders MA (1998) Atomic decomposition by Basis Pursuit. SIAM J Sci Comput 20(1):33–61
6. Pati YC, Rezaiifar R, Krishnaprasad PS (1993) Orthogonal matching pursuit: recursive function approximation with applications to wavelet decomposition. In: IEEE 1993 conference record of the twenty-seventh Asilomar conference on signals, systems and computers, 1–3 Nov 1993, Pacific Grove. IEEE, pp 40–44
7. Wipf D, Rao BD (2004) Sparse Bayesian learning for basis selection. IEEE Trans Signal Process 52(8):2153–2164

8. Zhang Y, Mei S, Chen Q, Chen Z (2008) A novel image/video coding method based on compressive sensing theory. In: Proceedings of the international conference on acoustics, speech and signal processing (ICASSP), pp 1361–1364
9. Sun J, Lian QS (2013) An image compression algorithm combined nonuniform sample and compressed sensing. J Signal Process 29(1):31–37
10. Cen YG, Chen XF, Cen LH, Chen SM (2010) Compressed sensing based on the single layer wavelet transform for image processing. J Commun 31(8A):52–55

Chapter 74
Ground-based Cloud Detection Using Automatic Graph Cut

Shuang Liu, Zhong Zhang, Shuaiqi Liu, and Liang Han

Abstract Clouds are one of the most important meteorological phenomena related to the hydrological cycle and affect earth radiation balance. Ground-based cloud classification, as a key component of cloud analysis has received great concern in recent years and a number of algorithms have been proposed. However, there is no comprehensive study concerning the different classification methods. In this paper, we first make a survey on various classification methods. Further, we detail the current algorithms for classification and give theoretical analysis. Finally, we evaluate the performance of different algorithms under two ground-based cloud datasets. The experimental findings firmly justify our theoretical analysis.

Keywords Ground-based clouds • Cloud classification

74.1 Introduction

74.1.1 Motivation

Cloud is one of the most important meteorological phenomena related to the hydrological cycle and affects the earth radiation balance. Most cloud-related research requires ground-based cloud classification, which refers to classify the type of cloud in a ground-based cloud image. since successful classification of cloud type can improve the precision of weather prediction and help us to understand climatic conditions, we put our focus on cloud classification in this paper. Nowadays, clouds are studied by means of satellites or ground-based remote sensing [1, 2]. Satellites can provide global cloud information, but information of the lower cloud under the upper cloud is often lost. In addition, the global cloud information, which is at a low spatial resolution, cannot meet the need of meteorological research and weather forecasting. On the contrary, ground-based cloud

S. Liu • Z. Zhang (✉) • S. Liu • L. Han
College of Electron and Communication Engineering, Tianjin Normal University, Tianjin, China
e-mail: ls1665@sina.com; dreamzhangzhong@163.com; shdkj-1918@163.com; hanliang@mail.tjnu.edu.cn

J. Mu et al. (eds.), *The Proceedings of the Third International Conference on Communications, Signal Processing, and Systems*, Lecture Notes in Electrical Engineering 322, DOI 10.1007/978-3-319-08991-1_74

observation can provide detail information of local region, which can be used to support cloud studies.

At present, ground-based clouds are classified by the observers who have received professional training. However, different observers will obtain discrepant classification results due to different level of professional skill. Moreover, this work is complicated and time-consuming. Therefore, automatic ground-based cloud classification technique is eagerly required in this area.

To achieve this goal, many devices have been developed to translate the ground-based cloud into digital representation in the past few years, which provides the data base for ground-based cloud classification. Representative devices includes WSI (whole sky imager) [3], TSI (total sky imager) [4] and ICI (infrared cloud imager) [5]. Based on the above devices, a lot of methods have been proposed for ground-based cloud classification [6–8]. Most of the existing research on cloud identification from sky images is based on single cloud images [6]. However, the cloud-measuring devices on the ground actually take one image of the clouds every few minutes and collect a series of cloud images. Thus, the existing methods neglect the temporal information exhibited by contiguous cloud images. To overcome this drawback, method based on ground-based cloud sequences (GCSs) is proposed for cloud classification [6]. Although those methods can improve the performance of classification, there is still no work that comprehensively studies this significative field. Our work in this paper makes such a timely survey, in which classification methods are introduced and their relationships are exploited. We believe that this work will afford guiding and reference both beginners and practitioners in the field greatly.

74.1.2 Taxonomy

Since feature extraction is the foundation of automatic image classification. This is because if the extracted feature vectors in the feature space is inseparable, even if superior classifiers also helpless. Therefore, feature extraction techniques are mainly discuss in this paper, and most of existing cloud classification methods put focus on feature extraction techniques. For clarity, we group the existing feature extraction algorithms into three major categories according to their motivations.

- Global feature extraction techniques focus on the global description of all feature rather than each individual feature. This form of feature extraction is applied in previous techniques. Typical methods include co-occurrence matrix [9], fourier transformation, and LAWS [10]. Recently, some researches indicate that the performance with global feature extraction techniques is poor.
- Local feature extraction is proposed to describe each individual feature. Typical methods include local binary pattern (LBP) [11], bag of words (BOW) [12], and some extensions based on the two techniques. At present, feature extraction techniques with local information is the mainly techniques, and our attention also will be focused on this in this paper.

- The above techniques are both extracting feature of single cloud images. However, the cloud-measuring devices on the ground actually take one image of the clouds every few minutes and collect a series of cloud images. Thus, the above methods neglect the temporal information exhibited by contiguous cloud images. Method based on ground-based cloud sequences (GCSs) [6] overcomes this drawback, and we also introduce this technique in detail.

74.1.3 Contributions

The major contributions of this paper are summarized as follows:

- Provide a survey on recent process in feature extraction for ground-based cloud classification. To the best of our knowledge, we are the first to review ground-based cloud classification in automatical form.
- Evaluate several representative cloud classification methods on two ground-based cloud dataset.

74.2 Ground-Based Cloud Classification Methods

74.2.1 Techniques Based on LBP

In this section, we present a brief overview of the local binary pattern (LBP) proposed by Ojala et al. [11]. The LBP operator is a gray-scale texture operator which describes the spatial structure of the local image texture. Given a pixel in the image, the LBP operator labels it by computing the sign of the difference between the values of the given pixel and its neighborhood pixels. The result is a binary string or a decimal number, and then the image is represented by the histogram of them. The LBP label for the central pixel is given by:

$$LBP^{ri}_{P,R} = \min_{0\le l<P}\{\sum_{p=0}^{P-1} s(g_p - g_c)\times 2^{[(p+l)mod\,p]}\},\ s(x)=\begin{cases}1, x\ge 0\\ 0, x<0\end{cases} \tag{74.1}$$

where P is the total number of involved neighbors, R is the radius of the circle, which determines the distance between the neighbors and the central pixel, g_c is the gray value of the central pixel, and g_p is the gray value of the sample point that is angularly evenly distributed around the central pixel with radius R. $s(x)$ is a step function.

Based on LBP, many variants such as [7, 13–15] have been proposed. Typical extension are displayed as following. CLBP [16] is an extension of LBP, which represents a local region by its center pixel and a local difference sign-magnitude.

LTP [17] introduces a small tolerative range to deal with local noise. SLBP [7] define salience as the most frequently occurred patterns in an image via statistical analysis, and use those salient patterns for classification. All of those methods obtain better performance than conventional LBP.

74.2.2 Techniques Based on BOW

The bag of words model [12] originated from text classification has show superior performance in image classification. BOW model images as distributions over a set of dictionary, which is learned by clustering algorithm from original image patches, and then find one or several words for each patch based on this dictionary. Finally, a histogram is constructed by hard quantization or soft quantization. Based on BOW, a lot of improved algorithms have developed in recent years [18–20]. Among them, sparse coding is one of the most popular algorithms and has obtain more and more attention. In the following, we will introduce the process of sparse coding.

Sparse coding modeling of data assumes an ability to describe the signals as a linear combination of a few atoms from an over-complete dictionary. Formally, given a signal $x \in \mathbf{R}^{M\times 1}$ and a dictionary $D = [d_1, d_2, \ldots, d_N] \in \mathbf{R}^{M\times N}$, where typically $M < N$, then we can obtain the SC coefficient a for x which satisfies:

$$\min_{a} \|a\|_0$$

$$s.t. \ \ \|x - \mathbf{D}a\|^2 \leq \varepsilon \tag{74.2}$$

where $\|\cdot\|_0$ denotes the l_0-norm, which counts the number of non-zeros elements in a vector, and ε is a small threshold. Given the dictionary $\mathbf{D}$, the model tries to seek the sparsest representation for the signal x, i.e. a few elements in a is non-zero. However, the optimization for Eq. (74.2) is NP-hard. Recent works show that, under some mild conditions, this NP-hard problem can be tackled by replacing the l_0-norm with l_1-norm regularization. In many applications, the dictionary $\mathbf{D}$ is unknown and we need to construct it from training data $\mathbf{X} = [x_1, x_2, \ldots, x_L]$. The dictionary $\mathbf{D}$, as well as the SC coefficient vector a_i for x_i, can be learned by the optimizing the following objective function:

$$\min_{\mathbf{D},\mathbf{A}} \sum_{i=1}^{L} \|\mathbf{x}_i - \mathbf{D}a_i\|^2 + \lambda \|a_i\|_1 \tag{74.3}$$

$$s.t. \ \ \|\mathbf{d}_k\|^2 \leq 1, \forall k = 1, 2, \ldots, N$$

where $\mathbf{A} = [a_1, a_2, \ldots, a_L]$ ($a \in \mathbf{R}^{M \times 1}$) and λ is the regularization parameter controlling the sparsity of coefficient vector. $\| \cdot \|_1$ denotes the l_1-norm, which counts the sum of the absolute value of each element in a_i, and the unit l_2-norm constraint on d_k is to avoid trivial solutions.

The theory and algorithms of sparse coding have been successfully used in image processing and pattern recognition [21, 22]. On this basis, a lot of improved algorithms have been proposed, such as nonnegative SC and soft-sign SC. All of them obtain good performance.

74.2.3 Techniques Based on Cloud Sequences

Observation previous researchers, we can find that most of them only consider the classification task of cloud images while less attention has been paid to the synthesis one. In addition, all the existing research on cloud identification from sky images is based on single cloud images. However, the cloud-measuring devices on the ground actually take one image of the clouds every few minutes and collect a series of cloud images. Thus, the existing methods neglect the temporal information exhibited by contiguous cloud images. To overcome this drawback, Liu et al. proposed the Tensor Ensemble of Ground-based Cloud Sequences model (eTGCS) [6], which utilizes cloud sequences for classification. In the eTGCS model, an ensemble of GCSs forms a single tensor, and each GCS is a subtensor of the single tensor. To utilize the spatial relationship, each frame of the cloud sequence uses the Image-As-Matrix representation. In the framework of an ensemble, all GCSs share an identical class mode subspace, which makes the classification convenient. Furthermore, the eTGCS model goes beyond mere classification, and it can be applied to conduct other tasks such as synthesis and compression in a very convenient manner.

74.3 Experimental Results and Analysis

To evaluate the performance of different algorithms, we carry out a series of experiments on two ground-based cloud databases: Kiel database and IapCAS database, and compare the performance of several methods, which includes LBP [11], SLBP [7], SC [21], SSC [19], and eTGCS [6]. Prior to the discussion of experimental results, we first introduce the cloud datasets and then give the experimental setup. Finally, experimental results and analysis will be provided.

74.3.1 Datasets

The first cloud dataset is Kiel dataset, which is provided by Kiel University in Germany. According to the International cloud classification system published in WMO, the dataset is divided into seven classes. The sample number of each class is different and the total number is 1,500. This dataset has large illumination variations and intra-class variation. Samples for each class are shown in Fig. 74.1.

The second cloud dataset is IapCAS-S dataset, which is provided by IAPCAS. The dataset includes 156 ground-based cloud sequences (GCSs), and each GCS consists of 50 frames with the size of 120 × 120 pixels (totally 7,800 frames). The time interval between each of a GCS is 3 minutes. GCSs samples from each class are shown in Fig. 74.2.

74.3.2 Experimental Results and Analysis

Experimental results in Kiel dataset: Methods based on LBP, SLBP, SC and SSC are compared, while exclusive of eTGCS. This is because method based on eTGCS is for cloud Sequences. Specifically, 1/3 samples are randomly chosen from each class as training data while the remaining images are used for testing, and the process is repeated 100 times. The experiment results of different algorithms on the Kiel dataset are listed in Table 74.1. From Table 74.1, we can see that method based

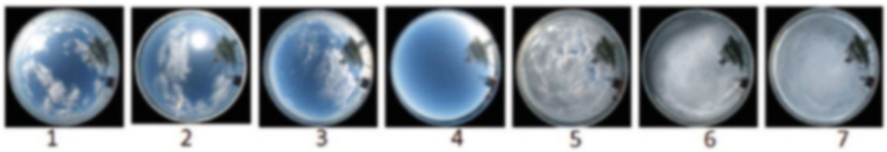

Fig. 74.1 Cloud samples from the Kiel dataset

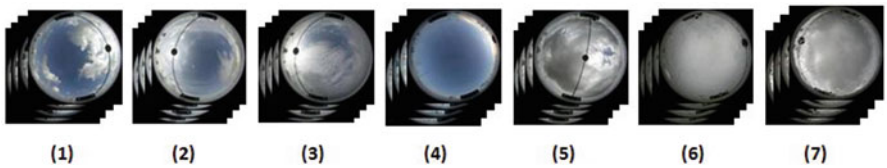

Fig. 74.2 The GCS samples of seven classes from IapCAS-S dataset

Table 74.1 Average classification accuracy for the four algorithms on the Kiel dataset

LBP	SLBP	SC	SSC
86.59	91.67	90.58	93.21

Table 74.2 Average classification accuracy for the five algorithms on the IapCAS-S dataset

LBP	SLBP	SC	SSC	eTGCs
83.02	87.97	88.23	89.31	92.31

on SSC obtain the highest accuracy. This is because that Adaptive sparse coding mode can better express the essential structure of ground-based clouds.

Experimental results in IapCAS-S dataset: In this experiment, All of methods will been compared. For fair comparison, we conduct the experiments in the following manners: (1) for image-based methods, the accuracy for each sample is calculated as the percentage of correctly classified frames, which is between 0 and 1; then all accuracies are averaged to be the final accuracy; (2) method based on eTGCs classifies each sample directly, so the accuracy is either 1 or 0. The final accuracy is also computed by averaging the classification accuracies of all the cloud sequences. In our experiment, 50 GCSs samples are randomly chosen as training data while the remaining ones as testing data, and the partition process is repeated 50 times. Table 74.2 shows the experimental results of different methods. We can see that method based on eTGCs achieves the highest recognition accuracy. This performance improvement is brought out because eTGCs uses cloud sequences to classify cloud which fully takes advantage of time information between frames. Furthermore, rather than simply utilizing single cloud images, eTGCs adopts the powerful framework of tensor analysis to give a thorough analysis of cloud image sequences in three dimensions.

Conclusions

In this paper, we do a comprehensive study concerning the different classification methods. We analyze the performance of different methods and their relations. Experimental results show that SSC algorithm can effectively represent the structure of clouds, and method based on GCSs can obtain better performance for classification.

References

1. Ebert EE (1992) Pattern recognition analysis of polar clouds during summer and winter. Int J Remote Sens 13(1):97–109
2. Lamei N, Hutchison KD, Crawford MM (1994) Cloud type discrimination via multispectral textural analysis. Opt Eng 33(4):1303–1313
3. Shields JE, Karr ME, Tooman TP (1998) The whole sky imagerłA year of progress. In: Proc. eighth atmospheric radiation measurement (ARM) science team meeting
4. Long CN, Sabburg JM, Calbó J, Pagès D (2006) Retrieving cloud characteristics from ground-based daytime color all-sky images. J Atmos Ocean Technol 23(5):633–652
5. Shaw JA, Thurairajah B (2003) Short-term Arctic cloud statistics at NSA from the infrared cloud imager. In: Proc. thirteenth ARM science team meeting
6. Liu S, Wang C, Xiao B, Zhang Z, Cao X (2013) Tensor ensemble of ground-based cloud sequences: its modeling, classification and synthesis. IEEE Geosci Remote Sens Lett 10 (5):1190–1194

7. Liu S, Wang C, Xiao B, Zhang Z, Shao Y (2013) Salient local binary pattern for ground-based cloud classification. Acta Meteorol Sin 27(2):211–220
8. Heinle A, Macke A, Srivastav A (2010) Automatic cloud classification of whole sky images. Atmos Meas Tech 3(1):557–567
9. Singh M, Glennen M (2005) Automated ground-based cloud recognition. Pattern Anal Appl 8:258–271
10. Calbó J, Sabburg J (2008) Feature extraction from whole-sky groundbased images for cloud-type recognition. J Atmos Ocean Technol 25:3–14
11. Ojala T, Pietikäinen M, Mäenpää T (2002) Multiresolution gray-scale and rotation invariant texture classification with local binary patterns. IEEE Trans Pattern Anal Mach Intell 24 (7):971–987
12. Zhu L, Rao AB, Zhang A (2002) Theory of keyblock-based image retrieval. ACM Trans Inf Syst 20(2):224–257
13. Zhang Z, Wang C, Xiao B, Liu S, Zhou W (2012) Multi-scale fusion of texture and color for background modeling. In: International conference on advanced video and signal-based surveillance, pp 154–159
14. Zhang Z, Wang C, Xiao B, Zhou W, Liu S (2011) Background modeling by exploring multi-scale fusion of texture and intensity in complex scenes. In: Asian conference on pattern recognition, pp 402–406
15. Liu S, Wang C, Xiao B. Zhang Z, Shao Y (2012) Illumination-invariant completed LTP descriptor for cloud classification. In: International congress on image and signal processing, pp 449–453
16. Guo Z, Zhang L, Zhang D (2010) A completed modeling of local binary pattern operator for texture classification. IEEE Trans Image Process 19(6):1657–1663
17. Tan X, Triggs B (2010) Enhanced local texture feature sets for face recognition under difficult lighting conditions. IEEE Trans Image Process 19(6):1635–1650
18. Zhang Z, Wang C, Xiao B, Zhou W, Liu S, Shi C (2013) Cross-view action recognition via a continuous virtual path. In: IEEE conference on computer vision and pattern recognition, pp 2690–2697
19. Liu S, Wang C, Xiao B, Zhang Z, Shao Y (2012) Soft-signed sparse coding for ground-based cloud classification. In: International conference on pattern recognition, pp 2214–2217
20. Liu S, Wang C, Xiao B, Zhang Z, Shao Y (2012) Ground-based cloud classification using multiple random projections. In: International conference on compute vision in remote sensing, pp 7–12
21. Xie J, Zhang L, You J, Zhang D (2010) Texture classification via patch-based sparse texton learning. In: IEEE international conference on image processing, pp 2737–2740
22. Yang J, Yu K, Gong Y, Huang T (2009) Linear spatial pyramid matching using sparse coding for image classification. In: IEEE conference on computer vision and pattern recognition, pp 2032–2047

Chapter 75
Identifying Image Splicing Based on Local Statistical Features in DCT and DWT Domain

Yujin Zhang, Shenghong Li, Shilin Wang, and Xudong Zhao

Abstract In this paper, an effective image splicing detection algorithm based on the local statistical features in DCT and DWT domain is proposed. The local ternary pattern (LTP) operator is introduced to characterize the statistical changes of DCT and DWT coefficients caused by image splicing. The LTP histograms are generated from the magnitude components of the block DCT coefficients with varying block sizes and the DWT coefficients in three detail subbands, respectively. All these LTP histograms are concatenated together to form the discriminative feature set for splicing detection. The effectiveness of the proposed detector is evaluated on the Columbia image splicing detection evaluation dataset. Simulation results have shown that the proposed method can perform better than several state-of-the-art methods investigated.

Keywords Passive image forensics • Splicing detection • Local ternary pattern • DCT • DWT

75.1 Introduction

With the rapid development of electronic information technology, the performance of digital image acquisition equipment is constantly changing and the function of image editing software is increasingly powerful. Such techniques make it easy and convenient to tamper an image. Image splicing is one of the most common means of image content tampering which creates a composite image by cropping an image

Y. Zhang (✉) • S. Li • X. Zhao
Department of Electronic Engineering, Shanghai Jiao Tong University, Shanghai 200240, China
e-mail: eeyjzhang@gmail.com; shli@sjtu.edu.cn

S. Wang
School of Information Security Engineering, Shanghai Jiao Tong University, Shanghai 200240, China
e-mail: wsl@sjtu.edu.cn

J. Mu et al. (eds.), *The Proceedings of the Third International Conference on Communications, Signal Processing, and Systems*, Lecture Notes in Electrical Engineering 322, DOI 10.1007/978-3-319-08991-1_75

patch from a source image and pasting it onto a target image. The tampered patch may also be accompanied by some kinds of geometric transformations, such as scaling, rotation, and skewing, etc. The composite image could be so realistic-looking that they may scarcely be distinguished from authentic ones. Once the tampered images are used in scientific discovery, news media and legal evidence and so on, they may bring the negative influence to society and public. As a result, the detection of image splicing is of particular significance.

Traditional active authentication methods [1] have some limitations due to the need of prior information, such as digital watermark and digital signature, many passive splicing detection methods have therefore been developed in recent years [2]. Image splicing detection can be viewed as a two-class pattern recognition problem. Therefore, developing the effective feature set is the key to capturing the traces of image splicing. Many approaches have been devoted to reveal image splicing forgery from the specific feature perspective. Ng et al. in [2] proposed to use third order moment spectra (i.e. bicoherence) based features for splicing detection with the assumption that bicoherence is sensitive to quadratic phase coupling (QPC) caused by splicing discontinuity. In [3], Fu et al. constructed discriminative features from Hilbert-Huang Transform (HHT) and moments of characteristic function of wavelet subbands. In [4], Chen et al. adopted 2-D phase congruency and statistical moments of wavelet characteristic function to detect splicing. In [5], Shi et al. presented two types of statistical features derived from moments of characteristic functions of wavelet subbands and Markov transition probabilities of difference 2-D arrays to identify splicing forgery, which boost the detection accuracy compared with the prior arts in the field of image splicing detection. He et al. in [6] extended the Markov based splicing detection approach [5] to DWT domain to capture the splicing traces more effectively.

Different from the above methods, in this paper, a novel image splicing detection method based on local statistics in DCT and DWT domain is developed. We use the local ternary pattern (LTP) operator to capture the statistical changes of DCT and DWT coefficients caused by image splicing. We show that the LTP features in the cross-domain (DCT + DWT) can provide the superior performance for splicing detection.

The rest of this paper is organized as follows. The next section describes the proposed method. Section 75.3 gives the experimental results. Finally, Sect. 75.4 concludes the paper.

75.2 Proposed Method

In this section, we begin with a brief review of the local ternary pattern operator. We then describe the proposed feature extraction procedure for image splicing detection.

75.2.1 Local Ternary Patterns

Tan and Triggs in [7] proposed the local ternary pattern (LTP) descriptor for face recognition. Considering the central pixel g_c of a local image region, g_l ($l = 0, 1, 2 \ldots L-1$) is the value of its neighbors and R is the radius of the neighborhood. Suppose the coordinate of g_c is (x_c, y_c), then the coordinates of g_p are $(x_c + R\cos(2\pi l/L), y_c - R\sin(2\pi l/L))$. The gray values of neighbors which do not fall exactly on pixels can be estimated by bilinear interpolation [8]. For the central pixel g_c, the LTP is given by

$$LTP(x_c, y_c) = \{t(g_0, g_c, \varepsilon), t(g_1, g_c, \varepsilon), \cdots, t(g_{L-1}, g_c, \varepsilon)\} \tag{75.1}$$

Where ε is the threshold parameter and the three-valued coding function $t(g_l, g_c, \varepsilon)$ [7] is defined as

$$t(g_l, g_c, \varepsilon) = \begin{cases} 1, & g_l - g_c \geq \varepsilon \\ 0, & |g_l - g_c| < \varepsilon \\ -1 & g_l - g_c \leq -\varepsilon \end{cases} \tag{75.2}$$

To avoid the high dimensionality of the LTP histogram with the ternary codes, each LTP is first split into two binary components [7], denoted by LTP_P ("−1" is coded as "0") and LTP_N ("1" is coded as "0". Meanwhile, "−1" is coded as "1"). The histograms computed from such two descriptors (i.e.LTP_P and LTP_N) can be calculated as

$$\begin{gathered} H_\alpha(k) = \sum_i \sum_j \delta(LTPC_\alpha(i, j), k) \\ k \in \left[0, 2^L - 1\right], \quad \alpha \in \{P, N\} \end{gathered} \tag{75.3}$$

Where $LTPC_\alpha$ (i, j) ($\alpha \in \{P, N\}$) is the decimal number corresponding to the binary pattern LTP_α (i, j) and the δ function is defined as

$$\delta(m, n) = \begin{cases} 1 & if \ \ m = n \\ 0 & else \end{cases} \tag{75.4}$$

The alternative LTP histogram can be formulated as

$$F = \left\{H_\alpha \middle| \alpha \in \{P, N\}\right\} \tag{75.5}$$

75.2.2 Feature Extraction

For an original digital image, there would have some inner dependencies in transform domain. Splicing operation itself can more or less disturb this underlying regularity. Two popular transforms, i.e., DCT and DWT, have been proved to be

effective for splicing detection in the previous works [5, 6]. In this paper, the LTP operator is used to model the magnitude components of DCT and DWT coefficients to capture the traces left by splicing. The proposed feature extraction procedure is described as follows.

75.2.2.1 LTP Features in DCT Domain

Block discrete cosine transform (BDCT) has been commonly used in the popular image and video compression schemes such as JPEG and H.264 owing to its good property of decorrelation and energy compaction. To reduce the effects caused by the diversity of image content and highlight the splicing artifacts [5], BDCT is first used to preprocess the test image, and resulting BDCT coefficient 2-D arrays are used for subsequent feature extraction.

For an image with size of $N_1 \times N_2$, the LTP feature extraction in DCT domain can be divided into the following steps:

1. Split the given image into $r \times s$ ($r = \lfloor N_1/b \rfloor, s = \lfloor N_2/b \rfloor$) non-overlapping blocks $X_{i,j}^b (1 \le i \le r, 1 \le j \le s)$, where the superscript $b\,(b \in \{4, 8, 16\})$ denotes the block size.
2. Perform 2-D DCT on each spatial image block $X_{i,j}^b$ independently. The corresponding BDCT coefficient 2-D array Y can be written as

$$Y = \begin{pmatrix} Y_{1,1}^b & Y_{1,2}^b & \cdots & Y_{1,s}^b \\ Y_{2,1}^b & Y_{2,2}^b & \cdots & Y_{2,s}^b \\ \vdots & \vdots & \ddots & \vdots \\ Y_{r,1}^b & Y_{r,2}^b & \cdots & Y_{r,s}^b \end{pmatrix} \tag{75.6}$$

Where $Y_{i,j}^b = C^T X_{i,j}^b C$, and

$$\begin{cases} C(k,l) = \dfrac{1}{\sqrt{b}}, & 0 \le k \le b-1, l = 0 \\ C(k,l) = \sqrt{\dfrac{2}{b}} \cos\left(\dfrac{\pi(2k+1)l}{2b}\right), & 0 \le k \le b-1, 1 \le l \le b-1 \end{cases} \tag{75.7}$$

3. Calculate the corresponding LTP histograms with $L = 8$ and $R \in \{1,2\}$ from the magnitude components of each of the above BDCT coefficient arrays, respectively.
4. Concatenate the LTP histograms generated from step (3) to form the LTP feature set in DCT domain as

$$\Pi_{DCT} = \left\{ F_{L,R}^b \middle| b \in \{4, 8, 16\}, L = 8, R = \{1, 2\} \right\} \tag{75.8}$$

75.2.2.2 LTP Features in DWT Domain

Discrete wavelet transform (DWT) has been widely used in many fields due to its good capabilities of the spatial-frequency localization and multi-resolution representation. It performs well in catching the local changes in signals such as breakdown points and discontinuities. Since splicing operations may lead to sharp edges, DWT is fit for splicing detection. For an original image, there exists some dependencies among the DWT coefficients [5, 6], and splicing operations will also inevitably destroy these dependencies to certain extent. In order to catch the artifacts caused by image splicing more sensitively and obtain more discriminative information between authentic images and spliced images, the detail subbands after 1-level discrete Meyer wavelet transform (DMWT) are considered in this paper. For an image, the LTP features in DWT domain are extracted as follows:

1. Apply 1-level DMWT to the given image to get four subbands, i.e., the approximation subband CA, the horizontal detail subband CH, the vertical detail subband CV and the diagonal detail subband CD.
2. Calculate the corresponding LTP histograms with $L = 8$ and $R = 1$ from the magnitude components of three detail subbands (i.e., CH, CV and CD), respectively.
3. Concatenate the above LTP histograms to form the LTP feature set in DWT domain as

$$\Pi_{DWT} = \left\{ F^{\Theta}_{L,R} \middle| \Theta \in \{CH, CV, CD\}, L = 8, R = 1 \right\} \tag{75.9}$$

75.2.2.3 Summary of Feature Generation

The LTP features in both DCT and DWT domain are utilized for image splicing detection. The framework of the proposed feature extraction procedure is summarized in Fig. 75.1. In summary, $512 \times 3 \times 2 = 3{,}072$ LTP features in DCT domain and $512 \times 3 = 1{,}536$ LTP features in DWT domain are first obtained. These features are further merged together to form the final feature vector. Hence, there are $3{,}072 + 1{,}536 = 4{,}608$ elements in the proposed feature vector for one image.

75.3 Experiments and Results

75.3.1 Experimental Setup

The Columbia Image Splicing Detection Evaluation Dataset [9], which consists of 933 authentic and 912 spliced images, is used to evaluate the efficiency of the proposed method. All of images in this dataset are in BMP format and with size of 128×128. LIBSVM [10] and the RBF kernel function is adopted for classification. The classification procedure is given as follows:

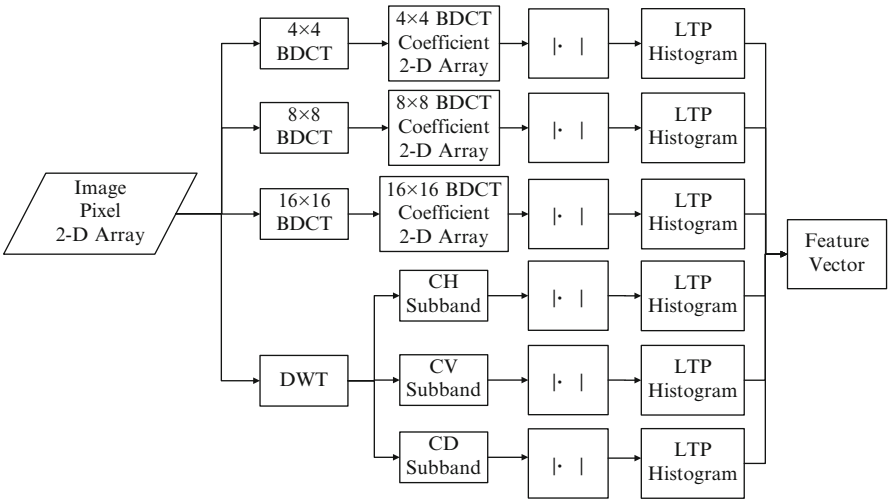

Fig. 75.1 Feature extraction procedure

1. Randomly pick out 5/6 of the authentic images (negative class) and 5/6 of the spliced images (positive class) to construct the training set, and the remaining images are used for evaluation.
2. Perform the cross-validation and grid-searching procedure to get the best parameters C and γ for the RBF kernel function, and then apply them to train the SVM classifier on the training set.
3. Use the trained classifier to evaluate on the testing set and record the true positive rate (TPR), true negative rate (TNR) and detection accuracy rate (AR).
4. Repeat the step 1–3 one hundred times for eliminating the effect of randomness caused by image selection. If the above experimental procedure is finished, then compute the average TPR, TNR and AR over 100 times random experiments for evaluation.

75.3.2 Detection Results of Image Splicing

To verify the effectiveness of the proposed method, two state-of-the-art methods (i.e.NIM-based method [5] and MFDD-based method [6]) have also been investigated for comparison on the same dataset. For the proposed method, the threshold parameter ϵ is empirically set to 0.9 and 1.5 for feature generation in DCT and DWT domain, respectively. Detection results of the proposed LTP features are shown in Table 75.1. Detection performance comparison of the proposed method and the other two methods is summarized in Table 75.2. The averaged receiver operating characteristic (ROC) curves and area under the receiver operating characteristic curve (AUC) [11] for the above three methods are presented in Fig. 75.2.

From Tables 75.1, 75.2 and Fig. 75.2, the following observations can be made:

Table 75.1 Detection results of the LTP features (standard deviation in *parentheses*)

	DCT	DWT	DCT + DWT
Feature size	3,072	1,536	4,608
TPR	91.76 % (2.07 %)	85.15 % (2.97 %)	92.18 % (2.01 %)
TNR	91.10 % (2.23 %)	86.50 % (2.41 %)	92.42 % (2.34 %)
AR	91.43 % (1.43 %)	85.83 % (1.79 %)	92.30 % (1.48 %)

Table 75.2 Detection performance comparison of the proposed method, the NIM-based method, and the MFDD-based method (standard deviation in *parentheses*)

Method	NIM [5]	MFDD [6]	Proposed
Feature size	266	7,290	4,608
TPR	90.80 % (2.32 %)	88.82 % (2.67 %)	92.18 % (2.01 %)
TNR	90.24 % (2.36 %)	88.16 % (2.31 %)	92.42 % (2.34 %)
AR	90.52 % (1.73 %)	88.49 % (1.74 %)	92.30 % (1.48 %)

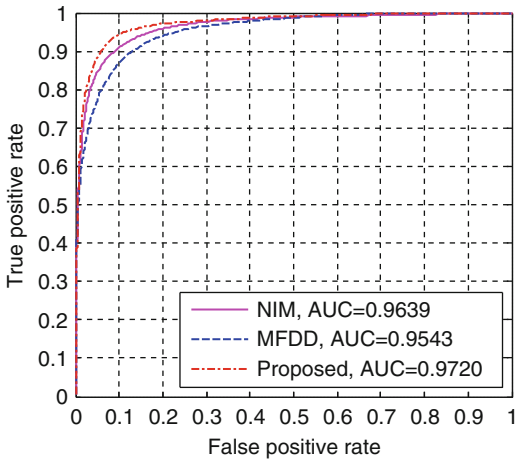

Fig. 75.2 ROC curves for three detection methods

1. Each of LTP feature sets in DCT and DWT domain can effectively expose the traces left by image splicing. In addition, combining these two feature sets can perform better than the individual feature set.
2. The proposed method achieves a detection accuracy of 92.30 %, increased by 1.78 % and 3.81 % compared with the other two methods, respectively.
3. Among all these three method, the ROC performance of the proposed feature is better than other two, which also indicates that the proposed feature is more effective for splicing detection.

In order to evaluate the computational complexity, the computational costs for feature extraction and training/testing SVM (including the optimum parameter searching) have been recorded. The time cost ratio of the above three methods (i.e., the NIM-based method, the MFDD-based method and the proposed method) is

about 1:2.15:1.20, which demonstrate the computational complexity of the proposed method is higher than the NIM-based method and lower than the MFDD-based method.

Conclusions

In this paper, a passive image splicing detection method has been proposed. The brief review of the LTP operator is first given. Then the LTP operator is applied to capture the statistical changes of DCT coefficients and DWT coefficients caused by image splicing. Specifically, the LTP histograms are calculated from the magnitude components of the block DCT coefficients with varying block sizes and the DWT coefficients in three detail subbands, respectively. The concatenated LTP histograms are treated as the discriminative features for splicing detection. Experimental results have proved that the proposed method can perform well in exposing the traces of image splicing. In addition, it can achieve better detection performance than other two state-of-the-arts.

Acknowledgments This work is mainly funded by National Science Foundation of China (61271316, 61271319, 61071152, and 61271180), 973 Program (2010CB731403, 2010CB731406, and 2013CB329605) of China, Chinese National "Twelfth Five-Year" Plan for Science and Technology Support (2012BAH38 B04), Key Laboratory for Shanghai Integrated Information Security Management Technology Research, and Chinese National Engineering Laboratory for Information Content Analysis Technology.

References

1. Paquet H, Ward RK, Pitas I (2003) Wavelet packets-based digital watermarking for image verification and authentication. Signal Process 83(3):2117–2132
2. Ng T-T, Chang S-F, Sun Q (2004) Blind detection of photomontage using higher order statistics. In: IEEE international symposium on circuits and systems, Vancouver, Canada, pp. V688–V691
3. Fu D, Shi YQ, Su W (2006) Detection of image splicing based on Hilbert-Huang transform and moments of characteristic functions with wavelet decomposition. In: International workshop on digital watermarking, LNCS, vol 4283. Springer, Heidelberg, pp 177–187
4. Chen W, Shi YQ, Su W (2007) Image splicing detection using 2-D phase congruency and statistical moments of characteristic function. In: Society of photo-optical instrumentation engineers conference series, vol 6505. SPIE, Washington, DC, pp 65050R.1–65050R.8
5. Shi YQ, Chen C, Chen W (2007) A natural image model approach to splicing detection. In: The 9th workshop on multimedia & security, Dallas, Texas, USA, pp. 51–62
6. He Z, Lu W, Sun W, Huang J (2012) Digital image splicing detection based on Markov features in DCT and DWT domain. Pattern Recogn 45(12):4292–4299
7. Tan X, Triggs B (2010) Enhanced local texture feature sets for face recognition under difficult lighting conditions. IEEE Trans Image Process 19(6):1635–1650

8. Ojala T, Pietikainen M, Maenpaa T (2002) Multiresolution gray-scale and rotation invariant texture classification with local binary patterns. IEEE Trans Pattern Anal Mach Intell 24 (7):971–987
9. Ng T-T, Chang S-F (2004) A dataset of authentic and spliced image blocks. ADVENT technical report, #203-2004-3, Columbia University, New York, USA
10. Chang CC, Lin CJ (2001) LIBSVM: a library for support vector machines. http://www.csie.ntu.edu.tw/cjlin/libsvm
11. Fawcett, T. Roc graphs: notes and practical considerations for researchers. http://home.comcast.net/~tom.fawcett/public_html/papers/ROC101.pdf

Chapter 76
Estimation of Partially Linear Regression for Errors-in-Variables Models with Validation Data

Yanyan Zhang

Abstract This paper develops an estimation approach for error-in-covariables partially linear model with the help of validation data. A feasible least squares estimator of the parameter is defined by means of local linear kernel estimator. Further, the estimator of non-parametric component is also defined by the Fourier transformation method. A small simulation studies are given and the convergent behaviors for the proposed parametric and nonparametric estimators are shown respectively.

Keywords Partially linear model • Validation data • Least squares estimator • Local linear kernel estimator • Fourier transformation • Monte-Carlo simulation

76.1 Introduction

Over the last two decades, a great deal of efforts have been devoted to errors-in-variables (EV) models. When the relationship between the surrogate variables and the true variables are rather complicated compared to the classical additive error structure usually assumed, it is challenging to obtain the correct statistical analysis. An important solution can be used to capture the underlying relationship between them is by the help of validation data. When the covariate is measured erroneously in which some validation data is available to relate the surrogate and true variables without specifying any error model structure, the nonparametric regression provides a useful tool. In such situations, semi-parametric regression models become natural alternatives. Most semi-parametric regression models, such as the partial linear regression model, are modified to allow one or more predictor variables to have complicated effects on the response, and they have been widely applied in many areas due to its flexibility. When the covariate is measured erroneously without specifying any error model structure, we consider in this paper to adopt

Y. Zhang (✉)
College of Mathematical Science, Tianjin Normal University, Tianjin 300387, PR China
e-mail: yanyanzhang1973@163.com

J. Mu et al. (eds.), *The Proceedings of the Third International Conference on Communications, Signal Processing, and Systems*, Lecture Notes in Electrical Engineering 322, DOI 10.1007/978-3-319-08991-1_76

the partially linear model to estimate the regression function by the help of the validation between the surrogate and true variables.

To be specific, we assume that independent validation dataset $\upsilon = \{(t_j, \tilde{t}_j)\}_{j=N+1}^{N+n}$ is available, in addition to the primary surrogate dataset $\varsigma = \{(y_i, x_i, \tilde{t}_i)\}_{i=1}^{N}$, which is generated by the following partially linear model

$$Y = X\beta + m(t) + \varepsilon, \tag{76.1}$$

where Y is a scalar response variable, $X = (X_1, X_2, \ldots, X_p)$ is a p-dimension explanatory vector, and the unknown parameter vector is $\beta = (\beta_1, \beta_2, \ldots, \beta_p)^T$. For convenience, we denote the sample $X = (x_1, x_2, \ldots, x_N)^T$, and $x_i = (x_{i1}, x_{i2}, \ldots, x_{ip})^T$. t is a univariate explanatory variable, $\tilde{t}$ is the surrogate variable of t and ε is the random error with mean zero and finite variance. t_i's are independent and identically distributed, and given $\tilde{t}_i$'s and x_i's, the errors ε_i's are also assumed to be independent and identically distributed. Our aim is to estimate the unknown regression function $m(\cdot)$ and parameter vector β with the dataset υ and ς simultaneously.

76.2 Methodology

According to model (76.1) and the assumptions below it, we consider to rewrite it as the following form

$$y_i = x_i^T\beta + m(U(\tilde{t}_i) + \eta_i) + \varepsilon_i, \quad i = 1, 2, \ldots, N \tag{76.2}$$

$$t_j = U(\tilde{t}_j) + \eta_j, \quad j = N+1, N+2, \ldots, N+n \tag{76.3}$$

where $U(\tilde{t}_i), \varepsilon_i$ and η_i are mutually independent and identically distributed. Taking $U(\cdot)$ as a new variable, this can be regarded as a Berkson EV model the one as reference [1] and [2]. Note that the nonparametric technique for solving Berkson EV problem developed in [3] and [4] can be applied here as long as we could obtain all of the three estimations for the distribution of η_i, $E[(y_i - x_i^T\beta)|U(\tilde{t}_i) = z]$ and the parametric component β on which we will study next.

76.2.1 Estimating $\boldsymbol{\beta}$ *and* $E[(y_i - x_i^T\beta)|U(\tilde{t}_i) = z]$

According to the above idea and model (76.1), represent (76.2) as

$$y_i = x_i^T\beta + M(U(\tilde{t}_i)) + \xi_i, \quad i = 1, 2, \ldots, N \tag{76.4}$$

For the true parameters of β, we have $M(z,\beta) = E[(y_i - x_i^T\beta)|U(\tilde{t}_i) = z]$. We assume that $E[\xi_i|\tilde{t}_i, x_i] = 0, E[\xi_i]^3 < \infty$ and $E[\xi_i]^2 = \sigma^2$. Generally, M is not equal to m and $\xi_i \neq \varepsilon_i + \eta_i$. For the unknown function $U(\cdot)$, based on the validation data set $\upsilon = \{(t_j, \tilde{t}_j)\}_{j=N+1}^{N+n}$, we can estimate $U(\cdot)$ by means of kernel, namely

$$\hat{U}(\tilde{t}) = \sum_{j=N+1}^{N+n} t_j \cdot L_{nj}(\tilde{t}). \tag{76.5}$$

We choose to use the local linear kernel estimator (LLKE) here for the reason that this method possesses superior boundary behavior, that is

$$L_{nj}(\tilde{t}) = \frac{L\left(\frac{\tilde{t}_j - \tilde{t}}{b_n}\right)\{S_{n2} - (\tilde{t}_j - \tilde{t})S_{n1}\}}{\sum_{j=N+1}^{N+n} L\left(\frac{\tilde{t}_j - \tilde{t}}{b_n}\right)\{S_{n2} - (\tilde{t}_j - \tilde{t})S_{n1}\}},$$

where

$$S_{n\gamma} = \frac{1}{nb_n}\sum_{j=N+1}^{N+n} L\left(\frac{\tilde{t}_j - \tilde{t}}{b_n}\right)(\tilde{t}_j - \tilde{t})^{\gamma}, \quad \gamma = 0, 1, 2,$$

$L(\cdot)$ is a symmetric density kernel function and b_n is the bandwidth.

On the other hand, based on the corresponding surrogate data set $\varsigma = \{(y_i, x_i, \tilde{t}_i)\}_{i=1}^{N}$, we can construct a positive weight functions $w_{Ni}(z)$ depending on $U(\cdot)$. For every given β, we define an estimator of $M(z)$ by

$$M(z,\beta) = \sum_{i=1}^{N} w_{Ni}(z) \cdot (y_i - x_i^T\beta),$$

and $w_{Ni}(z) = w_{Ni}(z|U(\tilde{t}_1), U(\tilde{t}_2), \ldots, U(\tilde{t}_N))$. Given the estimator $\hat{U}(\cdot)$ in Eq. (76.5), we can obtain the positive weight functions $K_{Ni}(z)$ to be taken as $w_{Ni}(z)$. That is

$$\begin{aligned} K_{Ni}(z) &= K_{Ni}\left(z|\hat{U}(\tilde{t}_1), \hat{U}(\tilde{t}_2), \ldots, \hat{U}(\tilde{t}_N)\right) \\ &= \frac{K\left(\frac{\hat{U}(\tilde{t}_i) - z}{h_N}\right)\{S_{N2} - (\hat{U}(\tilde{t}_i) - z)S_{N1}\}}{\sum_{i=1}^{N} K\left(\frac{\hat{U}(\tilde{t}_i) - z}{h_N}\right)\{S_{N2} - (\hat{U}(\tilde{t}_i) - z)S_{N1}\}}, \end{aligned}$$

it is also a form of LLKE, where

$$S_{N\gamma} = \frac{1}{Nh_N}\sum_{i=1}^{N} K\left(\frac{\hat{U}(\tilde{t}_i) - z}{h_N}\right)(\hat{U}(\tilde{t}_i) - z)^{\gamma}, \quad \gamma = 0, 1, 2,$$

$K(\cdot)$ is another symmetric density kernel function and h_N is its corresponding bandwidth.

Then we can estimate $M(z, \beta)$ based on the weights $K_{Ni}(z)$ by

$$\widehat{M}(z, \beta) = \sum_{k=1}^{N} K_{Nk}(z) \cdot (y_k - x_k^T \beta),$$

and the value of $M(z, \beta)$ at $\hat{U}(\tilde{t}_i)$ can be estimated by

$$\widehat{M}(\hat{U}(\tilde{t}_i), \beta) = \sum_{k=1}^{N} K_{Nk}(\hat{U}(\tilde{t}_i)) \cdot (y_k - x_k^T \beta).$$

Further, replacing $M(U(\tilde{t}_i))$ by $\widehat{M}(\hat{U}(\tilde{t}_i), \beta)(i = 1, 2, \ldots, N)$ in model (76.4), using the least squares Estimation (LSE) criterion, we can obtain estimator of β by

$$\widehat{\beta}_N = \underset{\beta}{\operatorname{argmin}} \sum_{i=1}^{N} (y_i - x_i^T \beta - \widehat{M}(\hat{U}(\tilde{t}_i), \beta))^2.$$

So the LSE of β is

$$\widehat{\beta}_N = (\tilde{X}^T \tilde{X})^{-1} \left(\sum_{i=1}^{N} \tilde{x}_i \tilde{y}_i\right), \tag{76.6}$$

where $\tilde{y}_i = y_i - \sum_{k=1}^{N} K_{Nk}(\hat{U}(\tilde{t}_i)) y_i$, $\tilde{x}_i = x_i - \sum_{k=1}^{N} K_{Nk}(\hat{U}(\tilde{t}_i)) x_i$ and $\tilde{X} = (\tilde{x}_1, \tilde{x}_2, \ldots, \tilde{x}_N)^T$.

Thus, we at last obtain the estimator of $M(z)$ by

$$\hat{M}^*(z) = \sum_{i=1}^{N} K_{Ni}(z) \cdot (y_i - x_i^T \widehat{\beta}_N). \tag{76.7}$$

So far, we obtain the final estimators of the parameters and the nonparametric function in (76.4) simultaneously, which are expressed in Eqs. (76.7) and (76.8).

76.2.2 *Estimating* m(z)

Noted that in the partially linear regression model if we regard $y_i - x_i^T\beta$ as a working response $y_i(\beta)$, the Fourier transformation method can also be employed to recover the non-parametric function $m(\cdot)$. Without loss of generality, we assume that the support intervals of the densities of t_j, $\tilde{t}_j$ and η_j have been re-scaled respectively so that they are contained within $\Omega = [-\pi, \pi]$. In addition, to assure $m(\cdot)$ is identifiable, we suppose that the support of the density of t is contained within the range of $U(\tilde{t}_i)$. After obtaining $\hat{M}^*(z)$, we can accommodate the Fourier transformation method to find the relationship between $m(\cdot)$ and $M(\cdot)$ so that $\widehat{m}(z)$ can be estimated by $\hat{M}^*(z)$. This is similar to the method in [3] and here we only recall the main steps integrated with our proposed estimators.

On Ω we may write the trigonometric series for $m(z)$ as

$$m(z) = m_0 + \sum_{l=1}^{\infty}\{m_{1l}\cos(lz) + m_{2l}\sin(lz)\},$$

where

$$m_0 = \frac{1}{2\pi}\int_{\Omega} m(t)dt, \quad m_{1l} = \frac{1}{\pi}\int_{\Omega} m(t)\cos(lt)dt, \quad m_{2l} = \frac{1}{\pi}\int_{\Omega} m(t)\sin(lt)dt.$$

Analogously, $M(U)$ can be represented as

$$M(U) = M_0 + \sum_{l=1}^{\infty}\{M_{1l}\cos(lU) + M_{2l}\sin(lU)\},$$

where the constants M_0, M_{1l}, M_{2l} for $l = 1, 2, \ldots$, are the Fourier coefficients determined by function M. If U and η are independent which implied by the Berkson model (76.2) and (76.3), then the relationship between the coefficients m_{1l}, m_{2l} and M_{1l}, M_{2l} is

$$\begin{pmatrix} m_{1l} \\ m_{2l} \end{pmatrix} = \frac{1}{\alpha_{1l}^2 + \alpha_{2l}^2}\begin{pmatrix} \alpha_{1l} & -\alpha_{2l} \\ \alpha_{2l} & \alpha_{1l} \end{pmatrix}\begin{pmatrix} M_{1l} \\ M_{2l} \end{pmatrix}, \tag{76.8}$$

where $\alpha_{1l} = E\{\cos(l\eta)\}$ and $\alpha_{2l} = E\{\sin(l\eta)\}$ provided that $\alpha_{1l}^2 + \alpha_{2l}^2 \neq 0$ for $l \geq 1$.

With the help of validation data, the empirical distribution of $\widehat{\eta}_j's$ can be used to obtain the distribution of η, that is

$$\widehat{\eta}_j = t_j - \widehat{U}(\tilde{t}_j), \quad j = N+1, \ldots, N+n.$$

Then, the estimators of α_{1l}, α_{2l} are given by

$$\widehat{\alpha}_{1l} = \frac{1}{n}\sum_{j=N+1}^{N+n} \cos(l\widehat{\eta}_j), \quad \widehat{\alpha}_{2l} = \frac{1}{n}\sum_{j=N+1}^{N+n} \sin(l\widehat{\eta}_j)$$

and the estimated coefficients of m_{1l}, m_{2l} can be represented as

$$\begin{pmatrix} \widehat{m}_{1l} \\ \widehat{m}_{2l} \end{pmatrix} = \frac{1}{\widehat{\alpha}_{1l}^2 + \widehat{\alpha}_{2l}^2} \begin{pmatrix} \widehat{\alpha}_{1l} & -\widehat{\alpha}_{2l} \\ \widehat{\alpha}_{2l} & \widehat{\alpha}_{1l} \end{pmatrix} \begin{pmatrix} \widehat{M}_{1l}^* \\ \widehat{M}_{2l}^* \end{pmatrix}, \tag{76.9}$$

where

$$\widehat{M}_{1l}^* = \frac{1}{\pi}\int_H \widehat{M}^*(t)\cos(lt)dt, \quad \widehat{M}_{2l}^* = \frac{1}{\pi}\int_H \widehat{M}^*(t)\sin(lt)dt,$$

$$\widehat{m}_0 = \widehat{M}_0^* = \frac{1}{2\pi}\int_H \widehat{M}^*(t)dt$$

$H \subseteq \Omega$ contains the support of M^*. Then the final estimator for $m(\cdot)$ is given by

$$\widehat{m}(z) = \widehat{m}_0 + \sum_{l=1}^{q}\{\widehat{m}_{1l}\cos(lz) + \widehat{m}_{2l}\sin(lz)\},$$

where q is the number of Fourier coefficients included in the estimators and it can be deemed as another smoothing parameter besides b_n and h_N.

76.3 Simulation Studies and Conclusions

Because there are consistent procedures for all the steps, it is possible to obtain a consistent estimator. A small simulation studies are given next.

76.3.1 Smoothing Parameters Selections

Reference [4] proposed an automatic way of choosing the smoothing parameters q, h_N and b_n for the nonparametric circumstance. Since our estimator $\widehat{\beta}_N$ is related to two parameters h_N and b_n, first, we yield $\widehat{b}_n$ by the leave-one-out CV criterion, that is the minimizer of

$$CV(b_n) = \frac{1}{n}\sum_{j=N+1}^{N+n}[t_j - \widehat{U}^{(-j)}(\tilde{t}_j; b_n)]^2,$$

where $\hat{U}^{(-j)}$ denotes the leave-one-out version of $\hat{U}$ using b_n. Then, $\widehat{\beta}_N$ relies only on the smoothing parameter h_N and we can defining $\hat{U}$ using $\widehat{b}_n$. On the other hand, $\widehat{m}(z)$ involves three regularization parameters h_N, b_n and q. If we replace b_n by $\widehat{b}_n$, we can yield the other two parameters h_N and q in one step, that is

$$(\hat{h}_N, \widehat{q}) = \underset{h_N, q}{argmin}\frac{1}{N}\sum_{i=1}^{N}[y_i - x_i^T\widehat{\beta}(h_N) - \widehat{m}^{(-i)}(\hat{U}(\tilde{t}_i), \widehat{\beta}(h_N); h_N, q)]^2. \tag{76.10}$$

where $\widehat{m}^{(-i)}$ denotes the version of $\widehat{m}$ which is constructed on omitting $(y_i, x_i, \tilde{t}_i)$ from the surrogate data using h_N and q terms in the trigonometric series. We write the procedure in Fortran language and it requires a few minutes to complete each simulation of the corresponding model.

76.3.2 Numerical Results

We conduct a moderate sample Monte-Carlo simulation to show the behavior of the estimator $\widehat{\beta}_N$ and $\widehat{m}(\cdot)$. Suppose the data is drawn from (76.2) and (76.3). Our purpose is to show the effectiveness of the proposed estimators and thus we only choose certain representative examples for illustration.

We take the true parameter vector $\beta_0 = (1.0, 1.1, 1.2)$ and the three-dimensional regressor vector $x_i \sim N(0, \Sigma_x)$ with two cases,

$$(1)\Sigma_x = I_3, \quad (2)\Sigma_x = \begin{pmatrix} 0.81 & 0.1 & 0.2 \\ 0.1 & 2.25 & 0.1 \\ 0.2 & 0.1 & 1 \end{pmatrix} \tag{76.11}$$

where I_3 is a three-order unit matrix which means the regression variables are independent. Case (2) means the regression variables are somewhat correlated. For the regression function $m(\cdot)$ could be chosen

$$(1)m(z) = (1-z^2)^2 I[-1 \le z \le 1], (2)m(z) = (1-z^2)^2 exp(2z) I[-1 \le z \le 1] \tag{76.12}$$

Three cases for $U(\cdot)$ are considered

Table 76.1 The estimated bias and MSE of β_N for each model

	$\beta_1 = 1.0$		$\beta_2 = 1.1$		$\beta_3 = 1.3$	
Model	Bias	MSE	Bias	MSE	Bias	MSE
(111)	0.037027	0.002286	0.038411	0.002317	0.037446	0.002279
(112)	0.035963	0.00209	0.035989	0.002005	0.035821	0.002057
(113)	0.039242	0.002414	0.040466	0.002654	0.03937	0.0025
(121)	0.054826	0.00469	0.054246	0.004693	0.05225	0.00439
(122)	0.052467	0.004384	0.050864	0.004086	0.051824	0.004261
(123)	0.051959	0.004338	0.051118	0.004199	0.051253	0.004299
(211)	0.04274	0.002972	0.02575	0.001042	0.038458	0.002404
(212)	0.040924	0.002694	0.024082	0.000894	0.036789	0.00217
(213)	0.044927	0.003199	0.027079	0.001191	0.040434	0.002637
(221)	0.061472	0.005946	0.036324	0.002104	0.053661	0.004631
(222)	0.059193	0.005667	0.034132	0.001832	0.053224	0.004494
(223)	0.060171	0.005741	0.034321	0.001895	0.052638	0.004534

$$(1)t = \tilde{t} \ + \delta, \qquad (2)t = \tilde{t}^2 - \frac{1}{4} + \delta, \qquad (3)t = \cos(2\pi\tilde{t}) + \delta \tag{76.13}$$

where $\tilde{t} \sim N(0, 0.5^2)$ and $\delta \sim U[-1, 1]$ which is independent of $\tilde{t}$. The first setting of $U(\cdot)$ in (76. 13) is just considered as the additive Berkson error model. Throughout this section we assumed that $\varepsilon_i \sim N(0, 0.25^2)$. For each of several choices of $\Sigma_x, m(\cdot)$ and $U(\cdot)$, 1000 simulated datasets were generated for each sample size combination of $(n, N) = (30, 120)$. The kernel functions $K(\cdot)$ and $L(\cdot)$ are both chosen to be the Epanechnikov form $0.75(1 - x^2)I[-1 \le z \le 1]$. Table 76.1 show us both the bias and MSE for $\widehat{\beta}_N$ corresponding to the true value β_0, where $(ijk), i = 1, 2; j = 1, 2; k = 1, 2, 3,$ means the true model is obtained from the form of (i), (j) and (k) in (76. 11), (76. 12), (76. 13) respectively.

Table 76.1 shows us that it makes little difference for the bias and MSE of $\widehat{\beta}_N$ when the variance structure in (76. 11) are considered. But it is not the case when the nonparametric function $m(z)$ in (76. 12) and the error model in (76. 13) are considered. We can notice that the bias and MSE get larger when the complexity is increased. This is intuitive because the estimator $\widehat{\beta}_N$ relies strongly on the function $\hat{U}(\tilde{t})$.

Our final estimators $\widehat{m}(\cdot)$ are shown in Fig. 76.1, where (ijk) is the same meaning as the one in Table 76.1. From the 12 figures we can observe that $\widehat{m}(z)$ can capture the patterns of the true curves although it tends to have larger bias at boundaries and peaks due to its explicit dependence on the size of data set.

From the results above we can see that the performance of $\widehat{m}(\cdot)$ can totally capture the main profile of the underlying regression function. However,we must notice that the proposed method requires relatively large sample size,especially at the boundary.

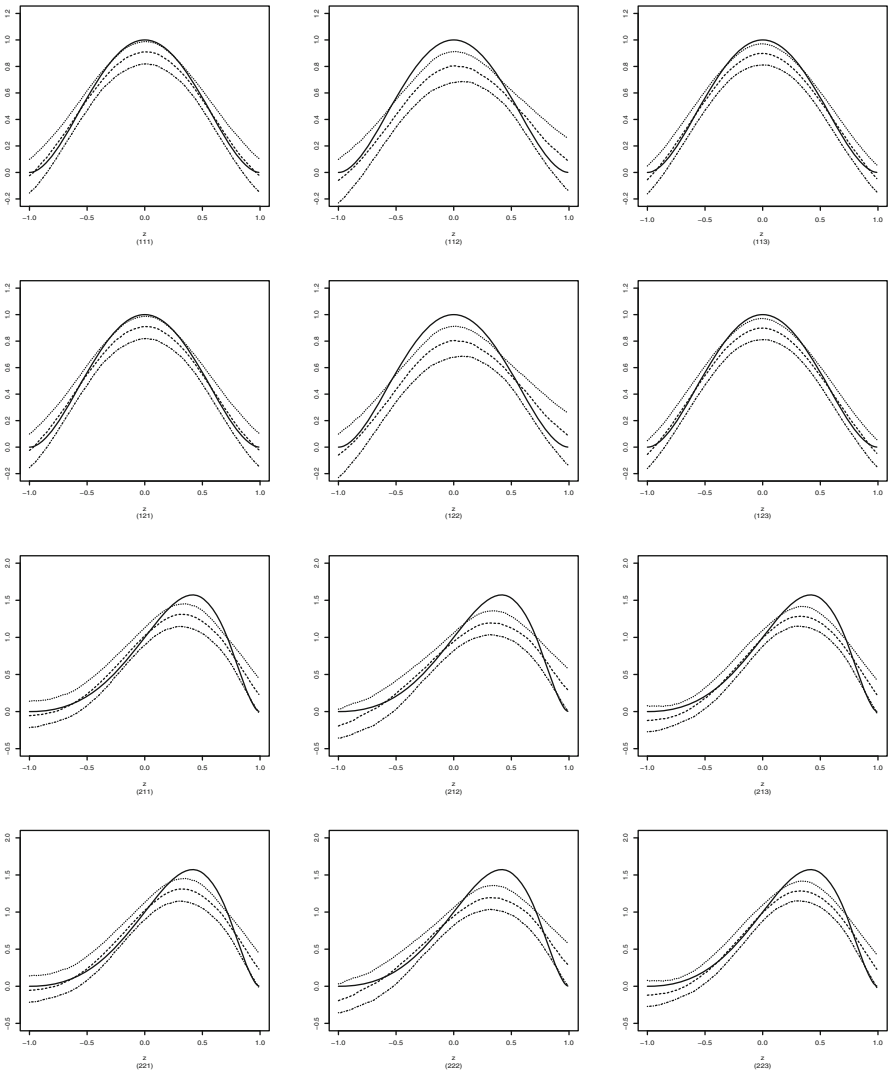

Fig. 76.1 The estimated curves of $m(\cdot)$ for the regression functions in (76. 12) for the 12 models, where the *solid, dashed, dotted and dashed-dotted curves* represent $m(\cdot)$, the median of $\widehat{m}(\cdot)$ and the quartiles of $\widehat{m}(\cdot)$ respectively

Acknowledgements The author gratefully acknowledges the editors for their constructive suggestions that helped greatly improve this paper. This research is supported by the Science and Technology Development Fund of Tianjin Education Commission for Higher Education (201307015).

References

1. Berkson J (1950) Are there two regression problems? J Am Stat Assoc 45:164–180
2. Carroll RJ et al (2006) Measurement error in nonlinear models: A modern perspective, 2nd edn. Chapman and Hall, London
3. Delaigle A, Hall P, Qiu P (2006) Nonparametric methods for solving the Berkson errors-in-variables problem. J R Stat Soc Ser B 68:201–220
4. Du L, Zou C, Wang Z (2010) Nonparametric regression function estimation for errors-in-variables models with validation data. Stat Sin 21:1093–1113

Chapter 77
A Fast PN Synchronization Algorithm in CDMA2000 Spread Spectrum Systems

Zengshan Tian, Jie Gu, and Mu Zhou

Abstract The traditional algorithms are normally suffered from large computation complexity and serious acquisition performance. This paper proposes a fast pseudo noise (PN) phase synchronization algorithm for mobile station downlink channels. Based on overlap-saving method and fast Fourier transform (FFT), the proposed algorithm achieves phase synchronization with less time and resource consumption. Simulation results indicate that the proposed algorithm could significantly decrease PN codes acquisition time cost and is proved to perform well in PN phase synchronization.

Keywords CDMA • Pseudo noise phase acquisition • Fast synchronization • Overlap-saving method • Computation complexity

77.1 Introduction

In the area of Code Division Multiple Access (CDMA) communication systems, the transceivers are precisely synchronized for pseudo noise (PN) sequence phase since the accuracy of PN sequence synchronization significantly affects the carrier synchronization and the bit error rate (BER) of digital information to be recovered. Therefore, the receiver should capture the instantaneous phase of PN sequence which is sent from the transmitter accurately and quickly.

As far as we know, the algorithms for PN phase acquisition in CDMA systems generally contain three main categories: serial acquisition method [1], parallel acquisition method [2, 3] and window-based search method [4, 5]. In [1], the authors studied the advantages and disadvantages of serial acquisition algorithm. The serial acquisition algorithm has simple composition structure of addition and multiplication, nevertheless the long acquisition time limits its performance. The authors in [2] and [3] introduced the parallel frequency acquisition algorithm which is featured that the received signals are processed by fast Fourier transform

Z. Tian (✉) • J. Gu • M. Zhou
Chongqing Key Lab of Mobile Communications Technology, Chongqing University of Posts and Telecommunications, Chongqing 400065, People's Republic of China
e-mail: tianzs@cqupt.edu.cn; cqgujie@gmail.com

J. Mu et al. (eds.), *The Proceedings of the Third International Conference on Communications, Signal Processing, and Systems*, Lecture Notes in Electrical Engineering 322, DOI 10.1007/978-3-319-08991-1_77

algorithm (FFT) for the sake of searching for the correlation peaks. Compared with the algorithm in [1], this algorithm reduces acquisition time cost, but it consumes more hardware resources. Window-based search algorithm, exploited in [4] and [5], can be recognized as the most widely used method for PN codes acquisition. The limitation of this method lies in that it is difficult to determine the window size and decision thresholds. When the determination criterion is appropriate, this algorithm can speed up the acquisition process, however, it is restricted by large arithmetic complexity due to the calculations of time-domain correlation.

In the CDMA2000 systems, the downlink pilot channel only uses low transmission power to conduct carrier synchronization. Furthermore, the Doppler shift and instability of local sampling clock increase the difficulty in phase synchronization. This paper proposes a high-efficient fast PN synchronization algorithm which can be applied to the circumstances of low power and large system frequency deviation.

The paper is organized as follows. Section 77.2 describes an overview of the overall structure of CDMA2000 downlink model. Section 77.3 addresses the steps of our proposed algorithm and discusses the complexity analysis of our algorithm in detail. The performance of our proposed algorithm is verified in Sect. 77.4. Finally, section "Conclusion" concludes this paper.

77.2 CDMA2000 Downlink Model

Since each base station transmits pilot signals to be synchronized within the local cell, the mobile station can capture PN phase by using the pilot channel. The baseband model of downlink pilot channel structure is shown in Fig. 77.1.

The PN sequence is produced by 15-stage linear feedback shift register (LFSR) and the actual rate reaches 1.2288 million chips per second (Mc/s). The I, Q generator polynomials are listed below:

$$\begin{cases} P_I(x) = x^{15} + x^{13} + x^9 + x^8 + x^7 + x^5 + 1 \\ P_Q(x) = x^{15} + x^{12} + x^{11} + x^{10} + x^6 + x^5 + x^4 + x^3 + 1 \end{cases} \tag{77.1}$$

Considering the real-time data transmission and computational complexity, overlength PN sequences may not satisfy the requirements of real-time signals demodulation. On the contrary, the too short PN sequence in low SNR condition cannot ensure that the correlation peak exceeds a given threshold. In this case, the monitoring failure may occur.

In [6], the authors proposed a PN phase acquisition algorithm using signal difference. In concrete terms, the sequence with length of M chips is first divided into P equal-length segments, which means $M = P \times X$ where X is number of chips in each segment. The output of level-l correlator is given by

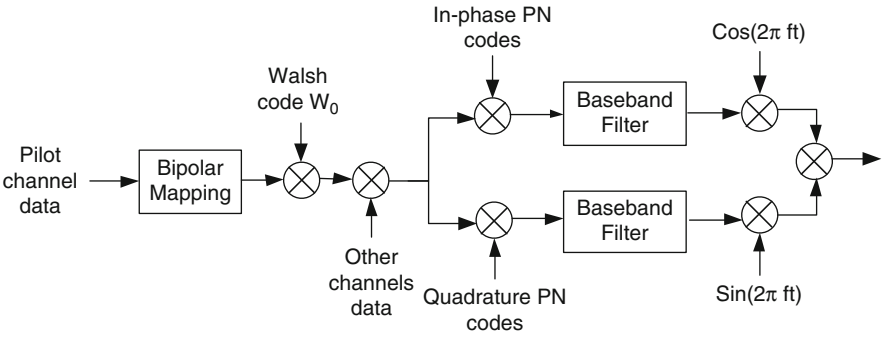

Fig. 77.1 Downlink pilot channel model

$$z_l = \sum_{k=0}^{X-1} y_I(k) + j \times \sum_{k=0}^{X-1} y_Q(k) \tag{77.2}$$

Then, we conduct shift conjugate multiplication on the correlation outputs of P segments for all the possible synchronization phase sampling point s. The maximum likelihood estimate of the phase synchronization time can be calculated as

$$\hat{s} = \text{argmax}|v(s)|^2, v(s) = \sum_{l=0}^{P-1} z_l z_{l-1}^* \tag{77.3}$$

The algorithm in [6] is one kind of window-based search methods. From the view of time-domain correlation, the methods of using shift conjugate to eliminate the effects of frequency deviation and achieving PN phase synchronization quickly can be applied to the situation that the PN sequence is not overlong. The disadvantages of the algorithm in [6] to be used in CDMA2000 can be summarized in two aspects. On the one hand, it requires a huge amount of storage space for computing the correlation of PN sequence directly. On the other hand, the high rate of baseband data transmission causes the algorithm cannot meet application requirements.

77.3 Fast PN Synchronization Method

77.3.1 Algorithm Description

The linear discrete convolution in time-domain can be calculated according to the definition, as well as being solved by using z-transform analysis method. Both the convolution calculation and z-transform analysis are complicated due to the large amount of computation cost. In response to this compelling problem, we use FFT to reduce the cost of convolution operation dramatically.

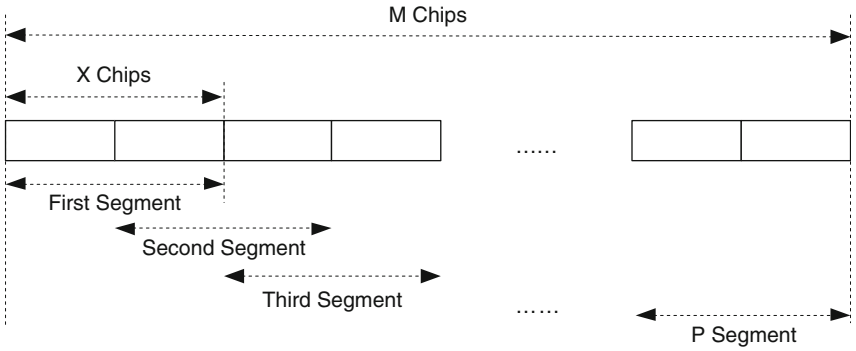

Fig. 77.2 Backtracking course of convolution searching

Although the FFT can be used to obtain the correlation peaks more quickly compared with the method in [6], the memory storage cost is significantly large by conducting FFT on the entire PN sequence. Therefore, it is not appropriate to apply FFT into PN phase acquisition directly. The combination of overlap-saving method and FFT improves operational efficiency in achieving fast convolution of long sequences and significantly saves storage space, thus a fast synchronization algorithm is proposed in this paper.

First of all, to conduct convolution, we divide the sequence with lengths of M into P equal-length segments, where the length of each segment is X. We backtrack $X/2$ chips for every segment calculations. Figure 77.2 shows the backtracking course of convolution searching. In general, X is determined by the length of short sequence. We set the length of short sequence as N where $X \geq 2N$.

Second, we use FFT and IFFT to obtain cross-correlation of two sequences segment by segment. After that, we stitch the fragments of correlation results together.

Finally, we scan through the correlation results to locate the peak position which is also recognized as the target chip in PN sequence. Based on the periodic characteristic of PN codes, we can easily find the baseband sampling data alignment with the PN phase of zero offset.

77.3.2 Algorithm Steps

To sum up, PN codes are synchronized following the five steps below.

Step 1: We first generate the local PN codes. In concrete terms, we generate the complex PN sequence according to the I, Q polynomials which are defined in (1).

Step 2: As discussed in Sect. 77.3.1, we set total sequence contain M chips and $p(n)$ sequence as the segment containing X chips. In this case, we have $P = M.X$. In

addition, we define baseband signal as $r(n)$ sequence with the length of N. Then, zero padding is aligned by the criteria in (4) and (5).

$$p(n) = \begin{cases} p(n), & n = 0, 1, \ldots, X-1 \\ 0, & n = X, X+1, \ldots, L-1 \end{cases} \tag{77.4}$$

and

$$r(n) = \begin{cases} 0, & n = 0, 1, \ldots, X-2 \\ r(n), & n = X-1, X, \ldots, X+N-2 \\ 0, & n = X+N-1, X+N, \ldots, L-1 \end{cases} \tag{77.5}$$

where L is the length for FFT, such that

$$\begin{cases} L = 2^{\alpha}, \ \alpha \in N+ \\ L \geq X + N - 1 \end{cases} \tag{77.6}$$

Step 3: With respect to the updated sequences $p(n)$ and $r(n)$, we apply FFT to calculate the corresponding frequency-domain sequences $P(k)$ and $R(k)$. We obtain correlation sequence $Z(k) = P^*(k)R(k)$, where $P^*(k)$ is the complex conjugate.

Step 4: We conduct IFFT on $Z(k)$ to obtain sequence $z(n)$. Then, we truncate $X - N$ elements in $z(n)$ starting from the N-th element and reverse the truncated sequence to calculate segment correlation. The calculation of segment correlation is shown in Fig. 77.3.

Step 5: After executing loops over the steps (3) to (4) for P iterations, the calculation of sliding correlation for all the segments shown in Fig. 77.2 is completed. We stitch those truncated sequences together to construct a new sequence with the length of M. After the peak position is located by scanning through the entire sequence, the PN sequence can be synchronized.

Based on the previous five steps, the receiver can acquire the initial PN phase assigned to the base station. In addition, the synchronization of PN sequence is necessary to the signal demodulation and decoding for the downlink channels.

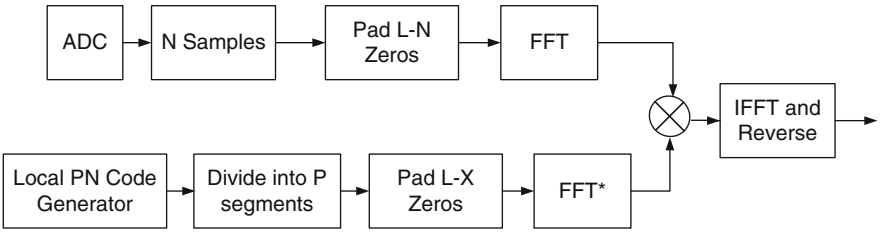

Fig. 77.3 PN correlation acquisition scheme

77.3.3 Complexity Analysis

To show the results clearer, we give the formula of computational complexity for the L-point FFT, which is same with IFFT [7]. We assume that $2^{\alpha} = L$, in the condition of α series, the amount of computation is as follows:

$$CMul: \ \left(\frac{L}{2}\right)\log_2 L = \frac{L\alpha}{2} \ CAdd: \ L\log_2 L = L\alpha \tag{77.7}$$

where *CMul* and *CAdd* are the count of complex multiplication and the count of complex addition respectively. Each segment correlation by the fast synchronization algorithm involves of two L-point FFT, one L-point complex multiplication and one L-point IFFT. Hence, the total amount of computation can be updated as

$$CMul: \ L + \frac{3}{2}L\alpha \ CAdd: \ 3L\alpha \tag{77.8}$$

In general, the execution efficiency of algorithm depends on the multiplication computation. The ratio of multiplications required by time-domain correlation algorithm [6] and multiplications by our proposed algorithm is given by

$$K = \frac{L_1 L_2}{L\left(1 + \frac{3\alpha}{2}\right)} = \frac{L_1 L_2}{L\left(1 + \frac{3}{2}\log_2 L\right)} \tag{77.9}$$

where L_1 and L_2 are the lengths of sequences $p(n)$ and $r(n)$. Complexity of the time-domain correlation algorithm is $\Theta(n^2)$, while the complexity of our proposed algorithm is $\Theta(n\log_2 2n)$.

Figure 77.4 shows the comparison of the count of complex multiplication with respect to α series between our proposed algorithm and the conventional time-domain correlation algorithm. The results in Fig. 77.4 demonstrate that our proposed method performs well in computation efficiency. In concrete terms, our proposed algorithm is about 58 times faster when $\alpha = 11$ and about 107 times faster when $\alpha = 12$ compared to the time-domain correlation algorithm.

77.4 Simulation Results

We establish a platform to acquire downlink PN phase of CDMA2000 signals and analyze algorithm performance by using Matlab R2009. According to CDMA2000 standard, the power of pilot channel occupies 20 % of the transmit power and the maximum range of frequency deviation is $\pm$ 2 kHz.

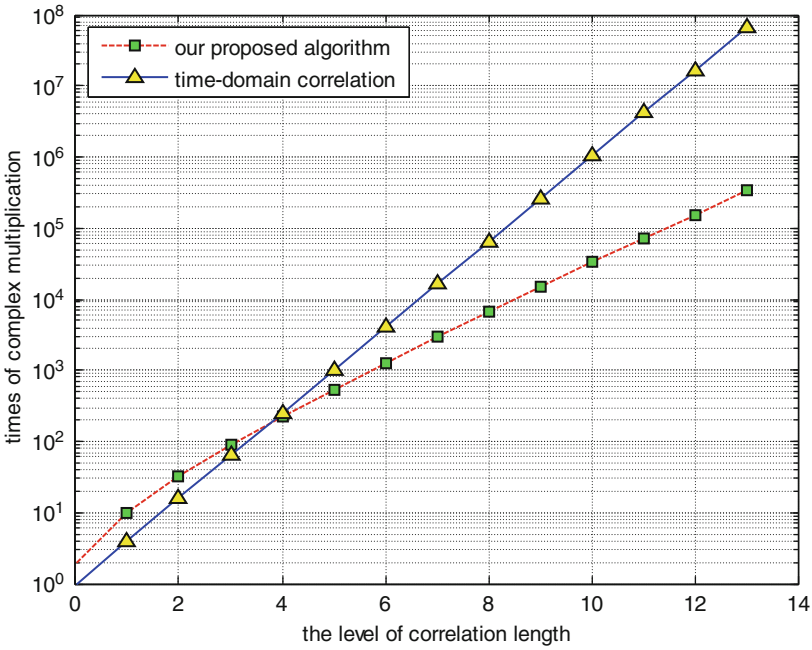

Fig. 77.4 Comparison of algorithmic efficiency

Table 77.1 Comparison of efficiency between our proposed algorithm and the CS algorithm

Algorithms	Complexity	Run time (μs)
Proposed algorithm	$\Theta(n^2)$	87
CS algorithm	$\Theta(n\log_2 2n)$	5,481

In this paper, the complexity of our proposed algorithm and the correlation search (CS) algorithm [6] are evaluated by computation time. By setting the block length as $L = 2,048$, Table 77.1 compares the complexity and run time of two algorithms. Our proposed algorithm speeds up the signal processing.

To achieve algorithm efficiency, we conduct the experiments for 1,000 times using Monte Carlo simulation method for the sake of comparing the correctness probabilities of acquired PN phase in different SNR conditions and by different methods.

In the same conditions of received power and frequency deviation, Fig. 77.5 compares the synchronization probabilities between our algorithm and the CS algorithm with respect to the SNR. In Fig. 77.5, we can find that when $SNR \leq -17$ dB, the acquiring probability by our proposed fast synchronization algorithm is more stable, while the acquiring performance by the CS algorithm deteriorates significantly as the SNR decreases. For example, the acquired probability by the correlation search algorithm is only about 55 % when $SNR = -20$ dB.

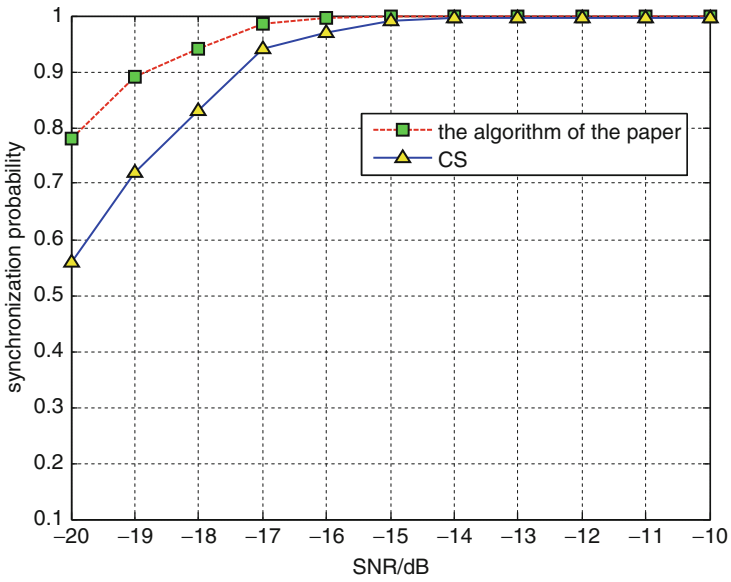

Fig. 77.5 Comparison of synchronization probabilities between proposed algorithm and CS algorithm

Fig. 77.6 Correlation peaks by proposed algorithm

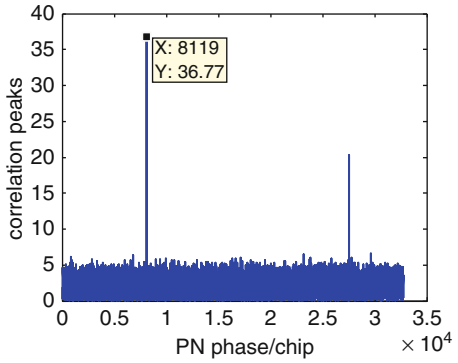

Finally, to verify the feasibility of acquisition algorithm, we collected real CDMA2000 signals using software radio platform with the sampling clock of intermediate frequency of 1.2288 MHz.

Figures 77.6 and 77.7 show the results of correlation peaks by our proposed synchronization algorithm and CS algorithm respectively. In Figs. 77.6 and 77.7, we can find that the correlation peaks achieved by our proposed algorithm are more obvious than the peaks by CS algorithm. We can use the peak-to-average ratio (PAR) to illustrate the synchronization performance. Obviously, the PAR by our proposed algorithm is much higher than the PAR by CS algorithm, which means our proposed algorithm can acquire PN phase more effectively.

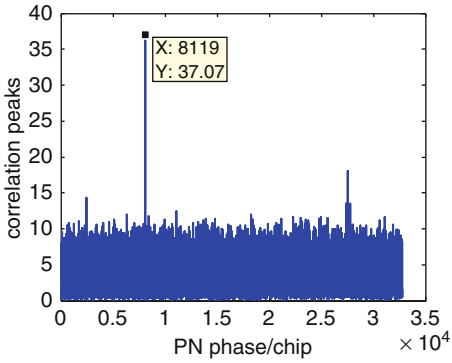

Fig. 77.7 Correlation peaks by CS algorithm

Conclusion

In this paper, we propose a fast synchronization algorithm to solve the problem of PN phase acquisition in CDMA2000 systems. By using FFT and overlap-saving method, our proposed algorithm reduces algorithm complexity and saves storage space. Based on Monte Carlo method, the simulation results show that our proposed algorithm can capture the PN phase reliably in low SNR and large frequency deviation conditions.

References

1. Feng Z, Yao R, Wang L, Huang D (2012) Fast acquisition implementation nd analysis with multi-channel search on FPGA for GNSS systems. In: IEEE international conference on signal processing, communication and computing, pp 495, 498, 12–15
2. De Angelis G, Baruffa G, Cacopardi S (2010) Parallel PN code acquisition for wireless positioning in CDMA handsets. In: Advanced satellite multimedia systems conference and signal processing for space communications workshop, pp 343, 348, 13–15
3. Song W, Zhang Y, Shao D et al (2011) Novel fast acquisition algorithm for DS/FH system. In: International conference on business management and electronic information, vol 2, pp 460, 462, 13–15
4. Chen G (2012) Parameter optimization of frequency domain narrowband interference suppression algorithm in satellite navigation. In: International conference on wireless communications networking and mobile computing, pp 1, 4, 21–23
5. Ok KM, Kang CG (2006) Improvement of window-based PN code acquisition scheme in CDMA spread spectrum systems. In: IEEE international conference on communications, vol 11, pp 4941, 4946
6. Burshtein D, Rainish D, Shamai S, Ben-Eli D (2001) Fast synchronization method for CDMA communication systems. IEEE J Select Areas Commun 19(12):2396, 2405
7. Huang P, Zu B (2009) Performance analysis of PN code acquisition using fast fourier transform. In: International conference on wireless communications networking and mobile computing, pp 1, 5, 24–26

Chapter 78
Research and Development of Wireless Data Value-Added Service System Based on Java

Lei Fan, Xin Yin, Cui-ping Zhang, Yue-yang Cui, and Rong-rong Zhang

Abstract With the development of mobile information and intelligent mobile phone, wireless data services have changed in content and form. This paper expounds the function and design of wireless test system based on J2ME platform, using RMS for data persistence, meet the needs of learning anywhere and anytime possible, to achieve efficient and timely communication between teachers and students, provides a new mode for a new mobile education system.

Keywords J2ME • MIDP • Record management system • Wireless test system

78.1 Research Status Introduction

The mobile communication and the Internet have become indispensable to modern society. Integrating these two technologies in development will open up a new space for the development of the value-added service. The mobile Internet in China mainly entertainment games mainly in the prophase development, but with the social situation changes and the popularization of mobile Internet, mobile e-commerce will become the main content of the mobile Internet application. J2ME is a kind of new mobile data service and value-added service, it provides an open platform for users, provide users a better graphical, dynamic and mobile value-added service [1].

In today's development prospects, paperless examination system has been applied to many fields, such as the company's entry test, driving test etc. This paper focuses on the system of learning. At present, the online examination system database developed, based largely on WAP, function more concentrated on the server side, the lack of certain interactive and real-time. For example, teachers need to be detected to accept students' knowledge of the extent, or some class exercises, arrangement of classroom work, the traditional application system based on WAP can't meet the students whenever and wherever possible access to education

L. Fan • X. Yin (✉) • C.-p. Zhang • Y.-y. Cui • R.-r. Zhang
College of Electronics and Communications Engineering, Tianjin Normal University, Tianjin 300380, China
e-mail: yinxin1025@126.com

J. Mu et al. (eds.), *The Proceedings of the Third International Conference on Communications, Signal Processing, and Systems*, Lecture Notes in Electrical Engineering 322, DOI 10.1007/978-3-319-08991-1_78

information and resources, teachers can't grasp the knowledge grasping level, which greatly reduces the effectiveness of instruction. Wireless test terminal so how to construct a simple and easy to operate and safe and reliable has become a new development opportunity. Mobile learning is a new learning style and with the mobile device applications. And in the intelligent mobile phone popularity today, students use the mobile phone frequency is far more than the use of the Internet, the development of mobile terminal to meet the students in any place, any time for learning, causes between the teacher and the student communication more smooth.

78.2 Systems Theory Framework

J2ME is a highly optimized Java runtime environment, definition and standardization of a portable wireless application development environment [2], J2ME program can be developed on the PC machine and simulation run, relatively easy to transplant to the target machine. Compared with WAP, J2ME has a strong cross platform, and has direct access to the network capacity, the realization of wireless devices and the server communication security. For mobile J2ME development using CLDC/MIDP structure.

MIDP is a Profile used for mobile phone developed, the core of MIDP is a MIDlet application [3], it is mainly realized these three abstract methods contain startApp (), pauseApp () and destroyApp (). Through transfer related time to change the state of the application.

The conversion between the three state diagram is shown in Fig. 78.1.

The project mainly adopts HTTP communication protocol to connect, to realize the network communication based on HTTP protocol using the HttpConnection interface, the wireless test system client through the Connector class in MIDP to create a HttpConnection object [4], realize the communication process and servers on the Internet online for a mobile, after the establishment, it can be more

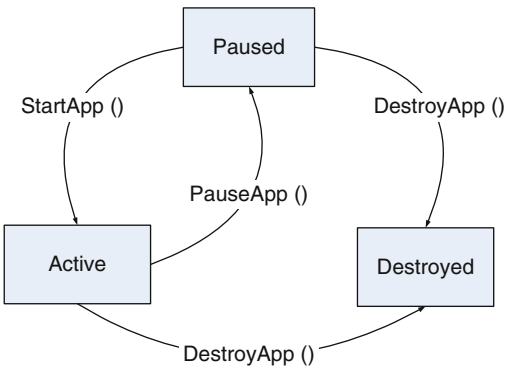

Fig. 78.1 Three state diagram conversion

convenient to operate the data, through the XML to realize the data exchange between the client and server, the user's operation request through the XML conversion is transmitted to the server, After the server receives XML information, call the relevant processes, do database access operations, and send the results back to the client. J2ME program receives the XML information, the information is converted into data that can be processed for Java, which was displayed on the mobile phone screen.

For data storage using RMS of the associated data in terminal storage system [5], mainly used the RecordStore class, MIDP support for persistent storage of data, in RMS, can create multiple records storage, data is recorded as being in the form of permanent storage in the record store, not because of equipment shutdown or other emergencies causing loss of data. Before using the record store, the first thing is create a record store, create and open record stores need to use the openRecordStore () method. After recording successfully created, can operate these such as adding and reading records, and modify and delete records. Database system can store relevant learning resources, such as the subject of questions, answers, user information and user feedback information in the process to use.

The whole system is developed by using WTK as a development platform, the application using the WTK can run J2ME, it contains the complete generation tool, and the device emulator, can simulate J2ME application [6].

Design block diagram of system program is shown in Fig. 78.2.

78.3 Systems Research and Programs

The university has gradually spread the Internet teaching management, but the mobile phone has become the product that people would not leave the body in modern society, the WAP system can't meet obtain information whenever and wherever [7], so the realization of wireless teaching management more in line with the development trend of modern. In this paper, mainly introduce a teaching program to the realization of wireless module based on J2ME. Develop test system based on WAP, teachers can decorate the classroom work, review homework, also can get feedback from students on the spot test, timely. Students can sort out the wrong question to facilitate future inquiries.

Specific functions as follows:

1. User management: user login, registration and query.
2. Test question management: classify the test subject and the degree of ease, managers can increase questions in, modify or delete and answer set.
3. Title generation: according to the user account, knowledge points, degree of difficulty, such as the choice of the set type, testing time, automatic generation of test paper.
4. The examination management: examination time limit, in a predetermined set time, the system automatically submits the examination paper and return to the

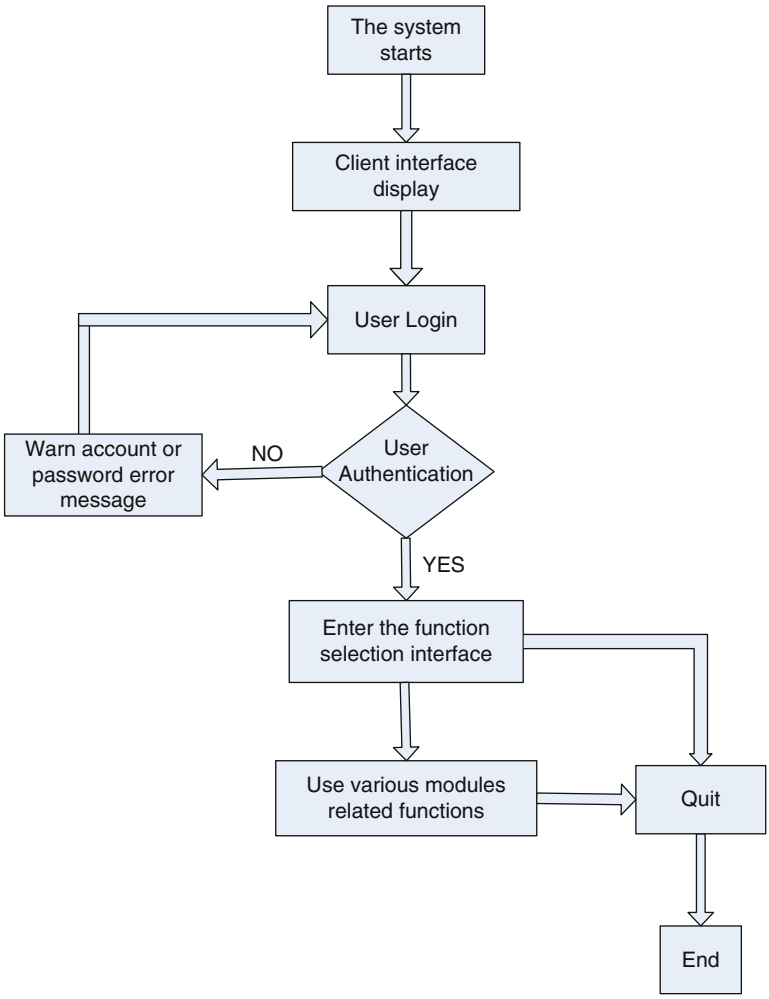

Fig. 78.2 Design block diagram

main interface. In the test after the evaluation, the user can organize for their useful topics by category, and the answer record feedback, feedback of results are uploaded to the management office.

The system structure and function structure diagram is shown in Fig. 78.3.

78.3.1 Login Module Design

The login module is designed with Alert class, after the set time, to enter the login interface,; using the LoginForm class, enter the correct account and password to log

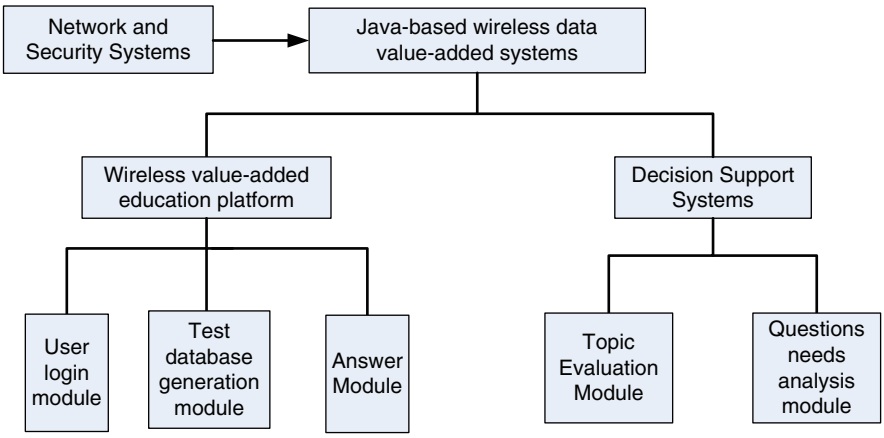

Fig. 78.3 The system structure and function structure diagram

on. In this process, the client will start the server, open the local default port, the account and password transfer user input to the server, the server to verify that the information is correct, enter the main interface program. In the login module, recognition of the identity of teachers and students, teachers can do the identity view of students, the answer and modify database. A student can do, proofreading, error management function, can the accounts to view the past preserved under the historical information.

78.3.2 Functions Selection Interface Design

In the user interface, using MIDP class List and class Form function selection, user input and other operations, provide a range of options for the user. The user can choose to enter the module, you can choose the test subjects, difficulty, error query, after selection into the corresponding interface.

In the design of test mode, the need for regular operation, at the time the user must stop the answer, need to use MIDP API in the TimerTask class and the Timer class, Timer class is responsible for the task execution to create and manage thread.

78.3.3 Records Management and Test Database Design

Data storage is operated through the record management system operation, the need to import the package javax.microedition.rms. In records management system, data can be created, add, delete, access and create multiple record storage area, when it comes to many records of the operation, need to implement the RMS three interface

in the package, data is recorded as the form of permanent storage in the record store, will not be lost because of exit or equipment shutdown.

78.4 System Implementation and Testing

78.4.1 Development Environment

1. Operating system: Microsoft Windows 7
2. Development platform: J2ME
3. Programming languages: Java
4. Integrated development environment: WTK, Eclipse
5. Data storage: RMS, TXT

78.4.2 Module Test

See Figs. 78.4, 78.5, 78.6, and 78.7.

Fig. 78.4 Login module

Fig. 78.5 Function selection module

Conclusion

Wireless test system for a wireless test base, including test questions library module, examination module and evaluation module. A part of the mobile learning, improve classroom teaching efficiency, overcome time, space restrictions on communication between teachers and students, the educational system will be wireless data increment of Java System Based on mobile terminal application to this, students can master the information whenever and wherever possible, the absorption test of knowledge, some download applications more secure college education, make more intelligent. With the development of mobile communication technology, the performance of mobile services will be more and more higher, wireless education system will have a more broad application prospect.

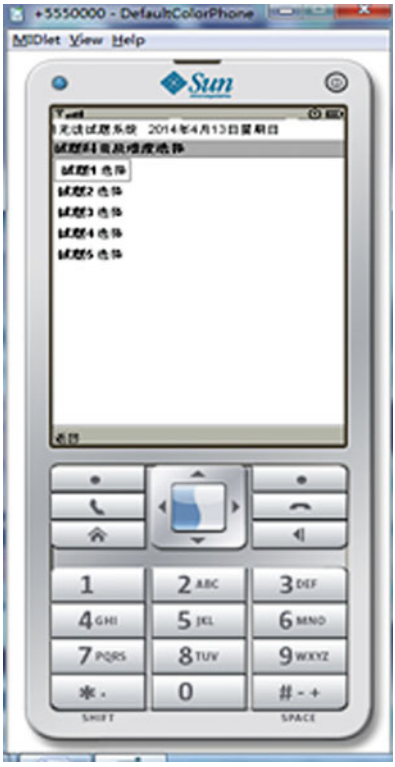

Fig. 78.6 Test module

Fig. 78.7 Questions add module

References

1. Keogh J (2004) J2ME The complete reference. Tsinghua Publisher, Beijing, China
2. Long Z, Jianhua W, Jun Z, Jiaqi D (2010) The application of mobile learning in higher education reform. Comput Educ 6:34–37
3. Xiaoying S, Dongben L (2004) Design of application platform for location based service based on J2ME. Comput Appl 24(11):146–148
4. Yushun L, Ding M (2008) The current situation and trend of development of mobile learning. China Inf Technol Educ 3:9–11
5. Dye A et al, (2003) Mobile education-a glance at the future. http://www.dye.no/articles/a_glance_at_the_future/index.html
6. Yun Z (2006) Exercise of streaming media on J2ME mobile phone. http://blog.csdn.net
7. Muchow J (2003–2006) Implementing push technology with J2ME and MIDP. http://www-128.ibm.com/developerworks/edu/ wi-dw-wi-midpreg-i.html

Chapter 79
Recognition of OFDM Signal Based on Cyclic Cumulant Reconstruction with Sub-Nyquist Sampling

Siyuan Liu, Zhuo Sun, Sese Wang, Xuantong Chen, and Wenbo Wang

Abstract In recent years,to meet the challenge of spectrum sensing with ultra wide band and big data in cooperative and cognitive radio networks,the theory of compressed sensing is introduced in,which can solve the problem of high sampling rate requirement due to Shannon-Nyquist sampling theory. In this paper,considering the property of signals' cyclostationarity, we innovatively propose a method in OFDM signal detection using sub-Nyquist samples. By doing sparsity analysis combined with detection necessities,we present a partial-scale reconstruction method to reduce the recovery iteration and lower the algorithm complexity. Furthermore,we find out an equivalent cyclic cumulant calculation method for OFDM signals to simplify the calculation and lower the high memory consumption during signal processing. From the simulations we can see the optimized method introduced in effectively eliminates the constraints for compressed detection of OFDM signals and possesses a far-reaching significance in further researches and applications.

Keywords Cognitive radio • Compressive sampling • Feature detection • Cyclic autocorrelation

79.1 Introduction

As an intelligent radio technology, cognitive radio (CR) is widely applied in wireless communication systems for its ability of spectrum sensing over wide band and can do spectrum management flexibly and efficiently. Traditional sensing process is based on Nyquist sampling theory, and the data scale to be dealt with can be enormous with a quite wide band especially in the cooperation networks. Recently, compressed sensing has been brought in to reduce the sensing

S. Liu (✉) • Z. Sun • S. Wang • X. Chen • W. Wang
Key Laboratory of Universal Wireless Communication, Ministry of Education, Beijing University of Posts and Telecommunications, Beijing 100876, China
e-mail: lsy0627@bupt.edu.cn

J. Mu et al. (eds.), *The Proceedings of the Third International Conference on Communications, Signal Processing, and Systems*, Lecture Notes in Electrical Engineering 322, DOI 10.1007/978-3-319-08991-1_79

redundancy [1], which makes it possible for signal recognition and detection to conduct with lower dimension. The combination of the two popular technology has broken up the bottleneck of the ultra high sampling rate, not only minimizing spectrum sensing redundancy, but also bringing down the cost during storage, processing and transmission.

In the 4G communication system, the application of Orthogonal Frequency Division Multiplexing (OFDM) shows a clear advantage on counteracting the degeneration caused by multi-path propagation. When it comes to the spectrum detection and analysis, several methods on multi-carrier detection have been studied extensively [2]. For most communication signals, Feature detection on signals' cyclostationarity is proved as an effective method [2]. Signal cyclostationarity is spreaded on the two-dimensional (2D) cyclic frequency-time domain while the values of noise on both of the two domains are almost zero. So, it is conducive to achieve signal recognition, detection and parameter identification in noisy environments.

Our study focuses on the physical layer process of CR, especially on the detection of OFDM signals based on compressed sampling. There are two main approaches in relevant studies. In the first method [3], the signal's 2D spectral correlation function (SCF) is set as sparse domain, and then recovery of the whole 2D SCF is achieved by establishing the projection relationship between the compressed samples and the sparse cyclic spectrum. However, the accomplishment costs a large scale of memory, which makes it only available for single carrier linear digital (SCLD) signals [4]. Another method is conducted by one-dimension recovery of cyclic autocorrelation with a fixed time-delay or a fixed cycle frequency (CF) [5], while it can't be adopted for the information obtained isn't enough for parameter detections.

Inspired by both of the methods,we will innovatively set up the relationship between sub-Nyquist samples and original OFDM signal's second order cyclic cumulant, using the sparsity of OFDM signal in cyclic cumulant domain, and specially introduce a simplified equivalent method in calculating the cyclic cumulant avoiding large memory and also reducing the complexity of the algorithm. Furthermore, considering we only need some of the information over the cyclic cumulant domain in feature detection, we render a partial-scale reconstruction strategy to lower the sampling rate and reduce the iterations in recovery without weakening the detection performance. The algorithm we propose in the paper provides an effective approach on the practical applications of OFDM signal detection and triggers further studies.

The remaining part of this paper is organized as follows. Section 79.2 presents the system model. Section 79.3 describes the algorithm of partial-scale reconstruction of OFDM signal's sparse cyclic cumulant. Section 79.4 presents simulation and analysis. Finally, we present the conclusion in section "Conclusion" and then make some suggestions for future work.

79.2 System Model

In the following analysis, we consider the OFDM signal as a zero-mean cyclostationary process. The OFDM symbol consists of N modulated multiple subcarriers and we denote the OFDM signal as follows:

$$x(t) = \frac{1}{\sqrt{N}} \sum_{k=-\infty}^{\infty} \sum_{n=0}^{N-1} d_{n,k} \mathrm{e}^{j2\pi((f_c+n\Delta f)(t-kT)+\phi_0)} \times g(t - t_0 - kT) \tag{79.1}$$

where the k-th OFDM symbol $d_{n,k}$ is identically distributed after constellation mapping and $g(t)$ is the pulse shaping filter. The symbol period $T = T_u + T_{cp}$, where T_{cp} is cyclic prefix (CP) duration and $T_u = 1/\Delta f$ is the useful symbol duration. Δf is the frequency interval between two adjacent sub-carriers. The initial phase is ϕ_0, the carrier frequency is f_c and the signal's initial time is t_0.

In our model, the signal is transmitted to the receiver through AWGN channel. At the receiver, compressed sampling is launched at first and detection comes followed.

79.3 Partial-Scale Reconstruction of Sparse Cyclic Cumulant

79.3.1 Sparsity Exploration of OFDM Signals

As the theory of compressive sensing presents, as long as the signal has sparsity in some transform domain, the original signal can be perfectly recovered with seldom samples by solving an optimization problem. According to the definition of cyclic cumulant and OFDM signal's cycle ergodic, the second order cyclic cumulant which is also known as the cyclic autocorrelation function (CAF) can be represented as:

$$C_{2x}^{\alpha}(\alpha;\tau) = \lim_{T_0\to\infty} \frac{1}{T_0} \int_{-T_0/2}^{T_0/2} x(t+\tau/2)x^*(t-\tau/2)e^{-j2\pi\alpha t}dt \tag{79.2}$$

where T_0 is the cyclic period, $C_{2x}(t;\tau) = E[x(t+\tau/2)x^*(t-\tau/2)]$ is the second order time varying autocorrelation function (AF) and $E[\cdot]$ denotes expectation. As is known that OFDM signals are orthogonal among subcarriers and symbols, considering the cyclostationary, the CAF of OFDM signal consists only several peaks on certain delay and cyclic frequency position α= m/T and we can see from Fig. 79.1 that it shows perfect sparsity in the time-frequency domain, where m is an integer.

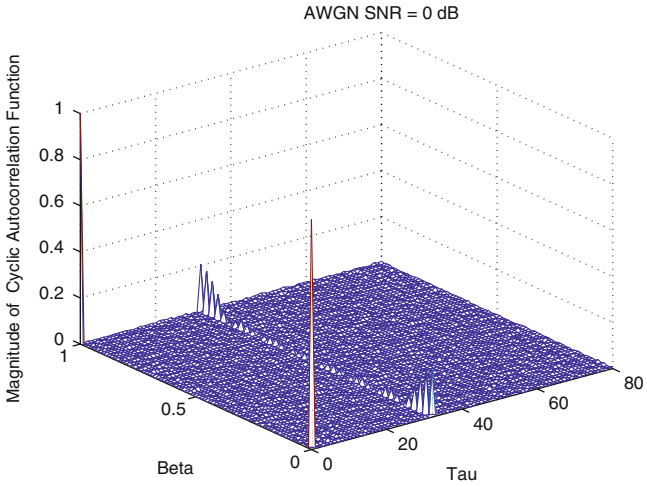

Fig. 79.1 The cyclic cumulant of OFDM signal

79.3.2 Build the Sparse Projection Relationships

Considering the digital format of the OFDM signal, $x[n] = x(t) \mid (t = nT_s)$, where $T_s = 1/f_s$ and f_s is the sampling rate. The AF can be expressed as:

$$r_x(n,\tau) = E\{x(nT_s)x^*(nT_s + \tau T_s)\} = E\{x[n]x^*[n+\tau]\} \tag{79.3}$$

For the signal cyclostationary, we suppose AF is periodical with period T, $r_x(n,\tau)$=$r_x(n + kT, \tau)$. Accordingly, the cyclic cumulant (79.2) can be estimated as

$$r_x^{(c)}(m,\tau) = \frac{1}{\tilde{N}} \sum_{n=0}^{\tilde{N}-1} x[n]x^*[n+\tau]e^{-j\frac{2\pi}{D}mn} \tag{79.4}$$

where $m \in [0, \tilde{N} - 1]$, $\tau \in [0, \tilde{N} - 1]$, $D = N_{fft} + N_{cp}$ represents the number of samples over an OFDM symbol, $\tilde{N} = D \times N_s$ is the length of discrete input signal and N_s denotes the number of symbols. The non-zero cyclic frequency $\alpha = (m/D)f_s$. When $x[n]$ is complex-valued, the matrix of signal AF(3) is conjugate symmetric positive semi-definite. So to consolidate and simplify the information, we formulate the autocorrelation matrix as follows [3]:

$$\mathbf{R} = \begin{bmatrix} r_x(0,0) & r_x(0,1) & \cdots & r_x(0,N-1) \\ r_x(1,0) & r_x(1,1) & \cdots & 0 \\ \vdots & \vdots & & \vdots \\ r_x(N-1,0) & 0 & \cdots & 0 \end{bmatrix} \tag{79.5}$$

Then we extract the elements of $\mathbf{R}$ by column as $\mathbf{r}_x$: $vec\{\mathbf{R}\} = \mathbf{B}\mathbf{r}_x$, where $\mathbf{r}_x$ is of size $\tilde{N}(\tilde{N}+1)/2 \times 1$. From (79.4) we can get the relationship between cyclic cumulant matrix $\mathbf{R}_x^{(c)}$ and $\mathbf{R}$ by $\mathbf{R}_x^{(c)} = \sum_{\tau=0}^{\tilde{N}} -1\mathbf{G}_\tau \mathbf{R}\mathbf{D}_\tau$

Note that the $\tilde{N} \times \tilde{N}$ matrix $\mathbf{G}_\tau = [(1/\tilde{N})e^{-j2\pi mn/\tilde{N}}]_{(m,n)}$ achieves FFT and Matrix $\mathbf{D}_\tau$ contains only (τ,τ)-th diagonal element being 1 and all the other elements being 0 is of size. In the next we use the property $\text{vec}\{\mathbf{UXV}\} = (\mathbf{V}^T \otimes \mathbf{U})\text{vec}\{\mathbf{X}\}$ and the relationship matrix turns to:

$$vec\{\mathbf{R}_x^{(c)}\} = \sum_{\tau=0}^{N-1}(\mathbf{D}_\tau^T \otimes \mathbf{G}_\tau)vec\{\mathbf{R}\} = \mathbf{H}\mathbf{r}_x \Rightarrow \mathbf{r}_x = \mathbf{H}^\dagger vec\{\mathbf{R}_x^{(c)}\} \tag{79.6}$$

where $\mathbf{H}^\dagger$ is the pseudo-inverse matrix of $\mathbf{H}$. In the following, we denote the sampling process as $\mathbf{z}_t = \mathbf{A}\mathbf{x}_t$, where $\mathbf{z}_t$ is the sub-Nyquist sample vector and $\mathbf{A}$ is the measurement matrix. Therefore we obtain

$$\mathbf{R}_z = \mathbf{A}\mathbf{R}_x\mathbf{A}^H \tag{79.7}$$

where $\mathbf{R}_z = E\{\mathbf{z}_t\mathbf{z}_t^T\}$ is of size $M \times M$. Similar to the derivation of (79.8), we get

$$\mathbf{r}_z = \mathbf{Q}_M vec\{\mathbf{A}\mathbf{R}_x\mathbf{A}^H\} = \mathbf{Q}_M(\mathbf{A} \otimes \mathbf{A})vec\{\mathbf{R}_x\} = \Theta\mathbf{r}_x \tag{79.8}$$

By plugging (79.6) into (79.8), we obtain the projection relationship between signal CAF matrix $\mathbf{R}_x^{(c)}$ and the sample autocorrelation vector $\mathbf{r}_z$:

$$\mathbf{r}_z = \Theta\mathbf{H}^\dagger vec\{\mathbf{R}_x^{(C)}\} = \Psi vec\{\mathbf{R}_x^{(C)}\} \tag{79.9}$$

where $\Psi = \Theta\mathbf{H}^\dagger$ is of size $M(M+1)/2 \times \tilde{N}^2$.

79.3.3 Equivalent Cyclic Cumulant Calculation

As is discussed above, the projection matrix Ψ contains several matrixes size of $O(\tilde{N}^2 \times \tilde{N}^2)$ which would expand as $\tilde{N}$ increases. Especially when detecting OFDM signals, $\tilde{N}$ is dozens of times(D) larger than N_s in single-carrier signal scenario. So the memory size needed is extremely large and hard to satisfy in practice.

To solve the problem we propose a novel statistic method for OFDM signals. As is stated in Sect. 79.3.1, we merely interested in the non-zero cyclic frequency set α and from (79.4) we can see that $r_x^{(c)}(m,\tau)$ is periodic with period D. Then we can

split the accumulation by OFDM symbols and in our study, we do the simplification by every two OFDM symbols:

$$r_x^{(c)}(m,\tau) = \frac{1}{\tilde{N}} \sum_{k=0}^{(N_s-1)/2} \sum_{n=0}^{2D-1} x(n+2kD) \times x^*(n+\tau+2kD) e^{\frac{-j2\pi mn}{2D}} \tag{79.10}$$

Thus the frequency set we obtain turns to $\alpha = m/(2D)$.

The accumulation method above does benefit on memory saving. In the approach, the signal matrix dimension is limited to $\tilde{N} = 2D$. Set a case with 800 OFDM symbols as an example, where FFT size is 64 and the length of CP is 16 for each symbol. The matrix dimension successfully get diminished from $800 * 80^2 \times 800 * 80^2$ to $2 * 80^2 \times 2 * 80^2$ and the memory size needed got a reduction by $2.5 * 10^{10}$ times. Furthermore, considering the statistic feature, the accuracy of estimated CAF improves as the number of input symbols increases.

79.3.4 Cyclic Cumulant Recovery

Base on the sparsity of CAF depicted in Sect. 79.3.1, we can recover the cyclic cumulant of the original signal according to the compressed sensing theory.

Given the covariance vector of sub-Nyquist $\mathbf{r}_z$, the reconstruction issue of vector $vec\{\mathbf{R}_x^{(C)}\}$ comes down to solving the NP-hard puzzle as follows:

$$\widetilde{vec\{\mathbf{R}_x^{(C)}\}} = \text{argmin} \left\| vec\{\mathbf{R}_x^{(C)}\} \right\|_0 s.t. \mathbf{r}_z = \Psi vec\{\mathbf{R}_x^{(C)}\} \tag{79.11}$$

79.3.4.1 Traditional Perfect Reconstruction

Traditionally, we solve the problem (79.12) by a linear programming method:

$$\min_{vec\{\mathbf{R}_x^{(C)}\}} \left\| \mathbf{r}_z - \Psi vec\{\mathbf{R}_x^{(C)}\} \right\|_2^{1/2} + i \left\| vec\{\mathbf{R}_x^{(C)}\} \right\|_1 \tag{79.12}$$

which is called $l1$-norm least square programming problem and is proved to be convex that exists an unique optimum solution. $i > 0$ is a weighing scalar that balances between the sparsity of the solution induced by the $l1$-norm term and the data reconstruction error reflected by the $l2$-norm LS term.

Under the theory, considering the Gaussian random matrix is uncorrelated with almost all matrixes [6], we choose the Gaussian random matrix of size $M \times N$ as the sub-sample(measurement) matrix. So, the original signal of length N can be recovered from M samples when the number of compressive sample satisfies $M \geq cK \log(N/K)$ [6], where c is a small constant and K indicates the sparsity. As

for the reconstruction method, we prefer OMP algorithm for its well performance on incomplete reconstruction and the accomplishment is simple and fast.

79.3.4.2 Novel Partial-Scale Reconstruction

From the analyses in Sect. 79.3.1, we can see that the CAF of OFDM signal is quite sparse. Thus OMP algorithm can perfectly recover the original signal if only the model satisfies the compress sensing theory. Under the detecting method in Sect. 79.3.5, if only the top 5 points are recovered, the information they contain will be sufficient to do the following signal detection, which we called partial-scale reconstruction. More work on the feasibility and performance will be shown in Sect. 79.4.

79.3.5 Signal Recognition and Detection

At the receiver, before parameter identification, we would firstly verify that whether the received signal is OFDM. If it is, then we would do the following detections for further spectrum analyses.

1. OFDM FFT size estimation: Detect whether there is peak at on CF zero and time delay $\tilde{N}_{FFT}$. If there is, we can judge that $N_{FFT} = \tilde{N}_{FFT} - 1$.
2. CP length N_{cp} estimation: By searching the frequency domain with the estimated $\tilde{N}_{FFT}$, N_{cp} can be estimated by the following formula:

$$(p-1)/N = 1/(N_{FFT} + N_{cp}) \Rightarrow N_{cp} = N/(p-1) - N_{FFT} \tag{79.13}$$

where p is the position of the second peak and here $N = 2 \times (N_{fft} + N_{cp})$.

79.4 Simulation and Analysis

In our simulation, a OFDM symbol consists of 32 sub-carriers with QPSK modulated, the whole signal bandwidth is 480 kHz, and the useful symbol period is set as 0.8us with 0.2us CP length. At the sampler, we deal with two symbols as a unit according to (79.11) andin the tests we choose the probability of correct detection as our evaluation criterion.

When analyzing the performance of the algorithm, we find that there are three main factors that may affect the detection: the signal to noise ratio (SNR), sampling rate *M*/*N* and the number of OFDM symbols L. We did simulations to see how they affect the performance separately. Then we try to find a minimum sampling rate

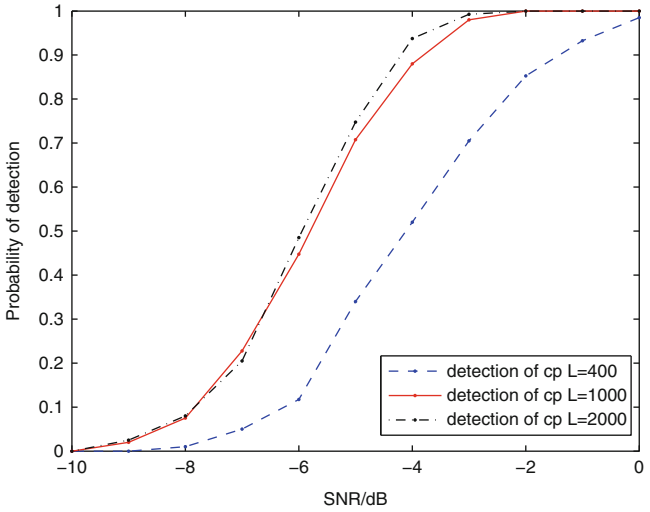

Fig. 79.2 The correct probability of detection with different L

that sufficient to the detection accuracy to get a balance between the algorithm complexity and performance.

At first, we set the sampling rate as 0.3 and $L = 1000$ when it is noiseless. We can see from the result that the correct detection probability of both FFT size N and CP improve as the increase of the SNR. And when the SNR is better than -3dB, the accuracy reaches to 95 %, which is a pretty high.

In the case when monitoring the observation time of the signal, we set the sampling rate as 0.3 similarly. Setting CP detection as an example, from Fig. 79.2 we can see that the probability gets higher as the number of symbols(L) increases, which is because the more symbols we observe the closer the AF reach to its ideal statistical average. At the same time, we can see that when L is up to 1000, the AF accuracy is sufficient and can't be better with larger L.

In our tests, N is fixed. From simulations we can see that the probability of detection gets higher as M increases, which is understandable that larger M means more signal information containing in the samples Practically, to minimize the processing complexity, it is significant to find the minimum M. As the simulation result showing in Fig. 4, when M = 24, the probability can reach 80 % under the SNR of -3dB and up to 95 % under the SNR of 0dB. However, when M is smaller, the performance deteriorates significantly. So we conjecture that under the condition we simulated the minimize value of M is 24 and the corresponding sampling rate is 0. 3 (Fig. 79.3).

At last we do comparison on the detection performance between the proposed partial-scale method with the least reconstruction iteration and the perfect reconstruction of CAF. From the result in this case we confirmed that the two methods show almost the same performance. When the SNR is larger than 3dB, both the two methods can get a high detection accuracy of 95 %. Thus, by reducing the iterations, we can achieve detection faster without degrading the performance.

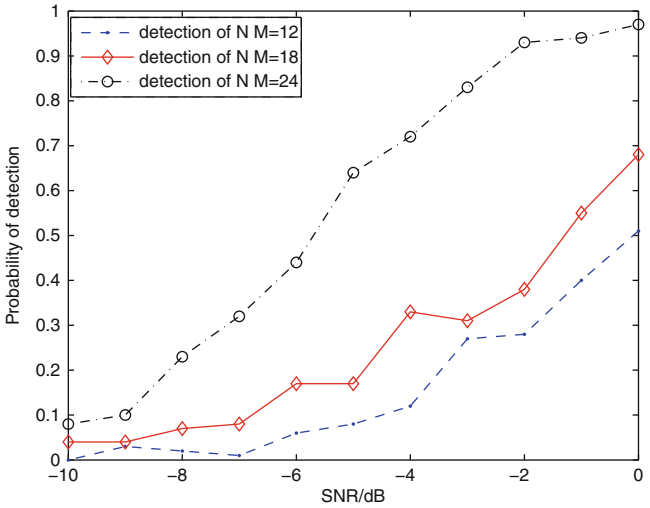

Fig. 79.3 The correct probability of detection with few M

Conclusion

This paper has proposed an optimized method in recognizing OFDM signals with sub-Nyquist samples. We fomulated the CS projection relation based on the property of OFDM CAF. And also we successfully solve the trouble of insufficient memory in practice by presenting an equivalent AF statistic approach. In addition, we explained and verified the feasibility of the partial-scale method with minimized iterations by simulation tests and also discussed the algorithm performance.

Acknowledgements This work was supported by the National Science and Technology Major Project of China under grant 2013ZX03001003-003, and the BUPT Research Innovation Project under grant 2013RC0104.

References

1. Candes EJ (2006) Compressive sampling [A]. In: Proceedings of the international congress of mathematicians [C], vol. 3. Madrid, Spain, pp. 1433–1452
2. Bolcskei H (2001) Blind estimation of symbol timing and carrier frequency offset in wireless OFDM systems [J]. IEEE Trans Commun 49(6):988–999P
3. Tian Z (2011) Cyclic feature based wideband spectrum sensing using compressive sampling. In: Proc. IEEE ICC

4. Khalaf Z, Nafkha A, Palicot J (2012) Blind spectrum detector for cognitive radio using compressed sensing and symmetry property of the second order cyclic autocorrelation. In: 7th international ICST conference on IEEE
5. Rebeiz E, Jain V, Cabric D (2012) Cyclostationary-based low complexity wideband spectrum sensing using compressive sampling. In: Proc. IEEE ICC, pp. 1619–1623
6. Baraniuk RG (2007) Compressive sensing [lecture notes]. IEEE Signal Process Mag 24.4:118–121

Chapter 80
Ka-band Rectangular Waveguide to HMSIW Transition Based on Trapezoidal-shaped Probe

Jun Dong, Yu Liu, Yihong Zhou, Ziqiang Yang, and Tao Yang

Abstract In this letter, a novel rectangular waveguide-to-half mode substrate integrated waveguide (HMSIW) transition is presented. The transition is realized by using a trapezoidal-shaped probe to terminate the TE_{10} mode of the standard waveguide within a wide frequency band. A back-to-back transition at Ka-band is designed and fabricated. The simulated results show that the proposed structure has less than 0.35 dB insertion loss and a better than 20 dB return loss within a frequency range from 25 to 40 GHz for a back-to-back structure. In addition, there is no need of intermediate transition for this design. The size of the proposed transition is reduced by approximately 81.8 % as compared with the Waveguide-to-HMSIW transition using antipodal fin-line. The proposed transition has the advantages of compact size and sample structure, and it is suitable for the application of HMSIW technology.

Keywords Rectangular waveguide • HMSIW • Trapezoidal-shaped probe

80.1 Introduction

Recently, substrate integrated waveguide (SIW) is a promising candidate for microwave and millimeter-wave applications for its excellent features such as low loss and easy integration with planar circuit [1]. Half mode substrate integrated waveguide (HMSIW) is a type of miniaturized SIW, which keeps the advantages of SIW but the size is nearly half reduced [2, 3]. Based on HMSIW technology, various kinds of microwave and millimeter-wave devices are designed [4–7]. However, rectangular waveguides are still widely used in microwave/millimeter-wave systems because of their high performance in terms of quality factor and power-handling capacity. Therefore, the development of a broadband and low loss transition between the rectangular waveguide and other planar transmission lines is required.

J. Dong (✉) • Y. Liu • Y. Zhou • Z. Yang • T. Yang
University of Electronic Science and Technology of China, Chengdu, Sichuan 611731, P. R. China
e-mail: jundong.ee@gmail.com

J. Mu et al. (eds.), *The Proceedings of the Third International Conference on Communications, Signal Processing, and Systems*, Lecture Notes in Electrical Engineering 322, DOI 10.1007/978-3-319-08991-1_80

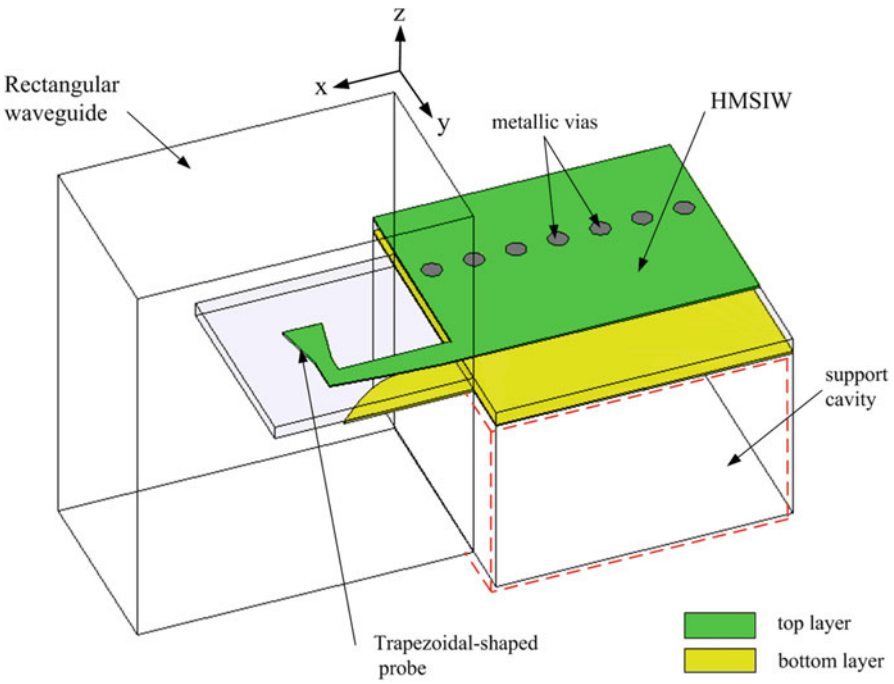

Fig. 80.1 Structure of Waveguide-to-HMSIW transition based on trapezoidal-shaped probe

Various transitions between rectangular waveguide and SIW have been investigated by some researchers [8–12]. In this work, a novel Waveguide-to-HMSIW transition is introduced for the application of half-mode substrate integrated waveguide technology.

A broad rectangular waveguide to HMSIW transition using an antipodal fin-line is realized for the first time [13]. Although the bandwidth of such transition is wide enough for uses, the circuit size is large owing to the length of the short-circuited tapered fin-line. Besides, an intermediate transition between HMSIW and antipodal fin-line is needed for this transition, which results in circuit size increasing and design complexity.

This work presents a new type of waveguide-to-HMSIW transition based on trapezoidal-shaped probe, as shown in Fig. 80.1. The trapezoidal-shaped probe is placed quarter-wavelength away from a waveguide short-back, which is also used as a support cavity for the HMSIW substrate. It transforms the TE_{10} mode of the rectangular waveguide to the quasi-$TE_{0.5,0}$ mode of the HMSIW. The circuit size of the proposed transition reduced largely since there is no need of an intermediate transition. Compared with the Waveguide-to-HMSIW transition using the antipodal fin-line [13], the proposed transition has a reduction of 81.8 % in circuit size. The probe size is half of the one in [14], which is a waveguide-to-microstrip transition. An extra square notch is needed for impendence matching [14], which make the transition more sensitive to fabrication errors. In addition to the features of compact size, the novel proposed transition is shown to operate well over Ka-band. In order to verify the proposed design, a back-to-back transition has been designed.

80.2 Proposed Transition and Design

The structure of the proposed transition is shown in Fig. 80.1. It can be seen that the transition structure consists of three parts, which are the rectangular waveguide, the trapezoidal-shaped probe and the HMSIW. The waveguide is a standard WR-28 rectangular waveguide. The planar circuit for the proposed transition consists of the trapezoidal-shaped probe and the HMSIW. The HMSIW is fabricated by implementing a row of metallic vias on a substrate with metal coating on both sides [2, 3]. The support cavity made by a solid block of metal that supports the ground plane side of the HMSIW. The trapezoidal-shaped probe extended from the top layer of HMSIW and inserted into the centre of a waveguide, which is approximately quarter-wavelength away from a waveguide short-back. A tapered ground plane extended from the bottom of HMSIW is made to achieve a good field matching.

The planar circuit for waveguide to HMSIW transition is shown in Fig. 80.2, the top view for both the top layer and bottom layer is given. Due to the large ratio of HMSIW width to height and the discrete arrangement of the metallic vias, only the quasi-$TE_{p\text{-}0.5,0}$ ($p = 1, 2, \ldots$) modes can propagate in the HMSIW and the dominant mode is the $TE_{0.5,0}$ mode [3]. The trapezoidal-shaped probe is employed to

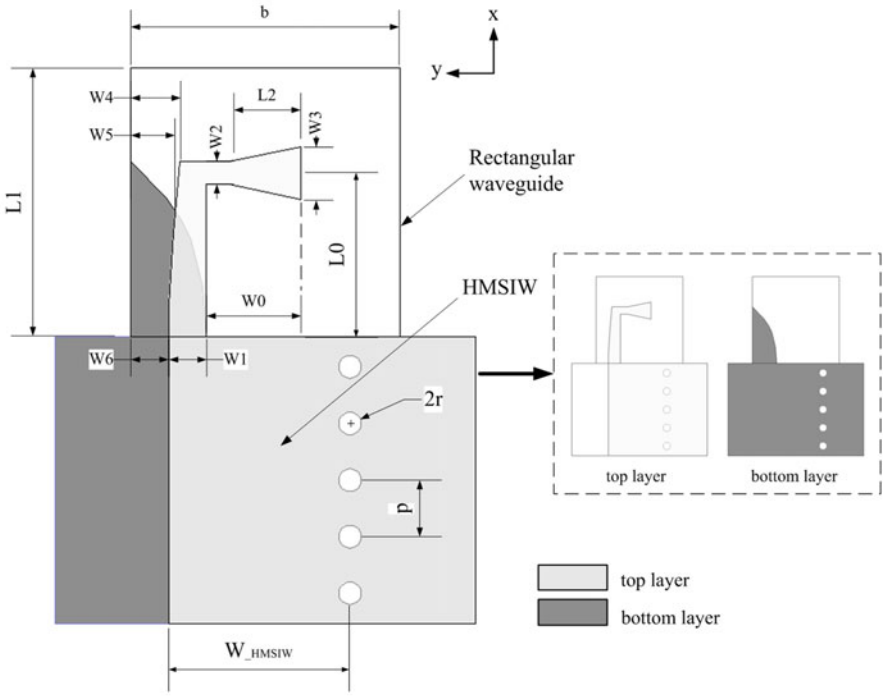

Fig. 80.2 View of planar circuit for waveguide to HMSIW transition

terminate the TE_{10} mode of the waveguide, which results in transforming the y-polarized E-field of the TE_{10} mode of the waveguide to the z-polarized E-field of $TE_{0.5,0}$ mode of the HMSIW. An extended ground plane is made to alleviate the effects of the discontinuity between the HMSIW and the probe. This extended ground plane ends at the center of the probe. An arc curvature is employed in the design of extended section.

As shown in Fig. 80.1, the trapezoidal-shaped probe is put at the center of the E-plane of a standard waveguide together with a support cavity a quarter-wavelength away from it. The support cavity can not only function as the mechanical support for the substrate of the HMSIW but also serve as a short-plane for reference. By properly choosing the dimension of the probe, the TE_{10} mode in the waveguide can be terminated efficiently within a wide frequency range. The proposed transition is simulated and optimized using Ansoft high-frequency structure simulator (Ansoft HFSS). The rectangular waveguide is a standard WR-28 with dimensions of 7.112×3.556 mm. The HMSIW and trapezoidal-shaped probe are integrated into an RT/Duroid 5880 substrate with relative dielectric constant of 2.22, loss tangent of 0.009 and thickness of 0.254 mm. After optimisation with Ansoft HFSS, the design parameters for the transition circuit are obtained. The key parameters of transition circuit are $r = 0.2$ mm, $p = 0.8$ mm, $W0 = 1.25$ mm, $L0 = 2.17$ mm, $W1 = 0.5$ mm, $W4 = 0.65$ mm, $W5 = 0.6$ mm, $L1 = 4$ mm, the narrow wall of rectangular waveguide is $b = 3.556$ mm, the broad wall of the HMSIW $W\_{HMSIW} = 2.5$ mm, Probe size in the x-axis is shown as $L0 = 2.17$ mm or around a quarter-wavelength away from the cavity short-back. The dimensions of the trapezoidal-shaped probe are $W2 = 0.3$ mm, $W3 = 0.7$ mm and $L2 = 0.95$ mm. The whole length of the rectangular waveguide to the HMSIW transition is $L1 = 4$ mm. Compared with the transition in [13], the transition length is reduced from 22 to 4 mm, corresponding to an 81.8 % reduction. It demonstrated that the size of transition circuit is reduced largely.

80.3 Simulation Results and Discussion

To verify this design, a back-to-back transition circuit is designed for the need of experiment. As shown in Fig. 80.3, the planar circuit of the back-to-back transition was fabricated. The simulated results of the back-to-back transition are shown in Fig. 80.4. It shows a better than 20 dB return loss from 25 to 40 GHz. The simulated insertion loss of the back-to-back transition, including the loss of a 17.5 mm HMSIW transmission line, is less than 0.35 dB within the frequency range 25–40 GHz.

Table 80.1 summarizes the performances of the proposed waveguide-to-HMSIW transition along with previously published transitions for comparison. The simulated results of this work are shown in Table 80.1 while the previous works are obtained by measurement. However, based on the Ansoft HFSS simulation, a feasible result can be expected.

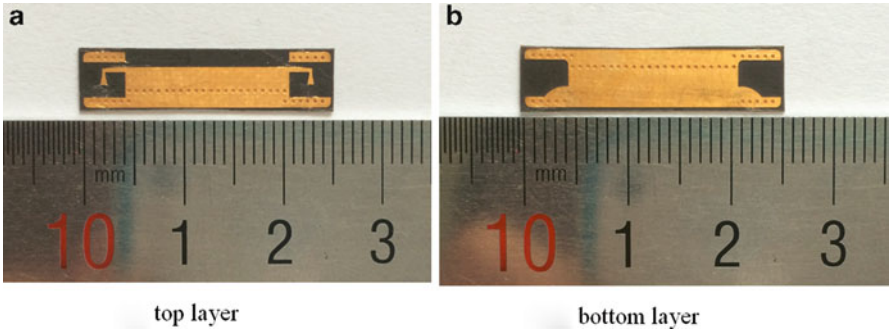

Fig. 80.3 Layout of the fabricated back-to-back transition. (**a**) Top layer. (**b**) Bottom layer

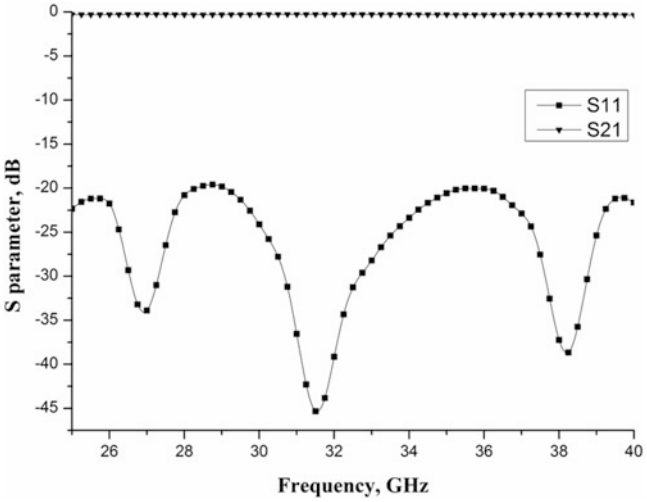

Fig. 80.4 The simulated results of the back-to-back transition

Table 80.1 Comparison of waveguide to SIW/HMSIW transitions

	Frequency	Transition	BW (GHz)	RL (dB)	IL (dB)	Fabrication	Transition lengths (mm)
[8]	Ka	Waveguide-to-SIW	28.3–39.5	>14	<2.5	Complex	8.15
[9]	Ka	Waveguide-to-SIW	26.5–40	>12	<1.6	Easy	21.00
[10]	Ka	Waveguide-to-SIW	25–40	>15	<1.4	Easy	16.20
[13]	Ka	Waveguide-to-HMSIW	26.5–40	>15	<1.3	Easy	22
This work	Ka	Waveguide-to-HMSIW	25–40	>20 (simu)	<0.35 (simu)	Easy	4

There are some differences in the design of waveguide-to-SIW and waveguide-to-HMSIW transition due to the different transmission mode in the SIW and HMSIW. The dominant transmission mode in the SIW is TE_{10} mode, while the HMSIW is quasi-$TE_{0.5,0}$ mode [3]. The transition both in [9] and [13] are realized by using antipodal fin-line, the difference is that an intermediate transition is needed in the design of waveguide-to-HMSIW transition. Compared with the transition using the antipodal fin-line in [13], the transition length of this work has been reduced by 81.8 %, which means more than 81.8 % reduction in circuit size. Due to this advantage of compact size, it can be widely adopted in the application of HMSIW technology.

Conclusion

In this work, a novel compact Waveguide-to-HMSIW transition based on the trapezoidal-shaped probe is proposed. This improved probe can provide a high performance and compact size for Waveguide-to-HMSIW transition. There is no need of intermediate transition for this design. A back-to-back transition circuit is designed and fabricated at Ka band. With the features of compact size and sample structure, such a broad transition is suitable for various millimeter-wave applications.

Acknowledgments This work was supported by the Fundamental Research Funds for the Central Universities of China (Grant No. ZYGX2012J030 and ZYGX2013J059).

References

1. Bozzi M, Georgiadis A, Wu K (2011) Review of substrate-integrated waveguide circuits and antennas. IET Microw Antennas Propag 5(8):909–920
2. Hong W, Liu B, Wang YQ, Lai QH, Wu K (2006) Half mode substrate integrated waveguide: a new guided wave structure for microwave and millimeter wave application. In: Proceedings joint 31st international infrared millimeter wave conference/14th international Terahertz electron conference, Shanghai, September 2006, pp 18–22
3. Lai QH, Fumeaux C, Hong W, Vahldieck R (2009) Characterization of the propagation properties of the half-mode substrate integrated waveguide. IEEE Trans Microw Theory Tech 57(8):1996–2004
4. Suntives A, Hum SV (2012) A fixed-frequency beam-steerable half-mode substrate integrated waveguide leaky-wave antenna. IEEE Trans Antennas Propag 60(5):2540–2544
5. Senior DE, Cheng XY, Yoon Y-K (2012) Electrically tunable evanescent mode half-mode substrate-integrated-waveguide resonators. IEEE Microw Wireless Compon Lett 22 (3):123–125
6. Ho M-H, Li C-S (2013) Novel balanced bandpass filters using substrate integrated half-mode waveguide. IEEE Microw Wireless Compon Lett 23(2):78–80
7. Ali AAM, El-Shaarawy HB, Aubert H (2011) Compact wideband double-layer half-mode substrate integrated waveguide 90° coupler. Electron Lett 47(10):598–599
8. Xia L, Xu R, Yan B, Li J, Guo Y, Wang J (2006) Broadband transition between air-filled waveguide and substrate integrated waveguide. Electron Lett 42(24):1403–1405

9. Zhong CL, Xu J, Zhi ZY (2009) Broadband substrate integrated waveguide to rectangular waveguide transition with fin-line. Electron Lett 45(4):205–207
10. Li J, Wen G, Xiao F (2010) Broadband transition between rectangular waveguide and substrate integrated waveguide. Electron Lett 46(3):223–224
11. Jin H, Chen W, Wen G (2012) Broadband transition between waveguide and substrate integrated waveguide based on quasi-Yagi antenna. Electron Lett 48(7):355–356
12. Głogowski R, Zürcher J-F, Peixeiro C, Mosig JR (2013) Broadband Ka-band rectangular waveguide to substrate integrated waveguide transition. Electron Lett 49(9):602–604
13. Zhong CL, Xu J, Zhi ZY, Jin CX (2009) Broadband transition between half mode substrate integrated waveguide and rectangular waveguide. Electron Lett 45(3):168–170
14. Lou Y, Chan C-H, Xue Q (2008) An in-line waveguide-to-microstrip transition using radial-shaped probe. IEEE Microw Wireless Compon Lett 18(5):311–313

Chapter 81
The First Robust Mongolian Text Reading Dataset CSIMU-MTR

Yunxue Shao, Guanglai Gao, Linbo Zhang, and Zhong Zhang

Abstract Text extraction from various text containers like document, born digital images, real scenes and videos has been a continuous interest in this field for more than a decade. Although a lot of work has been done on printed Mongolian document image analysis, there has little work on Mongolian text extraction from complex images. For the design and evaluation of Mongolian text extraction algorithms and systems, the availability of large-scale dataset is important. This paper first introduces a dataset named CSIMU-MTR which is built by the College of Computer Science of Inner Mongolia University. And then presents benchmark results using two state-of-the-art methods in text detection on this new dataset. The reported results serve as a baseline for evaluating the further works.

Keywords Mongolian text extraction dataset • Scene text detection • Maximally stable extremal regions

81.1 Introduction

Past research has shown that a considerable amount of text on Web pages is presented in image form (17 %), while an important fraction of this text (76 %) is not to be found anywhere else in the Web page [1]. The use of images as text carriers stems from a number of reasons, for example in order to make the Web pages more beautiful (e.g. titles, headings etc.), to attract attention (e.g. advertisements), to hide information (e.g. images in spam emails used to

Y. Shao (✉) • G. Gao
College of Computer Science, Inner Mongolia University, Inner Mongolia, PR China
e-mail: csshyx@imu.edu.cn; csggl@imu.edu.cn

L. Zhang
China Academy of Transportation Sciences (CATS), Beijing, China
e-mail: zhanglinbo@163.com

Z. Zhang
College of Electronic and Communication Engineering, Tianjin Normal University, Tianjin, China
e-mail: zhong.zhang8848@gmail.com

J. Mu et al. (eds.), *The Proceedings of the Third International Conference on Communications, Signal Processing, and Systems*, Lecture Notes in Electrical Engineering 322, DOI 10.1007/978-3-319-08991-1_81

avoid text-based filtering). Automatically extracting text from images would provide the enabling technology for a number of applications such as improved indexing and retrieval of Web content, enhanced content accessibility, content filtering etc. At the same time, efficient and fast comprehension of text in our environment is an important aspect of scene understanding for a variety of application areas, e.g. for automatic and assisted navigation of robots and humans respectively [2, 3].

In Asia, classical Mongolian is used by more than five millions of people. Mongolian text can be seen everywhere on the street in Inner Mongolia. Although there has been a lot of work on Latin text, Arabic text or Chinese text extraction from complex images [4–8] and born-digital images [9–12], and a lot of work on printed Mongolian document image analysis [13–16]. There has little work on Mongolian text extraction from complex images or born-digital images. For the design and evaluation of Mongolian text extraction algorithms and systems, the availability of large-scale dataset is important. This paper introduces a dataset named CSIMU-MTR built by the College of Computer Science of Inner Mongolia University. This dataset contains more than 500 complex real-scene images captured by high-resolution camera and born-digital images downloaded from Web pages. The dataset is publicly available for academic research.

The rest of the paper is organized as follows. Section 81.2 describes the CSIMU-MTR dataset. Section 81.3 presents the experimental results of two text detection methods. Finally, the last section gives conclusions.

81.2 Dataset

The dataset was built up similarly to ICDAR2011 robust reading datasets. Overall, we collected a set of 560 images which includes real-scene images and born-digital images. The dataset was split into a training set of 400 images and a test set of 160 images randomly. Real-scene images were captured with digital camera using auto focus and natural lighting. This kind of images containing text in a variety of colors and fonts on many different backgrounds and in various orientations, which pose considerable challenges to text detection, such as blurred or out of focus frames, low-contrast, over-exposure, uneven lighting, complex backgrounds, and lens distortion. Born-digital were collected by downloading from search engines. Born-digital images are usually low-resolution (for fast transmitting or displaying), non-uniform color and often suffer from compression artefacts and severe anti-aliasing.

Reading text in images consisted of two steps. The first step is to identify text regions and mark their location with axis-aligned rectangular bounding boxes. The second step is to recognize cropped word images of scene text. Accordingly, the ground truth is prepared in two phases. In the first phase, we prepared text location ground truth. The bounding boxes are tight so they touch most of the boundary pixels of a word. In the second phase, we will prepare word recognition ground truth.

Fig. 81.1 An example image in the dataset and its corresponding ground truth file

At the current stage, the first phase is finished and the dataset is open for the study of text localization. Each image in the dataset corresponds to a ground truth TXT file which contains the set of bounding rectangles. Each bounding rectangle is determined by the top-left point and the bottom-right point. Each line in the TXT file corresponds to: x-axis value and y-axis value of the top-left point, x-axis value and y-axis value of the bottom-right point. An example image and its corresponding ground truth file is shown in Fig. 81.1.

81.3 Benchmark Results

A text localization system generally consists of two major components: candidate text region extraction and text region filtering. In candidate text region extraction step, according to the features utilized, text localization methods can be categorized into region-based and texture-based. The problem with traditional texture-based methods is their computational complexity in the texture classification stage, which accounts for most of the processing time. In particular, texture-based filtering methods require an exhaustive scan of the input image to detect and localize text regions. This makes the convolution operation computationally expensive. Region-based methods use the properties of the color or gray scale in a text region or their differences with the corresponding properties of the background. These methods can be further divided into two sub-approaches: connected component (CC)-based and edge-based. These two approaches work in a bottom-up fashion: by identifying sub-structures, such as CCs or edges, and then merging these sub-structures to mark bounding boxes for text. Due to their relatively simple implementation and effectiveness, region-based methods are widely used. In this paper, we present benchmark results using two region-based methods on this new dataset. One is based on

the Canny edges and the other one is based on the Maximally Stable Extremal Regions (MSER). In recent years, MSER is usually used for extracting character like regions and ICDAR2013 robust reading competition results [17] demonstrate that MSER based methods perform better.

The flowchart of edge based text detection method used in our experiments is shown in Fig. 81.2. In the pre-processing stage, the input image is first resized into different scales. And at each image scale, the resized image is smoothed by 5 × 5 gaussian mask and Canny edge image is computed on the pre-processed image. Before edge merging, the edge image is first smoothed into a gray image and then been binarized for eliminating small edges and connecting adjacent edges. In the edge merging step, some heuristic knowledge, such as closeness, alignment, and comparable height is used and the candidate text regions are generated in this step. For each candidate region, a SVM classifier with RBF kernel is used to determinate whether or not this region is a Mongolian text like region, this string level classifier is denoted as StringSVM in this paper. StringSVM was trained on a set of 2,000 Mongolian text regions and 5,000 non-Mongolian text regions obtained by manually selected from candidated text regions extracted by the edge merging step. Bag of visual words (BoVW) model is used for feature extraction on each region. Finally, some refinement processes, such as region reduction or expansion are done on the text like regions. Figure 81.3 illustrates an example of the results in each step.

In the BoVW model, the extracted feature is a vector of occurrence counts of a vocabulary of local image features. To achieve this, it usually includes three steps:

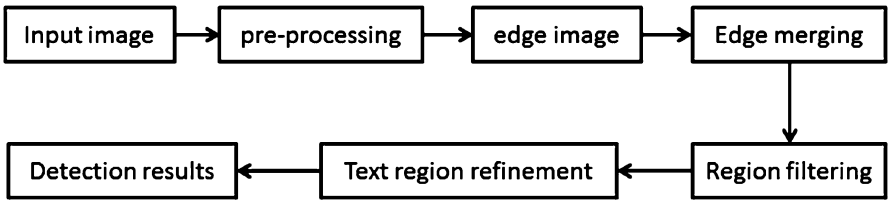

Fig. 81.2 The flowchart of edge based text detection method

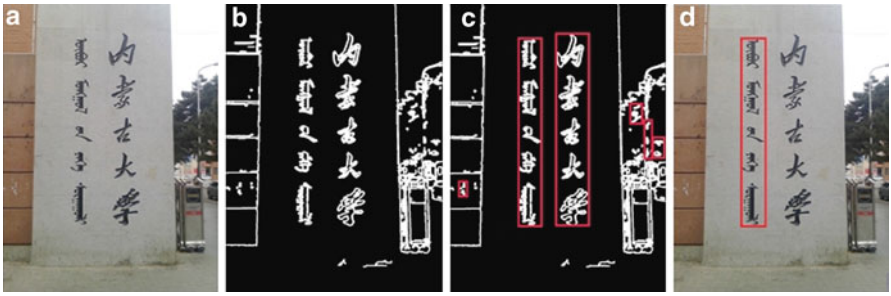

Fig. 81.3 An example of the results in each step of edge based method. (**a**) the input image (**b**) the smoothed Canny edge image (**c**) edge merging result (**d**) text detection result

feature detection, feature description and codebook generation. In this paper, dense sampling with different sliding window size is used in the feature detection step. In the feature description step, three HOG [18] feature vectors are extracted on each sampled image patch at three scales. Three codebooks are generated at each scale accordingly by K-means clustering method. Finally, each HOG feature is projected into its corresponding codebook. Join these histograms together results in the final feature vector. The feature extraction method is illustrated in Fig. 81.4.

The flowchart of MSER based text detection method used in our experiments is shown in Fig. 81.5. The pre-processing and the text region refinement methods used in this method are the same as used in edge based method. In the MSER detection stage, the Vlfeat open source library [19] was used to detect MSER regions. Then the MSER regions are merged into a candidate text regions using the same heuristic knowledge as used in edge based method. Finally, the candidate text regions are classified by StringSVM. An example of the results in each step is illustrated in Fig. 81.6.

For the evaluation of text localization results, the framework proposed by Wolf and Jolion [20] is used in our experiments. The key principle of the scheme is that evaluation is done at the object level over the whole collection, taking into account the quality of each match between detected and ground truth text boxes. Matches are first determined based on area overlapping. Then different weights for one-to-one, one-to-many and many-to-one matches are used when pooling together the results.

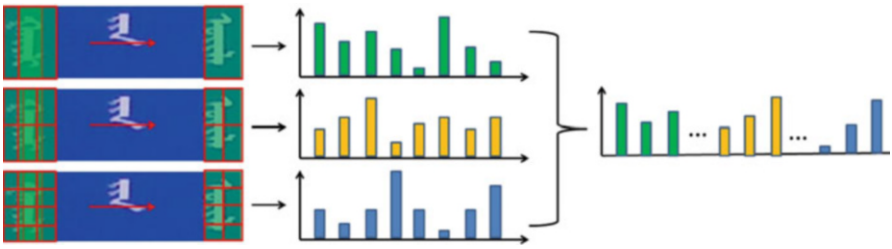

Fig. 81.4 Feature extraction method used in text region classification

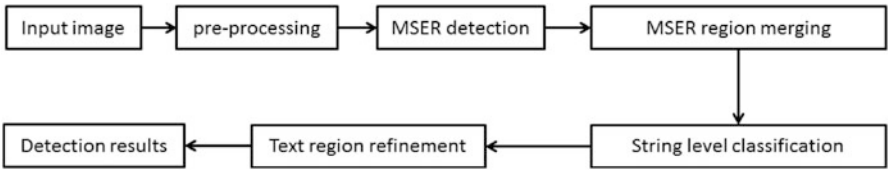

Fig. 81.5 The flowchart of MSER based text detection method

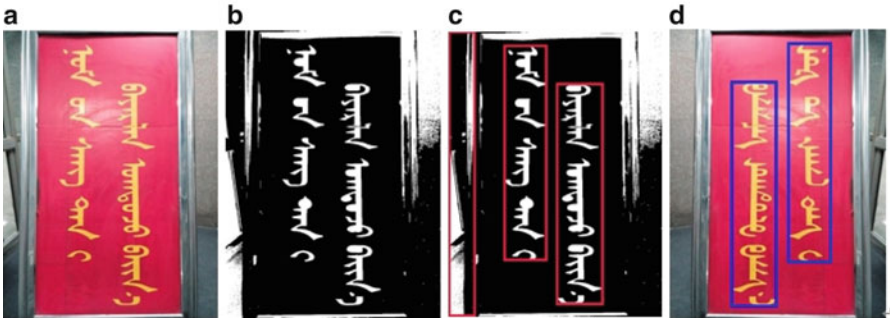

Fig. 81.6 An example of the results in each step of MSER based method. (**a**) the input image (**b**) MSER regions (**c**) region merging result (**d**) text detection result

Table 81.1 Text localization results

Method	Recall (%)	Precision (%)	F-score (%)
Edge based	61.13	72.36	66.27
MSER based	63.56	74.25	68.49

Results of this two method on this new dataset are shown in Table 81.1. MSER based method performs a little better than edge based method. Form these results we can see that this problem is still a challenge and it opens a large room for research and improvement.

An crucial problem of the proposed edge based method is that if text edges connect with background edges, the edge merging step would fail to give an accurate candidate text region. The problem of the proposed MSER based method is that if the gray value or color in the same text differs, the MSER detection step would fail to detect an accurate MSER region. Some examples of detection failures are depicted in Fig. 81.7. Most of them are caused by nonuniform color, lower resolution, uneven illumination, low-contrast or over-exposure which cannot generate complete MSERs or Canny edges for component merging. Some others are caused by non-regular text such as hand-written fonts and art fonts, since they are difficult to be correctly predicted by text classifier.

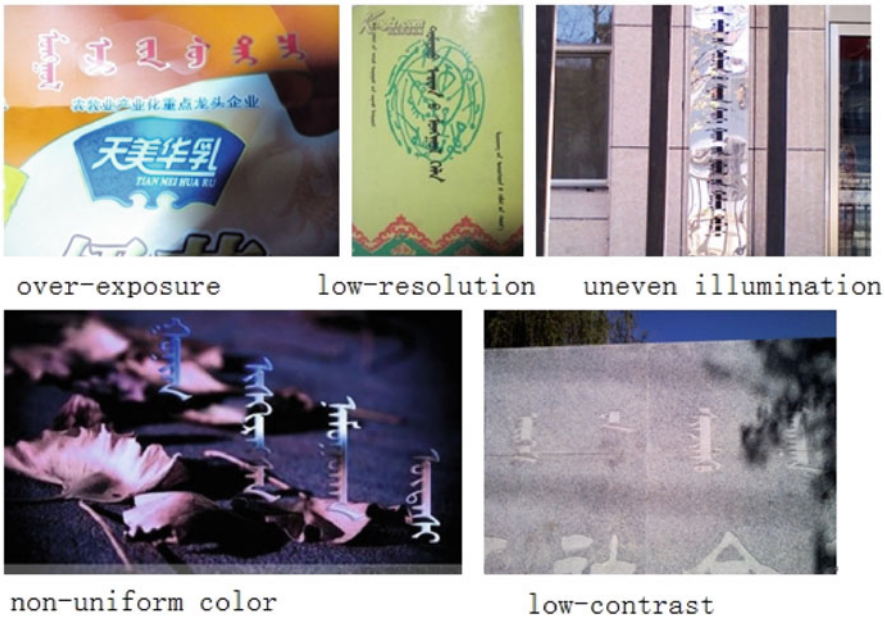

Fig. 81.7 Detection failures of MSER based or edge based method

Conclusion

In this paper, the first robust Mongolian text reading dataset named CSIMU-MTR which is built by the College of Computer Science of Inner Mongolia University is introduced. This dataset poses considerable challenges to text detection such as blurred image, low-contrast, over-exposure, uneven lighting, complex backgrounds, non-uniform color. Benchmark results are presented using two state-of-the-art methods in text detection on this new dataset. The reported results serve as a baseline for evaluating the further works.

Acknowledgements This work was supported by program of higher-level talents of Inner Mongolia University.

References

1. Antonacopoulos A, Karatzas D, Ortiz Lopez J (2001) Accessing textual information embedded in internet images. In: Proceedings of SPIE, Internet Imaging II, vol 4311, pp 198–205
2. Merino-Gracia C, Lenc K, Mirmehdi M (2012) A head-mounted device for recognizing text in natural scenes. In: CBDAR'11, LNCS, vol 7139, pp 29–41

3. Gao J, Yang J (2001) An adaptive algorithm for text detection from natural scenes. In: CVPR'01, vol 2, pp 84–89
4. Epshtein B, Ofek E, Wexler Y (2010) Detecting text in natural scenes with stroke width transform. In: 2010 I.E. conference on computer vision and pattern recognition, pp 2963–2970
5. Weinman JJ, Butler Z, Knoll D, Feild J (2014) Toward integrated scene text reading. IEEE Trans Pattern Anal Mach Intell 36(2):375–387
6. Yi C, Tian Y (2011) Text string detection from natural scenes by structure-based partition and grouping. IEEE Trans Image Process 20(9):2594–2605
7. Koo H, Kim D (2013) Scene text detection via connected component clustering and nontext filtering. IEEE Trans Image Process 22(6):2296–2305
8. Shahav A, Shafait F, Dengel A (2011) ICDAR 2011 robust reading competition challenge 1: reading text in scene images. In: 2011 international conference on document analysis and recognition, pp 1491–1496
9. Karatzas D, Mestre SR, Mas J, Nourbakhsh F, Roy PP (2011) ICDAR 2011 robust reading competition-challenge 1: reading text in born-digital images (web and email). In: 2011 international conference on document analysis and recognition (ICDAR), pp 1485–1490
10. Karatzas D, Antonacopoulos (2007) A colour text segmentation in web images based on human perception. Image Vision Comput 25(5):564–577
11. Lopresti D, Zhou J (2000) Locating and recognizing text in WWW images. Inf Retr 2:177–206
12. Perantonis SJ, Gatos B, Maragos V (2003) A novel web image processing algorithm for text area identification that helps commercial OCR engines to improve their web image recognition efficiency. In: Second international workshop on web document analysis (WDA2003), pp 61–64
13. Gao G, Li W, Hou H, Li Z (2003) Multi-agent based recognition system of printed Mongolian characters. In: Proceedings of the international conference on active media technology, pp 376–381
14. Gao G, Su X, Wei H, Gong Y (2011) Classical Mongolian words recognition in historical document. In: Proceedings of the 11th international conference on document analysis and recognition (ICDAR), pp 692–697
15. Wei H, Gao G (2014) A keyword retrieval system for historical Mongolian document images. Int J Doc Anal Recognit 17(2):33–45
16. Peng L, Liu C, Ding X et al (2010) Multi-font printed Mongolian document recognition system. Int J Doc Anal Recognit 13(2):93–106
17. Karatzas D et al (2013) ICDAR 2013 robust reading competition. In: 2013 international conference on document analysis and recognition, pp 1484–1493
18. Dalal N, Triggs B (2005) Histograms of oriented gradients for human detection. In: Proceedings of IEEE conference on computer vision and pattern recognition, pp 886–893
19. Vedaldi A, Fulkerson B (2008) An open and portable library of computer vision algorithms. http://www.vlfeat.org/
20. Wolf C, Jolion J.-M (2006) Object count/area graphs for the evaluation of object detection and segmentation algorithms. Int J Doc Anal Recognit 8(4):280–296

Chapter 82
Detection of High-Frequency Signals Based on Stochastic Resonance and Ensemble Average

Yao Sun, Chenglin Zhao, and Xiao Peng

Abstract The traditional signal detection methods mainly focus on suppressing noise to extract the weak signal. However, stochastic resonance (SR) can enhance the signal component by converting energy from the noise to the signal. Base on the theory of SR, a novel approach to detect weak signal with a short data record is proposed. Ensemble average and cross-correlation operation are applied in this method to improve detection performance. In order to settle the limitation of stochastic resonance to detect large parameters signal, scale transformation stochastic resonance (STSR) is presented. The result of simulation proves the effectiveness of this designed method.

Keywords Stochastic resonance • Signal detection • Short data record • Scale transformation • Ensemble average • Cross-correlation

82.1 Introduction

The concept of stochastic resonance was put forward by Benzi in the study of ancient glaciers weather [1]. The characteristic of SR is that it can transfer energy from the noise to the signal when nonlinear system gets matching relation with the signal and the noise, which is similar to the familiar "resonance phenomenon" in dynamics. The signal to noise ratio (SNR) of the output of SR system will greatly increase [2], which provides a new way to detect weak signal submerged in heavy noise.

However, restricted by adiabatic approximation and linear response theory, the original stochastic resonance can only deal with small parameters signals [3]. To solve this problem, Refs. [4, 5] proposed modulated stochastic resonance, shifting signals from the original signal frequency to the difference frequency of the input signal and the given signal, which needs a small frequency scanning step. References [6, 7] put

Y. Sun (✉) • C. Zhao • X. Peng
Key Lab of Universal Wireless Communications, MOE Wireless Network Lab, Beijing University of Posts and Telecommunications, Beijing, China
e-mail: sunyao9116@126.com

J. Mu et al. (eds.), *The Proceedings of the Third International Conference on Communications, Signal Processing, and Systems*, Lecture Notes in Electrical Engineering 322, DOI 10.1007/978-3-319-08991-1_82

forward secondary sample stochastic resonance, compressing high-frequency signals to the low-frequency band, which requires a large amount of data.

In this paper, we present a novel method of high-frequency weak signals detection with a short data record based on stochastic resonance. Scale transformation stochastic resonance is presented to settle the limitation of stochastic resonance to detect large parameters signals. Ensemble average and cross-correlation operation are applied in this method to improve detection performance. In Sect. 82.2, stochastic resonance was introduced. In Sect. 82.3, the theory of the weak signal detection was described in details. In Sect. 82.4, the result of simulation was given. Finally, section "Conclusion" closed the paper with brief summary.

82.2 Bistable Stochastic Resonance Model

Stochastic resonance consists of three basic elements: sinusoidal signals, noise and nonlinear system. The model of the system affected by sinusoidal periodic signals and Gaussian white noise can be described as the Langevin equation

$$\frac{dx}{dt} = ax - bx^3 + s(t) + n(t) \tag{82.1}$$

In Eq. (82.1), a, b are real parameters of the system, $s(t) = Asin(2\pi f_0 t)$, $n(t)$ is Gaussian white noise with intensity D.

The corresponding potential function of Eq. (82.1) can be written as follow

$$U(x) = \frac{1}{2}ax^2 - \frac{1}{4}bx^4 + [s(t) + n(t)] \times x \tag{82.2}$$

The potential function can be described in a double-well potential diagram shown in Fig. 82.1.

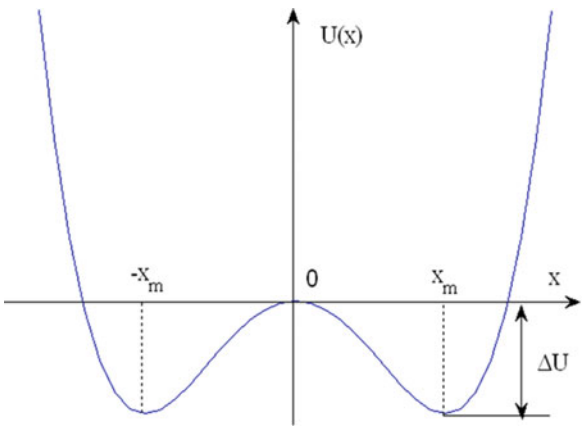

Fig. 82.1 Potential function chart

Potential function curve is composed by two potential trap points and a barrier point. When $A=0$, $D=0$, the potential trap points are $\pm x_m = \pm\sqrt{a/b}$, and the barrier height is $\Delta U = a^2/4b$. The system describes an overdamped Brownian motion. In the absence of the input, the state of the system is confined to one of the two potentials that determined by the initial condition. When $0 < A < A_c = \sqrt{4a^3/27b}$, particles can only have partial periodic motion in one side of the potential well with signal frequency. However, when $D \neq 0$, even if $A < A_c$, particles will switch between two potential wells. The period change driven by signals and the switching caused by noise are effectively synchronized, so that the small periodic component in the output signal will be enhanced, which is a concise explanation of why stochastic resonance can strengthen the weak signal.

According to the adiabatic approximation theory, the power spectrum of the output signal expressed as $S(f)$ consists of two parts [7]: $S_1(f)$ corresponds to the output generated by the periodic signal and $S_2(f)$ corresponds to the output generated by the noise. According to the Lorentz distribution of $S_2(f)$, the spectral energy of noise concentrates in the low frequency band. $S(f), S_1(f)$ and $S_2(f)$ can be expressed as Eqs. (82.3–82.5) (system parameters are set as: $a=1, b=1$).

$$S(f) = S_1(f) + S_2(f) \tag{82.3}$$

$$S_1(f) = \frac{2A^2\exp(-1/2D)/\left(\pi D^2\right)}{(2\exp(-1/2D)/\pi^2) + (2\pi f_0)^2} \times \delta(f_0 - f) \tag{82.4}$$

$$\begin{aligned} S_2(f) = &\left[1 - \frac{A^2\exp(-1/2D)/\left(\pi^2 D^2\right)}{(2\exp(-1/2D)/\pi^2) + (2\pi f_0)^2}\right] \\ &\times \left[\frac{4\sqrt{2}\exp(-1/4D)/\pi}{(2\exp(-1/2D)/\pi^2) + (2\pi f)^2}\right] \end{aligned} \tag{82.5}$$

82.3 The Proposed Detection Method

82.3.1 The Principle of STSR

According to the adiabatic approximation theory and the linear response theory, we can notice that the original stochastic resonance model can only be applied to detect low-frequency signals. In order to achieve high-frequency signal detection, scale transformation stochastic resonance method is proposed. The scale parameter R is mixed into the STSR model as follow

$$\frac{dx}{dt} = R \times \left[ax - bx^3 + s(t) + n(t)\right] \tag{82.6}$$

In the STSR model, the role of parameter R is compressing high-frequency signals to the low-frequency band to obtain stochastic resonance phenomenon. Then the

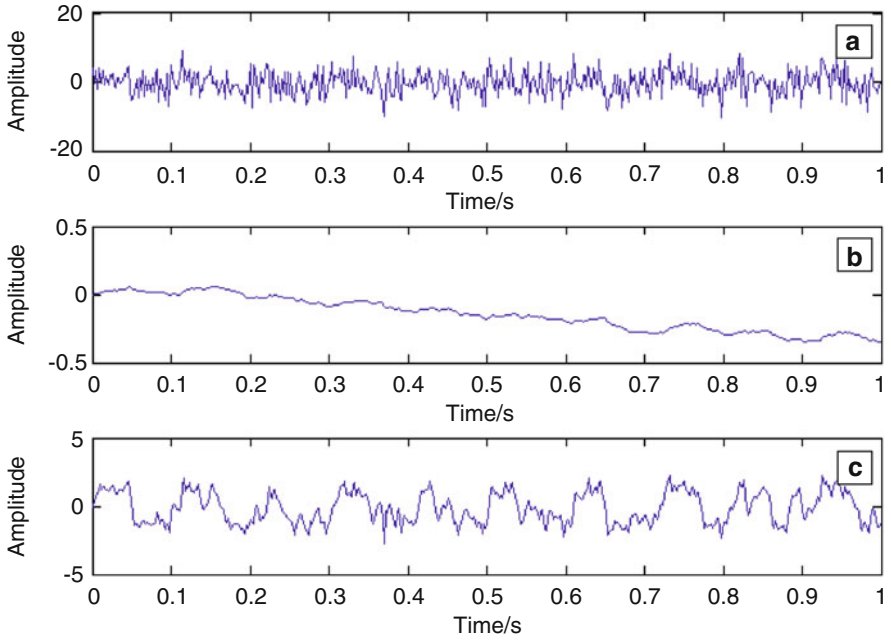

Fig. 82.2 Time domain waveforms of original SR system and STSR system. (**a**) The input signal. (**b**) The output signal of the original SR system. (**c**) The output signal of the STSR system

frequency of the signal will be recovered to achieve the detection of the high-frequency signal and the estimation of signal frequency. R is the scaling ratio, f_h stands for the original signal frequency, f_l stands for the low frequency after scaled down, $f_l = f_h/R < 1$.

The parameters in the simulation shown in Figs. 82.2 and 82.3 are set as: $A = 1$, $f_0 = 10$ Hz, $D = 10, a = 1, b = 1, R = 100$.

In Fig. 82.3b, before the signal scaled down, the weak signal under strong noise is difficult to detect since the SR phenomenon does not occur. However, as shown in Fig. 82.3c, after the signal scaled down, a very sharp spectrum peak at frequency $f_0 = 10$ Hz appears in the spectrum graph and signal detection is achieved successfully by STSR method.

82.3.2 Ensemble Average and Cross-Correlation

The concept of ensemble average comes from statistics. In recent years, scholars have applied this idea to many areas and achieved unexpected effect. The ensemble average method deals with multiple sets of data and calculates the average to eliminate deviation and suppress noise.

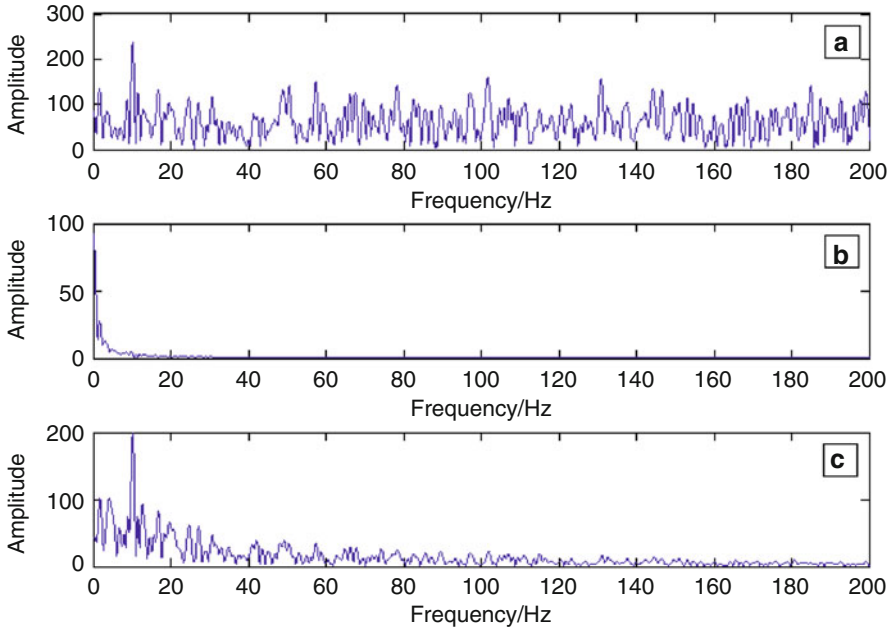

Fig. 82.3 Spectrums of original SR system and STSR system. (**a**) The spectrum of the input signal. (**b**) The spectrum of the output signal of the original SR system. (**c**) The spectrum of the output signal of the STSR system

It is well known that the performance of a signal detection method is closely related to the observation time and the number of the sampling points. In the SR system with added noise, due to the randomness of additional noise, we can get several different data samples by adding noise to one sample of experimental data. The proposed method combining with ensemble average can detect weak signal effectively even if the received data record is short.

The substance of correlation detection method is to calculate the correlation function of the input signal. According to the irrelevance between the periodic signal and the random noise, the method of correlation can be used in signal processing to achieve the elimination of part of noise. The algorithm employs cross-correlation operation to suppress noise further.

82.3.3 The Principle of Detection

Firstly, appropriate extra noise is added to the input signal to get several different data samples. Secondly, the STSR system processes the weak signal mixed with extra noise, which realizes the energy transformation from the noise to the signal. As noise is weakened and the signal is enhanced, the SNR of the output signal will

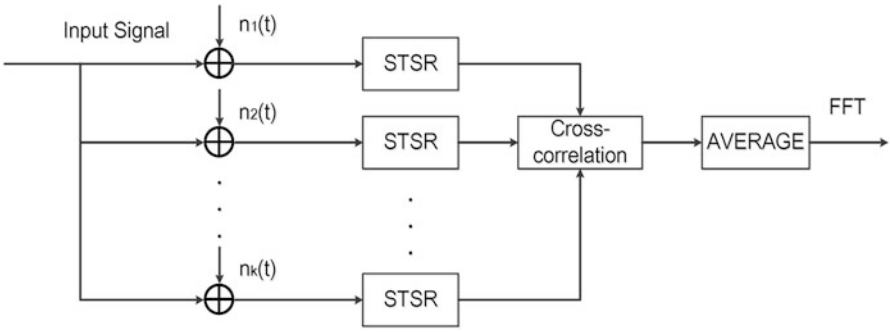

Fig. 82.4 The principle of the proposed signal detection

greatly increase. Finally, the cross-correlation function of these output data is calculated and averaged to suppress noise. The proposed signal detection system chart is shown in Fig. 82.4.

82.4 Simulation and Performance Analysis

In our simulation, parameters are set as: $f_0 = 100\,\text{Hz}, D = 9, a = 1, b = 1, R = 1,000$. The data length of the received signal is 2,000 points. In order to outstand the superiority of the algorithm, we set the amplitude of the periodic signal is $A = 1.34$ ($SNR = -10\,\text{dB}$) in the time domain analysis and $A = 0.425$ ($SNR = -20\,\text{dB}$) in the frequency domain analysis. The results of simulation experiment are shown in Figs. 82.5 and 82.6.

From the two figures above, it can be seen that Figs. 82.5a and 82.6a show the time–frequency diagram of the input signal, the weak signal submerged in heavy noise is difficult to detect. Figures 82.5b and 82.6b show the time–frequency diagram of the output signal of the STSR system, obviously, the periodic component of the time domain signal has been enhanced in Fig. 82.5b but the spectral line at frequency $f_0 = 100\,\text{Hz}$ is not distinct enough to be detected in Fig. 82.6b. Figures 82.5c and 82.6c show the time–frequency diagram of the output signal of the proposed method. In Fig. 82.5c, noise is markedly inhibited and the waveform is close to the original periodic signal. Compared with Fig. 82.6a, b, a very sharp spectrum peak at frequency $f_0 = 100\,\text{Hz}$ can be found in Fig. 82.6c, the weak signal can be detected easily.

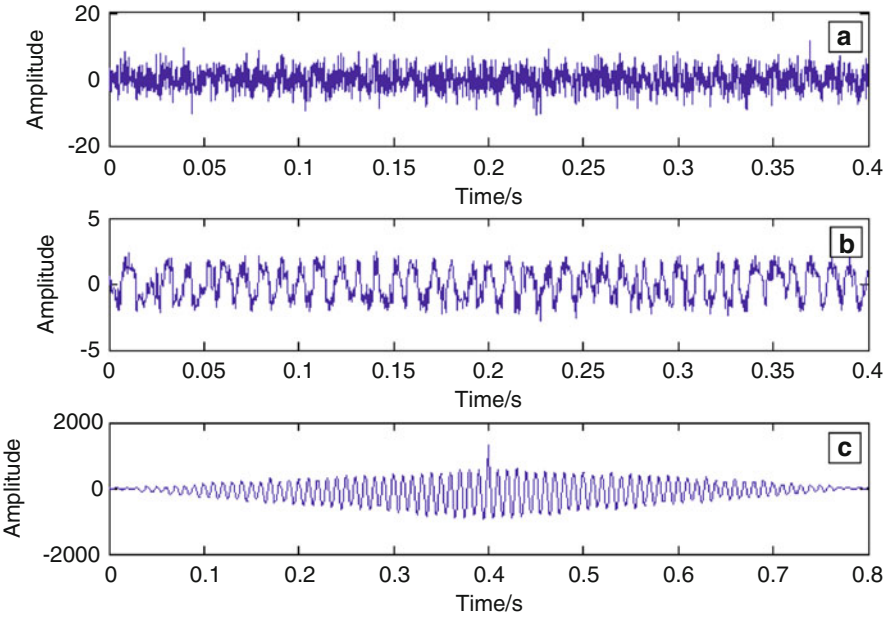

Fig. 82.5 Time domain waveforms of the STSR system and the proposed method. (**a**) The input signal. (**b**) The output signal of the STSR system. (**c**) The output signal of the proposed method

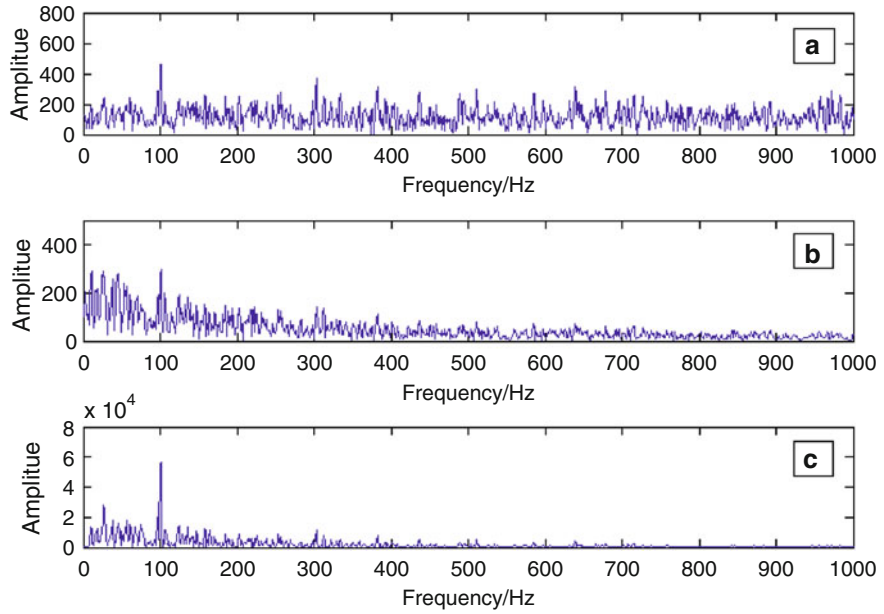

Fig. 82.6 Spectrums of the STSR system and the proposed method. (**a**) The spectrum of the input signal. (**b**) The spectrum of the output signal of the STSR system. (**c**) The spectrum of the output signal of the proposed method

Conclusion

The paper analyzes the principle of stochastic resonance. Based on the stochastic resonance method, we proposed a novel method to detect high-frequency weak signal submerged in heavy noise with a shot data record. The algorithm combines with ensemble average and cross-correlation operation to suppress noise. By compressing high-frequency signals to the low-frequency band to achieve stochastic resonance phenomenon, high-frequency weak signal will be detected. The numerical simulation result shows that the performance of the proposed method is better than the traditional stochastic resonance.

Acknowledgements This work was supported by the National Natural Science Foundation of China (61379016, 1271180), Major National Science and Technology Projects (2013zx03001015).

References

1. Benzi R, Sutera A, Vulpiani A (1981) The mechanism of stochastic resonance. J Phys A 14:453–457
2. De-Chun G, Gang H, Xiao-Dong W (1992) Experimental study of signal-to-noise ratio of stochastic resonance systems. Phys Rev A 46:3243–3249
3. Duan F, Chapeau-Blondeau F, Abbott D (2008) Stochastic resonance in a parallel array of nonlinear dynamical elements. Phys Lett A 372:2159
4. Shuo S, Wan-Yi Yin Y, Ming-Chuan Y (2012) A high-resolution weak signal detection method based on stochastic resonance and superhet technology. In: Seventh international ICST conference on communications and networking in China (CHINACOM), pp 329–333
5. Hai-Lin Z, Long-Quan Z, Chan-Juan L (2013) Detecting parameters of high frequency signals with frequency modulation stochastic resonance. In: Sixth international Congress on Image and Signal Processing (CISP), vol 2, pp 1090–1095
6. Yong-Gang L, Tai-Yong W (2003) Numerical research of twice sampling stochastic resonance for the detection of a weak signal submerged in a heavy noise. Acta Phys Sin 52(10):2432–2437
7. Yong-Gang L, Tai-Yong W (2004) Power spectrum research of twice sampling stochastic resonance response in a bistable system. Acta Phys Sin 53(3):717–723

Chapter 83
Square Root Unscented Kalman Filter Based on Strong Tracking

Meng Zhao, Xue-lian Yu, Ming-lei Cui, Xue-gang Wang, and Jing Wu

Abstract To solve the numerical instability in the recursive process of unscented Kalman filter (UKF), as well as the unsatisfactory performance in case of abrupt changes, a new adaptive target tracking method, called square root unscented Kalman filter based on strong tracking (STF–SRUKF), is presented. On the one hand, inspired by the idea of square-root filter, the square root of the covariance matrix is substituted for the covariance matrix itself in the recursive process, to guarantee numerical stability. On the other hand, based on the idea of strong tracking filter, a time-varied fading factor is introduced into the recursive process, which is helpful to adjust the gain matrix timely, and thus enabling STF–SRUKF more power to deal with sudden changes. Experimental results demonstrate that STF–SRUKF performs well and steadily, especially when target motion changes suddenly.

83.1 Introduction

The state estimation of nonlinear dynamic system exists widely in many practical applications. In theory, the optimal solution to this problem is to calculate the posterior probability distribution of state, which is usually difficult in most cases. Consequently, many sub-optimal filtering techniques were proposed.

The most classical method for nonlinear estimation is the extended Kalman filter (EKF) based on the linearization technique with Taylor's series expansion, but its performance is significantly limited because of low accuracy, bad stability and convergence [1, 2], especially for highly nonlinear systems. To overcome the shortcomings of EKF, proposed the strong tracking filter (STF). Its kernel is to introduce a fading factor to adjust the gain matrix adaptively according to the

M. Zhao • X.-l. Yu • M.-l. Cui • X.-g. Wang (✉) • J. Wu
University of Electronic Science and Technology of China (UESTC),
No. 2006, Xiyuan Avenue, West High-Tech Zone, Chengdu 611731, China
e-mail: zhaom524@163.com; xgwang@ee.uestc.edu.cn

J. Mu et al. (eds.), *The Proceedings of the Third International Conference on Communications, Signal Processing, and Systems*, Lecture Notes in Electrical Engineering 322, DOI 10.1007/978-3-319-08991-1_83

current measurement [2–4], which makes STF very effective for abrupt state change and target maneuver. However, it still needs linearization operation.

Afterwards, Julier and Uhlmann proposed the unscented Kalman filter (UKF). Instead of linearization, UKF adopts a minimal set of sampled points, to approximate the probability density distribution of the nonlinear function. UKF can obtain second-order accuracy [5, 6], but its accuracy still cannot completely satisfy the high requirements of some practical applications. Moreover, the covariance matrix is likely to lose positive definition during propagation, which may be hazardous and makes UKF out of work.

One effective and simple solution to the above problem is the square-root filter. That is, the square root of the covariance matrix instead of itself is propagated in the recursive process [7, 8]. Inspired by the idea, Wan et al. proposed the square root unscented Kalman filter (SRUKF). Compared with UKF, SRUKF has good numerical stability, without additional computational complexity as well. However, the performance may lower greatly in case of sudden state change or target maneuver.

The recently proposed particle filter (PF), along with its variant ones [9, 10], based on Monte-Carlo technique, is a kind of optimal regression Bayesian method. It improves the estimation accuracy of nonlinear dynamic system greatly, but has limited applications in practical systems due to tremendous computation.

For the purpose of improving the performance of maneuvering target tracking and guaranteeing the numerical stability, a new nonlinear filter, called square root unscented Kalman filter based on strong tracking (STF–SRUKF), is presented in this paper. The time-varying fading factor of STF is introduced into SRUKF, which can improve the estimation performance of SRUKF for the uncertainty of system models, abrupt state change, and target maneuver. At the same time, the inherent numerical stability of SRUKF is retained fully in STF–SRUKF. At first, SRUKF is reviewed briefly. Then, the derivation process of the proposed STF–SRUKF algorithm is detailed. Next, the effectiveness of the algorithm is verified with an example. Finally, conclusions are given.

83.2 Square Root Unscented Kalman Filter

The discrete nonlinear system can be expressed as:

$$\mathbf{x}_k = f(\mathbf{x}_{k-1}) + \mathbf{w}_{k-1} \tag{83.1}$$

$$\mathbf{z}_k = h(\mathbf{x}_k) + \mathbf{v}_k \tag{83.2}$$

where $\mathbf{x}_k \in \Re^{n_x}$ is the state vector, $\mathbf{z}_k \in \Re^{n_z}$ is the measurement, and $\mathbf{w}_{k-1} \sim N(0, \mathbf{Q}_{k-1})$ and $\mathbf{V}_{k-1} \sim N(0, \mathbf{R}_k)$ are both Gaussian white noise with zeros means and covariance $\mathbf{Q}_{k-1}$ and $\mathbf{R}_k$, respectively.

To avoid the problem that the covariance matrix may loses positive definition during the process of iteration and update in UKF, SRUKF uses the square root of covariance matrix directly in the recursive process.

The calculation procedure of SRUKF can be summarized as follows [7].

Initialize with:

$$\hat{\mathbf{x}}_0 = E(\mathbf{x}_0), \mathbf{S}_0 = chol\left\{E\left[(\mathbf{x}_0 - \hat{\mathbf{x}}_0)(\mathbf{x}_0 - \hat{\mathbf{x}}_0)^T\right]\right\} \tag{83.3}$$

For $k \in \{1, \cdots, \infty\}$,

Step 1: Sigma points calculation

$$\boldsymbol{\chi}_{k-1|k-1} = \left[\hat{\mathbf{x}}_{k-1|k-1} \quad \hat{\mathbf{x}}_{k-1|k-1} + \sqrt{n+\kappa}\mathbf{S}_{k-1|k-1} \quad \hat{\mathbf{x}}_{k-1|k-1} - \sqrt{n+\kappa}\mathbf{S}_{k-1|k-1}\right] \tag{83.4}$$

$$W_i = [\kappa/(n+\kappa) \quad 1/2(n+\kappa) \quad 1/2(n+\kappa)] \tag{83.5}$$

Step 2: Time update

$$\begin{cases} \boldsymbol{\chi}_{k|k-1,i} = f\left(k, \boldsymbol{\chi}_{k-1|k-1,i}\right) \\ \hat{\mathbf{x}}_{k|k-1} = \sum_{i=0}^{2n} W_i \boldsymbol{\chi}_{k|k-1,i} \end{cases} \tag{83.6}$$

$$\begin{cases} \mathbf{S}_{k|k-1} = qr\left\{\left[\sqrt{W_{1:2n}}\left(\boldsymbol{\chi}_{k|k-1,1:2n} - \hat{\mathbf{x}}_{k|k-1}\right) \quad \sqrt{\mathbf{Q}_k}\right]\right\} \\ \mathbf{S}_{k|k-1} = cholupdate\left(\mathbf{S}_{k|k-1}, \boldsymbol{\chi}_{k|k-1,0} - \hat{\mathbf{x}}_{k|k-1}, sign(W_0)\sqrt{W_0}\right) \end{cases} \tag{83.7}$$

$$\begin{cases} \boldsymbol{\zeta}_{k|k-1,i} = h\left(k, \boldsymbol{\chi}_{k|k-1,i}\right) \\ \hat{\mathbf{z}}_{k|k-1} = \sum_{i=0}^{2n} W_i \boldsymbol{\zeta}_{k|k-1,i} \end{cases} \tag{83.8}$$

Step 3: Measurement update

$$\begin{cases} \mathbf{S}_{zz,k|k-1} = qr\left\{\left[\sqrt{W_{1:2n}}\widetilde{\boldsymbol{\zeta}}_{1:2n} \quad \sqrt{\mathbf{R}_k}\right]\right\} \\ \mathbf{S}_{zz,k|k-1} = cholupdate\left(\mathbf{S}_{zz,k|k-1}, \widetilde{\boldsymbol{\zeta}}_0, \mathrm{sgn}(W_0)\sqrt{W_0}\right) \end{cases} \tag{83.9}$$

$$\mathbf{P}_{x_k z_k} = \sum_{i=0}^{2n} W_i \left(\boldsymbol{\chi}_{k|k-1,i} - \hat{\mathbf{x}}_{k|k-1} \right) \left(\boldsymbol{\zeta}_{k|k-1,i} - \hat{\mathbf{z}}_{k|k-1} \right)^T \tag{83.10}$$

$$\mathbf{K}_k = \left(\mathbf{P}_{x_k z_k} / \mathbf{S}_{zz,k|k-1}^T \right) / \mathbf{S}_{zz,k|k-1} \tag{83.11}$$

$$\hat{\mathbf{x}}_{k|k} = \hat{\mathbf{x}}_{k|k-1} + \mathbf{K}_k \left(\mathbf{z}_k - \hat{\mathbf{z}}_{k|k-1} \right) \tag{83.12}$$

$$\mathbf{S}_{k|k} = cholupdate \left(\mathbf{S}_{k|k-1}, \mathbf{K}_k \mathbf{S}_{zz,k|k-1}, -1 \right) \tag{83.13}$$

where $\widetilde{\boldsymbol{\zeta}}_i = \boldsymbol{\zeta}_{k|k-1,i} - \hat{\mathbf{z}}_{k|k-1}$, the function $qr\{\cdot\}$ and $cholupdate\{\cdot\}$ denote QR decomposition and the updates of the Cholesky factor.

83.3 STF–SRUKF

83.3.1 Strong Tracking Filter

Based on the extended Kalman filter and orthogonality principle, STF is deduced by introducing a fading factor λ_k into the predicted error covariance of EKF. It makes the residual error series orthogonal to each other. The sub-optimal time-varying factor can be calculated as [3, 4]:

$$\lambda_{k+1} = \begin{cases} \lambda_0, \lambda_0 > 1 \\ 1 \quad , \lambda_0 \leq 1 \end{cases} \tag{83.14}$$

$$\lambda_0 = \frac{\mathbf{tr}[\mathbf{N}_{k+1}]}{\mathbf{tr}[\mathbf{M}_{k+1}]} \tag{83.15}$$

$$\begin{cases} \mathbf{N}_{k+1} = \mathbf{V}_{k+1} - \mathbf{H}_k \mathbf{Q}_k \mathbf{H}_k^T - \beta \mathbf{R}_{k+1} \\ \mathbf{M}_{k+1} = \mathbf{H}_k \mathbf{F}_k \mathbf{P}_{k|k} \mathbf{F}^T(k) \mathbf{H}^T{}_k \end{cases} \tag{83.16}$$

$$\mathbf{V}_{k+1} = E\{\boldsymbol{\gamma}_k \boldsymbol{\gamma}_k^T\} = \begin{cases} \boldsymbol{\gamma}_1 \boldsymbol{\gamma}_1^T & k = 0 \\ \dfrac{[\rho \mathbf{V}_k + \boldsymbol{\gamma}_{k+1} \boldsymbol{\gamma}_{k+1}^T]}{1+\rho} & k \geq 1 \end{cases} \tag{83.17}$$

where, $0 < \rho \leq 1$ is the forgetting factor and $\beta \geq 1$ is the weakening factor. Both are set empirically.

83.3.2 STF–SRUKF

STF–SRUKF is a combination of the strong tracking filter and the square root unscented Kalman filter. In STF–SRUKF, the square root of the covariance matrix is used in the recursive process instead of covariance matrix itself to guarantee numerical stability. Simultaneously, a time-varied fading factor is introduced into the filter to enhance the quick-response ability to deal with state sudden change.

The only difference between SRUKF and STF–SRUKF is the calculation of prediction error covariance. By introducing the time-varying fading factor, the prediction error covariance can be described as:

$$\begin{aligned}\mathbf{P}_{k|k-1} &= \lambda_k\left(\sum_{j=0}^{2n} W_j \widetilde{\mathbf{x}}_{k|k-1,j}\widetilde{\mathbf{x}}^T_{k|k-1,j} + \mathbf{Q}_{k-1}\right)\\ &= \sum_{j=1}^{2n}\lambda_k W_j \widetilde{\mathbf{x}}_{k|k-1,j}\widetilde{\mathbf{x}}^T_{k|k-1,j} + \lambda_k\mathbf{Q}_{k-1} + \lambda_k W_0\widetilde{\mathbf{x}}_{k|k-1,0}\widetilde{\mathbf{x}}^T_{k|k-1,0}\\ &= \lambda_k T^T T + \lambda_k W_0\widetilde{\mathbf{x}}_{k|k-1,0}\widetilde{\mathbf{x}}^T_{k|k-1,0}\end{aligned} \tag{83.18}$$

Where $\widetilde{\mathbf{x}}_{k|k-1,1:2n} = \hat{\mathbf{x}}_{k|k-1} - \boldsymbol{\chi}_{k|k-1,1:2n}$, $\mathbf{T} = \left[\sqrt{\lambda_k W_{1:2n}}\widetilde{\mathbf{x}}_{k|k-1,1:2n} \quad \sqrt{\lambda_k\mathbf{Q}_{k-1}}\right]^T$.

To facilitate the calculation, we can express the transpose of T in terms of an orthogonal matrix $\mathbf{O}_k$ and an upper triangular matrix $\mathbf{S}^T_{k|k-1}$ using the QR-decomposition. Thus, Eq. (83.18) can be rewritten as:

$$\begin{aligned}\mathbf{P}_{k|k-1} &= \mathbf{S}_{k|k-1}\mathbf{O}_k^T\mathbf{O}_k\mathbf{S}^T_{k|k-1} + \lambda_k W_0\widetilde{\mathbf{x}}_{k|k-1,0}\widetilde{\mathbf{x}}^T_{k|k-1,0}\\ &= \mathbf{S}_{k|k-1}\mathbf{S}^T_{k|k-1} + \lambda_k W_0\widetilde{\mathbf{x}}_{k|k-1,0}\widetilde{\mathbf{x}}^T_{k|k-1,0}\end{aligned} \tag{83.19}$$

The square root of forecast covariance matrix of STF–SRUKF can be acquired:

$$\begin{cases}\mathbf{S}_{k|k-1} = \sqrt{\lambda_k}qr\left\{\left[\sqrt{W_{1:2n}}\left(\boldsymbol{\chi}_{k|k-1,1:2n} - \hat{\mathbf{x}}_{k|k-1}\right) \quad \sqrt{\mathbf{Q}_k}\right]\right\}\\ \mathbf{S}_{k|k-1} = cholupdate\left(\mathbf{S}_{k|k-1}, \boldsymbol{\chi}_{k|k-1,0} - \hat{\mathbf{x}}_{k|k-1}, sign(\lambda_k W_0)\sqrt{\lambda_k W_0}\right)\end{cases} \tag{83.20}$$

Then, the running sequence of the STF–SRUKF algorithm is Eqs. (83.3–83.6), (83.8), (83.14–83.17), (83.20), (83.9–83.13).

83.4 Simulation Results

Consider a typical air traffic control circumstance, which is given in [8]. We set two state mutations from 20 to 40 s. Figure 83.1 shows the trajectories of aircraft.

The nonlinear system of equations corresponding to the turning motion and the measurement equation can be represent as:

$$\mathbf{x}_k = \begin{bmatrix} 1 & \frac{\sin \Omega T}{\Omega} & 0 & -\left(\frac{1-\cos \Omega T}{\Omega}\right) \\ 0 & \cos \Omega T & 0 & -\sin \Omega T \\ 0 & \left(\frac{1-\cos \Omega T}{\Omega}\right) & 0 & \cos \Omega T \\ 0 & \sin \Omega T & 0 & \cos \Omega T \end{bmatrix} \mathbf{x}_{k-1} + \mathbf{w}_k \tag{83.21}$$

$$\mathbf{z}_k = \begin{bmatrix} r_k \\ \theta_k \end{bmatrix} = \begin{bmatrix} \sqrt{x_k^2 + y_k^2} \\ \tan^{-1}\left(\frac{y_k}{x_k}\right) \end{bmatrix} + \mathbf{v}_k \tag{83.22}$$

The state vector $\mathbf{x}_k = [x_k, v_k^x, y_k, v_k^y]$, where x_k and y_k are the displacement components of x and y direction, v_k^x and v_k^y are the corresponding velocity components, here $T = 1$ s is the time interval between radar measurements. The turn rate Ω is unknown. The process noise $\mathbf{w}_k$ and measurement noise $\mathbf{v}_k$ are Gaussian sequence with zero mean and the covariance of them are $\mathbf{Q} = diag[\mathbf{M} \quad \mathbf{M}]$ and $\mathbf{R} = diag[\sigma_r^2 \quad \sigma_\theta^2]$.

The initial state is $\mathbf{x}_0 = [1000 \quad 300 \quad 1000 \quad 0]$ and the initial associated covariance is $\mathbf{P}_{0|0} = diag[100 \quad 10 \quad 100 \quad 10]$. The system parameters are

$$\mathbf{M} = \begin{bmatrix} \frac{T^3}{3} & \frac{T^2}{3} \\ \frac{T^2}{2} & T \end{bmatrix}, \quad \sigma_r = 10 \text{ m}, \quad \sigma_\theta = \sqrt{10}\text{mrad}.$$

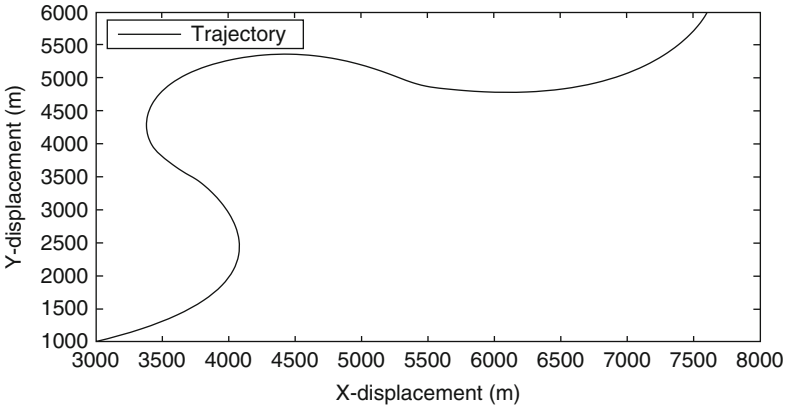

Fig. 83.1 Aircraft trajectory

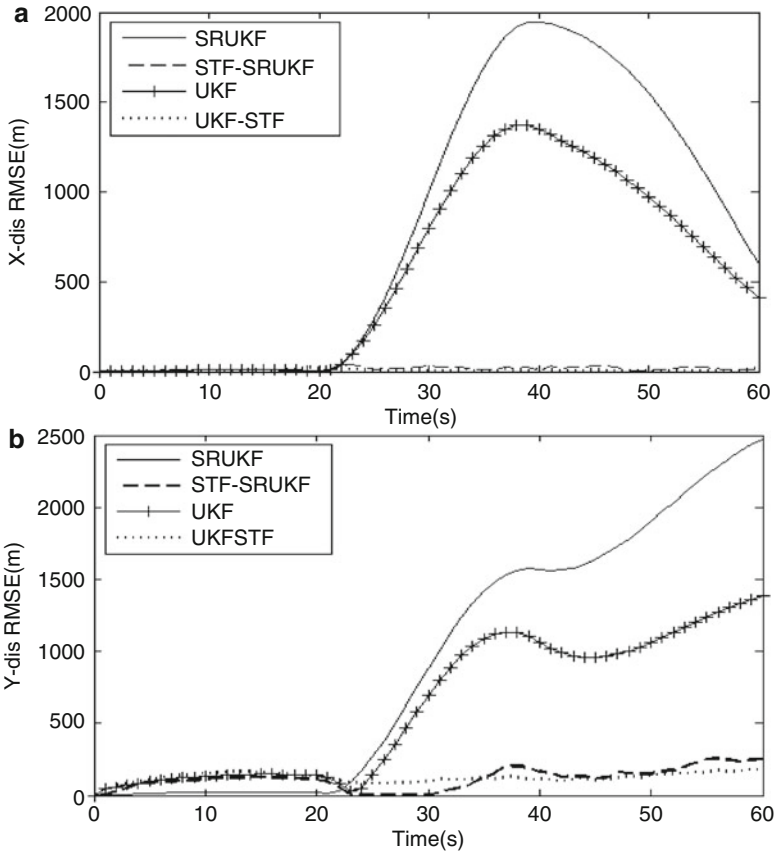

Fig. 83.2 RMSE of X-displacement (**a**) and Y-displacement (**b**)

This simulation is performed to compare the estimation performance between the proposed STF–SRUKF, UKF, UKF–STF and SRUKF. For a fair comparison, we make 100 independent Monte Carlo runs. All the filters are initialized with the same condition.

The Fig. 83.2 shows that the performance of the filter which have introduced into time-varying factor is superior to those without time-varying factor when state change happen suddenly. The tracking result of UKF and SRUKF exhibit a divergent trend. But contrast, the result of STF–SRUKF and UKF–STF are stability and the errors of them are credible. Therefore, it can be concluded that STF–SRUKF make a good showing in numerical stability, as well as the ability of dealing with unexpected sate change.

Conclusion

A new adaptive maneuvering target tracking method, called square root unscented Kalman filter based on strong tracking (STF–SRUKF), is presented in this paper. STF–SRUKF has two prominent merits. First, by introducing a time-varying fading factor, STF–SRUKF can adjust the gain matrix online and the ability of tracking abrupt changes is improved. Second, the square root filtering method has been used in this filter, which can help the filter gain high stability. Simulation results show that STF–SRUK performs well in case of sudden state changes and target maneuvering, and keeps satisfactory stability during the tracking process.

Acknowledgments This research was supported by National Natural Science Foundation of China (No. 61139003), The China Postdoctoral Science Foundation (No. 2013 M531948), and The National Key Technology Research and Development Program of the Ministry of Science and Technology of China (No. 2011BAH24B05).

References

1. Sadeghi B, Moshiri B (2007) Second-order EKF and unscented Kalman filter fusion for tracking maneuvering targets. In: IEEE international conference on information reuse and integration, pp 514–519
2. Wu C, Han C (2007) Strong tracking finite-difference extended Kalman filtering for Ballistic target tracking. In: ROBOI 2007 IEEE, pp 1540–1544. doi:10.1109/ROBOI.2007.4522393
3. Yu X, Bin Y (2002) Comparison between a strong tracking filter and Kalman filter for target tracking. J Air Force Rad Acad 16:17–22 (in Chinese)
4. Ge QB, Li WB, Wen CL (2011) SCKF-STF-CN: a universal nonlinear filter for maneuver target tracking. J Zhejiang University-Science C, pp 678–686. doi:10.1631/jzus.C10a0353
5. Liu C, Shui P, Li S (2011) Unscented extended Kalman filter for target tracking. Syst Eng Electron. doi:10.3969/j.issn.1004-4132.2011.02.002
6. Chang Guobin X, Jiangning LA (2011) A target tracking method of iterative unscented Kalman filter. J Xi'an JiaoTong Univ 45:70–74 (in Chinese)
7. Van der Merve R, Wan EA (2001) The square-root unscented Kalman filter for state and parameter-estimation. In: ICASSP'01, pp 3461–3464. doi:10.1109/ICASSP.2001.940586
8. Arasaratnam I, Haykin S (2009) Cubature Kalman filters. IEEE Trans Automat Control, 1254–1269. doi:101109/TAC.2009.2019800
9. Yb K, Feng XX, Lu CG (2012) Passive target tracking algorithm based on improved Gaussian mixture particle filter. Mod Radar 34:44–58 (in Chinese)
10. Wang Z, Liu Z et al (2011) Particle filter algorithm based on adaptive resampling strategy. In: International conference on EMEIT, pp 3138–3143. doi:10.1109/EMEIT.2011.6023752

Chapter 84
A Method of Availability Measurement Based on Resource Integration

Wang Qiurong, Zhao Ningshe, and Luo Yaguo

Abstract To estimate resources availability measurement in system integration, a new method is discussed. Firstly it analyzes the change of system resource state and discusses the mechanism of transmission of failures based on resource faults. Secondly the method of resource faults-based health measurement, the representation of classification and formalization for resources in system integration, and the theoretical means of availability metrics of resources and resource platform are proposed. Finally an algorithm for availability measurement of resource integrated platform is proposed.

Keywords Integration system • Resource availability • Measurement

84.1 Introduction

The resource platform is the base for system tasks execution, and the availability of resource components is the starting point to achieve function and operation [1, 2]. Using computer modeling and simulating to depict the resource organization of system integration can support a base of formal expression for researching health management of electronic systems integration [3, 4]. Health measurement is to analyze the availability of current resources in according with current resource capacity structure and design capacity. Resource testing from resource characterizations to defects discovery belongs to BIT (Build-in Test) program business while derivation issues based on resource availability are classified to health metrics category (resource availability measures) [5].

W. Qiurong (✉)
Modern Educational Technology & Network Information Center,
Xi'an Physical Education University, Xi'an, China
e-mail: jorland@163.com

Z. Ningshe
School of Software Engineering, Xi'an University, Xi'an, China
e-mail: zhaoningshe@gmail.com

L. Yaguo
School of Mathematics and Computer Engineering, Xi'an University, Xi'an, China
e-mail: 26487944@qq.com

J. Mu et al. (eds.), *The Proceedings of the Third International Conference on Communications, Signal Processing, and Systems*, Lecture Notes in Electrical Engineering 322, DOI 10.1007/978-3-319-08991-1_84

84.2 Availability Measurement of the System Resources

The availability measurement system resource (ASR) estimates the distance between current resources and expected resource based on existing ability of current resource. So $D(R_i, \hat{R}_i)$ is used to express the degree of difference between their abilities of resource i and expected one. Its calculation is shown by formula (84.1):

$$D(R_i, \hat{R}_i) = \frac{ASR(i) =}{A\hat{S}R(i) =} = \frac{\delta_r(e_r) \cdot u_r \cdot \sum_{i=1}^{x} (\theta_i \cdot a_i)}{\delta_r(e_r) \cdot u_r \cdot \sum_{i=1}^{x} (\theta_i \cdot \hat{a}_i)} \tag{84.1}$$

Then in the traditional sense, the ability availability of resource can be measured by formula (84.2):

$$ASR(i) = \delta_r(e_r) \cdot u_r \cdot \sum_{i=1}^{x} (\theta_i \cdot a_i) \tag{84.2}$$

where, $\delta_r(e_r)$ denotes the mapping function of resource faults, whose value range is [0,1], commonly reflecting the relation between resource r and others in platform.

Because single resource remaining capabilities concern its capability structure, capability weight should be considered in measurement. For example, one resource of R1 exists capability degradation (fault weights are 0.15 and 0.2), so the remaining capability is estimated as 0.65 in according with capability weight.

The remaining capability of some resource is associated with not only its capability but also change in resource scale. For example, R1:10 split into R1:6 + R11:3 + R12:1, then the variability of this resource is 0.4, where R11 remains 80 % of original capability structure, R12 remains 75 %, so resource remaining capability of R1 is 0.915(0.6*1 + 0.3*0.8 + 0.1*0.75). Besides, the remaining capabilities of resource integrated platform are associated with platform integration capability, so resource type weight must also be considered.

Combining the remaining usage life (RUL) prediction result in resources faults detection process, time availability of resource could be estimated, which essentially depends on its capability items aging. Consuming the RUL of resource is associated with system tasks being executed, with system function being called. To a task demand at some certain moment, the resources age will be affected by function call for the fixed function demand. In an integrated system, the age of resource platform is showed by capability age integration.

84.3 The Principle of Availability Measurement of Resources Integrated Platform

In the traditional sense, based on the result of ASR described in mathematical form, the availability of resource platform abbreviated AR can be measured by formula (84.3):

$$AR = \sum_{i=1}^{x} (\alpha_i \cdot ASR(i)) \tag{84.3}$$

where α_i represents the proportion of scale of resource i in resource platform.

The availability of whole platform is measured by the integrated distance between current and designed availability. To acquire this integrated distance, an algorithmic process is proposed: suppose resource capability vector group is $R = [R_1 : m_1, R_2 : m_2, \cdots, R_x : m_x]$, where x is the number of resource type, n_1:n_x is scale sequence. The designed resource capability vector is $\hat{R} = \left[\hat{R}_1 : n_1, \hat{R}_2 : n_2, \cdots, \hat{R}_r : n_r\right]$, where r is number of resource type, N_1:N_r is scale sequence of designed resources, then $\boldsymbol{AR}$ is estimated in according with the degree Linear-Expressed of $\boldsymbol{R}$ to $\hat{R}$, namely according to the supporting degree of whole platform to resource $\boldsymbol{R_i}$. The estimation matrix inequality (84.4) is as follows:

$$(R_1, R_2, \cdots, R_x) \cdot Y \geq \hat{R}_i \tag{84.4}$$

where Y is supporting matrix which represents the description for supported situation of the current resources overall capability structure to the expected resource capability demands. If formula (84.4) has any solution, it shows that the demand support platform to resource $\boldsymbol{R_i}$ is satisfied.

A function process is constructed as formula (84.5):

$$s(i) = \begin{cases} \omega_i, & if \quad R \cdot Y \geq R_i \\ 0 & else \end{cases} \tag{84.5}$$

then

$$A_{PoR} = \sum_{i=0}^{r} f(i) \tag{84.6}$$

84.4 The Algorithm Description for Availability Measurement of Resource Integrated Platform

The problem for resource measurement is whether expected demand capability structure can be supported by current resources capabilities. During measuring the whole availability of resources integrated platform, the support for resource demands depends on the integrated status of resource platform, so the tactics of

resource integration will affect the result. To solve the problem that resources capability degradation helps to generating new structure, during the system running, resource integrated platform management software must integrate resources capability.

Here is an algorithm for resource capacity integration:

① If the counter i is the number of types of existing resources, turn to ⑧, else to continue.
② If the counter j reaches the companion number of resource class I, turn to ①, else to continue.
③ If capability structure of element(i,j) is not empty, turn to ①, else to continue.
④ To reset seek symbol mark as 0.
⑤ To seek for other main element which is not i.
⑥ If found, to set seek mark as 1, link resource R(i,j) to the main element, turn to ①.
⑦ To generate new resource vector, and let the number of main element companion of ith type resource as 1, turn to ①.
⑧ To delete redundant representation of resource and the resources which are exhausted (scale = 0).

Conclusion

The following issues are settled by means of simulation process for resource availability measurement: (1) the formulation for resource ability structure, which expresses several management properties of kind, nature and status of resource objects. (2) Resource degradation to faults occurrence and the expression, where the degradation of resource platform is simulated with the introducing random ability mutation. (3) simulating the difference between resource integration management and traditional management. (4) Implementing of the construction algorithm process for availability measurement of resources and resource platform, which gives the effective result of resources to functions.

Acknowledgments This study was funded by Shaanxi Province "12th Five-Year" Planning Project of Education Science (No. SGH12501) and XI'AN Science and Technology Plan Innovation Fund "Arts and Sciences Special" project (No. CX12189WL34) and Xi'an University Education Reform Project (No. 12C103).

References

1. Gouging WANG (2011) Thinking about developing integrated avionics system. Int Aviat 8:55–58
2. Wei C, Bo J (2013) Failure prediction of integrated avionic system. Electron Opt Control 20 (5):53–57, 62

3. Wenkui C, Fengming Z, Xiaoguang F (2009) Overview on software architecture of integrated modular avionic systems. Acta Aeronaut Astronaut Ica Sinica 30(10):1912–1917
4. Avizienis A, Randell B, Landwehr C (2004) Basic concepts and taxonomy of dependable and secure computing. IEEE Trans Dependable Secure Comput 1(1):11–33
5. Zhao N (2014) Modeling resource availability measurement for system integration. Appl Mech Mater 845–848. In Proceedings of 2013 International Symposium on Vehicle, Mechanical, and Electrical Engineering, ISVMEE 2013. December 21, 2013[C]. Switzerland: Trans Tech Publications

Chapter 85
Compact Waveguide to HMSIW Transition Using Antisymmetric Tapered Probes

Jun Dong, Ziqiang Yang, Yihong Zhou, Yu Liu, and Tao Yang

Abstract A compact and broadband rectangular waveguide-to-half mode substrate integrated waveguide (HMSIW) transition based on antisymmetric tapered probes is proposed. The antisymmetric tapered probes are used to change the quasi-$TE_{0.5,0}$ mode in the HMSIW to the TE_{10} mode in the rectangular waveguide. To verify the proposed transition circuit, a back-to-back transition structure has been designed, fabricated and measured. The measured results show that an insertion loss less than 1.6 dB and a return loss better than 14 dB at 26–40 GHz are obtained for a back-to-back transition. Compared with the waveguide-to-HMSIW transition using antipodal fin-line, the size of the proposed transition circuit is reduced by approximately 71 %. The high performance, compact size and simple structure, enable such transition to be employed in a number of other millimeter-wave applications.

Keywords Compact • HMSIW • Rectangular waveguide • Transition • Antisymmetric tapered probes

85.1 Introduction

Recently, due to the good characteristics of low loss, low cost, high power handling capability and easy integration, substrate integrated waveguide (SIW) has drawn much attention [1, 2]. Half mode substrate integrated waveguide (HMSIW) is a type

J. Dong (✉)
University of Electronic Science and Technology of China, Chengdu, China
e-mail: jundong.ee@gmail.com

Z. Yang • Y. Liu • T. Yang
School of Electronic Engineering, University of Electronic Science and Technology of China, No.2006, Xiyuan Ave, West Hi-Tech Zone, Chengdu 611731, China

Y. Zhou
School of Physics and Electronic, University of Electronic Science and Technology of China, Jianshe Road, Chengdu 610054, China

J. Mu et al. (eds.), *The Proceedings of the Third International Conference on Communications, Signal Processing, and Systems*, Lecture Notes in Electrical Engineering 322, DOI 10.1007/978-3-319-08991-1_85

of miniaturized SIW, which keeps the advantages of SIW but the size is nearly half reduced [3, 4]. Based on HMSIW technology, many kinds of microwave/millimeter-wave devices have been designed [5–8]. Nevertheless, acting as an effective transmission structure, rectangular waveguide has been widely used in microwave/millimeter-wave systems for many years because of their excellent performance in terms of quality factor and power-handling capacity. Therefore, it is necessary to design compact, broadband, high performance transition between rectangular waveguide and HMSIW. The transitions between rectangular waveguide and SIW/HMSIW have been investigated by many researchers [9–12]. However, the circuit size is usually large owing to the dimension of these transition circuits.

The bandwidth and circuit size are two important considerations in the design of transition circuit. To enhance the bandwidth, a transition between rectangular waveguide and SIW using a radial probe extended from SIW inserted into a height-tapered waveguide was implemented [9]. Although the bandwidth of this transition is almost cover all Ka-band, the insertion loss is big and the fabrication of height-tapered waveguide is more complicated. Some broad waveguide-to-SIW transitions are achieved in open literature [10, 11]. There are some differences in the design of waveguide-to-SIW and waveguide-to-HMSIW transition due to the different transmission mode in the SIW and HMSIW. The dominant transmission mode in the SIW is TE_{10} mode, while the HMSIW is quasi-$TE_{0.5,0}$ mode [3]. The transition both in [10] and [12] are realized by using antipodal fin-line, the difference is that an intermediate transition is needed in the design of waveguide-to-HMSIW transition. Unlike those transitions, a novel waveguide-to-HMSIW transition is presented in this work for the application of half-mode substrate integrated waveguide technology.

A broad rectangular waveguide to HMSIW transition using antipodal fin-line is presented for the first time [12]. Experimental results show about 1.3 dB insertion loss and better than 15 dB return loss for a back-to-back transition structure over 10 GHz bandwidths from 26.5 to 40 GHz. Although the bandwidth of such transition is wide enough for uses, the circuit size is large owing to the tapered fin-line. The bulky size of this transition limits the use of HMSIW in compact millimeter-wave circuits.

To reduce the circuit size, a waveguide-to-HMSIW transition based on antisymmetric tapered probes is proposed in this work. Compared with the waveguide-to-HMSIW transition using short-circuited tapered fin-line [12], the size of the proposed transition circuit is reduced by approximately 71 %. In addition to the compact size, it exhibits a broad band characteristic over the full Ka-band. A back-to-back prototype of the proposed transition had been fabricated and measured to verify the proposed design.

85.2 Proposed Transition

As shown in Fig. 85.1, the proposed transition structure consists of three parts, which are the rectangular waveguide, the antisymmetric tapered probes and the HMSIW. The HMSIW is fabricated by implementing a row of metallic vias on a low-loss substrate with metal coating on both sides. The antisymmetric tapered

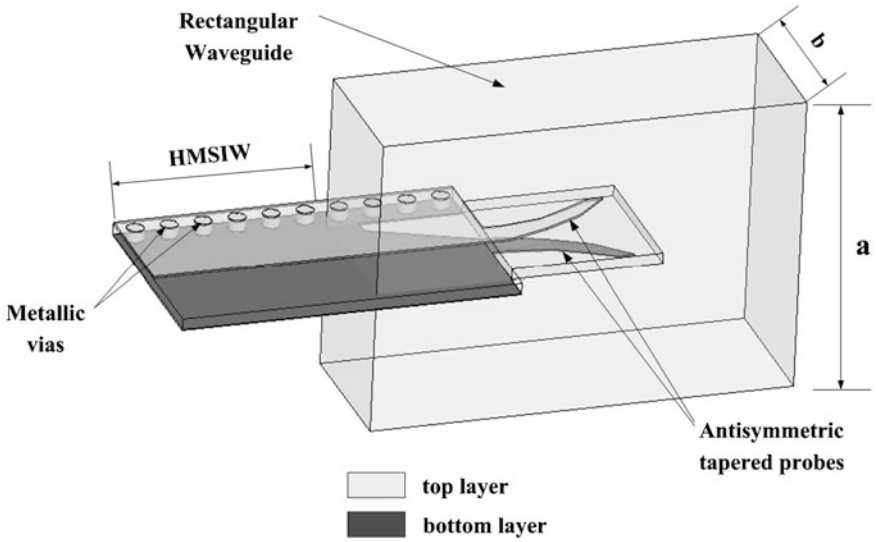

Fig. 85.1 Configuration of waveguide-to-HMSIW transition using antisymmetric tapered probes

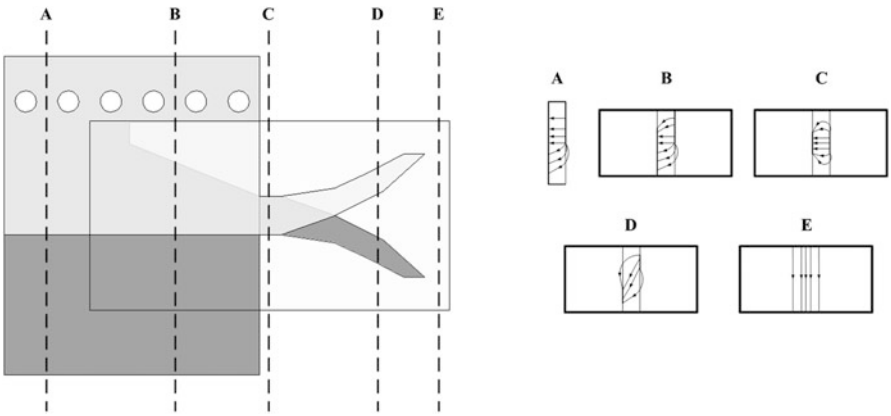

Fig. 85.2 The process of waveguide-to-HMSIW transition

probes are placed at the E-plane of the rectangular waveguide, which not only act as an impedance transformer, but also change the quasi-$TE_{0.5,0}$ mode in the HMSIW to the TE_{10} mode in the rectangular waveguide gradually. The rectangular waveguide is a standard WR-28 with dimensions of 7.112×3.556 mm. The antisymmetric tapered probes and HMSIW are integrated on a single RT/Duroid 5880 substrate with relative dielectric constant of 2.22, loss tangent of 0.0009 and thickness of 0.254 mm.

The E-field matching for the transition between waveguide and HMSIW are showed in Fig. 85.2. In operation, the quasi-$TE_{0.5,0}$ mode in the HMSIW is

gradually converted into the quasi-TEM mode in the antisymmetric tapered probes by a tapered gap, and then the quasi-TEM mode in the antisymmetric tapered probes is gradually converted into TE_{10} mode in the rectangular waveguide.

In the simulation, the transition between HMSIW and the antisymmetric tapered probes, a gradual impedance variation has been made by etching a small gap in the ground plane. With the enlarging of the gap, the width of the overlapped strip between the top and bottom layer is decreased, which results in an increase in characteristic impedance. Therefore, the low characteristic impendence of HMSIW and the high impedance of the tapered probes can be changed smoothly by adjusting the width of gap in a suitable outline. To achieve the low insertion loss and low reflection, all the proposed transition circuit was simulated with software (Ansoft HFSS).

85.3 Simulation and Experiment Results

The planar circuits for the proposed transition on both sides of the substrate are shown in Fig. 85.3. The impedance matching between the rectangular waveguide and HMSIW can be achieved via gradual change of the tapered probes. A spline curve is adopted to optimize the tapered probes. After optimization with Ansoft HFSS, the key dimensions of the proposed transition are obtained as shown in Fig. 85.3. It shows that the transition length between waveguide and HMSIW is very small, with only 6.36 mm. Two identical transitions were cascaded back-to-back for the need of experiment. As shown in Fig. 85.4, a back-to-back transition

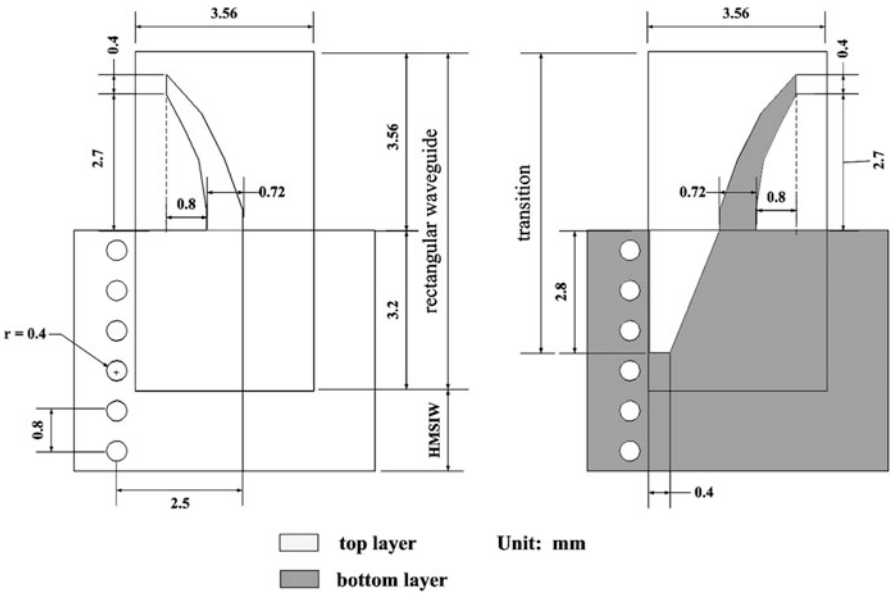

Fig. 85.3 The key dimensions of planar circuit for proposed transition

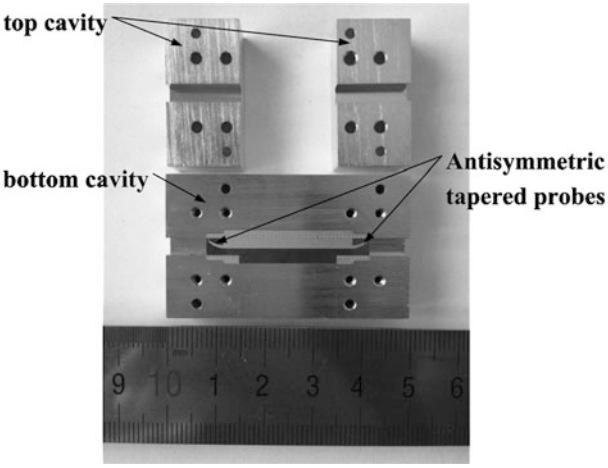

Fig. 85.4 Photograph of the fabricated back-to-back transition

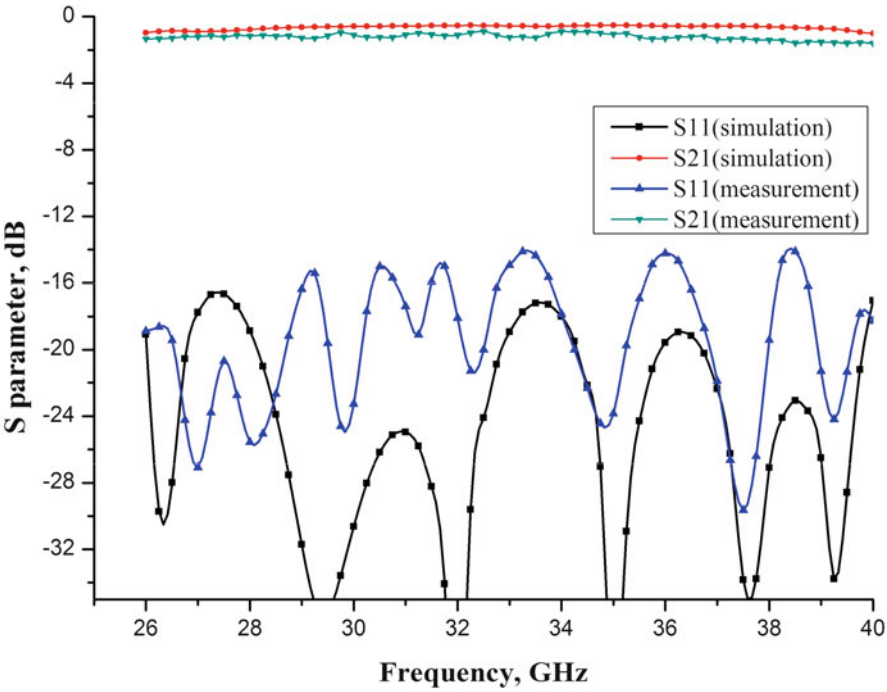

Fig. 85.5 Simulation and measurement results of the back-to-back transition

prototype is fabricated. The measurements were carried by an Agilent N5230A network analyzer. Fig. 85.5 shows the simulation and measurement results of the back-to-back transition. The measurement results show that the return loss is better than 14 dB and the insertion loss is less than 1.6 dB (which contains the

transmission loss of a 20 mm HMSIW line) in the frequency range 26–40 GHz. The measurement results show good agreement with the simulation results.

Conclusion

In this Letter, a novel compact and broadband waveguide-to-HMSIW transition based on the antisymmetric tapered probes is proposed. To verify the simulation result, a back-to-back transition prototype has been fabricated and measured. Compared with the waveguide-to-HMSIW transition using antipodal fin-line, the length of this proposed transition structure is reduced from 22 to 6.36 mm, which means 71.1 % reduction in size. In addition, it exhibits a good transmission characteristic over the full Ka-band. The measured results show that such transition has an insertion loss less than 1.6 dB and a return loss better than 14 dB over the Ka-band. The measured results are well agreed with the simulated results which verify the feasibility of the proposed waveguide-to-HMSIW transition.

Acknowledgments This work was supported by the Fundamental Research Funds for the Central Universities of China (Grant No. ZYGX2012J030 and ZYGX2013J059).

References

1. He FF, Wu K, Hong W, Han L, Chen X-P (2012) Low-cost 60-GHz smart antenna receiver subsystem based on substrate integrated waveguide technology. IEEE Trans Microwave Theory Tech 60(4):1156–1165
2. Bozzi M, Georgiadis A, Wu K (2011) Review of substrate-integrated waveguide circuits and antennas. IET Microwave Antenna Propag 5(8):909–920
3. Hong W, Liu B, Wang Y, Lai Q, Tang H, Yin XX, Dong YD, Zhang Y, Wu K (2006) Half mode substrate integrated waveguide: a new guided wave structure for microwave and millimeter wave application. In: Proceedings of the joint 31st international conference, infrared millimeter waves 14th international conference terahertz electronics, Shanghai, p 219
4. Lai QH, Fumeaux C, Hong W, Vahldieck R (2009) Characterization of the propagation properties of the half-mode substrate integrated waveguide. IEEE Trans Microwave Theory Tech 57(8):1996–2004
5. Liu B, Hong W, Wang Y-Q, Lai Q-H, Wu K (2007) Half mode substrate integrated waveguide (HMSIW) 3 dB coupler. IEEE Microwave Wirel Compon Lett 17(1):22–24
6. Ho M-H, Li C-S (2013) Novel balanced BPF design using half-mode substrate integrated waveguide with common-mode suppression. Microwave Opt Technol Lett 55(5):1112–1115
7. Wu L-S, Xia B, Mao JF, Yin W-Y (2012) A half-mode substrate integrated waveguide ring for two-way power division of balanced circuit. IEEE Microwave Wirel Compon Lett 22 (7):333–335
8. Senior DE, Cheng XY, Yoon Y-K (2012) Electrically tunable evanescent mode half-mode substrate-integrated-waveguide resonators. IEEE Microwave Wirel Compon Lett 22 (3):123–125
9. Xia L, Xu R, Yan B, Li J, Guo Y, Wang J (2006) Broadband transition between air-filled waveguide and substrate integrated waveguide. Electron Lett 42(24):1403–1405

10. Zhong CL, Xu J, Zhi ZY (2009) Broadband substrate integrated waveguide to rectangular waveguide transition with fin-line. Electron Lett 45(4):205–207
11. Li J, Wen G, Xiao F (2010) Broadband transition between rectangular waveguide and substrate integrated waveguide. Electron Lett 46(3):223–224
12. Zhong CL, Xu J, Zhi ZY, Jin CX (2009) Broadband transition between half mode substrate integrated waveguide and rectangular waveguide. Electron Lett 45(3):168–170

Part VIII
Biological and Medical Signal Processing

Chapter 86
A Multi-Label Classification Framework to Predict Disease Associations of Long Non-coding RNAs (lncRNAs)

Ashis Kumer Biswas, Baoju Zhang, Xiaoyong Wu, and Jean X. Gao

Abstract In this paper, the automated detection of tissue specific disease association of long non-coding RNAs (lncRNAs) is modeled as a multi-label classification task, where a single lncRNA transcript may be associated with several diseases in a tissue specific manner. Four algorithms are evaluated and compared in this task. Furthermore, in this article we put emphasis on the fact that secondary structure and the composition features of the lncRNAs dictate their functions that led us to develop a new multi-label feature extraction scheme. Experiments are conducted on a set of 7,566 lncRNA transcripts with 22 tissue labels, and the results provide interesting insights into the quality of the discussed algorithms and the features.

Keywords Long non-coding RNA • Multi-label classification • Association

86.1 Introduction

With the advent of the Next Generation Sequencing (NGS) platform it is now experimentally verified that in a typical Eukaryote, up to 90 % of its genomic DNA undergo transcription, and only 1–2 % of these transcripts code for proteins, and the remaining large population of transcripts are classified as non-coding RNAs (ncRNAs). Due to the size of the transcripts, the long non-coding RNAs (lncRNAs) form a major portion of the transcribed ncRNAs. The lncRNAs have been shown to play key roles in various biological processes, such as imprinting control, epigenetic regulation, cell cycle control, nuclear and cytoplasmic trafficking,

A.K. Biswas (✉) • J.X. Gao
Department of Computer Science and Engineering,
The University of Texas at Arlington, Arlington, TX 76019, USA
e-mail: ashis.biswas@mavs.uta.edu; gao@uta.edu

B. Zhang • X. Wu
School of Communications and Electronic Information, Tianjin Normal University,
Tianjin 300387, China
e-mail: wdxyzbj@163.com

J. Mu et al. (eds.), *The Proceedings of the Third International Conference on Communications, Signal Processing, and Systems*, Lecture Notes in Electrical Engineering 322, DOI 10.1007/978-3-319-08991-1_86

differentiation, immune responses and chromosome dynamics. It is not surprising to discover the fact that the dysregulations and mutations of lncRNAs are implicated in variety of human diseases [1].

Previous lncRNA-disease association studies employed a graph mining paradigm over a constructed coding and non-coding transcript network [2]. Several experimental studies revealed that more than 227 human diseases are associated with 266 lncRNAs resulting nearly 650 lncRNA-disease associations [3]. Thus, using the pigeonhole principle we can realize that an lncRNA may be associated to several different diseases, and hence several different lncRNAs may develop a complex disease exploiting their functional combinations. Such associations can also be realized through a multi-label classification methods that motivated us for an investigation conducted in this study.

A secondary contribution of this paper is a new multi-label dataset with 89 composition features, 21 structural features of 7,566 tissue-specific lncRNAs that are categorized into one or more out of 22 classes of tissues. The dataset is made available in a publicly accessible website,[1] in order to allow comparative experiments by other researchers.

The primary contribution of this paper is twofold:

- A comparative experimental evaluation of four multi-label classification algorithms on the aforementioned dataset using a variety of evaluation metrics.
- $O(n)$ algorithms to extract various secondary structural properties from given dot-bracket secondary structures of lncRNAs, where n is the length of the lncRNA in nucleotides unit. Since lncRNAs can have huge number of nucleotides, any quadratic algorithm for the similar purpose would not be applicable in large scale application developments.

The remaining of this paper is structured as follows: Sect. 86.2 presents the details of the dataset used in this study, along with the composition and structural feature extraction schemes and the algorithms to perform the multi-label classification and their evaluation criteria. Section 86.3 presents experimental results comparing the four multi-label classification algorithms. Finally, conclusions and future work are drawn in Sect. 86.4.

86.2 Materials and Methods

86.2.1 Dataset and Preprocessing

The Human Body Map Project [4] presents a catalog of human long non-coding RNAs (lncRNA) with corresponding 22 tissue specific RNA-seq expression profiles. The current project website provides annotation and expression information of

[1] http://biomecis.uta.edu/~ashis/res/csps2014/suppl.

21,626 distinct lncRNAs. We first selected 18,657 transcripts (more than 85 % of the catalog) that have length less than or equal to 2,000 bases to bypass quadratic computational cost imposed by the off-the-shelf secondary structure prediction methods. Then by using a tissue-specificity threshold we extracted 89 composition-based features, 21 secondary structure-based features of 7,566 lncRNAs from this pool.

86.2.2 Composition and Structure-Based Profile Generation

From the nucleotide sequences of transcripts we computed global G+C content, G+C content in the first, second and third positions of the codon bases. The compositions of unigrams, bigrams and trigrams for the entire length of the transcripts were calculated. Finally if we include the transcript length as another composition based feature, the total number of composition features become 89 (4 G+C content related, 4 unigrams, 16 bigrams, 64 trigrams and 1 length measure).

Mercer et al. [5] reported that in many cases, the secondary structure of lncRNAs dictates their functions, and functional identifications can be observed through investigation of the conservation at the secondary structure level than at the sequence level of the lncRNA transcripts. In this study, we investigated the functional association of lncRNAs through using their secondary structural properties.

Most RNA molecules are single stranded that fold back onto itself to form double helical regions stabilized by the Watson–Crick base pairs (A-U and C-G) and wobbling base pair (G-U). Given a primary sequence S, a secondary structure is defined as a set $P = (i, j)|1 \leq i < j \leq N$ of base-pairs represented as tuples of positions in the sequence of length n such that for any two base-pairs (i_1, i_2), $(j_1, j_2) \in P$ with $i_1 < j_1$ either $i_1 < i_2 < j_1 < j_2$ or holds. Figure 86.1 illustrates various components of secondary structure of a synthetic RNA molecule. If all the internal nucleotides in the sequence interval $[i + 1, \cdots, j - 1]$ with base-pair (i, j) are contiguous and non-binding, then we call this element a hairpin. If the base-pair (i, j) is adjacent to another base-pair (h, l) such that $i < h < l < j$, then various structure element formations are possible:

1. if $h > i + 1$ and $j = l + 1$, then we call this structure element a left bulge
2. if $h = i + 1$ and $j > l + 1$, then it is a right bulge.
3. if $h > i + 1$ and $j > l + 1$, then it is an internal loop
4. if $h = i + 1$ and $j = l + 1$, then it is a stack (i.e., stem).

A multi-loop consists in addition to the base-pair (i, j) of at least two base-pairs from which several stems radiate.

GCGCCCGUAGCUCAAUUGGAUAGAGCGUUUGACUACGGAUCAAAAGGUUAGGGGUUCGACUCCUCUCGGGCGCG

(((((((. . ((((. . . . .)))) (((. . (((. . . ((((. . . .)))) . . .))) . .))) . . . . . .))))))) .

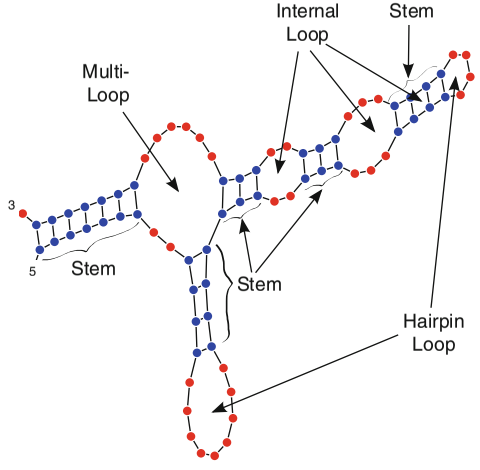

Fig. 86.1 A dot-diagram plot for the corresponding dot-bracket notation of the predicted secondary structure (second line from the *top*) for the RNA sequence shown at the *top*

Minimum Free Energy (MFE) based RNA secondary structures can be predicted using the well known Vienna RNA package [6]. However, it was later discovered that the non-coding RNA sequences do not always form MFE based secondary structures that may lead to a wrong predictions of the structure by Vienna RNA package. We, therefore, in conjunction with the Vienna RNA package, applied a non-MFE based secondary structure predictor, CentroidFold [7]. The later package applied a posterior decoding method including the γ-centroid estimator that can provide more reliable RNA structures, especially non-coding RNA structures.

Both the Vienna RNA and CentroidFold package provide predicted secondary structures in dot-bracket notation, from which we extracted the following features (10 scores from each predicted structures and the MFE):

1. Normalized AU, CG, GU pair frequencies, and base pair frequencies. All these scores can be computed in $O(N)$ time through scanning the N length sequence and its corresponding predicted secondary structure.
2. Average hairpin length occurring in a predicted secondary structure. Any occurrence of the pattern starting with an open-bracket, followed by at least one dot then a closing bracket represents a hairpin. For instance, the three patterns `(.)`, `(..)`, `(...)` denote three hairpins of length 3, 4 and 5 bases respectively. This search can be accomplished in $O(N)$ time.
3. Average length of the left bulges occurring in a secondary structure. Any occurrence of the pattern starting with an open-bracket, followed by at least one dot then another open-bracket represents a left-bulge. For instance, the three patterns `(.(`, `(..(`, `(...(` denote three left-bulges of length 3, 4 and 5 bases respectively. Again, this search can be accomplished in $O(N)$ time.
4. Average length of the right bulges occurring in a secondary structure. Essentially the right bulges are symmetric to left bulges, and so the procedure to get the left-bulge score can be symmetrically modified to compute the average length of the right bulges in length N structure T, and the computational cost would be $O(N)$.
5. Average length of the interior loop in secondary structures. An interior loop does have a left bulge and a right bulge. Thus, the score can be computed in $O(N)$ time.
6. Average length of the stems occurring in a secondary structure. By exploiting the properties of stack data structure and keeping track of subsequent base-pairs the stem score can also be computed in $O(N)$ time.
7. Average number of base-pairs forming the multi-loops. The procedure GET-MULTI-LOOP-SCORE returns the average value in $O(N)$ time, given an N length secondary structure of a long non-coding RNA T in dot-bracket notation.

GET-MULTI-LOOP-SCORE(T)

$n = 0$; $sum = 0$; $depthValue = 0$
$K = \emptyset$ // Stack maintains the matched open and closing brackets
$BPList = \emptyset$ // multi-list contains list of base-pairs forming multi-loops
for $i = 1$ **to** $T.length$
    if $T[i] =$ char'('
        $depthValue = depthValue + 1$
        push(K, i)
    elseif $T[i] =$ char')'
        $depthValue = depthValue - 1$
        $j =$ pop(K)
        if $depthValue > 0$ and (i, j) is not part of a stem
            $BPList[depthValue] =$ append($BPList[depthValue], < i, j >$)
n = frequency of $BPList$ entries having at least $2 < i, j >$ pairs
sum = total number of $< i, j >$ pairs forming those n multi-loops
return $\frac{sum}{n}$

86.2.3 Tissue Specificity Profile Generation

We computed the tissue specificity scores of each of the 18,657 long non-coding RNAs under study based on the expression scores computed in each of the 22 different human tissue samples. The tissue specificity score τ of a given lncRNA transcript is defined as:

$$\tau = \frac{1}{N-1}\sum_{i=1}^{N}(1 - X_i) \tag{86.1}$$

where N is the number of tissues, and x_i is the expression level of the lncRNA at tissue i normalized by maximum possible expression level in the N tissues of the lncRNA. We filtered out those lncRNAs that has tissue specificity greater than 1 and below 0. Then we attached 22 binary labels corresponding to the 22 tissues in the following manner:

$$L_{i,j} = \begin{cases} 1 & X_{i,j} \geq 0.10 \\ 0 & \text{otherwise} \end{cases} \tag{86.2}$$

where $L_{i,j}$ denotes the label of ith transcript for jth tissue with $1 \leq i \leq 7,566, 1 \leq j \leq 22$, and $X_{i,j}$ represents the normalized expression score of ith transcript in the jth tissue observed in the RNA-seq expression data obtained through the Human BodyMap project.

86.2.4 Multi-Label Classification

Traditional single-label classification methods are concerned with learning from a set of training instances which are associated with a single label l from a set of disjoint labels, L, with $|L| > 1$. However, in multi-label classification, the instances are associated with a set of labels $Y \subseteq L$. There are two main categories of multi-label classification techniques [8]: (i) Problem transformation methods—that transform the original problem into one or more single label classification problem, and (ii) Algorithm adaptation methods—that extend the learning algorithms to tackle the multi-label problem. We compared four multi-label classification algorithms: Random k-labelsets (RAkEL), multi-label k-nearest neighbor (ML-kNN), Binary relevance (BR) and Back-Propagation Multi-Label Learning (BPMLL). The first two are problem transformation methods, and the last two are the algorithm adaptation methods.

Multi-label classifiers are evaluated with different set of metrics than those used in the case of single-label problems. Unlike in a single-label classification problem where a prediction result is considered either correct or incorrect, in a multi-label classification problem, the classifier deserves partial credit for correctly predicting some of the labels as per the problem requirements. Three categories of evaluation metrics have been proposed in the literature: (i) Example-based, (ii) Label-based and (iii) ranking based. All the algorithms and the evaluation metrics are nicely presented in [9] among some other publications.

86.2.5 Experimental Setup

We used Weka-based package of java classes, called Mulan (http://mulan.sourceforge.net/) for all the multi-label classification methods and the supervised learning algorithms used by the algorithms. BR and RAkEL were run using Sequential Minimal Optimization based Support Vector Machines (SVMs) as the base classifier. The SVM was trained with a linear kernel and the complexity constant C was set to 1. For MLkNN, the number of nearest neighbors were set to 10. Tenfold cross validation experiments were conducted with the dataset for each of the four algorithm evaluations, and the results are reported in the following section. All the experiments were performed in 64-bit Ubuntu 12.04 operating system installed in a machine with Intel Core i3-2310M CPU @ 2.10 GHz $\times$ 4 processor, 8GB of RAM, 500GB SATA Hard drive (5,400 rpm).

86.3 Results and Discussions

In the Tables 86.1, 86.2 and 86.3, an up-arrow beside a metric name denotes that a higher value is better, and the down-arrow denotes a lower value is better. Best performance values among the four multi-label classifiers are shown in bold-faces for each of the metric. By analyzing the performance of the algorithms, it is possible to observe that there is no predominance of a single multi-label classification algorithm. However, if we extend our observation on the results we can find that ML*k*NN with $k = 10$ delivered the best possible results in most of the cases as compared with the other three algorithms.

Table 86.1 Example-based evaluation of the predictive performances of the multi-label classifiers

Example-based measures	RAkEL	ML*k*NN	BR	BPMLL
Hamming loss ↓	0.2032 ± 0.0059	$\mathbf{0.1970 \pm 0.0056}$	0.2048 ± 0.0056	0.2241 ± 0.0060
Accuracy ↑	0.5474 ± 0.0137	$\mathbf{0.5610 \pm 0.0126}$	0.5441 ± 0.0137	0.5191 ± 0.0096
Precision ↑	0.7781 ± 0.0147	0.7599 ± 0.0143	$\mathbf{0.7804 \pm 0.0142}$	0.6900 ± 0.0200
Recall ↑	0.6133 ± 0.0128	0.6486 ± 0.0149	0.6050 ± 0.0131	$\mathbf{0.6660 \pm 0.0213}$
F1-measure ↑	0.6409 ± 0.0135	$\mathbf{0.6627 \pm 0.0118}$	0.6405 ± 0.0137	0.6412 ± 0.0087
Subset accuracy ↑	$\mathbf{0.1980 \pm 0.0100}$	0.1807 ± 0.0103	0.1965 ± 0.0092	0.1006 ± 0.0245

Table 86.2 Label-based evaluation of the predictive performances of the multi-label classifiers

Label-based measures	RAkEL	ML*k*NN	BR	BPMLL
Micro-avg precision ↑	0.7680 ± 0.0106	0.7698 ± 0.0126	$\mathbf{0.7766 \pm 0.0105}$	0.7043 ± 0.0165
Micro-avg recall ↑	0.6219 ± 0.0124	0.6439 ± 0.0146	0.6029 ± 0.0116	$\mathbf{0.6497 \pm 0.0205}$
Micro-avg F1 ↑	0.6872 ± 0.0104	$\mathbf{0.7011 \pm 0.0111}$	0.6788 ± 0.0101	0.6754 ± 0.0077
Macro-avg precision ↑	0.6625 ± 0.0117	$\mathbf{0.6998 \pm 0.0226}$	0.5787 ± 0.0092	0.5753 ± 0.0641
Macro-avg recall ↑	0.4948 ± 0.0129	$\mathbf{0.5237 \pm 0.0177}$	0.4588 ± 0.0115	0.4827 ± 0.0202
Macro-avg F1 ↑	0.5494 ± 0.0113	$\mathbf{0.5804 \pm 0.0171}$	0.5058 ± 0.0099	0.4700 ± 0.0212

Table 86.3 Ranking-based evaluation of the predictive performances of the multi-label classifiers

Ranking-based measures	RAkEL	ML*k*NN	BR	BPMLL
One error ↓	0.2865 ± 0.0218	0.1075 ± 0.0110	0.2959 ± 0.0210	$\mathbf{0.1034 \pm 0.0115}$
Coverage ↓	14.2869 ± 0.2559	$\mathbf{11.5804 \pm 0.2154}$	14.5713 ± 0.2224	12.5604 ± 0.2064
Average precision ↑	0.7382 ± 0.0123	$\mathbf{0.8155 \pm 0.0087}$	0.7274 ± 0.0123	0.7867 ± 0.0104

Table 86.4 Time required by the multi-label classifiers to perform the tenfold cross-validation with the dataset with 7,566 lncRNA each with 110 features and 22 labels

Algorithm	CPU time (in seconds)
RAkEL	14,061
ML*k*NN	773
BR	5,890
BPMLL	289

Table 86.4 shows the CPU time in seconds that was consumed during the tenfold cross validation phase of each of the algorithms. We notice that BPMLL, ML*k*NN and BR algorithms require little time as compared to the RAkEL method, since their complexity is linear with respect to the number of labels. The complexity of RAkEL is bounded by the subset size parameter, and its increased time comes from the multiple label powerset models that it builds, since it is an ensemble approach.

Conclusions and Future Works

The task of multi-label classification of tissue-specific long non-coding RNAs (lncRNA) into tissues was investigated. An evaluation of four multi-label classification algorithms was performed on a collection of 7,566 lncRNAs. Among these algorithms, ML*k*NN was the most effective and is proposed for lncRNA-tissue specific disease categorization. The overall predictive performance was high and encourages further investigation of multi-label methods.

Future work will explore the effectiveness of new features, with different strategies to feature selection, as well as hierarchical multi-label classification approach which we believe has great potential in the lncRNA-disease association studies.

References

1. Sacco LD, Baldassarre A, Masotti A (2012) Bioinformatics tools and novel challenges in long non-coding RNAs (lncRNAs) functional analysis. Int J Mol Sci 13(1):97–114
2. Liu M-X, Chen X, Chen G, Cui Q-H, Yan G-Y (2014) A computational framework to infer human disease-associated long noncoding RNAs. PLoS ONE 9(1):e84408
3. Chen G, Wang Z, Wang D, Qiu C, Liu M, Chen X, Zhang Q, Yan G, Cui Q (2013) LncRNADisease: a database for long-non-coding RNA-associated diseases. Nucleic Acids Res 41(D1):D983–D986
4. Cabili MN, Trapnell C, Goff L, Koziol M, Tazon-Vega B, Regev A, Rinn JL (2011) Integrative annotation of human large intergenic noncoding RNAs reveals global properties and specific subclasses. Genes Dev 25(18):1915–1927
5. Mercer TR, Mattick JS (2013) Structure and function of long noncoding RNAs in epigenetic regulation. Nat Struct Mol Biol 20(3):300–307
6. Hofacker IL, Fontana W, Stadler PF, Bonhoeffer LS, Tacker M, Schuster P (1994) Fast folding and comparison of RNA secondary structures. Chem Mon 125(2):167–188
7. Sato K, Hamada M, Asai K, Mituyama T (2009) CENTROIDFOLD: a web server for RNA secondary structure prediction. Nucleic Acids Res 37(suppl 2):W277–W280

8. Tsoumakas G, Katakis I (2007) Multi-label classification: an overview. Int J Data Warehouse Min 3(3):1–13
9. Santos AM, Canuto AMP, Neto AF (2011) A comparative analysis of classification methods to multi-label tasks in different application domains. Int J Comput Inf Syst Ind Manag Appl 3:218–227

Chapter 87
Function Annotation of Proteins in *Eriocheir sinensis* Based on the Protein-Protein Interaction Network

Tong Hao, Ailing Yu, Bin Wang, Anan Liu, and Jinsheng Sun

Abstract *Eriocheir sinensis* is a highly-commercial aquaculture species as an important aquatic product source. The protein-protein interaction network (PIN) of *E. sinensis* has been constructed based on the RNA transcriptional sequencing. Many unknown proteins exist in the PIN, which seriously restricts the further mechanism researches on regulation, immunity and development of *E. sinensis*. In this work, we predicted the functions of the unknown proteins in *E. sinensis* based on the modularity feature of the PIN. The functions of 677 (93 %) proteins were annotated. The analysis of ribosome module indicates that the annotation of proteins and modules provides important references to be studied in the further in vivo experiment as well as the biological capability of the *E. sinensis* PIN.

Keywords *Eriocheir sinensis* • Protein-protein interaction network • Function annotation • Modularity

87.1 Introduction

The Chinese mitten crab (*Eriocheir sinensis*) (Henri Milne Edwards, 1854) is one of the most important aquaculture species with high commercial value as an important aquatic product source [1]. Many studies have been performed to accelerate the

T. Hao • A. Yu • B. Wang
Tianjin Key Laboratory of Animal and Plant Resistance/College of Life Science, Tianjin Normal University, Tianjin 300387, P. R. China

A. Liu
School of Electronic Information Engineering, Tianjin University, Tianjin 300072, China

J. Sun (✉)
Tianjin Key Laboratory of Animal and Plant Resistance/College of Life Science, Tianjin Normal University, Tianjin 300387, P. R. China

Tianjin Aquatic Animal Infectious Disease Control and Prevention Center, Tianjin 300221, China
e-mail: jinshsun@163.com

J. Mu et al. (eds.), *The Proceedings of the Third International Conference on Communications, Signal Processing, and Systems*, Lecture Notes in Electrical Engineering 322, DOI 10.1007/978-3-319-08991-1_87

growth or improve the immunity or signaling transduction system of *E. sinensis*, focusing on single or several genes [2], proteins [3] or a specific pathway [4]. Recently, the RNA sequencing has been executed for *E. sinensis* eyestalk, Y-organ, hepatopancreas and 21,678 unigenes were obtained. A protein-protein interaction network (PIN), including 3,223 proteins and 35,787 interactions, was constructed based on the RNA sequencing, which providing a paradigmatic blueprint of *E. sinensis* interactome [5]. According to the GO biological process annotation of proteins, the functions of 2,496 proteins related to 4,981 unigenes in the *E. sinensis* PIN were annotated, whereas the functions of the other 727 proteins related to 1,187 unigenes were still unknown, which makes up approximately 23 % of all the proteins and 19 % of all the unigenes. The large amount of unknown proteins seriously restricts the further mechanism researches on regulation, immunity and development of *E. sinensis*. On the other hand, PIN is a key to understand the complex world of biological processes inside the cell [6]. Knowledge of PINs have helped us solving many problems such as recognition of functional modules [7], investigation of signaling transduction mechanism [8], and prediction of protein functions [9]. Given the significant importance of PINs, proteome-wide interaction networks based on protein interactions has been constructed for many organisms [10–12]. For example, *Saccharomyces cerevisiae* [13], *Helicobacter pylori* [14] and *Bacillus subtilis* [15]. In the decades-long development of PIN, interest has shifted from microbial systems [16, 17] to mammalian [18] and a greater emphasis on more kinds of organisms [10]. For all the PINs, modularity is the basic feature of these biological networks. It is proved that the proteins with similar functions were inclined to assemble into the same module [10]. Therefore, with the construction of *E. sinensis* PIN, which supplied a comprehensive relationship network of proteins, the functions of unknown proteins in the network are possible to be predicted based on these relationships.

In this work, we predicted the function of unknown proteins in *E. sinensis* using its PIN based on the modularity of the network. The ribosome module was analyzed to show the biological significance of function annotation. The annotated proteins supplied important references for the further functions and mechanism study of *E. sinensis* eyestalk, Y-organ and hepatopancreas.

87.2 Methods

87.2.1 Decomposition of PIN

The decomposition method includes two steps:

1. A network was firstly decomposed into a dendrogram tree based on the topological structure. Then the dendrogram tree was searching downwards from root to each branch for identifying the proper modules. When a branch of the tree contains the number of leaves less than the 30, the leaves in that branch was

output as a module. Such searching was executed from top to bottom and the left to the right of the tree to obtain a preliminary result of decomposition.
2. Some of the preliminary decomposed modules (query modules) contain too few nodes to form independent biological function. Therefore an optimization was executed to eliminate these query modules. Firstly, the threshold for the maximal size for query modules was set to be 10. Then the number of boundary edges between each query module and all the other modules were investigated. The query module was combined into the module having the most boundary edges with it. Whereas when a query module connected to two or more modules with the same number of boundary edges, it was combined with the one with smallest boundary edges.

87.2.2 Function Annotation of Unknown Proteins

The biological process GO terms of known proteins was obtained from *E. sinensis* PIN [5]. For each module, the number of nodes included in each GO term was calculated. The GO term(s) included more than 40 % of all the proteins in the module were considered as the module GO function(s). As the proteins in the same module were inclined to have the same biological function, these module GO function(s) were annotated to all the unknown proteins in this module.

87.3 Results and Discussion

87.3.1 Function Annotation of Proteins

The *E. sinensis* PIN contains 3,223 proteins and 35,787 interactions. Firstly, 318 modules were obtained in the searching of dendrogram tree, with 180 small modules having less than 10 proteins. These small modules were then combined each other or with other modules in the network according to the method described in the method section. We finally obtained 149 modules from the whole network. These modules indicated 149 relatively separated biological functions in *E. sinensis*. The distribution of proteins in different modules was shown in Fig. 87.1. The largest module contained 230 proteins and the smallest contained 10 proteins. Most of modules contained less than 100 proteins.

As it is described in the *E. sinensis* PIN [5], in all the 2,496 proteins in the network, the functions of 2,496 proteins were annotated and the function of the rest 727 proteins were still unknown. These unknown proteins distributed in the 149 modules. In all the 727 proteins, 677 (93 %) were finally annotated with the method mentioned in the Method section in eight turns of iteration. As the GO terms were distributed as a tree-like structure, with deeper level having more detailed description of the function, we investigated the function distributions of

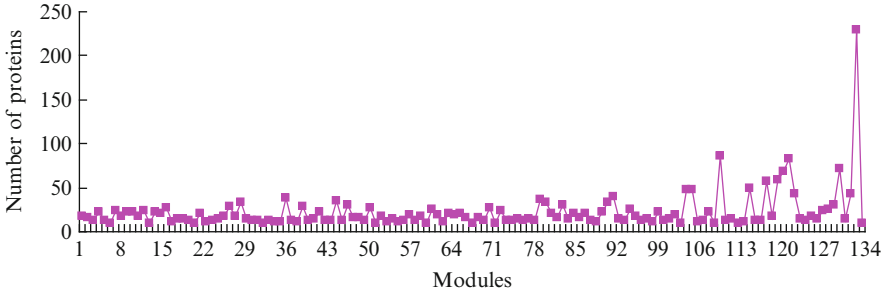

Fig. 87.1 Distribution of proteins in different modules

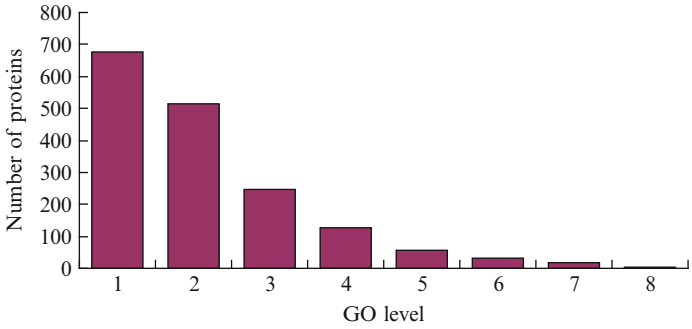

Fig. 87.2 The number of assigned unclassified protein with GO level

new annotated proteins in different GO levels. All the functions were traced to their higher GO levels and the number of annotated proteins in each level were investigated (Fig. 87.2). From Fig. 87.2 we can see that with the increase of GO level, the number of proteins decreased. In the eighth level, only four proteins were annotated. Actually, the number of proteins in level 1 (677 proteins) was the total number of newly annotated proteins in the global PIN.

87.3.2 Annotation of Ribosome Module

We took module 128 as an example to show the result of annotation. Module 128 contains 49 proteins and 272 interactions, with 34 known and 15 unknown proteins before function annotation. The module functions of module 145 are: cellular process, metabolic process, cellular macromolecule metabolic process, gene expression, biosynthetic process, cellular macromolecule biosynthetic process and translation. Therefore, all the unknown proteins in this module were annotated with these module functions. From these annotations we deduced that the function of module 128 have closely relationship with the gene expression and translation of proteins in

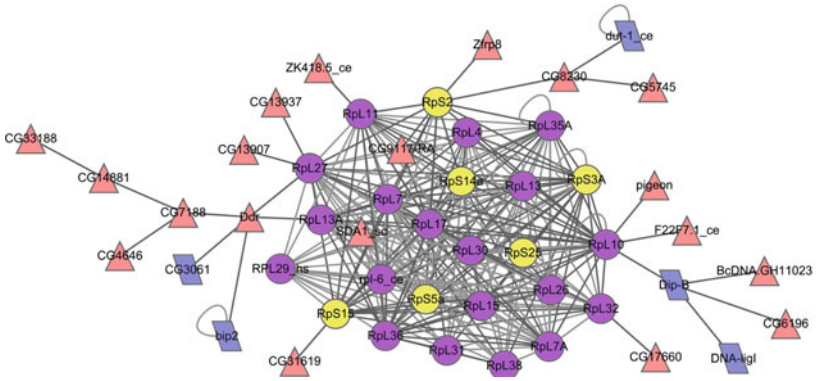

Fig. 87.3 The ribosomal module of *E. sinensis*. *Round* nodes represent the ribosome proteins, with *purple* standing for large subunit protein and *yellow* standing for small subunit protein. *Red triangle* nodes stand for the proteins with no pathways in KEGG database. *Blue quadrangle* nodes stand for the non-ribosome proteins in KEGG database

the protein biosynthetic process. In order to verify the function of these proteins, we then matched all these proteins in module 128 to the pathways in KEGG database. The pathway composition of module 128 was shown in Fig. 87.3. In all the 49 proteins, 25 were ribosome proteins, which composed the core of this module, indicating that this module is a ribosome module. Ribosome is an important organelle in cell widely existing in most prokaryotic and eukaryotic organisms. The biological function of ribosome is accurately translating mRNA sequences into peptide chains [19]. It is exactly the gene expression and translation of proteins in the protein biosynthesis process, which is consistent with the function annotation of the proteins in this module. The ribosome in eukaryotic organisms was composed of large subunit and small subunit, which contains 49 and 33 kinds of ribosome proteins. In the 25 identified ribosome proteins in ribosome module, 19 were identified as large subunits and 6 were small subunits. In addition, 24 other candidate ribosome proteins were annotated in this module. Therefore, the function annotation of module 128 shows the protein translation capability contained in the *E. sinensis* PIN as well as providing important candidate proteins to be studied in the further in vivo experiment.

Conclusion

As PIN supplies a comprehensive relationship network of proteins, the functions of unknown proteins in the network can be predicted based on these relationships. In this work, we predicted the functions of 677 previously unknown proteins in *E. sinensis* PIN, which accounts for 93 % of all the unknown proteins in the network. The function annotations can be used as important guidance for the further investigation by biological experiment. In addition, the function annotation of modules also showed the biological capability of the *E. sinensis* PIN.

Acknowledgments This work was supported by National High-Tech Research and Development Program of China (863 programs, 2012AA10A401 and 2012AA092205), Grants of the Major State Basic Research Development Program of China (973 programs, 2012CB114405), National Natural Science Foundation of China (21106095, 61100124), National Key Technology R&D Program (2011BAD13B07 and 2011BAD13B04), Foundation of Introducing Talents to Tianjin Normal University, the Tianjin Research Program of Application Foundation and Advanced Technology (15JCYBJC30700), Project of introducing a thousand high level talents in three years and "131" Innovative Talents cultivation of Tianjin.

References

1. Zhang Y, Sun Y, Liu Y, Geng X, Wang X, Wang Y, Sun J, Yang W (2011) Molt-inhibiting hormone from Chinese mitten crab (Eriocheir sinensis): cloning, tissue expression and effects of recombinant peptide on ecdysteroid secretion of YOs. Gen Comp Endocrinol 173:467–474
2. Yu AQ, Jin XK, Guo XN, Li S, Wu MH, Li WW, Wang Q (2013) Two novel Toll genes (EsToll1 and EsToll2) from Eriocheir sinensis are differentially induced by lipopolysaccharide, peptidoglycan and zymosan. Fish Shellfish Immunol 35:1282–1292
3. Yanhua Wang YZ, Sun Y, Liu Y, Geng X, Sun J (2013) Cloning and molecular structure analysis of crustacean hyperglycemic hormone (Ers-CHH) in Eriocheir sinensis. J Fish China 37:987–993
4. Li X, Cui Z, Liu Y, Song C, Shi G (2013) Transcriptome analysis and discovery of genes involved in immune pathways from hepatopancreas of microbial challenged mitten crab Eriocheir sinensis. PLoS One 8:e68233
5. Hao T, Zeng Z, Wang B, Zhang Y, Liu Y, Geng X, Sun J (2014) The protein-protein interaction network of eyestalk, Y-organ and hepatopancreas in Chinese mitten crab Eriocheir sinensis. BMC Syst Biol 8
6. Mosca R, Pons T, Ceol A, Valencia A, Aloy P (2013) Towards a detailed atlas of protein-protein interactions. Curr Opin Struct Biol 23(6):929–940
7. Chen B, Fan W, Liu J, Wu FX (2014) Identifying protein complexes and functional modules from static PPI networks to dynamic PPI networks. Brief Bioinform 15(2):177–194
8. Navlakha S, Gitter A, Bar-Joseph Z (2012) A network-based approach for predicting missing pathway interactions. PLoS Comput Biol 8:e1002640
9. Zeng E, Ding C, Narasimhan G, Holbrook SR (2008) Estimating support for protein-protein interaction data with applications to function prediction. Comput Syst Bioinformatics Conf 7:73–84
10. Guruharsha KG, Rual JF, Zhai B, Mintseris J, Vaidya P, Vaidya N, Beekman C, Wong C, Rhee DY, Cenaj O, McKillip E, Shah S, Stapleton M, Wan KH, Yu C, Parsa B, Carlson JW, Chen X, Kapadia B, VijayRaghavan K, Gygi SP, Celniker SE, Obar RA, Artavanis-Tsakonas S (2011) A protein complex network of Drosophila melanogaster. Cell 147:690–703
11. Kuhner S, van Noort V, Betts MJ, Leo-Macias A, Batisse C, Rode M, Yamada T, Maier T, Bader S, Beltran-Alvarez P, Castano-Diez D, Chen WH, Devos D, Guell M, Norambuena T, Racke I, Rybin V, Schmidt A, Yus E, Aebersold R, Herrmann R, Bottcher B, Frangakis AS, Russell RB, Serrano L, Bork P, Gavin AC (2009) Proteome organization in a genome-reduced bacterium. Science 326:1235–1240
12. Hu P, Janga SC, Babu M, Diaz-Mejia JJ, Butland G, Yang W, Pogoutse O, Guo X, Phanse S, Wong P, Chandran S, Christopoulos C, Nazarians-Armavil A, Nasseri NK, Musso G, Ali M, Nazemof N, Eroukova V, Golshani A, Paccanaro A, Greenblatt JF, Moreno-Hagelsieb G, Emili A (2009) Global functional atlas of Escherichia coli encompassing previously uncharacterized proteins. PLoS Biol 7:e96
13. Schwikowski B, Uetz P, Fields S (2000) A network of protein-protein interactions in yeast. Nat Biotechnol 18:1257–1261

14. Kim KK, Kim HB (2009) Protein interaction network related to Helicobacter pylori infection response. World J Gastroenterol 15:4518–4528
15. Marchadier E, Carballido-Lopez R, Brinster S, Fabret C, Mervelet P, Bessieres P, Noirot-Gros MF, Fromion V, Noirot P (2011) An expanded protein-protein interaction network in Bacillus subtilis reveals a group of hubs: exploration by an integrative approach. Proteomics 11:2981–2991
16. Uetz P, Giot L, Cagney G, Mansfield TA, Judson RS, Knight JR, Lockshon D, Narayan V, Srinivasan M, Pochart P, Qureshi-Emili A, Li Y, Godwin B, Conover D, Kalbfleisch T, Vijayadamodar G, Yang M, Johnston M, Fields S, Rothberg JM (2000) A comprehensive analysis of protein-protein interactions in Saccharomyces cerevisiae. Nature 403:623–627
17. Yu H, Braun P, Yildirim MA, Lemmens I, Venkatesan K, Sahalie J, Hirozane-Kishikawa T, Gebreab F, Li N, Simonis N, Hao T, Rual JF, Dricot A, Vazquez A, Murray RR, Simon C, Tardivo L, Tam S, Svrzikapa N, Fan C, de Smet AS, Motyl A, Hudson ME, Park J, Xin X, Cusick ME, Moore T, Boone C, Snyder M, Roth FP et al (2008) High-quality binary protein interaction map of the yeast interactome network. Science 322:104–110
18. Rual JF, Venkatesan K, Hao T, Hirozane-Kishikawa T, Dricot A, Li N, Berriz GF, Gibbons FD, Dreze M, Ayivi-Guedehoussou N, Klitgord N, Simon C, Boxem M, Milstein S, Rosenberg J, Goldberg DS, Zhang LV, Wong SL, Franklin G, Li S, Albala JS, Lim J, Fraughton C, Llamosas E, Cevik S, Bex C, Lamesch P, Sikorski RS, Vandenhaute J, Zoghbi HY et al (2005) Towards a proteome-scale map of the human protein-protein interaction network. Nature 437:1173–1178
19. Garrido C, Brunet M, Didelot C, Zermati Y, Schmitt E, Kroemer G (2006) Heat shock proteins 27 and 70: anti-apoptotic proteins with tumorigenic properties. Cell Cycle 5:2592–2601

Chapter 88
MNetDec: A Flexible Algorithm for Metabolic Network Decomposition

Tong Hao, Bin Wang, Ailing Yu, Anan Liu, and Jinsheng Sun

Abstract Relevant modules of a metabolic network can reveal the underlying structure of the metabolic system and hence provide the insight into its function. Modularity is a useful standard for decomposing a complex network. However, it has been shown that simply optimizing modularity failed to find the most natural community structure by overpartition or under partition the network. Here, a novel network decomposition algorithm, called MNetDec, is proposed by integrating the dendrogram and modularity features of a metabolic network. By dealing with MNetDec, the small modules with questionable biological function are eliminated. Moreover, the size of the smallest module and final number of the modules in the decomposition result can be flexibly set by the users based on their own specific needs. The application of this algorithm on brain specific human metabolic network shows that MNetDec can generate biological reasonable modules with high modularity.

Keywords Metabolic network • Decomposition • Modularity • Dendrogram

88.1 Introduction

In recent years, there has been a surge of interest in the analysis of complex systems as networks. The literature is extensive, spanning areas as diverse as gene regulation, protein interaction and metabolic network, social networks or engineering

T. Hao • B. Wang • A. Yu
Tianjin Key Laboratory of Animal and Plant Resistance/College of Life Science, Tianjin Normal University, Tianjin 300387, P. R. China

A. Liu
School of Electronic Information Engineering, Tianjin University, Tianjin 300072, China

J. Sun (✉)
Tianjin Key Laboratory of Animal and Plant Resistance/College of Life Science, Tianjin Normal University, Tianjin 300387, P. R. China

Tianjin Aquatic Animal Infectious Disease Control and Prevention Center, Tianjin 300221, China
e-mail: jinshsun@163.com

J. Mu et al. (eds.), *The Proceedings of the Third International Conference on Communications, Signal Processing, and Systems*, Lecture Notes in Electrical Engineering 322, DOI 10.1007/978-3-319-08991-1_88

systems [1, 2]. Due to the large-scale, complex nature of many systems under study, an appealing idea is to obtain relevant modules of the network (also called partitions or communities) that can reveal the underlying structure of the system and hence provide the insight into its function [3]. Compared to other methods, modularity does not require the number of communities to be specified in advance. However, it has been shown that optimizing modularity can overpartition or underpartition the network, failing to find the most natural community structure [4]. Besides, the algorithm depends on modularity such as the simulated annealing algorithm [5, 6] is always time consuming due to the huge computational complexity.

Dendrogram is another important feature to investigate the structure of biological network, which shows the overall evolution of the network [7]. Hierarchical clustering organizes objects into a dendrogram whose branches are the desired modules [8]. The process of module detection is referred to as dendrogram tree cutting, branch cutting or branch pruning. However, the cutting level of dendrogram often poses a challenge to cluster definition [9]. In addition, the state-of-the-art decomposition methods [10–13] commonly produce some very small modules with only few nodes which are questionable to represent a biological function. These small modules trouble the further functional analysis of the metabolic network.

In this work a novel network decomposition algorithm, called MNetDec, is proposed. It integrates dendrogram and modularity features of a metabolic network. A network is firstly decomposed into a dendrogram and then further optimized based on the size of module and the modularity of the network. Another advantage of this algorithm is that it costs little computational complexity. Furthermore, the application of MNetDec on a brain specific human metabolic network verified that the modules generated by this algorithm are biological reasonable and well partitioned into different groups with relative independent functions.

88.2 Methods

88.2.1 Decomposition Based on Dendrogram Tree

A network was firstly decomposed into a dendrogram based on the topological structure: It was transformed to be an undirected network firstly. The shortest path length matrix of a network was calculated. Then a dendrogram tree was generated based on the average/UPGMA algorithm. Subsequently, the dendrogram tree was searching downwards from root to each branch for identifying the proper modules. An experienced threshold (threshold 1) for the maximal size of modules can be set by the users. When the number of leaves in a branch is less than the threshold, the leaves in that branch was outputted as an isolated module. Such searching was executed from left to right and from top to bottom of the tree to obtain a preliminary decomposition result with vertices in each module less than threshold 1.

88.2.2 First Step of Refinement

The preliminary decomposition result usually contains some very small modules with only few nodes, which have questionable biological function or even isolated leave nodes in the tree. Therefore an optimization was needed to combine those small modules into other modules. Firstly, a threshold (threshold 2) for the maximal number of nodes in the small modules can be set by the users. Then we searched in all the other modules with more nodes than threshold 2 in the preliminary decomposition to find a proper module which can be combined with the small ones. Generally, the small module was combined with the module having most boundary edges with it. Whereas when a small module connected to two or more modules with the same boundary edges, it is combined with the one with fewer/fewest number of nodes. As a result of this optimization, all the small modules with number of nodes below threshold 2 were combined with other modules in the network. Thus, the small modules with questionable biological function are eliminated.

88.2.3 Second Step of Refinement

The second step of refinement is the optimization of network modularity. For each module (module A), when it is combined with one of its connected module, the modularity change (ΔQ) of the network was defined as following:

$$\Delta Q = e_{ij} + e_{ji} - 2a_i a_j = 2\left(e_{ij} - a_i a_j\right) \tag{88.1}$$

In which e_{ij} is one-half of the fraction of edges in the network that connect vertices in module i to those in module j. a_i is the fraction of all ends of edges that are attached to vertices in group i. We can calculate a_i straightforwardly by noting that $a_i = \sum_j e_{ij}$. The ΔQ of module A and each of its connected modules were calculated respectively. The module with largest positive ΔQ was considered to be the best candidate (module B) that can be combined with. Then module A and B were combined to be one module. After each combination, a new module list was generated and the search restarts from the very beginning again. A threshold (threshold 3) for the final number of modules can be set by the users as the end of the iterative calculation. Otherwise the iteration will be executed successively until the number of modules decreased to be 1.

88.3 Application on Brain Specific Human Metabolic Network

We applied MNetDec to the brain specific Human Metabolic Network constructed by Tong Hao et al. [14]. Before the decomposition, some pretreatments were needed to transform the metabolic network into a reaction graph. Firstly, to focus on the main metabolites flow in the metabolic network, the misleading currency metabolites were removed and the metabolite links in the network were obtained with the method Ma and Zeng have developed [15]. A directed arc from reaction node A to reaction node B is added if the product of reaction A is the substrate of B. If there are two directed links from A to B and from B to A respectively, the two links were combined as an undirected edge. In this way the metabolic network was represented as a directed reaction graph, whose nodes are reactions and arcs/edges are metabolites which connect reactions [16]. As a result, we obtained a directed reaction graph with 1,500 vertices, 2,196 directed arcs and 947 undirected edges. Then the reaction graph was decomposed into 74 weak connected components (WCC) with most of the WCC contains less than 10 nodes (Fig. 88.1a). The biggest WCC contains 872 vertices which takes 58 % nodes in the network.

As the other WCCs were too small to be further decomposed, MNetDec was applied to the biggest WCC from brain specific network. The dendrogram tree of the biggest WCC is shown in Fig. 88.1b. Threshold 1 for the maximal size of the modules in the preliminary decomposition was set to be 50, and 45 modules were obtained based on the dendrogram (Fig. 88.1c). In the refinement of the decomposition, threshold 2 was set to be 10. Thirteen small modules were found and combined with other modules (Fig. 88.1d). Then the final number of modules (threshold 3) was set to be 20 and the decomposition result is shown in Fig. 88.1e. The parameters and result of the three-step decomposition and links between and within modules were listed in Table 88.1. It can be seen that the number of links within modules has been increased, but that between modules has been decreased after two-step refinement. The modularity of the network is also increased, which indicates that the structure of the modules is optimized on the point of topological view.

To verify the biological function of the modules obtained by MNetDec, we analyzed the metabolic subsystem distribution of all the WCCs and final 20 modules (Fig. 88.2). The metabolic subsystems are obtained from KEGG database [17]. As it is shown in Fig. 88.2, most biological functions concentrate in the biggest WCC and most of the modules generated by MNetDec contains no more than three metabolic functions. Each module is dominated by one metabolic function. It can also been see in Fig. 88.2 that the neural signal metabolites metabolism takes large proportion in the brain metabolic network as well as the basic metabolism such as lipid, amino acid, nucleotide and carbohydrate metabolism, which is in consistent with the main function of human brain—nerve centre and signal transduction. In addition, Different modules in Fig. 88.2 represent relative independent function. For example, for the same lipid metabolism, module 1 mainly focuses on the de novo synthesis of

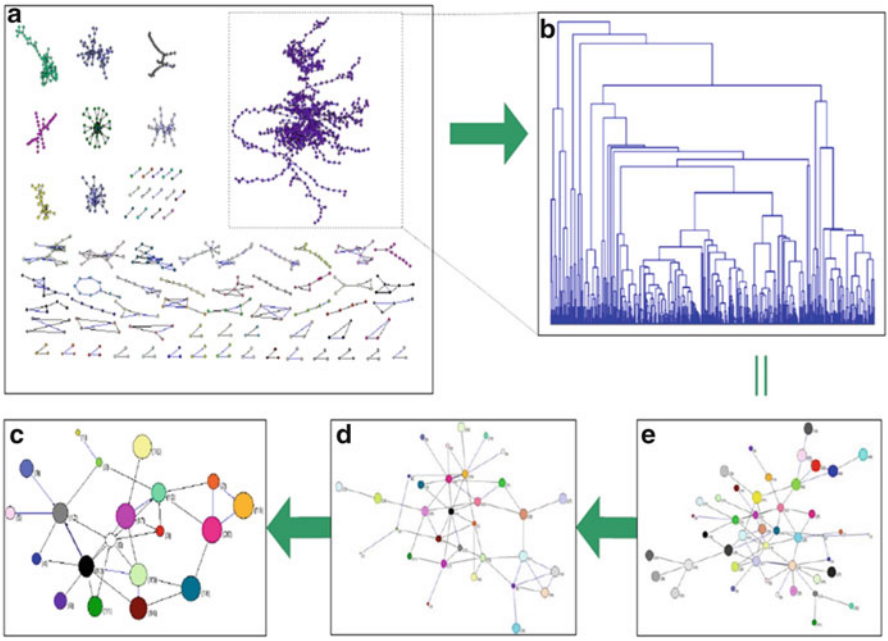

Fig. 88.1 the result of three-step decompositions. (**a**) Brain specific metabolic network; (**b**) dendrogram tree of the biggest WCC; (**c**) preliminary decomposition based on dendrogram; (**d**) result of first-step refinement; (**e**) result of second-step refinement

Table 88.1 The decomposition parameters and results of the biggest WCC in brain metabolic network

	Threshold	Clusters	Link in clusters	Link between clusters	Modularity
Preliminary	50	45	1,709	203	0.847683
First refinement	10	32	1,726	186	0.852279
Second refinement	20	20	1,786	126	0.861626

fatty acids; module 2 mainly represents the β-oxidation of monounsaturated fatty acid; reactions in module 3 mostly distributed in the β-oxidation of polyunsaturated fatty acid and glyceryl phosphatide metabolism; module 10 is the arachidonic acid metabolism and module 16 represents the glycosylsphingolipid synthesis.

On the other hand, since the reactions with similar functions were inclined to be classified into the same module, the topological structure may indicate the close relationship between different metabolisms which were grouped into one module. For example, module 4 contains all the reactions in neural signal metabolites metabolisms and the reactions have closed relationship with neural signal metabolites metabolisms. The central carbon metabolism distributed in several different modules (11, 12, 13, 14, 15, 17) interacting with many the other metabolisms,

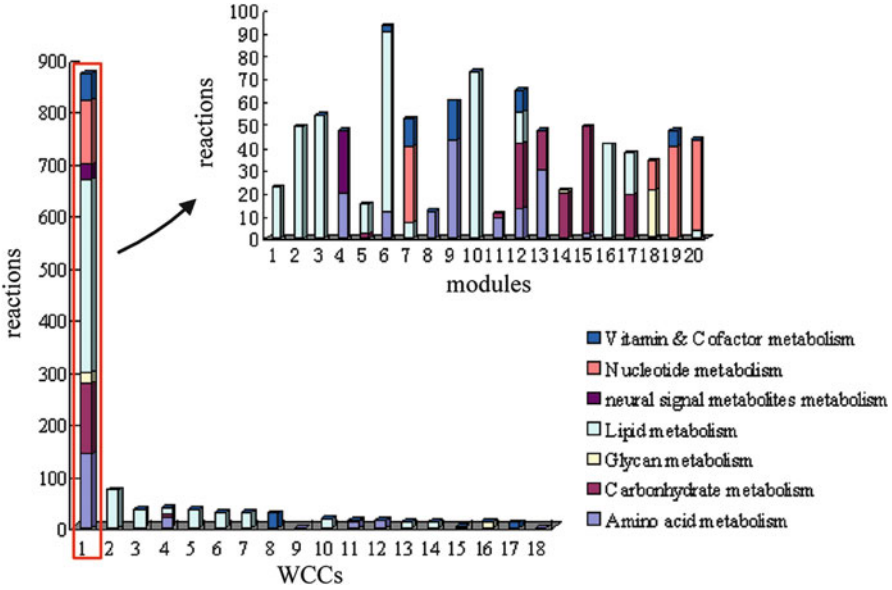

Fig. 88.2 Function distribution of WCCs and modules in brain specific metabolic network

which is agree with its diversity. Thus, the function distribution of the modules reveals the reasonable biological meaning of the network decomposition. It is interesting that vitamin and cofactor metabolism is strongly intent to be coupled with nucleotide, amino acid and glycan metabolism, which may indicate the essential role of vitamins and cofactors in these metabolisms.

Conclusion

In this work a novel decomposed algorithm MNetDec was proposed. This method integrated dendrogram and modularity features of the biological metabolic network. The flexibility of MNetDec is reflected in the fact that the initial number of modules in the preliminary decomposition, the maximal number of nodes in the smallest module and the final number of modules can all be set by the users based on their own specific needs. The application of MNetDec on brain specific human metabolic network produces a reasonable functional classification. Therefore, the generated modules with reasonable biological functions can benefit the further functional and structural analysis of metabolic networks.

Acknowledgements This work was supported by National High-Tech Research and Development Program of China (863 programs, 2012AA10A401 and 2012AA092205), Grants of the Major State Basic Research Development Program of China (973 programs, 2012CB114405), National Natural Science Foundation of China (21106095, 61100124), National Key Technology R&D Program (2011BAD13B07 and 2011BAD13B04), Foundation of Introducing Talents to

Tianjin Normal University, the Tianjin Research Program of Application Foundation and Advanced Technology (15JCYBJC30700), Project of introducing a thousand high level talents in three years and "131" Innovative Talents cultivation of Tianjin.

References

1. Strogatz SH (2001) Exploring complex networks. Nature 410(6825):268–276
2. Delvenne JC, Yaliraki SN, Barahona M (2010) Stability of graph communities across time scales. Proc Natl Acad Sci U S A 107(29):12755–12760
3. Fortunato S, Barthelemy M (2007) Resolution limit in community detection. Proc Natl Acad Sci U S A 104(1):36–41
4. Newman ME (2004) Fast algorithm for detecting community structure in networks. Phys Rev E Stat Nonlin Soft Matter Phys 69(6 Pt 2):066133
5. Guimera R, Sales-Pardo M, Amaral LA (2004) Modularity from fluctuations in random graphs and complex networks. Phys Rev E Stat Nonlin Soft Matter Phys 70:025101
6. Guimera R, Nunes Amaral LA (2005) Functional cartography of complex metabolic networks. Nature 433:895–900
7. Lee H, Kang H, Chung MK, Kim BN, Lee DS (2012) Persistent brain network homology from the perspective of dendrogram. IEEE Trans Med Imaging 31(12):2267–2277
8. Narayanan T, Gersten M, Subramaniam S, Grama A (2011) Modularity detection in protein-protein interaction networks. BMC Res Notes 29(4):569
9. Langfelder P, Zhang B, Horvath S (2008) Defining clusters from a hierarchical cluster tree: the Dynamic Tree Cut package for R. Bioinformatics 24(5):719–720
10. Newman ME, Girvan M (2004) Finding and evaluating community structure in networks. Phys Rev E Stat Nonlin Soft Matter Phys 69:026113
11. Clauset A, Newman ME, Moore C (2004) Finding community structure in very large networks. Phys Rev E Stat Nonlin Soft Matter Phys 70:066111
12. Newman ME (2006) Finding community structure in networks using the eigenvectors of matrices. Phys Rev E Stat Nonlin Soft Matter Phys 74:036104
13. Pascal Pons ML (2005) Computing communities in large networks using random walks. Comput Sci 3733:284–293
14. Hao T, Ma HW, Zhao XM, Goryanin I (2010) Compartmentalization of the Edinburgh human metabolic network. BMC Bioinformatics 11:393
15. Ma HW, Zeng AP (2003) Reconstruction of metabolic networks from genome data and analysis of their global structure for various organisms. Bioinformatics 19(2):270–277
16. Ma HW, Zhao XM, Yuan YJ, Zeng AP (2004) Decomposition of metabolic network into functional modules based on the global connectivity structure of reaction graph. Bioinformatics 20(12):1870–1876
17. Kanehisa M, Goto S (2000) KEGG: Kyoto encyclopedia of genes and genomes. Nucleic Acids Res 28:27–30

Chapter 89
Throat Polyp Detection Based on the Neural Network Classification Algorithm

Shan Qin, Baoju Zhang, Wei Wang, and Sijie Cheng

Abstract This paper realizes the judgment that whether patients have throat polyp by normalization processing, principal component analyzing and Neural Network Classifying the extracted audio data. This implementation replaces the traditional approach to diagnosis of throat polyps. Conventional laryngoscopy need to cutout, clamp or puncture from the patient to remove the lesions to do pathological examinations, which is so hurt to the patient. The test for throat polyp prediction with the neural network classification algorithm are carried out. The results shows that the correct rate of prediction is stable under different number of samples and different random measurement matrices.

Keywords Principal component analysis • Neural network • Normalization

89.1 Introduction

Throat polyp detection is a field that demands more investigation. It is common to have throat polyps and to be completely unaware of them, particularly if they are fairly small. Traditionally, the methods of diagnosis are indirect laryngoscope, video-laryngoscope, and stroboscope light [1]. These polyps then break off and disappear inside the body or clear up by themselves. However, throat polyps can increase in size to the extent that they affect a person's ability to speak. Furthermore, most of these methods need special instrument, and mainly depend on the experience of the pathologists. Also, the patients will feel uncomfortable pain usually. It would be desirable if throat polyps could be detected based on the patient vowel voices only [2].

Traditional pattern recognition techniques such as Bayesian classifier, known as the optimal classifier, could be used if the voice samples follow certain distribution, and this belongs to model-based statistical processing. In [3], the statistical characteristic root-mean square-delay spread and standard deviation were employed to

S. Qin (✉) • B. Zhang • W. Wang • S. Cheng
College of Electronic and Communication Engineering, Tianjin Normal University, Tianjin, China
e-mail: videolab@163.com

J. Mu et al. (eds.), *The Proceedings of the Third International Conference on Communications, Signal Processing, and Systems*, Lecture Notes in Electrical Engineering 322, DOI 10.1007/978-3-319-08991-1_89

describe the speech frequency domain characteristic and used as two antecedents. The Fuzzy logic system was used to make polyp patients' diagnosis. The results demonstrated that the proposed method could detect the throat polyps with low prob-48 ability of miss detection and 0 % false alarm rate. In [4], some methods of speech analysis for the diagnosis of the laryngeal function have been discussed. In humans' voices, the voice amplitude is highly bursty, and we believe that no statistical model can really demonstrate the uncertain nature of the voice [5].

Because of the complexity and unpredictability of voice, the data and information in many aspects, such as analysis, making discissions are non linear connection and complex. As an important branch of artificial intelligence, Neural network implements a mapping function from the input to the output, which is proved by mathematical theory that three layer neural network can approximate any nonlinear continuous function with arbitrary precision [6]. This makes it particularly suitable for solving complex problems, namely that has strong nonlinear mapping ability.

This paper builds a BP neural network, which realizes the judgment that whether patients have throat polyp. Some popular industry technologies, including normalization processing, principal component analyzing and neural network classifying are appropriately combined.

89.2 Theory

89.2.1 Principal Component Analysis

There are random variables $X_1, X_2, \ldots, X_p$, whose standard deviations of the sample is recorded as $S_1, S_2, \ldots, S_p$. First, standardization transformation is $C_j = a_{j1 \times 1} + a_{j2 \times 2} + \ldots + a_{jp \times p}$, $j = 1, 2, \ldots, p$. We have the following definitions:

If $C_1 = a_{11 \times 1} + a_{12 \times 2} + \ldots + a_{1p \times p}$, and $\mathrm{Var}(C_1)$ is the biggest, C_1 is called the first principal component;

If $C_2 = a_{21 \times 1} + a_{22 \times 2} + \ldots + a_{2p \times p}$, and $(a_{21}, a_{22}, \ldots, a_{2p})$ perpendicular to the $(a_{11}, a_{12}, \ldots, a_{1p})$, and $\mathrm{Var}(C_2)$ is the biggest, C_2 is called the second principal component;

Similarly, there is a third, fourth, fifth ... the main ingredient, and at most p points.

Principal component analysis is a statistical approach allows to reduce the dimensionality, which is implemented by an orthogonal transformation translating the related component of the original random vector into uncorrelated components of new random vector. On the respect of algebra, it means that the covariance matrix of original random vector is transformed into a diagonal matrix. In geometry, it means that the original coordinate system is transformed into a new orthogonal coordinate system, which point to the P orthogonal directions of the

sample points that spread most open. Then, the multidimensional variable system will reduce the dimension [7]. The math algorithm is as follows.

P dimensional random vectors of standard collection of the original data is $x = (x_1, x_2, \ldots, x_p)^T$, n samples is $x_i = (x_{i1}, x_{i2}, \ldots, x_{ip})^T, i = 1, 2, \ldots, n$

When $n > p$, construct the sample matrix, and make the standard transformation to the sample array element as follows:

$$Z = \frac{x_{ij} - \overline{x}_j}{s_j}, i = 1, 2, \ldots, n; j = 1, 2, \ldots, p \tag{89.1}$$

$$\overline{x}_j = \frac{\sum_{i=1}^{n} x_{ij}}{n}, s^2 j = \frac{\sum_{i=1}^{n} \left(x_{ij} - \overline{x}_j\right)^2}{n-1} \tag{89.2}$$

and the standardization matrix is Z.

Second, demand the correlation coefficient matrix of Z.

$$R = \left[r_{ij}\right]_p \; xp = \frac{Z^T Z}{n-1} \tag{89.3}$$

$$r_{ij} = \frac{\sum z_{kj} \cdot z_{kj}}{n-1}, i, j = 1, 2, \ldots, p \tag{89.4}$$

Third, demand the characteristic equation of sample correlation matrix R, which is $|R - \lambda I_p| = 0$, have p characteristic roots to determine the main ingredient. Then, according to $\frac{\sum_{j=1}^{m} \lambda_j}{\sum_{j=1}^{p} \lambda_j} \geq 0.85$ to determine the value of m, and ensure the utilization rate of information is more than 85 %, Solution of equations, $Rb = \lambda_j b$, for each λ_j, $j = 1, 2, \ldots, m$, get the unit eigenvector b_j^o.

Last, conversion the normalized indicator variables to main component $U_{ij} = z_i^T b_j^o, j = 1, 2, \ldots, m$, U_1 is the first main ingredient.

89.2.2 Neural Network Algorithm

Artificial neural network has the characteristics of self-adaption, self-organization and self-learning. It is already well known that an ANN consists of a number of artificial neurons and connections among them. An artificial neuron is generally regarded as a nonlinear device with multiple inputs and a single output. An ANN model is shown in Fig. 89.1.

Where $x_n(t)$ is the output of the n - th neuron at time t which is also the n - th input to the i - th neuron at the same time, w_{in} is the weight representing the connection strength between the n - th and i - th neuron, net(t) is the net total input to the i - th neuron at time t, $a_i(t)$ is the activation of the i - th neuron at time t which is a function

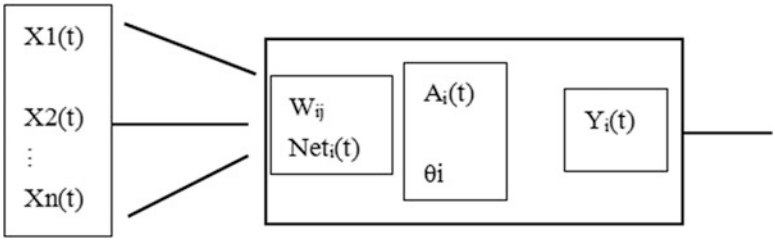

Fig. 89.1 An ANN mode

of $net_i(t)$, θ_i is the threshold of the i - th neuron, and $y_i(t+1)$ is the output which is a nonlinear function of $a_i(t)$ and θ_i, as shown in Eqs. 89.5, 89.6, and 89.7 respectively [8].

$$net_i(t) = \sum_{n=1}^{N} W_{in} x_n(t) \tag{89.5}$$

$$a_i(t) = g(net_i(t)) \tag{89.6}$$

$$y_i(t+1) = f(a_i(t), \theta_i) \tag{89.7}$$

BP neural network algorithm is the most widely used, which is based on the error back propagation to adjust the network weights and thresholds constantly, and establishes a network with the minimum of sum of squared errors. Actually, the data flow information is positive, but the error propagation is reversed [9].

89.3 Experiment and Simulation

MATLAB is a useful industrial, educational and research tool, which can enough to help users find what can be done and what not to do, which can help develop and broaden the field of neural networks work. In this lab, each person has two sound samples, /a:/and /i:/. In MATLAB, the function of premnmx is used to normalize the original data between −1 and 1, and the function of princomp is used to extract the characteristic values. We take five characteristic values from /a:/and /i:/ sample of each person in a column as one input of net. There are 18 training samples, and 15 testing samples [10].

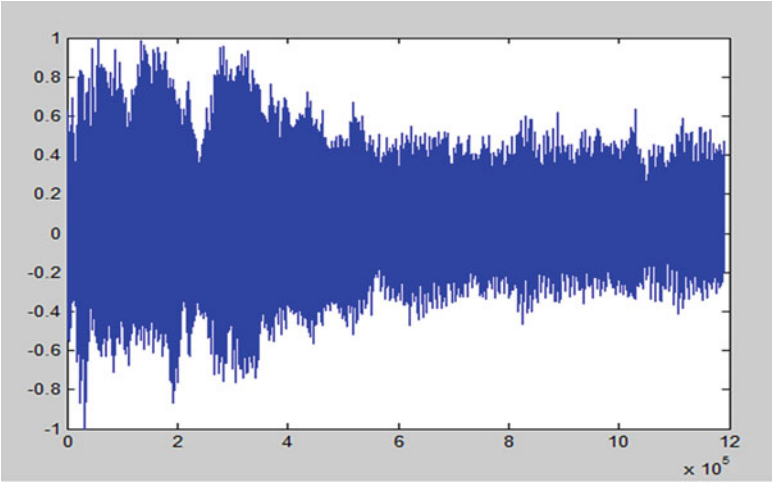

Fig. 89.2 The data distribution of data normalization

89.3.1 The Result of Experiment

89.3.1.1 The Result of the Data Normalization

The main idea of data normalization is to define the data within a fixed range, by setting up a normalization factor, which is subtracted by the original data, and at same time, to eliminate systematic errors in the experimental data. In this experiment, the collected data samples of voice normalized between −1 and 1. The normalized data will be very convenient, and ensure a faster convergence during running programs in subsequent processing. Figure 89.2 is a sample in which the data distribution of data normalization.

89.3.1.2 The Result of Principal Component Analysis

In the samples, the original data is a matrices of n rows and 1 column, after matrix deformation, they become a matrix of m rows and 100 columns. Principal component analysis was performed on the raw data, and we get the triangular matrix of 100 rows and 100 columns and achieve the effect of reducing the dimensions. In the MATLAB, we can obtain the characteristics of each vector value directly.

Dimension reduction will cause a loss of information. However, the loss of information is rarely. Because the main part of the information is extracted. Figure 89.3 shows the main ingredients of one sample.

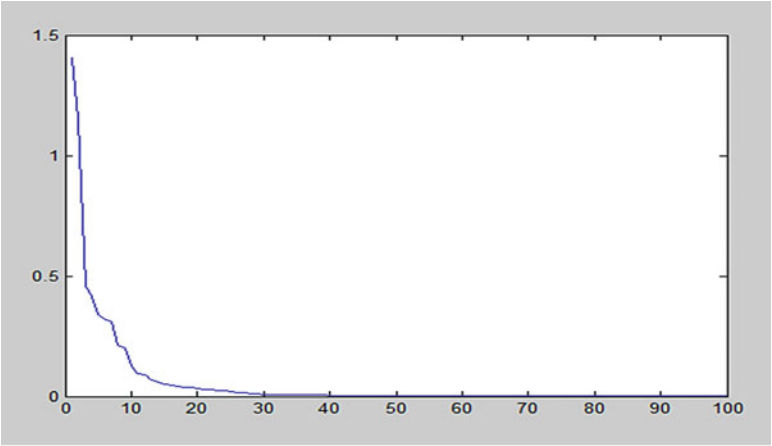

Fig. 89.3 The main ingredients of one sample

89.3.1.3 The Result of Neural Network Classifying

The experiment choose Back Propagation network algorithm, which is the most widely used. And learning rules is quasi-Newton method.

Compared with the standard steepest descent method, quasi-Newton method has a high convergence speed in the vicinity of the area closed to the optimal solution, and we can improve the learning speed of neural networks. In addition, iterative direction of Quasi-Newton method has conjugation, which has a limited secondary termination. In fact, this property is one of evaluation standards to judge a algorithm whether is good or bad. If a convergence algorithm does not have this property, then it would be difficult to have the super linear convergence speed.

The experiment uses eight-layer hidden layer. Increasing the number of layers can reduce the learning error and improve the training accuracy. But, network becomes complex, and training time of the network weights will be longer.

The expected outputs of training sample is [1,1,1,1,1,1,1,1,1,1,0,0,0,0,0,0,0,0], and the actual output is [0.9975, 0.9973, 0.9973, 0.9975, 0.9974, 0.9961, 0.9902, 0.9975, 0.9975, 0.9971, 0.0611, 0.0339,0.0200, 0.0560, 0.0339, 0.0339, 0.0129, −0.0103], in which illness output is 1, not illness output is 0. The result of training is shown in Figs. 89.4 and 89.5.

89.3.2 The Result of Simulation

There are 15 testing samples. The expected output is [1, 1, 1, 1, 1, 1, 1, 1, 1, 1, 0, 0, 0, 0, 0], and the real output is [0.9975 0.9975 0.9967 0.9797 0.0339 0.9975 0.0070 0.0273 0.9267 0.9975 0.9922 0.0069 0.9975 0.0345 0.3247]. The result is shown in Figs. 89.6 and 89.7.

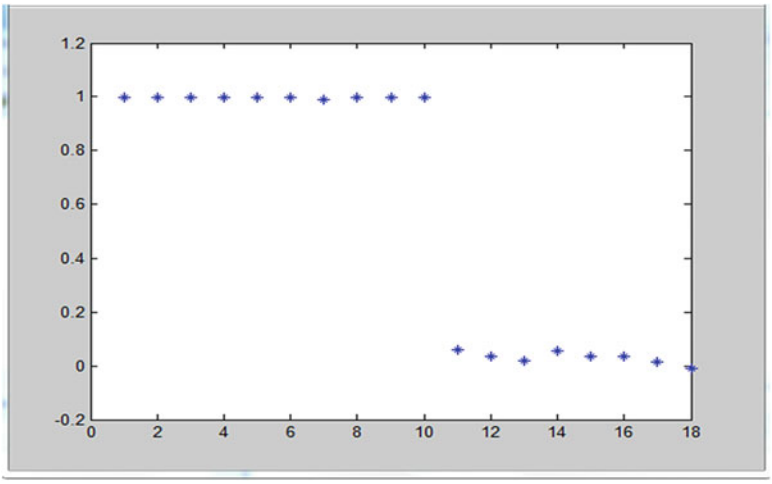

Fig. 89.4 The output of training

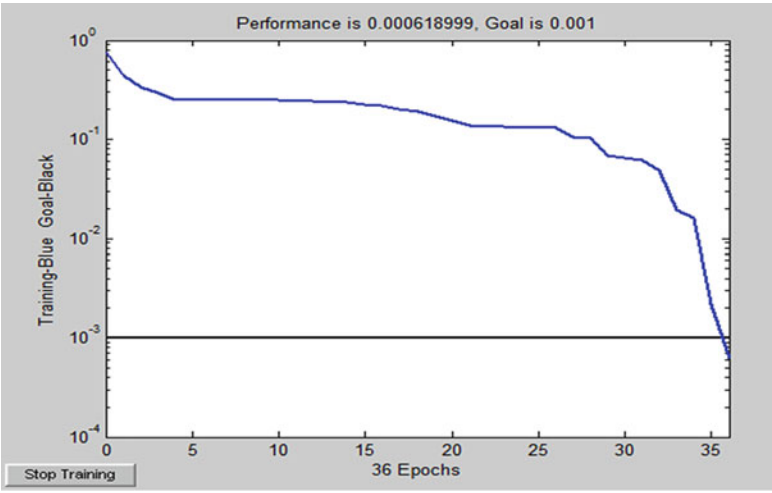

Fig. 89.5 The target error of training

89.3.3 Error Analysis

The results of simulation displays that the correct rate of prediction is believable under different number of samples and different random measurement matrices. By calculating, It can be drawn that the of the sick can reach 70 %, and the judgment accuracy of the health rate is up to 60 %. So, the judgment accuracy of wether is sick or health is about 67 %.

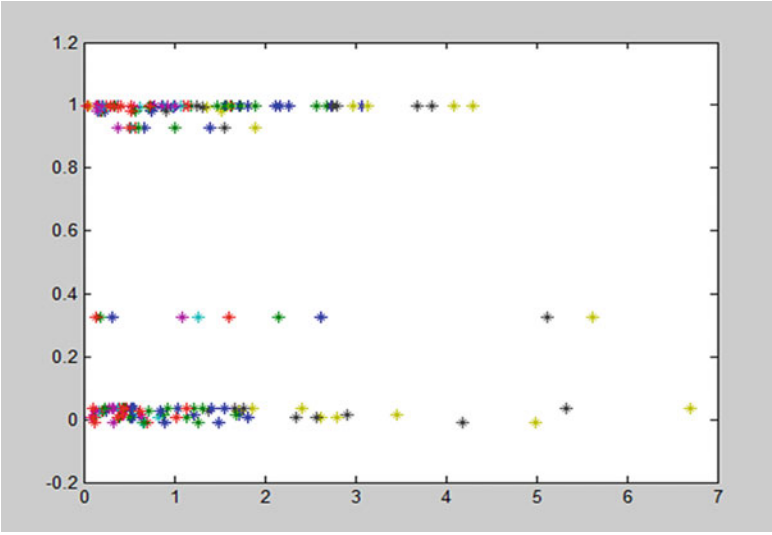

Fig. 89.6 The result of simulation of 10-dimensional

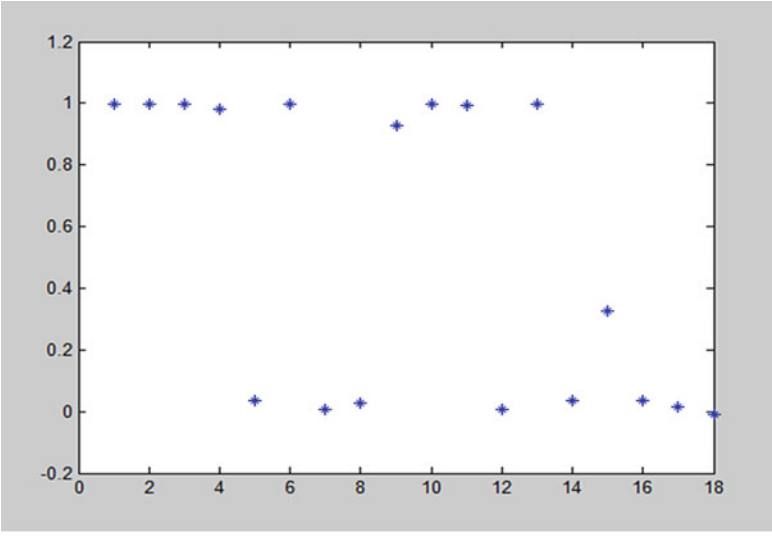

Fig. 89.7 The result of simulation of 1-dimensional

Conclusion

In this experiment, we analyze the data, extract its characteristic values, and then use the neural network learning to train the samples. We get the classification data. The simulation results of test samples are also ideal, indicating that the experiment can be replicated in reality to alleviate the pain of patients in the process of diagnosis.

The results shows that the correct rate of prediction is stable under different number of samples and different random measurement matrices. But However, more voice data should be sampled in order to reach a better diagnosis result, and the test accuracy still need to be improved by improved algorithm. We will continue to study in the future.

Acknowledgments This work was supported by National Natural Science Foundation of China (61271411), National Natural Science Foundation of China (61372097), and University Students' Innovative Training Program. This work is also supported by the University Students' Innovative Training Program.

References

1. Zhong Z, Chen Z, Liang Q, Xiao S (2012) Throat polyps detection based on patient voices. Lect Notes Electr Eng 202:531–539
2. Wei Wang, Zhangliang Chen, Jiasong Mu, Tingting Han (2014) Throat polyp detection based on compressed big data of voice with support vector machine algorithm. EURASIP J Adv Signal Process. doi:10.1186/1687-6180-2014-1
3. Zhong Z, Jiang T, Zhang WS, Yao H (2010) Analysis speech of polypus patients based on channel parameters and fuzzy logic systems. In: Proceedings of the 2010 seventh international conference on fuzzy systems and knowledge discovery, Yantai, pp 529–532
4. Choi JM, Sung MW, Park KS (2002) New method in acoustic analysis for the diagnosis of the laryngeal functions. Proc Second Jt EMBS/BMES Conf 10:135–136
5. Budhaditya S, Pham D-S, Lazarescu M, Venkatesh S (2009) Effective anomaly detection in sensor networks data streams. In: Ninth IEEE international conference on data mining, pp 722–727
6. Wei Wang et al (2014) Intelligent throat polyp detection with separable compressive sensing. EURASIP J Adv Signal Process 2014:6
7. Pham D-S, Venkatesh S, Lazarescu M, Budhaditya S (2012) Anomaly detection in large scale data stream networks. Data Min Knowl Discov. doi:10.1007/s10618-012-0297-3
8. Dardari D et al (2008) Threshold-based time of arrival estimators in UWB dense multipath channels. IEEE Trans Commun 56(8):1366–1378. doi:10.1109/TCOMM.2008.050551
9. Zhong yixin, Chi huisheng (1992) A survey of artificial neural networks. Acta Electron Sin 10:20–25
10. He qingbi, Hu jiuyong (2004) An overview of data mining. J Southwest Univ Natl 29:328–330

Chapter 90
Ridge-Slope-Valley Feature for Fingerprint Liveness Detection

Feng Wang, Jian Cheng, and Yan Jiang

Abstract Attacking fingerprint-based biometric systems by presenting fake fingers is a serious threat for unattended devices. In this work, we introduce a novel algorithm, by extracting features along the fingerprint curves, to discriminate between fake fingers and real ones on static images. Pairs of mean value and standard deviation are sampled from the ridge, slope and valley of the curves. Then bag-of-words model is used to select cluster centers and form a 128-dimension feature of words' frequency. We test our method on a dataset collected by Chinese Academy of Science, which contains 960 live fingerprints and 960 fake ones made by silicon. Though the fake fingerprints is too verisimilar to be distinguished by naked eyes, we still get an accuracy of 98.85 %. Because our method is based on single static fingerprint image, it can be freely embedded into existing fingerprint-based biometric systems.

Keywords Fingerprint liveness detection • Bag-of-words model • Image texture analysis.

90.1 Introduction

In recent years, fingerprint verification systems for personal identity recognition reached a high degree of accuracy. Unfortunately, as the ancient Chinese proverb says, while the priest climbs a post, the devil climbs ten, various of fake fingerprint molds have been developed to attack the biometric authentication system [1]. Materials of Play-Doh, gelatin, latex, silicone, and even the printed paper can pass some authentication systems. From a security and accountability perspective, fingerprint authentication systems should have the ability to detect when fake finger samples are presented. This requirement gives huge motivation for researchers to find effective method to discriminate fake fingers from real ones. One of the solution

F. Wang (✉) • J. Cheng • Y. Jiang
School of Electronic Engineering, University of Electronic Science and Technology of China, Chengdu, Sichuan, PR China
e-mail: feng.wff@gmail.com

J. Mu et al. (eds.), *The Proceedings of the Third International Conference on Communications, Signal Processing, and Systems*, Lecture Notes in Electrical Engineering 322, DOI 10.1007/978-3-319-08991-1_90

is to analyse the difference of the texture between real and fake fingerprint images. It is cheap, convenient and easy to be embedded in to a present fingerprint verification system.

Up to now, no obviously physical feature in static images has been found to provide a clear standard of judging the liveness of fingerprint. Some researchers did preliminary analyse in using statistical methods, such as power spectrum [2], wavelet [3–5], curvelet [6], fusion of multiple static feature [7]. Perspiration pattern and other noise in valley of fingers are widely considered to be a useful information [8–10], however, whether perspiration exists or not is more determined by the users, not the machine. Pores on the ridge are also extensively used pattern [7, 10], while the abraded fake fingers would not contain the tiny details.

Due to the speciality of the classification of live and fake fingerprint, that the direction of fingerprint curves change everywhere, an isotropous statistical method cannot get a satisfied performance. The useful but subtle information will be diluted with the high response of the magnitude difference of ridges and valleys. Moreover, the width of ridges and valleys mainly depends on the pressure of the users, so statistical features like whether black or white gray levels cannot be used as the basis of judgement.

To bypass the difficulty caused by variation of direction and width, some researchers started to extract features along the fingerprint curves. Derakhshani et al. [8] and Choi et al. [7] use a 1-D long signal on the ridges, and find that the 11–33 FFT points have considerable ability of discrimination. Tan and Schuckers [10] add signal samples from valleys, which denotes the perspiration and noise. Maybe because they intent to avoid the influence of the width, they only use the thinned skeletons of ridges and valleys, leaving the rest information from slopes apart. Furthermore, in a fingerprint of good quality, the valleys should be clean white, and the ridges are expected to be almost totally black except for pores. Whether the ridges and valleys have enough information are still in doubt.

In our approach, we use not only features extracted from ridges and valleys, but also from the slopes between them, which are ignored by most previous researchers. Unlike real human fingers, fake fingers made by silicon, gelatin and latex have smoother edges located between the ridges and valleys. With the fraying of the material, the smooth degree of the edges will be more prominent. Mathematically, signal sampled alone the slope of live fingers should have a higher variance compared with that from fake fingers. Utilizing this property, we designed our proposed method.

90.2 Algorithm

As we aim at gathering the subtle difference between live and fake fingerprint, it is suggested that *no* pre-processing should be taken on the fingerprint image, to preserve all the details captured by the hardware. Some pre-processing method,

e.g. histogram equalization, may enhance the fingerprint to a better visualization, but also simultaneously change the local distribution of pixel intensity.

Our algorithm contains the following procedures.

1. Partition the fingerprint image into 16 × 16 blocks. Calculate the directions of fingerprint curves in all blocks.
2. Generate sampling lines along the fingerprint curves. Each line collect three information: the pixel intensity distribution $\widehat{X}$, mean value $E[X]$ and standard deviation $Std[X]$.
3. Calculate the conditional distribution $P(\widehat{X}|E[X])$. Generate a filter that allows all $\widehat{X}$ with $P(\widehat{X}|E[X]) > 0.01$ pass the filter.
4. Use the filter to recalculate the $E[X]$ and $Std[X]$ of all sampling lines.
5. Execute k-means algorithm to get 128 cluster centers of all the 2D points ($E[X]$, $Std[X]$). By aggregating the frequency of each word, a 128-dimension feature is extracted to describe a fingerprint's texture.
6. kNN classifier is used to discriminate fake fingerprints from real ones.

90.2.1 Feature Extraction

The fingerprint is firstly partitioned into blocks of 16 × 16 pixels, in which the fingerprint ridge can be approximately treated as some straight lines of a certain direction. Ridge orientation is calculated using the method suggested in [11].

In each block, we define the ridge orientation as the y-direction, and the orthogonal orientation as the x-direction. Then a series of lines is generated, with width of 1 pixel and length of 16 pixels, parallel with the y-direction (Fig. 90.1a). Different from the method in [11], we introduce a over-sampling strategy: our lines are overlapped with the neighbors to get a more accurate ridge-valley envelope. The method to generate the lines can be Wu's antialiasing algorithm [12] or the overlapping area of the lines and the pixel grids (Fig. 90.1b). The method of overlapping area is strongly recommended because it is more similar to a sampling procedure.

Here, the intensity (0–1) of a pixel on the line is considered as the probability p_i, and the intensity of the pixel on the covered position of the fingerprint is considered as the magnitude x_i. The mean value and standard deviation on each sampling line can be calculated as:

$$E[X] = \frac{\sum_i p_i x_i}{\sum_i p_i} \tag{90.1}$$

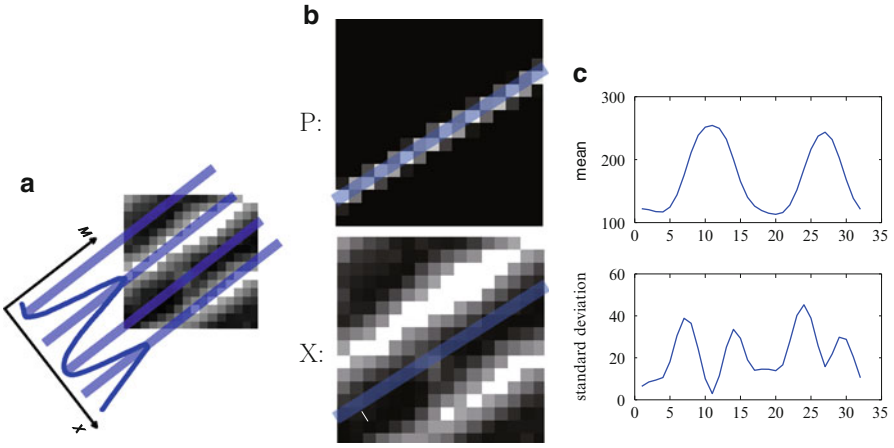

Fig. 90.1 (**a**) Four sampling lines and sampled mean value. (**b**) The method of overlapping area to generate a sampling line: pixels' intensity is defined by the overlapping area between pixels and the sampling line. $E[X]$ and $Std[X]$ can be calculated by simply multiplying the matrix P, X and X^2. (**c**) The sampled mean value and standard deviation from (**b**)

$$Std[X] = \sqrt{\frac{\sum_i p_i x_i^2 - \left(\sum_i p_i x_i\right)^2}{\sum_i p_i}} \tag{90.2}$$

where p_i denotes each pixel in line image P and x_i denotes each pixel in image block X. The mean values is one-to-one correspondence to the standard deviations (Fig. 90.1c).

When press on the fingerprint scanner, people always use different pressure with different parts of finger, which leads to asymmetrical local contrast. Here we normalize the $E[X]$ signal with the maximum and minimum values in 5×5 neighbour blocks[1] to eliminate this effect. Since $Std[X]$ is proportional to X, the same scale transform should be applied to $Std[X]$ in each block, too.

90.2.2 Noise Filter

In Sect. 90.2.1, we assume that the orientation of fingerprint curve is straight in each block. The assumption is quite precise in most blocks. However, it is not always correct, which leads to a bad performance. For example, in the middle of the fingerprint the curves are always like a circle. Moreover, at the edge of the finger

[1] The accuracies of different sizes of normalization window are illustrated in Fig. 90.4.

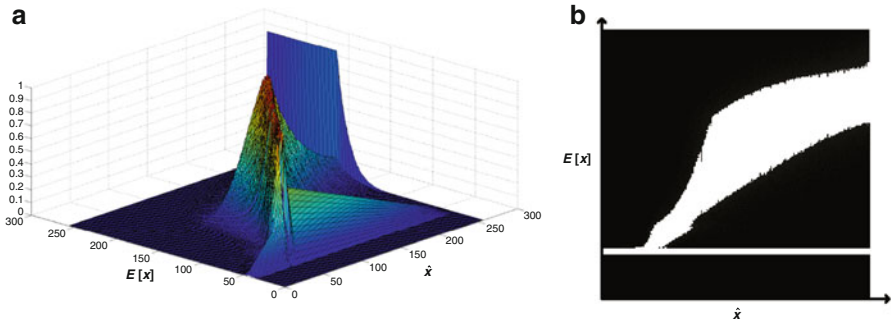

Fig. 90.2 (**a**) Normalized filter map $P(\widehat{X}|E[X])$. (**b**) Manually fixed filter matrix. The *white horizontal line* is where the pore pattern lies in

where the curves break, the sampling line will mistaken the blank pixels as useful information.

To fix these mistakes, we introduce a two-stage noise filter method. In the first stage, we generate the joint distribution of $\widehat{X}$ and $E[X]$ as $P(\widehat{X}|E[X])$. Under an assumption that the noise is much weaker than the useful signals, we design a filter to allow the signal with $P(\widehat{X}|E[X]) > 0.01$ pass only.

Notice that this filter can be modified arbitrarily. There are some obvious noises in the map. For example, in the middle levels of $E[X]$ (slope), there are too much X values of 255, which should be erased manually. Note that some of the areas with low $E[X]$ and high $\widehat{X}$ have considerable probability. These are the pores on the edge, so it is necessary to let all of them pass the filter. Finally, the prior map (or filter) is shown in Fig. 90.2b.

In the second stage, we calculate the $E[X]$ and $Std[X]$ again, using the filter matrix to filtering the noise out. This filter method is a big qualitative leap that increases the accuracy from about 89–98.85 %, and makes this algorithm to be one of the state-of-the-art algorithms.

90.2.3 Bag-of-Words Model and Feature Representation

One easiest method to represent the feature is to quantize the mean-standard deviation scatter to a grid, and use the frequency of each node as the feature.[2] This would cause a problem that some of the dimensions of the feature are always zero. On account of this phenomenon, we use bag-of-words model instead to avoid the waste of dimension.

[2] The result has also been illustrated in Fig. 90.4 labeled by "Grid Feature".

After the filter step, we collect all the pairs of mean value and standard deviation and use a 2D k-means algorithm to select 128 cluster centers ($k = 128$). We use the frequency of the appearance of the 128 words in one image as the feature.

To judge the ability to distinguish between the live and fake finger of each word, we modified the Fishers linear discriminant.

$$J(w_i) = \frac{|\mu_{live} - \mu_{fake}|}{\sqrt{\sigma_{live}^2 + \sigma_{fake}^2}} \tag{90.3}$$

where $\mu_{live}(\mu_{fake})$ and $\sigma_{live}^2(\sigma_{fake}^2)$ represent the mean and variance of the word w_i in the training live(fake) class. The word is considered to be enough distinctive to classify if $J(w_i) > 1$.

All the words and their ability of discrimination is shown in Fig. 90.3. It can be concluded from the plot that the ridge and slope patterns have better performance. However, the slope patterns have been ignored by researchers for a long time [7, 10].

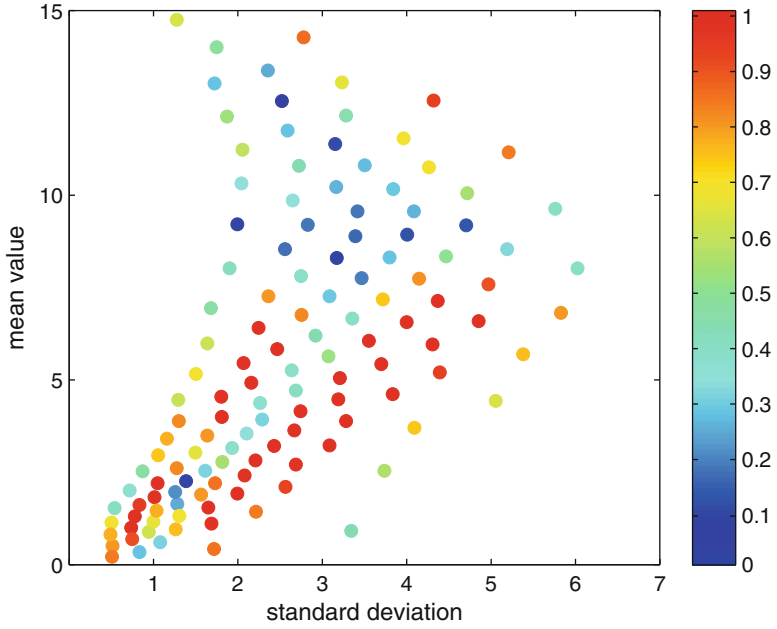

Fig. 90.3 Centers in bag-of-words model and the ability of discrimination of the words. All the words w_i with $J(w_i) > 1$ are colored by *red*, regarding that they have enough ability of discrimination

90.3 Experiment

We use *k*NN classifier to discriminate fake subjects from the live ones. It is almost the simplest classifier, with only one parameter k and one method to measure the distance from samples. One of the disadvantage of *k*NN classifier is the time and space complexity increase as the training set grows. We have also tested other classifier, such as SVM and random forest, they get about 4–5 % less classify rate than the *k*NN classifier. This may because we have not found the latent manifold of our feature.

Hellinger distance, ℓ 2 distance, KL-divergence is utilized to determine the distance between the features. As the result illustrated in Fig. 90.4, there are no apparent differences between the three distances.

The dataset is provided by Chinese Academy of Sciences [13]. It contains 960 fake fingerprint made by silicon and 960 corresponding live fingerprint. The fingerprints have been divided into two subsets, one for training and another for testing. To make our results more persuasive, we have also implemented some of other algorithms such as LBP [14], Choi's method [7] and Tan's method [10]. The recognition rate are listed in Table 90.1.

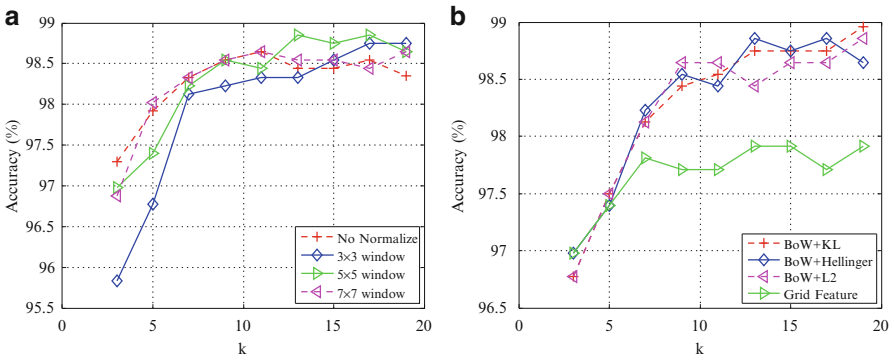

Fig. 90.4 (**a**) The affect of different sizes of the normalization window. (**b**) The recognition rate of different measurements of distance and the affect of various *k* in *k*NN. Note that the performance of "Grid Feature" mentioned in Sect. 90.2.3 is also displayed here. The results of more algorithms is listed in Table 90.1

Table 90.1 Recognition rate of different algorithms

BoW +KL	**Grid feature**	**No noise filter**	LBP [14]	Choi's method [7]	Tan's method [10]
98.85 %	97.92 %	89.17 %	91.75 %	79.167 %	85.52 %

The bold accuracy is the performance of our proposed algorithm

Conclusion

In this paper, we proposed a fingerprint texture extraction algorithm for fingerprint liveness detection. Our method overcomes the shortage of previous ones, ignoring the information from the slope. Experiment results show that the slope patterns perform no less than the feature extracted from the ridge, and beyond the valley signals. By combining all the patterns together, our algorithm promote the recognition rate to more than 98 % on the dataset from Chinese Academy of Sciences.

Acknowledgements This research was supported by the National Natural Science Foundation of China (61201271, 61301269), the Fundamental Research Funds for the Central Universities (ZYGX2013J019, ZYGX2013J017), Sichuan Science and Technology Support Program (cooperated with the Chinese Academy of Sciences) (2012JZ001), and Science and Technology Support Program of Sichuan Province, China (2014GZX0009).

References

1. Ratha NK, Connell JH, Bolle RM (2001) Enhancing security and privacy in biometrics-based authentication systems. IBM Syst J 40(3):614–634
2. Coli P, Marcialis GL, Roli F (2007) Power spectrum-based fingerprint vitality detection. In: IEEE workshop on automatic identification advanced technologies. IEEE, pp 169–173
3. Abhyankar AS, Schuckers SC (2004) A wavelet-based approach to detecting liveness in fingerprint scanners. In: Defense and security. International society for optics and photonics, pp. 278–286
4. Moon YS, Chen JS, Chan KC, So K, Woo KC (2005) Wavelet based fingerprint liveness detection. Electron Lett 41(20):1112–1113
5. Tan B, Schuckers S (2006) Liveness detection for fingerprint scanners based on the statistics of wavelet signal processing. In: Conference on computer vision and pattern recognition workshop (CVPRW'06). IEEE, pp 26–26
6. Nikam SB, Agarwal S (2008) Fingerprint liveness detection using curvelet energy and co-occurrence signatures. In: Fifth international conference on computer graphics, imaging and visualisation (CGIV'08). IEEE, pp 217–222
7. Choi H, Kang R, Choi K, Jin ATB, Kim J (2009) Fake-fingerprint detection using multiple static features. Opt Eng 48(4):047202–047202
8. Derakhshani R, Schuckers SAC, Hornak LA, O'Gorman L (2003) Determination of vitality from a non-invasive biomedical measurement for use in fingerprint scanners. Pattern Recogn 36(2):383–396
9. Parthasaradhi STV, Derakhshani R, Hornak LA, Schuckers SAC (2005) Time-series detection of perspiration as a liveness test in fingerprint devices. IEEE Trans Syst Man Cybern Part C 35 (3):335–343
10. Tan B, Schuckers S (2010) Spoofing protection for fingerprint scanner by fusing ridge signal and valley noise. Pattern Recogn 43(8):2845–2857
11. Hong L, Wan Y, Jain A (1998) Fingerprint image enhancement: algorithm and performance evaluation. IEEE Trans Pattern Anal Mach Intell 20(8):777–789

12. Wu X (1991) An efficient antialiasing technique. ACM SIGGRAPH Comput Graph 25(4):143–152
13. Fake fingerprint database from Chinese Academy of Sciences. http://www.fingerpass.csdb.cn
14. Ojala T, Pietikäinen M, Harwood D (1996) A comparative study of texture measures with classification based on featured distributions. Pattern Recogn 29(1):51–59

Part IX
Circuit Processing System, Intelligent System and Technology

Chapter 91
The Implementation and Analysis of Compressive Sensing Algorithm Based on DSP OMAP-L138

Baoju Zhang, Yulong Gu, Wei Wang, and Sijie Cheng

Abstract According to the basic principle of Compressive Sensing, a method of implementation of CS theory on DSP by the CCSLink is proposed. In Matlab, we utilize the CCSLink tool to create suitable embedded target to analyze parameter visually and discuss the basic factors which can effect the reconstruction algorithm on the platform of OMAP-L138. By improving and optimizing the algorithm, we accomplish the implementation of the theory of compressive sensing on DSP finally.

Keywords Compressive sensing • CCSLink • DSP • Reconstruction

91.1 Introduction

Traditional signal acquisition technology is ways based on signal waveforms. Firstly, we take no distortion sample, according to the Nyquist theory, then we discard those data which value is too small and unimportant, which is called compression. Usually, the quantity of data reduced significantly, which means that there is great waste in the process of sampling, that is a lot of hardware resources is consumed to sample those data which would be abandoned. The theory of compressive sensing (CS) [1, 2] is a new way of data compression and sampling method. The theory says, if the signal is sparse, or sparse on the certain basis, then we only need to sample a few projection value of the signal to realize the construction of origin accurately or approximately. The sampling rate does not rely on the bandwidth of signal, but on the structure and content of the signal. It could reduce the hardware cost in practical application greatly.

The hardware design of compressive sensing theory can be divided into two parts: design simulation and implementation. In the part of design and simulation

B. Zhang (✉) • Y. Gu • W. Wang • S. Cheng
College of Electronic and Communication Engineering, Tianjin Normal University, Tianjin, China
e-mail: wdxyzbj@163.com

J. Mu et al. (eds.), *The Proceedings of the Third International Conference on Communications, Signal Processing, and Systems*, Lecture Notes in Electrical Engineering 322, DOI 10.1007/978-3-319-08991-1_91

we complete the overall planning and algorithm design, then we make simulation. When the result of simulation satisfy the system requirement, we begin hardware design. Due to Matlab has great abilities of analysis, calculation and visualization, we use the software in the first part. Matlab link for Code Composer Studio (CCSLink) [3] is a link tool of hardware target developed by MathWorks company and Ti company. It can be used to connect Matlab, CCS, and Target board of DSP. It can make the designer operates on CCS and target board, so it can satisfy the need of current design and implementation. Therefore we utilize the tool to optimize and analyze the system we design. In order to obtain higher performance, the hardware platform we take is OMAP-L138 [4], which is a CPU of TI product. The OMAP-L138 applications processor contains two primary CPU cores: an ARM RISC CPU for general-purpose processing and systems control; and a powerful DSP to efficiently handle communication and audio processing tasks.

91.2 CS Theory Principle

Compressive sensing, which also can be called compressed sampling. It can realize the compression at the same time of sampling of signal. The theory skip the traditional process of compressing and sampling, in which sampling N samples, obtain the representation of compressed signal. The theory of CS utilize the feature of the natural signal has sparse representation on basis of sparse basis. We can obtain the origin signal projection on measurement matrix, then we can reconstruct the signal by apposite reconstruction algorithm. The process of compressive sensing can be seen in the block diagram (Fig. 91.1).

91.3 CS Simulation in Matlab

The whole process of compressive sensing can be explain below.

Firstly, analyze the signal which could be compressed. To find sparse basis to sparse the signal mostly. Assuming we have a N-dimensional discrete-time signal $x \in R^{N \times 1}$, which could be represented by a linear combination of matrix of sparse basis $\Psi^T = [\psi_1, \psi_2, \ldots\ldots \psi_k \ldots\ldots \psi_N]$, $x = \sum_{k=1}^{N} \psi_k \alpha_k = \Psi\alpha$ If x only has k nonzero coefficients α_k on the basis of Ψ, we can say that Ψ is the sparse basis of x, x is k sparse, and we think that this signal is sparse on the base of these primary functions.

Secondly, design a suitable measurement matrix and projecting the sparse signal on the measurement matrix to gain observed value. By this way, we can realize the purpose of sampling a few projection values of origin signal. In the theory of

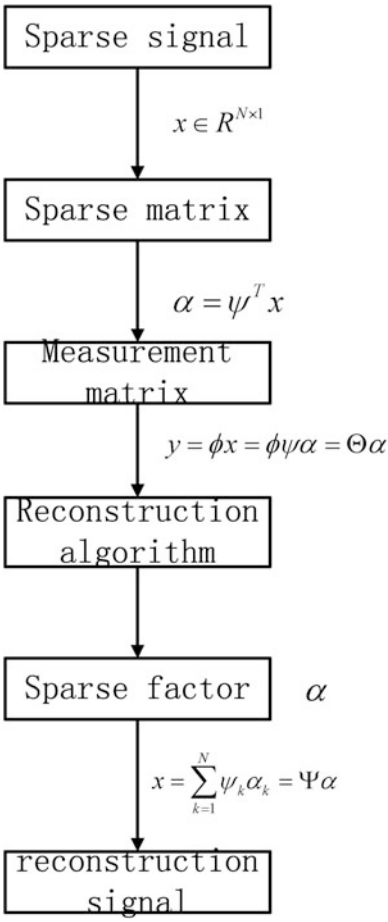

Fig. 91.1 The block diagram of CS

compressive sensing, we do not measure the sparse signal x, but to project the signal x to a group of measurement vectors $\Phi = [\phi_1, \phi_2 ..... \phi_k ..... \phi_M]$. We obtain a group of measurement values of M-dimensional, that is $y = \Phi x = \Phi\Psi\alpha = \Theta\alpha$. The projection values of y should consist of enough information to reconstruct the origin signal.

Thirdly, design a optimal reconstruction algorithm. Reconstruct the signal according to the projection values of origin signal to accomplish the process of coding and decoding of signal. Since the dimension of the measurement value is M, which is smaller than the dimension of origin signal x. So it is a NP-Hard question. But due to the signal is sparse, which sparsity is k, also $k < M \ll N$. We can find the solution of x or sparse coefficients α, according to the reconstruction algorithm.

In our design, we choose the Gabor overcomplete dictionary, the Gaussian random matrix as the measurement matrix, orthogonal matching pursuit (OMP)

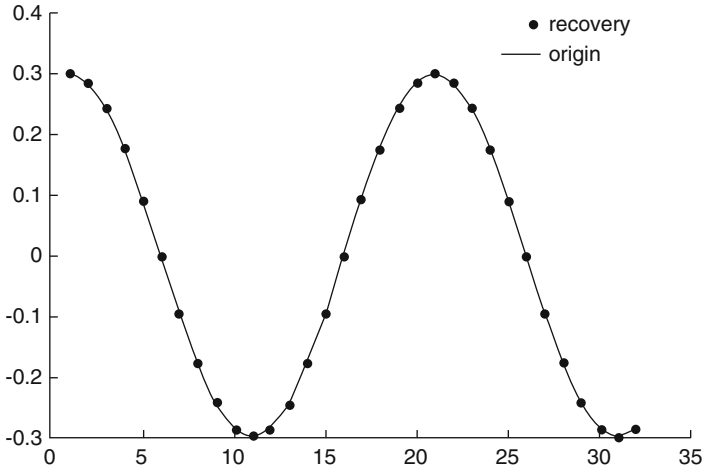

Fig. 91.2 The result of CS simulation in Matlab

[5] as the reconstruction algorithm. For the sake of analysis of the factors which can effect the reconstruction process, we choose a 32 points discrete signal as the initial signal. M is the sample points of CS, m is the sparsity of origin signal. We have a simulation here (Fig. 91.2).

91.4 The Implementation of CS on the OMAP-L138

After we accomplished the simulation in Matlab, we apply the method to OMAP-L138 to verify the feasibility of the CS theory's implementation on DSP.

The specific implementation process can be seen below:

(1) Storing the sparse matrix in the specified address space in the RAM of OMAP-L138.
(2) Using the linear congruential method (LCG) and central limit theory (CLT) to gain Gaussian random Matrices to act as measurement matrix.
(3) Using the orthogonal matching pursuit algorithm (OMP) to reconstruct signal from the measurement values.

We can get the conclusion from the Fig. 91.3, the reconstructed signal keep the essential features of origin signal. It can verify the feasibility of the CS theory's implementation on DSP. But we find that we cannot see the detailed problems clearly like we have done in Matlab.

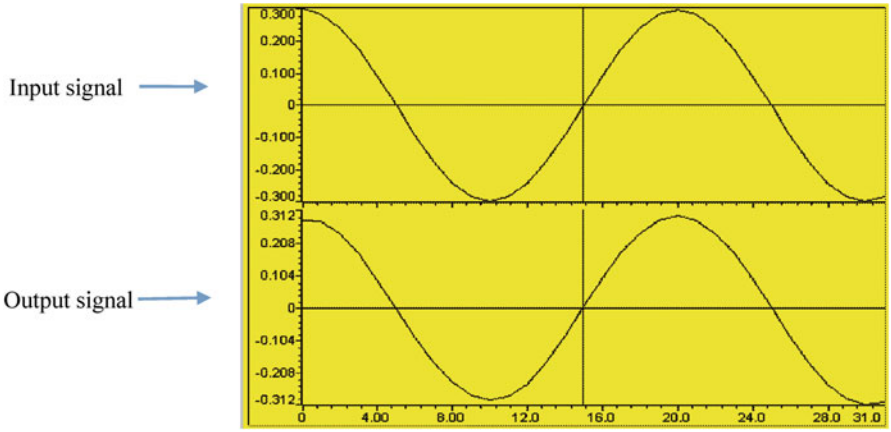

Fig. 91.3 The implementation of CS on OMAP-L138

91.5 Using CCSLink to Analyze the CS Theory

Matlab link for CCS Development Tool [3] can operate the registers of DSP through the Matlab's commands and objects simply, conveniently and visually. Thanks to the Matlab has the abilities of analysis and calculation, we can analyze the precision of CS theory implementation on DSP and kinds of errors. It solves a lots of problems. Such as we must keep the intermediate results on PC by development tool and we must call in the results to Matlab to compare with the simulation if we don't have the CCSLink tool. By its function of visualization, we can see the difference between reconstructed signal and origin signal. Thus, we can optimize the algorithm. CCSLink can connect the Matlab, CCS and OMAP-L138 together. The relationship between them can be seen in the figure below (Fig. 91.4).

91.5.1 The Process of Experiment

(1) Choose the target DSP
(2) Cerate CCS IDE to connect the target
(3) Use Matlab to load files to CCS IDE
(4) Operate the target of CCS IDE in Matlab
(5) Close the connection

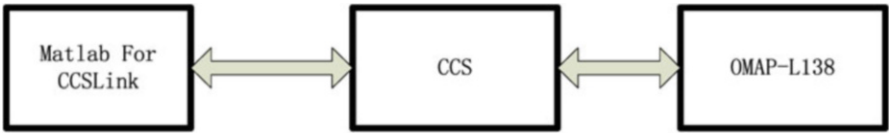

Fig. 91.4 The connection between CCSLink, CCS and DSP

91.5.2 Analysis About the Result of Experiment

The connection target and embedded target both be operated with object-oriented technology. The connection target connect Matlab and OMAP-L138, the embedded target visit and operate the C symbols in the target DSP.

(1) Analysis of algorithm

In the implementation of compressive sensing, we firstly setup the embedded target of input signal and output signal: inp_buffer and out_buffer, then operate the embedded target of DSP in Matlab, and then analyze the parameters in the process of implementation. The simulation of Matlab and the errors of implementation on DSP can be seen in the tables below (Tables 91.1, 91.2).

According to the tables, we can conclude that the reconstruction errors of the CS theory on DSP can fit with the simulation in Matlab. We have accomplish the verification of the feasibility and validity of CS theory implemented on DSP.

(2) The factors which effect the implementation on DSP

1. When the number of measurement M is certain, the reconstruction errors change with the sparsity m. It can be seen in Fig. 91.5

   From the Fig. 91.5, when the sample points keep the same, the results of simulation in Matlab and implementation on DSP show that reconstruction error change with the sparsity in same trend. Moreover, the reconstruction error make a great change with sparsity within limit. The sparsity m is bigger, the reconstruction error is smaller. When the m reaches a certain value, the error keep the same approximately.
2. When the sparsity m is defined, the reconstruction error change with the number of measurement M, which can be seen in Fig. 91.6

   From the Fig. 91.6, when the sparsity of signal is certain, the reconstruction error change in the same trend in Matlab simulation and DSP implementation. When the M reach a certain value, the error keep the same. We also verify that if $M \geq \kappa \times \log(N/\kappa)$, the origin signal can be reconstructed accurately.

Table 91.1 The reconstruction error change with the sparsity

Reconstruction error	m	Simulation in Matlab	Implementation of DSP
	2	0.37347350383227	0.37351998439005
	3	0.331069522943899	0.33116726786609
	4	0.14351034574599	0.14349679881114
	5	0.11827534137123	0.11828899954650
	6	0.08934423010329	0.08931563672474
	7	0.04875054648026	0.04875585601670
	8	0.03984971034685	0.03986661831408
	9	0.03589392678239	0.03591345716226
	10	0.02370342665450	0.02370862368992
	11	0.02611479549253	0.02612316855154
	12	0.02816088535563	0.02817190332547
	13	0.02574368812161	0.02575410085436
	14	0.02758378065924	0.02759988712440

M is defined, the reconstruction error change with m

Table 91.2 The reconstruction error change with the measurement number M

Reconstruction error	m	Simulation in Matlab	Implementation of DSP
	10	0.04094116668559	0.04096663335103
	11	0.04124325312550	0.04126895527942
	12	0.02328320991889	0.02328790600412
	13	0.02354160802044	0.02354673646906
	14	0.02370116902901	0.02370625193975
	15	0.02370342665450	0.02370862368992
	16	0.02274532342814	0.02275011985996
	17	0.02258376777193	0.02258825499037
	18	0.02370116902901	0.02261958589668
	19	0.02376484531263	0.02261754207333
	20	0.02376484531263	0.02377033763343

m is defined, the reconstruction error change with M

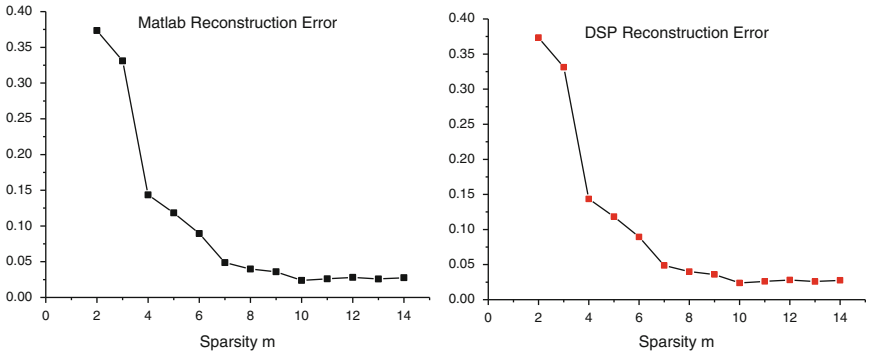

Fig. 91.5 M is defined, the error change with the sparsity m

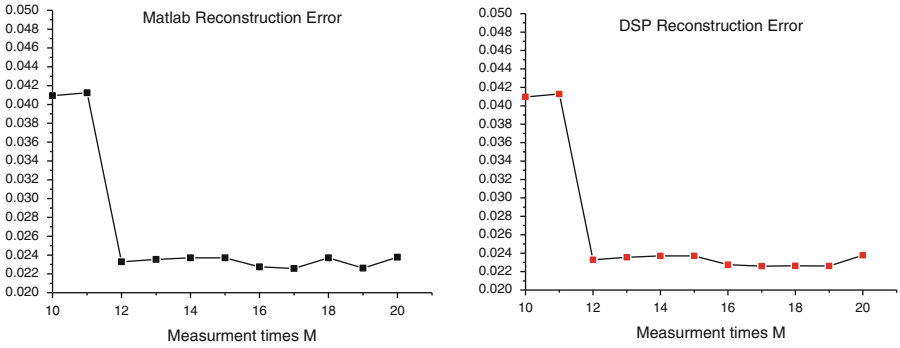

Fig. 91.6 m is defined, the error change with the measurement number M

Conclusion

In this paper, we introduce the basic principle about the theory of Compressive sensing. On the base of simulation in Matlab, we accomplish the algorithm of CS implementation on DSP by CCSLink. The results show that the time of DSP development can be reduced greatly by the auxiliary of Matlab. Not only reduce the inventory, but also improve the accuracy of reconstruction. Through the analysis and comparison about the experiment results, we conclude the basic factors which effect the reconstruction of signal, and improve and optimize the algorithm of reconstruction, accomplish the accurate reconstruction on the platform of OMAP-L138.

Acknowledgments This research was supported by the National Natural Science Foundation (61271411), The Tianjin Natural Science Foundation (10JCYBJC00400), High Education Science & Technology Foundation Planning Project of Tianjin (20100716) & Tianjin Younger Natural Science Foundation (12JCQNJC00400) and University Students' Innovative Training Program.

References

1. Donoho DL (2006) Compressive sensing. IEEE Trans Info Theory 52(4):1289–1306
2. Candes EJ, Romberg J, Tao T (2006) Robust uncertainty principle: exact signal reconstruction from highly incomplete frequency information. IEEE Trans Info Theory 52(2):489–509
3. MATLAB®Link for code composer studio development tools new for version 1.0. http://cn.mathworks.com/products/embedded-coder/index.html?s_cid=0909_webg_9b_ccslink_trans_268513
4. OMAP-L138 C6000 DSP + ARM processor technical reference manual (Rev.A). http://www.ti.com/general/docs/litabsmultiplefilelist.tsp?literatureNumber=spruh77a
5. Tropp JA, Gilbert AC (2007) Signal recovery from random measurements via orthogonal matching pursuit. IEEE Trans Info Theory 53(12):4655–4666

Chapter 92
Combination of Adaptive Filter Design and Application

Jia Huang, Ruian Liu, Daxi Liu, Chenxian Luo, and Lan Wang

Abstract Individual Adaptive Filter only allows one input signal through, so doped with a signal source when there are different types of noise or interference, an individual Adaptive Filter is not a good mix of original signal noise and therefore cannot fully restore the initial signal. Combining adaptive filters introduced precisely to address this issue. This article introduces the basic ideas of Adaptive filter design portfolio illustrates combined Adaptive Filter theory. And a combination filter was introduced in the practical application of spread spectrum technology. By simulating the experiments confirmed the combination filter has good filtering effect.

Keywords Adaptive filtering • Combination filter • Spread spectrum techniques

92.1 Development Status

In the late 1950, study of the Adaptive Filter began. This filter method is optimal filtering that developed from Wiener and Kalman filter linear filter. In 1959, the formulation of the least mean square algorithm for adaptive technology development has a major role. At present, this kind of algorithm widely used to calculate weights. Adaptive Filter can be adjusted according to the different needs of its own arguments, therefore it has a wide applications in various areas. In the next 40 years, adaptive filters has rapid developed. In addition, combination of the adaptive filter proposed in order to meet a variety of interference in the signal source issue.

J. Huang • R. Liu (✉) • D. Liu • C. Luo • L. Wang
College of Physical and Electronic Information, Tianjin Normal University, Tianjin, China
e-mail: ruianliu@sina.com

J. Mu et al. (eds.), *The Proceedings of the Third International Conference on Communications, Signal Processing, and Systems*, Lecture Notes in Electrical Engineering 322, DOI 10.1007/978-3-319-08991-1_92

92.2 The Basic Idea of a Combination of Design

Combination of the adaptive filter is the combination of different types of filters together as a group, to meet the different needs of the application. Filter bank constitute by N adaptive filters F_1, F_2, ... F_N that independently of one another [1]. While signal sources contain several different types or intensity of additive noise, filter bank can select several filters according to the type and intensity of noise. Each filter filtering a particular noise in the signal source. Then combine these filters, that combination filters can achieve a good filter effect. If the signal contains only one noise source, the combination of the filter used for filtering not only can the noise cancel better but also can retain details of the signal [2] to improve the signal quality. Therefore, filter bank can at least achieve the best results for a single filter.

According to different combinations of multiple filters, filter combinations can be divided into linear and nonlinear combinations.

92.2.1 Linear Combination

$x_i(n)$ represents the i-th input of the adaptive filter; $y_i(n)$ represents the i-th output of the filter at time n; $w_i(n)$ represents the weight vector of the i-th adaptive filter; $e_i(n)$ represents the i-th output error signal of the adaptive filter; $d_i(n)$ represents the desired signal of the i-th adaptive filter, $i = 1,2,\ldots,N$;

Filter Bank overall error signal:

$$e(n) = \lambda_1 e_1(n) + \lambda_2 e_2(n) + \ldots + \lambda_N e_N(n) \tag{92.1}$$

Type (92.1): $e_i(n) = d_i(n) - y_i(n)$, $y_i(n) = w_i^T(n)\, x_i(n)$, $i = 1,2,\ldots,N$;

$\lambda_i(i = 1,2,\ldots N)$ is combination coefficients of the adaptive filter.

A linear combination filter required: (a) each filter is an adaptive filter (b) the length of each of the adaptive filter is same. (c) combination coefficients $\lambda_i \in (0,1)$ $(i = 1,2,\ldots,N)$ is constant, and it also must be satisfied: $\sum_{1}^{N} \lambda_i = 1. \in$.

92.2.2 Nonlinear Combination

In nonlinear Adaptive Filter combination, combination coefficient is no longer a constant. Here use $\lambda_i(n)$ to represent, then the filter's overall output error is:

$$e(n) = \lambda_1(n) e_1(n) + \lambda_2(n) e_2(n) + \ldots + \lambda_N(n) e_N(n) \tag{92.2}$$

Type (92.2): $e_1(n)$, $e_2(n),\ldots$, $e_N(n)$ are the output error of each adaptive filter, combining the design also requires a combination coefficient: $\sum_{1}^{N} \lambda_i(n) = 1$.

92.3 The Noise Cancellation Principle of Adaptive Combinations Filters

Adaptive filters in various fields widely used in noise cancellation. When the adaptive filter offset noise, the desired signal is subjected to interference plus noise of the original signal. Adaptive filter input enter a noise signal, this signal and signal interference is related, but it has nothing to do with the original signal. If the above conditions are met, we use a example of two Adaptive Filter combination filters to prove that is optimal filtering which meet minimum criteria [3, 4].

Assuming the desired signal $d(n) = s(n) + v(n)$, is the filter-i's input is signal is $V_i(n)$, and s (n), v (n) are zero mean stationary random process, at the n time, filter-i always output signal is $y_i(n) = w_i^T(n)V_i(n)$, $i = 1,2,\ldots N$, The error signal is $e_i(n)$, then the whole system out is the combination of various filters and get e(n), namely:

$$\text{out} = e(n) = \lambda_1 e_l(n) + \lambda_2 e_2(n) + \ldots + \lambda_N e_N(n)$$

λ in the type must satisfy $\sum_1^N \lambda_i = 1$, we obtain the mean square error is $E[e^2(n)] = E\left\{\left[\sum_1^N \lambda_i e_i(n)\right]^2\right\}$. If there are two filters, $E[e^2(n)] = E\{[\lambda_1 e_1(n) + \lambda_2 e_2(n)]^2\} = E[\lambda_1{}^2 e_1{}^2(n)] + E[\lambda_2{}^2 e_2{}^2(n)] + 2\lambda_1\lambda_2 E[e_1(n)e_2(n)]$

If there are two kinds of noise in the signal source, and these two types of noise are not related, namely $v(n) = v_l(n) + v_2(n)$. At this point we can design a filter that contains two filters that can offset these two noise respectively. Filter the input signal $V_1(n)$ and $v_1(n)$ is related to the noise signal from the same noise source; $V_2(n)$ is $v_2(n)$ is related to the noise signal from the same noise source, and that the two noise more relevant then filtering effect get better [5]. Pay attention to the signal source contains more than one type of noise, therefore need to be added noise that related with the $v_2(n)$ in the first Adaptive filter, added noise that related with the $v_1(n)$ in a second adaptive filters, makes a filter whose output error sign $e_1(n)$ and $e_2(n)$ meet the following formula:

$$e_1(n) = d(n) - y_1(n) = s(n) + v_1(n) + v_2(n) - y_1(n)$$
$$e_2(n) = d(n) - y_2(n) = s(n) + v_1(n) + v_2(n) - y_2(n)$$

Because the system error signal is $e(n) = \lambda_1 e_l(n) + \lambda_2 e_2(n)$.

So mean square error is $\xi = E[e^2(n)] = E\{[\lambda_1 e_1(n) + \lambda_2 e_2(n)]^2\} = \lambda_1{}^2 E[s^2(n)] + \lambda_2{}^2 E[s^2(n)] + 2\lambda_1\lambda_2 E[s^2(n)]$

$e_1(n)$ and $e_2(n)$ into the mean-square error equation where: $v_l(n)$ and $V_l(n)$ is from the same source of noise, so a high level of correlation between them. $v_2(n)$ and $V_2(n)$ the same way. And expect s(n) and $v_l(n)$, $v_2(n)$, $V_1(n)$, $V_2(n)$ is irrelevant. So when $y_l(n)$, $y_2(n)$ tends to $v_l(n)$, $v_2(n)$, we can prove: $\xi = E[e^2(n)] = E[s^2(n)]$. At this time the error signal e(n) is noise reduction and enhancement signals that obtain in adaptive filter [6].

In this way, we can discover the error signal e(n) is noise reduction and enhancement signals that obtain in adaptive filter. Single noise is a special case of noise, $v_1(n)$, $V_1(n)$, $v_2(n)$ and $V_2(n)$ are all from the same source of noise. When using combination filters filter the signal noise source can also serve to eliminate noise, enhance the role of the signal.

92.4 Application of Combination of Adaptive Filter in Spread Spectrum Communication

A new combination filter need two identical in structure Adaptive Filter, besides the filter coefficients corresponding to the right to equal. Combined filter weights can be controlled by the adaptive algorithm of the adaptive filter [7]. At this point, call them filter N and filter M. For the filter M, it is supplied to the optimum filter weights to N, we will sent signal x(k) to the delay then subtracted with e(k), since information data is then despread by n to a summation of outputs, the s(k) is spread over the same PN sequence then the spread data, its magnitude is reduced to 1/N value. With the number of iterations increases, the relevant the processed data bit values tended to the true value. From the above discussion, filter M provides the best weights for filter N. N filters use the optimal weights to signal filtering. According to the analysis, combination filter will provide better filtering effect [8].

Now, take the length of the adaptive filter is: $M = 8$, the output power is 1. The signals were generated using a combination of linear predictor constituted the basic filter model and linear adaptive predictor performance simulation under different disturbances.

92.4.1 The Simulation Results Under the Single-Frequency Interference

Assuming single-frequency interference frequency offset is obtained after panning sinusoidal signal. The filter output is stable, a plurality of sampling points taken to calculate the SNR. Signal to noise ratio is improved on average, as follows (Table 92.1):

Table 92.1 SNR under the interference sinusoidal signal

Input SNR (dB)	Linear prediction SNR (dB)	Combined forecast SNR (dB)	Performance improvement SNR (dB)
−22	27.5	39.0	11.5
−16	20.1	34.3	14.2
−10	16.2	27.1	10.9
−4	10.9	23.2	12.3

Table 92.2 SNR under narrowband interference

Input SNR (dB)	Linear prediction SNR (dB)	Combined forecast SNR (dB)	Performance improvement SNR (dB)
−22	22.9	35.1	12.2
−16	17.1	32.0	14.9
−10	11.7	24.3	12.6
−4	8.1	20.6	12.5

92.4.2 Performance Simulation in the Case of Narrow-Band Interference

Interference is white noise with variance 0.01. Changing the size of the interference signal power, the two predictors improve noise at different signal to noise ratio, as follows (Table 92.2):

By a comparison of the above two tables, we can draw the following conclusions. In single frequency interference conditions, the combination of linear predictor of signal to noise ratio compared to linear predictor increased 12.45 dB; In the narrow-band interference conditions, the combination of linear predictor SNR improvement compared to linear predictor, increased 13. 05 dB; SNR of the input signal does not directly affect the size of the filtering effect of the combination filter.

Combination filter design compared with other adaptive filter design, combination filter and did not increase the complexity of algorithms and SNR significantly improved performance. In particular, the noise is large, the combined filter to improve the SNR of the input channel has maintained a stabilizing. Combined filter anti-interference ability is significantly better than a single adaptive filter.

Conclusions

This article describes the combination of adaptive filter design, describes the basic principles of combination of adaptive filters. And combination of adaptive filters is mean-square performance analysis. Through analysis, we can conclude: the applicability of the combined filter is universal, we can apply to this combination of practical engineering. Combined with an instance of the combination filter should be used for communication and using simulations, eventually confirmed combination filter has good filtering effect.

Acknowledgments This research was supported by the Tianjin natural science fund (13JCYBJC15800)

References

1. Arenas-Gareia J, Gomez-Verdejo V, Figueiras-Vidal AR (2005) New algorithms for improved adaptive convex combination of LMS transversal filters. IEEE Trans Instrum Meas 54(6): 2239–2249
2. Zhang YG, Chambers JA (2006) Convex combination of adaptive filters for variable tap-length LMS algorithm. IEEE Signal Process Lett 13(10):628–631
3. Rong Mei, Shanhua Yao (2008) Adaptive filter application in the noise cancellation system. Instrum Technol 37(8):13–15
4. Xiao Zhe (2006) RLS adaptive speech noise canceling based on MATLAB system design and implementation. J Changsha Univ 20(2):83–86
5. Zhang Xiangfen, Chen Wufan (2010) Image noise removal method based on a combination of filters. In: Proceedings of the 15th national conference on image and graphics 391(41)
6. Tang Yu, Yan Mei, Hong Fuming (2008) Combination of adaptive anti-jamming technique in spread spectrum communications. J Electron Sci Technol Univ 27(2)
7. Nascimento VH, Sliver MTM (2013) A low-cost implementation strategy for combinations of adaptive filters. In: 2013 I.E. international conference, pp 5671–5675
8. Chamon LFO, Lopes WB (2012) Combination of adaptive filters with coefficients feedback. In: 2012 I.E. international conference, pp 3785–3788

Chapter 93
The Research and Application of Wireless Intelligent Network System Based on STM32F407

Jincheng Wu, Aiqian Du, Hongbin Lu, Shouqing Yang, Di Yun, and Jingrui Sun

Abstract This topic takes STM32F407ZGT6 MCU as the master chip, has designed the wireless intelligent system of fire alarm, which includes 2.4G wireless communication module, smoke transducer, temperature transducer, the audible and visual alarm module, TFT LCD module and GSM communication module. Moreover, the research and application of wireless intelligent system would be discussed further in this topic. It's convenient and flexible for wireless system to erect and move freely. Also the wireless system doesn't need large-scale wiring. Currently, the wireless system has replaced the traditional wired network gradually and becomes a new trend in the development of communication technology. It's so different from the way of traditional wired connection for wireless network that it can reduce the restriction of factors such as topography, terrain and price to the intelligent system. As a result, the intelligent system can be used widely in various fields without restrictions. According to the test, this design has accomplished each function basically and achieved the expected results. Therefore it will show a bright prospect about its application.

Keywords STM32F407 • NRF24L01 • Smoke transducer • GSM mobile communication

93.1 Introduction

The science and technology are the powerful weapons of promoting the social progress. Nowadays, it emerges so many previously unimaginable high-tech products around us which have made our daily life change with each passing day as the technology develops rapidly. In the field of communication, there exist numerous

J. Wu (✉) • A. Du • H. Lu • S. Yang • D. Yun • J. Sun
College of Electronic and Communication Engineering,
Tianjin Normal University, Tianjin, China
e-mail: wdxywjc@mail.tjnu.edu.cn; 243073975@qq.com

J. Mu et al. (eds.), *The Proceedings of the Third International Conference on Communications, Signal Processing, and Systems*, Lecture Notes in Electrical Engineering 322, DOI 10.1007/978-3-319-08991-1_93

limitations of the previous traditional wired transmission. For instance, there is no possibility for completed construction to bury wire while installing some equipment. Also, laying exposed wire has bad effects on the appearance, and some buildings are not allowed to destroy the decoration and so on. In these cases, the wireless communication comes in handy and will come into play. The wireless communication technology has been gradually turning into a new developmental tendency instead of wired communication with its advantages of flexibility, convenience, no need to wire extensively and so on. The wireless communication technology can be seen everywhere in modern life because of the widespread use of the high-tech. It has been widely used in various fields such as satellite communication, telemetry sensing of aerospace, intelligent home, wireless video access door system, industrial data collecting, biological signal collecting, hydrology and meteorology monitoring, operation of subway dispatching, and medical treatment and so on.

Due to the population aging and the need to develop economy of Chinese society, more and more aged people and children live at home alone. They are generally lack of the awareness of fire precaution. They are far more easily threatened by the fire because their ability of escaping from fire is relatively poor. According to statistics the proportion of the old and kids injured in the fire accounts for more than 60 % of all the fire casualties every year. In particular, the elderly people might use the electrical appliances improperly or forget to unplug some devices timely which can cause fire accident, as a consequence, lead to a serious fire disaster. Therefore, it's urgent and important to guarantee security of living place for the old and children. So, this topic selected to design wireless intelligent system of fire alarm based on STM32F407 aimed at fire precaution. The system can send alarm messages to the designated number automatically at the beginning of fire. Even though there is no one at the scene of the fire, the fire also can be noticed immediately so that people can eliminate the fire in the embryonic stage. The system can alarm via intensive light and sound while fire breaks out. In this way, people such as the old, children, security guard and neighbors can put out the fire after receiving information of fire and avoid causing more acute casualties or damage.

93.2 System Architecture Overview

The fire detector made up of smoke transducer and temperature transducer detects the fire signal such as temperature and smog concentration. The detected signal is transmitted to the CPU, and the CPU will make a judgment whether a fire accident happens (compare with the set value). If the received temperature and smog concentration are equal to the set value in the master chip, it is certain that a fire has occurred. After that, the audible and visual alarm module gives an alarm. Then, it will drive the linkage to take corresponding measures.

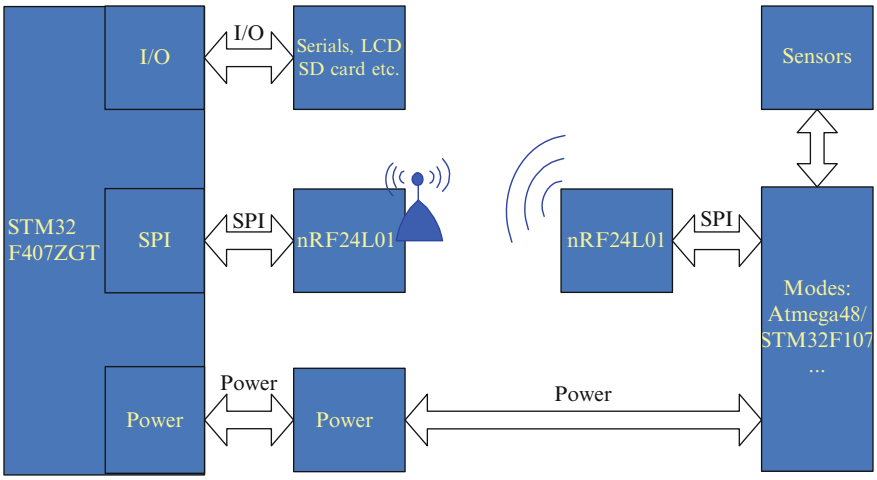

Fig. 93.1 System hardware schematics

As shown in Fig. 93.1, the controlling terminal selects STM32F407 as the master chip and accomplishes to transmit data and information via NRF24L01 wireless communication module. The detected information will be transmitted to the master MCU. Then, the MCU makes a judgment whether there is a fire accident according to the information of surroundings read by the smoke transducer and temperature transducer. All the real-time information will be shown on the TFT LCD screen. The alarm equipment can alarm through intensive light and sound as the combustible gas density and the temperature increase sharply in environment. The advantage of this system is alarming through lights if the fire breaks out at midnight. The sound section alerts via reading the audio files stored in advance in SD card. GSM communication module takes an alarm through calling the number configured by users ahead of time such as 119 or sending text messages to the users outdoor.

93.3 Hardware Flow Diagram of System

As shown in Fig. 93.2, it is the hardware flow diagram of the system. System selected STM32F407ZGT6 as the master chip which is produced by ARM Corporation [1]. It has the most abundant peripheral resources and pin resources. It adopts the package technology of LQFP. This processor is Cortex-M4 kernel which is structured based on ARM V7. Its basic frequency is 120 MHz. It has 1 M bytes FLASH and 128 k bytes SRAM internally. The new Thumb-2 instruction set is embedded within Cortex-M4 kernel by ARM Company. It simplifies software development and code maintenance, it also provides modified performance and energy efficiency [2].

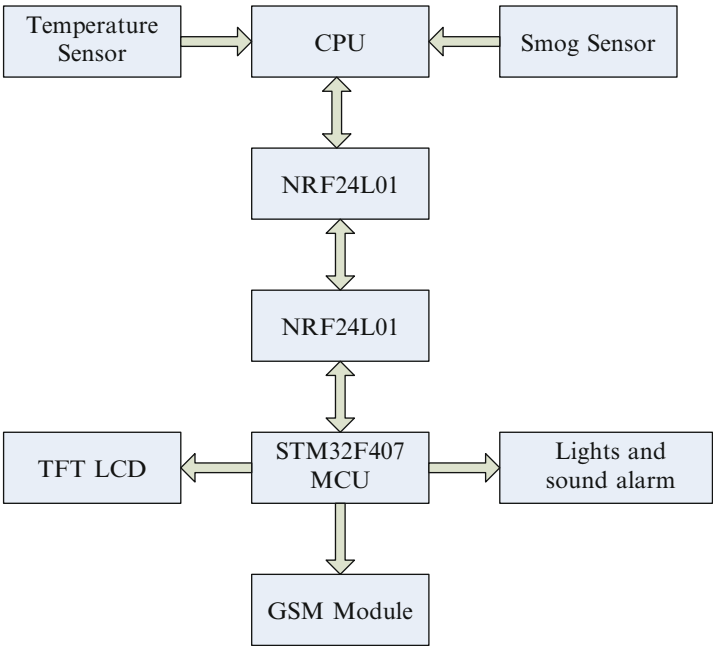

Fig. 93.2 System structure

Table 93.1 NRF2401 operating mode

Mode	PWR_UP register	PRIM_RX register	CE	FIFO state
RX mode	1	1	1	–
TX mode	1	0	1	Data in TX FIFO
TX mode	1	0	$1 \rightarrow 0$	Stays in TX mode until packet transmission is finished
Standby-II	1	0	1	TX FIFO empty
Standby-I	1	–	0	No ongoing packet transmission
Power down	0	–	–	–

System uses NRF24L01 produced by Nordic Company. It operates at ISM frequency, and it can complete the wireless transmission of data. Its work rate can be up to 2 Mb per second. It has wide voltage range and a plurality of communication channel and the data channel.

It adopts high-efficient GFSK modulation and has great capacity of resisting disturbance [3]. As shown in Table 93.1, it is NRF24L01.

A breakthrough of this design, the section of sound alarm breaks the limitation of buzzer whose sound is invariable, alarms through reading the audio files stored in

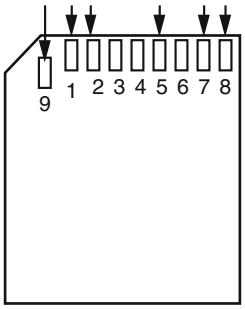

PIN	1	2	3	4	5	6	7	8	9
SD MODE	CD/DATS	CMD	VSS	VCC	CLK	VSS	DAT0	DAT1	DAT2
SPI MODE	CS	MOSI	VSS	VCC	CLK	VSS	MTS0	NC	NC

Fig. 93.3 SD card pin data

advance in SD card. Therefore users can change the audio files randomly and select the sensitive music for themselves so that they can notice rapidly when a fire occurs. SD card is a new generation of memory device based on semiconductor flash memory. There are numerous features such as high memory capacity, rapid transmission rate of data, great mobile flexibility and good security although it looks like a stamp and it weighs only 2 g. The SD card supports two kinds of operating modes: SD mode and SPI mode. The SD mode allows high-speed data transmission. By contrast, SPI mode loses speed. So, the system accesses the SD card through SDIO interface which is so-called SD mode. As shown in Fig. 93.3, it is SD Card Pin Data.

The section of sound alarm uses the VS1003 chip produced by Finland semiconductor Company. The advantages of VS1003 are low price, easy to use and powerful functions. It has the function of audio decoding and encoding.

The smoke transducer is a kind of sensor which can detect smog density. The smog detecting of the design uses the gas sensitive smoke transducer, MQ-2, which is a low power consumption microprocessor. Its operating property is stable and reliable, it's more sensitive, and more convenient to maintain. The internal material of MQ-2 is SnO_2 which has low conductivity in the clean air. If exist combustible gases around, its conductivity will increase as the combustible gas density increases. So, it can turn the physical signal of combustible gas density changing into corresponding voltage signal through the gas-electric conversion circuit. Then, turn the analog signal into digital signal through A/D conversion circuit. The signal will be transmitted to the CPU and the CPU finishes the work of processing data [4]. With the continuous development of industry automation, in underground coal mine, at the explosive places full of gas and coal dust, it's more and more important to detect the combustible gas. So, the smoke transducer plays an indispensable role in numerous fields such as industry, petrochemical industry, gas transmission and distribution, crowded station and so on [5].

Table 93.2 AT instruction set

Instruction	Function
AT&F	Initialization of module
AT + CMGF = 1	Configure the message at text format
AT + CMGF = 0	Configure the message at PDU format
AT + CSCS = "GSM"	Select the character set of TE
AT + CMGS = "number"	Set the number of sending text message
ATD number	Dialing instruction
ATH	Hanging on instruction

The system alarms via sending text message or calling by GSM communication module. GSM network becomes mature gradually after several years' development. Nowadays, it has few blind spots, its signal is stable and roaming is fully automatic [6]. Also, the communication distance is not influenced by surrounding. Especially, the text message is flexible and convenient, and can be transmitted across the province and city even internationally. It is reliable and cheap as it only needs 10 cents. So, it is a nice choice to alarm via GSM communication module [7].

As shown in the Table 93.2 is the frequently-used AT instruction set:

93.4 System Software Design

As shown in Fig. 93.4, the system is initialized after powering-on or resetting. Some initialization information is displayed on the TFT LCD screen. The information got through temperature transducer and smoke transducer detecting surrounding environment also is displayed on the screen. In the loop of the program, the temperature and smog density is compared with the threshold value every time. When the data equal to the value, system alarms by sending text message [8]. Meanwhile, the lights and sound make an alarm. If the fire is more serious, the system will call the phone number configured by users such as 119 along with the intensive light and sound alarm. For example, the source program of the lights and sound alarm part is as follows:

```
for( index = 0; index < sizeof(MP3_DATA); index += 32 )
 {
  while(MP3_DREQ ==0);
  VS1003_WriteData( (void*)( MP3_DATA + index ) );
  GPIO_SetBits(GPIO_LED,DS1_PIN|DS2_PIN|DS3_PIN|DS4_PIN);
  LED_ON(i%4);
  i++;
 }
USART1_putstr("AT&F\r\n");
delay_ms(300);
```

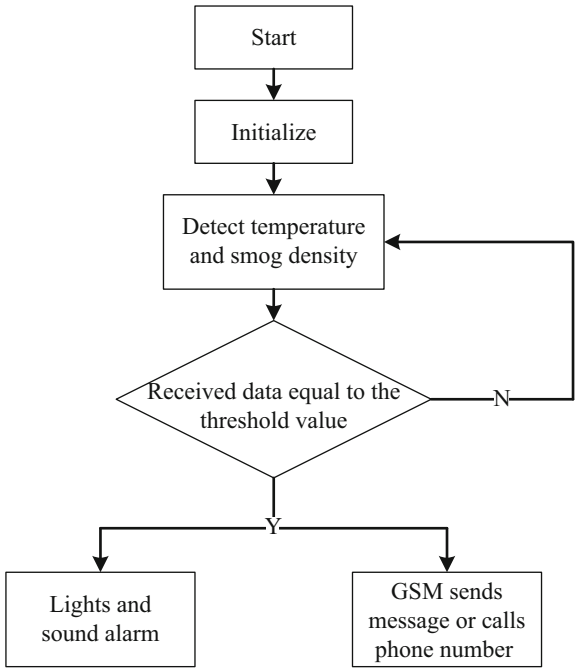

Fig. 93.4 Software flow chart

```
USART1_putstr("AT\r\n");
delay_ms(300);
USART1_putstr("AT+CMGF=1\r\n");
 delay_ms(300);
 USART1_putstr("AT+CSCS=");
delay_ms(1);
USART_SendData(USART1, 0x22);
delay_ms(1);
USART1_putstr("GSM");
delay_ms(1);
USART_SendData(USART1, 0x22);
delay_ms(1);
USART1_putstr("\r\n");
delay_ms(300);
USART1_putstr("AT+CMGS=");
delay_ms(1);
USART_SendData(USART1, 0x22);
delay_ms(1);
USART1_putstr("xxxxxxxxxxx");
delay_ms(1);
USART_SendData(USART1, 0x22);
delay_ms(1);
```

```
USART1_putstr("\r\n");
delay_ms(300);
USART1_putstr("Emergency! Warning!");
delay_ms(300);
USART_SendData(USART1, 0x1A);
USART1_putstr("AT&F\r\n");
delay_ms(300);
USART1_putstr("AT\r\n");
delay_ms(300);
USART1_putstr("ATDxxxxxxxxxxx");
delay_ms(1);
USART_SendData(USART1, 0x3B);
delay_ms(1);
USART1_putstr("\r\n");
```

Conclusion

The wireless intelligent system of fire alarm in this design, includes mainly sensor circuit and wireless communication circuit. The sensor of detecting section can be selected by users, it is used to detect the temperature and smog density surrounding. The intelligent system can be used flexibly and conveniently, and it is of low price and high performance. Especially, it communicates via wireless communication rather than the traditional wired communication. It can be moved randomly, don't need wire on large scale, can be erected easily. It also can't be influenced by the region, terrain and landform. So the intelligent system designed in this topic has a widely application prospects, a large space for development, and can be extended to other fields.

References

1. Liao Yikui (2013) ARM Cortex-M4 precise solution of embedded practice development based on STM32F4. Beijing University of Aeronautics and Astronautics Publisher, Beijing
2. Zhang Yang, Liu Jun, Yan Hanyu (2013) Atom teaches you learning STM32 (library edition). Beijing University of Aeronautics and Astronautics Publisher, Beijing
3. Wu Jiangyuan, Liu Yubing, Zhang Yu (2012) Design and implementation of 2.4G wireless file transmission system. China Integr Circuit 11:72–75
4. Hu Guyue, Huang Lihua (2013) The burglar-proof and fire-proof system in dormitory based on MCU. Technol Wind 7(13):22
5. Nie Wei, Li Xiaoqing (2012) The design of intelligent fire alarm system. Inf Commun 02:92
6. Long Guangli, Li Baiping, Wang Shaohua (2011) Design of wireless alarming system based on GSM/GPRS. J Shaanxi Univ Technol (Nat Sci) 9(27):12–15
7. Zhang Sheng, Xu Xiaobing, Gong Liangwu, Zeng Binbin (2010) Use AT89S52 to accomplish the design of GSM SMS fire alarm system. Silicon Val 3(15):62
8. STMicroelectronics (2010) STM32 Chinese reference manual, 10th edn. STMicroelectronics (China) Investment Company, Shanghai.

Chapter 94
A Design of Multi-rate Matched uPP Based on FPGA

Donghui Huang, Chaohai Li, Jiefeng Wang, and Shangce Yuan

Abstract The design of spectrum monitoring receiver usually use FPGA (Field Programmable Gate Arrays) + DSP (Digital Signal Processor) hardware model, which requires the baseband data and spectral data under different bandwidths can be real-time transmitted between the FPGA and DSP. According to the characteristics of the receiver, a multi-rate matched universal parallel port (uPP), which is used to transmit data between FPGA and DSP, is implemented in this paper. The port achieves a high-speed data transmission, which is up to 150 MBtye/s with only 20 I/O lines. The adaptation of different input data rates is implemented by a ping-pong buffer in dual-FIFO (First In First Out).

Keywords FPGA • uPP • Multi-rate matched • Ping-pong buffer

94.1 Introduction

With the developing of radio application, the spectrum resource of radio is more and more inadequate [1]. It is particularly important to monitor the radio spectrum. The FPGA + DSP hardware model is usually used in the digital processing of spectrum monitoring receiver. Some preprocessing of digital intermediate frequency signal after analog-to-digital converter (ADC) sampling is made in FPGA, such as digital down conversion (DDC), filtering and fast Fourier transform (FFT). Then the baseband data and spectral data are supposed to be obtained, which should be real-time transmitted to DSP for further processing, such as signal demodulation, parameter estimation and measurement.

To improve the quantified signal-noise-ratio (SNR) of ADC sampling, a higher sampling rate is generally chosen if the device allows. While the data rate is increased, the processing of baseband data required for a corresponding increase in the processing speed of hardware. As we all know, different bandwidths require different data rates. To achieve the resource and power optimization of FPGA, data

D. Huang (✉) • C. Li • J. Wang • S. Yuan
School of Electronic Engineering, University of Electronic Science and Technology of China, Chengdu, Sichuan 611731, PR China
e-mail: 493272936@qq.com; ysctrnt@126.com

J. Mu et al. (eds.), *The Proceedings of the Third International Conference on Communications, Signal Processing, and Systems*, Lecture Notes in Electrical Engineering 322, DOI 10.1007/978-3-319-08991-1_94

rates decelerations is correspondingly made in different bandwidths. In order to meet the real-time characteristic, the data interface between FPGA and DSP requires a fast enough transmission speed. However the general serial interface, such as McBSP, is difficult to meet the requirement of the transmission speed. Therefore a multi-rate matched uPP which is used in data transmission between FPGA and DSP is to be implemented in this paper.

94.2 About uPP

This design is based on a dual-core application processor OMAP-L138, which is produced by TI. The uPP provided by OMAP-L138 is a multi-channel, high-speed parallel interface with dedicated data lines and minimal control signals, which includes two channels that can independently work at the same time [2]. It means that, the uPP can operate in receive mode, transmit mode, or duplex mode, in which its individual channels operate in opposite directions. Each channel can be set in 8-bit mode or 16-bit mode, and controlled by the signal of 'start', 'enable' and 'wait'. With the different supply voltages, the maximum operating frequency is different, which is 50 MHz in 1.1 V and 75 MHz in 1.2 V or 1.3 V. In 16-bit mode, the transmission rate can be up to 150 MByte/s. However, each channel of uPP contains only 1 clk signal, 3 control signals, and 16 data lines, which means that the transmission rate can be up to 150 MByte/s with only 20 I/O lines.

Benefit from the excellent parallel transmission capacity, uPP is widely used in real-time processing system with high data rate. It is designed to interface cleanly with high-speed ADC or DAC (Digital-to-Analog Converter) with up to 16-bit data width (per channel). It may also be interconnected with FPGA or other uPP devices to achieve high-speed digital data transmission.

94.3 The Implement of Multi-rate Matched uPP by FPGA

The rate of data after preprocessing by FPGA is different in different bandwidth. To simplify the design, the clock frequency of uPP is supposed to be unchanged. In order to match different data rates, a ping-pong buffer in dual-FIFO is added in front of uPP, so that a certain length data can be continuously transmitted without missing any data. The certain length of data is determined by the depth of the FIFO. After cached by dual-FIFO, the baseband data and spectral data are independently transmitted through the two channels of uPP. Because the operating modes of the two channels are the same, only one of them is introduced. The system data path is shown in Fig. 94.1.

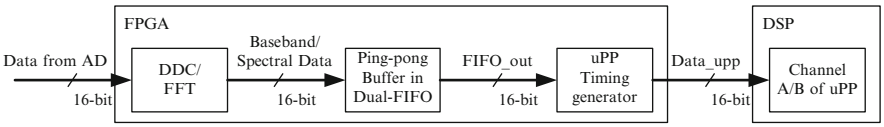

Fig. 94.1 Diagram of the system data path

94.3.1 The Implement of Ping-Pong Buffer in Dual-FIFO

When the transmission rate of uPP remains unchanged, if the data rate is larger than the transmission rate, it will lead to miss some data in the transmission, what is called distortion. On the contrary, if the data rate is less than the transmission rate, it will make the transmission discontinuous. To match the different data rates, a method of ping-pong buffer in dual-FIFO [3] is used in this design. The data width and depth of the two FIFOs are both the same. The operating flow of dual-FIFO is shown in Fig. 94.2.

When the data rate is larger than the transmission rate, which means that the writing speed of FIFO is faster than the reading speed, the step of operating the dual-FIFO is shown as following.

(1) Reset the system and clear both the two FIFOs;
(2) Write the input data into FIFO_A;
(3) After the FIFO_A is written full, write the input data into FIFO_B and read the data of FIFO_A at the same time;
(4) Wait for reading empty of FIFO_A, when FIFO_B is written full;
(5) After the FIFO_A is read empty, write the input data into FIFO_A and read the data of FIFO_B at the same time;
(6) Wait for reading empty of FIFO_B, when FIFO_A is written full;
(7) After the FIFO_B is read empty, write the input data into FIFO_B and read the data of FIFO_A at the same time;
(8) Repeat steps 4–7.

When the data rate is less than the transmission rate, which means that the writing speed of FIFO is slower than the reading speed, the step of operating the dual-FIFO is shown as following.

(1) Reset the system and clear both the two FIFOs;
(2) Write the input data into FIFO_A;
(3) After the FIFO_A is written full, write the input data into FIFO_B and read the data of FIFO_A at the same time;
(4) Wait for writing full of FIFO_B, when FIFO_A is read empty;
(5) After the FIFO_B is written full, write the input data into FIFO_A and read the data of FIFO_B at the same time;
(6) Wait for writing full of FIFO_A, when FIFO_B is read empty;
(7) Repeat steps 3–6.

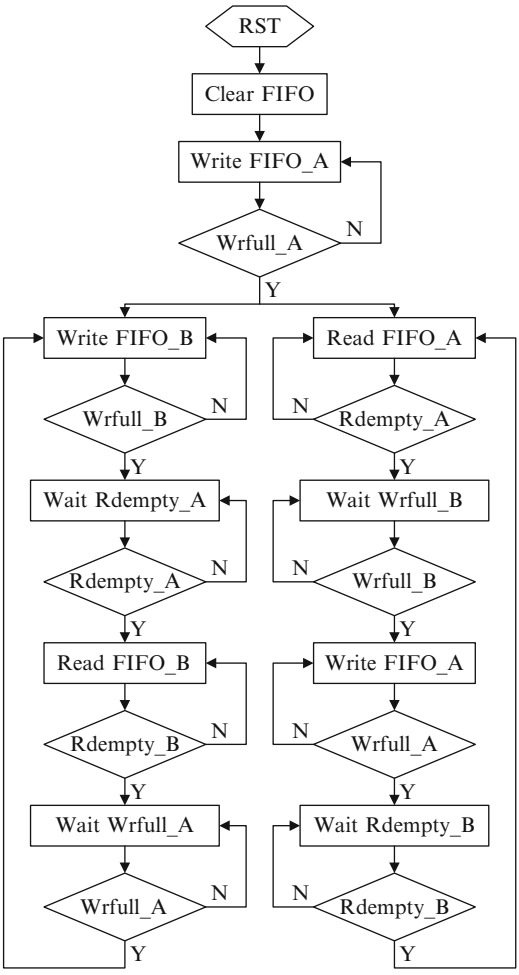

Fig. 94.2 The flow diagram of ping-pong buffer in dual-FIFO

The data with different rates is cached in the two FIFOs, which are set in front of uPP, and then sent to the uPP in an unchanged rate. Suppose that the depth of FIFO is 2048, and the data width is 16-bit. It can be guaranteed that the transmission of at least 2048 16-bit data is continuous and undistorted, and the data rate is the same with the transmission rate.

94.3.2 The Generator of uPP Timing

Each channel of uPP can operate in single-data-rate or double-data-rate. Each of them can operate in transmit direction or receive direction. Only single-data-rate in receive direction is introduced in this paper. Here the direction is from the point of

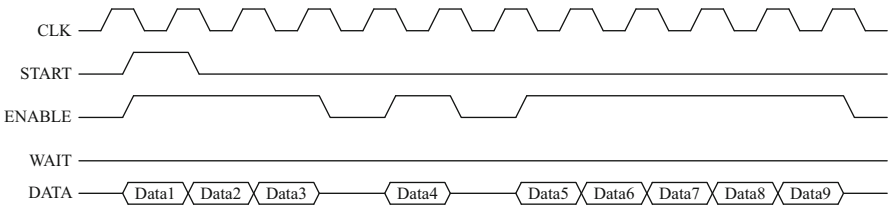

Fig. 94.3 uPP single-data-rate receive timing diagram

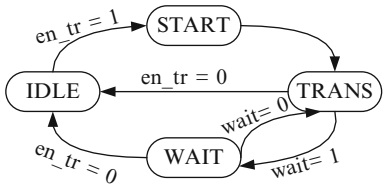

Fig. 94.4 State diagram of uPP

the DSP, which means that the data is transmitted from FPGA and received by DSP. The single-data-rate receive timing diagram is shown in Fig. 94.3. From the timing diagram, it can be seen that the first data should be in synchronization with the signal 'start', and the signal 'data', 'enable' and 'start' are all delay to the rising edge of the signal 'clk'.

What shown in Fig. 94.4 is the state diagram of uPP, in which the signal 'en_tr' is the enable signal of uPP. When the signal is high, it means that the data cached in the dual-FIFO is ready to be transmitted. Conversely, when the signal is low, it means that there is no data to be transmitted or the data is being cached. The operation that the four states do is shown as following.

IDLE	Initial all the signal of the interface
START	Generate the signal 'start' and 'enable', and transmit the first data at the same time
TRANS	Transmit the data
WAIT	Wait for data request of DSP.

By inversing the phase of clock or using the falling edge to trigger the circuit, the delay between the other signals and the clock signal can be easily implemented.

94.3.3 The Implement of Multi-rate Matched uPP

The different data rates under different bandwidths can be matched by a ping-pong buffer in dual-FIFO. The data after cached is transmitted to the uPP timing generator, and then transmitted to DSP. As the name suggests, what the uPP timing generator does is generating the timing of uPP. By compositing the modules as

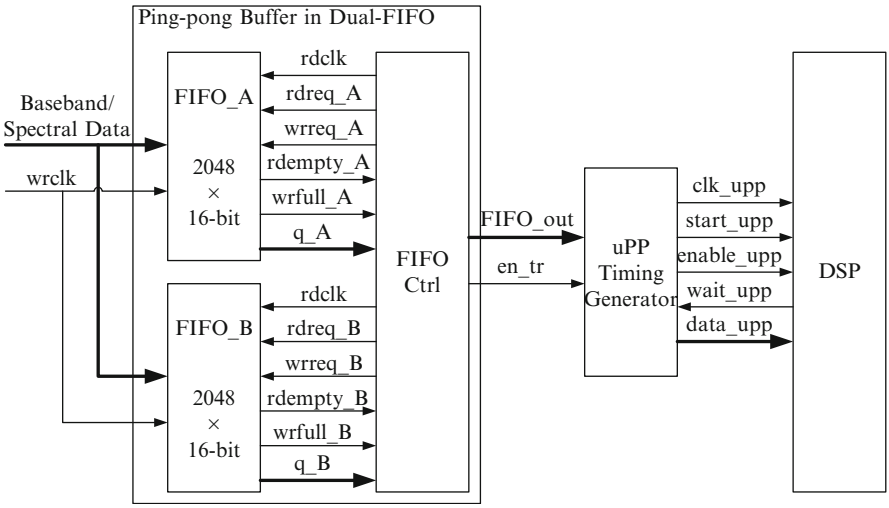

Fig. 94.5 The block diagram of multi-rate matched uPP

described above in FPGA and connecting with DSP, a multi-rate matched real-time data transmission can be implemented. What shown in Fig. 94.5 is the block diagram of multi-rate matched uPP. After preprocessed, the baseband data or spectrum data is cached by a ping-pong buffer in dual-FIFO, and then transmitted to DSP for further processing through the uPP timing generator.

94.4 Simulation and Testing

In order to verify the correctness of the design, simulation and testing are essential. Firstly, the logic circuit of this design is simulated in Modelsim, which is a simulation software developed by Mentor. After simulation, the code is supposed to be loaded into the FPGA chip. Then all the signals of uPP interface will be sampled by SignaltapII, which is embedded in QuartusII developed by Alter. Finally, the result of sampling will be contrasted with the data received in DSP. The design in this paper can be proved to be correct and feasible, if the transmitted data and the received data are the same.

94.4.1 Simulation in Modelsim

Modelsim is the best HDL language simulation software, in which the result of simulation is reliable. To reflect the process of multi-rate matching, the rate of input data is set to be half of the interface rate. Meanwhile, to make the simulation simple

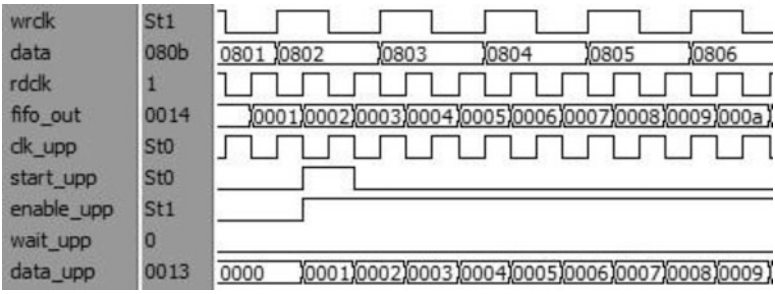

Fig. 94.6 Modelsim simulation diagram of uPP

and intuitive, the input data is set to self-increase from 1 to 65535. The depth of both the two FIFOs is 2048, and the data width is 16-bit.

As the Fig. 94.6 shown, the frequency of write clock is half the read clock. After the first FIFO is written full (note that, the depth of FIFO is 2048, and the 2048th data is 0x0800), the first data is beginning to be outputted from the dual-FIFO, and then transmitted to DSP through uPP. It is obvious that the logic of this design is correct by the comparison of Figs. 94.3 and 94.6.

94.4.2 Testing in Hardware

StratixII series chip EP2S180F1020, which is an FPGA chip developed by Altera, is selected in this design. While the DSP chip is the OMAP series chip OMAP_L138, which is developed by TI. The frequency of system clock is 60 MHz, and the uPP clock is 75 MHz, while the data rate is 37.5 MHz, which is half of the uPP clock. A phase locked loop (PLL) called from IP-core of Altera is used to generate the clock of 75 MHz and 37.5 MHz. The two FIFOs are also called from IP-core, of which the depth, data width and input data are all the same with the description in Sect. 94.4.1.

Comparing Figs. 94.6 and 94.7, it is obvious that the logic of the design can be implemented in hardware. What shown in Fig. 94.8 is the data received by DSP, which is the same with the input data. It means that, the uPP design in this paper can correctly transmit the 16-bit data from FPGA to DSP with a clock frequency of 75 MHz. Making a sample calculate, a conclusion can be easily gotten that the transmission rate of this interface is up to 150 MByte/s.

94.5 Summary

A multi-rate matched uPP is designed in this paper for the requirement of spectrum monitoring receiver that the multi-rate data can be real-time transmitted. By simulating in Modelsim and testing in hardware, it is proved that the baseband data and

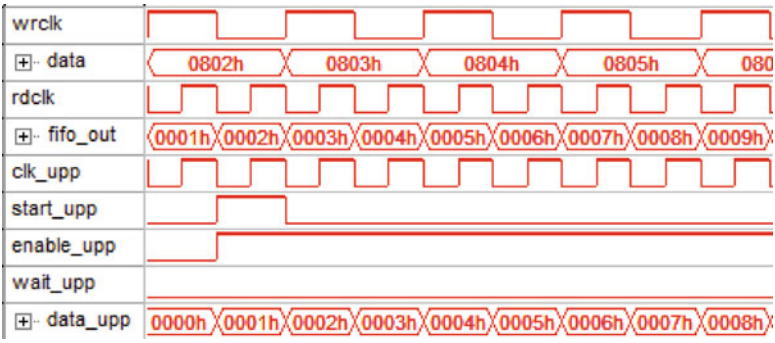

Fig. 94.7 Sampling diagram of uPP in SignaltapII

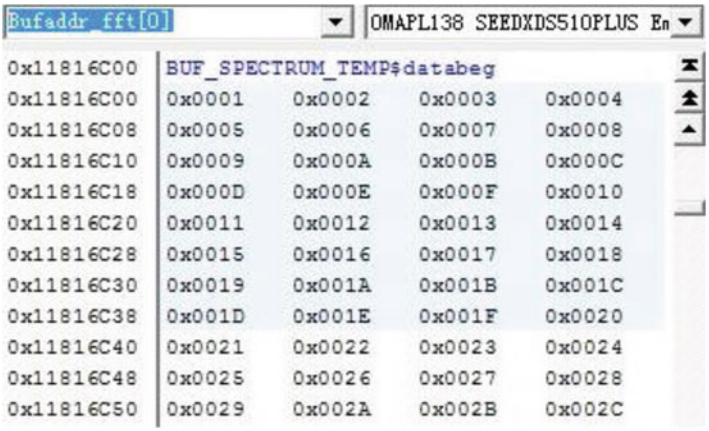

Fig. 94.8 The data received by DSP

spectral data in different bandwidths can be correctly transmitted through uPP from FPGA to DSP. In this paper, a high transmission rate interface which is up to 150 MByte/s is implemented with only 20 I/O lines, and the adaption of multi-rate input data is implemented by a ping-pong buffer in dual-FIFO. This design can be also used in other systems with the requirement of real-time transmission of high-rate data.

References

1. Lian F (2009) Renovation in Radio Monitoring System. J Electron Meas Instrum
2. Texas Instrument (2011) OMAP L-138 C600 DSP + ARM processor technical datasheet. http://www.ti.com/product/omap-l138
3. Ping X, Hong-cheng Z, Ting X (2011) A design of McBSP interface for multiple rate matching based on ping-pong catching in two FIFO. Electron Qual 9:011

Chapter 95
Interrelation Analysis of Behavioral Measures of Power Amplifier Nonlinearity

Yiming Lei and Liaoyuan Zeng

Abstract Nonlinear distortion is generated when signals are driven through nonlinear power amplifiers (PAs), and it is a major degradation in orthogonal frequency-division multiplexing (OFDM) like multi-carrier signal transmitter systems. The nonlinearity of PAs is mostly evaluated by three measures, i.e., 1dB compression point (P1dB), the 3rd order intercept point (IP3), and percentage linearity (PL). In this paper, the interrelationship between these three measures of PA nonlinearity are derived by using a truncated complex power series model.

Keywords Power amplifier • Nonlinear distortion • P1dB • IP3 • PL

95.1 Introduction

In orthogonal frequency-division multiplexing (OFDM) communications systems, power amplifiers (PAs) generate the nonlinear distortion, which is a major signal impairment, [1]. OFDM-like multi-carrier communication systems have a nature of high peak-to-average power ratio (PAPR) performance, and this is because that these signals are companied with a large number of independent subcarriers and non-constant envelope modulation (NoCEM) schemes, [2]. Measurements of PA nonlinearity is an elemental concern in behavioural research of nonlinear PAs, and the most frequent measures of PA nonlinearity are, 1dB compression-point (P1dB), output 3rd intercept-point (IP3), and a newly established one - percentage linearity (PL) [3, 4].

The focuses of these three measures are different. For example, P1dB focuses on the medium nonlinearity range of PA envelope obtained in a single-tone

Y. Lei (✉)
School of Electronics Engineering and Computer Science, Peking University, Beijing, China
e-mail: leiym@pku.edu.cn

L. Zeng
School of Electronics Engineering, University of Electronic Science and Technology of China, Chengdu, China
e-mail: lyzeng@uestc.edu.cn

J. Mu et al. (eds.), *The Proceedings of the Third International Conference on Communications, Signal Processing, and Systems*, Lecture Notes in Electrical Engineering 322, DOI 10.1007/978-3-319-08991-1_95

experiment; IP3 is based on a two-tone experiment, and it focuses on the relation between fundamental carriers and the 3rd order intermodulation products (IMPs); and PL focuses on the power of saturation point of PA envelope; Although these measures are frequently used, the analysis of their interrelationship is still lacked. This paper present our efforts seeking the answer to this question.

This paper is organized as follows. In Sect. 95.2, the theoretical derivation of application of the power series model is introduced. Expression of three measures by using a 3rd order power series model is given in Sect. 95.3. Finally the conclusions are shown in section "Conclusion".

95.2 Modeling of PA Nonlinear Distortion

Complex power series model is widely used in general derivation of PA behavioural modelling [5]. The link between input and output signals can be expressed as,

$$s_o(t) = k_1 s_i(t) + k_2 s_i^2(t) + k_3 s_i^3(t) \tag{95.1}$$

Equation (95.1) is a 3rd order truncated power series model, and it can satisfy the modelling accuracy in most cases [6]. Assuming the investigated PA is a solid state PA (SSPA), its AM/PM conversion can neglected here, and thus, the coefficients are treated as real values [7].

In a single tone experiment, the input signal can be written as:

$$s_i(t) = A[\cos(\omega t + \varphi(t))] \tag{95.2}$$

The power of zonal output of a single-tone signal (out_1tone) may be written as:

$$P_{out\_1tone} = \left(k_1 A + \frac{3}{4} k_3 A^3\right)^2 \tag{95.3}$$

Also, the power of input single-tone signal (in_1tone) is,

$$P_{in\_1tone} = A^2 \tag{95.4}$$

Rewritten Eqs. (95.3) and (95.4) in unit of decibels, we may obtain:

$$P_{out\_1tone}(dB) = 20 * \lg\left(k_1 A + \frac{3}{4} k_3 A^3\right) \tag{95.5}$$

and

$$P_{in\_1tone}(dB) = 20 * \lg(A) \tag{95.6}$$

In a two-tone experiment, the input signal can be written as,

$$s_i(t) = A[\cos(\omega_1 t + \varphi_1(t)) + \cos(\omega_2 t + \varphi_2(t))] \tag{95.7}$$

Introducing (95.7) into (95.1), the powers of each fundamental carrier (*fund_2tone*), 3rd order IMP (*IMP*3_2*tone*), and input signal (*in_2tone*) can be written as,

$$P_{fund\_2tone} = \left[k_1 A + \frac{9}{4} k_3 A^3\right]^2 \tag{95.8}$$

$$P_{IMP3\_2tone} = \left[\frac{3}{4} k_3 A^3\right]^2 \tag{95.9}$$

$$P_{in\_2tone} = 2A^2 \tag{95.10}$$

Similarly with (95.5) and (95.6), we can have that

$$P_{fund\_2tone}(dB) = 20 * \lg\left[k_1 A + \frac{9}{4} k_3 A^3\right] \tag{95.11}$$

$$P_{IMP3\_2tone}(dB) = 20 * \lg\left[\frac{3}{4}|k_3|A^3\right] \tag{95.12}$$

$$P_{in\_2tone}(dB) = 20 * \lg[\sqrt{2}A] \tag{95.13}$$

95.3 Interrelation Analysis of PA Nonlinearity Measures

The definition of P1dB is based on the linear extrapolation curve (LEC) of PA single-tone envelope characteristics. Thus, the slope and intercept have to be derived to extract the track function of LCE, which can be written as,

$$Slope\_LEC_{1tone} = \lim_{A \to 0}\left[\frac{k_1 A + \frac{9}{4} k_3 A^3}{k_1 A + \frac{3}{4} k_3 A^3}\right] = 1 \tag{95.14}$$

Then, the LEC of single tone characteristics can be written as,

$$y_{LEC\_1tone}(dB) = P_{in\_1tone}(dB) + b_{LEC\_1tone}(dB) \tag{95.15}$$

where y_{LEC_1tone} denotes LEC, and b_{LEC_1tone} is the intercept of LEC of single tone characteristics with y-axis.

Since Eq. (95.15) shows the asymptote of single-tone output characteristics, we can have that,

$$\begin{aligned}
&\lim_{A\to 0}\left[1*P_{in_1tone}(dB)+b_{LEC_1tone}(dB)-P_{out_1tone}(dB)\right]=0\\
&\Rightarrow\\
&b_{LEC_1tone}(dB)=\lim_{A\to 0}\left[P_{out_1tone}(dB)-1*P_{in_1tone}(dB)\right]\\
&\qquad=\lim_{A\to 0}\left[20*\lg\frac{k_1A+\frac{3}{4}k_3A^3}{A}\right]=20*\lg(k_1)
\end{aligned}\tag{95.16}$$

From the definition of P1dB, we may obtain:

$$\begin{aligned}
&P_{out_1tone}(dB)-P_{in_1tone}(dB)=y_{LEC_1tone}(dB)-1\\
&\Rightarrow\\
&20*\lg\left[\frac{k_1A+\frac{3}{4}k_3A^3}{A}\right]=20\lg(10^{-1/20}k_1)
\end{aligned}\tag{95.17}$$

Simplifying (95.17), the input power of P1dB, i.e., $P_{in\_1tone\_P1dB}(dB)$, can be derived as,

$$\begin{aligned}
&k_1+\frac{3}{4}k_3A^2=10^{-120}k_1\\
&\Rightarrow\\
&P_{in_1tone_P1dB}=\frac{4}{3}(10^{-120}-1)k_1k_3\cong -0.145k_1k_3
\end{aligned}\tag{95.18}$$

From the definition of PL, we can have that,

$$\begin{aligned}
&d[P_{out_1tone}(dB)]d[P_{in_1tone}(dB)]=0.1\\
&\Rightarrow\frac{k_1A+\frac{9}{4}k_3A^3}{k_1A+\frac{3}{4}k_3A^3}=0.1\\
&\Rightarrow P_{in_1tone_PL}=-3.6k_18.7k_3
\end{aligned}\tag{95.19}$$

where $P_{in\_1tone\_PL}$ denotes the input power of PL in single-tone experiment.

Calculation of IP3 is a bit more complex than other two measures above, since the definition of IP3 explores linear extrapolations of both fundamental carriers and IMPs. In a two-tone experiment, the slope of linear extrapolations of each fundamental carrier may be calculated as:

$$\begin{aligned}
&\lim_{A\to 0} d[P_{fund_2tone}(dB)]d[P_{in_2tone}(dB)] \\
&= \lim_{A\to 0} d\left[\lg(k_1A + \frac{9}{4}k_3A^3)\right] d\left[\lg(\sqrt{2}A)\right] \\
&= \lim_{A\to 0} \frac{\sqrt{2}A\left(k_1 + \frac{27}{4}k_3A^2\right)}{\sqrt{2}\left(k_1A + \frac{9}{4}k_3A^3\right)} = 1
\end{aligned} \tag{95.20}$$

The slope of linear extrapolations of single 3rd IMP may be calculated as:

$$\begin{aligned}
&\lim_{A\to 0} d[P_{IMP3_2tone}(dB)]d[P_{in_2tone}(dB)] \\
&= \lim_{A\to 0} d\left[\lg\left(\frac{3}{4}|k_3|A^3\right)\right] d[\lg(\sqrt{2}A)] \\
&= \lim_{A\to 0} \frac{-3\sqrt{2}A\frac{3}{4}k_3A^2}{-\sqrt{2}\frac{3}{4}k_3A^3} = 3
\end{aligned} \tag{95.21}$$

Thus, based on above derivations, the track equation of LEC of fundamental carrier in a two-tone experiment may be written as:

$$y_{LEC\_fund\_2tone}(dB) = 1*P_{fund\_2tone}(dB) + b_{LEC\_IMP3\_2tone}(dB) \tag{95.22}$$

where the $y_{LEC\_fund\_2tone}$ denotes the LEC of fundamental carrier, and $b_{LEC\_fund\_2tone}$ denotes the intercept of LEC of fundamental carrier with y-axis in a two-tone experiment. Since Eq. (95.22) is the asymptote of fundamental component in two tone experiment, as derived in Eqs. (95.11)–(95.13), we may obtain:

$$\begin{aligned}
&\lim_{A\to 0}[1*P_{in_2tone}(dB) + b_{LEC_fund_2tone}(dB)] = P_{fund_2tone}(dB) \\
&\Rightarrow \\
&b_{LEC_fund_2tone}(dB) = \lim_{A\to 0}[P_{fund_2tone}(dB) - P_{in_2tone}(dB)] \\
&\qquad = \lim_{A\to 0}\left[20*\lg\frac{k_1A + \frac{9}{4}k_3A^3}{\sqrt{2}A}\right] \\
&\qquad = 20*\lg(k_1/\sqrt{2})
\end{aligned} \tag{95.23}$$

The track equation of LEC of single IMP3 component in two tone experiment may be written as:

$$y_{LEC\_IMP3\_2tone}(dB) = 3*P_{IMP3\_2tone}(dB) + b_{LEC\_IMP3\_2tone}(dB) \tag{95.24}$$

where the $y_{LEC\_IMP3\_2tone}$ denotes the LEC of IMP3, and $b_{LEC\_IMP3\_2tone}$ denotes the intercept of LEC of IMP3 with y-axis in a two-tone experiment. Since Eq. (95.24) is the asymptote of IMP3 component in a two-tone experiment, as derived in Eqs. (95.11)–(95.13), we may obtain:

$$\begin{aligned}
&\lim_{A\to 0}\left[3*P_{IMP3_2tone}(dB) + b_{LEC_IMP3_2tone}(dB)\right] = P_{IMP3_2tone}(dB)\\
&\Rightarrow\\
&b_{LEC_IMP3_2tone}(dB) = \lim_{A\to 0}\left[P_{IMP3_2tone}(dB) - 3*P_{in_2tone}(dB)\right]\\
&\qquad = \lim_{A\to 0}\left[20*\lg\frac{\frac{3}{4}|k_3|A^3}{2\sqrt{2}A^3}\right]\\
&\qquad = 20*\lg(|k_3|/8\sqrt{2})
\end{aligned} \tag{95.25}$$

According to definition of IP3, we may have,

$$\begin{aligned}
&P_{fund_2tone}(dB) = P_{IMP3_2tone}(dB)\\
&\Rightarrow\\
&3*P_{in_2tone}(dB) + b_{LEC_IMP3_2tone}(dB)\\
&\qquad = 1*P_{in_2tone}(dB) + b_{LEC_fund_2tone}(dB)\\
&\Rightarrow\\
&40*\lg[\sqrt{2}A] = 20*\lg(k_1/\sqrt{2}) - 20*\lg(|k_3|/8\sqrt{2})\\
&\Rightarrow\\
&P_{in_2tone_IMP3} = \frac{8k_1}{|k_3|} = \frac{-8k_1}{k_3}
\end{aligned} \tag{95.26}$$

where $P_{in\_2tone\_IMP3}$ denotes the input power of IP3.

Observing (95.18), (95.19), and (95.26), it is interesting to find that, when the 3rd order nonlinearity dominates PA behavior, the measures of PA nonlinearity P1dB, IP3, and PL are actually equivalent.

Conclusion

The derivation presented in this paper discloses the relationship among P1dB, IP3 and PL, three popular measures for PA nonlinearity. The three measures are equivalent with an approximately fixed distance in input decibels over considered dynamic range that three-term power series shows acceptable modelling accuracy. From the derivation results, it can be seen that it is interesting to find that, when the 3rd order nonlinearity dominates PA behavior, the measures of PA nonlinearity P1dB, IP3, and PL are actually equivalent.

References

1. Lei Y, O'Droma M, Jin Y (2014) A practical analysis of performance optimization in OSTBC based nonlinear MIMO-OFDM systems. IEEE Trans Commun 62:930–938. doi:10.1109/TCOMM.2014.010414.130533
2. Lei Y, Dong M, Jin Y (2014) The sensitivity of modulation fidelity on PA envelope variation in OFDM transmitter systems. EURASIP J Wirel Commun Netw 52:1–15. doi:10.1186/1687-1499-2014-52
3. O'Droma M, Mgebrishvili N (2005) On quantifying the benefits of SSPA linearization in UWC-136 systems. IEEE Trans Signal Process 53:2470–2476. doi:10.1109/TSP.2005.849190
4. Maas S (2003) Nonlinear microwave and RF circuits. Artech House, Norwood
5. Fager C, Pedro C, Carvalho B, Zirath H, Fortes F, Rosario J (2004) A comprehensive analysis of IMD behavior in RF CMOS power amplifiers. IEEE J Solid State Circuits 39:24–34. doi:10.1109/JSSC.2003.820860
6. Chorti A, Brookes M (2006) On the effects of memoryless nonlinearities on M-QAM and DQPSK OFDM signals. IEEE Trans Microw Theory Tech 54:3301–3315. doi:10.1109/TMTT.2006.879129
7. Minkoff J (1985) The role of AM-PM conversion in memoryless nonlinear systems. IEEE Trans Commun 33:139–144. doi:10.1109/TCOM.1985.1096262

Chapter 96
The Relationship Between Color Gamut and Brightness of Multi-primary Color Displayer

Yuli Ding, Yan Li, Na Li, Yanlin Du, Xinzhi Wang, and Zhe Wang

Abstract Colors show vivid colorful images displayed by three or more primary colors on each individual pixel. However, the brightness of the color greatly limits the color gamut of the displayer. According to the color mixture principle, the total color gamut shrinks with the increase of brightness. When the maximal brightness, the displayers only show white point of display system. This paper puts forward a theory of the relationship between brightness and color gamut based on multi-primary displayer. The paper simulates and estimates the color gamut boundary of multi-primary colors under the required brightness, which was proved by the experimental results of three primary colors displayer.

Keywords Brightness • 3-D color gamut • Multi-primary • Reconstruction

96.1 Introduction

Recently, many applications require accurate color images reproduction, such as desktop electronic publishing and network office system. For these applications, color displayer market emphasizes that not only display panel size but also color gamut is larger. In addition, some systems requiring original colors, such as medical and military applications or visual communication, are extremely important and are now being developed. But the color gamut of three primary colors displayer, such as the traditional Cathode Ray Tube (CRT) and Liquid Crystal Display (LCD), can't meet these requirements. The color gamut displayed by three primary colors is a triangle on the chromaticity diagram, but a big area on a chromaticity diagram is beyond the triangle. These colors are cut or mapped to the similar colors in the

This paper is subsidized by the Undergraduate Training Programs for Innovation and Entrepreneurship of Tianjin (201410065027)

Y. Ding • Y. Li (✉) • N. Li • Y. Du • X. Wang • Z. Wang
College of Electronic and Communication Engineering,
Tianjin Normal University, Tianjin, China
e-mail: wdxyliy@163.com

J. Mu et al. (eds.), *The Proceedings of the Third International Conference on Communications, Signal Processing, and Systems*, Lecture Notes in Electrical Engineering 322, DOI 10.1007/978-3-319-08991-1_96

reproduction of the color gamut. In general, the reproduced colors and the original colors are different, although the color gamut mapping technology has been studied to compensate the differences of the color gamut between different display devices [1–4].

It is clear that the color gamut is determined by the primary colors of the displayer. In order to display higher saturation colors, there are two methods to expand the color gamut. One method is to widen chromaticity_coordinate triangle by increasing the purity of primary colors. RGB laser display, Light-Emitting Diode (LED) display and Organic Light Emitting Diode (OLED) displays have a high degree of saturation, because their spectrum width of primary colors are narrower than the width of the CRT, plasma displays, and LCD. When each maximal luminous flux of the three primary colors is limited, the maximal brightness of display will be limited by the total maximal brightness of three primary colors. However, color gamut is still limited in the triangle area. Another way to expand the color gamut of displayer is to create four or more primary colors display system, which have polygon color gamut in chromaticity diagram. The display system with more than three primary colors is called Multi-primary color display (MPD).

Regardless of any primary colors, brightness of color displayer greatly limits color gamut of the system. From the principle of additive color mixture, the area of color gamut decreases with the increase of the brightness. When the maximal brightness, the displayer can only represent the system white point [5]. In order to establish the relationship between the brightness and color gamut, relevant primary colors brightness method was put forward in 2005 [2]. For N primary colors displayer whose white point is given, it only need (N-3) degrees of freedom to determine the relative brightness of N primary colors . Yet even reduce the three degrees of freedom, the method of reference [2] is almost not possible for seven or more primary colors. Because it is very difficult to analyze the locus of four or higher dimensions in the current coordinates. This paper proposes a method that the gamut of multi-primary colors displayer is mapped to two dimensional chromaticity diagram by the polygon area. Thus the problem of multi-primary colors is solved in two dimensional color space, the complexity of algorithms is reduced.

96.2 The Principle of Mixed Color

In essence, the light is made up of a series of spectrum of electromagnetic waves . In order to standardize presentation of color, International Commission on Illumination (IEC) set the wavelength of monochromatic light of three primary colors (red, Green, Blue) as 700, 546.1 and 435.8 nm respectively in 1931. And then, CIEXYZ color system was defined, in which the relationship between color coordinates and tristimulus values X, Y, and Z was provided as shown in formula (96.1):

$$\begin{cases} x = \dfrac{X}{X+Y+Z} \\ y = \dfrac{Y}{X+Y+Z} \\ z = \dfrac{Z}{X+Y+Z} \end{cases} \tag{96.1}$$

As the coordinates of color C_1 and C_2 used to match are (X_1,Y_1,Z_1) and (X_2,Y_2,Z_2) respectively, according to the superposition principle of tristimulus values, X_3, Y_3 and Z_3 ,the tristimulus values of mixed color C_3, can be calculated with the formula (96.2).

$$\begin{cases} X_3 = X_1 + X_2 \\ Y_3 = Y_1 + Y_2 \\ Z_3 = Z_1 + Z_2 \end{cases} \tag{96.2}$$

From formula (96.1) and (96.2), 2-D chromatic coordinates of color C_3 are obtained, which is represented as formula (96.3).

$$\begin{cases} x_3 = \dfrac{X_3}{X_3+Y_3+Z_3} = \dfrac{X_1+X_2}{(X_1+Y_1+Z_1)+(X_2+Y_2+Z_2)} = \dfrac{m_1x_1+m_2x_2}{m_1+m_2} \\ y_3 = \dfrac{Y_3}{X_3+Y_3+Z_3} = \dfrac{Y_1+Y_2}{(X_1+Y_1+Z_1)+(X_2+Y_2+Z_2)} = \dfrac{m_1y_1+m_2y_2}{m_1+m_2} \end{cases} \tag{96.3}$$

Where m_1 and m_2 represent (Y_1/y_1) and (Y_2/y_2) respectively, and the coordinates of mixed color $C_3(x_3, y_3)$ is at the center of gravity position of the weight $m_1(Y_1/y_1)$ of C_1 and the weight $m_2(Y_2/y_2)$ of C_2. The result is based on the center of gravity law of color mixing [6, 7].

96.3 The Color Gamut of Three Primary Colors Displayer

The coordinates of three primary colors (Red, Green and Blue) were measured as (x_r,y_r), (x_g,y_g),(x_b,y_b) respectively, and the maximal brightness is $Y_{r,max}$,$Y_{g,max}$,$Y_{b,max}$ respectively. The brightness of colors mixed is determined by the brightness values of primary colors. As the maximal brightness of each of three primary colors is fixed, the display system has a fixed maximal brightness value. So color gamut boundary is discussed with different brightness area combined by the maximal brightness of possible primary colors. The possible combination of the maximal brightness of primary colors is expressed as formula (96.4).

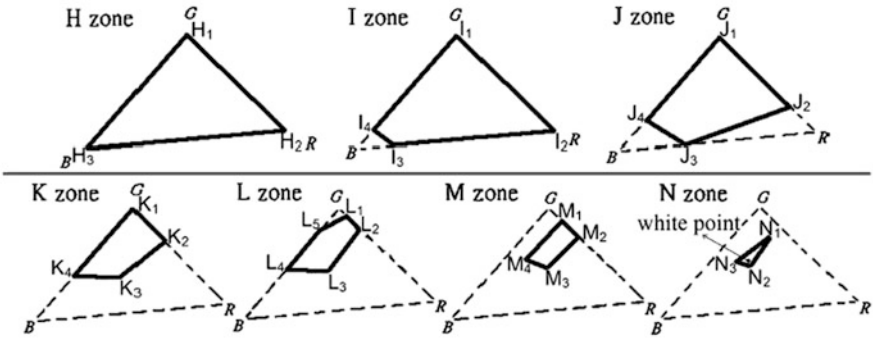

Fig. 96.1 The seven areas determined by brightness of three-primary system

$$\sum_{m=1}^{n} C(n,m) \tag{96.4}$$

where C(n,m) = n!/[m!(n-m)!], and n! = n*(n − 1)*(n − 2)*. . .*3*2*1. The meaning of m! is same as n!. So the color gamut of three primary colors is discussed in seven areas which are get from C(3,1) + C(3,2) + C(3,3). The seven areas are represented by H to N area respectively, shown in Fig. 96.1.

There are four steps to determine color gamut boundary in different brightness regions. The first step is to choose the total brightness value will be discussed. The second step is to determine which region that the specific Y belongs to. Then the mixed coordinates of color gamut vertex are calculated by formula (96.1). The last step is to get color gamut boundary in the corresponding brightness

96.4 The Color Gamut of Multi-primary Colors Displayer

When considering the gamut of N primary colors, where N is larger than three, it needs to discuss the color gamut boundary of Y through different brightness in $\sum_{i=0}^{N-1} C(N,i)$ areas. But it is different from three primary colors system. The difference is that N primary colors system contains un-adjacent primary colors, as shown C_1 and C_3 in Fig. 96.2a. The color gamut boundary vertex of C_1C_3, M_3 is on the line linked by C_1C_3, and M_3 is contained in the color gamut boundary, which is made of adjacent primary colors. Where the color gamut boundary vertexes of the adjacent primary colors refer to M_1 and M_2. Because M_3 is included in the color gamut boundary, M_3 is not true color gamut boundary vertex. The situation appears in the range of 2 to N − 2. When N is larger than four, the gamut vertexes of some non-adjacent primary colors are not suitable. Therefore, for multi-primary colors display system, only color gamut boundary points of adjacent primary colors are considered.

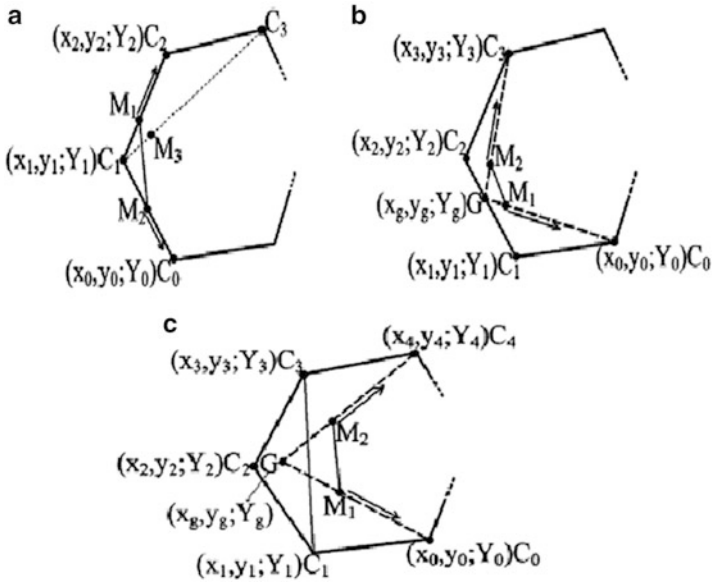

Fig. 96.2 (**a**) When the value of lightness of C_1 is smaller than that of total system, (**b**) when the value of lightness of C_1 and C_2 is smaller than that of total system, (**c**) when the value of lightness of C_1, C_2 and C_3 is smaller than that of total system

The theory above suggests that when the maximal brightness of the primary color is smaller than the total luminance Y, with the increase of Y, color gamut boundary vertexes approach to the two adjacent primary colors, which is also the nearest primary colors , as shown in M area of Fig. 96.1. In M area of Fig. 96.1, when the maximal brightness of blue primary color is smaller than the total luminance Y, with the increase of Y, two vertexes of color gamut boundary M_3 and M_4 approach to the red and green coordinates respectively. In other words, the coordinates of the M_3 and M_4 were the center of gravity position of blue and red, blue and green respectively.

The conclusion is applicable for mixing more colors, as shown in Fig. 96.2a. When maximal brightness of primary color C_1 is smaller than the total luminance Y, with the increase of Y, two vertexes of color gamut boundary, M_1 and M_2 approach to primary C_0 and C_2 respectively. In other words, the coordinates of the M_3 and M_4 were the center of gravity position of C_0 and C_1, C_1 and C_2 respectively. The above characteristics is expressed as $B[M_1,M_2] = B[P(C_1,C_0), P(C_1,C_2)$, the coordinates are represented as Eqs. 96.5 and 96.6.

$$M_1 = \left(\frac{\frac{Y_1}{y_1}x_1 + \frac{Y-Y_1}{y_0}x_0}{\frac{Y_1}{y_1} + \frac{Y-Y_1}{y_0}}, \frac{\frac{Y_1}{y_1}y_1 + \frac{Y-Y_1}{y_0}y_0}{\frac{Y_1}{y_1} + \frac{Y-Y_1}{y_0}} \right) \tag{96.5}$$

$$M_2 = \left(\frac{\frac{Y_1}{y_1}x_1 + \frac{Y - Y_1}{y_2}x_2}{\frac{Y_1}{y_1} + \frac{Y - Y_1}{y_2}}, \frac{\frac{Y_1}{y_1}y_1 + \frac{Y - Y_1}{y_2}y_2}{\frac{Y_1}{y_1} + \frac{Y - Y_1}{y_2}} \right) \tag{96.6}$$

Where $B[M_1,M_2]$ represents color gamut boundary to connect two vertexes M_1 and M_2, $P(C_0,C_1,C_2,C_3,....C_N)$ represents the center of gravity position of C_0,C_1,C_2, $C_3,....$ and C_N. In other words, the coordinates of mixed colors, M_1 and M_2, is the center of gravity position of the weights $(Y - Y_1)/y_0$, Y_1/y_1, and the weights of $(Y - Y_1)/y_2$ and Y_1/y_1.

Similarly, if the maximal brightness of the two adjacent primary colors is smaller than the total brightness, with the increase of Y, the vertex of color gamut boundary approach to the adjacent primary colors, as shown in K area of Fig. 96.1. K_3 is the center of gravity position of blue, red and green. This conclusion is also applied to multi-primary colors mixture, as shown in Fig. 96.2b. In Fig. 96.2b, when the brightness of two adjacent primary colors, C_1 and C_2 are smaller than the total brightness Y, with the increase of Y, two vertexes of color gamut boundary , M_1 and M_2 approach to C_0 and C_3 respectively. In other words, coordinates of M_1 and M_2 are the center of gravity position of C_1, C_2 and C_0, C_1, C_2 and C_3. The above characteristics expressed in mathematical form is: $B[M_1,M_2] = B[P(P(C_1,C_2), C_0),P(P(C_1,C_2), C_3)] = B[P(G,C_0),P(G,C_3)]$. Where G is the center of gravity position of C_1 and C_2. That is to say, coordinates of mixed color G is the center of gravity position of the weights Y_1/y_1 and Y_2/y_2. The relation between G and color gamut boundary point, M_1 and M_2 is as follows:

$$G = \left(x_g, y_g\right) = \left(\frac{\frac{Y1}{y1}x1 + \frac{Y2}{y2}x2}{\frac{Y1}{y1} + \frac{Y2}{y2}}, \frac{\frac{Y1}{y1}y1 + \frac{Y2}{y2}y2}{\frac{Y1}{y1} + \frac{Y2}{y2}} \right) \tag{96.7}$$

$$M_1 = \left(\frac{\frac{Y1+Y2}{yg}xg + \frac{Y-Y1-Y2}{y0}x0}{\frac{Y1+Y2}{yg} + \frac{Y-Y1-Y2}{y0}}, \frac{\frac{Y1+Y2}{yg}yg + \frac{Y-Y1-Y2}{y0}y0}{\frac{Y1+Y2}{yg} + \frac{Y-Y1-Y2}{y0}} \right) \tag{96.8}$$

$$M_2 = \left(\frac{\frac{Y1+Y2}{yg}xg + \frac{Y-Y1-Y2}{y3}x3}{\frac{Y1+Y2}{yg} + \frac{Y-Y1-Y2}{y3}}, \frac{\frac{Y1+Y2}{yg}yg + \frac{Y-Y1-Y2}{y3}y3}{\frac{Y1+Y2}{yg} + \frac{Y-Y1-Y2}{y3}} \right) \tag{96.9}$$

Similarly, when the maximal brightness of the three adjacent primary colors is smaller than the total brightness, with the increase of Y, the two vertexes of color gamut boundary approach to the adjacent primary colors, as shown in Fig. 96.2c. In Fig. 96.2c, the brightness of the three adjacent primary colors C_1, C_2 and C_3, is smaller than the total brightness Y, with the increase of Y, two vertexes of color gamut boundary, M_1 and M_2 approach to the primary colors C_0 and C_4 respectively. In other words, coordinates of M_1 and M_2 are the center of gravity position of C_1, C_2, C_3 and C_0, C_1, C_2, C_3 and C_4. The above characteristics expressed in mathematical form is: $B[M_1,M_2] = B[P(P(C_1,C_2), C_0), P(P(C_1,C_2), C_3)] = B[P(G,C_0), P(G,C_3)]$. Where G is the center of gravity position of C_1 and C_2. That is to say, coordinates of mixed color G is the center of gravity position of the weights Y_1/y_1 and Y_2/y_2. The relation between G and color gamut boundary point, M_1 and M_2 is as follows:

$$G = \left(x_g, y_g\right) = \left(\frac{\frac{Y1}{y1}x1 + \frac{Y2}{y2}x2 + \frac{Y3}{y3}x3}{\frac{Y1}{y1} + \frac{Y2}{y2} + \frac{Y3}{y3}}, \frac{\frac{Y1}{y1}y1 + \frac{Y2}{y2}y2 + \frac{Y3}{y3}y3}{\frac{Y1}{y1} + \frac{Y2}{y2} + \frac{Y3}{y3}} \right) \tag{96.10}$$

$$M_1 = \left(\frac{\frac{Y1+Y2+Y3}{yg}xg + \frac{Y-Y1-Y2-Y3}{y0}x0}{\frac{Y1+Y2+Y3}{yg} + \frac{Y-Y1-Y2-Y3}{y0}}, \frac{\frac{Y1+Y2+Y3}{yg}yg + \frac{Y-Y1-Y2-Y3}{y0}y0}{\frac{Y1+Y2+Y3}{yg} + \frac{Y-Y1-Y2-Y3}{y0}} \right) \tag{96.11}$$

$$M_2 = \left(\frac{\frac{Y1+Y2+Y3}{yg}xg + \frac{Y-Y1-Y2-Y3}{y4}x4}{\frac{Y1+Y2+Y3}{yg} + \frac{Y-Y1-Y2-Y3}{y4}}, \frac{\frac{Y1+Y2+Y3}{yg}yg + \frac{Y-Y1-Y2-Y3}{y4}y4}{\frac{Y1+Y2}{yg} + \frac{Y-Y1-Y2}{y4}} \right) \tag{96.12}$$

Thus, the three relations of G and color gamut boundary, M_1 and M_2 are shown in formula (96.14) and (96.15). According to this theory, the color gamut boundary of multi-primary color display can be gotten, and the color gamut is the lines linked by the suitable color gamut vertexes. Finally, the color gamut boundary of multi-primary color is determined.

$$G = \left(x_g, y_g\right) = \left(\frac{\sum_{k=i}^{j} \frac{Yk}{yk}xk}{\sum_{k=i}^{j} \frac{Yk}{yk}}, \frac{\sum_{k=i}^{j} \frac{Yk}{yk}yk}{\sum_{k=i}^{j} \frac{Yk}{yk}} \right) \tag{96.13}$$

$$M_1 = \left(\frac{\frac{\sum_{k=i}^{j} Yk}{yg} xg + \frac{Y - \sum_{k=i}^{j} Yk}{yi-1} xi - 1}{\frac{\sum_{k=i}^{j} Yk}{yg} + \frac{Y - \sum_{k=i}^{j} Yk}{yi-1}}, \frac{\frac{\sum_{k=i}^{j} Yk}{yg} yg + \frac{Y - \sum_{k=i}^{j} Yk}{yi-1} yi - 1}{\frac{\sum_{k=i}^{j} Yk}{yg} + \frac{Y - \sum_{k=i}^{j} Yk}{yi-1}} \right) \tag{96.14}$$

$$M_2 = \left(\frac{\frac{\sum_{k=i}^{j} Yk}{yg} xg + \frac{Y - \sum_{k=i}^{j} Yk}{yj+1} xj + 1}{\frac{\sum_{k=i}^{j} Yk}{yg} + \frac{Y - \sum_{k=i}^{j} Yk}{yj+1}}, \frac{\frac{\sum_{k=i}^{j} Yk}{yg} yg + \frac{Y - \sum_{k=i}^{j} Yk}{yj+1} yj + 1}{\frac{\sum_{k=i}^{j} Yk}{yg} + \frac{Y - \sum_{k=i}^{j} Yk}{yj+1}} \right) \tag{96.15}$$

96.5 Simulation Experiment of the Four Primary Display

96.5.1 The Experimental Condition

Experimental instrument consists of three parts: signal generator, the monitor to be tested and colorimeter. Experimental equipments are set up according to Fig. 96.3, and the optical axis of colorimeter and central area of the display to be tested should be orthogonal, where h is an effective and visual height of the display to be tested, d refers to the horizontal distance between colorimeter lens and the display to be tested, Moreover the test distance should be three times as large as the effective visual height of the screen (HDTV), or four times (SDTV). Experimental measurements were conducted in the darkroom, in order to ensure that the feature of display does not significantly change over time, all experimental apparatus needs to be preheated for more than 30 min before the experiment.

96.5.2 The Results of Chromaticity Experiment

The chromaticity coordinates and the maximal brightness of four primary monitor measured by experiment are shown in Table 96.1. According to the experimental data, the boundary vertexes of the total luminance Y is determined by the method mentioned in Sect. 96.4. The three-dimensional figure of gamut boundary of four primary color is shown in Fig. 96.4. In the figure, x, y coordinates represent the coordinates of the primary colors in CIE 1931, the Z coordinate represents corresponding total maximal brightness. From the figure, the color gamut of the high brightness is smaller than that of the low brightness.

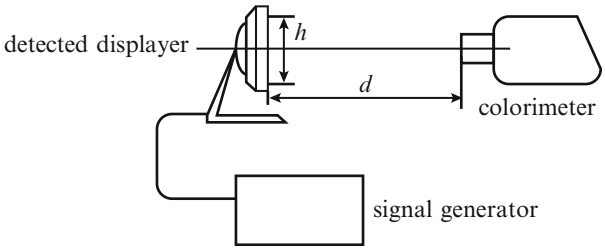

Fig. 96.3 The sketch of experimental equipment

Table 96.1 Chromaticity coordinates and maximum value of lightness of four-primary system

Primary colors	Chromaticity coordinates	Maximum value of lightness
Red	(0.64,0.34)	19.04
Green	(0.30,0.64)	79.76
Blue	(0.15,0.06)	7.49
Yellow	(0.45,0.52)	195.92

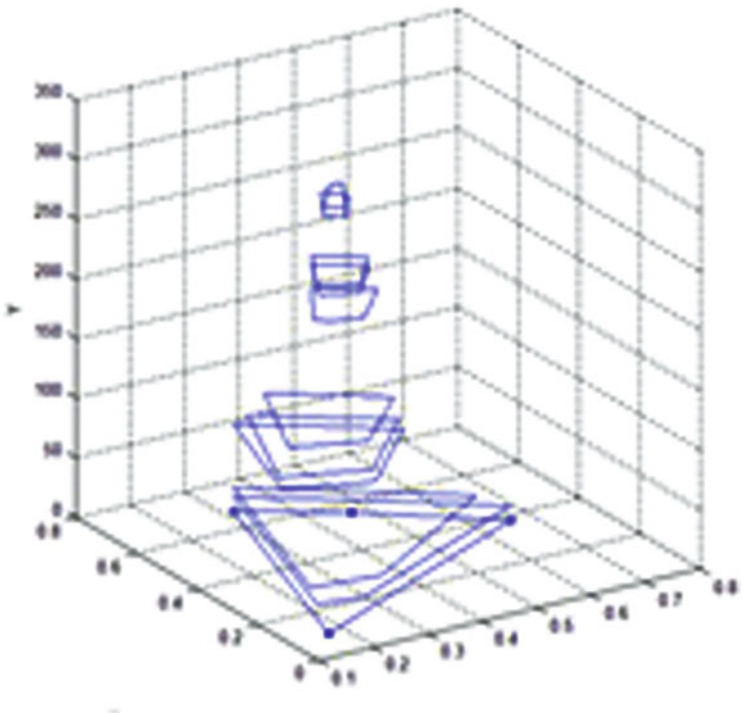

Fig. 96.4 The gamut of four-primary system in different lightness

Conclusion

This article shows that the color gamut of the higher brightness boundary is covered by the color gamut boundary of the lower brightness. From Fig. 96.4, when the brightness of the displayer is larger, the colors it can display is less. As a result, certain colors can only be displayed under a certain brightness value. Through the construction of the color gamut boundary of three primary colors, this article proposes the method to get directly colors on the gamut boundary for building the color gamut boundary of N primary colors video system. So it is not required to calculate the brightness equation of the system for establishing the three dimensional color gamut diagram, which is like three primary system. In fact, the data in the Table 96.1 is sufficient for reconstruction of N primary colors system. The arithmetic presented in this article not only reduces the times of experiments, but also dramatically reduces the computation.

References

1. Wang Y, Xu H (2005) In: Li CS, Yeung MM (eds) Determination of CRT color gamut boundaries in perceptual color space, 5637th edn. SPIE, Beijing, pp 332–338
2. Wen S (2005) Design of relative primary luminances for four-primary displays. Displays 26(4–5):171–176
3. Yamaguchi M, Iwama R, Ohya Y, Obi T, Ohyama N, Komiya Y, Wada T (1997) In: Kim Y (ed) Natural color reproduction in the television system for telemedicime, 3031st edn. SPIE, Newport Beach, pp 482–489
4. Murakami Y, Hatano N, Takiue J, Yamaguchi M, Ohyama N (2004) In: Chien LC, Wu MH (eds) Evaluation of smooth tonal change reproduction on multiprimary display: comparison of color conversion algorithms, 5289th edn. SPIE, San Jose, pp 275–283
5. Travis D (1991) Effective color displays: theory and practice. Academic, London
6. Hunt RWG (1991) Measuring colour, 2nd edn. Ellis Horwood, London
7. Berns RS (2000) Principles of color technology, 3rd edn. Wiley, New York

Chapter 97
Hydrological Visualization and Analysis System

Piraporn Jangyodsuk, Dong-Jun Seo, Baoju Zhang, Xiaoyong Wu, Ramez Elsmasri, and Jean Gao

Abstract While many hydrological data have been collected and produced from hydrological models, the new data from the Office of Hydrologic Development, NOAA has a benefit over others in terms of high resolution both in temporal and spatial resolutions. In this work, the web-based Hydrological Visualization and Analysis System (HyVAS) is developed to help both hydrologists and local people examine and analyze this high resolution hydrological data. The HyVAS provides both temporal and spatial visualization and analysis tools. In total, there are two visualization tools and two analysis tools. Both 2D and 3D graphics have been implemented in these tools to aid users to view and to understand information hidden in the numerical data. In the first stage, this system focuses only on soil moisture visualization and analysis. Later if more data are available and more functions are needed, they can be added because this system does not depend on any environments, operating systems, or commercial software. This web-based Hydrological Visualization and Analysis System is hoped to help the hydrological community visualize and analyze data and extract useful information from the data.

Keywords Visualization • Analysis • Map • Time series • Hydrological data • Web application

P. Jangyodsuk (✉) • R. Elsmasri • J. Gao
Computer Science and Engineering Department, The University of Texas at Arlington, Arlington, TX 76019, USA
e-mail: piraporn.jangyodsuk@mavs.uta.edu; gao@uta.edu

D.-J. Seo
Department of Civil Engineering, The University of Texas at Arlington, Arlington, TX 76019, USA

B. Zhang • X. Wu
School of Electronics and Communications, Tianjin Normal University, Tiajin 300387, China

J. Mu et al. (eds.), *The Proceedings of the Third International Conference on Communications, Signal Processing, and Systems*, Lecture Notes in Electrical Engineering 322, DOI 10.1007/978-3-319-08991-1_97

97.1 Introduction

Visualization is an important tool to find spatial and temporal relationship in numerical data. The purpose of this web-application, the Hydrological Visualization and Analysis System (HyVAS), is visualizing and also analyzing the historical hydrological data from the Office of Hydrologic Development at the National Oceanic and Atmospheric Administration (OHD-NOAA). This web-application is hoped to help the hydrological community view the data and find the relationship, trend, hidden pattern, and mine useful information out of it.

There are many applications for hydrological data visualization, such as HydroDesktop [1–3] from CUAHSI, and HDMRAS (Hydrologic Data Management, Retrieval & Analysis System) [4], GISHydro2000 [5], WHAT1 [6], ArcGIS [7], and China Geo-Explorer [8].

The HydroDesktop has been developed since 2009 by CUAHSI (Consortium of Universities for the Advancement of Hydrologic Science, Inc.). It accesses data from two sources, the HIS Central, which data is from HydroServer, and the HydroServer, which data is from more than 70 water data web services. The purposes of HydroDesktop are downloading, visualizing, and analyzing integrated hydrologic and climate data from heterogeneous formats. The HydroDesktop can visualize spatial data and time series data. The drawbacks are OS and environment dependent because it must be run on Windows XP or Windows 7 with.NET framework, data coverage is not high, and the visualization is only available in two dimensions.

The Hydrologic Data Management, Retrieval and Analysis System (HDMRAS) is designed to integrate data from heterogeneous sources and formats, and provide them for searching, retrieving, and visualizing. The prototype is a Java based application and provides data in California, Washington, Oregon, and Arizona. The first drawback is its complicated installation. It provides both temporal and spatial visualizations. Still, its lack of data is the main drawback. For some data, e.g. stream-flow, provided for very few points on the map.

Our HyVAS aims to help both researchers and local government visualize the hydrological data from the NOAA-OHD. This data set has an advantage over others in term of the coverage, and high spatial and temporal resolution (see Sect. 97.2.1 for more detail). Thus, our system provides more accurate information for users who interest in small areas like in state, county, or city level. This can also help the local hydrological organizations view and manage the water supplies.

The HyVAS has another advantage that it is a web-based application. So it is platform independent and no complicated installation and license fee is needed. Also, From the experiment result in [9], the design of the HyVAS, which uses server for retrieving and filtering data and uses client for rendering data, yields the best result in terms of balancing workload between client and server.

Finally, this system provides both spatial and temporal visualization while some of others provide only spatial or only temporal functions. Moreover, the HyVAS provides 3D-visualization that is lacked in many web-based hydrological applications.

97.2 Data Set and Methods

The HyVAS has two tools for spatial visualization and two tools for temporal visualization. In this section, the data set will be introduced, followed by the overall architecture, then each of the four visualization tools will be discussed.

97.2.1 Data Set

The hydrological data in this work uses HRAP (Hydrologic Rainfall Analysis Project) coordinate system [10]. This data set has 32 variables in high spatial resolution (every 4×4 km^2 of the US except Alaska and Hawaii) and high temporal resolution (every 6 h from January 2, 1979 to December 31, 2008).

Although the data covers all states in the US, the current system focuses only on the local area, the West Gulf River Forecast Center (WGRFC) area, which includes Texas, Oklahoma, New Mexico and some part of the nearby states as shown in the Fig. 97.1. Also, from 32 variables, the HyVAS currently focuses on four soil moisture variables (soilm1-soilm4) because these variables are highly related to drought which is an important issue in this area. Each soil moisture variable represents soil moisture in different soil layer. The top soil layer is 0–10 cm. from the surface, the second layer is 10–40 cm., the third is 40–100 cm, and the bottom layer is 100–200 cm.

97.2.2 Architecture

In order to keep the system simple and not redundant, all four tools in the HyVAS share the same architecture which covers the database, data-flow, and web-interface.

97.2.2.1 Database

MATLAB is chosen to be the database. The relational database is not used because the 3D Trend of Soil Moisture Range Tool (see Sect. 97.2.4) needs to process Region Connecting algorithm which is implemented using MATLAB so it is faster to read and process data using only MATLAB than to retrieve data from a relational database and send it to be processed in MATLAB. For the rest three tools, to make the system simple and non-redundant, MATLAB is chosen as the database.

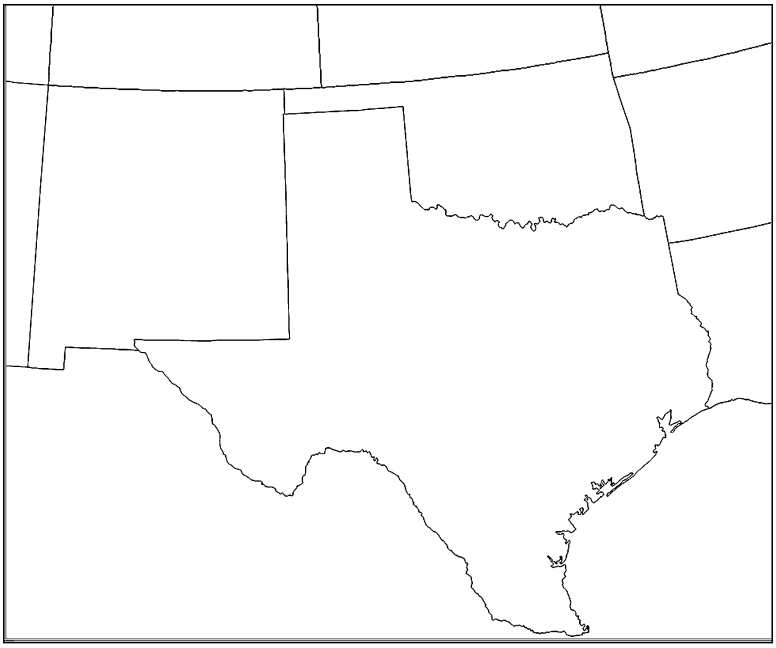

Fig. 97.1 West Gulf River Forecast Center (WGRFC) area

97.2.2.2 Data Flow

The data flow, shown in the Fig. 97.2, starts when the web-interface receives input from a user. It then sends a data request via Ajax to a PHP page to triggers MATLAB using the *system* command. MATLAB writes the requested data to a CSV file. After waiting for MATLAB, the PHP page reads the CSV file and sends the requested data back to the web-interface. Finally, the web-interface renders graphic visualization using JavaScript.

97.2.2.3 Web-Interface

The four tools in the HyVAS can also be categorized based on the graphic rendering modes into 2D and 3D Graphic Visualization Tools.

1. 2D Graphic Visualization Tools
   The tools in this category are Full Time Series Tool, and Time Series Comparison Tool. The visualization, which is either map or graph, is rendered by canvas tag of HTML5. These tools have the same set of visualization-aid functions (see Tool box in the top right of the Fig. 97.2) as the following,

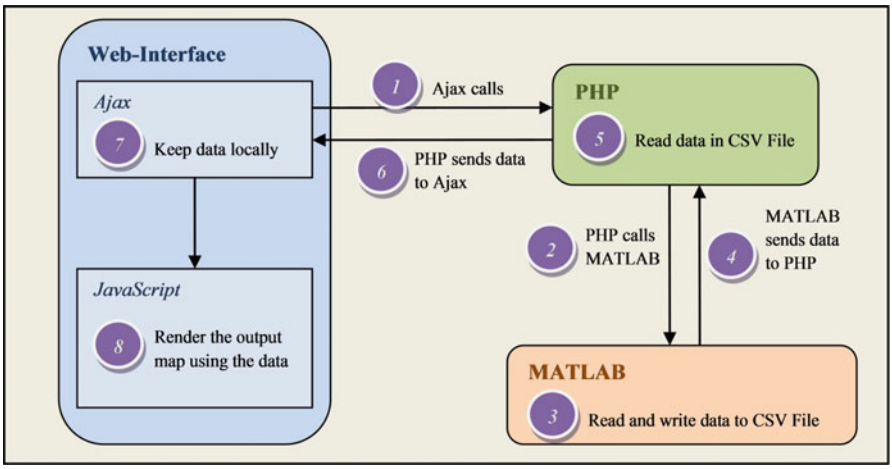

Fig. 97.2 Data flow of the HyVAS

- Zoom: The map/graph can be zoomed in and out in eight levels.
- Pan: When the map/graph is zoomed in, it can be panned to any area of interest but is limited within the WGRFC area.
- Information Tool-tip: If this function is enabled, the information of that data point is displayed on the tool-tip.

2. 3D Graphic Visualization Tools
   The tools in this category are 4-Layer-Soil Moisture Maps Tool and 3D Soil Moisture Trend Tool. The visualization, which is either a 3D map and a four layered map, is rendered by a WebGL library called *three.js*. The visualization-aid functions are as the following,

   - Zoom: The map can be zoomed in and out in by the zoom-in and zoom-out buttons, and also by dragging mouse up or down.
   - Rotate: The map can be rotated in all three axis by six buttons (two buttons for each axis) and also by dragging mouse to left or right.
   - Area Selection: This allows user to select the area of interest. Only the selected area will be visualized.

97.2.3 4-Layer Soil Moisture Maps Tool

This tool is for spatially visualizing any of four soil moisture variables smoothly without re-retrieving data or re-rendering map. Four maps are rendered at the same time and stacked on top of the other based on the order of layers. Then, user can choose one layer to visualize at a time (Fig. 97.3).

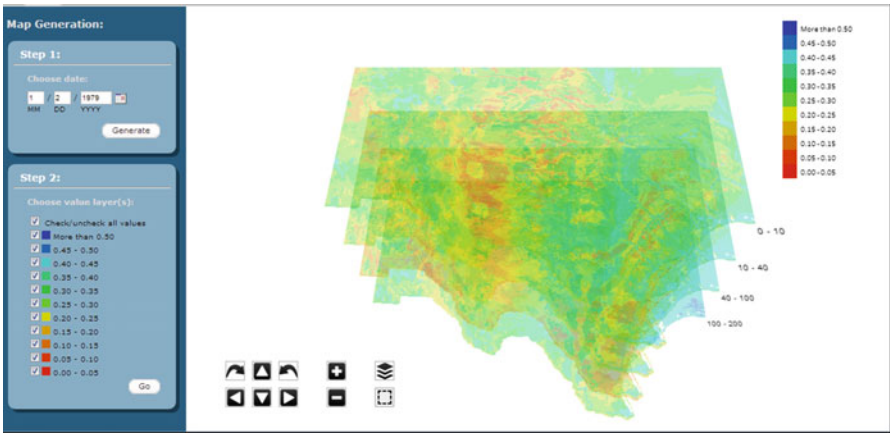

Fig. 97.3 4-Layer of Soil Moisture Maps on January 2, 1979

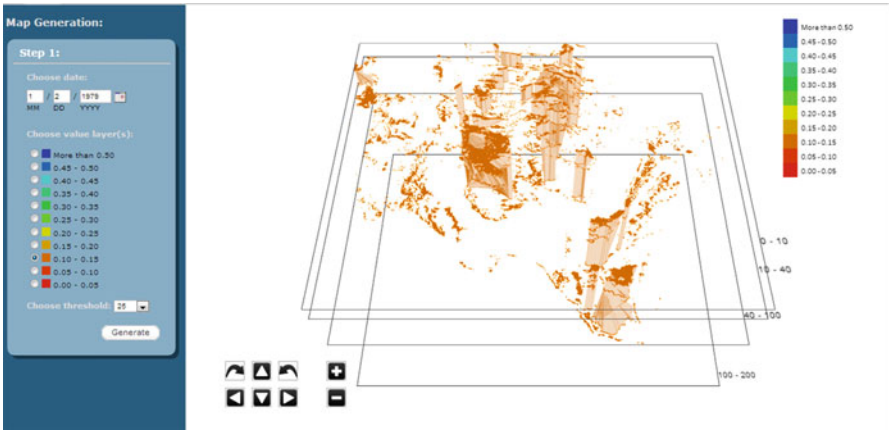

Fig. 97.4 3D trend of the 0.10–0.15 soil moisture on January 2, 1979

97.2.4 3D Distribution of Soil Moisture Range Tool

The motivation of this tool is for analyzing and visualizing the distribution or relationship of soil moisture between soil layers. The maps are stacked as in the 4-Layer of Soil Moisture Maps Tool but, in this tool, one range of soil moisture is displayed at a time (Fig. 97.4).

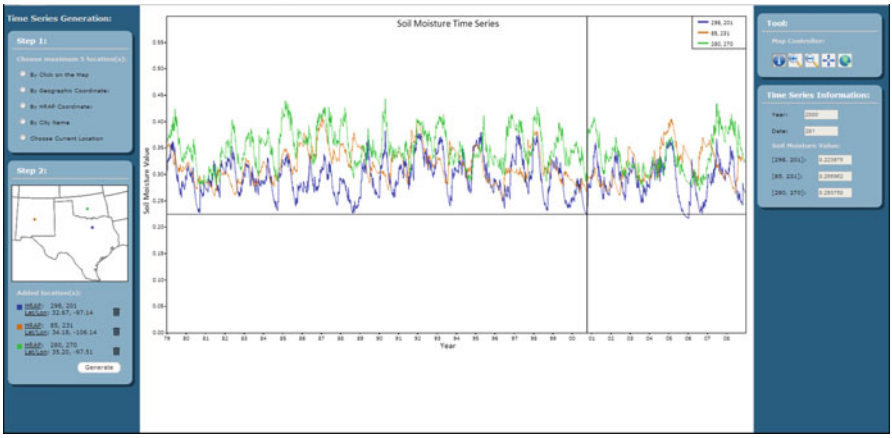

Fig. 97.5 Full time series visualization tool

97.2.4.1 Region Connecting Algorithm

To visualize the distribution of a range of soil moisture value between layers, quadrilateral sides are put to connect the top layer edges to the bottom layer edges. This process creates a prism-like object which two bases, or regions, are not required to have the same shape or area.

Algorithm 1 The summarized region connecting algorithm

Data: S is a set of soil moisture layers
P is a set of pairs of adjacent soil moisture layers
R is a set of regions in the top soil moisture layer
begin
  for $s \in S$ **do**
    Cut out the HRAP cells that are out of the user's specified range
    Put the adjacent within-range-cells to the same region
    Assign a number to each region
    Remove regions that have less than 25 cells
  end
  for $p \in P$ **do**
    Find overlap regions in the bottom layer
    for $r \in R$ **do**
      Extract edge cells of those regions from both layers
      Determine a starting cell in both layers
      Use greedy algorithm to match top layer's edges to the bottom
      Put a quadrilateral face to connect the top to the bottom layer
    end
  end
end

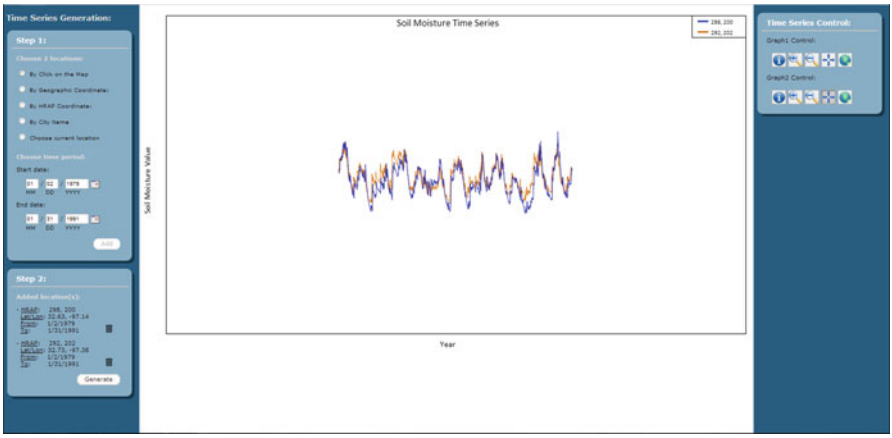

Fig. 97.6 Time series comparison tool

97.2.5 Full Time Series Tool

The purpose of this tool is to temporally visualize the average soil moisture time series from up to five HRAP cells at a time. This should help users visualize and find the monthly/seasonal/annual trend hidden in the historical data. In addition, it helps visualize some statistic properties, such as mean and variant of the data at the specified HRAP cell (Fig. 97.5.).

97.2.6 Time Series Comparison Tool

This tool is for visually comparing the similarity of two average soil moisture time series/sub-sequences. These two time series/sub-sequences can be from the same or different HRAP cell and date (Fig. 97.6).

Conclusion
In this work, a web-based system that provides spatial and temporal visualization tools is developed. It is designed to help hydrological community visualizing the OHD-NOAA data set without license fee or platform dependence. This system has many advantages over existing systems which provides both spatial and temporal visualizations. It is flexible to add more functions and data set than commercial programs. Moreover, it provides both 2D and 3D visualization.

References

1. Ames DP, Horsburgh JS, Cao Y, Kadlec J, Whiteaker T, Valentine D (2012) Environ Model Softw 37:146
2. Piasecki M, Ames DP, Goodall J, Hooper R, Horsburgh JS, Maidment DR, Tarboton DG, Zaslavsky I (2010) In: HIC 2010, pp 1407–1416
3. Ames DP, Horsburgh JS, Goodall J, Whiteaker T, Tarboton DG, Maidment DR (2009) In: 18th world IMACS congress and MODSIM09 international congress on modelling and simulation modelling and simulation society of Australia and New Zealand and international association for mathematics and computers in simulation, pp. 4353–4359, 2009
4. Jeong S, Liang Y, Liang X (2006) Environ Model Softw 21(12):1722
5. Moglen GE (2000) In: GISHydro2000: a tool for automated hydrologic analysis in Maryland, Chap 50, pp 1–12
6. Lim KJ, Engel BA, Tang Z, Choi J, Kim KS, Muthukrishnan S, Tripathy D (2005) J Am Water Resour Assoc 41(6):1407
7. Arcgis. http://www.esri.com/software/arcgis
8. Zhang X, Zhu X, She B, Bao S (2009) In: The spatial data integration and analysis with China Geo-Explorer, pp 1–8, 2009
9. Huang B (2003) Comput Environ Urban 27(6):623
10. Reed SM, Maidment DR (1999) J Hydrol Eng 4(2):174

Chapter 98
Design and Implementation of Intelligent Field Monitoring and Irrigation System for Radix Ophiopogonis

Yu Xiang, Zhaoguang Xuan, Jun Zhang, Ting Yang, and Wenyong Wang

Abstract Sichuan province is one of main producing areas of Radix Ophiopogonis which is a valuable herb in Chinese traditional medicine. It is important to monitor the field's environment parameters during the growing period and maintain the soil moisture value to ensure both the quality and yield of Radix Ophiopogonis. This paper designs and implements the intelligent monitoring wireless network and automatic irrigation system for Radix Ophiopogonis. Our system includes hardware modularity, which separates PSU (Power Supply Unit) from sensor nodes, monitoring network with diversifying field environmental data, and irrigation expert model for Radix Ophiopogonis. Combined with weather data, such as temperature, humidity, and rainfall data from meteorological observatory, environmental data (such as soil humidity and surface temperature) gathered from our network are served as input of the irrigation expert model to make decision, then the result is fed back to SV Node (Solenoid Valve Node) to form a closed loop, which reaches the goal of field monitoring and irrigation control. The result shows that our system can provide moisture accurately for Radix Ophiopogonis, thus realize automatic, real-time and appropriate amount of irrigation. Our system also provides high control accuracy, reliable communication, and is especially suitable for medium-large-size farmland of Medicinal herbs.

Keywords Radix Ophiopogonis • Wireless sensor • Irrigation expert model • Hardware modularity

Y. Xiang • Z. Xuan (✉) • J. Zhang • T. Yang • W. Wang
School of Computer Science and Engineering, University of Electronic Science and Technology of China, Chengdu, China
e-mail: jcxiang@uestc.edu.cn; braveheart_xzg@163.com; zhangjun@uestc.edu.cn; yting@uestc.edu.cn; wangwy@uestc.edu.cn

J. Mu et al. (eds.), *The Proceedings of the Third International Conference on Communications, Signal Processing, and Systems*, Lecture Notes in Electrical Engineering 322, DOI 10.1007/978-3-319-08991-1_98

98.1 Introduction

Radix Ophiopogonis, a perennial evergreen herb of liliaceae ophiopogon, has a great medicinal value. Santai county of Sichuan province is one of main producing areas of Radix Ophiopogonis, its outputs are accounted for 60 %, and exports accounted for 80 % in China. It is important to maintain the soil moisture to keep Radix Ophiopogonis' healthy, high soil moisture will lead to rot the root of plants, and the resource will be wasted due to high number of fertilizer loss. Therefore, reasonable irrigation produces large strength to guarantee the high yield and high profit in the process of planting Radix Ophiopogonis of large-scale farmland.

In recent years, an increasing number of technologies are applied to agriculture. International and domestic researchers have had lots of work about intelligent irrigation system [1]. For example, Jin Zhaorong designs the spraying irrigation automatic controller based on fuzzy decision [2], Xie Shouyong's team design and implement fuzzy control for irrigating system with PLC [3], Zhang Wei implements precision irrigation system based on WSN and fuzzy control [4], Yunseop (James) Kim and Robert G. Evans design the remote sensing and control of an irrigation system using a distributed WSN [5]. There are three problems in these studies, first, sources of data are simplex, the researchers only consider about soil humidity, but ignore other environmental information, resulting in low accuracy of irrigation decision. Second, the irrigation expert models are not mature. At last, the mechanism of estimated time adopted by most of researches increases the probability of lower precision of expert models. In order to guarantee the growth environment of crops, a field monitoring and irrigation system targeted for Radix Ophiopogonis with the aid of WSN has become a rational solution. Our system have the characteristics of low power consumption, diversifying field environmental data, hardware modularity, irrigation expert model for Radix Ophiopogonis, it is able to unattended for a long time and form the closed-loop feedback subsystem, the system like this has not yet been reported.

This paper presents the overall framework of our system, the software and hardware design of WSN. It introduces the function of DCS (Data Communication Station) of monitoring center and the process of the irrigation expert model. Finally, it presents our implementation and conclusion.

98.2 System Architecture

98.2.1 System Overview

As shown in Fig. 98.1, our field monitoring system gathers a variety of environment parameters (such as soil humidity and surface temperature) with the aid of the WSN nodes deployed in fields, it transmits data to monitoring center via wireless network with the combination of long and short distance transmission (i.e. for GSM and

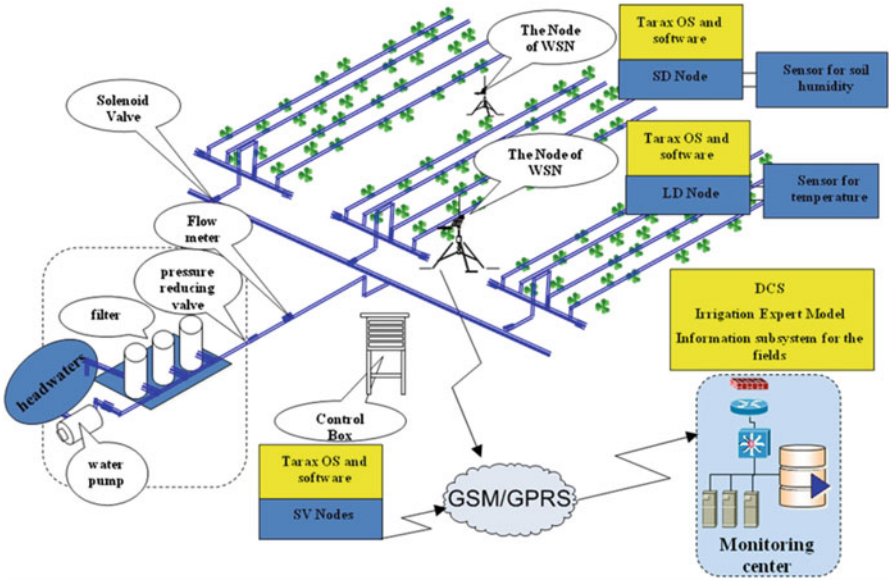

Fig. 98.1 Overall architecture of the system

Zigbee). The irrigation expert model in monitoring center determines whether a corresponding field area needs irrigation or not, and updates irrigation management data. Administrators send irrigation commands to control solenoid valves, and complete the irrigation.

From Fig. 98.1, three types of nodes are deployed in fields, the first is a SD Node (Short Distance Node) with Zigbee network; the second one is a LD Node (Long Distance Node) with not only Zigbee network but also GSM network; the third is a SV Node (Solenoid Valves control Node) with GSM network. In order to obtain field environmental parameters, multiple SD Nodes deployed in the area center on their own LD Nodes to form a WSN with multiple sets of data collection. LD Nodes sort out the current set of data, and then transfer the data to monitoring center according to the rules which have been set in advance via GSM network.

In conclusion, the system has two closed-loop feedback subsystems (Fig. 98.2). One is that DCS submits field environmental data collected by WSN to the irrigation expert model, and then the expert model feeds back the result to DCS after it makes irrigation decision. The other is that sensor nodes gather environmental data and transmit them to DCS, and DCS sends the commands to SV Nodes to control irrigation.

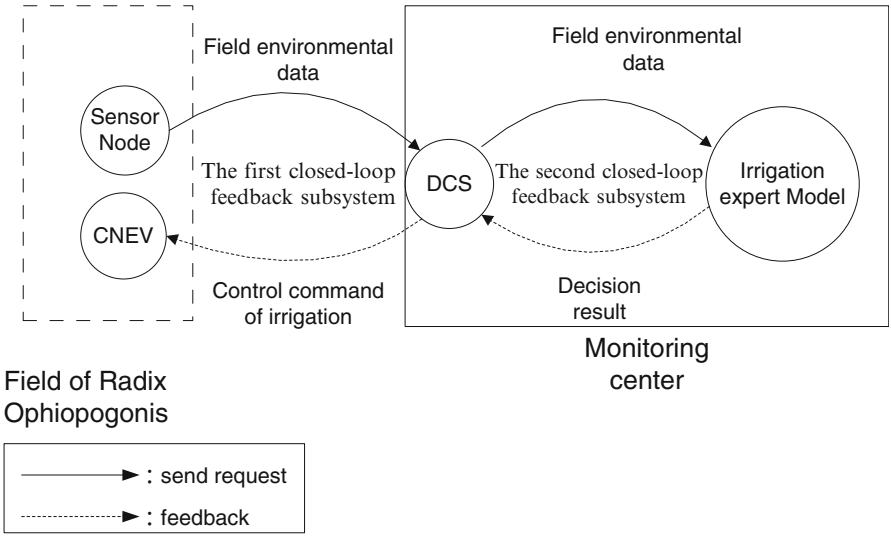

Fig. 98.2 Schematic diagram of the closed-loop feedback mechanism

98.3 The Monitoring Solution of WSN in the Farmland

98.3.1 The Network Architecture

A LD Node and several SD Nodes are deployed in an area of fields to form a star subnet of WSN, and Zigbee wireless transmission protocol is used in internal communication of the subnet. In the process of multiple sets of data collection, LD Nodes organize the current set of data, and upload them to monitoring center through GSM network. Monitoring center receives data, and resolve and save them. After the irrigation expert model makes decision, monitoring center sends commands to SV Nodes to control irrigation under the result of decision.

98.3.2 The Hardware of Nodes

The WSN nodes of our system include LD Nodes, SD Nodes and SV Nodes. Consider the replacements of old modules, function scalabilities of sensor nodes, different power requirements of sensor nodes and precision requirements of collecting data, our system adopts the hardware modular design, which is mainly represented in two points: First, the power module is separated from WSN nodes to form the modular management of the combination of sensor nodes and PSU. PSU supply power for sensor nodes under their requirements. Second, sensor nodes adopt a common core module, and extend different modules according to their

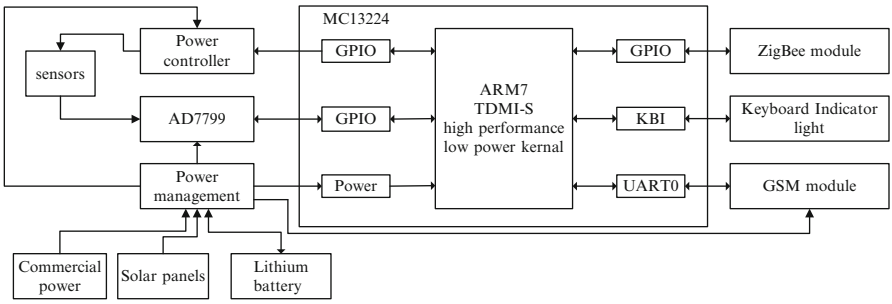

Fig. 98.3 The hardware structure diagram of the WSN nodes

functional requirements. Three kinds of nodes are based on MC13224 chip hardware architectures. According to functional requirements, sensor nodes can extend Zigbee wireless and GSM communication module, serial communication interface, AD conversion module, GPIO interface, etc.. . .

98.3.2.1 LD Node and SD Node

LD Nodes and SD Nodes serve as the nodes used in data collection, and receive output data of a sensor. The sensor's data is dealt with a low-pass filter, and sampled by the AD module. MC13224 module corrects the data, and sends it to protocol processing module to modulate. The signal modulated by protocol processing module is transmitted to monitoring center through the antenna. Hardware block diagram is shown as Fig. 98.3. SD Nodes don't have GSM module In that they have no requirement of communication with monitoring center.

98.3.2.2 SV Node

SV Nodes receive commands from monitoring center to control the relays on the nodes, but possess no function of data acquisition. Two pins of the relays connect to an external solenoid valve. The solenoid valve is closed when no power is supplied. On the contrary, it will be open. So it is feasible to control states of the relay to achieve the purpose of controlling the solenoid valve. The hardware block diagram is shown as Fig. 98.4.

98.3.2.3 Design of PSU

Energy consumption has always been a bottleneck problem in WSN, so the power module has become the premise of the stability, robustness, and reliability of WSN. The system adopts modular hardware design, and separates PSU from sensor nodes.

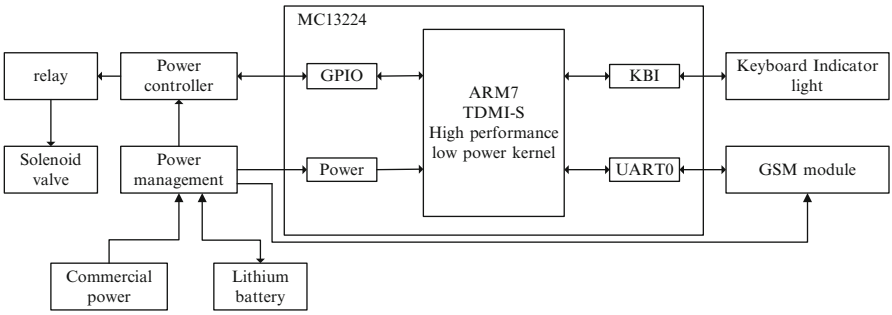

Fig. 98.4 The hardware structure diagram of SV Nodes

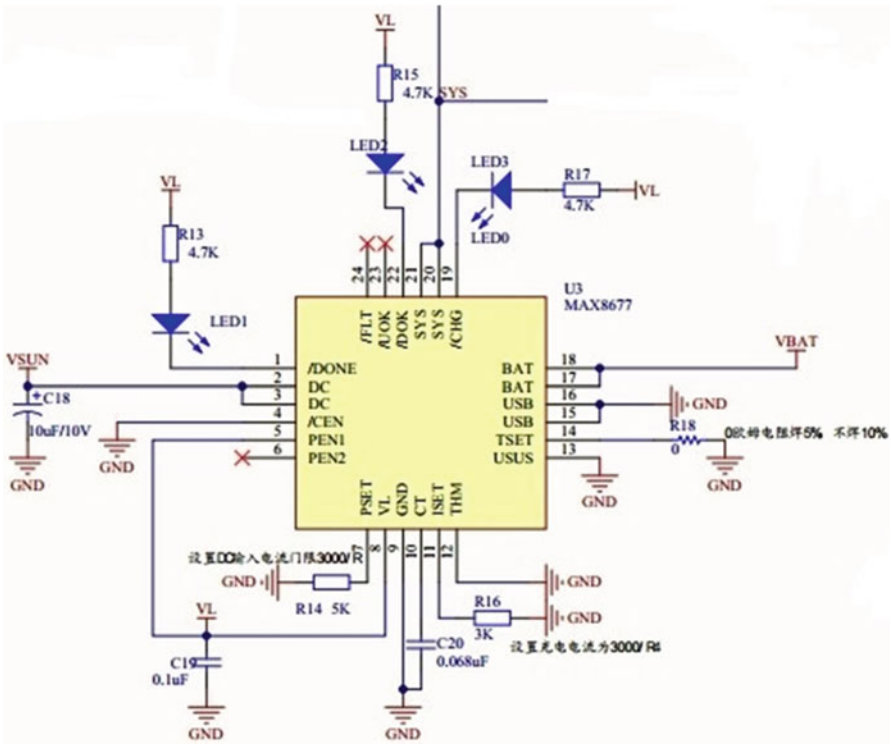

Fig. 98.5 The circuit and principle diagram for PSU

PSU (Fig. 98.5) offers power to the other modules on the nodes according to their requirements. Considering the application environment of system, including sunshine, weather and other factors in fields of Radix Ophiopogonis in Santai, we adopt the solution of combination of commercial power, solar power and lithium battery power. According to types of nodes and deployment locations, we choose two ways of power supply:

1. "Electricity-Lithium battery" mode. Considering that the solenoid valve's working voltage is DC12V, and rated power is 20 W, its power consumption is relatively high. On the other hand, it is convenient to deploy power lines for SV Nodes. So we use "Electricity-Lithium battery" to supply power for SV Nodes. In the power supply design, commercial power is directly supplied for solenoid valve via PSU and for lithium batteries at the same time. Then lithium batteries supply power for other modules on the nodes via PSU, such as MC13224 chips, AD7799 chips, and SIM300C module.
2. "Solar-Battery" mode. Since deployment locations of SD Nodes and LD Nodes are not fixed and their low power consumption, so we choose "Solar-Battery" mode for sensor nodes. Of course, "Electricity- Lithium battery" mode can be used when the power lines can be deployed reasonably. In this mode, batteries directly supply power for sensor nodes via PSU. Solar panels generate electricity to charge batteries. If solar panels supply directly power for the power modular, it will cause the instability of the system because of the working power of solar panels influenced violently by weather, sunshine intensity and other factors. However, batteries possess the characteristic of limiting current, overcharge protection, and power supply stability, "Solar-Battery" mode improves stabilities of our system. Therefore, "Solar-Battery" mode is more suitable for the system.

98.3.3 The Design of System Software

98.3.3.1 The Main Function

The main function is the entry point of the software, primarily responsible for initialization of each module, including interruption, platform, task scheduling, timer, serial communication module, and protocol stack of wireless communication.

After all the initialization is completed, event handlers are added, and interrupts are enabled. Then our system enters into the cycle of task scheduling. The execution flow of the main function is shown in Fig. 98.6.

This system uses a WSN operating system based on task scheduling mechanisms. Mechanisms used includes: priority-based, fixed-priority, non-preemptive and "Task + event". By the way of submitting an event to activate a task, it achieves the target of the resource scheduling. Each task includes a number of events, and each event corresponds to an event flag. When an event occurs, the corresponding task event flag is set to true, then the even handler function is called to deal with the event. The scheduler determines when they are executed if multiple tasks are added.

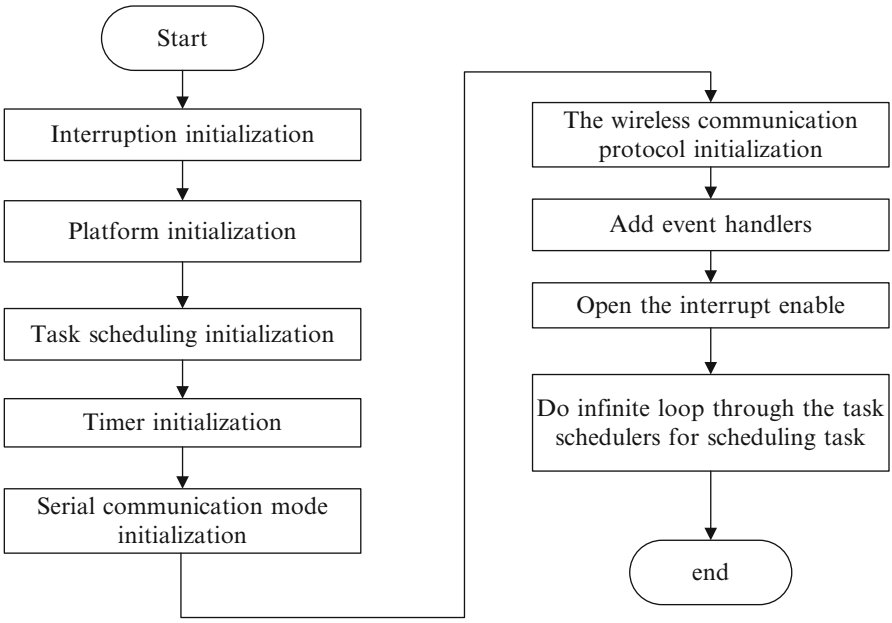

Fig. 98.6 The flow chart of the main function

98.3.3.2 Software Design for Sensor Node

In each subnet of WSN, the LD Node is regarded as the master node, responsible for gathering data from wireless network, organizing and configuring the network, completing the protocol conversion of WSN to GSM and receiving commands of decision from monitoring center. It not only resolves commands but also sends them to SD Nodes. The SD Node is mainly in charge of data acquisition and transmits the data to LD Node. The SV Node works as an independent node to receive irrigation commands from the monitoring center to control solenoid valves, it has no function of Zigbee network communication. Software modules of the LD Node include task scheduling, wireless communication, timer management, and serial port communication, storing and processing data, and power management, data collection. The relationship among the modules is shown in Fig. 98.7. Due to differences among sensor nodes, compared with LD Nodes, SD Nodes lack the functions of serial port and GSM communication, and SV Nodes are short of the functions of data collection and wireless communication.

98.4 Decision and Control Scheme for Monitoring Center

The monitoring center is in charge of receiving a variety of environmental parameters from LD Nodes. The parameters are stored after resolved. In the second closed-loop feedback subsystem, the irrigation expert model obtains water

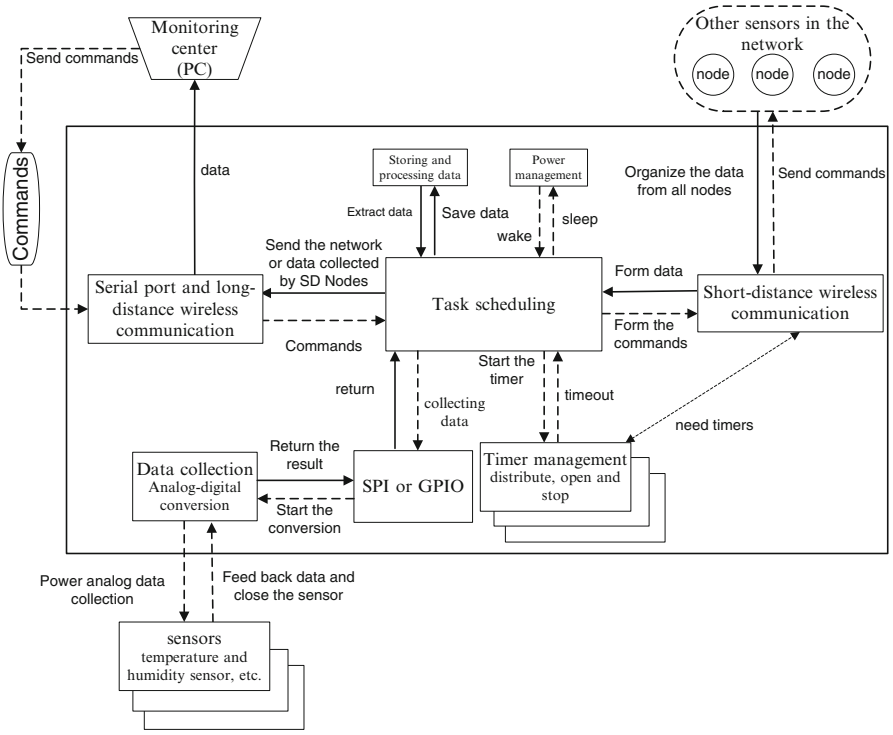

Fig. 98.7 Relationship among the modules of LD Nodes

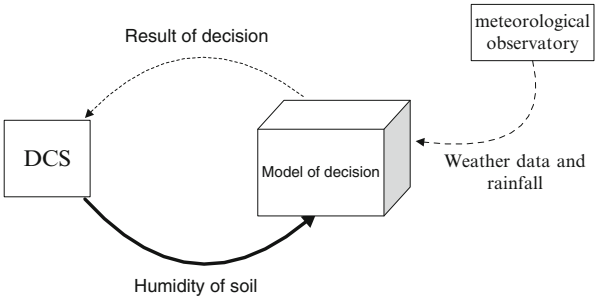

Fig. 98.8 Data flow diagram of the second closed-loop feedback subsystem

requirement on the basis of environmental data, determines whether the corresponding area of fields needs irrigation or not combined with weather data. Finally the expert model feeds back the decision result to DCS. The data flow among them is shown as Fig. 98.8.

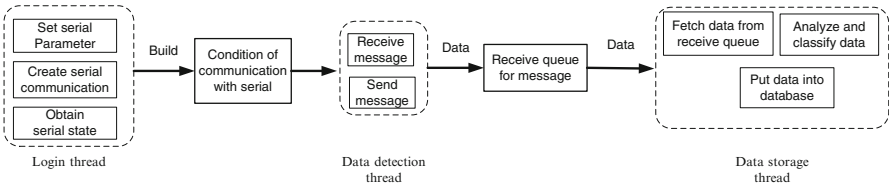

Fig. 98.9 The thread of DCS and relations among the threads

98.4.1 DCS

DCS is an integrated platform communicated with sensor nodes, and the key to realize the closed-loop feedback system. From the first closed-loop feedback system of Figs. 98.1 and 98.2, it receives environmental data from LD Nodes to resolve and store. It also takes charge of sending collection commands and irrigation commands respectively to the sensor nodes and SV Nodes. For the second closed-loop feedback subsystem, the expert model makes decisions based on the data stored by DCS, and then feeds back the decision result to DCS.

DCS is an application based on Window API and the runtime library of MFC. It communicates with LD Nodes through the Modem which can be connected to the serial port of PC (Modem is a terminal device communicated with LD Nodes via GSM network). It establishes three threads to complete all the functions, respectively, including the login thread, data detection thread and data storage thread. The specific relations are shown in Fig. 98.9.

Login thread builds the serial communication connection automatically and gets the state of Modem. Finally the data detection thread and data storage thread are started up.

Data detection thread receives and sends data messages automatically after the qualification of communication with serial ports is obtained. The messages are put into the receive queue.

Data storage thread resolves data from the receive queue of messages automatically, and then store them.

98.4.2 The Irrigation Expert Model

The irrigation expert model is the core of our system, and it directly affects the precision, feasibility and efficiency of irrigation. It judges whether the corresponding area requires irrigation or not. The irrigation of fields is affected by multiple parameters of soil, such as humidity of soil, moisture, and temperature and so on. But considering the feasibility and operability, the model gives priority to the humidity of soil, and complementary to the temperature of soil surface, weather, and rainfall for making decision.

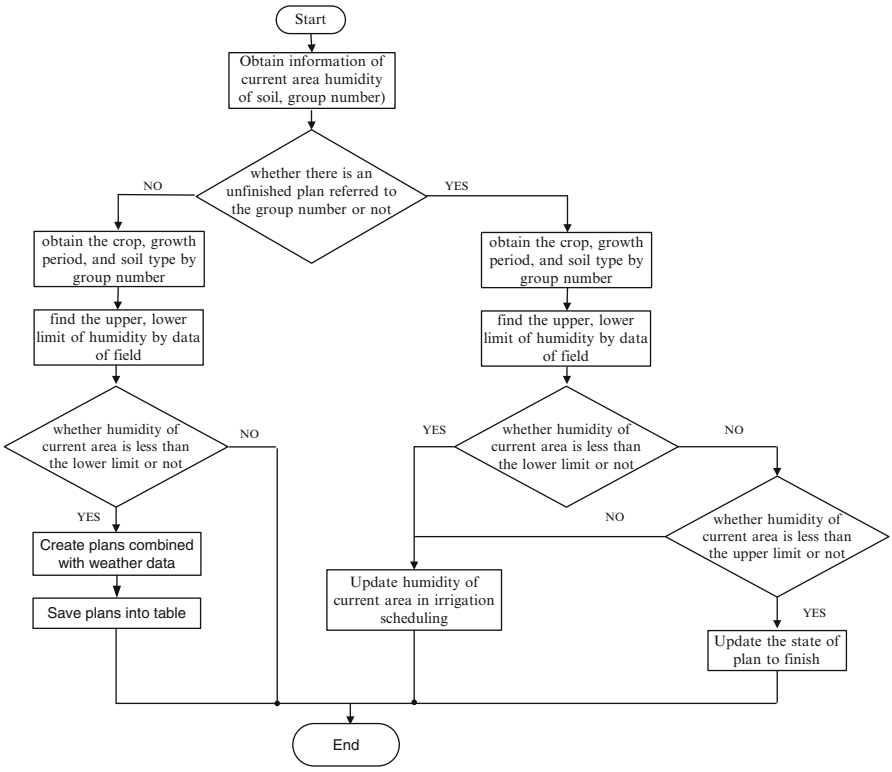

Fig. 98.10 The flow chart for irrigation decision

In the process of making decision, the model sets the upper limit (Hupper) and the lower limit (Hlower) of soil humidity, it gets the relation of current humidity value and the humidity threshold of soil to make irrigation decision combined with weather data. When a group of data is input, the model would obtain an attribute "group number" of area and humidity of soil. The specific process is shown in Fig. 98.10.

Obviously, Hlower and Hupper of soil is the core of the irrigation model, and directly determine whether the current area requires irrigation or not. In the model, it obtains the crops, the soil type, and growth period with the aid of "group number" of area. Eventually it can find Hlower and Hupper of soil. So Hlower and Hupper of soil depend on the crops, the soil type and growth period.

From the results of scientific research [6–8], there are lots of factors related to Hlower and Hupper of soil, such as the crop, growth period, properties of soil, the growth area, and Immeasurable factors and so on. These factors increase difficulties to make Hlower and Hupper of soil precise, which makes the upper and lower limit of humidity tend to fuzzification. However, if the aim of setting the limit of soil humidity precisely is achieved, the only way is that we have to eliminate impact

factors referred to soil humidity limit, which is an important idea of this article. The system is aimed at the fields of Santai County in Sichuan, and rules out the factors of crop and soil which influence soil humidity threshold. The result shows that Hlower and Hupper of Radix Ophiopogonis of Santai are respectively 15.6 % and 23.2 %.

98.5 Implementation for System

Sensor nodes and SV nodes deployed in fields reach the target of monitoring environmental data and controlling the valves, these nodes are based on TaraxOS system.

From the view of circuit design, sensor nodes achieve the modular management of separating PSU from sensor nodes. The function parts of sensor nodes also complete the modular management, so that sensor nodes extend some functions effectively according to their own requirements. The display of hardware is shown in Fig. 98.11a. So, compared with the traditional sensor nodes, sensor nodes of the system own the advantage of more flexibility and extensibility.

The system provides administrators with the sketch map of farmlands and the interface of irrigation management, which are shown as Figs. 98.12 and 98.13. The sketch map of fields with the service of display and management of information is a platform based on WebGIS. Combined with geographical information, it provides intuitively the functions of obtaining field environmental data, querying real-time data, downloading data, displaying the histogram of data and so on for administrators.

Interface of irrigation management is a Web application which provides irrigation management and query of data related to irrigation for administrators. It offers

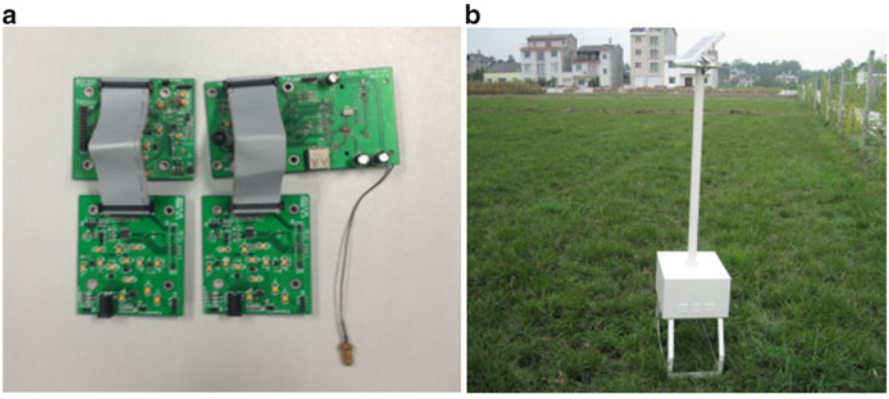

Fig. 98.11 Sensor nodes and sketch diagram of the field. (**a**) The sketch diagram of sensor nodes. (**b**) Sensor nodes in farmland of Radix Ophiopogonis

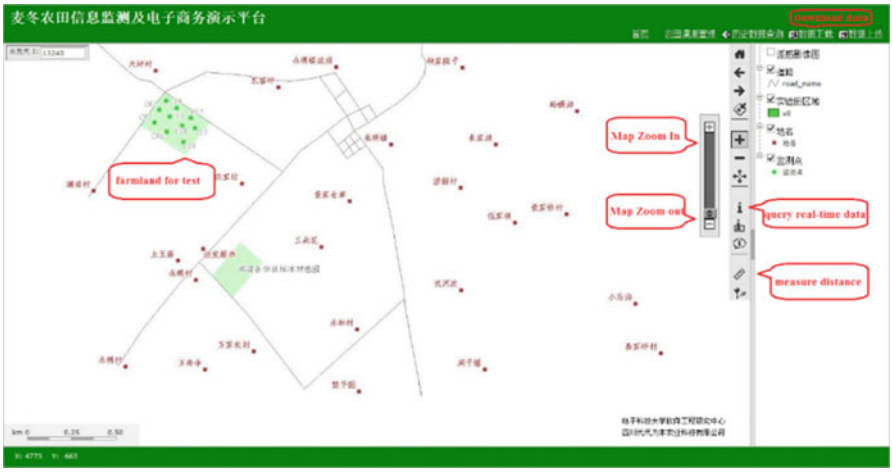

Fig. 98.12 Display of map for farmland

Fig. 98.13 The interface for irrigation management

four operators, respectively including starting irrigation, being irrigation, closing irrigation and completing irrigation. These operators can help administrators control directly solenoid valves deployed in fields and get the schedule, state, time, consumption of irrigations.

The system is aimed at the farmlands of Santai County, so we select 100 km^2 farmland for Radix Ophiopogonis (Fig. 98.11b) in Santai to carry out the monitoring and irrigation experiment. From the result of the experiment, the range of power consumption of system is from 370.28 to 380.76 mW, the average is 378.76 mW, reduced by 148 % compared with the index requirement of the system. The control range of system is 60–80 mu per set, and the average is 72 mu per set, 140 % higher than the index requirement.

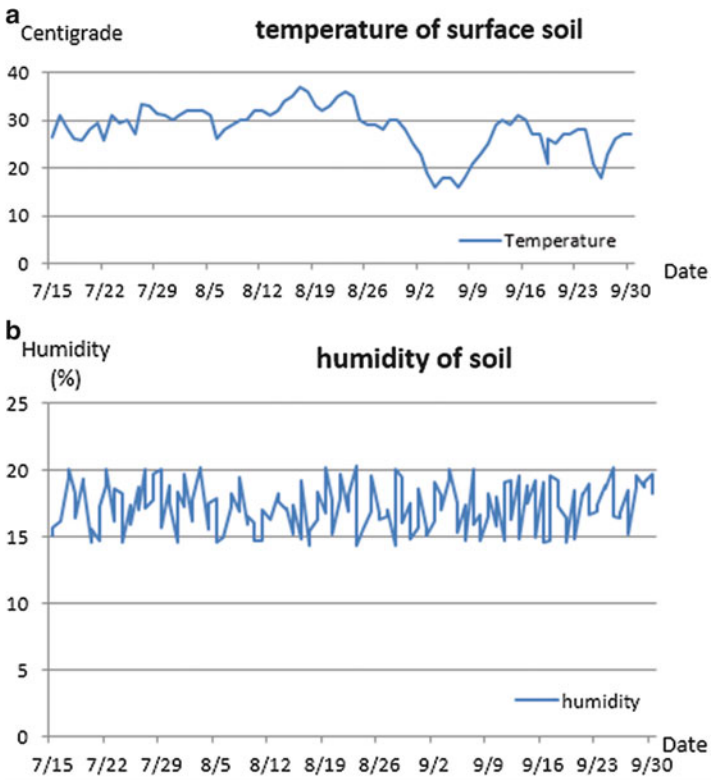

Fig. 98.14 The result of soil humidity and temperature of surface soil. (**a**) The result of temperature of surface soil. (**b**) The result of soil humidity

In the application of system, the sensor nodes get the corresponding voltage values of field environmental data firstly, and their actual values are obtained through their voltage values conversed. The result is shown in Fig. 98.14.

Conclusion

Radix Ophiopogonis in Santai has the very high commercial value. In order to provide moisture for fields more effectively, this paper puts forward a design scheme of intelligent monitoring and irrigation system based on Zigbee wireless transmission and the mechanism of closed-loop feedback.

The system can obtain accurately water requirement of Radix Ophiopogonis after it collects and analyzes soil humidity and temperature of surface soil. It also realizes automatic, real-time and effective irrigation. Our system has the characteristics of practicability, low power consumption, and it is suitable for large-scale irrigation area of Radix Ophiopogonis. The

(continued)

(continued)

result shows that the system can reach the target of reliable communication and precise irrigation control, and has higher practical value for application.

The system proposes a modular management scheme of sensor nodes, which makes WSN more flexible and easier to extend other functions. At the same time, it also provides a new train of thought for the research of energy consumption of WSN.

References

1. Han Huafeng, Du Keming, Sun Zhongfu et al (2009) Design and application of ZigBee based telemonitoring system for greenhouse environment data acquisition. Trans CSAE 25 (7):158–163
2. Jin Zhaorong, Xu Minjie, Wei Xueliang et al (2004) Study and design of spraying irrigation automatic controller based on fuzzy decision. Drain Irrig Mach 22(5):26–28
3. Xie Shouyong, Li Xiwen, Yang Shuzi et al (2007) Design and implementation of fuzzy control for irrigating system with PLC. Trans CSAE 23(6):208–210
4. Zhang Wei, He Yong, Qiu Zhengjun et al (2009) Design of precision irrigation system based on wireless sensor network and fuzzy control. Trans CSAE 25(Supp 2):7–12
5. Kim Y, Evans RG (2008) Remote sensing and control of an irrigation system using a distributed wireless sensor network. IEEE Trans Instrum Meas 57(7):1379–1387
6. Zhou Guoxiang, Zhou Jun, Miao Yubin et al (2005) Development and application on GSM-based monitoring system for digital agriculture. Trans CSAE 21(6):87–91
7. Wang Zi, Wang Ruihui, Zuo Haijun, Liu Jian (2009) Transpiration water consumption characteristics of five kinds of landscape ground cover plants in Hunan, southern China. J Beijing Forest Univ 31(6):139–144
8. Chen Shaoyong, Guo Kaizhong, Dong Anxiang (2008) Research of variety rule of soil humidity in Loess Plateau of China. Plateau Meteorol 27(3):530–537

Chapter 99
The Design of Taxi Mileage Pricing Table

Jingrui Sun, Jingya Zhao, and Jincheng Wu

Abstract This system is mainly based on ATMEL Corporation AT89S52 microcontroller as the core, with using a 12 MHz crystal oscillator to provide the clock signal, and the Hall sensor detects the vehicle speed, timing through software programming, mileage detection, costing the same time the visual image of the LED digital tube display mileage and total costs, so as to achieve the purpose of billing. The system has a total of five buttons (Clear, query/verify, stop, one way/return function selection), corresponding to the button operation can be achieved one way/round-trip pattern selection, stop charging, waiting for the time to query, cleared reset and other functions. Not only does it have quite simple structure, but also it has a bright future with a stable, intuitive display and easy operation.

Keywords Taxi mileage pricing table • MCU AT89S52 • Hall sensor, control circuit

99.1 The Design Requirements

The design has a certain function of taxi mileage valuation system, can use sensors to detect the speed, to process and display mileage and amount.

To display real-time mileage number and amount Using digital tube. Taxi single price of 2 yuan/km, round-trip price is 1.5 yuan/km; Single/return two modes can be made of button switch, taxi speed <5 km/h accumulation for the total waiting time, every 5 min of waiting time is equal to 1 km mileage.

Start mileage of 3 km, 8 yuan. If the actual operation is more than 3 km, mileage than at 2 yuan/km. Turn the simulation speed by rotary photoelectric sensor, according to the number of wheel rotation circle skillfully mileage calculation.

J. Sun (✉) • J. Zhao • J. Wu
College of Electronic and Electronic communication engineering,
Tianjin Normal University, Tianjin, China
e-mail: 243073975@qq.com

J. Mu et al. (eds.), *The Proceedings of the Third International Conference on Communications, Signal Processing, and Systems*, Lecture Notes in Electrical Engineering 322, DOI 10.1007/978-3-319-08991-1_99

After arriving at the destination, press the "stop" key, the valuation table stop valuation: Press "clear" key, valuation table can record data (mileage, waiting time and price, etc.) automatic reset: Press "query" button, can display the total waiting time automatically, and then press the key valuation table display mileage and amount to return to the state.

99.2 The Overall Design Scheme

The design table of valuation system is mainly composed of two parts of hardware and software. The software design using C language programming to achieve; AT89S52 single chip microcomputer as main control chip of hardware design, the external circuit including reset circuit, crystals circuit, digital tube display circuit, the speed detection circuit, independent keyboard circuit, indicator light circuit, storage circuit, clock circuit, etc. Overall scheme design is shown in Fig. 99.1:

Design principle diagram is shown in Fig. 99.2:

The design of the mileage calculation and cost calculation scheme is as follows:

99.2.1 Mileage Calculation

1. Hall sensor detects wheel signal, and outputs pulse signal to the microcontroller.
2. Single-chip microcomputer to count of hall sensor output pulse signal, and mileage (unit: km) conversion. One revolution every pulse signal on behalf of

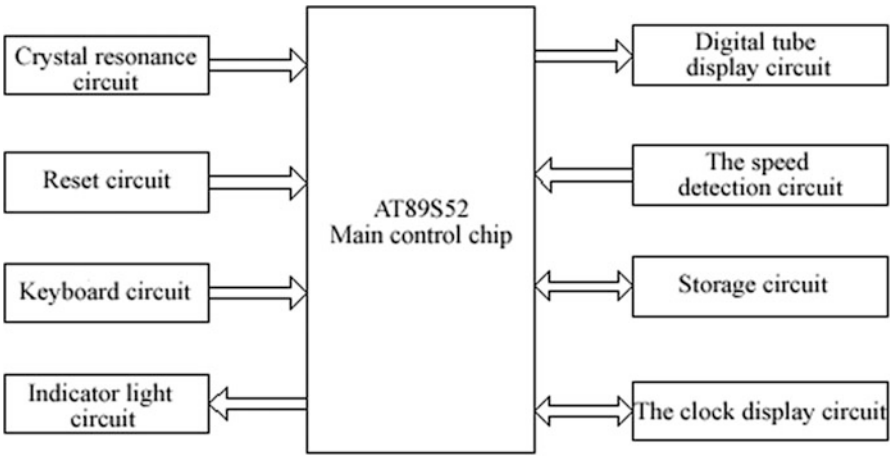

Fig. 99.1 The overall scheme

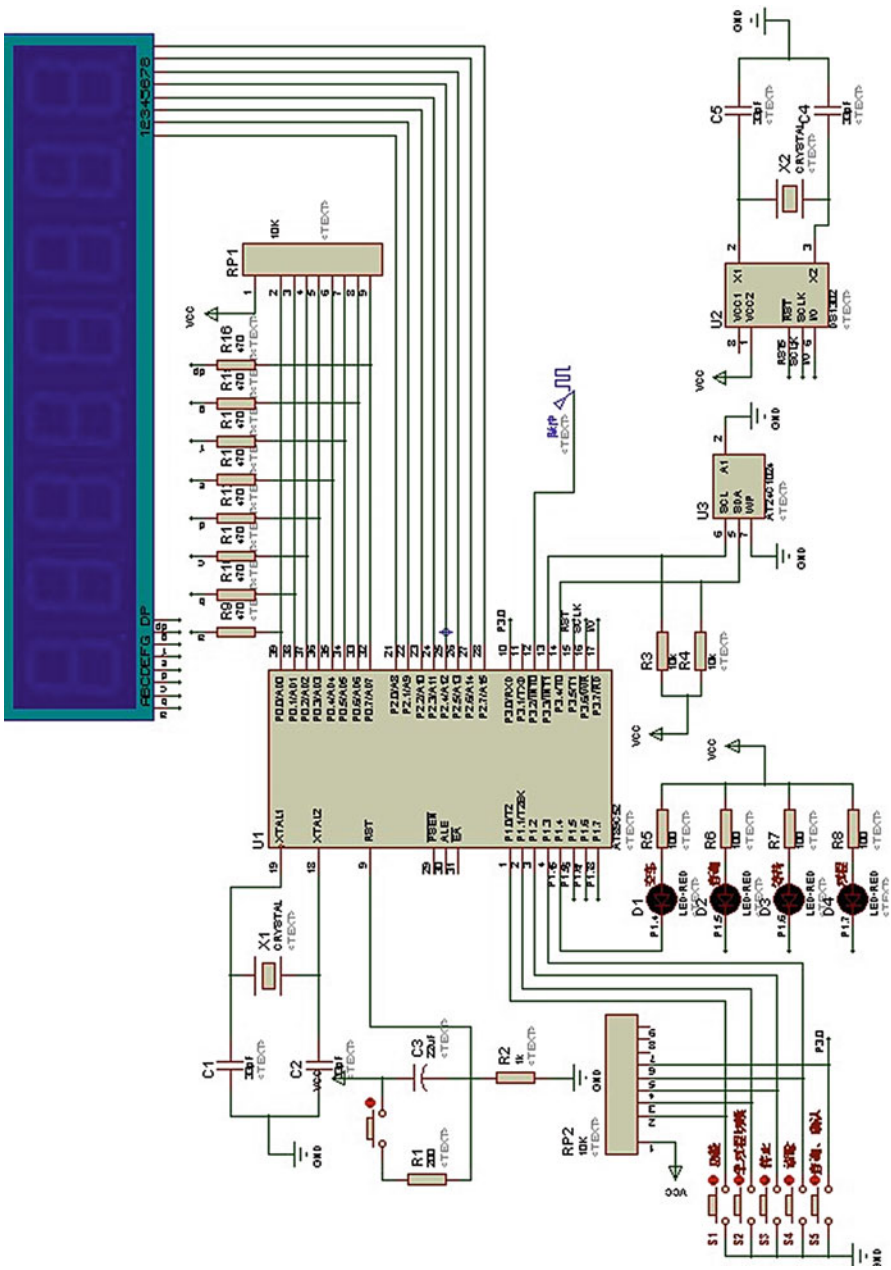

Fig. 99.2 The principle diagram of the design

the tire, the diameter of the tire for d = 0.5 m; Tire revolutions to N, then the distance Z = PI * d * N/1,000 (km). A speed V, and the pulse signal frequency F, the V = PI * d * F (m/s) = 3.6 PI * d * F (km/h).

99.2.2 Cost Calculation

1. The start of the taxi is 8 yuan, and requires no additional valuation in 3 km.
2. Driving a taxi after 3 km, one-way is 2 yuan/km, roundtrip is 1.5 yuan/km.
3. Waiting for the charge standard for 5 min press 1 km to hold.
4. Pauses taxi valuation table suspended valuation, no charge.

99.3 Each Unit Control Circuit Design

99.3.1 The Hardware System Design

99.3.1.1 Reset Circuit

AT89S52 reset end is a Schmitt trigger input, high level effectively [15]. If RST end from low level to high level and lasts two machine cycle, system will achieve a reset operation [1]. This reset circuit, the power or press the reset switch can appear on the RST end a period of high level, make the system reset. As shown in Fig. 99.3.

99.3.1.2 Crystal Resonance Circuit

Its XTAL1 input for the chip pin, its output XTAL2 for chip pin. Through these two pins in the chip and quartz crystal oscillator and two capacitors, thus form a stable self-excitation oscillator. As shown in Fig. 99.4.

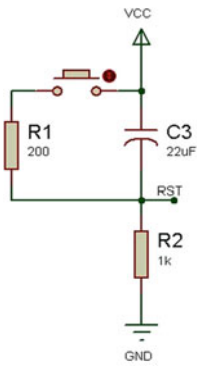

Fig. 99.3 Reset circuit

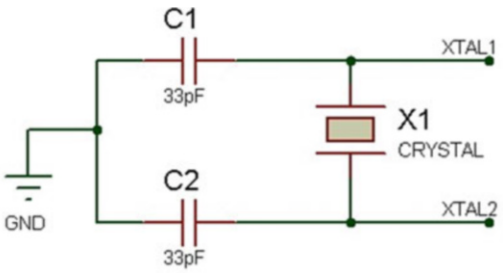

Fig. 99.4 Crystal resonance circuit

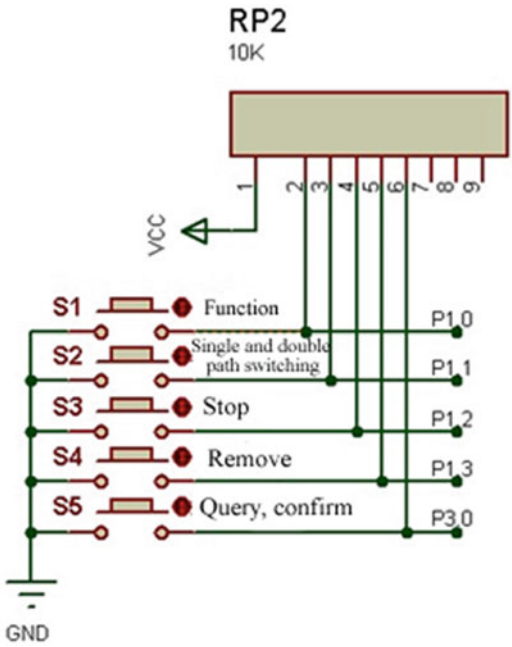

Fig. 99.5 Independent keyboard circuit

99.3.1.3 Independent Keyboard Circuit

The design of the keyboard circuit is composed of five separate buttons, as shown in Fig. 99.5.

Keys function is as follows:

S1 The function keys. When pressed into the single and double path choice model, then return to the real time display state.

S2 The "switch" button. According to the function keys into single and double path selection mode and then click this button to switch between single and double.

S3 The "stop" button. Running state press this button or stop taxi billing.

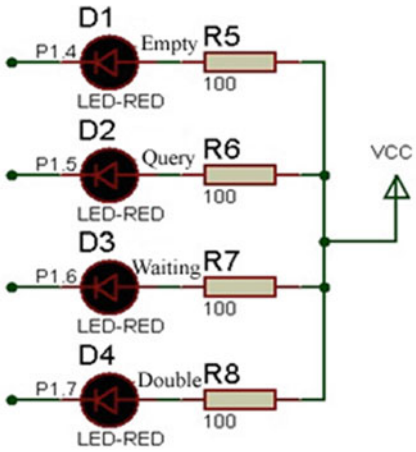

Fig. 99.6 Indicator light circuit

S4 Remove the key. Press the clear mileage and the amount of data information, and storing the information is sent to storage circuit.

S5 Query, confirm the key. Function selection mode by pressing this button to confirm selection, runtime push down this button can query latency, press return to display mileage, amount again.

99.3.1.4 Indicator Light Circuit

It is composed of four LED, including the empty light, querying, indicator light, waiting for light, double indicator light. As shown in Fig. 99.6.

These lights to tip taxi each kind of condition, there is a waiting indicator, a query is a query indicator, when the speed is less than 5 km/h. If the mode to return the double is selected, the indicator is on, one-way without light.

99.3.1.5 Digital Tube Display Circuit

Four digital tube display circuit consists of two integrated LED digital tube, LED digital tube is composed of LED array display device. The main characteristic of LED digital tube as follows:

1. It can work under the condition of low voltage, low current drive. It is compatible with CMOS, ITL circuit.
2. It has small size, light weight. Shock resistant performance is good.
3. Life is long, life in 100,000 h, or even up to 1 million hours. The cost is low. So it is widely used as a digital instrumentation, numerical control equipment, computer digital display device.

Fig. 99.7 Digital tube

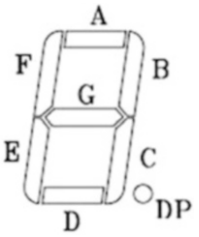

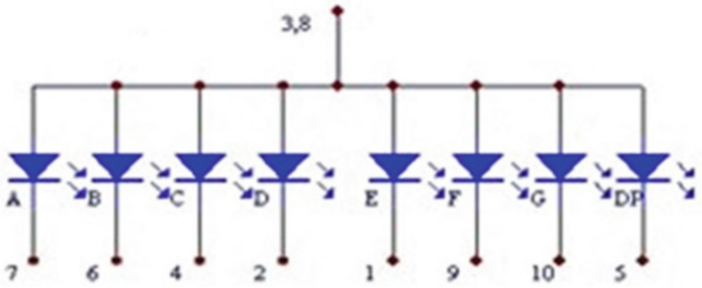

Fig. 99.8 Period of Yang digital tube

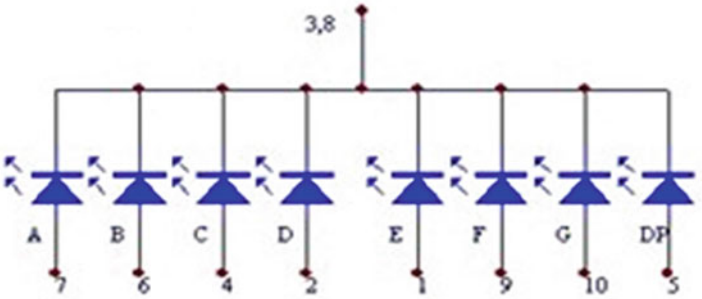

Fig. 99.9 Period of Yin digital tube

4. Inside of each digital tube is composed of eight LEDs, schematic diagram as shown in Fig. 99.7, among them A–G on behalf of the seven LEDs constitute 7 t glyph, remaining A DP constitute A decimal point, known as 8 LEDs. Section 8 of LED digital tube can display 0–9 ten numbers and the decimal point, such as wide use [2]. As shown in Fig. 99.7.

This kind of digital tube can be divided into a total of anode and cathode two, a total of anode is all the LED anode is connected to the common contact, and each LED cathode respectively a, b, c, d, e, f, g, dp. Common cathode is all the LED the cathode is connected to the common contact, and each LED anode respectively, a, b, c, d, e, f, g, dp. As shown in Figs. 99.8 and 99.9.

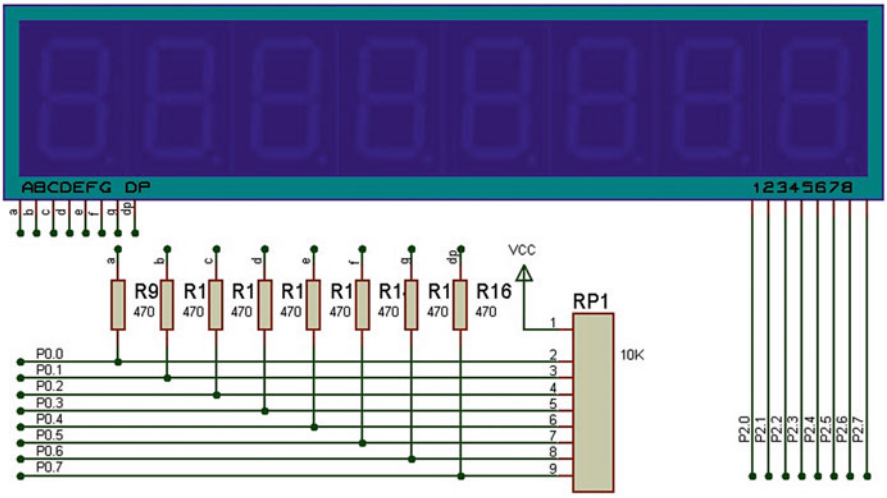

Fig. 99.10 Digital tube display circuit

By controlling the public side, can make the corresponding LED light or dark. When a total of Yin extreme ground or high level of anode, the display is effective, the opposite is invalid. This design USES is Yin LED digital tube.

Digital tube has two ways of a static display and dynamic display, this design USES the dynamic display. In comparison, dynamic display method has the advantages of low power consumption, less interface [3]. Used in the design of two of the four digital tube integrated the as segment P0 port, the as a P2 port. Empty, display the current time, began to charge, in four show mileage, after four show amount. When to query latency is shown as waiting time. As shown in Fig. 99.10.

99.3.1.6 The Speed Detection Circuit

The design selected the hall sensor to test the mileage. The design selected the hall sensor to test the mileage.

Mileage is measured by using a hall sensor IC mounted on the wheel at the top of the iron plate, install the magnet on the wheel, rotating wheel aim the magnet IC, hall sensor outputs a pulse signal, sent to the single-chip microcomputer, after a single-chip processing, mileage to display unit and display. Hall sensor range detection diagram as shown in Fig. 99.11.

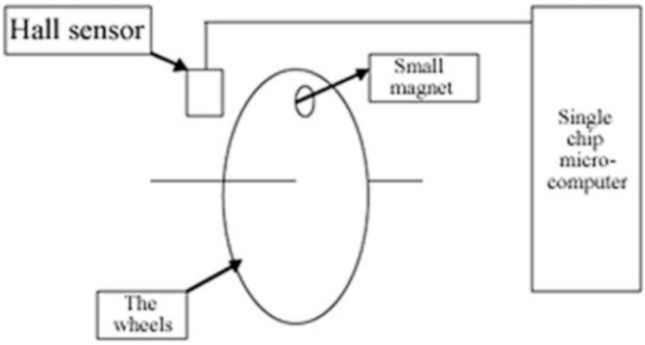

Fig. 99.11 Miles detection schemes

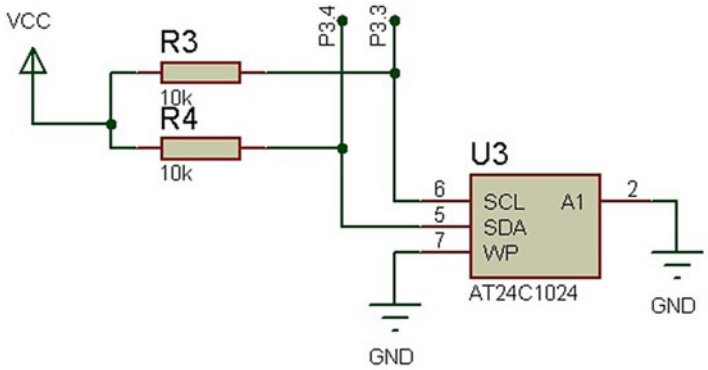

Fig. 99.12 Storage circuit

99.3.1.7 Storage Circuit

Before the storage circuit is used to store the amount of time, mileage and waiting time. This design adopts AT24C1024 can erase the memory chips, adopt the two-wire serial bus and the single chip microcomputer communication, information on chip under the condition of power can still save more than 40 years, in order to use convenient, DIP encapsulation, with 8 ft. Storage circuit as shown in Fig. 99.12. Pull up resistors R3 and R4 is in the figure, because AT24C1024 data and address lines are reusable, adopt the way of serial transmission data, so only two wires SCL and SDA connected with MCU P3.3 and P3.4 mouth [9], thus to transmit data.

99.3.1.8 The Clock Display Circuit

This design based on DS1302 clock circuit, empty, display the current time. DS1302 is a high-performance, low power consumption, real-time clock circuit with RAM, DS1302 pin arrangement, including VCC1 as backup power supply,

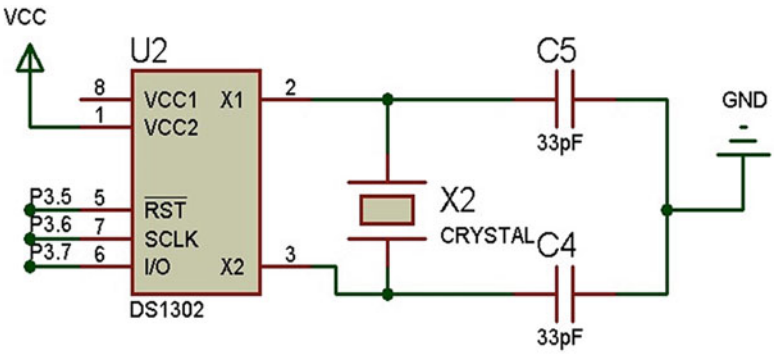

Fig. 99.13 Clock display circuit

mainly VCC2 power supply. In the case of main power supply shut down, also can keep the clock run continuously. X1 and X2 is oscillating source, external crystals. RST is reset/plate line selection, through the RST input driver set high level to start all data transfer [10]. The I/O for the serial data input/output end (bidirectional), SCLK as the clock input. As shown in Fig. 99.13.

References

1. Qihua Dai (2006) Circuit design and simulation based on Proteus. J Mod Electron Technol 19
2. Wenxiu Liu (2005) Single-chip microcomputer application system simulation study. J Mod Electron Technol 286
3. Qiaoyuan Cao (1997) Single-chip microcomputer principle and application. Electronic Industry Press, Beijing, pp 220–230
4. Yongchang Wei (2006) MCU peripheral circuit design. Electronic Industry press, Beijing, pp 136–141
5. Guangdi Li (2006) Single chip microcomputer based. Beijing University of Aeronautics and Astronautics Press, Beijing, pp 104–110
6. Zhongmei Ma (2003) Single chip C language programming. Beijing University of Aeronautics and Astronautics Press, Beijing, pp 92–99
7. Hua Li (1993) MCU practical interface technology. Beijing University of Aeronautics and Astronautics Press, Beijing, pp 140–148
8. Jia Dai (2007) 51 microcontroller C language application design example. Electronic Industry Press, Beijing, pp 200–210
9. Yongxiong Pan (2003) New single chip microcomputer principle and application. Xi'an University of Electronic Science and Technology Press, Xi'an, pp 82–85
10. Meie Dai, Jiaquan Shi (2003) Microcomputer technology and application. Tsinghua University Press, Beijing, pp 104–109
11. Limin He (1990) Single chip microcomputer application system design. Beijing University of Aeronautics and Astronautics Press, Beijing, pp 210–220

12. Weiping Wang (2004) Electronic technology foundation. Electronic Industry Press, Beijing, pp 180–188
13. Mingying Chen (2004) 8051 single-chip computer curriculum design training materials. Tsinghua University Press, Beijing, pp 154–159
14. Jingwu Zhang (2009) Principle of single chip microcomputer application and PROTEUS simulation. Electronic Industry Press, Beijing, pp 251–257
15. Lei Sun (2011) Based on the Protel DXP2004 printed circuit board design method research. J Mod Electron Technol 22

Chapter 100
Deep Learning Based Digital Signal Modulation Recognition

Junqiang Fu, Chenglin Zhao, Bin Li, and Xiao Peng

Abstract In this investigation, we proposed a promising digital signal modulation recognition scheme which is inspired by the deep learning. Firstly, the signal discriminations are constructed, which are composed of the full temporal characteristics of digital signals, its frequency spectrum as well as several higher-order spectral characteristics. Subsequently, the deep learning algorithm, with the powerful ability of interpretations and learning, is further suggested to realize modulation recognitions. A major advantage of this new scheme is that it may fully exploit the complete information of digital signals, rather than only utilizing several extracted features. It is verified by experimental simulations that the recognition accuracy of the proposed new scheme is much superior to other traditional recognition methods, which therefore provides an attractive approach to realistic modulation recognition.

Keywords Modulation recognition • Spectral characteristics • Amplitude characteristics • Deep learning

100.1 Introduction

Nowadays, the applications of modulation recognition have been invading almost every domain of commercial and military communications. In general, there are three kinds of traditional methods, i.e., decision tree classifier, cluster analysis, neural network classifier.

Nandi [1] and Azzouz [2] proposed a decision tree algorithm which makes a hard decision based on several characteristic parameters. It has low computational complexity and is intuitive, which, however, is susceptible to noise. Therefore, in practice, it has to usually be combined with some other methods. Cluster analysis [3] is a multivariate statistical classification method, which blindly classifies unlabeled samples according to the pattern similarity among them. Unfortunately,

J. Fu (✉) • C. Zhao • B. Li • X. Peng
Key Lab of Universal Wireless Communications, MOE Wireless Network Lab, Beijing University of Posts and Telecommunications, Beijing, China
e-mail: 750450554@qq.com

J. Mu et al. (eds.), *The Proceedings of the Third International Conference on Communications, Signal Processing, and Systems*, Lecture Notes in Electrical Engineering 322, DOI 10.1007/978-3-319-08991-1_100

cluster analysis seems to be noise sensitive and, accordingly, the identification performance will be influenced significantly by the extraction of characteristic parameters. As the most popular method, the back propagation (BP) [4] and radial basis function (RBF) [5] neural networks (NN) have the ability self-learning and generalization which is hence suitable to identify the underlying nonlinear mapping of input signal and output classification. However, it is easy to fall into some local optimal solutions. Besides, it may have a slow decline in the convergence rate closed to the optimal solution and also the poor generalization ability and low recognition rate in low signal to noise ratio (SNR).

In this investigation, we proposed a promising digital signal modulation recognition scheme based on the learning scheme. In sharp contrast to existing NN schemes, the deep learning algorithm is suggested to further promote the interpretation and classification capability. Firstly, the signal discriminations are constructed, which is composed of the full temporal characteristics of digital signals, its frequency spectrum as well as several higher-order spectral characteristics. Subsequently, the deep learning [6] algorithm, with the powerful ability of interpretations and learning, is further suggested to realize modulation recognitions. A major advantage of this new scheme is that it may fully exploit the complete information of digital signals, rather than only utilizing several extracted features. It is verified by experimental simulations that the recognition accuracy of the proposed new scheme is much superior to other traditional recognition methods, which therefore provides an attractive approach to realistic modulation recognition.

100.2 Signal Characteristic Extraction

100.2.1 Characteristics of the Signal Frequency Spectrum

This paper processed automatic modulation identification of several commonly used methods, including MASK, MPSK, MFSK and MQAM signals, by utilizing differences in time-domain, frequency spectrum and higher-order spectrum in the AWGN channel. Digital sampling signal in time-domain can be represented as

$$s(n) = \sum_{k=1}^{K} a_k \cos\left(2\pi f_0 n T_s + \varphi(n)\right), n = 1, 2, \ldots, N, \tag{100.1}$$

where N is the total number of sampling points, K is the number of sampling point per symbol, T_s is the sampling period, f_0 is the carrier frequency, $\varphi(n)$ is the carrier phase and a_k is the symbol amplitude. Then the signal frequency spectrum is given by the Fourier transform

$$F(w) = FFT\{s(n)\} = \langle s(n), \exp(-jwn) \rangle \tag{100.2}$$

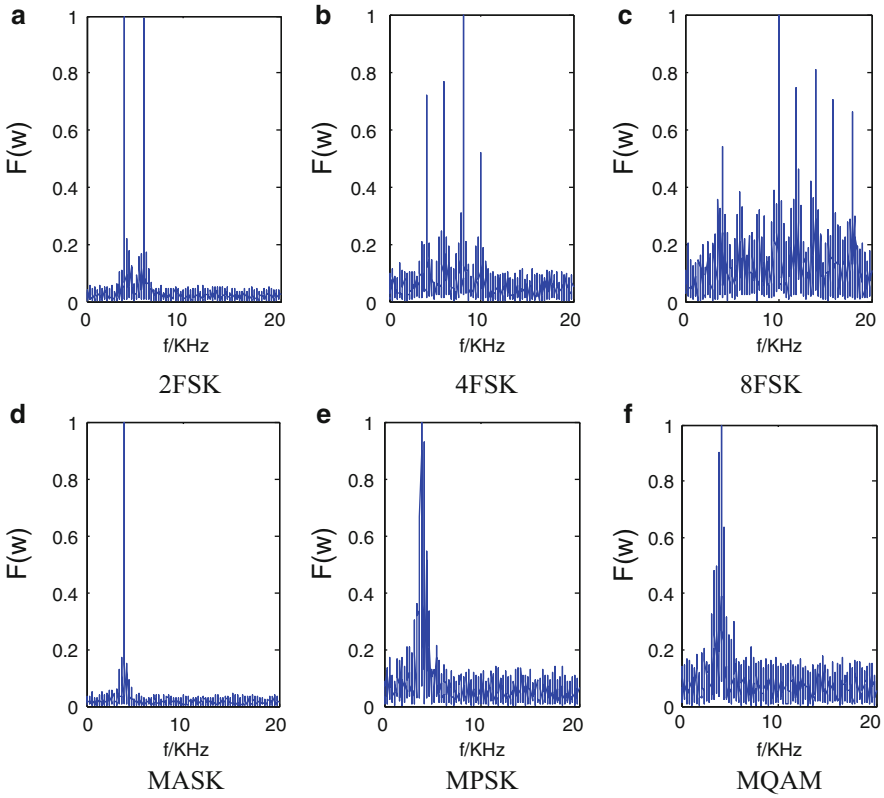

Fig. 100.1 Signal frequency spectrum

For the MFSK signals, there are M peaks the signal frequency spectrum. But there is only one for other signals. For the MASK signals, there will be a large impulse of the carrier. For the MPSK and MQAM signal, however, the spectrum line near the carrier will decline slowly and not appear obvious pulsing because of sudden phase anomalies (SPA) (Fig. 100.1).

100.2.2 Time-Domain Amplitude Characteristics

In time-domain MPSK and MFSK signals are constant envelope signals, but MASK and MQAM signals exist amplitude variation. In Eq. 100.1 we can get the absolute sum value of all sample points amplitude within each symbol

$$M_k = \sum_{n=k-1}^{(k-1)*m+m-1} |\cos(2\pi f_0 n T_s + \varphi(n))|, \tag{100.3}$$

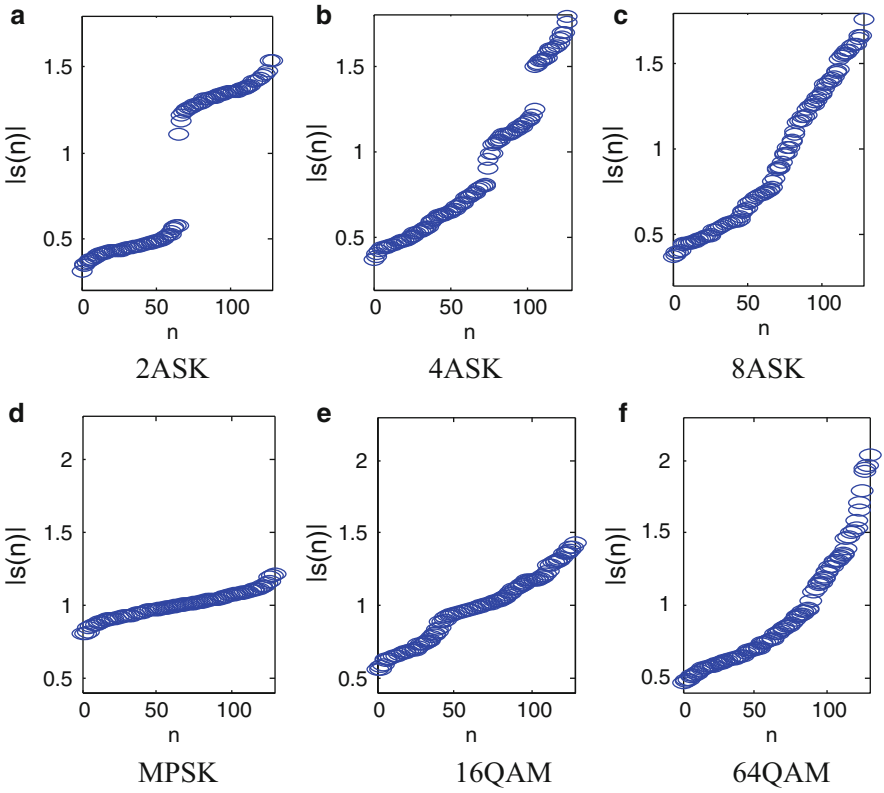

Fig. 100.2 Signal time-domain normalized amplitude

where $M = N/K$ is the number of sampling point per symbol.

The energy-normalized amplitude is given as follows

$$\alpha_k = M_k / \sqrt{\sum_k M_k / K}, \tag{100.4}$$

Then α_k are sorted as a feature vector (Fig. 100.2).

100.2.3 Higher-Order Spectral Characteristics

Square spectrum of BPSK appears at a noticeable discrete spectral line in double carrier frequency. Four order spectrum of QPSK and 8 PSK have different characteristic line in quadruplicated carrier frequency. 8 PSK signals exist relatively high lines near the zero frequency. 4 PSK signals, however, do not. The higher-order spectrum can be given as (Figs. 100.3 and 100.4)

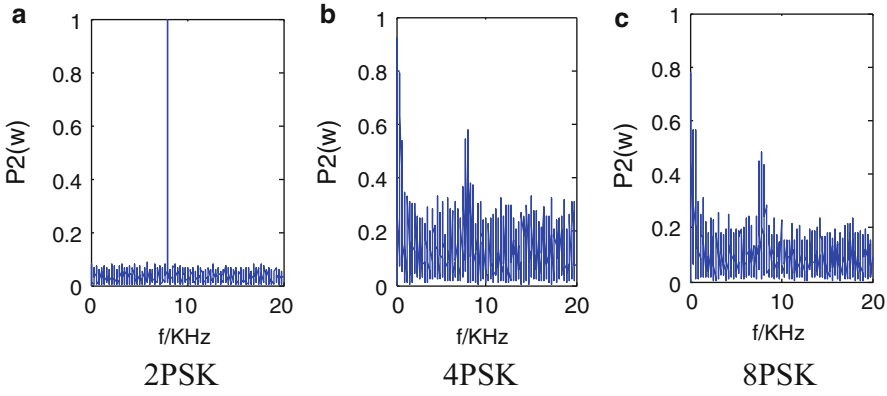

Fig. 100.3 Two-order frequency spectrum

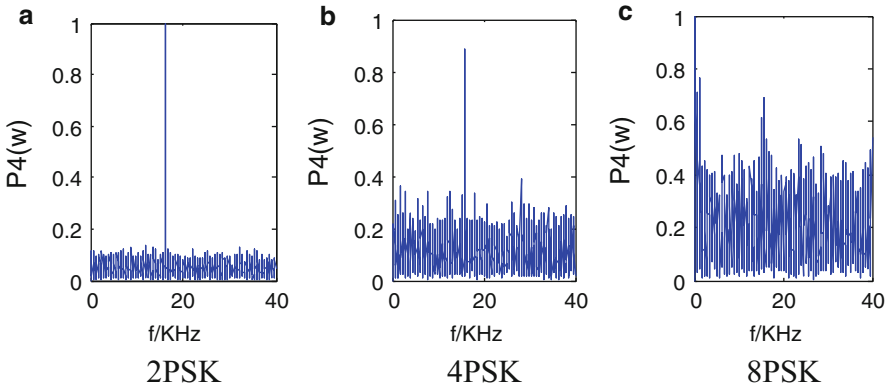

Fig. 100.4 Four-order frequency spectrum

$$P_2(w) = FFT\left\{s^2(n)\right\} \tag{100.5}$$

$$P_4(w) = FFT\left\{s^4(n)\right\}. \tag{100.6}$$

100.3 Deep Learning Algorithm

The deep learning is a neural network, which contains many hidden units between its input layer and its output layer. Pre-training, an unsupervised and undirected Restricted Boltzmann Machine [7] (RBM) process, is essential to the next training. Training has two parts: top-down generation model and down-top recognition model (Fig. 100.5).

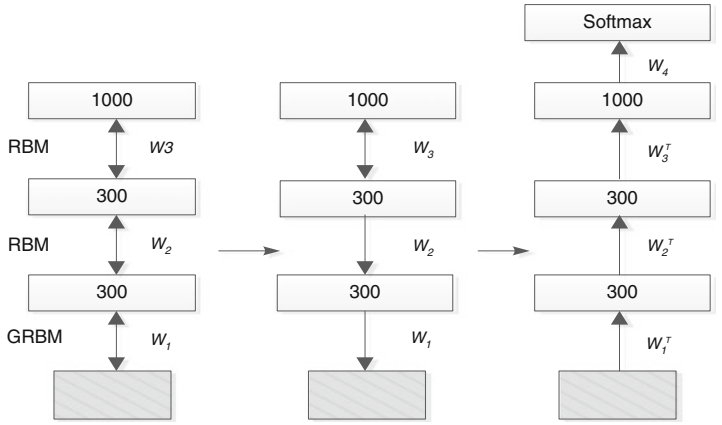

Fig. 100.5 Deep learning

100.3.1 Pre-training

A RBM consists of a binary visible layer that represents binary data and a binary hidden layer. It uses a parameter of weight, W, to set the joint probability of visible vectors, v, and hidden vector, h, by a energy function, E

$$\begin{aligned} p(v,h;W) &= \exp(-E(v,h;W))/Z, \\ Z &= \sum\nolimits_{v',h'} \exp\left(-E\left(v',h';W\right)\right), \end{aligned} \tag{100.7}$$

where Z is a normalized factor.

The joint (v, h) in a RBM defines a energy

$$E(v,h) = -\sum_{i\in\text{visible}} a_i v_i - \sum_{j\in\text{hidden}} b_j h_j - \sum_{i,j} v_i h_j w_{ij}. \tag{100.8}$$

where a_i, b_j is respectively the bias of visible unit, v_i, and hidden unit, h_j, w_{ij} is a connection to unit, j, from unit, i, in the lower layer.

Given hidden vector, h, the probability of visible units, v_i, is given as follows

$$p(v) = \sum\nolimits_h \exp(-E(v,h))/Z. \tag{100.9}$$

The change in a weight is linear with the derivate of log probability

$$\begin{aligned} \Delta w_{ij} &= \varepsilon\left(< v_i h_j >_{\text{data}} - < v_i h_j >_{\text{model}}\right) \\ &= \varepsilon/N \sum\nolimits_{n=1}^{n=N} \partial \log p(v^n)/\partial w_{ij}, \end{aligned} \tag{100.10}$$

where ε is a learning factor.

However, $<v_i h_j>_{\text{model}}$ will be difficult to get and be replaced by $<v_i h_j>_{\text{recon}}$. Given a random binary vector, v, the hidden unit, h_j, is reconstructed by conditional probability

$$p(h_j = 1|v) = \text{logistic}\left(b_j + \sum\nolimits_i v_i w_{ij}\right), \tag{100.11}$$

And then given a hidden vector, h, the visible unit, v_i, is reconstructed by

$$p(v_i = 1|h) = \text{logistic}\left(a_i + \sum\nolimits_j h_i w_{ij}\right). \tag{100.12}$$

The learning rule for a weight is given by

$$\Delta w_{ij} = \varepsilon\left(< v_i h_j >_{\text{data}} - < v_i h_j >_{\text{recon}}\right). \tag{100.13}$$

RBM which input vector is real vale with Gaussian noise is called Gaussian-Bernoulli RBM (GRBM). Two conditional probabilities for GRBM are given as follows

$$p(h_j|v) = \text{logistic}\left(b_j + \sum\nolimits_i v_i/\sigma_i w_{ij}\right), \tag{100.14}$$

$$p(v_i|h) = N\left(a_i + \sigma_i \sum\nolimits_j h_i w_{ij}, {\sigma_i}^2\right). \tag{100.15}$$

100.3.2 Top-Down Generation Model

After pre-training, we train network on a directed connection in a mandatory registration. Each hidden unit utilizes logistic function as a transfer function. We input x_j to get output y_j by a weight, w_{ij}

$$y_j = \text{logistic}(x_j) = 1/(1 + \exp(-x_j)), \tag{100.16}$$

$$x_j = b_j + \sum\nolimits_i y_i w_{ij}. \tag{100.17}$$

A top-down generation model has a top-down, directed connection, but the top two layers are a top-down RBM. The RBM can get a probability

$$p(v; W) = \sum\nolimits_h p(h; W) p(v|h; W). \tag{100.18}$$

It is required to reverse the roles of the visible and hidden layer and remain $p(v/h;W)$ fixed. Then $p(h;W)$ is replaced with a hidden vector inferred using Eq. 100.14 from a sampled visible vector, v.

100.3.3 Down-Top Recognition Model

A down-top recognition model has a down-top directed connection and adds a "Softmax" multiclass classifier that contains one unit for each modulation in the top layer. A class probability, p_j, is given by using the softmax function

$$p_j = \exp(x_j) / \sum_n x_n. \tag{100.19}$$

Then it defines a cost function

$$C = -\sum_j d_j \log p_j, \tag{100.20}$$

Where d_j, taking values of 0 or 1, is target probability.

A weight is updated by

$$\Delta w_{ij}(n) = \delta \Delta w_{ij}(n-1) - \varepsilon \partial C / \partial w_{ij}(n), \tag{100.21}$$

where $0 < \delta < 1$.

100.4 Simulation and Performance Analysis

We first set carrier frequency 4 KHz, symbol rate 1 KHz, MFSK spacing frequency 2 KHz, the sampling frequency 40 KHz, the number of symbols 300 and then sampled from all signals in the AWGN channel. SNR takes values of 0/5/10/20 dB, 20 groups of them are selected as training sequences and 200 groups as test sequences. There are three hidden layers and the number of units per layer was 300\300\1,000. The number of units in the input layer is consistent with dimension of input visible vectors. The number of units in the output layer is consistent with modulation classes.

In Fig. 100.6, it represents the decision feature extraction process. Feature vectors are extracted in sequence to be as input data for digital signal modulation recognition.

In Fig. 100.7a it shows the BP network based recognition accuracy where SNR takes values of 0, 5, 10 and 15 dB. When the SNR = 5 dB, the recognition rate can reach 93 %. However, the recognition rate of 8PSK is relatively low. With the increase of SNR, the recognition rate approaching 100 %. It is easy to fall into local optimal solution for BP network and its generalization ability is poor.

In Fig. 100.7b it represents the deep learning based recognition accuracy where SNR takes values of 0, 5, 10 and 15 dB. Deep learning overcomes the problem of falling into local optimal solution and has fast convergence speed and good

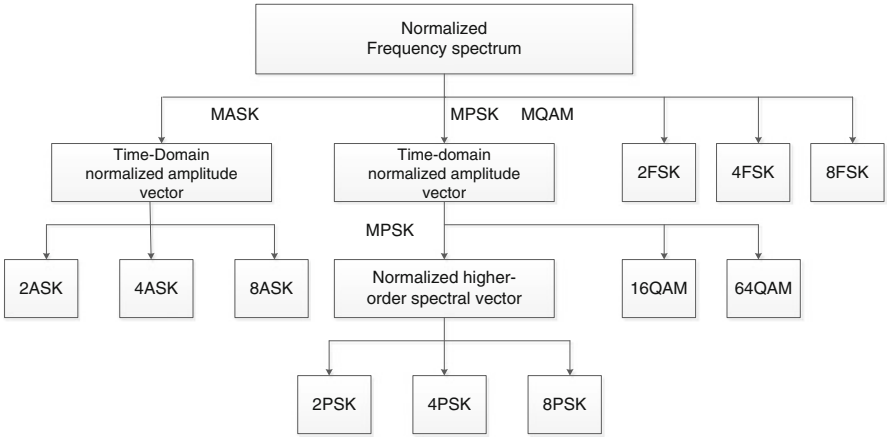

Fig. 100.6 The whole recognition process

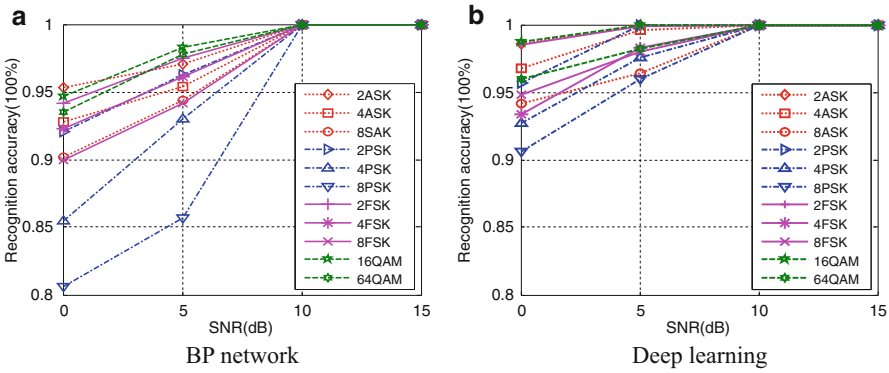

Fig. 100.7 Recognition accuracy

generalization ability. By comparing (a) with (b), we can clearly see that the deep learning scheme has a higher recognition rate than BP. When the SNR = 0 dB, the recognition rate even can reach 90 %. Although deep learning has a higher computational complexity, the performance has been significantly improved.

Conclusion

This paper proposes a promising digital signal modulation recognition scheme which is inspired by the deep learning. A major advantage of this new scheme is that it may fully exploit the complete information of digital signals, rather than only utilizing several extracted features. It is verified by

(continued)

(continued)

experimental simulations that the recognition accuracy of the proposed new scheme is much superior to other traditional recognition methods, which therefore provides an attractive approach to realistic modulation recognition. Compared to the current BP neural network, deep learning based the recognition accuracy is significantly higher than BP network. In a complex channel environment, the next step is to do deeper research about how to further reduce the complexity of the algorithm.

Acknowledgement This work was supported by National Science and Technology Major Project (2013ZX03001015-003), NSFC (61379016, 61271180), Doctoral Fund of Ministry of Education of China (20130005110016).

References

1. Nandi AK, Azzouz EE (1998) Algorithms for automatic modulation recognition of communication signals. IEEE Trans Cornrn 46(4):431–436
2. Azzouz EE, Nandi AK (1996) Automatic modulation recognition of communications signals. Kluwer, Boston
3. Chen H, Liu C (2013) Research and application of cluster analysis algorithm[C]. In: Measurement, information and control (ICMIC), 2013 international conference on IEEE, vol 1, pp 575–579
4. Hassan K, Dayoub I, Hamouda W et al. (2010) Automatic modulation recognition using wavelet transform and neural networks in wireless systems. EURASIP J Adv Signal Process
5. Savitha R, Suresh S, Sundararajan N (2012) Metacognitive learning in a fully complex-valued radial basis function neural network. Neural Comput 24(5):1297–1328
6. Hinton G, Deng L, Yu D et al (2012) Deep neural networks for acoustic modeling in speech recognition: the shared views of four research groups. Signal Process Mag IEEE 29(6):82–97
7. Hinton G (2010) A practical guide to training restricted Boltzmann machines. Momentum 9(1):926

Chapter 101
Finite Time Proportional-Integral Sliding Mode Control of Theodolite Aiming Chaotic Motor with Time Varying Parameters

Zhenxin He, Chuntong Liu, Hongcai Li, Zhili Zhang, and Xianxiang Huang

Abstract In the angle measuring using theodolite, the telescope is driven by the aiming motor to sight the target automatically. The parameters of aiming motor will vary with duty conditions to bring about aiming control system chaotic, which is harmful for the aiming system and the aiming results. The aiming motor control system exist the time-varying load and the inside disturbances, the dynamic model is established and analyzed. The behavior of chaos is proved. Due to terminal sliding control with good robustness, fast dynamic response, finite time convergence and high tracking precision, The finite time proportional-integral (PI) sliding mode structure and control strategy are given, and the system stability is analyzed. The chaotic orbits of the aiming motor control system are stabilized to arbitrary chosen the fixed points and periodic orbits by means of sliding mode method. Simulation results show that finite time PI sliding mode control can realize the stability and accuracy of aiming motor control system, and overcome the negative influence of the chaos for the aiming system.

Keywords Chaotic motor • Finite time sliding mode control • Theodolite aimiomg • Time-varying parameters

101.1 Introduction

Electronic theodolite is the key equipment as weapon measuring system, whose automation is the trend of its development. Theodolite vertical shaft is driven by installing brushless dc motor, which can achieve the automatic sighting and automatic measuring angle for the goal. But in the process of actual measuring, the parameters of the motor will change with conditions changing, such as temperature. Therefore, the motor control system of electronic theodolite is a strongly nonlinear system. The unpredictable random nonlinear phenomenon for a long time can lead to intermittent

Z. He • C. Liu (✉) • H. Li • Z. Zhang • X. Huang
Precision Instrument Department, Xi'an Research Institute of High Technology, Xi'an, Shaan Xi 710025, China
e-mail: hezhenxin1986@126.com; liuchuntong2001@163.com

J. Mu et al. (eds.), *The Proceedings of the Third International Conference on Communications, Signal Processing, and Systems*, Lecture Notes in Electrical Engineering 322, DOI 10.1007/978-3-319-08991-1_101

oscillation of motor torque and speed, the irregular electromagnetic noise of the system, more system loss and unstable control performance [1, 2]. When chaos is bad in the motor driving, it is important to restrain and keep chaotic behavior stable effectively.

To curb and stabilize chaotic behavior, many control methods have been proposed, such as the OGY method, feedback method, adaptive control method and intelligent control method [3–6]. The disturbance is not considered when these control methods are adopted. But in the actual theodolite measuring, the motor system is influenced by external and internal disturbances badly. Sliding mode variable structure control is a class of special nonlinear control with fast response, no-sensitivity for parameter variation and disturbance, no need for on-line identification system and the simple physical realization, which can be well used in brushless dc motor control to inhibit motor system interference [7, 8]. The traditional sliding mode variable structure control is using linear control, and the deviation between the system state the given trajectory is asymptotic convergence. In recent years, some scholars put forward terminal sliding mode control strategy [9–11]. The nonlinear function is introduced to construct the terminal sliding mode surface in the design of sliding hyperplane, which makes the tracking error of the sliding surface converge to zero in finite time.

In this article, the chaotic phenomenon of theodolite motor system is analyzed; Based on the theory of sliding mode control, PI terminal sliding mode surface and sliding mode control strategy is established to control the chaotic trajectory at the specified fixed point and the periodic orbit; Simulation results are shown to verify the proposed strategy

101.2 Problem Description

Based on the working principle of brushless dc motor and the control system structure of the measuring motor, through Clark transform and Scale transform, when parameter perturbation and time-varying load disturbance happens, the measuring motor dynamic model can be expressed as [12]:

$$\begin{cases} \dfrac{d\widetilde{i}_q}{d\widetilde{t}} = -\widetilde{i}_q - \widetilde{i}_d\widetilde{\omega}_r + \rho\widetilde{\omega}_r + V_q \\ \dfrac{d\widetilde{i}_d}{d\widetilde{t}} = \widetilde{i}_q\widetilde{\omega}_r - \widetilde{i}_d + V_d \\ \dfrac{d\widetilde{\omega}_r}{d\widetilde{t}} = \eta(1 + m\sin(2\pi t))\left(\widetilde{i}_q - \widetilde{\omega}_r\right) - \widetilde{T}_L \end{cases} \tag{101.1}$$

where $\widetilde{i}_q$, $\widetilde{i}_d$ and $\widetilde{\omega}_r$ are motor direct axis, quadrature axis current and mechanical angular velocity, respectively. ρ is free parameter, $V_q = \frac{p^2\tau^2 k_t}{LB_v} v_q$, $V_d = \frac{p^2\tau^2 k_t}{LB_v} v_d + \frac{\rho LB_v + p^2 k_t^2 \tau}{LB_v}$, $\eta = \frac{\tau B_v}{J}$, $\tau = \frac{L}{R}$, $\widetilde{T}_L = \frac{p\tau^2}{J} T_L$.

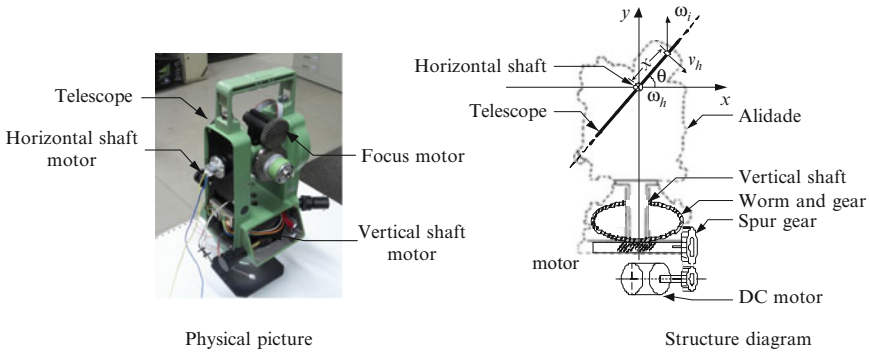

Fig. 101.1 Auto aiming theodolite

R and L are winding resistance and inductance. J is moment of inertia of rotor; B_v is viscous coefficient; p is the logarithmic motor pole; k_t is coefficient of motor torque; T_L is load torque; v_q and v_d are direct axis and quadrature axis voltage, respectively. η is decided by four motor parameters itself, which will change in the process of the motor running. m represents the degree of motor parameter perturbation.

Auto aiming theodolite is shown in Fig. 101.1. For theodolite horizontal axis drive motor, load T_L is constant and relatively easy to control. But in the horizontal axis rotation system, T_L is a function of telescope angle θ, and is a time-varying system, which can be used as a system disturbance. The ordinary PID control is difficult to meet the control requirements. In order to design terminal sliding mode control law, the upper limit of T_L is requested. T_L is calculated using system modeling method in this paper.

Telescope structure is complex, and its shape is not a simple symmetry space stereo, and it needs to be simplified. Due to the telescope's center of mass is generally located in the horizontal axis, and to simplify the model, the telescope is simplified to a symmetrical rigid body about the horizontal axis. The telescope's length is l, and linear density is ρ. The rotating angular speed of the telescope and sighting department are represented by ω_h, ω_i respectively.

A tiny particle dx on a telescope is chosen. According to the definition of the moment of inertia, its moment of inertia of the y axis can be obtained:

$$dJ_y = (x\cos\theta)^2 \rho dx \tag{101.2}$$

Total moment of inertia of the telescope is as follows:

$$J_y = J_y(\theta) = \int_{-l/2}^{l/2} dJ_y = \frac{l^2}{12} m_t \cos^2\theta \tag{101.3}$$

From Eq. 101.3, the maximum moment of inertia of the motor shaft is as follows:

$$J_{\max} = \frac{J_0 + J_y(0)}{j^2} + J$$

where J_0 is the moment of inertia of sighting, which excepts the telescope part. Reduction ratio $j = 736{:}1$.

Telescope moves 180° in 8 s to meet the design requirement, and the maximum angular acceleration θ'' is $21.1°/s^2$. So, the maximum load torque is: $T_{L\max} = J_{\max}\theta''_{\max} j$.

101.3 Chaos Analysis

To illustrate the chaotic behavior of brushless dc motor drive, phase track and Lyapunov index system spectrum is given, respectively. With an actual brushless dc motor as an example, the main parameters as follows:

$P = 1$, $L = 0.147\,mH$, $R = 0.997\ \ \Omega$, $J = 4.2\,gcm^2$, $B_v = 6 \times 10^{-3}\,Nm/(r/s)$, $k_t = 13.6\,mNm/A$. Get the motor parameters $\eta = 2.7$, $\widetilde{T}_{L\max} = 0.035$.

101.3.1 2-D and 3-D System Phase Diagram

Phase track can visually distinguish the chaotic behavior, balance, and cycle behavior. Balance and phase trajectory of periodic behavior is point and closed curve, respectively, but chaotic behavior of the phase trajectory is random distribution in a bounded area. The load torque is time-varying in the process of measuring and exists the maximum value 0.035, and $\widetilde{T}_L = 0.020 + 0.015 \times \sin(2\pi t)$. Three system state variables $\widetilde{i}_q$, $\widetilde{i}_d$, $\widetilde{\omega}_r$ can be written as x_1, x_2, x_3, respectively, setting their initial values for [3, 3, −0.3657], $V_q = 20.66$, $V_d = 0.168$. When the free number $\rho = 45$, motor parameters $\eta = 2.7$, and perturbation parameter $m = 0.02$, Fig. 101.2 shows the state trajectory of the chaos system.

When initial value, the free number ρ and η meet certain condition, the motor parameters theodolite aiming system will appear chaotic phenomenon by observing the system phase diagram.

101.3.2 Lyapunov Index

Lyapunov index can be used to determine the stability of chaotic behavior, measure the attractor in state space stretching and contraction rate, the max Lyapunov index

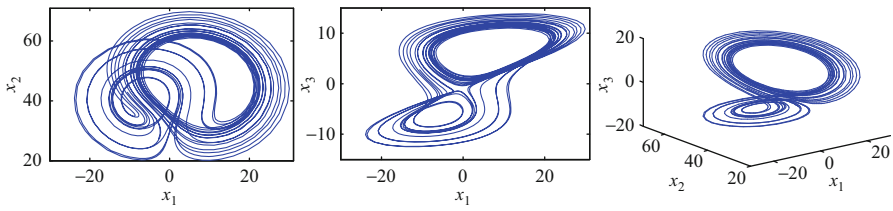

Fig. 101.2 The system phase trajectory in the chaos states

$\lambda_{\max}$ can judge the stability of the chaotic system. The system state variables are represented as follows,

$$X(t) = T^t X_0 \tag{101.4}$$

where T^t describes the evolution of the state variable X at time axis t. The evolution of the differential equation of δX can be represented as follows,

$$\delta X(t) = U^t_{X_0} \delta X_0 \tag{101.5}$$

where $U^t_{X_0}$ describes δX change from initial state. Therefore, Lyapunov index λ_i of three dimensional system can be calculated according to Eq. 101.6 [13],

$$\lambda_i = \lim_{h\to\infty} \frac{1}{h\Delta t} \sum_{j=0}^{h-1} \ln \frac{\left\| U^{\Delta t}_{X_j} e^j_i \right\|}{\left\| e^j_i \right\|}, i = 1, 2, 3 \tag{101.6}$$

where Δt is the time evolution, e^j_i is the ith baseline vector of the jth step in three dimensional state space. In reference [14], if $\Delta t << 1$ and $\|e^j_i\| << 1$, λ_i can approximate to,

$$\lambda_i = \lim_{h\to\infty} \frac{1}{h\Delta t} \sum_{j=0}^{h-1} \ln \frac{\left\| T^{\Delta t}\left(X_j + e^j_i\right) - T^{\Delta t} X_j \right\|}{\left\| e^j_i \right\|}, i = 1, 2, 3 \tag{101.7}$$

If Lyapunov index $\lambda_{\max} > 0$, the measuring system is in the state of chaos. For the system (101.1), the system parameters are set the same as Sect. 99.3.1 to show the existence of chaotic behavior. Figure 101.3 shows Lyapunov index changing with parameter η.

By observing Fig. 101.3, it is easy to find the parameter area η, when the system is in the critical state and the chaotic state.

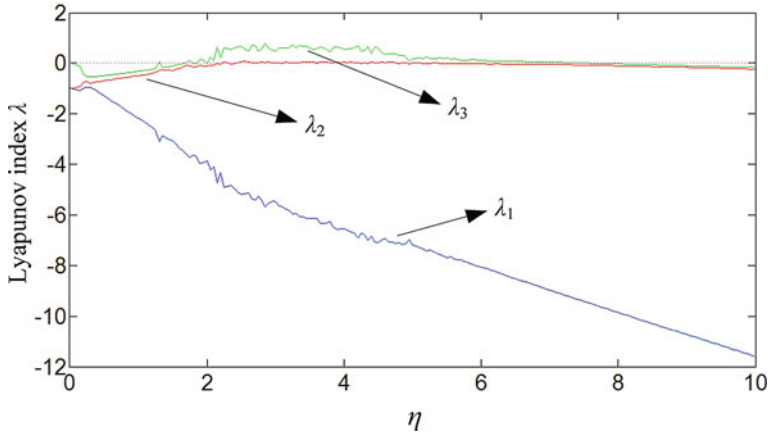

Fig. 101.3 The Lyapunov exponential spectrum

101.4 Finite Time Proportional-Integral Sliding Mode Control

In this paper, the proportion coefficient and integral coefficient k_d, k_p of the finite time proportional-integral sliding mode control is based on the type PI control, which can improve the dynamic performance of the control system.

101.4.1 The Controller Design

In order to analysis the system, the aiming motor control system can be represented as follows,

$$\begin{cases} \dot{x}_1 = -x_1 + \rho x_3 - x_2 x_3 + V_q + u_1 \\ \dot{x}_2 = -x_2 + x_1 x_3 + V_d + u_2 \\ \dot{x}_3 = \eta(1 + m\sin(t))(x_1 - x_3) - T_L + u_3 \end{cases} \tag{101.8}$$

where $\begin{cases} x_1 = \widetilde{i}_q \\ x_2 = \widetilde{i}_d \\ x_3 = \widetilde{\omega}_r \end{cases}$, u_1, u_2, u_3 are the control inputs.

Define the matrixes: Linear matrix of system $A = [-1\ 0\ \rho; 0\ -1\ 0; \eta\ 0\ -\eta]$; Control matrix $B = [1\ 0\ 0; 0\ 1\ 0; 0\ 0\ 1]$. Nonlinear term $\xi = [-x_2x_3 + V_q; x_1x_3 + V_d; \eta m\sin(t)(x_1 - x_3) - T_L]$.

Design goal: for the aiming motor chaotic system (101.8) with the bounded load and parameters perturbation of brushless dc motor, Finite time PI sliding mode

control is designed to realize the control of the chaotic states rapidly and accurately, and has the strong robustness for the nonlinear uncertain part.

Define the control target state $x_d = [x_{d1};x_{d2};x_{d3}]$, the error between the system state $x = [x_1;x_2;x_3]$ and the target state is $e = x - x_d$. Error system equation is as follows,

$$\dot{e} = \dot{x} - \dot{x}_d = Ax + B\xi + Bu - \dot{x}_d \tag{101.9}$$

In order to design controller of the chaotic system, the sliding mode function is designed as follows,

$$S = Ke - \int_{0_-}^{t} K(A - BL)e(\lambda)d\lambda \tag{101.10}$$

where matrix $K \in R^{3\times 3}$ satisfying $\det(KB) \neq 0$. L is designed using pole assignment method, and A-BL is negative positive definite matrix. Therefore, the design of the parameter matrix K and L is the key of sliding mode (101.10) design.

For the nonlinear uncertain systems (101.8), under the condition of the sliding mode, i.e., $S = \dot{S} = 0$, the controller u is put forward as follows,

$$u = -[\xi + Le] - (KB)^{-1}[KAx_d - K\dot{x}_d] - (KB)^{-1}[\varepsilon + \|KB\xi\|]sign(S) \tag{101.11}$$

where ε is constant, and $\varepsilon > 1$.

101.4.2 Stability Analysis

For the nonlinear system (101.8), the sliding mode surface (101.10) and the sliding mode control strategy (101.11) is designed. The error system (101.9) can be convergence in the finite time. Choose the Lyapunov function as follows,

$$V(S) = \frac{1}{2}S^T S$$

Derive $V(S)$ along time for the error system (101.9):

$$\begin{aligned} \dot{V}(S) &= S^T\dot{S} + \dot{S}^T S \\ S^T\dot{S} &= S^T(KB\xi + KBLe + KAx_d - KA\dot{x}_d + KBu) \\ &= S^T[-(\varepsilon + \|KB\xi\|)sign(S)] \\ &\leq -\varepsilon S^T sign(S) = -\varepsilon\|S\| \leq -\|S\| \end{aligned}$$

In the same way, we can obtain: $\dot{S}^T S \leq -\|S\|$

As a result, $\dot{V}(S) \leq -2\|S\| \leq 0$

Prove up.

101.5 Simulation Analysis

In the aiming motor control system (101.8), the parameters are set as follows: $x_1(0)=3$, $x_2(0)=3$, $x_3(0)=-0.3657$, $V_q=20.66$, $V_d=0.168$, free number $\rho=45$, motor parameter $\eta=4.2$, motor perturbation parameter $m=0.02$, $T_L=0.020+0.015\times\sin(2\pi t)$. The control system exists chaos when $u=0$, matrix $K=\mathrm{diag}(0.25,0.25,0.25)$ is designed to reach the target value x_d of control system the xd, and to guarantee the KB reversible. The eigenvalues $\mathrm{P}=[-5,-5,-5]$ of A-BL are selected, and matrix L is determined using pole assignment method as follows,

$$L=\begin{bmatrix}4 & 0 & 45\\ 0 & 4 & 0\\ 1.5 & 0 & 3.5\end{bmatrix}$$

Finite time sliding mode function S is designed as follows,

$$S_i=0.25e_i+\int_0^t 1.25e_i(\lambda)d\lambda,\quad \lambda=1,2,3$$

In the controller Eq. 101.11 u, the constant ε is 2.

101.5.1 Control to the Fixed Point

The method presented in this paper can control the system (101.8) steadily to the arbitrary point, The goal point is set for (5,5,5), namely $x_d=5$. The controller is joined at the moment of 1 s. The controlled system state and control input as shown in Figs. 101.4 and 101.5, respectively.

Figure 101.4 shows that, aiming control system (101.8) can converge to target state in a limited time (5,5,5) after joining PI sliding mode controller. Tracking error can decrease along, and achieve high tracking precision to meet the precision

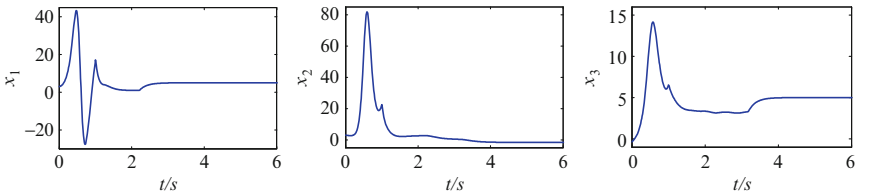

(1) motor direct axis current x_1 (2) motor quadrature axis current x_2 (3) motor angular velocity x_3

Fig. 101.4 The state variables of the system when the control signals are activated at the time $t=1$ s

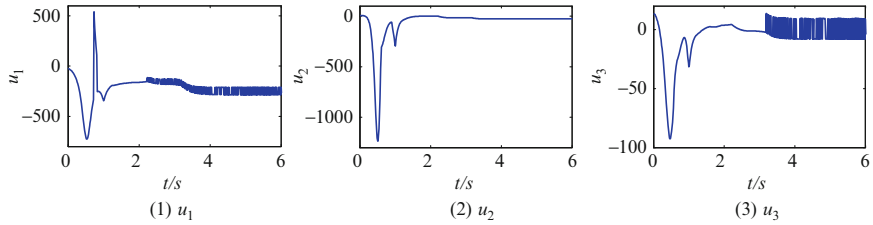

Fig. 101.5 Control input u

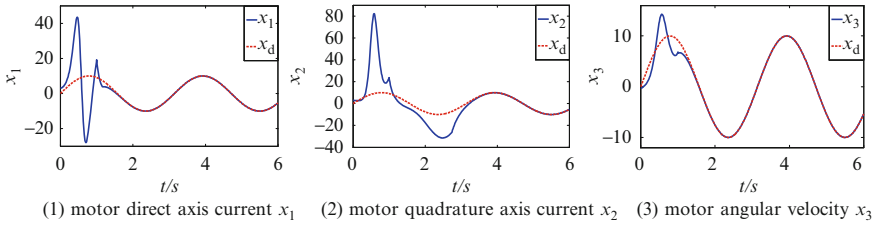

Fig. 101.6 The state variables of the system when the control signals are joined at $t = 1$ s

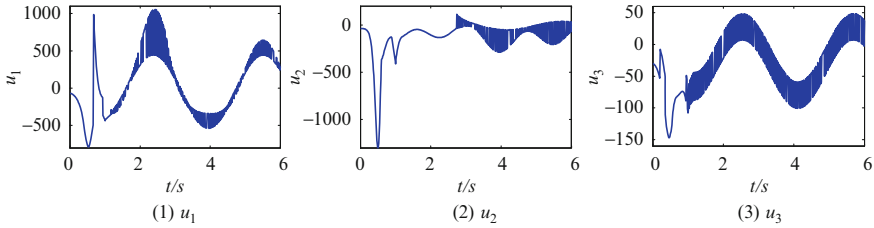

Fig. 101.7 Controller output u

aiming demand, which means the system go into sliding mode surface. From Fig. 101.5, the final control input value u has certain range change, but the system is stable. The fluctuation is generated by the symbolic function of controller.

101.5.2 Control to the Fixed Cycle

The finite time PI sliding mode control method can also make chaotic systems (101.8) stability to the preset periodic orbit to control theodolite velocity to realize the axis rotation. Here, assuming the default cycle target xd = 10 × sin(2 t), the controller is joined at 1 s. The control system states and the controller output u are as shown in Figs. 101.6 and 101.7, respectively.

Figure 101.6 shows that the designed controller can accurately track the setting cycle track, and has very strong robustness for the time-varying parameter perturbation and load torque of the aiming system (101.8). When the state waveform is stable, the target trajectory can be tracked well; In addition, the motor angular velocity can quickly reach to the target orbit with the finite time.

Conclusion

Complex working environment leads to a parameter perturbation for the theodolite aiming motor. The existence of chaos is proved in the motor system using Lyapunov index spectrum, which shows motor parameters range of the chaotic behavior. Under the motor parameters perturbation and the time-varying load torque, the general controller cannot achieve the ideal performance. The conventional sliding mode control method has robustness for parameter perturbation and external disturbance, but the convergence time and the tracking accuracy affect the actual application. Based on the obtained maximum load torque adopting the modeling method, the finite time proportional integral sliding mode control is proposed. The simulation results show that the method is very simple and easy to implement, with the fast response and the high control precision. The stability of the chaotic system can well satisfy the motor control requirement, which paves the way for the theodolite aiming.

Acknowledgments This work is partially supported by the National Nature Science Foundation of China under Grant 41174162.

References

1. Chen J, Chau K, Chan C (1999) Chaos in voltage-mode controlled dc drive system. Int J Electron 86:857–874
2. Han W, Xu S, Chen L (2001) Prospect and review on the chaotic phenomena in engineering and applications of chaos. Electric Mach Control 5:251–255
3. Aline S, Marcelo A (2009) A multiparameter chaos control method based on OGY approach. Chaos Solit Fract 40:1376–1390
4. Casa F, Grebogi C (1997) Control of chaotic impacts. Int J Bifurc Chaos 7:951–955
5. Boccalettis S, Farini A, Arecchi F (1997) Adaptive strategies for recognition, control and synchronization of chaos. Chaos Solit Fract 8:1431–1448
6. Wang J, Xue H, Si S (2009) Hybrid control of chaotic systems based on PSO and OGY method. Acta Phys 58:3729–3733
7. Utkin V (1978) Sliding modes and their application in variable structure system. Nauka, Moscow
8. Liu J, Sun F (2007) Research and development on theory and algorithms of sliding mode control. Control Theory Appl 33:407–416
9. Zak M (1988) Terminal attractors for addressable memory in neural networks. Phys Lett 33:18–22

10. Iglesias W, Xu L, Saito O (1996) Fast convergence for tracking problem of Nth degree system by sliding mode control. In: Proceedings of the 35th conference on decision and control, Kobe, pp 4607–4612
11. Harashima F et al (1987) Adaptive control of a flexible arm with a variable payload. In: Proceedings of IACS/ IFAC international symposium on modeling and simulation of distributed parameter systems, Osaka, Japan, pp 323–328
12. Ge Z, Cheng J (2005) Chaos synchronization and parameter identification of three time scales brushless DC motor system. Chaos Solit Fract 24:597–616
13. Shimada I, Nagashima T (1970) A numerical approach to ergodic problem of dissipative dynamical systems. Prog Theor Phys 61:1605–1616
14. Benettin G, Galgani L, Strelcyn J (1976) Kolmogorov entropy and numerical experiments. Phys Rev A 14:2338–2345

Index

J. Mu et al. (eds.), *The Proceedings of the Third International Conference on Communications, Signal Processing, and Systems*, Lecture Notes in Electrical Engineering 322, DOI 10.1007/978-3-319-08991-1

Z